

申 报	系列：教师系列
	教学科研并重型
	专业：材料学
	职称：教授

业绩成果材料

（申报人的业绩成果材料包括论文、科研项目、获奖以及其他成果等）

单 位（二级单位） 材料与能源学院

姓 名 林雅铃

材料核对人：

单位盖章：

核对时间：

华南农业大学制

目 录

一、教学研究业绩

1. 教学研究项目

- 1.1 在制药工程专业设立“创新学分”的探索研究（校级教改项目） 1
- 1.2 药物分析（校级质量工程） 3
- 1.3 课程育人与科研育人相结合——《药物分析》研究性教学探索（校级教改项目） 4
- 1.4 深度学习视域下《药物分析》课程线上线下混合式教学模式探索（广东省高等教育学会研究课题） 10

2. 教改论文

- 2.1 基于离子氢键的聚硅氧烷超分子弹性体的制备及其实验设计（C类） 11
- 2.2 聚丙烯酰胺季铵盐大分子药物的环境毒性评价及其实验设计（C类） 21

二、科研项目

1. 主持

- 1.1 两亲性大分子季铵盐的合成及其对水稻纹枯病菌的抑制作用与机理（国家自然科学基金项目，31772202）有关佐证材料 31
- 1.2 两亲性大分子季铵盐的合成及其在水稻纹枯病防治中的应用研究（广州市科技计划项目，201704020084）有关佐证材料 33
- 1.3 两亲性聚硅氧烷接枝季铵盐的合成及其在香蕉枯萎病防治中的应用（广东省科技计划项目，2016A020210105）有关佐证材料 37

1.4 甜菜碱型两性离子聚合物的合成及其在甜菜夜蛾无公害防治中的应用（教育部博士点新教师基金项目，20124404120025）有关佐证材料.....	40
1.5 含聚硅氧烷两亲性大分子季铵盐的合成及其在香蕉枯萎病防治中的应用（广州市科技计划项目，201803020015）有关佐证材料	43
1.6 基于微区分离与动态可逆键的人工心脏瓣膜用超分子弹性体（广东省自然科学基金，2023A1515011264）有关佐证材料	49
1.7 人工心脏瓣膜用抗凝抗钙化聚氨酯弹性体（其他纵向，20240010）有关佐证材料.....	54
1.8 聚合物材料的生物相容性评价（横向项目，h20220413）有关佐证材料	57
1.9 覆铜板基板树脂材料的开发研究（横向项目，h20240612）有关佐证材料	63
2. 主要参加	
2.1 基于抑制昆虫雌性生殖干细胞分化活性的骆驼蓬碱构效（教育部博士点博导项目，20134404110019）有关佐证材料	66

三、论文、著作等

1. 检索证明	67
2. 以第一作者发表本专业论文情况	
2.1. Synergistic enhancement of the robustness of multifunctional polyurethane via an ionic noncovalent cross-linking network and aromatic disulfides (<i>Chemical Engineering Journal</i> , 2024)	76
2.2 Surface-imprinted polysiloxane with recognition ability based on an	

ITO layer for rapid detection of <i>Fusarium oxysporum</i> f. sp. <i>cubense</i> by the naked eye (<i>ACS Applied Materials & Interfaces</i> , 2024)	90
2.3 Amphiphilic polysiloxane graft guanidine salts with a combination of low environmental toxicity and high antifungal activity (<i>European Polymer Journal</i> , 2024)	100
2.4 Fluorine-containing amphiphilic quaternary ammonium salts for the suppression of Banana fusarium wilt (<i>Reactive & Functional Polymers</i> , 2023)	109
2.5 Polymeric diallyl quaternary ammonium salts for inhibiting banana <i>Fusarium</i> wilt (<i>Reactive & Functional Polymers</i> , 2022)	119
2.6 Molecularly Imprinted Photonic Crystals Based on Fusaric Acid for the Detection of Banana <i>Fusarium</i> Wilt (<i>ACS Applied Polymer Materials</i> , 2021)	125
2.7 The interactions between bovine serum albumin and carboxybetaine-functionalized polysiloxanes in solution (<i>Colloid and Polymer Science</i> , 2016)	133
2.8 Synthesis and antimicrobial activities of polysiloxane-containing quaternary ammonium salts on bacteria and phytopathogenic fungi (<i>Reactive & Functional Polymers</i> , 2014)	142
2.9 多臂星形聚乙二醇-聚乳酸嵌段共聚物的降解特性 (<i>高分子材料科学与工程</i> , 2013)	151

3. 以通讯作者发表本专业论文情况

3.1 Polyacrylamide quaternary ammonium salts based on stable adsorption in soil and its application on the control of soil-borne fungal disease (<i>European Polymer Journal</i> , 2024)	158
3.2 Simultaneously enhancing the mechanical robust and conductivity of	

ionogel by in situ formation of coordination complexes as physical crosslinks (<i>Journal of Materials Chemistry A</i> , 2024)	165
3.3 Siloxane-based segmented poly(urethane-urea) elastomers with enhanced mechanical properties, hydrophobicity and anti-calcification based on hierarchical phase separation for potential applications of polymeric heart valve (<i>European Polymer Journal</i> , 2024)	177
3.4 The robustness waterproof ionogel based on the phase separation to form soft hard heterostructures and the interaction of cation- π realizes underwater adhesion and sensing (<i>Chemical Engineering Journal</i> , 2024)	189
3.5 Prediction and explanation of properties in multicomponent polyurethane elastomers: Integrating molecular dynamics and machine learning (<i>Macromolecules</i> , 2024)	202
3.6 Antifungal mechanisms of polymeric quaternary ammonium salts against conidia of <i>Fusarium oxysporum</i> f. sp. <i>cubense</i> , race 4 (<i>European Journal of Plant Pathology</i> , 2023)	216
3.7 A systematic study on Zn(II)-Iminocarboxyl complexation applied in supramolecular PDMS networks (<i>Polymer</i> , 2022)	231
3.8 Tough, self-Healing, recyclable bottlebrush polyurethane elastomer with a skin-like strain-adaptive-strengthening property (<i>ACS Applied Polymer Materials</i> , 2022)	239
3.9 Polydimethylsiloxane-polymethacrylate block copolymers containing quaternary ammonium salts against <i>Fusarium oxysporum</i> f. sp. <i>cubense</i> race 4 in soil: Antifungal activities and pot experiments (<i>Reactive and Functional Polymers</i> , 2021)	249
3.10 Stretchable, robust and reprocessable poly(siloxane-urethanes) elastomers based on exchangeable aromatic disulfides (<i>Polymer</i> , 2021)	

.....	259
3.11 A solvent-free, transparent, self-healing polysiloxanes elastomer based on unsaturated carboxyl-amino ionic hydrogen bonds (<i>Polymer</i> , 2021)	268
3.12 Interpenetrating covalent adaptable networks with enhanced mechanical properties and facile reprocessability and recyclability (<i>Polymer Chemistry</i> , 2021)	277
3.13 超声细胞粉碎法快速提取真菌中的麦角甾醇 (<i>南京农业大学学报</i> , 2021)	288
3.14 Reprocessability of dynamic polydioxaborolane networks activated by heat, moisture and mechanical force (<i>Polymer</i> , 2020)	298
3.15 Anti-Rhizoctonia solani activity by polymeric quaternary ammonium salt and its mechanism of action (<i>Reactive and Functional Polymers</i> , 2018)	307
3.16 Polymeric quaternary ammonium salt activity against Fusarium oxysporum f. sp. cubense race 4: Synthesis, structure-activity relationship and mode of action (<i>Reactive & Functional Polymers</i> , 2017)	317
3.17 Controllable synthesis and antimicrobial activities of acrylate polymers containing quaternary ammonium salts (<i>Reactive & Functional Polymers</i> , 2017)	327
3.18 The synthesis and protein resistance of amphiphilic PDMS-b-(PDMS-g-Cysteine) copolymers (<i>Applied Surface Science</i> , 2017)	336
3.19 Synthesis and antimicrobial activities of acrylamide polymers containing quaternary ammonium salts on bacteria and phytopathogenic fungi (<i>Reactive & Functional Polymers</i> , 2015)	342

3.20 The synthesis and characterization of supramolecular elastomers based on linear carboxyl-terminated polydimethylsiloxane oligomers (<i>Polymer Chemistry</i> , 2014)	350
--	-----

四、科研成果

1. 知识产权

1.1. 专利授权证书：大分子季铵盐在抑制水稻纹枯病菌菌核萌发中的用途（专利号：201610278530.1）	358
1.2. 专利授权证书：嵌段大分子季铵盐在抑制香蕉枯萎病菌生长中的用途（专利号：201610278195.5）	360
1.3. 专利授权证书：非渗透性的聚硅氧烷的无规共聚物及其制备方法和应用（专利号：202011328953.2）	362
1.4. 专利授权证书：具有两嵌段结构的含氟大分子季铵盐及其制备方法和应用（专利号：202210337163.3）	364

五、其他业绩

1. 指导学生学科竞赛

1.1. 指导学生参加学科竞赛（广东省第十届大学生材料创新大赛总决赛 三等奖，2020 年）	366
--	-----

2. 近五年本科评教有 3 个学期以上在本单位排名前 10%的证明材料	367
---	-----

华南农业大学2013年度教育教学改革与研究一般、自筹项目一览表

序号	项目名称	项目负责人	项目类别
1	单片机课程网络教学资源建设与考核方式改革	邓小玲	一般项目
2	《企业网组网实验》课程的优化研究	韩方珍	一般项目
3	国际班双语教学PBL教学模式研究与实践	张霞	一般项目
4	《包装印刷工艺实验》课程的整合设计与教学实践	范小平	一般项目
5	基于研究型实验的《化学生物学》实验教学的探索与实践	熊亚红	一般项目
6	园林专业《园林工程学》课程实践教学改革创新研究	汤辉	一般项目
7	《汽车构造》精品课程建设的研究与实践	武涛	一般项目
8	专业大类教学模式《概率论与数理统计》课程教学改革与实践	徐小红	一般项目
9	教师角色理论在《植物学》实验课程教学组织中的应用研究	白玫	一般项目
10	《植物制片与形态结构》课程内容体系改革和优化的研究与实践	梁社坚	一般项目
11	《大学物理》实验教学模式改革的研究	刘勇	一般项目
12	院级实验教学示范中心公共创新平台运行模式的探讨	黄九九	一般项目
13	高校移动网络教学模式的探索与研究	曾鸣	一般项目
14	基于Moodle的《大学计算机基础》课程在线学习平台的设计与应用研究	杨磊	一般项目
15	基于移动计算技术的高等教育信息化服务体系的研究与探索	梁茹冰	一般项目
16	《汽车试验学》课程改革与实践研究	吴伟斌	一般项目
17	《森林生态学》双语课程教学资源整合与实践	贾小容	一般项目
18	《生物质能源工程》课程教学改革与探索	王明峰	一般项目
19	《环境保护与可持续发展》课程教学改革与实践	赵本良	一般项目
20	《食品生物技术》“快捷式”教学过程探索与实践	陈忠正	一般项目
21	本科生推荐免试研究生后期质量跟踪调查与信息反馈——基于地方重点院校的实证研究	孟成民	一般项目
22	基于网络平台的高等农业院校参与公益性农技推广人员培训的模式研究	宋欢	一般项目
23	师生互动环节在《毛泽东思想和中国特色社会主义理论体系概论》课程中的方法设计与应用研究	崔慧霞	一般项目
24	我校大类招生人才培养模式下本科生专业分流机制优化研究	刘春桃	一般项目
25	工商管理本科应用型人才培养的问题与对策研究——以华南农业大学为例	郭萍	一般项目
26	阳光体育运动下的普通高校耐力跑课程的教学设计改革与实践	周华锋	一般项目
27	《创业管理》课程教学内容体系改革和整体优化研究与实践	杨学儒	一般项目
28	文化素质教育课程建设与教学改革——基于大学生心理素质教育课程建设与教学改革研究	宋迎秋	一般项目
29	基于文化创意产业特点的《基础写作》课程教学研究	王青	一般项目
30	社会化背景下学校社区工作的育人功能研究	李敏	一般项目
31	高校人才培养与企业需求有效对接的研究——以法学专业为例	郑大睿	一般项目
32	基于珠三角会展经济发展的《展示设计》课程教学改革研究	李女仙	一般项目
33	构建“华农文库”，推动华南农业大学学科建设	何建新	一般项目
34	汉语言文学专业百篇作文训练培养模式研究	韦盛年	一般项目
35	高校《思想道德修养与法律基础》课师生互动教学模式的效果评估指标体系研究	张机	一般项目
36	电子沙盘模拟在管理类专业课程实验教学中的应用研究	张程	一般项目
37	中外合作办学项目教学质量监控体系的构建与实践——基于华南农业大学的实证研究	魏旭娇	一般项目
38	基于WebQuest的大学英语研究性教学模式的建构与实践	仇如慧	一般项目
39	视觉化下的英语口语教学研究	魏清华	一般项目
40	基于校企联合培养模式的财会专业学生创业教育研究	刘卫民	一般项目
41	基于自建专门用途英语（ESP）教学语料库的词块研究——探索大学英语教师向ESP教师转型的途径	秦建华	一般项目
42	以校园文化讲坛为载体的大学生文化素质教育模式的创新与实践	汪路勇	一般项目
43	新人才培养方案指导下的法学专业课程整合与优化	李文丽	一般项目
44	高校思政课对话教学模式的建构与研究	蔡小婷	一般项目
45	创意思维训练模式在动画剧作教学中的实践	王柯	一般项目
46	以创新型人才培养为目标的艺术素质教育改革的研究与实践	石娟娟	一般项目
47	优化整合校内媒体资源建设广播电视编导专业教育实训基地	王敏	一般项目
48	基于企业合作的动画专业实践教学研究与实施	吴祝元	一般项目
49	开放·交叉·融合——普通高校体育课双语教学模式的研究与实践	单宇	一般项目
50	基于协同创新的高校校企合作人才培养模式研究	欧阳倩兰	一般项目
51	高校校园文化品牌培育模式的研究与实践	张春苑	一般项目
52	教学团队建设的研究与实践——以A系列课程《创业学》为例	陈建	一般项目
53	少学时条件下的课程教学改革研究——以《工程光学》课程教学为例	刘建斌	自筹项目
54	《食品工程原理课程设计》课程的教学改革	李雁	自筹项目
55	基于聚合算子决策的学科交叉课程设计培养方案	刘鹏飞	自筹项目
56	茶艺美学资源开发及《茶艺学》教学内容体系改革研究与实践	张凌云	自筹项目

67	适于高等农业院校的入侵生物学教学课程体系的构建与探索	陆永跃	自筹项目
68	高等教育大众化视域下大学生学习动力系统分析与构建研究	房三虎	自筹项目
69	基于DUS三性判定的农事训练模式的探索与实践	徐振江	自筹项目
70	《摄影测量学》课程实践教学模式创新和实践教学基地建设改革与实践	王长委	自筹项目
71	农林院校化学类专业开放性实验室的管理与改革实践	温青	自筹项目
72	在制药工程专业设立“创新学分”的探索研究	林雅铃	自筹项目
73	《植物检疫学》课程教学改革探索	胡琼波	自筹项目
74	《生物统计附试验设计》课程教学改革与实践	张哲	自筹项目
75	以问题求解能力为核心的渐进式程序设计实验教学改革研究与实践	林毅申	自筹项目
76	工科类工业设计专业产品设计表现技法课程实践教学改革	郭晓燕	自筹项目
77	高等农业院校统计学专业实践教学的研究和探讨	肖莉	自筹项目
78	动物科学学院《微生物学》课程教学团队的改革与建设	刘丽	自筹项目
79	工程训练模式下教学管理的创新与实践	任春涛	自筹项目
80	面向卓越工程师教育培养的电子科学与技术专业实践教学体系研究	罗霞	自筹项目
81	以培养应用能力为导向的《生物防治》课程教学改革与实践	许小霞	自筹项目
82	《食品工艺原理》课程教学改革的实践与探索	赵雷	自筹项目
83	基于学生综合能力培养的机械实验课程改革探索与实践	甄文斌	自筹项目
84	以实践教学改革为核心的道路与桥梁工程应用型人才培养模式研究	黄俐	自筹项目
85	《环境化学》课程教学内容与教学过程的优化建设	蒋成爱	自筹项目
86	《土壤农化分析》实验课实验方法的改进与探索	赵兰凤	自筹项目
87	精品课程《森林经理学》信息技术服务体系的构建与实践	王本洋	自筹项目
88	《生物化学实验》课程教学改革与实践	蒋珺	自筹项目
89	大学生课外学术创新能力培养模式的探索与实践	许益镌	自筹项目
90	学研结合的《动物营养与饲料学》实践教学改革探索与实践	叶慧	自筹项目
91	基于创新能力培养的实验教学改革与实践——以《动物遗传学》课程为例	刘满清	自筹项目
92	以兴趣培养为核心的《植物学》课程教学的改革	龚维	自筹项目
93	非英语专业大学生英语学习“动机缺失”研究	彭英	自筹项目
94	我校专门用途英语（ESP）课程建设研究	李飞武	自筹项目
95	基于高校学生社区的社会工作专业校本实践平台建设研究	周志荣	自筹项目
96	《制度经济学》课程设计创新与教学体系改革实践	何一鸣	自筹项目
97	大学英语分层教学模式下《跨文化交际》作为拓展课程的教学实践与探索	赵勇	自筹项目
98	综合性高校音乐学科改造与特色建设的研究与实践	胡远慧	自筹项目
99	历史学专业课程中教学方法的创新研究	殷小平	自筹项目
100	英语分层教学模式下学生需求、认知风格与自我效能的分析与应对策略研究	吕丽珊	自筹项目
101	《马克思主义基本原理概论》课教学设计研究	黄浩	自筹项目
102	高校校外实践模式、创业教育对大学生就业影响研究	李尚蒲	自筹项目

2019年、2020年校级课程立项汇总表

学院名称	课程类别	课程名称	课程负责人	立项时间
材料与能源学院	课程思政	基础化学实验AⅢ (物理化学实验)	丁唯嘉	2019
材料与能源学院	课程思政	无机化学	刘晓璿	2019
材料与能源学院	课程思政	无机功能材料	倪春林	2019
材料与能源学院	大国三农	农业新能源与新材料	简秀梅	2019
材料与能源学院	线下课程	无机及分析化学实验	倪春林	2020
材料与能源学院	线上线下混合式	有机化学 (公共课)	李春远	2020
材料与能源学院	线上线下混合式	家具设计	郭琼	2020
材料与能源学院	线上线下混合式	药物分析	林雅铃	2020
材料与能源学院	线上线下混合式	(药物)毒理学	王 颖	2020
材料与能源学院	线上线下混合式	基础化学实验Ⅱ	肖 勇	2020
创新创业学院	课程思政	大学生创新创业基础	顾美霞	2019
电子工程学院	课程思政	微电子技术基础 (双语)	刘洪山	2019
电子工程学院	全英课程	光纤通信	徐初东	2019
电子工程学院	线上线下混合式	人工智能技术智慧农业应用导论	韩宇星	2020
电子工程学院	线上线下混合式	光电图像处理技术	杨初平	2020
动物科学学院	大国三农	农科大学生创新创业基础与实践	何冬梅	2019
动物科学学院	全英课程	蚕业经济与管理	刘吉平	2019
动物科学学院	线下课程	动物生产学	孙宝丽	2020
动物科学学院	线下课程	家畜环境卫生学	吴银宝	2020
动物科学学院	线下课程	动物营养与饲料综合实验	曹庆云	2020
动物科学学院	线上线下混合式	家畜育种学	张 哲	2020
工程基础教学与训练中心	大国三农	农用无人机工程技能训练课程	卢玉华	2019
工程基础教学与训练中心	线上线下混合式	工程制图	文 晟	2020
工程基础教学与训练中心	线上线下混合式	工程力学B	陈海波	2020
工程学院	大国三农	精准农业航空技术与应用	兰玉彬	2019
工程学院	线上线下混合式	单片机原理及接口技术	魏德仙	2020
工程学院	线上线下混合式	自动控制原理	张铁民	2020
公共管理学院	课程思政	田野调查与社会实践	廖 杨	2019
公共管理学院	线下课程	社会工作导论	卓彩琴	2020
公共管理学院	线下课程	土地信息系统	王 枫	2020
公共管理学院	线下课程	公共政策学	武玉坤	2020
公共管理学院	线上线下混合式	田野调查与社会实践	廖 杨	2020

033

项目编号: JG19 1 06

华南农业大学教育教学研究和改革项目

申报书

项目名称 课程育人与科研育人相结合——

《药物分析》研究性教学探索

项目负责人 林雅铃

职 称 副教授

工作单位 材料与能源学院 (盖章)

移动电话 13380097023

电子邮箱 linyaling@scau.edu.cn

申报日期 2019-06-13

华南农业大学 教务处 制

211

2019 年 6 月

申请者的承诺与成果使用授权

本人自愿申报华南农业大学教育教学改革项目，承诺对所填写的《申报书》所涉及各项内容的真实性负责，保证没有知识产权争议。课题申请如获准立项，在研究工作中，接受华南农业大学教务处及本人所在单位的管理，并对以下约定信守承诺：

1.遵守相关法律法规。遵守我国著作权法和专利法等相关法律法规；遵守我国政府签署加入的相关国际知识产权规定。

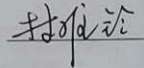
2.遵循学术研究的基本规范，恪守学术道德，维护学术尊严。研究过程真实，不得以任何方式抄袭、剽窃或侵吞他人学术成果，杜绝伪注、伪造、篡改文献和数据等学术不端行为；成果真实，不重复发表研究成果；维护社会公共利益，不以项目名义牟取不当利益。

3.遵守华南农业大学教育教学改革项目有关管理规定以及华南农业大学财务规章制度。

4.凡因项目内容、成果或研究过程引起的法律、学术、产权或经费使用问题引起的纠纷，责任由相应的项目研究人员承担。

5.项目获批后务必按项目计划要求及时开展研究工作，确保研究工作如期完成。

6.同意华南农业大学或其授权（委托）单位有权基于公益需要公布、使用、宣传《项目申请·评审书》内容及相关成果。

项目负责人（签章）： 

2019 年 6 月 19 日

六、单位、评审小组及学校意见

所在单位意见:

同意推荐.

(公章)

单位负责人签字:

2019年 6月 24日

张俊双

评审小组意见:

同意立项

评审小组长签字:

2019年 月 日

张平亮

学校主管部门意见:

同意立项

签章:

2019年 月 日

附件： 2021年度校级质量工程暨教改项目验收结果

序号	项目类别	项目名称	负责人	所在单位	验收结果	备注
1	一流专业	生态学	章家恩	资源环境学院	验收通过	已入选国家一流专业建设点
2	一流专业	食品质量与安全	孙远明	食品学院	验收通过	已入选国家一流专业建设点
3	一流专业	植物保护	徐汉虹	农学院	验收通过	已入选国家一流专业建设点
4	大学生校外实践教育基地	华南农业大学广东海印股份有限公司实践教学基地	刘辉	公共管理学院	验收通过	
5	大学生校外实践教育基地	华南农业大学上达电子（深圳）股份有限公司实践教学基地	杨卓鸿	材料与能源学院	验收通过	
6	大学生校外实践教育基地	华南农业大学广州博物馆实践教学基地	赵飞	人文与法学学院	暂缓通过	延迟结题
7	大学生校外实践教育基地	华南农业大学索菲亚家居股份有限公司实践教育基地	孙瑾	材料与能源学院	验收通过	
8	大学生校外实践教育基地	华南农业大学通联支付广东分公司实践教学基地	左伟	经济管理学院	验收通过	
9	大学生实践教学基地	华南农业大学广东粤建设计研究院有限公司校外实践教育基地	闫恩诚	水利与土木工程学院	验收通过	
10	实验教学示范中心	工程通识训练实验教学示范中心	陶冶	基础实验与实践训练中心	验收通过	
11	实验教学示范中心	生物质材料与能源实验教学示范中心	胡传双	材料与能源学院	验收通过	
12	实验教学示范中心	工业设计实验教学示范中心	高锐涛	工程学院	验收通过	
13	实验教学示范中心	基于云平台的计算机实验教学示范中心	田绪红	数学与信息学院、软件学院	验收通过	
14	战略新兴产业特色专业	信息与计算科学	蔡贤资	数学与信息学院、软件学院	验收通过	
15	战略新兴产业特色专业	环境设计	郑欣	艺术学院	验收通过	
16	教学团队	制药工程系列实践课程教学团队	倪春林	材料与能源学院	验收通过	
17	教学团队	面向非遗文创的设计学跨专业课程群教学团队	曾智林	艺术学院	验收通过	
18	教学团队	百篇作文教学团队	王瑛	人文与法学学院	验收通过	
19	教学团队	经济管理专业《统计学原理》教学团队	谭莹	经济管理学院	验收通过	
20	教学团队	岭南城乡特色营造实践教学团队	卢丹梅	林学与风景园林学院	验收通过	
21	教学团队	压花艺术教学团队	陈国菊	园艺学院	验收通过	
22	教学团队	国际经济与贸易教学团队	熊启泉	经济管理学院	验收通过	
23	教学团队	刑事法实践教学团队	杜国明	人文与法学学院	验收通过	
24	教学团队	音乐表演专业教学团队	郑颜文	艺术学院	验收通过	
25	在线开放课程	传统园林技艺	高伟	林学与风景园林学院	验收通过	
26	在线开放课程	最优化方法	张昕	数学与信息学院、软件学院	验收通过	

序号	项目类别	项目名称	负责人	所在单位	验收结果	备注
27	在线开放课程	电视摄像	李俊良	艺术学院	验收通过	
28	在线开放课程	发展社会学	程启军	公共管理学院	验收通过	
29	在线开放课程	微生物学	马金成	生命科学学院	暂缓通过	延迟结题
30	在线开放课程	电机学	孙振刚	工程学院	验收通过	
31	在线开放课程	水力学	韦未	水利与土木工程学院	验收通过	
32	在线开放课程	结构力学	唐贵和	水利与土木工程学院	验收通过	
33	在线开放课程	机械制造基础	刘天湖	工程学院	验收通过	
34	在线开放课程	形势与政策	项赠	马克思主义学院	验收通过	
35	专业认证	木材科学与工程	胡传双	材料与能源学院	验收通过	已通过SWST认证
36	专业认证	网络工程	周敏	数学与信息学院、软件学院	验收通过	已通过IEET认证
37	专业认证	土木工程	刘爱华	水利与土木工程学院	验收通过	已通过IEET认证
38	专业认证	建筑学	吴运江	水利与土木工程学院	验收通过	
39	产业学院	华南农业大学华顺农林产业学院	曹藩荣	园艺学院	验收通过	
40	精品视频公开课(选题)	生活中的数据分析	杨德贵	数学与信息学院、软件学院	验收通过	
41	精品资源共享课	广告管理	张蓓	经济管理学院	验收通过	
42	精品资源共享课	林业经济学	李怡	经济管理学院	验收通过	
43	精品资源共享课	兽医外科手术学(双语)	李守军	兽医学院	验收通过	
44	精品资源共享课	水污染控制工程	崔理华	资源环境学院	验收通过	
45	线上线下结合精品课程	动物学	李海云	动物科学学院	验收通过	
46	线上线下结合精品课程	人类学与现代生活(基于微信平台的精品视频公开课改造)	廖杨	公共管理学院	验收通过	
47	特色专业	社会学	廖杨	公共管理学院	验收通过	
48	教学研究与改革项目	基于云课堂的混合式教学在《药剂学实验》中的应用研究与实践	胡洋	材料与能源学院	验收通过	
49	教学研究与改革项目	国际认证背景下新工科专业的品牌化建设与实践——以家具专业为例	易欣	材料与能源学院	验收通过	
50	教学研究与改革项目	《物理化学》教学中落实“课程思政”理念的改革与探索	秦为为	材料与能源学院	验收通过	
51	教学研究与改革项目	基于校企联合培养基地的实践教学改革创新	孙理超	材料与能源学院	验收通过	
52	教学研究与改革项目	新媒体平台在《有机化学》课程教学改革中的应用	李兆栋	材料与能源学院	验收通过	
53	教学研究与改革项目	《无机化学》课程思政的建设与实践	刘晓璠	材料与能源学院	验收通过	

序号	项目类别	项目名称	负责人	所在单位	验收结果	备注
54	教学研究与改革项目	基于雨课堂及精品网课资源的农业院校公共有机化学混合式教学改革	丁唯嘉	材料与能源学院	验收通过	
55	教学研究与改革项目	基于国际标准培养木材科学与工程新工科专业特色人才的研究与实践	古今	材料与能源学院	验收通过	
56	教学研究与改革项目	新工科背景下化工原理虚拟仿真实验教学改革与实践	袁腾	材料与能源学院	验收通过	
57	教学研究与改革项目	课程育人与科研育人相结合——《药物分析》研究性教学探索	林雅铃	材料与能源学院	验收通过	
58	教学研究与改革项目	基于“互联网+”技术在基础化学实验教学的改革与实践	肖勇	材料与能源学院	验收通过	
59	教学研究与改革项目	基于速课微课堂教学平台的物理化学教学难点突破研究	陈明洁	材料与能源学院	验收通过	
60	教学研究与改革项目	校企合作背景下材料化学专业人才培养模式探讨	张超群	材料与能源学院	验收通过	
61	教学研究与改革项目	多媒体网络技术在基础化学实验教学中的应用探索	唐小兰	材料与能源学院	验收通过	
62	教学研究与改革项目	结合从业上岗证培训的“实验动物学”课程的改革与实践	余文兰	测试中心（实验动物中心）	验收通过	
63	教学研究与改革项目	基于能力结构的卓越农林教师教学发展模式研究	朱蕾	党委教师工作部、人力资源处	验收通过	
64	教学研究与改革项目	高校创新创业教育的慕课体系建设研究	曾璇	党委学生工作部（党委研究生工作部）	验收通过	
65	教学研究与改革项目	《舞蹈鉴赏》课程中“艺术+思政”的改革探索与实践研究	殷舒	党委学生工作部（党委研究生工作部）	验收通过	
66	教学研究与改革项目	艺术类专业人才培养的创新创业教育改革研究	陈志远	党委学生工作部（党委研究生工作部）	验收通过	
67	教学研究与改革项目	基于人工智能背景下的教学教务管理信息化探索与研究	王宣琳	党政办公室（研究室）	暂缓通过	延迟结题
68	教学研究与改革项目	知识传授、文化传承、价值引领三位一体的课程思政教学改革与创新——以大学物理基础课程为例	徐初东	电子工程学院（人工智能学院）	验收通过	
69	教学研究与改革项目	《数字电子技术》课程思政建设研究	赵文锋	电子工程学院（人工智能学院）	验收通过	
70	教学研究与改革项目	可编程器件原理与应用实验在线课程建设与应用	徐海涛	电子工程学院（人工智能学院）	验收通过	
71	教学研究与改革项目	《物联网技术导论》课程校企协同育人机制创新实践研究	贾维卿	电子工程学院（人工智能学院）	验收通过	
72	教学研究与改革项目	结合企业实训的实践教学体系的创新与研究	徐梅宣	电子工程学院（人工智能学院）	验收通过	
73	教学研究与改革项目	新工科背景下通信工程专业多方协同育人模式改革与实践	俞龙	电子工程学院（人工智能学院）	验收通过	
74	教学研究与改革项目	《养羊学》课程内容优化及微课、翻转课堂在教学实践中的应用研究	柳广斌	动物科学学院	验收通过	
75	教学研究与改革项目	基于蚕病学课程的全英教学和管理模式研究	孙京臣	动物科学学院	验收通过	
76	教学研究与改革项目	在生物化学课程中构建低年级大学生研究性学习引导机制研究	孙加节	动物科学学院	验收通过	
77	教学研究与改革项目	学分制模式下动物科学专业人才培养方案的修订	吴银宝	动物科学学院	验收通过	
78	教学研究与改革项目	新时代背景下产业学院本科生实践能力提升机制研究——以华南农大一温氏集团产业学院为例	何小敏	动物科学学院	验收通过	
79	教学研究与改革项目	通过丝绸文化课程提升大学生对中华文化自信	陈芳艳	动物科学学院	验收通过	



广东省高等教育学会
2022年度高等教育研究课题
(一般课题)

结题证书

课题编号: 22GYB060
课题名称: 深度学习视域下《药物分析》课程线上线下
混合式教学模式探索
课题承担单位: 华南农业大学
课题主持人: 林雅铃
课题组成员: 聂燕芳、宋高鹏、霍理坚、高永峰
获得等级: 合格

该课题经审核准予结项, 特发此证。

广东省高等教育学会

2024年11月25日



中国高等教育学会实验室管理工作分会会刊
中文核心期刊
RCCSE中国权威学术期刊

ISSN 1002-4956
CN 11-2034/T
CODEN SJYGAR

实验技术与管理

Shiyan Jishu yu Guanli

Experimental Technology and Management

10
2022

第39卷 第10期
Vol. 39 No. 10

月刊

中西亚地区野外科学观测台站建设实践

现代极地科考破冰船实验室管理

改良标记点线栓法建立大鼠脑缺血再灌注模型

六自由度液体旋转晃动实验平台设计

往复式杆套类柱面摩擦副的摩擦磨损模拟试验机研制

悬索桥模型结构设计及其动力学分析

2021年重庆市实验室生物安全管理现状调查分析

我国医药卫生相关科技创新基地建设简析

ISSN 1002-4956



9 771002 495224

10

中华人民共和国教育部主管

清华大学主办

主管：中华人民共和国教育部
主办：清华大学

主编：吕志刚

副主编：彭远红

编辑部主任：彭远红(兼)

编辑：张文杰 彭远红 张利芳

孙浩 杨荫蔚

编务：杨荫蔚 陈昕

发行：段然 吴岩

封面题字：刘仙洲院士、清华大学原第一副校长，
1963年题

编辑：《实验技术与管理》编辑部

地址：北京市海淀区清华大学科技服务楼

邮编：100084

在线投稿：http://syjl.cbpt.cnki.net

编辑部电话：010-62783005

邮箱：sjg@tsinghua.edu.cn

广告电话：010-62788738

订刊发行电话：010-62792635

邮箱：syjsygl@tsinghua.edu.cn

出版与发行：清华大学出版社有限公司

地址：北京市海淀区双清路学研大厦A座6层

邮编：100084

印刷：北京卓诚恒信彩色印刷有限公司

发行范围：国内外公开发行

国际标准连续出版物号：ISSN 1002-4956

国内统一连续出版物号：CN 11-2034/T

国际期刊编码：CODEN SJYGAR

广告发布登记：京海市监广登字20200045号

出版日期：10月20日

定价：26.00元/期 全年12期 312.00元

收录本刊内容的国内外数据库与媒体：

- 中国学术期刊(光盘版)
- 中国核心期刊(遴选)数据库
- 万方数据资源系统数字化期刊群
- 中国期刊网
- 中国学术期刊综合评价数据库
- 中国期刊全文数据库
- 中文科技期刊数据库
- 中文电子期刊服务
- 中国学术期刊文摘(中文版)
- 中国科技论文在线
- 美国《剑桥科学文摘》(CSA)
- 美国《化学文摘(网络版)》(CA)
- 美国《乌利希期刊指南(网络版)》(Ulrichsweb)
- 英国《世界陶瓷文摘(网络版)》(WCA)
- 日本《日本科学技术振兴机构数据库(中国)》(JST China)
- 美国《艾博思科数据库》(EBSCOhost)

目次

第39卷 第10期(总第314期) 2022年10月

特约专栏——高水平实验室建设

- 中亚地区野外科学观测台建设实践.....洪永欣, 张新, 郝丽静, 等 1
现代极地科考破冰船实验室管理.....陈清满, 廖周鑫, 沈悦 6

实验技术与方法

- 页岩气开发水基钻屑的生物急性毒性测试研究
.....朱天莉, 宋娇, 黄涛, 等 12
基于脑电实验的高铁调度员工作负荷识别方法
.....张光远, 邓一平, 王亚伟 18
基于COMSOL的光学压力传感器的仿真与实验
.....杨福铃, 梁帅, 李艳 24
不同卸围压速率下灰岩卸荷力学特性试验研究.....周传涛 30

基于离子氢键的聚硅氧烷超分子弹性体的制备及其实验设计

-林雅铃, 霍理坚, 莫家亨, 等 36

改良标记点线栓法建立大鼠脑缺血再灌注模型

-王梦洁, 李炜健, 宋心怡, 等 42

茶多酚功能化的还原氧化石墨烯的制备和生物性能

-郝丽英, 罗萌, 康茂萍 49

水压致裂煤体分区渗流试验装置及教学实验方法设计

-张村, 宋子玉, 刘晨熙, 等 54

基于注意力残差网络的甲状腺结节分类研究.....杨行, 惠雨, 李菁菁, 等 59

- 山梨酰胺对胁迫下小麦种子萌发的影响.....陈蔚燕, 李建忠 65

虚拟仿真技术

- 螺纹连接松动机理有限元仿真分析.....何佳龙, 郭继超, 李雨露, 等 69

- 基于忆阻器的多模式识别CNN电路设计.....陈鑫辉, 王宇轩, 张跃军, 等 75

- 一种改进型RetinaFace的遮挡人脸检测算法.....党宏社, 狄国栋, 张逸德 80

基于ANSYS的海上风机雷电电磁暂态虚拟仿真实验

-张萍, 杨晓磊, 李永健, 等 86

融合随机游走MFPT特征的链接预测仿真与实证分析

-伍杰华, 高学勤, 王涛, 等 91

基于数字孪生技术的智能医学影像实验室构建及应用

-陈珊珊, 汪红志, 夏天, 等 101

仪器设备研制

- 六自由度液体旋转晃动实验平台设计.....王志亮, 周炳红, 孙志斌 108

往复杆套类柱面摩擦副的摩擦磨损模拟试验机研制

-高雷雷, 姜浩, 李肖, 等 115

实验教学研究与管理

- 组合夹具设计“虚实结合”实验平台开发.....尚振国, 蔡卫国, 安相华, 等 122

热蒸汽改性FeS₂制备及光催化降解罗丹明B综合实验

-王海涛, 邹菁, 江吉周 130

期刊基本参数: CN11-2034/T * 1963 * m * A4 * 248 * zh * P * ¥26.00 * 6500 * 44 * 2022-10

基于离子氢键的聚硅氧烷超分子弹性体的制备及其实验设计

林雅铃¹, 霍理坚¹, 莫家亨², 赵 颖², 张安强²

(1. 华南农业大学 材料与能源学院, 广东 广州 510642;

2. 华南理工大学 材料科学与工程学院, 广东 广州 510641)

摘 要: 基于非共价键构建超分子弹性体是近年来超分子领域研究的热点之一, 其中离子氢键因其结构简单且性能可控而受到重视。通过将该领域最新科研成果引入实验教学, 设计、制备了两类结构相似但性能迥异的超分子弹性体, 通过 FT-IR、¹H-NMR、GPC、流变行为、力学性能及自愈合效率等表征手段, 建立了超分子弹性体的结构与性能关系。该实验内容涵盖了聚合物合成与改性、制备方案设计和实施、聚合物结构表征等诸多环节, 具有一定的综合性与探索性, 有利于提高学生的综合素质, 以及科研与创新能力。

关键词: 超分子弹性体; 离子键-氢键; 流变特性

中图分类号: TQ33 文献标识码: A 文章编号: 1002-4956(2022)10-0036-06

Experimental design and preparation of polysiloxane supramolecular elastomer based on ionic hydrogen bond

LIN Yaling¹, HUO Lijian¹, MO Jiaheng², ZHAO Ying², ZHANG Anqiang²

(1. College of Material and Energy, South China Agricultural University, Guangzhou 510642, China; 2. School of Materials Science and Engineering, South China University of Technology, Guangzhou 510641, China)

Abstract: Supramolecular elastomers based on non-covalent bonds is one of the hotspots recently in the field of supramolecular, in which the ionic hydrogen bond associations have attract much attention for their simple structure and controllable properties. By introducing the latest scientific research achievements in this field into experimental teaching, two serials supramolecular elastomers with similar structures but different properties are designed and prepared, and relationship between structure and properties is established based on FT-IR, ¹H-NMR, GPC, rheological behavior, mechanical properties and self-healing efficiency. The experimental content covers many subjects such as polymer synthesis and modification, preparation scheme design and implementation, polymer structure characterization and so on, it is comprehensive and exploratory to a certain extent, and is conducive to improve students' comprehensive quality, scientific research and innovation ability.

Key words: supramolecular elastomer; ionic hydrogen bond; rheological behaviors

将材料领域的最新科研成果引入本科探索性实验教学, 是科研与教学结合的重要方式之一, 在此过程

中应注意科研成果的前沿性与学生认知水平及实验教学条件的匹配^[1]。基于可逆键(如: 氢键^[2]、配位键^[3-4]、

收稿日期: 2022-05-06

基金项目: 国家自然科学基金项目(51473051、31772202、52073098); 广东省教育厅质量工程项目(GD2019-185); 华南农业大学教育教学改革与研究重点项目(JG19106); 华南理工大学教学研究项目(2021-C9213066); 华南理工大学探索性实验项目(2021-C9212110)

作者简介: 林雅铃(1978—), 女, 福建罗源, 博士, 副教授, 主要研究领域为大分子药物与超分子弹性体, linyaling@scau.edu.cn。

通信作者: 张安强(1976—), 男, 湖南安仁, 博士, 教授, 主要研究方向为功能高分子材料, aqzhang@scut.edu.cn。

引文格式: 林雅铃, 霍理坚, 莫家亨, 等. 基于离子氢键的聚硅氧烷超分子弹性体的制备及其实验设计[J]. 实验技术与管理, 2022, 39(10): 36-41.

Cite this article: LIN Y L, HUO L J, MO J H, et al. Experimental design and preparation of polysiloxane supramolecular elastomer based on ionic hydrogen bond[J]. Experimental Technology and Management, 2022, 39(10): 36-41. (in Chinese)

离子键^[5-6]或可逆共价键^[7-8]等)构建超分子弹性体(supramolecular elastomers),是弹性体领域的热点和重要方向之一^[9]。以可穿戴的柔性传感为例,要求柔性基材可多次动态弯折、易于贴合皮肤、无不适感、生物相容性好以及与传感器黏合好等^[10],而这些恰好是超分子弹性体区别与传统共价交联弹性体的优势^[11-13]。

基于此要求,本文提出了以主链柔顺且生物相容性好的聚二甲基硅氧烷(PDMS)为基材,在其侧基上引入廉价且无毒的羧酸和伯胺,合成得到氨基接枝聚硅氧烷(APS)和羧基接枝聚硅氧烷(包括:不饱和羧基接枝聚硅氧烷(UCS)与饱和羧基接枝聚硅氧烷(SCS)),通过调控有机酸和有机碱的相互作用强度,使二者之间在产生氢键的同时发生质子转移,形成具有较强相互作用的离子氢键(ionic hydrogen bonds, IHBs),继而通过调节二者的混合比例,制备得到基于离子氢键交联且具有不同黏弹特性的聚硅氧烷超分子弹性体^[12]。该方案解决了传统共价交联的聚硅氧烷弹性体无自黏性、模量较高且不易调节、不能自愈等问题,可为柔性可穿戴传感器提供良好的弹性体基材^[13]。

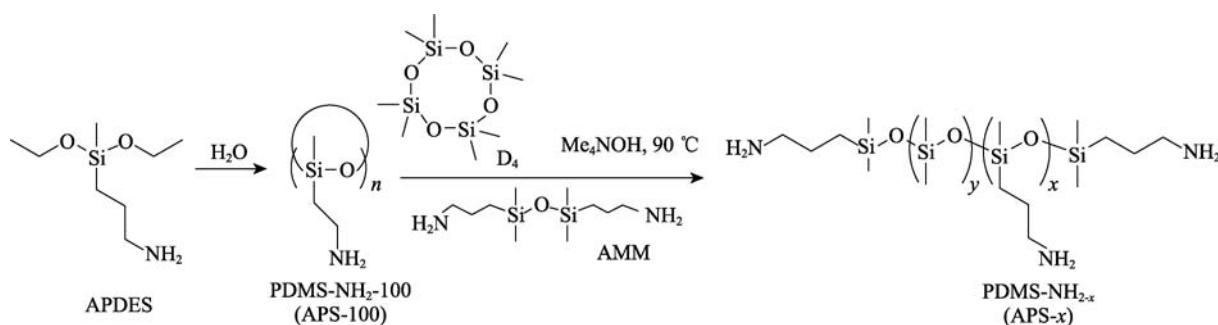


图1 氨基接枝聚硅氧烷(APS-x)的合成路线

在单口瓶中加入 APDES、过量的去离子水,升温至 50 °C,磁力搅拌 4 h 后在 120 °C、1 mbar 下减压蒸馏 2 h 除去副产物乙醇和多余的水,得到无色透明黏稠状液体 APS-100,产率约为 95%。

APS-x 的分子量和接枝密度由 APS-100、D₄ 和封头剂 AMM 三者投料配比给出,其中 AMM 在控制分子量的同时带有氨基,在合成分子量不大的 APS 时还应该考虑其对氨基接枝密度的影响,从而更精准控制氨基接枝密度。APS 的分子量和接枝密度与 APS-100、D₄ 和封头剂 AMM 三者投料质量比由式(1)给出:

$$\begin{cases} m_{\text{APS-100}} = 117 \frac{Ma - 148 - 100a}{43a + 74} \\ m_{\text{D}_4} = M - 248 - m_{\text{APS-100}} \\ m_{\text{AMM}} = 248 \end{cases} \quad (1)$$

式中, $m_{\text{APS-100}}$ 、 m_{D_4} 和 m_{AMM} 分别表示 APS-100、D₄ 和 AMM 的投料量(g); M 为所合成的 APS-x 的设

1 实验部分

1.1 实验试剂

八甲基环四硅氧烷(D₄, 99%),美国道康宁公司;3-氨丙基甲基二乙氧基硅烷(APDES, 96%),山东曲阜化工有限公司;1,3-双(3-氨基丙基)-1,1,3,3-四甲基二硅氧烷(AMM, 99%),四甲基氢氧化铵·五水合物(Me₄NOH·5H₂O, 97%),马来酸酐(MAH, 99%),琥珀酸酐(SAH, 99%),3-氨丙基三甲氧基硅烷(APTMS, 99%),均为上海麦克林生化科技有限公司产品;其余试剂均为常规分析纯,广州化学试剂厂。

1.2 样品制备

1.2.1 氨基接枝聚硅氧烷(APS)的合成

氨基接枝聚硅氧烷是双端和侧基都接枝有氨基丙基的聚二甲基硅氧烷。其合成分为两步:先合成全侧氨基丙基聚硅氧烷(APS-100, 100 表示 100%的硅氧烷单元上都接枝氨基),继而与八甲基环四硅氧烷(D₄)和封头剂 AMM 调聚,得到一定氨基接枝密度以及分子量的氨基接枝聚硅氧烷(APS-x, x 表示 $x\%$ 的硅氧烷单元上接枝有氨基),其合成路线如图1所示。

计数均分子量; a 为氨基的比例($a = x/(x+y)$, $0 < a < 1$)。

根据以上公式,以接枝率为 10%,分子量为 10 kDa 的氨基接枝聚硅氧烷(记为 APS-10-10 kDa)为例,说明其合成过程:将 APS-100 (31 g)、封头剂 AMM (6.2 g) 和催化剂 Me₄NOH·5H₂O (1.2 g, 占单体总质量约 0.5%) 加入 500 mL 三口烧瓶,通入氮气,升温至 90 °C,敞口机械搅拌 1 h 除去体系中微量的水分。接着加入 D₄ (213 g),装上冷凝管继续反应 10 h。升温至 160 °C 并保持 1.5 h 分解催化剂,得到无色透明粗产物。将得到的粗产物在 160 °C、1 mbar 条件下减压蒸馏 2 h 除去低沸点杂质,得到均一无色透明液体 APS-10-10 kDa,产率为 95%。

1.2.2 羧基硅油(UCS 和 SCS)的合成

不饱和羧基接枝聚硅氧烷(UCS)和饱和羧基接枝聚硅氧烷(SCS)由 APS-x 在无溶剂条件下分别与马来酸酐(MAH)和琥珀酸酐(SAH)反应得到,其合成路线如图2所示。

以接枝率为 10% 的羧基硅油的合成为例, 在烧杯中加入一定量的 APS-10-10 kDa, 升温至 80 °C, 开动机械搅拌, 缓慢加入氨基的 1.05 eq 的 MAH 或 SAH,

继续搅拌 10 min, 得到淡黄色黏稠液体 UCS-10 或 SCS-10。

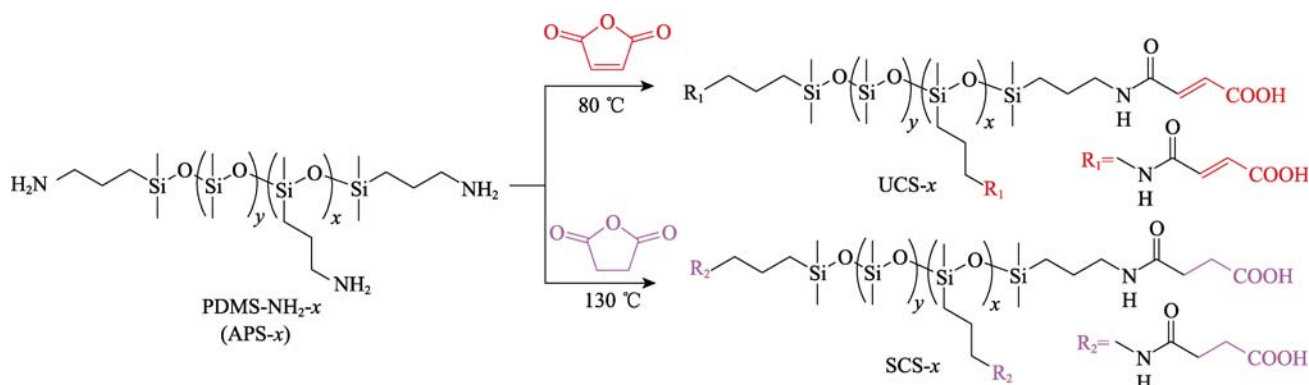


图 2 不饱和羧基接枝聚硅氧烷 (UCS) 与饱和羧基接枝聚硅氧烷 (SCS) 的合成路线

1.2.3 聚硅氧烷超分子弹性体的制备

在 APS 和对应的 UCS 控制羧基和氨基的比值为 1 : 1 的条件下, 在室温无溶剂条件下直接混合, 机械搅拌 5~10 min 至均一透明黏稠液体, 倒入聚四氟乙烯模具中, 抽真空排除气泡后放入 60 °C 真空烘箱 48 h, 得到无色透明弹性薄膜, 其代号为 APS-UCS-x, 例如: APS-UCS-10 表示 UCS-10 和 APS-10 按 $n(-\text{COOH}) : n(-\text{NH}_2) = 1 : 1$ 混合而得到的产物。

如果将 APS 和对应的 SCS 控制羧基和氨基的比值为 1 : 1 的条件下, 在室温无溶剂条件下直接混合, 所得产物标记为 APS-SCS-x。

1.2.4 羧基与伯胺基之间离子氢键作用结合力常数的测定

为了更准确表征超分子弹性体内不同结构的羧基与伯胺基之间的离子氢键作用, 参照文献[12]的方法合成得到 3-氨丙基三甲氧基硅烷 (APTMS) 与 MAH 或 SAH 的酰胺化产物 (APTMS-MA 和 APTMS-SA, 其结构分别如图 7 所示)。采用核磁滴定的方法测定和计算羧基与伯胺基之间的离子氢键作用强度, 简述如下: 将 APTMS、APTMS-MA 及 APTMS-SA 分别溶于氘代 DMSO 中, 将 APTMS 浓度固定为 0.12 mol/L, 向 APTMS 溶液中分别加入不同量的 APTMS-MA (或 APTMS-SA), 使核磁管中的 APTMS/APTMS-MA (或 APTMS/APTMS-SA) 浓度比为 0.12 mol/L : 0.02 mol/L 至 0.12 mol/L : 0.12 mol/L 之间的多个浓度, 并测定相应的核磁氢谱, 以 APTMS 中紧邻 $-\text{NH}_2$ 的亚甲基的核磁位移为观察对象, 按照文献[14]所述方法计算 APTMS 与 APTMS-MA (或 APTMS-SA) 之间的结合力常数 K_1 (或 K_2), 以此分别作为 APS 与 UCS (或 SCS) 之间的羧基与伯胺基之间的离子氢键作用强度。

1.3 测试与表征

用傅立叶变换红外光谱仪 (美国赛默飞 Nicolet iS5) 测定样品的红外光谱; 用核磁共振仪 (德国布鲁克 Avance III-600) 测定样品的核磁氢谱 (以氘代氯仿或氘代 DMSO 为溶剂, 室温下测试); 用凝胶渗透色谱仪 (美国 Waters515-2414) 测定样品的分子量和分子量分布 (以单分散 PS 为标样, 氯仿作为流动相, 流速为 1 mL/min, 柱温 40 °C, 其中, APS 样品中含有反应性的伯胺基, 在进行 GPC 测试前需用间甲苯异氰酸酯进行封端处理); 用平板流变仪 (奥地利安东帕 MCR102) 测试弹性体的流变行为; 用恒温恒湿拉力试验机 (东莞科建 KJ-2091) 测试弹性体样品的拉伸应力应变特性。

将 50 mm×10 mm×1 mm 样条用锋利的刀片从中间划开, 小心拼接, 在不受外力作用下水平放置, 待其进行自愈合, 愈合效率定义为

$$\text{愈合效率} = \frac{TS_{\text{healed}}}{TS_{\text{virgin}}} \times 100\% \quad (2)$$

式中, TS_{virgin} 和 TS_{healed} 表示样品愈合前后的拉伸强度。

2 结果与分析

2.1 APS-x、UCS-x 和 SCS-x 的结构表征

为便于说明, 下文以接枝率为 10% 的不同阶段产物为例进行说明, 图 3(a) 为接枝率为 10% 的 APS-10、UCS-10 和 SCS-10 的红外图谱对比。可以看到在所有的样品中, 有 2966 cm^{-1} 和 2906 cm^{-1} 处的甲基上的 C—H 伸缩振动吸收峰、1262 cm^{-1} 处的变形振动吸收峰以及 1096 cm^{-1} 和 1026 cm^{-1} 伸缩振动双驼峰, 这些特征吸收峰表明这 3 种产物具有相同的聚硅氧烷主链。1614 cm^{-1} 为 APS 接枝伯胺上 N—H 弯曲振动吸收峰, 3300~3200 cm^{-1} 范围内为 UCS 和 SCS 接枝羧基上 O—H 振动吸收峰, 1714 cm^{-1} 和 1725 cm^{-1} 分别是 UCS-10

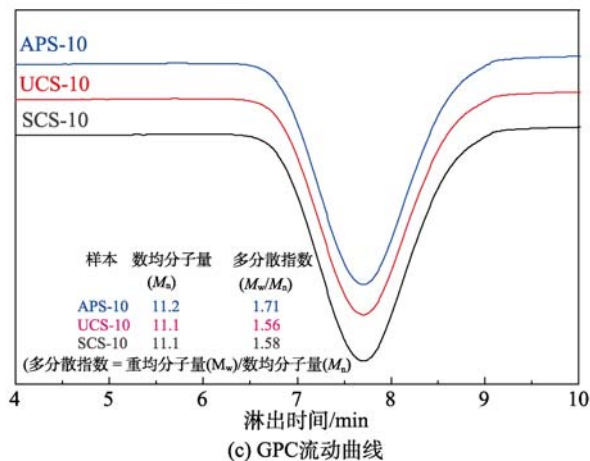
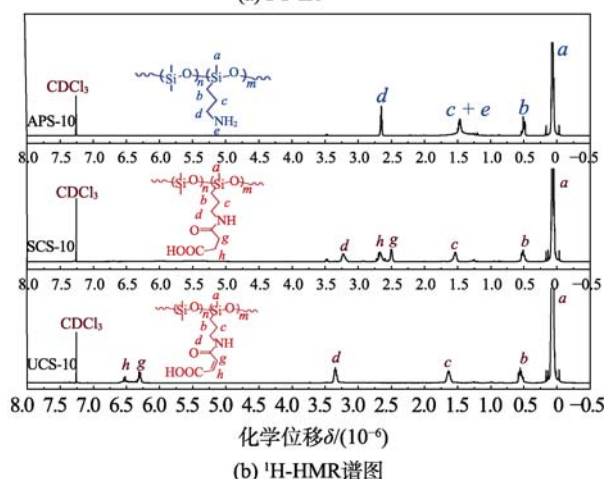
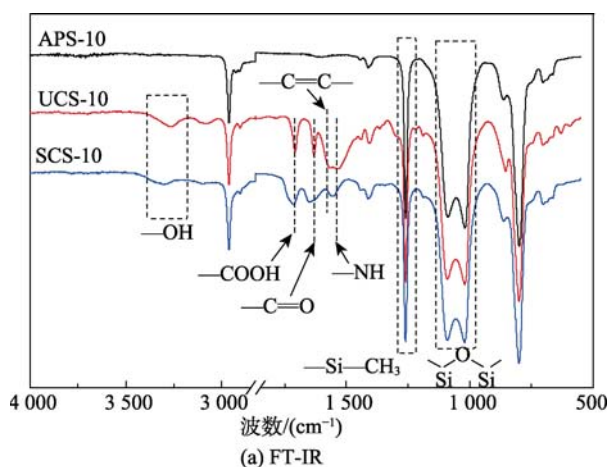


图3 APS-10、UCS-10和SCS-10的FT-IR、¹H-NMR谱图和GPC流动曲线

和SCS-10接枝羧基上C=O的伸缩振动吸收峰, 1640 cm⁻¹和1652 cm⁻¹分别是UCS和SCS接枝酰胺基上C=O的伸缩振动吸收峰, 1445 cm⁻¹是酰胺基上N—H的弯曲振动吸收峰, 这些特征吸收峰表明羧基成功接枝到聚硅氧烷主链上。此外, 在1800~1750 cm⁻¹处没有酸酐的特征吸收峰, 表明体系中酸酐已反应完全。

图3(b)是APS-10、UCS-10和SCS-10的¹H-NMR谱图。其中, δ 0.46~0.55、 δ 1.40~1.50和 δ 2.63~2.68分

别对应APS-10中氨基丙基上离硅原子由近到远3个亚甲基上的质子峰; δ 0.50~0.58、 δ 1.57~1.68和 δ 3.29~3.38分别对应UCS-10中离硅原子由近到远3个亚甲基上的质子峰, 相比APS-10, 受到酰胺基的影响这3个质子峰均向低场移动, 且越靠近酰胺基位移越大; δ 0.46~0.57、 δ 1.48~1.61和 δ 3.16~3.27则分别对应SCS-10中离硅原子由近到远3个亚甲基上的质子峰, 虽然同样受到酰胺基的影响, 但是位移程度比UCS-10的稍小。 δ 2.45~2.56和 δ 2.60~2.72分别是酰胺基和羧基中间两个亚甲基的质子峰。核磁测试结果说明氨基全部转化为对应的不饱和或者饱和羧基, 且没有酸酐的残留。

图3(c)是APS-10、UCS-10和SCS-10的GPC曲线、分子量以及分子量分布数据, 可见三者的数均分子量与设计值(10×10^3)十分接近。需要注意的是, 直接测量得到的APS-10分子量并非其真实值, 这是因为在测量前需要用间甲苯基异氰酸酯(mTI)把氨基封端(防止伯胺基与色谱柱填料发生反应), 这将会稍微增大分子量。

2.2 两种超分子产物(APS-UCS和APS-SCS)的结构表征与分子模拟

2.2.1 两种超分子产物(APS-UCS和APS-SCS)的结构表征

将APS-10与UCS-10(或SCS-10)在无溶剂条件下直接混合, 得到的两种产物, 分别标记为: APS-UCS-10、APS-SCS-10, 图4是其FT-IR谱图, 由图可见, APS-10与UCS-10或SCS-10混合后, 1750~1700 cm⁻¹处羧基上C=O伸缩振动吸收峰消失, 同时出现1560 cm⁻¹处的羧酸盐振动吸收峰, 这表明氨基和羧基发生酸碱中和反应且不再有羧基剩余。实验发现, APS-UCS-10为无色透明的弹性体薄膜, 而APS-SCS-10产物为黏稠状液体。

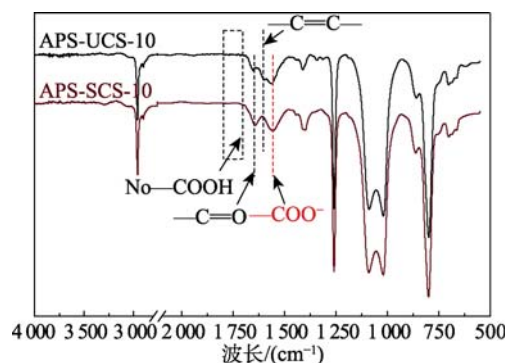


图4 APS-UCS-10和APS-SCS-10的FT-IR谱图

图5是APS-UCS-10和APS-SCS-10的流变行为主曲线, 在25℃的参考温度下, APS-UCS-10整个测试频率范围内都处于橡胶平台: 即储能模量 G' >损耗模量 G'' , 随着频率的增加, G' 小幅上升, G'' 则出现显

著上升;而在整个测试频率范围内,APS-SCS-10的主曲线都呈现 $G' < G''$ 的特征,表现为黏流态的液体。

如前所述,UCS和SCS的差异仅仅在于聚硅氧烷所接枝的羧基中含的是 $C=C$ 双键还是 $C-C$ 单键,其产物的性能却迥然不同,这主要是两个体系中离子氢键的作用强度相差较大造成的:在氨基基团结构不变的条件下,影响氨基与羧基之间离子氢键强度的主要因素是羧基的酸性(常用羧基电离常数的负对数, pK_a 值来表示)。其中,含有不饱和 $C=C$ 双键的马来酸与含有 $C-C$ 单键的琥珀酸的 pK_a 值分别为1.92和4.21,前者的电离常数较后者高了两个数量级,即UCS具有更强的酸性,导致APS-UCS体系中的离子氢键强度更高,更有利于构建稳定的交联体系,表现在宏观上,APS-UCS为交联弹性体,而APS-SCS为黏性流体(如图5所示)。

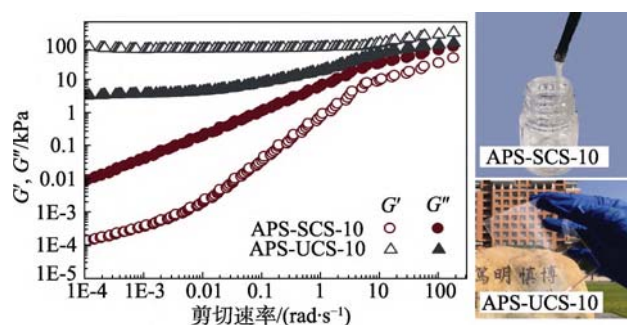


图5 APS-UCS-10和APS-SCS-10的流变主曲线及产物外观

2.2.2 两种不同结构羧基与氨基之间离子氢键作用强度的小分子模拟

为了更清晰地表征两种不同结构羧基与氨基之间的离子氢键作用强度,使得学生更直观地了解羧基酸性强弱对其与氨基之间相互作用强度的影响,考虑到大分子结构和作用力的复杂性,引入小分子模拟物APTMS、APTMS-MA和APTMS-SA(结构如图6所示),利用核磁滴定可用于测定化合物间的非共价相互作用的强度^[12,14],结果如图6所示。

对于APTMS和APTMS-MA组合,随着APTMS-MA浓度的从0.02 mol/L上升到0.12 mol/L,APTMS中紧邻 NH_2 的亚甲基的化学位移从2.51移动到2.77,通过最小二乘法拟合算得结合常数 K_1 为45.5 L/mol;对于APTMS和APTMS-SA组合,其化学位移从2.51移动到2.69,算得结合常数 K_2 为7.25 L/mol。结合常数是可逆非共价相互作用强度的良好度量,不饱和羧基与氨基的结合常数远大于饱和羧基与氨基的结合常数说明前者组合产生的离子氢键强度更强。

2.3 APS-UCS的力学性能和自愈合特性表征

APS-UCS的拉伸测试结果如图7所示。随着氨基和羧基接枝率的提高,APS-UCS的拉伸强度和杨氏模量也显著增加,而断裂伸长率则从900%急剧下降到260%;自愈合效率也随之下降。这主要是因为离子氢键交联密度的提高会增加链间相互作用力和限制聚硅氧烷主链的运动,在提高拉伸强度和模量的同时降低

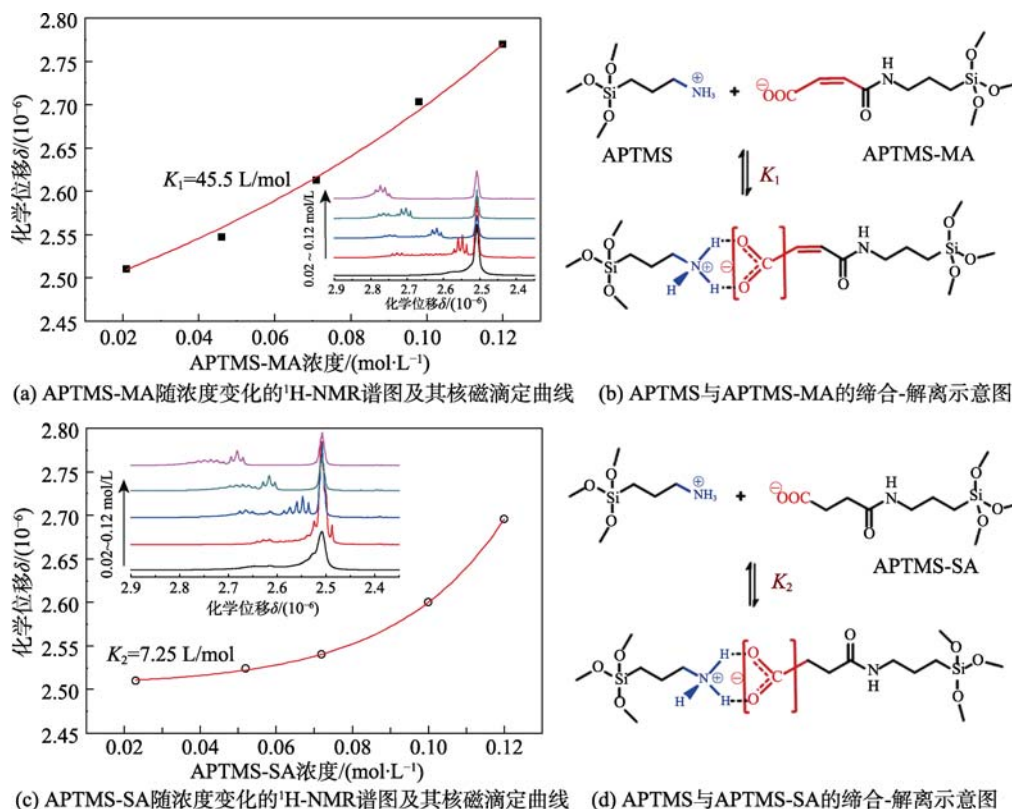


图6 APTMS-MA和APTMS-SA随浓度变化的 1H -NMR谱图、核磁滴定曲线及其缔合-解离示意图

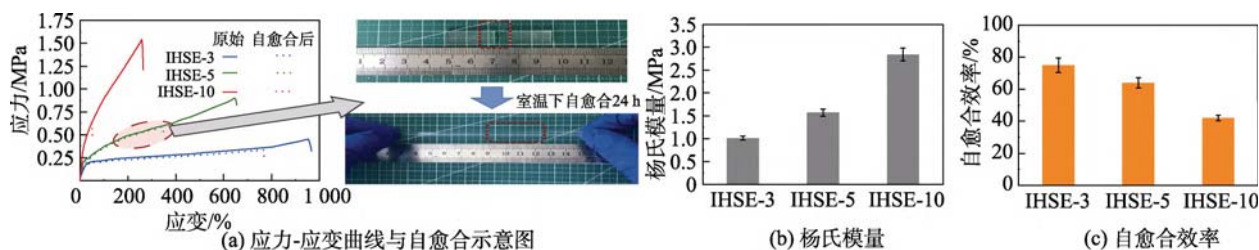


图7 APS-UCS-x 的应力-应变曲线、杨氏模量、自愈合效率

了扯断伸长率;自愈合的机理在于离子氢键的断裂、迁移和重组,同时还跟界面的扩散有关,这些过程受链段运动能力控制,随着聚合物链运动能力的下降,其自愈合的效率也会降低。

3 结语

通过两步法合成了氨基接枝聚硅氧烷 (APS-x),利用 APS 与马来酸酐或琥珀酸酐在无溶剂条件下反应获得 UCS-x 和 SCS-x。通过 FT-IR、¹H-NMR 和 GPC 表征证明合成产物能准确符合预先设计值。APS 与 UCS 在无溶剂条件下简单共混能获得离子氢键超分子弹性体,而同样条件下 APS 与 SCS 的共混则得到弹性体,流变行为表征亦清晰证实了上述结果;通过引入小分子模型化合物,结合核磁滴定,较好地解释了 APS-UCS 和 APS-SCS 体系产物性能差异的原因。APS-UCS 的拉伸强度和模量随着氨基和羧基接枝率的提高而降低,而室温自愈合能力则表现出相反的趋势。

该实验大大丰富了传统弹性体制备的实验内容,涵盖了材料的设计、合成到制备、性能分析与验证,既增强了实验的综合性,也提高了学习难度和要求。通过该实验,学生能够掌握聚合物结构表征的常用方法,更深入理解高分子材料结构与性能之间的构效关系,分析和解决问题的能力也都得到了有效的提升。

参考文献 (References)

- [1] 陈世良, 黄亦军, 黄嘉驰. 教师科研项目融入高分子专业实验教学的探索与实践[J]. 实验技术与管理, 2020, 37(9): 170-173, 178.
- [2] 张安强, 陆合承, 王炼石. 基于氢键作用的超分子弹性体材料的研究进展[J]. 高分子材料科学与工程, 2012, 28(2): 161-164.
- [3] MOZHDEHI D, AYALA S, CROMWELL O R, et al. Self-healing multiphase polymers via dynamic metal-ligand interactions[J]. Journal of the American Chemical Society, 2014, 136(46): 16128-16131.

- [4] LEI Y F, HUANG Q P, SHAN S J, et al. A stretchable and rapidly self-healable polysiloxane elastomer based on reversible aluminum- amino coordination[J]. New Journal of Chemistry, 2019, 43, 17441-17445.
- [5] LEI Y F, HUANG W Y, HUANG Q P, et al. A novel polysiloxane elastomer based on reversible aluminum-carboxylate coordination[J]. New Journal of Chemistry, 2019, 43, 261-268.
- [6] XU C H, CAO L M, LIN B, et al. Design of self-healing supramolecular rubbers by introducing ionic cross-links into natural rubber via a controlled vulcanization[J]. ACS Applied Materials & Interfaces, 2016, 8, 17728-17737.
- [7] GARCÍA F, SMULDERS M M J. Dynamic covalent polymers[J]. Journal of Polymer Science Part A Polymer Chemistry, 2016, 54, 3551-3577.
- [8] ZOU W, DONG J, LUO Y, et al. Dynamic covalent polymer networks: From old chemistry to modern day innovations[J]. Advanced Materials, 2017, 29(14): 1606100.
- [9] 莫家亨, 陈心渝, 傅育槟, 等. 基于可逆键构筑超分子弹性体的研究进展[J]. 弹性体, 2019, 29(6): 67-75.
- [10] DROZDOV A D, CHRISTIANSEN J D. Multi-cycle deformation of supramolecular elastomers: Constitutive modeling and structure-property relations[J]. International Journal of Engineering Science, 2018, 133: 311-335.
- [11] WEI S M, YOU Y, MA Y Y, et al. Bi-layer supramolecular polydimethylsiloxane elastomer film: Synthesis, characterization, and application in wound dressing on normal and diabetic rat[J]. Reactive and Functional Polymers, 2019, 141, 21-32.
- [12] MO J H, CHEN X Y, FU Y B, et al. A solvent-free, transparent, self-healing polysiloxanes elastomer based on unsaturated carboxyl-amino ionic hydrogen bonds[J]. Polymer, 2021, 228, 123903.
- [13] MAI D D, MO J H, SHAN S J, et al. Self-healing, self-adhesive strain sensors made with carbon nanotubes/polysiloxanes based on unsaturated carboxyl-amine ionic interactions[J]. ACS Applied Materials & Interfaces, 2021, 13(41): 49266-49278.
- [14] CORTESE J, SOULIÉ-ZIAKOVIC C, LEIBLER L. Binding and supramolecular organization of homo- and heterotelechelic oligomers in solutions[J]. Polymer Chemistry, 2014, 5(1): 116-125.

智慧实验室



安全准入管理系统

安全准入学习 | 考试自动阅卷
准入资格管理 | 准入门禁联动



大型仪器共享管理系统

预约授权使用 | 数据统计分析
账单汇总推送 | 数据一键上报



实验动物管理系统

实验培训考试 | 动物伦理审查
动物实验申请 | 动物订购寄养



环境监测管理系统

温湿度监测 | 气体监测
多级智能预警 | 实验室声光报警

可视化数据中心



试剂耗材管理系统

耗材档案管理 | 采购自动入库
领用审核出库 | 库存管理预警

智能终端

独特的蓝牙方案：仪器共享行业创新研发，150多家客户成熟应用，不受限于网络，不受限于地域。

智慧的人脸识别方案：人脸识别、语音交互、联动控制、AI人脸智能追踪。



蓝牙版电源控制器



网络版电源控制器



人脸识别终端



蓝牙版电脑控制器



网络版电脑控制器



智慧人脸门牌



智能门禁



动物管理手持终端



冰箱锁



环境监测

400-6969-039

广州佰能信息科技有限公司

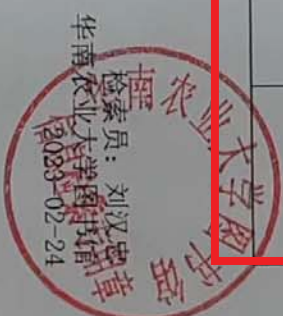
地址：广州市番禺区兴南大道483号华粤大厦

网址：<http://www.bynonco.com>



10	ammonium salts against conidia of Fusarium oxysporum f. sp. cubense, race 4	PATHOLOGY 出版年: 2022 卷期: 页码: - 文献类型: Article; Early Access	通讯作者	B类	华南农业大学	SCI	IF2-year=2.224 IF5-year=2.262 (2021)	农林科学 3区 Top期刊: 否 (2022)
11	Polymeric diallyl quaternary ammonium salts for inhibiting banana Fusarium wilt	REACTIVE & FUNCTIONAL POLYMERS 出版年: 2022 MAR 卷期: 172 文献号: 105174 文献类型: Article	第一作者	B类	华南农业大学	SCI	IF2-year=4.966 IF5-year=4.266 (2021)	工程技术 3区 Top期刊: 否 (2022)
12	基于离子氢键的聚硅氧烷超分子弹性体的制备及其实验设计	实验技术与管理 出版年: 2022 卷期: 39 10 页码: 36-41 文献类型: Article	第一作者	C类	华南农业大学	北大核心		

报告免责声明: 如未盖章, 报告无效





中国高等教育学会实验室管理工作分会会刊
中文核心期刊
中国科技核心期刊
科技期刊世界影响力指数(WJCI)科学技术综合学科01区
RCCSE中国权威学术期刊

ISSN 1002-4956
CN 11-2034/T
CODEN SJYGAR

实验技术与管理

Shiyan Jishu yu Guanli

Experimental Technology and Management

8

2024

第41卷 第8期
Vol. 41 No. 8

月刊

高分辨液相色谱质谱联用仪在蛋白质化学修饰中的应用

基于异构图和语义融合的实体关系抽取

竖直管道内三种粉体抑爆剂对聚乙烯燃爆火焰传播的影响

基于VRX的无人水面船智能控制虚拟仿真实验平台设计

基于液压储能器的制动能量回收试验台研制

聚乙烯醇/SAPO-34混合基质膜制备及渗透汽化性能综合实验教学设计

基于遗传算法的元胞自动机复杂楼宇人员疏散模型

ISSN 1002-4956



9 771002 495248

中华人民共和国教育部主管

清华大学主办

主管：中华人民共和国教育部

主办：清华大学

主编：王玉军

副主编：彭远红

编辑部主任：彭远红（兼）

编辑：张文杰 彭远红 张利芳 孙浩

责任编辑：孙浩

编务：陈昕

发行：吴岩

封面题字：刘仙洲院士、清华大学原第一副校长，

1963年题

编辑：《实验技术与管理》编辑部

地址：北京市海淀区双清路学研大厦B座908

邮编：100084

在线投稿：<http://syjl.cbpt.cnki.net>

编辑部电话：010-62783005

邮箱：sjg@tsinghua.edu.cn

广告电话：010-62788738

订刊发行电话：010-62792635

邮箱：syjsygl@tsinghua.edu.cn

出版与发行：清华大学出版社有限公司

地址：北京市海淀区双清路学研大厦A座6层

邮编：100084

印刷：北京卓诚恒信彩色印刷有限公司

发行范围：国内外公开发行

国际标准连续出版物号：ISSN 1002-4956

国内统一连续出版物号：CN 11-2034/T

国际期刊编码：CODEN SJYGAR

广告发布登记：京海市监广登字20200045号

出版日期：8月20日

定价：30.00元/期 全年12期 360.00元

收录本刊内容的国内外数据库与媒体：

- 中国学术期刊(光盘版)
- 中国核心期刊(遴选)数据库
- 万方数据资源系统数字化期刊群
- 中国期刊网
- 中国学术期刊综合评价数据库
- 中国期刊全文数据库
- 中文科技期刊数据库
- 中文电子期刊服务
- 中国学术期刊文摘(中文版)
- 中国科技论文在线
- 美国《剑桥科学文摘》(CSA)
- 美国《化学文摘(网络版)》(CA)
- 美国《乌利希期刊指南(网络版)》(Ulrichsweb)
- 英国《世界陶瓷文摘(网络版)》(WCA)
- 日本《日本科学技术振兴机构数据库(中国)》(JST China)
- 美国《艾博思科数据库》(EBSCOhost)

目次

第41卷 第8期(总第336期) 2024年8月

特约专栏——蛋白质化学修饰研究进展

高分辨液相色谱质谱联用仪在蛋白质化学修饰中的应用

汪会玲, 孟祥高, 肖凤萍, 等 1

实验技术与方法

Gleeble 高温拉伸样品标距段的选定对拉伸曲线的影响

赵冠琳, 吴东亭, 刘树帅, 等 15

基于异构图和语义融合的实体关系抽取 唐贤伦, 丁河长, 唐瑜泽, 等 22

超声空化诱导煤微观孔隙损伤的原位测试技术研究

李傲, 王玉娟, 郭晓阳, 等 30

海洋食品酶解物改善精神疲劳功能性评价的综合实验设计

张恬恬, 马磊, 邹宏宇, 等 36

基于透明物体深度补全的机器人抓取实验设计

张倩, 朱美强, 王惠, 等 43

竖直管道内三种粉体抑爆剂对聚乙烯燃爆火焰传播的影响

苏明清, 多英全, 陈思凝, 等 53

基于三维建模的喷油器流量系数在线测试 董全, 王迪, 周谈庆, 等 60

[Emim]NTF₂/MIL-53(Al)复合材料制备及其硫酸羟基氯喹吸附性能探索型实验设计 李正杰, 刘苗, 刘忆贤, 等 66

聚丙烯酰胺季铵盐大分子药物的环境毒性评价及其实验设计

林雅铃, 吴明阳, 张卫, 等 77

双级可转导叶压气机性能研究 王忠义, 李政, 王瑞浩, 等 82

基于双折射晶体透镜的自干涉全息成像系统 许灿华, 薛礼松, 范德辉, 等 88

矿物分选中低阶多孔煤的药剂吸附及表征实验设计

解维伟, 周玲娟, 李海门, 等 96

核电领域高阻抗纯水体系 IR 降控制的研究 蔡双雨, 雷应, 王峰, 等 104

虚拟仿真技术

井底流固耦合环境下 PDC 钻头切削齿冷却仿真实验

王京印, 耿明远, 廖华林 111

基于 VRX 的无人水面船智能控制虚拟仿真实验平台设计

张宇, 李洪宇, 王宗省 121

基于 Unity 3D 的瓦斯燃烧与烟气排放仿真实验建设

李乃良, 王利军, 刘常松, 等 129

断层破碎带隧道结构破坏离散元数值试验 杨青林, 李醒, 王永雷 136

仪器设备研制

高铁司机警觉度监测与干预穿戴装置研制 史磊, 周文慧, 魏方传, 等 143

期刊基本参数: CN11-2034/T * 1963 * m * A4 * 259 * zh * P * ¥30.00 * 6500 * 36 * 2024-08

基于液压储能器的制动能量回收试验台研制	徐平, 马宗正, 王赛飞, 等	150
动水条件下煤岩单轴蠕变试验监测装置研制	杨东辉, 张星星, 陈晓鹏, 等	156
一种用于缆上控制与保护装置 (IC-CPD) 测试的剩余电流模拟系统设计	陈聪, 倪峰, 李春	161
液位控制实训平台设计	王振浩, 专祥涛	169

实验教学研究与管理

区域综合能源系统两阶段鲁棒优化实验案例教学	邵振国, 林勇棋, 陈煜超, 等	175
多孔有机笼膜材料纳滤机理的分子模拟教学实验设计	刘捷, 谭晓艳, 薛亚楠, 等	182
基于高精度激光光斑质心定位技术的教学实验设计	沈利荣, 张文博, 隆嘉瑾, 等	188
聚乙烯醇/SAPO-34 混合基质膜制备及渗透汽化性能综合实验教学设计	蔡卫滨, 宋美洁, 焦健, 等	195
基于实际工程项目的装配参数视觉检测实践教学设计与实践	杨义, 陈宗涛, 徐刚, 等	201
创新型传热学导热系数教学实验的设计与实践	孙始财, 谷林霖	208
集成 AI 大语言模型的在线编程实验平台设计与实现	厉旭杰, 顾雨辰, 姚持恩	215
LSTM 智能导向的电子信息实践教改探索	包建荣, 秦艺鹏, 刘超, 等	222

实验室环境健康与安全

标杆管理理论在高校实验室安全管理中的应用	范寒寒, 朱久娟, 冯嘉靖, 等	230
基于遗传算法的元胞自动机复杂楼宇人员疏散模型	白鹏, 刘楠, 董卓龙, 等	236

实验室建设与管理

新工科背景下提高教学类仪器设备利用率的探索与实践——以吉林大学工程训练中心为例	丁连涛, 吴彤, 刘思含, 等	244
实验技术队伍先进技术集群建设	郑娜, 吴哲敏, 徐丽, 等	251
地方院校实验室科研用房绩效考核改革与实践——以徐州医科大学为例	赵冲, 郑友广, 徐红岩	255

· 广告索引 ·

江苏埃德伯格电气有限公司 (封二)
2024 年《实验技术与管理》征订单 (后一)
外应环球科技 (北京) 有限公司 (封三)
上海万欣计算机信息科技有限公司 (封底)



《实验技术与管理》
微信公众号

实验技术与管理

第十二届编辑委员会名单

主任: 曾嵘

顾问: (按姓名拼音排序)

陈小明 程建平 高松 邱爱慈 瞿振元
席葆树 周玉 周远清 朱静

副主任: (按姓名拼音排序)

毕卫民 董林 胡国庆 蒋兴浩 金永东
李长利 刘克新 孙小平 唐睿康 王海洁
王小力 王玉军 席海涛 熊宏齐 张社荣
钟代笛 朱臻 宗俊峰

编委: (按姓名拼音排序)

蔡以兵 曹蓓 陈越 陈晓猛 陈心浩
丁元明 董华青 董绍辉 杜华云 冯建刚
盖宏伟 郭庆 郭建中 韩英霞 郝志强
侯珏 黄富贵 蒋开东 蒋文春 康传红
赖廷清 李崧 李格升 李立光 李鹏健
李天书 李向阳 梁勇 刘锋 刘刚
刘哲 刘红军 刘兼唐 刘崎峰 刘琦晖
刘雯杰 刘拥军 芦燕 罗茂斌 马国杰
马国玉 毛昌杰 毛继泽 孟兆磊 牛晓滨
彭远红 任志波 邵岚 邵光辉 沈勇
沈清明 沈如群 孙胜春 唐俊峰 汪必琴
王建 王强 王耀峰 王哲强 王中亮
魏永前 闻毓民 吴卫 吴雁 吴祝武
向坚持 熊龙彪 许燕滨 薛凌云 杨立成
杨立功 杨小兵 杨旭静 杨原志 姚丽蓉
姚作芳 于江华 余自中 袁洪学 占金华
张东 张莉 张巍 张文 张润峰
张明生 张若好 张新生 章明卓 赵国
赵冬梅 钟华勇 周晔 朱正茂 朱仁卿
庄志鸿

特邀编委: (按姓名拼音排序)

敖天其 毕大强 蔡峰 陈小鸿 丁建伟
冯建跃 桂南 韩小涛 金仁东 刘明文
雷敬炎 李赛 李震彪 史天贵 唐强
王兵 王杰 邢志 姚文清 袁志
张云怀 章立军 钟茂华

特别支持单位

江苏埃德伯格电气有限公司 董事长 杨勇
上海万欣计算机信息科技有限公司 总经理 谢卫民
中国分析测试协会高校分析测试分会 秘书长 姚文清
清华四川能源互联网研究院 副院长 曹宗相
浙江清华长三角研究院 副院长 冯叶成

聚丙烯酰胺季铵盐大分子药物的环境毒性评价及其实验设计

林雅铃¹, 吴明阳¹, 张卫¹, 孙凯伦², 张安强²

(1. 华南农业大学 材料与能源学院, 广东 广州 510642;

2. 华南理工大学 材料科学与工程学院, 广东 广州 510641)

摘要: 聚丙烯酰胺季铵盐 (PAM-QAS) 是丙烯酰胺 (AM) 与丙烯酰胺季铵盐 (AM-QAS) 的无规共聚物, 因兼具聚丙烯酰胺的土壤改良特性和大分子季铵盐的抑菌特性, 在抑制土壤病原真菌、改良和修复病土等领域有良好的应用前景。但人们对季铵盐具有较高环境毒性的传统认识, 极大地限制了这类新型大分子药物的应用。如何结合 PAM-QAS 的应用环境, 综合、客观地评价其环境毒性, 是大分子药物设计和应用中亟待解决的问题。通过在 PAM-QAS 中修饰荧光基团直观地观察其在土壤中的吸附与淋溶特性, 以及结合土壤吸附和淋溶实验用鱼类经口急性毒性实验和蚯蚓毒性实验评价 PAM-QAS 经土壤吸附后的实际环境毒性, 为 PAM-QAS 的田间应用提供了一定科学依据。该实验内容涉及聚合物结构表征与应用、大分子药物在复杂环境下的定性检测, 以及药物的环境毒性评价等诸多环节, 具有一定的综合性与探索性, 有利于提高学生的综合素质、科研能力和创新能力。

关键词: 聚丙烯酰胺季铵盐; 荧光基团修饰; 土壤吸附特性; 环境毒性评价

中图分类号: TQ33 **文献标识码:** A **文章编号:** 1002-4956(2024)08-0077-05

将药物的评价标准与实际应用条件相结合, 客观评价药物的综合性能, 一直是药物分析和评价领域的难题, 将这些领域的研究成果引入本科探索性实验教学, 是科研与教学结合的重要方式。在此过程中, 应注意测试标准的普适性与实际应用环境的有机结合, 以及学生认知水平与实验教学条件的匹配^[1]。聚丙烯酰胺季铵盐 (PAM-QAS) 是丙烯酰胺 (AM) 与丙烯酰胺季铵盐 (AM-QAS) 的无规共聚物, 因兼具聚丙烯酰胺的土壤改良特性^[2-4]和大分子季铵盐的抑菌特性^[5-6], 在抑制土壤的病原真菌^[7]、改良和修复病土^[8]等领域有良好的应用前景。但基于人们关于传统小分子季铵盐具有广谱抑菌活性^[9-13], 具有较高环境毒性的惯性思维, 往往也认为大分子季铵盐也具有较高环境毒性, 这极大地限制了这类新型大分子药物的应用。

针对上述问题, 我们设计了多个可直观表现 PAM-QAS 低环境毒性的实验。首先, 在 PAM-QAS 的聚合过程中引入极少量的乙烯基荧光单体, 得到荧光修饰

的聚丙烯酰胺季铵盐 (PAM-QAS-FL), 通过土壤淋溶实验证实 PAM-QAS-FL 在土壤中具有良好的吸附和难迁移特性; 其次, 结合 PAM-QAS 的土壤吸附与淋溶实验, 用斑马鱼毒性实验 (鱼类急性毒性实验) 证实 PAM-QAS 经土壤吸附后, 极大地降低了对环境水体的影响; 最后, 用蚯蚓毒性实验证实吸附了 PAM-QAS 的土壤对蚯蚓的毒性极低。本综合实验内容涵盖了功能聚合物的荧光特性表征、结合实际应用条件和国家标准开展实验设计等诸多环节, 还具有一定的趣味性, 能够使学生较为系统地学习功能高分子材料的分子设计、结构表征及应用等方面知识, 训练灵活掌握大分子药物和功能高分子材料学科的研究方法与思维方式。

1 实验部分

1.1 实验材料

N, N-二甲基十二烷基苄基氯化铵 (商品名: 苯扎

收稿日期: 2024-02-28

基金项目: 国家自然科学基金项目 (31772202); 广州市科技计划项目 (201803020015); 广东省高等教育教学改革项目 (2022-397); 广东省高等教育学会课题 (22GYB060); 华南理工大学探索性实验项目 (2021-11)

作者简介: 林雅铃 (1978—), 女, 福建罗源, 博士, 副教授, 主要研究领域为大分子药物与超分子弹性体, linyaling@scau.edu.cn。

通信作者: 张安强 (1976—), 男, 湖南安仁, 博士, 教授, 主要研究方向为功能高分子材料, aqzhang@scut.edu.cn。

引文格式: 林雅铃, 吴明阳, 张卫, 等. 聚丙烯酰胺季铵盐大分子药物的环境毒性评价及其实验设计[J]. 实验技术与管理, 2024, 41(8): 77-81.

Cite this article: LIN Y L, WU M Y, ZHANG W, et al. Environmental toxicities evaluation and experimental design of polymeric drugs based on polyacrylamide quaternary ammonium salts[J]. Experimental Technology and Management, 2024, 41(8): 77-81. (in Chinese)

氯铵, BC), >99%, 麦克林生化科技有限公司产品。根据季铵盐结构的不同, 聚丙烯酰胺季铵盐 (PAM-QAS) 分为 PAM-BB 和 PAM-BC 两种, 对应的荧光基团产物 (PAM-QAS-FL), 也分为 PAM-BB-FL 和 PAM-BC-FL, 其结构如图 1 所示, 均参考文献[8]合成。实验用土取自华南农业大学科研基地农场 (菜园土), 风干

后去除非土物质, 碾碎, 过 20 目筛, 备用。土壤的理化性质如下: pH 5.54, 有机质含量 21.1 g/kg, 全 N、P、K 含量分别为 824、108、226 mg/kg。斑马鱼购于上海市费曦生物科技有限公司, 全长 2 ± 0.5 cm, 体重 0.2 ± 0.1 g。蚯蚓品种为赤子爱胜蚓 (*Eisenia foetida*), 购于河北省鑫伊达蚯蚓养殖场, 全长 5~8 cm, 体重 0.3~0.6 g。

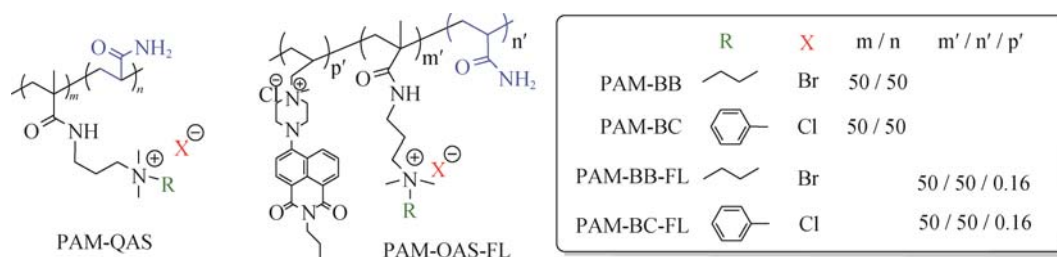


图 1 PAM-QAS (PAM-BB 和 PAM-BC) 和 PAM-QAS-FL (PAM-BB-FL 和 PAM-BC-FL) 的结构示意图

1.2 土壤淋溶实验

根据 PAM-QAS 在土壤中的常用施用量 (0.2 g/kg 干土), 预先把 PAM-QAS (或 PAM-QAS-FL) 按 3 倍常用施用量 (0.6 g/kg 干土) 与风干并过筛的土壤混合均匀 (阳性对照为苯扎氯铵/BC, 阴性对照为不加任何药物), 然后将 700 g 混合土壤装入内径为 4 cm、长度为 30 cm、带有出口控制阀的玻璃柱中 (装置如图 2 所示), 需边轻微振动边添加土壤以实现均匀填充, 最后用石英砂覆盖土柱的上表面。加入 0.01 mol/L CaCl_2 溶液使土柱中水分达到饱和, 以去除土壤颗粒中存在的空气, 平衡 24 h 后, 在 24 h 内于每个土柱上滴加 320 mL (相当于 255 mm/ 24 h 的“特大暴雨”级别的降雨量) 的人工降雨 (去离子水), 收集土柱淋出液, 静置 12 h 后, 得到土壤淋溶液。当混入药物为 PAM-QAS-FL 时, 淋溶液浓缩后用荧光分光光度计测定其荧光吸收特性; 当混入药物为 PAM-QAS 时, 在收集的淋溶液中加入斑马鱼, 以评价 PAM-QAS 土壤淋溶液对斑马鱼的急性毒性。

1.3 PAM-QAS 对斑马鱼的急性毒性实验

参照《GB/T 31270.12—2014: 鱼类急性毒性试验》



图 2 土壤淋溶装置示意图

测试 PAM-QAS 在不同条件下 (直接投入、土壤淋溶液、药物与水土混合物) 对水生生物斑马鱼的急性毒性, 选用 $2.0 \sim 2.2$ cm 体长和 $0.2 \sim 0.3$ g 体重的斑马鱼作为实验对象。

在直接投入条件下, 以 PAM-BB、PAM-BC 和 BC 作为实验药物, 重铬酸钾为参照毒物, 不含任何药物的清水为对照组。在预实验中, 将重铬酸钾、BC、PAM-BB 和 PAM-BC 的浓度设置为 0 、 0.01 、 0.1 、 1.0 、 10 和 100 mg/L, 以确定导致斑马鱼 $0 \sim 100\%$ 死亡率时的浓度范围。每个处理组放入 7 尾鱼, 每隔 24 h 记录斑马鱼的存活情况。预实验中, 浓度为 100 mg/L 的处理组即为限度实验, 若此测试浓度下 7 尾鱼全部存活, 则证明所测试药物对斑马鱼无急性毒性。根据预实验 96 h 毒性结果, 在正式实验中, 将药物在 $10 \sim 100$ mg/L 区间配置成不同浓度持续进行, 记录 96 h 鱼的死亡率。根据毒力方程求出 BC、PAM-BB 和 PAM-BC 对斑马鱼的半数致死浓度 LC_{50} [14]。

针对土壤淋溶液环境, 以 PAM-BB、PAM-BC 和 BC 作为实验药物, 参照本文 1.2 节中所述方法获得土壤淋溶液, 每组放入 7 尾鱼, 每组重复三次。空白对照组为不含药物土壤的淋溶液, 其他条件与实验组相同。以每公斤干土中所含的药物为基础, 估算所得淋溶液在 96 h 后对斑马鱼的半数致死浓度, 为了与 LC_{50} 相区分, 采用 LC_{50L} 来表示, 下标 “L” 表示淋溶液。

针对水土共混环境, 以 PAM-BB、PAM-BC 和 BC 作为实验药物, 将其加入到水土比约为 $5:1$ 的模拟鱼塘水中, 充分混匀后静置 24 h 后, 每组放入 7 尾鱼, 每组重复三次。空白对照组为不含药物的水溶液, 其他条件与实验组相同。观察并记录 96 h 后斑马鱼的中毒症状和死亡率, 所得的对斑马鱼的半数致死浓度标记为 LC_{50S} , 下标 “S” 表示含土壤的水土共混环境。

1.4 PAM-QAS 对蚯蚓的急性毒性实验

参照 GB/T31270.12—2014, 选取二月龄以上、体重在 0.4 ± 0.1 g 的健康赤子爱胜蚓。在进行实验之前, 在室内对蚯蚓培养 7 d 以上。配制由 10% 泥炭藓、68% 50~100 μm 的石英砂、20% 高岭土、2% 碳酸钙组成的人工土壤, 调节其 pH 值至 6.0 ± 0.5 , 加入蒸馏水调节人工土壤含水量为 30%~35%。以 PAM-BB、PAM-BC 和 BC 作为实验药物, 按一定比例间距设置 6 个浓度组和 1 个空白对照组, 每个浓度重复三组。不同处理组分别放入蚯蚓 10 条, 用保鲜膜封好瓶口并扎小孔, 将烧杯置于 20 ± 2 $^{\circ}\text{C}$ 、湿度 80% 左右、光照强度 400~800 lx 的培养箱中。根据蚯蚓 14 d 的死亡率, 计算药物对蚯蚓的毒性 LC_{50} 值及 95% 置信限^[10-11,15]。

2 结果与讨论

2.1 PAM-QAS 在土壤中的淋溶与迁移特性

与诸多小分子药物不同的是, PAM-QAS 自身并没有明显的特征吸收峰, 难以用常规的光谱分析方法表征其在土壤中的吸附、迁移与淋溶特性, 故需在其分子链中共聚极少量的荧光基团 ($<0.2\%$ mol), 得到荧光基团修饰的 PAM-QAS, 即: PAM-QAS-FL。图 3 是 PAM-BB-FL 及含 PAM-BB-FL 土壤的淋溶液的荧光光谱图。由图 3 可以看出, PAM-BB-FL 水溶液在紫外灯下能够发出明亮的绿光, 且在 515 nm 处有最大的荧光强度, 而含 PAM-BB-FL 土壤的淋溶液浓缩后在紫外灯下只有暗蓝色光, 为土壤本身所带荧光物质颜色, 且在 515 nm 处的荧光强度极低。这一实验结果直观地表明, PAM-QAS 在土壤中难以移动, 不容易随水迁移, 可以较长时间稳定地待在土壤中, 有利于长期发挥抑菌作用。

2.2 PAM-QAS 在不同环境下对斑马鱼和蚯蚓的急性毒性

图 4 是 PAM-QAS 和 BC 在不同环境下对斑马鱼和蚯蚓的急性毒性。由图可见, 当按照 GB/T 31270.12—2014 的要求, 将药物直接投入水中来评价药物对鱼类的急性毒性时, 季铵盐类药物都表现出较高的毒性, 其中, BC 的 $\text{LC}_{50} < 1$ mg/L, 表现为高毒, PQDXAM 的 LC_{50} 较 BC 略高一些, 在 1~10 mg/L 间, 但仍属于中毒范畴, 这与文献报道^[9-12]大致吻合, 这也是人们对季铵盐类药物在田间施用感到担忧的一个原因。众所周知, 季铵盐可经由不同途径释放到环境中, 在水体、沉积物、土壤等多种介质中均可检出, 由于其较强的表面活性和非专一性的生物毒性, 对生态环境构成潜在威胁^[12]。PAM-QAS 作为一类新型的具有较大分子量的水溶性大分子季铵盐类药物, 其分子特性及土壤吸附特性与小分子季铵盐存在较大差异, 主要以水溶液与土壤预拌方式施用。鉴于其与土壤之间具有很强的吸附作用^[8], 绝大部分的 PAM-QAS 被土壤有效吸附, 难以被淋溶进入环境水体 (如图 3 所示)。实际上, 图 4 中的蚯蚓急性毒性实验结果也证实了, 经

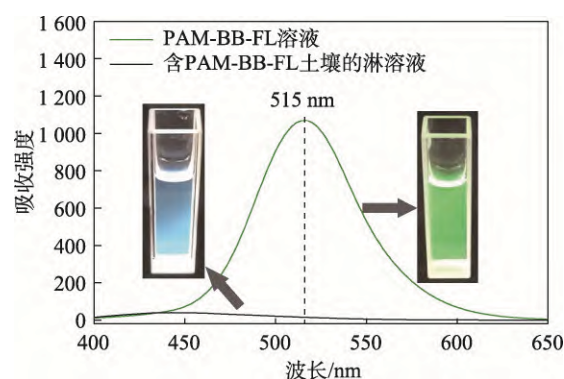


图 3 PAM-BB-FL 在土壤中的淋溶行为

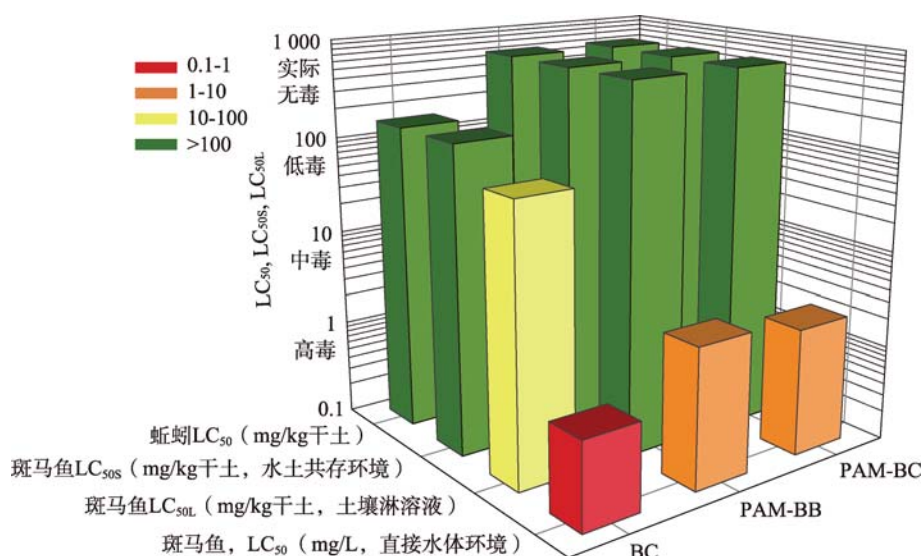


图 4 PAM-QAS 和 BC 在不同环境条件下对斑马鱼和蚯蚓的急性毒性

过与土壤的吸附, PAM-QAS 和 BC 对蚯蚓的急性毒性均处于低毒范畴。相应地, 需要针对不同的施用方式使用不同的鱼类毒性评价方法。

基于上述理念, 我们通过模拟药物在实际生产应用中随雨水渗入地下水以及与水土混合后对环境水体的影响, 引入 LC_{50L} 和 LC_{50S} 两个指标分别用于评价土壤淋溶液和水/土/药混合液的鱼类毒性。我们发现, 由于 PAM-QAS 在土壤中具有较强的吸附和难迁移特性, 大大降低了进入环境水体中的游离药物浓度。由图 4 可见, 在 3 倍田间常用施用量 (即: $0.6 \text{ g}/(\text{kg} \text{ 干土})$) 条件下, PAM-QAS 的土壤淋溶液及水土混合液中, 所有斑马鱼经过 96 h 后均都可以正常存活, 即相应的 LC_{50L} 和 LC_{50S} 均大于 $600 \text{ mg}/(\text{kg} \text{ 干土})$, 说明在田间常用施用量下, PAM-QAS 对鱼类和蚯蚓均是安全的。而在同样的施用量下, BC 的土壤淋溶液和水土共混液中的斑马鱼全部死亡, 说明 PAM-QAS 环境毒性较 BC 显著降低。这与直接施用于水体中所测得的 LC_{50} 有显著差异, 也是更符合实际使用条件的测试结果。我们认为, 这主要得益于聚丙烯酰胺较高的主链分子量及其与土壤之间的良好吸附作用。上述实验结果, 为在土壤中具有较强吸附作用药物 (尤其是大分子药物) 的环境评价, 提供了新的思路和方法。

3 结语

通过模拟药物在实际生产应用中随雨水渗入地下水以及与水土混合后对环境水体的影响, 引入 LC_{50L} 和 LC_{50S} 指标分别用于评价土壤淋溶液和水/土/药混合液的鱼类毒性, 较为准确地建立了 PAM-QAS 的环境毒性评价方法。实验结果表明, 在田间常用施用量为 $0.6 \text{ g}/(\text{kg} \text{ 干土})$ 条件下, PAM-QAS 可在土壤中稳定地吸附和存留, 对鱼类和蚯蚓均是安全的。与小分子季铵盐 BC 相比, 其环境毒性显著降低。

该实验大大丰富了大分子药物的环境毒性评价实验内容, 涵盖了功能聚合物的荧光特性表征、结合实际应用条件和国家标准开展环境毒性评价实验设计等诸多环节, 有助于学生深入理解高分子材料结构与性能之间的构效关系, 灵活掌握药物分析和功能高分子材料学科的研究方法与思维方式。在此过程中, 学生的材料结构表征能力、分析和解决问题能力也得到有效提升。

参考文献 (References)

- [1] 陈世良, 黄亦军, 黄嘉驰. 教师科研项目融入高分子专业实验教学的探索与实践[J]. 实验技术与管理, 2020, 37(9): 170-173, 178.
CHEN S L, HUANG Y J, HUANG J C. Exploration and practice

- of combining scientific research projects with experimental teaching of polymer materials and engineering[J]. Experimental Technology and Management, 2020, 37(9): 170-173, 178. (in Chinese)
- [2] ZHANG H L, WANG G H, DU J, et al. Effects of several polymeric materials on the improvement of the sandy soil under rainfall simulation[J]. Journal of Environmental Management, 2023(345): 118847.
- [3] MAMEDOV A I, HUANG C H, ALIEV F A, et al. Aggregate stability and water retention near saturation characteristics as affected by soil texture, aggregate size and polyacrylamide application [J]. Land Degradation and Development, 2017, 28(2): 543-552.
- [4] KEBEDE B, TSUNEKAWA A, HAREGEWEYN N, et al. Effectiveness of polyacrylamide in reducing runoff and soil loss under consecutive rainfall storms[J]. Sustainability, 2020, 12(4): 1597.
- [5] JIAO Y, NIU L N, MA S, et al. Quaternary ammonium-based biomedical materials: State-of-the-art, toxicological aspects and antimicrobial resistance[J]. Progress in Polymer Science. 2017(71): 53-90.
- [6] LU G Q, WU D C, FU R W. Studies on the synthesis and antibacterial activities of polymeric quaternary ammonium salts from dimethylaminoethyl methacrylate[J]. Reactive and Functional Polymers, 2007, 67(4): 355-366.
- [7] ZHANG A Q, LIU Q Q, LEI Y F, et al. Synthesis and antimicrobial activities of acrylamide polymers containing quaternary ammonium salts on bacteria and phytopathogenic fungi [J]. Reactive and Functional Polymers, 2015(88): 39-46.
- [8] ZHANG W, YU J G, WU M Y, et al. Polyacrylamide quaternary ammonium salts based on stable adsorption in soil and its application on the control of soil-borne fungal disease[J]. European Polymer Journal, 2024(202): 112604.
- [9] TONG Y H, LU P L, ZHANG W Y, et al. The shock of benzalkonium chloride on aerobic granular sludge system and its microbiological mechanism[J]. The Science of the Total Environment, 2023(895): 165010.
- [10] CHEN Y, GEURTS M, SJOLLEMA S B, et al. Acute toxicity of the cationic surfactant C12-benzalkonium in different bioassays: How test design affects bioavailability and effect concentrations[J]. Environmental Toxicology and Chemistry, 2014, 33(3): 606-615.
- [11] WANG Y H, CANG T, ZHAO X P, et al. Comparative acute toxicity of twenty-four insecticides to earthworm, *Eisenia fetida*[J]. Ecotoxicology and Environmental Safety, 2012(79): 122-128.
- [12] 李北兴, 李华, 张大侠, 等. 季铵盐和有机硅助剂对啮虫脉杀虫活性及水生生物毒性的影响[J]. 农药学报, 2017, 19(1): 93-99.
LI B X, LI H, ZHANG D X, et al. Influence of quaternary ammonium and organic silicon adjuvant on insecticidal activity of acetamiprid and environmental toxicity against aquatic organisms[J]. Chinese Journal of Pesticide Science, 2017, 19(1): 93-99. (in Chinese)

- [13] LARSSON Y, MONGELLI A, KISIELIUS V, et al. Microbial biofilm metabolism of benzalkonium compounds (benzyl dimethyl dodecyl ammonium & benzyl dimethyl tetradecyl ammonium chloride)[J]. Journal of Hazardous Materials, 2024(463): 132834.
- [14] EL-HARBAWI M. Toxicity measurement of imidazolium ionic liquids using acute toxicity test[J]. Procedia Chemistry, 2014(9): 40–52.
- [15] 陈吉祥, 于伟丽, 王广友, 等. 氯虫苯甲酰胺对环境生物的急性毒性与安全性评价[J]. 生态毒理学报, 2022, 17(6): 452–461.
- CHEN J X, YU W L, WANG G Y, et al. Acute toxicity and safety evaluation of chlorantraniliprole to environmental organisms[J]. Asian Journal of Ecotoxicology, 2022, 17(6): 452–461 (in Chinese)

Environmental toxicities evaluation and experimental design of polymeric drugs based on polyacrylamide quaternary ammonium salts

LIN Yaling¹, WU Mingyang¹, ZHANG Wei¹, SUN Kailun², ZHANG Anqiang²

(1. College of Materials and Energy, South China Agricultural University, Guangzhou 510642, China;

2. School of Materials Science and Engineering, South China University of Technology, Guangzhou 510641, China)

Abstract: [Objective] Because of the huge damage caused by soil-borne fungal diseases in agriculture, polyacrylamide quaternary ammonium salts (PAM-QAS) have been introduced to control soil-borne fungal diseases, such as banana *Fusarium* wilt, which is caused by *Fusarium oxysporum* f. sp. *cubense* (Foc). As a random copolymer of acrylamide and acrylamide quaternary ammonium salt, PAM-QAS shows significant improvement properties on soil and good antifungal activities against soil-borne fungal diseases, such as Foc. Thus, PAM-QAS has a good application prospect in the control of soil-borne fungal diseases and improving soil. However, traditional small molecular quaternary ammonium salts have been well-known to show high environmental toxicities, greatly limiting their application. Thus, visually evaluating the environmental toxicities of PAM-QAS based on exact application environments has become an urgent issue in the design and application of PAM-QAS. In this work, multiple experiments were designed to visually demonstrate the low environmental toxicity of PAM-QAS. [Methods] To visualize PAM-QAS, a very small amount of a fluorescent group (FL) was introduced into PAM-QAS to obtain fluorescent-labeled PAM-QAS (PAM-QAS-FL). Thus, its adsorption and leaching characteristics in soil could be observed intuitively. From the soil adsorption and leaching experiments, the actual environmental toxicities of PAM-QAS after soil adsorption could be evaluated using fish oral acute toxicity and earthworm toxicity experiments, which gave a good perspective for the field application of PAM-QAS. [Results] The soil adsorption and leaching experiments intuitively showed that under an application rate of 0.6 g per kilogram of dry soil in the field, which was about three times the commonly applied amount, PAM-QAS-FL could be stably adsorbed and retained in the soil, with only a few free PAM-QASs leaching into environmental water. Thus, the impact of PAM-QAS on the environment could be greatly reduced. The fish acute toxicity of simulated rain leaching solution containing PAM-QAS and soil (LC_{50L}), the fish acute toxicity of a suspension containing PAM-QAS and soil (LC_{50S}), and the earthworm toxicity of PAM-QAS (LC_{50}) were all higher than 600 mg per kilogram of dry soil. Meanwhile, the LC_{50L} , LC_{50S} , and LC_{50} (earthworm) for small molecule quaternary ammonium salt (benzalkonium chloride (BC)) were about 70, 150, and 150 mg per kilogram of dry soil, respectively. These results demonstrate that compared with BC, the environmental toxicity of PAM-QAS is significantly reduced, and it is safe for both fish and earthworms. [Conclusions] By simulating the effects of drugs infiltrating groundwater with rainwater and mixing with soil and water in practical production applications, LC_{50L} and LC_{50S} were introduced to evaluate the fish toxicity of soil leaching solutions and water/soil/drug mixtures, respectively. A more accurate environmental toxicity assessment method for PAM-QAS was thus established. This work covers several aspects, such as structure characterization and application of functional polymers, qualitative detection of polymeric drugs in complex environments, and environmental toxicity evaluation of drugs. It is comprehensive and exploratory to a certain extent and is conducive to improving students' comprehensive quality, scientific research, and innovation ability.

Key words: polyacrylamide quaternary ammonium salt; fluorescent group modification; soil adsorption characteristics; environmental toxicity evaluation

(编辑: 张文杰)

智慧可视化管理平台

万欣可视化维视(VIIS维视)智慧管理平台

· 挖掘数据价值 · 赋能综合治理 · 支撑建设决策 · 展示应用成效

应用成果
智慧展示数据

展示



建设管理
科学利用数据

利用

专项
建设

仪器
购置

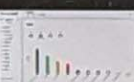
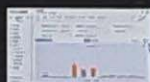
绩效
考核

数据
上报

安全
治理

统计报表
智能分析数据

分析



运行过程
采集使用数据

采集

安全
管控

资源
开放

实验
教学

物联
终端

整合治理
规范基础数据

规范

房间

人员

设备

耗材

安全
信息

万欣高校智慧实验室信息化管理



上海万欣计算机信息科技有限公司

A: 上海市虹口区花园路128号7街区A座3001 T: 400-008-1581 W: <http://www.wanxinsoft.com>



扫码关注万欣

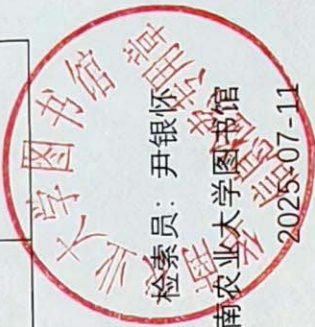
检索证明

根据委托人提供的论文材料，委托人华南农业大学材料与能源学院 林雅铃 1 篇论文收录情况如下表。

序号	论文名称	发表刊物及发表的年月卷期/页码等	作者排名	论文等级	作者工作单位	收录情况	影响因子	中科院大类分区
1	聚丙烯酰胺季铵盐大分子药物的环境毒性评价及其实验设计	实验技术与管理 出版年：2024 卷期： 页码： - 文献号： 文献类型：	第一作者	C 类	华南农业大学 材料与能源学院	北大核心	无	无

说明：论文等级和中科院大类分区按《华南农业大学学术论文评价方案（试行）》划分。

报告免责声明：如未盖章，报告无效



关于国家自然科学基金资助项目批准及有关事项的通知

林雅铃 先生/女士：

根据《国家自然科学基金条例》的规定和专家评审意见，国家自然科学基金委员会（以下简称自然科学基金委）决定批准资助您的申请项目。项目批准号：

31772202，项目名称：两亲性大分子季铵盐的合成及其对水稻纹枯病菌的抑制作用与机理，直接费用：55.00万元，项目起止年月：2018年01月至2021年12月，有关项目的评审意见及修改意见附后。

请尽早登录科学基金网络信息系统（<https://isisn.nsfc.gov.cn>），获取《国家自然科学基金资助项目计划书》（以下简称计划书）并按要求填写。对于有修改意见的项目，请按修改意见及时调整计划书相关内容；如对修改意见有异议，须在计划书电子版报送截止日期前提出。**注意：请严格按照《国家自然科学基金资助项目资金管理办法》填写计划书的资金预算表，其中，劳务费、专家咨询费科目所列金额与申请书相比不得调增。**

计划书电子版通过科学基金网络信息系统（<https://isisn.nsfc.gov.cn>）上传，由依托单位审核后提交至自然科学基金委进行审核。审核未通过者，返回修改后再行提交；审核通过者，打印为计划书纸质版（一式两份，双面打印），由依托单位审核并加盖单位公章后报送至自然科学基金委项目材料接收工作组。计划书电子版和纸质版内容应当保证一致。

向自然科学基金委提交和报送计划书截止时间节点如下：

- 1、提交计划书电子版截止时间为**2017年9月11日16点**（视为计划书正式提交时间）；
- 2、提交计划书电子修改版截止时间为**2017年9月18日16点**；
- 3、报送计划书纸质版截止时间为**2017年9月26日16点**。

请按照以上规定及时提交计划书电子版，并报送计划书纸质版，未说明理由且逾期不报计划书者，视为自动放弃接受资助。

附件：项目评审意见及修改意见表

国家自然科学基金委员会
生命科学部
2017年8月17日

表9 科研课题情况
林雅铃 主持的课题

序号	项目名称	评审等级	项目来源	合同经费/实到经费	立项时间	结题时间	课题组总人数	本人排名	是否结题	备注
1	两亲性大分子季铵盐的合成及其对水稻纹枯病菌的抑制作用与机理	A	国家自然科学基金委员会	65.0	2017-08-17	2021-12-31	4	1	是	

科技处审核人及盖章：

年 月 日



201704020084

广州市科技计划项目合同书

批文号:穗科创字(2017)107号

项目编号: 201704020084

广州市科技计划项目 合同书

(前期资助一次性拨付类)

项目名称: 两亲性大分子季铵盐的合成及其在水稻纹枯病防治中的应用研究

计划类别: 产学研协同创新重大专项

专题名称: 民生科技研究

起止时间: 2017-05-01到2019-12-31

承担单位: 华南农业大学材料与能源学院

组织单位: 华南农业大学

责任处室: 社基处

填表日期: 2017-01-17 19:07

广州市科技创新委员会制
(2016年版)



201704020084

广州市科技计划项目合同书

一、项目基本信息表

项目名称		两亲性大分子季铵盐的合成及其在水稻纹枯病防治中的应用研究					
研究类别/所属技术领域		农业与食品/农业生产资料/农药的研制与生产					
承担单位	名称	华南农业大学材料与能源学院					
	通信地址	广州市天河区五山路483号					
	邮政编码	510642	传真	02085282366			
	单位特性	其他	单位类型				
	组织机构代码	45541656-3	统一社会信用代码	暂无			
	法定代表人	陈晓阳	电子邮箱	linyaling@scau.edu.cn			
	联系人	房翊	联系电话	13380055703			
参加单位	序号	名称	单位类型	分工	联系人	联系电话	
	1	华南理工大学	高等院校	(参见项目承担单位与参与单位合作内容)	张安强	133 188 188 95	
(一) 项目负责人							
姓名	林雅铃	性别	女	出生年月	1978-07-15		
国籍	中国	民族	汉族	学位授予国家(或地区)	中国		
学历	博士研究生	学位	博士	手机号码	13380097023		
证件名称	身份证	证件号码	350123197807150045	固定电话	020-85280319		
职务	副教授	职称	副高	电子邮箱	linyaling@scau.edu.cn		



广州市科技计划项目合同书

八、合同书各方签章

签订地点：广州市越秀区

广州市科技创新委员会（甲方）：

项目经办人（签章）

胡宁

联系电话

83124044

责任处室负责人（签章）

华国彭

（公章）



2017月-06-05

项目承担单位（乙方）：华南农业大学材料与能源学院

项目负责人（签章）

林雅玲

财务负责人（盖章）

郑晓月

财务负责人联系电话：

8128)402

帐户名：华南农业大学

帐号：3602002609000310520

开户银行：中国工商银行广东省广州市五山支行

法定代表人：（签章）

（Signature）

（公章）

2017年3月22日

组织单位（丙方）：华南农业大学

项目经办人（签章）

（Signature）

（公章）

2017年3月22日

表9 科研课题情况
林雅铃 主持的课题

序号	项目名称	评审等级	项目来源	合同经费/实到经费	立项时间	结题时间	课题组总人数	本人排名	是否结题	备注
1	两亲性大分子季铵盐的合成及其在水稻纹枯病防治中的应用研究	A	广州市科技局	100.0	2017-04-27	2019-12-31	5	1	是	

科技处审核人及盖章：

年 月 日

受理编号: c1630550100241

项目编号: 2016A020210105

文件编号: 粤科规财字(2016)47号



2016A020210105

广东省省级科技计划项目 合同书

项目名称: 两亲性聚硅氧烷接枝季铵盐的合成及其在香蕉枯萎病防治中的应用

计划类别: 农村科技领域

项目起止时间: 2016-01-01 至 2018-12-31

管理单位(甲方): 广东省科学技术厅

承担单位(乙方): 华南农业大学

乙方主管部门(丙方): 华南农业大学

通讯地址: 广东省广州市天河区五山路483号

邮政编码: 510642

单位电话: 020-38632819

项目负责人: 林雅铃

联系电话: 020-38297109

项目联系人: 林雅铃

联系电话: 020-38297109

广东省科学技术厅
二〇一四年制

九、本合同签约各方

管理单位（甲方）：广东省科学技术厅（盖章）

单位地址：广东省广州市连新路171号

法定代表人（或授权代表）：黄宁生

联系人（经办人）姓名：刘世伟

Email: liusw@gdstc.gov.cn

电话：020-83163909



2015年 9月 1日

承担单位（乙方）：华南农业大学

（盖章）

二级部门：华南农业大学材料与能源学院

单位地址：广东省广州市天河区五山路483号

法定代表人（或法人代理）：陈晓阳

联系人（项目主管）姓名：石睿

Email: 77909213@qq.com

电话：020-85283435

开户单位名称：华南农业大学

开户银行及帐号：广东广州工行五山支行 3602002609000310520

（签章）
（签章）



2015年 9月 1日

乙方主管部门（丙方）：华南农业大学

（盖章）

单位地址：广东省广州市天河区五山路483号

法定代表人（或法人代理）：陈晓阳

联系人（项目主管）姓名：石睿

Email: 77909213@qq.com

电话：020-85283435

开户单位名称：华南农业大学

开户银行及帐号：广东广州工行五山支行 3602002609000310520

（签章）
（签章）



2015年 9月 1日

表9 科研课题情况
林雅铃 主持的课题

序号	项目名称	评审等级	项目来源	合同经费/实到经费	立项时间	结题时间	课题组总人数	本人排名	是否结题	备注
1	两亲性聚硅氧烷接枝季铵盐的合成及其在香蕉枯萎病防治中的应用	B	广东省科技厅	15.0	2016-04-22	2018-12-31	3	1	是	

科技处审核人及盖章：

年 月 日

教育部科技发展中心

[首 页](#) | [机构设置](#) | [科研基金](#) | [科技奖励](#) | [科技成果](#) | [产学研合作](#) | [大学科技园](#) | [科技产业化](#) | [计量认证](#) | [教育信息化](#)

2023年5月24日 星期三 [\[公告\]](#) [·2021年《中国教育网络》杂志征订函](#) [·2021年《中国高校科技》杂志征订](#)  站内搜索:

您的位置: [首页](#) >> [中心工作动态](#)

2012年博士点基金立项课题公布

来源: 教育部科技发展中心

发布时间: 2012-12-18

访问次数:

【字体: 大 中 小】

2012年度高等学校博士学科点专项科研基金课题评审工作结束, 现将批准项目公布。

2012年12月18日

附件: [2012年博士点基金资助课题名单-博导类](#)

[2012年博士点基金资助课题名单-新教师类](#)

[2012年博士点基金资助课题名单-优先发展领域](#)

[2012年博士点基金资助课题名单-与香港研资局研究用途补助金合作项目资助课题](#)


相关信息

没有相关信息

[打印本页](#)

[关闭窗口](#)

客户服务信箱 Fax: 010-62514678 京ICP备: 05004627号

 京公网安备 11040202430024号

位来客

Copyright © 2007-2012 版权所有: 教育部科技发展中心 未经书面许可 不得转载本站信息



2012年度高等学校博士学科点专项科研基金资助课题名单（新教师类）						
序号	课题编号	课题名称	申请学校	申请人	学科组名称	资助额度 (万元)
1						
2						
3	20120001120097	Hermite 向量丛的半稳定性	北京大学	陈华一	数学	4
4	20120001120098	三维流形的福勒结构及应用	北京大学	王家军	数学	4
485	20123702120014	基于Ren的实时及组成连接性建模与验证片 测填补灌条件下小麦水氮高效利用的生理机 制研究	山东农业大学	石玉	农林渔牧一组	4
486	20124306120006	异源四倍体鲫鲫雌核发育后代的遗传和生殖 特性研究	湖南师范大学	覃钦博	农林渔牧一组	4
487	20124320120001	稻米蛋白质基因QD6的精细定位与克隆	湖南农业大学	雷东阳	农林渔牧一组	4
488	20124404120002	基于无线地下传感网的中尺度土壤含水量测 定方法	华南农业大学	徐兴	农林渔牧一组	4
489	20124404120007	水稻稻瘟病抗性基因Pik-m抗病机理的研究	华南农业大学	王加峰	农林渔牧一组	4
490	20124404120008	林木根系形态特征对稳态营养供应的响应机 理研究	华南农业大学	何茜	农林渔牧一组	4
491	20124404120009	同步深施肥机械精量穴直播水稻的氮素利用 效率研究	华南农业大学	潘圣刚	农林渔牧一组	4
492	20124404120011	硅提高大豆白粉病抗性的分子机制研究	华南农业大学	沈雪峰	农林渔牧一组	4
493	20124404120025	甜菜碱型两性离子聚合物的合成及其在甜菜 夜蛾无公害防治中的应用	华南农业大学	林雅铃	农林渔牧一组	4
494	20124404120031	水稻细菌性基腐病菌zeamine毒素基因簇的 结构来源及关键基因的功能分析	华南农业大学	周佳暖	农林渔牧一组	4
495	20125103120008	组蛋白甲基转移酶基因Lhd1调控的水稻开花 分子机制研究	四川农业大学	孙昌辉	农林渔牧一组	4
496	20125103120011	锌指蛋白基因OsGCZ2在水稻稻瘟病致病过程 中的调控机制	四川农业大学	李伟滔	农林渔牧一组	4
497	20125103120018	亚热带天然次生林地下碳循环过程对氮沉降 的响应	四川农业大学	涂利华	农林渔牧一组	4
498	20126518120002	干旱胁迫下棉花叶黄素循环的响应机制及与 抗性的关系	石河子大学	张亚黎	农林渔牧一组	4
499	20120008120001	降解吸吐毒素有益菌的筛选及其在饲料单端 孢霉烯类毒素降解中的应用	中国农业大学	赵丽红	农林渔牧二组	4
500	20120014120004	农作物秸秆纤维素素清洁分离及功能产品制备 研究	北京林业大学	王堃	农林渔牧二组	4
501	20120014120006	纳米纤维素基高强度水凝胶制备研究	北京林业大学	杨俊	农林渔牧二组	4

表9 科研课题情况
林雅铃 主持的课题

序号	项目名称	评审等级	项目来源	合同经费/实到经费	立项时间	结题时间	课题组总人数	本人排名	是否结题	备注
1	甜菜碱型两性离子聚合物的合成及其在甜菜夜蛾无公害防治中的应用	B	教育部	4.0	2012-12-28	2015-12-31	9	1	是	

科技处审核人及盖章：

年 月 日

项目编号： 201803020015

广州市科技计划项目 合同书

项目名称： 含聚硅氧烷两亲性大分子季铵盐的合成及其在香蕉枯萎病防治中的应用

计划类别： 民生科技攻关计划

专题名称： 都市型现代农业专题

起止时间： 2018年04月01日 至 2021年03月31日

承担单位： 华南理工大学

组织单位： 华南理工大学

责任处室： 社会发展与基础研究处

填表日期： 2018年02月13日

广州市科技创新委员会
(2017年版)

八、项目承担单位（乙方）与合作单位合作内容

承担单位名称：华南理工大学

任务分工：材料合成与结构表征、材料物理性能表征与生物相容性测试

知识产权分配：双方共享

市科创委经费分配额度（万元）：65.00

自筹经费出资额度（万元）：0.00



合作单位（1）名称：华南农业大学

任务分工：材料生物相容性表征、抑菌实验与抑菌机理与盆栽实验等

知识产权分配：双方共享

市科创委经费分配额度（万元）：35.00

自筹经费出资额度（万元）：0.00



九、合同书各方签章

签订地点：广州市越秀区

广州市科技创新委员会（甲方）：广州市科技创新委员会

项目经办人（签章）：

秀珍

联系电话：

83124044

责任处室负责人（签章）

华国彭



章)

2018-05-10日

项目承担单位（乙方）：华南理工大学

二级部门：华南理工大学材料科学与工程学院

项目负责人（签章）：

张华

财务负责人（签章）：

马红

财务负责人联系电话：87110372

帐户名：华南理工大学

帐号：3602002609000733759

开户银行：工行广州五山支行

法定代表人（签章）：

王迎军



组织单位（丙方）：华南理工大学

项目经办人（签章）：

吴婷婷



联合申报项目协议书

甲方：华南理工大学

乙方：华南农业大学

甲方与乙方经友好协商决定联合申报 2018 年度 广州市科技计划项目(民生科技攻关计划项目) 项目，项目名称：含聚硅氧烷两亲性大分子季铵盐的合成及其在香蕉枯萎病防治中的应用研究。并达成如下合作协议：

第一条：项目研究工作详细分工：

甲方(主持方)：材料合成与结构表征、材料物理性能表征与生物相容性测试；

乙方(参与方)：材料物理性能表征、抑菌实验与抑菌机理、盆栽实验等。

第二条：经费分配：

1、如果本申报项目获批立项，按政府下达的资助经费，甲方、乙方同意此经费分别按政府资助经费的甲方：65 %、乙方：35 % 进行分配。

2、甲方在收到 广州市科技创新委员会 下达的资助经费后的一个月将乙方所占经费支付给乙方指定帐户。

账 户：华南农业大学

帐 号：3602002609000310520

开户行：工商银行广州五山支行

第三条：企业配套经费比例：

无。

第四条：知识产权归属：

1. 项目实施过程中所产生的知识产权，优先执行任务下达单位的知识产权管理政策，在此前提下，作如下规定：

①各方独立完成的所有权归各自所有；双方共同完成的由双方共享，具体按照双方的贡献大小进行分配或双方另行商定。

②项目成果的转让，须在双方同意的前提下进行，任何一方不得私自转让或许可实施。

2. 项目成果申报各级奖项，双方单位排名根据具体情况另行商定，人员排

名原则上按贡献大小先后排名。

第五条：合作项目各方应严格遵守共同签订的合作协议书，除因不可抗拒的客观原因，不得中途撤消或中止合同。在合同期内，某方要求修改合同条款，须各方协商，确认后方能生效。

第六条：如合作方因各种原因无法履行合同条款时，由项目负责人报项目主管部门同意后，另寻合作者。

第七条：经批准中途退出合作的一方，应视具体情况将所余经费退回项目主持方，已用经费由项目负责人提出审查报告，报项目主管部门审批。

第八条：合作一方在工作进行中有问题不及时报告，影响项目整体的年度进展者，项目负责人有权缓拨或停拨下一年度经费，并通报项目主管部门。如影响项目整体无法完成者，将承担相关责任，并报主管部门。

第九条：本协议自双方签字盖章之日起生效，至项目完成之日起终止；若合作申请未获资助，本协议自动废止。

大
农
业
科
技
合
同
专
用
章

甲方单位（盖章）：

委托代理人：

项目负责人（签字）：

2017年6月9日

吴婷婷
张书强

乙方单位（盖章）：

委托代理人：

项目负责人（签字）：

2017年6月9日

大
农
业
科
技
合
同
专
用
章
(1)
林明论

表9 科研课题情况
林雅铃 主持的课题

序号	项目名称	评审等级	项目来源	合同经费/实到经费	立项时间	结题时间	课题组总人数	本人排名	是否结题	备注
1	含聚硅氧烷两亲性大分子季铵盐的合成及其在香蕉枯萎病防治中的应用	C	广州市科技局	35.0	2017-10-31	2021-12-31	5	1	是	

科技处审核人及盖章：

年 月 日

受理编号: c23140500001255

项目编号: 2023A1515011264

文件编号: 粤基金字(2023)2号

广东省基础与应用基础研究基金项目 任务书

项目名称: 基于微区分离与动态可逆键的人工心脏瓣膜用超分子弹性体

项目类别: 广东省自然科学基金-面上项目

项目起止时间: 2023-01-01 至 2025-12-31

管理单位(甲方): 广东省基础与应用基础研究基金委员会

依托单位(乙方): 华南理工大学

通讯地址: 广东省广州市天河区广州市天河区五山路381号

邮政编码: 510640

单位电话: 020-87110630

项目负责人: 张安强

联系电话: 020-87112466



(广东科技微信公众号)



(查看任务书信息)



(受理纸质材料二维码)

广东省基础与应用基础研究
基金委员会
二〇二〇年制

五、人员信息

项目负责人

姓名	证件号码	年龄	性别	职称	学历	在项目中承担的任务	所在单位	签名
张安强	432831197610172419	47	男	教授	博士研究生	项目负责人	华南理工大学	张安强

项目组主要成员

姓名	证件号码	年龄	性别	职称	学历	在项目中承担的任务	所在单位	签名
林雅铃	350123197807150045	45	女	副教授	博士研究生	生物相容性与血流动力学评价	华南农业大学	林雅铃
黄皓浩	330222197412061975	49	男	副教授	博士研究生	材料结构表征	华南理工大学	黄皓浩
吴雄辉	430424199409138210	29	男	未取得	博士研究生	材料合成、结构表征与生物相容性评价	华南理工大学	吴雄辉
单世洁	370202199604201128	27	女	未取得	博士研究生	材料合成与结构表征	华南理工大学	单世洁
夏宇	36062220001205003x	23	男	未取得	本科	材料合成、生物相容性与血流动力学评价	华南理工大学	夏宇

六、工作分工及财政经费分配

承担/参与单位名称 (盖章)	工作分工	省级财政科技资金分配 (万元)
华南理工大学	材料合成与结构分析、瓣膜制备	7.00
华南农业大学	生物相容性评价与血流动力学测试。	3.00
	合计	10.00

2023 年度广东省自然科学基金项目申报合作协议书

甲方：华南理工大学

乙方：华南农业大学

甲乙双方本着相互协作的精神，合作申报 2023 年广东省自然科学基金面上项目，项目名称“基于微区分离与动态可逆键的人工心脏瓣膜用超分子弹性体”，经过协商达成如下协议，并由双方共同恪守。

一、 双方负责人：

甲方 华南理工大学 为项目依托单位，项目负责人为 张安强。

乙方 华南农业大学 为项目合作单位，合作方联系人为 林雅铃。

二、 研究分工：

甲方：材料合成与结构表征；

乙方：材料生物相容性与动物实验研究。

三、 研究成果归属：各自所有。

四、 经费分配：

该项目申请经费 10 万元，甲方经费比例 70 %，乙方经费比例 30 %。

本协议一式两份。若本项目未被批准，该协议自动失效；若项目获批，则甲乙双方根据实际获批经费，重新签订正式合作任务书。

甲方：华南理工大学

法人代表/委托代理人：

项目负责人（签章）：

张安强

联系电话：13318818895

2022 年 8 月 18 日

乙方：华南农业大学

法人代表/委托代理人：

项目负责人：

林雅铃

联系电话：13380097023

2022 年 8 月 18 日

科技合同-20230146

表9 科研课题情况
林雅铃 主持的课题

序号	项目名称	评审等级	项目来源	合同经费/实到经费	立项时间	结题时间	课题组总人数	本人排名	是否结题	备注
1	基于微区分离与动态可逆键的人工心脏瓣膜用超分子弹性体	按照个人到位经费定级	广东省基础与应用基础研究基金委员会	3.0	2023-01-01	2025-12-31	1	1	否	

科技处审核人及盖章：

年 月 日

项目编号：20240010

华南理工大学

广东省高性能与功能高分子材料重点实验室开放基金 项目合同书

项目名称：人工心脏瓣膜用抗凝抗钙化聚氨酯弹性体

项目负责人：林雅铃

联系电话：13380097023

起止年月 2024 年 6 月 至 2025 年 5 月

广东省高性能与功能高分子材料重点实验室学术委员会

- 第三条 甲方所设开放基金项目资金来源是其承担的广东省科学技术厅“广东省高性能与功能高分子材料重点实验室开放运行”项目经费，按照科研项目经费管理办法，甲方财务处已扣科研管理费、公摊水电费等间接费用。乙方在收到甲方转入的开放基金课题费用时，不能再重复扣管理费、水电费等任何间接费用。
- 第四条 乙方项目负责人务必于每年十二月底前，报送《广东省高性能与功能高分子材料重点实验室开放基金科研资助计划项目年度进展报告》。
- 第五条 乙方阶段性研究成果或最终研究成果，在出版或发表时，必须注明“广东省高性能与功能高分子材料重点实验室开放基金资助”（英文：The Open Fund for Key Lab of Guangdong High Property and Functional Macromolecular Materials, China）字样。否则，此成果不能视作本项目成果，不予结题。
- 第六条 乙方研究工作完成后必须及时结题，填写《广东省高性能与功能高分子材料重点实验室开放基金资助计划项目总结报告》。
- 第七条 乙方若不能按上述条款执行，未按期完成项目，将终止经费使用，在三年内不得申请新项目。
- 第八条 本合同正式文本一式肆份，甲、乙方各持贰份，自签约之日起生效，各合同具有同等法律效力。

甲方：华南理工大学

签字：

盖章：

乙方：华南农业大学

签字：

盖章：

乙方银行账户信息：汇款时请注明：林雅铃华工省重开放基金项目经费）

账户户名：华南农业大学

银行账号：3602 0026 0900 0310 520

开户银行：中国工商银行广州五山支行

签约日期 年 月 日

表9 科研课题情况
林雅铃 主持的课题

序号	项目名称	评审等级	项目来源	合同经费/实到经费	立项时间	结题时间	课题组总人数	本人排名	是否结题	备注
1	人工心脏瓣膜用抗凝抗钙化聚氨酯弹性体		其他纵向	2.0	2024-06-30	2025-05-31	1	1	否	

科技处审核人及盖章：

年 月 日

合同编号:

技术服务合同

项目名称: 聚合物材料的生物相容性评价

委托方: 华南理工大学
(甲方)

受托方: 华南农业大学
(乙方)

签订时间: 2022年6月 日

签订地点: 广州市

有效期限: 2022年6月15日至2023年12月31日

中华人民共和国科学技术部印制

填 写 说 明

一、本合同为中华人民共和国科学技术部印制的技术服务合同示范文本，各技术合同认定登记机构可推介技术合同当事人参照使用。

二、本合同书适用于一方当事人（受托方）以技术知识为另一方（委托方）解决特定技术问题所订立的合同。

三、签约一方为多个当事人的，可按各自在合同关系中的作用等，在“委托方”、“受托方”项下（增页）分别排列为共同委托人或共同受托人。

四、本合同书未尽事项，可由当事人附页另行约定，并作为本合同的组成部分。

五、当事人使用本合同书时约定无需填写的条款，应在该条款处注明“无”等字样。

技术服务合同

委托方（甲方）： 华南理工大学

住 所 地： 广州市天河区五山路 381 号

法定代表人： 高松

项目联系人： 张安强

联系方式：

通讯地址： 广州市天河区五山路 381 号

电 话： 020-87112466 传真：

电子信箱：

受托方（乙方）： 华南农业大学

住 所 地： 广州市天河区五山路

法定代表人： 刘雅红

项目联系人： 林雅铃

联系方式

通讯地址： 广州市天河区五山路 483 号

电 话： 13380097023 传 真：

电子信箱： linyaling@scau.edu.cn

本合同甲方委托乙方就 聚合物材料的生物相容性评价 项目进行的专项技术服务，并支付相应的技术服务报酬。双方经过平等协商，在真实、充分地表达各自意愿的基础上，根据《中华人民共和国合同法》的规定，达成如下协议，并由双方共同恪守。

1. 技术背景资料：无；
2. 可行性论证报告：无；
3. 技术评价报告：无；
4. 技术标准和规范：无；
5. 原始设计和工艺文件：无；
6. 其他：无；

第十五条：双方约定本合同其他相关事项为：无。

第十六条：本合同一式肆份，具有同等法律效力。

第十七条：本合同经双方签字盖章后生效。

甲方：华南理工大学（盖章）

法定代表人 / 委托代理人：高晓明（签名）

年 月 日

经办人：丁楚怡

乙方：华南农业大学（盖章）

法定代表人 / 委托代理人：刘雅红（签名）

年 月 日

印花税票粘贴处：



(以下由技术合同登记机构填写)

合同登记编号：

--	--	--	--	--	--	--	--	--	--	--	--	--	--	--	--

1. 申请登记人：_____

2. 登记材料：(1) _____

(2) _____

(3) _____

3. 合同类型：_____

4. 合同交易额：_____

5. 技术交易额：_____

技术合同登记机构（印章）

经办人：

年 月 日



表9 科研课题情况
林雅铃 主持的课题

序号	项目名称	评审等级	项目来源	合同经费/实到经费	立项时间	结题时间	课题组总人数	本人排名	是否结题	备注
1	聚合物材料的生物相容性评价		横向	6.0	2022-06-13	2023-12-31	2	1	是	

科技处审核人及盖章：

年 月 日

HX1GHT2024.879

合同编号：

技术开发（合作）合同

项目名称： 覆铜板基板树脂材料的开发研究

甲方： 湖南方锐达科技有限公司

乙方： 华南农业大学

签订时间： 2024 年 7 月 日

签订地点： 湖南省浏阳市经开区康平路 175 号

有效期限： 2024 年 7 月 15 日至 2026 年 7 月 15 日

中华人民共和国科学技术部印制

任一方违反本条，守约方有权终止本合同且无须承担违约责任，且违约方应立即停止违约行为，如导致另一方声誉受损或经济损失的，违约方应当同时承担相应的损害赔偿责任，守约方保留进一步追究违约方法律责任的权利。

第十八条 合作各方约定本合同其他相关事项为：为有效履行本合同，合作各方确定，在本合同有效期内，甲方指定李玉新为甲方项目联系人，乙方指定林雅铃为乙方项目联系人。项目联系人承担以下责任：

1. 及时联络双方项目进展工作，组织双方研讨会；
 2. 一方变更项目联系人的，应当及时并以书面形式通知其合作方。
- 未及时发现并影响本合同履行或造成损失的，应承担相应的责任。

第十九条 本合同一式四份，具有同等法律效力。

第二十条 本合同经合作各方签字盖章后生效。

甲方：湖南方锐达科技有限公司 (盖章)

法定代表人/委托代理人：林雅铃 (签名)

2024年7月5日

乙方：华南农业大学 (盖章)

法定代表人/委托代理人：林雅铃 (签名)

年 月 日

表9 科研课题情况
林雅铃 主持的课题

序号	项目名称	评审等级	项目来源	合同经费/实到经费	立项时间	结题时间	课题组总人数	本人排名	是否结题	备注
1	覆铜板基板树脂材料的开发研究		横向	30.0	2024-07-05	2026-07-15	1	1	否	

科技处审核人及盖章：

年 月 日

表9 科研课题情况
林雅铃 参与的课题

序号	项目名称	评审等级	项目来源	合同经费/实到经费	立项时间	开始时间	结题时间	负责人	课题组总人数	本人排名	是否结题
1	基于抑制昆虫雌性生殖干细胞分化活性的骆驼蓬碱构效关系研究		教育部	12.0	2013-10-28	2014-01-01	2016-12-31	钟国华	9	3	是

科技处审核人及盖章：

年 月 日

检索证明

根据委托人提供的论文材料，委托人华南农业大学材料与能源学院 林雅铃 9 篇论文收录情况如下表。

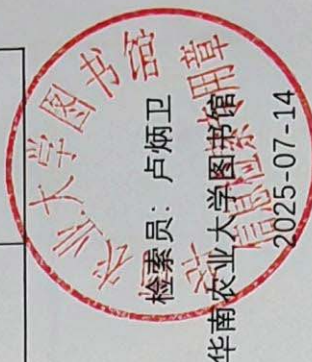
序号	论文名称	发表刊物及发表的年月卷期/页码等	作者排名	论文等级	作者文中单位	收录情况	影响因子	中科院大分类区
1	Synergistic enhancement of the robustness of multifunctional polyurethane via an ionic noncovalent cross-linking network and aromatic disulfides	CHEMICAL ENGINEERING JOURNAL 出版年: 2024 出版日期: FEB 1 卷期: 481 页码: - 文献号: 148229 文献类型: Article	第一作者, 共同通讯作者	T2 类	华南农业大学 材料与能源学院	SCI	IF2-year=13.2 IF5-year=13.5 (2024)	材料科学 1 区 Top 期刊: 是 (2025)
2	Surface-Imprinted Polysiloxane with Recognition Ability Based on an ITO Layer for Rapid Detection of Fusarium oxysporum f. sp. cubense by the Naked Eye	ACS APPLIED MATERIALS & INTERFACES 出版年: 2024 出版日期: JUN 21 卷期: 16 26 页码: 33182-33191 文献类型: Article	第一作者, 共同通讯作者	A 类	华南农业大学 材料与能源学院	SCI	IF2-year=8.2 IF5-year=8.5 (2024)	材料科学 2 区 Top 期刊: 否 (2025)
3	Amphiphilic polysiloxane graft guanidine salts with a combination of low environmental toxicity and high antifungal activity	EUROPEAN POLYMER JOURNAL 出版年: 2024 出版日期: AUG 7 卷期: 216 页码: -	第一作者, 共同通讯作者	A 类	华南农业大学 材料与能源学院	SCI	IF2-year=6.3 IF5-year=6.0 (2024)	化学 2 区 Top 期刊: 否 (2025)

	文献号: 113258 文献类型: Article								
4	Fluorine-containing amphiphilic quaternary ammonium salts for the suppression of Banana fusarium wilt	REACTIVE & FUNCTIONAL POLYMERS 出版年: 2023 出版日期: JAN 卷期: 182 页码: - 文献号: 105488 文献类型: Article	第一作者, 共同 通讯作者			华南农业大学 材料与能源学院	SCI	IF2-year=4.5 IF5-year=4.1 (2023)	工程技术 3 区 Top 期刊: 否 (2023)
5	Polymeric diallyl quaternary ammonium salts for inhibiting banana Fusarium wilt	REACTIVE & FUNCTIONAL POLYMERS 出版年: 2022 出版日期: MAR 卷期: 172 页码: - 文献号: 105174 文献类型: Article	第一作者, 共同 通讯作者			华南农业大学 材料与能源学院	SCI	IF2-year=5.1 IF5-year=4.3 (2022)	工程技术 3 区 Top 期刊: 否 (2022)
6	Molecularly Imprinted Photonic Crystals Based on Fusaric Acid for the Detection of Banana Fusarium Wilt	ACS APPLIED POLYMER MATERIALS 出版年: 2021 出版日期: NOV 12 卷期: 3 11 页码: 5818-5825 文献类型: Article	第一作者, 共同 通讯作者			华南农业大学 材料与能源学院	SCI	IF2-year=4.855 IF5-year=4.855 (2021)	化学 3 区 Top 期刊: 否 (2021)

7	The interactions between bovine serum albumin and carboxybetaine-functionalized polysiloxanes in solution	COLLOID AND POLYMER SCIENCE 出版年: 2016 出版日期: DEC 卷期: 294 12 页码: 2029-2037 文献类型: Article	第一作者, 共同通讯作者	B类	华南农业大学材料与能源学院	SCI	IF2-year=1.723 IF5-year=1.749 (2016)	化学 3区 Top 期刊: 否 (2016)
8	Synthesis and antimicrobial activities of polysiloxane-containing quaternary ammonium salts on bacteria and phytopathogenic fungi	REACTIVE & FUNCTIONAL POLYMERS 出版年: 2014 出版日期: DEC 卷期: 85 页码: 86-44 文献类型: Article	第一作者, 共同通讯作者	A类	华南农业大学资源与环境学院	SCI	IF2-year=2.515 IF5-year=2.535 (2014)	工程技术 2区 Top 期刊: 否 (2014)
9	多臂星形聚乙二醇-聚乳酸嵌段共聚物的降解特性	高分子材料科学与工程 出版年: 2013 卷期: 页码: - 文献号: 文献类型:	第一作者, 通讯作者	B类	华南农业大学资源与环境学院	北大核心	无	无

说明: 论文等级和中科院大类分区按《华南农业大学学位论文评价方案(试行)》划分。

报告免责声明: 如未盖章, 报告无效



检索证明

根据委托人提供的论文材料，委托人华南农业大学材料与能源学院 林雅铃 20 篇论文收录情况如下表。

序号	论文名称	发表刊物及发表的年月卷期/页码等	作者排名	论文等级	作者文中单位	收录情况	影响因子	中科院大类分区
1	Polyacrylamide quaternary ammonium salts based on stable adsorption in soil and its application on the control of soil-borne fungal disease	EUROPEAN POLYMER JOURNAL 出版年: 2024 出版日期: JAN 5 卷期: 202 页码: - 文献号: 112604 文献类型: Article	共同通讯作者/倒数第一	A类	华南农业大学 材料与能源学院	SCI	IF2-year=6.3 IF5-year=6.0 (2024)	化学 2 区 Top 期刊: 否 (2025)
2	Simultaneously enhancing the mechanical robustness and conductivity of ionogels by in situ formation of coordination complexes as physical crosslinks	JOURNAL OF MATERIALS CHEMISTRY A 出版年: 2024 出版日期: MAY 21 卷期: 12 20 页码: 12134-12145 文献类型: Article	共同通讯作者	A类	华南农业大学 材料与能源学院	SCI	IF2-year=9.5 IF5-year=10.3 (2024)	材料科学 2 区 Top 期刊: 否 (2025)
3	Siloxane-based segmented poly(urethane-urea) elastomers with enhanced mechanical properties, hydrophobicity and anti-calcification based on hierarchical	EUROPEAN POLYMER JOURNAL 出版年: 2024 出版日期: SEP 18 卷期: 218 页码: - 文献号: 113349	共同通讯作者	A类	华南农业大学 材料与能源学院	SCI	IF2-year=6.3 IF5-year=6.0 (2024)	化学 2 区 Top 期刊: 否 (2025)

	phase separation for potential applications of polymeric heart valve	文献类型: Article							
4	The robustness waterproof ionogel based on the phase separation to form soft hard heterostructures and the interaction of cation-It realizes underwater adhesion and sensing	CHEMICAL ENGINEERING JOURNAL 出版年: 2024 出版日期: OCT 1 卷期: 497 页码: - 文献号: 155046 文献类型: Article	共同通讯作者		华南农业大学材料与能源学院	SCI	IF2-year=13.2 IF5-year=13.5 (2024)	材料科学 1 区 Top 期刊: 是 (2025)	
5	Prediction and Explanation of Properties in Multicomponent Polyurethane Elastomers: Integrating Molecular Dynamics and Machine Learning	MACROMOLECULES 出版年: 2024 出版日期: NOV 26 卷期: 57 23 页码: 10912-10925 文献类型: Article	共同通讯作者		华南农业大学材料与能源学院	SCI	IF2-year=5.2 IF5-year=5.2 (2024)	化学 1 区 Top 期刊: 是 (2025)	
6	Antifungal mechanisms of polymeric quaternary ammonium salts against conidia of <i>Fusarium oxysporum</i> f. sp. <i>cubense</i> , race 4	EUROPEAN JOURNAL OF PLANT PATHOLOGY 出版年: 2023 出版日期: FEB 卷期: 165 2 页码: 317-331 文献类型: Article	通讯作者		华南农业大学材料与能源学院	SCI	IF2-year=1.7 IF5-year=1.9 (2023)	农林科学 3 区 Top 期刊: 否 (2023)	

7	A systematic study on Zn(II)-Iminocarboxyl complexation applied in supramolecular PDMS networks	POLYMER 出版年: 2022 出版日期: MAY 26 卷期: 250 页码: - 文献号: 124896 文献类型: Article	共同通讯作者	A类	华南农业大学 材料与能源学院	SCI	IF2-year=4.6 IF5-year=4.2 (2022)	化学 2 区 Top 期刊: 否 (2022)
8	Tough, Self-Healing, Recyclable Bottlebrush Polyurethane Elastomer with a Skin-like Strain-Adaptive-Strengthening Property	ACS APPLIED POLYMER MATERIALS 出版年: 2022 出版日期: SEP 12 卷期: 4 10 页码: 7554-7563 文献类型: Article	共同通讯作者	A类	华南农业大学 材料与能源学院	SCI	IF2-year=4.6 IF5-year=5.1 (2022)	化学 2 区 Top 期刊: 否 (2022)
9	Perspective Article Polydimethylsiloxane-polymethacrylate block copolymers containing quaternary ammonium salts against Fusarium oxysporum f. sp. cubense race 4 in soil: Antifungal activities and pot experiments	REACTIVE & FUNCTIONAL POLYMERS 出版年: 2021 出版日期: MAR 卷期: 160 页码: - 文献号: 104848 文献类型: Article	共同通讯作者/倒数第一	B类	华南农业大学 材料与能源学院	SCI	IF2-year=4.966 IF5-year=4.266 (2021)	工程技术 3 区 Top 期刊: 否 (2021)
10	Stretchable, robust and reprocessable poly(siloxane-urethanes) elastomers based on exchangeable aromatic disulfides	POLYMER 出版年: 2021 出版日期: APR 14	共同通讯作者	A类	华南农业大学 材料与能源学院	SCI	IF2-year=4.432 IF5-year=4.161 (2021)	化学 2 区 Top 期刊: 否 (2021)

		卷期: 221 页码: - 文献号: 123588 文献类型: Article							
11	A solvent-free, transparent, self-healing polysiloxanes elastomer based on unsaturated carboxyl-amino ionic hydrogen bonds	POLYMER 出版年: 2021 出版日期: JUL 16 卷期: 228 页码: - 文献号: 123903 文献类型: Article	共同通讯作者	A类	华南农业大学材料与能源学院	SCI	IF2-year=4.432 IF5-year=4.161 (2021)	化学 2 区 Top 期刊: 否 (2021)	
12	Interpenetrating covalent adaptable networks with enhanced mechanical properties and facile reprocessability and recyclability	POLYMER CHEMISTRY 出版年: 2021 出版日期: JUL 28 卷期: 12 28 页码: 4052-4062 文献类型: Article	共同通讯作者 (倒数第一)	A类	华南农业大学材料与能源学院	SCI	IF2-year=5.364 IF5-year=5.056 (2021)	化学 2 区 Top 期刊: 否 (2021)	
13	超声细胞破碎法快速提取真菌中的麦角甾醇	南京农业大学学报 出版年: 2021 出版日期: 2021-05-31 11:32 卷期: 44 06 页码: 1090-1096 文献号: 文献类型: 期刊论文	通讯作者	B类	华南农业大学材料与能源学院	北大核心	无	无	

14	Reprocessability of dynamic polydioxaborolane networks activated by heat, moisture and mechanical force	POLYMER 出版年: 2020 出版日期: NOV 17 卷期: 209 页码: - 文献号: 123037 文献类型: Article	共同通讯作者/倒数第一	A类	华南农业大学材料与能源学院	SCI	IF2-year=4.43 IF5-year=4.186 (2020)	化学 2 区 Top 期刊: 否 (2020)
15	Anti-Rhizoctonia solani activity by polymeric quaternary ammonium salt and its mechanism of action	REACTIVE & FUNCTIONAL POLYMERS 出版年: 2018 出版日期: APR 卷期: 125 页码: 1-10 文献类型: Article	共同通讯作者/倒数第一	A类	华南农业大学材料与能源学院	SCI	IF2-year=3.074 IF5-year=3.076 (2018)	工程技术 2 区 Top 期刊: 否 (2018)
16	Polymeric quaternary ammonium salt activity against Fusarium oxysporum f. sp cubense race 4: Synthesis, structure-activity relationship and mode of action	REACTIVE & FUNCTIONAL POLYMERS 出版年: 2017 出版日期: MAY 卷期: 114 页码: 13-22 文献类型: Article	通讯作者	A类	华南农业大学材料与能源学院	SCI	IF2-year=2.975 IF5-year=2.843 (2017)	工程技术 2 区 Top 期刊: 否 (2017)
17	Controllable synthesis and antimicrobial activities of acrylate polymers containing quaternary ammonium salts	REACTIVE & FUNCTIONAL POLYMERS 出版年: 2017 出版日期: DEC 卷期: 121 页码: 110-118	共同通讯作者	A类	华南农业大学材料与能源学院	SCI	IF2-year=2.975 IF5-year=2.843 (2017)	工程技术 2 区 Top 期刊: 否 (2017)

	文献类型: Article							
18	The synthesis and protein resistance of amphiphilic PDMS-b-(PDMS-g-cysteine) copolymers	APPLIED SURFACE SCIENCE 出版年: 2017 出版日期: OCT 15 卷期: 419 页码: 393-398 文献类型: Article	共同通讯作者	A类	华南农业大学 材料与能源学 院	SCI	IF2-year=4.439 IF5-year=3.743 (2017)	工程技术 2区 Top 期刊: 是 (2017)
19	Synthesis and antimicrobial activities of acrylamide polymers containing quaternary ammonium salts on bacteria and phytopathogenic fungi	REACTIVE & FUNCTIONAL POLYMERS 出版年: 2015 出版日期: MAR 卷期: 88 页码: 39-46 文献类型: Article	通讯作者	A类	华南农业大学 材料与能源学 院	SCI	IF2-year=2.725 IF5-year=2.706 (2015)	工程技术 2区 Top 期刊: 否 (2015)
20	The synthesis and characterization of supramolecular elastomers based on linear carboxyl-terminated polydimethylsiloxane oligomers	POLYMER CHEMISTRY 出版年: 2014 卷期: 51 页码: 153-160 文献类型: Article	共同通讯作者	A类	华南农业大学 材料与能源学 院	SCI	IF2-year=5.52 IF5-year=5.723 (2014)	化学 2区 Top 期刊: 否 (2014)

说明: 论文等级和中科院大分区按《华南农业大学学位论文评价方案(试行)》划分。

报告免责声明: 如未盖章, 报告无效

检索员: 欧群

华南农业大学图书馆

2025-08-08



Synergistic enhancement of the robustness of multifunctional polyurethane via an ionic noncovalent cross-linking network and aromatic disulfides

Yaling Lin^{a,*}, Ning Yu^{b,1}, Shijie Shan^b, Anqiang Zhang^{b,*}

^a College of Materials and Energy, South China Agricultural University, 483 Wushan Rd., Guangzhou 510642, Guangdong, China

^b School of Materials Science and Engineering, South China University of Technology, 381 Wushan Rd., Guangzhou 510641, Guangdong, China

ARTICLE INFO

Keywords:

Ionic noncovalent cross-linking
Mechanical robustness
Self-healing
Recyclability
Multifunctionality

ABSTRACT

The preparation of functional polyurethane materials with high strength, toughness, and excellent self-healing ability is currently challenging. In this study, a multifunctional bi-dynamic supramolecular crosslinked network PU elastomer was successfully prepared by introducing ionic bonds and aromatic disulfide bonds into a PU matrix. The resulting ionic PU elastomers exhibited impressive mechanical properties, including high tensile strength (39.9 ± 4.4 MPa) and excellent elongation at break (1930 ± 345 %). They also demonstrated efficient self-healing capability (94.4 %), recyclability and processability. The distribution of hydrophilic ion bonds within the polymer networks enabled the elastomers to possess water-induced shape memory and antibacterial activity. Additionally, the hydrophilicity of the elastomers provided a self-cleaning ability when used as a coating material. The covalent bonding of the cations with the PU matrix prevented the leaching of bactericidal substances, ensuring good biocompatibility of the ionic PU. Furthermore, a double-layered self-healing composite flexible sensor was developed using the ionic PU as the substrate and carboxylated carbon nanotubes (CNTs-COOH) as the conductive medium to detect human motion. These multifunctional ionic PU elastomers offer great potential for the design and preparation of robust materials with self-healing ability for various applications across multiple fields.

1. Introduction

The development of society has increased the demand for versatile and progressive elastomer materials. PU elastomers have a wide range of raw materials and offer strong control over molecular structure. The unique 'microphase separation' structure of the molecular chain, consisting of soft and hard segments, provides excellent overall performance [1]. These elastomers have adjustable mechanical properties and can be easily produced [2]. They also possess shape memory [3], are non-toxic, highly transparent, and have found widespread applications in various technical fields such as biomedical [4], antifouling and antibacterial coatings [5], intelligent textiles [6], and flexible electronic devices [7–9]. However, due to the complexity and harshness of their usage environment, PU elastomers are susceptible to mechanical damage throughout their lifecycle. If such damage is not repaired promptly, it can lead to a rapid decline in performance and render them unusable. Therefore, integrating self-healing ability and recyclability into elastomers is considered a promising approach to enhance their lifespan,

reduce raw material consumption, and lower carbon emissions [10].

In recent years, researchers have focused on developing reversible dynamic covalent bonds, such as Diels-Alder crosslink bonds [11,12], imine bonds [13,14], acylhydrazone bonds [15,16], and intrinsic self-healing and recyclable elastomers with disulfide bonds [17–19]. Additionally, noncovalent interactions, including hydrogen bonds [20], metal coordinates [21], and ionic bonds [22,23], have also been explored. However, the mechanical strength of materials has often been overlooked in the pursuit of effective self-healing ability. Numerous studies have demonstrated the challenge of balancing the mechanical strength and self-healing properties [24–26]. To enhance the self-healing efficiency and mechanical strength of PU materials, researchers have proposed various strategies. Noncovalent bonds, such as supermolecular self-assembly bonds, offer advantages over covalent bonds due to their dynamic reversibility and physical cross-linking. These bonds can be destroyed and rebuilt, effectively dissipating energy and improving the flexibility, resilience, and self-healing performance of PU materials. Ureidopyrimidone (UPy) is a self-

* Corresponding authors.

E-mail addresses: linaling@scau.edu.cn (Y. Lin), aqzhang@scut.edu.cn (A. Zhang).

¹ These authors contribute equally.

complementary quaternary hydrogen bonding group that has the potential to enhance the mechanical strength and toughness of polymer networks. This is achieved by increasing the noncovalent cross-linking and sacrificial bonds. However, the synthesis of polyurethane or polyurea elastomers with UPy groups is complex and these materials have low solubility in common polar solvents. As a result, they are not suitable for large-scale production and preparation [27,28]. To address this limitation, researchers have proposed the incorporation of a dual dynamic mechanism into a single polymer system. This exciting concept aims to achieve synergistic effects between the two mechanisms, enhancing both self-healing and mechanical properties. Qin and colleagues [29] introduced diazoalkylurea (DU) and aromatic disulfide into the PU matrix to overcome the trade-off between mechanical robustness and room temperature self-healing. The strong hydrogen bonding cross-linking points improved the robustness of the cross-linking structure, while the rapid chemical decomposition of disulfide bonds contributed to the kinetics of the cross-linking network. The obtained PU elastomer had high tensile strength (14.08 MPa), high toughness (64.6 MJ/m³), and excellent self-healing ability (~81 % at room temperature). Sun et al. [21] investigated the combination of disulfide exchange and metal coordination interaction. The introduction of coordinate covalent bonds disrupted the hydrogen bond sequence, resulting in the destruction of the hard phase. This disruption was beneficial for disulfide exchange. The material exhibited a tensile strength of 9.4 ± 0.1 MPa and a self-healing efficiency of 96.6 ± 1.5 %. Wu et al. [30] synthesized a supramolecular elastomer with exceptional toughness (14.7 MJ/m³) and high tensile properties (1700 %) by incorporating strong metal coordinate covalent bonds and weak tetrahydrogen bonds into the molecule. However, the mechanical strength was only 2.6 MPa. Despite significant advancements in the development of high-strength, high-toughness self-healing materials in recent years, there are still numerous challenges in achieving simultaneous high strength, high toughness, and self-healing capabilities in polymer materials.

Ionic bonds, with their strong noncovalent bond interaction (50–250 kJ/mol), play a crucial role in enhancing energy dissipation through bond fracture, thereby toughening materials. However, there have been limited studies on how to enhance PU through interchain ionic bonds. In this study, we present a novel approach that involves the introduction of dynamic disulfide bonds, which contain rigid benzene ring structures, and ionic chain extenders into prepolymers. This leads to the formation of PU ionomers, enabling the development of room temperature self-healing and recyclable PU elastomers with exceptional mechanical strength. In this study, it was observed that ionic interactions displayed a higher interaction strength compared to the relatively weaker π - π stacking interactions and hydrogen bonds. The presence of ionic groups in the polymer matrix resulted in the formation of clusters, which in turn enhanced the physical crosslinking by dispersing within the soft polyester network domain [31]. The dithio diphenylamine, with its rigid structure consisting of two benzene rings, exhibited excellent double decomposition ability [32,33]. The PU elastomer obtained in this study demonstrated several desirable properties, including high tensile strength, toughness, self-healing ability, water-induced shape memory, antibacterial and antifouling properties, and other multifunctional properties. These properties were achieved through a combination of hydrogen bonds, ion interactions, and the dynamic disulfide effect, which induced the formation of soft and hard microphase separation structures in the network. Moreover, the PU elastomers showed good recyclability due to their reversible cross-linking structure, making them suitable for multiple cycles of use. Additionally, the potential application of ionic PU in wearable flexible electronic products was demonstrated by coating a layer of conductive CNT-COOH on the surface of the prepared flexible ionic PU matrix.

2. Experimental section

2.1. Materials

Polytetramethylene ether glycol (PTMG, $M_n = 2000$), isophorone diisocyanate (IPDI, 99 %), ditin butyl dilaurate (DBTDL, 95 %), 3-dimethylaminopropane-1,2-diol (DP, 98 %), 4,4'-thiodianiline (AFD, 98 %), *n*-butyl bromide (99.0 %), castor-oil and carboxylated multiwalled carbon nanotubes (CNTs-COOH, 95 % purity, length: 10–30 μ m, -COOH: ~3.9 wt%) were purchased from Shanghai Macklin Inc. *Escherichia coli* (*E. coli*), *Staphylococcus albus* (*S. albus*) and human fibroblast cells were provided by South China Agricultural University. Fluorescein isothiocyanate-labelled bovine serum albumin (FITC-BSA) was obtained from Solarbio Science & Technology Co., Ltd. (Beijing, China). Dulbecco's modified Eagle's medium (DMEM) and fetal bovine serum (FBS) were purchased from Hyclone (Thermo Fisher, USA). All chemicals were used without further purification.

2.2. Synthesis of QDP

DP (4.77 g, 40 mmol) and *n*-butyl bromide (8.22 g, 60 mmol) were dissolved in isopropanol (~50 mL) and added into a 100 mL three-neck round-bottom flask equipped with magnetic stirring and condensation reflux. The system was heated to 75 °C and stirred for 24 h in a N₂ atmosphere. Appropriate amounts of water and chloroform were added to the product for extraction, and the extraction was repeated to obtain the aqueous phase three times to fully extract the final product. The aqueous phase was evaporated to remove water, resulting in a transparent and colorless liquid. The sample was dried in a 60 °C oven for 12 h and had a yield of approximately 90 %. For convenience, this product was named QDP.

2.3. Synthesis of PU-QDP_x-SS

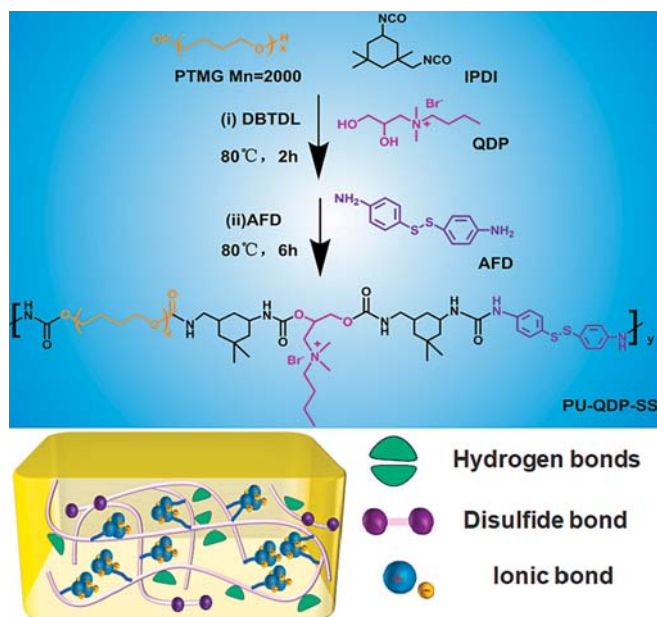
QDP was added dropwise to a mixture of IPDI and DBTDL in anhydrous N, N-dimethylformamide (DMF) (50 mL) at 80 °C for 2 h under stirring with the protection of a nitrogen atmosphere, and then AFD was added for another 6 h of reaction. The resultant mixture was poured into a mold and then maintained at 60 °C for 24 h. The obtained ionic PU were named PU-QDP_x-SS ($x = 3/1$ or $2/2$). The amount of each reactant is listed in Table S1. PU-DP_x-SS ($x = 3/1$ or $2/2$), PU-DP, PU-QDP and PU-SS were synthesized similarly. Their synthetic routes are shown in Scheme 1, Schemes S1 and S2.

2.4. Electrospinning of EPU-QDP_{3/1}-SS

A 10 mL medical syringe was used to draw 10-mL of a THF/DMF (1/1, v/v) PU-QDP_{3/1}-SS solution with a concentration of 10 % (w/w). The syringe was connected to the 19 # flat mouth spinneret, the positive and negative electrodes of the high-voltage power supply were connected to the positions of the nozzle and the receiving device, and the solution propulsion flow rate was controlled through a micro-injection pump. The extrusion rate was 3 mL/h. The positive voltage of spinning was 15 kV, the distance between the receiver and the spinneret was adjusted to 12 cm, and the electrospinning process lasted for 1 h at room temperature. After the spinning was completed, the collected nanofiber film was placed in a vacuum drying oven at 30 °C for 48 h and repeatedly weighed until the fiber film was at constant weight. Record the fiber membrane obtained by electrospinning as EPU-QDP_{3/1}-SS.

2.5. Fabrication of the self-healable electrode film

First, 10 mg of CNTs was added to 20 mL of ethanol and sonicated for 10 min to obtain a uniform dispersion. Second, the obtained CNT dispersion (1 g) was sprayed onto the surface of EPU-QDP_{3/1}-SS (40 mm \times 60 mm) using an air compressor equipped with a spray gun (DUN-30



Scheme 1. Schematic diagram of the preparation process of PU-QDP-SS.

L, Anjieshun, China) at a pressure of 0.5 MPa and a distance of 20 cm. The sample was placed in a 60 °C vacuum oven and cured for 24 h to remove residual solvents. The mold was peeled off to obtain a carbon nanotube ionic PU composite film, denoted as EPU-CNT.

2.6. Characterizations

The NMR spectra were obtained from a Bruker AVANCE III HD 600 using methanol- d_4 as the solvent. The FTIR spectra of the samples were acquired with a Thermo Nicolet iS5 spectrometer (Thermo Scientific, USA) with a ZnSe ATR accessory. The TGA curves were measured on a Netzsch TG 209 F1. The samples (~10 mg) were heated from 30 °C to 900 °C at a rate of 20 °C/min in a N_2 atmosphere. XRD measurements (D8 Advance, Bruker, Germany) were taken to determine the phase structure and composition of the ionic PU, with a 2 θ scanning range of 5–60°. Stress–strain curves were measured on a KJ-1067 tensile test machine with a controlled temperature and humidity chamber (Dongguan Kejian Instrument Co. Ltd., China). The measurements were carried out at room temperature at a stretching speed of 100 mm/min. At least three specimens were tested for each elastomer sample, and the average values with standard errors were calculated. For cyclic tensile tests, both loading and unloading processes were carried out at a strain rate of 100 mm min^{−1} at room temperature. The dissipated energy was evaluated from the closed area between the loading–unloading curves. The toughness was acquired by integrating the area under the stress–strain curves. DMA (dynamic mechanical thermal spectrometer) (Mettler Toledo Star 1 system) from Mettler Toledo was used to evaluate the dynamic properties. The measurements were carried out in a temperature range of −100 °C to 50 °C with a heating rate of 5 °C/min at a frequency of 1 Hz. Rheological sweeping curves were measured with an Anton Paar MCR 102 rheometer (Austria) equipped with a stainless-steel parallel-plate geometry (diameter: 25 mm). For temperature sweeping tests, a constant frequency of 1 Hz and 1 % strain were applied, and the temperature was increased from 20 °C to 160 °C at a heating speed of 2 °C/min. The stress relaxation behavior was tested in parallel plate mode on an Anton Paar MCR-102 rheometer; a circular specimen with a diameter of 35 mm and a thickness of 1 mm was initially equilibrated at the set temperature for 10 min, and then a strain of 1.5 % was applied to the sample. The relaxation modulus changes over time were recorded at a constant temperature. X-ray photoelectron spectroscopy (XPS) of samples was recorded by a Thermo Fisher Scientific ESCALAB 250xi.

The energy scanning range was 0–1300 eV, the step size was 1 eV, and analysis was performed using the Advantage software system. The films were tested using a Raman spectroscopy (HJY LabRAM Aramis) with a laser wavelength of 785 nm and silicon wafer calibration. The micro-phase separation structure of polyurethane was observed with a Bruker NT-MDT Prima atomic force microscope (AFM). Transmission electron microscopy (TEM) characterization were carried out on JEM 2100F (JEOL) electron microscope. Ultrathin sections about 200 nm in thickness of the samples were cut by an ultramicrotome Leica EMUC6 under liquid nitrogen atmosphere. Scanning electron microscopy (SEM) of the morphology of the film was carried out using ZEISS EVO 18 Special Edition (Merlin, Carl Zeiss Jena, Germany) at 1000 \times magnification. The surface morphology of ionic PU after immersion was examined using a three-dimensional optical profilometer (UP Dual Model, RTEC, USA). The sample film was vacuum-dried at room temperature for 24 h and placed on the platform of a contact angle measuring instrument (DSA25, Krüss Company, Germany). Deionized water was added dropwise onto the film surface using a microsyringe. The shape of the droplet was recorded using a camera and analyzed using software to obtain the contact angle. The test was repeated at least three times for each sample.

2.7. Antifouling assay

After UV sterilization, all samples were cultured with FITC-BSA solution (0.05 mg/mL) in the dark at 37 °C for 2 h. Afterward, the samples were gently rinsed with PBS to remove unadhered proteins. Finally, the adhesion of proteins on the surface were observed by fluorescent inverted microscope (Olympus IX73). To further clarify the adhesion level of FITC-BSA, ImageJ software was used to evaluate the relative fluorescence intensity (RFI) results (setting the RFI of PU-SS to 100 %).

2.8. Antimicrobial activities

The antibacterial performance of ionic PU was measured using the plate counting method [34]. The experimental bacteria were *S. albus* and *E. coli*. The bacteria were inoculated in lysogeny broth and incubated overnight under shaking at 37 °C and 150 rpm to reach the growth index stage. The number of live bacteria in this bacterial solution should be $(1 \sim 5) \times 10^5$ CFU/mL. A bacterial suspension (100 μ L) was dripped onto the sample surface and then covered with the sterile polyethylene film (2 \times 2 cm²) to make the bacterial suspension evenly spread across the surface. After incubation at 37 °C for 24 h, all samples were washed with 5 mL of sterilized PBS, and then the number of CFUs was counted. Each colony determination test was repeated independently more than 3 times. For comparison, polyethylene film was used as the control group.

2.9. Cytotoxicity evaluation

To evaluate the cytotoxicity of PU-QDP_{3/1}-SS elastomers on human fibroblasts through MTT experiments [35], human dermal fibroblasts (3×10^5) in 1 mL of DMEM supplemented with 10 % fetal bovine serum were cultured in a 24-well plate for 72 h. The membrane was cut into 10 \times 10 mm² squares and sterilized under a UV lamp for 30 min, and the sample was immersed in 30 mL of PBS at pH 7.4 for 24 h to obtain the leachate. Then, 20 μ L leachate was added and cultured at 37 °C for 12, 24 and 48 h, respectively; 20 μ L PBS with pH 7.4 was added in the control group. Next, 100 μ L of the MTT solution (5 g/L PBS) was added to each well. After being placed at 37 °C for 4 h, 100 μ L dimethyl sulfoxide (DMSO) was added to each well, and the optical density (OD) value at 490 nm was measured with a microplate reader (Spectra Max M5, Molecular Devices, USA). All measurements were repeated three times.

2.10. Sensing performance

The EPU-CNT film with a size of 10 mm \times 30 mm \times 0.5 mm was

attached onto the finger or wrist of a volunteer. Copper tapes at both ends of the film were used to connect the film with output metallic wires, and commercial tapes were used to firmly fix the film with the finger/wrist. As a result, the real-time electrical signal changes of this film during stretching were recorded through the digital source table.

3. Results and discussion

3.1. Structural characterization of ionic PU and thermodynamic properties

Fig. S1 presents the ^1H NMR spectra of DP and QDP following the quaternary ammonium reaction. The triplet peak at 2.50 ppm and the quartet peak at 2.19 ppm were assigned to the methylene protons directly attached to the nitrogen atom. After reacting DP with n-butyl

bromide, the resonating protons for these methylene protons were observed at 3.44 ppm due to increased electronegativity. The signals corresponding to the methyl and methylene protons of the butyl groups appeared in the range of 0.97–1.79 ppm. These results indicate the successful transformation of QDP into a quaternary ammonium compound. The structure of the ionic PU was analyzed using FTIR spectroscopy, as shown in Fig. 1a. Strong peaks were observed in the range of 1750 cm^{-1} and 1600 cm^{-1} . Specifically, the peaks at 1718 cm^{-1} and 1633 cm^{-1} were assigned to the carbonyl tensile vibration peaks of nonhydrogen bond and disordered hydrogen bond carbamate bonds, respectively. Additionally, the peaks at 1692 cm^{-1} and 1652 cm^{-1} were attributed to the ordered and disordered hydrogen bond urea bond carbonyl tensile vibration peaks (gray area), respectively [21,28]. Notably, no-NCO stretching vibration peak was observed near 2230 cm^{-1} (Fig. S2), indicating the complete depletion of the highly active

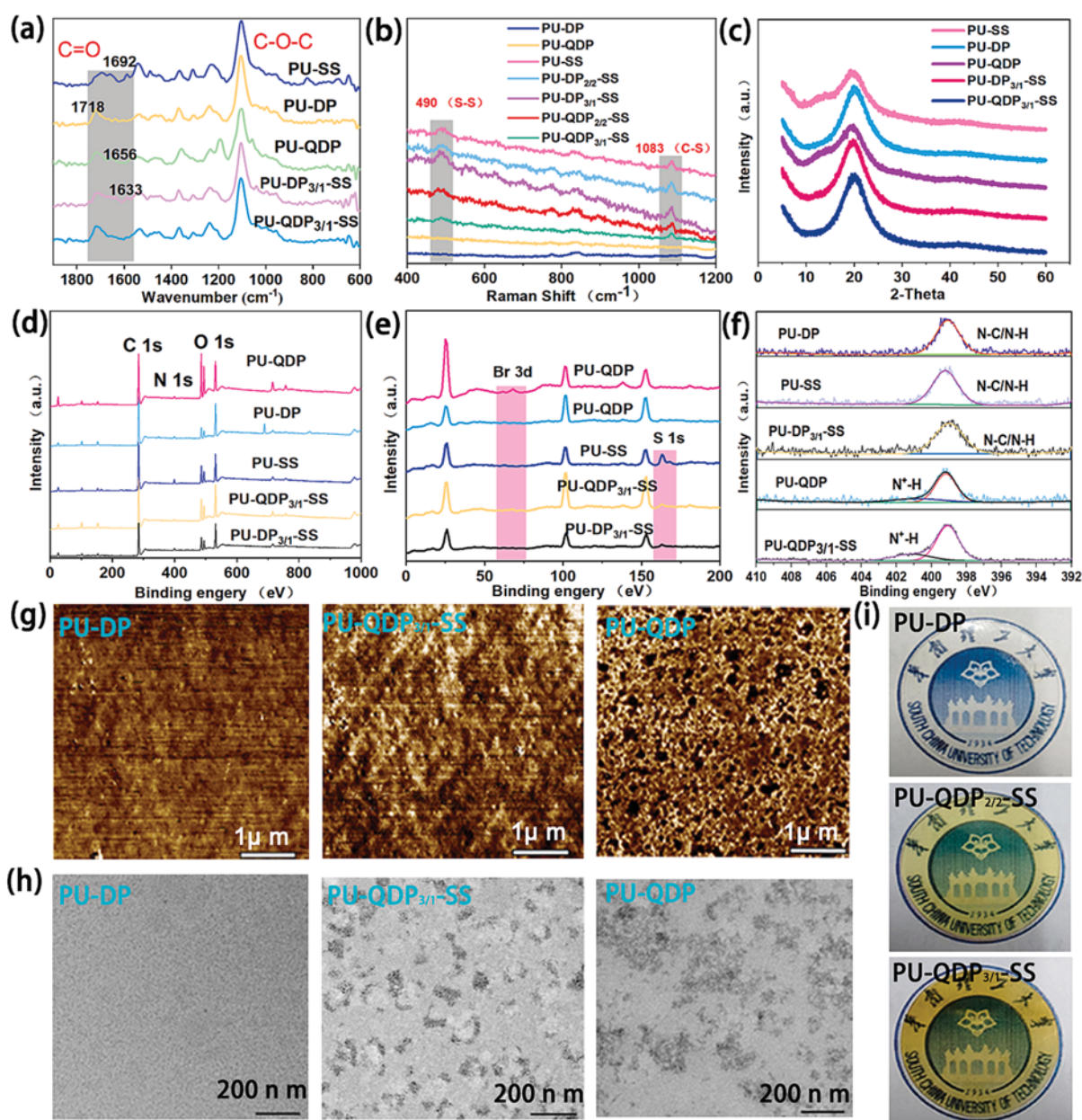


Fig. 1. (a) FTIR spectra of the ionic noncovalent interaction-enhanced PU with dynamic aromatic disulfides. (b) Raman spectra of the PU samples. (c) XRD curves of the PU-DP, PU-QDP, PU-SS, PU-DP_{3/1}-SS and PU-QDP_{3/1}-SS samples. (d) (e) XPS wide-scan spectra of PU-DP, PU-QDP, PU-SS, PU-DP_{3/1}-SS and PU-QDP_{3/1}-SS samples. (f) XPS N1s signals of the PU samples. (g) AFM 2D analysis of the PU samples. (h) TEM images of PU samples. (i) Digital optical images of the PU-DP, PU-DP_{2/2}-SS and PU-QDP_{3/1}-SS samples.

isocyanate bond.

Based on the Raman spectrum in Fig. 1b, the absorption peak of the S-S bond in PU-SS, PU-DP_{3/1}-SS and PU-QDP_{3/1}-SS was observed at 490 cm⁻¹, and the characteristic peak at 1083 cm⁻¹ was C-S. However, the PU-DP and PU-QDP samples did not show any evident characteristic peak at 490 cm⁻¹ and 1083 cm⁻¹, indicating the successful introduction of disulfide bonds in the polymers. The XPS spectrum of ionic PU, shown in Fig. 1d and e, revealed that all PU samples were mainly composed of C, N, and O elements, with corresponding binding energies appearing at 284, 400, and 532 eV, respectively. In comparison, the signals for Br3d (~68 eV) were observed in PU-QDP_{3/1}-SS and PU-QDP, while S1s (~163 eV) appeared in PU-SS, PU-QDP_{3/1}-SS, and PU-DP_{3/1}-SS. In Fig. 1f, the N1s peak of PU-QDP and PU-QDP_{3/1}-SS, which contained quaternary ammonium ionic groups consisted of two components: N⁺-C (~402 eV) and N-C/N-H (~399 eV). However, the N1s peak of PU-DP, PU-SS and PU-DP_{3/1}-SS without quaternization only had N-C/N-H (~399 eV). After quaternization, the electron cloud density of N decreased, causing its binding energy to increase [36]. Therefore, based on the above analysis, ionic PU was successfully synthesized. The microphase separation, a structural characteristic of polyurethane, is influenced by various factors and affects its performance. Atomic force microscopy (AFM) was used to examine the microphase separation morphology of ionic PU. Fig. 1g shows the presence of discontinuous areas where bright (hard segments) and dark regions (soft segments) are

observed, indicating the microphase separation of the soft and hard segments of PU. The microphase separation in ionic PU is more pronounced compared to PU-DP due to the formation of ion clusters and aggregation of hard segments [37,38]. TEM was employed to further investigate the microstructure of the ionic PU. Fig. 1h clearly shows the presence of hard domains in the microphase separation of the membrane. These dark regions are nanoclusters, while the bright regions correspond to the soft segments where PTMG is located. In contrast, PU-DP did not exhibit significant differences in brightness. The presence of ion clusters promotes the formation of microphase separation, consistent with the AFM results. The XRD pattern in Fig. 1c indicates a macroscopic homogeneous amorphous structure in ionic PU, resulting in excellent transparency (Fig. 1i).

The storage modulus and loss factor (tan δ) of various materials were measured using DMA within different temperature ranges. In Fig. 2a, the addition of ionic bonds increased the storage modulus of ionic PU. This could be attributed to the enhanced interaction between chain segments due to the presence of ionic bonds, which limited their mobility and flexibility. For polytetrahydrofuran, the T_g of all samples was concentrated within the range of -69 °C to -65 °C. When the temperature exceeded T_g, a significant decrease in the storage modulus was observed, indicating the condition for shape memory [39]. Fig. 2b and c depict the TGA curves of the ionic PU under a N₂ atmosphere. The starting decomposition temperatures (T_{Start}) of the PU-DP, PU-QDP and

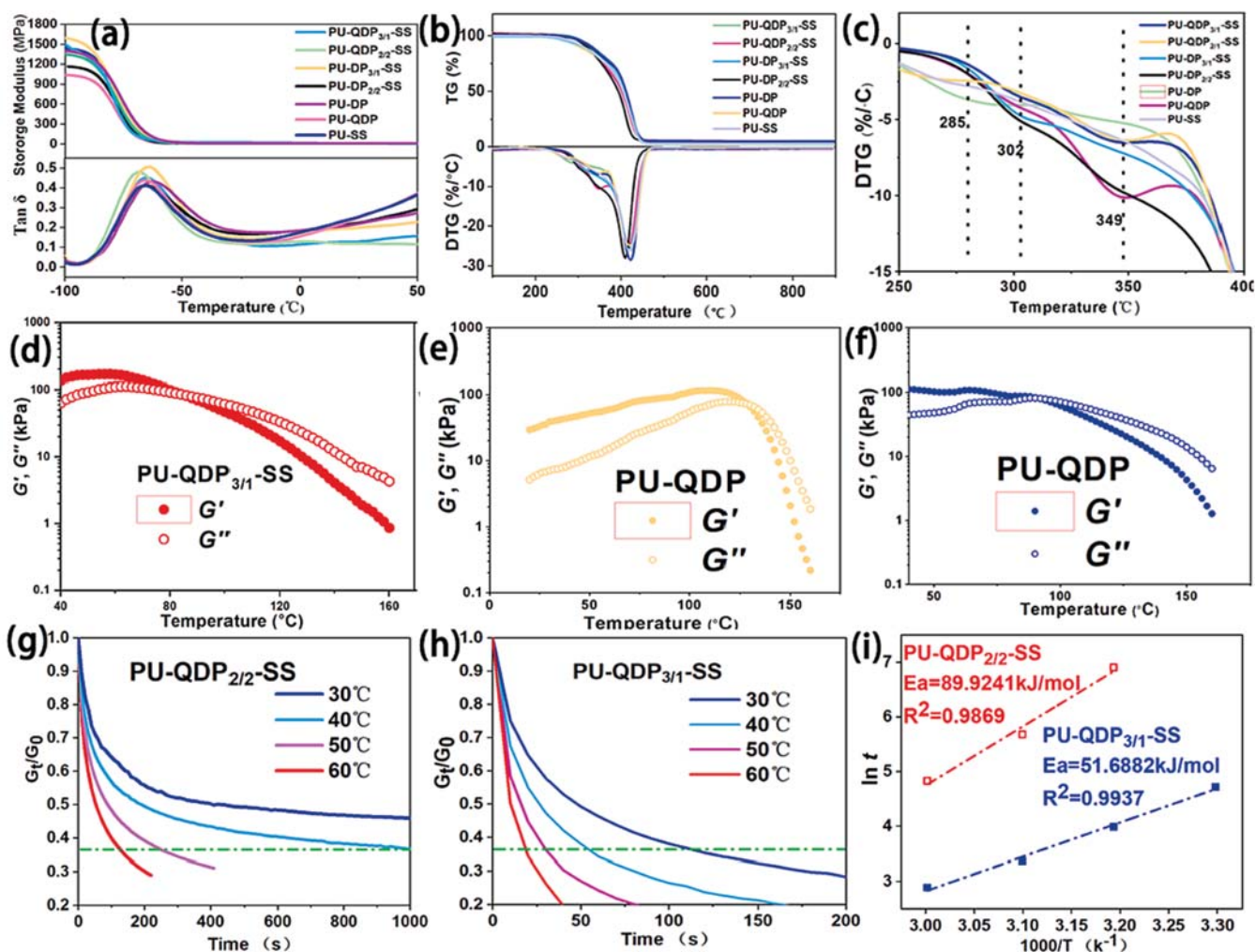


Fig. 2. (a) Overlaid plots of the storage modulus and tan δ against temperature of ionic PU from the DMA tests. (b-c) TGA curves of ionic PU. (d-f) Storage modulus (G') and loss modulus (G'') against temperature of PU-QDP_{3/1}-SS, PU-QDP and PU-SS from the temperature sweeping tests of rheology analysis. (g-h) Normalized stress relaxation experiments of the PU-QDP_{2/2}-SS and PU-QDP_{3/1}-SS under different conditions. (i) Linear fitting of relaxation time at different temperatures according to the Arrhenius law.

PU-SS samples were 392.4 °C, 399.1 °C and 373.6 °C, respectively. These differences can be attributed to the heat resistance of the quaternary ammonium groups in the polyurethane formulation (Table S2). As the degree of [DP]/[AFD] (or [QDP]/[AFD]) increased from 2/2 to 3/1, the T_{Start} values of PU-QDP_x-SS were higher than those of the corresponding PU-DP_x-SS. The introduction of quaternary ammonium led to improved thermal stabilities of the PU.

The viscous flow transition temperature of PU-SS was approximately 142 °C, as shown in Fig. 2d–f. However, for ionized PU-QDP, the viscous flow transition temperature occurred at a lower temperature due to the physical cross-linking effects produced by ion interactions. When the system contained both aromatic disulfide and ion bonds, the viscous flow transition temperature reached 92 °C, potentially due to the synergistic effect of the two dynamic bonds. From Fig. 2g and h, it can be observed that a lower temperature correlated with a larger friction within the molecular chain and a more difficult stress relaxation. According to the Maxwell model of viscoelastic fluids, the relaxation time is defined as the time corresponding to the decay of the modulus to the original value of 37 % (1/e) [40]. As shown in Fig. 2g and h and Fig. S3 show the relaxation times of PU-QDP_{3/1}-SS, PU-DP_{3/1}-SS, PU-QDP_{2/2}-SS and PU-DP_{2/2}-SS at 50 °C, which are 32 s, 51 s, 228 s and 312 s, respectively. The relaxation time decreased with increasing ion content. The relationship between the characteristic relaxation time (s) and

temperature followed the Arrhenius formula. Fig. 2i and Fig. S4, display the activation energies E_a of PU-QDP_{3/1}-SS, PU-QDP_{2/2}-SS, PU-DP_{3/1}-SS and PU-DP_{2/2}-SS calculated from the slope, which were 51.6, 89.9, 24.9 and 69.9 kJ/mol, respectively. A lower activation energy provided a greater topological rearrangement and resulted in good healing performance due to rapid exchange reactions.

3.2. Mechanical properties and self-healing behaviors

By introducing ionic bonds and aromatic disulfide bonds, a dynamic double cross-linked structure was formed in PU-QDP-SS, resulting in significant improvement in its mechanical properties. Fig. 3(a–c) illustrates that ionic PU exhibited higher tensile strength, elongation at break, and toughness compared to nonionized PU. Among the variants, PU-QDP_{3/1}-SS demonstrated the highest elongation at break (1930 %), tensile strength (39.9 MPa), and toughness (288.0 MPa). In an ionized PU network, anions and cations interacted directionally within a specific range, forming ion clusters of a certain scale. The strong polarity of ion bonds facilitated the formation of microphase separation structures in non-polar soft phases, while the physical crosslinking effect of hard aggregates enhanced both tensile strength and stretchability. Additionally, the incorporation of a small amount of rigid disulfide structure increased spatial hindrance and further restricted the segmental

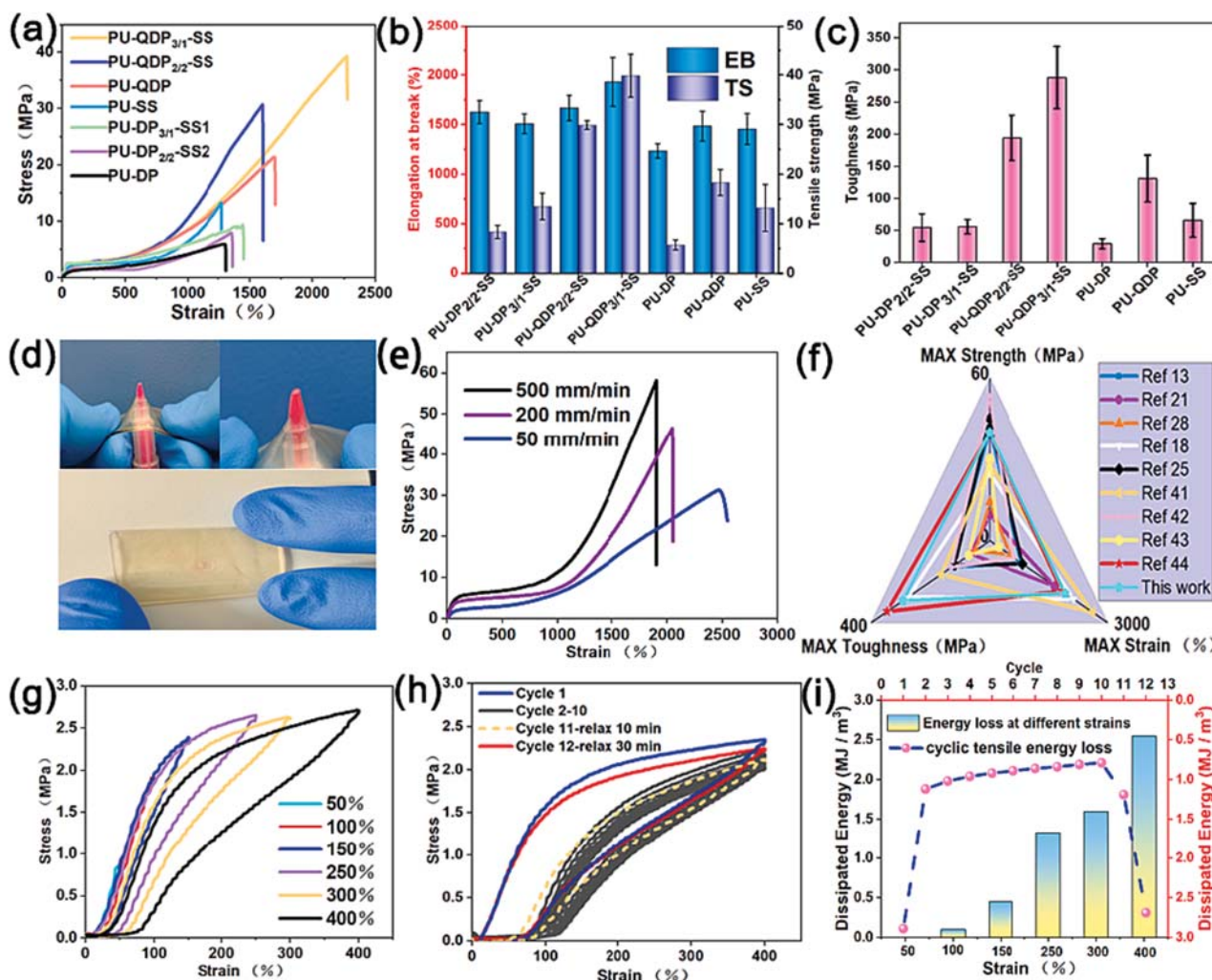


Fig. 3. (a) Typical stress-strain curves of ionic PU. (b) Tensile strength and breaking elongation. (c) Toughness. (d) Photographic images of PU-QDP_{3/1}-SS puncture resistance. (e) Tensile stress-strain curves of PU-QDP_{3/1}-SS specimens under different deformation rates. (f) Comparison of tensile strength, elongation at break, and toughness of PU-QDP_{3/1}-SS with data from other literature. (g) Successive cyclic tensile behavior of PU-QDP_{3/1}-SS at different strains. (h) Consecutive cyclic tensile curves of PU-QDP_{3/1}-SS at a strain of 400%. (i) Cyclic tensile energy loss value.

movement of PU. This resulted in a more regular chain arrangement, thereby enhancing the robustness of hard segments in the PU matrix. In contrast, nonionized PU solely relied on polymer chain entanglement and intermolecular hydrogen bonds between urethane and urea groups, leading to insufficient mechanical strength due to the absence of hard domains. A sample from the PU-QDP_{3/1}-SS series demonstrated excellent mechanical robustness, successfully resisting puncture from a writing pen (Fig. 3d). The stress-strain behaviors of PU varied depending on the frequency of stress transfer. When subjected to low stretching speeds, PU molecular chains were able to unfold more easily, thereby improving its stretchability. However, at high stretching rates, the molecular chains of PU were unable to fully stretch within a short period of time, resulting in chain aggregation and a significant increase in modulus and tensile strength (Fig. 3e). Among several self-healing PU

reported in [9,13,18,21,25,28,41–43], the tensile strength and toughness values of ionic PU were particularly noteworthy (Fig. 3f).

Cyclic tensile tests were performed to investigate the deformation recovery and recoverable energy dissipation capability. Fig. 3g illustrates the single cyclic stress-strain curves of PU-QDP_{3/1}-SS at various strains (50 %, 100 %, 150 %, 250 %, 300 %, and 400 %) during the successive tensile process. It is evident that the hysteresis loop becomes more pronounced with increasing tensile strain. Furthermore, Fig. 3i provides quantification results for the lag region. The energy dissipated by the material increases from 0.01 to 2.54 MJ/m³ as the deformation (elongation) rises from 100 to 400 %. This indicates that PU-QDP_{3/1}-SS effectively dissipates strain energy resulting from the breaking of ionic bonds, S-S bonds, and H-bonds during stretching-retraction cycles at different strains. During the cyclic stretching process with a fixed strain

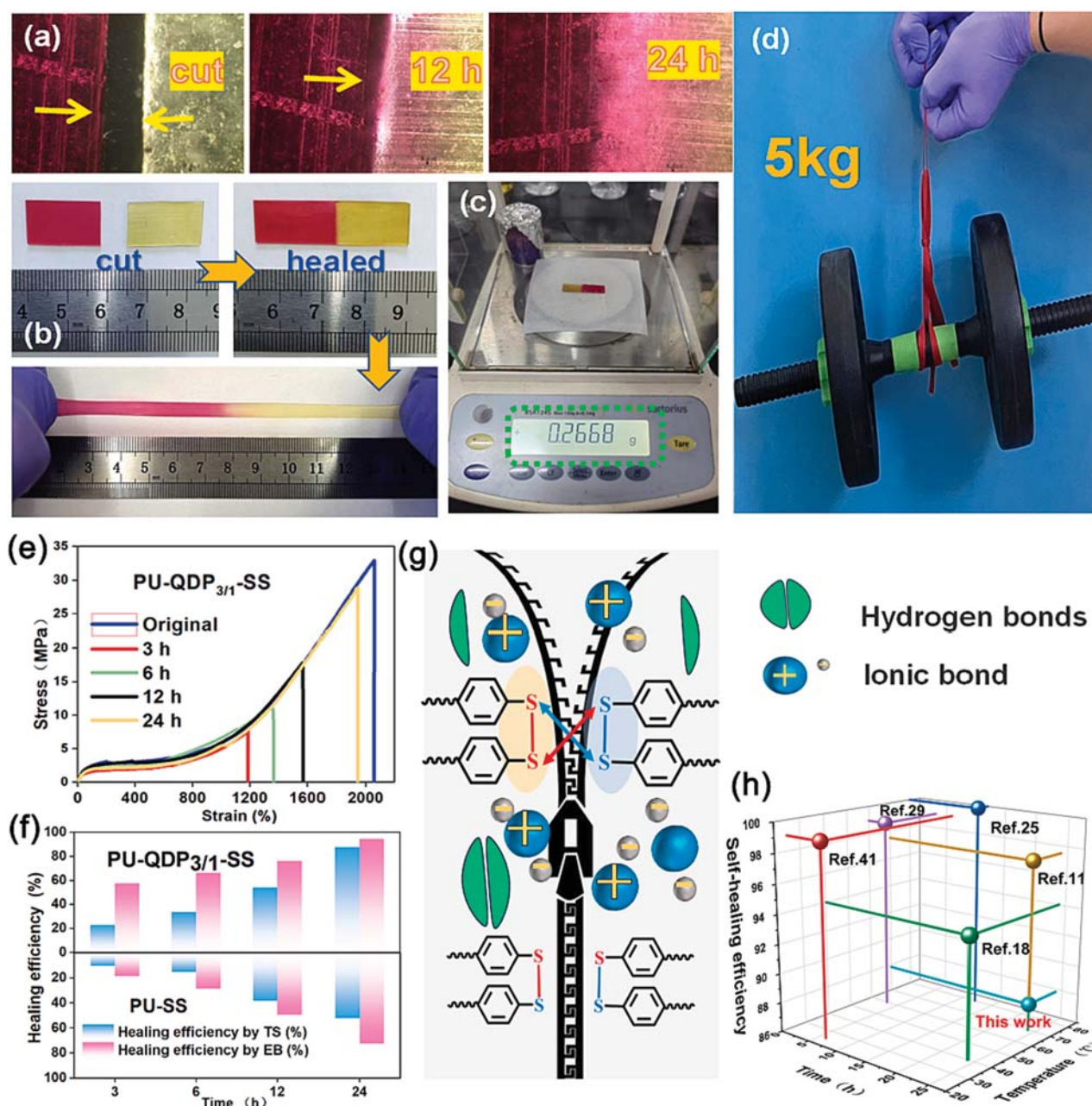


Fig. 4. (a) Digital images of the fracture-healing process of PU-QDP_{3/1}-SS under an optical microscope. (b) Healed PU-QDP_{3/1}-SS sample stretched to ~500 %. (c) Weighing the mass of PU-QDP_{3/1}-SS with an electronic balance. (d) Photograph of the PU-QDP_{3/1}-SS lifting a 5 kg dumbbell. (e) Stress-strain curves of the self-healing PU-QDP_{3/1}-SS under different healing times. (f) Healing efficiency of PU-QDP_{3/1}-SS and PU-SS under different repair conditions. (g) Self-healing mechanism. (h) Comparison of the self-healing efficiency, temperature and time of PU-QDP_{3/1}-SS with other literature data.

of 400 %, the energy dissipated in the 1st cycle was 2.89 MJ/m³, which was four times higher than the dissipated energy in the 10th cycle (0.68 MJ/m³). This difference can be attributed to the partially unrecovered dissociated dynamic bonds from the first cycle (Fig. 3h and i). After a resting time of 30 min (Fig. 3h), the hysteresis loop of the PU-QDP_{3/1}-SS almost returned to its original state, and the energy dissipated also reached 94 % of the initial situation, demonstrating excellent elastic restorability. This time-dependent self-recovery property primarily relies on the reversible dissociation/reassociation of relatively weak H-bonds, ion clusters, and S-S bonds in the dynamic hard domains.

To express the self-repairing behavior of our prepared samples more intuitively, a pristine and a methyl red dyed PU film were respectively cut into two pieces and then placed directly at 70 °C for a period of time without any external force. After 24 h, the incision on the surface was almost completely repaired (Fig. 4a). The healed sample exhibited a certain level of tensile strength and elongation, capable of stretching up to 5 times its own length (~2.5 cm) (Fig. 4b). Furthermore, a sample weighing 0.2688 g could withstand a weight of 5 kg of dumbbells without sustaining any damage (Fig. 4d). Additionally, its load-bearing capacity was found to be 18,600 times its own weight (Fig. 4c).

The self-healing efficiency refers to the percentage of recovery to the original sample. After being subjected to a temperature of 70 °C for 24 h, the tensile strength and tensile rate of the sample showed a self-healing efficiency of 87.8 % and 94.4 % respectively, as depicted in Fig. 4e and f. This indicates that PU-QDP_{3/1}-SS possesses a good self-healing ability. Additionally, Fig. S5 demonstrates that reducing the temperature significantly decreases the healing efficiency. For instance, when the healing time was 24 h at 50 °C, the self-healing efficiency of the sample was equivalent to that achieved by heating to 70 °C for 12 h. Furthermore, the self-healing efficiency of PU-QDP_{3/1}-SS is substantially higher than that of PU-SS, as shown in Fig. 4f. Fig. 4g provides a schematic diagram illustrating the self-healing process of PU-QDP_{3/1}-SS samples. The self-healing ionic PU sample primarily consists of ordinary

hydrogen bonds, ion interactions, and aromatic disulfide bonds within the main chain. When exposed to a temperature of 70 °C, the small-sized anions and cations on the polymer chain are attracted to each other, leading to diffusion at the interface. This local diffusion enhances the overall segmental motion of the polymer chains. The rapid diffusion of small-sized anions promotes the double decomposition reaction of disulfide bonds, which is crucial for crack healing. However, the presence of a single aromatic disulfide bond in PU-SS, which is locked in the hard domain, affects the self-healing efficiency due to the tightly arranged hard segments. Therefore, the self-healing performance of PU-QDP_{3/1}-SS is a result of the combined action of ionic bonds and disulfide bonds. In comparison to experimental data in the literature, the self-healing efficiency of ion elastomers was not particularly remarkable (Fig. 4h). This can be attributed to the strong ion interactions and the structure of the biphenyl ring, which hindered chain segment motion.

3.3. Shape memory properties

The storage modulus of the PU-QDP_{3/1}-SS sample showed a significant dependence on temperature. By disrupting the dynamic ionic and disulfide bonds, the sample could rearrange its network topology, leading to shape memory behavior under appropriate programming. Fig. 5a provides a visual representation of the strong correlation between shape memory behavior and temperature. It is evident that a flat sample can be gradually transformed into a cubic shape by heating it to 90 °C and then cooling it to room temperature. The stretching chain's limited relaxation allows for the maintenance of macroscopic deformation at room temperature [2]. When subjected to additional heating and cooling cycles, each deformed part of the sample exhibited simultaneous recovery to its initial state (Fig. 5a). However, the lack of control mechanisms for thermally induced shape memory processes has significantly impeded their widespread application on a large scale. The distinguishing feature of water-induced shape memory is the precise

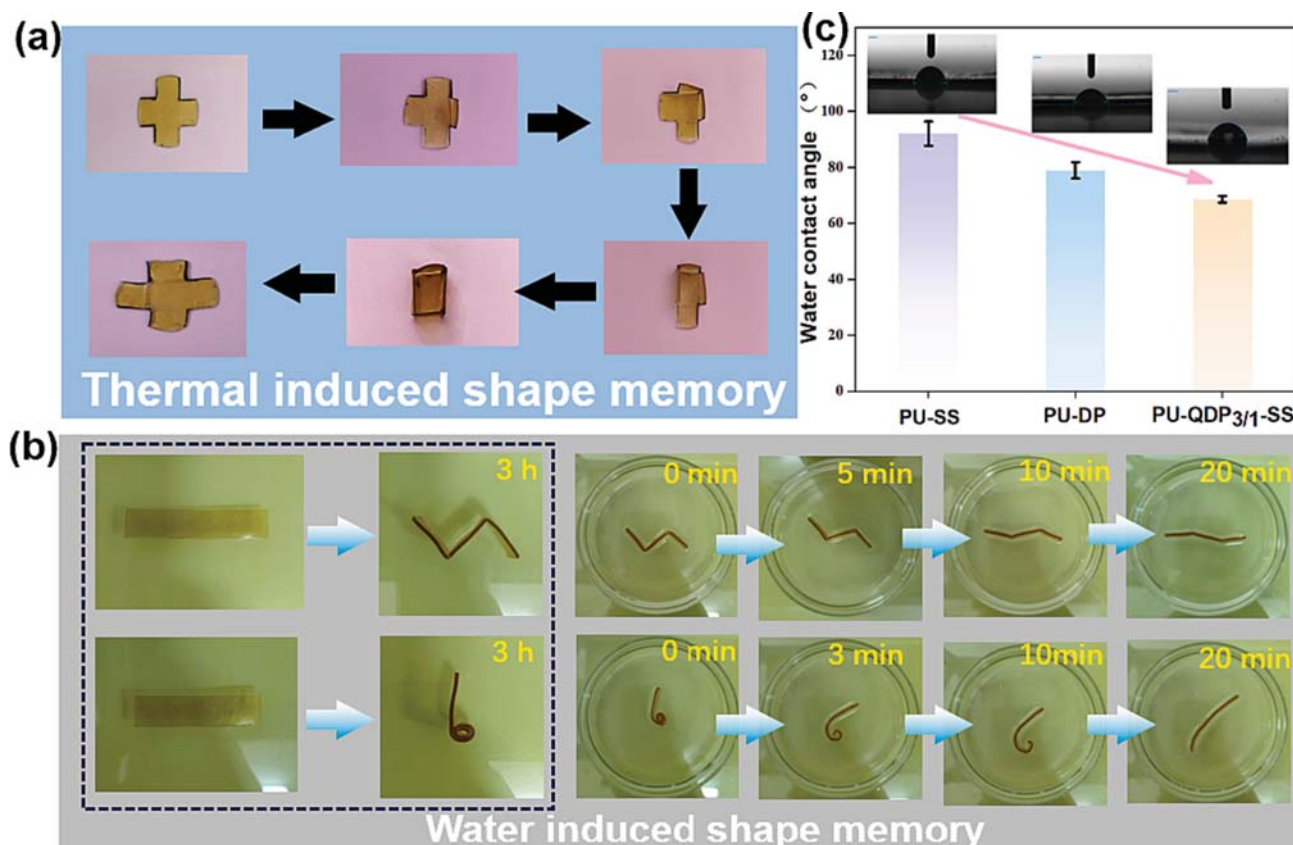


Fig. 5. (a) and (b) Photographs showing the shape memory behavior of PU-QDP_{3/1}-SS in heat and water. (c) Water contact angle of PU-SS, PU-DP and PU-QDP_{3/1}-SS.

control over the order of deformation, which introduces a control switch in addition to the traditional heat-induced shape memory.

The original straight specimens PU-QDP_{3/1}-SS were initially bent into a temporary shape (Fig. 5b) at 90 °C and then cooled back to room temperature (20 °C) to fix the shape. At room temperature, the shape of the elastomer remained unchanged without any additional stimulation. Subsequently, the deformed specimens were immersed in water (~5 °C) to observe the water-induced shape recovery process. It was observed that all the specimens could recover their original shape after being immersed for more than 20 min. The excellent hydrophilicity of the ion segment of ionic PU facilitated the quick absorption of water molecules by PU in the aqueous environment. These absorbed water molecules then participated in the hydration of ions. Consequently, with the

assistance of water molecules, both ionic and hydrogen bonds rapidly dissociated, leading to the destruction of the hard phase and providing the necessary structural conditions for the reconstruction of a new temporary shape. Fig. 5c illustrates that the water contact angle of PU is 68°, which is lower than that of nonionized PU, indicating the contribution of ions to the hydrophilicity of the material.

3.4. Self-cleaning characteristics

Ionic PU elastomers can be used as coatings to firmly bond with substrates, such as glass and metal [44]. However, due to the hydrophilic properties of ionic PU, it leads to a high surface energy and is easily contaminated by substances with low surface energy, such as

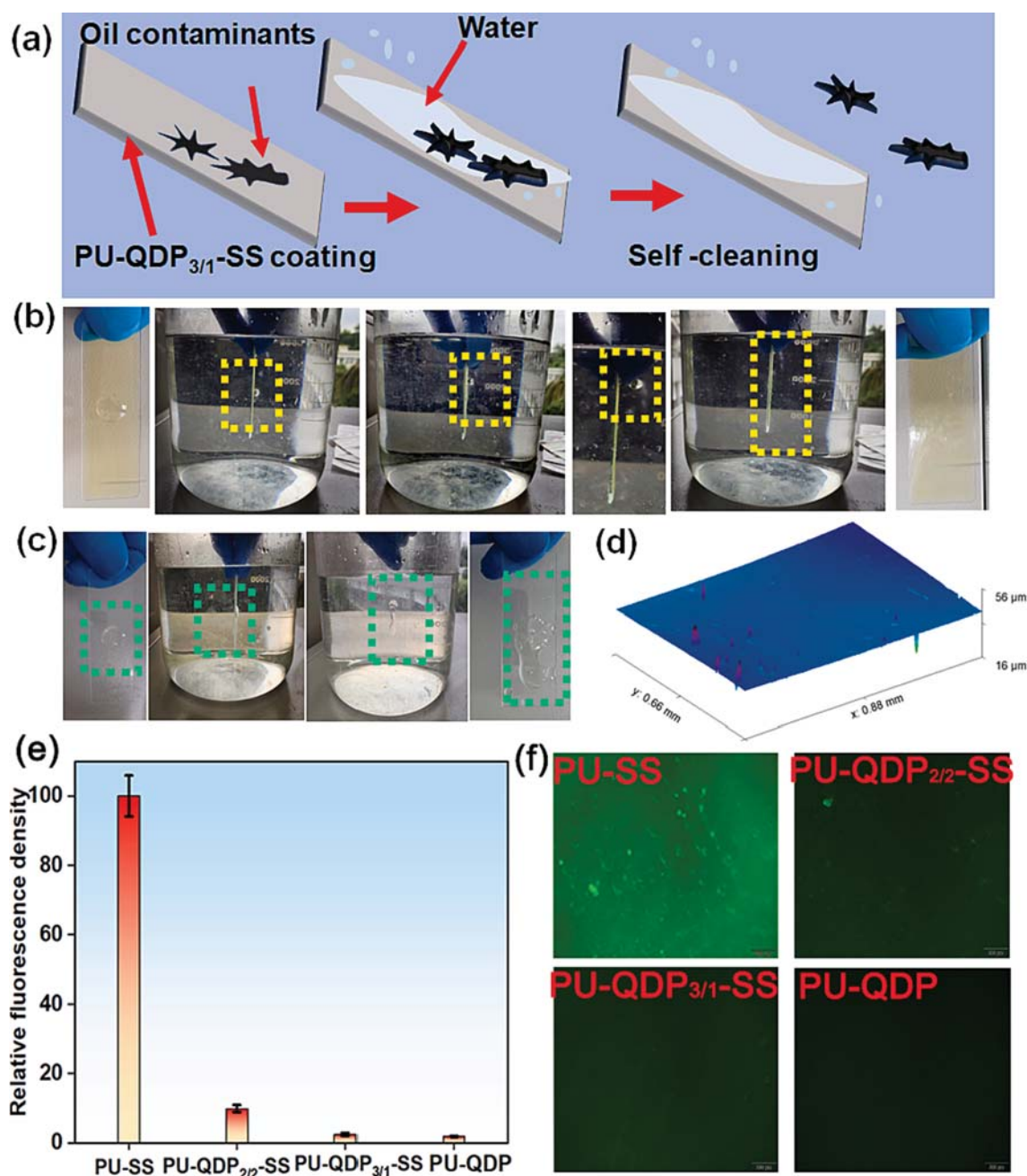


Fig. 6. (a) Schematic diagram of the self-cleaning of the PU-QDP_{3/1}-SS coating. (b) Digital photo of the separation process of castor oil in water by the PU-QDP_{3/1}-SS coating. (c) Digital photos of a glass plate adhering to castor oil in water. (d) 3D contour map of the PU-QDP_{3/1}-SS membrane surface after soaking in water for 72 h. (e) Relative fluorescence density of different types of ionic PU. (f) Fluorescence photos of BSA-FITC protein adsorption on different ionic PU sample surfaces. Scale bar: 200 μm.

various oil stains. Therefore, the antifouling performance of ionic PU coatings is crucial in practical applications [23]. The self-cleaning performance of PU-QDP_{3/1}-SS was evaluated by conducting tests. Castor oil was added dropwise onto a glass plate coated with ionic PU. When the glass plate was submerged in water, the hydrophilic PU-QDP_{3/1}-SS coating surface quickly interacted with a layer of water molecules (Fig. 6a and b). The oil stain on the glass plate formed a ball in the water, gradually sliding off the ionic PU coating surface and floating in the water, leaving a clean surface. In contrast, when the uncoated glass plate was immersed in water, the oil stains remained on the surface and could not be removed, leading to surface contamination (Fig. 6c). SEM images, microscope magnified views, and three-dimensional optical contour line diagrams (Fig. 6d and Fig. S6) demonstrated that after 72 h of immersion in water, the coating surface remained smooth and crack-free, exhibiting excellent water stability. These findings indicate the potential application of this coating in the field of antifouling coatings.

Fig. 6e and f present both qualitative and quantitative results of BSA-FITC protein adsorption on the ionic PU surfaces. The stained protein images (Fig. 6f) reveal a significant amount of green BSA-FITC protein adsorbed on the surface of PU-SS. The adsorption capacity of BSA-FITC protein decreases noticeably with the increase in ion bond content, and fluorescence signals are barely observable on the surface of PU-QDP. By using the fluorescence intensity of PU-SS as the baseline (100 %), the relative fluorescence intensity of ionic PU was calculated (Fig. 6e). It can be deduced that the relative absorbance of the PU-QDP surface is the smallest (<1.3 %), indicating that the hydrophilicity of the substrate surface effectively resists protein adsorption.

3.5. Recyclability, antimicrobial activity and cytotoxicity evaluation

Ionic PU offers the advantage of reconstructing network topology through postprocessing techniques such as solvent-assisted recovery and heat recovery. Fig. 7a demonstrates the process where the PU-QDP_{3/1}-SS

sample is cut into small pieces, rapidly dissolved in organic solvents (such as THF and DMF) for 20 min, dried in a vacuum at 50 °C, and finally transformed into the original transparent film, which can also be recovered through heating. Additionally, Fig. 7b illustrates how the ionic PU fragments acquire a heart shape when subjected to hot working at 100°C. Cationic polymers possess broad-spectrum bactericidal properties and do not exhibit bacterial resistance. The antibacterial mechanism of these polymers can be summarized as follows: firstly, cationic polymers adhere to the negatively charged cell membrane of bacteria through electrostatic interactions. Secondly, the hydrophobic alkyl chains of the polymers are inserted into the lipid layer of the bacterial membranes, resulting in leakage of the cytoplasm and subsequent bacterial death [45]. The antibacterial activity of ionic PUs was studied using the plate counting method. Fig. 7b and c show the antibacterial rates of the raw and recycled elastomer films. The antibacterial rate was calculated by Eq. (1):

$$\text{Antibacterial rate (\%)} = \frac{CFU(\text{control}) - CFU(\text{sample})}{CFU(\text{control})} \times 100 \quad (1)$$

The study found that the ionized PU (PU-QDP-SS series) exhibited antibacterial properties, with antibacterial rates of 98.36 % and 99.93 % against *E. coli* and *S. albus*, respectively. The antibacterial rate of recycled PU-QDP_{3/1}-SS against the two types of bacteria did not show significant change. The distribution of quaternary ammonium cations on the polymer remained unaffected by the recovery process of the antibacterial elastomer through thermoforming, indicating that its antibacterial performance was not compromised. Furthermore, the structural differences between *E. coli* and *S. albus* led to the cell membrane of *S. albus* being more susceptible to damage caused by cation charge interference, resulting in higher antibacterial activity of the elastomers against *S. albus* compared to *E. coli* [46].

Electrospinning is a fiber preparation technology known for its

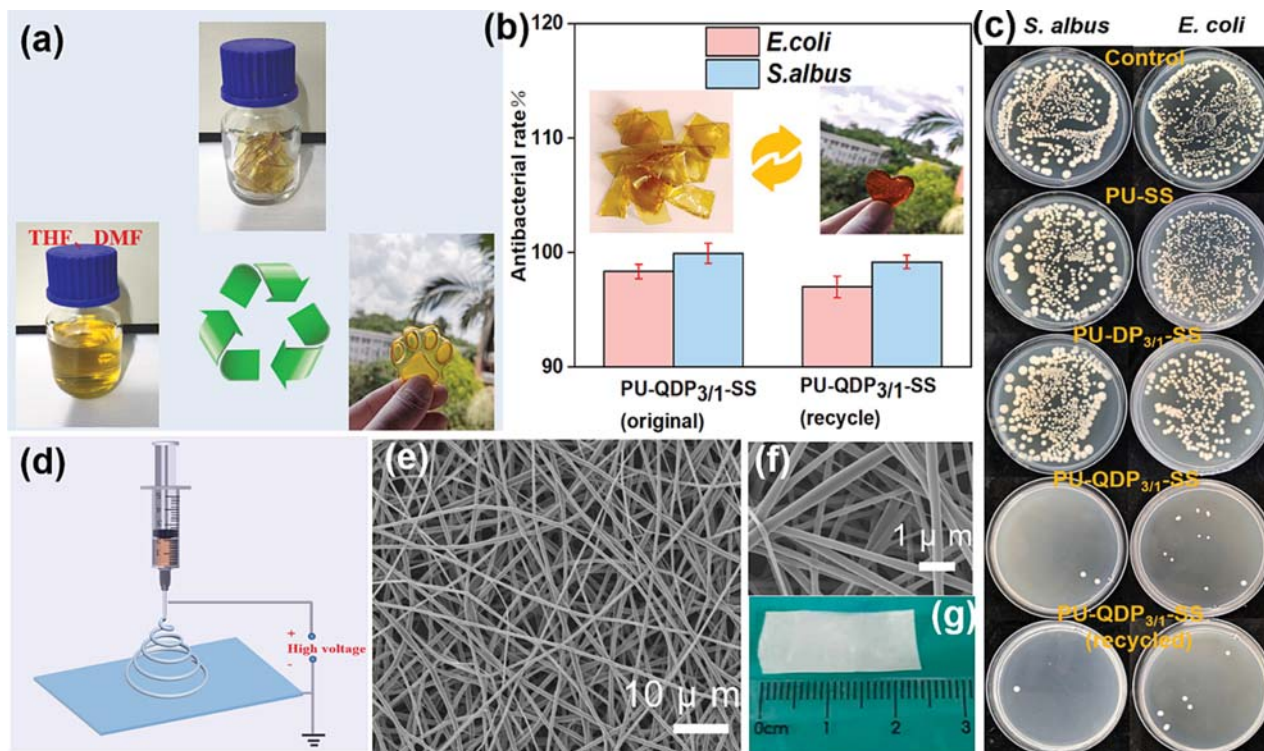


Fig. 7. (a). Process for recycling the PU-QDP_{3/1}-SS elastomer, where the elastomer was cut into pieces and dissolved in DMF and then cast into a cat claw shape. (b) Antibacterial rate of the original and recycled PU-QDP_{3/1}-SS samples. Illustration: chopped PU-QDP_{3/1}-SS and thermoplasticized it into a heart shape at 100 °C. (c) Plate photos of the antibacterial efficiency and bacterial colony count determined by the plate counting method. (d) Schematic diagram of PU-QDP_{3/1}-SS electrospinning. (e-g) SEM images and digital photo of the electrospun film.

simple process and high repeatability. In this study, the processability of PU-QDP_{3/1}-SS was investigated using electrospinning technology (Fig. 7d). The morphology and digital photo of the electrospun PU film were observed through SEM, as depicted in Fig. 7e–g. The fiber size was uniformly distributed without any defects, and the electrospun fiber membrane exhibited a smooth surface morphology. Our research highlights the potential applications of ionic PUs in various fields, particularly in the biomedical sector.

Calculate the relative growth rate (RGRs) of dermal fibroblasts based on the 490 nm OD value obtained by the MTT assay to evaluate the cytotoxicity of ionic PU. The RGR values for PU-SS, PU-DP_{3/1}-SS, and PU-QDP_{3/1}-SS membranes were determined to be 92 %, 92 %, and 88 %, respectively. These results indicate that the synthesized ionic PU membranes exhibit low cytotoxicity (Fig. 8a and Table S3). The morphology of normal fibroblasts stained with the live/dead kit after 48 h is depicted in Fig. 8b and c. All cells exhibited strong green fluorescence signals, and the fibroblasts displayed the typical fusiform (diffusion) morphology. These findings confirm that the ionic PU membranes do not generate cytotoxic byproducts. *E. coli* was chosen as the model microorganism to demonstrate the contact antibacterial properties of the ionic PU membrane using the inhibition zone method. A sterilized PU-QDP_{3/1}-SS (with a diameter of 20 mm) was placed on an agar plate containing the *E. coli* strain (at a concentration of 10⁵ CFUs/mL) and then incubated at 37 °C for 24 h. As depicted in Fig. 8d, no inhibition zone was observed around the PU films, indicating that antimicrobial properties required direct contact between the biocidal surface and microorganisms. Since the quaternary ammonium was attached to the PU systems through reactions, there was no release of antimicrobial agents. Without the release of antimicrobial agents, these films could prevent contamination of the environment and long-term antibacterial activity. The surface zeta potential of the membrane (Fig. 8e) revealed that PU-QDP_{3/1}-SS had a positive charge on its surface, but these cations did not leach out. Thus, these films exhibited both surface antibacterial properties and good biocompatibility.

3.6. Sensing performance

Due to its unique mechanical and self-healing properties, the self-healing ionic PU can be used as a flexible conductive substrate or as a composite material with conductive materials for flexible wearable electronic devices and human motion detection [47–49]. A flexible stretchable strain sensor based on ionic PU was obtained by spraying CNTs-COOH as conductive fillers on the surface of EPU-QDP_{3/1}-SS (Fig. 9a). The electrospun ionic PU frameworks in Fig. 9-b1 exhibited smooth surfaces and similar diameters, forming different pore sizes. When CNTs precipitated onto the surface of the porous framework, they densely stacked and connected to create a network, establishing a continuous conductive pathway for current transmission (Fig. 9-b2 and b3). Additionally, the fiber mesh structure of the sensor contributed to its excellent sensing performance, enabling high sensitivity (gauge factor (GF)) over a wide strain range. Fig. S7 demonstrates that EPU-CNT acted as a wire to light up LED bulbs. Notably, the CNTs-COOH formed ion interactions with the ionic PU, significantly enhancing the interfacial adhesion between the two materials. The study investigated the self-healing behavior of CNTs as conductive fillers on the surface of ionic PU films. Initially, the resistance of the original sample was measured as 1.0 K Ω using a multimeter (Fig. 9c, original sample). To assess the impact of damage, a cut mark was made on the EPU-CNT conductive film using a razor blade, resulting in the disconnection of CNTs on both sides of the cut. This led to a reading of 0 on the electricity meter, indicating the loss of conductivity in the EPU-CNT conductive film (Fig. 9c, the sample with a cut mark). However, when the damaged film was allowed to heal at room temperature for 10 s and 1 min, the resistance value gradually approached the initial value, suggesting a recovery of conductivity. Fig. 9d illustrates that the resistance-time curve exhibited a sharp increase in the peak value when the EPU-CNT film had a cut mark, indicating a discontinuity in the circuit transmission of the separated part. Conversely, when the separated parts came into contact again, the transmission path was reconstructed,

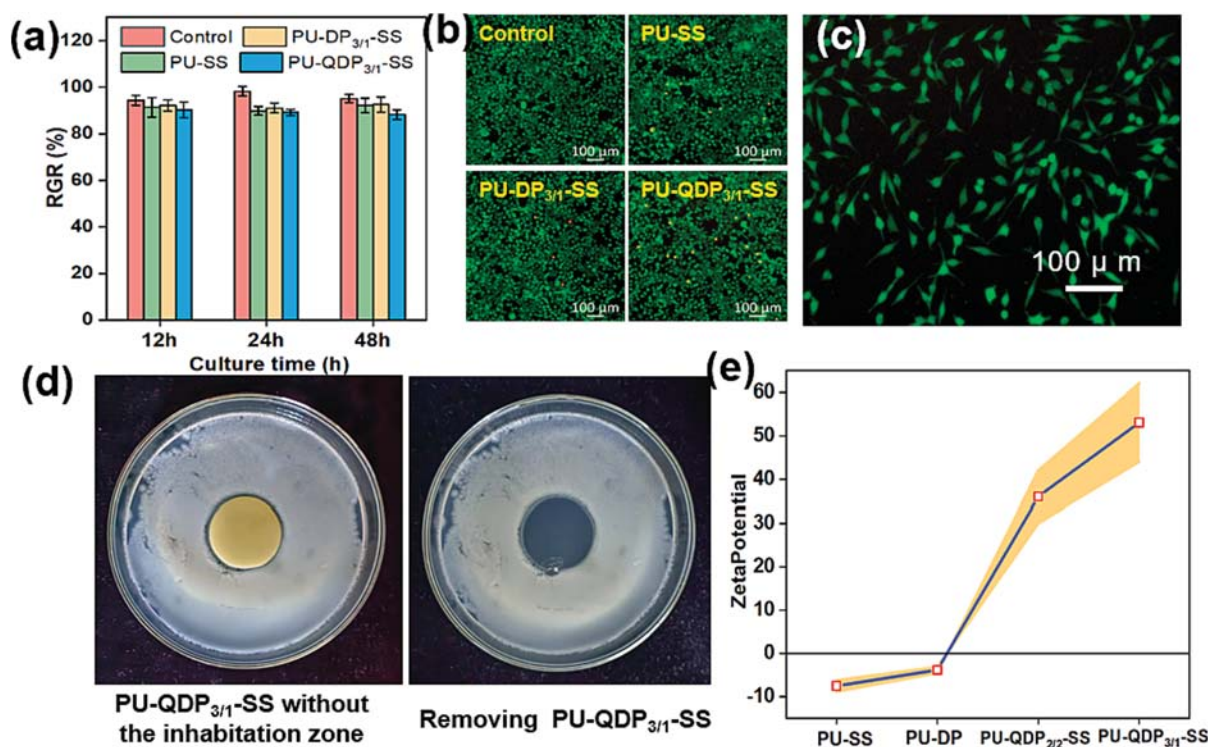


Fig. 8. (a) Relative growth rate (RGR %) of the fibroblasts cultured in the extracted leachate of PU-QDP_{3/1}-SS. (b) Morphology under a microscope of the cells cultivated after 48 h (c) Microscopic enlarged view of the spindle-forming fibroblasts. (d) Inhibition zones of the PU-QDP_{3/1}-SS films against *E. coli*. (e) Surface zeta potential of ionic PU.

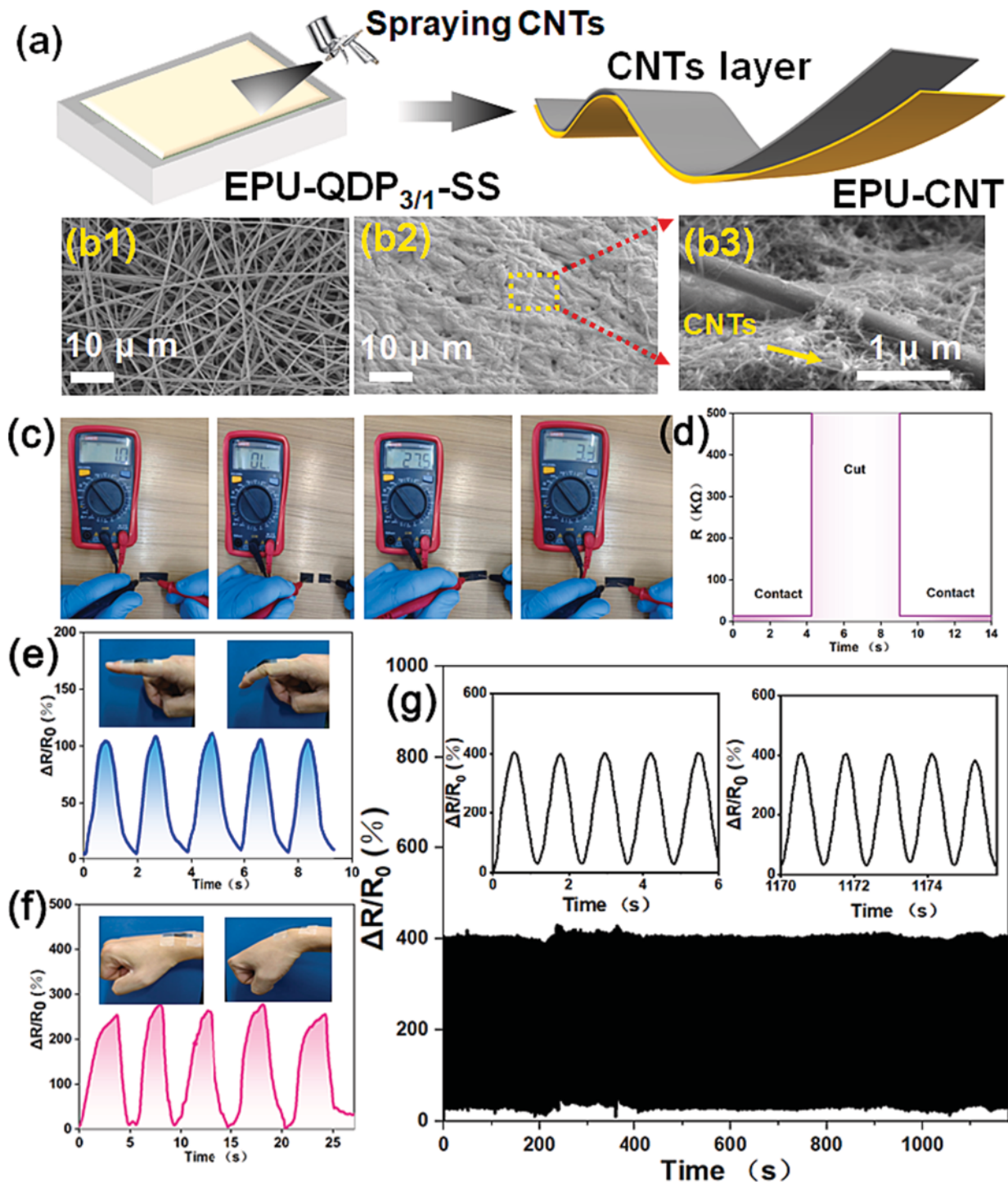


Fig. 9. (a) Preparation process of EPU-CNT flexible composite materials. (b) SEM images of electrospun ion PU and EPU-CNT. (c) Measurement of the resistance of the EPU-CNT composite flexible sensor with a multimeter in the initial state, state with a cut mark, and state when healing at room temperature for 10 s and 1 min. (d) Electrical resistance changes of EPU-CNT during the cut-reconnection. (e) Change rate of relative resistance when detecting the bending motion of the human index finger. (f) Change rate of relative resistance when detecting the bending motion of the human wrist. (g) Response stability of the strain sensor at a constant strain of 50 % for 1000 cycles.

demonstrating the restoration of conductivity in the EPU-CNT membrane.

The changes in the relative resistance of flexible sensors within the tensile strain range of 0–400 % $\Delta R/R_0$ and GF values are depicted in Fig. S8. The stretching process can be divided into two strain regions: 0–200 % and 200–400 %. The corresponding GFs for these regions are 7.52 and 4.31, respectively. As the strain amplitude increases, the slope

of the curve decreases and GF decreases, indicating an increase in resistance during the stretching process. Fig. 9e and f demonstrate the sensor's response to different bending angles of the fingers and wrists. In addition, $\Delta R/R_0$ increased with increasing bending angle. The results illustrated that the strain sensor based on EPU-CNT has high sensitivity in a wide sensing range. Stability is another important parameter for strain sensors, and the response stability of the strain sensor was

evaluated by continuously monitoring the resistance change under constant deformation for 1000 cycles. The results displayed a uniform response curve waveform for each deformation, as shown in Fig. 9g, indicating that the sensor exhibited good stable strain response. Overall, real-time monitoring of $\Delta R/R_0$ changes was achieved with accuracy, highlighting the potential of EPU-CNT as a sensitive self-repairing wearable strain sensor for monitoring various human activities.

4. Conclusions

In this study, a self-healing ionic PU with ionic bonds and an aromatic disulfide structure was synthesized. The formation of ion clusters through the aggregation of anions and cations resulted in physical cross-linking networks. The combination of these ion clusters and dynamic aromatic disulfide bonds effectively addressed the trade-off between mechanical robustness and healing efficiency. Compared to PU without cationic noncovalent interactions, the PU-QDPx-SS exhibited a high decomposition temperature and demonstrated high tensile strength (39.9 ± 4.4 MPa), elongation at break (1930 ± 345 %), and toughness (288 ± 48.4 MPa). The self-healing efficiency of the PU-QDP_{3/1}-SS after 24 h reached 94.4 %. Furthermore, biological experiments showed that even the recovered PU-QDP_{3/1}-SS samples exhibited excellent contact killing and antibacterial activity. The quaternary ammonium attached to the PU system through a reaction and did not release antibacterial agents, ensuring good biocompatibility. The presence of ionic bonds also demonstrated the water-induced shape memory ability of the ionic PU, which, due to its high hydration ability resulting from hydrophilicity, also exhibited self-cleaning ability as a coating material. Finally, the study explored the practical application of composite films assembled using CNTs-COOH as conductive materials and EPU-QDP_{3/1}-SS as substrates in flexible wearable strain sensors. This research presents a novel approach for designing flexible, multifunctional, high-strength, and high-toughness elastomers.

Author contributions

This manuscript was written through contributions of all authors. All authors have given approval to the final version of the manuscript.

CRediT authorship contribution statement

Yaling Lin: Writing – review & editing, Writing – original draft, Supervision, Project administration, Methodology. **Ning Yu:** Writing – original draft, Methodology, Investigation, Data curation. **Shijie Shan:** Writing – original draft, Methodology. **Anqiang Zhang:** Writing – review & editing, Supervision, Project administration, Funding acquisition, Conceptualization.

Declaration of competing interest

The authors declare that they have no known competing financial interests or personal relationships that could have appeared to influence the work reported in this paper.

Data availability

Data will be made available on request.

Acknowledgements

The authors acknowledge the financial support from the National Natural Science Foundation of China (No. 52073098, 31772202) and the Natural Science Foundation of Guangdong Province (No. 2022A1515011570, 2023A1515011264).

Appendix A. Supplementary data

Supplementary data to this article can be found online at <https://doi.org/10.1016/j.cej.2023.148229>.

References

- [1] Y. Zhang, Y. Li, H. Wang, Z. Zhang, Y. Feng, Q. Tian, N. Li, J. Mei, J. Su, H. Tian, Measuring the microphase separation scale of polyurethanes with a vibration-induced emission-based ratiometric “fluorescent ruler”, *ACS Appl. Mater. Interfaces*. 11 201939351–39358, <https://doi.org/10.1021/acsami.9b13193>.
- [2] S. Yang, S. Wang, X. Du, Z. Du, X. Cheng, H. Wang, Mechanically robust self-healing and recyclable flame-retarded polyurethane elastomer based on thermoreversible crosslinking network and multiple hydrogen bonds, *Chem. Eng. J.* 391 (2020) 123544, <https://doi.org/10.1016/j.cej.2019.123544>.
- [3] C. Liu, H. Yang, L. Shen, L. Shi, Q. Yin, Y. Bao, J. Ma, Mechanically robust waterborne polyurethane with excellent room temperature self-healing and shape memory performance, *Eur. Polym. J.* 196 (2023) 112288, <https://doi.org/10.1016/j.eurpolymj.2023.112288>.
- [4] S. Wendels, L. Averous, Biobased polyurethanes for biomedical applications, *Bioact. Mater.* 6 (2021) 1083–1106, <https://doi.org/10.1016/j.bioactmat.2020.10.002>.
- [5] H. Guo, L. Song, J. Hu, T. Lin, X. Li, H. Yu, D. Cheng, Y. Hou, X. Zhan, Q. Zhang, Enhanced antifouling strategy with a strong synergistic effect of fluorescent antifouling and contact bacteriostasis using 7-amino-4-methylcoumarin, *Chem. Eng. J.* 420 (2021) 127676, <https://doi.org/10.1016/j.cej.2020.127676>.
- [6] Y. Dai, K. Qi, K. Ou, Y. Song, Y. Zhou, M. Zhou, H. Song, J. He, H. Wang, R. Wang, Ag nw-embedded coaxial nanofiber-coated yarns with high stretchability and sensitivity for wearable multi-sensing textiles, *ACS Appl. Mater. Interfaces* 15 (2023) 11244–11258, <https://doi.org/10.1021/acsami.2c20322>.
- [7] N. Jiang, X. Chang, D. Hu, L. Chen, Y. Wang, J. Chen, Y. Zhu, Flexible, transparent, and antibacterial ionogels toward highly sensitive strain and temperature sensors, *Chem. Eng. J.* 424 (2021) 130418, <https://doi.org/10.1016/j.cej.2021.130418>.
- [8] W.B. Ying, Z. Yu, D.H. Kim, K.J. Lee, H. Hu, Y. Liu, Z. Kong, K. Wang, J. Shang, R. Zhang, J. Zhu, R. Li, Waterproof, highly tough, and fast self-healing polyurethane for durable electronic skin, *ACS Appl. Mater. Interfaces* 12 (2020) 11072–11083, <https://doi.org/10.1021/acsami.0c00443>.
- [9] Z. Liu, W. Guo, W. Wang, Z. Guo, L. Yao, Y. Xue, Q. Liu, Q. Zhang, Healable strain sensor based on tough and eco-friendly biomimetic supramolecular waterborne polyurethane, *ACS Appl. Mater. Interfaces* 14 (2022) 6016–6027, <https://doi.org/10.1021/acsami.1c21987>.
- [10] Z. Guo, X. Lu, X. Wang, X. Li, J. Li, J. Sun, Engineering of chain rigidity and hydrogen bond cross-linking toward ultra-strong, healable, recyclable, and water-resistant elastomers, *Adv. Mater.* 35 (2023), <https://doi.org/10.1002/adma.202300286>.
- [11] P.K. Behera, S.K. Raut, P. Mondal, S. Sarkar, N.K. Singha, Self-healable polyurethane elastomer based on dual dynamic covalent chemistry using diels-alder “click” and disulfide metathesis reactions, *ACS Appl. Polym. Mater.* 3 (2021) 847–856, <https://doi.org/10.1021/acspapm.0c01179>.
- [12] Y. Song, J. Li, G. Song, L. Zhang, Z. Liu, X. Jing, F. Luo, Y. Zhang, Y. Zhang, X. Li, Self-healing polyurethane elastomers with high mechanical properties based on synergistically thermo-reversible and quadruple hydrogen bonds, *ACS Appl. Polym. Mater.* 5 (2023) 1302–1311, <https://doi.org/10.1021/acspapm.2c01849>.
- [13] Z. Shi, J. Kang, L. Zhang, Water-enabled room-temperature self-healing and recyclable polyurea materials with super-strong strength, toughness, and large stretchability, *ACS Appl. Mater. Interfaces* 12 (2020) 23484–23493, <https://doi.org/10.1021/acsami.0c04414>.
- [14] M. Grosjean, D. Berne, S. Caillol, V. Ladmiral, B. Nottel, Dynamic peg-pla/hydroxyurethane networks based on imine bonds as reprocessable elastomeric biomaterials, *Biomacromolecules* (2023), <https://doi.org/10.1021/acs.biomac.3c00229>.
- [15] R. Liang, H. Zhang, Y. Wang, J. Ye, L. Guo, L. He, X. Li, T. Qiu, X. Tuo, Dual dynamic network system constructed by waterborne polyurethane for improved and recoverable performances, *Chem. Eng. J.* 442 (2022) 136204, <https://doi.org/10.1016/j.cej.2022.136204>.
- [16] X. Zhu, K. Han, C. Li, J. Wang, J. Yuan, Z. Pan, M. Pan, Tough, photoluminescent, self-healing waterborne polyurethane elastomers resulting from synergistic action of multiple dynamic bonds, *ACS Appl. Mater. Interfaces*. 15 (2023) 19414–19426, <https://doi.org/10.1021/acsami.3c00333>.
- [17] C. Liu, Q. Yin, Q. Yuan, L. Hao, L. Shi, Y. Bao, B. Lyu, J. Ma, A wear-resistant, self-healing and recyclable multifunctional waterborne polyurethane coating with mechanical tunability based on hydrogen bonding and an aromatic disulfide structure, *Polym. Chem.* 13 (2022) 5647–5658, <https://doi.org/10.1039/D2PY00958G>.
- [18] F. Dong, X. Yang, L. Guo, Y. Wang, H. Shaghaleh, Z. Huang, X. Xu, S. Wang, H. Liu, Self-healing polyurethane with high strength and toughness based on a dynamic chemical strategy, *J. Mater. Chem. A* 10 (2022) 10139–10149, <https://doi.org/10.1039/D2TA00802E>.
- [19] K. Chang, H. Jia, S. Gu, A transparent, highly stretchable, self-healing polyurethane based on disulfide bonds, *Eur. Polym. J.* 112 (2019) 822–831, <https://doi.org/10.1016/j.eurpolymj.2018.11.005>.
- [20] G. Wu, J. Li, Q. Zhang, H. Zhang, Synergistic effect of multiple hydrogen bond and disulfide bond on healing waterborne conductive polyurethane composite, *Polymer* 258 (2022) 125240, <https://doi.org/10.1016/j.polymer.2022.125240>.

- [21] Y. Li, W. Guo, W. Li, X. Liu, H. Zhu, J. Zhang, X. Liu, L. Wei, A. Sun, Tuning hard phase towards synergistic improvement of toughness and self-healing ability of poly(urethane urea) by dual chain extenders and coordinative bonds, *Chem. Eng. J.* 393 (2020) 124583, <https://doi.org/10.1016/j.cej.2020.124583>.
- [22] Z. Wei, Z. Liu, X. Fu, Y. Wang, A. Yuan, J. Lei, Effect of crystalline structure on water resistance of waterborne polyurethane, *Eur. Polym. J.* 157 (2021) 110647, <https://doi.org/10.1016/j.eurpolymj.2021.110647>.
- [23] H. Luo, H. Wei, L. Wang, Q. Gao, Y. Chen, J. Xiang, H. Fan, Anti-smudge and self-cleaning characteristics of waterborne polyurethane coating and its construction, *J. Colloid. Interface. Sci.* 628 (2022) 1070–1081, <https://doi.org/10.1016/j.jcis.2022.08.017>.
- [24] D. Wang, Z. Wang, S. Ren, J. Xu, C. Wang, P. Hu, J. Fu, Molecular engineering of a colorless, extremely tough, superiorly self-recoverable, and healable poly(urethane-urea) elastomer for impact-resistant applications, *Mater. Horiz.* 8 (2021) 2238–2250, <https://doi.org/10.1039/d1mh00548k>.
- [25] H. Xu, J. Tu, J. Ji, L. Liang, H. Li, P. Li, X. Zhang, Q. Gong, X. Guo, Ultra-high-strength self-healing supramolecular polyurethane based on successive loose hydrogen-bonded hard segment structures, *Eur. Polym. J.* 177 (2022) 111437, <https://doi.org/10.1016/j.eurpolymj.2022.111437>.
- [26] W. Yang, Y. Zhu, T. Liu, D. Puglia, J.M. Kenny, P. Xu, R. Zhang, P. Ma, Multiple structure reconstruction by dual dynamic crosslinking strategy inducing self-reinforcing and toughening the polyurethane/nanocellulose elastomers, *Adv. Funct. Mater.* 33 (2023) 2213294, <https://doi.org/10.1002/adfm.202213294>.
- [27] X. Chen, Q. Zhong, C. Cui, L. Ma, S. Liu, Q. Zhang, Y. Wu, L. An, Y. Cheng, S. Ye, X. Chen, Z. Dong, Q. Chen, Y. Zhang, Extremely tough, puncture-resistant, transparent, and photoluminescent polyurethane elastomers for crack self-diagnose and healing tracking, *ACS Appl. Mater. Interfaces* 12 (2020) 30847–30855, <https://doi.org/10.1021/acsami.0c07727>.
- [28] J. Xu, X. Wang, X. Zhang, Y. Zhang, Z. Yang, S. Li, L. Tao, Q. Wang, T. Wang, Room-temperature self-healing supramolecular polyurethanes based on the synergistic strengthening of biomimetic hierarchical hydrogen-bonding interactions and coordination bonds, *Chem. Eng. J.* 451 (2023) 138673, <https://doi.org/10.1016/j.cej.2022.138673>.
- [29] Y. Xu, S. Zhou, Z. Wu, X. Yang, N. Li, Z. Qin, T. Jiao, Room-temperature self-healing and recyclable polyurethane elastomers with high strength and superior robustness based on dynamic double-crosslinked structure, *Chem. Eng. J.* 466 (2023) 143179, <https://doi.org/10.1016/j.cej.2023.143179>.
- [30] X. Wu, J. Wang, J. Huang, S. Yang, Robust, stretchable, and self-healable supramolecular elastomers synergistically cross-linked by hydrogen bonds and coordination bonds, *ACS Appl. Mater. Interfaces* 11 (2019) 7387–7396, <https://doi.org/10.1021/acsami.8b20303>.
- [31] K.I. Winey, Designing tougher elastomers with ionomers, *Science* 358 (2017) 449–450, <https://doi.org/10.1126/science.aap8114>.
- [32] C. Zhang, H. Liang, D. Liang, Z. Lin, Q. Chen, P. Feng, Q. Wang, Renewable castor-oil-based waterborne polyurethane networks: simultaneously showing high strength, self-healing, processability and tunable multishape memory, *Angew. Chem. Int. Ed.* 60 (2021) 4289–4299, <https://doi.org/10.1002/anie.202014299>.
- [33] S. Kim, H. Jeon, S. Shin, S. Park, J. Jegal, S.Y. Hwang, D.X. Oh, J. Park, Superior toughness and fast self-healing at room temperature engineered by transparent elastomers, *Adv. Mater.* 30 (2018) 1705145, <https://doi.org/10.1002/adma.201705145>.
- [34] Q. Xu, Z. Zheng, B. Wang, H. Mao, F. Yan, Zinc ion coordinated poly(ionic liquid) antimicrobial membranes for wound healing, *ACS Appl. Mater. Interfaces* 9 (2017) 14656–14664, <https://doi.org/10.1021/acsami.7b01677>.
- [35] Z. Luo, H. Cui, J. Guo, J. Yao, X. Fang, F. Yan, B. Wang, H. Mao, Poly(ionic liquid)/ce-based antimicrobial nanofibrous membrane for blocking drug-resistance dissemination from mrsa-infected wounds, *Adv. Funct. Mater.* 31 (2021) 2100336, <https://doi.org/10.1002/adfm.202100336>.
- [36] Y. Wang, R. Chen, T. Li, P. Ma, H. Zhang, M. Du, M. Chen, W. Dong, Antimicrobial waterborne polyurethanes based on quaternary ammonium compounds, *Ind. Eng. Chem. Res.* 59 (2020) 458–463, <https://doi.org/10.1021/acs.iecr.9b04828>.
- [37] C. Yu, M. Salzano De Luna, A. Russo, I. Adamiano, F. Scherillo, Z. Wang, X. Zhang, H. Xia, M. Lavorgna, Role of diisocyanate structure on self-healing and anticorrosion properties of waterborne polyurethane coatings, *Adv. Mater. Interfaces* 8 (2021) 2100117, <https://doi.org/10.1002/admi.202100117>.
- [38] Q. Qu, J. He, Y. Da, M. Zhu, Y. Liu, X. Li, X. Tian, H. Wang, High toughness polyurethane toward artificial muscles, tuned by mixing dynamic hard domains, *Macromolecules* 54 (2021) 8243–8254, <https://doi.org/10.1021/acs.macromol.1c01098>.
- [39] X. Wang, J. Xu, Y. Zhang, T. Wang, Q. Wang, Z. Yang, X. Zhang, High-strength, high-toughness, self-healing thermosetting shape memory polyurethane enabled by dual dynamic covalent bonds, *Polym. Chem.* 13 (2022) 3422–3432, <https://doi.org/10.1039/D2PY00564F>.
- [40] J. Rong, J. Zhong, W. Yan, M. Liu, Y. Zhang, Y. Qiao, C. Fu, F. Gao, L. Shen, H. He, Study on waterborne self-healing polyurethane with dual dynamic units of quadruple hydrogen bonding and disulfide bonds, *Polymer* 221 (2021) 123625, <https://doi.org/10.1016/j.polymer.2021.123625>.
- [41] J. Chen, Y. Gao, L. Shi, W. Yu, Z. Sun, Y. Zhou, S. Liu, H. Mao, D. Zhang, T. Lu, Q. Chen, D. Yu, S. Ding, Phase-locked constructing dynamic supramolecular ionic conductive elastomers with superior toughness, autonomous self-healing and recyclability, *Nat. Commun.* 13 (2022), <https://doi.org/10.1038/s41467-022-32517-4>.
- [42] Z. Zheng, D. Liang, H. Deng, F. Xie, X. Chen, Y. Luo, C. Zhang, Castor oil-based, robust, non-leaching and durable antibacterial waterborne polyurethane/polyhexamethylene guanidine composites prepared via an electrostatic self-assembly strategy, *Chem. Eng. J.* 462 (2023) 142060, <https://doi.org/10.1016/j.cej.2023.142060>.
- [43] H. Wu, Y. Chen, W. Zhu, Y. Shangguan, Q. Zheng, Highly adhesive and tough thermoplastic polyurethanes using a furandicarboxamide rigid chain extender with noncovalent interactions, *ACS Appl. Polym. Mater.* 5 (2023) 3515–3523, <https://doi.org/10.1021/acsapm.3c00198>.
- [44] C. Li, P. Wang, D. Zhang, S. Wang, Near-infrared responsive smart superhydrophobic coating with self-healing and robustness enhanced by disulfide-bonded polyurethane, *ACS Appl. Mater. Interfaces* 14 (2022) 45988–46000, <https://doi.org/10.1021/acsami.2c08496>.
- [45] H. Yang, L. Jin, D. Zhao, Z. Lian, M. Appu, J. Huang, Z. Zhang, Antibacterial and antibiofilm formation activities of pyridinium-based cationic pillar[5]arene against *Pseudomonas aeruginosa*, *J. Agric. Food. Chem.* 69 (2021) 4276–4283, <https://doi.org/10.1021/acs.jafc.1c01032>.
- [46] S. He, M. Hou, S. Shan, R. Li, N. Yu, Y. Lin, A. Zhang, Synthesis and anti-bacterial/fungal activities of amphiphilic polysiloxanes primary ammonium salts, *Reactive Funct. Polymers* 183 (2023) 105495, <https://doi.org/10.1016/j.reactfunctpolym.2022.105495>.
- [47] T. Guan, X. Wang, Y. Zhu, L. Qian, Z. Lu, Y. Men, J. Li, Y. Wang, J. Sun, Mechanically robust skin-like poly(urethane-urea) elastomers cross-linked with hydrogen-bond arrays and their application as high-performance ultrastretchable conductors, *Macromolecules* 55 (2022) 5816–5825, <https://doi.org/10.1021/acs.macromol.2c00492>.
- [48] E.K. Boahen, B. Pan, H. Kweon, J.S. Kim, H. Choi, Z. Kong, D.J. Kim, J. Zhu, W. B. Ying, K.J. Lee, D.H. Kim, Ultrafast, autonomous self-healable iontronic skin exhibiting piezo-ionic dynamics, *Nat. Commun.* 13 (2022), <https://doi.org/10.1038/s41467-022-35434-8>.
- [49] X. Xun, Z. Zhang, X. Zhao, B. Zhao, F. Gao, Z. Kang, Q. Liao, Y. Zhang, Highly robust and self-powered electronic skin based on tough conductive self-healing elastomer, *ACS Nano* 14 (2020) 9066–9072, <https://doi.org/10.1021/acsnano.0c04158>.

Surface-Imprinted Polysiloxane with Recognition Ability Based on an ITO Layer for Rapid Detection of *Fusarium oxysporum* f. sp. *cubense* by the Naked Eye

Yaling Lin,^{*,§} Rui Li,[§] Ning Yu, Jianjun Chen, and Anqiang Zhang^{*}



Cite This: *ACS Appl. Mater. Interfaces* 2024, 16, 33182–33191



Read Online

ACCESS |



Metrics & More



Article Recommendations



Supporting Information

ABSTRACT: Direct observation by the naked eye of fluorescence-stained microbes adsorbed on surface imprinted polymers (SIPs) is highly challenging and limited by speed, accuracy and the semiquantitative nature of the method. In this study, we tested for the presence of spores of *Fusarium oxysporum* f. sp. *cubense* race 4 (*Foc4*), which cause severe banana Fusarium wilt disease and reduces the area of banana plants. This kind of spore can become dormant in soil, which means that the detection of secreted molecules (molecular imprinting) in soil may be inaccurate; detection methods such as polymerase chain reaction (PCR) and Raman spectroscopy are more accurate but time-consuming and inconvenient. Therefore, a semiquantitative and rapid SIP detection method for *Foc4* was proposed. Based on the ITO conductive layer, a reusable and naked-eye-detectable *Foc4*-PDMS SIP film was prepared with a site density of approximately 9000 mm⁻². Adsorption experiments showed that when the *Foc4* spore concentration was between 10⁴ to 10⁷ CFU/mL, the number of *Foc4* spores adsorbed and the fluorescence intensity were strongly correlated with the concentration and could be fully distinguished by the naked eye after fluorescence staining. Adsorption tests on other microbes showed that the SIP film completely recognized only the *Foc* series. All the results were highly consistent with the naked-eye observations after fluorescence staining, and the results of the *Foc4*-infected soil experiment were also close to the ideal situation. Taken together, these results showed that *Foc4*-PDMS SIPs have the ability to rapidly and semiquantitatively detect the concentration of *Foc* in soil, which can provide good support for banana cultivation. This method also has potential applications in the detection of other fungal diseases.

KEYWORDS: on-site rapid detection, surface imprinted polymers, naked eye, fluorescence staining, *Fusarium oxysporum* f. sp. *cubense*



1. INTRODUCTION

In the past few decades, due to the development of material and biochemical science and technology, related detection technologies for small molecules, macromolecules, viruses, and microbes have rapidly developed.^{1–9} In these studies, imprinted polymers (IPs), including molecular imprinted polymers (MIPs) and surface imprinted polymers (SIPs), which simulate antigen–antibody binding effects, serve as on-site rapid detection materials with simple sensing capabilities.¹⁰

Fusarium oxysporum f. sp. *cubense* (*Foc*) is a plant fungus that causes banana Fusarium wilt disease in vast regions of the world and is capable of long-term dormancy; in particular, race 1 (*Foc1*) and race 4 (*Foc4*) of the *Foc* series pose great harm.¹¹ Banana fusarium wilt disease caused by *Foc4* and *Foc1* is a devastating disease faced by the banana industry worldwide, but suitable disease-resistant varieties and effective treatment measures for this disease are lacking. Therefore, it is particularly important to use rapid and accurate detection techniques for banana fusarium wilt to identify pathogenic fungi and control the spread of this disease. On the other hand,

banana Fusarium wilt disease has also led to a large number of abandoned banana fields and a continuous reduction in banana planting areas. Studies have shown that the number of pathogenic fungi in the soil is positively correlated with disease severity. Therefore, timely detection of the amount of *Foc* in the soil is highly important for banana field replanting. The current mainstream detection methods for fungal spores are coating plates, polymerase chain reaction (PCR), and spectral analysis.^{12,13} For the detection of *Foc*, the coating plate wastes much time and high-end manpower; PCR technology is the most common technology, but due to cross contamination and incorrect nucleic acid sequences (DNA and RNA),¹⁴ it is

Received: April 17, 2024

Revised: June 12, 2024

Accepted: June 13, 2024

Published: June 21, 2024



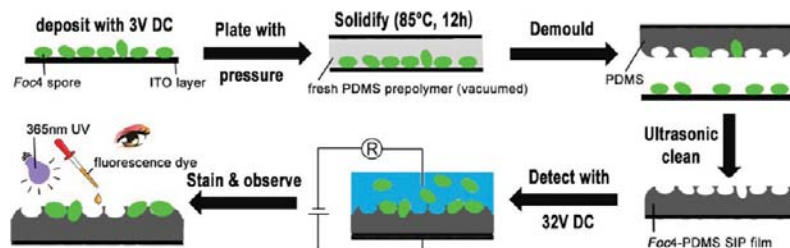


Figure 1. Complete process of preparation, adsorption, and detection of the *Foc4*-PDMS SIP film.

not completely reliable, and Raman spectroscopy instruments are very expensive and inconvenient to carry, which means that a new method must be proposed, and imprinting technology, especially IP, is much more suitable for the above conditions. Therefore, to quickly obtain reliable detection data on site, the use of MIPs to detect small molecules secreted by *Foc* with the naked eye has been considered.¹⁵ However, Compared with hyphae, *Foc* spore secretes a limited amount of small molecules in specific environments, and in most cases, it only undergoes normal metabolism and even directly enters a dormant state, which results in a minimum metabolic rate;¹¹ this makes the detection of small molecules such as fusaric acid (FA) based on MIP ineffective, and without PCR, the detection of secreted proteins such as those secreted in xylem protein (SIX) is also considered difficult.¹⁶ Inexpensive SIPs usually allow for rapid microbe detection,¹⁷ which means that SIPs are more suitable for detecting *Foc* spores than MIPs; therefore, the preparation of whole-cell SIPs and the establishment of good detection methods are absolute priorities.

The preparation of *Foc4*-PDMS SIPs and related detection methods face daunting challenges, which mainly include (1) the dispersion of microbial sedimentary layers, (2) changes in the size of imprinted sites caused by the death and dehydration of microbes during the preparation of SIP, (3) surface recognition efficiency and recognition accuracy, (4) rapid detection and sensing, especially by the naked eye, and (5) the reusability of thin smooth films.¹⁸

Many strategies have been designed to address these issues. In the initial research, a large number of scholars used glutaraldehyde to fix cells and sizes of imprint sites and then measured the adsorption capacity of imprinted polymers by using QCM.^{19–21} The application of conductive electrochemical cell SIPs enables rapid preparation, and impedance is subsequently used to detect microbial suspensions, which greatly increases the detection efficiency.^{22–24} Zhu et al.²⁵ improved the preparation of electrochemical SIPs and obtained electrodes with surface-grafted quaternary ammonium salt-imprinted polymers, which had a detection limit as low as 2 CFU/mL for *Escherichia coli* and *Staphylococcus albus*. More detection methods, such as PDMS microfluidic chip sensing²⁶ and heat transfer,^{27–29} are being explored. Ren and Zare²⁰ reported that when a modified surface is more lipophilic, more microorganisms can be adsorbed. Gennaro et al.³⁰ used electrostatic relaxation technology on adsorbed brewing yeast, indicating that in addition to surface geometric information, deeper surface information is transferred to the imprinted polymer film layer, which explains the enhanced adhesion of yeast under the action of imprinted polymers³¹ and explains why surface imprinted polymers can distinguish ABO blood groups.³² Fluorescence staining is a good auxiliary method that is sometimes used to assist in impedance detection and heat transfer detection,^{33,34} and faster on-site

detection has also been achieved via this method. Dulay et al.³⁵ labeled *E. coli* with fluorescent proteins, and the number of effectively recognized *E. coli* on the imprinted membranes was determined. Gao et al.³⁶ used AO/EB fluorescent dyes to stain tumor cells on the imprinted polymer with antibodies and achieved efficient capture of tumor cells. Bezdekova et al.³⁷ used magnetic MIP to adsorb *S. aureus* in the milk samples, and the detection limit is approximately 10^3 CFU/mL.

As mentioned above, most of the *Foc4* would be in the state of dormant spores due to the lacking of nutrients and host in real-world soil. This study was guided by rapid on-site naked-eye detection, without any host, the extremely inactive fungus *F. oxysporum* f. sp. *cubense* race 4 (*Foc4*) which spores could be in dormant state for long was selected for imprinting and detection. This kind of spore easily aggregates,³⁸ which is inconsistent with bacteria and single-cell biological spores.^{21,39} This study applied direct voltage to achieve high density and uniform dispersion to facilitate the preparation of SIPs and enhanced recognition by applying a higher voltage. A fluorescent agent that can strongly stain *F. oxysporum* is used, and solid fluorescence is used for detection to evaluate the actual effectiveness of fluorescence detection by the naked eye.⁴⁰

2. EXPERIMENTAL SECTION

2.1. Design Strategy for the *Foc4*-PDMS SIP Film. The core idea of this work is to use the good spreadability of the prepolymer and the flexibility of PDMS to prepare a relatively flat *Foc4*-PDMS surface-imprinted polymer layer on a conductive and transparent ITO layer that has been plated on a glass substrate to facilitate the observation of the electrostatic adsorption process of spores on the SIP film under an optical microscope and to collect real-time adsorption statistics. The entire process is shown in Figure 1. The preparation processes for the other fungal SIP films (changing *Foc4* to other fungi and changing the deposition time) and NIP films (without deposition) were nearly the same as those for the *Foc4*-PDMS SIP film.

2.2. Materials. ITO layered glass ($0.2\ \mu\text{m}$, $32\ \Omega$) was obtained from Luoyang Guluo (China), SYLGARD 184 was obtained from Dow Corning (Midland), *F. oxysporum* f. sp. *cubense* race 4. (*Foc4*), *F. oxysporum* f. sp. *cubense* race 1. (*Foc1*), *F. oxysporum* f. sp. *benincasae* (*Fob*), *E. coli* (*E. coli*), and *Staphylococcus albus* (*S. albus*) were obtained from South China Agricultural University, *Saccharomyces* was bought from Angel Yeast Co., Ltd. (China), and *n*-pentane, CaCl_2 , NaCl, NaOH, benzyltrimethyldecylammonium chloride (DDBAC), and Calcofluor White M2R (Fluorescent Brightener 28, FB-28) were obtained from Macklin (Shanghai, China). All chemicals were of analytical grade and used as received.

2.3. Characterization. The characterization instruments used included an optical microscope (XDS200-PH, Phenix Optics, China), a scanning electron microscope (SEM, EVO-18, Zeiss, German), a fluorescence spectrophotometer with a solid holder (F-2700, Hitachi, Japan), a microplate reader (Wellscan Mk3, Thermo LabSystems),

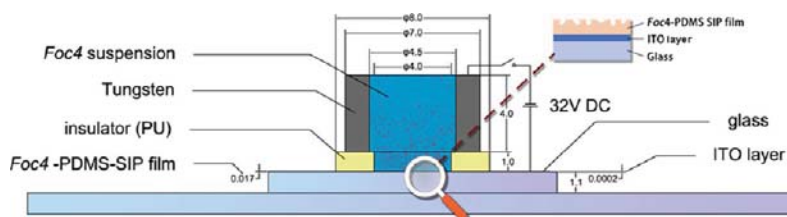


Figure 2. Diagram of the device for *Foc* spore electrodeposition detection (unit: mm).

and a three-dimensional (3D) surface profile instrument (RETC UP Dual Model, RETC).

2.4. Preparation of the *Foc4* Spore Suspension and other Microbe Suspensions. *Foc4*, *Foc1*, *Fob*, and *Staphylococcus* were flushed from solid media to a CaCl_2 solution (0.01 M, pH 7.0) to prepare suspensions, which were then manually counted after dilution to obtain accurate concentrations. *E. coli* was removed from the liquid culture medium directly to prepare a suspension, and a microplate reader was used to determine its concentration. Finally, all the suspensions were sealed at 6 °C for future use.

2.5. Preparation of the *Foc4* Spore Stamp. *Foc4* spore suspension ($1 \times 10^8 \text{ mL}^{-1}$, 15 μL . To be consistent with other papers, all mL^{-1} units in this study were written as CFU/mL), and sterile CaCl_2 solution (0.01 M, 385 μL) was mixed in a sterile centrifuge tube until the prominent uneven white turbidity disappeared. Then, all the well-mixed liquid was carefully transferred to a special tungsten model whose bottom was protected by PDMS on an ITO layer of glass to prevent any damage to the ITO layer and provide insulation protection. Afterward, a 3 V direct current was applied for 60 min, the negative electrode was set on the tungsten model, and the positive electrode was set on the ITO layer. Then, the direct current, the tungsten model, and all the liquid on the ITO layer were removed, and the ITO layer was washed with ultrapure water with a slow current for 2 min to clean the *Foc4* spore layer. Finally, the ITO layer with the *Foc4* spore layer on glass was dried without dust or other microbes for 30 min. The white transparent layer, which was subsequently plated on glass, was the *Foc4* spore stamp, and all steps were carried out at 25 °C.

2.6. Preparation of the *Foc4*-PDMS Surface Imprinted Polymer Film (*Foc4*-PDMS SIP Film, SIP Film) and PDMS Nonimprinted Polymer Film (NIP Film). Components A and B of SYGARD 184 were well mixed at a mass ratio of 10:1 as the prepolymer mixture (prepolymer), and then the mixture was vacuumed at room temperature for 10 min. After the prepolymer was placed at -18°C for 60 min to ensure that the polymerization activity of the prepolymer was minimized, a pipet was used to accurately aspirate 3.0 μL of the prepolymer and carefully drop it on another clean ITO layer. Then, this ITO layer with the mixture was placed in a clean environment for 15 min to allow the mixture to have full contact with the ITO surface for subsequent operations. With the two pieces of ITO layered glass placing contactless cross, the mixture was scrupulously covered with the well-prepared *Foc4* spore stamp. After all the area between the two pieces of ITO layered glass was filled with the mixture, the ITO-mixture-*Foc*-ITO sandwich was placed in an environment at 85 °C for 12 h. Finally, the two pieces of ITO glass were separated, and the piece of ITO layered glass with the PDMS film was the final detection piece with the *Foc4*-PDMS SIP film. In addition to the use of a clean ITO layer instead of a *Foc4* spore stamp, the preparation steps for the NIP film were the same as those for the SIP film.

2.7. Establishment of the *Foc* Spore Electrodeposition Detection Device. Inspired by a thermal transport sensor,²⁷ a *Foc* spore electrodeposition detection device composed of a glass gasket, ITO glass, *Foc4*-PDMS SIP film, tungsten ring, microbe suspension, polyurethane spacer (insulator), and a downward steady electric field on SIP film was developed. The self-established device with the detection area is shown in Figure 2.

2.8. Adsorption and Detection. In a conventional adsorption experiment at 25 °C, 15 μL of NaCl solution (0.1 M, pH 7.0) and 50

μL of *Foc4* spore suspension were mixed uniformly first, and then the mixture was added to the detection area of the SIP film, and an approximately $1.88 \text{ V}/\mu\text{m}$ ($32 \text{ V}/17 \mu\text{m}$) downward electric field was applied to adsorb the *Foc4* spores. After 60 min of adsorption, the remaining suspension, tungsten ring, and electric field were removed, and the SIP film was washed with ultrapure water under slow flow for 2 min to remove the nonadsorbed *Foc4* spores. Then, the SIP film with adsorbed *Foc4* spores was completely dried in a clean environment. Similar methods will also be used for the adsorption of other microbes for comparison. After adsorption, 50–100 μL of staining solution containing FB-28 and NaOH (1 g/L FB-28, pH = 12.0) was added to the detection area of the SIP film with adsorbed *Foc4* spores, and a piece of sterile cover glass was immediately added to the SIP film to provide the staining solution. After the entire system was put in a dark environment and dyed for 2 min, the cover glass was peeled, and the SIP film was washed with ultrapure water under slow flow for 2 min. Then, all the liquid attached to the SIP film was removed. Then, solid-state fluorescence was used to detect the fluorescence intensity of the detection area with adsorbed *Foc4* spores on the SIP film, and an ultraviolet lamp with a 365 nm wavelength was used for illumination in a dark environment to take photos and observe the sample with the naked eye. The detection and adsorption processes of the other microbes and SIP film were the same as those of *Foc*. All adsorption experiments were repeated 3 times.

2.9. Detection of *Foc* in Soil. After mixing 1 g of sterilized dry soil with 1 mL of a 10^8 CFU/mL *Foc4* spore suspension and leaching with a 20 μm metal filter 3 times, as shown in Figure 3, filtrates with

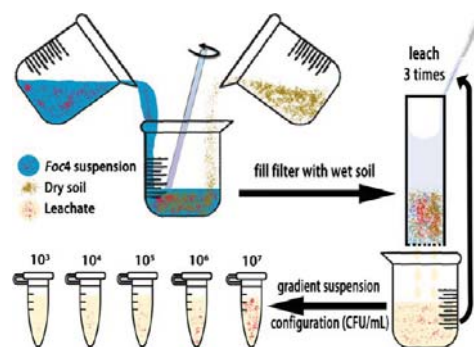


Figure 3. Processing of *Foc4*-soil leachate.

spore concentrations ranging from 10^3 to 10^7 CFU/mL were prepared after counting and adjusting the concentration of the sterile soil extract. The adsorption and detection processes were the same as in Section 2.8.

2.10. Reuse Experiments. The deposited layer was reused after demolding, the ITO layer was reused after thoroughly cleaning the deposited layer by ultrasonication, and the *Foc4*-PDMS SIPs were reused after ultrasonic cleaning. The remaining operating steps were the same as those described in Section 2.8.

3. RESULTS AND DISCUSSION

3.1. Statistics of *Foc4* Spore Number Density on the Deposited Layer. When the *Foc4* spores were deposited, the real-time number density, which varied with time, was

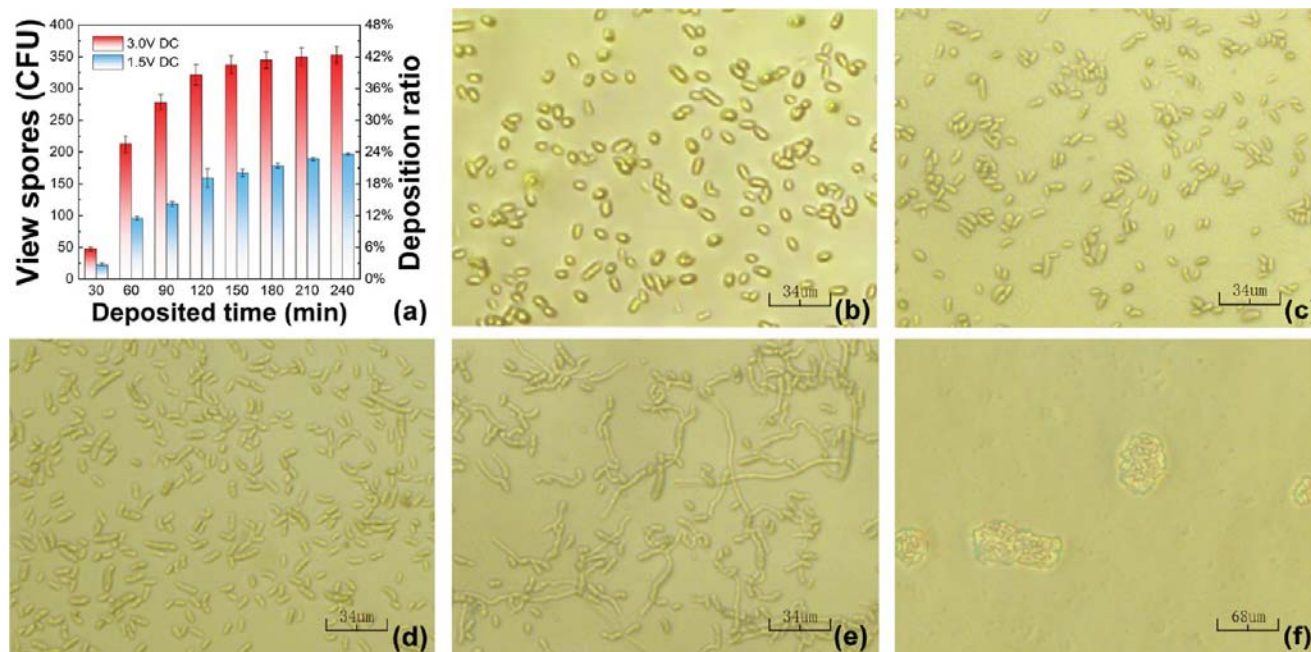
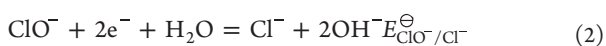


Figure 4. (a) Relationships between *Foc4* spore number density and deposition ratio, voltage, and deposition time; (b) *Foc4* spores deposited at 3 V for 60 min; (c) *Foc4* spores deposited at 3 V for 90 min; (d) *Foc4* spores deposited at 3 V for 120 min; (e) *Foc4* spores deposited at 3 V for 240 min; (f) *Foc4* spores deposited at 120 min without electricity.

determined under an optical microscope by taking micrographs after washing, and the dispersity of the *Foc4* spores could be observed at the same time. To avoid spore death caused by electrochemical reactions, according to eqs 1–3, with a 0.01 mol/L CaCl_2 solution, the lowest voltage at which the reaction begins was 1.54 V in theory, and a pre-experiment indicated that the iron sheet and stainless-steel sheet were all corroded under this voltage. Considering that the pre-experiment of the ITO layer in which the surface potential (E_c) cannot be ignored, the reaction began at 3.05 V.



$$E = (E_{\text{H}_2\text{O}/\text{H}_2}^\ominus - E_{\text{ClO}^-/\text{Cl}^-}^\ominus) - \frac{2RT}{nF} \ln[\text{Cl}^-] + E_c \quad (3)$$

The statistical data of the deposition voltage at 3.0 and 1.5 V under the same view area (0.0552 mm^2), which included 3 layers per deposition time from 30 to 240 min, are shown in Figure 4a. According to this figure, for deposition, the 3.0 V voltage was better than the 1.5 V voltage, and the number density of *Foc4* spores increased rapidly first and then increased slowly until it tended to nearly stabilize, which indicated that the best deposition time was between 120 and 240 min, when the number density under 3.0 V of *Foc4* spores was between 5500 and 6500 CFU/mm^2 . The micrographs shown in Figure 4b–e, which included different deposition times of 60 min, 90, 120 and 240 min, indicated that excessive electrodeposition time led to *Foc4* spore germination. The abovementioned phenomena implied that the best deposition time was approximately 120 min.

Compared with the layer deposited without electricity for 120 min, as shown in Figure 4f, the layer deposited with electricity, as shown in Figure 4d, could significantly disperse *Foc4* spores. Due to the presence of well-dispersed spores, the

subsequent use of a *Foc4* spore surface imprinting polymer, which is sensitive to the shape of a single spore, was convenient. The deposition methods used are shown in Table S1.

3.2. Characterization of the *Foc4*-PDMS SIP Film. After solvent-free film formation with quantitative plating, as shown in Figure S1, the two pieces of ITO glass were cured and separated, and Fourier-transform infrared (FT-IR) was used to ensure that the prepolymer fully reacted. After an electronic microgauge was used to approximately measure the thickness of the film, SEM and optical microscopy were used to obtain micrographs to determine the thickness three times, as shown in Figure 5a,b. Figure 5c shows the NIP film. And at the same time, imprinting sites could also be observed, as shown in Figure 5d–e. Compared with Figure 5f, which shows the SIP film, and Figure 5g, which shows the stamp before the SIP film, the consistency between the positions of the imprinting sites on the SIP film and the positions of the spores on the stamp indicated that the positions of the spores did not change during the preparation of the SIP film. The 3D surface profiling images shown in Figure 5h,i, which also implied that the sizes of the imprinting sites were nearly the same as those of single spores, and the surface density of the imprinted site was $9000 \pm 500 \text{ mm}^{-2}$, as shown in Figure S2.

3.3. Adsorption and Detection of *Foc4* Spores. Due to the negative charge on the spore surface, the spores could be better deposited by applying a voltage. When the device was used to adsorb *Foc4* spores, the adsorption curves shown in Figure 6a,b indicated that the optimal adsorption time was greater than 45 min. Note that in Figure 6b, the adsorption efficiency (η), which was calculated by eq 4, changed sharply when the adsorption time was between 20 and 40 min, possibly because of the permeation of ions in the film, which reduced the resistance to the appropriate value.

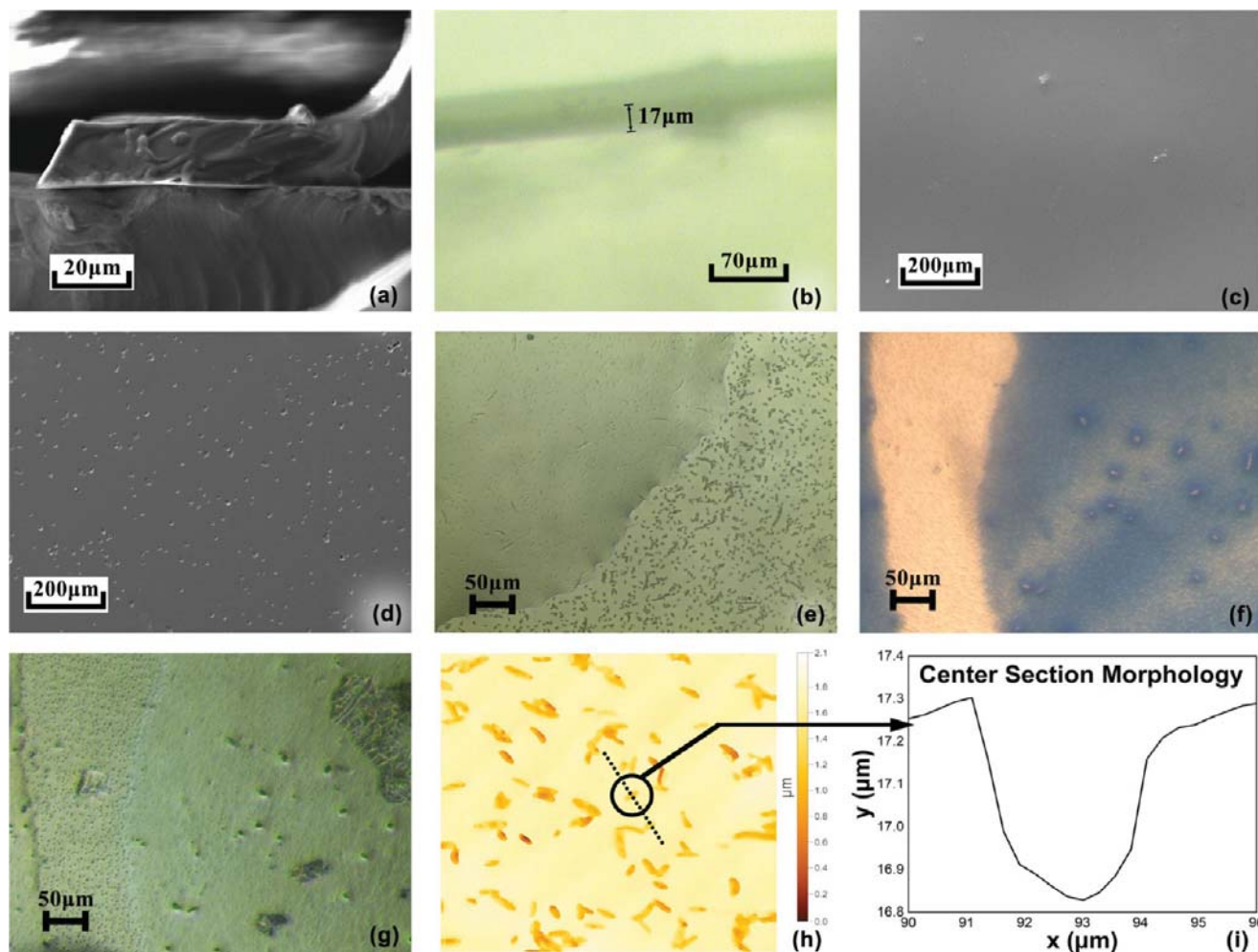


Figure 5. (a) SEM image of the film with a thickness of 17 μm ; (b) optical microscopy image of the film with a thickness of 17 μm ; (c) SEM image of the NIP film; (d) SEM image of the *Foc4*-PMDS SIP film; (e) optical microscopy image of the *Foc4*-PMDS SIP film; (f) marking area before imprinting (stamp); (g) marking area after imprinting (film); (h) 3D surface profiling image of the *Foc4*-PMDS SIP film; (i) site size.

$$\eta = \frac{\text{view number after washing}}{\text{view number before washing}} \times 100\% \quad (4)$$

After converting the number of *Foc4* spores in the view area ($10^4 \sim 2 \times 10^6$ CFU/mL: 0.37775 mm^2 ; $10^7 \sim 2 \times 10^7$ CFU/mL: 0.055224 mm^2) to the number of *Foc4* spores per unit area (CFU/ mm^2), the relationship between the adsorption number/adsorption efficiency and concentration of the *Foc4* suspension was determined, as shown in Figure 6c, and the results demonstrated that the optimal concentration for detection seemed to be between 10^5 and 10^7 CFU/mL. However, Figure 6d–f, which represent the excitation spectrum, emission spectrum and fit curve of the maximum light intensity (420 nm), respectively, showed that after fluorescence staining and analysis of the fluorescence intensity, the absolute degree of deviation from the fluorescence intensity fit curve was much smaller than that of the microscopic statistics fit curve at a spore concentration of 10^4 CFU/mL. Based on this phenomenon, we believe that the statistics are imprecise because an insufficient view area cannot reflect the real distribution of extremely few *Foc4* spores with poor distribution on a small scale, which means that the lower detection limit of this method is between 10^3 and 10^4 CFU/

mL, and the upper detection limit is between 10^7 and 2×10^7 CFU/mL.

In addition to the above results, photos taken by the camera (as shown in Figure 7a–e) strongly indicated that the best detection interval for the naked eye was 10^4 to 10^7 CFU/mL. Long-term tracking by optical microscopy and SEM was subsequently used to prove the effective adsorption of the *Foc4* spores. The adsorption process was successfully tracked (photos are shown in Figure 7f–i, and a video of the adsorption process is shown in Videos S1 and S2), and a static adsorption photo (SIP film produced with 0.1 wt % *n*-pentane), as shown in Figure 7j, was also obtained. These results well illustrated that *Foc4* spores were indeed adsorbed on the SIP film effectively.

3.4. Immunity and Selectivity of the *Foc4*-PDMS SIP Film. To compare the adsorption effects of other microbes with those of *Foc4*, *Foc1*, *Fob*, *E. coli*, and *S. albus*, a concentration of 10^7 CFU/mL was chosen. The statistical results and optical microscopy images of *Foc4*, *Foc1*, and *Fob* shown in Figure 8a–c indicate that the recognition of the *Foc4*-PDMS SIP film was likely based on the morphology of the imprint sites. The ratios of the overlap length and width of the same interval for these three kinds of microbes are shown in Figure S3, and the adsorption ratio (k) was calculated

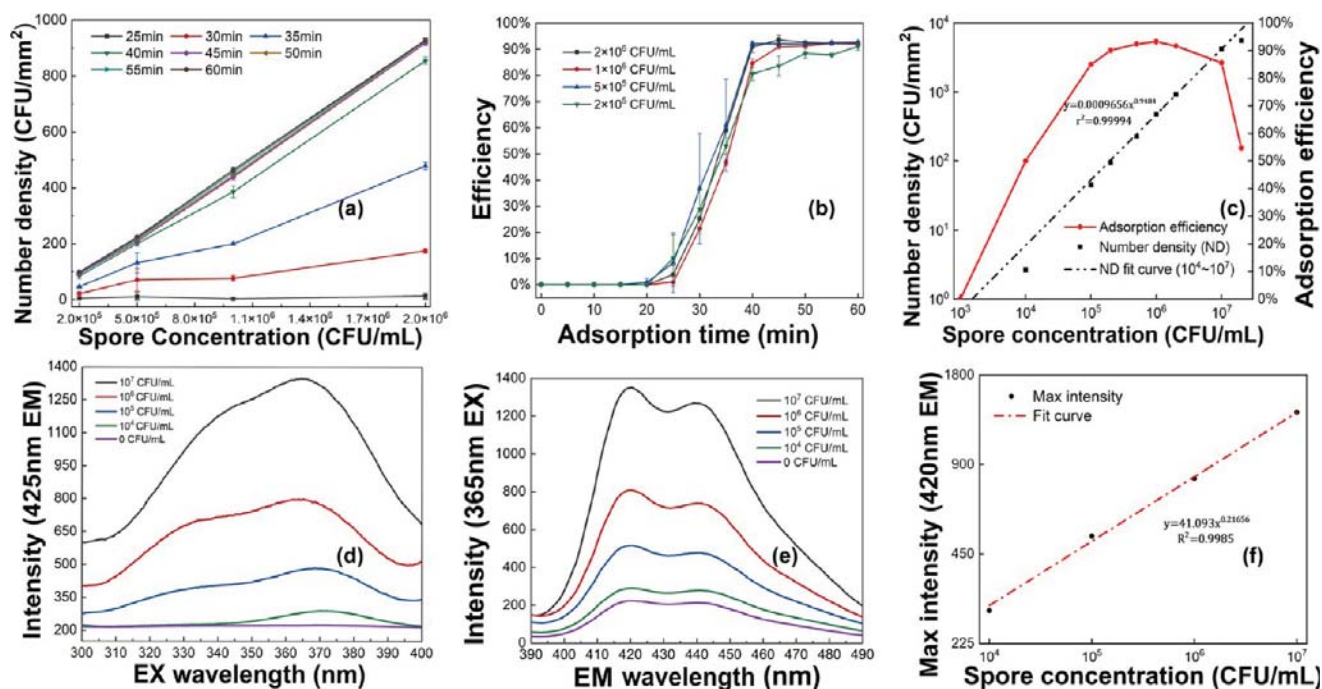


Figure 6. (a) Spore number density of *Foc4* at different concentrations at the same adsorption time; (b) Spore adsorption efficiency of *Foc4* at different adsorption times at the same concentrations; (c) Spore adsorption efficiency and number density of *Foc4* at different concentrations after adsorbing for 60 min; (d) Excitation spectrum after adsorbing for 60 min; (e) Emission spectrum after adsorbing for 60 min; (f) Maximum intensity after adsorbing for 60 min.

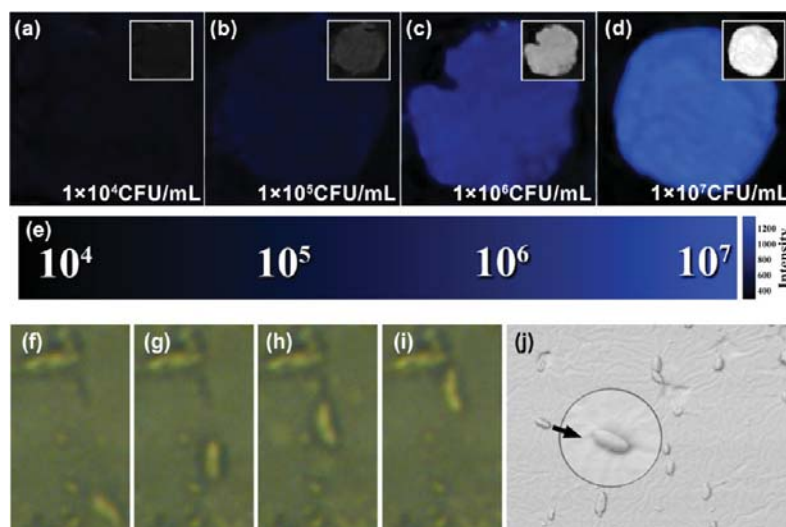


Figure 7. (a–d) Photos taken by camera (naked eye observed) with different *Foc4* spore concentrations; (e) cubic-interpolated light intensity color bar at 420 nm emission; (f–i) adsorption process; (j) static adsorption on film produced with 0.1 wt % *n*-pentane.

according to eq 5, while the η of eq 5 was calculated according to eq 4. All the statistical data were combined and calculated via eqs 4 and 5, the value of k for *Foc4* and *Fob* was 9.88% (7.34–11.36%), while that for *Foc4* and *Foc1* was approximately 100%, which confirmed that the recognition of the *Foc4*-PDMS SIP film was based on the morphology of the imprint sites. Furthermore, the abovementioned phenomena and data indicated that the *Foc4*-PDMS SIP film was not able to distinguish between *Foc4* and *Foc1*; however, considering that *Foc1* is also the main pathogenic fungus of banana Fusarium wilt disease and that the difference in virulence

between *Foc1* and *Foc4* is not significant, recognition was still considered effective.

$$k = \frac{\eta(\text{another microbe})}{\eta(\text{Foc4})} \times 100\% \quad (5)$$

Then, all the chosen microbes were adsorbed via the same methods first and tested via solid-state fluorescence. Figure 8d shows the maximum intensity of the different microbes, which was used to verify the identification mechanism of the *Foc4*-PDMS SIP film.

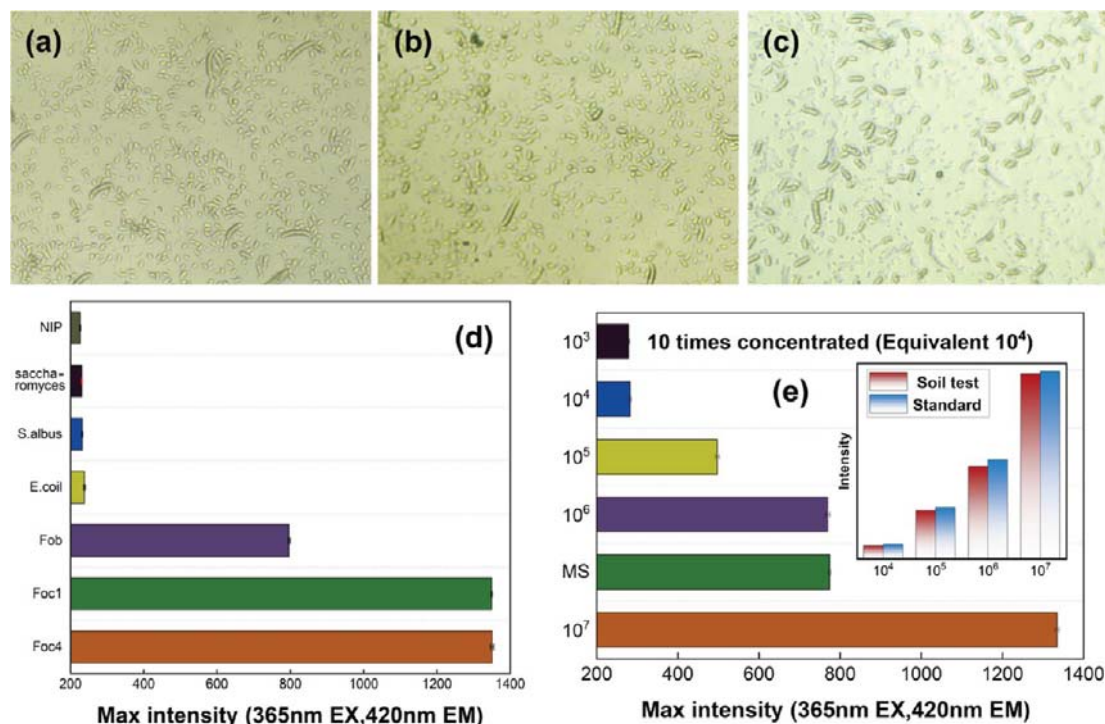


Figure 8. (a) Adsorption of *Foc4*; (b) adsorption of *Foc1*; (c) adsorption of *Fob*; (d) maximum solid-state fluorescence intensity of different microbes and NIP adsorption. (e) Soil detection with MS and different concentrations of *Foc4* spores and comparison with standard data.

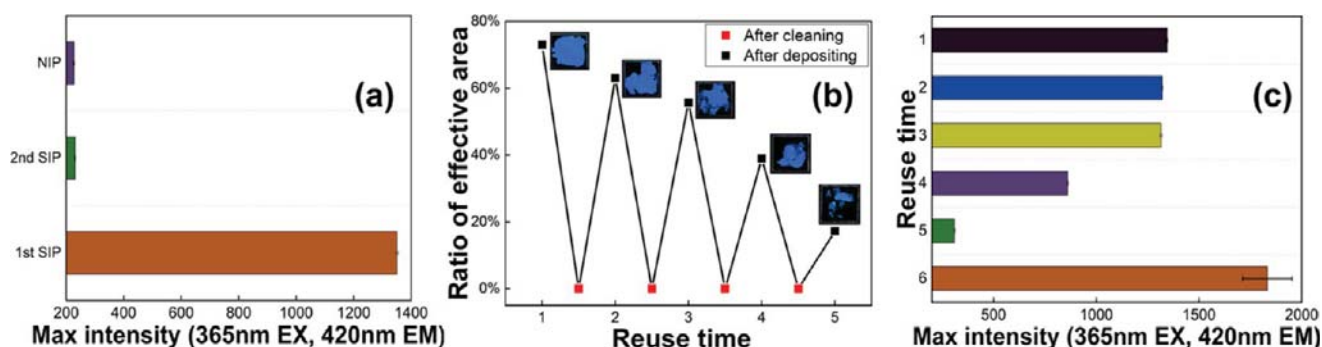


Figure 9. (a) Solid-state fluorescence intensity of NIPs, SIPs (first SIP), and reimage SIPs (second SIP); (b) ratio of the effective area of the ITO layer when reusing; (c) solid-state fluorescence intensity with different reuse times of SIPs.

To verify the detection sensitivity of the film layer in real situations, different concentrations of *Foc4* spores were detected in soil. The detection of 10⁴ to 10⁷ CFU/mL and 10 times the concentration (by centrifugation) of 10³ CFU/mL are shown in Figure 8e. And according to Figure 3, the mixed suspension (MS) with 10⁶ CFU/mL of each type microbe (*Foc4*, *E. coli*, *S. albus*, and *Saccharomyces*) was also prepared, and the result is shown in Figure 8e as well. All results indicate that the *Foc4*-PDMS SIP film had good sensitivity in real situations. One additional clarification is that *Fob* and *Foc* hardly appear in the same piece of land in the real environment, and the toxicity of *Foc1* to bananas is similar to that of *Foc4*, so the results were acceptable with a simple survey of soil history.

3.5. Reuse Experiment. To explore the recycling effect of the ITO layer with deposited spores, a second imprint was generated, as shown in Figure 9a. After a second processing at 85 °C for 12 h and reimprinting, the second *Foc4*-PDMS SIP film was not able to be used to identify *Foc4* spores, which was

similar to the identification of dead *Foc4* spores (treated with 1 g/L DDBAC for 24 h) on the first *Foc4*-PDMS SIP film; this finding indicated that the *Foc4*-deposited layer had no reuse value because an environment with long-term high temperature and low humidity killed all the spores. Due to the inability to reuse the deposited *Foc4* layer, the reuse of ITO layered glass was tested. With ultrasonic cleaning after deposition and subsequent deposition, by fluorescence staining with FB-28, Figure 9b shows that the effective deposition area of the layer decreased with increasing deposition time, so it was considered that the damage to the ITO layer caused by reuse was irreversible, but reusing twice was acceptable. A reuse experiment of the *Foc4*-PDMS SIP film was also carried out, and the solid fluorescence results of this experiment are shown in Figure 9c. The results indicated that when reused no more than 3 times, the *Foc4*-PDMS SIP film exhibited good adsorption. When it was reused 3–5 times, the adsorption capacity of the film rapidly decreased, which might be related to the total time of voltage application and the total time of

water adsorption, which greatly accelerated the failure of the film when the film was about to deform. When it was reused more than 5 times, the film was destroyed by voltage and water. Sketch maps of deformation with water adsorption and destroyed films are shown in Figure S4.

3.6. Contrast Experiment. To show that the *Foc4*-SIP film had a certain degree of specificity, SIP films of *Fob* and *S. albus* were prepared via the same process. Because adsorption kinetic of different microbes has significant differences which causes significant differences of absolute fluorescence intensity of each SIP film, all fluorescence intensity was normalized to relative intensity $I'_{Y/X}$ with eq 6. In this equation, X represents spore suspension corresponding to the SIP film, Y represents spore suspension to be tested, and I represents the absolute fluorescence intensity.

$$I'_{Y/X} = \frac{I_Y - I_{\text{NIP}}}{I_X - I_{\text{NIP}}} \times 100\% \quad (6)$$

Figure 10 shows that after normalization of fluorescence intensity, each fungi-SIP PDMS film prepared by this method

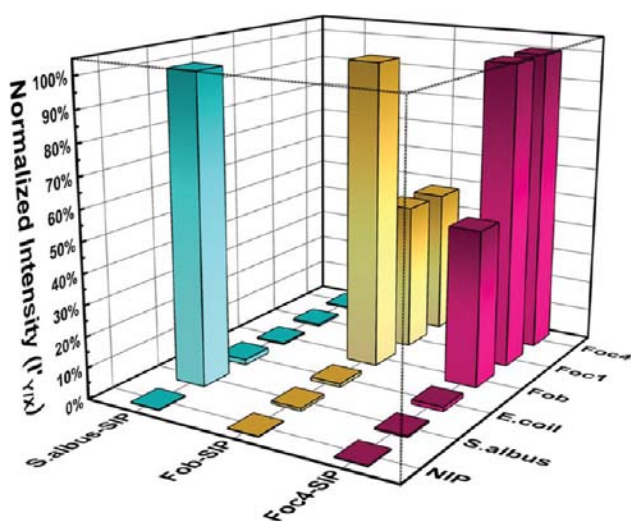


Figure 10. Detection of different SIP films.

has a response to the corresponding fungal spores, and has an incomplete response to spores with similar shapes and sizes. All results indicated that this preparation, adsorption, and detection method has considerable potential for application.

4. CONCLUSIONS

This work demonstrated a preparation strategy for smooth SIP films different from that for other SIP films and showed an easy way to detect *Foc4* spores on site by the naked eye within 1 h (the particular detection range was thought to be limited to *Foc*, including *Foc1* and *Foc4*). Compared with preparations of other microbe-deposited layers that were not easily agglomerated, the difficulty of strongly agglomerating *Foc4* spores was overcome by treatment with a stable low-voltage direct current, which led to the successful preparation of a layer of uniformly dispersed *Foc4* spores. This was the first time that the SIP dynamic adsorption process was recorded. Compared with other detection methods, the advantages of *Foc4* detection methods are as follows: (i) easy operation and visibility to the naked eye, which means that instruments are not necessary; (ii) portable SIP films and staining agents, which have great

potential for real-time and rapid detection; and (iii) easy cleaning, which shows the reusability of SIP films. Benefiting from the advantages of the preparation and detection methods, the efficiency and practicality of the *Foc4*-PDMS SIP film were confirmed. By providing a history of disease, this work may provide a new approach for on-site rapid economic detection of low-activity fungal spores or other low-activity microbes. Above all, with an acceptable limit of detection (LOD), this work has taken a significant step toward identifying microorganisms with the naked eye rather than instrument detection.

■ ASSOCIATED CONTENT

Supporting Information

The Supporting Information is available free of charge at <https://pubs.acs.org/doi/10.1021/acsami.4c06275>.

Deposition and adsorption method (processing method) selection; *Foc4*-PDMS SIP film preparation method selection; thickness selection of *Foc4*-PDMS SIP film; statistics on the length and width of *Foc1*, *Foc4* and *Fob*; explanation of destroy of reused film (PDF)
Adsorption process (MP4)
Demonstration that spores with poor adsorption could be wash by water (MP4)

■ AUTHOR INFORMATION

Corresponding Authors

Yaling Lin – College of Materials and Energy, South China Agricultural University, Guangzhou 510642 Guangdong, China; orcid.org/0000-0002-5289-4304; Email: linyaling@scau.edu.cn

Anqiang Zhang – School of Materials Science and Engineering, South China University of Technology, Guangzhou 510641 Guangdong, China; orcid.org/0000-0001-7499-8406; Email: aqzhang@scut.edu.cn

Authors

Rui Li – School of Materials Science and Engineering, South China University of Technology, Guangzhou 510641 Guangdong, China; orcid.org/0000-0003-4866-5821

Ning Yu – School of Materials Science and Engineering, South China University of Technology, Guangzhou 510641 Guangdong, China; orcid.org/0000-0002-0671-6216

Jianjun Chen – College of Materials and Energy, South China Agricultural University, Guangzhou 510642 Guangdong, China; orcid.org/0009-0003-2872-3817

Complete contact information is available at: <https://pubs.acs.org/doi/10.1021/acsami.4c06275>

Author Contributions

[§]Y.L. and R.L. contributed equally to this work. This manuscript was written through contributions of all authors. All authors have given approval to the final version of the manuscript.

Notes

The authors declare no competing financial interest.

■ ACKNOWLEDGMENTS

The authors acknowledge the financial support from the National Natural Science Foundation of China (Nos. 52073098, 31772202), the Scientific and Technological Planning Project of Guangzhou City (201803020015), and

the Natural Science Foundation of Guangdong Province (Nos. 2022A1515011570, 2023A1515011264).

REFERENCES

- (1) Vlatakis, G.; Andersson, L. I.; Müller, R.; Mosbach, K. Drug assay using antibody mimics made by molecular imprinting. *Nature* **1993**, *361*, 645–647.
- (2) Hu, X.; Li, G.; Huang, J.; Zhang, D.; Qiu, Y. Construction of Self-Reporting Specific Chemical Sensors with High Sensitivity. *Adv. Mater.* **2007**, *19* (24), 4327–4332.
- (3) Gong, C. B.; Wong, K. L.; Lam, M. H. W. Photoresponsive molecularly imprinted hydrogels for the photoregulated release and uptake of pharmaceuticals in the aqueous media. *Chem. Mater.* **2008**, *20* (4), 1353–1358.
- (4) Cumbo, A.; Lorber, B.; Corvini, P. F. X.; Meier, W.; Shahgaldian, P. A synthetic nanomaterial for virus recognition produced by surface imprinting. *Nat. Commun.* **2013**, *4* (1), No. 1503.
- (5) Wangchareansak, T.; Thitithanyanont, A.; Chuakheaw, D.; Gleeson, M. P.; Lieberzeit, P. A.; Sangma, C. Influenza A virus molecularly imprinted polymers and their application in virus subtype classification. *J. Mater. Chem. B* **2013**, *1* (16), 2190–2197.
- (6) Hou, J.; Zhang, H.; Yang, Q.; Li, M.; Jiang, L.; Song, Y. Hydrophilic-Hydrophobic Patterned Molecularly Imprinted Photonic Crystal Sensors for High-Sensitive Colorimetric Detection of Tetracycline. *Small* **2015**, *11* (23), 2738–2742.
- (7) Dinc, M.; Esen, C.; Mizaikoff, B. Recent advances on core-shell magnetic molecularly imprinted polymers for biomacromolecules. *TrAC, Trends Anal. Chem.* **2019**, *114*, 202–217.
- (8) Li, Z.-y.; Jing, L.-p.; Gu, L.-l.; Tong, Z.-h.; Du, K.; Zhang, H. Preparation and application of highly sensitive myclobutanil sensor based on molecularly imprinted photonic crystals. *Polymer* **2021**, *228*, No. 123921.
- (9) Kotsiri, Z.; Vidic, J.; Vantarakis, A. Applications of biosensors for bacteria and virus detection in food and water-A systematic review. *J. Environ. Sci.* **2022**, *111*, 367–379.
- (10) Dar, K. K.; Shao, S.; Tan, T.; Lv, Y. Molecularly imprinted polymers for the selective recognition of microorganisms. *Biotechnol. Adv.* **2020**, *45*, No. 107640.
- (11) Ploetz, R. C. Fusarium Wilt of Banana. *Phytopathology* **2015**, *105* (12), 1512–1521.
- (12) Ray, M.; Ray, A.; Dash, S.; Mishra, A.; Achary, K. G.; Nayak, S.; Singh, S. Fungal disease detection in plants: Traditional assays, novel diagnostic techniques and biosensors. *Biosens. Bioelectron.* **2017**, *87*, 708–723.
- (13) Lin, Y. J.; Lin, H. K.; Lin, Y. H. Construction of Raman spectroscopic fingerprints for the detection of Fusarium wilt of banana in Taiwan. *PLoS One* **2020**, *15* (3), No. e0230330.
- (14) Arnheim, N.; Erlich, H. Polymerase Chain Reaction Strategy. *Annu. Rev. Biochem.* **1992**, *61* (1), 131–156.
- (15) Lin, Y.; Feng, X.; Zhang, W.; Li, R.; Zhang, A. Molecularly Imprinted Photonic Crystals Based on Fusaric Acid for the Detection of Banana Fusarium Wilt. *ACS Appl. Polym. Mater.* **2021**, *3* (11), 5818–5825.
- (16) Adusei-Fosu, K.; Dickinson, M. Detecting Fusarium oxysporum f. sp. elaeidis by using loop-mediated isothermal amplification. *J. Plant Pathol.* **2023**, *105* (4), 1637–1643.
- (17) Cui, F.; Zhou, Z.; Zhou, H. S. Molecularly Imprinted Polymers and Surface Imprinted Polymers Based Electrochemical Biosensor for Infectious Diseases. *Sensors* **2020**, *20* (4), No. 996, DOI: 10.3390/s20040996.
- (18) Mamipour, Z.; Nematollahzadeh, A.; Kompany-Zareh, M. Molecularly imprinted polymer grafted on paper and flat sheet for selective sensing and diagnosis: a review. *Microchim. Acta* **2021**, *188* (8), 279.
- (19) Dickert, F. L.; Hayden, G. Bioimprinting of polymers and sol-gel phases. Selective detection of yeasts with imprinted polymers. *Anal. Chem.* **2002**, *74* (6), 1302–1306.
- (20) Ren, K.; Zare, R. N. Chemical Recognition in Cell-Imprinted Polymers. *ACS Nano* **2012**, *6* (5), 4314–4318.
- (21) Werner, M.; Gluck, M. S.; Brauer, B.; Bismarck, A.; Lieberzeit, P. A. Investigations on sub-structures within cavities of surface imprinted polymers using AFM and PF-QNM. *Soft Matter* **2022**, *18* (11), 2245–2251.
- (22) Namvar, A.; Warriner, K. Microbial imprinted polypyrrole/poly(3-methylthiophene) composite films for the detection of Bacillus endospores. *Biosens. Bioelectron.* **2007**, *22* (9–10), 2018–2024.
- (23) Lahcen, A. A.; Arduini, F.; Lista, F.; Amine, A. Label-free electrochemical sensor based on spore-imprinted polymer for Bacillus cereus spore detection. *Sens. Actuators, B* **2018**, *276*, 114–120.
- (24) Yasmeen, N.; Etienne, M.; Sharma, P. S.; El-Kirat-Chatel, S.; Helu, M. B.; Kutner, W. Molecularly imprinted polymer as a synthetic receptor mimic for capacitive impedimetric selective recognition of Escherichia coli K-12. *Anal. Chim. Acta* **2021**, *1188*, No. 339177.
- (25) Zhu, L.; Wang, L.; Zhang, X.; Li, T.; Wang, Y.; Riaz, M. A.; Sui, X.; Yuan, Z.; Chen, Y. Interfacial engineering of graphenic carbon electrodes by antimicrobial polyhexamethylene guanidine hydrochloride for ultrasensitive bacterial detection. *Carbon* **2020**, *159*, 185–194.
- (26) Regiart, M.; Rinaldi-Tosi, M.; Aranda, P. R.; Bertolino, F. A.; Villarreal-Rocha, J.; Sapag, K.; Messina, G. A.; Raba, J.; Fernandez-Baldo, M. A. Development of a nanostructured immunosensor for early and in situ detection of Xanthomonas arboricola in agricultural food production. *Talanta* **2017**, *175*, 535–541.
- (27) Eersels, K.; van Grinsven, B.; Ethirajan, A.; Timmermans, S.; Monroy, K. L. J.; Bogie, J. F.; Punniyakoti, S.; Vandenryt, T.; Hendriks, J. J.; Cleij, T. J.; et al. Selective identification of macrophages and cancer cells based on thermal transport through surface-imprinted polymer layers. *ACS Appl. Mater. Interfaces* **2013**, *5* (15), 7258–7267.
- (28) Yongabi, D.; Khorshid, M.; Losada-Pérez, P.; Eersels, K.; Deschaume, O.; D'Haen, J.; D'Haen, J.; Bartic, C.; Hooyberghs, J.; Thoenen, R.; Wübbenhorst, M.; Wagner, P. Cell detection by surface imprinted polymers SIPs: A study to unravel the recognition mechanisms. *Sens. Actuators, B* **2018**, *255*, 907–917, DOI: 10.1016/j.snb.2017.08.122.
- (29) Stilman, W.; Lenzi, M. C.; Wackers, G.; Deschaume, O.; Yongabi, D.; Mathijssen, G.; Bartic, C.; Gruber, J.; Wübbenhorst, M.; Heyndrickx, M.; Wagner, P. Low Cost, Sensitive Impedance Detection of E. coli Bacteria in Food-Matrix Samples Using Surface-Imprinted Polymers as Whole-Cell Receptors. *Phys. Status Solidi A* **2021**, *219* (23), No. 2100405, DOI: 10.1002/pssa.202100405.
- (30) Gennaro, A.; Yongabi, D.; Deschaume, O.; Bartic, C.; Wagner, P.; Wübbenhorst, M. Cell detection by surface imprinted polymers (SIPs) — A study of the sensor surface by optical and dielectric relaxation spectroscopy. *IEEE Trans. Dielectr. Electr. Insul.* **2018**, *25* (3), 816–821.
- (31) Hachułka, K.; Lekka, M.; Okrajni, J.; Ambroziak, W.; Wandelt, B. Polymeric sensing system molecularly imprinted towards enhanced adhesion of Saccharomyces cerevisiae. *Biosens. Bioelectron.* **2010**, *26* (1), 50–54.
- (32) Hayden, O.; Mann, K. J.; Krassnig, S.; Dickert, F. L. Biomimetic ABO blood-group typing. *Angew. Chem., Int. Ed.* **2006**, *45* (16), 2626–2629.
- (33) Wang, R.; Wang, L.; Yan, J.; Luan, D.; Tao, S.; Wu, J.; Bian, X. Rapid, sensitive and label-free detection of pathogenic bacteria using a bacteria-imprinted conducting polymer film-based electrochemical sensor. *Talanta* **2021**, *226*, No. 122135.
- (34) Arreguin-Campos, R.; Eersels, K.; Rogosic, R.; Cleij, T. J.; Dillen, H.; van Grinsven, B. Imprinted Polydimethylsiloxane-Graphene Oxide Composite Receptor for the Biomimetic Thermal Sensing of Escherichia coli. *ACS Sens.* **2022**, *7* (5), 1467–1475.
- (35) Dulay, M. T.; Zaman, N.; Jaramillo, D.; Mody, A. C.; Zare, R. N. Pathogen-Imprinted Organosiloxane Polymers as Selective Biosensors for the Detection of Targeted E. coli **2018** *4* 2 29 DOI: 10.3390/c4020029.
- (36) Gao, S.; Chen, S.; Lu, Q. Cell-imprinted biomimetic interface for intelligent recognition and efficient capture of CTCs. *Biomater. Sci.* **2019**, *7* (10), 4027–4035.

- (37) Bezdekova, J.; Zemankova, K.; Hutarova, J.; Kociova, S.; Smerkova, K.; Adam, V.; Vaculovicova, M. Magnetic molecularly imprinted polymers used for selective isolation and detection of *Staphylococcus aureus*. *Food Chem.* **2020**, *321*, No. 126673.
- (38) Whitehead, K. A.; Liauw, C. M.; Lynch, S.; El Mohtadi, M.; Amin, M.; Preuss, A.; Deisenroth, T.; Verran, J. Diverse surface properties reveal that substratum roughness affects fungal spore binding. *iScience* **2021**, *24* (4), No. 102333.
- (39) Sarkhosh, T.; Mayerberger, E.; Jellison, K.; Jedlicka, S. Development of cell-imprinted polymer surfaces for *Cryptosporidium* capture and detection. *Water Res.* **2021**, *205*, No. 117675.
- (40) Stewart, A.; Deacon, J. W. Vital fluorochromes as tracers for fungal growth studies. *Biotech. Histochem.* **1995**, *70* (2), 57–65.



Amphiphilic polysiloxane graft guanidine salts with a combination of low environmental toxicity and high antifungal activity

Yaling Lin^{a,*}, Shiqi He^b, Mingyang Wu^a, Meng Hou^a, Rui Li^b, Anqiang Zhang^{b,**}

^a College of Materials and Energy, South China Agricultural University, 483 Wushan Rd., Guangzhou 510642, Guangdong, China

^b School of Materials Science and Engineering, South China University of Technology, 381 Wushan Rd., Guangzhou 510641, Guangdong, China

ARTICLE INFO

Keywords:

Polysiloxane graft guanidine salts
Antifungal activity
Banana Fusarium wilt
Environmental toxicity

ABSTRACT

Banana Fusarium wilt is one of the most serious diseases that restricts the banana industry. How to achieve efficient, low toxicity, and long-term inhibition of pathogenic fungal spores (*Fusarium oxysporum* f. sp. *cubense*, race 4, Foc4) that grow in soil has become a challenge in the field of chemical control of plant diseases in recent years. Based on the special antimicrobial mechanism of guanidine salts, which can effectively inhibit microbes by forming transmembrane stomata on the plasma membrane, we were inspired to introduce hydrophilic guanidine salts to hydrophobic PDMS chains to potentially balance high antimicrobial activity and low environmental toxicity. In this work, a series of novel amphiphilic polysiloxane graft guanidine salts (PDMS-g-GH) were synthesized based on our previous works, i.e., polysiloxane graft primary amine salts (PDMS-g-AH), in which the primary amine salt groups were converted to guanidine salt groups. The molecular weight of the polymer, the grafting density of guanidine salts, the distribution of guanidine salt units on the main chain (random or block), the *in vitro* antifungal activities and the anti-Foc4 activities in soil, the adsorption characteristics in soil, and the environmental toxicity after soil adsorption were systematically studied. The results confirmed that compared with PDMS-g-AH, PDMS-g-GH showed stronger antifungal activity against Foc4 and long-term antifungal activity against Foc4 in soil, but its environmental toxicity was significantly reduced. These results support the potential application of PDMS-g-GH for the prevention and control of banana Fusarium wilt and other soil-borne fungal diseases.

1. Introduction

Banana Fusarium wilt is one of the most common and devastating soilborne diseases in banana-producing regions worldwide and is caused by *Fusarium oxysporum* f. sp. *cubense* (Foc). [1] With regards to the pathogen responsible for banana Fusarium wilt, there are multiple physiological races in which race 4 (Foc4) is the most harmful and can infect almost all banana varieties. [2] Once banana plants are infected with Foc4, the pathogen enters the vascular bundle through the root system, and conventional drugs have little effect on prevention and control; hence, this pathogen is called “banana cancer”. [3] Even worse, the chlamydospores of Foc4 can survive in soil for several years or more. The occurrence of banana Fusarium wilt is significantly related to the concentration of Foc4 spores in soil; [4,5] thus, reducing the concentration of Foc4 in the soil is currently the main goal for the control of

banana Fusarium wilt, and the control and prevention methods include cultivating resistant varieties of banana, crop rotation, soil disinfection, and biological control. [6,7] Among these methods, crop rotation has certain effects, but these effects are highly limited by market factors, such as supply and sales. [6] Soil disinfection, also called soil fumigation, involves the use of disinfectants/fumigants (such as lime nitrogen and chlorine dioxide) to kill almost all microorganisms in the soil, including Foc4; thus, new organic matter needs to be introduced after treatment to restore the soil, [7,8] and it should be noted that both residual and escaping disinfectants can also pollute the environment, and due to the difficulty of long-term retention in the soil, it is almost ineffective in the spread and diffusion of pathogens caused by the transplantation stage of banana plants after soil disinfection. [9] Biological control has been a research hotspot in recent years, and its main prevention and control strategy is to inhibit pathogens while maintaining

* Corresponding author at: College of Materials and Energy, South China Agricultural University, 483 Wushan Rd., Guangzhou 510642, Guangdong, China.

** Corresponding author at: School of Materials Science and Engineering, South China University of Technology, 381 Wushan Rd., Guangzhou 510641, Guangdong, China.

E-mail addresses: linyaling@scau.edu.cn (Y. Lin), aqzhang@scut.edu.cn (A. Zhang).

<https://doi.org/10.1016/j.eurpolymj.2024.113258>

Received 9 May 2024; Received in revised form 19 June 2024; Accepted 20 June 2024

Available online 26 June 2024

0014-3057/© 2024 Elsevier Ltd. All rights reserved, including those for text and data mining, AI training, and similar technologies.

the diversity of soil microbial communities. [7] However, the effectiveness of biological control is influenced by many external factors and is not widely applicable. Thus, an urgent challenge for the control and prevention of banana *Fusarium* wilt should be reducing the concentration of Foc4 in soil while maintaining microbial diversity in soil at the same time. [2,3].

In previous studies, [10–18] it was found that the molecular weight, hydrophilicity and hydrophobicity of the main chain, as well as the sequence structure of the main chain (random or block) of polymeric quaternary ammonium salts (PQASs), had different impacts on the antimicrobial activities of PQASs, and these PQASs showed some commonalities, such as significantly enhanced antimicrobial activity compared to that of the corresponding monomers containing cations, strong adsorption and difficulty migrating in soil; after being adsorbed by soil, their toxicity to the environment was significantly reduced, and their impact on soil microbial populations was relatively small. [12,14–16] For example, both amphiphilic polysiloxane-polyacrylate quaternary ammonium salt block copolymers (S_5Q_5) [12] and hydrophilic polyacrylamide containing quaternary ammonium salt (PAM-X) [15] can effectively adsorb in soil, and their inhibitory effect on Foc4 spores in soil can last for 60–90 d. When a more hydrophobic fluorinated acrylic monomer unit is introduced into the main chain of the polyacrylate quaternary ammonium salts, the anti-Foc4 activity can be significantly enhanced. [14] Unlike commercial small-molecule quaternary ammonium salts (such as benzalkonium chloride/BC), which can significantly destroy soil microbial diversity, the abovementioned PQASs, which have vastly different structures, have relatively small overall impacts on soil microbial populations. [15,16] Although these PQASs are basically nontoxic to earthworms when applied to soil and their soil/water mixtures and soil leaching solutions are almost nontoxic to fish, their acute oral toxicity to fish when directly applied to water is moderate, which hinders their application in the field.

Compared with quaternary ammonium salts, other cationic groups, such as primary ammonium salts and guanidine salts, can increase electrostatic binding to anionic lipopolysaccharides, which strongly disrupts cell wall integrity. [18,19] It was found that polymers containing guanidine salts could effectively inhibit microbes by forming transmembrane stomata on the plasma membrane in contact with microorganisms, which is different from the mechanism of action of QASs, indicating that the guanidine polymer could be effective against microbial activity without severe membrane damage; in other words, the introduction of guanidine salts into polymer chains might be a potential strategy for the synthesis of polymers with low toxicity and high antimicrobial activity. [20–23].

These results also prompt us to consider the following questions: can we simultaneously reduce the environmental toxicity while obtaining higher antifungal activity by introducing different cations into the polymer chain? [24–26] Therefore, in this work, based on previous work, i.e., the synthesis of a series of polydimethylsiloxane-grafted primary amine hydrochlorides (PDMS-g-AH), [16] we attempted to convert the primary amine salt into a guanidine salt, thus affording a series of polydimethylsiloxane-grafted guanidine salts (PDMS-g-GH) with different main chain lengths, main chain structures (random or block), and guanidine salt grafting rates. The inhibitory effects of PDMS-g-GH on Foc4 in culture media and in the soil environment and its environmental toxicity, including its impact on the soil microbial population and fish, and its relationship with polymer structure were also evaluated. In these works, we hope that a novel cationic polymer with low toxicity and high antifungal activity can be obtained.

2. Experimental section

2.1. Materials

1H-Pyrazole-1-carboxamide hydrochloride (HPC, 99 %), N,N-diisopropylethylamine (DIEA, 99 %), and benzalkonium chloride (BC,

99 %) were obtained from Shanghai Macklin Biochemical Technology Co., Ltd. (Shanghai, China).

Fusarium oxysporum f. sp. *cubense* race 4 (Foc4) was donated by the Fungal Laboratory, Department of Plant Pathology, South China Agricultural University. The soil (crushed and screened through a 20-mesh sieve) was taken from the banana field of the scientific research base of South China Agricultural University. The physicochemical properties of the soil are shown in Table S2. Zebrafish with a total length of 2 ± 0.5 cm and a weight of 0.2 ± 0.1 g were purchased from Shanghai Feixi Biotechnology Co., Ltd.

2.2. Synthesis of amphiphilic polysiloxane graft guanidine salts (PDMS-g-GH)

Polysiloxanes grafted with primary ammonium (PDMS-g-AH) with different chain lengths and structures, i.e., random copolymer (PDMS-co-AH) or block copolymer (PDMS-b-AH), as shown in Scheme 1, were synthesized via a thiol-ene “click” reaction between cysteamine hydrochloride and polydimethylsiloxane-polymethylvinylsiloxane (PDMS-PVMS), including random copolymer (PDMS-co-PVMS) and block copolymer (PDMS-b-PVMS), according to our previous work, where the chain lengths of PDMS-co-PVMS or PDMS-b-PVMS are 3, 5, and 8 kDa, and the graft ratios of primary ammonium, which are determined by the contents of PVMS in PDMS-PVMS, are 50 % and 75 %, respectively, as shown in Table S1. [16].

PDMS-g-GH was synthesized via a guanidine reaction between PDMS-g-AH and 1H-pyrazole-1-carboxamide hydrochloride (HPC), as shown in Scheme 1. Predetermined amounts of PDMS-g-AH and HPC were dissolved in 50 g of anhydrous ethanol in a 250 mL three-neck flask, and predetermined amounts of DIEA were added as catalysts under a nitrogen atmosphere. The mixture was reacted for 12 h at 55 °C, and most of the solvent was removed by rotary steaming at 70 °C. Then, the residue was precipitated three times using a mixed solvent of methanol and acetone and finally vacuum dried overnight at 60 °C (approximately 93 % yield).

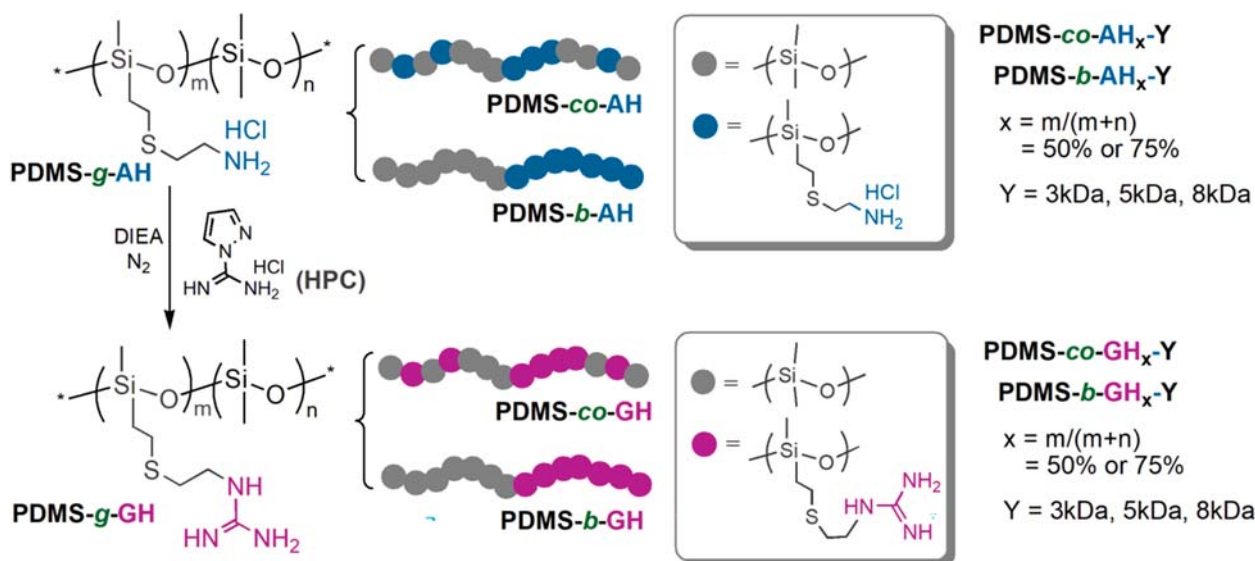
For convenience, PDMS-g-GH with a random structure and block structure are represented as PDMS-co-GH_x-Y and PDMS-b-GH_x-Y, respectively, where x represents the graft ratio of GH in PDMS-g-GH (50 % or 75 %), i.e., m/(m + n) in Scheme 1, and Y is the theoretical molecular weight of PDMS-PVMS (3 kDa, 5 kDa and 8 kDa).

¹H NMR (600 MHz, D₂O, δ , ppm): δ = 0–0.30 (m, 9H, –SiCH₃); 1.03 (t, 2H, –SiCH₂CH₂S–); 2.75 (t, 2H, –SiCH₂CH₂S–); 2.86 (t, 2H, –CH₂SCH₂–), 3.48 (t, 2H, –SCH₂CH₂NH); FT-IR (ν , KBr, cm^{–1}): 3400 (ν_{NH}), 2963 (ν_{asCH_3} , –CH₃), 1640 ($\delta_{\text{C=N}}$), 1095 ($\nu_{\text{Si-O}}$), 1020 ($\nu_{\text{Si-O}}$), 866 ($\nu_{\text{Si(CH}_3)_2}$), 802 ($\nu_{\text{asSi(CH}_3)_2}$).

2.3. Characterization and methods

FT-IR spectra were collected on a Nicolet iS5 Fourier transform infrared spectrometer (Thermo Scientific, USA) equipped with an iD7-ZnSe ATR accessory. ¹H NMR spectra were obtained using a Bruker Avance III HD 600 (Bruker Instrument Corp., Germany) spectrometer with CDCl₃ (for PDMS-PVMS) or D₂O (for PDMS-g-AH or PDMS-g-GH) as the solvent. The critical micelle concentration (CMC) was determined using a DDS-11A conductivity meter (Shanghai Hongyi Instrument Co. Ltd., China). Zeta potentials and particle size distributions were analyzed using a Brookhaven BI-90 Plus particle size analyzer (Brookhaven Instrument Corp., USA) with ultrapure water as the solvent. TEM was performed with a JEM-2100 transmission electron microscope (JEOL, Japan), in which PDMS-g-GH was prepared in a 1 g/L solution with ultrapure water, followed by dropping and drying onto a copper net with a carbon film.

The other methods, including the testing method for the adsorption of PDMS-g-GH in soil, the antifungal assay of PDMS-g-GH on Foc4 (in vitro and in soil), and the biotoxicity evaluation (culturable microbes in soil and fish acute toxicity evaluation), are detailed in the Supporting



Scheme 1. The synthetic route of PDMS-g-AH and PDMS-g-GH.

Information (Parts S2 to S4).

3. Results and discussion

3.1. Structural characterization of PDMS-g-GH

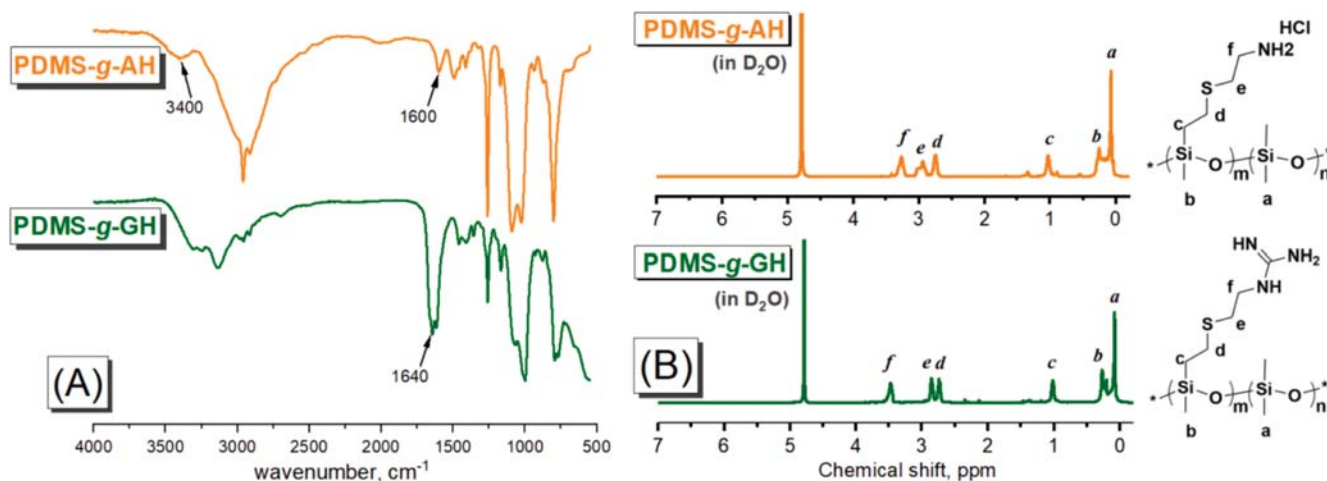
With respect to the guanidine products of PDMS-g-AH, the disappearance of the characteristic peak of the primary ammonium salts and the appearance of the characteristic peak of the guanidine salts could effectively support the synthesis of PDMS-g-GH. As shown in Fig. 1-A, the peak at 1640 cm^{-1} for PDMS-g-GH can be assigned to the guanidine groups, and the protons at 3.48 ppm ($-\text{SCH}_2\text{CH}_2\text{NH}$) (Fig. 1-B) confirmed the successful connection of the guanidine salts to the PDMS chain.

As shown in Scheme 1, there is only one simple side functional group conversion between PDMS-g-AH and PDMS-g-GH, and the molecular weight and molecular weight distribution of PDMS-g-GH are basically consistent with those of PDMS-g-AH, as described in our previous work [16].

3.2. Aggregation characteristics of PDMS-g-GH in water

The critical micelle concentration (CMC) of PDMS-g-GH was measured by the electrical conductivity method. Fig. 2-A shows the CMCs of PDMS-g-GH with different molecular weights and grafting degrees. The CMCs of the block type (PDMS-b-GH) were lower than those of the random type (PDMS-co-GH), while the molecular weights and grafting degrees were the same. Compared with those of PDMS-g-AH, [16] the CMCs of PDMS-g-GH are slightly greater, which might be related to the greater hydrophilicity of the guanidine salts.

The zeta potential and particle morphology of PDMS-g-GH in water are shown in Fig. 2-B and Figure S1, respectively. The results showed that polymers with low molecular weights exhibited low zeta potentials, indicating that it was easier for polymers to aggregate in water. Compared with PDMS-g-AH, [16] PDMS-g-GH with the same structure, i. e., the same chain length and chain structure (random or block), showed a lower zeta potential (Fig. 7-B) and larger particle size. Moreover, at concentrations much greater than the CMC, PDMS-g-GH could form spherical or hollow micelles (Figure S1), and a higher molecular weight would result in a larger diameter of the micelles.

Fig. 1. FTIR spectra (A) and ^1H NMR spectra (B) of PDMS-g-AH and PDMS-g-GH.

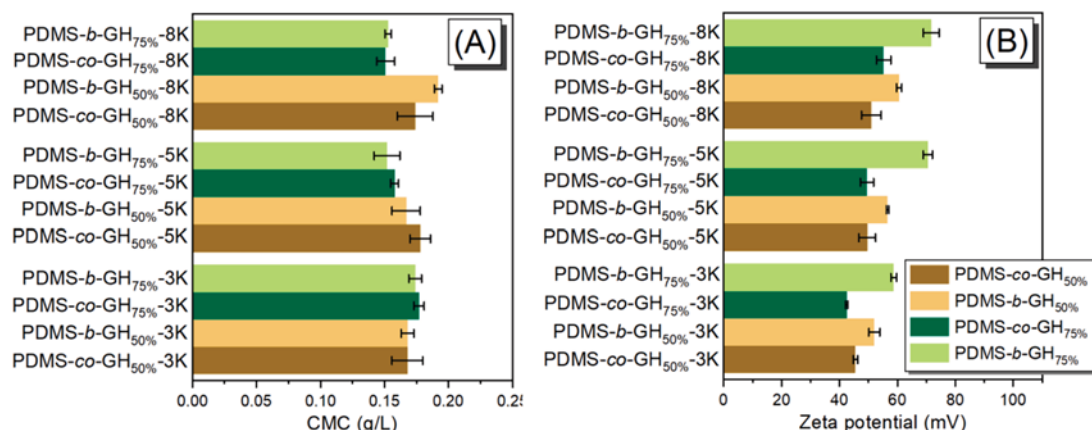


Fig. 2. The critical micelle concentration (CMC) (A) and zeta potentials (B) of PDMS-co-GH and PDMS-b-GH with different molecular weights (3, 5, and 8 kDa) and grafting degrees (50 % and 75 %, respectively). (Vertical bars represent the standard error of the means.).

3.3. The absorption effect of PDMS-g-GH in soil

Fig. 3 shows the sorption kinetics of PDMS-g-GH, PDMS-g-AH and BC in soils. After less than 3h, equilibrium adsorption of the three tested fungicides in soil was observed, after which the concentration of fungicides in the soil was almost unchanged (Fig. 3-A). Moreover, the overall adsorption kinetics of these three fungicides on the soil conformed to a pseudo-second-order model with coefficients of correlation (R^2) above 0.99 (Fig. 3-B). Both the Freundlich and Langmuir models were selected to fit the results (Fig. 3-C, D and Table S3), where the

Freundlich model showed a better regression coefficient (R^2), indicating that the adsorption of PDMS-g-GH, PDMS-g-AH and BC to the tested soil tended to be a multilayer adsorption process. The Freundlich constant ($1/n$) (Table S3) is related to the adsorption strength of the adsorbent: $1/n$ values of 0.1–0.5, 0.5–1.0, and > 1.0 indicate that adsorption is good, easy to adsorb, and difficult to adsorb, respectively. Thus, the $1/n$ values of PDMS-g-GH, PDMS-g-AH and BC are all greater than 0.5, indicating that they can be easily adsorbed in soil. The strong absorption effect of PDMS-g-GH and PDMS-g-AH in soil might be due to two main factors: first, the positive charge carried by the polymers can combine

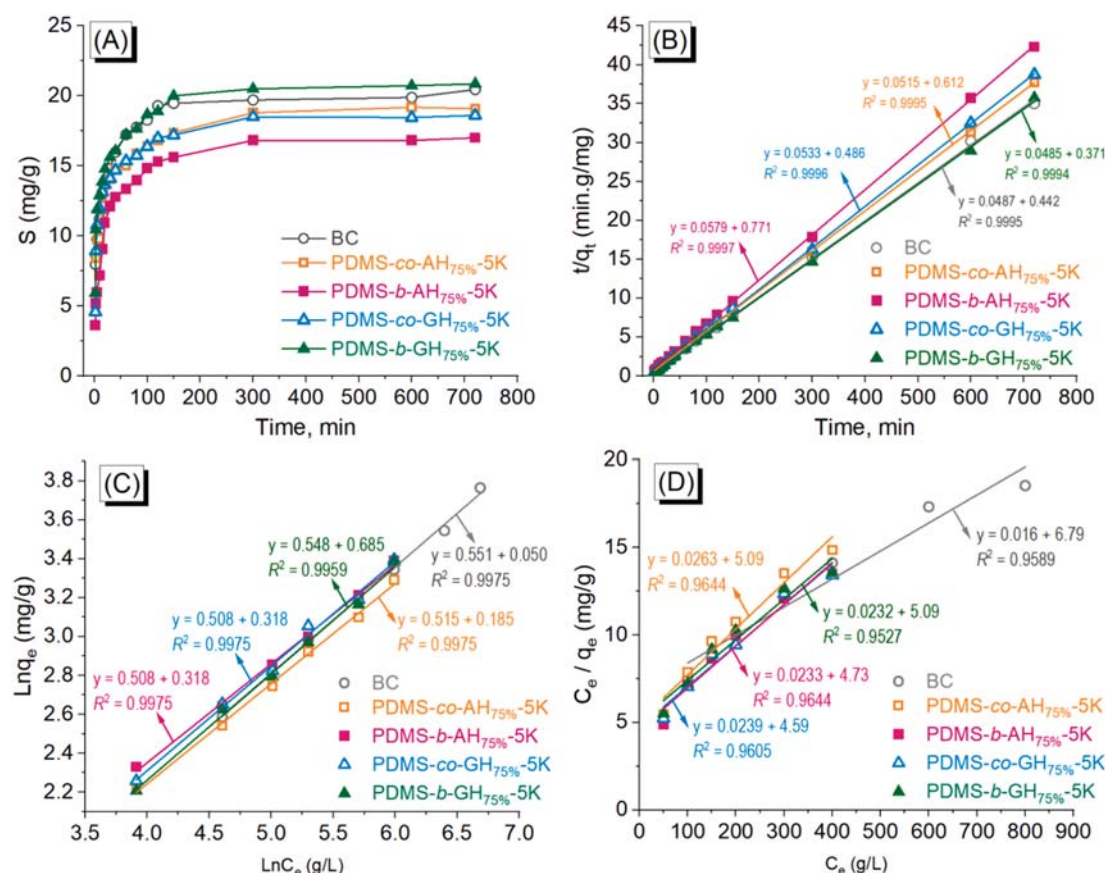


Fig. 3. Sorption kinetics and isotherms of PDMS-g-GH, PDMS-g-AH and BC in soils: (A) relationships between the sampling time and the PDMS-g-GH, PDMS-g-AH and BC concentrations in soils; (B) the pseudo-second-order model fit to the PDMS-g-GH, PDMS-g-AH and BC sorption kinetics data; (C) Freundlich sorption isotherms and (D) Langmuir sorption isotherms.

with the negative charge normally carried by soil particles (such as sludge and sediments); second, the long chain of polymers and the entanglement between polymer chains and soil particles. For BC, the first aspect mentioned above is the main reason.

3.4. Antifungal activities of PDMS-g-GH based on different evaluation methods

According to the different application scenarios of fungicides, there are several commonly used methods for evaluating antifungal activities, such as the TTC coloration method, inhibition of mycelial growth, and the spore counting method, which simulate the antifungal activities of fungicides in soil. The TTC coloration method evaluates the antifungal activity of fungicides when they come into free contact with fungal spores or mycelia in a liquid environment, in which the minimum inhibitory concentration (MIC) and minimum fungicidal concentration (MFC) are used to evaluate the antifungal activities. While for the method of inhibition of mycelial growth, fungal mycelia were cultured on solid or gel cultures containing fungicide, and the 50 % effective concentration (EC_{50}) and 90 % effective concentration (EC_{90}) were used to evaluate the antifungal activities. Since the contact between the mycelia and the culture medium is limited, the results might not reflect the true environment of fungicides in soil.

Considering that fungicides might be used in soil to inhibit soil-borne fungal spores, it is necessary to introduce the soil environment during the testing process. The spore counting method was designed for the application of fungicides in soil. To distinguish it from the aforementioned methods, EC_{50s} and EC_{90s} were used to evaluate the antifungal activities of fungicides in soil; here, the subscript “s” indicates soil.

The *in vitro* antifungal activities of PDMS-g-GH against Foc4, i.e., MIC and MFC and EC_{50} and EC_{90} , are shown in Figs. 4 and 5, respectively. Although the testing methods are different, the general trends of the polymer structure and antifungal activities are similar. For example, for the same molecular weight of the main chain, block polymers and polymers with higher graft rates showed stronger antifungal activities. Additionally, for both PDMS-g-AH and PDMS-g-GH, the MIC and MFC values on Foc4 are much lower than their CMC values, which means that micelles formed by single polymer chains play a dominant role in antifungal activity. Due to the different methods used for testing antifungal activities, the antifungal activities of the polymers were slightly different: PDMS-g-GH-5 K and PDMS-g-GH-8 K showed better antifungal

activities (Fig. 4) based on the MIC and MFC results, while PDMS-g-GH-5 K showed stronger antifungal activities based on the EC_{50} and EC_{90} results (Fig. 5). When the side group of the primary ammonium salt (AH) was converted to a guanidine salt (GH), the antifungal activity significantly increased, and the antifungal activity of PDMS-g-GH was almost double that of PDMS-g-AH.

In the subsequent evaluation of antifungal activities in soil, PDMS-g-AH and PDMS-g-GH, which have main chain molecular weights of 3 k and 5 k and high *in vitro* antifungal activity, respectively, were chosen for further evaluation of their EC_{50s} and EC_{90s} . Fig. 6 shows the 50 % inhibitory concentration (EC_{50s}) and 90 % inhibitory concentration (EC_{90s}) of PDMS-g-GH and PDMS-g-AH in inhibiting Foc4 spores in soil. Compared to the EC_{50} , the EC_{50s} had a much lower value, which is only approximately half of the EC_{50} . Although the *in vitro* anti-Foc4 activity of PDMS-g-GH was much lower than that of BC, the anti-Foc4 activity of PDMS-g-GH in soil was similar to or even greater than that of BC, which might be related to the chemical structure of the guanidine group and the hydrophilic-hydrophobic balance of PDMS-g-GH. Although the antifungal activity of PDMS-g-GH was stronger than that of PDMS-g-AH, these two series of fungicides exhibited a pattern of greater zeta potential and stronger anti-Foc4 activities, in which the block polymers showed greater zeta potential and stronger anti-Foc4 activities than the random polymers (Fig. 7-B), which might be due to the tighter aggregation of cations in the block copolymers. It was also found that there was a good linear relationship between the EC_{50s} and EC_{50} , as shown in Fig. 7-A. The difference between the EC_{50} and EC_{50s} might be related to the testing conditions of the EC_{50s} , in which the polymer chains have more opportunities and sufficient contact with soil and Foc4 spores, and effective contact between fungicides and spores would result in better antifungal activities. These results provide us with some inspiration for designing and synthesizing cationic polymers with high zeta potentials to obtain fungicides with better antifungal activity.

The rapid spread of Foc4 caused by agricultural production (banana seedling transportation, the use of production equipment, etc.) was one of the main reasons for the rapid spread of banana Fusarium wilt; thus, the ability to continuously and repeatedly inhibit newly transmitted Foc4 spores, i.e., the persistence of fungicides on Foc4 in soil, should be important for the control of banana Fusarium wilt. Therefore, by adding a Foc4 spore suspension to soil every 10 d, the persistence of different concentrations of fungicides in the soil was evaluated. As shown in Figure S3, both PDMS-g-AH and PDMS-g-GH were unable to kill all the

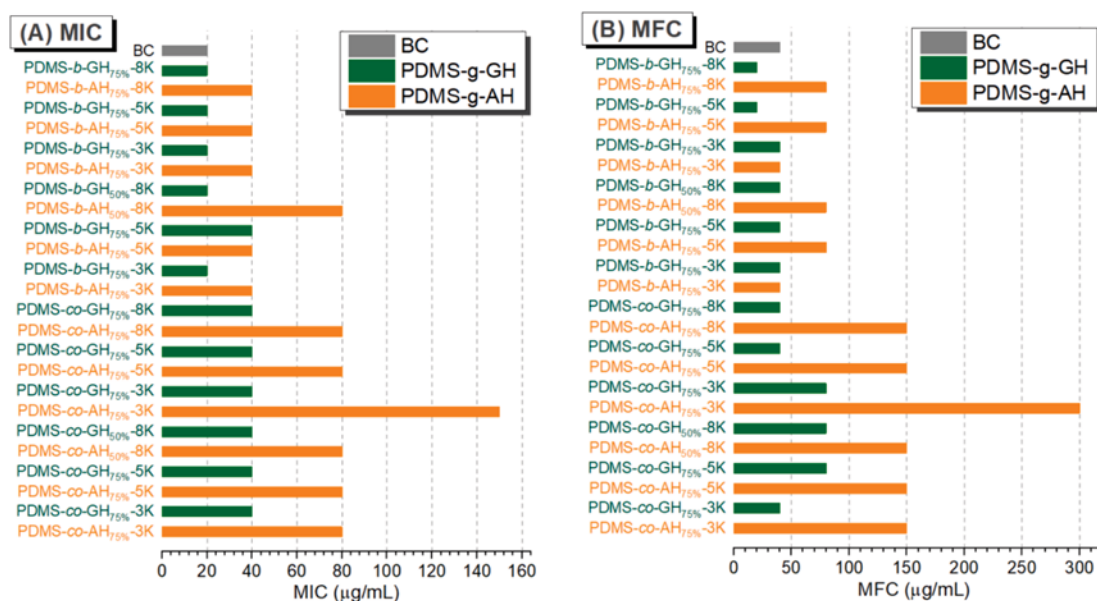


Fig. 4. MICs (A) and MFCs (B) of PDMS-g-GH and PDMS-g-AH against Foc4.

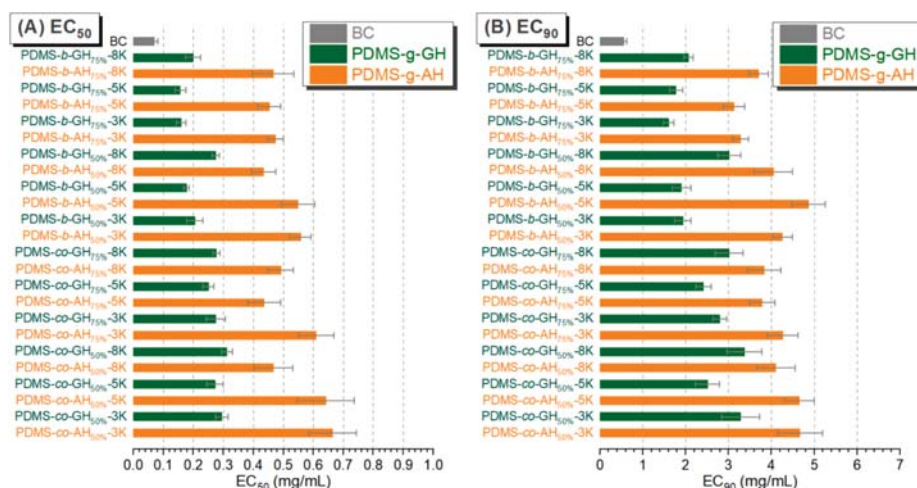


Fig. 5. EC_{50} and EC_{90} of PDMS-g-GH and PDMS-g-AH against Foc4 (Vertical bars represent the standard error of the means.).

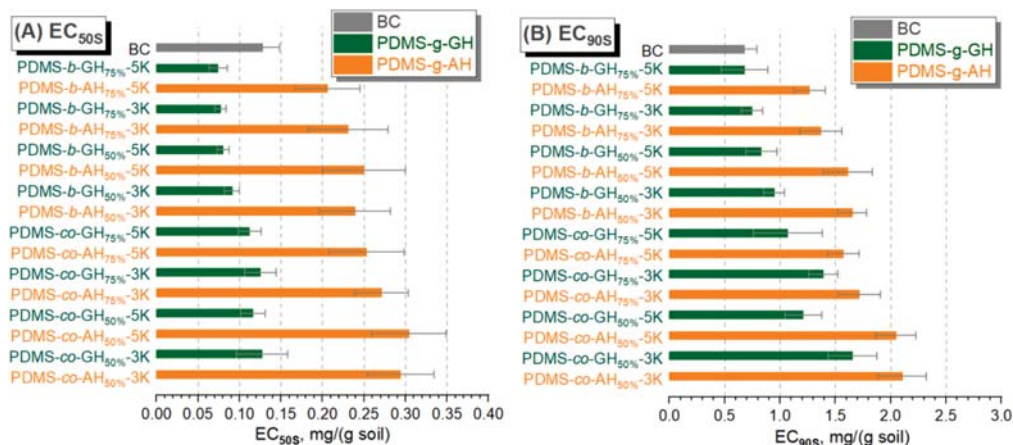


Fig. 6. EC_{50S} (A) and EC_{90S} (B) of PDMS-g-GH and PDMS-g-AH against Foc4 in soil (Vertical bars represent the standard error of the means.).

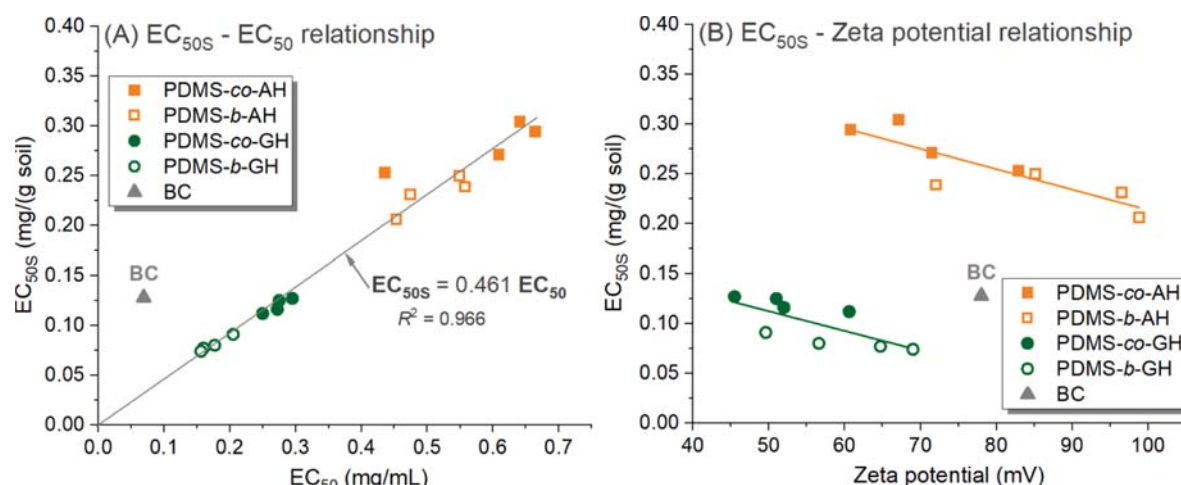


Fig. 7. The EC_{50S} – EC_{50} relationship (A) and the EC_{50S} – zeta potential relationship (B) of PDMS-g-GH and PDMS-g-AH.

Foc4 spores in the soil at concentrations of 1 x EC_{50S} and 4 x EC_{50S} . When the concentration exceeded 16 x EC_{50S} , it could effectively kill Foc4 spores in the soil for a duration of 30 d. However, for BC, after the second addition of Foc4 spores, Foc4 colonies appeared on PDA media at 20 d, indicating that compared with PDMS-g-AH and PDMS-g-GH, BC

had a shorter persistence of Foc4 in soil. The results indicate that lower concentrations of PDMS-g-AH and PDMS-g-GH can effectively inhibit Foc4 spores in soil for longer durations.

3.5. The environmental impact of PDMS-g-GH

The development of antimicrobial agents with low toxicity and high efficiency is one of the important principles for the design of fungicides. Here, so-called low toxicity refers to minimizing the impact on other living organisms in the environment, such as soil microorganisms, environmental water that is in direct contact with soil, and the fish that survive in the environment, while suppressing pathogenic fungi.

Fig. 8 shows the effects of the PDMS-g-AH, PDMS-g-GH and BC treatments on the total number of culturable populations of bacteria, fungi and actinomycetes in the soil. Compared to BC, PDMS-g-AH and PDMS-g-GH effectively inhibited fungal growth, while the total number of bacterial and actinomycete communities increased. PDMS-g-GH had a greater inhibitory effect on the total number of fungal colonies than did PDMS-g-AH.

The influence of BC, PDMS-g-AH and PDMS-g-GH on the number of soil microbes might be related to the stable adsorption of PDMS-g-AH and PDMS-g-GH in soil and their antifungal activities in soil. As mentioned above, most of the PDMS-g-AH and PDMS-g-GH chains were stably adsorbed on the surface of the soil particles, which greatly reduced the effective contact probability between the free polymer chains and the microorganisms in the soil; thus, the antimicrobial activities of these cation polymers would be reduced and prolonged. In comparison, the weaker absorption of BC in soil might help to maintain the strong antimicrobial activities of BC, thus resulting in broad-spectrum inhibition of microorganisms in soil.

One possible explanation is that the bacteria, fungi, and actinomycetes in the soil ecosystem are in a dynamic equilibrium relationship. Since both PDMS-g-AH and PDMS-g-GH have different inhibitory effects on microorganisms in the soil, when they have a good inhibitory effect on fungi and greatly reduce their number, the bacteria and actinomycetes in the soil will be relatively conducive to reproduction and increase due to the reduction in competition. [14] In summary, the application of PDMS-g-GH in soil can shift the soil toward bacterial soil, which is beneficial for plant growth. Notably, the detailed strains of bacteria, fungi and actinomycetes after treatment with BC, PDMS-g-AH and PDMS-g-GH should be intensively investigated in the future.

Fig. 9 shows the acute toxicity of PDMS-g-AH and PDMS-g-GH to zebrafish under different conditions, i.e., direct toxicity (LC_{50}), soil/water mixture (LC_{50S}) and leachate of soil (LC_{50L}). Compared to the high toxicity of BC ($LC_{50} < 1.0$ mg/L), the direct toxicity of PDMS-g-AH was

lower and remained in the moderate toxicity range ($1.0 < LC_{50} < 10.0$ mg/L), while the direct toxicity of PDMS-g-GH was much lower and already located in the low toxicity range ($LC_{50} > 10.0$ mg/L), indicating that the conversion of primary amine salts (AH) to guanidine salts (GH) is beneficial for reducing the biological toxicity of PDMS-g-GH. In addition to direct application to aqueous solutions, considering that PDMS-g-GH is mainly applied to soil in the form of aqueous solutions, we also measured the toxicity of PDMS-g-AH, PDMS-g-GH, and BC after being adsorbed by soil and leached into environmental water by rainwater, namely, LC_{50L} and LC_{50S} . As shown in Fig. 9, due to the strong adsorption effect of these three fungicides in the soil, the amount of free fungicides lost to the environment after soil adsorption is significantly reduced, resulting in a significant reduction in their environmental toxicity. The LC_{50L} and LC_{50S} of BC were 50 mg/(kg soil) and 110 mg/(kg soil), respectively, reaching the range of low toxicity or practically nontoxic, while for PDMS-g-AH and PDMS-g-GH, their LC_{50L} and LC_{50S} are greater than 600 mg/(kg soil), which means that they are practically nontoxic and can be safely used in farmland soil.

4. Conclusions

In this paper, a series of random and block-type polysiloxane graft guanidine salts (PDMS-g-GHs) with tunable molecular weights, grafting degrees, and chain structures (random or block) were synthesized based on the guanidine reaction of polysiloxane graft primary amine salts (PDMS-g-AHs). Compared with PDMS-g-AH, PDMS-g-GH showed stronger antifungal activity against Foc4 and long-term antifungal activity against Foc4 in soil, but its environmental toxicity was significantly reduced. Block-type PDMS-g-GH, i.e., PDMS-b-GH, showed greater zeta potential, stronger anti-Foc4 activity and lower environmental toxicity than did the random type (PDMS-co-GH). These results support the potential application of PDMS-g-GH for the prevention and control of banana Fusarium wilt and other soil-borne fungal diseases.

CRediT authorship contribution statement

Yaling Lin: Writing – review & editing, Writing – original draft, Supervision, Funding acquisition, Conceptualization. **Shiqi He:** Writing – original draft, Methodology, Data curation. **Mingyang Wu:** Data curation. **Meng Hou:** Data curation. **Rui Li:** Writing – original draft, Methodology, Data curation. **Anqiang Zhang:** Writing – review &

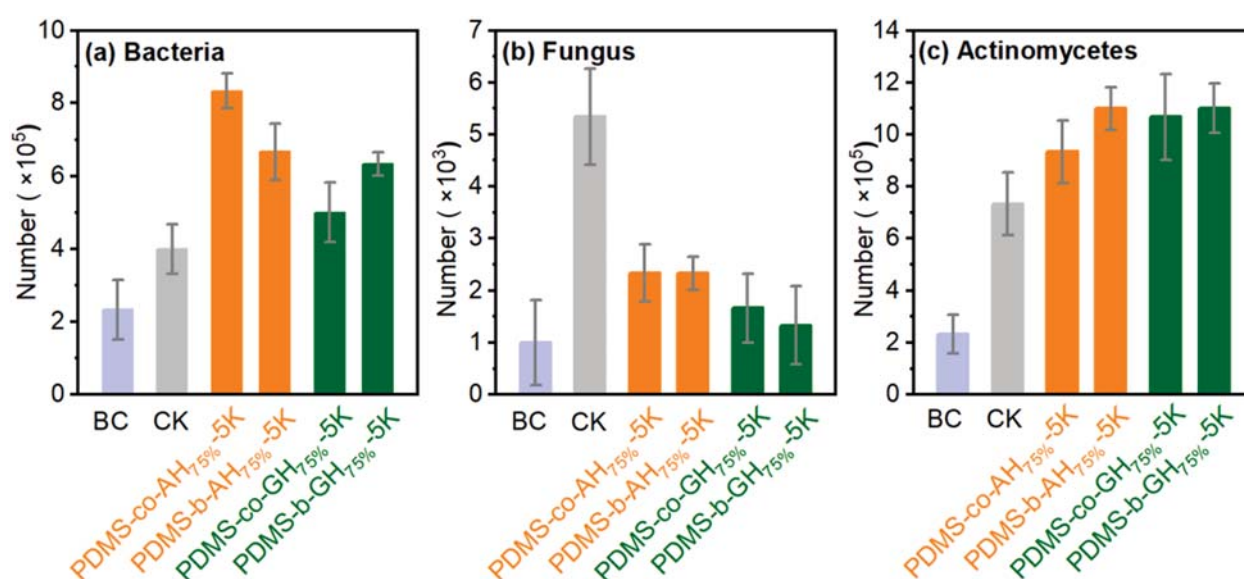


Fig. 8. Culturable populations of bacteria (A), fungi (B) and actinomycetes (C) in soil from the PDMS-g-GH and PDMS-g-AH treatments (Vertical bars represent the standard error of the means.)

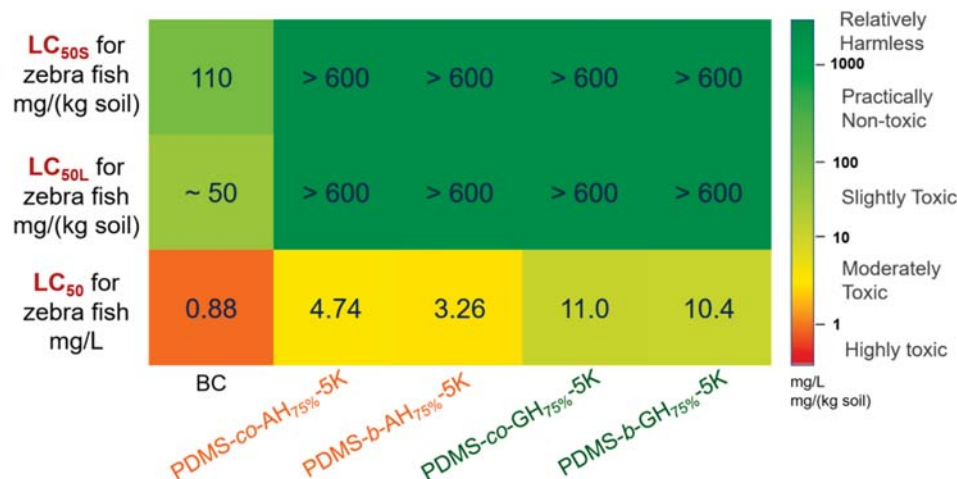


Fig. 9. LC₅₀, LC_{50L}, and LC_{50S} of PDMS-g-AH, PDMS-g-GH and BC for zebrafish (*Danio rerio*) (96 h) (Potassium dichromate and chloroacetamide were used as zebrafish and earthworm reference poisons, respectively. BC was used as a positive control. Average of three replicates.).

editing, Supervision, Methodology, Funding acquisition, Conceptualization.

Declaration of competing interest

The authors declare that they have no known competing financial interests or personal relationships that could have appeared to influence the work reported in this paper.

Data availability

Data will be made available on request.

Acknowledgements

The authors acknowledge the financial support from the National Natural Science Foundation of China (Nos. 52073098 and 31772202) and the Scientific and Technological Planning Project of Guangzhou City (201803020015).

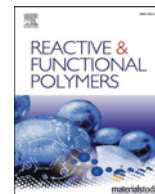
Appendix A. Supplementary material

Detailed methods and results including molecular weight of PDMS-co-PVMS and PDMS-b-PVMS, the methods for soil-polymer interaction experiments, the methods for evaluation of antifungal activities, the methods and results for the evaluation of persistence of PDMS-g-AH and PDMS-g-GH on Foc4 in soil, the methods for biotoxicity evaluation, can be found in Supporting Information. Supplementary data to this article can be found online at <https://doi.org/10.1016/j.eurpolymj.2024.113258>.

References

- [1] R.C. Ploetz, *Fusarium wilt of banana is caused by several pathogens referred to as Fusarium oxysporum f. sp. cubense*, *Phytopathology* 96 (6) (2006) 653–656.
- [2] Janet MR, Lilia CC, Cecilia O'D, Vivian AR, Andre D. Diagnostics of *Fusarium wilt* in banana: Current status and challenges. *Plant Pathology*. 2024, 1-17, DOI: 10.1111/ppa.13863.
- [3] B.G. Siddhesh, K.S.S. Upendra, R.G. Thumballi, *Fusarium wilt of banana: Biology, epidemiology and management*, *Int. J. Pest Manage.* 61 (3) (2017) 250–263.
- [4] D. Miguel, B. Marcia, H. Daniel, S. Eduardo, P.S. Charles, *Fusarium wilt of banana: current knowledge on epidemiology and research needs toward sustainable disease management*, *Front. Plant Sci.* 9 (10) (2018) 146.
- [5] W.M. Li, M. Dita, W. Wu, G.B. Hu, X.J. Ge, *Resistance sources to Fusarium oxysporum f. sp. cubense tropical race 4 in banana wild relatives*, *Plant Pathol.* 64 (5) (2015) 1061–1067.
- [6] S. Hong, H.L. Jv, M. Lu, B.B. Wang, Y.Z. Ruan, *Significant decline in banana Fusarium wilt disease is associated with soil microbiome reconstruction under chilli pepper-banana rotation*, *Eur. J. Soil Biol.* 97 (2020) 103154.
- [7] Z.Z. Shen, C.R. Penton, N.N. Lv, C. Xue, X.F. Yuan, Y.Z. Ruan, R. Li, Q.R. Shen, *Banana Fusarium wilt disease incidence is influenced by shifts of soil microbial communities under different monoculture spans*, *Microb. Ecol.* 75 (2018) 739–750.
- [8] T.V. Nguyen, L.T.T. Tran-Nguyen, C.L. Wright, et al., *Evaluation of the efficacy of commercial disinfectants against Fusarium oxysporum f. sp. cubense race 1 and tropical race 4 propagules*, *Plant Dis.* 103 (4) (2019) 721–728.
- [9] T. Bratec, N. Kirchhübel, N. Baranovskaya, et al., *Towards integrating toxicity characterization into environmental studies: case study of bromine in soils*, *Environ. Sci. Pollut. Res.* 26 (2019) 19814–19827.
- [10] G.Q. Lu, D.C. Wu, R.W. Fu, *Studies on the synthesis and antibacterial activities of polymeric quaternary ammonium salts from dimethylaminoethyl methacrylate*, *React. Funct. Polym.* 67 (4) (2007) 355–366.
- [11] W.Q. Zhong, Y. Chang, Y.L. Lin, A.Q. Zhang, *Synthesis and antifungal activities of hydrophilic cationic polymers against Rhizoctonia solani*, *Fungal Biol.* 124 (2020) 735–741.
- [12] Y.Y. Chang, W.Q. Zhong, J.Q. Liang, A.Q. Zhang, Y.L. Lin, *Polydimethylsiloxane-polymethacrylate block copolymers containing quaternary ammonium salts against Fusarium oxysporum f. sp. cubense race 4 in soil: Antifungal activities and pot experiments*, *React. Funct. Polym.* 160 (2021) 104848.
- [13] X.Q. Yin, P.F. Tan, Z.P. Gu, Z.M. Liu, L. Tan, *Polymeric antibacterial materials: design, platforms and applications*, *J. Mater. Chem. B* 9 (12) (2021) 2802–2815.
- [14] Y.L. Lin, D.Q. Zhang, S.J. Shan, W. Zhang, R. Li, A.Q. Zhang, *Fluorine-containing amphiphilic quaternary ammonium salts for the suppression of Banana fusarium wilt*, *React. Funct. Polym.* 182 (2023) 105488.
- [15] W. Zhang, J.G. Yu, M.Y. Wu, R. Li, A.Q. Zhang, Y.L. Lin, *Polyacrylamide quaternary ammonium salts based on stable adsorption in soil and its application on the control of soil-borne fungal disease*, *Eur. Polym. J.* 202 (2024) 112604.
- [16] S.Q. He, M. Hou, S.J. Shan, R. Li, N. Yu, Y.L. Lin, A.Q. Zhang, *Synthesis and antibacterial/fungal activities of amphiphilic polysiloxanes primary ammonium salts*, *React. Funct. Polym.* 183 (2023) 105495.
- [17] Y.L. Lin, W.Q. Zhong, C.Y. Dong, C. Zhang, X.X. Feng, A.Q. Zhang, *Synthesis and antifungal activities of amphiphilic PDMS-b-QPDMAEMA copolymers on Rhizoctonia solani*, *ACS Appl. Bio Mater.* 1 (6) (2018) 2062–2072.
- [18] K. Kuroda, W.F. DeGrado, *Amphiphilic polymethacrylate derivatives as antimicrobial agents*, *J. Am. Chem. Soc.* 127 (2005) 4128–4129.
- [19] G.J. Gabriel, A.E. Madkour, J.M. Dabkowski, et al., *Synthetic mimic of antimicrobial peptide with nonmembrane-disrupting antibacterial properties*, *Biomacromolecules* 9 (2008) 2980–2983.
- [20] K.E.S. Locock, T.D. Michl, J.D.P. Valentin, et al., *Guanylated polymethacrylates: A class of potent antimicrobial polymers with low hemolytic activity*, *Biomacromolecules* 14 (2013) 4021–4031.
- [21] H. Liu, M.M. Han, X. Liu, S.X. Ji, *Guanylation significantly enhances the antifungal activity of poly(L-lysine)*, *ACS Appl. Mater. Interfaces* 4 (10) (2022) 7508–7517.
- [22] X.Y. Zhou, J. He, C.C. Zhou, *Strategies from nature: polycaprolactone-based mimetic antimicrobial peptide block copolymers with low cytotoxicity and excellent antibacterial efficiency*, *Polym. Chem.* 10 (8) (2019) 945–953.
- [23] X. Liu, Y.L. Yang, M.M. Han, J.W. Guo, et al., *Guanylated hyperbranched polylysines with high in vitro and in vivo antifungal activity*, *Adv. Healthc. Mater.* 11 (2022) 2201091.

- [24] P. Pham, S. Oliver, C. Boyer, Design of antimicrobial polymers, *Macromol. Chem. Phys.* 224 (3) (2023) 1–28.
- [25] H. Choi, K.J. Kim, D.G. Lee, Antifungal activity of the cationic antimicrobial polymer-polyhexamethylene guanidine hydrochloride and its mode of action, *Fungal Biol.* 121 (2017) 53–60.
- [26] N.D. Koromilas, G.C. Lainioti, G. Vasilopoulos, A. Vantarakis, J.K. Kallitsis, Synthesis of antimicrobial block copolymers bearing immobilized bacteriostatic groups, *Polym. Chem.* 7 (2016) 3562–3575.



Fluorine-containing amphiphilic quaternary ammonium salts for the suppression of Banana fusarium wilt

Yaling Lin^{a,*}, Deqiang Zhang^b, Shijie Shan^b, Wei Zhang^a, Rui Li^b, Anqiang Zhang^{b,*}

^a College of Materials and Energy, South China Agricultural University, 483 Wushan Rd., Guangzhou 510642, Guangdong, China

^b School of Materials Science and Engineering, South China University of Technology, 381 Wushan Rd., Guangzhou 510641, Guangdong, China

ARTICLE INFO

Keywords:

Polymeric quaternary ammonium salt
Fluoroalkyl group
Banana fusarium wilt
Antifungal activities

ABSTRACT

As the pathogen of banana Fusarium wilt, *Fusarium oxysporum* f. sp. *cubense* race 4 (Foc4) has the strongest toxicity and pathogenicity due to its long-term viability in soil, but there is still no effective way to control it at present. Based on the activity parameters of polymeric quaternary ammonium salt in our previous work, this paper hopes to enhance the amphiphilicity of polymeric quaternary ammonium salt by introducing a fluoroalkyl group to improve the antifungal property of polymeric quaternary ammonium salt and achieve stable adsorption and long-term inhibition of saprophytic Foc4 conidia in soil. Here, we prepared a series of fluorine-containing ammonium salts with random and block structures by atom transfer radical polymerization (ATRP), and we systematically studied the effects of the introduction of fluoroalkyl groups, the proportion of hydrophobic segments and polymer structure on micelle properties, antifungal properties, adsorption, migration and long-term antifungal properties against Foc4 in soil. Finally, the preferred polymeric quaternary ammonium salts were selected for pot experiments in the prevention and control of banana Fusarium wilt caused by Foc4, and positive experimental results were achieved. In conclusion, we made an exploratory attempt at the practical application of polymeric amphiphilic quaternary ammonium salt in plant disease control.

1. Introduction

Banana Fusarium wilt is a common soil-borne disease in banana plantations that causes immeasurable losses to the agricultural economy every year. *Fusarium oxysporum* f. sp. *cubense* race 4 (Foc4) has the strongest toxicity and pathogenicity due to its strict asexual reproduction ability and long-term viability in soil. Foc4 initially infects a plant by invading the xylem of the plant and establishing a biological nutritional relationship with the host. Then, the plant is killed by transforming the host tissue into necrotic nutrients [1–3]. Infected plants continue to release pathogens into the surrounding soil and infect surrounding plants or exist in the soil as chlamydospores for a long time. Once the environment changes, they infect the plants again and cause disease [4].

Two methods of chemical control used in practice are as follows. The first uses chemical agents to inhibit the number of pathogens in the soil. Some small-molecule drugs screened based on indoor virulence determination and pot experiments such as prochloraz, propiconazole, and pentachloronitrobenzene have a certain control effect on Foc4. However, small-molecule drugs easily lose their effect on soil erosion and

decomposition in soil. As a result, the control effect in practice is poor [5,6]. The second method can be called “soil disinfection,” where all microorganisms in the soil are killed by physical, chemical, or biological methods such as soil heating and fumigation. Among them, fumigation with small-molecule chemicals represented by minocycline (tetrahydro-3,5-dimethyl-2-h-1,3,5-thiadiazine-2-thione) [7], lime nitrogen (calcium cyanamide), and chlorine dioxide is the main method of field control at present. However, this method completely destroys the microbial community structure in the soil, so it is necessary to introduce new organic matter to restore the soil after treatment, which is not conducive to the stability of the soil ecosystem. In addition, biological control and crop rotation are difficult to implement effectively on a large scale due to the high economic cost and the inability to plant continuously [8,9]. As a result, there is no economically feasible way to treat Foc4 while maintaining the diversity of the soil ecosystem [10–12].

Based on the severe situation of Foc4 and the lack of strategies of small-molecule drugs, polymeric quaternary ammonium salts, which are also used as antifungal agents [13], have become a research hot spot of plant disease control. Compared with small-molecule antibiotics, the amphiphilic structure of antibacterial cationic polymers can make them

* Corresponding authors.

E-mail addresses: linyinling@scau.edu.cn (Y. Lin), aqzhang@scut.edu.cn (A. Zhang).

<https://doi.org/10.1016/j.reactfunctpolym.2022.105488>

Received 8 October 2022; Received in revised form 11 December 2022; Accepted 12 December 2022

Available online 15 December 2022

1381-5148/© 2022 Published by Elsevier B.V.

fold into a secondary structure with surface affinity and cations to produce a strong interaction with biofilm [14,15]. In addition, the structure and performance of antifungal cationic polymers have advantages such as the possibility of regulation, low synthesis cost, non-volatility, impermeability to skin, long circulation time, strong biological activity, stability, low residual toxicity to the environment, and delayed development of drug resistance. In the past ten years, new antifungal cationic polymers and their related research have developed rapidly [16,17].

In our previous work, we obtained a series of polymeric quaternary ammonium salts by changing the main chain structure, molecular weight, cationic group, hydrophilic-hydrophobic ratio, and other parameters of antibacterial cationic polymers [18–20]. It was found that the appropriate molecular weight and hydrophilic-hydrophobic balance might have an important impact on the antibacterial activity of antifungal cationic polymers [21,25]. In addition, the type of hydrophobic group seriously affected the antifungal activity. A series of studies were conducted on the relationship between quaternary ammonium salt structures [26,27], hydrophilic-hydrophobic balance, molecular weight [28,29], lateral base length [30], anti-ion [31,32], and antifungal activity. However, research on the effects of strong hydrophobic fluoroalkyl groups in quaternary ammonium salts has rarely been reported.

Compared with conventional antibacterial or antifungal agents, the antifungal agents for soil-borne disease have to face the complex interactions with soil, such as adsorption and inactivation, which might obviously affect their antifungal efficacy. Although our previous studies have confirmed that amphiphilic polymeric quaternary ammonium salts showed strong adsorption in soil [41,42], it is still unclear on the effect of the introduction of fluorine containing hydrophobic groups. As a potential antifungal agents for the control of banana *Fusarium* wilt, the environmental impact, such as the effect on the microbial diversity in soil, the toxicity of its leaching solution to zebra fish, and also including the pot experiments, should be comprehensively evaluated.

In this work, fluoroalkyl segments, which are more hydrophobic than carbon-hydrogen chains, are introduced into polymeric quaternary ammonium salts. Two types of polymeric fluorine-containing quaternary ammonium salts, i.e., F_1 -co- Q_5 and F_1 -b- Q_5 , are obtained by controlling the feeding sequence and reaction time in an atom transfer active radical polymerization method (ATRP). We hope that the introduction of fluoroalkyl groups into polymeric quaternary ammonium salts will enhance the amphiphilicity of polymers with lower surface tension, excellent water-soluble stability, good adsorption in soil, and low environmental toxicity, and thus enhance long-term antifungal activities in soil. We systematically studied the effect of the fluoroalkyl group ratio and position of the fluoroalkyl group in the polymer chain on antifungal activities against *Foc4* in vitro or in soil, biological toxicity, soil adsorption, and migration characteristics. Then, pot experiments were conducted to confirm the growth-promoting effect of the synthesized fluorine-containing polymeric quaternary ammonium salts on normal banana plants and the control effect on *Foc4*.

2. Experimental

2.1. Materials

2-(Dimethylamino)ethyl methacrylate (DMAEMA, 99%), 2,2,2-trifluoroethyl methacrylate (DMAFMA, 99%), ethyl 2-bromoisobutyrate (EtBrIB, 98%), N, N, N', N''-pentamethyldiethylenetriamine (PMDETA, 98%), and copper(I) bromide (CuBr, 99%) were purchased from Aladdin (Shanghai, China). Benzyl chloride and 2,3,5-triphenyltetrazolium chloride (TTC) were purchased from Sangon Biotech (Shanghai) Co., Ltd. (Shanghai, China). Potato dextrose agar medium (PDA) and beef extract peptone medium were prepared according to [20,22]. The fungal strain *Fusarium oxysporum* f. sp. *cubense* race 4 (*Foc4*), *Candida albicans* (*C. albicans*), and the bacterial strains *Escherichia coli* (*E. coli*) and *Staphylococcus albus* (*S. albus*) used in this study

were kindly supplied by the Fungal Laboratory of the University of South China Agricultural. Soil samples and banana seedlings were obtained from the Institute of Fruit Trees, Guangdong Academy of Agricultural Sciences, China.

2.2. Synthesis of QPDMAEMA (Q_5)

PDMAEMA (D_3) was synthesized as shown in Scheme 1.

The polymerization procedure was as follows: A calculated amount of EtBrIB, PMDETA, and CuBr was added to 80 g mixed solvent (toluene/ethanol = 1/1, m/m) in a 250-mL Schlenk flask. After three freeze-pump-thaw cycles, the reaction system was filled with nitrogen, DMAEMA was injected into the mixture, and the reaction mixture was stirred at 50 °C for a set time. Subsequently, the reaction mixture was exposed to air, and the catalyst was removed by neutral alumina column chromatography with acetone as the eluent. Then, the reaction mixture was dried under vacuum at 130 °C for 3 h, and the product (D_3) was obtained (ca. yield 73%). Here, the number average molecular weight of PDMAEMA was designed as approximately 3 kDa, so it is abbreviated as D_3 , and the antifungal activity of D_3 after quaternization is better according to [18].

^1H NMR (400 MHz, CDCl_3 , δ , ppm): 0.9–1.25 (s, C- CH_3), 1.82–1.94 (s, C- CH_2 -C), 2.28 (s, N(CH_3) $_2$), 2.57 (t, N- CH_2 - CH_2), 4.06 (t, O- CH_2 - CH_2). FT-IR (KBr, ν , cm^{-1}): 2952–2773 (ν_{CH}), 1730 ($\nu_{\text{C=O}}$).

QPDMAEMA (Q_5) was designed with a number average molecular weight of 5 kDa and synthesized via a quaternization reaction between D_3 and benzyl chloride: D_3 was dissolved in 80 g mixed solvent (toluene/ethanol = 1/1, m/m) in a 250-mL Schlenk flask. After three freeze-pump-thaw cycles, the reaction system was filled with a nitrogen atmosphere, then 4 times the amount of BC was injected into the mixture, and the reaction system was stirred at 70 °C for 48 h. Subsequently, the reaction system was dried under vacuum at 70 °C to remove most of the solvent, and anhydrous diethyl ether was added to the mixture to precipitate the product. After washing with diethyl ether three times, the precipitate was dried under vacuum at 40 °C overnight (ca. yield 90%).

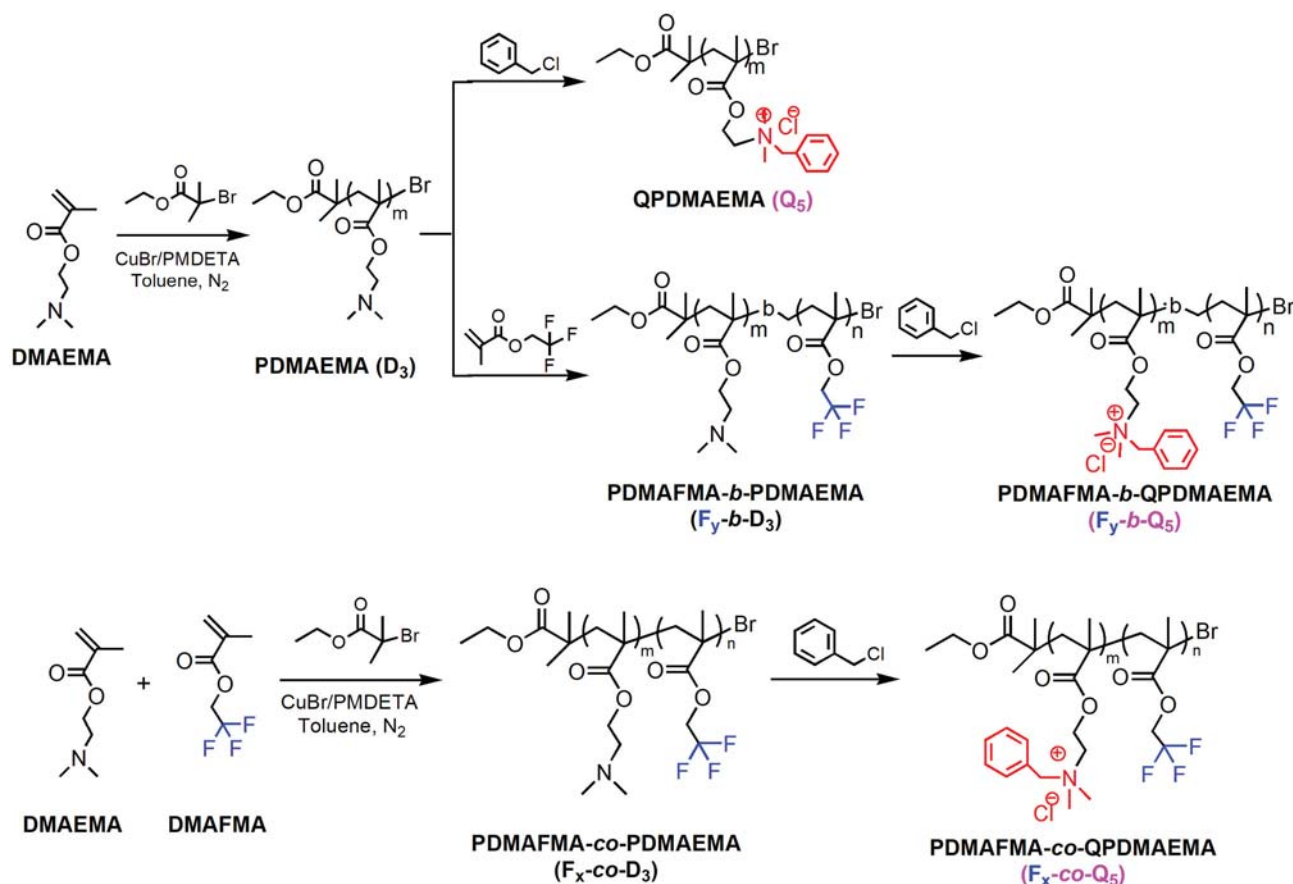
^1H NMR (600 MHz, methanol- d_4 , δ , ppm): 1.2 (s, C- CH_3), 3.28 (s, N $^+$ (CH_3) $_2$), 4.05 (t, CH_2 - CH_2 -N $^+$), 4.65 (m, CH_2 - CH_2 -N $^+$), 7.56, 7.72 (s, Φ -H). FT-IR (KBr, ν , cm^{-1}): 2983 (ν_{CH}), 1734 ($\nu_{\text{C=O}}$), 717, 768 ($\gamma_{\Phi\text{-H}}$).

2.3. Synthesis of PDMAFMA-co-QPDMAEMA (F_x -co- Q_5) and PDMAFMA-b-QPDMAEMA (F_y -b- Q_5)

PDMAFMA-b-PDMAEMA (labeled F_y -b- D_3) and PDMAFMA-co-PDMAEMA (labeled F_x -co- D_3) were synthesized by atom transfer free radical polymerization similar to the synthesis route of D_3 . The difference is that the synthesis of F_y -b- D_3 is a two-step process. First, the calculated DMAEMA monomer is added to the reaction system and reacts to a set time, and then the DMAFMA monomer is added to react. The F_x -co- D_3 is synthesized by adding the calculated DMAEMA and DMAFMA monomers into the reaction system together through a one-step method, reacting to the set time and processing to obtain the product (ca. yield 70–75%). For F_y -b- D_3 and F_x -co- D_3 , the subscript “3” indicates that the designed molecular weight of the DMAEMA unit is approximately 3 kDa, and the subscripts “x (1 to 5)” and “y (1 to 5)” indicate that the designed molecular weights of the DMAFMA unit are 1, 2, 3, and 5 kDa, respectively.

^1H NMR (600 MHz, CDCl_3 , δ , ppm): 4.36 ppm (s, 2H, CH_2CF_3 from PDMAFMA); 4.07 ppm (s, 2H, $\text{CH}_2\text{CH}_2\text{N}(\text{CH}_3)_2$ from PDMAEMA); 2.56 ppm (s, 2H, $\text{CH}_2\text{CH}_2\text{N}(\text{CH}_3)_2$ from PDMAEMA); 2.21 ppm (s, 6H, $\text{CH}_2\text{CH}_2\text{N}(\text{CH}_3)_2$ from PDMAEMA); 1.92 to 1.50 ppm (m, 2H, CH_2 -from backbone); 1.25 to 0.81 ppm (m, 3H, CH_3 from backbone). FT-IR (KBr, ν , cm^{-1}): 2955–2773 (ν_{CH}), 1725 ($\nu_{\text{C=O}}$), 660 ($\delta_{\text{C-F}}$).

F_x -co- Q_5 and F_y -b- Q_5 were synthesized via a quaternization reaction between F_x -co- D_3 , F_y -b- D_3 and benzyl chloride, respectively. The F_x -co- D_3 and F_y -b- D_3 were dissolved in 80 g mixed solvent (toluene/ethanol = 1/1, m/m) in a 250-mL Schlenk flask. After three freeze-pump-thaw



Scheme 1. Synthesis routes of QPDMAEMA (Q₅), PDMAFMA-*b*-QPDMAEMA (F_y-*b*-Q₅), and PDMAFMA-*co*-QPDMAEMA (F_x-*co*-Q₅).

cycles, 4 times the amount of benzyl chloride was injected into the mixture, and the reaction system was stirred at 70 °C under a nitrogen atmosphere for 48 h. Subsequently, the reaction system was dried under vacuum at 70 °C to remove most of the solvent, and anhydrous diethyl ether was added to the mixture to precipitate the product. After washing with diethyl ether three times, the precipitate was dried under vacuum at 40 °C overnight (ca. yield 87% ~ 91%).

¹H NMR (600 MHz, methanol-D₄, δ , ppm): 1.15, 1.95 (s, C-CH₃), 3.24 (s, N⁺(CH₃)₂), 4.01 (t, CH₂-CH₂-N⁺), 4.59 (m, CH₂-CH₂-N⁺, O-CH₂-CF₃), 7.56, 7.72 (s, Φ -H). FT-IR (KBr, ν , cm⁻¹): 3011–2963 (ν CH), 1726 (ν C=O), 717, 768 (γ Φ -H).

2.4. Characterization

¹H NMR spectra were collected in CDCl₃ or methanol-*d*₄ solvent using a Bruker Avance III-600 (Bruker Instrument Corp., Germany) spectrometer. Size exclusion chromatography (SEC) with simultaneous ultraviolet (UV) and refractive index (RI) detection was conducted in THF at 35 °C using two identical 7.5 mm × 300 mm columns (PLgel, 5 μ m, Mixed-C) at a flow rate of 1 mL/min (1260 Infinity, Agilent). This was calibrated with a series of polystyrene standards to obtain the apparent number-average molecular weight ($M_{n, SEC}$) and molar mass distribution (D). FT-IR spectra were obtained on a Nicolet iS5 spectrometer (Thermo Fisher, USA) by using KBr pellets. Critical micelle concentrations (CMC) were determined by using a DDS-11A conductivity meter (Shanghai Hongyi Instrument Co. Ltd., China) [23,24]. Zeta potentials and particle size distributions were analyzed by using a Brookhaven BI-90 Plus particle size analyzer (Brookhaven Instrument Corp., USA) using ultrapure water as the solvent.

Detailed characterization results on the products and the methods of antifungal testing, adsorption and migration characteristics, antifungal

bioassays in soil, toxicity tests, and pot experiments are provided in the Supporting Information.

3. Results and discussion

3.1. Structure characterization of Q₅, F_x-*co*-Q₅, and F_y-*b*-Q₅

Since there were many factors affecting the polymeric quaternary antifungal properties, we know that hydrophilic-hydrophobic balance [21,25] is a necessary condition for good antifungal properties of polymeric quaternary ammonium salts. This conclusion is based on research work regarding the design and antifungal structure of quaternary ammonium salt in our group [18–20]. There is a series of studies on the effects of quaternary ammonium salt structures, rope, molecular weight, lateral base length, anti-ion, and other parameters. The preliminary results showed that the polymeric quaternary had better antifungal properties when using ohmic chloride as a counterion. There is a series of studies on the relationship between quaternary ammonium salt structures [26,27], hydrophilic-hydrophobic balance, molecular weight [28,29], lateral base length [30], anti-ion [31,32], and antifungal activity. However, research reports on the effects of strong hydrophobic fluoroalkyl groups in quaternary ammonium salts are relatively rare. Here, the fluoroalkyl group is introduced into the quaternary ammonium salt. On the one hand, this could improve the structure and chemical stability of the quaternary ammonium salt, which had lower surface tension and excellent water solubility. On the other hand, the biological activity of the quaternary ammonium salt could promote its binding and enhance permeability.

For Q₅, F_x-*co*-Q₅, and F_y-*b*-Q₅, the number average molecular weight of the D₃ chain was designed as 3 kDa [18], and the molecular weights of the DMAFMA chain were designed as 1–5 kDa. The molecular weights of

Q₅, F_x-co-Q₅, and F_y-b-Q₅ are listed in Table 1 and are basically consistent with the design. The ¹H NMR and FT-IR spectra of the products are shown in Fig. 1. As shown in Figs. 1, 2988, 1725, 1640, 1146 cm⁻¹, and 774 and 720 cm⁻¹ are the infrared absorption bands of saturated -CH₂-, C=O, C=C, C-N, and C-H on the benzene ring, respectively, and F_x-co-Q₅ and F_y-b-Q₅ have infrared absorption peaks of C-F at 658 and 564 cm⁻¹, while Q₅ does not. The signals for the CH₂CH₂N(CH₃)₂, O-CH₂-CF₃ protons appear at 4.36 and 4.07 ppm in F_x-co-D₃, F_y-b-D₃ and move to 4.59 ppm after quaternization. The proton signal of benzene ring in benzyl group appears at 7.56 and 7.72 ppm after quaternization. Thus, Q₅, F_x-co-Q₅, and F_y-b-Q₅ were synthesized as expected.

3.2. Micellar conformation of Q₅, F_x-co-Q₅ and F_y-b-Q₅ in water

The characteristics of Q₅, F_x-co-Q₅ and F_y-b-Q₅ in aqueous solution are shown in Fig. 2. From the conductivity test data of Q₅, F_x-co-Q₅ and F_y-b-Q₅ in Fig. 2(a), it can be seen that the introduction of fluoroalkyl groups is conducive to the formation of micelles. In terms of the same molecular weight and fluorine segment, the CMC of the block structure fluorine-containing quaternary ammonium salt is smaller than that of the random structure. This is because when the fluorine-containing ammonium salt concentration is relatively low, the polymeric quaternary ammonium salt is present in a single molecule or several-molecule aggregate. As the polymeric quaternary ammonium salt concentration is increased in solution, it gradually reaches saturation to aggregate to form a micelle. As a result, the higher molecular weight, higher fluorine-containing segment, and stronger block structure fluorine-containing quaternary ammonium salt are more easily aggregated to form a micelle core and grow. Therefore, the CMC is lower [33].

The zeta potential [Fig. 2(b)] of fluorine-containing quaternary ammonium salt with random and block structures shows that the formed micelle zeta potential and dynamic stability of the micelles [34] constantly improve as the hydrophobicity increases. A schematic diagram of the particle size distribution [Fig. 2(c)] and transmission electron microscopy of fluorine-containing ammonium salt (Fig. S3) indicate that with increasing molecular weight and fluoroalkyl groups, the space position between fluorine-containing side groups increases, which prevents the main chain of quaternary ammonium salts from bending greatly. The micelles are prone to hollow phenomena and form vesicles. The shape orientation is irregular, and the particle size of micelles is relatively large.

3.3. Antifungal activities of Q₅, F_x-co-Q₅, and F_y-b-Q₅

3.3.1. Antifungal activities against *Foc4*

The MIC and MFC of fluorine-containing quaternary ammonium salts and BC against *Foc4* are shown in Fig. 3 using the TTC coloration

Table 1

Molecular weights of Q₅, F_x-co-Q₅ and F_y-b-Q₅ prepared at different [DMAEMA]/[DMAFMA] feeding ratios.

Samples	[DMAEMA]/ [DMAFMA] feeding molar ratio	<i>M_n</i> , SEC of [PDMAEMA] (kDa)	<i>M_n</i> , SEC of final sample (kDa)	<i>D</i> (<i>M_w</i> / <i>M_n</i>)
Q ₅	1.00	3.0	5.4	1.29
F ₁ -co-Q ₅	0.34	–	6.2	1.36
F ₂ -co-Q ₅	0.68	–	7.3	1.55
F ₃ -co-Q ₅	1.00	–	7.9	1.53
F ₅ -co-Q ₅	1.70	–	11.3	1.61
F ₁ -b-Q ₅	0.34	2.8	6.3	1.34
F ₂ -b-Q ₅	0.68	2.8	7.6	1.41
F ₃ -b-Q ₅	1.00	2.9	8.4	1.39
F ₅ -b-Q ₅	1.70	3.1	11.6	1.58

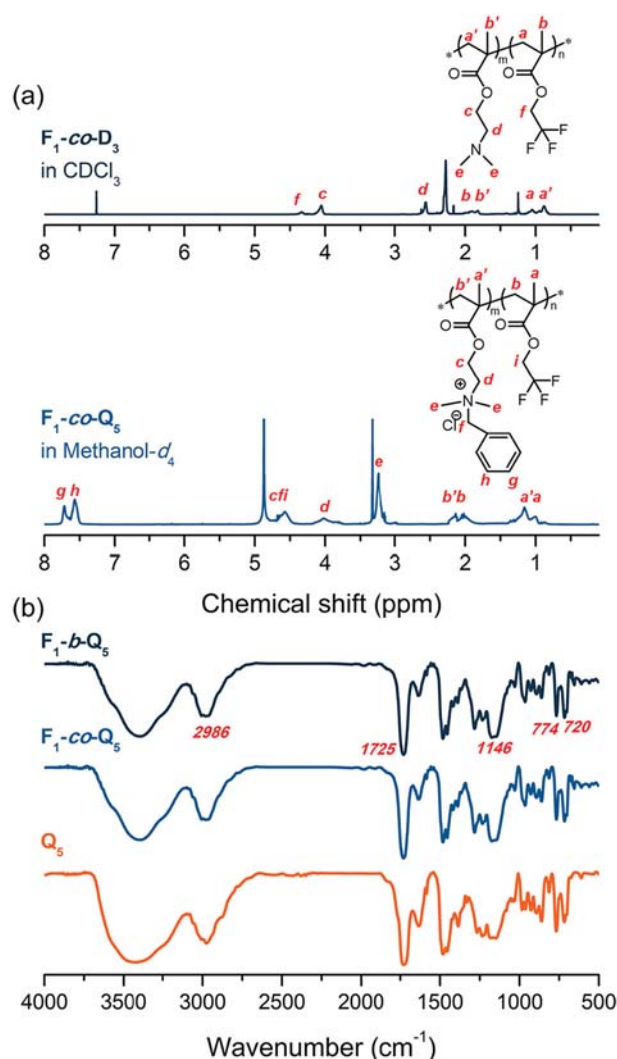


Fig. 1. (a) ¹H NMR spectra and (b) FT-IR spectra of Q₅, F₁-co-Q₅, and F₁-b-Q₅.

method [13]. From the experimental data, we can see that Q₅, F₁-co-Q₅, and F₁-b-Q₅ have a positive inhibitory effect on *Foc4* in vitro, in which F₁-co-Q₅ is equivalent to BC against *Foc4* with both at 40 μg/mL. In addition, the fluorine-containing ammonium salts exhibited a trend of antifungal activities with hydrophobicity: the antifungal activity of the quaternary ammonium salt increased at first and then decreased with increasing hydrophobicity of the quaternary ammonium salt. The fluoroalkyl group of quaternary ammonium salt with a better antifungal activity is preferably approximately 15%, the Q₅ is free of fluoroalkyl group, and the antifungal activity is poor, which also illustrates an element necessary for the hydrophobic segment to exhibit good antifungal performance. Additionally, in the case of similar hydrophobic (fluorine-containing) segments, the random structural antifungal properties are generally better than those of the block. This may be related to the micelle morphology and antifungal mechanism of quaternary ammonium salt in aqueous solution.

The 50% and 90% maximum inhibitory concentrations represent the concentrations of quaternary ammonium salt at which 50% or 90% of *Foc4* growth is inhibited. For the convenience of distinction, we define the concentrations of 50% and 90% inhibition of fluorine-containing quaternary ammonium salt against *Foc4* measured in vitro and in soil as IC₅₀, IC₉₀ and IC_{50S}, and IC_{90S}, respectively. The ratio of the growth inhibition of *Foc4* by typical mycelial growth in vitro and the spot plate method in soil on PDA medium are shown in Fig. 4. The experimental results show that the 50% and 90% maximum inhibitory concentrations

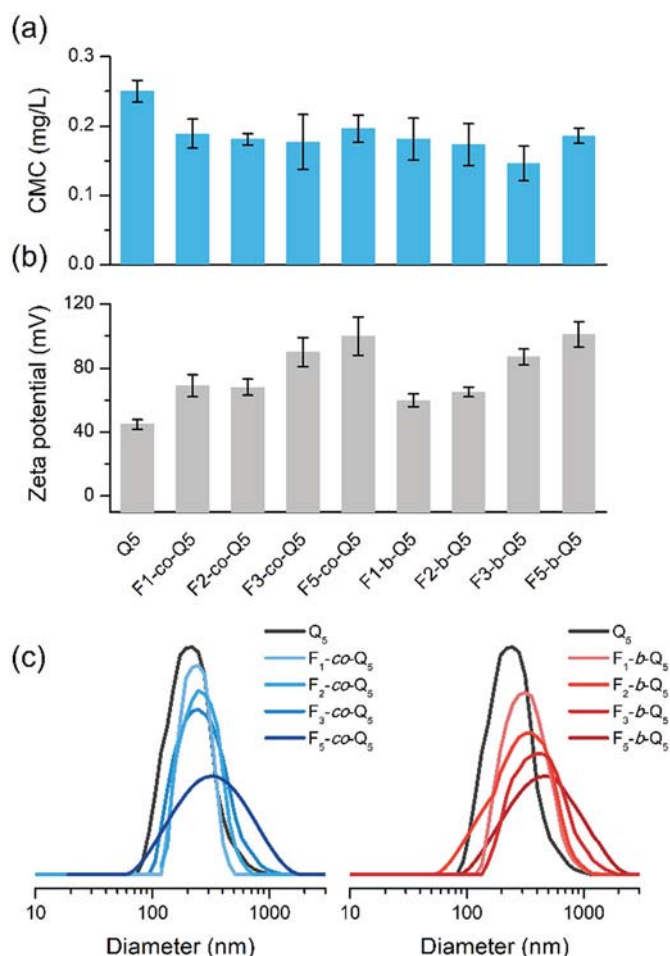


Fig. 2. (a) CMC values of Q5, F_x-co-Q5 and F_y-b-Q5 with different molecular weights and fluorine segments. (b) Zeta potentials and (c) particle size distributions of Q5, F_x-co-Q5 and F_y-b-Q5 with different molecular weights and fluorine segments.

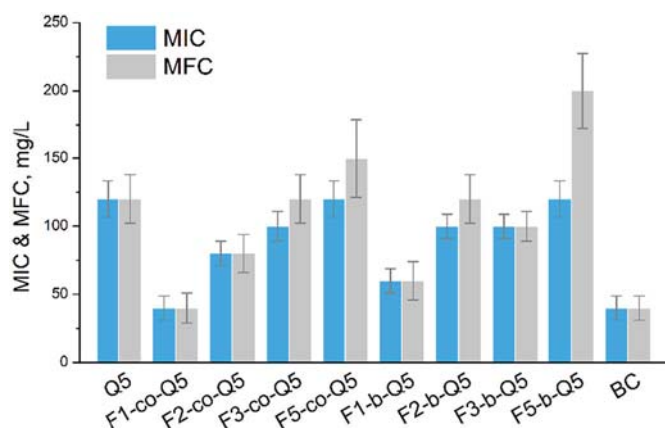


Fig. 3. MIC and MBC (for bacteria) or MFC (for fungi) values of Q5, F_x-co-Q5 and F_y-b-Q5 against Foc4.

of fluorine-containing quaternary ammonium salt are positively correlated with the antifungal activity (MIC) both in vitro and in soil. The difference is that the 50% and 90% maximum inhibitory concentrations of fluorine-containing quaternary ammonium salt are much higher than those of BC. This may occur because the mobility of fluorine-containing polymeric quaternary ammonium salt is much worse than that of BC,

resulting in its reduced utility. Additionally, it can be seen that the IC_{50s} and IC_{90s} of quaternary ammonium salt in soil are much smaller than the IC₅₀ and IC₉₀, which may be explained as follows: IC₅₀ and IC₉₀ were measured by the poison plate test method. In the test process, the quaternary ammonium salts and medium were mixed evenly to make culture medium, and the Foc4 mushroom dish was inoculated on the prepared culture medium. Then, in the process of inhibiting the growth of Foc4 mycelium, the quaternary ammonium salt on the surface of the medium plays a greater role because the solid medium limits the movement of quaternary ammonium salt drugs to a certain extent. In contrast, in the process of testing IC_{50s} and IC_{90s}, it is easier for quaternary ammonium salts to contact and interact with Foc4 in soil through shock culture. Therefore, the measured IC_{50s} is smaller than the IC₅₀.

3.3.2. Antimicrobial activities against *C. albicans*, *E. coli*, and *S. albus*

To explore the wide range of antimicrobial activities of Q5, F_x-co-Q5, and F_y-b-Q5, another fungus, *C. albicans*, and bacteria (*E. coli* and *S. albus*) were selected to determine their MIC and MFC (MBC) using the TTC coloration method [13]. The results are shown in Fig. S1. The MBC/MIC (or MFC/MIC) ratio of Q5, F_x-co-Q5, and F_y-b-Q5 against the three kinds of microbial is less than 4, which indicates that they have bactericidal/fungicidal effects. Specifically, the antifungal and antibacterial activities of both F_x-co-Q5 and F_y-b-Q5 showed a trend of first increasing and then decreasing with the increase of hydrophobicity, in which F1-co-Q5, F2-co-Q5, and F1-co-Q5/F1-co-Q5 showed the best antimicrobial activities on *C. albicans*, *E. coli* and *S. albus*, respectively.

The different antimicrobial activities of amphiphilic polymeric quaternary ammonium salt on different bacterial/fungal strains is different, which is related to the bacteriostatic/fungistatic mechanism and the structure of different kinds of bacteria/fungi. For example, compared with *S. albus*, the structure and components of the outer membrane of *E. coli* are more complex, and the resistant to the damage of quaternary ammonium cations would be stronger.

3.3.3. Effect on microbial diversity in soil

Traditional low-molecular-weight antimicrobial agents are typically used to kill pests and microorganisms in terms of plant protection, but low-molecular-weight antimicrobial agents kill all microorganisms and destroy the soil ecosystem due to their strong efficacy and toxicity. To explore the effect of fluorine-containing quaternary ammonium salts when used in the control of Banana Fusarium wilt, an experiment of preferred quaternary ammonium salt on microorganisms in soil is carried out [35]. Fig. 5 shows the number of bacteria, fungi, and actinomycetes in the soil after the addition of quaternary ammonium salts and BC. It can be seen from the chart that the number of bacteria, fungi, and actinomycetes were greatly reduced after BC application, while the number of bacteria and actinomycetes increased and the number of fungi decreased after the effect of the preferred quaternary ammonium salt on microorganisms in the soil. One possible explanation is that the bacteria, fungi, and actinomycetes in the soil ecosystem are in a dynamic equilibrium relationship. The prepared fluorine-containing quaternary ammonium salts have different inhibitory properties on microorganisms in the soil. When quaternary ammonium salts have a good inhibitory effect on fungi and greatly reduce their number, the bacteria and actinomycetes in the soil will be relatively conducive to reproduction and increase due to the reduction in competition.

3.3.4. Persistence of preferred quaternary ammonium salt on Foc4 in soil

In the practical application of fluorine-containing quaternary ammonium salt toward the prevention and control of Foc4 in plant protection, the stability and efficacy persistence are also very important parameter indicators. In this experiment, the preferred quaternary ammonium salts were mixed with soil, Foc4 was calculated, and the persistence of fluorine-containing quaternary ammonium salt was explored. Fig. S5 is a schematic diagram of the sampling and coating

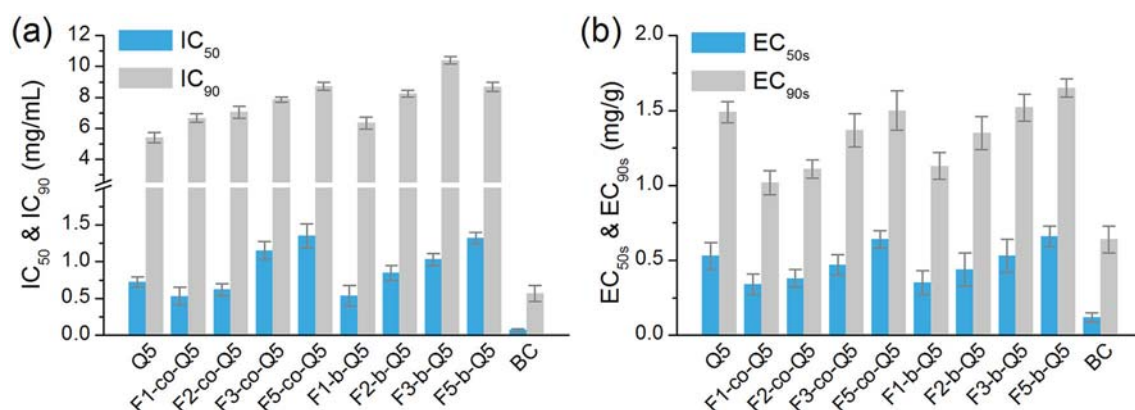


Fig. 4. (a) IC_{50} & IC_{90} and (b) EC_{50s} & EC_{90s} of Q_5 , F_x-co-Q_5 , and F_y-b-Q_5 .

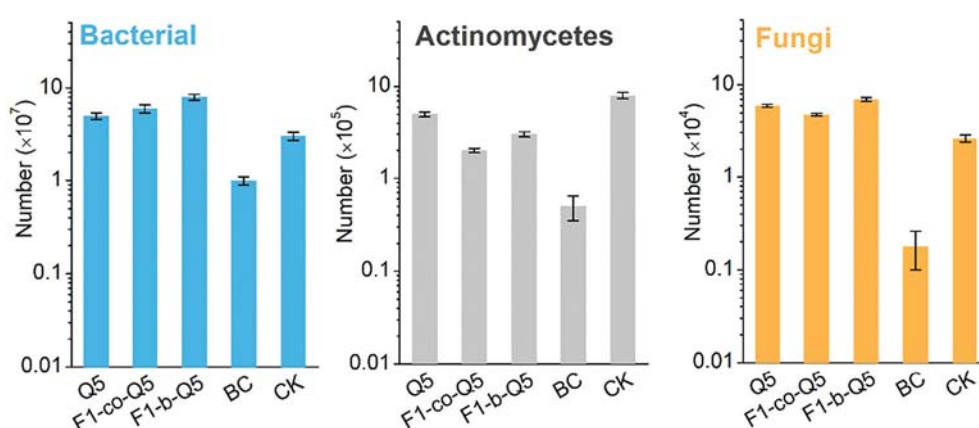


Fig. 5. Number of bacterial, actinomycetes, and fungi of Q_5 , F_x-co-Q_5 , F_y-b-Q_5 , BC, and CK as references.

results on PDA medium of the preferred quaternary ammonium salt at different concentrations after a certain time. The figure shows that the quaternary ammonium salt cannot kill all Foc4 in the soil at low concentrations, and there are still a certain number of Foc4 after coating on PDA medium. When the concentration of quaternary ammonium salt is more than 6 times that of IC_{50s} , it can effectively kill most bacteria in the soil and has a persistence of up to 30 days. This may be because the preferred quaternary ammonium salt is easy to adsorb in the soil and is not easy to migrate, which is conducive to its long-term role in the soil and the achievement of long-term antifungal performance at a high concentration against Foc4.

3.4. Adsorption and migration characteristics in soil

The physical and chemical properties of soil are important factors [36–38] that affect the interaction of Q_5 , F_x-co-Q_5 , and F_y-b-Q_5 with soil and then affect their characteristics in the soil environment. The characteristics of Q_5 , F_x-co-Q_5 , and F_y-b-Q_5 in agricultural soil can be detected according to the 260-nm absorption peak in the UV spectrophotometer due to the benzene ring structure.

Fig. 6(a)–(b) shows the adsorption curves of Q_5 , F_x-co-Q_5 , F_y-b-Q_5 , and BC in soil. We find that the adsorption process of quaternary ammonium salt in soil mainly occurs in the first 120 min, and the adsorption amount changes little with time after 120 min, reaching the saturated adsorption state between 8 and 10 h. The adsorption of fluorine-containing quaternary ammonium salt in soil is affected by many factors including electrostatic interactions, hydrophobic interactions, hydrogen bonding, physical and chemical properties of soil, and adsorption mechanisms. In the experiment, we selected the soil to

explore the effects of electrostatic interactions, hydrophobic interactions, and hydrogen bonding on the adsorption of fluorine-containing quaternary ammonium salts. An explanation of the saturated adsorption capacity and adsorption kinetic process is as follows: the experimental soil is negatively charged and has high cation exchange capacity on its surface. Therefore, when adsorbed with the soil, the fluorine-containing cationic quaternary ammonium salt is combined with the soil through electrostatic adsorption, which is the rapid adsorption stage of ion exchange. Then, the fluorocarbon chain is adsorbed and combined with the soil through hydrophobic interactions and hydrogen bonding. This is a relatively slow process. Figs. S2 and S3 show that the cation content of fluorine-containing amphiphilic quaternary ammonium salt mainly affects its adsorption rate, and the hydrophobic and electrostatic effects of fluorine-containing chain segments are more conducive to combination and desorption. This is consistent with the stronger hydrophobic effect, larger adsorption coefficient, and greater adsorption capacity [39,40].

The migration of Q_5 , F_x-co-Q_5 , and F_y-b-Q_5 with rainwater in soil is an important factor that affects their long-term antifungal performance against Foc4 in plant protection. The soil migration experiment simulates the leaching of quaternary ammonium salt in the soil layer by rainwater and explores the retention capacity of Q_5 , F_x-co-Q_5 , F_y-b-Q_5 , and BC in soil. Fig. 6(c)–(d) is a relationship chart showing the migration depth and leaching rate of Q_5 , F_x-co-Q_5 , F_y-b-Q_5 , and BC in soil. The migration capacity of fluorine-containing quaternary ammonium salt and BC in soil is poor, and the maximum leaching depth is less than 10 cm from the experimental data. The outflow rate R1 (0–10 cm) of various fluorine-containing quaternary ammonium salts and leaching solutions is more than 50%, which is difficult to leach according to GB

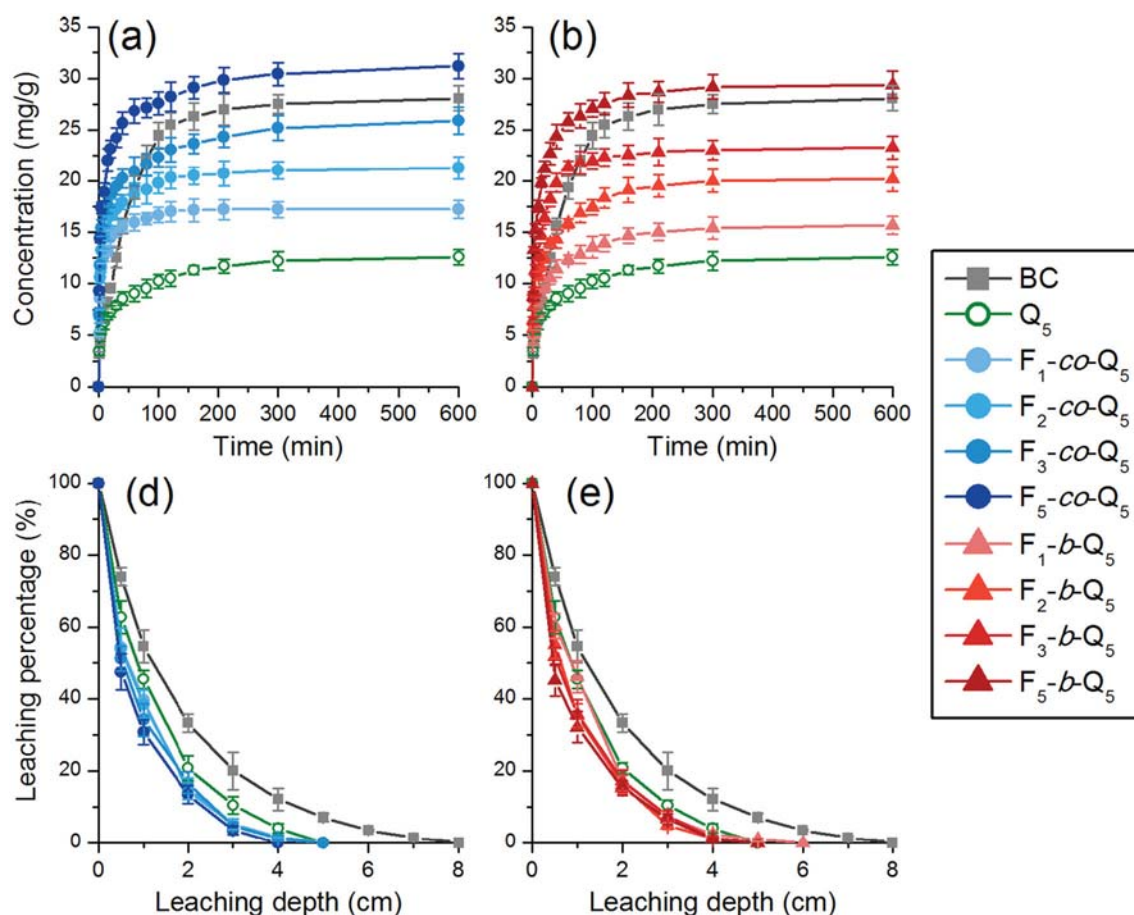


Fig. 6. (a-c) Saturated adsorption capacity of Q₅, F_x-co-Q₅, F_y-b-Q₅, and BC in soil. (d-f) Typical leaching curves of leaching depth against leaching percentage of Q₅, F_x-co-Q₅, and F_y-b-Q₅.

31270.5–2014. Therefore, Q₅, F_x-co-Q₅, and F_y-b-Q₅ do not easily migrate with water in the soil and can stay in the soil stably for a long time. This is conducive to long-term antifungal performance against Foc4.

3.5. Toxicity tests

Fig. 7 shows the toxicity data of Q₅, F_x-co-Q₅, F_y-b-Q₅, and BC to zebrafish according to GB/T 31270.12–2014. The oral toxicity LC₅₀ data of Q₅, F_x-co-Q₅, and F_y-b-Q₅ to zebrafish are between 1 and 10 mg/L,

showing an acute oral toxicity to zebrafish according to the classification standard of toxicity level. In addition, the oral acute toxicity LC₅₀ data of Q₅, F_x-co-Q₅, and F_y-b-Q₅ to zebrafish decreased as time elapsed, which indicates that the toxicity and side effects of Q₅, F_x-co-Q₅, and F_y-b-Q₅ on zebrafish are cumulative and long-lasting. Based on Q₅, F_x-co-Q₅ and F_y-b-Q₅ are easy to adsorb and difficult to migrate in the soil, and the toxicity LC₅₀ of quaternary ammonium salt in soil to zebrafish after soil adsorption and rainwater leaching is greater than 10 mg/L. This indicates that Q₅, F_x-co-Q₅, and F_y-b-Q₅ have great application prospects in the prevention and control of Foc4 in plant protection.

3.6. Pot experiments

In a pot experiment regarding the prevention and control effects of the preferred quaternary ammonium salt on Foc4 during the growth of banana seedlings, we set the growth of banana seedlings in four experimental groups (Table S2). Fig. 8(a), Fig. S6(a), and Fig. S7(a) show that when Foc4 is not inoculated, banana seedlings grow healthily, which indicates that fluorine-containing quaternary ammonium salts have little effect on the growth of banana seedlings under the experimental conditions without Foc4. Fig. 8(b), Fig. S6(b), and Fig. S7(b) indicate that when Foc4 is inoculated, the symptoms of Foc4 infection in banana seedlings are different: banana seedlings have better growth and fewer disease symptoms under higher concentrations of quaternary ammonium salt but have relatively poor growth under low concentrations of drugs. Fig. 8(b) shows that the leaves of banana seedlings turned yellow or withered seriously, and the pseudostem appeared as a dark or brown area at a concentration of IC_{50S} quaternary ammonium salt. The infection of Foc4 in banana seedling roots and leaves was relatively mild

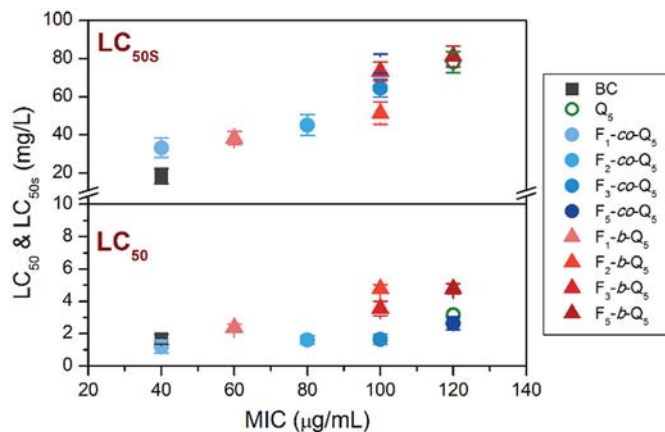


Fig. 7. Distribution of antifungal activity against Foc4 and biotoxicity to zebrafish: (a) acute toxicity and (b) toxicity after adsorption of soil.

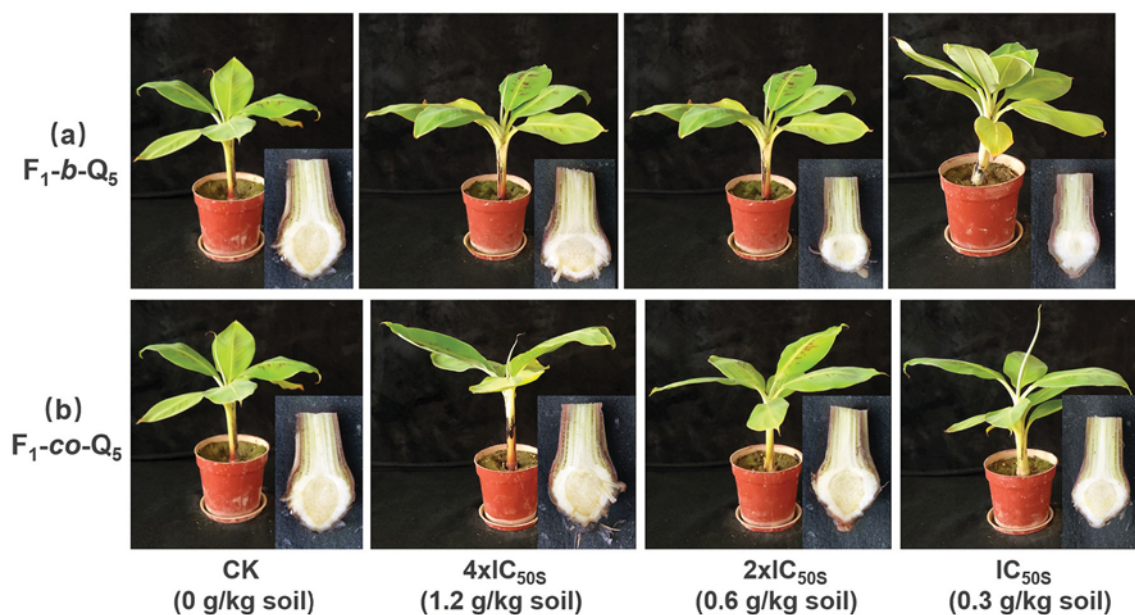


Fig. 8. Classic diagram of effect of (a) F_1-b-Q_5 and (b) F_1-co-Q_5 on growth of banana seedlings after 40 d. Small illustration in lower right corner shows longitudinal bisection of corms.

under a $4 \times IC_{50S}$ concentration of F_1-co-Q_5 . This may be because the high concentration of quaternary ammonium salt easily contacts Foc4 more fully in the soil and kills most of the Foc4, which leads to a small amount of residual Foc4 causing mild and minor infection of banana seedlings. (See Fig. 9.)

The $4 \times IC_{50S}$ concentration of quaternary ammonium salt is roughly equivalent to the IC_{90S} value measured by antifungal properties against Foc4 in soil (Fig. 4). At this concentration, fluorine-containing quaternary ammonium salt can kill most of the Foc4 in the soil, which is consistent with the growth of banana seedlings in the pot experiment. In addition, comparing the effect of Q_5 , F_1-co-Q_5 , and F_1-b-Q_5 on the growth parameters of banana seedlings in the process of controlling banana Fusarium wilt in Table S3 and Fig. S8, we found that the disease

index of banana seedlings under the $4 \times IC_{50S}$ (1.2 mg/g soil) action of F_1-co-Q_5 and F_1-b-Q_5 decreased to disease grade I (the degree of infection was approximately 11%). This indicated that the introduction of quaternary ammonium salt with an appropriate proportion of fluorine groups can enhance its antifungal performance to better control banana Fusarium wilt during the growth of banana seedlings.

4. Conclusions

This study showed that fluorine-containing amphiphilic quaternary ammonium salts with random and block structures (Q_5 , F_x-co-Q_5 , and F_y-b-Q_5) have good broad-spectrum antimicrobial properties, especially the fluoroalkyl group introduced into quaternary ammonium salt, which



Fig. 9. Classic diagram of effect of (a) F_1-b-Q_5 and (b) F_1-co-Q_5 on growth of banana seedlings after 40 d under different concentrations of fluorine-containing amphiphilic quaternary ammonium salts, in which Foc4 conidia concentration is 2×10^6 conidia/g soil. Small illustration in lower right corner shows longitudinal bisection of corms.

exhibits better antifungal performance on Foc4, as the MIC of F_{1-co-Q5} is equivalent to BC. In addition, Q₅, F_{x-co-Q5}, and F_{y-b-Q5} are easy to adsorb in the soil and will not move, which is conducive to their long-term stable existence in the soil. In addition, they are unlikely to flow into groundwater to cause water pollution. This verified their low toxicity to zebrafish and long-term antifungal performance against Foc4 after application. Additionally, the application of fluorine-containing polymeric quaternary ammonium salt does not destroy the diversity of the microbial system in soil. Finally, the results of a pot experiment showed that the fluorine-containing quaternary ammonium salt had a more positive effect on the control of Foc4, while the fluoroalkyl group was introduced into the quaternary ammonium salt. Through the systematic characterization and research of fluorine-containing amphiphilic quaternary ammonium salts with random and block structures (Q₅, F_{x-co-Q5}, and F_{y-b-Q5}), we hope to provide a new way to protect banana plants against banana Fusarium wilt and promote the healthy and stable development of the banana industry.

Notes

The authors declare no competing financial interest.

Author contributions

The manuscript was written through the contributions of all authors.

Declaration of Competing Interest

The authors declare that they have no known competing financial interests or personal relationships that could have appeared to influence the work reported in this paper.

Data availability

No data was used for the research described in the article.

Acknowledgements

The authors acknowledge the financial support from the National Natural Science Foundation of China (Nos. 31772202 and 52073098) and the Scientific and Technological Planning Project of Guangzhou City (201803020015).

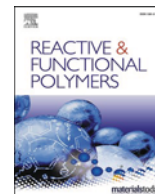
Appendix B. Supplementary data

Detailed methods for the antimicrobial testing; the characterization of F_{x-co-Q5} and F_{y-b-Q5}, D₃ and Q₅; the adsorption and migration characteristics of Q₅, F_{x-co-Q5} and F_{y-b-Q5} in agricultural soil; the antifungal properties against Foc4 in soil; the toxicity test; the methods & results for pot experiments, can be seen in Supporting Information. Supplementary data to this article can be found online at <https://doi.org/10.1016/j.reactfunctpolym.2022.105488>.

References

- [1] J.P. Jones, S.S. Woltz, Fusarium wilt of tomato: interaction of soil liming and micronutrient amendments on disease development, *Phytopathology* 60 (2) (1970) 812–813.
- [2] E.I. Jonathan, G. Rajendran, Interaction of *Meloidogyne incognita* and *Fusarium oxysporum* f. sp. *cubense* on banana, *Nematol. Mediterr.* 26 (1) (1998) 9–11.
- [3] M. Dita, M. Barquero, D. Heck, E.S.G. Mizubuti, C.P. Staver, Fusarium wilt of banana: current knowledge on epidemiology and research needs toward sustainable disease management, *Front. Plant Sci.* 9 (2018) 1468.
- [4] C.E. Alvarez, V. Garcia, J. Robles, Influence of soil characteristics on the incidence of Panama disease, *Fruits* 36 (2) (1981) 71–81.
- [5] Y. Qi, X. Zhang, J. Pu, H. Zhang, Y. Xie, Inactivation effect of 10 compounds on *Fusarium oxysporum* f. sp. *cubense* and its toxin, *Int. J. Fruit Sci.* 25 (3) (2008) 78–82.
- [6] Y. Pushpavathi, S.N. Dash, Y.A. Reddy, V. Triveni, Evaluation of fungicides and biocontrol agents for potential application in fusarium wilt management of banana cv Bantal, *Int. J. Farm Sci.* 7 (2) (2017) 115–118.
- [7] M. Rokunuzzaman, A. Hayakawa, S. Yamane, S. Tanaka, K. Ohnishi, Effect of soil disinfection with chemical and biological methods on bacterial communities, *Egyptian J. Basic & Appl. Sci.* 3 (2) (2016) 141–148.
- [8] T. Raguchander, V. Shanmugam, R. Samiyappan, Biological control of Panama wilt disease of banana, *Madras Agric. J.* 87 (4) (2000) 320–321.
- [9] Z. Shen, Y. Ruan, X. Chao, J. Zhang, R. Li, Q. Shen, Rhizosphere microbial community manipulated by 2 years of consecutive biofertilizer application associated with banana fusarium wilt disease suppression, *Biol. Fertil. Soils* 51 (5) (2015) 553–562.
- [10] T. Chang, R. Chang, Generation of volatile ammonia from urea fungicidal to *Phellinus noxius* in infested wood in soil under controlled conditions, *Plant Pathol.* 48 (3) (1999) 337–344.
- [11] A.B. Pattison, C.L. Wright, T.L. Kukulies, A.B. Molina, Ground cover management alters development of fusarium wilt symptoms in Ducasse bananas, *Australas. Plant Pathol.* 43 (4) (2014) 465–476.
- [12] A.K. Sharma, D. Sharma, A.K. Chopra, An overview of pesticides in the development of agriculture crops, *J. Appl. Nat. Sci.* 12 (2) (2020) 101–109.
- [13] Z. Huang, R. Liuyang, C. Dong, Y. Lei, A. Zhang, Y. Lin, Polymeric quaternary ammonium salt activity against *Fusarium oxysporum* f. sp. *cubense* race 4: synthesis, structure-activity relationship and mode of action, *React. Funct. Polym.* 114 (2017) 13–22.
- [14] M. Schulz, A. Olubummo, W.H. Binder, Beyond the lipid-bilayer: interaction of polymers and nanoparticles with membranes, *Soft Matter* 8 (2012) 4849–4864.
- [15] K.A. Brogden, Antifungal peptides: pore formers or metabolic inhibitors in bacteria? *Nat. Rev. Microbiol.* 3 (3) (2005) 238–250.
- [16] P. Gilbert, L.E. Moore, Cationic antiseptics: diversity of action under a common epithet, *J. Appl. Microbiol.* 99 (4) (2005) 703–715.
- [17] E.R. Kenawy, F.I. Abdel-Hay, A.E.R.R. El-Shanshoury, M.H. El-Newehy, Biologically active polymers. V. Synthesis and antifungal activity of modified poly (glycidyl methacrylate-co-2-hydroxyethyl methacrylate) derivatives with quaternary ammonium and phosphonium salts, *J. Polym. Sci. A Polym. Chem.* 40 (14) (2002) 2384–2393.
- [18] W. Zhong, C. Dong, R. Liuyang, Q. Guo, H. Zeng, Y. Lin, A. Zhang, Controllable synthesis and antifungal activities of acrylate polymers containing quaternary ammonium salts, *React. Funct. Polym.* 121 (2017) 110–118.
- [19] Y. Lin, W. Zhong, C. Dong, C. Zhang, X. Feng, A. Zhang, Synthesis and antifungal activities of amphiphilic PDMS-b-QPDMAEMA copolymers on *Rhizoctonia solani*, *ACS Appl. Bio Mater.* 1 (2018) 2062–2072.
- [20] A. Zhang, Q. Liu, Y. Lei, S. Hong, Y. Lin, Synthesis and antifungal activities of acrylamide polymers containing quaternary ammonium salts on bacteria and phytopathogenic fungi, *React. Funct. Polym.* 88 (2015) 39–46.
- [21] E. Palermo, I. Sovadinova, K. Kuroda, Structural determinants of antifungal activity and biocompatibility in membrane-disrupting methacrylamide random copolymers, *Biomacromolecules* 10 (11) (2009) 3098–3107.
- [22] Y. Lin, Q. Liu, L. Cheng, Y. Lei, A. Zhang, Synthesis and antifungal activities of polysiloxane-containing quaternary ammonium salts on bacteria and phytopathogenic fungi, *React. Funct. Polym.* 85 (2014) 36–44.
- [23] A. Dominguez, A. Fernandez, N. Gonzalez, E. Iglesias, L. Montenegro, Determination of critical micelle concentration of some surfactants by three techniques, *J. Chem. Educ.* 74 (10) (1997) 1227–1231.
- [24] A.M. Khan, S.S. Shah, Determination of critical micelle concentration (CMC) of sodium dodecyl sulfate (SDS) and the effect of low concentration of pyrene on its CMC using origin software, *J. Chem. Soc. Pak.* 30 (2) (2008) 186–191.
- [25] C. Cheng, J. Wang, R. Kausik, K. Lee, S. Han, Nature of interactions between PEO-PPO-PEO triblock copolymers and lipid membranes: (II) role of hydration dynamics revealed by dynamic nuclear polarization, *Biomacromolecules* 13 (9) (2012) 2624–2633.
- [26] K.E.S. Locock, T.D. Michl, J.D.P. Valentin, K. Vasilev, J.D. Hayball, Y. Qu, A. Traven, H.J. Griesser, L. Meagher, M. Haeussler, Guanylated polymethacrylates: a class of potent antifungal polymers with low hemolytic activity, *Biomacromolecules* 14 (11) (2013) 4021–4031.
- [27] K.E.S. Locock, T.D. Michl, N. Stevens, J.D. Hayball, K. Vasilev, A. Postma, H. J. Griesser, L. Meagher, M. Haeussler, Antifungal polymethacrylates synthesized as mimics of tryptophan-rich cationic peptides, *ACS Macro Lett.* 3 (4) (2014) 319–323.
- [28] Y. Chen, P.A. Wilbon, Y.P. Chen, Z.H. Zhou, M. Nagarkatti, C.P. Wang, F.X. Chu, A. W. Decho, C.B. Tang, Amphipathic antibacterial agents using cationic methacrylic polymers with natural rosin as pendant group, *RSC Adv.* 2 (27) (2012) 10275–10282.
- [29] K. Kuroda, G.A. Caputo, W.F. DeGrado, The role of hydrophobicity in the antifungal and hemolytic activities of polymethacrylate derivatives, *Chemistry-a, Eur. J. Dermatol.* 15 (5) (2009) 1123–1133.
- [30] A. King, S. Chakrabarty, W. Zhang, X.M. Zeng, D.E. Ohman, L.F. Wood, S. Abraham, R. Rao, K.J. Wynne, High antifungal effectiveness with low hemolytic and cytotoxic activity for PEG/quaternary copolyoxetanes, *Biomacromolecules* 15 (2) (2014) 456–467.
- [31] W. Jaeger, J. Bohrisch, A. Laschewsky, Synthetic polymers with quaternary nitrogen atoms—synthesis and structure of the most used type of cationic polyelectrolytes, *Prog. Polym. Sci.* 35 (5) (2010) 511–577.
- [32] M. Werner, J.U. Sommer, V.A. Baulin, Homo-polymers with balanced hydrophobicity translocate through lipid bilayers and enhance local solvent permeability, *Soft Matter* 8 (46) (2012) 11714–11722.

- [33] S.C. Owen, D. Chan, M.S. Shoichet, Polymeric micelle stability, *Nano Today* 7 (1) (2012) 53–65.
- [34] S. Creutz, J.V. Stam, F.C.D. Schryver, R. Jérôme, Dynamics of poly ((dimethylamino) alkyl methacrylate-block-sodium methacrylate) micelles. Influence of hydrophobicity and molecular architecture on the exchange rate of copolymer molecules, *Macromolecules* 31 (3) (1998) 681–689.
- [35] M. Teimouri, P. Mohammadi, A. Jalili, Microbial properties and dehydrogenase activity in semiarid area, Kerman Province, Iran, *Polish J. Environ. Stud.* 28 (2) (2019) 853–860.
- [36] S. Paria, K.C. Khilar, A review on experimental studies of surfactant adsorption at the hydrophilic solid-water interface, *Adv. Colloid Interf. Sci.* 110 (3) (2004) 75–95.
- [37] S. Xu, S.A. Boyd, Cationic surfactant sorption to a vermiculitic subsoil via hydrophobic bonding, *Environ. Sci. Technol.* 29 (2) (1995) 312–320.
- [38] S. Xu, S.A. Boyd, Cationic surfactant adsorption by swelling and nonswelling layer silicates, *Langmuir* 11 (7) (1995) 2508–2514.
- [39] V.C. Hand, G.K. Williams, Structure-activity relationships for sorption of linear alkylbenzenesulfonates, *Environ. Sci. Technol.* 21 (4) (1987) 370–373.
- [40] C.P. Higgins, R.G. Luthy, Sorption of perfluorinated surfactants on sediments, *Environ. Sci. Technol.* 40 (23) (2006) 7251–7256.
- [41] Y. Chang, W. Zhong, J. Liang, A. Zhang, Y. Lin, Polydimethylsiloxane-polymethacrylate block copolymers containing quaternary ammonium salts against *fusarium oxysporum* f. sp. *cubense* race 4 in soil: antifungal activities and pot experiments, *React. Funct. Polym.* 160 (2021), 104848.
- [42] W. Zhang, Y. Chang, W. Zhong, A. Zhang, Y. Lin, Antifungal mechanisms of polymeric quaternary ammonium salts against conidia of *fusarium oxysporum* f. sp. *cubense*, race 4, *Eur. J. Plant Pathol.* (2022), <https://doi.org/10.1007/s10658-022-02608-5>.



Polymeric diallyl quaternary ammonium salts for inhibiting banana Fusarium wilt

Yaling Lin^{a,*}, Chang Zhang^b, Meng Hou^a, Rui Li^b, Anqiang Zhang^{b,*}

^a College of Material and Energy, South China Agricultural University, 483 Wushan Rd., Guangzhou 510642, Guangdong, China

^b School of Material Science and Engineering, South China University of Technology, 381 Wushan Rd., Guangzhou 510641, Guangdong, China

ARTICLE INFO

Keywords:

Polymeric diallyl quaternary ammonium salt
Banana Fusarium wilt
Antifungal activity
Biototoxicity
Long-term inhibition

ABSTRACT

Banana Fusarium wilt is a typical soil-borne pathogen disease caused by *Fusarium oxysporum* f. sp. *cubense* (Foc) and is difficult to control because Foc conidia can survive for many years in soil. Thus, the inhibition of Foc conidia in soil would be an effective and possible way to control banana Fusarium wilt. In this work, three kinds of poly(N,N-diene propyl quaternary ammonium salts) (PDPQASs), namely, poly(methyl butyl diallyl ammonium chloride) (PM), poly(methyl benzyl diallyl ammonium chloride) (PB) and poly(dimethyl diallyl ammonium chloride) (PD), were synthesized, and the antifungal activities on Foc4, the adsorption and leaching properties in soil, and the biotoxicieties on silkworms, zebrafish and mice were evaluated. It was found that the three kinds of PDPQAS showed obvious and stronger inhibiting effects on Foc4 conidia, and they were essentially nontoxic to silkworms and mice. Their toxicities were much lower than that of benzalkonium chloride (BC, a typical commercial small molecular QAS) to zebrafish, in which PB showed the best comprehensive properties in antifungal activities and biotoxicieties. Benefitting from the stronger polymer-soil interaction, PB could absorb in soil more easily and hardly be leached from the soil, which helped PB stay in the soil more stably and effectively inhibited Foc4 conidia in the long term, giving PB a potential application in the control of banana Fusarium wilt.

1. Introduction

Banana Fusarium wilt is caused by *Fusarium oxysporum* f. sp. *cubense* (Foc). There are four categories of pathogenic fungi, among which tropical race 4 (Foc4) shows the strongest pathogenicity and can infect all the current banana varieties [1,2]. Banana Fusarium wilt is a typical soil-borne disease. Once Foc4 conidia enter a banana garden, they will reproduce in the soil, penetrate the intercellular space of the root epidermis cell walls and colonized the root vascular tissues of corms of bananas, leading to water blockage and resulting in pseudostem and leaf wilting [3]. So, in a conducive soil even low levels of pathogen inoculum can cause serious damages [4]. Thus, banana Fusarium wilt is considered a “cancer” in the banana growing industry, which has greatly restricted the development of the banana industry in South China and even in the world.

At present, chemical control and biological control are two important methods to control banana Fusarium wilt. For biological control, some fungi and bacteria that have antagonistic effects on the target pathogen have been used, but the current research is still mainly in the laboratory stage; furthermore, the fungi that have antagonistic effects on banana Fusarium wilt might change with the environment in the actual soil, showing instability [5]. For chemical control, the inhibitory effects of chemical reagents on banana Fusarium wilt have been studied. However, most of the chemical reagents used in chemical control are single and small molecules, which are prone to be lost with rain in the process of chemical control, making it difficult to achieve the effect of killing Foc conidia in the soil over a period of time [5,6]. Polymeric quaternary ammonium salts (PQASs) are novel antimicrobial agents. Due to their long molecular chain length and higher charge density, their immigration ability is lower than those of small molecule

Abbreviations: Foc, *Fusarium oxysporum* f. sp. *cubense*; Foc4, *Fusarium oxysporum* f. sp. *cubense* race 4; QAS, quaternary ammonium salts; PQAS, polymeric quaternary ammonium salts; PDPQASs, poly(N,N-diene propyl quaternary ammonium salts); MBDAC, methyl butyl diallyl ammonium chloride; PB, methyl benzyl diallyl ammonium chloride; DMDAC, dimethyl diallyl ammonium chloride; PM, poly(methyl butyl diallyl ammonium chloride); PB, poly(methyl benzyl diallyl ammonium chloride); PD, poly(dimethyl diallyl ammonium chloride); LC₅₀, median lethal concentration; LD₅₀, median lethal dose; MIC, minimum inhibitory concentration; MFC, minimal fungicidal concentration; TTC, 2,3,5-triphenyltetrazolium chloride..

* Corresponding authors.

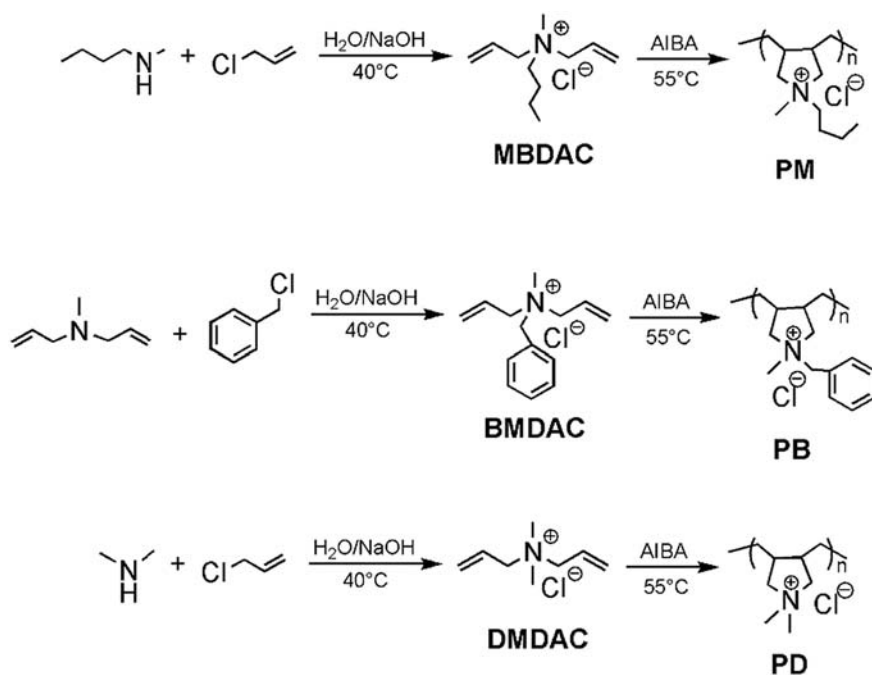
E-mail addresses: linyinling@scau.edu.cn (Y. Lin), aqzhang@scut.edu.cn (A. Zhang).

<https://doi.org/10.1016/j.reactfunctpolym.2022.105174>

Received 8 October 2021; Received in revised form 7 January 2022; Accepted 10 January 2022

Available online 20 January 2022

1381-5148/© 2022 Elsevier B.V. All rights reserved.



Scheme 1. Structures and synthesis routes of MBDAC, BMDAC, DMDAC, PM, PB and PD.

quaternary ammonium salts (SQASs); thus, the inhibitory effect might be prolonged [7,8].

According to the position of quaternary ammonium (N^+) in the macromolecules, PQAS can be divided into three categories: main chain type, side chain type and branch type [9]. In main chain cationic polymers, multiple cationic centers densely appear in the polymer skeleton, which can enhance the polymer's adsorption to the microbial membrane surface. Liu [10] and Cakmak [11] found that the main chain cationic polymers could greatly inhibit the growth of most pathogenic bacteria. There are many types of main chain cationic polymers, including polyguanidine [12,13], polyimidazole [10], diallyl quaternary ammonium polymer [14] and other main-chain macromolecular quaternary ammonium salts [11,15].

Compared with the side-chain quaternary ammonium salts most studied now [16], diallyl polymeric quaternary ammonium salt showed higher charge density, for example, the average molecular per quaternary ammonium (N^+) for polyacrylamide-based QAS (such as PQD-BC) [17] and the PDPQASs discussed in the work (such as PB), are about 280 and 227, respectively. Thus the PDPQASs have stronger adsorption characteristics to bacteria or fungi, and its antibacterial/antifungal activities could be further improved to meet the current needs of efficient sterilization. In addition, most of the current main chain type PQASs were synthesized based on the condensation method [18,19], while N,N-diene propyl types of PQASs (PDPQASs) can be obtained by traditional radical polymerization via a ring-closing mechanism, and the molecular weights are easy to control [20,21]. In addition, the polymerization of PDPQASs can be carried out in water without organic solvent, which is low cost and environmentally friendly and makes the synthetic method highly advantageous to a wide range of development and application in the future [22,23].

Although SQASs have been studied for decades, the applications of SQASs in the control of soil-borne disease have rarely been reported [24,25], which might be due to their broad-spectrum antimicrobial activity and their potential pollution to soil and water environments. Therefore, in this work, based on the synthesis of a series of N,N-diene propyl quaternary ammonium salts (DPQASs) with different side groups and the corresponding homopolymers (PDPQASs), the influence of molecular structure on the antifungal activities, biotoxicities (including toxicities to fish, silkworm and mice), polymer-soil

interactions and long-term antifungal properties of PDPQASs in Foc4-containing soil were studied in detail. We hope this work will help to further the understanding of the relationship between polymer structure and long-term antifungal properties and will assist in finding potential polymeric antimicrobial agents for plant protection.

2. Experimental

2.1. Materials

N-methyldiallyl amine (98%), azodiisobutyramidine hydrochloride (AIBA), benzyl chloride, dimethylamine, N-methyl-butylamine, and benzalkonium chloride (BC) were purchased from Shanghai Macklin Biochemical Technology Co., Ltd. (Shanghai, China). 2,3,5-Triphenyltetrazolium chloride (TTC) was purchased from BBI Life Sciences. *Fusarium oxysporum* f. sp. *cubense* race 4 (Foc4) was donated by the Fungal Laboratory, Department of Plant Pathology, South China Agricultural University and subcultured on potato dextrose agar medium (PDA). The soil (crushed and screened through a 20-mesh sieve) was taken from the banana field of the Institute of Fruit Tree Research, Guangdong Academy of Agricultural Sciences. The physicochemical properties of the tested soil are shown in Table S1.

2.2. Synthesis of quaternary ammonium monomers and their homopolymers

N, N-methyl butyl diallyl ammonium chloride (MBDAC) and its homopolymer (PM), N,N-dimethyl benzyl diallyl ammonium chloride (BMDAC) and its homopolymer (PB), and N,N-dimethyl diallyl ammonium chloride (DMDAC) and its homopolymer (PD) were synthesized according to Scheme 1, and the synthesis procedures were described briefly in the Supporting Information (Part S1).

2.3. Characterization

FT-IR spectra were collected on a Nicolet iS5 (Thermo Fisher Scientific Corp., USA) using KBr pellets. ^1H NMR spectra were obtained using a Bruker Avance III-400 (Bruker Instrument Corp., Germany) spectrometer with D_2O as the solvent. Size exclusion chromatography

Table 1
Molecular weights and distributions of PD, PM and PB.

Sample	M_n^a	M_w^a	$D (M_w/M_n)^a$
PD	7.36×10^3	12.9×10^3	1.95
PM	4.93×10^3	8.19×10^3	2.06
PB	2.41×10^3	4.37×10^3	2.11

a : based on GPC testing.

(SEC) was performed on a Waters 515–2414 system (Waters Corp., USA) equipped with Ultrahydrogel 250 columns, and the samples were measured at 40 °C using 0.5 M acetic acid and 0.5 M sodium acetate solution as the eluent, and the instrument was calibrated using PEG standards.

2.4. Antifungal properties of the PDPQASs on *Foc4*

The antifungal activities of PDPQASs, namely PM, PB, and PD, were evaluated based on the method of inhibition of mycelial growth and the TTC coloration method [26]. The 50% inhibitory concentration (IC_{50}) and 90% inhibitory concentration (IC_{90}) were determined by the hyphal growth inhibition test to measure the diameters of the fungal colonies on PDA plates with different concentrations of PDPQASs; the minimum inhibitory concentrations (MICs) of PDPQASs on *Foc4* were determined by the broth microdilution method with 2,3,5-triphenyltetrazolium chloride (TTC), and the minimal fungicidal concentrations (MFCs) on *Foc4* were determined by the spot plate method [26]. All tests were conducted in triplicate.

2.5. Biototoxicity evaluation methods

The evaluation methods for determining the biotoxicities of PM, PB, PD and BC on insects (silkworms), fish (zebrafish) and mammals (Kunming mice) are listed in detail in the Supporting Information, Part S2.

2.6. Characterization of the interaction between PDPQASs and soil

The testing methods for the adsorption and leaching properties of PB in soil [7] and the inhibition characteristics of PB on *Foc4* in soil are listed in the Supporting Information (Part S3).

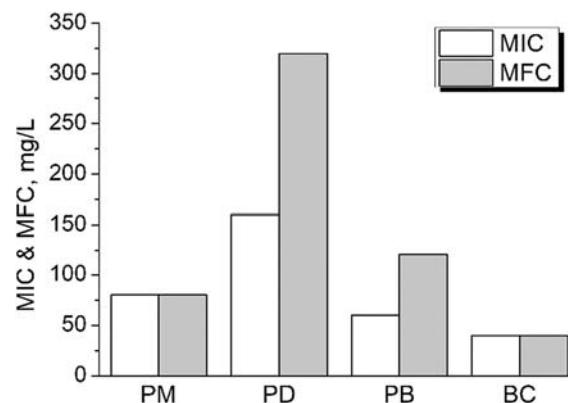


Fig. 2. MICs and MFCs of PD, PM, PB and BC against *Foc4* based on the TTC coloration method.

3. Results and discussion

3.1. Synthesis and characterization of PD, PM and PB

The FTIR and 1H NMR spectra of the three kinds of monomers, namely, DMDAC, MBDAC and BMDAC, are shown in Figs. S3 and S4, respectively. In which, the peaks in 958 cm^{-1} in the FTIR spectra, and the 5.60 ppm & 5.95 ppm in the 1H NMR spectra were assigned to the vinyl group of the monomers, and peaks in 1640 cm^{-1} were assigned to the N^+ groups.

Generally, the hygroscopic nature of quaternary ammonium salts was demonstrated strongly, and there was a wide water peak at 3422 cm^{-1} for each monomer. The characteristic peaks marked in Figs. S3 and S4 show that the monomers had the expected structure.

The homopolymers, namely, PD, PM and PB, were synthesized from DMDAC, MBDAC and BMDAC based on radical polymerizations, and their FTIR and 1H NMR spectra are shown in Figs. S5 and S6, respectively. The peaks for $C=C$ bonds (958 cm^{-1} in the FTIR spectra, and 5.60 ppm & 5.95 ppm in the 1H NMR spectra) almost disappeared, demonstrating the successful synthesis of the polymers. The molecular weights and distributions of PD, PM and PB are shown in Table 1. Table S2 showed that with different feed ratio of the monomers/initiators, overall, the polymerization activity decreased with increasing volume of the side group. And we noticed that although the molecular weight would be different, the molecular weight distribution and their anti-bacterial or antifungal activities were almost the same, which mean the molecular weight of PDPQASs was not the significant factor. Thus in

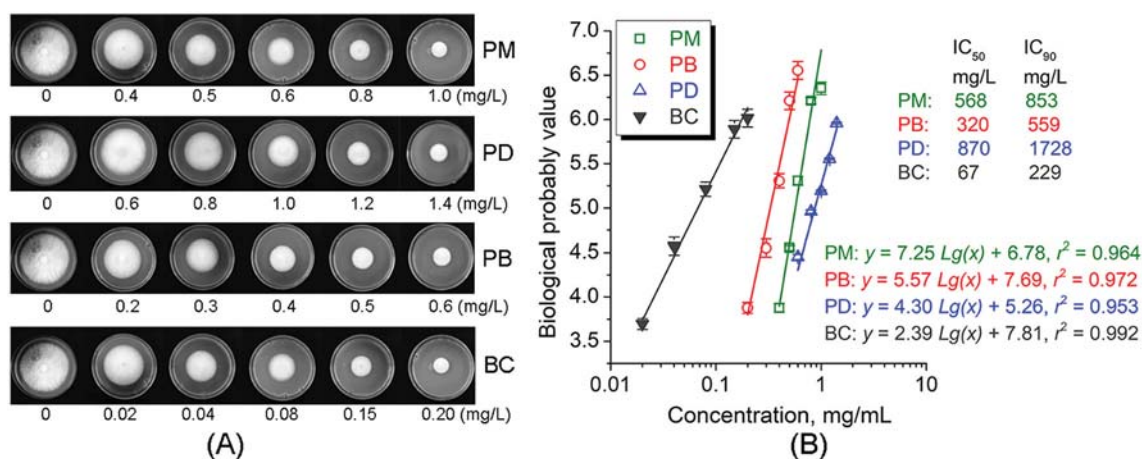


Fig. 1. (A) Antifungal activities of PD, PM, PB and BC against *Foc4* (after incubation for 5 d) based on the method of inhibition of mycelial growth and (B) the fitting curves and results of IC_{50} and IC_{90} .

Table 2

Toxicities of PD, PM, PB and BC to silkworm, zebrafish and Kunming mice.

Sample	LC ₅₀ for silkworm, mg/L	LC ₅₀ for zebrafish, mg/L	LD ₅₀ for Kunming mice, mg/kg
PM	> 2000	3.45	4500
PD	> 2000	4.31	> 5000
PB	> 2000	2.29	2000
BC	1320	1.79	555

this paper, for each polymer, only one sample was pick out for representative, as shown in Table 1.

3.2. Anti-fungal activities of PDPQASs on *Foc4*

The IC₅₀ and IC₉₀ are regarded as the two most important indicators for antifungal drugs [26]. Fig. 1-(A) shows the growth state of the typical fungus dish after being injected into the solid medium with the drug for 5 d. The inhibitory effect of the drug on mycelial growth was reflected in the size of mycelial growth under different concentrations. Fig. 1-(B) shows the fitting curves, and the IC₅₀ and IC₉₀ values could be calculated from the curves. Although BC showed the lowest IC₅₀ and IC₉₀, PB seemed to have the best anti-*Foc4* activities among the three kinds of PDPQASs. Similar results are shown in Fig. 2. PB also showed the lowest MIC among the three PDPQASs, which was slightly higher than that of BC. The differences between IC₅₀ & IC₉₀ and MIC & MFC for the same drug are mainly due to the testing methods; for the former, the fungal mycelium only contacts one side of the PDA plates containing drugs, while for the latter, the mycelium could mix with the drugs in solution uniformly, thus resulting in a much lower inhibitory concentration.

According to the mechanisms of electrostatic adsorption and bacteriostatic inhibition [27], the strength of the inhibition effect is determined by the binding property between the molecular chain and the outer membrane when the polymer adsorbs on the surface of the fungus. The stronger the hydrophobicity is, the more favorable it is to combine the polymer chain with the phospholipid layer of the fungal membrane structure through hydrophobic effects to destroy the integrity. The above three types of PDPQASs have a certain inhibitory effect on *Foc4* mycelia, and their inhibitory activity will decrease with increasing molecular weight. The stronger the side group hydrophobicity is, the better the inhibitory effect will be [17,28].

3.3. Biotoxicities of PDPQASs

As a typical cationic ammonium salt bacteriostatic agent, both the bacteriostatic effect and the biotoxicity should be evaluated. In this work, BC was chosen as a reference commercial cationic ammonium salt bacteriostatic agent, and the toxicity test results of BC and three kinds of

PDPQASs on silkworms, zebrafish and mice are shown in Table 2.

As shown in Table 2, the LC₅₀ values of PD, PM and PB for silkworms were greater than 2000 mg/L, indicating that the acute toxicity to silkworms was essentially nontoxic, while BC showed low toxicity to silkworms, which was consistent with the literature [29,30]. For zebrafish, although both PDPQASs and BC are labeled “moderate toxicity” (1–10 mg/L), the toxicity of PDPQASs is slightly lower than that of BC. PB showed a lower LC₅₀ for zebrafish, which might be due to the higher hydrophobicity, indicating that the toxicity would also be enhanced with the improvement of hydrophobicity of the side groups of PDPQASs [31,32]. This regularity between side group and toxicity could also be found in the toxicity to mice; the LD₅₀ of PD was greater than 5000 mg/kg, indicating that it was nontoxic to mice, and although PB had the lowest LD₅₀ of the three kinds of PDPQASs, LD₅₀ values of 2000 mg/kg or more indicate that they have low toxicity to mammals and are much safer than BC.

Based on the comprehensive evaluation of the antifungal activities and biotoxicities of the three kinds of PDPQASs, PB could be considered an ideal cationic ammonium salt bacteriostatic agent with higher anti-*Foc4* activities and lower biotoxicities and was chosen for further polymer-soil interaction studies.

3.4. Adsorption and leaching properties of PB

As a typical soil-borne pathogen, *Foc4* spores can survive in soil for several years, and anti-fungi agents should be applied in soil; thus, the interaction between polymeric cationic ammonium salts (here, PB was chosen for extensive study) and soil, including adsorption and leaching properties, should be evaluated. Although both PB and BC had good water solubility, the adsorption and leaching properties of PB were much different from those of BC, as shown in Fig. 3-(A). The saturated absorption (C_s) of PB was much higher than that of BC, while the time for equilibrium adsorption was also longer (approximately 16 h) than that of BC (approximately 9 h). Due to the broad-spectrum bacteriostatic effect, the drugs applied in soil hope to show good adsorption and should hardly be leached and lost from the soil, as shown in Fig. 3-(B). Compared with BC, the leaching rate of PB was much lower (the 350 mL leaching volume is equivalent to 70 mm rainfall in a day, that is, the level of a rainstorm), indicating that PB could easily absorb in soil and hardly be leached from soil [33].

3.5. Long-term anti-*Foc4* properties of PB in soil

Different loadings of PB with varied water/soil ratios were applied to the soil, where the initial concentration of *Foc4* spores in the soil was set as 2.25×10^5 conidia/(g dry soil). At this concentration, banana seedlings were susceptible to banana *Fusarium* wilt. By checking whether

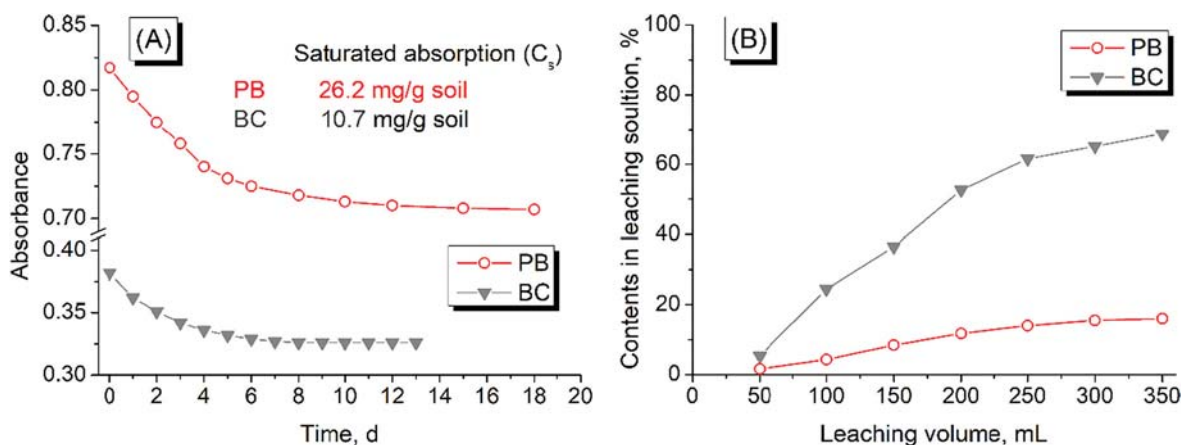


Fig. 3. Absorbance (A) and leaching (B) properties of PB and BC in soil.

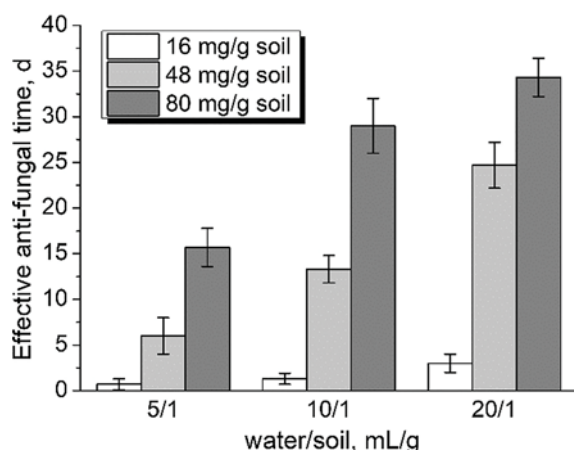


Fig. 4. Influence of PB loadings and the water/soil ratio on the long-term anti-Foc4 time of PB in soil.

there were live Foc4 conidia in the soil, the effective anti-Foc4 time in the soil could be determined. Fig. 4 shows that at a PB loading of 16 mg/(g dry soil) (roughly equivalent to $10 \times IC_{50}$), the effective anti-Foc4 time was very short under different water/soil ratios, which was mainly due to the PB loading of 16 mg/(g soil) being much lower than the saturated absorption (C_s) of PB in the soil (26.2 mg/g soil, as shown in Fig. 3-(A)). Thus, most of the PB was adsorbed on the surface of the soil particles, and PB chains were free in water, resulting in a poor anti-fungal effect. When the PB loadings were larger than C_s , with the increase in PB loading and water/soil ratio, more PB chains could be free in the soil/water mixture and result in better long-term anti-Foc4 properties. When the PB loading reached 80 mg/(g dry soil) (roughly equivalent to $50 \times IC_{50}$) under a water/soil ratio of 20/1, the effective anti-Foc4 time could be longer than one month, making PB a potential long-term anti-Foc4 agent.

4. Conclusions

In this work, three kinds of poly(N,N-diene propyl quaternary ammonium salts) with different side groups, namely, PM, PD and PB, were synthesized, and then the anti-Foc4 activities and biotoxicities were evaluated. PB showed higher anti-Foc4 activities and lower biotoxicities than small molecular quaternary ammonium salts, such as BC. Benefitting from the stronger polymer-soil interaction, PB could more easily absorb in soil and hardly be leached from soil, which helped PB remain in soil more stably and effectively inhibited Foc4 conidia. The more than one-month antifungal persistence time showed that PB had potential application prospects in the prevention of Foc4.

Author contribution statement

Yaling LIN: Conceptualization, writing- reviewing and editing, supervision; Chang ZHANG: Data collecting and writing; Meng HOU: Data collecting and writing; Rui LI: Data collecting and writing; Anqiang ZHANG: Conceptualization, writing- reviewing and editing, supervision.

Declaration of Competing Interest

The authors declare that they have no known competing financial interests or personal relationships that could have appeared to influence the work reported in this paper.

Acknowledgments

This work was supported by the National Natural Science Foundation of China under grant 31772202; the Scientific and Technological

Planning Project of Guangzhou City under grants 201803020015.

Appendix A. Supplementary data

Supplementary data to this article can be found online at <https://doi.org/10.1016/j.reactfunctpolym.2022.105174>.

References

- [1] K. Pegg, L. Coates, W. O'Neill, D. Turner, The epidemiology of Fusarium wilt of banana, *Front. Plant Sci.* 10 (2019) 1395.
- [2] R. Ploetz, Fusarium wilt of banana, *Phytopathology* 105 (2015) 1512–1521.
- [3] L. Zhang, T. Yuan, Y. Wang, D. Zhang, T. Bai, S. Xu, Y. Wang, W. Tang, S. Zheng, Identification and evaluation of resistance to *Fusarium oxysporum* f. sp. *cubense* tropical race 4 in *Musa acuminata* Pahang, *Euphytica* 214 (2018) 106.
- [4] M. Dita, M. Barquero, D. Heck, E.S. Mizubuti, C.P. Staver, Fusarium wilt of banana: current knowledge on epidemiology and research needs toward sustainable disease management, *Front. Plant Sci.* 9 (2018) 1468.
- [5] R. Ploetz, S. Freeman, J. Konkol, A. Al-Abed, Z. Naser, K. Shalan, R. Barakat, Y. Israeli, Tropical race 4 of Panama disease in the Middle East, *Phytoparasitica* 43 (2015) 283–293.
- [6] B. Wang, J. Yuan, J. Zhang, Z. Shen, M. Zhang, R. Li, Y. Ruan, Q. Shen, Effect of novel bioorganic fertilizer produced by *Bacillus amyloliquefaciens* W19 on antagonism of *Fusarium* wilt of banana, *Biol. Fertil. Soils* 49 (2013) 435.
- [7] Y. Chang, W. Zhong, J. Liang, A. Zhang, Y. Lin, Polydimethylsiloxane-polymethacrylate block copolymers containing quaternary ammonium salts against *Fusarium oxysporum* f. sp. *cubense* race 4 in soil: antifungal activities and pot experiments, *React. Funct. Polym.* 160 (2021) 104848.
- [8] Y. Jiao, L. Niu, S. Ma, J. Li, R. Fanklin, J. Chen, Quaternary ammonium-based biomedical materials: state-of-the-art, toxicological aspects and antimicrobial resistance, *Prog. Polym. Sci.* 71 (2017) 53–90.
- [9] Y. Xue, H. Xiao, Y. Zhang, Antimicrobial polymeric materials with quaternary ammonium and phosphonium salts, *Int. J. Mol. Sci.* 16 (2015) 3626–3655.
- [10] L. Liu, Y. Huang, S. Riduan, S. Gao, Y. Yang, W. Fan, Y. Zhan, Main-chain imidazolium oligomer material as a selective biomimetic antimicrobial agent, *Biomaterials* 33 (2012) 8625–8631.
- [11] I. Cakmak, Z. Ulukanli, M. Tuzcu, S. Karabuga, K. Genctav, Synthesis and characterization of novel antimicrobial cationic polyelectrolytes, *Eur. Polym. J.* 40 (2004) 2373–2379.
- [12] Y. Zhang, J. Jiang, Y. Chen, Synthesis and antimicrobial activity of polymeric guanidine and biguanidine salts, *Polymer* 40 (1999) 6189–6198.
- [13] M. Ahmed, T. Annamalai, X. Li, A. Seddek, P. Teng, Y. Tse-Dinh, J. Moon, Synthesis of antimicrobial poly(guanylurea)s, *Bioconjug. Chem.* 29 (2018) 1006–1009.
- [14] J. Olsson, T. Pham, P. Jannasch, Poly(N,N-diallylazacycloalkane)s for anion-exchange membranes functionalized with n-spirocyclic quaternary ammonium cations, *Macromolecules* 50 (2017) 2784–2793.
- [15] Y. Zhu, C. Xu, N. Zhang, X. Ding, B. Yu, F. Xu, Polycationic synergistic antibacterial agents with multiple functional components for efficient anti-infective therapy, *Adv. Funct. Mater.* 28 (2018) 1706709.
- [16] Y. Oda, S. Kanaoka, T. Sato, S. Aoshima, K. Kuroda, Block versus random amphiphilic copolymers as antibacterial agents, *Biomacromolecules* 12 (2011) 3581–3591.
- [17] A. Zhang, Q. Liu, Y. Lei, S. Hong, Y. Lin, Synthesis and antimicrobial activities of acrylamide polymers containing quaternary ammonium salts on bacteria and phytopathogenic fungi, *React. Funct. Polym.* 88 (2015) 39–46.
- [18] W. Jaeger, J. Bohrisch, A. Laschewsky, Synthetic polymers with quaternary nitrogen atoms-synthesis and structure of the most used type of cationic polyelectrolytes, *Prog. Polym. Sci.* 35 (2010) 511–577.
- [19] Y. Yang, J. Enbert, Synthesis and catalytic properties of hydrophobically modified poly(alkylmethyl diallyl ammoniumbromides), *J. Organomet. Chem.* 56 (1990) 4300–4304.
- [20] C. Wandrey, J. Hernandez-Barajas, D. Hunkeler, Diallyldimethylammonium chloride and its polymers, in: I. Capek, J. Hernández-Barajas, D. Hunkeler, J. L. Reddinger, J.R. Reynolds, C. Wandrey (Eds.), *Radical Polymerisation Polyelectrolytes. Advances in Polymer Science* 145, Springer, Berlin, Heidelberg, 1999, pp. 123–182, https://doi.org/10.1007/3-540-70733-6_3.
- [21] R. Losada, C. Wandrey, Copolymerization of a cationic double-charged monomer and electrochemical properties of the copolymers, *Macromolecules* 42 (2009) 3285–3293.
- [22] Y. Yang, B.F.N. Jan, Engberts. Synthesis and catalytic properties of hydrophobically modified poly(alkylmethylallylammonium bromides), *J. Organomet. Chem.* 56 (1991) 4300–4304.
- [23] G. Wang, B.F.N. Jan, Engberts. Synthesis and catalytic properties of hydrophobically modified poly(alkylmethyl-diallylammonium chlorides), *Eur. Polym. J.* 31 (1995) 409–417.
- [24] R. Meldrum, A. Daly, L. Tran-Nguyen, E. Aitken, The effect of surface sterilants on spore germination of *Fusarium oxysporum* f. sp. *cubense* tropical race 4, *Crop Prot.* 54 (2013) 194–198.
- [25] B. Nela, C. Steinberg, N. Labuschagne, A. Viljoena, Evaluation of fungicides and sterilants for potential application in the management of Fusarium wilt of banana, *Crop Prot.* 26 (2007) 697–705.
- [26] Z. Huang, R. Liuyang, C. Dong, Y. Lei, A. Zhang, Y. Lin, Polymeric quaternary ammonium salt activity against *Fusarium oxysporum* f. sp. *cubense* race 4: synthesis,

- structure-activity relationship and mode of action, *React. Funct. Polym.* 114 (2017) 13–22.
- [27] B. Mowery, S. Lee, D. Kissounko, R. Epand, R. Epand, B. Weisblum, S. Stahl, S. Gellman, Mimicry of antimicrobial host-defense peptides by random copolymers, *J. Am. Chem. Soc.* 129 (2007) 5474–5476.
- [28] D. Sha, J. Xu, X. Yang, Y. Xue, X. Liu, C. Li, M. Wei, Z. Liang, K. Shi, B. Wang, Y. Tang, X. Ji, Synthesis and antibacterial activities of quaternary ammonium salts with different alkyl chain lengths grafted on polyvinyl alcohol-formaldehyde sponges, *React. Funct. Polym.* 158 (2021) 104797.
- [29] Punyavathi Sudhakumari, C. Das, M. Bhat, H. Manjunatha, evaluation of the medically important compounds TASKI protasan and combatan for its efficacy using *Bombyx mori* as a model system, *J. Pharm. Res.* 7 (2013) 184–188.
- [30] Y. Lin, W. Zhong, C. Dong, C. Zhang, X. Feng, A. Zhang, Synthesis and antifungal activities of amphiphilic PDMS-*b*-QPDMAEMA copolymers on *Rhizoctonia solani*, *ACS Appl. Bio Mater.* 1 (2018) 2062–2072.
- [31] A. Engler, J. Tan, Z. Ong, D. Coady, V. Ng, Y. Yang, J. Hedrick, Antimicrobial polycarbonates: investigating the impact of balancing charge and hydrophobicity using a same-centered polymer approach, *Biomacromolecules* 14 (2013) 4331–4339.
- [32] M. Ganewatta, C. Tang, Controlling macromolecular structures towards effective antimicrobial polymers, *Polymer* 63 (2015) A1–A29.
- [33] Y. Wang, H. Gao, Z. Xie, L. Zhang, X. Ma, Effects of different agronomic practices on the selective soil properties and nitrogen leaching of black soil in Northeast China, *Sci Rep-UK.* 10 (2020) 14939.

Molecularly Imprinted Photonic Crystals Based on Fusaric Acid for the Detection of Banana Fusarium Wilt

Yaling Lin,* Xixiang Feng, Wei Zhang, Rui Li, and Anqiang Zhang*

Cite This: *ACS Appl. Polym. Mater.* 2021, 3, 5818–5825

Read Online

ACCESS |



Metrics & More



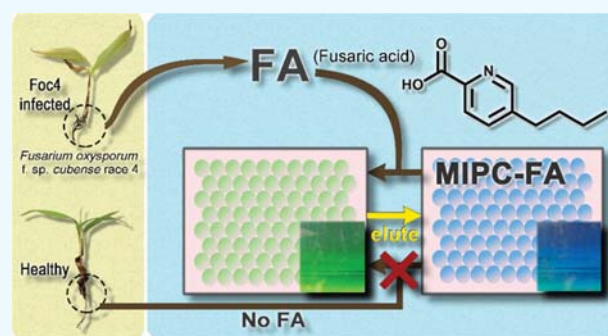
Article Recommendations



Supporting Information

ABSTRACT: Banana Fusarium wilt is a soil-borne disease caused by *Fusarium oxysporum* f. sp. *cubense* (Foc) in which *F. oxysporum* f. sp. *cubense* race 4 (Foc4) could infect all kinds of banana and has caused great damage to the banana planting industry. The most important means to prevent and control banana Fusarium wilt in agricultural production is to control the spread and invasion of pathogens. Among them, the detection and determination of banana Fusarium wilt in the field is essential and thus is the basis of protection. Since fusaric acid (FA) is one of the specific products present during the metabolic processing of Fusarium wilt pathogens, by combining FA with molecularly imprinted photonic crystal (MIPC) technologies, a series of MIPCs based on monodispersed silica, FA, and cross-linked polymers, i.e., MIPC-FA, which could be recycled, were designed and prepared. It was found that the responses of MIPC-FA were affected by the cross-linking degree of the polymer matrix and the pH values. The results showed that MIPC-FA could effectively detect FA in a solution of FA in a minute scale, Foc4-containing medium, and banana plants infected by Foc4, and the response was related to the FA concentration, which makes it an effective and fast method to detect and determine banana Fusarium wilt caused by Foc4 in the field.

KEYWORDS: molecularly imprinted photonic crystal, banana Fusarium wilt, fusaric acid, Foc4, field testing



1. INTRODUCTION

Banana Fusarium wilt is a typical vascular wilt disease caused by a special species of a complex of *Fusarium oxysporum* f. sp. *cubense* (Foc).¹ According to banana planting technology and the perennial and single-variety cultivation characteristics of banana plantations, it is obvious that the management of banana wilt is not simple.² At present, there are no effective fungicides or other eradication methods that can eradicate *F. oxysporum* f. sp. *cubense* race 4 (Foc4), and the affected plants lead to a rapid decline in the output of an entire banana plantation.

Banana wilt is considered to be a “polycyclic” plant disease,³ which means that the invasion of a small amount of pathogens may cause large-scale losses. Proactive prevention, containment of the disease, and isolation of infected plants appear to be extremely important. Therefore, the fast detection of infected plants is particularly important.

The detection of banana Fusarium wilt traditionally relies on the identification of disease symptoms. The main feature is that the leaves are yellow and the banana pseudostems become reddish brown.⁴ However, due to the long incubation period of the pathogen, by the time symptoms are found in the banana host, the pathogen has already begun to spread.⁵ The routine diagnosis of Foc requires long-term culture, microscopy and

pathogenicity tests, and distinguishing Foc from other *Fusarium* species based on its morphological characteristics, which requires testing personnel to have an excellent *Fusarium* species research background. This method cannot distinguish between pathogenic and nonpathogenic strains.⁶ The pathogenicity test can distinguish whether it is pathogenic but this test is extremely time-consuming, and different environments may bring different results.

DNA-based diagnosis can effectively improve the speed and accuracy of testing. Polymerase chain reaction (PCR) using specific primers is a relatively common method of identification, but it requires cultivation and can only provide qualitative results.⁷ Quantitative PCR was developed to solve the shortcomings of conventional PCR and is often applied to the quantification of pathogen DNA in environmental samples.⁸ Lin and co-workers⁹ developed the SCAR primer set FocSc-1/FocSc-2, and primers for real-time PCR

Received: August 16, 2021

Accepted: October 5, 2021

Published: October 15, 2021



amplification can be applied to the quantitative detection of Foc4. The Food and Agriculture Organization (FAO) uses a PCR technique that uses specific primers to detect FocTR4-F/FocTR4-R.¹⁰ This specific method is only for FocTR4 (VCG-01213), which causes great damage to Cavendish bananas. This detection method can detect infected plants and soil- and water-containing pathogens.

In the process of Foc invading banana plants, the pathogen produces a series of phytotoxins to invade the host. Among them, fusaric acid (FA) is a phytotoxin produced by several species of *Fusarium*.¹¹ In banana *Fusarium* wilt, FA is closely related to the symptoms of banana *Fusarium* wilt. FA may destroy the cell membrane of the host cell at the stage when the bacteria causing banana *Fusarium* wilt invades the plant and causes an imbalance in the water level in the leaves.¹² Some studies also suggest that FA is related to the destruction of chloroplasts, and the reduction of photosynthesis and the presence of FA can be detected in leaves showing yellowing.¹³ It is believed that FA plays a very important role in the infection cycle of banana *Fusarium* wilt, which means that FA can be used as a target substance to detect banana *Fusarium* wilt caused by Foc.

Molecularly imprinted polymers (MIPs) are considered to be the closest synthetic analogues of the antibody–antigen system in biological systems. A molecularly imprinted polymer identifies the selective binding of the template molecule in the synthesis process through the “lock–key” structure.^{14,15} MIP provides the specificity of natural biological receptors and is inexpensive.

Currently, to solve the signal problem after molecular imprinting recognition, an increasing number of reports use electrochemical¹⁶ and optical technologies¹⁶ to transform molecular imprinted materials into “sensors”. Molecularly imprinted photonic crystals (MIPCs) prepared by combining molecular imprinting technology and photonic crystals are an ideal sensing material with high selectivity and fast response, and the most significant advantage of MIPCs is that their response signal can be directly observed by the naked eye. MIPCs based on many recognition molecules have been synthesized for the recognition of specific compounds, such as nitrobenzene,¹⁷ ethanol,¹⁸ formaldehyde,¹⁹ cocaine,²⁰ deltamethrin,²¹ etc. MIPC sensors enable low-cost, small, and rugged identification systems and could be suitable for portable systems for drug detection and environmental monitoring.

This work was designed to synthesize molecularly imprinted photonic crystals (MIPCs) using fusaric acid (FA) as a template molecule and to detect fusaric acid in a standard solution, Foc4 culture medium, and Foc4-infected seedlings.

2. MATERIALS AND METHODS

2.1. Chemicals and Materials. Tetraethyl orthosilicate (TEOS), methacrylic acid (MAA), ethylene glycol dimethacrylate (EGDMA), 2,2'-azobis(2-methylpropionitrile) (AIBN), and hydrofluoric acid (HF, 40%) were purchased from Macklin (Shanghai, China) and used directly. 5-Butylpicolinic acid (fusaric acid, FA) was purchased from Biosynth Carbosynth (Suzhou, China). Phosphate buffer solution (PBS, 0.01 M, pH 7.6) was prepared by dissolving Na₂HPO₄ and KH₂PO₄ in Milli-Q water. Glass slides (25 × 70 × 2 mm³) were immersed in a 98% H₂SO₄/30% H₂O₂ (70/30, v/v) mixture for 12 h, rinsed three times with deionized water in an ultrasonic bath, and then dried before use. Poly(methyl methacrylate) (PMMA) slides (50 × 25 × 2 mm³) were cleaned with anhydrous ethanol. All of the solvents and chemicals used were of reagent quality and used without further purification unless indicated.

2.2. Preparation of Monodispersed Silica. The multistep preparation method of monodispersed silica preceded based on the Stober method.^{22–24} In brief, 27.5 mL of anhydrous ethanol, 3.5 mL of ammonia, and 16 mL of deionized water were mixed in a 250 mL flask, stirred intensively with a magnetic stirrer, and then 50 mL of anhydrous ethanol and 3 mL of TEOS were added and the mixture was made to react for 4 h. After that, 2 mL of TEOS and 0.32 mL of deionized water were added every 4 h to the reaction. After repeating feeding eight times, monodispersed silica particles were obtained by centrifugation and resuspended in anhydrous ethanol five times. Afterward, the obtained monodispersed particles were fully dispersed in anhydrous ethanol with concentrations by weight of approximately 10–30%.

2.3. Preparation of the SiO₂ Photonic Crystal. The above-synthesized monodispersed SiO₂ ethanol concentrated emulsion was diluted to a 0.5–2% SiO₂ ethanol emulsion with anhydrous ethanol in a 25 mL beaker. A glass slide treated with piranha solution was inserted vertically into the beaker with the SiO₂ emulsion. After ethanol completely evaporated naturally, SiO₂ photonic crystals were prepared on both sides of the glass slide.

2.4. Fabrication of Molecularly Imprinted Photonic Crystal Films. In this work, we fabricated four kinds of MIPC-FA films and one nonmolecularly imprinted photonic crystal (N-MIPCs) film. The MIPC-FA films were imprinted with fusaric acid under different polymer compositions (including MAA, EGDMA, methanol, and water), while for the N-MIPC film, FA was not added during the preparation of polymers, as shown in Table 1. The scheme of the

Table 1. Formula for the Preparation of MIPC-FA Using a 250 nm SiO₂ Photonic Crystal as the Matrix

sample	FA (mmol)	MAA (mmol)	EGDMA (mmol)	methanol (μL)	water (μL)
MIPC-FA-1	1	4	1	400	100
MIPC-FA-2	1	6	1	400	100
MIPC-FA-3	1	6	1	500	0
MIPC-FA-4	1	8	1	400	100
N-MIPC	0	6	1	400	100

synthesis process of MIPCs is shown in Figure 1. For the fabrication of MIPC-FA, fusaric acid, MAA, and EGDMA were mixed with methanol and deionized water and stored at 6 °C overnight. Then, 0.01 g of AIBN was added to the stored homogeneous monomer mixtures and degassed with nitrogen for 10 min. The prepared glass slide with SiO₂ photonic crystals was closely attached to a PMMA

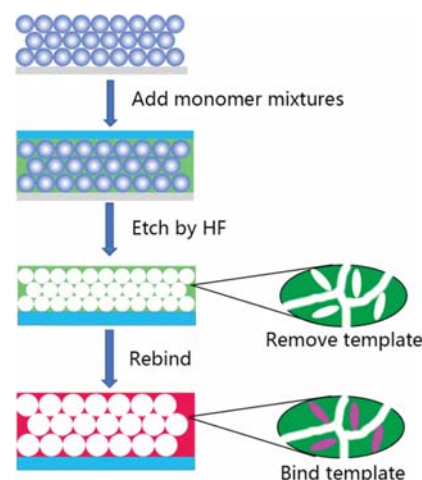


Figure 1. Schematic diagram of the preparation process of the MIPC-FA polymer film.²⁷

slide to form a sandwich structure, and the edge of the sandwich was immersed into the prepared mixture until the sandwich structure became transparent. The homogeneous monomer mixtures entered the gap of the photonic crystal due to capillary action. Then, the “sandwich” structure was fixed with clamps, and the remaining mixture was photopolymerized at 2 °C under UV light at 365 nm for 2 h.

After photopolymerization, the sandwiches were immersed in 1% hydrofluoric acid for 2 h until the two slides separated and the silica particles were etched fully. After rinsing the PMMA slide with deionized water for 3 min, the PMMA slide was immersed in an acetic acid/methanol (1/9, v/v) mixture for 2 h to remove the template molecules on the imprinted polymer. After removing the template, the PMMA slides were immersed in PBS to reach an equilibrium state for storage.

The fabrication of N-MIPCs is the same as that for the others except that no fusaric acid is added.

2.5. Determination of MIPC-FA Films toward Recognition.

All of the concentrations of the analytes were prepared with the same PBS (0.01 M, pH 7.6). For determination in a competitive environment, the analytes were changed to a mixture of PB buffer and extracted with the original concentration. For each analyte, testing began from the blank state of MIPC-FA films and followed a sequence from low to high concentrations to eliminate interference. After testing the highest concentration, the MIPC-FA films were soaked in an acetic acid/methanol mixture for recovery.

2.6. Extraction of Crude Toxin from Foc4. To extract the crude toxin of Foc4, Foc4 was inoculated in 200 mL of Czapek-Dox Medium (10^6 CFU/mL) for 7 days at 28 °C on a shaker at 180 rpm. The resulting medium was filtered through four layers of gauze, and the filtered liquor was collected and centrifuged at 8000g for 20 min. The supernatant was collected. The centrifugations were passed through a 0.45 μ m filter membrane, and the filtrate was collected. The filtrate was adjusted to pH 2.0 with 2 M HCl and then extracted five times with ethyl acetate to obtain the metabolite extract. Then, the solvent was removed by rotary evaporation at 40 °C under vacuum. The dried residue was dissolved in 5 mL of methanol and then filtered through a 0.45 μ m filter to obtain a methanol solution of the crude toxin.

2.7. Plant Cultivation. Banana seedlings (*Musa AAA Cavendish* cv. *Brazil*) were obtained from the South China Botanical Garden in Guangdong Province, China. Potted soil was provided by the Crop Nutrition and Fertilization Laboratory of South China Agricultural University.

The soil samples were sieved over a 5 mm mesh and then divided into two groups: an infected group and a blank group (each group contained 20 replications). The total amount of soil in the pot for each replication was 300 g in which Foc4 conidial suspension in the infected group and deionized water in the blank group were mixed with soil before being added to the pots (upper diameter of 7 cm, lower diameter of 5 cm, and height of 10 cm). Banana seedlings with a height of ~10 cm (2–3 leaves) were transplanted to the pots. Then, 200 mL of tap water was added, and 75 mL of tap water was added every afternoon to each pot. All potted plants were cultured in a greenhouse at a typical temperature of 28 °C and humidity of 60–80% under natural sunshine for ~12 h. After 15 days of banana seedling growth, various parts of the banana were prepared for observation and extraction.

2.8. Extraction of Fusaric Acid from Banana Seedlings. The cultivated banana plants were removed from the soil, and then banana seedlings were washed to remove the soil. Then, the roots, pseudostems, and leaves of the banana seedlings were separated. After pretreatment, the obtained roots, pseudostems and leaves were washed, dried, and weighed, and the weight was recorded; then, the extract was prepared in methanol/1% K_2HPO_4 with a volume ratio of 1:1 (pH = 2.5). Then, 3 mL of the extract was added to the weighed roots, pseudostems, and leaves, and they were ground until there were no obvious lumps. After grinding, the slurry was centrifuged at 8000g for 30 min, and the supernatant was collected and acidified with 2 M HCl to pH = 2.5. After acidification, excess ethyl acetate was added in

three extractions, the organic phases were finally combined, and ethyl acetate was removed by rotary evaporation under reduced pressure. The dried residue was dissolved in 3 mL of methanol to obtain a methanol extract of the banana roots, pseudostems, and leaves.

2.9. Crude Extraction Analysis by High-Performance Liquid Chromatography (HPLC). To identify the presence of FA in crude toxin extracted from the pathogen culture and seedlings, we employed an HPLC system (Waters 600s-2998, Waters Corporation) with a Hypersil ODS-2 column (4.6×250 mm², Thermo Fisher Scientific). Aliquots of 10 μ L of the extracts were injected and eluted with MeOH/0.43% H_3PO_4 (68/32, v/v) for 10 min with a UV detector at 280 nm. The flow rate was 1 mL/min. Before injection, the samples were filtered through 0.45 μ m filters.

2.10. Testing Procedure for the MIPC-FA Slide. Before testing, the extract of crude toxin from Foc4, the extract of fusaric acid from banana seedlings, or the FA standard solution should be diluted using phosphate buffer solution to the set concentration. After immersing the MIPC-FA slide into the above solution for about 1 min until the color of MIPC-FA no longer changes, the slide was taken out to observe with naked eyes or test using a UV–vis spectrometer. After testing, the MIPC-FA slide was soaked in acetic acid/methanol (1/9, v/v) solution for 20 min until the color of MIPC-FA no longer changes, and then the MIPC-FA slide was soaked in phosphate buffer solution for storage and reuse.

2.11. Instrumentation. The morphologies of SiO_2 templates and the obtained MIPC films were viewed by a scanning electron microscope (ZEISS EVO18, Germany) operating at 10 kV. UV–vis spectra were recorded using a PerkinElmer Lambda 950 spectrometer. A common digital camera was used to obtain the color image of MIPCs. The particle size of SiO_2 was measured by a nanoparticle size analyzer (HORIBA SZ-100Z, Japan).

3. RESULTS AND DISCUSSION

3.1. Characterization of Silica Photonic Crystals and MIPCs. The preparation of monodispersed silica photonic crystals and the influence of silica particle sizes on the reflectance spectra of silica photonic crystals are discussed in the Supporting Information (Parts S1 and S2).

Molecularly imprinted photonic crystals (MIPCs) can be prepared using SiO_2 photonic crystals as a template, filling the prepolymer, and etching and removing the SiO_2 microspheres after polymerization. As shown in Figure S3B, the molecularly imprinted polymer occupied the gaps in the original SiO_2 arrangement and became rigid using EGDMA as a cross-linking agent after silica was etched. In the end, a molecularly imprinted polymer with a certain rigidity and maintaining a highly ordered and periodic structure is obtained, and this photonic crystal structure is called an inverse opal.²⁵

Finally, considering the visible light wavelength range of the human eye and human sensitivity to different colors of light,²⁶ we chose the 250 nm SiO_2 microspheres as a template to prepare MIPCs and for further testing.

3.2. Recognition of MIPCs in Relation to pH. As mentioned before, MIPC-FA was prepared based on methacrylic acid (MAA) as a functional monomer. The typical pH response performance of MIPC-FA based on SiO_2 photonic crystals was tested and is shown in Figure S4. As shown in Figure S4A, the Bragg diffraction peak of MIPCs gradually shifts to red with increasing pH, and the intensity of the diffraction peaks reaches a maximum when pH = 5. This phenomenon may be caused by the irregular volume change of MIPCs. When pH = 3–11, the position of the diffraction peak changes in a roughly linear pattern with the pH value, and when pH is higher than 11 or lower than 3, the position of the diffraction peak appears more shifted, as shown in Figure S4B. This result indicated that the carboxyl group of the functional

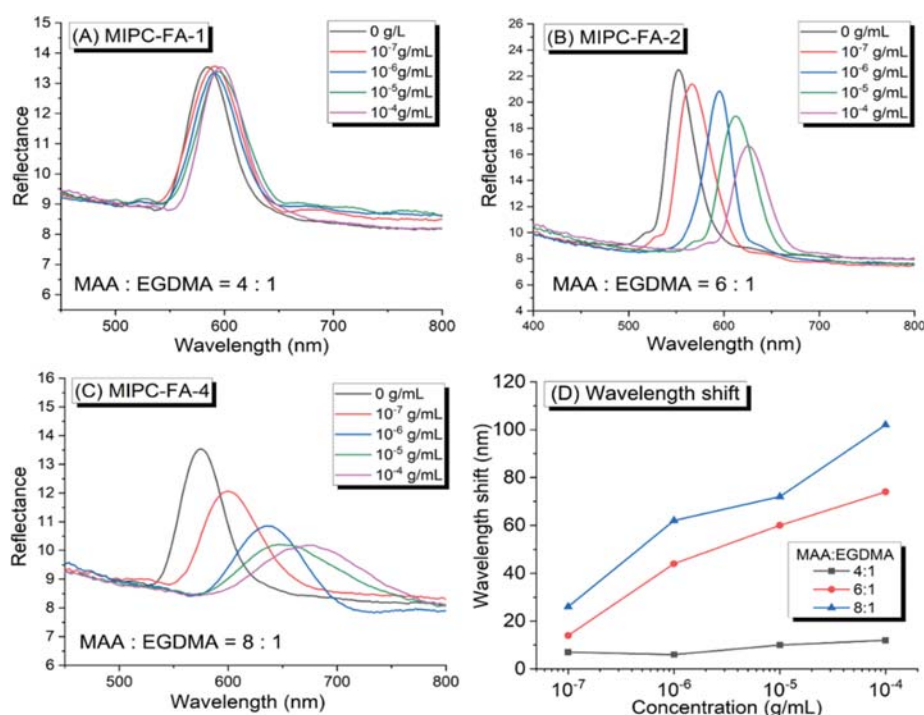


Figure 2. Reflectance spectra of MAA/EGDMA = 4:1 (A), 6:1 (B), and 8:1 (C) MIPC-FA to fusaric acid and chart of the diffraction peak shift (D).

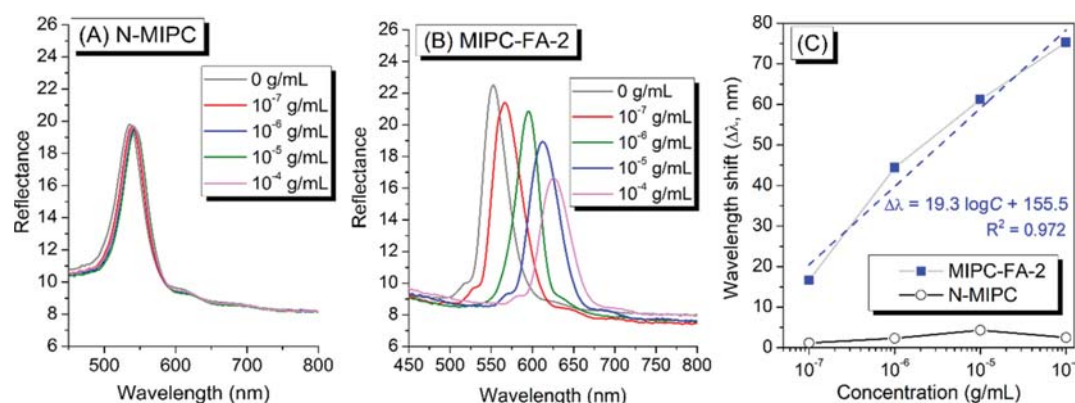


Figure 3. Responses of N-MIPC (A) and MIPC-FA-2 (B) and wavelength changes between N-MIPC and MIPC-FA-2 (C).

monomer (MAA) might be neutralized in an acid–base environment, which caused the swelling or shrinkage of MIPC-FA.

Based on this result, a phosphate buffer solution (PBS, pH = 7.6) is used as the test solvent in subsequent responsive experiments of MIPC to avoid the influence of the changes in diffraction peaks caused by pH changes.

3.3. Influence of Polymer Precursors on Response.

Figure 2 presents the response of MIPCs to fusaric acid under different cross-linking degrees. Different degrees of cross-linking were achieved at different ratios of MMA and EGDMA. As shown in Figure 2A, MIPC-FA-1 with MAA/EGDMA = 4:1 still has no obvious response under 10^{-4} g/mL fusaric acid (diffraction peak shift is only 8 nm under 10^{-4} g/mL). MIPC-FA-4 with MAA/EGDMA = 8:1 is obviously more responsive to fusaric acid, as illustrated in Figure 2C (diffraction peak shifts above 100 nm at 10^{-4} g/mL), but it can also be observed

that the diffraction peak intensity decreases and the peak width gradually widens with increasing FA concentration. Figure 2D indicates that the degrees of cross-linking of the imprinted polymer has a strong effect on the response. High degrees of cross-linking will cause little deformation of the polymer but a high degree of mechanical stability and low degrees of cross-linking will have the opposite effect. Therefore, a moderate cross-linking degree of the polymer (Figure 2B) can be used to obtain MIPCs that can cause deformation without significantly changing the ordered structure. Therefore, MIPC-FA-2, which has the best performance and with moderate cross-linking, is used for the following preparations.

According to the mechanism of molecularly imprinted photonic crystals, the response of MIPCs is based on hydrogen bonding between functional and template molecules. Water, as a highly polar substance, will affect the adsorption function of the molecularly imprinted polymer. The responses of the

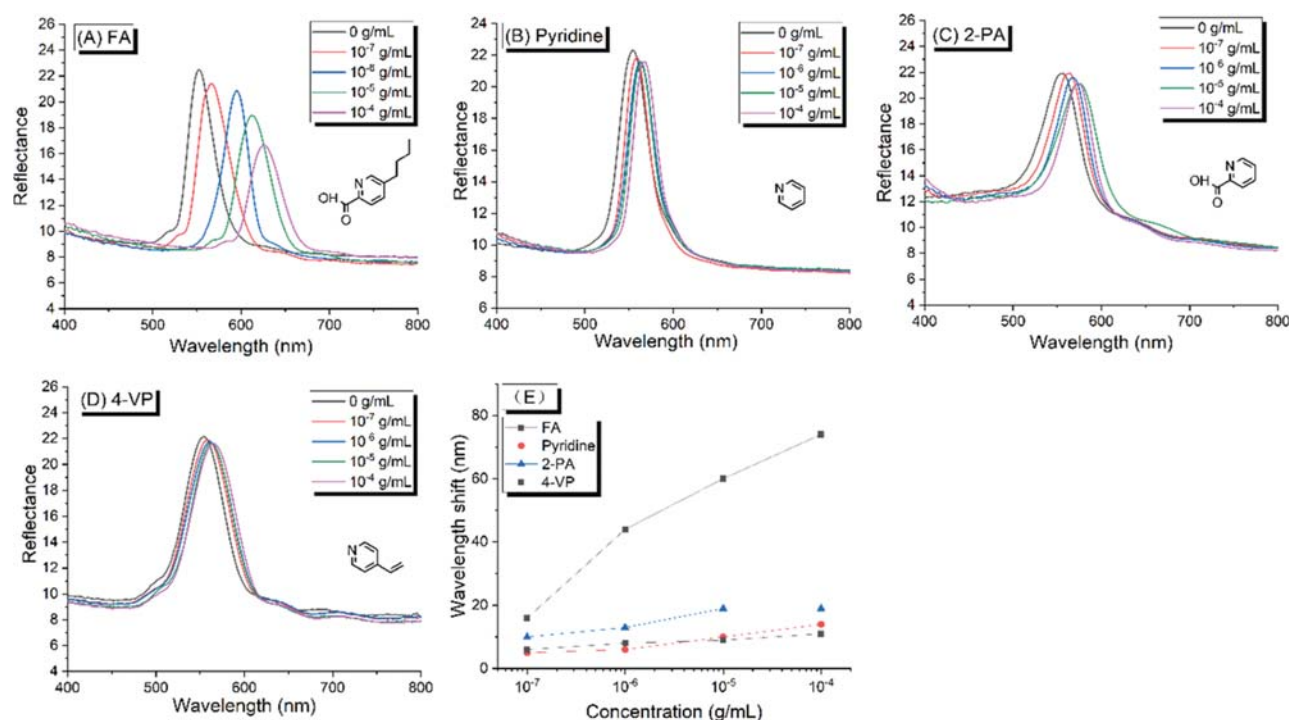


Figure 4. Response spectra of MIPC-FA caused by fusaric acid (A), pyridine (B), 2-picolinic acid (C), and 4-vinylpyridine (D) and wavelength shift chart (E); the insert picture is the corresponding chemical structure of the target molecule.

MIPCs with and without water during the preparation technique are shown in Figure S5. The response performance of MIPCs actually decreases without water, and a sudden decrease in diffraction peak intensity and shift can be observed at high concentrations of FA (Figure S5A). This phenomenon may be caused by water affecting the bonding of MIPCs and fusaric acid as well as the permeability in the test environment. A small amount of water can improve the permeability of the entire MIPC system in water (Figure S5B), which may offset the adverse effects caused by water molecules.

Finally, the wavelength changes of nonmolecularly imprinted photonic crystals (N-MIPCs) and MIPC-FA-2 under the same ratio of mixture in addition to the template molecule (FA) under fusaric acid are shown in Figure 3. This result indicates that the wavelength change caused by the molecularly imprinted polymer is caused by the template molecule selected during its synthesis, and N-MIPCs do not have the ability to recognize or change the diffraction peak. And for MIPC-FA-2, the relationship between the wavelength shift ($\Delta\lambda$) with the logarithmic concentrations of FA solutions ($\log C$) was almost linear, as shown in Figure 3C.

Based on the above discussion, the optimal synthesis process of MIPC-FA is determined as follows: SiO_2 photonic crystals with a particle size of 250 nm are selected to prepare templates; thus, λ_{max} at different FA concentrations (0 – 10^{-4} g/mL) would be between 550 and 650 nm, and the polymerization ratio of MIPC-FA-2 is used to prepare molecularly imprinted photonic crystals to synthesize MIPC-FA.

3.4. Specificity of Molecularly Imprinted Photonic Crystals. The specificity of MIPC-FA depends on the recognition selectivity of the molecular imprinting technique and the changes in photonic crystal properties caused by recognition. To study the specificity of MIPCs based on fusaric

acid, MIPC-FA was used to respond to fusaric acid, pyridine, 2-picolinic acid, and 4-vinylpyridine, as shown in Figure 4A–D, respectively, which have pyridine ring but different side groups.

All of the substances used were prepared in the same concentration series. Compared with the result with fusaric acid (Figure 4A), a slight shift was observed when MIPC-FA was immersed in solutions of other substances. For example, the maximum red shift reached only 20 nm when the concentration of 2-picolinic acid was up to 10^{-4} g/mL, as shown in Figure 4B. The wavelength change caused by other substances hardly changes with the change in concentration. From the wavelength comparison in Figure 4E, it can be found that compared with the reaction to other substances, MIPC-FA shows obvious specificity to fusaric acid.

3.5. Recoverability of Molecularly Imprinted Photonic Crystals. It is known that the response of photonic crystals mainly depends on hydrogen bonding between the molecularly imprinted polymer and the template molecule, and this hydrogen bonding is reversible. Therefore, the recoverability of MIPC-FA was tested under a 1×10^{-4} g/mL fusaric acid combine-elute cycle. The spectrum of the repeated test and wavelength changes are shown in Figure S6. After five cycles of elute and response, MIPC-FA showed great reproducibility, and this reproducibility also showed that the structure of MIPC-FA is highly stable.

3.6. Analysis of Crude Toxin of the Foc4 Culture Medium. Former research results¹³ show that Foc4 produces a large number of metabolites during proliferation among which fusaric acid is typical. Following extraction of the crude toxin in the Foc4 culture medium, it was further tested by HPLC, as shown in Figure S7. Fusaric acid was found in the crude toxin after the extraction method, and then the standard curve was corrected according to the standard sample. The

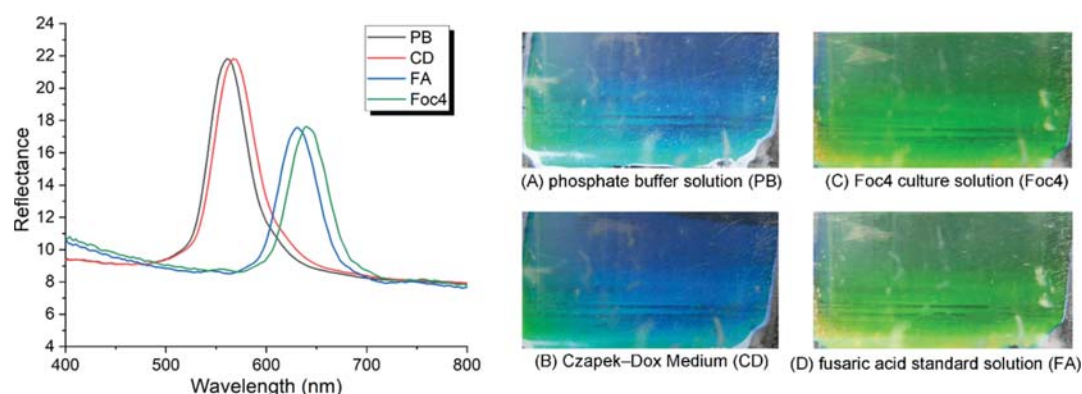


Figure 5. Comparison of the spectra of fusaric acid MIPC against phosphate buffer (PB) solution (A), Czapek-Dox (CD) Medium (B), Foc4 culture solution (C), and fusaric acid (FA) standard solution (D).

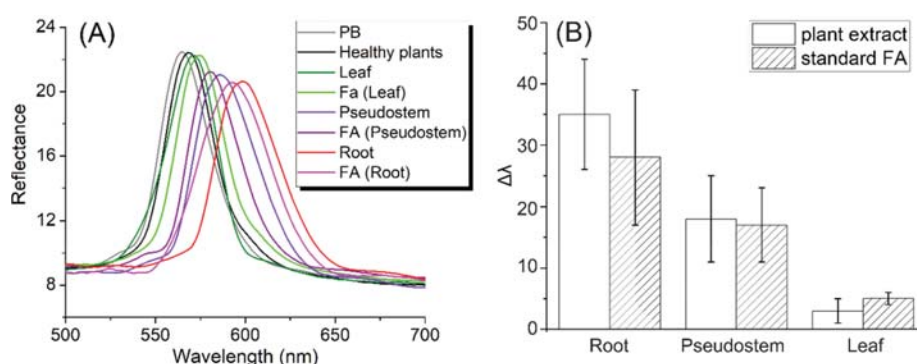


Figure 6. Reflectance spectrum (A) and Bragg diffraction peak shift (B) responses by plant extract and FA standard solution with the same concentration measured by HPLC.

concentration of fusaric acid in the Foc4 culture medium was $145.8 \pm 20.6 \mu\text{g/mL}$.

3.7. Response of MIPC-FA to Foc4 Culture Medium.

MIPC-FA was used to test the blank phosphate buffer solution and phosphate buffer solution of the blank Czapek-Dox medium, Foc4 culture medium, and FA standard solution with the same FA concentration (determined by the HPLC method) as the Foc4 culture medium. The results of the wavelength change and the corresponding MIPC-FA discoloration are shown in Figure 5.

Figure 5 shows that the Foc4 culture medium and FA standard solution with the same FA concentration ($145.8 \mu\text{g/mL}$, measured by HPLC) can cause obvious and similar wavelength shifts (69–75 nm) of MIPC-FA, while the Czapek-Dox medium causes almost no wavelength shifts. This result indicates that the FA in the Foc4 culture medium is the main reason for the wavelength shifts, which again verifies the specificity of MIPC-FA for fusaric acid.

In Figure 5A, about 15 nm shift can be observed between FA and Foc4, so we guess that it might be due to the complex components of the Foc4 culture medium, compared to the single component of the standard FA solution.

3.8. Distribution of Fusaric Acid in Banana Plants.

In Figure S8, it can be seen that the growth status of the banana seedlings inoculated with Foc4 was obviously worse: the roots of the plants inoculated with Foc4 were severely atrophied and almost brown, and there was no new root development; the pseudostems of the inoculated plant were relatively small, and there were spots similar to those seen in diseased plants; the

leaves of the inoculated plants obviously turned yellow from the top.

The inside of the banana was also observed by cutting the bulbs of different banana plants along the center part, as shown in Figure S8C,D. The bulbs of the inoculated plants were smaller than those of healthy bananas. After zooming in on the roots of the inoculated plants, it can be seen that the roots of the inoculated banana seedlings turned red, which may be due to xylem infection. In general, Foc4 banana seedlings were successfully infected based on multiple symptoms.

The phytotoxins in the banana plants from roots, pseudostems, and leaves were extracted separately, and the concentrations were analyzed by HPLC, as shown in Figure S9A. In contrast to the cultured Foc4 medium, there are more complex substances in plants. However, there was still a clear difference between the inoculated plant and the blank plant near 4.1 min. Comparing the peak time (4.1 min) of the fusaric acid standard under the same conditions, it was determined that the peak was the characteristic peak of fusaric acid. Finally, the concentration of fusaric acid was detected in three different positions from the roots, pseudostems, and leaves of the infected plants. As shown in Figure S9B, the distribution of fusaric acid was not uniform in banana plants, which may be related to the invasion stage of Foc4. The infection of Foc4 in plants started from the roots and gradually moved upward, which may cause uneven concentrations in banana seedlings.

3.9. Response of MIPC-FA to Extracts of Banana Plants. The extracts of plant roots, pseudostems, and leaves were selected for responsiveness experiments, and the same

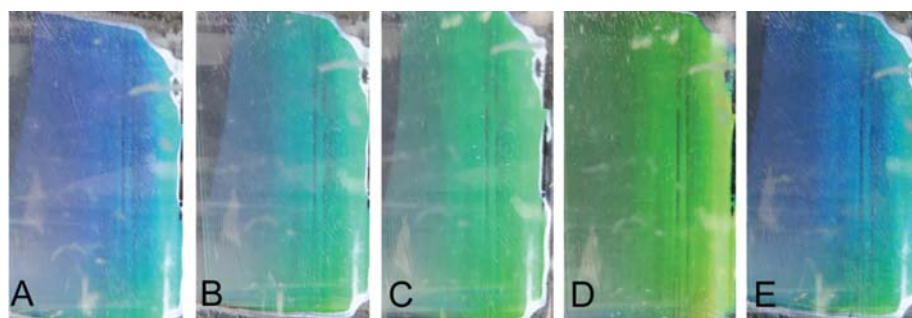


Figure 7. Color changes of MIPC-FA in blank PBS (A), leaves (B), pseudostems (C), and roots (D) of Foc4-infected and healthy banana seedlings (E).

concentration of fusaric acid obtained by HPLC was used for testing and comparison. The eluted MIPC-FA diffraction peak was used as the zero point to record the diffraction peak shift ($\Delta\lambda$) of different groups. The Bragg diffraction peak shift is shown in Figure 6, and the corresponding color changes of MIPC-FA are shown in Figure 7.

Comparing the HPLC data with the shift of the Bragg diffraction peak, it can be found that the difference between the peak shifts of the plant extracts is almost the same as the extraction concentration measured by HPLC. The diffraction peak shift caused by the root extract with FA concentration of about 150 ng/mL reached 35 nm, while the shift for pseudostem extract with FA concentration of about 50 ng/mL reached 28 nm. These degrees of diffraction peak shift can be observed with the naked eye, but the leaf extract with FA concentration of about 0.2×10^{-7} g/mL (as shown in Figure S9) only showed a 5 nm diffraction peak shift, which is difficult to identify by the naked eye, as shown in Figure 7B. Thus, the lower detection limit of MIPC-FA could be roughly inferred as about 50 ng/mL (0.5×10^{-7} g/mL).

Comparing the diffraction peak shifts of the fusaric acid standard and the extracted liquid at the same point, we found that the shift caused by root extraction was larger than that of the FA standard solution (5–15 nm), as shown in Figure 6A. The reason for this obvious gap might be that fusaric acid homologues or precursors are produced during toxin metabolism in Foc4 infection, and the presence of these similar substances may affect the detection. The gap between the peaks of other extracts and the corresponding standard solution was significantly smaller, which indicated that after Foc4 enters the vasculature, the Foc4 living environment has relatively less resistance, so the concentration of fusaric acid produced becomes low.

4. CONCLUSIONS

In conclusion, molecularly imprinted photonic crystals (MIPCs) of fusaric acid and their response to fusaric acid and to extracts of Foc4 culture medium and banana seedlings infected by Foc4 were studied. Monodispersed silica particles synthesized by a multistep method were used to fabricate silica photonic crystals by vertical deposition to provide templates for MIPCs. The degree of cross-linking of the polymer matrix and polymerization process parameters were adjusted to optimize the stability and response ability in fabricating the appropriate MIPC. The fabricated MIPCs show both a certain color change and spectroscopic differences under fusaric acid and have a specific response to FA. MIPC-FA can detect the concentrations of fusaric acid in the Foc4 culture medium and

Foc4-infected banana seedling extract, thus verifying that Foc4 produces fusaric acid in infected banana plants. Thus, we could afford a fast and effective field testing method, which could qualitatively or semiquantitatively determine whether a banana plant is infected by Foc4 or not and the approximate concentration of FA in the plant.

■ ASSOCIATED CONTENT

Supporting Information

The Supporting Information is available free of charge at <https://pubs.acs.org/doi/10.1021/acsapm.1c01032>.

Characterization of silica microspheres; SEM photographs of the photonic crystals; results for the influence of pH and water on the recognition of MIPCs; recoverability of MIPC-FA; determination of FA in the crude toxin of Foc4 culture medium; overall view of healthy and Foc4-infected banana seedlings (PDF)

■ AUTHOR INFORMATION

Corresponding Authors

Yaling Lin – College of Material and Energy, South China Agricultural University, Guangzhou 510642 Guangdong, China; orcid.org/0000-0002-5289-4304; Email: linyaling@scau.edu.cn

Anqiang Zhang – School of Materials Science and Engineering, South China University of Technology, Guangzhou 510641 Guangdong, China; orcid.org/0000-0001-7499-8406; Email: aqzhang@scut.edu.cn

Authors

Xixiang Feng – School of Materials Science and Engineering, South China University of Technology, Guangzhou 510641 Guangdong, China

Wei Zhang – College of Material and Energy, South China Agricultural University, Guangzhou 510642 Guangdong, China; orcid.org/0000-0003-1583-1555

Rui Li – School of Materials Science and Engineering, South China University of Technology, Guangzhou 510641 Guangdong, China; orcid.org/0000-0003-4866-5821

Complete contact information is available at: <https://pubs.acs.org/doi/10.1021/acsapm.1c01032>

Notes

The authors declare no competing financial interest.

ACKNOWLEDGMENTS

The authors acknowledge the financial support from the National Natural Science Foundation of China (Nos. 31772202 and 52073098) and the Scientific and Technological Planning Project of Guangzhou City (201803020015).

ABBREVIATIONS

Foc, *Fusarium oxysporum* f. sp. *cubense*; Foc4, *Fusarium oxysporum* f. sp. *cubense* race 4; TEOS, tetraethyl orthosilicate; MAA, methacrylic acid; EGDMA, ethylene glycol dimethacrylate; PMMA, poly(methyl methacrylate); FA, fusaric acid (5-butylpicolinic acid); MIPs, molecularly imprinted polymers; MIPCs, molecularly imprinted photonic crystals; UV, ultraviolet; HPLC, high-performance liquid chromatography

REFERENCES

- (1) Ploetz, R. C. Fusarium wilt of banana is caused by several pathogens referred to as *Fusarium oxysporum* f. sp. *cubense*. *Phytopathology* **2006**, *96*, 653–656.
- (2) D'hont, A.; Denoeud, F.; Aury, J. M.; Baurens, F. C.; Carreel, F.; Garsmeur, O.; Noel, B.; Bocs, S.; Droc, G.; Rouard, M.; Da Silva, C.; Jabbari, K.; Card, C.; Poulain, J.; Souquet, M.; Labadie, K.; Jourda, C.; Lengelle, J.; Rodier-Goud, M.; Alberti, A.; Bernard, M.; Correa, M.; Ayyampalayam, S.; McKain, M. R.; Leebens-Mack, J.; Burgess, D.; Freeling, M.; Mbeguie-A-Mbeguie, D.; Chabannes, M.; Wicker, T.; Panaud, O.; Barbosa, J.; Hribova, E.; Heslop-Harrison, P.; Habas, R.; Rivallan, R.; Francois, P.; Poirion, C.; Kilian, A.; Burthia, D.; Jenny, C.; Bakry, F.; Brown, S.; Guignon, V.; Kema, G.; Dita, M.; Waalwijk, C.; Joseph, S.; Dievart, A.; Jaillon, O.; Leclercq, J.; Argout, X.; Lyons, E.; Almeida, A.; Jeridi, M.; Dolezel, J.; Roux, N.; Risterucci, A. M.; Weissenbach, J.; Ruiz, M.; Glaszmann, J. C.; Quetier, F.; Yahiaoui, N.; Wincker, P. The banana (*Musa acuminata*) genome and the evolution of monocotyledonous plants. *Nature* **2012**, *488*, 213–217.
- (3) Ploetz, R. C. Management of Fusarium wilt of banana: A review with special reference to tropical race 4. *Crop Prot.* **2015**, *73*, 7–15.
- (4) Gordon, T. R. *Fusarium oxysporum* and the Fusarium wilt syndrome. *Annu. Rev. Phytopathol.* **2017**, *55*, 23–39.
- (5) Dita, M. A.; Waalwijk, C.; Buddenhagen, I. W.; Souza, J. M. T.; Kema, G. H. J. A molecular diagnostic for tropical race 4 of the banana fusarium wilt pathogen. *Plant Pathol.* **2010**, *59*, 348–357.
- (6) Meldrum, R. A.; Fraser-Smith, S.; Tran-Nguyen, L. T. T.; Daly, A. M.; Aitken, E. A. B. Presence of putative pathogenicity genes in isolates of *Fusarium oxysporum* f. sp. *cubense* from Australia. *Australas. Plant Pathol.* **2012**, *41*, 551–557.
- (7) Niu, G.; Zhang, J.; Zhao, S.; Liu, H.; Boon, N.; Zhou, N. Bioaugmentation of a 4-chloronitrobenzene contaminated soil with *Pseudomonas putida* ZWL73. *Environ. Pollut.* **2009**, *157*, 763–771.
- (8) Pabinger, S.; Rödiger, S.; Krieger, A.; Vierlinger, K.; Weinhäusel, A. A survey of tools for the analysis of quantitative PCR (qPCR) data. *Biomol. Detect. Quantif.* **2014**, *1*, 23–33.
- (9) Lin, Y.; Su, C.; Chao, C.; Chen, C.; Chang, C.; Huang, J.; Chang, P. A molecular diagnosis method using real-time PCR for quantification and detection of *Fusarium oxysporum* f. sp. *cubense* race 4. *Eur. J. Plant Pathol.* **2013**, *135*, 395–405.
- (10) Magdama, F.; Monserrate-Maggi, L.; Serrano, L.; Sosa, D.; Jiménez-Gasco, M. D. M. Comparative analysis uncovers the limitations of current molecular detection methods for *Fusarium oxysporum* f. sp. *cubense* race 4 strains. *PLoS One* **2019**, *14*, No. e0222727.
- (11) Fakhouri, W.; Walker, F.; Armbruster, W.; Heinrich, B. Detoxification of fusaric acid by a nonpathogenic *Colletotrichum* sp. *Physiol. Mol. Plant Pathol.* **2003**, *63*, 263–269.
- (12) Singh, V. K.; Singh, H. B.; Upadhyay, R. S. Role of fusaric acid in the development of 'Fusarium wilt' symptoms in tomato: Physiological, biochemical and proteomic perspectives. *Plant Physiol. Biochem.* **2017**, *118*, 320–332.
- (13) Dong, X.; Ling, N.; Wang, M.; Shen, Q.; Guo, S. Fusaric acid is a crucial factor in the disturbance of leaf water imbalance in Fusarium-infected banana plants. *Plant Physiol. Biochem.* **2012**, *60*, 171–179.
- (14) Andersson, L.; Sellergren, B.; Mosbach, K. Imprinting of amino acid derivatives in macroporous polymers. *Tetrahedron Lett.* **1984**, *25*, 5211–5214.
- (15) Wulff, G.; Oberkobusch, D.; Minárik, M. Enzyme-analogue built polymers, 18 chiral cavities in polymer layers coated on wide-pore silica. *React. Polym., Ion Exch., Sorbents* **1985**, *3*, 261–275.
- (16) Wang, J.; Pinkse, P. W. H.; Segerink, L. I.; Eijkel Jan, C. T. Bottom-up Assembled Photonic Crystals for Structure-Enabled Label-Free Sensing. *ACS Nano* **2021**, *15*, 9299–9327.
- (17) Alizadeh, T.; Hamedsoltani, L. Graphene/graphite/molecularly imprinted polymer nanocomposite as the highly selective gas sensor for nitrobenzene vapor recognition. *J. Environ. Chem. Eng.* **2014**, *2*, 1514–1526.
- (18) Alizadeh, T.; Rezaloo, F. A new chemiresistor sensor based on a blend of carbon nanotube, nano-sized molecularly imprinted polymer and poly methyl methacrylate for the selective and sensitive determination of ethanol vapor. *Sens. Actuators, B* **2013**, *176*, 28–37.
- (19) Tang, X.; Raskin, J.-P.; Lahem, D.; Krumpmann, A.; Decroly, A.; Debliquy, M. A formaldehyde sensor based on molecularly-imprinted polymer on a TiO₂ nanotube array. *Sensors* **2017**, *17*, No. 675.
- (20) Smolinska-Kempisty, K.; Ahmad, O. S.; Guerreiro, A.; Karim, K.; Piletska, E.; Piletsky, S. New potentiometric sensor based on molecularly imprinted nanoparticles for cocaine detection. *Biosens. Bioelectron.* **2017**, *96*, 49–54.
- (21) Martins, N.; Carreiro, E. P.; Locati, A.; Ramalho, J. P. P.; Cabrita, M. J.; Burke, A. J.; Garcia, R. Design and development of molecularly imprinted polymers for the selective extraction of deltamethrin in olive oil: An integrated computational-assisted approach. *J. Chromatogr. A* **2015**, *1409*, 1–10.
- (22) Masalov, V. M.; Sukhinina, N. S.; Kudrenko, E. A.; Emelchenko, G. A. Mechanism of formation and nanostructure of Stöber silica particles. *Nanotechnology* **2011**, *22*, No. 275718.
- (23) Han, Y.; Lu, Z.; Teng, Z.; Liang, J.; Guo, Z.; Wang, D.; Han, M.; Yang, W. Unraveling the growth mechanism of silica particles in the stöber method: In situ seeded growth model. *Langmuir* **2017**, *33*, 5879–5890.
- (24) Weidemüller, M.; Hemmerich, A.; Görlitz, A.; Esslinger, T.; Hänsch, T. W. Bragg diffraction in an atomic lattice bound by light. *Phys. Rev. Lett.* **1995**, *75*, 4583–4586.
- (25) Schroden, R. C.; Al-Daous, M.; Blanford, C. F.; Stein, A. Optical properties of inverse opal photonic crystals. *Chem. Mater.* **2002**, *14*, 3305–3315.
- (26) Biersdorf, W. R.; Armington, J. C. Response of the human eye to sudden changes in the wavelength of stimulation. *J. Opt. Soc. Am.* **1957**, *47*, 208–215.
- (27) Wu, Z.; Hu, X.; Tao, C.-a.; Li, Y.; Liu, J.; Yang, C.; Shen, D.; Li, G. Direct and label-free detection of cholic acid based on molecularly imprinted photonic hydrogels. *J. Mater. Chem.* **2008**, *18*, 5452–5458.

The interactions between bovine serum albumin and carboxybetaine-functionalized polysiloxanes in solution

Yaling Lin¹ · Weiyan Huang² · Yang You² · Yufeng Lei² · Anqiang Zhang²

Received: 25 August 2016 / Revised: 8 October 2016 / Accepted: 17 October 2016 / Published online: 27 October 2016
© Springer-Verlag Berlin Heidelberg 2016

Abstract The interactions between carboxybetaine-functionalized polydimethylsiloxanes (PDMS-g-CB) and bovine serum albumin (BSA) in water solution were investigated from varied aspects based on different techniques, including fluorescence spectroscopy, UV-Vis spectroscopy, circular dichroism spectroscopy, isothermal titration calorimetry, and atomic force microscopy. Due to the weak interaction between PDMS-g-CB and BSA, another polymer with similar structure as PDMS-g-CB, i.e., quaternary ammonium salt-functionalized polydimethylsiloxanes (PDMS-g-QAS), was synthesized and chosen as the positive control, and the results indicated that the free PDMS-g-CB in solution could exhibit good resistance against proteins, which was mainly due to the zwitterions-side groups' binding ability between PDMS chain and protein. Both the characterization methods and the results could help us to understand the interaction between free water-soluble polymers and protein, and extend the application of PDMS-g-CB and design new antifouling materials.

Keywords Carboxybetaine functionalized polydimethylsiloxanes · Protein · Polymer/protein interactions · Fluorescence spectroscopy · Isothermal titration calorimetry

Introduction

Proteins exist extensively in plants, animals, and many other creatures and play vital roles in life processes. Polymer-protein interactions are important for the design and preparation of polymer materials for biomedical applications. The strength of polymer-protein interactions should be tailored depending on the application. Appropriate protein absorption to polymers is required in polymer scaffolds and targeted drug and gene delivery [1–3]. The interactions between polymers and proteins should be weak for marine coating, antifouling membranes, implanted devices, and drug delivery carriers [4–7]. PEG-based polymers, a type of hydrophilic polymer materials, have been widely studied as an antifouling material [8–11], and the hydration induced by hydrogen bonds between water molecules and such materials can be used to account for their antifouling behavior [12, 13]. However, their chemical instability restricts the application of this group of materials [14].

Polybetaine is a new generation of antifouling material [14–16]. With a negative and positive charge on a monomer unit, polybetaines are electrically neutral and hydrophilic and can bind water molecules more tightly via ionic solvation, which is stronger than hydrogen bond [13, 17, 18]. Polybetaines exhibit excellent protein-resistance properties and stabilities [19]. In recent years, antifouling materials based on polybetaines, such as poly(carboxylbetaine) (pCB) and poly(sulfobetaine) (pSB), have received an increasing amount of attention because of the inexpensive raw material and

Electronic supplementary material The online version of this article (doi:10.1007/s00396-016-3969-5) contains supplementary material, which is available to authorized users.

✉ Yaling Lin
linyaling@scau.edu.cn

✉ Anqiang Zhang
aqzhang@scut.edu.cn

¹ College of Materials and Energy, South China Agricultural University, 483 Wushan Rd., Guangzhou, Guangdong 510642, China

² College of Material Science and Engineering, South China University of Technology, 381 Wushan Rd., Guangzhou, Guangdong 510641, China

excellent antifouling properties [20–26]. However, in most cases, these polybetaines have been immobilized on a certain surface, and their antifouling properties are evaluated through quartz crystal microbalance (QCM), surface plasmon resonance (SPR) methods [27, 28]. Thus, the interactions between proteins and free polybetaines in solution have rarely been reported.

In our previous work, water-soluble carboxybetaine-functionalized polydimethylsiloxanes (PDMS-g-CB), which consisted of a PDMS backbone and carboxybetaine pendant-side groups, were synthesized and were mixed with PDMS or grafted on PDMS surface, which could significantly improve the material's ability of resisting protein and bacterial absorption [29, 30]. The carboxybetaine-side group electrostatically combined with water, and the induced hydration layer resisted the absorption of protein and bacteria. Considering spraying operation would be more acceptable for some applications like plant protection, thus the interactions of free and water-soluble polymers with protein were more expected, unfortunately, it's rarely reported.

PDMS-g-CB is considered to be a potential environmentally friendly pesticide. A soluble antifouling material can be an excellent out way to pest prevention. Insects, such as *Spodoptera exigua* (beet armyworm), secrete mucus on the abaxial leaf surface to assist in the adhesion of eggs, and this mucus mainly contains water, proteins, and a small amount of carbohydrates [31]. We believe that it is possible to form an antifouling coating on leaf surfaces by spraying a PDMS-g-CB solution, thus resisting the adhesion of insect eggs and restraining the reproduction of pests. Thus, the interactions between proteins and free PDMS-g-CB are a fundamental issue.

In this study, experiments were conducted to gain an understanding of the interaction between free PDMS-g-CB and protein. Bovine serum albumin (BSA), a convenient and widely studied model globular protein in biological process, was chosen as the model protein for its well water-solubility, unique ligand-binding properties, and well-established structure [32]. We detected the interaction in solution between BSA and PDMS-g-CB using different analytical methods, including fluorescence spectroscopy, UV-Vis spectroscopy, circular dichroism spectroscopy, isothermal titration calorimetry, and atomic force microscopy. PDMS-g-QAS, [33] which is similar to PDMS-g-CB in structure, containing a PDMS backbone and quaternary ammonium salt pendant-side groups was chosen as the positive comparison. The results obtained from different measurements showed that the interactions between PDMS-g-CB and proteins in solution were weak, or even too weak to be detected, benefiting the design and application of this group of antifouling materials.

Experimental

Materials

Octamethylcyclotetrasiloxane (D^4 , >99.5 %, Dow Corning, USA), 1, 3, 5, 7-tetramethylcyclotetrasiloxane (D^4_H , >99 %, Hangzhou Silong Material Technology Co. Ltd., China), and hexamethyldisiloxane (MM, >99 %, Dow Corning, USA) were dried before use. N, N-Dimethylallylamino (DMAA, >99 %, Haining City Huangshan Chemical Industry Co. Ltd., China) was purified by distillation before use. Benzyl chloride (GC, >99 %) and sodium chloroacetate (SC) were purchased from Aladdin Reagent Co. Ltd. (Shanghai, China) and were used as received. Platinum (0)-1, 3-divinyl-1, 1, 3, 3-tetramethyldisiloxane complex solution (Karstedt's catalyst solution, Pt~2 %, Aladdin Reagent Co. Ltd., China) was used as the catalyst for the hydrosilylation reaction. Purolite™ CT175 (Purolite (China) Co. Ltd) is a clay containing sulfonic acid and was used as received. Other solvents, such as isopropanol, were used without any pretreatment. Bovine serum albumin (BSA) was purchased from the Bio Science & Technology Co. Ltd. (Shanghai, China). Water used in these experiments was purified by an Ultrapure water purification system with a minimum resistivity of 18.0 MΩ.cm. The phosphate buffer solution (PBS) had a pH of 7.0 and an ionic strength of 0.01 mol/L.

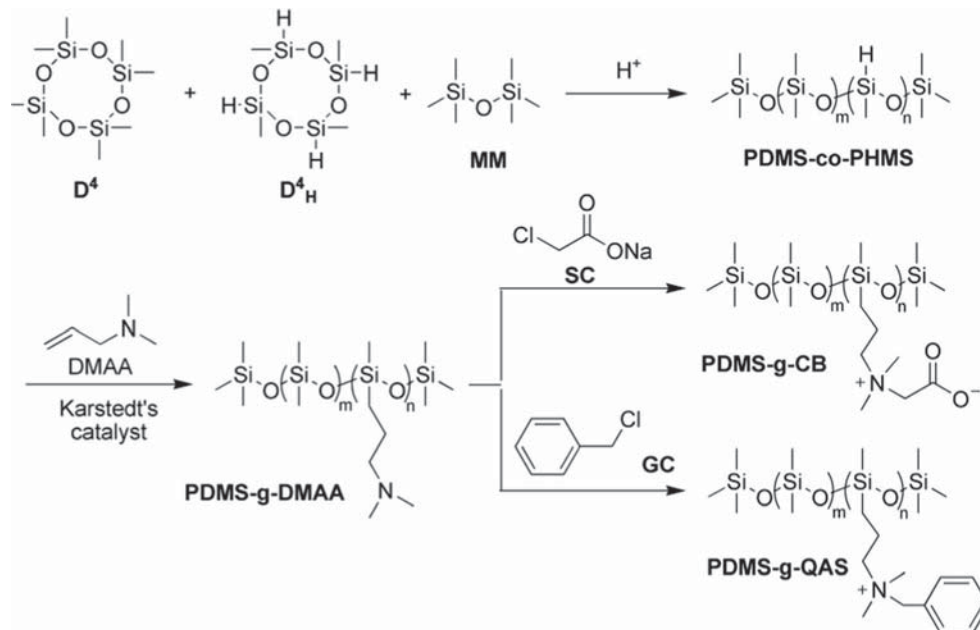
Syntheses of PDMS-g-CB and PDMS-g-QAS

In this paper, PDMS-g-CB series and PDMS-g-QAS were synthesized via a three-step procedure according to our previous report (Scheme 1) [29, 33]. The two polymers shared the same first two steps, but were different from each other when it comes in the third step.

Firstly, hydrogen-containing polysiloxanes (PDMS-co-PHMS) were synthesized through ring-opening polymerization of D^4 and D^4_H . Secondly, DMAA was grafted to PDMS-co-PHMS via a hydrosilylation reaction in the presence of Karstedt's catalyst to obtain PDMS-g-DMAA. Finally, carboxybetaine-functionalized polysiloxanes (PDMS-g-CB) were prepared by subsequent quaternization reaction with sodium chloroacetate (SC), while benzyldimethylaminopropyl chloride grafted polysiloxane (PDMS-g-QAS) were prepared with benzyl chloride (GC).

The control group for the series of experiments in this paper was PDMS-g-QAS, which had a similar construction to PDMS-g-CB and has been shown to interact with proteins [33].

The grafting ratio and molecular weight (determined by GPC) of the polymers are presented in Table 1.

Scheme 1 The synthetic route of PDMS-g-CB and PDMS-g-QAS

Fluorescence spectroscopy

Steady-state fluorescence experiments were carried out with an FM-4P spectrofluorometer (HORIBA, France) using a 1.0-cm quartz cell at 25 °C. Fluorescence spectra were measured upon adding different amounts of polymers to a fixed BSA solution of 0.1 mg/mL, and the mass ratio of the polymer/BSA was varied from 0 to 0.1, 0.5, 1, 2, 4, and 8. The samples were prepared with PBS with pH = 7.0 and incubated for 5 h before analyses. Intrinsic fluorescence spectra were recorded between 310 and 400 nm with an excitation wavelength of 275 nm, where the contribution of polymers was negligible. Excitation and emission slits comprised of nominal 2 nm bandwidths. The fluorescence spectra were acquired as an average of three repeated scans.

Circular dichroism spectroscopy

Far-UV circular dichroism (CD) spectroscopy was performed using a Chirascan CD spectropolarimeter (Applied Photophysics Ltd., UK) in a wavelength range of 190–260 nm. Considering the accuracy of the CD spectra, we used

a fixed BSA solution of 0.3 mg/mL, and the mass ratio of polymer/BSA was varied from 0 to 1/30, 5/30, 10/30, 20/30, 40/30, and 80/30. The samples were prepared with PBS with pH = 7.0 and incubated for 5 h before testing. The samples were filled in a 0.1-cm path length cuvette where the temperature was kept at 25 °C with a circulation water bath. The CD spectra were acquired as an average of three repeated scans with a scanning rate, response time, and step of 20 nm/min, 0.5 s, and 1 nm, respectively. The recorded spectra were corrected for background signals using buffer solution.

UV–Vis spectroscopy

UV-Vis spectra were obtained using a UV-2550 spectrometer (Shimadzu, Japan) with a 1.0-cm quartz cell at 25 °C. The spectra were recorded in a wavelength range from 200 to 300 nm with a step of 1 nm. The measurements used the same concentration series as the fluorescence spectroscopy measurements. The solutions were incubated at 25 °C for 5 h before analyses. A buffer solution was used as a blank to eliminate the disturbance from the adsorption of polymers. The UV-Vis spectra were acquired as an average of three repeated scans.

Isothermal titration calorimetry

The calorimeter used was the Nano ITC (TA Instruments, USA). A 2 μ L aliquot of a BSA solution was added stepwise using an automatic injection syringe containing 50 μ L of a 0.02 mg/mL BSA solution into a cell of 300 μ L that contained either water or a polymer solution with a 3-min interval between each injection at 25 °C. The concentrations of the

Table 1 Molecular weight and grafting ratio of polymers

Sample	Molecular weight (Mn)	Grafting ratio
PDMS-g-CB _{1/3}	4.85×10^3	1/3
PDMS-g-CB _{1/4}	3.10×10^3	1/4
PDMS-g-CB _{1/6}	2.22×10^3	1/6
PDMS-g-CB _{1/8}	3.69×10^3	1/8
PDMS-g-QAS	2.22×10^3	1/6

polymer solutions were four times their CMC values, i.e., 0.2, 0.3, 0.2, 0.25, and 0.2 mg/mL for PDMS-g-CB_{1/3}, PDMS-g-CB_{1/4}, PDMS-g-CB_{1/6}, PDMS-g-CB_{1/8}, and PDMS-g-QAS, respectively [29]. The solution was prepared with ultrapure water and degassed before testing.

Atomic force microscopy

Morphological changes of the proteins in the absence and presence of polymers were imaged using tapping-mode AFM. A drop of the mixed protein–polymer solution with a polymer/BSA mass ratio of 10/1 (BSA concentration of 0.05 mg/mL) was deposited on fresh peeled mica and dried for 24 h (under the normal conditions) before AFM imaging. AFM images were acquired by a Bruker Multimode 8. Commercial Si cantilever (Bruker) with an elastic modulus of 40 N/m was used. All images were acquired at a typical scan rate of 1.0 Hz and scan angle of 0°. Representative images of each sample were collected by scanning at least three different locations.

Results and discussion

The interactions between the polymers and proteins could be evaluated from different aspects. The addition of a polymer may change the conformation of a protein, which consists of tertiary and secondary structures, resulting in the release of heat or aggregation. Here, we used varied detection methods to evaluate the interaction between PDMS-g-CB (or PDMS-g-QAS) and BSA, as discussed in the following.

Fluorescent spectroscopy

The fluorescent spectroscopy of proteins was used to measure the change in the tertiary structure of the protein induced by different polymers. The intrinsic fluorescence of BSA recorded in the range of 280–480 nm mainly results from aromatic amino acids residues of Tyr and Trp [34]. Once the protein undergoes a conformational change, the fluorescence of the aromatic amino acids depends not only on the exposure or accessibility of their residues but also on the local protein environment immediately surrounding the aromatic amino acids [28]. Here, the polymer-induced conformational changes of proteins at different polymer/protein mass ratios (i.e., 0, 0.1, 0.5, 1, 2, 4, and 8) as a function of polymer grafting ratios was monitored by observing changes in the intensity of BSA fluorescence (Fig. 1). A blue shift from 348 to 329 nm was observed in PDMS-g-QAS/BSA systems (Fig. 1e), which suggests that the fluorescence residues were surrounded by a more hydrophobic environment resulting from the absorption of PDMS-g-

QAS molecules near the amino acid residues. The fluorescence intensity decreased with an increase in polymer concentration, as illustrated by Fig. 1e, where PDMS-g-QAS demonstrated a stronger ability to induce fluorescence quenching of BSA.

In contrast, for any PDMS-g-CB/BSA mixtures, the fluorescence curves of different concentrations were almost overlapped. There were no detectable red/blue shifts or clear intensity changes (Fig. 1a–d, f), which illustrated that PDMS-g-CB did not influence the microenvironment of aromatic amino acids or induce fluorescence quenching of BSA. It also illustrated that the faint influence of PDMS-g-CB on BSA aromatic amino acids residues was independent of its grafting ratio. The fluorescence intensities of PDMS-g-CB/BSA systems slightly decreased, which may have been induced by shading of the high concentration solution.

Different interactions between proteins and PDMS-g-CB or PDMS-g-QAS are likely attributed to their different side groups. PDMS-g-QAS is a polymeric quaternary ammonium salt, where the polymer chain is positively charged in aqueous media. While BSA is a negatively charged protein [35] and can combine with PDMS-g-QAS through electrostatic interactions and form aggregates in solution, resulting fluorescence quenching. PDMS-g-CB is a zwitterionic polymer, and the polymer chain is electrically neutral in solution. Additionally, the amount of carboxybetaine side groups is large and allows water molecules to bind strongly via ionic solvation, which can block the adhesion of protein molecules.

Circular dichroism spectroscopy

Far-UV circular dichroism (CD) spectroscopy is a useful tool for detecting changes in the secondary structure of BSA, which is composed of an α -helix, β -sheet, β -turn, and random coil [36]. The CD spectra for the PDMS-g-CB/BSA and PDMS-g-QA/BSA systems in the range of 190–260 nm are shown in Fig. 2. Two negative bands at approximately 210 and 222 nm were characteristic CD spectra of a BSA α -helix. The negative molar ellipticity decreased with an increase in the polymer concentration, indicating a decrease in the α -helix content [34]. The CD spectra curves of all PDMS-g-CB/BSA solution mixtures at different polymer concentrations were almost overlapping (Fig. 2a–d). The negative molar ellipticity decreased with an increase in the PDMS-g-QAS/BSA mass ratio (Fig. 2e), indicating that the addition of PDMS-g-QAS induced an α -helix transformation. The calculated contents of α -helix, β -sheet, β -turn, and random coil structures at the lowest and highest polymer concentrations (Fig. 2f) showed that PDMS-g-CB almost did not affect the secondary structure of BSA, while the 0.8 mg/mL PDMS-g-

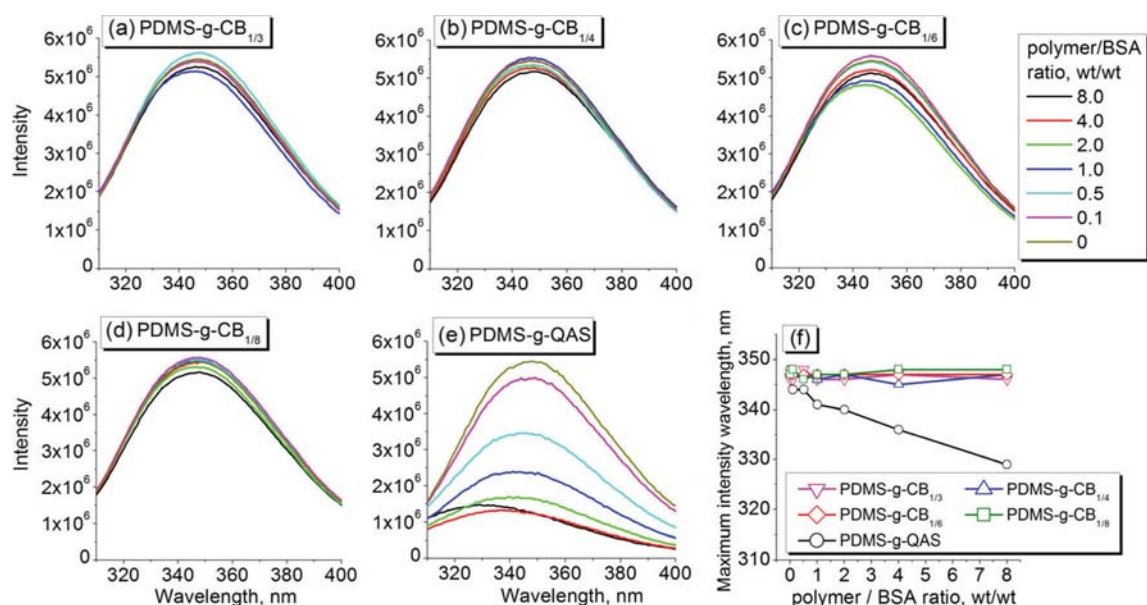


Fig. 1 The fluorescence curves of different polymer/BSA mixture solutions in varied concentrations **a** PDMS-g-CB_{1/3}, **b** PDMS-g-CB_{1/4}, **c** PDMS-g-CB_{1/6}, **d** PDMS-g-CB_{1/8}, **e** PDMS-g-QAS, and **f** the maximum intensity wavelength vs. polymer/BSA ratios

QAS could introduce a 50 % drop in the α -helix content, indicating the strong ability of PDMS-g-QAS in unfolding the BSA molecule.

UV–Vis measurements

Except for detecting the microenvironment of aromatic amino acid residues, UV-Vis spectroscopy can also detect changes in polypeptide backbone structures. Figure 3 shows the UV-Vis spectra for the polymer/BSA mixture

solutions, where two absorption peaks at approximately 204 and 278 nm are clearly presented. In PDMS-g-CB/BSA mixture solutions, the absorbance curves of different polymer concentrations were almost overlapped, and no red/blue shift and absorbance changes were observed at either 204 or 278 nm (Fig. 3a–d, and Fig. 4). For the PDMS-g-QAS/BSA mixtures, the addition of PDMS-g-QAS into the BSA buffer solution resulted in a significant red shift ($\Delta\lambda_{\max} \sim +8$ nm) of the maximum absorbance peak accompanied with an intensity increase at

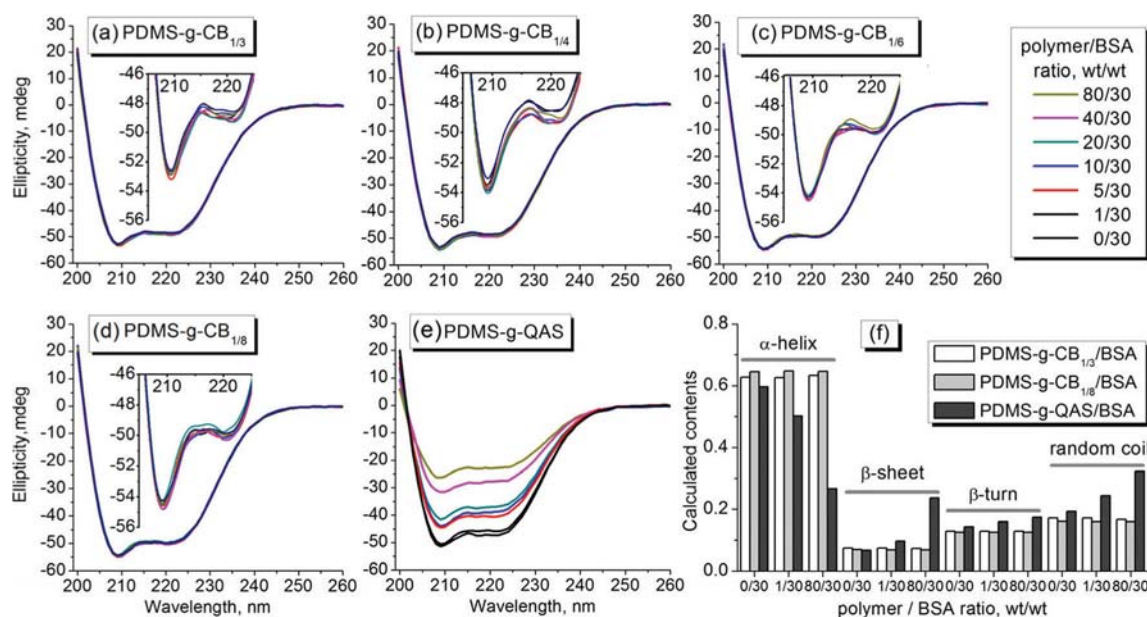
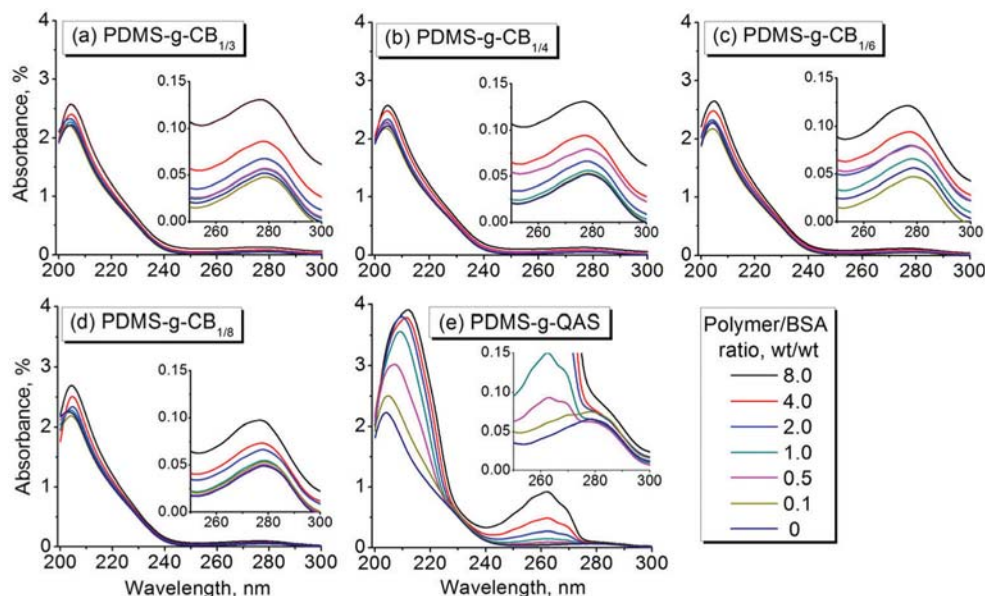


Fig. 2 CD spectra of polymer/BSA solution in varied polymer/BSA ratio **a** PDMS-g-CB_{1/3}, **b** PDMS-g-CB_{1/4}, **c** PDMS-g-CB_{1/6}, **d** PDMS-g-CB_{1/8}, **e** PDMS-g-QAS, and **f** The calculated contents of α -helix, β -sheet, β -turn, and random coil, with BSA concentration of 0.3 mg/mL

Fig. 3 The UV-Vis spectra of polymer/BSA solutions with different polymer/BSA ratio **a** PDMS-g-CB_{1/3}, **b** PDMS-g-CB_{1/4}, **c** PDMS-g-CB_{1/6}, **d** PDMS-g-CB_{1/8}, and **e** PDMS-g-QAS, with BSA concentration of 0.1 mg/mL



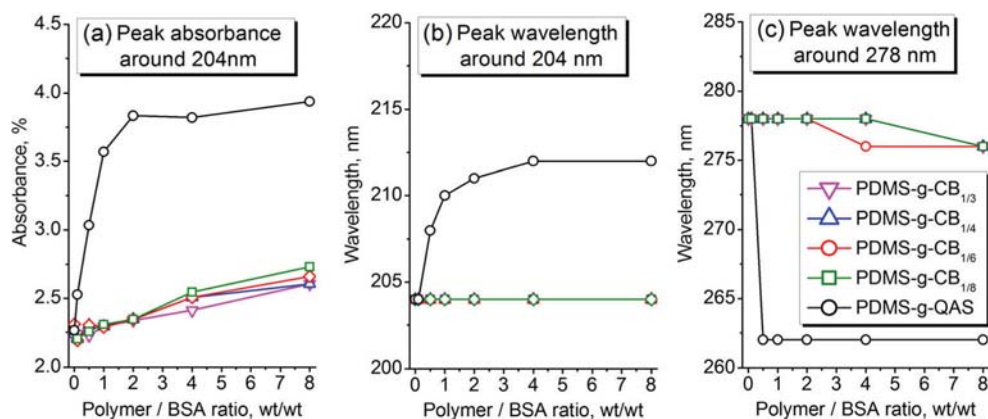
204 nm (Fig. 4a), which was attributed to the π - π^* transition of the polypeptide backbone structure ($C=O$) of BSA. It is reported that π^* electron clouds have higher polarity than that of π ; therefore, in a polar solvent, the energy of π^* should decrease more than that of π , which would reduce the energy gap between π^* and π and result in a red shift of absorbance at approximately 204 nm (Fig. 4b) [34]. These observations and CD measurements suggested that BSA was unfolded by PDMS-g-QAS and exposed the structures in a more polar environment.

There was also a blue shift ($\Delta\lambda_{\max} \sim -16$ nm) and intensity increase of the maximum absorbance peak at approximately 278 nm (Fig. 4b), which was due to the n - π^* transition of the aromatic amino acid residues [34]. This observation was consistent with the fluorescence spectra, and the aromatic amino acid residues were found to be surrounded by a more hydrophobic environment.

Isothermal titration calorimetry

From a macro perspective, heat absorption and emissions are always observed in the presence of reactions. Figure 5 shows the calorimetric titration curves upon the addition of a 0.2 mg/mL BSA solution into water and the polymer solutions (detailed titration curves are shown in Fig. S1, Electronic Supplementary Material). The curves of all the PDMS-g-CB/BSA systems almost overlapped, which suggested that the heat release of PDMS-g-CB/BSA systems was independent of polymer grafting ratios. Moreover, the curve shapes of the BSA/water and BSA/polymer mixtures were similar except for PDMS-g-QAS, as shown in Fig. S1a-f. When BSA was added to any of the PDMS-g-CB solutions, there was a heat release difference of approximately 1.5 μ J/mol between the BSA/water and BSA/PDMS-g-CB systems, which can be attributed to changes in the solution environments. PDMS-g-QAS had a

Fig. 4 The polymer maximum absorbance of varied grafting ratio at different concentration **(a)** and corresponding wavelength near 204 **(b)**, and 278 nm **(c)**, respectively



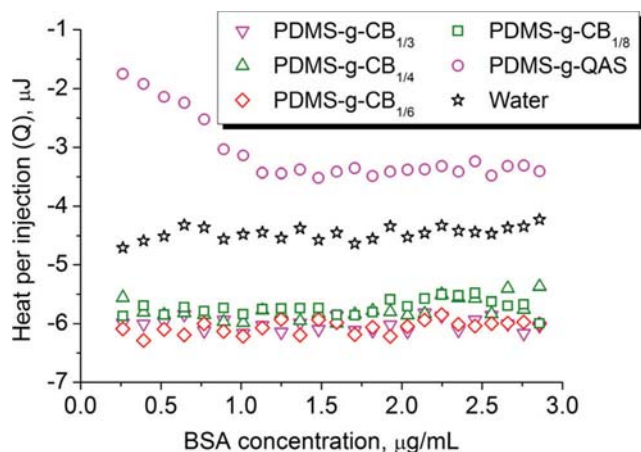


Fig. 5 ITC data for titration of BSA (0.2 mg/mL) into different polymer solution or water at 25 °C

different curve shape: the heat per injection (Q) decreased with an increase in protein content and then appeared to plateau. In the beginning, BSA interacted with PDMS-g-QAS and this process was exothermic. With an increase in the protein concentration in a sample cell, the bond reached saturation, as shown in Fig. S1f.

AFM experiments

AFM protocols provide morphological reproduction of microsurfaces and are generally used to characterize protein interactions with polymers. Thus, the morphological changes of the proteins upon incubation with polymers (PDMS-g-CB and PDMS-g-QAS) were examined. The mass ratio of polymer/BSA was 10/1, and the sample had a BSA concentration of 0.05 mg/mL. The morphologies of the deposited aggregates firmly adsorbed on mica were then analyzed by tapping-mode AFM. For BSA-involved systems, some small and uniform sphere-like molecules of 5–8 nm were observed in pure BSA solutions (Fig. 6a). Upon incubation of BSA with PDMS-g-CB, spherical particles similar in size, shape, and quantity were clearly observed (Fig. 6b). Conversely, a mixture of BSA and PDMS-g-QAS

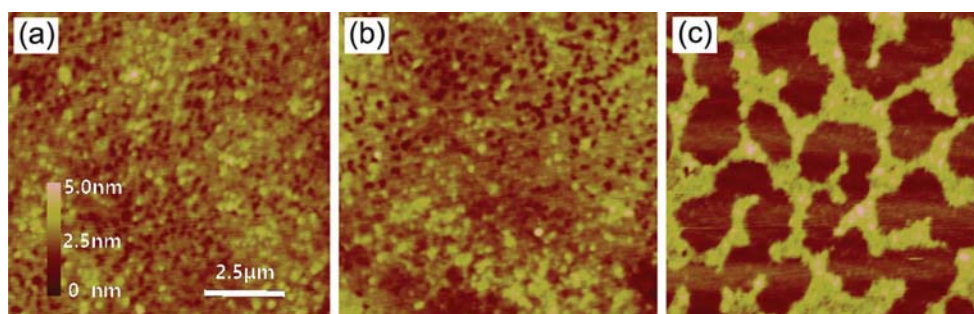
produced irregular aggregation, in sharp contrast to the morphologies of pure BSA and mixed BSA-PDMS-g-CB solutions (Fig. 6c). The aggregation of BSA may account for PDMS-g-QAS unfolding BSA molecules and changing the charge around the protein surface.

Overall, qualitative AFM images provided additional evidence that PDMS-g-CB had a relatively faint interaction with proteins than PDMS-g-QAS, complementary to the more quantitative results from all the experiments described above. Similar morphologies between protein and protein/PDMS-g-CB systems indicated that PDMS-g-CB in aqueous solutions did not induce morphological changes of proteins.

Conclusions

In this work, we studied the interaction between BSA and PDMS-g-CB or PDMS-g-QAS in solution from different aspects via optical techniques, ITC, and AFM. The CD spectra and UV-Vis spectra demonstrated that PDMS-g-QAS could unfold protein molecules, which consequently resulted in the exposure of aromatic amino acid residues to more hydrophobic environments, as observed in the fluorescence spectra. The ITC curves confirmed that interactions occurred between PDMS-g-QAS and BSA, and AFM protocols showed that this type of interaction induced protein aggregation. From a wide analysis of the data, we did not detect dramatic interactions between PDMS-g-CB and BSA compared with PDMS-g-QAS, which was attributed to its strong ability to bind with water molecules via the zwitterions on the side groups. The optical spectra and ITC results demonstrated that the grafting ratio did not influence the ability of PDMS-g-CB to resist the absorption of proteins and made it obvious that PDMS-g-CB had good anti-fouling properties. Because the PDMS-g-CBs were obtained by modified polyorganosiloxane (PDMS) through grafting betaine, the bio-inert properties of the PDMS backbone, and the super-hydrophilic side carboxybetaine groups allowed for effective insect prevention. This work helped clarify our understanding of the interaction

Fig. 6 AFM images of **a** pure BSA, **b** PDMS-g-CB_{1/6}/BSA, and **c** PDMS-g-QAS/BSA with BSA concentration of 0.05 mg/mL and polymer/BSA ratio of 10/1 (wt/wt)



between polymers and proteins in solution and can serve as a guide for the design and syntheses of anti-fouling materials applied in solution.

Acknowledgments This work was supported by the National Natural Science Foundation of China under Grant 31201552 and 51473051; the Specialized Research Fund for the Doctoral Program of Higher Education under Grant 20124404120025; and the Science and Technology Planning Project of Guangdong Province under Grant 2016A020210105.

Compliance with ethical standards

Conflict of interest The authors declare that they have no conflict of interest.

References

- Place ES, George JH, Williams CK, Stevens MM (2009) Synthetic polymer scaffolds for tissue engineering. *Chem Soc Rev* 38:1139–1151
- Ma Z, Mao Z, Gao C (2007) Surface modification and property analysis of biomedical polymers used for tissue engineering. *Colloid Surface B* 60:137–157
- Kabanov AV, Batrakova EV, Alakhov VY (2002) Pluronic® block copolymers as novel polymer therapeutics for drug and gene delivery. *J Control Release* 82:189–212
- Yang WJ, Neoh K, Kang E, Teo SL, Rittschof D (2014) Polymer brush coatings for combating marine biofouling. *Prog Polym Sci* 39:1017–1042
- Zhao Y, Zhu L, Yi Z, Zhu B, Xu Y (2013) Improving the hydrophilicity and fouling-resistance of polysulfone ultrafiltration membranes via surface zwitterionization mediated by polysulfone-based triblock copolymer additive. *J Membrane Sci* 440:40–47
- Shen M, Wagner MS, Castner DG, Ratner BD, Horbett TA (2003) Multivariate surface analysis of plasma-deposited tetraglyme for reduction of protein adsorption and monocyte adhesion. *Langmuir* 19:1692–1699
- Yuan Y, Mao C, Du X, Du J, Wang F, Wang J (2012) Surface charge switchable nanoparticles based on zwitterionic polymer for enhanced drug delivery to tumor. *Adv Mater* 24:5476–5480
- Pale-Grosdemange C, Simon ES, Prime KL, Whitesides GM (1991) Formation of self-assembled monolayers by chemisorption of derivatives of oligo (ethylene glycol) of structure $\text{HS}(\text{CH}_2)_{11}(\text{OCH}_2\text{CH}_2)_m\text{OH}$ on gold. *J Am Chem Soc* 113:12–20
- Prime KL, Whitesides GM (1993) Adsorption of proteins onto surfaces containing end-attached oligo (ethylene oxide): a model system using self-assembled monolayers. *J Am Chem Soc* 115:10714–10721
- Guo D, Han H, Wang J, Xiao S, Dai Z (2007) Surface-hydrophilic and protein-resistant silicone elastomers prepared by hydrosilylation of vinyl poly (ethylene glycol) on hydrosilanes-poly (dimethylsiloxane) surfaces. *Colloids Surfaces A* 308:129–135
- Kingshott P, Thissen H, Griesser HJ (2002) Effects of cloud-point grafting, chain length, and density of PEG layers on competitive adsorption of ocular proteins. *Biomaterials* 23:2043–2056
- Ostuni E, Chapman RG, Holmin RE, Takayama S, Whitesides GM (2001) A survey of structure-property relationships of surfaces that resist the adsorption of protein. *Langmuir* 17:5605–5620
- Chen S, Li L, Zhao C, Zheng J (2010) Surface hydration: principles and applications toward low-fouling/nonfouling biomaterials. *Polymer* 51:5283–5293
- Jiang S, Cao Z (2010) Ultralow-fouling, functionalizable, and hydrolyzable zwitterionic materials and their derivatives for biological applications. *Adv Mater* 22:920–932
- Chen S, Jiang S (2008) A new avenue to nonfouling materials. *Adv Mater* 20:335–338
- Cheng G, Zhang Z, Chen S, Bryers JD, Jiang S (2007) Inhibition of bacterial adhesion and biofilm formation on zwitterionic surfaces. *Biomaterials* 28:4192–4199
- Leng C, Han X, Shao Q, Zhu Y, Li Y, Jiang S, Chen Z (2015) In situ probing of the surface hydration of zwitterionic polymer brushes: structural and environmental effects. *J Phys Chem C* 118:15840–15845
- Leng C, Hung H, Sieggreen OA, Li Y, Jiang S, Chen Z (2015) Probing the surface hydration of nonfouling zwitterionic and poly (ethylene glycol) materials with isotopic dilution spectroscopy. *J Phys Chem C* 119:8775–8780
- Cheng G, Li G, Xue H, Chen S, Bryers JD, Jiang S (2009) Zwitterionic carboxybetaine polymer surfaces and their resistance to long-term biofilm formation. *Biomaterials* 30:5234–5240
- Chen S, Chang Y, Lee K, Wei T, Higuchi A, Ho F, Tsou C, Ho H, Lai J (2012) Hemocompatible control of sulfobetaine-grafted polypropylene fibrous membranes in human whole blood via plasma-induced surface zwitterionization. *Langmuir* 28:17733–17742
- Yang W, Chen S, Cheng G, Vaisocherova H, Xue H, Li W, Zhang J, Jiang S (2008) Film thickness dependence of protein adsorption from blood serum and plasma onto poly (sulfobetaine)-grafted surfaces. *Langmuir* 24:9211–9214
- Zhang Z, Finlay JA, Wang L, Gao Y, Callow JA, Callow ME, Jiang S (2009) Polysulfobetaine-grafted surfaces as environmentally benign ultralow fouling marine coatings. *Langmuir* 25:13516–13521
- Wang M, Yuan J, Huang X, Cai X, Li L, Shen J (2013) Grafting of carboxybetaine brush onto cellulose membranes via surface-initiated ARGET-ATRP for improving blood compatibility. *Colloid Surface B* 103:52–58
- Quintana R, Gosa M, Jańczewski D, Kutnyanszky E, Vancso GJ (2013) Enhanced stability of low fouling zwitterionic polymer brushes in seawater with diblock architecture. *Langmuir* 29:10859–10867
- Sin M, Sun Y, Chang Y (2014) Zwitterionic-based stainless steel with well-defined polysulfobetaine brushes for general bioadhesive control. *ACS Appl Mater Inter* 6:861–873
- Chang Y, Chang W, Shih Y, Wei T, Hsue G (2011) Zwitterionic sulfobetaine-grafted poly (vinylidene fluoride) membrane with highly effective blood compatibility via atmospheric plasma-induced surface copolymerization. *ACS Appl Mater Inter* 3:1228–1237
- Leng C, Hung H, Sun S, Wang D, Li Y, Jiang S, Chen Z (2015) Probing the surface hydration of nonfouling zwitterionic and PEG materials in contact with proteins. *ACS Appl Mater Inter* 7:16881–16888
- Wu J, Zhao C, Hu R, Lin W, Wang Q, Zhao J, Bilinovich SM, Leeper TC, Li L, Cheung HM, Chen S, Zheng J (2014) Probing the weak interaction of proteins with neutral and zwitterionic anti-fouling polymers. *Acta Biomater* 10:751–760
- Cheng L, Liu Q, Lei Y, Lin Y, Zhang A (2014) The synthesis and characterization of carboxybetaine functionalized polysiloxanes for the preparation of anti-fouling surfaces. *RSC Adv* 4:54372–54381
- Zhang A, Cheng L, Hong S, Yang C, Lin Y (2015) Preparation of anti-fouling silicone elastomers by covalent immobilization of carboxybetaine. *RSC Adv* 5:88456–88463

31. Jin F, Ji B, Liu S, Tian L, Gao J (2009) Deposition modes, components and functions of secretions associated with oviposition in insects. *Acta Entomol Sin* 52:1008–1016
32. Bujacz A (2012) Structures of bovine, equine and leporine serum albumin. *Acta Crystallogr D Biol Crystallogr* 68: 1278–1289
33. Lin Y, Liu Q, Cheng L, Lei Y, Zhang A (2014) Synthesis and antimicrobial activities of polysiloxane-containing quaternary ammonium salts on bacteria and phytopathogenic fungi. *React Funct Polym* 85:36–44
34. Yin T, Qin M, Shen W (2014) Physicochemical investigations on the interactions between gemini/single-chain cationic surfactants and bovine serum albumin. *Colloid Surf A* 461:22–29
35. Martin VI, Rodriguez A, Maestre A, Moya ML (2013) Binding of cationic single-chain and dimeric surfactants to bovine serum albumin. *Langmuir* 29:7629–7641
36. Sreerama N, Woody R (2000) Estimation of protein secondary structure from circular dichroism spectra: comparison of CONTIN, SELCON, and CDSSTR methods with an expanded reference set. *Anal Biochem* 287:252–260



Contents lists available at ScienceDirect

Reactive & Functional Polymers

journal homepage: www.elsevier.com/locate/react

Synthesis and antimicrobial activities of polysiloxane-containing quaternary ammonium salts on bacteria and phytopathogenic fungi

Yaling Lin ^{a,*}, Qiongqiong Liu ^b, Liujun Cheng ^b, Yufeng Lei ^b, Anqiang Zhang ^{b,*}

^a Department of Pharmaceutical Engineering, College of Resource and Environment, South China Agriculture University, 483 Wushan Rd., Guangzhou 510642, Guangdong, China

^b Department of Polymer Material Science and Engineering, College of Material Science and Engineering, South China University of Technology, 381 Wushan Rd., Guangzhou 510641, Guangdong, China

ARTICLE INFO

Article history:

Received 26 July 2014

Received in revised form 30 September 2014

2014

Accepted 6 October 2014

Available online 14 October 2014

Keywords:

Polysiloxane graft quaternary ammonium salts

Antimicrobial activity

Phytopathogenic fungi

ABSTRACT

A series of dimethylaminopropyl benzyl chloride grafted polysiloxanes (PDMS-g-BCs) with tunable molecular weights and cationic content were synthesized, and the effect of polymer structure on the antimicrobial activities against bacteria (*Escherichia coli* (*E. coli*) and *Staphylococcus albus* (*S. albus*)) and phytopathogenic fungi (*Rhizoctonia solani* (*R. solani*) and *Fusarium oxysporum* f. sp. *cubense* race 4 (*Foc4*)) were systematically assessed. The antibacterial activity was evaluated by determining the minimum inhibitory concentration (MIC) against *E. coli* and *S. albus* by the broth dilution method, and the antifungal activity was measured by mycelia growth inhibition as well as by the MIC and minimum fungicidal concentration (MFC) values. The molecular weight and cationic content were major determinants of the activities of PDMS-g-BCs; when the molecular weight was approximately 2500 g/mol and the cationic content was approximately 20 mol% of the total siloxane units, PDMS-g-BCs gained strong antimicrobial activities toward both *E. coli* and *Foc4*, comparable to those of a commonly used broad-spectrum microbicide benzalkonium chloride, making PDMS-g-BCs promising fungicidal agents for plant disease control.

© 2014 Elsevier B.V. All rights reserved.

1. Introduction

Antimicrobial agents generate a great deal of interest from researchers in both academia and industry, as these agents are capable of destroying or inhibiting the growth of microbes. Quaternary ammonium salts (QASs) are widely used as disinfectants to control microbial growth. Both ionic and hydrophobic interactions between the QASs and microbial walls or cytoplasmic membranes lead to cell death or malfunctions in cellular processes [1]. However, low-molecular-weight QASs suffer from many disadvantages, including toxicity to the environment and short-lived antimicrobial activity [2]. Therefore, antimicrobial agents are often designed to contain reactive functional groups for covalent linkage to polymers.

Polymers with antimicrobial groups chemically bonded to the polymer chain have attracted a great deal of attention, as they effectively inhibit the growth of bacteria and other microbes without releasing toxic low-molar-mass compounds to the environment. The strong antimicrobial potency of these polymers is a

result of the high local concentration of active groups [2–4]. Their antimicrobial activity is attributed to the destructive interaction through electrostatic forces with the negatively charged microbial cell wall, cytoplasmic membrane, or both [2].

Among the polycationic antimicrobial agents, polysiloxanes are particularly attractive, as they show exceptionally high static and dynamic flexibility in many solvents as well as high permeability and unusual surface properties. All of these features make the QAS groups attached to the backbone readily available for the destructive interaction with microbial walls [5,6]. In addition, polysiloxanes are physiologically inert, chemically stable and, after modification with the ionic QAS groups, water-soluble [1].

To our knowledge, although polysiloxane QASs [5–10] are effective for inhibiting bacteria that cause diseases in humans and animals, few reports have been published about QAS-containing polysiloxanes as antifungal polymers applied to control phytopathogenic fungi that cause plant diseases.

To this end, in this paper, we synthesized dimethylaminopropyl benzyl chloride grafted polysiloxanes (PDMS-g-BCs) with tunable molecular weights and cationic content through three steps, and systematically investigated the structure and antibacterial (gram-positive bacteria *Staphylococcus albus* (*S. albus*) and the gram-negative bacteria *Escherichia coli* (*E. coli*)) and antifungal

* Corresponding authors. Tel./fax: +86 20 8711 2466.

E-mail addresses: linyaling@scau.edu.cn (Y. Lin), aqzhang@scut.edu.cn (A. Zhang).

(phytopathogenic fungi, including rice sheath blight pathogen (*Rhizoctonia solani*, *R. solani*) and banana fusarium wilt (*Fusarium oxysporum* f. sp. *cubense* race 4, *Foc4*)) properties of the PDMS-g-BCs.

2. Experimental

2.1. Materials

Benzalkonium chloride (dodecylbenzyltrimethylammonium chloride) and Karstedt's catalyst were supplied by Aladdin Reagent Co Ltd. (Shanghai, China). Octamethylcyclotetrasiloxane (D_4 , 99%) and 1,1,1,3,3,3-hexamethyldisiloxane (MM, 98%) was supplied by Dow Corning in USA. 1,3,5,7-tetramethylcyclotetrasiloxane (D_4^H , 99%) was supplied by Hangzhou Sloan Materials Technology Co, Ltd. (Hangzhou, China). Strong-acid cation exchange resin (Purolite® CT175) was supplied by Purolite (China) Co Ltd. N,N-dimethylallylamine (DMAA, 98%) was supplied by Haining Huangshan Chemical Co Ltd. (Haining, China). Beef extract was supplied by Sinopharm Chemical Reagent Co Ltd. (Shanghai, China). Peptone was supplied by Guangdong Ring Kay Microbial Technology Co Ltd. (Guangzhou, China). Agar was supplied by MYM Biological Technology Company (Shanghai, China). RPMI-1640 liquid medium was supplied by America Hyclone Company. All of the microorganisms were kindly supplied by the Fungus Laboratory, Department of Plant Pathology, South China Agricultural University.

2.2. Synthesis of benzyldimethylaminopropyl chloride grafted polysiloxane (PDMS-g-BC)

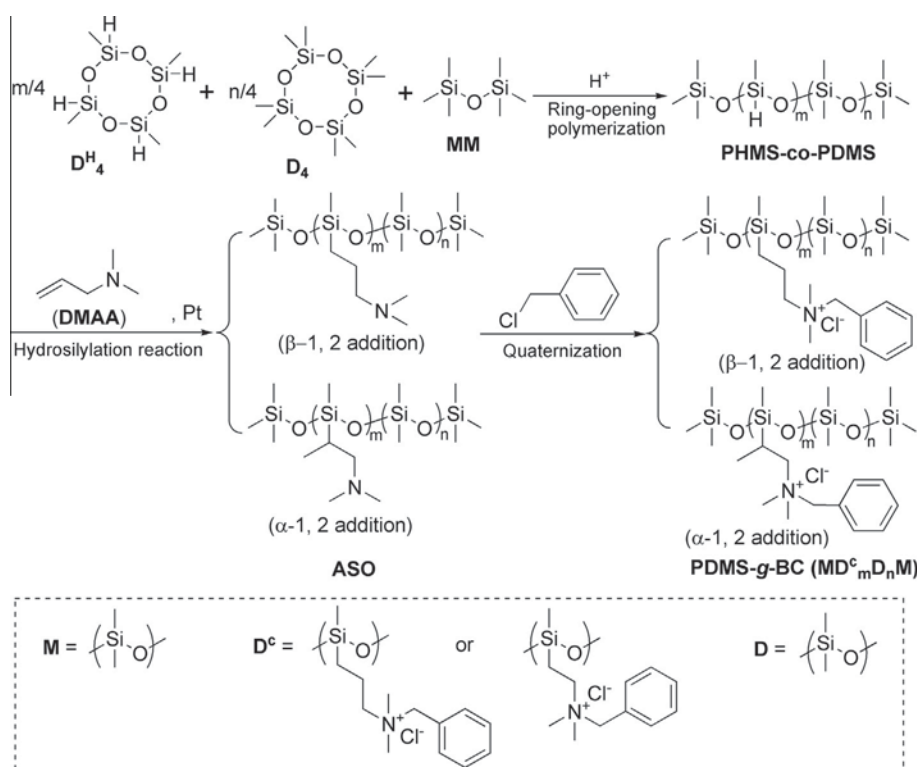
PDMS-g-BC series were prepared through the three-step process presented in Scheme 1.

Poly(hydromethylsiloxane-co-dimethylsiloxane) terminated by trimethylsiloxane groups (PHMS-co-PDMS) was synthesized by ring-opening polymerization. Calculated D_4 , D_4^H , MM and Purolite® CT175 (1 wt.%) were charged into a three-necked flask and stirred at 65 °C under a nitrogen atmosphere for 12 h. Then, the mixture was

filtered to remove the catalyst, and the volatile oligomers were distilled off under reduced pressure at 150 °C. ^1H NMR (400 MHz, CDCl_3 , δ , ppm): 0.07–0.09 (m, Si- CH_3), 4.68 (s, Si-H). FT-IR (ν , cm^{-1}): 2154 ($\nu_{\text{Si-H}}$), 1260 ($\nu_{\text{Si-CH}_3}$), 1027–1094 ($\nu_{\text{Si-O-Si}}$).

Tertiary amine substituted silicone oil (ASO) was obtained by the hydrosilylation reaction between PHMS-co-PDMS and DMAA. First, calculated N,N-dimethylallylamine (DMAA) and Karstedt's catalyst was charged into a three-neck flask equipped with a condenser, a magnetic stirrer and a nitrogen inlet. After purging the flask with nitrogen, PHMS-co-PDMS was dripped via the dropping funnel, and the mixture was heated to 100 °C. During the course of the reaction, samples were removed periodically, and conversions were monitored by FT-IR spectroscopy. The reaction was conducted until no Si-H absorption (2154 cm^{-1}) was detected by FT-IR spectroscopy. Then, the resulting mixture was distilled under reduced pressure to remove the remaining DMAA. ^1H NMR (400 MHz, CDCl_3 , δ , ppm): 0.05–0.09 (m, Si- CH_3), 0.49 (t, Si- CH_2CH_2), 0.91 (m, Si-CH), 0.98 (d, $\text{CH}_3\text{-CH}$), 1.51 (m, $\text{CH}_2\text{-CH}_2\text{-CH}_2$), 2.17–2.22 (m, $\text{N}^+(\text{CH}_3)_2$), 2.27 (m, $\text{CH}_2\text{-CH}_2\text{-CH}_2$). FT-IR (ν , cm^{-1}): 2771 ($\nu_{\text{N}(\text{CH}_3)_2}$), 1260 ($\nu_{\text{Si-CH}_3}$), 1027–1094 ($\nu_{\text{Si-O-Si}}$).

Benzyldimethylaminopropyl chloride grafted polysiloxane (PDMS-g-BC) was synthesized by the quaternization reaction. ASO and anhydrous ethanol were charged into a three-necked flask with a condenser, a magnetic stirrer and a nitrogen inlet, and the mixture was heated to 90 °C under nitrogen. Then, benzyl chloride (BC) dissolved in anhydrous ethanol was dripped via the dropping funnel, and the reaction was maintained at 90 °C for 30 h. After removing the solvent, the resulting product was dissolved in distilled water and washed with petroleum ether several times to remove the remaining BC. Finally, the mixture was subjected to rotary evaporation and vacuum drying to obtain a purified product of PDMS-g-BC. For simplicity of nomenclature, each polymer was given a letter based on its cationic content and molecular weight. For example, PDMS-g-BC_{17L}, composed of 17 mol% quaternary ammonium units, was named 17L, with "L" representing low molecular weight and the "17" representing mole percentage of



Scheme 1. Synthesis of PDMS-g-BCs.

Table 1

Characterization of PDMS-g-BCs with different molecular weights and cationic content.

Samples	MD _m D _n M	Molecular weight (g/mol)	m/(m + n)	Yield (%)
PDMS-g-BC _{17L}	MD ₅ D ₂₀ M	2700	1/6	58.6
PDMS-g-BC _{20L}	MD ₄ D ₁₆ M	2400	1/5	61.9
PDMS-g-BC _{25L}	MD ₄ D ₁₂ M	2100	1/4	62.5
PDMS-g-BC _{33L}	MD ₅ D ₈ M	1800	1/3	63.7
PDMS-g-BC _{50L}	MD ₈ D ₈ M	2900	1/2	53.4
PDMS-g-BC _{17H}	MD ₁₀ D ₅₀ M	6600	1/6	23.3
PDMS-g-BC _{20H}	MD ₁₂ D ₄₈ M	7000	1/5	6.5
PDMS-g-BC _{25H}	MD ₁₆ D ₄₈ M	8100	1/5	18.25

quaternary ammonium salt units. Similarly, the letter “H” represented the high-molecular-weight polymers. The characterization of PDMS-g-BC is presented in Table 1. ¹H NMR (400 MHz, D₂O, δ, ppm): 0.06 (m, Si–CH₃), 0.53 (m, Si–CH₂CH₂), 1.01 (m, Si–CH), 1.22 (d, CH₃–CH), 1.84 (m, CH₂–CH₂–CH₂), 2.98 (m, N⁺(CH₃)₂), 3.15 (m, CH₂–CH₂–CH₂), 4.41 (s, CH₂–Φ), 7.48 (s, Φ–H). FT-IR (ν, cm^{−1}): 3010 (ν_{Φ-H}), 1260 (ν_{Si-CH₃}), 1082 (ν_{Si-O-Si}), 704, 736 (ν_{Φ-H}).

2.3. Characterization

FT-IR spectra were obtained with a VERTEX spectrometer (Bruker Instrument Corp., Germany) by the KBr disk method. ¹H NMR spectra were obtained using an AV-400 FT-NMR (Bruker Instrument Corp., Germany) and D₂O or CDCl₃ as a solvent. GPC experiments were performed in chloroform (1 mL/min) at room temperature with an Elite EC2000 GPC apparatus (Dalian, China) equipped with a Shodex K-G guard column and a Shodex K-804L chromatographic column. The molecular weights were estimated with a polystyrene calibration.

2.4. Antimicrobial tests

2.4.1. Test microorganisms

The microorganisms included the gram-positive bacteria *S. albus* and the gram-negative bacteria *E. coli*. The phytopathogenic fungi associated with plant diseases included the rice sheath blight pathogen (*R. solani*) and the banana fusarium wilt (*Foc4*).

2.4.2. Media

Beef extract peptone medium was used as the growth medium for the tested bacteria and was prepared as follows: 3.0 g of beef extract, 10.0 g of tryptone, and 5.0 g of NaCl were added into 1000 mL of distilled water and heated to dissolve, and the solution's pH was adjusted to 7.0. To the solution, 15–20 g of agar powder was added to obtain solid medium. Then, the medium was sterilized by autoclaving (HVE-50, Japan Hirayama Corporation) at 121 °C for 20 min and cooled down.

Potato dextrose agar (PDA) was used as the growth medium for the tested fungi, and the PDA was prepared as follows: 200 g of sliced potato was boiled in water for 30 min, and the liquid was then strained through a cheese-cloth. Distilled water was added to adjust the total volume of suspension to 1000 mL, and then 20 g of dextrose and 15 to 20 g of agar powder were added. Finally, the medium was transferred to a flask, sealed, sterilized by autoclaving at 121 °C for 30 min and cooled down.

RPMI-1640 liquid medium was obtained by buffering RPMI-1640 (with L-glutamine and without bicarbonate) with 10 M NaOH to pH 7.0; the medium was sterilized by filtering with a 0.22-μm membrane.

2.4.3. Determination of minimum inhibitory concentration (MIC)

The antibacterial properties of PDMS-g-BCs against *E. coli* and *S. albus* were quantitatively evaluated using the broth dilution

method [11]. Bacterial growth rates were determined by measuring the optical density at 600 nm (OD₆₀₀) using a UV-vis spectrophotometer (UV-2300, Shanghai Techcomp Instrument Co Ltd.) based on the turbidity of the cell suspension. The minimum inhibitory concentration (MIC) against the tested bacteria was defined as the concentration of PDMS-g-BC at which bacterial growth was completely inhibited. The main procedures were as follows. The sterilized tubes were grouped and bundled according to concentrations; each group consisted of four bundles, and each bundle consisted of a number of branches (number determined by the sampling time), of which three bundles were parallel experiments, and the fourth was the control. Different concentrations of the sample solution were added to the corresponding tubes: 4 mL was added into the reference group, and 2 mL was added into the parallel group; then, 2 mL of the bacteria suspension was charged into the parallel group, and 4 mL of medium was charged into the reference group. The initial optical density (OD₆₀₀) from one tube from each bundle was tested using an UV spectrophotometer, with the solution in the corresponding reference tube as the reference solution. The remaining tubes were incubated at 37 °C in a shaker incubator (DHZ-D, Taicang Experimental Equipment Factory, China) under 120 rpm. During incubation, the OD₆₀₀ of one tube from each bundle was tested to record the bacterial suspension concentration. The MIC was the lowest concentration at which there was no visible growth of bacteria, i.e. the OD₆₀₀ did not change with time compared with the initial value.

2.4.4. Determination of mycelial growth inhibition

The antifungal activities of the samples were tested by the inhibition of mycelial growth. To prepare solutions of different concentrations, the samples were dissolved in sterilized water, mixed with PDA and poured onto sterile Petri dishes (with diameter of 9 cm). Control plates consisted of PDA only. A 5-mm disc containing mycelia was transferred to the center of the PDA plate containing the samples and incubated at 28 °C. Sterilized water was used as a negative control. Each experiment was conducted in three replicates. The diameter of fungal colonies was measured three times and averaged. Growth inhibition was calculated according to Formulas (1) and (2).

$$\text{Radial growth (mm)} = \text{The average fungi colony diameter (mm)} - 5 \text{ mm} \quad (1)$$

$$\text{Mycelia growth inhibition} = (C - T)/T \times 100\% \quad (2)$$

whereby C = radial growth of fungi in the control plate, T = radial growth of fungi in the treatment plate.

2.4.5. Determination of minimum inhibitory concentration (MIC) and minimum fungicidal concentration (MFC)

Foc4 was chosen as the tested microorganism to determine the MIC and MFC values of the samples. *Foc4* microorganisms were incubated at 28 °C for 7 days in PDA medium; the fungal suspension was prepared by adding 1 mL of 0.85% saline containing 0.01 mL of Tween 20 to the incubated colony. Then, the upper homogeneous liquid was transferred to a sterilized tube and diluted with RPMI-1640 liquid medium to give inoculation suspensions of 0.4×10^4 – 5×10^5 CFU/mL with twice the final concentration. The broth microdilution method was used to determine the MIC of the samples. The samples were dissolved in water and diluted in RPMI-1640 medium. The sample solution (100 μL) with concentrations ranging from 5×10^{-5} to 3 mg/mL was added into 96-well plates. The same volume of mycelial suspension containing approximately 0.4×10^4 – 5×10^5 CFU/mL was incubated at 28 °C for 46–50 h. In addition, a reference liquid medium without samples was used as a negative control. MIC was measured at least

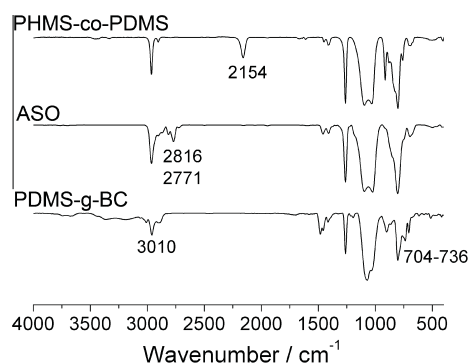


Fig. 1. FT-IR spectra of PHMS-co-PDMS, ASO and PDMS-g-BC.

three times and recorded as the lowest concentration that completely inhibited visible growth [12].

The MFC test was the most common estimation of fungicidal activity and was defined as the lowest concentration of antimicrobial agent needed to kill 99.9% of the initial inoculums after incubation [13]. To determine the MFC, 100 μ L from each of the wells at or above the MIC was plated on PDA and incubated at 28 $^{\circ}$ C for 48 h. The MFC was defined as the lowest concentration at which no colonies were detected on the PDA.

3. Results and discussions

3.1. Design, synthesis and characterization of PDMS-g-BC

By designing and synthesizing a series of polysiloxane QASs with controllable compositions, we examined the relationship between antimicrobial activities and the structure (molecular weight and cationic content) of polysiloxane QASs. Polysiloxane QASs possess rather flexible hydrophobic backbones, allowing potent antimicrobial activities to be achieved by finely tuning the molecular weight and cationic content. Thus, polysiloxane QASs (PDMS-g-BCs) were synthesized through three steps as described in Scheme 1. First, PHMS-co-PDMS was synthesized by the ring-opening polymerization of D_4 , D_4^H and MM, followed by a hydrosilylation reaction between PHMS-co-PDMS and *N,N*-dimethylallylamine (DMAA). PDMS-g-BC was finally obtained after the quaternization

of ASO with benzyl chloride (BC). The chemical structures of products were confirmed by FT-IR and 1 H NMR spectroscopy.

By adjusting the mole ratio of D_4 , D_4^H and MM, a series of PHMS-co-PDMS with various molecular weights and hydrogen content were synthesized by ring-opening polymerization. As shown in Figs. 1 and 2, the adsorption peaks at 2154, 1260, 1094 and 1027 cm^{-1} represented the stretching vibration of Si–H, Si–CH₃ and Si–O–Si, respectively, and the signal of Si–H protons appeared at $\delta = 4.68$ ppm and Si–CH₃ protons at $\delta = 0.07$ –0.09 ppm. The molecular weights of PHMS-co-PDMSs were determined by GPC, and the low- and high-molecular-weight serial PHMS-co-PDMSs varied from approximately 1600 to 2500 and from approximately 6300 to 7900, respectively.

ASO was synthesized by the hydrosilylation reaction of PHMS-co-PDMS with DMAA in the presence of Karstedt's catalyst. The disappearance of Si–H absorption (at 2154 cm^{-1}) and the appearance of $N(\text{CH}_3)_2$ (at 2816 and 2771 cm^{-1}) in the FT-IR analysis (Fig. 1) and the disappearance of a Si–H proton (at $\delta = 4.68$ ppm) and the appearance of a series of C–H protons in 1 H NMR analysis (Fig. 2) confirmed the reaction of PHMS-co-PDMS with DMAA leading to ASO.

A series of PDMS-g-BCs were obtained by the quaternization reaction between ASO and benzyl chloride (BC). In the FT-IR analysis (Fig. 1), Φ -H absorption at 704–736 and 3010 cm^{-1} appeared, and $N(\text{CH}_3)_2$ absorption at 2816 and 2771 cm^{-1} disappeared. In the 1 H NMR analysis (Fig. 2), after the quaternization reaction, the $N(\text{CH}_3)_2$ protons signals shifted from approximately 2.20 ppm to 2.98 ppm completely, and the characteristic protons signals of BC ($\delta = 4.41$ ppm and $\delta = 7.48$ ppm) appeared, which indicated the structure of PDMS-g-BC agreed well with our expectation. The characterization of PDMS-g-BC is presented in Table 1.

3.2. Antibacterial activities of PDMS-g-BCs

To investigate the antibacterial properties (MIC values) of PDMS-g-BCs, different concentrations of PDMS-g-BCs were added to the medium. Bacterial growth was monitored by measuring the optical density at 600 nm (OD_{600}) based on the turbidity of the cell suspension. In this experiment, OD_{600} curves were recorded in different concentrations of PDMS-g-BCs with medium, and the effect of PDMS-g-BCs on the bacterial growth was assessed from the curves. Taking PDMS-g-BC_{17L} (Fig. 3(A)) as an example, bacteria were first grown to $\text{OD}_{600} = 0.2$, and the bacterial growth

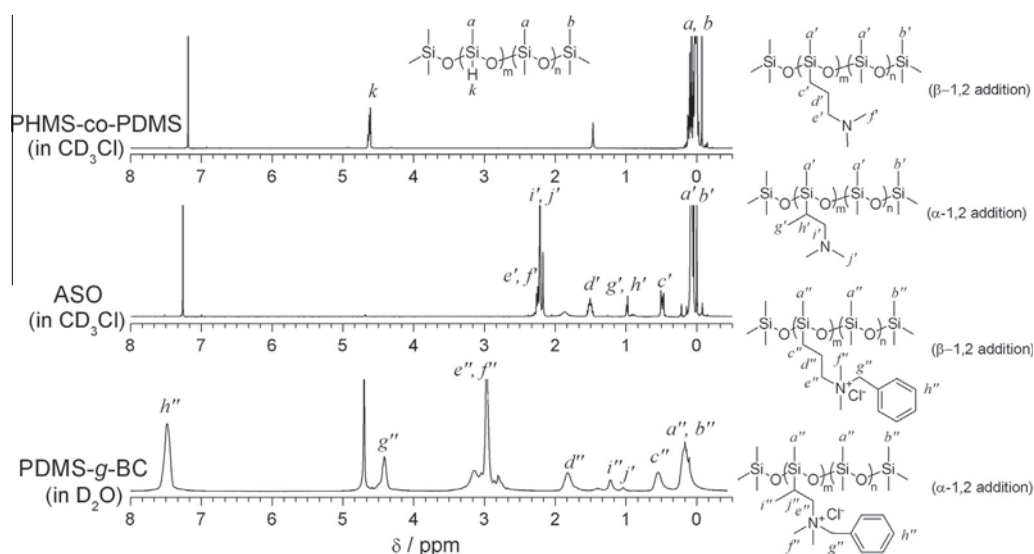


Fig. 2. 1 H NMR spectra of PHMS-co-PDMS, ASO and PDMS-g-BC.

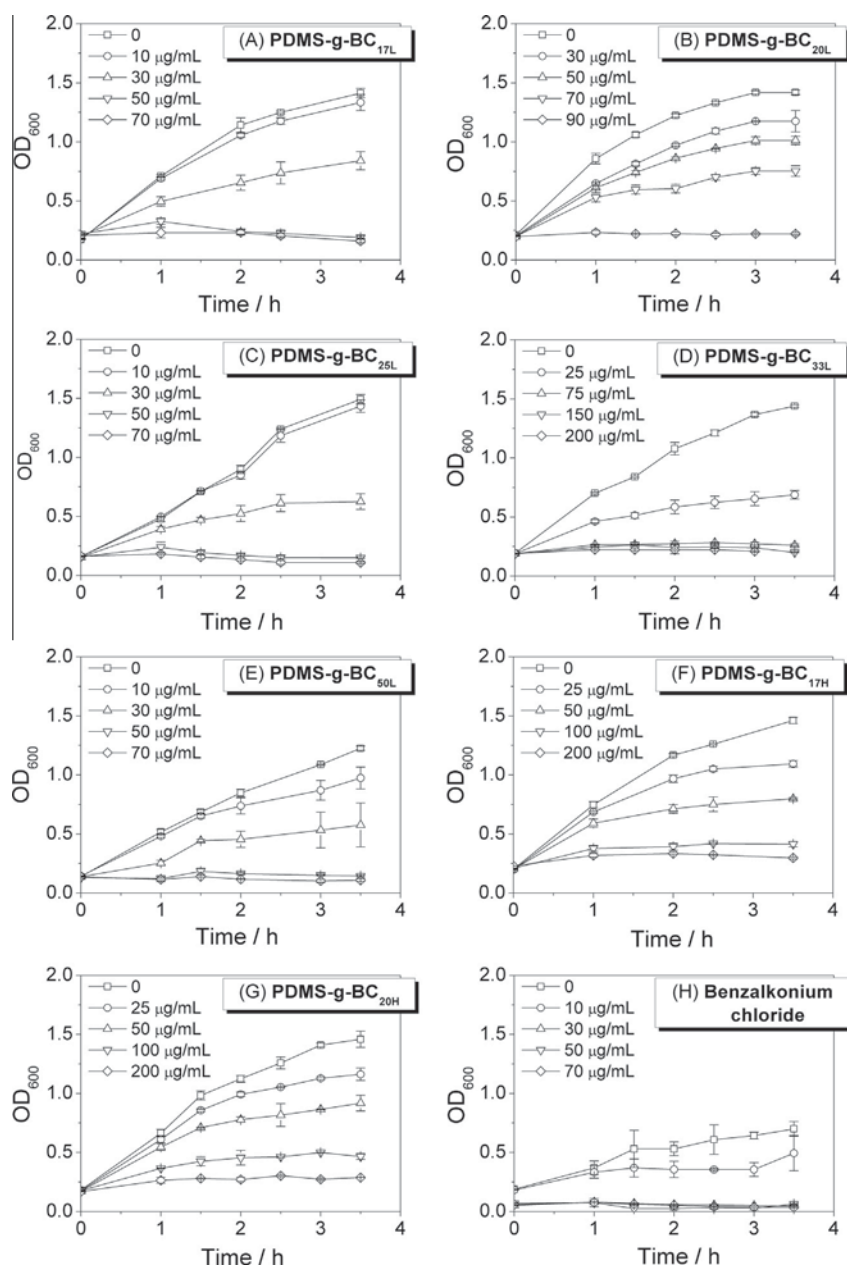


Fig. 3. MIC values for PDMS-g-BC and benzalkonium chloride against *E. coli*: (A) PDMS-g-BC_{17L}, (B) PDMS-g-BC_{20L}, (C) PDMS-g-BC_{25L}, (D) PDMS-g-BC_{33L}, (E) PDMS-g-BC_{50L}, (F) PDMS-g-BC_{17H}, (G) PDMS-g-BC_{20H}, and (H) benzalkonium chloride.

slowed as the concentration of PDMS-g-BC_{17L} increased, indicating that 10 $\mu\text{g/mL}$ was able to slow the growth of *E. coli*. When the concentration of PDMS-g-BC_{17L} was increased to 50 $\mu\text{g/mL}$, the bacterial growth was completely inhibited. Thus, the minimal inhibition concentration (MIC) of PDMS-g-BC_{17L} was 50 $\mu\text{g/mL}$ against *E. coli*.

The MIC values for PDMS-g-BCs against *E. coli* and *S. albus* are shown in Figs. 3 and 4, and the results are summarized in Tables 2 and 3.

As shown in Table 2, low-molecular-weight PDMS-g-BC_L (except PDMS-g-BC_{33L}) had low MIC values compared to those of benzalkonium chloride (dodecylbenzyltrimethylammonium chloride, a broad-spectrum and highly effective biocide, widely used in medical or industrial treatment), in which PDMS-g-BC_{25L} and PDMS-g-BC_{17L} had the best antibacterial effect, with MIC values of 50 $\mu\text{g/mL}$. Additionally, MIC values varied with cationic content, but there was no direct correlation between cationic content and MIC values.

MIC values of PDMS-g-BC_L demonstrated the importance of cationic content, hydrophobicity and molecular weight in the antimicrobial performance of polysiloxane QASs. PDMS-g-BC_L (except for PDMS-g-BC_{33L}) had potent antibacterial activities against *E. coli*, with the cationic content ranging between 17% and 50%, and the molecular weight of approximately 2500 g/mol. In addition, the molecular weight of polycations has been shown to profoundly impact the efficacy of many antimicrobial quaternized macromolecular systems, and an optimal molecular weight range exists for the biocidal action of polycations. Generally, the antimicrobial properties of conventional polymer biocides have a bell-shape dependence on molecular weight, while dendrimer biocides have a parabolic dependence. Ikeda found that the antibacterial activities of polycations strongly depended on molecular weight and had a bell-like shape [14]. Cooper and co-workers discovered a parabolic dependence on the molecular weight of the antimicrobial properties of the quaternary ammonium functionalized poly(pro-

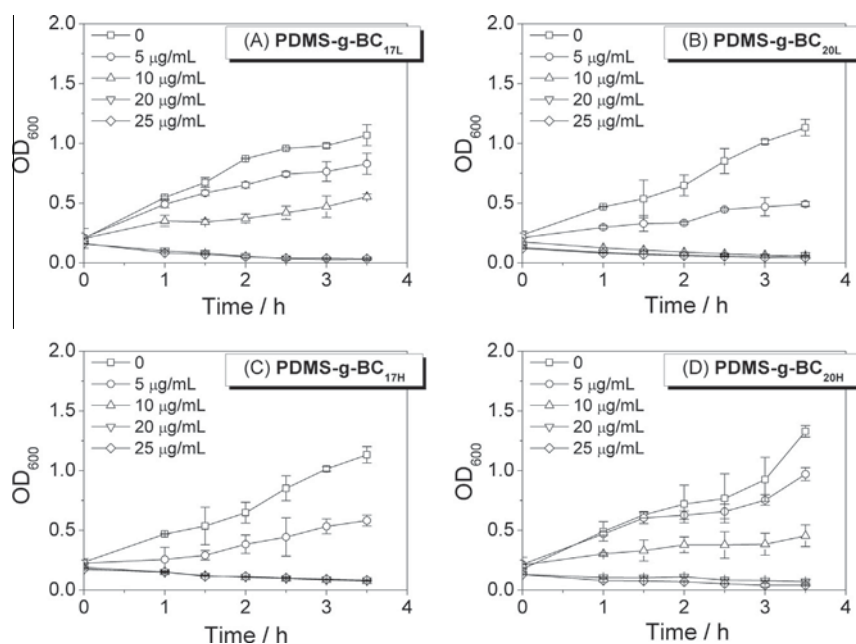


Fig. 4. MIC values for PDMS-g-BC against *S. albus*: (A) PDMS-g-BC_{17L}, (B) PDMS-g-BC_{20L}, (C) PDMS-g-BC_{17H}, (D) PDMS-g-BC_{20H}.

Table 2

MIC values of PDMS-g-BCs against *E. coli*.

Samples	Molecular weight (g/mol)	MIC (µg/mL)
PDMS-g-BC _{17L}	2700	50
PDMS-g-BC _{20L}	2400	90
PDMS-g-BC _{25L}	2100	50
PDMS-g-BC _{33L}	1800	200
PDMS-g-BC _{50L}	2900	70
PDMS-g-BC _{17H}	6600	200
PDMS-g-BC _{20H}	7000	200
Benzalkonium chloride	340	30

Table 3

Comparison of MIC values of PDMS-g-BCs against *E. coli* and *S. albus*.

Samples	MIC (µg/mL)	
	<i>E. coli</i>	<i>S. albus</i>
PDMS-g-BC _{17L} (<i>M</i> ~ 2700)	50	20
PDMS-g-BC _{20L} (<i>M</i> ~ 2400)	90	5
PDMS-g-BC _{17H} (<i>M</i> ~ 6600)	200	20
PDMS-g-BC _{20H} (<i>M</i> ~ 7000)	200	100

pyleneimine) dendrimers [3]. In our report, by comparing MIC values of low-molecular-weight PDMS-g-BC_L with high-molecular-weight PDMS-g-BC_H, we found that PDMS-g-BC_H had weaker antibacterial activities (displayed by higher MIC values) compared with those of PDMS-g-BC_L.

From Table 3, we found that PDMS-g-BCs showed lower MIC values against *S. albus* than against *E. coli*, which suggests that PDMS-g-BCs were more active against gram-positive bacteria *S. albus* than against gram-negative *E. coli* because of the difference in the structure of their cell walls [5,15]. Gram-positive bacteria possess a loosely packed polyglycane outer layer, which facilitated the deep penetration of PDMS-g-BC chains inside of the cell to interact with the cytoplasmic membrane, whereas gram-negative bacteria, with an additional membrane outside, protect the inner cytoplasmic membrane to a greater extent against the disruptive action of PDMS-g-BCs.

Polymers with QASs require sufficient hydrophobicity to impart substantial antimicrobial activity. In this article, the route of using

a flexible polysiloxane backbone was successful in endowing poly-cations with antibacterial properties as potent as those of the widely used broad-spectrum biocide (benzalkonium chloride). The high activity of the polysiloxane QASs can be explained by the larger conformational freedom of their chains, which was substantial in flexible dimethylsiloxane units. The high flexibility of the polymer chains facilitated the contact of the QAS groups with the microorganism, allowing polymers to adopt conformations favorable for the interaction with the bacterial wall [5,16,17]. Another important point is their amphiphilic character, with the hydrophilic inorganic portion and the hydrophobic organic groups, which augmented the concentration of the QAS groups in the vicinity of the microorganism cell wall.

3.3. Antifungal activities of PDMS-g-BCs

3.3.1. Effect of PDMS-g-BCs on mycelia growth of phytopathogenic fungi

Antifungal activities of PDMS-g-BC series were tested by the disc diffusion method. Fig. 5 displays the antifungal effect of PDMS-g-BCs against *R. solani* and *Foc4*, and the results are summarized in Fig. 6.

Fig. 6 demonstrates the antifungal activities of low-molecular-weight PDMS-g-BC_L against two phytopathogenic fungi, *R. solani* and *Foc4*. All of the samples exhibited a concentration-dependent inhibitory effect on the hyphal growth of *R. solani* and *Foc4*. When using a concentration of 1.6 mg/mL, there was a marked mycelial growth inhibition for PDMS-g-BC_{17L}, PDMS-g-BC_{20L}, PDMS-g-BC_{25L}, PDMS-g-BC_{33L} and PDMS-g-BC_{50L}, with a mycelial growth inhibition of approximately 80%. In particular, PDMS-g-BC_{25L} showed the highest activity toward both *R. solani* and *Foc4*. In addition, all PDMS-g-BCs exhibited significantly better inhibition ability against *R. solani* than against *Foc4*.

The effects of molecular weight on antifungal activity are evaluated in Figs. 7 and 8. The antifungal activity of higher-molecular-weight PDMS-g-BC_H tended to decrease compared to that of lower-molecular-weight PDMS-g-BC_L with the same cationic content.

Based on the above results, it is reasonable to infer that PDMS-g-BCs with relatively lower cationic content (20 mol% of the total

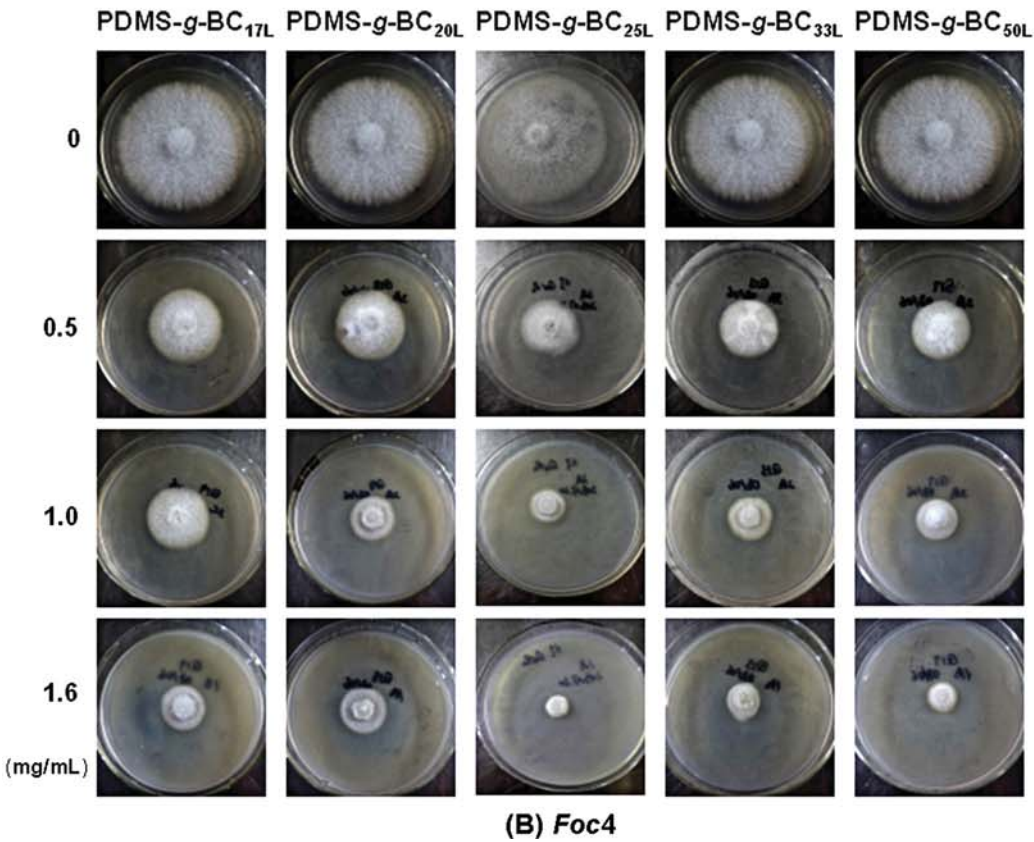
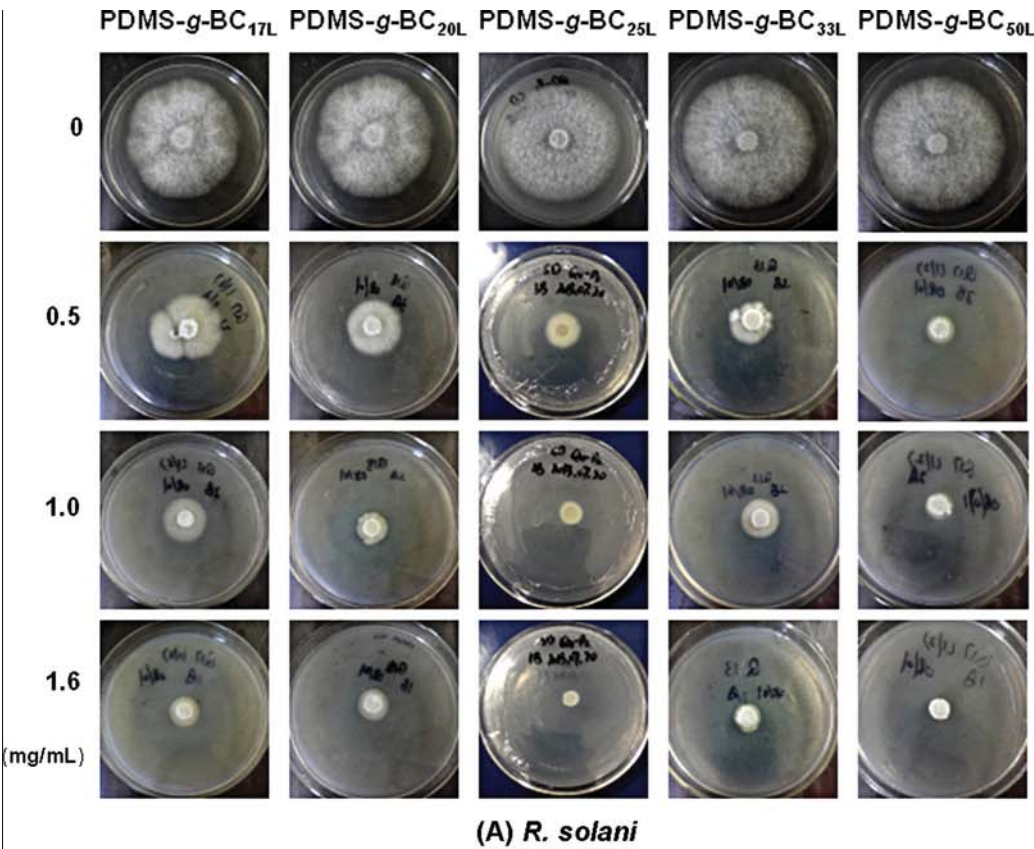


Fig. 5. Antifungal effects of PDMS-g-BC_L against (A) *R. solani* and (B) *Foc4*.

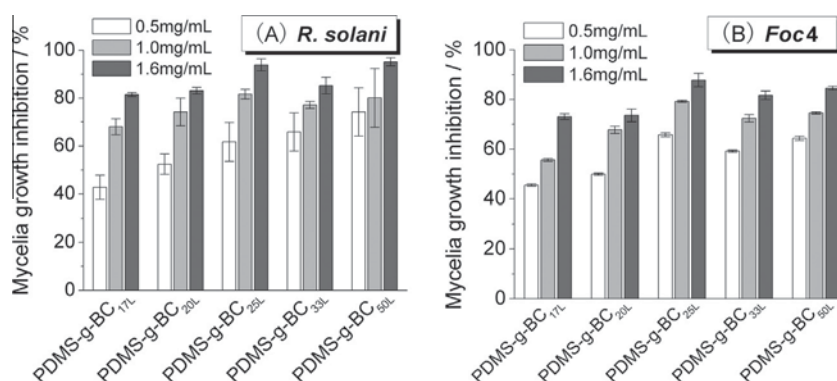


Fig. 6. Mycelial growth inhibition of PDMS-g-BC_L against (A) *R. solani* and (B) *Foc4*.

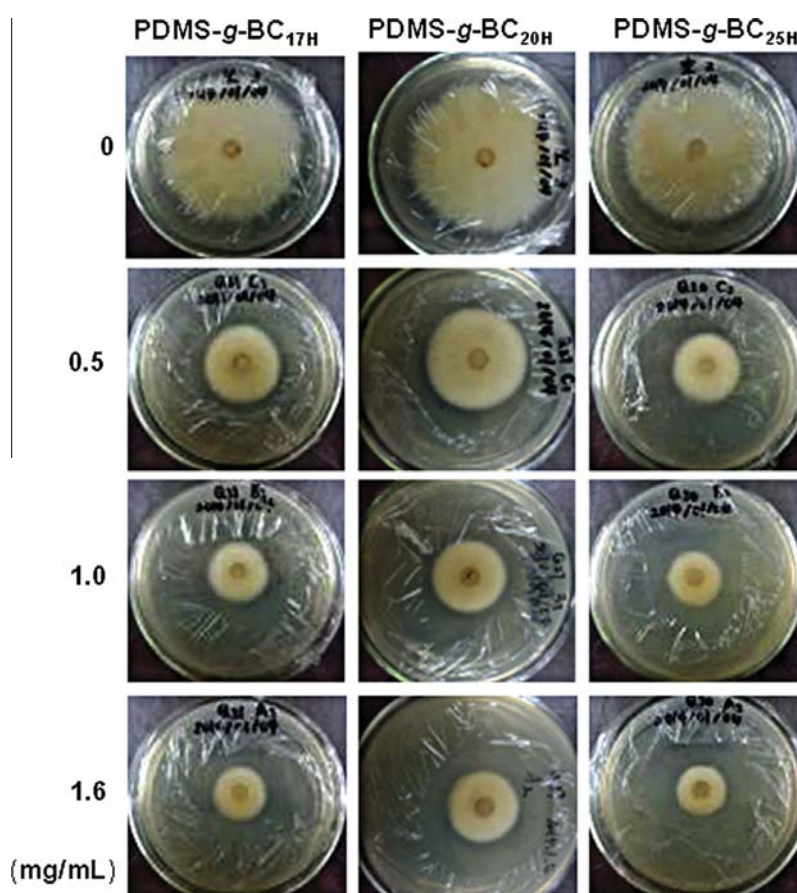


Fig. 7. Antifungal effects of PDMS-g-BC_H against *Foc4*.

siloxane units) and lower molecular weight (2500 g/mol) exhibit high inhibitory activity against the phytopathogenic fungi *Foc4*.

3.3.2. Minimum inhibitory concentration (MIC) and minimum fungicidal concentration (MFC) of PDMS-g-BC against *Foc4*

Based on the above results, the inhibitory effects of acrylamide QASs against *Foc4* were further estimated by the microdilution broth method. MIC was the minimum concentration that could completely inhibit fungal growth; MFC was the lowest concentration at which 99.9% of the fungi could be killed. The MFC/MIC ratio reflects the fungicidal activity of an antimicrobial agent: an antimicrobial agent has fungicidal activity when the MFC/MIC ratio is less or equal to 4, whereas an antimicrobial agent

only has fungistatic activity when the MFC/MIC ratio was greater than 4.

A series of sample solutions with concentration ranging from 0.05 to 3000 µg/mL mixed with a *Foc4* suspension was incubated in 96-well plates at 28 °C for 46–50 h. (MIC was defined as the lowest concentration that completely inhibited visible growth). The mixed liquid in each of the wells at or above the MIC was plated on PDA and incubated at 28 °C for 48 h, and MFC was defined as the lowest concentration at which no colony was detected.

PDMS-g-BCs had different molecular weights and cationic content, which indeed resulted in differences in their antifungal activities. The antifungal results, expressed in MIC and MFC values against *Foc4*, are grouped in Table 4.

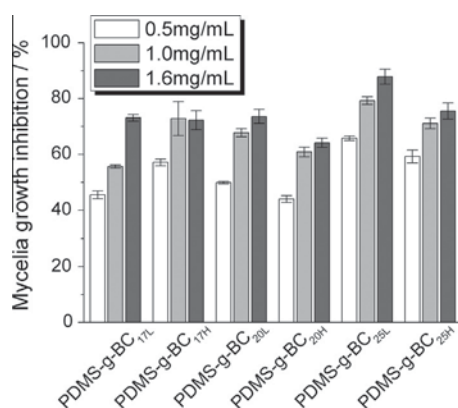


Fig. 8. Mycelial growth inhibition of PDMS-g-BC_L and PDMS-g-BC_H against *Foc4*.

Table 4
MIC and MFC values of PDMS-g-BCs against *Foc4*.

Samples	Molecular weight (g/mol)	MIC (μg/mL)	MFC (μg/mL)	MFC/MIC
PDMS-g-BC _{17L}	2700	5	25	5
PDMS-g-BC _{20L}	2400	5	5	1
PDMS-g-BC _{33L}	1800	250	1000	4
PDMS-g-BC _{50L}	2900	100	250	2.5
PDMS-g-BC _{17H}	6600	250	500	2
PDMS-g-BC _{20H}	7000	250	1000	4
PDMS-g-BC _{25H}	8100	50	100	2
Benzalkonium chloride	340	5	25	5

Low-molecular-weight PDMS-g-BC_L, PDMS-g-BC_{17L} and PDMS-g-BC_{20L} demonstrated better antifungal activities, with MIC and MFC values of 5.25 μg/mL and 5.5 μg/mL, respectively, compared to that of benzalkonium chloride (dodecyl benzyl dimethyl ammonium chloride), with MIC and MFC values of 5.25 μg/mL. Similar to the antibacterial effect of PDMS-g-BC_L, high-molecular-weight PDMS-g-BC_H had a molecular weight ranging from 6000 to 8000 g/mol but low antifungal effect, with MIC and MFC values between 50 and 1000 μg/mL. These results imply that a high molecular weight causes the loss of antifungal activity of PDMS-g-BCs, which is opposite to that of the quaternized chitosan [18]. The antifungal activities differed with regard to molecular weight and cationic content, and an appropriate molecular design of PDMS-g-BCs could strengthen their antifungal activity effectively. In addition, the MFC/MIC ratios of PDMS-g-BC_{20L}, PDMS-g-BC_{33L}, PDMS-g-BC_{50L}, PDMS-g-BC_{17H}, PDMS-g-BC_{20H} and PDMS-g-BC_{25H} are less than 4, implying that they are fungicidal agents.

4. Conclusions

In this experiment, benzyldimethylaminopropyl chloride grafted polysiloxane (PDMS-g-BCs) with tunable molecular weights and cationic content were synthesized successfully in

three steps. This paper systematically investigated the structure and antibacterial (gram-positive bacteria *S. albus* and gram-negative bacteria *E. coli*) and antifungal (phytopathogenic fungi, *R. solani* and *Foc4*) properties of the PDMS-g-BCs.

Antimicrobial results demonstrated the importance of cationic content and molecular weight in the antimicrobial performance of PDMS-g-BCs. With a cationic content of approximately 20 mol% of the total siloxane units and a molecular weight of approximately 2500 g/mol, PDMS-g-BC_L had great antimicrobial activities against *E. coli* and *Foc4* compared to that of a commonly used broad-spectrum microbicide benzalkonium chloride.

We conclude that polysiloxane QASs are worthy of further study as effective fungicidal agents to control plant diseases. Adequate control of phytopathogenic fungi growth using polysiloxane QASs requires an extensive knowledge of the factors that determine polysiloxane QAS performance.

Acknowledgments

The authors acknowledge financial support from the National Natural Science Foundation of China (Grants 31201552 and 51003032) and the Specialized Research Fund for the Doctoral Program of Higher Education (Grant 20124404120025).

References

- [1] G. Sauvet, S. Dupond, K. Kazmierski, J. Chojnowski, J. Appl. Polym. Sci. 75 (2000) 1005–1012.
- [2] E. Kenawy, S.D. Worley, R. Broughton, Biomacromolecules 8 (2007) 1359–1384.
- [3] C.Z. Chen, N.C. Beck-Tan, P. Dhurjati, T.K. van Dyk, R.A. LaRossa, S.L. Cooper, Biomacromolecules 1 (2000) 473–480.
- [4] A.M. Klivanov, J. Mater. Chem. 17 (2007) 2479–2482.
- [5] U. Mizerska, W. Fortuniak, J. Chojnowski, R. Hałasa, A. Konopacka, W. Werel, Eur. Polym. J. 45 (2009) 779–787.
- [6] K. Różga-Wijas, U. Mizerska, W. Fortuniak, J. Chojnowski, R. Hałasa, W. Werel, J. Inorg. Organomet. Polym. 17 (2007) 605–613.
- [7] P. Majumdar, J. He, E. Lee, A. Kallam, N. Gubbins, S.J. Stafslie, J. Daniels, B.J. Chisholm, J. Coat. Technol. Res. 7 (2009) 455–467.
- [8] U. Mizerska, W. Fortuniak, J. Chojnowski, K. Turecka, A. Konopacka, W. Werel, J. Inorg. Organomet. Polym. 20 (2010) 554–563.
- [9] L. Kou, J. Liang, X. Ren, H.B. Kocer, S.D. Worley, Y.M. Tzou, T.S. Huang, Ind. Eng. Chem. Res. 48 (2009) 6521–6526.
- [10] P. Majumdar, E. Crowley, M. Htet, S.J. Stafslie, J. Daniels, L. VanderWal, B. Chisholm, ACS Comb. Sci. 13 (2011) 298–309.
- [11] S.G. Chen, S.J. Chen, S. Jiang, Y.M. Mo, J.X. Luo, J.N. Tang, Z.C. Ge, Colloid Surf. B Biointerfaces 85 (2011) 323–329.
- [12] P. Plodpai, S. Chuenchitt, V. Petcharat, S. Chakthong, S.P. Voravuthikunchai, Crop Prot. 43 (2013) 65–71.
- [13] W. Sajomsang, P. Gonil, S. Saesoo, C. Ovatlarnporn, Int. J. Biol. Macromol. 50 (2012) 263–269.
- [14] T. Ikeda, H. Hirayama, H. Yamaguchi, S. Tazuke, M. Watanabe, Antimicrob. Agents Chemother. 30 (1986) 132–136.
- [15] T. Ikeda, S. Tazuke, Macromol. Chem. 185 (1984) 869–876.
- [16] W. Fortuniak, U. Mizerska, J. Chojnowski, T. Basinska, S. Slomkowski, M.M. Chehimi, A. Konopacka, K. Turecka, W. Werel, J. Inorg. Organomet. Polym. Mater. 21 (2011) 576–589.
- [17] P. Majumdar, E. Lee, N. Patel, S.J. Stafslie, J. Daniels, B.J. Chisholm, J. Coat. Technol. Res. 5 (2008) 405–417.
- [18] Z. Guo, R. Xing, S. Liu, Z. Zhong, X. Ji, L. Wang, P. Li, Carbohydr. Polym. 71 (2008) 694–697.

ISSN 1000-7555

CN 51-1293/06

CODEN GCKGEI

高分子材料 科学与工程

POLYMER MATERIALS SCIENCE & ENGINEERING

2013 Vol. 29 No. 11

目次

合成实验·工艺

- 正交试验法优化 BTDA-TDI/MDI 三元共聚聚酰亚胺聚合工艺 郭炳花, 陈 蕾, 于俊荣等(1)
- 超支化偶氮聚酯的合成及光致变色性能 冯宗财, 宋秀美, 王跃川等(6)
- 藻烷基端羟基聚醚的合成与表征 杜莉娟, 杨晓琴, 曾 韬等(10)
- 氧鎓离子法合成端羟基聚四氢呋喃-聚环氧丙烷嵌段共聚醚 汪存东, 潘洪波, 苏 玲等(15)
- 溶剂热法合成含异氰酸酯基的聚丙烯大分子相容剂 李 浩, 朱士洋, 张先明等(19)
- 聚氨酯/苯乙烯弹性体复合材料的合成及性能 赵亚丽, 李 莉, 李晓云等(24)
- 红外光谱法实时跟踪支化聚乙烯亚胺/甲基丙烯酸缩水甘油酯的官能团反应 茅群龙, 张 艳, 张 弢(28)

结构·性能

- 原位固相接枝 CaCO_3 /聚丙烯复合材料中界面相互作用与力学性能的关系 朱德钦, 生 瑜, 邹寅将等(31)
- 电袋复合除尘器内烟气成分对聚苯硫醚滤料的影响 黄 炜, 郑奎照, 郑辉东等(36)
- 预矿化丝素/壳聚糖复合支架的表征及细胞相容性 施李杨, 邓连霞, 杨明英等(42)
- 核壳型银/聚苯胺纳米复合材料的导电性能 李芝华, 华斯嘉, 卢健体(46)
- 液体橡胶增韧环氧树脂的力学性能及增韧机理 周恒石, 徐世爱(50)
- 氢氧化甲基丙烯酸锌/炭黑协同增强氢化丁腈橡胶硫化过程中的形态演变及性能 武守鹏, 纪彦玲, 徐文龙等(54)
- 石墨烯/碳纤维/聚偏氟乙烯导电复合材料的电性能 胡洪亮, 张 国, 陈 英等(58)
- 二元季铵盐化合物与明胶的相互作用 孟祥建, 崔月芝, 乔从德等(62)
- 多臂星形聚乙二醇-聚乳酸嵌段共聚物的降解特性 林雅铃, 吴敏儿, 邱艳舞等(67)
- 原位测量聚苯乙烯薄膜在溶剂气氛下的动态变化过程 李海东, 吕 鹤, 赖宇晴(71)
- 动态热机械分析法在材料耐老化性能分析中的应用 孟祥艳, 魏莉萍, 刘运传等(76)

材料测试·加工·应用

- 超高分子量聚乙烯-聚氨酯泡沫复合材料的抗爆实验与数值模拟 蔡军锋, 傅孝忠, 易建政(79)
- 模塑制品内部成型收缩特性的可视化测定方法 姜开宇, 孙合庆, 段 飞(84)
- 几种聚合物熔体黏度与超声波声速关系的表征 胡 坤, 王克俭(88)
- 基于响应面法的酚醛树脂固化条件优化 黄剑峰, 陈奶荣, 林巧佳等(92)
- 聚苯硫醚纤维氯甲基化反应条件的优化 周冬莉, 代立波, 惠跟雷等(97)
- 用于固体火箭发动机衬层固化过程监测的超声缓冲杆 杨亚军, 王召巴(101)

多臂星形聚乙二醇-聚乳酸嵌段共聚物的降解特性

林雅铃¹, 吴敏儿¹, 邱艳舞², 张安强²

(1. 华南农业大学资源环境学院制药工程系, 广东 广州 510642; 2. 华南理工大学材料科学与工程学院高分子系, 广东 广州 510641)

摘要:采用直接法合成了线型和多臂星形聚乙二醇-聚 L-乳酸嵌段共聚物((PLLA-b-PEG-b-PLLA 和 sPEG-b-PLLA)。研究了 3 种嵌段共聚物在 37 ℃、pH=7.2 的磷酸盐缓冲液中的降解机理。结果表明,共聚物降解后失重明显,亲水性降低;降解一定时间后共聚物的相对分子质量分布呈双峰分布,随着降解的进行,较低相对分子质量组分的相对分子质量并没有发生明显的变化。XRD 数据表明,降解前后的主要组成为结晶 PLLA 嵌段;¹H-NMR 分析证实,共聚物的降解过程中 PEG 嵌段和 PLLA 嵌段内部的降解程度很小。说明 sPEG-b-PLLA 在中性水性体系中的降解主要发生在连接 PLLA 和 PEG 的酯键上,而 PLLA 嵌段则由于处于结晶态,降解程度很低。

关键词:星形聚乙二醇-聚 L-乳酸嵌段共聚物;降解机理;结晶

中图分类号:TQ316.6⁺1

文献标识码:A

文章编号:1000-7555(2013)11-0067-04

聚乙二醇-聚乳酸嵌段共聚物(PEG-b-PLA)因其良好的两亲性、生物相容性和生物可吸收性,已被广泛应用于药物负载、组织工程等领域^[1~3]。与相同相对分子质量的线型共聚物相比,星形聚合物具有较小的流体力学体积,较高的热稳定性和较快的降解速率,更有利于药物的负载与输送。有关 PEG-PLA 嵌段共聚物的合成及降解已有广泛的研究^[3~8],但大部分的研究主要集中在不同形态的线型嵌段共聚物上,关于星形多臂 PEG-PLLA 共聚物降解行为的研究尚较少^[3]。本文在前期采用直接熔融缩聚法合成线型聚乙二醇-聚 L-乳酸三嵌段共聚物(PLLA-b-PEG-b-PLLA)和具有星形结构的多臂星形聚乙二醇-聚乳酸嵌段共聚物(sPEG-b-PLLA)的基础上,采用 FT-IR、GPC、¹H-NMR、接触角、降解失重等表征手段研究了上述线型和多臂星形 PEG-PLA 嵌段共聚物薄膜在中性 PBS 溶液(模拟体液)中的降解特性和降解规律。

1 实验部分

1.1 原料与试剂

线形聚乙二醇(PEG): $\bar{M}_n = 6000$, $\bar{M}_w/\bar{M}_n = 1.06$, Sigma-Aldrich 公司提供;四臂星形聚乙二醇(sPEG1): $\bar{M}_n = 0.43 \times 10^4$, $\bar{M}_w/\bar{M}_n = 1.05$, 黎明化工研究院提供;三臂星形聚乙二醇(sPEG2): $\bar{M}_n = 0.32 \times 10^4$, $\bar{M}_w/\bar{M}_n = 1.05$, 黎明化工研究院提供,使

用前用二氯甲烷溶解,冰乙醚沉析提纯 2 次,40 ℃真空干燥 48h 后备用;L-乳酸(LLA):耐热级,含水量约为 12%,武汉三江固德有限公司提供,采用文献[6]的方法制备得到提纯 LLA;辛酸亚锡($\text{Sn}(\text{Oct})_2$, 95%):Sigma-Aldrich 公司提供;pH=7.2 磷酸盐缓冲液(PBS):实验室配制;透析袋:截留相对分子质量 3500,上海绿鸟科技有限公司;其它试剂均为市售分析纯试剂。

1.2 仪器设备

Nicolet 6700 型红外光谱仪:美国 Thermo-Fisher 公司;Avance DRX-600 型核磁共振仪:瑞士 Bruker 公司;1515-2414 型凝胶渗透色谱仪:美国 Waters 公司;JC2000C 表面接触角分析仪:上海中晨数字技术设备有限公司;X' Pert Pro 型 X 射线衍射仪:荷兰 PANalytical 公司。

1.3 sPEG-b-PLLA 与 PLLA-b-PEG-b-PLLA 的合成

按文献[8]所述的方法合成。在装备冷凝器、机械搅拌的三口烧瓶中加入已提纯的 LLA 90g(1000 mmol),sPEG1 10g(2.33 mmol),按 LLA 质量的 1% 加入催化剂 $\text{Sn}(\text{Oct})_2$,从 120 ℃、10kPa 开始逐步升温聚合,每小时升温 5 ℃,至 165 ℃熔融聚合 9h。产物用二氯甲烷溶解、冰乙醚沉析 2 次,真空干燥后得到产物 sPEG1-b-PLLA。将 sPEG1 替换为 sPEG2 或 PEG 6000,可分别得到 sPEG2-b-PLLA 和 PLLA-b-PEG-b-

收稿日期:2013-01-14

基金项目:国家自然科学基金资助项目(51072055,51003032);广东省自然科学基金资助项目(07300675)

通讯联系人:林雅铃,主要从事药用高分子材料和药物分析的教学与研究, E-mail: linyaling@scau.edu.cn

PLLA。合成路线如 Fig.1 所示。

sPEG1-b-PLLA: FT-IR (KBr, cm^{-1}): 2960 ($-\text{CH}_3$); 2946 ($-\text{CH}-$); 2880 ($-\text{CH}_2-$); 1758 ($>\text{C}=\text{O}$); 1110 ($-\text{C}-\text{O}-$)。 $^1\text{H-NMR}$ (CDCl_3), δ : 5.17(a, 1H); 1.58(b, 6H); 3.64(c, 6H); 4.35(a', 1H); 3.41(c', 2H)。GPC(g/mol): $\bar{M}_n = 0.90 \times 10^4$, $\bar{M}_w = 1.29 \times 10^4$, $\bar{M}_w/\bar{M}_n = 1.43$ 。

sPEG2-b-PLLA: FT-IR (KBr, cm^{-1}): 2960 ($-\text{CH}_3$); 2946 ($-\text{CH}-$); 2880 ($-\text{CH}_2-$); 1758 ($>\text{C}=\text{O}$); 1110 ($-\text{C}-\text{O}-$)。 $^1\text{H-NMR}$ (CDCl_3) δ : 5.16(a, 1H); 1.58(b, 6H); 3.64(c, 6H); 4.36(a', 1H); 3.29(c', 2H)。GPC(g/mol): $\bar{M}_n = 1.07 \times 10^4$, $\bar{M}_w = 1.46 \times 10^4$, $\bar{M}_w/\bar{M}_n = 1.36$ 。

PLLA-b-PEG-b-PLLA: FT-IR(KBr, cm^{-1}): 2960 ($-\text{CH}_3$); 2946 ($-\text{CH}-$); 2880 ($-\text{CH}_2-$); 1758 ($>\text{C}=\text{O}$); 1110 ($-\text{C}-\text{O}-$)。 $^1\text{H-NMR}$ (CDCl_3) δ : 5.15(a, 1H); 1.57(b, 6H); 3.64(c, 6H); 4.35(a', 1H)。GPC(g/mol): $\bar{M}_n = 0.99 \times 10^4$, $\bar{M}_w = 1.48 \times 10^4$, $\bar{M}_w/\bar{M}_n = 1.50$ 。

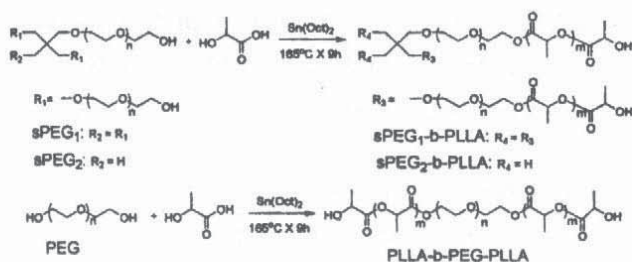


Fig.1 The Synthesis Route of sPEG-b-PLLA and PLLA-b-PEG-b-PLLA Copolymers

1.4 降解试验

将嵌段共聚物溶于二氯甲烷,配制成质量分数约为 10% 的溶液,将其倾倒在聚四氟乙烯平板上,涂抹均匀,待大部分溶剂自然挥干后,在真空干燥箱中常温

干燥 24 h,制得厚度约为 40 μm 的共聚物薄膜。将其剪裁成质量约为 100 mg 的 50mm \times 50mm 的降解试验用薄膜。将降解试验用薄膜装入透析袋中,加入 1 mL PBS 缓冲溶液,两端密封,放入含有 150mL PBS 缓冲溶液的锥形瓶中,瓶口用 Parafilm 薄膜密封,置于 $(37 \pm 0.5)^\circ\text{C}$ 水浴恒温振荡摇床(100 r/min)中进行降解。间隔一定时间取出样品,真空干燥后记录样品的质量,按式(1)计算共聚物的失重率(Mass loss),并对样品进行相应的结构表征。

$$\text{Mass loss} = (m_i - m_t) / m_i \quad (1)$$

式中: m_i ——降解前共聚物的质量, g; m_t —— t 时刻共聚物的质量, g。

1.5 sPEG-b-PLLA 及其降解产物的结构表征

采用 Nicolet 6700 型红外光谱仪(KBr 压片)、Avance DRX-600 型核磁共振仪(CDCl_3 为溶剂,四甲基硅烷为内标)分别测定降解产物的 FT-IR 谱图和 $^1\text{H-NMR}$ 谱图。采用 Waters 1515-2414 型凝胶渗透色谱仪(以四氢呋喃为流动相,单分散聚苯乙烯作为标样,流速 1mL/min,柱温 40°C)测定产物的相对分子质量及其分布。用 X' Pert Pro 型 X 射线衍射仪测定产物的结构参数, Cu K α 辐射,采用连续扫描方式,扫描步长 0.033° ,扫描范围 $5^\circ \sim 50^\circ$ 。用 JC2000C 表面接触角分析仪测定共聚物降解前后的接触角。

2 结果与讨论

2.1 共聚物降解过程中的结构变化

3 种嵌段共聚物在 $\text{pH} = 7.2$ 的 PBS 溶液中降解不同时间(0d~60d)后的 FT-IR 谱图如图 Fig.2 所示。由图中可见,归属于 PEG 嵌段或 sPEG 嵌段的亚甲基峰($-\text{CH}_2-$, 2880 cm^{-1})与 PLLA 嵌段的酯羰基峰($>\text{C}=\text{O}$, 1758 cm^{-1})的峰强度之比随着降解时间的延长而出现近似线性的下降趋势,说明残留在降解产物中的聚乙二醇嵌段的比例下降。

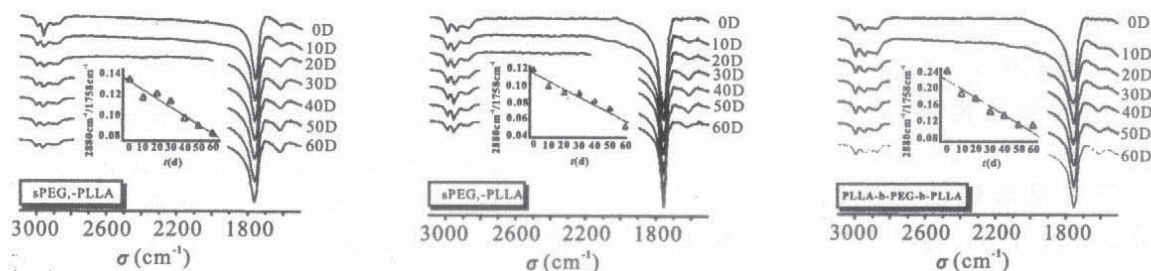


Fig.2 FT-IR Spectra of sPEG1-b-PLLA, sPEG2-b-PLLA, and PLLA-b-PEG-b-PLLA After 0d, 10d, 20d, 30d, 40d, 50d and 60d Degradation, and the Intensity Ratio of Peak 2880 cm^{-1} and 1758 cm^{-1}

由 Fig.3 可见,所有的共聚物在降解前的 GPC 曲

线都大致呈单峰分布,随着降解的进行,共聚物的相对

分子质量变小,出现较低相对分子质量的物质。其中, sPEG1-b-PLLA 降解 10d 后分子量分布变宽,开始出现较低相对分子质量的物质,降解 20d 时出现明显的双峰分布,继续降解,双峰分布稳定,低相对分子质量聚合物的相对分子质量基本保持不变, sPEG2-b-PLLA

和 PLLA-b-PEG-b-PLLA 的降解行为类似。3 种嵌段共聚物降解前后的 XRD 谱图均主要表现为结晶性 PLLA 嵌段的特征峰,且峰形未出现明显的变化,如 Fig.4 所示。

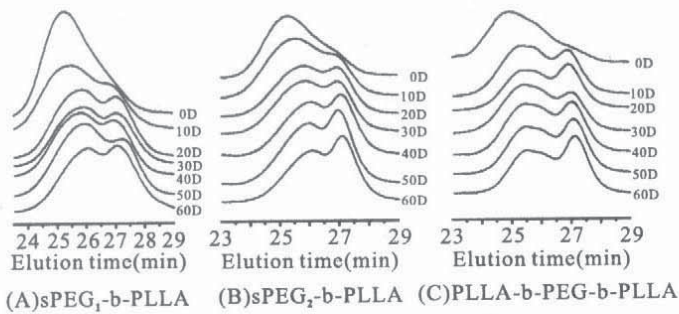


Fig. 3 GPC Curves of PEG-PLLA Copolymers After 0d, 10d, 20d, 30d, 40d, 50d, and 60d Degradation

由 Fig. 5(A)可见,共聚物中 PEG 嵌段降解前 $[c]/[c'] = 4n/2 = 2.47/0.06 = 41.2$;降解 60d 后, $[c]/[c'] = 4n/2 = 1.14/0.03 = 38.0$;降解前 PLLA 嵌段中 $[a]/[a'] = m = 1/0.05 = 20$;降解 60d 后 $[a]/[a'] = m = 1/0.05 = 20$,由此可知,降解前后的 n 值和

m 值变化小,说明在 PBS 缓冲液中,PEG 嵌段和 PLLA 嵌段的降解程度很小。sPEG2-b-PLLA(Fig. 5(B))和 PLLA-b-PEG-b-PLLA(Fig. 5(C))的 $^1\text{H-NMR}$ 谱图也有相似的结果。

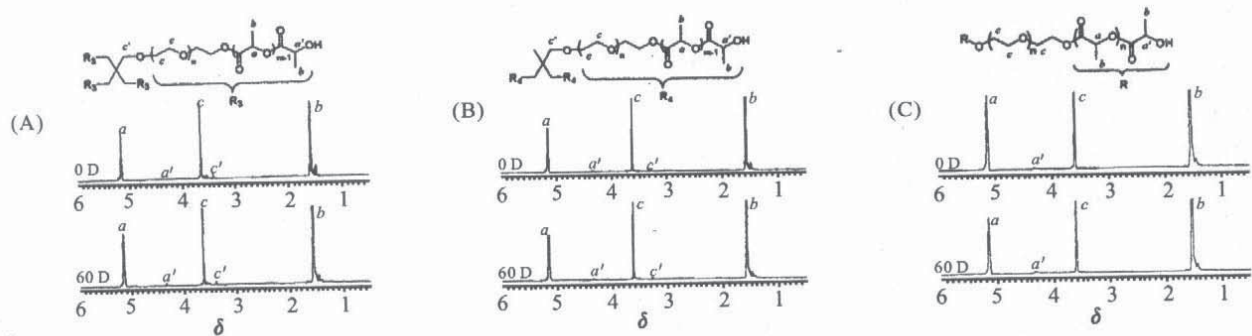


Fig. 5 $^1\text{H-NMR}$ Spectra of PEG-PLLA Copolymers Before and After 60d Degradation
(A): sPEG1-b-PLLA; (B): sPEG2-b-PLLA; (C): PLLA-b-PEG-b-PLLA

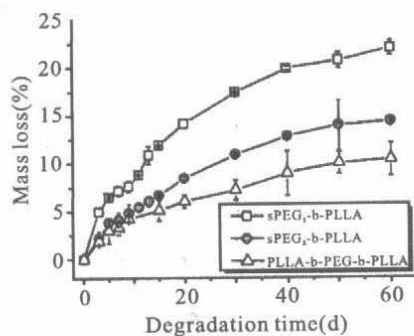


Fig. 6 Mass Loss of Different PEG-PLLA Films After Degradation in PBS (pH = 7.2)

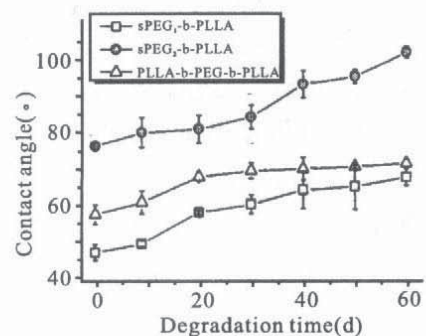


Fig. 7 The Contact Angle of PEG-PLLA Copolymers

共聚物的降解行为在宏观上表现为失重和亲水性的变化。Fig.6 是 3 种嵌段共聚物在降解过程中的失重行为,3 种嵌段共聚物在降解过程中都有明显的失重,且随着 PEG 臂数的增加,失重速率加快。这主要是由于 PEG 臂数的增加所引起的单位体积内连接 PLLA 嵌段与 PEG 嵌段的酯键密度增加所致。同时,降解产物的亲水性亦逐步降低,如 Fig.7 所示。接触角的变化趋势与 FT-IR 谱图(Fig.2)中亚甲基/羰基峰强度之比随着降解时间的延长而下降的现象相吻合。

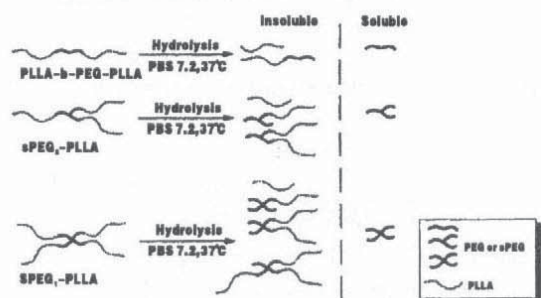


Fig. 8 The Degradation Mechanism of Star-Branched PEG-PLLA Copolymers

2.2 sPEG-PLLA 嵌段共聚物的降解机理

PEG-PLLA 嵌段共聚物在中性 PBS 中降解的基础是酯基的水解,而酯基水解的前提是水与酯基发生有效接触。PLLA 嵌段中有大量的酯基,但 PLLA 嵌段大多处于结晶态,水难以渗入,无法与 PLLA 嵌段内部的酯基发生有效接触,这也是 PLLA 嵌段的相对分子质量和结晶态结构在 PLLA-PEG 嵌段共聚物降解 60d 后依然未发生明显改变的主要原因。基于上述讨论,笔者推断,以 PLLA 为主体的线型和多臂星形 PEG-PLLA 嵌段共聚物在中性缓冲溶液中的降解机理主要为:PEG 嵌段与 PLLA 嵌段之间的酯键水解导致部分 PEG 嵌段完全从嵌段共聚物中游离出来,因其溶于水而流失,其他未完全水解的 PLLA-PEG 嵌段及残余的 PLLA 嵌段则因其水溶性不佳而未从降解产物中溶出,从而使得降解产物中 PEG 嵌段的含量降低、亲水性下降;而 PLLA 嵌段内部由于结晶度较高则未出现明显的降解(水解)。PEG-PLLA 嵌段共聚物在中性缓冲溶液中的降解过程如 Fig.8 所示。

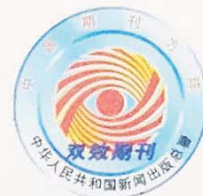
3 结论

采用直接熔融缩聚合成了线型和星形 PEG-PLLA 嵌段共聚物。通过考察其在 37 °C、pH=7.2 的 PBS 缓冲液(模拟体液)中的降解行为,证实了线型和星形 PEG-PLLA 嵌段共聚物的降解主要发生在连接 PLLA 嵌段和 PEG 嵌段的酯键上,而 PLLA 嵌段则由于处于结晶态,降解(水解)程度很低。

参考文献:

- [1] 林雅铃, 张安强, 观富宜, 等. sPEG-b-PLLA/布洛芬微球的制备与体外释放研究[J]. 药学学报, 2010, 45(12): 1570-1575.
Lin Y L, Zhang A Q, Guan F Y, *et al.* Preparation of ibuprofen/sPEG-b-PLLA copolymer microspheres and its in vitro release properties[J]. Acta Pharmaceutica Sinica, 2010, 45 (12): 1570-1575.
- [2] Jie P, Venkatraman S S, Min F, *et al.* Micelle-like nanoparticles of star-branched PEO-PLA copolymers as chemotherapeutic carrier[J]. Journal of Controlled Release, 2005, 110 (1): 20-33.
- [3] Salaam L T E, Dean D, Bray T L. In vitro degradation behavior of biodegradable 4-star micelles [J]. Polymer, 2006, 47 (1): 310-318.
- [4] Li S, Rashkov I, Espartero J, *et al.* Synthesis, characterization, and hydrolytic degradation of PLA/PEO/PLA triblock copolymers with long poly (L-lactic acid) blocks [J]. Macromolecules, 1996, 29 (1): 57-62.
- [5] Cai C, Wang L, Dong C M. Synthesis, characterization, effect of architecture on crystallization, and spherulitic growth of poly (L-lactide)-b-poly (ethylene oxide) copolymers with different branch arms [J]. Journal of Polymer Science Part A: Polymer Chemistry, 2006, 44 (6): 2034-2044.
- [6] 林雅铃, 张安强, 王炼石. 载药用聚外消旋乳酸的合成方法: 中国, 200810026430.5 [P]. 2010-11-10.
- [7] Lin Y L, Zhang A Q, Wang L S. Synthesis and characterization of star-shaped poly (ethylene glycol)-block-poly (L-lactic acid) copolymers by melt polycondensation [J]. Journal of Applied Polymer Science, 2012, 124(6): 4496-4501.
- [8] 张安强, 林雅铃, 魏芬芬, 等. 星形聚乙二醇-聚乳酸嵌段共聚物的合成与表征[J]. 高分子材料科学与工程, 2011, 27(11): 84-88.
Zhang A Q, Lin Y L, Wei F F, *et al.* Synthesis and characterization of multi-arm star-shaped poly (ethyleneglycol)-b-poly (L-lactide) copolymer prepared by ring-opening polymerization [J]. Polymer Materials Science & Engineering, 2011, 27(11): 84-88.

(下转第 75 页. to be continued on P.75)



《高分子材料科学与工程》征稿简则

1. 本刊系经国家科委批准、公开发行的专业性学术刊物。办刊宗旨为面向国民经济,注重学术性、信息性、实用性。读者对象是从事与高分子材料有关的具有大专以上文化程度的科研、教学、生产及科技管理人员,有关专业的大学生及研究生等。

本刊是全国核心期刊,进入了 Ei Compendex 数据库、CA、《俄罗斯文摘杂志》、美国《剑桥科学文摘》等国际检索系统,连续入选美国 CA 千名表。2008 年荣获中国科技期刊精品奖,进入全国科技期刊 300 强行列。

2. 本刊登载与高分子材料科学与工程领域有关的高分子化学、高分子物理和物化、反应工程、结构与性能、成型加工理论与技术、材料应用与技术开发、研究方法 & 测试技术等方面的研究成果,设有以下栏目:

专论·综述 刊登对高分子材料学科具有重要指导意义的专论和综述性文章。

合成实验·工艺 刊登有关高分子材料的合成实验、合成工艺、反应工程等方面具有创意的研究论文。

结构·性能 刊登有关高分子材料的结构与性能研究以及高分子物理方面的具有创意的研究论文。

材料测试·加工·应用 刊登有关高分子的测试技术、成型加工理论与技术,以及材料应用方面具有创意的研究论文。

新技术·产品开发 刊登紧密结合高分子材料工业生产的新技术、新产品的开发成果。

教学讨论 刊登有关高分子专业的教学研究与讨论。 研究快讯 刊登有关高分子材料科学与工程方面的最新科研成果。

3. 来稿应具有创新性、学术性、科学性、规范性。论文力求主题明确,内容充实,数据可靠,文字精练,文责由作者自负,论文请控制在 8000 字以内(包括图、表,参考文献在内)。

4. 作者须同意将该文的复制权,发行权,信息网络传播权,汇编权等转让给本刊编辑部,编辑部所付稿酬中包含了其著作权在印刷版,光盘版和网络版等各种使用方式的使用报酬,以后不再另付作者。

5. 文稿自收到之日起,审稿期限为 3 个月,若超过期限收不到录用通知,请及时向编辑部查询。查询电话:028-85401653。

高 分 子 材 料 科 学 与 工 程

GAOFENZI CAILIAO KEXUE YU GONGCHENG

POLYMER MATERIALS SCIENCE AND ENGINEERING

(月刊, 1985 年创刊)

第 29 卷 第 11 期 2013 年 11 月

· 公开发行 ·

Vol. 29, No. 11 Nov. 2013

主 管: 中华人民共和国教育部

主 办: 中国石油化工股份有限公司科技开发部

国家自然科学基金委员会化学科学部

高分子材料工程国家重点实验室

四川大学高分子研究所(中国·成都)

主 编: 徐 偃

副主编: 袁晴棠 赵一雯

编 辑 出 版 《高分子材料科学与工程》编辑部

地址: 四川大学(西区)高分子研究所

邮政编码: 610065 电话: (028) 85401653

总 发 行 处 四川省报刊发行局

订 购 处 全国各地邮局

国 外 发 行 中国国际图书贸易集团有限公司

印 刷 中国核动力院印刷厂

Edited & Published by Editorial Board of Polymer Materials Science & Engineering

(Address: Polymer Research Institute, Sichuan University, Chengdu 610065, China)

Editor-in-Chief Xu Xi

Distributed Abroad by China National Publications Import & Export Corporation

(P.O. Box 88, Beijing, China)

<http://pmse.scu.edu.cn>

Email: GFZCLBJB@163.net

ISSN 1000-7555



11>

ISSN 1000-7555

刊号: CN 51-1293/O6

邮发刊号 62-67

国外代号: M6669

每期定价: 28.00 元 全年定价 336.00 元



Polyacrylamide quaternary ammonium salts based on stable adsorption in soil and its application on the control of soil-borne fungal disease

Wei Zhang^{a,1}, Jiangang Yu^{b,1}, Mingyang Wu^a, Rui Li^c, Anqiang Zhang^{c,*}, Yaling Lin^{a,*}

^a College of Materials and Energy, South China Agricultural University, 483 Wushan Rd., Guangzhou 510642, Guangdong, China

^b College of Natural Resources and Environment, South China Agricultural University, 483 Wushan Rd., Guangzhou 510642, Guangdong, China

^c School of Materials Science and Engineering, South China University of Technology, 381 Wushan Rd., Guangzhou 510641, Guangdong, China

ARTICLE INFO

Keywords:

Polyacrylamide quaternary ammonium salt
Polymer/soil interaction
Soil-borne fungal disease
Banana Fusarium wilt

ABSTRACT

Currently, soil-borne fungal disease (SBFD) have caused a huge damage in agriculture, and small molecule soil disinfectants have been widely used for the prevention and control of SBFD, which could not only kill the chlamydospore of pathogenic fungi, but also completely destroy the microbial community and its functional diversity in the soil, and is not conducive to subsequent plant planting. Therefore, how to effectively inhibit plant pathogenic fungi while maintaining the general balance of microbial population in the soil to facilitate subsequent plant planting come to be critical problem in the prevention and control of SBFD. In this work, a series of polyacrylamide containing quaternary ammonium salts (PAM-X) were synthesized based on the radical copolymerization of acrylamide (AM) and acrylamide containing different quaternary ammonium salts groups (AMX). Owing to the entanglement between polymer chains and soil, PAM-X could be stably absorbed in the soil, thus effectively delaying the free migration of PAM-X chains in soil, and reducing the probability of being leached from soil, which might be the key to obtain novel polymeric quaternary ammonium salts that have less impact on the environment. Banana Fusarium wilt, also known as “banana cancer”, caused by *Fusarium oxysporum* f. sp. *cubense* (Foc), was chosen as a typical soil-borne pathogen disease to verify the rationality of the above thoughts. The results showed PAM-X had well anti-Foc4 activities in soil, and could maintain the general balance of microbial population in the soil, which are almost non-toxic to earthworms in soil and fish, thus provides a new prevention and control method for SBFD.

1. Introduction

Soil-borne fungal disease (SBFD) is caused by plant pathogenic fungi (such as *Fusarium*, *Verticillium*, *Sclerotinia*, *Gaeumannomyces*) that can survive in the soil for a long time (up to 10 years), it is hard to control for the reason that the pathogenic fungi can survive in soil in the form of chlamydospore, and is becoming a key factor to restrict sustainable development of agricultural production in the world. [1] Due to the

complexity of soil, many chemicals could not show ideal inhibitory effects on pathogenic fungi in soil, although they might show inhibitory effects on the SBFD in the laboratory. [2] Therefore, currently, SBFDs are prevented and controlled using the method of soil disinfection, i.e., killing all microorganisms in the soil. [3] For example, soil fungicides or soil disinfectants, such as methyl bromide or calcium cyanamide were usually used to control banana Fusarium wilt, also known as “Panama disease” and “banana cancer”, which is one of the most destructive soil-

Abbreviations: Foc, *Fusarium oxysporum* f. sp. *cubense*; Foc4, *Fusarium oxysporum* f. sp. *cubense* “tropical” race 4; AM, acrylamide; AMX, acrylamide quaternary ammonium salts; AMBB, (2-methacrylamido) propyltetrahydroxydimethylammonium bromide; AMHEB, (2-methacrylamido) propyltetrahydroxydimethylammonium bromide; AMBC, (2-methacrylamido) propyltetrahydroxydimethylammonium chloride; PAM-X, random copolymers of AM and AMX; PAM-BB, random copolymer of AM and AMBB; PAM-HEB, random copolymer of AM and AMHEB; PAM-BC, random copolymer of AM and AMBC; PAM-X-FL, fluorescently labelled PAM-X; PQASs, polymeric quaternary ammonium salts; BC, benzalkonium chloride; MIC, minimum inhibitory concentration; MFC, minimal fungicidal concentration; IC₅₀, the 50% maximal inhibitory concentration against Foc4; IC₉₀, the 90% maximal inhibitory concentration against Foc4; IC_{50S}, the 50% maximal inhibitory concentration against Foc4 in soil; IC_{90S}, the 90% maximal inhibitory concentration against Foc4 in soil; LC₅₀, the median lethal concentration; LC_{50S}, the median lethal concentration of the chemical/soil mixture; LC_{50L}, the median lethal concentration of the soil leaching solution.

* Corresponding authors.

E-mail addresses: aqzhang@scut.edu.cn (A. Zhang), linyaling@scau.edu.cn (Y. Lin).

¹ These authors contributed equally.

<https://doi.org/10.1016/j.eurpolymj.2023.112604>

Received 15 August 2023; Received in revised form 14 November 2023; Accepted 17 November 2023

Available online 24 November 2023

0014-3057/© 2023 Elsevier Ltd. All rights reserved.

borne vascular diseases of banana in South China and even in the world, and is caused by *Fusarium oxysporum* f. sp. *cubense* (Foc), in which tropical race 4 (Foc4) has a significant impact on global banana production. [4–5] Normally, the soil disinfectants are small molecule which showed strong broad-spectrum antibacterial/fungi activities, could not only kill the chlamydospore of pathogenic fungi, but also kill most microorganisms (including beneficial microorganisms) in the soil, thus completely destroy the microbial community and its functional diversity in the soil, and is not conducive to subsequent plant planting. [6] New organic fertilizer needs to be introduced to restore the soil in order to replant bananas, [7–8] and the fumigated areas might eventually be re-attacked by the pathogen, making the next fruit production impossible. [9–10] Moreover, the volatilization or leaching of the small molecule soil disinfectants might cause serious environmental hazards, such as air pollution, water pollution, soil residual pollution, etc. [6,11] Therefore, how to effectively inhibit plant pathogenic fungi in soil while maintaining the general balance of microbial population in the soil, and reduce the environmental hazards to facilitate subsequent plant planting come to be critical problem in the prevention and control of SBF. [1,2,4,8,11–13].

Quaternary ammonium salts (QASs) have been widely valued as daily disinfectants for their broad-spectrum anti-microorganism activities. [14–15] Although several type of QASs were applied to control plant pathogenic fungi in lab, when they were applied in soil, it may kill most microorganisms in the soil, [16] thus cause serious environmental risks and is detrimental to the subsequent planting. [16–17] Compared with small molecular QASs, by connecting the QASs groups with polymer chain to afford polymeric quaternary ammonium salts (PQASs) have attract more and more attentions for their excellent anti-microorganism properties, such as low toxicity, good environmental stability, none skin irritation, prolonged residence time and better biological activity. [18–21] However, they are less used in the prevention and control of plant diseases, especially soil-borne diseases. [22–24] On the other hand, polymeric compounds might improve soil structure by enhancing soil cohesion and increasing the stability and content of soil water-stable aggregates. For example, polyacrylamide (PAM) with different molecular weights has different effects on soil improvement, and all are effective. It maintains soil moisture and soil fertility, increases the content of soil water-stable aggregates, reduces soil bulk density, has no acute toxicity to aquatic organisms, and can promote the growth of corn plants after application. [25] Likewise, researchers have also reported the potential of crosslinked PAM for absorbing, retaining, and releasing extremely large amounts of water relative to its own weight. [26–27].

Therefore, we combined the virtue of PQASs with PAM, compared with previously reported PQASs, [18–19,24,31–32] the molecular weight of PAM is 1–3 orders of magnitude higher, which could help to enhance the interaction between polymer and soil particles, and effectively reduce the risk of quaternary ammonium salts loss by leaching, thus afford a series of polyacrylamide quaternary ammonium salts that have less impact on the environment. As talked above, PAM has been widely used for soil improvement for its good adsorption and aggregation properties on soil, thus it might be a suitable carrier for PQASs. According to this thought, a series of polyacrylamide copolymers (PAM-X) based on acrylamide (AM) and acrylamide containing different quaternary ammonium salts (AMX) [24] were synthesized via simple radical copolymerization, the adsorption and migration properties of PAM-X in soil, its impact on soil physical and chemical properties were studied in detail, and the biological and environmental toxicities were also evaluated by its impact on microbial population diversity in soil, earthworms and zebrafish. As for the persistency of PAM-X in soil, PAM-X could be considered as stable and none obvious harm to the environment before its degradation due to the PAM is hard to degrade in soil. Then, Foc4 was chosen as the typical pathogenic fungi of SBF, and the anti-Foc4 activities both *in vitro* and *in vivo* (in soil) of PAM-X were evaluated intensively. This work has taken an exploratory step towards

the subsequent practical application of PAM-X, especially in sustainable prevention and control of SBF.

2. Experimental

2.1. Materials

N, N-dimethylamine propyl methacrylamide (DMPMA), *n*-butyl bromide (BB, > 98 %), 1-hexyl bromide (HEB, 99 %), benzyl chloride (BC, 99 %) and 2,3,5-triphenyltetrazolium chloride (TTC, > 95 %), 2,2'-azobis(2-methylpropionamidine) dihydrochloride (AIBA, 98 %) and acrylamide (AM, 98 %), allyl chloride (99 %), 1-methylpiperazine (98 %), propylamine (98 %), 4-bromo-1,8-naphthalic anhydride (95 %) and ethylene glycol monomethyl ether (99 %) were purchased from Shanghai Macklin Biochemical Technology Co., Ltd. (Shanghai, China).

Fusarium oxysporum f. sp. *cubense* race 4 (Foc4) was donated by the Fungal Laboratory, Department of Plant Pathology, South China Agricultural University. The soil (crushed and screened through a 20-mesh sieve) was taken from the vegetable field of scientific research base of South China Agricultural University. The physicochemical properties of the soil are shown in Table S2, all the soil samples were passed through a 20-mesh sieve before using. Banana seedlings (*Musa AAA Cavendish* cv. *Brazil*) used in this experiment were provided by the South China Botanical Garden, Chinese Academy of Sciences. Zebrafish were purchased from Shanghai Feixi Biotechnology Co., Ltd., with a total length of 2 ± 0.5 cm and a weight of 0.2 ± 0.1 g. The earthworm species was *Eisenia foetida*, purchased from Xinyida Earthworm Farm in Hebei Province, China, with a total length of 5–8 cm and a weight of 0.3–0.6 g. Other chemical agents were used as received.

2.2. Synthesis of AMX (AMBB, AMHEB and AMBC)

The acrylamide quaternary ammonium salts, i.e., the AMX monomers, including (2-methacrylamido) propyltetra-butyl-dimethylammonium bromide (AMBB), (2-methacrylamido) propyltetra-hexyl-dimethylammonium bromide (AMHEB), and (2-methacrylamido) propyltetra-benzyl-dimethylammonium chloride (AMBC), were synthesized by the quaternization reaction of DMPMA with halogenated reagents, including *n*-butyl bromide, 1-hexyl bromide and benzyl chloride, according to the our previous work,²⁴ as shown in Scheme 1. The detailed synthesis procedure of AM was shown in Part S1 of Supporting Information.

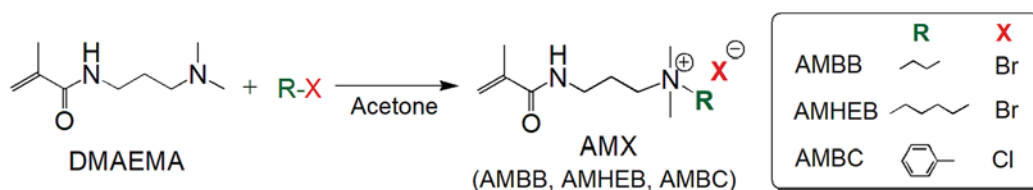
2.3. Synthesis of PAM-X (PAM-BB, PAM-HEB, and PAM-BC)

The random copolymer (PAM-X) of acrylamide (AM) and AMX (AMBB, AMHEB, and AMBC) with different AM / AMX feeding ratios were synthesized by radical copolymerization presented in Scheme 2.

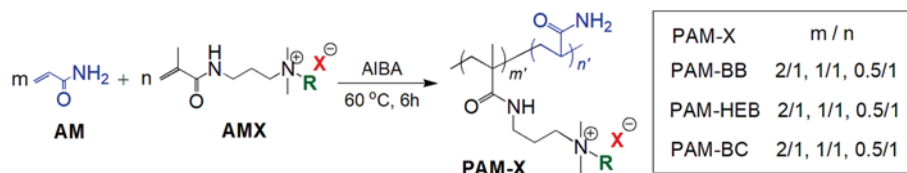
Taking PAM-BB with AM / AMBB feeding ratios (m/n) of 1/1 as the example, the typical procedure of PAM-BB was briefly stated as follows: first, under nitrogen atmosphere, AMBB (15.36 g, 0.05 mol) and AM (3.55 g, 0.05 mol) dissolved in sterile water (70 mL) was charged into a three-necked flask with a condenser, a magnetic stirrer and a nitrogen inlet, then heated to 60 °C under nitrogen atmosphere, and 0.28 g AIBA (dissolved in 5 mL sterile water) was dripped via the dropping funnel, and the reaction temperature was maintained at 60 °C for 6 h. After that, the mixture was condensed and added into acetone to precipitate the copolymers, the sticky copolymers were collected and then dried under vacuum at 70 °C for 24 h, and the product was denoted as PAM-BB. Similarly, PAM-HEB and PAM-BC with different AM / AMX feeding ratios were synthesized by identical procedure as above.

PAM-BB: ¹H NMR (600 MHz, D₂O, δ , ppm): 0.98–1.11 (bm, CH₂-C(CH₃), -CH₃), 1.39 (bs, -CH₂-CH₃), 1.75 (bs, -CH₂-CH₂-CH₃), 2.00 (bs, CH₂-C(CH₃), CH₂-CH₂-CH₂), 3.08 (bs, N⁺(CH₃)₂), 3.19 ~ 3.32 (bm, NH-CH₂, -CH₂-N⁺-CH₂). FT-IR (ν , cm⁻¹): 1661 (ν C=O amide), 1217 (ν C-N).

PAM-HEB: ¹H NMR (600 MHz, D₂O, δ , ppm): 0.89–1.10 (bm, CH₂-C



Scheme 1. The chemical structure and synthesis routine of the AMX (AMBB, AMHEB, and AMBC) monomers.



Scheme 2. The synthesis routine of polyacrylamide quaternary ammonium salts (PAM-X).

(CH₃), -CH₃), 1.35 (bs, -CH₂-(CH₂)₃-CH₃), 1.76–1.89 (bs, N⁺-CH₂-CH₂), 2.02 (bs, CH₂-C(CH₃), CH₂-CH₂-CH₂), 2.85 ~ 3.20 (bs, N⁺(CH₃)₂, NH-CH₂, -CH₂-N⁺-CH₂). FT-IR (ν , cm⁻¹): 1666 (ν C=O amide), 1215 (ν C-N).

PAM-BC: ¹H NMR (600 MHz, D₂O, δ , ppm): 0.96–1.13 (bm, CH₂-C(CH₃)), 1.53 ~ 1.96 (bm, CH₂-C(CH₃), 2.88 ~ 3.56 (bm, CH₂-CH₂-CH₂-N⁺-CH₂(CH₃)₂), 4.33 (bs, CH₂- Φ), 7.50 (bs, Φ -H). FT-IR (ν , cm⁻¹): 1665 (ν C=O amide), 1215 (ν C-N), 704, 734 (γ Φ -H).

The measurement residual monomers of PAM-X were shown in the [Supporting Information \(Part S4\)](#).

In order to realize the visualization of PAM-X, a very small amount of fluorescent group (FL) were introduced into PAM-X to obtain fluorescent labelled polyacrylamide quaternary ammonium salt (PAM-X-FL), and the detailed synthesis procedures of PAM-X-FL were shown in the [Supporting Information \(Part S2\)](#).

2.4. Characterization and methods

FT-IR spectra were collected on a Nicolet iS5 Fourier-Transform Infrared Spectrometer (Thermo Scientific, USA) equipped with an iD7-ZnSe ATR accessory. ¹H NMR spectra were obtained using a Bruker Avance III HD 600 (Bruker Instrument Corp., Germany) spectrometer with D₂O as the solvent. The viscosity average molecular weights (M_v) was measured using a capillary viscometer under 30 °C according GB/T 12005.1–1992.

The other methods, including the testing method for the soil/PAM-X interaction (adsorption, and migration), antifungal assay of PAM-X on *Foc4* (*in vitro* and in soil), biotoxicity evaluation (culturable microbes in soil, earthworm acute toxicity and fish acute toxicity evaluation), are detailed in the [Supporting Information \(Part S6 to S8\)](#).

3. Results and discussion

3.1. Structural characterization of PAM-X and anti-*Foc4* activities screening

To obtain high antifungal activities and improve soil characteristics, we designed and synthesized a series of polyacrylamide quaternary ammonium salts with different structures. The molecular structures of the target compounds were determined by ¹H NMR, FT-IR and fluorescence spectra, as detailed in the [Supporting Information \(Figures S2 and S3\)](#). As shown in [Figure S2](#), the peaks for C = C bonds (5.60 and 5.95 ppm in the ¹H NMR spectra) almost disappeared, and the absorption peaks at 1661, 1215 and 2881 cm⁻¹ represented the infrared absorption bands of -CONH- and -CH- of PAM-BB, PAM-HEB and PAM-BC ([Figure S3](#)), respectively. The spectra of the products were in complete

agreement with the expected structures and showed essentially no contaminants, which demonstrated the successful synthesis of the polymers.

As shown in [Table 1](#), the proportion of AMX monomer units in PAM-X was lower than that of the feeding ratio, and the viscosity average molecular weights of PAM-X were decrease with the increasing of AM/AMX feeding ratios, which mainly due to the steric hindrance effect of the bigger quaternary ammonium salt side groups. Due to the low contents of FL groups in PAM-X-FL (the feed ratio of FL-3 in the monomers was less than 1 wt%), although it is difficult to distinguish the characteristic peaks of FL groups in the FTIR and ¹H NMR spectra, we found that the maximum emission wavelength of PAM-X-FL moved from 523 nm (for FL-3) to 515 nm ([Figure S1](#)), indicating the copolymerization between AMX and FL-3.

In order to simplified the soil adsorption and environmental toxicity of PAM-X with different QASs structures, the *in vitro* anti-*Foc4* activities of PAM-X with different AM/AMX feeding ratios were tested based on the classical broth microdilution method with 2,3,5-triphenyl-tetrazoliumchloride (TTC), the results were shown [Table 1](#). It was found that for different PAM-X, the products with the feeding ratio of AM/AMX = 1/1 (mol/mol) showed the best anti-*Foc4* activities, thus in the following discussion, without special explanation, PAM-X refer to the products that are synthesized with the feeding ratio of AM/AMX = 1/1 (mol/mol).

3.2. The interactions between PAM-X and soil

Due to the weak light-absorbing properties of PAM-X, PAM-X containing fluorescent groups, i.e., PAM-X-FL, was chosen to determine the

Table 1
Molecular weight and anti-*Foc4* activities of PAM-X.

PAM-X	m / n ^a	m' / n' ^b	M_v^c (kDa)	MIC (mg/mL)	MFC (mg/mL)	MFC/MIC
PAM-BB	2/1	2.67/1	320	0.04	0.08	2
	1/1	1.30/1	300	0.04	0.04	1
	0.5/1	0.57/1	200	0.04	0.16	4
PAM-HEB	2/1	2.9/1	330	0.04	0.04	1
	1/1	1.18/1	290	0.04	0.04	1
	0.5/1	0.53/1	180	0.08	0.16	2
PAM-BC	2/1	2.77/1	330	0.04	0.04	1
	1/1	1.35/1	290	0.02	0.02	1
	0.5/1	0.51/1	180	0.02	0.04	2

a. The feeding ratio of AM / AMX (m / n, mol / mol).

b. The proportion of AM units / AMX units in PAM-X (m' / n', mol / mol) based on ¹H NMR measurements.

c. The viscosity average molecular weights (M_v) based on capillary viscometer.

adsorption kinetics of PAM-X in soil. Fig. 1 shows the sorption kinetics of 100 mg/L PAM-X-FL in soils. In less than 5 h, the equilibrium adsorption of the three kinds of PAM-X-FL in soil was observed, and afterward, the concentration of PAM-X-FL in the soil was almost unchanged, and the entire adsorption kinetics of these three PAM-X on the soil conformed to the pseudo-second-order model with coefficients of correlation (R^2) above 0.995 (Fig. 1-B). Both the Freundlich and Langmuir models were selected to fit the results (Fig. 1-C, D and Table 1), where the Freundlich model showed a better regression coefficient (R^2), indicating that the adsorption of PAM-X to the tested soil is more tend to be a multilayer adsorption process. The Freundlich constant ($1/n$) (Table 2) is related to the adsorption strength of the adsorbent: $1/n$ values of 0.1–0.5, 0.5–1.0, and > 1.0 indicate that adsorption is good, easy to adsorb, and difficult to adsorb, respectively. Thus, the $1/n$ value of the three PAM-X is PAM-HEB (0.366) $<$ PAM-BB (0.608) $<$ PAM-BC (0.685), indicating that these three kinds of PAM-X can be easily adsorbed in soil, in which PAM-HEB shows an excellent adsorption effect.

In addition to the absorption properties, the migration and leaching behaviour of PAM-X in soil are also important for polymer/soil and polymer/fungi interactions. Fig. 2 shows the fluorescence curves of the PAM-X-FL solution and the leachates of soil containing PAM-X-FL, from which we can see that the PAM-X-FL solution emitted bright green light under ultraviolet lamp irradiation and had a strong fluorescence intensity at 515 nm, while after leaching, the leachates of soil were only light blue under the ultraviolet lamp (365 nm) irradiation, and there was no fluorescence intensity at 515 nm. Thus, it can be concluded that PAM-X-FL is difficult to move in soil.

Both the soil adsorption and soil migration assays demonstrated that PAM-X is easily adsorbed and relatively immobile in soil, which might be mainly due to two aspects: first, the positive charge carried by PAM-X can combine with the negative charge normally carried by soil particles

Table 2

Sorption isotherm parameters of PAM-X sorption to soils.

	Freundlich parameters			Langmuir isotherm		
	K_f (mmol/g)	$1/n$	R^2	q_{max} (mg/g)	b	R^2
PAM-BB	1.57	0.608	0.9981	64.1	0.0084	0.9671
PAM-HEB	3.54	0.366	0.9909	69.4	0.0046	0.9974
PAM-BC	0.68	0.685	0.9996	64.9	0.0037	0.9478

(such as sludge and sediments), and second, the long chain of polymers and the entanglement between polymer chains and soil particles. Compared with alkyl groups, the presence of benzyl groups might strengthen the hydrophobic characteristics of quaternary ammonium salts and weaken the adsorption of polymeric quaternary ammonium salts in soil. These results are similar to previous studies on the behaviour of QASs in soil. [28–29].

The addition of polymers can change the physical conditions of soil for the interaction between soil particles and polymeric substances, and enhance the stability of aggregates by adhesions and adsorptions. Polymer adsorptions of soil particles could reduce the repulsive force between soil particles, and adhesions of polymers could bind the soil particles. [30] Thus the addition of PAM-X was assumed to act as a binding agent to stabilize the soil aggregates.

3.3. Anti-Foc4 activities of PAM-X

To evaluate the anti-fungal activities of chemicals, several antifungal parameters, such as the minimum inhibitory concentration (MIC) and minimal fungicidal concentration (MFC) based on the broth micro-dilution procedure with 2,3,5-triphenyl-tetrazoliumchloride (TTC), 50

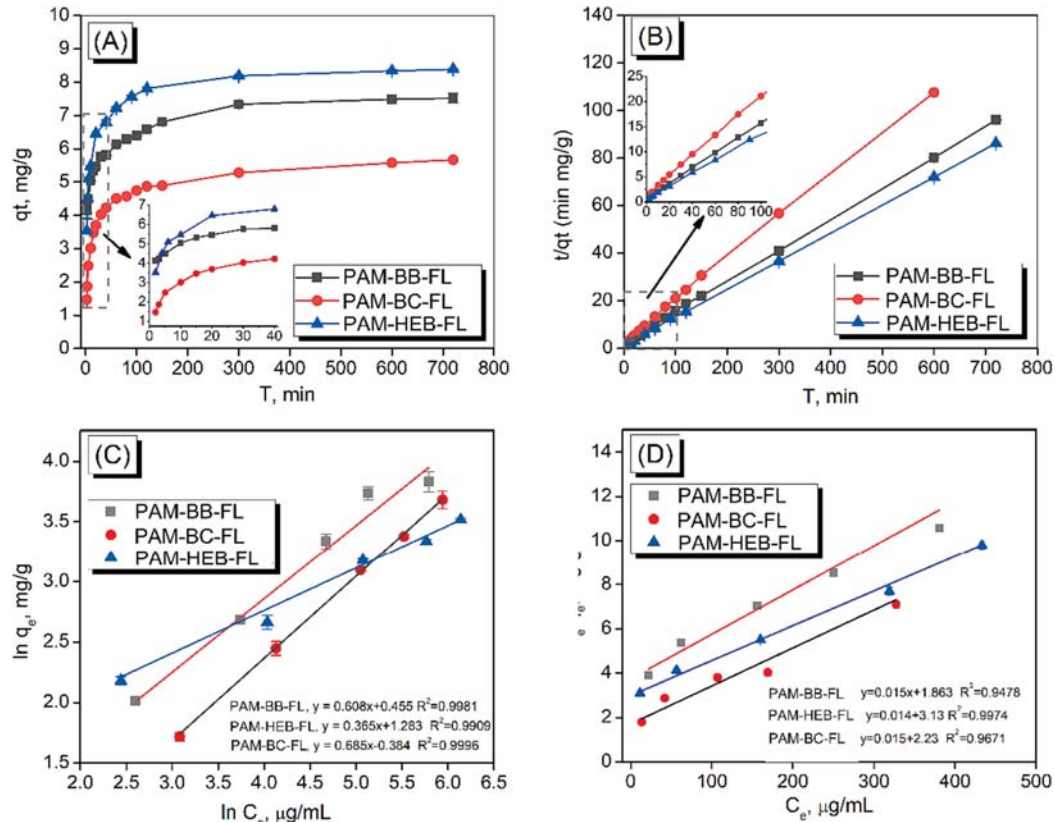


Fig. 1. Sorption kinetics and isotherms of PAM-X-FL (PAM-BB-FL, PAM-BC-FL and PAM-HEB-FL) in soils: (A) relationships between the sampling time and the PAM-X-FL concentration in soils; (B) the pseudo-second-order model fit to PAM-X-FL sorption kinetics data; (C) Freundlich sorption isotherms and (D) Langmuir sorption isotherms.

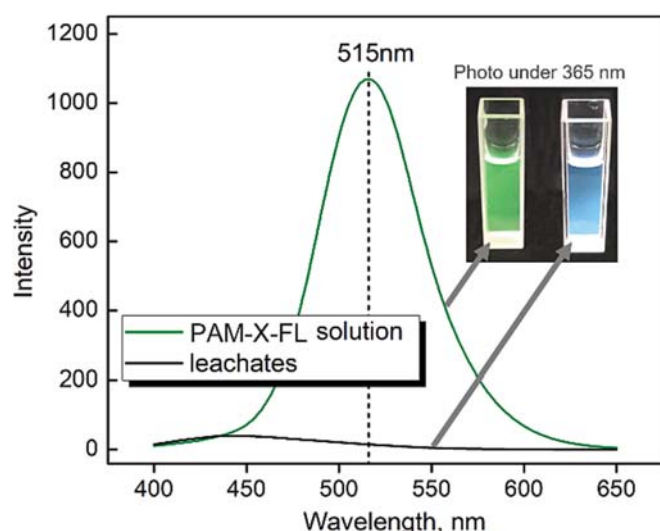


Fig. 2. Leaching behaviour of PAM-X-FL in soil.

% inhibitory concentration (IC_{50}) and 90 % inhibitory concentration (IC_{90}) based on the mycelia growth inhibition method, were often used. The culture media for these antifungal parameters were different: the culture media for MIC and MFC was liquid potato-dextrose (PD) media in which the chemicals could meet the *Foc4* conidia freely, while IC_{50} and IC_{90} were tested on solid potato-dextrose-agar (PDA) media, where the chemicals could meet the *Foc4* hyphae only on the surface of the PDA media. It should be noted that the *Foc4* conidia remained in the soil, which is much different from the culture media mentioned above; thus, we developed a new method in which the *Foc4* conidia were cultured in a mixture of sterilized soil and water, as detailed in the Part S8 of SI. This test condition is most similar to the actual environment of *Foc4* conidia in soil, and the results were labelled as IC_{50s} and IC_{90s} , in which the subscript “s” represents “Soil”. Fig. 3 shows the above mentioned typical anti-*Foc4* activities of PAM-X with different QAS structures in which a commercial bactericidal agent, benzalkonium chloride (BC),

was chosen as the positive control.

The results demonstrated that PAM-X exhibited antifungal activity against *Foc4* with MIC values ranging from 0.02 to 0.04 mg/mL, and the MFC/MIC ratios of the compounds were less than 4, indicating that both PAM-X and BC were fungicidally effective. [31] Although the IC_{50} values of PAM-X ranged from 0.56 to 0.65 mg/mL, which are much higher than those of BC, the difference between the IC_{50s} of PAM-X and BC was much smaller, as shown in Fig. 3, which demonstrates the good actual anti-*Foc4* activities of PAM-X in soil. We also noticed that compared with IC_{50} & IC_{90} , the IC_{50s} & IC_{90s} of BC increased, while the IC_{50s} & IC_{90s} of PAM-X decreased, which might be due to the better interaction of *Foc4* conidia and PAM-X in soil than in PDA media.

Although BC showed the lowest IC_{50} and IC_{90} in PDA media, in soil, PAM-X showed better sustained anti-*Foc4* activities. As mentioned above, during the measurements of IC_{50} & IC_{90} , the fungal mycelium only contacts one side of the PDA plates containing drugs, while for the IC_{50s} & IC_{90s} , the *Foc4* conidia could mix with the drugs in soil uniformly. [32] According to the mechanisms of fungistatic, the fungistasis of quaternary ammonium salts is a typical contact fungicidal, [33] and the effective contact between the fungistatic and the conidia is an important factor affecting its actual fungistatic activity in soil. Compared with BC, PAM-X was more easily adsorbed in soil and gradually desorbed, thus effectively promoting the effective contact between free PAM-X and *Foc4* conidia, resulting in increased antifungal activity. In particular, the slow desorption of the polymer chains is an important basis for the long-lasting antifungal activity of PAM-X. [34] This means that a single application of PAM-X in the field could prevent *Foc4* from invading banana plants through the soil for a certain period, and the results matched well with those of previous studies. [24,31–32].

3.4. Biototoxicity evaluation of PAM-X in the soil environment

Due to the broad-spectrum microbial inhibition characteristics of quaternary ammonium salt, the application of traditional small molecular quaternary ammonium salt in agriculture, especially in soil, is greatly limited due to its high environmental toxicity. Compared with small molecular quaternary ammonium salts, polymeric quaternary ammonium salts with higher molecular weight, such as the polyacrylamide-containing quaternary ammonium salt groups designed in this study, i.e., PAM-X, showed much difference in antifungal activities and soil adsorption properties, so it is necessary to evaluate their impact on the soil environments, including the impact on the culturable microbial populations in the soil, the effect on earthworms in soil and the acute toxicity of soil leachate containing PAM-X to fish.

The populations of total bacteria, fungi and actinomycetes in soil can also be used as indicators of soil health. [12–13,35] An appropriate microbial community structure is conducive to improving crop yield and soil defence ability. The effect of PAM-X on soil culturable microbial populations was evaluated based on plate counting methods in different media. After colony counting, the number of biological colonies in soil treated with PAM-X for 2 d was compared with that in untreated soil. The results of the culturable microbial analysis of soil amended with different PAM-X are presented in Fig. 4 A–C, which shows that PAM-X treatment increased the number of bacteria and actinomycetes in the soil in the order of PAM-BB > PAM-HEB > PAM-BC, and the total number of fungi decreased relatively, followed by PAM-BC > PAM-HEB > PAM-BB. Compared with PAM-X, traditional small molecular quaternary ammonium salts, such as benzalkonium chloride (BC), which has been widely commercially available, showed classic broad-spectrum bactericidal and fungicidal characteristics (Fig. 4: the culturable populations of bacteria, fungi and actinomycetes have decreased significantly; that is, BC could not only effectively inhibit *Foc4* conidia in soil but also destroy the ecology of the original microbial population in the soil, which is obviously not conducive to the growth of banana plants and not a sustainable way to control banana Fusarium wilt.

The changes in soil microbial numbers might be related to the stable

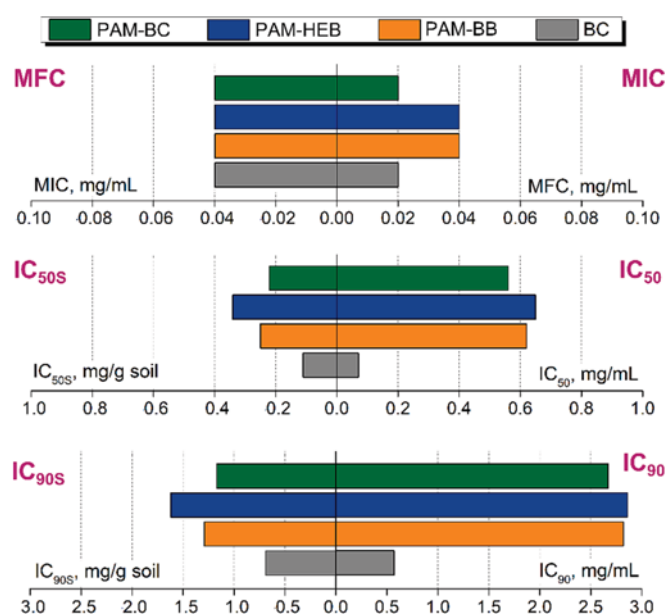


Fig. 3. Typical anti-*Foc4* activity parameters: (A) MIC & MFC, (B) IC_{50} & IC_{50s} and (C) IC_{90} & IC_{90s} of PAM-X and BC. (All the values are the average of 3 replicates; the data of the fungicidal activities were statistically analysed using Excel to give the IC_{50} & IC_{50s} and IC_{90} & IC_{90s} values.).

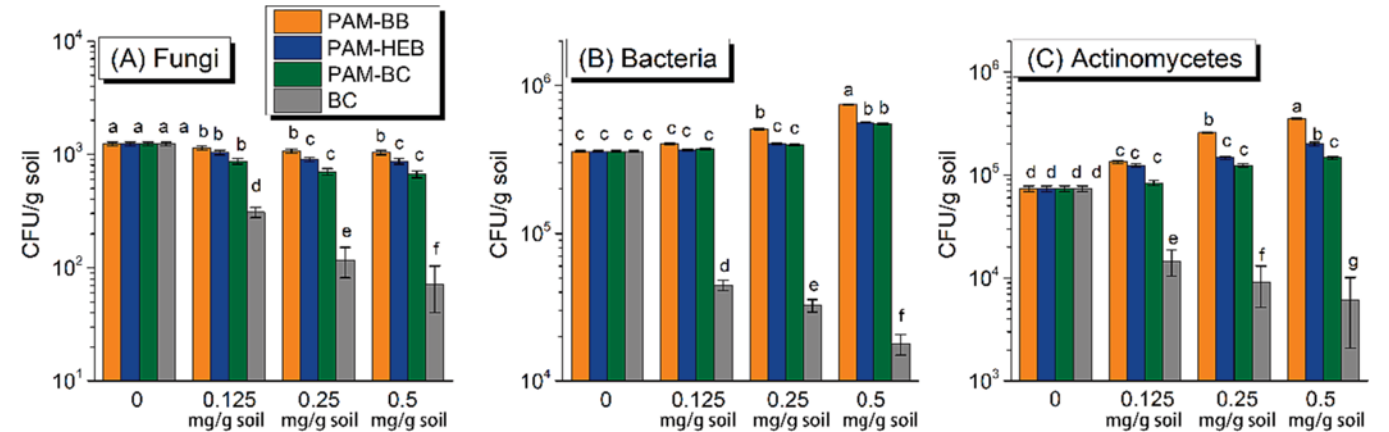


Fig. 4. Culturable populations of fungi (A), bacteria (B) and actinomycetes (C) in soils from the PAM-X treatments. (Vertical bars represent the standard error of the means. Treatments followed by different letters are significantly different according to Duncan's multiple range test ($p < 0.05$)).

adsorption of PAM-X in soil: due to the good adsorption of PAM-X in soil, most of the PAM-X chains were stably adsorbed on the surface of soil particles, which greatly reduces the effective contact probability between free PAM-X chains and microorganisms in soil. The increased bacterial numbers and decreased fungal numbers following PAM-X application represent an increase in soil fertility, possibly resulting in greater inhibition of *Foc4*.

In addition to the effect on the microbial community in the soil, the application of PAM-X to the soil also affected the earthworms living in the soil and the natural water environment in contact with the soil. Although quaternary ammonium salt showed high aquatic acute toxicity (e.g., zebrafish acute toxicity), considering that PAM-X is not directly applicable to natural water but applied to field soil, the only way to enter natural water (such as ponds and streams) is to be brought into or leached away by irrigation or rainwater. Therefore, in addition to routine evaluation of fish acute toxicity (LC_{50}) of PAM-X solutions, the fish acute toxicity of simulated rain leaching solution containing PAM-X soil (LC_{50L}) and a suspension containing PAM-X and soil (LC_{50S}) were also evaluated, which could help to simulate the actual application conditions of PAM-X in the field.

Fig. 5 shows the acute toxicities of three types of PAM-X, PAM-BB, PAM-HEB and PAM-BC on earthworms and zebrafish in which BC was chosen as the positive control. After 14 d of culture, the LC_{50} values for PAM-X and BC to earthworms were > 600 mg/kg and 150 mg/kg,

respectively, which means that both PAM-X and BC had no acute toxicity to earthworms. The acute toxicity of PAM-X and BC to zebrafish (*D. rerio*) is quite high; the LC_{50} of the three kinds of PAM-X is in the range of 1 to 10 mg/L (moderately toxic), and the LC_{50} of BC is less than 1 mg/L (highly toxic). After the application in soil, due to the good absorption of PAM-X in soil, the acute toxicity of both the leachate solution of the soil/PAM-X mixture (LC_{50L}) and the suspension of water/soil/PAM-X (LC_{50S}) could be significantly reduced: the LC_{50L} and LC_{50S} of three kinds of PAM-X were more than 600 mg/(kg soil), which is the actual maximum dosage of PAM-X in soil. For comparison, the LC_{50L} and LC_{50S} of BC under the same conditions are 70 mg/L and 150 mg/L. This means that the leaching solutions of the soil/PAM-X mixture and soil/BC mixture are non-acute-toxic and low-acute-toxic for zebrafish, respectively, according to GB/T 31270.12 (Test guidelines on environmental safety assessment for chemical pesticides).

4. Conclusions

Taken together, combining the strong adsorption effect of polyacrylamide in soil and the good anti-fungi activities of polymeric quaternary ammonium salts, polyacrylamide containing quaternary ammonium salts (PAM-X, including PAM-BB, PAM-HEB and PAM-BC) show strong soil-adsorption effect and exhibit inhibitory effects on the mycelial and conidial growth of *Foc4*, in which PAM-BC with a benzyl

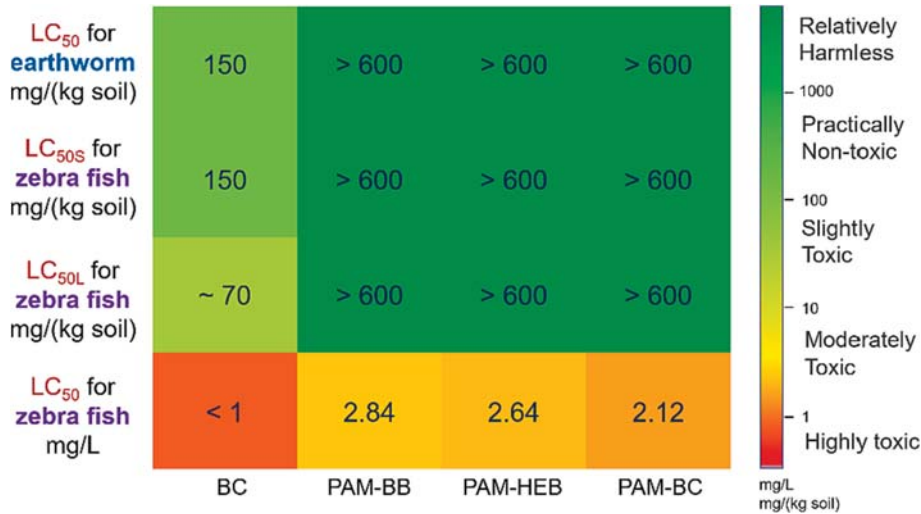


Fig. 5. LC_{50} , LC_{50L} , and LC_{50S} of PAM-X for zebrafish (*Danio rerio*) and earthworms (96 h). (Potassium dichromate and chloroacetamide were used as zebrafish and earthworm reference poisons, respectively. BC was used as a positive control. Average of three replicates.).

structure has better inhibitory and fungicidal effects. Due to the long chain of PAM-X, it exhibits easy adsorption in soil and is hard to move in soil, which makes it unlikely to flow into groundwater and cause water pollution. The IC_{50S} of PAM-X in soil is lower and more stable than that in indoor medium and can resist the invasion of *Foc4* conidia in soil. Unlike small molecule quaternary ammonium salts (such as benzalkonium chloride), which can kill almost all microorganisms in the soil, the adding of PAM-X can maintain the general balance of microbial population in the soil, in which the fungal population was effectively inhibited, while the bacteria and actinomycetes population was promoted, thus help to obtain a “bacterial soil” that is more conducive to plant growth. The good adsorption and difficult migration in the soil of PAM-X greatly reduce its impact on earthworms in the soil, and the soil drenching solution and soil suspension containing PAM-X are nontoxic to fish, which provides a new prevention and control method for SBF. It is also noticed that although PAM-X showed well anti-*Foc4* activities in soil and have less impact on environment, the non-degradability of PAM-X might be a risk for its application in soil, and degradable materials might be considered in the future work.

Declaration of competing interest

The authors declare that they have no known competing financial interests or personal relationships that could have appeared to influence the work reported in this paper.

Data availability

Data will be made available on request.

Acknowledgements

The authors acknowledge the financial support from the National Natural Science Foundation of China (Nos. 52073098 and 31772202) and the Scientific and Technological Planning Project of Guangzhou City (201803020015).

Appendix A. Supplementary data

Supplementary data to this article can be found online at <https://doi.org/10.1016/j.eurpolymj.2023.112604>.

References

- [1] W.W. Bockus, J.P. Shroyer, The impact of reduced tillage on soilborne plant pathogens, *Annu. Rev. Phytopathol.* 36 (1) (1998) 485–500.
- [2] H. Li, J. Huang, H. Yuan, Advances in control of plant soil-borne diseases by organic amendments, *Acta Phytopathologica Sinica* 32 (4) (2002) 289–295.
- [3] P. Gay, P. Piccarolo, D.R. Aimonino, C. Tortia, A high efficacy steam soil disinfection system, part II: Design and testing, *Biosyst. Eng.* 107 (3) (2010) 194–201.
- [4] B.G. Siddhesh, K.S.S. Upendra, R.G. Thumballi, Fusarium wilt of banana: biology, epidemiology and management, *International Journal of Pest Management* 61 (3) (2017) 250–263.
- [5] L. Teixeira, E. Nomura, E. Damatto, et al., Effectiveness of soil management practices on Fusarium wilt of banana in the Ribeira Valley, Brazil, *Tropical Plant Pathology* 47 (3) (2022) 1–10.
- [6] T. Bratec, N. Kirchhübel, N. Baranovskaya, et al., Towards integrating toxicity characterization into environmental studies: case study of bromine in soils, *Environ. Sci. Pollut. Res.* 26 (2019) 19814–19827.
- [7] T.V. Nguyen, L.T.T. Tran-Nguyen, C.L. Wright, et al., Evaluation of the efficacy of commercial disinfectants against *Fusarium oxysporum* f. sp. *cubense* race 1 and tropical race 4 propagules, *Plant Dis.* 103 (4) (2019) 721–728.
- [8] Z.Z. Shen, C. Xue, P.W.J. Taylor, Y.N. Ou, B.B. Wang, Y. Zhao, Y.Z. Ruan, R. Li, Q. R. Shen, Soil pre-fumigation could effectively improve the disease suppressiveness of biofertilizer to banana Fusarium wilt disease by reshaping the soil microbiome, *Biol. Fertil. Soils* 54 (2018) 793–806.
- [9] R.A. Segura, J.J. Stoorvogel, F.A. Blanco, J.A. Sandoval, A medium-term field experiment to study the effect of managing soil chemical properties on Fusarium wilt in banana (Musa AAA), *Journal of Fungi* 7 (2021) 261.
- [10] B. Nel, C. Steinberg, N. Labuschagne, et al., The potential of nonpathogenic *Fusarium oxysporum* and other biological control organisms for suppressing fusarium wilt of banana, *Plant Pathol.* 55 (2) (2006) 217–223.
- [11] L.F. Izquierdo-García, S.L. Carmona, P. Zuluaga, G. Rodríguez, M. Dita, M. Betancourt, M. Soto-Suárez, Efficacy of disinfectants against *Fusarium oxysporum* f. sp. *cubense* tropical race 4 isolated from La Guajira, Colombia, *Journal of Fungi* 7 (2021) 297.
- [12] S. Hong, H.L. Jv, M. Lu, B.B. Wang, Y.Z. Ruan, Significant decline in banana Fusarium wilt disease is associated with soil microbiome reconstruction under chilli pepper-banana rotation, *Eur. J. Soil Biol.* 97 (2020), 103154.
- [13] J. Yang, Y. Duan, X. Liu, et al., Reduction of banana fusarium wilt associated with soil microbiome reconstruction through green manure intercropping, *Agr Ecosyst Environ* 337 (2022), 108065.
- [14] J.W. Jr, B. Heldreth, W.F. Bergfeld, et al., Safety assessment of polyquaternium-22 and polyquaternium-39 as used in cosmetics, *Int. J. Toxicol.* 35 (s3) (2016) 47–53.
- [15] Y. Jiao, L.N. Niu, S. Ma, J. Li, R.T. Franklin, J.H. Chen, Quaternary ammonium-based biomedical materials: State-of-the-art, toxicological aspects and antimicrobial resistance, *Prog. Polym. Sci.* 71 (2017) 53–90.
- [16] C. Zhang, Y. Tezel, K. Li, et al., Evaluation and modeling of benzalkonium chloride inhibition and biodegradation in activated sludge, *Water Res.* 45 (3) (2011) 1238–1246.
- [17] B. Sarkar, M. Megharaj, Y. Xi, et al., Sorption of quaternary ammonium compounds in soils: implications to the soil microbial activities, *J. Hazard. Mater.* 184 (1–3) (2010) 448–456.
- [18] G.Q. Lu, D.C. Wu, R.W. Fu, Studies on the synthesis and antibacterial activities of polymeric quaternary ammonium salts from dimethylaminoethyl methacrylate, *React. Funct. Polym.* 67 (4) (2007) 355–366.
- [19] Y. Lei, S. Zhou, C. Dong, et al., PDMS tri-block copolymers bearing quaternary ammonium salts for epidermal antimicrobial agents: Synthesis, surface adsorption and non-skin-penetration, *React. Funct. Polym.* 124 (2018) 20–28.
- [20] C.C. Zhou, H. Wang, H.T. Bai, P.B. Zhang, L.B. Liu, S. Wang, Y.L. Wang, Tuning antibacterial activity of cyclodextrin-attached cationic ammonium surfactants by a supramolecular approach, *ACS Appl. Mater. Interfaces* 9 (2017) 31657–31666.
- [21] C.J. Raorane, Y. Kim, T. Periyasamy, J.H. Lee, S. Ulaganathan, T.J. Nam, S.C. Kim, J. Lee, Quaternary ammonium salt (QAS)-modified thermoresponsive PNIPAM-PDMAEA copolymer for antibiofilm and antimicrobial applications, *Polymer* 281 (2023), 126104.
- [22] W. Ji, R.R. Koepsel, H. Murata, et al., Bactericidal specificity and resistance profile of poly(quaternary ammonium) polymers and protein–poly(quaternary ammonium) conjugates, *Biomacromolecules* 18 (8) (2017) 2583–2593.
- [23] M. Rahman, M. Bam, E. Luat, et al., Macromolecular-clustered facial amphiphilic antimicrobials, *Nature, Communications* 9 (2018) 5231.
- [24] A. Zhang, Q. Liu, Y. Lei, et al., Synthesis and antimicrobial activities of acrylamide polymers containing quaternary ammonium salts on bacteria and phytopathogenic fungi, *React. Funct. Polym.* 88 (2015) 39–46.
- [25] A.I. Mamedov, S. Beckmann, C. Huang, G.J. Levy, Aggregate stability as affected by polyacrylamide molecular weight, soil texture, and water quality, *Soil Sci. Soc. Am. J.* 71 (6) (2007) 1909–1918.
- [26] A.I. Mamedov, C.H. Huang, F.A. Aliev, et al., Aggregate stability and water retention near saturation characteristics as affected by soil texture, aggregate size and polyacrylamide application, *Land Degrad. Dev.* 28 (2) (2017) 543–552.
- [27] B. Kebede, A. Tsunekawa, N. Haregeweyn, et al., Effectiveness of polyacrylamide in reducing runoff and soil loss under consecutive rainfall storms, *Sustainability* 12 (4) (2020) 1597.
- [28] Z.Z. Ismail, U. Tezel, S.G. Pavlostathis, Sorption of quaternary ammonium compounds to municipal sludge, *Water Res.* 44 (7) (2010) 2303–2313.
- [29] H. Jiang, L. Xu, Y. Hu, et al., Flotation and adsorption of quaternary ammonium cationic collectors on diaspore and kaolinite, *Trans. Nonferrous Met. Soc. Chin.* 21 (11) (2011) 2528–2534.
- [30] F.L. Santos, J.L. Reis, O.C. Martins, et al., Comparative assessment of infiltration, runoff and erosion of sprinkler irrigated soils, *Biosyst. Eng.* 86 (3) (2003) 355–364.
- [31] Z. Huang, R. Liuyang, C. Dong, et al., Polymeric quaternary ammonium salt activity against *Fusarium oxysporum* f. sp. *cubense* race 4: Synthesis, structure-activity relationship and mode of action, *React. Funct. Polym.* 114 (2017) 13–22.
- [32] Y.Y. Chang, W.Q. Zhong, J.Q. Liang, A.Q. Zhang, Y.L. Lin, Polydimethylsiloxane-polymethacrylate block copolymers containing quaternary ammonium salts against *Fusarium oxysporum* f. sp. *cubense* race 4 in soil: Antifungal activities and pot experiments, *React. Funct. Polym.* 160 (2021), 104848.
- [33] B.P. Mowery, S.E. Lee, D.A. Kissounko, et al., Mimicry of antimicrobial host-defense peptides by random copolymers, *J. Am. Chem. Soc.* 129 (50) (2007) 15474–15476.
- [34] M.T. Garcia, I. Ribosa, T. Guindulain, et al., Fate and effect of monoalkyl quaternary ammonium surfactants in the aquatic environment, *Environ. Pollut.* 111 (1) (2001) 169–175.
- [35] G. Bonanomi, V. Antignani, M. Capodilupo, et al., Identifying the characteristics of organic soil amendments that suppress soilborne plant diseases, *Soil Biol. Biochem.* 42 (2) (2010) 136–144.

PAPER



Cite this: *J. Mater. Chem. A*, 2024, 12, 12134

Simultaneously enhancing the mechanical robustness and conductivity of ionogels by *in situ* formation of coordination complexes as physical crosslinks†

Ning Yu,^a Yujiang Meng,^a Rui Li,^a Dongdong Mai,^c Shijie Shan,^a Xionghui Wu,^a Yaling Lin^{*b} and Anqiang Zhang^{id} ^{*a}

Ionogels with environmental tolerance have recently emerged as promising candidates for use in flexible electronics. However, a challenge still exists in simultaneously enhancing the mechanical robustness and conductivity of ionogels. In this paper, we demonstrate a facile and fast novel strategy for forming a high-strength metal-coordinated solvent-free ionogel through *in situ* polymerization in one pot. The resulting iongel exhibits high tensile strength (5.68 MPa) and elongation at break (600%) due to the presence of imidazole nitrogen–Ni²⁺ coordination complexes as physical crosslinks. Furthermore, the conductivity of the ionogel is increased to $68.63 \times 10^{-3} \text{ S m}^{-1}$ by incorporating metal ions as conductive fillers, which is 10 times higher than that of the ionogel without metal ions prepared under the same conditions. The strategy, based on the universal coordination between imidazole nitrogen and multivalent metal ions, is highly versatile and can be applied to a wide range of metal ions (Co²⁺/Zn²⁺). The ionogel can be utilized in the assembly of strain sensing and humidity sensors for human health monitoring. Additionally, its fast photo curing properties make it suitable as a 3D printing ink for customizing tough pressure sensors with microstructures, demonstrating its potential as an engineering material and wearable sensor.

Received 13th February 2024
Accepted 10th April 2024

DOI: 10.1039/d4ta01001a

rsc.li/materials-a

1. Introduction

Soft ionic conductors have a wide range of applications, including human-interactive technologies, biomedical devices, supercapacitors, wearable health monitors, and electronic skins.^{1–4} Among the various types, hydrogels and ionogels have gained significant attention in research due to their high ionic conductivity and their ability to withstand tension and compression. They also exhibit transparency and response to multiple stimuli. However, hydrogels are prone to instability in the environment, as they can lose water and freeze easily.^{5–7} On the other hand, ionogels, which are polymeric networks dispersed in ionic liquids, possess many unique features of ionic liquids, such as non-volatility, nonflammability, and high thermal and chemical stability. These properties make ionogels suitable for applications

in extreme environments with long-term reliability.^{8–10} Therefore, ionogels are considered an ideal alternative to hydrogel conductors. However, achieving the required conductivity in ionogels requires a significant amount of ionic liquid to be incorporated into the polymer network, which results in a notable decrease in the mechanical properties of the materials.

Numerous studies have focused on enhancing the mechanical performance of ionogels with high ionic liquid content. Chemical-crosslink ionogels typically exhibit satisfactory fracture strength and elasticity. However, they lack the ability to be repaired after damage, significantly reducing the ionogels' service life.¹¹ In contrast, physical crosslinking ionogels demonstrate remarkable self-healing ability due to the incorporation of dynamic interactions such as hydrogen bonds, ion-dipole interactions, and electrostatic interactions. For instance, Yue *et al.* successfully developed a transparent ionogel through hydrogen bonds and ion-dipole interactions.¹² These ionogels exhibited high conductivity and excellent self-healing ability at room temperature, albeit with a lower mechanical strength. Notably, as the ionic liquid content increased to 70%, the conductivity reached 2.92 mS cm^{-1} , but the tensile strength significantly decreased to 0.11 MPa. Consequently, the simultaneous achievement of high conductivity and mechanical properties in ionogels remains a significant challenge.

^aSchool of Materials Science and Engineering, South China University of Technology, 381 Wushan Rd., Guangzhou 510641, Guangdong, China. E-mail: aqzhang@scut.edu.cn

^bCollege of Materials and Energy, South China Agricultural University, 483 Wushan Rd., Guangzhou 510642, Guangdong, China. E-mail: linyaling@scau.edu.cn

^cSchool of Materials Science and Engineering, Guangdong University of Petrochemical Technology, Maoming 525000, Guangdong, China

† Electronic supplementary information (ESI) available. See DOI: <https://doi.org/10.1039/d4ta01001a>

Among the various non-covalent bonds investigated, metal coordination bonds are known to exhibit stronger binding, thereby enhancing the mechanical strength of coordination complexes. However, most research on metal-triggered complexation has primarily focused on hydrogels, with limited attention given to ionogels.^{13,14} Furthermore, previous studies on synthesizing metal coordination complexes have involved the use of large amounts of organic solvents and complex processes (specifically, the two-step controllable permeation method), which are time-consuming.^{15–18} It is also noteworthy that in polymer systems, multiple metal salts often serve a single function. For example, Lv *et al.* prepared a P (VI-co-VmimBF₄) ionogel with Zn²⁺ dynamic metal ligand interaction, resulting in a mechanical strength of only 0.58 MPa without contributing to conductivity.³ The potential of ions to produce tough and highly conductive ionogels has been overlooked in previous studies, but this work aims to address this issue. In this study, we present a simple and efficient method for preparing a solvent-free ionogel. This is achieved through a one-pot photo-initiated copolymerization of 2-hydroxyethyl acrylate (HA) and 1-vinylimidazole (IM) in a transparent and homogeneous solution of IL and NiCl₂·6H₂O. In particular, a hydrophilic room temperature quaternary ammonium based ionic liquid (IL) was prepared through a simple quaternization reaction. The IM–Ni²⁺ complex, formed by the coordination between Ni²⁺ and lone-pair-electrons of N atoms on imidazole rings, is introduced to enhance the mechanical strength. It is worth noting that Ni²⁺ also acts as a conductive filler, effectively balancing the trade-off between mechanical strength and conductivity, which is a novel finding. By adjusting the feeding molar fraction of Ni²⁺ and IL, the mechanical properties and ionic conductivity of the ionogel can be tailored over a wide range. The resulting solvent-free ionogel, named HAIM-IL-Ni, exhibits humidity sensitive characteristics and good sensing capabilities at low temperatures. Furthermore, the precursor solution can be rapidly solidified under digital light processing (3D printing) to create a durable metal supramolecular ionogel, allowing for the customization of a pressure sensor with a microstructure. This concept can also be extended to other monomers and metal ions (Co²⁺/Zn²⁺), offering a promising and straightforward approach for developing high strength and conductivity ionogels.

2. Results and discussion

2.1 Fabrication of HAIM-IL-Ni ionogels

The synthesis methodology of HAIM-IL-Ni ionogels is depicted in Fig. 1a. The ionogels were prepared by conducting a simple one-pot photo-initiated copolymerization of HA and IM in a transparent and homogeneous solution of ILs and NiCl₂·6H₂O, without the use of any chemical cross-linkers. The reaction took place in a PTFE mold (Fig. 1a), where imidazole–Ni²⁺ coordination complexes were formed *in situ*, acting as the physical crosslinks. The figure also displays the appearance of different metal coordination ionogels. In this process, HA monomers were chosen to create a flexible polymeric matrix. The PHA chains, rich in hydroxyl groups, formed a physical

cross-linked network through intramolecular hydrogen bonds. On the other hand, IM was selected as a comonomer to introduce rigid aromatic heterocyclic structures and hydrogen bond acceptors, thereby modifying the mechanical properties of the ionogel. IL was utilized to enhance the conductivity of the ionogel and increase its ductility. However, the solvation of PHAIM in IL resulted in a decrease in mechanical properties. To counteract this, Ni²⁺, Co²⁺, and Zn²⁺ were incorporated to improve the mechanical strength of the ionogel through coordination crosslinking with imidazole. Furthermore, these metal ions also acted as free ions, thereby enhancing the conductivity of the ionogel. This approach achieved a desirable balance between conductivity and mechanical strength.

To investigate the interactions between HAIM-IL-Ni components, MD simulations were performed. Fig. 1b shows the final snapshot of the HAIM-IL-Ni system obtained at the end of the simulation. Additionally, to gain a comprehensive understanding of the interactions in the gel system, the total potential energy of all interactions in HAIM-IL-Ni was calculated. The potential energy of HAIM₄₁-IL₄-Ni₆ was found to be lower than that of HAIM₄₁-IL₄, indicating a more stable system with stronger interactions due to the formation of coordination bonds (Fig. 1c). The radial distribution function *g*(*r*) of HA and IM was also calculated to examine the interactions between them (Fig. 1d). For HAIM₄₁ without IL, a peak is observed in the radial distribution function at an *r*-OH...N value of 1.96 Å, suggesting the presence of hydrogen bonds. However, in the presence of IL, the height of the peak decreases.¹⁹ The addition of Ni²⁺ in the ionogel leads to a higher peak height, indicating that the presence of Ni²⁺ suppresses the solvation of HAIM₄₁ chains by IL and promotes the formation of intermolecular hydrogen bonds in HAIM₄₁. This results in a reduced average distance between hydroxyl groups and imidazole nitrogen in HAIM polymer chains.²⁰

The FTIR spectroscopy and EDX analysis confirmed the chemical structures and elemental compositions of the HAIM-IL-Ni. As shown in Fig. 2a, the vibration stretching peak of C=O occurs at 1720 cm^{−1}, while the vibration stretching peak of C=N occurs at 1555 cm^{−1}, and the vibration stretching peak of C–N occurs at 1258 cm^{−1}. The presence of strong hydrogen bonding between the chains in HAIM₄₁ samples without IL causes the C=N and C–N vibration peaks to shift to lower wavenumbers. However, after the addition of IL, the solvation effect reduces the intermolecular force of the polymer, resulting in a change in the high wavenumber. In the case of HAIM₄₁-IL₄-Ni₆, the coordination of Ni²⁺ leads to a reduction in distance between the polymer chains, causing a shift of C=O, C=N, and C–N to lower wavenumbers, indicating the successful coordination of metal ions.^{21,22} The C, O, N, Cl, and Ni elements are uniformly distributed and arranged in the whole polymer network of HAIM₄₁-IL₄-Ni₆ (Fig. 2b and S2†). Notably, there is a uniform distribution of Ni²⁺ in the polymeric network without any aggregation, which is beneficial for the formation of dynamic metal coordination between Ni²⁺ and IM in one crosslinking network. The formation of coordination between Ni²⁺ and imidazole nitrogen was further confirmed by XPS. The XPS curves of NiCl₂·6H₂O and HAIM₄₁-IL₄-Ni₆ (Fig. 2c) show

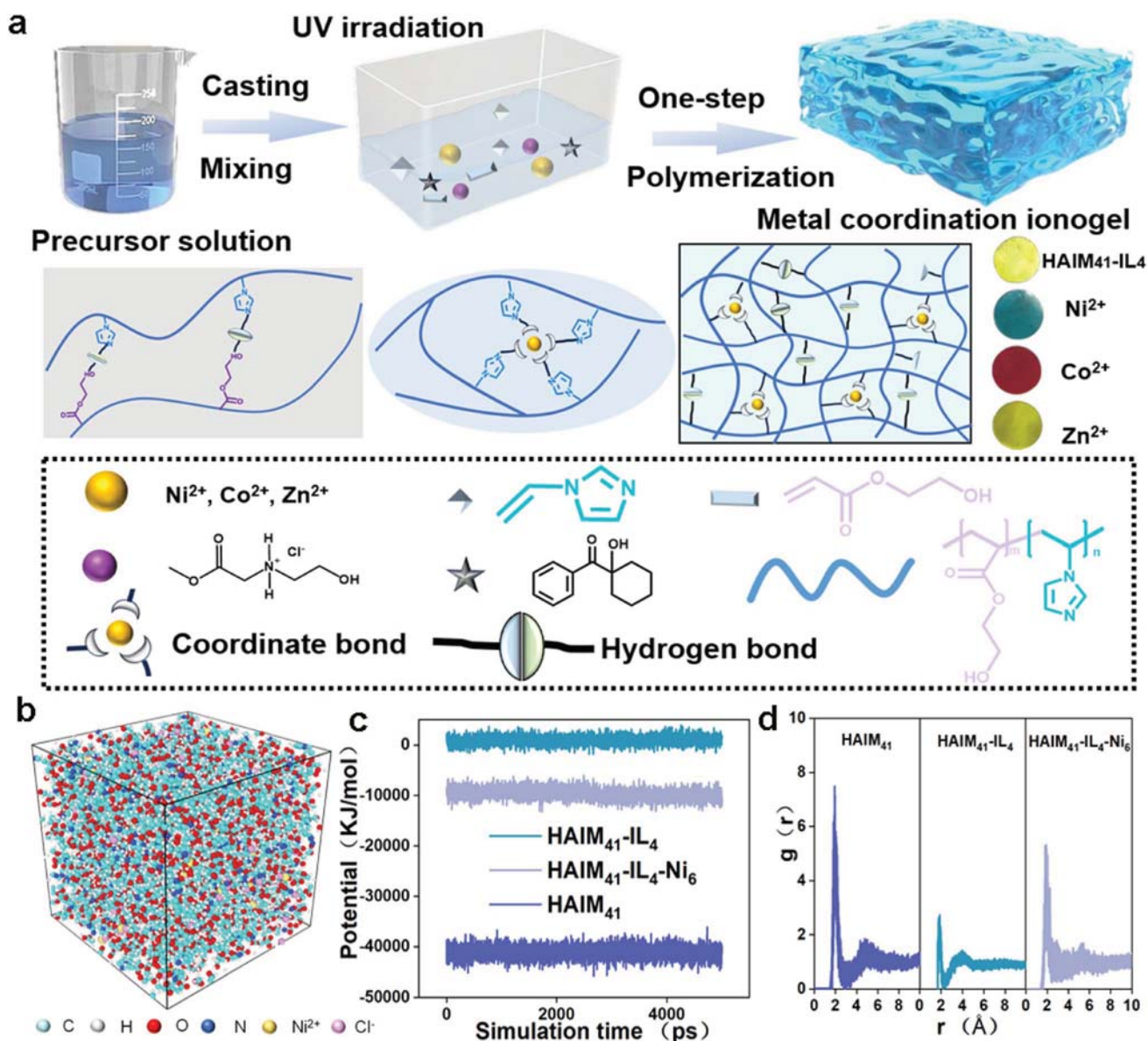


Fig. 1 (a) Schematic illustration of the syntheses and polymer network structures of the HAIM-IL-Ni ionogel. (b) Final snapshot of the metal coordination ionogel simulation system. (c) Potential energy of HAIM₄₁ and HAIM₄₁-IL₄ and HAIM₄₁-IL₄-Ni₆. (d) Radial distribution function $g(r)$ of the HA and IM.

that the Ni 2p peaks (854.3 eV) of HAIM₄₁-IL₄-Ni₆ shift towards lower binding energy (853.0 eV), indicating the interaction between Ni²⁺ and imidazole nitrogen.²³ The XRD diagram (Fig. 2d) of the metal coordination ionogel in the 2θ range from 5 to 60° indicates that the sample was in an amorphous form. However, the increase in the diffraction peak intensity of the HAIM₄₁ sample may be attributed to the high density of hydrogen bonds among polymer chains.²⁴ Furthermore, the input of Ni²⁺ was completely involved in the metal coordination reaction, and no residual crystalline solid was precipitated in the polymer network (Fig. S3†).

The aggregates in the polymer matrix of HAIM₄₁-IL₄-Ni₆ can be observed using transmission electron microscopy (TEM), as shown in Fig. S4.† These dark spherical spots are identified as

ion clusters formed by metal coordination. In contrast, no aggregation is observed in the TEM image of the HAIM₄₁-IL₄ sample. Elemental mapping of the scanning transmission electron microscopy (STEM) image was conducted using energy-dispersive X-ray spectroscopy (EDS) to identify elements present in the film (Fig. 2e). Strong signals of Ni, N, and Cl were observed in the nanoparticle regions, suggesting that the nanoparticles primarily consist of nitrogen-Ni²⁺ coordination ion clusters. The TGA curve demonstrates the excellent thermal stability of HAIM₄₁-IL₄-Ni₆, as there is no significant thermal degradation below 200 °C (Fig. 2f). However, above this temperature, the ionic liquid may decompose and the polymer network may undergo thermal degradation, such as depolymerization, random chain scission, and side-group elimination.

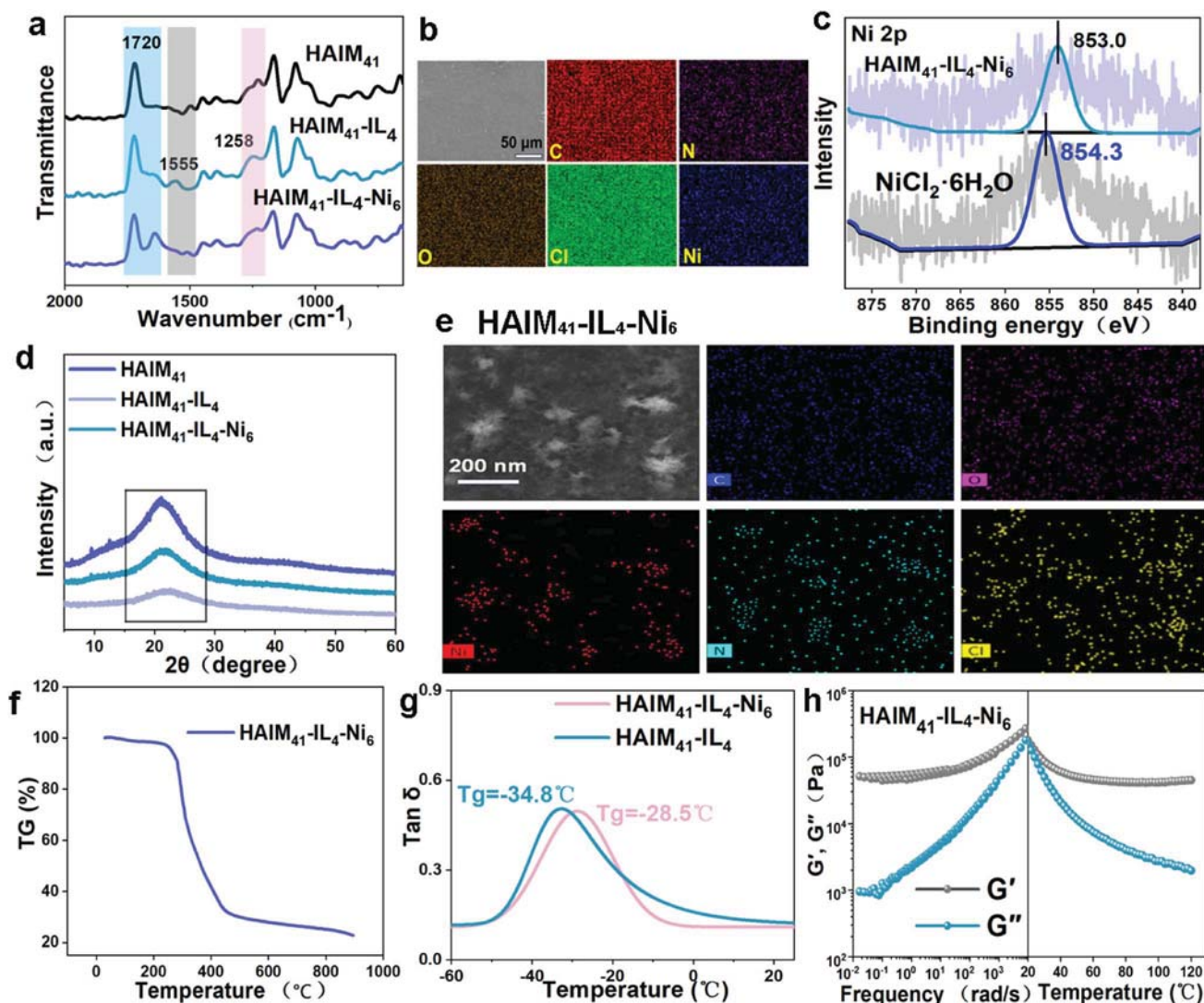


Fig. 2 (a) FTIR spectra. (b) EDS image of the HAIM₄₁-IL₄-Ni₆ surface. (c) XPS Ni 2p signals. (d) XRD curves. (e) STEM dark-field and STEM-EDS elemental mapping of the HAIM₄₁-IL₄-Ni₆. (f) TGA curve of HAIM₄₁-IL₄-Ni₆. (g) DMA curves. (h) Frequency and temperature rheological curves of HAIM₄₁-IL₄-Ni₆.

The DMA test reveals that the glass transition temperature (T_g) of HAIM₄₁-IL₄-Ni₆ is -28.5 °C, indicating that this ionogel material can operate effectively over a wide temperature range (Fig. 2g). The frequency-sweeping rheological results show that the storage modulus (G') of HAIM₄₁-IL₄-Ni₆ is consistently higher than its loss modulus (G'') across all frequencies, suggesting that HAIM-IL-Ni is in a highly elastic state (Fig. 2h). Temperature-sweeping rheological experiments indicate that G' and G'' of HAIM₄₁-IL₄-Ni₆ are similar at room temperature. However, with increasing temperature, the reversible hydrogen bonding and coordination bonding gradually weaken, resulting in a faster decrease in G'' compared to G' (Fig. 2h).

2.2 Mechanical properties and self-healing properties of HAIM-IL-Ni ionogels

The excellent mechanical properties of the fabricated HAIM-IL-Ni ionogel were confirmed through a series of tensile tests.

Fig. 3a shows that the tensile strength of HAIM increased from 45 MPa to 101 MPa as the molar ratios of HA to IM were adjusted from 4 : 1 to 4 : 2. Additionally, the stress-strain curve exhibited typical yielding characteristics.²⁵ The presence of IM, which provides a rigid aromatic heterocyclic structure and acts as a hydrogen-bond acceptor for the HAIM network, resulted in tightly entangled polymer chain segments. DSC tests revealed that the T_g of HAIM₄₁ was approximately 64.6 °C, indicating that the sample was in a glassy state at room temperature (Fig. 3b). The HAIM₄₁ sample was able to support a weight of 500 g (illustrated in Fig. 3b). A suite of stress-strain tests were conducted to investigate the mechanical properties of the ionogels (Fig. 3c). HA₄-IL₂ exhibited a low tensile strength of 0.3 MPa. Excessive input of IL into the samples led to failure in achieving a solid form. The addition of IM adjusted the strength of the HAIM-IL series. The tensile strength of HAIM₄₁-IL₂ significantly increased to 1.82 MPa. As the IL content was adjusted from 20

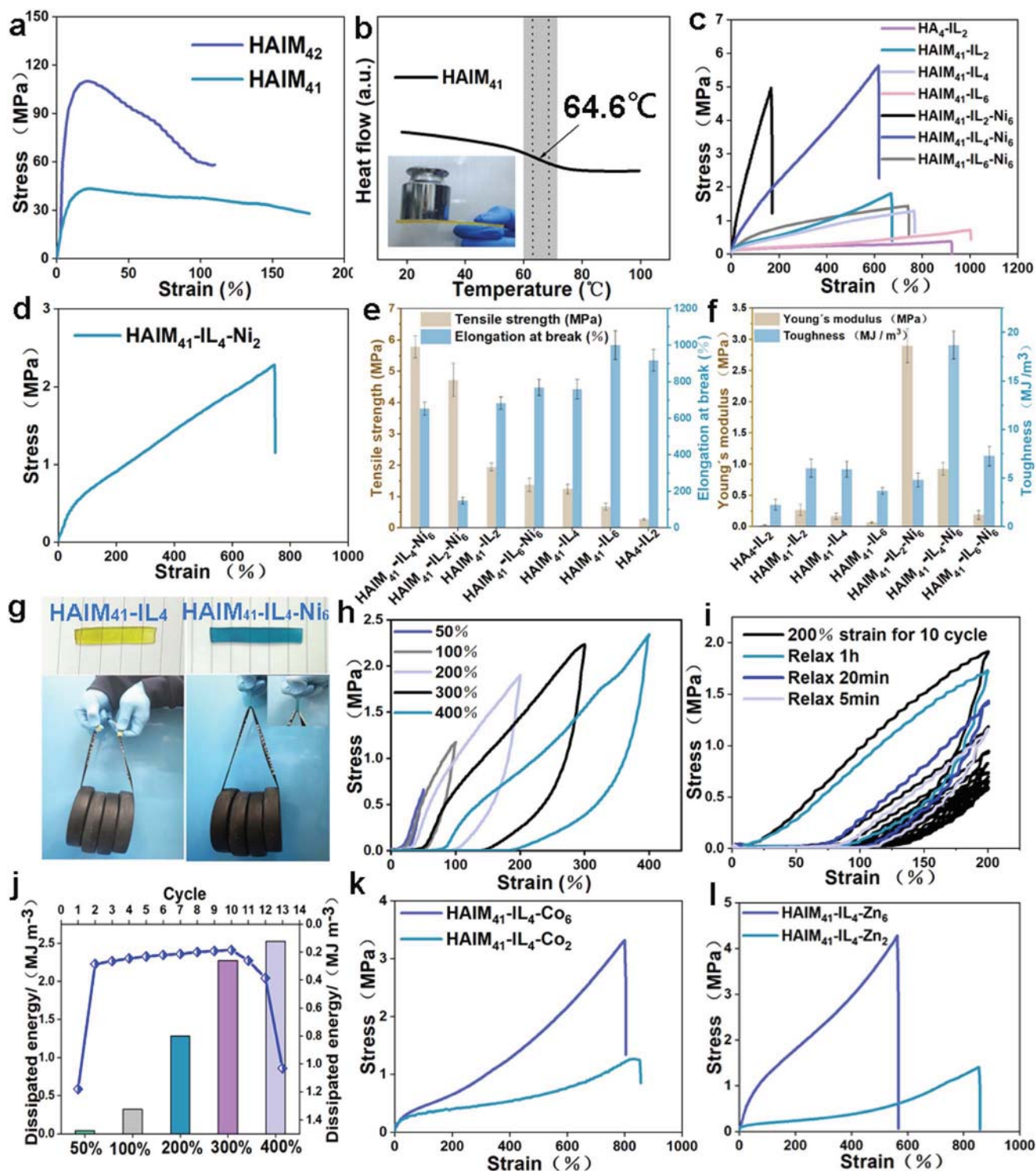


Fig. 3 (a) Tensile stress–strain curves of HAIM. (b) DSC determination T_g (illustration: demonstration of the HAIM₄₁ holding a 500 g weight). (c) Tensile stress–strain curves of the ionogels. (d) Tensile stress–strain curves of HAIM₄₁-IL₄-Ni₂. (e) Elongation at break and (f) Young's modulus/toughness of the ionogels. (g) Attempt to pull the dumbbell (5 kg) with HAIM₄₁-IL₄ and HAIM₄₁-IL₄-Ni₆. (h) Cyclic tensile mechanical curves of the HAIM₄₁-IL₄-Ni₆ under different strains. (i) Loading–unloading curves at a strain of 200% for different resting times. (j) Corresponding dissipated energy calculated by the area of cyclic tensile loops. Tensile stress–strain curves of different contents of (k) Co²⁺ and (l) Zn²⁺.

wt% to 60 wt% (from HAIM₄₁-IL₂ to HAIM₄₁-IL₆), the tensile strength of HAIM₄₁-IL decreased from 1.82 MPa to 0.88 MPa, while the elongation at break increased from 669% to 995%.

The addition of IL enhanced the solvation effect of the polymer chain, resulting in decreased interchain force, lower tensile strength, and increased stretchability. The effect of Ni²⁺

coordination on the mechanical properties of HAIM₄₁-IL-Ni was further investigated. In Fig. 3d, it can be observed that when the Ni²⁺ content is 2 wt%, HAIM₄₁-IL₄-Ni₂ exhibits a tensile strength of 2.20 MPa and an elongation at break of 756%. On the other hand, HAIM₄₁-IL₄-Ni₆, which contains 6 wt% of Ni²⁺, shows excellent tensile strength (5.68 MPa), toughness (18.72 MJ m⁻³), Young's modulus (0.93 MPa), and elongation at break (600%) (Fig. 3e and f). By adjusting the content of the metal ion, a wide range of adjustable mechanical properties can be achieved, similar to regulating physical crosslinking densities. To illustrate the significant difference in mechanical performance, we conducted a weight-lifting experiment using a rectangular ionogel (Fig. 3g). HAIM₄₁-IL₄ stretched significantly but failed to lift the weight, whereas HAIM₄₁-IL₄-Ni₆ successfully lifted the weight. In the ionogel with IL as the solvent, metal coordination acts as a physical crosslinking mechanism, reducing the distance between polymer chains and forming a high density of hydrogen bonds. The combination of multiple chemical or physical crosslinking structures, such as metal coordination, aromatic heterocycle rigid structure and high density of hydrogen bonds, provides an energy dissipation mechanism that greatly enhances the mechanical strength of the ionogel. In addition to mechanical strength, the elastic properties of the ionogel were investigated using loading-unloading tests at different strains and a fixed stretching speed of 100 mm min⁻¹. Fig. 3h and j display the loading-unloading curves and energy loss of HAIM₄₁-IL₄-Ni₆ at strains of 50%, 100%, 200%, 300%, and 400%, respectively. The stretching curve exhibits a significant hysteresis. As the deformation increases from 50% to 400%, the material's energy consumption rises from 0.06 to 2.49 MJ m⁻³, indicating that the disruption of dynamic coordination and hydrogen bonds within the network leads to effective energy dissipation. Additionally, 10 cycles of tensile tests were performed at a larger strain of 200% with no waiting time between consecutive trials. Fig. 3i demonstrates that the first cycle resulted in more energy loss due to the rearrangement of the polymer molecular chain. The lag decreased slightly with the number of cycles, possibly due to the un-recovery of dynamic bonds with partial dissociation in the first cycle.²⁶ Notably, after standing at room temperature for 1 h (Fig. 3i and j), the energy dissipation of the sample returned to almost 95% of the first cycle, indicating good elastic recovery with recovery ability varying over time. We believe this facile strategy can be universally applied to fabricate tough ionogels using other analogous formulas. As a demonstration, we synthesized tough ionogels using two ionic species, Co²⁺ and Zn²⁺, following a similar protocol. All the ionogels exhibited toughness and stretchability, with their mechanical properties easily regulated by changing the ion content (Fig. 3k and l).

The self-repair performance of HAIM₄₁-IL₄-Ni₆ was evaluated using a tensile test at 60 °C, with different healing times. The stress-strain curves of HAIM₄₁-IL₄-Ni₆ after 4 h, 8 h, and 24 h of healing are shown in Fig. S5a.† The mechanical strength and break elongation of the samples gradually recovered with longer self-healing time. Fig. S5b† demonstrates that when the healing time reached 24 h, the self-healing efficiency of stress and strain reached 85% and 90%, respectively, indicating good

self-healing properties. In Fig. S5(c1) and S5(c2),† pristine and rhodamine-dyed heart-shaped elastomer films were cut into two pieces, which were then brought into contact without any external force. Subsequently, the film was placed in a constant temperature and humidity box (40% RH and 60 °C) for a period of time (Fig. S5(c3)†), resulting in an ionogel film with a bicolor heart shape. This film remained intact even when stretched under external force (Fig. S5(c4)†). After 24 h of self-healing, light micrographs showed that the incision on the film had nearly disappeared (Fig. S5d†). Furthermore, Fig. S5e† demonstrates that the healed sample can even withstand a weight of 500 g. The real-time resistance of HAIM₄₁-IL₄-Ni₆ was measured and is depicted in Fig. S5f.† When the sample was severed, the resistance-time curve exhibited a sharp rising peak, indicating a discontinuous ion transport path in the separated section. Over time, as the separated part healed, the ionic resistance gradually returned to 98% of its original value within 0.3 s. This conductive self-healing process was successfully replicated in three cycle trials, and the luminous LED bulb also shows the electrical self-healing capability of the ionogel, as shown in Fig. S5g.† The self-healing process of the ionogel can be described as follows: when the gel breaks, the ionic, coordination, and hydrogen bonds at the interface are primarily disrupted, causing the entangled HAIM chains to untangle. Upon rejoining the two broken parts of the ionogel, the dynamic bonds quickly reestablish. Additionally, the HAIM chain exhibits good mobility in ionic liquids, allowing it to move between the two interfaces and re-entangle, thereby facilitating the self-repair process.

2.3 Ionic conductivity of HAIM-IL-Ni ionogels

The ionic conductivity of the HAIM-IL-Ni was determined using electrochemical impedance spectroscopy (EIS). Fig. S6† shows that the ionic conductivity increased from 0.12 to 49.79×10^{-3} S m⁻¹ as the IL content was adjusted from 20 wt% to 60 wt% (from HAIM₄₁-IL₂ to HAIM₄₁-IL₆). The electrical conductivity was also affected by the Ni²⁺ content. As depicted in Fig. 4a and b, the ionic conductivity increased from 3.93 to 68.63×10^{-3} S m⁻¹ as the NiCl₂·6H₂O content gradually increased from 0 to 6 wt% (from HAIM₄₁-IL₄ to HAIM₄₁-IL₄-Ni₆). However, when the NiCl₂·6H₂O content reached 10 wt%, the rigid network caused by the increased crosslinking density hindered the ion channel and led to a decrease in the ionic conductivity. The ionic conductivity was primarily influenced by carrier transfer and content. Ni²⁺ not only provided mechanical properties through metal coordination but also enhanced the conductivity as conductive ions. This enhancement can be attributed to an increase in the number of conducting ions. To further demonstrate the effect of ion migration in the ion gel, we analyzed the mean square shift (MSD) curve of the particles in Fig. 4c. In a particle system, atoms continuously move from their starting point to other areas. The MSD represents the average square displacement of the particles and is an important parameter for characterizing their dynamic behavior.²⁷ Among the particles, HAIM₄₁-IL₄-Ni₆ exhibits a high MSD value, indicating that the introduction of Ni²⁺ increases the number of ions and improves

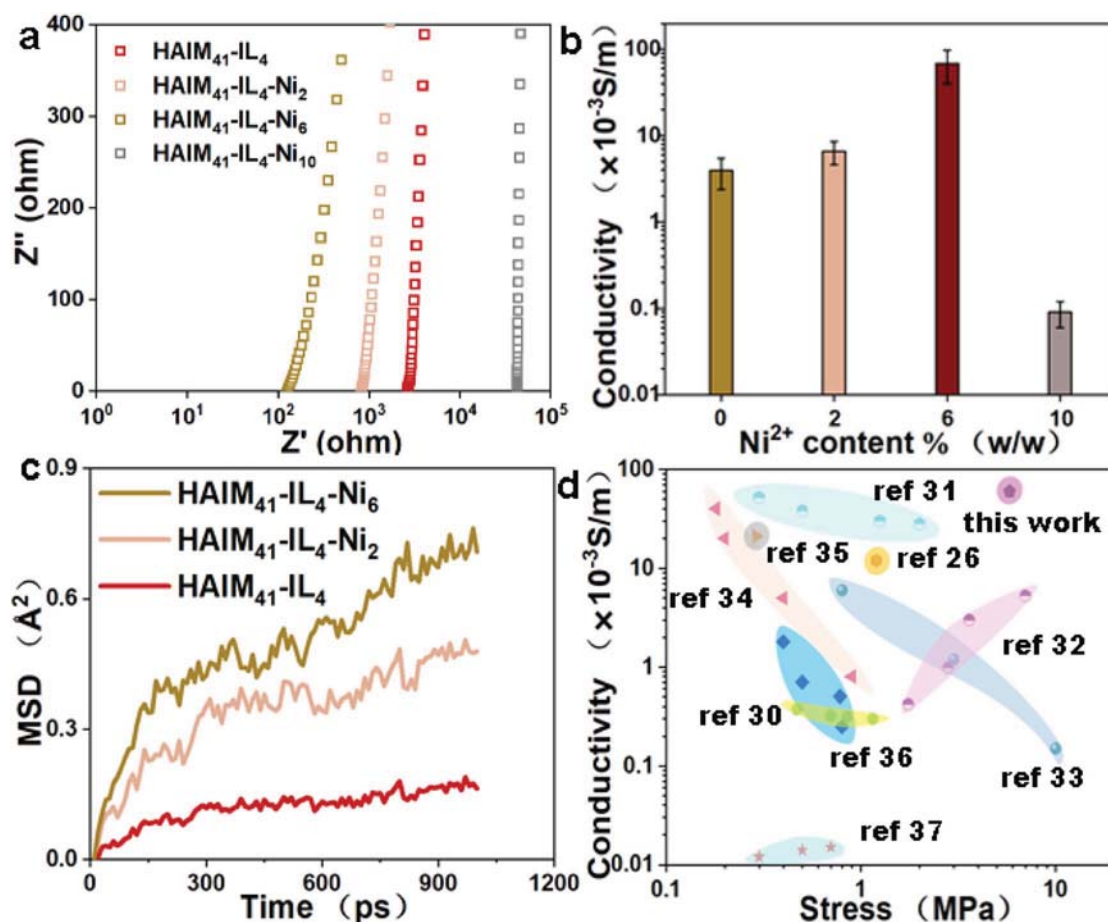


Fig. 4 (a) Impedance spectra of different HAIM-IL-Ni ionogels. (b) Effect of IL content on the conductivities of HAIM-IL-Ni. (c) Calculated MSD of HAIM-IL-Ni. (d) A comparison of ionic conductivity and fracture stress between state-of-the-art conductive ionogel and the $\text{HAIM}_{41}\text{-IL}_4\text{-Ni}_6$ in this work.

conductivity by enhancing the migration rate of anions and cations.^{28,29} Ionogels typically have low ionic conductivity due to strong intermolecular or intra-chain interactions.³⁰ However, in Fig. 4d, we compare the ionic conductivity and fracture stress of our metal coordination-toughened $\text{HAIM}_{41}\text{-IL}_4\text{-Ni}_6$ with other advanced conductive ionogels. Our tough ionogels are positioned in the rightmost area of the plot, indicating that they possess superior fracture strength compared to the best-in-class conductive ionogel while maintaining competitive ionic conductivity.^{26,30–37} This highlights the unique design and excellent properties of our ionogels.

2.4 Sensing properties of the $\text{HAIM}_{41}\text{-IL}_4\text{-Ni}_6$ ionogel

The sensing properties of the $\text{HAIM}_{41}\text{-IL}_4\text{-Ni}_6$ ionogel were further investigated based on its comprehensive mechanical, self-healing and electrical conductivity. The sensitivity of the ionogel strain sensor was assessed by calculating the GF. Fig. 5a illustrates the sensitivities of the $\text{HAIM}_{41}\text{-IL}_4\text{-Co}_6$, $\text{HAIM}_{41}\text{-IL}_4\text{-Zn}_6$, and $\text{HAIM}_{41}\text{-IL}_4\text{-Ni}_6$ ionogel sensors. The sensitivities of the three sensors all exhibited two linear relationship intervals in a small range of 0–50% and a large range of 50–400%. Specifically, the sensitivities of the $\text{HAIM}_{41}\text{-IL}_4\text{-Ni}_6$ ionogel

sensor were respectively 2.55 and 1.28 in the aforementioned ranges. In comparison, the sensitivities of the $\text{HAIM}_{41}\text{-IL}_4\text{-Co}_6$ and $\text{HAIM}_{41}\text{-IL}_4\text{-Zn}_6$ ionogel sensors were lower than those of the $\text{HAIM}_{41}\text{-IL}_4\text{-Ni}_6$ ionogel sensor. Furthermore, the $\text{HAIM}_{41}\text{-IL}_4\text{-Ni}_6$ ionogel sensor successfully detected stable electrical signals for small tensile strains (10%, 20%, 30%, 40%, and 50%), as well as for large tensile strains (100%, 150%, 200%, 250%, and 300%) in five cycle loading and unloading tests (Fig. S7a and b†). To further evaluate its performance, the $\text{HAIM}_{41}\text{-IL}_4\text{-Ni}_6$ was attached to the tester's fingers and tested at bending angles of 30°, 60° and 90° (Fig. 5b). The study found that the relative resistance changes of $\text{HAIM}_{41}\text{-IL}_4\text{-Ni}_6$ increased with the finger bending angle increased (Fig. 5c), indicating that $\text{HAIM}_{41}\text{-IL}_4\text{-Ni}_6$ can respond quickly to changes in the bending angle. When the $\text{HAIM}_{41}\text{-IL}_4\text{-Ni}_6$ was attached to the elbow (Fig. S7c†) and knee (Fig. S7d†) for repeated bending, the change signal of $\Delta R/R_0$ was also noticeable and consistent. In Fig. 5d, under 50% cyclic strain, our gel sensor showed remarkable stability, maintaining the consistency for 1000 cycles at room temperature, which can be attributed to the excellent fatigue resistance of the gel material. Additionally, when the word "SCUT", "福 (fu)", and a heart shape were written on a phone

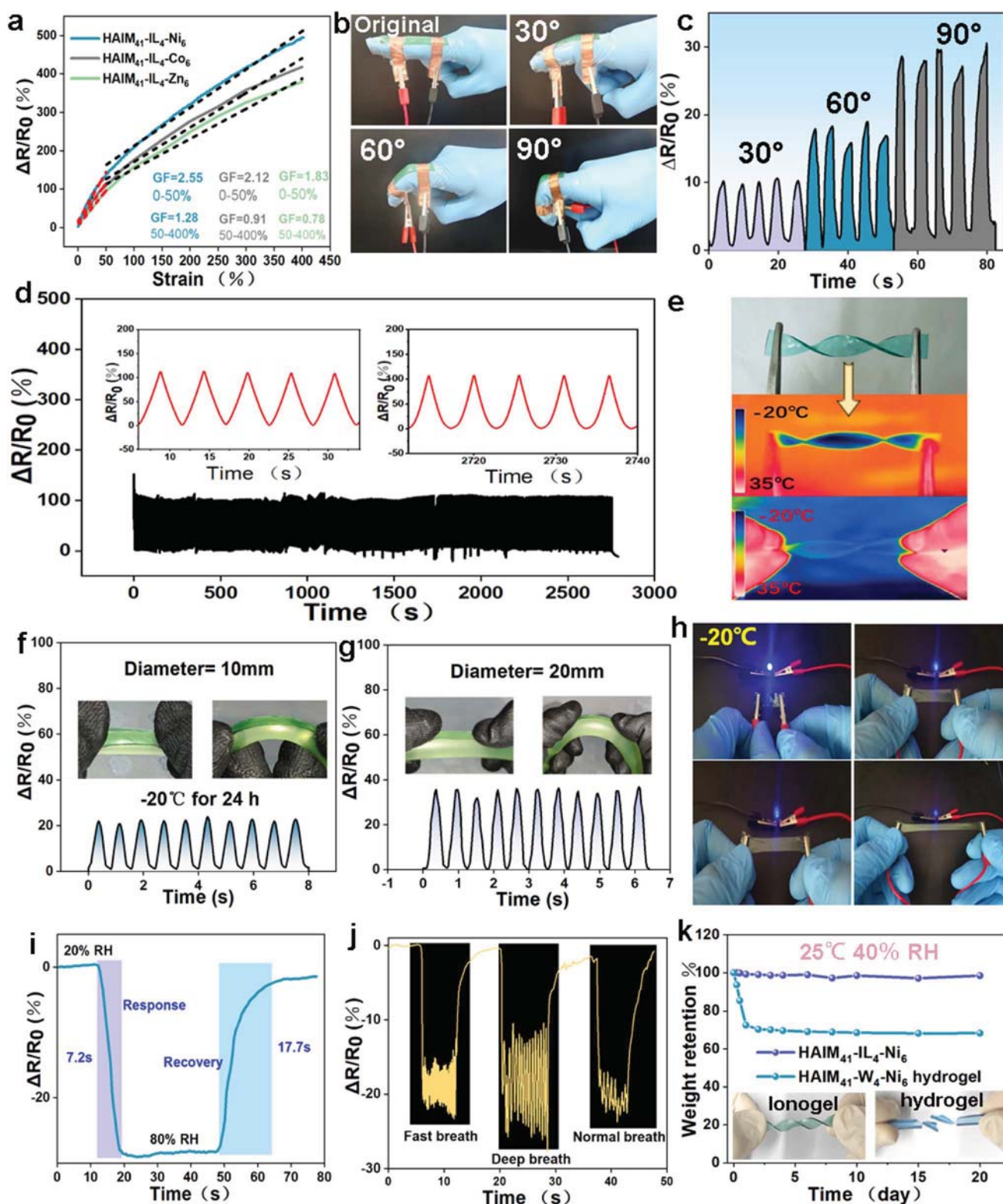


Fig. 5 (a) GF. (b) Sensors attached to the surface of fingers bent at different angles. (c) $\Delta R/R_0$ variation of the sensor to detect finger bending. (d) $\Delta R/R_0$ variation at 50% strain for 1000 cycles. (e) Infrared images of HAIM₄₁-IL₄-Ni₆ being twisted under the cold weather (−20 °C). $\Delta R/R_0$ variation when bending PU rods with diameters of 10 (f) and 20 mm (g) under the cold weather (−20 °C). (h) Change in LED brightness with the elongation of HAIM₄₁-IL₄-Ni₆ connected in the electric circuit in the series circuit at −20 °C. (i) The response/recovery time with an increase in the RH from 20 to 80%. (j) Sensor response to different breathing rates. (k) The weight variation of the hydrogel and ionogel during storage for 20 days at 25 °C and 40% RH environments (illustration: flexible ionogel and broken hydrogel after 20 days).

screen, the reaction speed was fast and accurate, mimicking the experience of writing with a finger on the screen (Fig. S8†). The above results show that the HAIM₄₁-IL₄-Ni₆ ionogel has potential sensing applications in human motions and intelligent screen writing.

Compared to other conductive elastomers or hydrogels, ionogels do not contain easily frozen liquid components and exhibit high mechanical flexibility at low temperatures. To evaluate the mechanical properties of the HAIM₄₁-IL₄-Ni₆ ionogel sample at $-20\text{ }^{\circ}\text{C}$, an infrared thermal imager was used. Fig. 5e demonstrates that the HAIM₄₁-IL₄-Ni₆ sample exhibits remarkable flexibility, being able to withstand complex twisting deformation when subjected to $-20\text{ }^{\circ}\text{C}$ for 24 h. Additionally, HAIM₄₁-IL₄-Ni₆ was assembled onto PU rods with varying diameters (10 mm and 20 mm) under the same conditions ($-20\text{ }^{\circ}\text{C}$ for 24 h) as shown in Fig. 5f and g. By subjecting the PU rod to repeated straightening and bending processes, we were able to effectively measure stable relative resistance changes. Moreover, we observed that PU rods with varying diameters produced response signals of different magnitudes. To further investigate the behavior of the gel at low temperatures, we connected HAIM₄₁-IL₄-Ni₆ in series with a light bulb in a series circuit at $-20\text{ }^{\circ}\text{C}$. Upon powering on the circuit, we observed a dazzling blue light emitted by the LED. Interestingly, as the gel strain increased, we noticed a decrease in the brightness of the LED, suggesting that the gel still exhibited good sensitivity even at low temperatures (Fig. 5h).

The presence of a higher number of hydrophilic groups in HAIM and IL is well-established, enabling them to absorb moisture from the atmosphere (Fig. S9a†). The hydrophilic nature of HA for humidity monitoring is demonstrated by the water contact angles measured on the bare HAIM₄₁-IL₄-Ni₆ surface, which were found to be 40° (Fig. S9b†). Upon exposure to moisture, the resistance of HAIM₄₁-IL₄-Ni₆ decreased, as depicted in Fig. S9c.† The humidity responsiveness of the HAIM₄₁-IL₄-Ni₆ was further explored (Fig. 5i). As the RH increases from 20% to 80%, the change in resistance ($\Delta R/R_0$) of HAIM₄₁-IL₄-Ni₆ decreases significantly to -29% . Additionally, the response time is 7.2 s and the recovery time is 17.7 s, indicating fast performance. To evaluate the repeatability of HAIM₄₁-IL₄-Ni₆, humidity cycling is conducted between 10% and 95% RH (Fig. S10†). During humidification, the $\Delta R/R_0$ generally decreases, while during dehumidification, it increases. Throughout the cycle, HAIM₄₁-IL₄-Ni₆ consistently produces repeatable and stable $\Delta R/R_0$ signals, demonstrating exceptional repeatability and recoverability. The sensor can be attached to a mask, which can be worn to monitor various respiration rates (Fig. S11†). The HAIM₄₁-IL₄-Ni₆ sensor could sensitively detect normal, fast, and deep breathing (Fig. 5j) and respond quickly to breathing. Additionally, the dehydration resistance of the hydrogel and ionogel was investigated under $25\text{ }^{\circ}\text{C}$ and 40%RH conditions, with the corresponding results shown in Fig. 5k. The water in the HAIM₄₁-W₄-Ni₆ hydrogel evaporated rapidly and almost completely disappeared within 200 min, indicating its instability. As a result of internal water evaporation, the hydrogel only retained 70% of its original weight and became fragile after 20 days (Fig. 5k illustration). In

contrast, the ionogel showed minimal size change, demonstrating excellent stability under ambient conditions. Despite this, the HAIM₄₁-IL₄-Ni₆ ionogel still maintained its flexibility (Fig. 5k illustration) and retained up to 98% of its original weight, showcasing its superior moisturizing and anti-drying properties.

2.5 3D printing performance of the HAIM₄₁-IL₄-Ni₆ ionogel

We demonstrate the fabrication of HAIM₄₁-IL₄-Ni₆ ionogel sensors with various hierarchical microstructures by 3D printing to investigate the structure-sensitivity relationship. The 3D-printed porous structures are loaded and unloaded at a 50% compression strain in Fig. 6a. The structures are synchronously compressed as they are loaded and restored as they are unloaded, and return to their original shape once completely unloaded (Fig. S12†), showing the good resilience. We observed that different microstructure geometries, such as cone, cubic, and hemispheres, exhibited enhanced sensitivity and detection limits by altering the contact area and stress concentrations under pressure (Fig. 6b and Fig. S13†). With the increase of external pressure from 0 to 100 kPa, the resistance variation of cone and hemisphere lattice-based pressure sensors is about 60.9% and 43.7%, respectively, which are 4.5- and 3.2-fold higher than that of the cubic one ($\approx 13.6\%$) (Fig. 6c). Hence, there exists a profound intrinsic correlation between the structure, pressure sensitivity, and sensing range, affording ample opportunities to enhance the sensing properties of ionogel-based sensors through targeted structural design, thereby catering to the demands of various applications.

Additionally, we tested the feasibility of using the resulting hemisphere micro pressure sensors in electronic devices by assembling an array pressure sensor, inspired by the array of neurons in the skin. Fig. 6d presents the representative prototype of the array pressure sensor, comprising multiple pixels assembled by a plurality of hemispheres micro pressure sensors ($10\text{ mm} \times 10\text{ mm} \times 5\text{ mm}$), enabling the transmission of real-time pressure signals. As a comparison, Fig. S14† shows the 2D mapping image of the sensor without applying pressure. We could observe a significant change in resistance at the location where the finger was pressed and no change in resistance at other locations, which indicated that each of our small ionogel cubes could work as a pressure sensor independently and stably. Furthermore, the sensor demonstrated a clear and accurate response to the magnitude and location of the pressure when a weight weighing up to 500 g was placed on the array. Inspired by the changes in the signal shapes of the hemisphere micro pressure sensors with the duration of deformation, it is possible to utilize Morse code for communication. The electrical signal changes caused by long-time compression represent the ‘dashes’, while the signal changes caused by short-time compression represent the ‘dots’. By rhythmically compressing the ionic conductor and recording the different combinations of ‘dots/dashes’ (Fig. 6e and f), it is possible to effectively transmit information such as “SCUT” and “HOPE”. Expanding the application prospects of flexible wearable electronic devices can be achieved by designing sensor

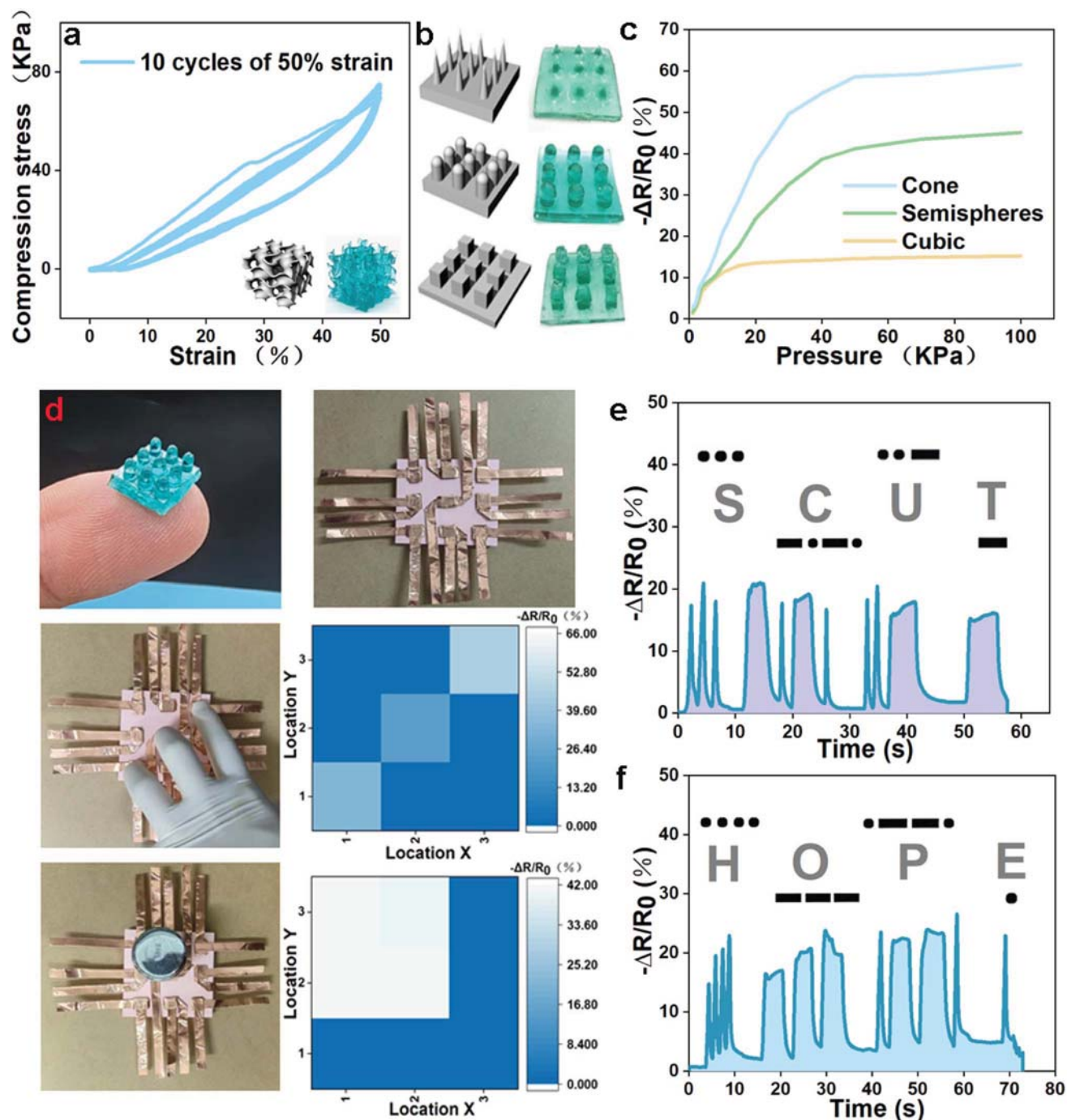


Fig. 6 (a) Fatigue test of the 3D printed with a bulk structure at 50% strain for 10 compression cycles. (b) 3D printed model and physical images of cubes, hemispheres, and cones. (c) Relative resistance changes of the different microstructure sensors with applied pressure increasing. (d) Hemispherical sensors, array pressure sensor diagram and 2D mapping sensing response diagram. (e) "SCUT" and (f) "HOPE" were transmitted through rhythmic compression of the hemispherical sensors according to the Morse code.

arrays with diverse microstructures to provide sensors with higher sensitivity.

3. Conclusions

In this study, we present a simple and efficient method for producing metal coordination ionogels with superior

mechanical properties and conductivity. By one-pot polymerizing precursor solutions containing HA, IM, IL and Ni^{2+} , the IM- Ni^{2+} coordination complexes are *in situ* formed during the synthesis of tough solvent-free ionogels. The incorporation of metal ions not only improved the mechanical strength of the ionogel through coordination crosslinking, but also enhanced its conductivity by serving as mobile ions. It is worth noting that

besides Ni^{2+} , other commonly found cations such as Co^{2+} and Zn^{2+} can also be utilized to fabricate solvent-free metal coordination ionogels using this approach. The significant impact of metal ions on enhancing the mechanical and electrical properties of HAIM-IL has been demonstrated through experiments and theoretical simulations. The resulting HAIM-IL-Ni ionogel exhibits tunable strength, remarkable stretchability, higher conductivity, outstanding fatigue resistance, and self-healing properties. Exploiting these advantages, various HAIM-IL-Ni ionogel based sensors have been demonstrated. HAIM₄₁-IL₄-Ni₆ resistive-type sensors exhibited diverse sensory capabilities towards humidity and strain. Furthermore, due to its fast photocuring properties, it can be used as a 3D printing ink for rapid customization of pressure sensors with microstructures. We believe that this study may provide a simple method from molecular design to multifunctional application of high strength and conductivity ionogels, which may promote the development of soft ion conductors.

4. Experimental section

4.1 Materials

2-Hydroxyethyl acrylate (HA, 99%), 1-vinylimidazole (IM, 99%), 1-hydroxycyclohexyl phenyl ketone (UV-184, 98%), $\text{NiCl}_2 \cdot 6\text{H}_2\text{O}$ (98%), ZnCl_2 (98%), $\text{CoCl}_2 \cdot 6\text{H}_2\text{O}$ (98%), methyl chloroacetate (99.5%), ethanol absolute (99.5%) and 2-aminoethanol (99%) were purchased from Macklin (Shanghai, China) and used as received.

4.2 Preparation of ionic liquid monomer (IL)

The schematic diagram of the preparation process of quaternary ammonium based ionic liquids (IL) is shown in Fig. S1a.† 2-Aminoethanol (10.0 g, 0.16 mol) and methyl chloroacetate (21.7 g, 0.20 mol) were dissolved in 50 mL of absolute ethanol. The resulting solution was stirred and reacted at 60 °C for 6 h. Once the reaction was completed, the ethanol was removed by rotary evaporation. The product was then dissolved in deionized water to extract the aqueous phase. The remaining viscous liquid was obtained by rotary evaporation to remove the water. Finally, the resulting product was vacuum dried at 60 °C for 12 h to obtain a yellow brown transparent ionic liquid (IL). The chemical structure of IL was characterized through the ^1H NMR spectrum (600 MHz, D_2O): δ/ppm 3.68 (3H, t, δH^a , $-\text{CH}_3$), 4.22 (2H, s, δH^b , $-\text{CH}_2^-$), 3.85 (2H, t, δH^c , $-\text{CH}_2^-$), 3.18 (2H, s, δH^d , $-\text{CH}_2^-$), as shown in Fig. S1b–d.† These results demonstrate the successful synthesis of the yellow brown transparent liquid IL (Fig. S1e†).

4.3 Preparation of solvent-free coordination ionogels

Taking HAIM₄₁-IL₄-Ni₆ as an example, 4.03 g of HA (equivalent to 34.45 mmol), 0.81 g of IM (equivalent to 8.61 mmol), 1.93 g of IL (40 wt% of HAIM monomer), 0.29 g of $\text{NiCl}_2 \cdot 6\text{H}_2\text{O}$ (6 wt% of HAIM monomer), and 0.088 g (0.4 mol% to HAIM) of photo-initiator UV-184 were mixed and stirred at 70 °C for 20 minutes until a blue-green transparent solution is formed. Subsequently, the formed homogeneous transparent precursor

solution was injected into a PTFE mold, followed by exposing it to a UV lamp (365 nm, 400 W) for 10 minutes to cure and shape it. The resultant ionogel is named HAIM₄₁-IL_x-Ni_y, where 41 is the molar ratio of HA and IM. The mass fraction of IL in the total mass of monomer HA and IM is denoted as x , with values of 20%, 40%, and 60%, represented as 2, 4, and 6, respectively. Similarly, the mass fraction of $\text{NiCl}_2 \cdot 6\text{H}_2\text{O}$ in the total mass of monomer HA and IM is denoted as y , with values of 2%, 6%, and 10%, represented as 2, 6, and 10, respectively. Ion types containing Zn^{2+} and Co^{2+} were fabricated in a similar way. The amount of each reactant is listed in Table S1.† The HAIM₄₁-W₄-Ni₆ hydrogel was also prepared using the same *in situ* photopolymerization method, but with deionized water instead of IL.

4.4 Statement

We have confirmed that informed written consent from all participants was obtained prior to the research.

Conflicts of interest

The authors declare that they have no known competing financial interests or personal relationships that could have appeared to influence the work reported in this paper.

Acknowledgements

The authors acknowledge the financial support from the National Natural Science Foundation of China (no. 52073098) and the Natural Science Foundation of Guangdong Province (no. 2022A1515011570 and 2023A1515011264). We thank Prof. Xiaodong Cao for providing the 3D printing support.

References

- 1 H. Wang, Q. Ding, Y. Luo, Z. Wu, J. Yu, H. Chen, Y. Zhou, H. Zhang, K. Tao, X. Chen, J. Fu and J. Wu, *Adv. Mater.*, 2024, **36**, 2309868.
- 2 Z. Chen, Y. Sun, X. Xiao, H. Wang, M. Zhang, F. Wang, J. Lai, D. Zhang, L. Pan and C. Li, *J. Mater. Chem. A*, 2023, **11**, 8359–8367.
- 3 J. Wu, L. Huang, S. Wang, X. Li, L. Wen, X. Li, T. Feng, P. Li, Z. Fang, M. Wu and W. Lv, *Energy Storage Mater.*, 2023, **57**, 549–556.
- 4 W. Li, L. Li, S. Zheng, Z. Liu, X. Zou, Z. Sun, J. Guo and F. Yan, *Adv. Mater.*, 2022, **34**, 2203049.
- 5 K. Tao, Z. Chen, J. Yu, H. Zeng, J. Wu, Z. Wu, Q. Jia, P. Li, Y. Fu, H. Chang and W. Yuan, *Adv. Sci.*, 2022, **9**, 2104168.
- 6 X. Huang, Z. Zheng, H. Wang, W. Xu, M. Wu, M. Wang, C. Chen, L. Wan, R. Du, T. Zhu, Z. Huang, X. Wang, X. Wang, Q. Zhang and X. Jia, *Adv. Funct. Mater.*, 2024, **34**, 2312149.
- 7 Y. Long, B. Jiang, T. Huang, Y. Liu, J. Niu, Z. L. Wang and W. Hu, *Adv. Funct. Mater.*, 2023, **33**, 2304625.
- 8 D. M. Correia, L. C. Fernandes, P. M. Martins, C. García-Astrain, C. M. Costa, J. Reguera and S. Lanceros-Méndez, *Adv. Funct. Mater.*, 2020, **30**, 130418.

- 9 Y. M. Kim and H. C. Moon, *Adv. Funct. Mater.*, 2019, **30**, 1907290.
- 10 P. Zhang, Y. Chen, Z. H. Guo, W. Guo, X. Pu and Z. L. Wang, *Adv. Funct. Mater.*, 2020, **30**, 144674.
- 11 S. Tan, C. Wang, B. Yang, J. Luo and Y. Wu, *Adv. Mater.*, 2022, **34**, 2206904.
- 12 L. Xu, Z. Huang, Z. Deng, Z. Du, T. L. Sun, Z. H. Guo and K. Yue, *Adv. Mater.*, 2021, **33**, 2105306.
- 13 X. Xu, F. A. Jerca, V. V. Jerca and R. Hoogenboom, *Macromolecules*, 2020, **53**, 6566–6575.
- 14 S. Kim, A. U. Regitsky, J. Song, J. Ilavsky, G. H. McKinley and N. Holten-Andersen, *Nat. Commun.*, 2021, **12**, 667.
- 15 C. Jiao, J. Zhang, T. Liu, X. Peng and H. Wang, *ACS Appl. Mater. Interfaces*, 2020, **12**, 44205–44214.
- 16 G. Dai, L. Sun, J. Xu, G. Zhao, Z. Tan, C. Wang, X. Sun, K. Xu and W. Zhong, *Acta Biomater.*, 2021, **129**, 84–95.
- 17 X. Xu, F. A. Jerca, V. V. Jerca and R. Hoogenboom, *Adv. Funct. Mater.*, 2019, **29**, 1904886.
- 18 S. H. Hong, Y. M. Kim and H. C. Moon, *ACS Appl. Mater. Interfaces*, 2023, **15**, 28516–28523.
- 19 J. Lyu, Q. Zhou, H. Wang, Q. Xiao, Z. Qiang, X. Li, J. Wen, C. Ye and M. Zhu, *Adv. Sci.*, 2023, **10**, 2206591.
- 20 W. Ge, S. Cao, Y. Yang, O. J. Rojas and X. Wang, *Chem. Eng. J.*, 2021, **408**, 127306.
- 21 J. Kim, K. Park, Y. Cho, H. Shin, S. Kim, K. Char and J. W. Choi, *Adv. Sci.*, 2021, **8**, 2004290.
- 22 Y. Guo, Z. Gao, Y. Liu, Z. Huang, C. Chai and J. Hao, *ACS Appl. Polym. Mater.*, 2019, **1**, 2370–2378.
- 23 X. Yu, Y. Zheng, Y. Wang, H. Zhang, H. Song, Z. Li, X. Fan and T. Liu, *Chem. Mater.*, 2022, **34**, 1110–1120.
- 24 W. Cui, Y. Zheng, R. Zhu, Q. Mu, X. Wang, Z. Wang, S. Liu, M. Li and R. Ran, *Adv. Funct. Mater.*, 2022, **32**, 122832.
- 25 S. Wu, J. Huang, S. Jing, H. Xie and S. Zhou, *Adv. Funct. Mater.*, 2023, **33**, 2303292.
- 26 J. Tie, Z. Mao, L. Zhang, Y. Zhong and H. Xu, *Adv. Funct. Mater.*, 2023, **33**, 2307367.
- 27 Y. Wang, Z. Liu, X. Wei, K. Liu, J. Wang, J. Hu and J. Lin, *Chem. Eng. J.*, 2021, **413**, 127493.
- 28 Z. Wang, W. Zheng, W. Sun, L. Zhao and W. Yuan, *ACS Appl. Energy Mater.*, 2021, **4**, 2808–2819.
- 29 Y. Zhai, W. Hou, M. Tao, Z. Wang, Z. Chen, Z. Zeng, X. Liang, P. Paoprasert, Y. Yang, N. Hu and S. Song, *Adv. Mater.*, 2022, **34**, 2205560.
- 30 Z. Wu, Y. Guo, M. Qin, C. Liao, X. Wang and L. Zhang, *J. Mater. Chem. A*, 2023, **11**, 16074–16083.
- 31 R. Zhou, Y. Jin, Y. Li, H. Jin, W. Zeng, J. Mei and Y. Liu, *Chem. Eng. J.*, 2023, **476**, 146840.
- 32 Z. Yu and P. Wu, *Adv. Mater.*, 2021, **33**, 2008479.
- 33 B. Yiming, Y. Han, Z. Han, X. Zhang, Y. Li, W. Lian, M. Zhang, J. Yin, T. Sun, Z. Wu, T. Li, J. Fu, Z. Jia and S. Qu, *Adv. Mater.*, 2021, **33**, 2006111.
- 34 B. Yiming, X. Guo, N. Ali, N. Zhang, X. Zhang, Z. Han, Y. Lu, Z. Wu, X. Fan, Z. Jia and S. Qu, *Adv. Funct. Mater.*, 2021, **31**, 2102773.
- 35 C. Ma, J. Wei, Y. Zhang, X. Chen, C. Liu, S. Diao, Y. Gao, K. Matyjaszewski and H. Liu, *Adv. Funct. Mater.*, 2023, **33**, 2211771.
- 36 S. Liu, Y. Li, J. Wen, Z. Shen, Q. Meng, Q. Liu, F. Yang, S. Yu Zheng, J. Li, Z. Sun, G. Zhuang and J. Yang, *Adv. Funct. Mater.*, 2024, **34**, 2313397.
- 37 Y. Gong, L. Yu, X. Lyu, S. Zheng, Y. Yu, P. Zhou, Z. Z. Luo and Z. Zou, *Adv. Funct. Mater.*, 2023, **33**, 2305314.



Siloxane-based segmented poly(urethane-urea) elastomers with enhanced mechanical properties, hydrophobicity and anti-calcification based on hierarchical phase separation for potential applications of polymeric heart valve

Xionghui Wu^a, Yichao Hu^a, Yu Xia^a, Yaling Lin^{b,*}, Anqiang Zhang^{a,*}

^a School of Materials Science and Engineering, South China University of Technology, 381 Wushan Rd., Guangzhou 510641, Guangdong, China

^b College of Materials and Energy, South China Agricultural University, 483 Wushan Rd., Guangzhou 510642, Guangdong, China

ARTICLE INFO

Keywords:

Poly(urethane-urea) elastomer
Microphase separation
Biocompatibility

ABSTRACT

The polymeric heart valves have attracted considerable attention for treating valvular heart diseases with favorable biocompatibility, stability and adjustable mechanical properties. However, the thrombosis, calcification, and mechanical durability in the dynamic blood environment have limited further applications. Polycarbonate (PCDL) and polysiloxane (PDMS) had high flexibility, low toxicity, excellent hydrolytic and oxidative stability and efficient biocompatibility, but PCDL was susceptible to calcification and PDMS was susceptible to protein adsorption. To solve these difficulties, PDMS and PCDL were chosen as soft segments to combine the virtues of excellent biocompatibility, hydrolytic stability, and good anti-calcification and anti-protein adsorption, and a series of PCDL-PDMS poly(urethane-urea) elastomers (PCDL-PDMS PUU) were synthesized using a two-step polymerization reaction based on the amino-terminated polydimethylsiloxane ($\text{H}_2\text{N-PDMS-NH}_2$), polycarbonate diol (PCDL) and isophorone diisocyanate. The thermodynamic incompatibility between PDMS and PCDL and hierarchical hydrogen bonds were used to construct microscopic micro-separation, enabling the combination of enhanced mechanical strength, toughness, tear resistance and biocompatibility. The effect of the molar ratio of PCDL and PDMS and hierarchical H-bonding interactions on the physical properties, biostability and biocompatibility of PCDL-PDMS PUU were investigated. It was found the PCDL-PDMS PUU could achieve relatively stable mechanical strength behavior, and the Young's modulus and tear strengths increased with the increasing proportion of $\text{H}_2\text{N-PDMS-NH}_2$. Meanwhile, PCDL-PDMS PUU showed low water uptake rate lower than 2 %, very good anti-hydrolysis performance, low hemolysis rate of less than 2 % and low adhesion to platelet cells. What's more, PCDL-PDMS PUU showed enhanced calcification resistance when compared with a commercial polyurethane, ElastollanTM 1180A. Therefore, the results demonstrated that PCDL-PDMS PUU elastomers showed great potential to be explored as heart valves material considering high biostability, superior biocompatibility and mechanical performances.

1. Introduction

Segmented thermoplastic polyurethanes (PU) and poly(urethane-urea)s (PUU) are a versatile class of polymers that exhibit many advantages such as excellent elasticity and mechanical properties, good processability and exceptional biocompatibility, etc., [1–7] and which have been widely application in different fields, especially in biomedical applications [8–11]. Due to the thermodynamic incompatibility between the hard and soft segments produces microphase separation, and

the hard segments are aggregated through hydrogen bonds and form hard domains while the soft segments are separated into soft domains, enhancing mechanical properties of PU material [12–15]. In addition, the biocompatibility of PUs is thought to be derived from the microphase separation structures that are similar to the cytomembrane structures. PU with different function structures can be used as implants biomaterials in heart valves, artificial blood vessels, biodegradable scaffolds and other biomedical devices by changing the type and composition of soft and hard segments [16–19].

* Corresponding authors.

E-mail addresses: linyaling@scau.edu.cn (Y. Lin), aqzhang@scut.edu.cn (A. Zhang).

<https://doi.org/10.1016/j.eurpolymj.2024.113349>

Received 23 June 2024; Received in revised form 26 July 2024; Accepted 28 July 2024

Available online 2 August 2024

0014-3057/© 2024 Elsevier Ltd. All rights are reserved, including those for text and data mining, AI training, and similar technologies.

When PU is used as polymeric heart valves material, the biocompatibility should be prioritized consideration [20,21]. However, the resistance of PU to degradation and calcification is largely determined by the chemical properties of the soft segments in the biological environment [22–24]. The polyester-based PUs suffered from hydrolytic degradation of ester groups while polyether-based PUs are prone to oxidative degradation, which limits their long-term implantation applications [22,25]. Compared to the other PUs, Polycarbonate urethanes (PCUs) have shown improved biostability [26–28], exhibiting excellent resistance toward hydrolysis and oxidation [29,30], but remain susceptible to calcification [31,32]. PDMS is commonly used in the manufacture of biomedical devices due to its high flexibility, low toxicity, excellent hydrolytic and oxidative stability, efficient biocompatibility and platelet adhesion [33–35]. However, the PDMS polyurethanes were likely to microphase separation occurs due to the thermodynamic incompatibility of polar hard segments and non-polar PDMS, which affects the mechanical properties of the material [36–39]. Therefore, it will be extensive attention to combine the advantages of the properties of poly(dimethyl siloxane) and polyurethane. In recent years, many research studies have been made to synthesize PDMS-based polyurethanes with good mechanical properties and biocompatibility [40–49]. PDMS-based PUs have good biostability and biocompatibility, but how to achieve a balance between high tensile strength and tear strength and dynamic modulus remains a forbidden challenge. Seifalian et al. reported a flexible nanocomposite polyurethane (POSS-PCU) with POSS nanoparticles covalently bonded to the hard segment of PCU, which not only ensures the flexibility and elasticity of the material, but also protects it from oxidation and hydrolysis degradation [50]. Meanwhile, POSS-PCU also showed resistance to the platelet adhesion and calcification [51]. However, POSS plays a role similar to covalent cross-linking, which makes the molding and processing of POSS-PCU more difficult [52]. Lin et al. reported a PCDL-PDMS- H_{12} MDI polyurethane samples, which varied molar ratios of PDMS (less than 30 %) were utilized to enhance the mechanical properties and biocompatibilities [53].

Several factors are essential for an ideal artificial heart valve, such as good mechanical properties, good biocompatibility, excellent anti-calcification and anti-coagulation properties, superior endothelial cell adhesion, great hydrodynamic and fatigue performance [54–56]. At present, most research studies emphasize the effects of hydroxy-terminated poly(dimethylsiloxane) (HO-PDMS-OH) contents on the performance of polyurethane, but few studies highlight the effect of amino-terminated poly(dimethylsiloxane) (H_2 N-PDMS- NH_2) and its high content contents on polyurethane. The introduction of H_2 N-PDMS- NH_2 into the polyurethane backbone, which will facilitate the formation of urea groups. This is conducive to aggregation between hard segments to obtain a more stable hard region cross-linking structure. Therefore, the research on PCDL-PDMS polyurethane is still worth further investigating. In this work, the heart valves demand materials with improved mechanical properties such as high tensile and tear strengths, low modulus and low cyclic creep in addition to long-term biostability. At present, how to achieve the balance between anti-thrombosis, anti-calcification, and mechanical durability of polymer valve materials in a dynamic blood environment has always been a difficult research and development challenge.

In this work, we report an approach that is different from the conventional soft and hard segment structure, two immiscible soft segments and hierarchical urethane/urea hydrogen bonds were implanted the network to form a unique molecular structure, enabling the combination of enhanced mechanical strength, toughness, tear resistance and biocompatibility. Herein, a series of PCDL-PDMS PUU elastomers, with the great biocompatible amino-terminated polysiloxane (H_2 N-PDMS- NH_2) and polycarbonate (PCDL) were selected as soft segments, were synthesized by adjusting the molar ratio of the PCDL and PDMS. On the one hand, the polymer exhibits an abundance of urethane ($-NH-COO-$) and urea ($-NH-CO-NH-$) groups, with hierarchical hydrogen bonds

interactions in the polyurethane network, facilitating energy dissipation during the stretching process. On the other hand, the thermodynamic incompatibility between PDMS and PCDL was used to construct nanoscopic microphase separation structures, which contributes to high strength, tear resistance and toughness. Due to the synergistic effects of microphase separation structures and hierarchical hydrogen bonds, the elastomers showed excellent mechanical strength (31.5 MPa), toughness (279.8 MJ/m³) and low dynamic modulus (3.8 MPa). Moreover, the PCDL-PDMS PUU elastomer is also highly biostability (anti-hydrolysis performance) and superior biocompatibility (anti-platelet adhesion and anti-calcification). Therefore, the PCDL-PDMS PUU elastomers has excellent tensile properties, high biostability and biocompatibility, showing a great potential for heart valves material.

2. Experimental section

2.1. Materials

Octamethylcyclotetrasiloxane (D_4 , > 99.5 %, Dow Corning, USA). Isophorone diisocyanate (IPDI, 99 %), 1,3-bis(3-aminopropyl)-1,1,3,3-tetramethyldisiloxane (AMM, 97 %), tetramethylammonium hydroxide pentahydrate (TMAH, 97 %) and dibutyltin dilaurate (DBTDL) were obtained from Shanghai Macklin, China. Tetrahydrofuran (THF, 99 %) is obtained from Shanghai Macklin and dried using 3 Å molecular sieves before use. Polycarbonate diol (PCDL) with a molecular weight of 2000 g/mol, which was obtained from Shandong Liduo, China, and was evaporated under reduced pressure at 110 °C for 3 h before use. Thermoplastic polyether polyurethane elastomers (Elastollan™ 1180 A) were obtained from BASF.

2.2. Synthesis of H_2 N-PDMS- NH_2

The synthetic route of H_2 N-PDMS- NH_2 is shown in Figure S1. D_4 (75.20 g, 0.254 mol), AMM (24.80 g, 0.10 mol) and tetramethylammonium hydroxide pentahydrate (0.5 wt%, 0.5 g) as a catalyst were added to a 250 mL flask with a reflux condensing flute. The system was first heated to 70 °C and maintained at this temperature for a while until all of the catalyst was dissolved. Then, the heater was set to 90 °C for 12 h. After reaction, the catalyst was decomposed under 150 °C for 1 h. Later, unreacted reagents were removed by a rotary evaporator at 150 °C /0.1 MPa. Yield: ~96 %.

FTIR (ATR, cm⁻¹): 2966, 2906, 1614, 1415, 1262, 1096, 1026, 868, 805.

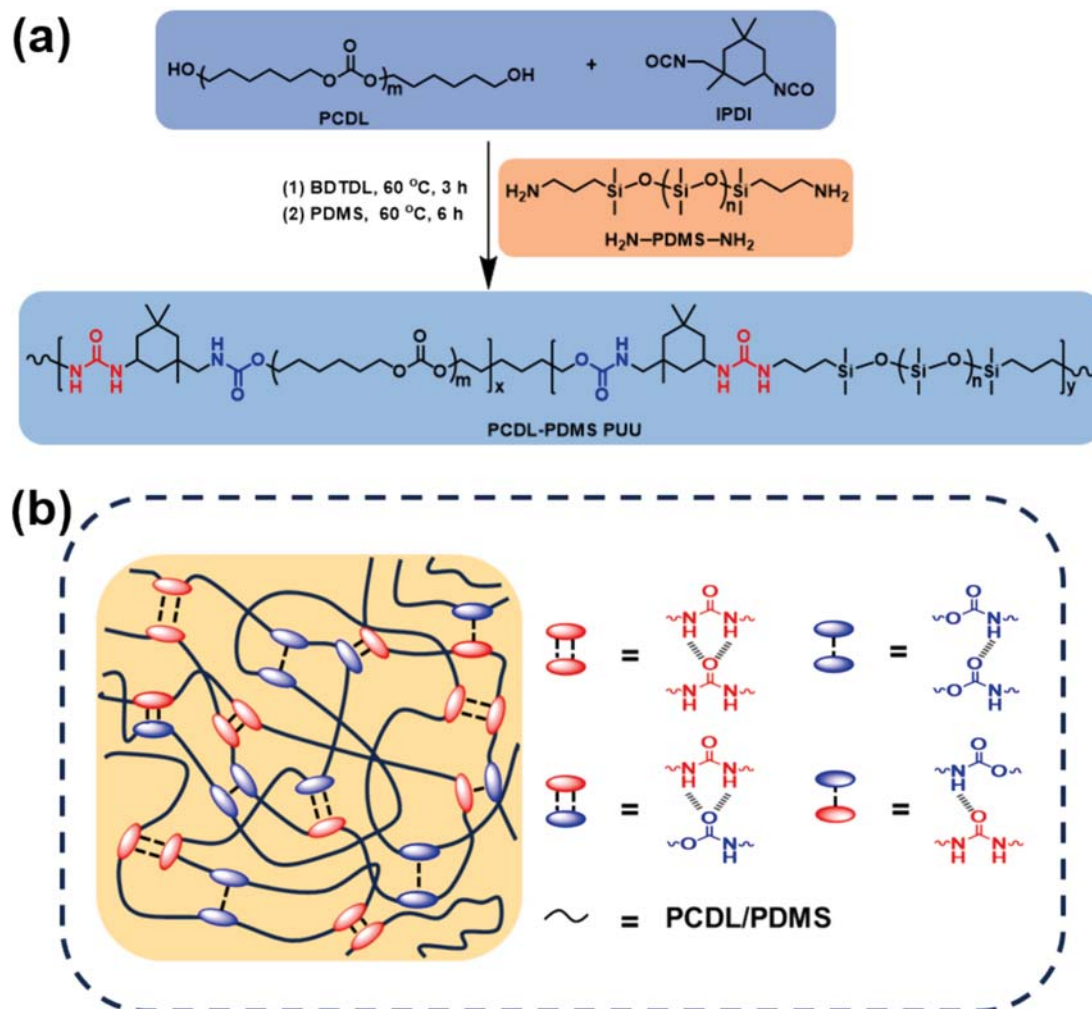
¹H NMR (400 MHz, CDCl₃, δ , ppm): 2.64 (m, $-CH_2-NH_2$), 1.44 (m, $-CH_2-CH_2-NH_2$), 0.51 (t, $-CH_2-CH_2-CH_2-NH_2$), 0.03–0.06 (m, Si- CH_3).

2.3. Synthesis of PCDL-PDMS PUU elastomers

The synthetic route of PCDL-PDMS PUU elastomers is shown in Scheme 1a. Taking PCDL₃-PDMS₂ PUU as an example, PCDL (6.0 g, 3.0 mmol), IPDI (1.11 g, 5.0 mmol), DBTDL (200 mg, 0.32 mmol) and 30 mL of tetrahydrofuran (THF) were charged into a three-neck round-bottom flask under a nitrogen atmosphere. The reaction was carried out at 60 °C for 3 h. Subsequently, H_2 N-PDMS- NH_2 (2.0 g, 2.0 mmol) dissolved in THF (10 mL) was added. And the mixtures were allowed to react at 60 °C for another 6 h. After reaction, the polymer was precipitated in a large amount of H₂O. The resulting polymers were collected by filtration and then dried under vacuum at room temperature. The dried samples were re-dissolved in THF, and the polymer products were poured into a mold and then stored at 50 °C for 24 h. The final product was named as PCDL_x-PDMS_y PUU (X and Y represents the molar ratio of PCDL and PDMS). Other samples were prepared using the same procedure, according to the recipes in Table S1. Yield: ~95 %.

FTIR (ATR, cm⁻¹): 3334, 2962, 1630, 1530, 1247, 1017, 960, 797.

¹H NMR (400 MHz, CDCl₃, δ , ppm): 4.02–4.12 (m, $-O-CH_2-(CH_2)_4-CH_2-O-$ in PCDL), 1.60–1.68 (m, $-O-CH_2-CH_2-(CH_2)_2-CH_2-CH_2-O-$ in



Scheme 1. (a) Synthesis routes of PCDL-PDMS PUU elastomers. (b) Hierarchical hydrogen bonds contained in PCDL-PDMS PUU elastomers.

PCDL), 1.25–1.41 (m, $-\text{O}-(\text{CH}_2)_2-\text{CH}_2-\text{CH}_2-(\text{CH}_2)_2-\text{O}-$ in PCDL), 0.03–0.07 (m, $-\text{Si}(\text{CH}_3)_2$ in PDMS), 2.58 (m, $-\text{CH}_2-\text{N}$ in PDMS), 1.48 (m, $-\text{CH}_2-\text{CH}_2-\text{N}$ in PDMS), 0.84 (s, $-\text{C}(\text{CH}_3)_2$ in IPDI), 1.06 (s, $-\text{C}-\text{CH}_3$ in IPDI), 2.04 (m, $-\text{CH}-$ in IPDI), 2.91 (m, $-\text{CH}-\text{CH}_2-\text{N}$ in IPDI).

2.4. Characterization and tests

The ^1H NMR spectra were recorded on a Bruker AVANCE III HD 600 NMR spectrometer at room temperature, CDCl_3 was used as the solvent.

Fourier transform infrared (FTIR) spectra were recorded on a Nicolet iS5 FT-IR spectrometer equipped with an iD7-ZnSe attenuated total reflectance (ATR) mode at a resolution of 4 cm^{-1} .

The number-average molecular weight (M_n) and polydispersity index (PDI) of polymers were performed on a Waters 515–2414 system as an eluent at $40\text{ }^\circ\text{C}$ with a flow rate of 1.0 mL/min , and narrow molecular weight distribution of polystyrenes were used as standards. The concentration of samples was approximately 10 mg/mL after filtration through a $0.45\text{ }\mu\text{m}$ pore-size membrane.

The thermogravimetric analysis (TGA) is carried out on the thermal analysis system, used a TG 209 F1 (Netzsch, Germany). The samples were heated at a rate of $20\text{ }^\circ\text{C/min}$ over a range of $30\text{ }^\circ\text{C}$ – $600\text{ }^\circ\text{C}$ under nitrogen atmosphere.

Differential scanning calorimetry (DSC) was performed using a DSC204F1 (Netzsch, Germany). The experimental process is carried out at a heating and cooling rate of $10\text{ }^\circ\text{C/min}$ in a nitrogen atmosphere. Each sample is measured between -80 and $150\text{ }^\circ\text{C}$. The heating and

cooling rates are both $10\text{ }^\circ\text{C/min}$. The first cycle is used to do away with the thermal history of the polymer, and the experimental data used is evaluated from thermograms collected during the second heating process.

Dynamic Mechanical Analysis (DMA) was performed on a Mettler Toledo DMA 1 system (Mettler-Toledo, Swiss) in the tension mode. The measurements were performed from $-150\text{ }^\circ\text{C}$ to $80\text{ }^\circ\text{C}$ with a heating rate of $3\text{ }^\circ\text{C min}^{-1}$ and a frequency of 1 Hz . The storage modulus (E'), loss modulus (E'') and loss factor ($\tan\delta$) were recorded as a function of temperature.

Rheological measurements were performed with a MCR102 rheometer (Anton Paar, Austria). The 25 mm steel plates were used. The dynamic frequency sweep ($100\text{--}0.1\text{ rad/s}$) was performed at $20\text{ }^\circ\text{C}$, $40\text{ }^\circ\text{C}$, $60\text{ }^\circ\text{C}$, $80\text{ }^\circ\text{C}$, $100\text{ }^\circ\text{C}$, and $120\text{ }^\circ\text{C}$ at 1% strain. Classic time–temperature superposition was applied to construct the master curves at $40\text{ }^\circ\text{C}$ as the reference temperature. The dynamic temperature ($20\text{--}160\text{ }^\circ\text{C}$) sweep was performed at a strain amplitude of 1% and a frequency of 1 Hz with a heating rate of $2\text{ }^\circ\text{C min}^{-1}$. The samples for rheological measurements were prepared in a cylindrical shape (diameter: 25 mm , thickness: $0.3\text{--}0.5\text{ mm}$).

X-ray photoelectron spectroscopy (XPS) of samples was conducted by a Thermo Fisher Scientific ESCALAB 250xi. The energy scanning range was $0\text{--}1300\text{ eV}$, the step size was 1 eV , and analysis was performed using the Advantage software system.

XRD measurements (D8 Advance, Bruker, Germany) were performed to determine the phase structure and composition of the PCDL-PDMS

PUU elastomers in the 2θ scanning range of 5 ~ 45°.

Small-angle X-ray scattering (SAXS) measurements were carried out on a Bruker NanoSTAR system and Cu Kα radiation ($\lambda = 0.1541$ nm) was used as the X-ray source. The distance from sample to detector is 1050 mm. The Periodic size (D) was calculated by the Bragg's law: $D = 2\pi/q_{\max}$.

The microphase separation structure of polyurethane elastomer was observed with a Bruker XE-100 Nano atomic force microscope (AFM).

Scanning electron microscopy (SEM) of the morphology of the elastomer surface was carried out using ZEISS EVO 18 Special Edition (Merlin, Carl Zeiss Jena, Germany).

The static water contact angles (WCAs) of PCDL-PDMS PUU elastomers surfaces were measured with a contact angle meter (DropMeter A-100, MAIST Vision Inspection & Measurement Co. Ltd., China) at room temperature. One drop of water (10 μL) was placed onto the surface and observed with an optical microscope. The WCA values were calculated from three measurements at different positions.

Tensile tests were performed on rectangular specimens (30 mm × 5 mm × 0.5 mm) using a KJ-2091 tensile testing machine (Kejian Instruments Co. Ltd, China) with a temperature and humidity-controlled chamber at a stretching rate of 200 mm/min. Three samples were tested for each group. Stress relaxation tests were also performed on the KJ-2091 tensile testing machine at 10 % strain at 25 °C. The Young's modulus was determined by the slope of the stress-strain curve in the initial linear region within 5 % of the strain. The toughness is defined as the area surrounded by the stress-strain curves. To evaluate the crack tolerance of the samples, tensile tests were conducted by the tensile experiment using the single-edge notched sample (1 mm notch, gauge length of 20 mm, width of 5 mm, thickness of 1.25 mm). The notched samples were both tested at the stretching rate of 50 mm min⁻¹. The creep behavior of the sample was also measured by MCR102 rheometer (Anton Paar, Austria). The sample was subjected to 1 N stress and the creep recovery time was 45 min.

2.5. Water uptake test

PCDL-PDMS PUU elastomer films (about 0.2 mm-thick) were cut into 2 mm × 2 mm rectangular ($n = 3$) and rinsing with distilled water 3 times, dried, weighed and the initial weights were recorded as m_w . The elastomer films were then immersed in water at room temperature for 48 h. Finally, the weight of the elastomer films after wiping the water on the surfaces were recorded as m_d . The water uptake rate (W) was calculated as following equation.

$$W(\%) = (m_d - m_w)/m_w \times 100\% \quad (1)$$

2.6. In vitro hydrolytic degradation

PCDL-PDMS PUU elastomer films (about 0.2 mm-thick) were cut into 1 cm × 1 cm rectangles and rinsing with PBS 3 times, dried, weighed and the initial weights were recorded as W_0 . The elastomer films were then incubated with PBS (pH=7.4) at 37 °C for 1 month and measured every 5 d. Finally, the elastomer films were dried in vacuum oven for 24 h to keep the weight constant. Dry weight of the elastomer films after water degradation were recorded as W_t . The percentage of weight loss for each elastomer films was calculated according to the following equation.

$$Weightloss(\%) = (W_0 - W_t)/W_0 \times 100\% \quad (2)$$

2.7. Hemolysis test

In the hemolysis tests, distilled water was used as positive control, and physiological saline was used as negative control. First, the PCDL-PDMS PUU elastomer films (5 mm × 5 mm, $n = 3$) were rinsed with distilled water 3 times, the samples were then put in a test tube containing 1.5 mL physiological saline. Six replicates were prepared for

each sample. These conical tubes were incubated at 37 °C for 30 min, 30 μL diluted blood was then added to each test tube, gently shaken at 37 °C for 2 h, and centrifuged at 3000 rpm for 10 min. The supernatant from each centrifuge tube was aspirated, and transferred to a 96-well plate, optical density value was read at a wavelength of 545 nm with a UV-vis spectrophotometer (UV2300). The hemolysis rate can be calculated according to the following equation.

$$HR(\%) = (OD_t - OD_{nc})/(OD_{pc} - OD_{nc}) \times 100\% \quad (3)$$

where OD_t , OD_{nc} and OD_{pc} mean the value of optical density at 545 nm of sample groups, negative groups and positive groups, respectively.

2.8. Cytotoxicity evaluation

To evaluate the cytotoxicity of PCDL-PDMS PUU elastomers on murine aneuploid fibrosarcoma cells (L929 cells) through MTT experiments [57]. The L929 cells were cultured on 96 well culture plates at a density of 1.0×10^5 cells/mL with RPMI 1640 culture medium (containing 10 % fetal bovine serum, 100 μL medium/well). The PCDL-PDMS PUU films were cut into 8×8 mm² squares and sterilized under a UV lamp for 30 min, and the sample was immersed in 30 mL of PBS at pH 7.4 for 24 h to obtain the leachate. Then, 20 μL leachate was added and cultured at 37 °C for 24 h. 20 μL PBS with pH 7.4 was added in the control group. Next, 100 μL of the MTT solution (5 g/L) was added to each well. After being placed at 37 °C for 4 h, 150 μL dimethyl sulfoxide (DMSO) was added to each well, and the optical density (OD) value at 570 nm was measured with a Wellsan MK 3 Microplate Reader (Labsystems Dragon, Finland). All measurements were repeated three times. The cell viability values are calculated according to the following formula:

$$Cellviability(\%) = (OD_{sample}/OD_{control}) \times 100\% \quad (4)$$

2.9. Platelet adhesion experiment

The PCDL-PDM PUU elastomer films (7 mm × 7 mm, $n = 3$) were rinsed with PBS 3 times, 500 μL platelet-rich plasma was then added to each test tube and incubated at 37 °C for 1 h. The samples were then rinsed with 0.9 % NaCl for 3 times to remove non-adhered platelets and fix the platelets with 2.5 % glutaraldehyde for 6 h. Finally, the samples were rinsed with 0.9 % NaCl for 3 times and 100 μL Rhodamine 123 was then added to each test tube and stand at 37 °C for 20 min in the dark. The samples were then rinsed with 0.9 % NaCl for 3 times. The adhesion numbers were observed by fluorescence microscopy.

2.10. Protein adsorption test

The PCDL-PDMS PUU elastomer films (1 cm × 1 cm, $n = 3$) were rinsed with PBS 3 times, then the 1.5 mL BSA solution (200 μg/mL) was added to each test tube and incubated at 37 °C for 3 h. After incubation, they were rinsed by de-ionic water and PBS buffer solution (pH 7.4) to remove the unabsorbed proteins on the surface. Then, the 4 mL Coomassie Brilliant Blue staining solution was added to each test tube and stand for 10 min. The absorbance of the solution at 595 nm was measured by UV-vis spectrophotometer (UV2300).

2.11. Recalcification whole blood clotting test

The PCDL-PDM PUU elastomer films were prepared into circle (6 mm in diameter, $n = 6$) and immersed in PBS buffer solution (pH 7.4) overnight. Fresh rabbit blood was added with 2 % (v/v) 0.1 mol/L CaCl₂ solution, and 200 μL of recalcified whole blood and the elastomers samples were quickly added into the 96-well plate, which were placed in a 37 °C incubator for 30 min. After completion, samples were taken out and cleaned with normal saline, then transferred to a new well plate and photographed for comparison. Finally, 300 μL of 0.5 % (v/v) Trion X-

100 solution was appended to each well and placed in a 37 °C incubator for 3 h to dissolve the thrombus. After the thrombus was entirely dissolved, the absorbance of 100 μ L supernatant was determined by a microplate reader (Multiskan FC) at 405 nm, which the values represent the amount of thrombus on the surface of PCDL-PDMS PUU elastomers.

2.12. In vitro calcium deposition

The PCDL-PDMS PUU elastomer films and Elastollan™ 1180 A were cut into 1 cm \times 1 cm rectangles ($n = 3$) and rinsing with PBS for 3 times, dried. The calcification test was conducted at 37 °C in simulated body fluid (SBF, pH 7.4) at a rate of 80 rpm for 14 d and changed the SBF every 2 d. After incubation, samples were rinsed 3 times with deionized water and dried. The calcium deposition on the surface of samples were

observed by SEM.

3. Results and discussion

3.1. Preparation and characterization of PCDL-PDMS PUU elastomers

The PCDL-PDMS PUU elastomers were synthesized through the polyaddition reaction of PCDL with IPDI together with the subsequent chain-extension reaction by PDMS (Scheme 1a). In this work, the structural design offers two advantages (Scheme 1b): (1) The polymer incorporates an abundance of urethane ($-\text{NH}-\text{COO}-$) and urea ($-\text{NH}-\text{CO}-\text{NH}-$), which contribute a significant number of hydrogen bond donors and acceptors to facilitate multi-scale hydrogen-bonding interactions within the hard microdomains. The reversible multi-scale hydrogen

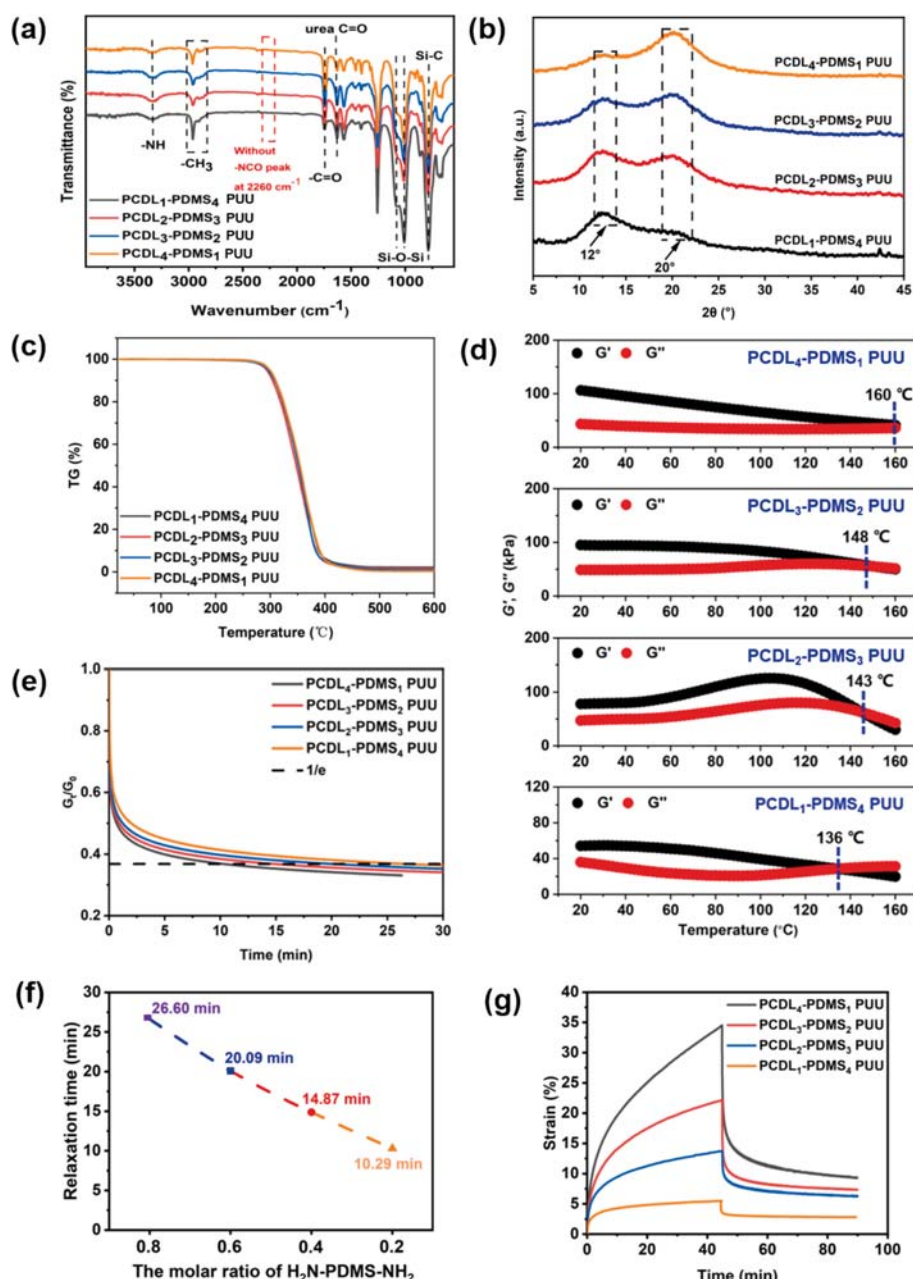


Fig. 1. (a) FTIR spectra, (b) XRD diffractograms, (c) TG curves and (d) Temperature scanning curves of PCDL-PDMS PUU elastomers with different molar ratios of PCDL and PDMS segments. (e) Stress-relaxation curves of PCDL-PDMS PUU elastomers with different molar ratios of PCDL and PDMS units at 25 °C, where the relaxation time is defined as the time for relaxation modulus reaching 1/e its original value. (f) Comparison of relaxation time calculated from (e) for PCDL-PDMS PUU elastomers. (g) Creep and recovery strain-time curve of PCDL-PDMS PUU elastomers.

bonds unfold and dissociate continuously to dissipate energy during the stretching process. (2) The forced compatibility and spontaneous separation of thermodynamically incompatible dual soft segments (PDMS and PCDL) are employed to effectively dissipate energy during elastomer stretching. The forced compatibility and spontaneous separation of two thermodynamically incompatible soft segments can synergistically incorporate hierarchical hydrogen bonds to effectively dissipate energy, thereby imparting excellent strength, toughness, and tear resistance to the elastomer. The sample composition and naming of the experimental process are shown in Table S1.

The successful synthesis of PCDL-PDMS PUU elastomers was characterized by FTIR, GPC and XPS. GPC molecular weights of synthesized PCDL-PDMS PUU elastomers are summarized in Table S2 and Figure S3. GPC trace of PCDL-PDMS PUU elastomers displayed a unimodal peak. The number average molecular weight of all PCDL-PDMS PUU elastomers in the series ranged from 64.8×10^3 g/mol to 118.5×10^3 g/mol, and the values of the polydispersity index (PDI, calculated as M_w/M_n) varied between 1.74 and 1.97. However, the molecular weight of PCDL-PDMS PUU elastomers decreases with the increase of H_2N -PDMS- NH_2 content, which should be attributed to the incompatibility of hydrophobic H_2N -PDMS- NH_2 with polyurethane during synthesis.

Fig. 1a shows the FTIR spectra of PCDL-PDMS PUU elastomers with different proportion of PDMS to PCDL. There are no absorption peaks at 2260 cm^{-1} in all the PCDL-PDMS PUU samples, indicating that the NCO group has disappeared. New peaks that appeared at 3334 cm^{-1} , 2962 cm^{-1} and 1630 cm^{-1} were assigned to N-H stretching, CH_3 stretching and C=O stretching vibration bands, respectively. The Si-C absorption peak at 797 cm^{-1} only existed in PDMS modified samples, and the intensity of the peak increased with the increase of PDMS content. Moreover, this rule is also applicable to the Si-O-Si absorption peak at 1017 cm^{-1} . It confirmed that H_2N -PDMS- NH_2 was introduced into PCDL-PDMS PUU elastomers. The peaks near 1530 cm^{-1} should be ascribed to the N-H bending vibrations and C-O vibration peaks in polycarbonate are located at 1247 cm^{-1} and 960 cm^{-1} . The XPS curves of these PCDL-PDMS PUU elastomers are shown in Figure S10. From the overview XPS charts, it was found that the characteristic peaks of O (1 s), C (1 s), N (1 s), and Si (2p) at 532.3 eV, 284.8 eV, 399.7 eV, and 102.3 eV, respectively. The above result shows that PCDL-PDMS PUU elastomers are successfully prepared.

Subsequently, the crystallization behavior of the PCDL-PDMS PUU elastomers were investigated using XRD. XRD diffractograms of PCDL-PDMS PUU elastomers are presented in Fig. 1b. All the PCDL-PDMS PUU elastomers films showed two different diffraction bands at about 12° and 20° . It indicated that there is an amorphous state in these elastomers. The characteristic peak of H_2N -PDMS- NH_2 is at $2\theta = 12^\circ$ [58], and it is also confirmed that H_2N -PDMS- NH_2 is successfully introduced into the polyurethane backbone. However, the diffraction peak intensity at $2\theta = 20^\circ$ continued to decrease with the increase of H_2N -PDMS- NH_2 content. The reason was mainly that the increase in PDMS had a destructive effect on the microstructure of PCDL-PDMS PUU elastomers.

The thermal properties of PCDL-PDMS PUU elastomers with different proportion of PDMS to PCDL were investigated with TGA and DTG analyses. The results are shown in Fig. 1c, Figure S4 and Table S3. The PCDL-PDMS PUU elastomer exhibits high thermal stability at a decomposition temperature of 300°C at 5 % weight loss (T5%). The weight loss (T5%) temperatures increase with increase the H_2N -PDMS- NH_2 content. According to the TGA and DTG curves, all PCDL-PDMS PUU elastomers show two-step weightlessness at $200\text{--}350^\circ\text{C}$ and $350\text{--}600^\circ\text{C}$, which indicates that there may be two thermally unstable parts in the polymer being synthesized. The degradation at $200\text{--}350^\circ\text{C}$ may be related to the fracture of the hard segment breakage of polyurethane. This is mainly due to the fact that the thermal stability of the hard segment of polyurethane is lower than that of the soft segment. The degradation of the soft segments in polyurethane and the breaking of Si-

O-Si chains in PDMS occur at $350\text{--}600^\circ\text{C}$. With the increase of H_2N -PDMS- NH_2 content, the residual carbon ratio of the polyurethane elastomer increased, thereby improving the heat resistance of the PCDL-PDMS PUU elastomers. On the one hand, it may be due to the formation of a large number of urea groups in the hard segments of polyurethane; on the other hand, it may be because an increase in the content of H_2N -PDMS- NH_2 changes the chemical structure of the polymer and increases the possibility of low surface energy Si enrichment on the surface. These results showed that increasing the PDMS content could slightly improve the thermal stability of PCDL-PDMS PUU elastomers.

The viscoelastic properties of PCDL-PDMS PUU elastomers with different proportion of PDMS to PCDL were evaluated with rheological measurements. The intersection of G' and G'' is considered to be a sign of the transition of the chain segment from an elasticity to a viscous flow state. According to Fig. 1d, the G' and G'' crossover temperatures of PCDL₄-PDMS₁ PUU, PCDL₃-PDMS₂ PUU, PCDL₂-PDMS₃ PUU, PCDL₁-PDMS₄ PUU were 136°C , 143°C , 148°C , 160°C , respectively. This indicated that the higher the urea bond density, the higher the activation energy required for the polymer state transition. Similar to the modulus-temperature curve, the molecular chain motion efficiency can be determined by the intersection frequency of G' and G'' . By conducting small-amplitude oscillatory shear at different temperatures ranging from 20°C to 120°C , we could construct a master curve (reference temperature = 40°C) for PCDL-PDMS PUU elastomers of frequency dependency of G' and G'' (Figure S5). A cross-point of G' and G'' at a critical shear frequency (ω_c) could be observed for PCDL-PDMS elastomers, indicating an average lifetime ($t = 1/\omega_c$) of the reversible crosslinks in these networks. The ω_c of PCDL-PDMS PUU shifted towards lower frequency with the increase of H_2N -PDMS- NH_2 , where the higher the urea bond density could hinder chain segment motion and result in a longer lifetime. Stress relaxation reflected the behavior of polymer to overcome the internal friction resistance with external force, and the decay rate depended on the internal friction resistance. The stress-relaxation experiments further demonstrate the dynamic viscoelasticity of PCDL-PDMS PUU elastomers, where completely different relaxation behaviors were observed with different molar ratios of PCDL and PDMS segments (Fig. 1e). The relaxation time increased with the increasing H_2N -PDMS- NH_2 content (Fig. 1f). That is consistent with the results of rheological measurements. PCDL₁-PDMS₄ PUU had the slowest stress attenuation rate, which indicated its maximum internal friction resistance. The main reason was the higher urea bond density in the hard segment, which increased the intensity of interaction between molecular chain segments and reduced the chain movement efficiency [59]. To evaluate the creep performance of PCDL-PDMS PUU elastomers, creep test was conducted. Fig. 1g shows the creep and recovery strain of PCDL-PDMS PUU as a function of time. Primary and secondary creep stages can be clearly observed in synthesized PCDL-PDMS PUU. In recovery phase, instantaneous recovery is rapid for all PCDL-PDMS PUU. Subsequently the recovery rate slowed for viscoelastic component due to time-dependent molecular relaxation. PCDL₂-PDMS₃ PUU and PCDL₁-PDMS₄ PUU showed enhanced creep resistance and recovery. In a word, the immiscible soft segments and hierarchical hydrogen bonds, which will facilitate the formation of hierarchical microstructures and enhance the physical cross-linking in chain segments. Figure S13 showed that the polymer had satisfactory solubility and recovery ability, indicating that it could be recycled.

3.2. Microphase separation structure of PCDL-PDMS PUU elastomers

The microphase separated structures of segmented polyurethane have significant effects on physical and biological properties. In this study, the microphase separation structure of PCDL-PDMS PUU elastomers were characterized by DSC, DMA and SAXS. The DSC curves of these PCDL-PDMS PUU elastomers are shown in Fig. 2c. In the DSC spectrum, neither the hard domain T_g , nor endothermic or exothermic peaks, indicating that all PCDL-PDMS PUU elastomers were amorphous,

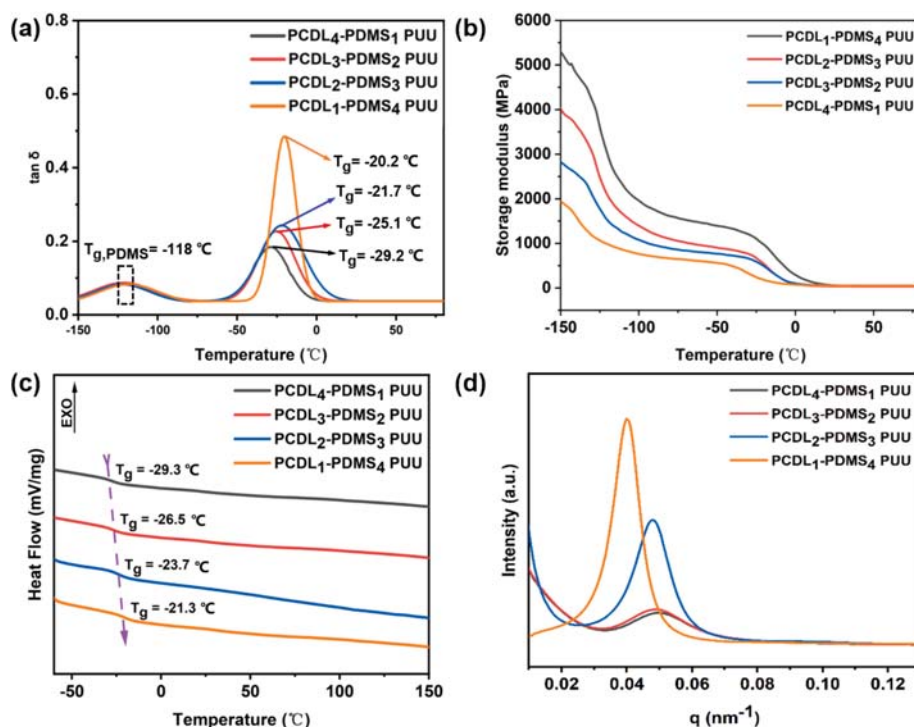


Fig. 2. (a) The loss factor ($\tan \delta$) curves, (b) The storage modulus, (c) DSC curves and (d) SAXS patterns of PCDL-PDMS PUU elastomers with different molar ratios of PCDL and PDMS segments.

which is consistent with the XRD test (Fig. 1b). With an increase in the content of H_2N -PDMS- NH_2 , the glass transition temperature ($T_{g, \text{PCDL}}$) of PCDL moved to higher temperatures, which means that more hard segments are dissolved in the PCDL phase and the PDMS phase, respectively [60]. The $T_{g, \text{PCDL}}$ of PCDL₄-PDMS₁ PUU, PCDL₃-PDMS₂ PUU, PCDL₂-PDMS₃ PUU and PCDL₁-PDMS₄ PUU are -29.3°C , -26.5°C , -23.7°C and -21.3°C , respectively. This was due to the fact that providing the number of hydrogen bonds and physical cross-linking sites with increasing PDMS content. The increase of $T_{g, \text{PCDL}}$ is beneficial for improving the mechanical properties of the material.

The curves of loss factor ($\tan \delta$) and storage modulus (E') as a function of temperature are shown in Fig. 2a and Fig. 2b. The PCDL-PDMS PUU elastomers had two T_g observed below room temperature. $T_{g1, \text{PDMS}}$ (from -130 to -110°C) and $T_{g2, \text{PCDL}}$ (from -35 to -15°C) were associated with the segmental movement of PDMS segments and PCDL segments, respectively. The T_g values of elastomers are consistent with those determined by DSC test. As shown in FTIR spectra, stronger hydrogen bonding in PCDL-PDMS PUU elastomers shows more phase separation. The appearance of two different $\tan \delta$ in DMA results, confirming the microphase separation in all PCDL-PDMS PUU elastomers. In addition, the addition of H_2N -PDMS- NH_2 increased the storage modulus of PCDL-PDMS PUU elastomers in Fig. 2b. This could be attributed to the enhanced interaction between chain segments due to more hydrogen bonds and physical cross-linking sites, which limited their mobility and flexibility.

As shown in Fig. 2d, the average distances between the hard domains of PCDL₄-PDMS₁ PUU, PCDL₃-PDMS₂ PUU, PCDL₂-PDMS₃ PUU and PCDL₁-PDMS₄ PUU elastomers have microphase separation and the average distances between the hard domains were calculated to be 127.4 nm, 128.2 nm, 131.2 nm and 157.5 nm, respectively (Table S4). From the results of SAXS, the distance between the hard segments and the degree of microphase separation increase with the increase of H_2N -PDMS- NH_2 content, suggesting a more distinct aggregation of the hard segments and the size of the hard domain increase. The microstructure of PCDL-PDMS PUU elastomers were further investigated by AFM. The obtained micrographs were shown in Figures S6 and S7, which

presented a clear microphase-separation structure. The bright and dark areas corresponded to hard and soft segment, respectively. With an increase in the content of H_2N -PDMS- NH_2 , the relatively dark part increases slightly, which may be related to the surface aggregate of H_2N -PDMS- NH_2 . The hard segments are partially dissolved in the soft segments of polyurethane.

3.3. Mechanical of PCDL-PDMS PUU elastomers

Considering that PCDL-PDMS PUU elastomers contain microphase separation structures and hierarchical hydrogen bonds interactions, these PCDL-PDMS PUU elastomers may exhibit excellent mechanical properties. The mechanical properties of PCDL-PDMS PUU elastomers were evaluated via a uniaxial tensile test with a stretching speed of 200 mm/min at room temperature. The stress-strain curves of PCDL-PDMS PUU elastomers are shown in Fig. 3a and the detailed results are summarized in Table S5. All PCDL-PDMS PUU elastomers are classical thermoplastic elastomer because they do not exhibit yielding phenomena during elongation. With H_2N -PDMS- NH_2 added to PCDL-PDMS PUU elastomers, the value of Elongation at break firstly increased and then decreased while tensile strength was not found remarkable changes. However, the Young's modulus and tear strengths increased with the increasing proportion of H_2N -PDMS- NH_2 . This main reason is the formation of strong intermolecular hydrogen bonds and microphase separations. The mechanical properties of the PCDL-PDMS PUU film were attributed to the two types of hydrogen bonds: (1) strong hydrogen bonds (urea units) conferring good mechanical reversibility to the PCDL-PDMS PUU film upon stretching, and (2) weak hydrogen bonds (urethane units) allowing effective dissipation of fracture energy. Among them, the representative PCDL₃-PDMS₂ PUU elastomer had a Young's modulus of 3.8 MPa, tensile strength of 31.5 MPa and toughness of 279.8 MJ/m^3 . Therefore, the microphase separation structures and hierarchical hydrogen bonds interactions are important factors for achieving excellent mechanical properties in terms of strength and toughness.

To investigate the fatigue resistance of the elastomers, the cyclic

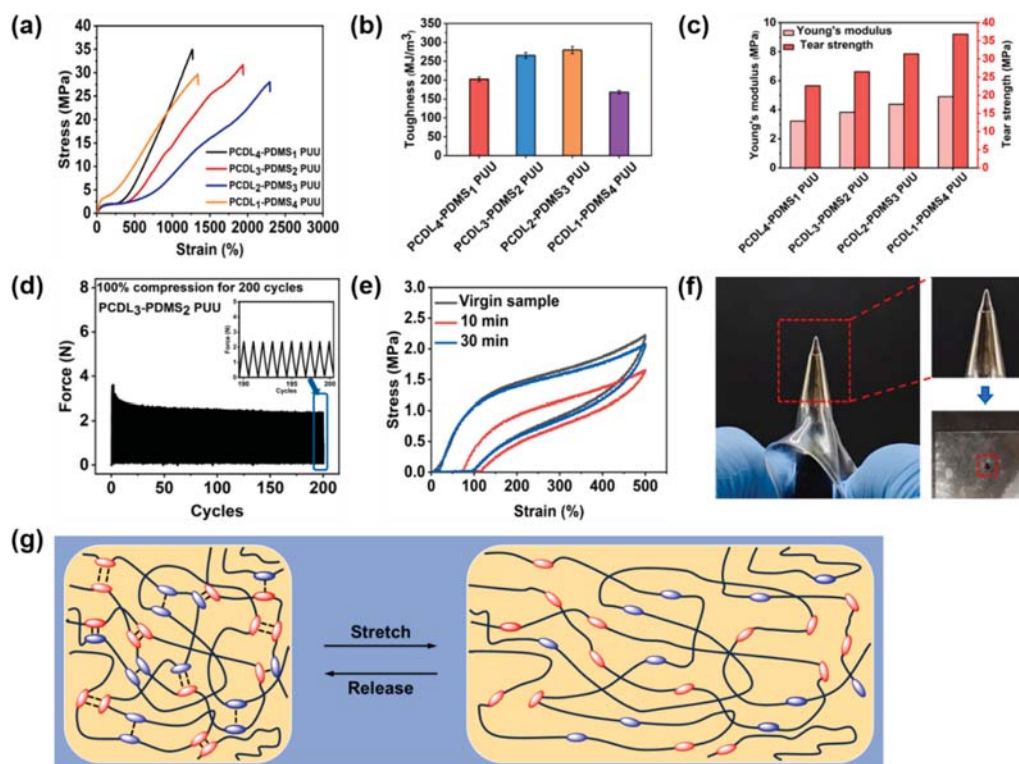


Fig. 3. (a) Typical stress-strain curves of PCDL-PDMS PUU elastomers with different molar ratios of PCDL and PDMS segments. (b) A histogram of toughness. (c) A histogram of Young's modulus and tear strength. (d) Variation of the force of PCDL₃-PDMS₂ PUU elastomer held at 100% strain for 200 cycles. (e) Cyclic loading-unloading tensile curves of the PCDL₃-PDMS₂ PUU elastomers at different waiting times. (f) Photographic images of PCDL₃-PDMS₂ PUU with excellent puncture resistance. (g) Schematic illustration of the structure of PCDL-PDMS PUU elastomer after being stretched and then released.

tensile tests were further conducted and continuous 200 cyclic stretching with a tensile rate of 50 mm/min and a strain of 100 % and the results are shown in Fig. 3d and Figure S8. The loading-unloading tensile curves of PCDL-PDMS PUU elastomers showed a distinct hysteresis loop. This could be attributed to partial hydrogen bond breakage in the elastomer. As the number of cyclic stretching increased, the maximum force tended to reach a stable state. This phenomenon could be attributed to the hydrogen bond achieving a dynamic balance between breakage and rapid reassociation. Notably, the curves corresponding to 91–100 cycles in the inset of Fig. 3d almost coincided with each other, which proved that PCDL₃-PDMS₂ PUU had good stability and fatigue resistance. The elastic restorability of the elastomers was also evaluated. Fig. 3e shows the cyclic tensile of PCDL₃-PDMS₂ PUU elastomer after loading 500 % strain and resting for different times. The first-cycle curve has obvious hysteresis. With the extension of the residence time, the cycle curve gradually approached the original state after a waiting period of 30 min, indicating that the broken hydrogen bonds were recombined and the mechanical properties of the elastomers were gradually recovered. Therefore, the PCDL₃-PDMS₂ PUU elastomer exhibited excellent elastic restorability and facilitating effectively mitigate the degradation of the elastomer's mechanical properties during biomedical applications. Meanwhile, the PCDL₃-PDMS₂ PUU elastomer also exhibited excellent puncture resistance, no puncture damage was observed, and the sample completely recovered to its original state following the puncture test (Fig. 3f), which confirms its great potential for application in biomedical devices. The reason could be primarily attributed to the dynamic dissociation and reassociation of hydrogen bonds within the hard microdomains. As a result, the energy was effectively dissipated and gradually transferred throughout the polymer network, resulting in exceptional puncture resistance. In summary, the outstanding fatigue-resistance and recovery ability of the elastomers the superhigh elastic restorability could be attributed to the following factors: (I) The polymer had a large number of urethane and urea bonds,

which will facilitate hierarchical hydrogen bonds interactions within the hard-phase microdomains; and (II) The forced compatibility and spontaneous separation of the thermodynamic incompatibility two segments facilitate the formation of nanoscopic microphase separation structures. These factors significantly improved the energy dissipation during the elastomer stretching (Fig. 3g).

Crack tolerance is considered to be crucial mechanical property parameters for elastomers. Adequate crack tolerance is crucial properties for elastomers as they enable them to withstand significant external forces without experiencing rapid damage. Therefore, in order to assess the crack tolerance of the samples, tensile tests were conducted on notched elastomers. Notched specimens were stretched at a speed of 50 mm/min. As shown in Figure S9, the results showed that PCDL₃-PDMS₂ PUU elastomer could be stretched to an elongation-at-break of 777 % and a breaking strength of 10.1 MPa even with a large notch of 1 mm. The excellent performance of the PCDL-PDMS PUU elastomer could be attributed to the breaking and rapid reorganization of hydrogen bonds within the hard microdomains. As a result, the stress at the notch of the sample was concentrated, allowing it to be transmitted and dispersed into the entire elastomer network structure, thereby effectively resisting the crack propagation.

3.4. Surface construction and in vitro degradation of the PCDL-PDMS PUU elastomers

The surface properties of materials influence chemical stability. PDMS could migrate to the surfaces of materials to protect materials. In the work, the surface properties of PCDL-PDMS PUU elastomers were characterized by XPS and WCA.

XPS test was used to characterize the surface elemental content of PCDL-PDMS PUU elastomers, and detailed C-spectrum and Si-spectrum of the samples are shown in Figure S10, Figure S11, Figure S12 and Table S6. H₂N-PDMS-NH₂ is a monomer with a molecular weight of

1000 consisting of 10–11 repeating Si-O units. The content of the Si element of the PCDL₄-PDMS₁ PUU, PCDL₃-PDMS₂ PUU, PCDL₂-PDMS₃ PUU and PCDL₁-PDMS₄ PUU obtained is calculated to be from 2.77 to 3.05 %, 6.15 to 6.76 %, 10.36 to 11.39 % and 15.75 to 17.33 %, respectively. However, it can be seen from Table S6 that the actual content of Si on the polymer surface is greater than the calculated data. As the molecular weight of H₂N-PDMS-NH₂ increases, the Si/C ratio increases, which also indicates that the surface is enriched with a large amount of Si, which is mainly attributed to the low surface energy properties of Si. That results in an increase in hydrophobicity of the surface (Fig. 4a). In addition, this is consistent with the results of TGA. In other words, by increasing the PDMS content, the thermal stability of the PCDL-PDMS PUU elastomers is increases, possibly due to the formation of a higher silicon-rich surface. The required elements and corresponding functional groups were detected, which further supported the successful preparation of PCDL-PDMS PUU elastomers (Figures S11 and S12).

The surface roughness may be related to the hydrophobicity of the material surface. As shown in Figure S7, it is observed that the samples show an uneven structure. The surface roughness values of PCDL₄-PDMS₁ PUU, PCDL₃-PDMS₂ PUU, PCDL₂-PDMS₃ PUU, and PCDL₁-PDMS₄ PUU are 7.86 nm, 5.22 nm, 4.28 nm, and 2.76 nm, respectively. As the content of H₂N-PDMS-NH₂ increases, the surface roughness shows a downward trend, which may be due to changes in the molecular structure of the polymer. Furthermore, the hydrophobicity/hydrophilicity of the surfaces of PCDL-PDMS PUU elastomers was measured with WCA. As shown in Fig. 4a, the WCA values increased from 94.8° to 116.8° as the molar fraction of H₂N-PDMS-NH₂ was increased from 20 % to 80 %. This is mainly related to the migration of Si to the surface, which reduces the surface energy and improves the hydrophobicity. That is consistent with the results of XPS.

To evaluate the water absorption of the PCDL-PDMS PUU elastomer films, the samples were immersed in water at room temperature for 48 h. As the shows Fig. 4b, all PCDL-PDMS PUU elastomers exhibited a low water absorption (<2%) and the value decreased with the proportion of H₂N-PDMS-NH₂ increased. This phenomenon was explained by the incremental surface hydrophobicity, which agrees well with the WCA and XPS results.

In addition, the *in vitro* hydrolytic degradation of the PCDL-PDMS PUU elastomers were also determined and the results are shown in Fig. 4c. This shows the *in vitro* hydrolytic degradation behavior of PCDL-PDMS PUU elastomers in PBS at 37 °C. All the elastomer films showed a mass loss of less than 2.5 % after degradation for 1 month, indicating a very slow degradation rate or high biostability. With the PDMS content increased in the elastomers, an obvious reduction in the degradation rate was found, which was consistent with the trend of the water absorption. These results indicated that the PCDL-PDMS PUU elastomers

have enough water resistance to meet the practical applications in biomedical devices.

3.5. Biocompatibility of the PCDL-PDMS PUU elastomers

The hemocompatibility of biomaterials were evaluated by cytotoxicity, hemolysis, protein adsorption, platelet adhesion and calcification test. As shown in Figure S14, the cell viability values based on MTT assay for all the PCDL-PDMS PUU samples were higher than 85 %, which indicated that the cytotoxicity of PCDL-PDMS PUU is quite low. As shown in Fig. 5a and Figure S15a, no obvious hemolysis phenomenon was observed in the PCDL-PDMS PUU elastomers, and the relative hemolysis rate of red blood cells in the PCDL-PDMS PUU elastomer films is less than 2 %, meeting the ISO 5840–3:2013 requirements [61]. Which shows that these elastomer films have a good blood compatibility. With the increased PDMS contents, the relative hemolysis rate of PCDL-PDMS PUU elastomer films decreased. That may be related to the hydrophobicity of the surface of the material, which is not conducive to the adhesion of red blood cells. Furthermore, the platelet adhesion on the PCDL-PDMS PUU elastomer film surface is shown in Fig. 5b. The number of platelets adhered to the surface presented a substantial reduction as the H₂N-PDMS-NH₂ content increased, which was also attributed to the low surface energy of the film surface. In addition, the recalcification whole blood clotting experiment was used to further evaluate the anti-coagulant ability of these PCDL-PDMS PUU elastomers. Fig. 5c and Figure S15b demonstrated PCDL-PDMS PUU elastomers have better anti-coagulant property, with almost no thrombus on its surface. This shows that these elastomer films have a good anticoagulant ability.

The rapid adsorption of plasma proteins on the surface of a blood-contacting implant is the first step in thrombus formation [62]. Plasma protein adsorption can initiate the aggregation and activation of platelets to ultimately form a clot backbone [63]. When thrombus occurred on the heart value materials, it would make them thicker and hinder their movements, finally leading to the failure of implantation. It has been hypothesized that calcification of polymer heart valves is the result of surface deposition of cellular debris, proteins and thrombi [64]. When calcification occurred on the heart value materials, it would make them thicker and hinder their movements and then decrease its lifetime. Therefore, protein adsorption and calcium deposition testing were carried out to characterize the Hemocompatibility properties of the materials.

As shown in Fig. 5d, the protein adsorption exhibited an opposite trend with the platelet adhesion. The most amount of adsorbed BSA was observed on PDMS PUU, meaning a relatively low ability for protein resistance. With the decrease in PDMS content in PCDL-PDMS PUU film, the BSA adsorption was reduced from 13.2 µg/cm² to 3.9 µg/cm². These results strongly indicate that less PDMS content in PCDL-PDMS PUU

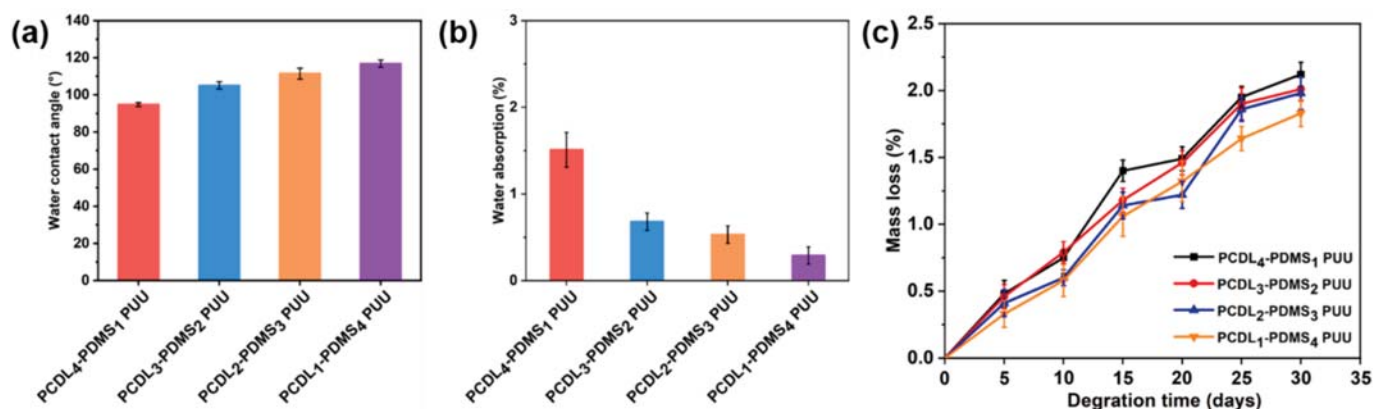


Fig. 4. (a) The water contact angle of PCDL-PDMS PUU elastomers. (b) Water absorption of PCDL-PDMS PUU elastomers in water for 48 h. (c) *In vitro* hydrolytic degradation behaviors of PCDL-PDMS PUU elastomers as function of time in PBS at 37 °C.

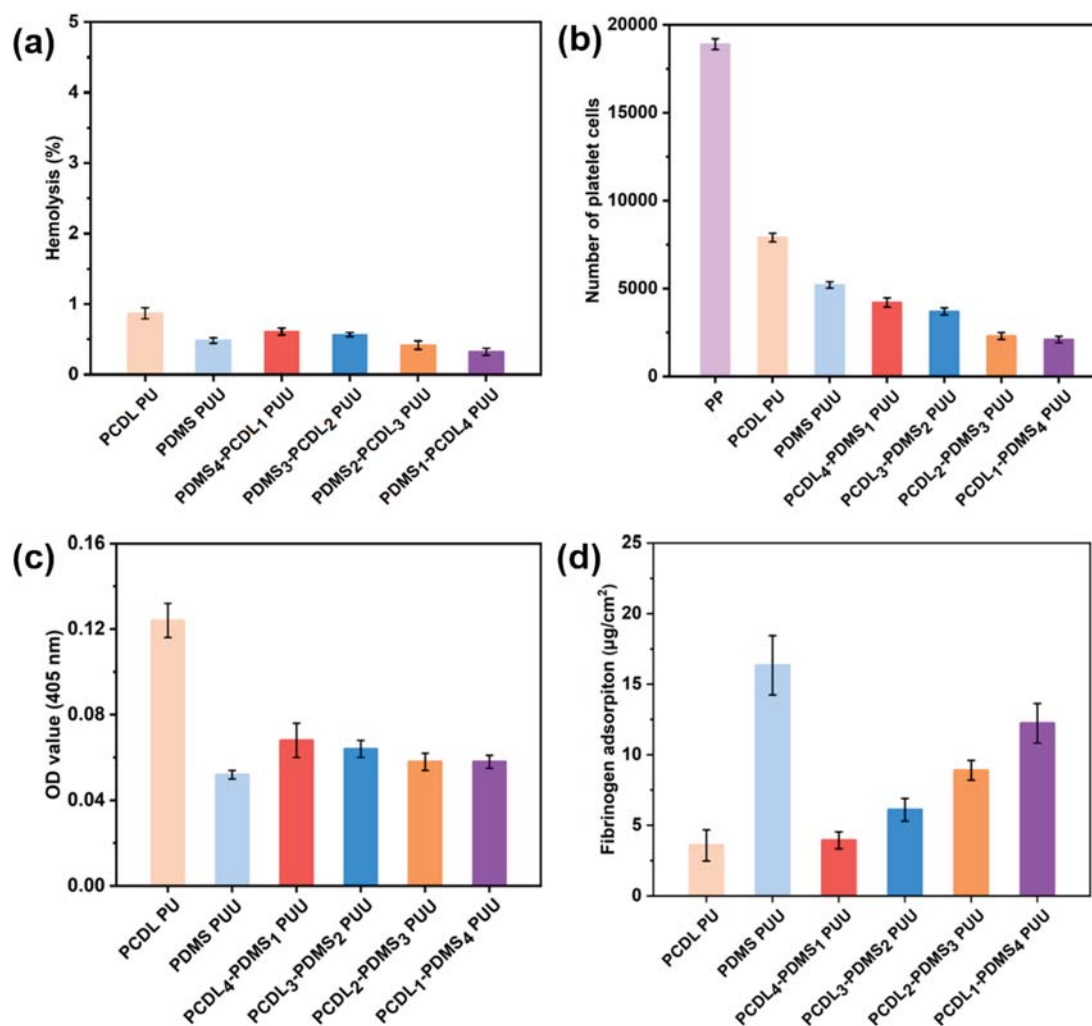


Fig. 5. (a) Hemolysis, (b) platelet adhesion, (c) recalcification whole blood clotting test and (d) BSA adsorption on the PCDL-PDMS PUU elastomer films surface.

elastomers owns stronger ability to resist protein adsorption. This behavior is usually associated with the synergy of microphase separation and the low interfacial energy.

To evaluate the calcium deposition on the PCDL-PDMS PUU elastomer films surface, the samples were immersed in a simulated body fluid (SBF) at 37 °C for 14 d. As shown in the SEM images, significant **calcific deposits** were observed on ElastollanTM 1180 A film (Figure S16a), while there were nearly no obvious calcific deposits in PCDL₃-PDMS₂ PUU elastomer (Figure S16b). Then the EDS test was used to quantitatively analyze the calcium contents of samples. EDS results further demonstrated the anti-calcification property of PCDL₃-PDMS₂ PUU elastomer (Figure S16d). For ElastollanTM 1180 A film, the amount of calcium is estimated to be about 25.7 wt% and the phosphorus to be about 14.5 wt% (Figure S16c). For PCDL₃-PDMS₂ PPU film, the amount of calcium is estimated to be about 0.02 wt% (Figure S16d). The result indicates the presence of PDMS effectively delays polymer calcification, which is consistent with the results of XPS (Figure S16e). All the results demonstrated that the PCDL-PDMS PUU elastomers possessed superior biocompatibility and could be explored as an artificial heart valve for biomedical applications.

4. Conclusions

In summary, we synthesized a series of PCDL-PDMS PUU elastomers with stable mechanical properties, good elastic recoverability, recyclable properties and good biocompatibility by two step

copolymerization method for medical applications. By adjusting the proportion of PCDL and PDMS, the influence of PDMS content on the chemical structure, surface morphology, mechanical behavior and biocompatibility was investigated. The synthesized PCDL-PDMS PUU elastomers with a hierarchical microphase separation structure has excellent mechanical properties, which can be attributed to the synergistic effect of the bi-incompatible soft phase and the hierarchical hydrogen bonds. The results of the water absorption and *in vitro* hydrolytic degradation showed that PCDL-PDMS PUU elastomers had high biostability. Because of the lower surface energy, the relative hemolysis rate of the elastomers to red blood cells is less than 2 %. Moreover, the PCDL-PDMS PUU elastomer is also superior biocompatibility with high anti-platelet adhesion and resistant to calcification. Therefore, the PCDL-PDMS PUU elastomers has excellent tensile properties, high biostability and biocompatibility, showing a great potential for heart valves material.

CRediT authorship contribution statement

Xionghui Wu: Writing – original draft, Methodology, Investigation, Data curation. **Yichao Hu:** Data curation. **Yu Xia:** Data curation. **Yaling Lin:** Writing – review & editing, Supervision. **Anqiang Zhang:** Writing – review & editing, Supervision, Project administration, Funding acquisition, Conceptualization.

Declaration of competing interest

The authors declare that they have no known competing financial interests or personal relationships that could have appeared to influence the work reported in this paper.

Data availability

Data will be made available on request.

Acknowledgements

The authors acknowledge the financial support from the National Natural Science Foundation of China (No. 52073098) and the Natural Science Foundation of Guangdong Province (No. 2022A1515011570, 2023A1515011264).

Appendix A. Supplementary data

Supplementary data to this article can be found online at <https://doi.org/10.1016/j.eurpolymj.2024.113349>.

References

- J.O. Akindoyo, M. Beg, S. Ghazali, M.R. Islam, N. Jeyaratnam, A.R. Yuvaraj, Polyurethane types, synthesis and applications-a review, *RSC Adv.* 6 (2016) 114453–114482.
- P.A. Gunatillake, L.S. Dandeniyage, R. Adhikari, M. Bown, R. Shanks, B. Adhikari, Advancements in the development of biostable polyurethanes, *Polym. Rev.* 59 (2019) 391–417.
- E. Ergene, B.S. Yagci, S. Gokyer, A. Eyidogan, E.A. Aksoy, P.Y. Huri, A novel polyurethane-based biodegradable elastomer as a promising material for skeletal muscle tissue engineering, *Biomed. Mater.* 14 (2019) 025014.
- Y. Zeng, Y. Chen, D. Sha, Y. Wu, R. Qiu, W. Liu, Highly stretchable fatty acid chain-dangled thermoplastic polyurethane elastomers enabled by H-bonds and molecular chain entanglements, *ACS Sustainable Chem. Eng.* 10 (2022) 11524–11532.
- N. Nasrollahi, M. Yousefpoor, A. Khataee, V. Vatanpour, Polyurethane-based separation membranes: A review on fabrication techniques, applications, and future perspectives, *J. Ind. Eng. Chem.* 116 (2022) 99–119.
- H. Xiong, H. Wu, J. Zhang, S. Huang, S. Gu, Y. Hou, Q. Wu, J. Wu, Healable and recyclable polyurethane with natural-rubber-like resilience via π -type tweezer structure stabilizing dynamical hard domains, *Macromolecules* 56 (2023) 8581–8591.
- Z.X. Fei, C. Yin, J.R. Sun, L. Yuan, L.Y. Shi, Healable and recyclable multiblock polyurethanes with mechanical performance tailorability based on hierarchical phase separation and dynamic bond interaction, *Polymer* 289 (2023) 126467.
- J. Chen, R. Dong, J. Ge, B. Guo, P.X. Ma, Biocompatible, biodegradable, and electroactive polyurethane-urea elastomers with tunable hydrophilicity for skeletal muscle tissue engineering, *ACS Appl. Mater. Interfaces* 7 (2015) 28273–28285.
- S. Kim, S. Liu, Smart and biostable polyurethanes for long-term implants, *ACS Biomater. Sci. Eng.* 4 (2018) 1479–1490.
- X. Ding, J. Gao, A.P. Acharya, Y.L. Wu, S.R. Little, Y. Wang, Azido-functionalized polyurethane designed for making tunable elastomers by click chemistry, *ACS Biomater. Sci. Eng.* 6 (2019) 852–864.
- A. Pierrard, S.F. Melo, Q. Thijssen, S. Van Vlierberghe, P. Lancellotti, C. Oury, C. Detrembleur, C. Jérôme, Design of 3D-photoprintable, bio-, and hemocompatible nonisocyanate polyurethane elastomers for biomedical implants, *Biomacromolecules* 25 (2024) 1810–1824.
- Q. Zhang, X. Lin, W. Chen, K. Jiang, D. Han, Applications of characterization methods in polyurethane materials: analysis of microphase-separated structures, *Appl. Spectrosc. Rev.* 57 (2022) 153–176.
- W. Zheng, C. Zhang, Y. Han, W. Wang, Z. Li, Highly durable silicone-based elastomers achieved through the synergy of bi-incompatible soft segments and multi-scale hydrogen bonds, *Small* 2402124 (2024).
- W. Li, H. Wu, Y. Huang, Y. Yao, Y. Hou, Q. Teng, M. Cai, J. Wu, Ultra-fast-healing glassy hyperbranched plastics capable of restoring 26.4 MPa tensile strength within one minute at room temperature, *Angew. Chem.* (2024) e202408250.
- F. Guo, R. Han, J. Ying, Z. Zhang, R. Yang, X. Zhang, Bioinspired polymeric heart valves derived from polyurethane and natural cellulose fibers, *J. Mater. Sci. Technol.* 144 (2023) 178–187.
- S. Li, L. Yang, Z. Zhao, X. Yang, H. Lv, A polyurethane-based hydrophilic elastomer with multi-biological functions for small-diameter vascular grafts, *Acta Biomater.* 176 (2024) 234–249.
- H.Y. Mi, X. Jing, G. Yilmaz, B.S. Hagerty, E. Enriquez, L.S. Turng, In situ synthesis of polyurethane scaffolds with tunable properties by controlled crosslinking of tri-block copolymer and polycaprolactone triol for tissue regeneration, *Chem. Eng. J.* 348 (2018) 786–798.
- R. Guo, Q. Zhang, Y. Wu, H. Chen, Y. Liu, J. Wang, X. Duan, Q. Chen, Y. Zhang, Extremely strong and tough biodegradable poly (urethane) elastomers with unprecedented crack tolerance via hierarchical hydrogen-bonding interactions, *Adv. Mater.* 35 (2023) 2212130.
- C. Xu, Y. Hong, Rational design of biodegradable thermoplastic polyurethanes for tissue repair, *Bioact. Mater.* 15 (2022) 250–271.
- S. Wendels, L. Avérous, Biobased polyurethanes for biomedical applications, *Bioact. Mater.* 6 (2021) 1083–1106.
- H. Wang, T. Li, J. Li, R. Zhao, A. Ding, F.J. Xu, Structural engineering of polyurethanes for biomedical applications, *Prog. Polym. Sci.* 151 (2024) 101803.
- F. Xie, T. Zhang, P. Bryant, V. Kurusingal, J.M. Colwell, B. Laycock, Degradation and stabilization of polyurethane elastomers, *Prog. Polym. Sci.* 90 (2019) 211–268.
- S.H. Hsu, J. Xu, S.H. Lin, S.D. Wu, Q.P. Cheng, C.W. Wong, Creative transformation of biomedical polyurethanes: from biostable tubing to biodegradable smart materials, *J. Polym. Res.* 29 (2022) 70.
- S. Chen, Y. Wang, L. Yang, C. Chu, S. Cao, Z. Wang, J. Xue, Z. You, Biodegradable elastomers for biomedical applications, *Prog. Polym. Sci.* 147 (2023) 101763.
- H. Wu, T. Dai, W. Ao, S. Shao, Z. Li, F. Luo, J. Li, D. Zhao, W. Lan, H. Tan, The role of segmental mixing on the mechanical properties and oxidative stability of polydimethylsiloxane-based polyetherurethane, *Polymer* 261 (2022) 125401.
- R.S. Labow, E. Meek, J.P. Santerre, Hydrolytic degradation of poly (carbonate)-urethanes by monocyte-derived macrophages, *Biomaterials* 22 (2001) 3025–3033.
- R. Zhu, Y. Wang, Z. Zhang, D. Ma, X. Wang, Synthesis of polycarbonate urethane elastomers and effects of the chemical structures on their thermal, mechanical and biocompatibility properties, *Heliyon* 2 (2016) e00125.
- Y. Eom, S.M. Kim, M. Lee, H. Jeon, J. Park, E.S. Lee, S.Y. Hwang, J. Park, D.X. Oh, Mechano-responsive hydrogen-bonding array of thermoplastic polyurethane elastomer captures both strength and self-healing, *Nat. Commun.* 12 (2021) 621.
- J. Kozakiewicz, G. Rokicki, J. Przybylski, K. Sylwestrzak, P.G. Parzuchowski, K. M. Tomczyk, Studies of the hydrolytic stability of poly(urethane-urea) elastomers synthesized from oligocarbonate diols, *Polym. Degrad. Stab.* 95 (2010) 2413–2420.
- I. Khan, N. Smith, E. Jones, D.S. Finch, R.E. Cameron, Analysis and evaluation of a biomedical polycarbonate urethane tested in an in vitro study and an ovine arthroplasty model, Part i: Materials Selection and Evaluation, *Biomaterials* 26 (2005) 621–631.
- A. D' Amore, S. K. Luketich, R. Hoff, S. H. Ye, W. R. Wagner, Blending polymer labile elements at differing scales to affect degradation profiles in heart valve scaffolds *Biomacromolecules* 20 2019 2494 2505.
- T. Al Kayal, P. Losi, M. Asaro, S. Volpi, W. Bonani, M. Bonini, G. Soldani, Analysis of oxidative degradation and calcification behavior of a silicone polycarbonate polyurethane-polydimethylsiloxane material, *J. Biomed. Mater. Res. Part A* 110 (2022) 1109–1120.
- F. Wang, Z.Q. Gao, C.P. Feng, D.Y. Wang, M.P. Jin, F. Zhang, Z.L. Peng, G. M. Zhang, X.Y. Zhu, H.B. Lan, Flexible electronics substrate with excellent tear-resistant and high toughness using multi-material 3D printing, *Addit. Manuf.* 81 (2024) 103985.
- S. Li, C.W.E. Lam, M. Donati, K. Regulagadda, E. Yavuz, T. Pfeiffer, P. Sarkis, E. Gogolides, A. Milonitis, D. Poulikakos, M. Kappl, Durable, ultrathin, and antifouling polymer brush coating for efficient condensation heat transfer, *ACS Appl. Mater. Interfaces* 16 (2023) 1941–1949.
- H.J. Lee, H. Kim, T.S. Kim, H.Y. Kim, J. Mun, G. Choi, H.E. Jeong, J. Yeo, Adhesive-free PDMS/PUA bilayer using selective photopolymerization for transparent, attachable, and wearable triboelectric nanogenerator, *Nano Energy* 121 (2024) 109274.
- T. Dai, C. Yi, S. Dong, M. Zhang, C. Long, Z. Li, W. Liu, F. Luo, J. Li, H. Tan, The influence of microphase separation structure of silicon-containing polyurethane on its wear resistance, *Polymer* 299 (2024) 126944.
- S. Hu, X. Chen, J.M. Torkelson, Isocyanate-free, thermoplastic polyhydroxyurethane elastomers designed for cold temperatures: Influence of PDMS soft-segment chain length and hard-segment content, *Polymer* 256 (2022) 125251.
- W. Liu, A. Wang, R. Yang, H. Wu, S. Shao, J. Chen, Y. Ma, Z. Li, Y. Wang, X. He, J. Li, H. Tan, Q. Fu, Water-triggered stiffening of shape-memory polyurethanes composed of hard backbone dangling PEG soft segments, *Adv. Mater.* 34 (2022) 2201914.
- J. Zhao, R. Xu, G. Luo, J. Wu, H. Xia, Self-healing poly (siloxane-urethane) elastomers with remoldability, shape memory and biocompatibility, *Polym. Chem.* 7 (2016) 7278–7286.
- D.J. Martin, L.A.P. Warren, P.A. Gunatillake, S.J. McCarthy, G.F. Meijs, K. Schindhelm, Polydimethylsiloxane/polyether-mixed macrodiol-based polyurethane elastomers: biostability, *Biomaterials* 21 (2000) 1021–1029.
- Z.H. Liu, Y.H. Xiao, X.Y. Ma, X. Geng, L. Ye, A.Y. Zhang, Z.G. Feng, Preparation and characterisation of zwitterionic sulfobetaine containing siloxane-based biostable polyurethanes *Mater. Adv.* 3 (2022) 4608–4621.
- L. Tang, X. Long, X. He, M. Ding, D. Zhao, F. Luo, J. Li, Z. Li, H. Zhang, Improved in vivo stability of silicon-containing polyurethane by fluorocarbon side chain modulation of the surface structure, *J. Mater. Chem. B* 9 (2021) 3210–3223.
- L. Tang, S. Shao, A. Wang, C. Tian, F. Luo, J. Li, Z. Li, H. Tan, H. Zhang, Influence of fluorocarbon side chain on microphase separation and chemical stability of silicon-containing polycarbonate urethane, *Polymer* 242 (2022) 124538.
- Y. Li, L. Yuan, H. Ming, X. Li, L. Tang, J. Zhang, R. Wang, G. Wang, Y. Jiang, Z. Li, F. Luo, J. Li, H. Tan, Q. Fu, Enhanced hydrolytic resistance of fluorinated silicon-containing polyether urethanes, *Biomacromolecules* 21 (2020) 1460–1470.
- X. Wu, H. Jia, W. Fu, M. Li, Y. Pan, Enhanced Tensile Properties, Biostability, and Biocompatibility of Siloxane-Cross-Linked Polyurethane Containing Ordered Hard Segments for Durable Implant Application, *Molecules* 28 (2023) 2464.
- C.A. Xu, B. Nan, M. Lu, Z. Qu, Z. Tan, K. Wu, J. Shi, Effects of polysiloxanes with different molecular weights on in vitro cytotoxicity and properties of

- polyurethane/cotton-cellulose nanofiber nanocomposite films, *Polym. Chem.* 11 (2020) 5225–5237.
- [47] G. Lv, J. Hu, X. Hao, N. Ning, B. Yu, M. Tian, Preparation and compatibility mechanism study of the polyurethane-polysiloxane copolymer with tunable polysiloxane content for TPU/MVQ blends with comfortable texture, *Polym. Chem.* 14 (2023) 2246–2255.
- [48] H. Wu, H. Wang, M. Luo, Z. Yuan, Y. Chen, B. Jin, W. Wu, B. Ye, H. Zhang, J. Wu, Mechanically robust, self-reporting and healable polyurethane elastomers by incorporating symmetric/asymmetric chain extenders, *Mater. Horiz.* 11 (2024) 1548–1559.
- [49] Z. Sun, J. Wen, C. Xu, W. Wang, H. Fan, Y. Chen, J. Xiang, Modification of two-package polyurethane by polyethersiloxanediol for non-polar substrate coating, *Chem. Phys. Lett.* 779 (2021) 138878.
- [50] A.G. Kidane, G. Burriesci, M. Edirisinghe, H. Ghanbari, P. Bonhoeffer, A. M. Seifalian, A novel nanocomposite polymer for development of synthetic heart valve leaflets, *Acta Biomater.* 5 (2009) 2409–2417.
- [51] H. Ghanbari, A.G. Kidane, G. Burriesci, B. Ramesh, A. Darbyshire, A.M. Seifalian, The anti-calcification potential of a silsesquioxane nanocomposite polymer under in vitro conditions: potential material for synthetic leaflet heart valve, *Acta Biomater.* 6 (2010) 4249–4260.
- [52] S. Sarkar, G. Burriesci, A. Wojcik, N. Aresti, G. Hamilton, A.M. Seifalian, Manufacture of small calibre quadruple lamina vascular bypass grafts using a novel automated extrusion-phase-inversion method and nanocomposite polymer, *J. Biomech.* 42 (2009) 722–730.
- [53] Z. Luo, H. Cui, J. Guo, J. Yao, X. Fang, F. Yan, B. Wang, H. Mao, Poly(ionic liquid)/ce-based antimicrobial nanofibrous membrane for blocking drug-resistance dissemination from mrsa-infected wounds, *Adv. Funct. Mater.* 31 (2021) 2100336.
- [54] S.F. Melo, A. Nondonfay, A. Aqil, A. Pierrard, A. Hulin, C. Delierneux, B. Ditkowski, M. Gustin, M. Legrand, B.M.E. Tullemans, S.L.N. Brouns, A. Nchimi, R. Carrus, A. Dejosé, J.W.M. Heemskerk, M.J.E. Kuijpers, J. Ritter, U. Steinseifer, J.C. Clauser, C. Jérôme, P. Lancellotti, C. Oury, Design, manufacturing and testing of a green non-isocyanate polyurethane prosthetic heart valve, *Biomater. Sci.* 12 (2024) 2149–2164.
- [55] R.L. Li, J. Russ, C. Paschalides, G. Ferrari, H. Waisman, J.W. Kysar, D. Kalfa, Mechanical considerations for polymeric heart valve development: Biomechanics, materials, design and manufacturing, *Biomaterials* 225 (2019) 119493.
- [56] M. Sun, M. Elkhodiry, L. Shi, Y. Xue, M.H. Abyaneh, A.P. Kossar, C. Giuglaris, S. L. Carter, R.L. Li, E. Bacha, G. Ferrari, J. Kysar, K. Myers, D. Kalfa, A biomimetic multilayered polymeric material designed for heart valve repair and replacement, *Biomaterials* 288 (2022) 121756.
- [57] R. Zhu, X. Wang, J. Yang, Y. Wang, Z. Zhang, Y. Hou, F. Lin, Influence of hydroxyl-terminated polydimethylsiloxane on high-strength biocompatible polycarbonate urethane films, *Biomed. Mater.* 12 (2016) 015011.
- [58] X. Wang, S. Zhan, Z. Lu, J. Li, X. Yang, Y. Qiao, J. Sun, Healable, recyclable, and mechanically tough polyurethane elastomers with exceptional damage tolerance, *Adv. Mater.* 32 (2020) 2005759.
- [59] D. Wang, Z. Wang, S. Ren, J. Xu, C. Wang, P. Hu, J. Fu, Molecular engineering of a colorless, extremely tough, superiorly self-recoverable, and healable poly (urethane-urea) elastomer for impact-resistant applications, *Mater. Horiz.* 8 (2021) 2238–2250.
- [60] L. Tang, S. Shao, A. Wang, C. Tian, F. Luo, J. Li, H. Zhang, Influence of fluorocarbon side chain on microphase separation and chemical stability of silicon-containing polycarbonate urethane, *Polymer* 242 (2022) 124538.
- [61] Q. Wang, L. Tan, K.J. Yang, Cytocompatibility and hemolysis of AZ31B magnesium alloy with Si-containing, Coating, *Mater. Sci. Technol.* 31 (2015) 845–851.
- [62] S. Kumar, D.N. Roy, V. Dey, A comprehensive review on techniques to create the anti-microbial surface of biomaterials to intervene in biofouling, *Colloid Interface Sci. Commun.* 43 (2021) 100464.
- [63] S. Yuan, S. Luan, S. Yan, H. Shi, J. Yin, Facile fabrication of lubricant-infused wrinkling surface for preventing thrombus formation and infection, *ACS Appl. Mater. Interfaces* 7 (2015) 19466–19473.
- [64] E.S. Fioretta, L. Von Boehmer, S.E. Motta, V. Lintas, S.P. Hoerstrup, M.Y. Emmert, Cardiovascular tissue engineering: from basic science to clinical application, *Exp. Gerontol.* 117 (2019) 1–12.



Contents lists available at ScienceDirect

Chemical Engineering Journal

journal homepage: www.elsevier.com/locate/cej

The robustness waterproof ionogel based on the phase separation to form soft hard heterostructures and the interaction of cation- π realizes underwater adhesion and sensing

Ning Yu^a, Peiqi Liu^a, Yaling Lin^{b,*}, Anqiang Zhang^{a,*}

^a School of Materials Science and Engineering, South China University of Technology, 381 Wushan Rd., Guangzhou 510641, Guangdong, China

^b College of Materials and Energy, South China Agricultural University, 483 Wushan Rd., Guangzhou 510642, Guangdong, China

ABSTRACT

Flexible ionic conductors hold significant promise for advancing the field of soft ion electronics in the future. However, the creation of flexible conductors that possess mechanical robustness, underwater adhesion and underwater motion monitoring remains a challenge. Drawing inspiration from the multiphase heterostructure found in biological connective tissues, such as high modulus fibers and low modulus water-rich matrices, this article proposes a one-pot polymerization in-situ design strategy to create a hydrophobic ionogel with a hetero structure of soft and hard domains. The mechanical robustness, elasticity, and toughness of the ionogel are achieved through a synergistic combination of a strong skeleton in the hard domain and an elastic matrix in the soft domain. Additionally, hydrophobic aromatic rings and quaternary ammonium cation simulated cation- π interactions in mussel foot silk protein. Upon contact with water, the hydrophobic clusters quickly aggregate, facilitating the expulsion of interfacial water and exposing salicylic acid groups and quaternary ammonium cationic groups, leading to outstanding underwater adhesion between the ionogel and various substrates. The resulting hydrophobic ionogel can be utilized in underwater wearable electronic devices for monitoring human movement and physiological information, underwater repair monitoring, and intelligent soft robotics, demonstrating its vast potential in the field of underwater sensors.

1. Introduction

Flexible ionic conductors are commonly utilized in wearable and implantable devices, solid-state batteries, flexible light-emitting devices, and human-computer interfaces due to their adjustable mechanical properties, extensibility, self-healing capabilities, and high conductivity [1–8]. Obviously, as an ideal interface that can be seamlessly compatible with human skin, the adhesive bonding between flexible electrodes and target substrates is crucial for recording high fidelity and stable interface sensing signals. Specifically, in various applications, soft electronic devices need to adhere to wet or submerged surfaces, such as implantable medical devices, wound dressings, underwater sensing devices, and underwater repair engineering. [9–11] Due to the presence of hydrophilic components, ionogel materials have a tendency to expand in moist or water-rich environments. This expansion results in the dilution of the polymer chain within the network, thereby reducing the bonding sites at the interface between the ionogel substrate and the ionogel, ultimately leading to ionogel debonding. At the same time, expansion can negatively impact the mechanical properties, electrical conductivity, and self-healing properties of ionogel. Additionally, the hydration film on the surface of the ionogel further hinders close contact between flexible

devices and substrates, weakening interface bonding and potentially leading to decreased sensitivity or failure [12]. Therefore, it is a great challenge to realize the stable adhesion of flexible ionic conductors materials in the water environment [13].

In fact, people have invested a lot of effort in devising effective strategies to address these challenges. One such approach involves creating hydrophobic anti-expansion ionogels through the incorporation of hydrophobic monomers like phenyl acrylate, *tert*-butyl acrylate, or fluorinated compounds. [14–19] The hydrophobic component can destroy the hydration film by repelling the interface water, and at the same time effectively resist water erosion. [20] For instance, Xu et al. prepare hydrophobic ionogel through the ion- dipole and ion- ion interaction between the fluoride rich polyionic liquid and the ionic liquid, as well as covalent cross-linking. The ionogel exhibits strong underwater adhesion, with an adhesion strength of 693 kPa to plastic. However, its mechanical properties, including a breaking strength range of 0.24–0.52 MPa and breaking strain range of 210 %–360 %, are considered suboptimal [21]. Zou et al. prepared solvent-free transparent poly (ionic liquid) elastomers (PILE) using acrylic monomers and acrylic ionic liquids. The combined hydrophobic and electrostatic interactions can effectively reduce the hydration of water molecules, although the

* Corresponding authors.

E-mail addresses: linyinling@scau.edu.cn (Y. Lin), aqzhang@scut.edu.cn (A. Zhang).

<https://doi.org/10.1016/j.cej.2024.155046>

Received 14 June 2024; Received in revised form 2 August 2024; Accepted 20 August 2024

Available online 22 August 2024

1385-8947/© 2024 Elsevier B.V. All rights are reserved, including those for text and data mining, AI training, and similar technologies.

mechanical strength remains relatively low with a breaking strength of 715 kPa and breaking strain of 1140 % [22]. Poor mechanical stability can decrease the longevity of materials and harm cohesion, thereby restricting their capacity for maintaining robust adhesion. Currently, the majority of ionogels exhibit low fracture strength (~ 1 MPa), toughness (~ 5 MJ/m³), and modulus (~ 0.1 MPa), which is insufficient. Hence, the advancement of multifunctional soft electronic materials with superior mechanical strength, strong underwater adhesion, and exceptional sensing capabilities remains a significant challenge, particularly within the realm of hydrophobic self-adhesive ionogel materials.

Most living organisms contain various soft tissues, such as skin, tendons, and ligaments, exhibiting excellent mechanical strength, toughness, and elasticity, capable of withstanding stress loads of tens to hundreds of megapascals (For example, the tensile strength of human skin ranged from 1 to 32 MPa). [23–25] These natural tissues contain heterogeneous structures such as hard collagen fiber scaffolds and soft, water rich matrices. (Fig. 1a). Taking inspiration from the phase separation heterostructure formed by the interweaving of high and low moduli in biological soft tissues, [26] we aimed to manipulate the conformation of ionogel molecular chains by leveraging differences in solubility (binding force) among monomers to create a hetero ionogel with distinct soft and hard domain structures [27–29]. A hydrophobic quaternary ammonium salicylate ionic liquid monomer (QSA) was initially designed and synthesized, demonstrating strong compatibility with hydrophobic choline chloride ionic liquid [Ch] [TFSI]. In contrast, benzyl acrylate (BZA) exhibited poor compatibility with [Ch] [TFSI]. Under different binding forces of [Ch] [TFSI], a highly solvated network forms a soft domain rich in solvent, which imparts softness and stretchability to the ionogel. Conversely, weak solvation networks form hard domains, causing polymer chains to become more tightly bound, leading to increased high cohesion and mechanical strength. What's even more exciting is that the short-range cation- π interactions between the cations and aromatic rings on QSA and the aromatic rings in BZA mimic the cation residues (e.g., lysine, arginine, and histidine) and hydrophobic aromatic amino acids (e.g., tyrosine, phenylalanine, and tryptophan) in mussel silk protein [30,31]. Cation- π interactions, which are formed between positively charged cations and the negatively charged electron clouds of π systems, have been shown to play a crucial role in the strong adhesion of marine mussels [32–34]. Upon contact with water, hydrophobic group chain segments come together to create interfacial phase separation, disrupting the surface hydration layer of the ionogel. Simultaneously, salicylic acid groups are revealed, enabling robust underwater adhesion and healing. [35] In addition, ionic liquids provide ionogels with inherent conductivity, making them suitable for use in soft ionogel electronics. The ionogels can be utilized to sensitively monitor human movement and physiological activities, as well as demonstrate promising application prospects in underwater operations and communication engineering. The soft ionogel conductor developed in this research, featuring adjustable mechanical strength and underwater adhesion, is expected to open up new avenues for advancements in human health monitoring and the design and manufacturing of underwater wearable electronic devices.

2. Results and Discussion

2.1. Preparation of QMBF ionogel and characterizations

In this work, an innovative design and material composition are proposed to incorporate exceptional mechanical, underwater adhesive, underwater self-healing, and transparent performance into a QMBF ionogel. This design is primarily built upon soft hard heterostructure and the interaction of cation- π . As shown in Fig. 1c and d, the four hydrophobic precursors monomers were polymerized by UV light without a chemical cross-linker and the formation of polymerization induced in situ soft hard heterostructure random copolymer ionogel was formed. Among them, QSA is designed and synthesized by a mild alkylation

reaction of 2-(dimethylamino) ethyl methacrylate with 5-bromosalicylic acid (Fig. 1d). The chemical structure of QSA is determined by ¹H NMR (Figure S3).

In this soft-hard heterostructure, a polymer rich phase is formed after polymerization due to the poor compatibility between PBZA and [Ch] [TFSI], while PQSA and [Ch] [TFSI] form a highly solvated network known as the solvent rich phase. Phase separation can make polymer chains tighter and promote supramolecular network interactions (H-bond, cations- π , ion-dipoles, etc.) are used to enhance the mechanical strength. In addition, hydrophobic aromatic groups can disrupt the hydration layer on the surface, form interfacial hydrophobic bonds, and achieve underwater adhesion. Our work provides a new strategy for preparing multifunctional ionogel with high strength, high toughness and underwater adhesion.

Fourier transform infrared (FTIR) spectrum was used to confirm the polymerization of vinyl groups in [Ch] [TFSI] (Figure S4). The typical peak at 1600 cm⁻¹ of the vinyl groups was not observed in any of the four types of ionogels, indicating complete polymerization of the monomer within the ionogel system. [36] Fig. 2a displays the optical image of ionogels with varying QSA and BZA weight ratios. The QMBF-2/0 ionogel, due to the favorable compatibility of QSA in [Ch] [TFSI], resulted in the formation of a homogeneous copolymer network, leading to high transparency of 88.5 % at 500 nm. In contrast, the QMBF-0/2 ionogel exhibited complete opacity attributed to the limited solubility of BZA in [Ch] [TFSI]. As expected, the transparency of the copolymer ionogels can be regulated by changing the weight ratios of QSA and BZA (Fig. 2a and b). The X-ray diffraction (XRD) spectra in Fig. 2c show no crystalline peaks, indicating that the inhomogeneous structure of the copolymer ionogels is due to phase behavior rather than crystal formation. The increase in diffraction peak intensity of the QMBF-0/2 sample may be attributed to phase separation narrowing the distance between polymer chains, leading to a higher density of non-covalent bonds.

Scanning electron microscopy (SEM) was used to reveal the evolution in the microscopic morphology of the ionogel as a function of composition. For the QMBF-1.5/0.5 ionogel, we observed a homogeneously disperse network with uniform and smooth morphologies (Fig. 2d). Upon the addition of BZA (1:1), the copolymer ionogel exhibited a heterogeneous structure with fine wrinkles appearing on the surface (Fig. 2e). Transmission electron microscopy (TEM) and atomic force microscopy (AFM) were utilized to analyze the soft-hard heterostructure formed within the QMBF ionogel. The AFM image of QMBF-1.5/0.5 ionogel revealed distinct soft (dark areas) and hard (bright areas) phases, with the hard phase exhibiting a relatively small size of a few hundred nanometers, corresponding to its reduced transparency (Figure S5a). The TEM image in Figure S5b reveals dark spherical spots within the matrix of QMBF-1.5/0.5 ionogel, indicating the separation of soft and hard domains. As the BZA content increases further, the AFM image of QMBF-1/1 ionogel exhibits a prominent light-dark contrast (Fig. 2f). The bright hard phase aggregates and grows, while the black spherical spots distributed in the transmission electron microscopy image aggregate to form larger sized nanoclusters (Fig. 2g). As the weight ratio of QSA and BZA increased to 0.5:1.5, the layered structure bi-continuous network that consisted of the polymer-rich and solvent-rich phases became clearly distinguishable (Fig. 2h). Further increasing the content of BZA (0:2) resulted in a sponge like pore structure due to the more complete soft hard heterostructure separation (Fig. 2i). Energy-dispersive spectrometer (EDS) elemental mapping analysis (Fig. 2j) confirms that the C, N, O, F, and S elements of the QMBF-0/2 are distributed in the ionogel, forming clear nanochannels. As a comparison, QMBF-1/1 has a uniform distribution of surface elements (Figure S6).

2.2. Mechanical properties and self-healing underwater of QMBF ionogel

The mechanical properties of ionogel play a crucial role in their

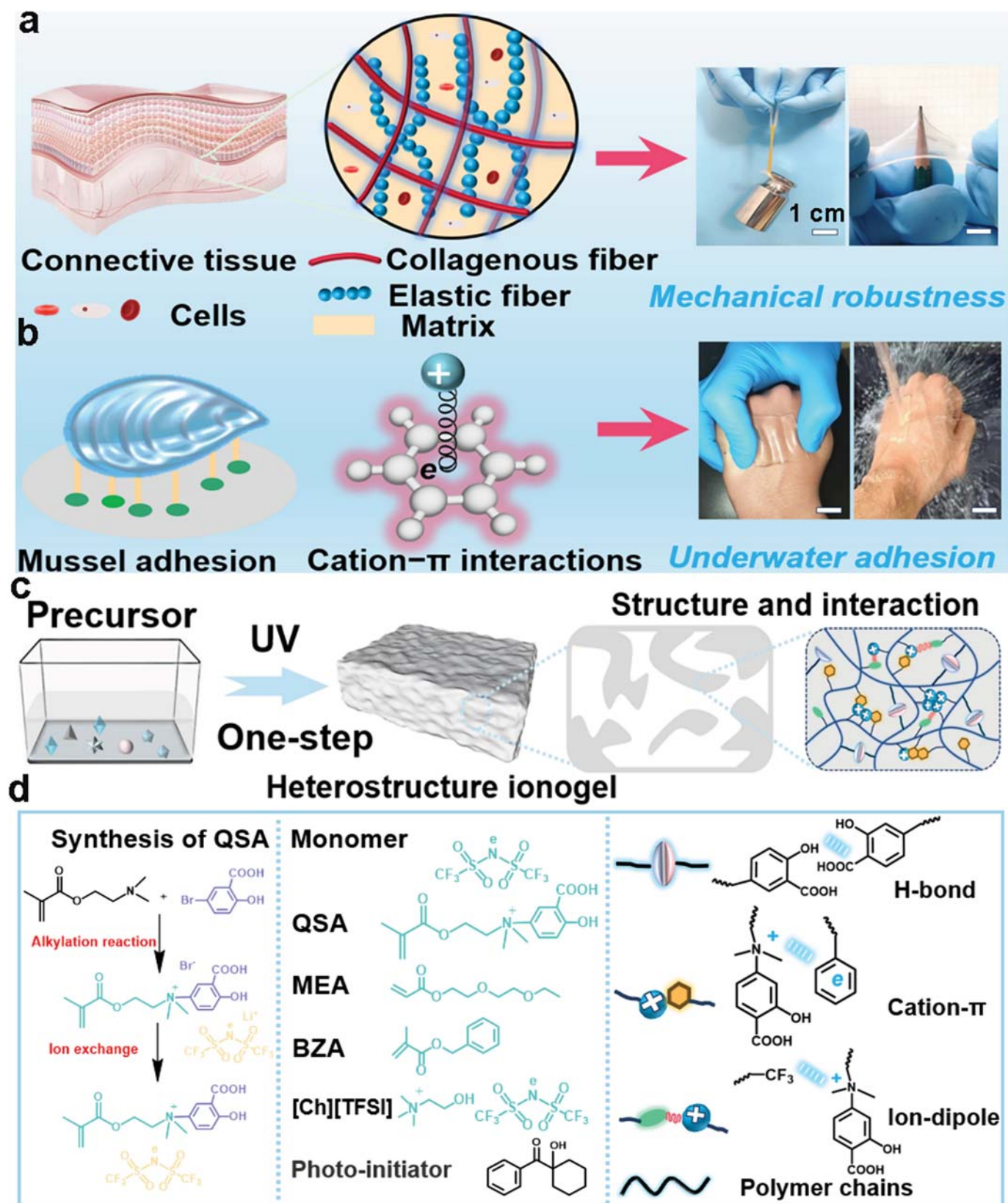


Fig. 1. Design and synthesis scheme of QMBF iongel. (a) Inspired by the phase separation inside the connective tissue, the designed mechanical robust iongel can lift the weight of 500 g. (b) Inspired by the cation- π in mussel mucin, the iongel designed has strong adhesion ability under water. (c) The synthesis route of QMBF iongel and (d) the schematic diagram of its internal structure.

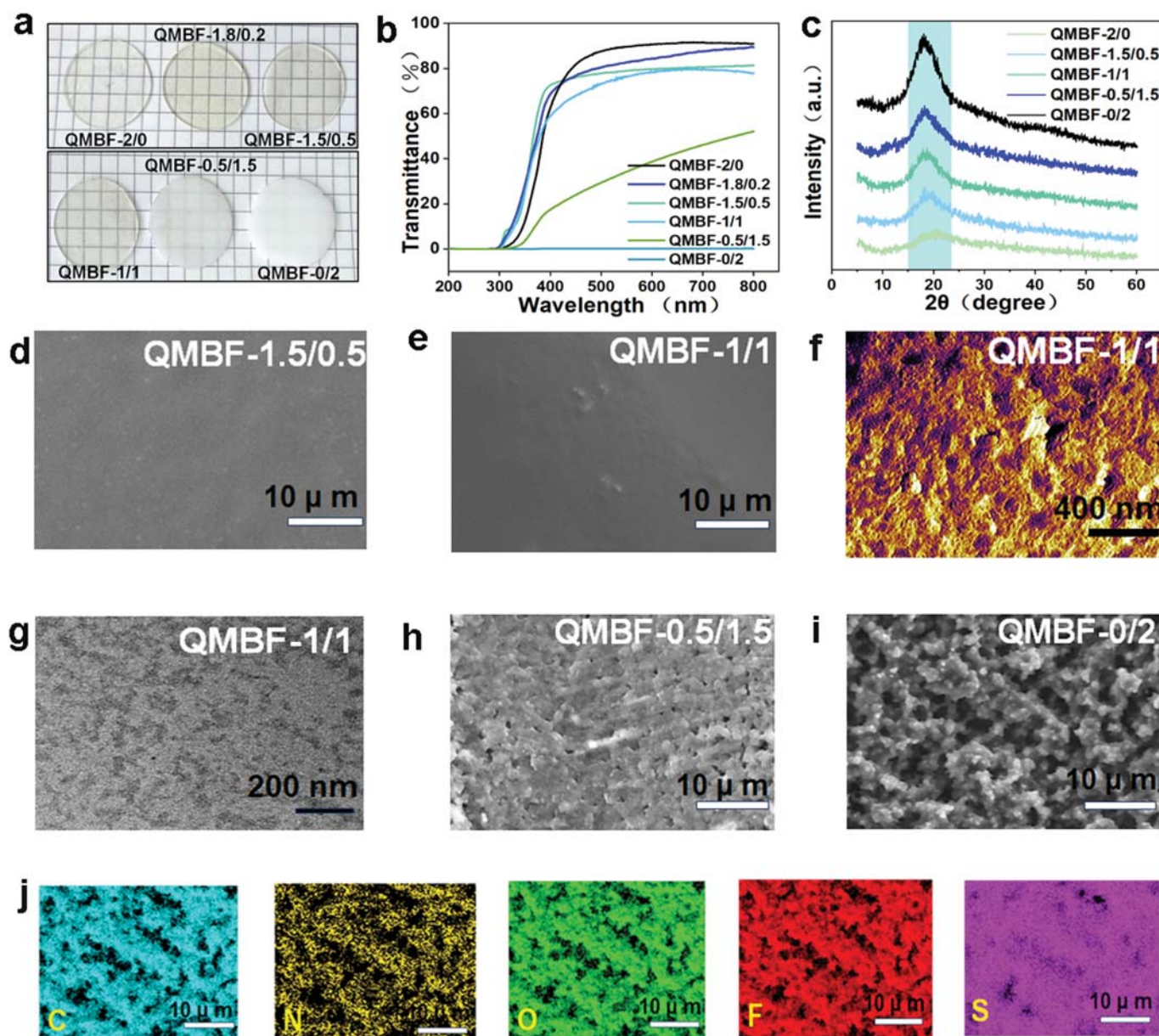


Fig. 2. Structure and morphology analysis of the ionogels. (a) Digital photos of QMBF ionogel. Each small square has a side length of 5 mm. (b) The transmission spectrum shows the change of transparency of QMBF ionogel with different compositions. (c) XRD spectrum of QMBF ionogel. (d) SEM image of QMBF-1.5/0.5. (e) SEM, (f) AFM, and (g) TEM images of QMBF-1/1. (h) SEM image of QMBF-0.5/1.5 and (i) QMBF-0/2. (j) EDS image of QMBF-0/2 surface.

application as adhesive materials and flexible electronics. By modifying the ratio of the monomers QSA and BZA, the mechanical properties of QMBF ionogel can be adjusted effectively. The copolymer ionogel showed an increase in fracture strength from 0.43 to 3.66 MPa when the weight ratio of BZA and QSA changed from 0:2 to 1.8:0.2, with a corresponding decrease in strain at failure from approximately 1460 % to 290 % (Fig. 3a and Figure S7). At a weight ratio of 1:1, the fracture strength, elongation and toughness of the copolymer QMBF-1/1 ionogel can reach 1.4 MPa, 1030%, and 6.8 MJ/m³, respectively. The impressive mechanical performance of this material is due to its unique soft-hard heterostructure. When stretched, the polymer-rich phase can efficiently dissipate energy by breaking hydrogen bonds, cation – π , ion-dipole interactions, etc. Meanwhile, the solvent-rich phase is responsible for distributing the loadings and maintaining the structural integrity of the ionogel. Further comparison was conducted on the effect of MEA content on the mechanical strength of the system (Figure S8). In the absence of MEA, higher ionic liquid content leads to solvation of

polymer segments, reducing mechanical strength. On the contrary, excessive MEA will enhance the compatibility between components, reduce the degree of phase separation, and thus have adverse effects on its mechanical properties. To showcase the distinct mechanical characteristics, a 500 g weight was lifted using three different ionogels in a rectangular shape. The QMBF-0/2 ionogel fractured brittly without successfully lifting the weight. The QMBF-2/0 ionogel exhibited significant stretching but ultimately failed before lifting the weight. Conversely, the copolymer ionogel successfully lifted the weight without any failure (Fig. 3b). In addition to its impressive tensile strength, ionogel also exhibits excellent mechanical flexibility (Fig. 3c). Fig. 3d illustrates the ionogel being wrapped around the surface of a balloon, which, when inflated, expanded to over 20 times its original volume. The expansion of the ionogel alongside the balloon was clearly visible under ultraviolet light, indicating its remarkable mechanical properties. To gain a deeper insight into the mechanical properties, cyclic tensile measurements with different cycle strains and times were conducted.

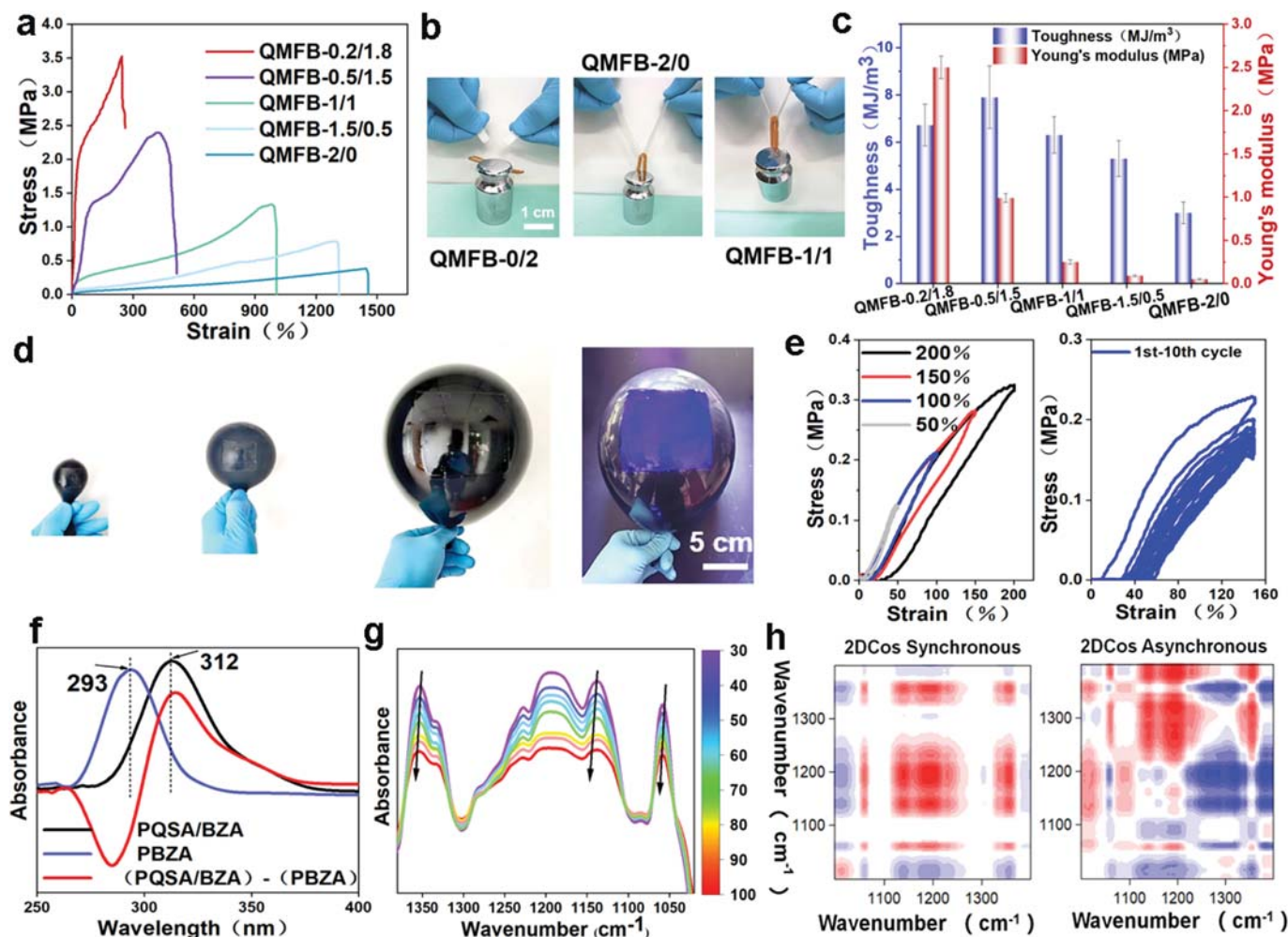


Fig. 3. (a) Tensile stress-strain curves of QMBF ionogel; (b) QMBF-1/1 can lift 500 g of weight, but both QMBF-0/2 and QMBF-2/0 failed to lift; (c) Young's modulus and toughness of QMBF ionogel; (d) The QMBF ionogel attached to the balloon can expand with the expansion of the balloon; (e) Loading-unloading tensile cycle curves of QMBF-1/1 ionogel under different strains at a deformation rate of 100 mm min⁻¹, and stress-strain curve of QMBF-1/1 ionogel continuously cycling for 10 cycles at 150 % strain; (f) Ultraviolet (UV)-vis spectra of PQSA/BZA and PBZA from 250 to 400 nm and the difference spectrum of PQSA/BZA minus PBZA; (g) Temperature-variable IR spectra of QMBF-1/1 ionogel upon heating from 30 to 100 °C (interval: 10 °C); (h) Two-dimensional correlation spectroscopy (2 DCOS) synchronous; (h) and asynchronous spectra of QMBF-1/1.

The cycle stress-strain curves of QMBF-1/1 with gradually increasing strain are shown in Fig. 3e. Initially, at a strain of 50 %, the sample experienced only elastic deformation due to the intact dynamic cross-linked network, enabling the ionogel to revert back to the original state driven by entropy. However, when the strain exceeded 100 %, the hysteresis areas of the curve notably expanded. This can be attributed to the disruption of dynamic interactions like hydrogen bonding, ionic bonding, cation- π and ion-dipole interactions under extensive deformation, with insufficient time for the reformation of these bonds. Notably, the hysteresis area was directly proportional to the strain, indicating increased energy dissipation at higher strains, effectively protecting QMBF-1/1 from damage (Figure S9a). Subsequently, via ten cyclic tensile tests were conducted under a relatively small strain of 150 %. As shown in Fig. 3e and Figure S9b, a large hysteresis area was observed during the first cyclic stretching, manifesting that the energy was significantly dissipated, which is mainly due to the partial cleavage of the noncovalent bonds during stretching. Subsequent observations reveal smaller hysteresis loops that decrease in size with each cycle.

The supramolecular interaction in the ionogel network was further explored. Cation- π interaction involves the electrostatic attraction between cations and π electron clouds in electron-rich aromatic systems. In Fig. 3f, the absorption peak of PBZA's aromatic ring is observed at 292

nm, while the aromatic ring UV absorption peak of PBZA/QSA is at 312 nm. This shift is primarily attributed to the cation- π interaction between the cation on QSA and the benzene ring, causing a blue shift in the UV absorption peak. Additionally, there are distinct positive and negative intensity changes in the UV difference spectra of the two at 312/290 nm, consistent with previous literature reports [37], suggesting the presence of cation- π dynamic non-covalent bonds in QMBF-1/1.

To investigate the ion-dipole interactions between the cation and C-F polar group and ion-ion interactions of the ionic conductors, variable-temperature FTIR spectra was performed (Fig. 3g). The asymmetric stretching bands of S=O and N-S of TFSI anions, initially located at 1351 and 1054 cm⁻¹, respectively, exhibited blue shifts to 1355 and 1058 cm⁻¹, respectively. This shift can be attributed to the increase in temperature, which leads to the dissociation of ionic bonds and consequently weakens the coulombic force between TFSI anions and cations. In addition, FT-IR spectroscopy analysis revealed that the peak corresponding to the C-F polar group in QMBF-1/1 shifted from 1137 cm⁻¹ at 30 °C to 1143 cm⁻¹ at 100 °C as the testing temperature increased. This shift suggests the dissociation of the C-F group from the quaternary ammonium cation of QSA, indicating an ion-dipole interaction. [38] 2DCOS was further employed to study the changes of v(C-N) of QMBF ionogel and v(C-F) bands during temperature increased (Fig. 3h). Both

synchronous and asynchronous spectra at ($1331, 1143\text{ cm}^{-1}$) and ($1331, 1137\text{ cm}^{-1}$) exhibited negative values. Following Noda's rule, the sequential changes in groups with temperature increment were identified as $1137\text{ cm}^{-1} \rightarrow 1142\text{ cm}^{-1}$, $1331\text{ cm}^{-1} \rightarrow \text{free } \nu(\text{C-F}\cdots\text{N}^+) \rightarrow \text{free } \nu(\text{C-N})$ and free $\nu(\text{C-F})$. This progression confirms the strong ion-dipole interaction between the C-F group of QMBF ionogel and the cation quaternary ammonium [39,40].

The QMBF ionogel exhibited exceptional self-healing properties due to the presence of abundant non-covalent interactions and a low glass transition temperature (Figure S10). The mechanical properties after healing under ambient and aquatic environments are illustrated in Fig. 4a–c. Following a 24 h repair period in air and water, the self-healing rates were 92 % and 83 %, respectively, with no significant difference observed. The impressive self-healing ability of ionogels in water can be attributed to the water-repelling surfaces facilitated by the TFSI units and hydrophobic aromatic group, eliminating the interfacial water layer and preserving the internal cation- π , ion-dipole, and ion-ion interactions, which collectively contribute to the ionogel's remarkable ability to self-heal in water (Figure S11). [41–43] The underwater self-healing process of QMBF-1/1 was illustrated in Fig. 4d. Upon gentle

contact between two separate specimens (dyed and neat ionogel) in fresh water, autonomous healing occurred without any external stress and the healed ionogel showed resilience against stretching without disintegration. Optical microscope images illustrate the healing process of crevices created by a blade, which completed within 2 h (Figure S12). Further testing the stability of ionogel after 5 cycles of cutting/healing in air and water respectively. After 5 cycles, the healing efficiency in air and water was 76.2 and 60.9%, respectively (Figure S13). Besides, QMBF-1/1 ionogel samples were immersed in water to assess their stability in a real water environment. The swelling ratio of the fully hydrophobic ionogel increased by 2.8 % on the first day, but remained stable over the following 6 d, as illustrated in Fig. 4e and f and Figure S14. Initially, the distribution of hydrophobic functional groups at the interface of the fresh ionogel was sparse, leading to ineffective prevention of water molecular diffusion. However, due to the inherent incompatibility between hydrophobic functional groups and water, the hydrophobic chain segment began to reorganize. This self-assembly process resulted in the formation of hydrophobic aggregates through hydrophobic interactions, akin to the self-assembly behavior observed in amphiphilic block copolymers in water, resulting in a lower surface free

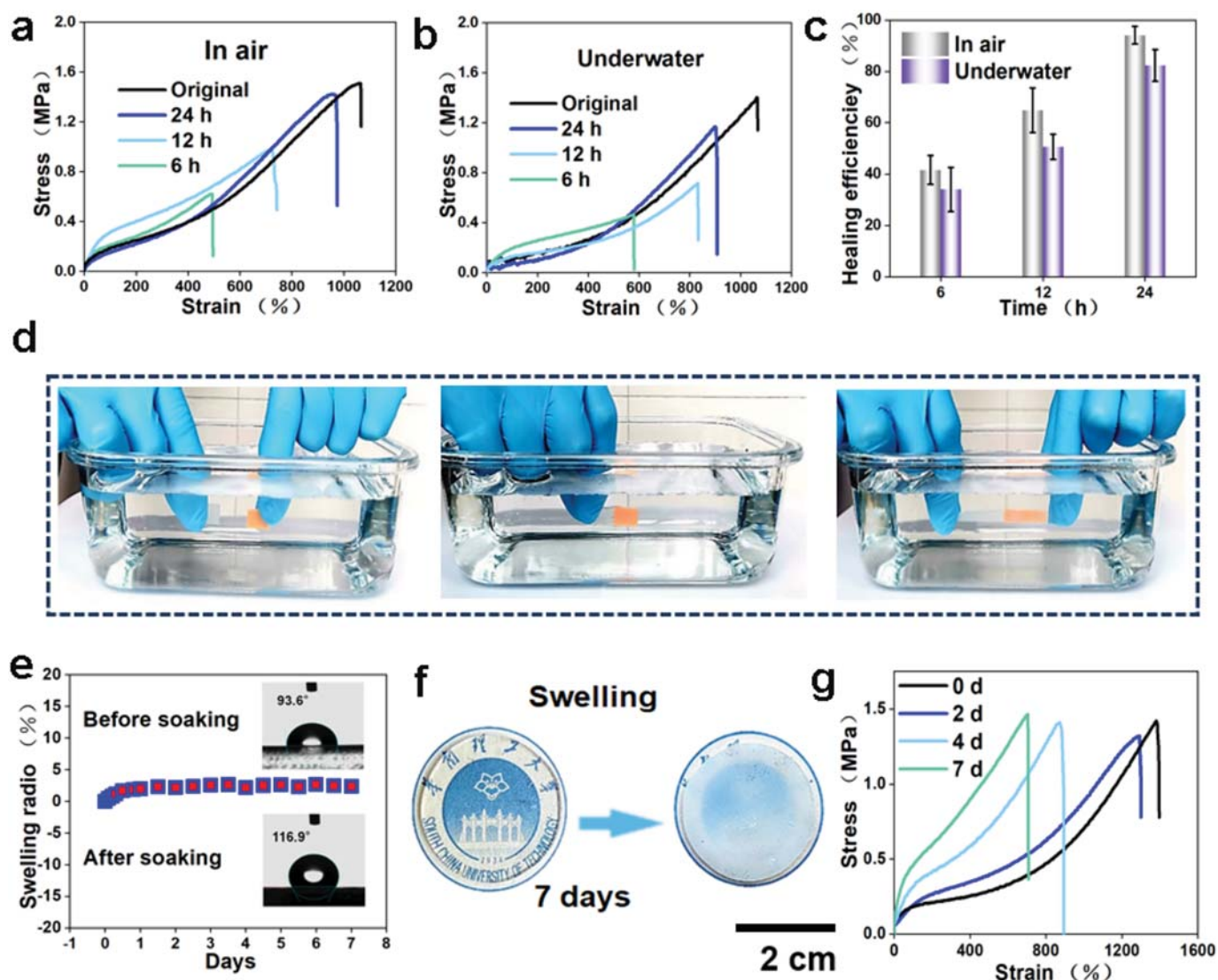


Fig. 4. Self-healing of the QMBF-1/1. Typical stress-strain curves of pristine and healed samples in (a) air and (b) underwater. (c) The self-healing efficiencies calculated by the tensile strength of original and healed samples. (d) Images showing underwater QMBF-1/1 healing. (e) Weight change rate of QMBF-1/1 immersed in water with time. (f) Optical photos showed that the volume of QMBF-1/1 did not change significantly after immersion for 7 d. (g) The tensile curve of QMBF-1/1 immersed in water for different time.

energy. [44,45] The mechanism was confirmed by observing the change in water contact angle (WCA) of the ionogel. Fig. 4e shows an increase in WCA from 93.8 to 116.3° after immersion in water.

In addition, the mechanical properties and surface topography of the soaked ionogel were evaluated, showing an increase in Young's modulus of the ionogel after 7 d of soaking (Fig. 4g and Figure S15). This increase

was attributed to the aggregation of hydrophobic chain segments during soaking, leading to phase separation within the ionogel and resulting in its hardening (Figure S16). The thermal stability of QMBF-1/1 was evaluated through thermogravimetric analysis (TGA) in nitrogen, showing an ultrahigh decomposition temperature of about 225 °C (Figure S17).

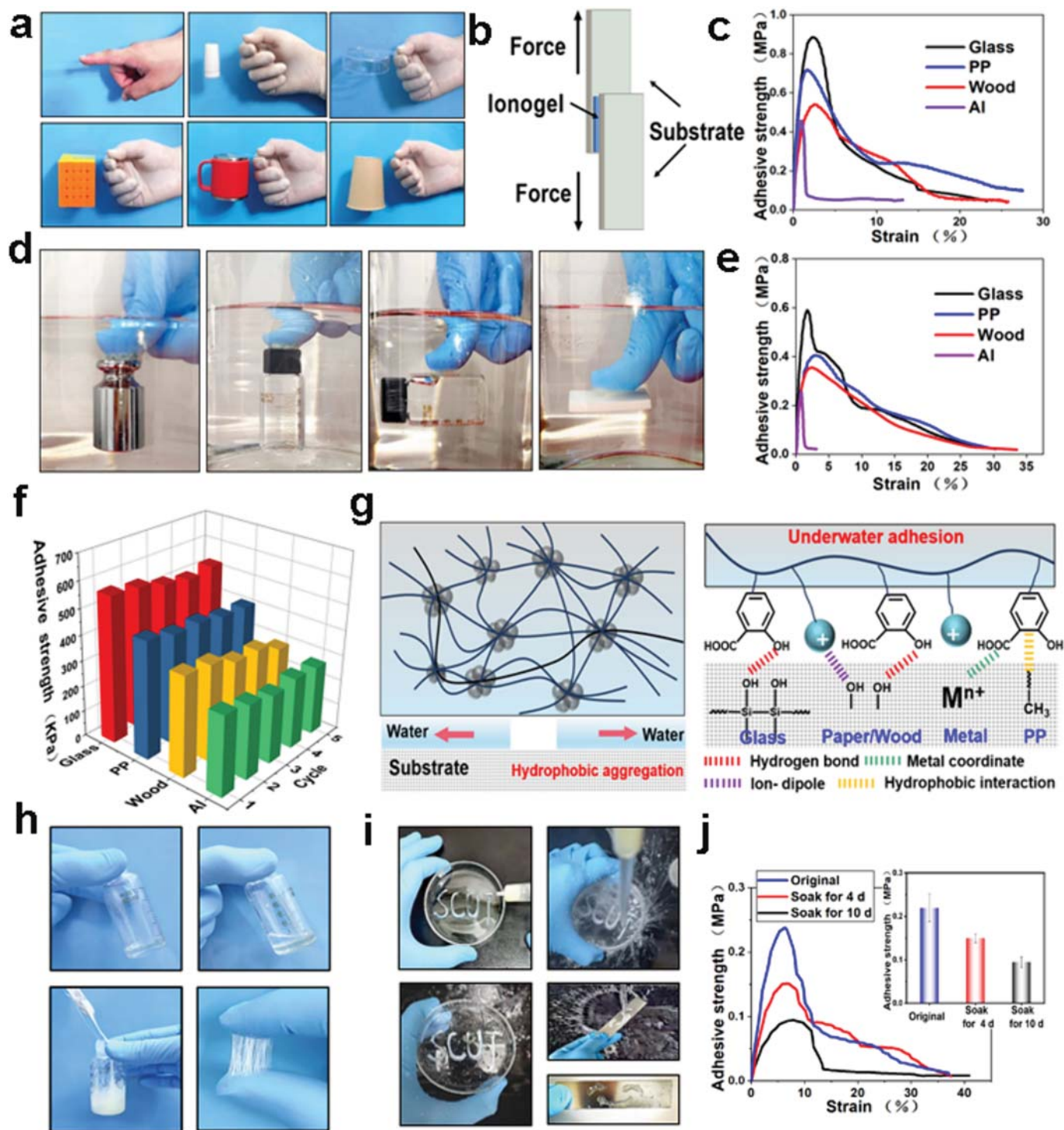


Fig. 5. The self-adhesive properties of QMBF ionogel. (a) Optical photographs of QMBF adhering in air. (b) Schematic diagram of the lap shear test. (c) The lap shear strength of ionogel with different materials at room temperature. (d) Optical photographs of QMBF adhering under water. (e) The lap shear strength of ionogel with different materials under water. (f) Repeated adhesive test of QMBF-1/1 for different substrates underwater. (g) Water triggered aggregation of hydrophobic segments of ionogel leads to interfacial drainage and underwater adhesion mechanism. (h) The self-aggregation behavior of QMBF in water. QMBF viscous fluid was used as an ink and pushed out of a syringe to paint the letters of (i) "SCUT" or a smiling face, the letters SCUT or smiling face were washed fiercely with water, still intact and firmly adhered to the glass or Al plate. (j) Adhesion properties of ionogel on Al plate immersed in water for different time.

2.3. Adhesion properties

Due to the excellent internal mechanical properties brought by abundant supramolecular interactions, the adhesion strength of QMBF ionogel are determined [46,47]. The QMBF ionogel (2.0 cm \times 1.0 cm) demonstrated effective adhesion to a variety of materials including glass, skin, Polytetrafluoroethylene (PTFE), plastic, kraft-paper, and alloy, as depicted in Fig. 5a and Figure S18. To assess the optimal adhesion of the ionogel to different materials, lap shear tests were conducted by placing the QMBF ionogel (2.0 cm \times 1.0 cm) between various materials (Fig. 5b). As shown in Fig. 5c, the optimal adhesion of glass, Al sheet, polypropylene (PP) and wood are 902 kPa, 725 kPa, 568 kPa and 469 kPa, respectively. It is worth noting that the presence of water can create a boundary layer on the substrate surface, potentially hindering the contact between the adhesive and the substrate, leading to a decrease in surface energy and adhesion strength. [48] Therefore, achieving fast, strong, and stable underwater adhesion remains a major challenge. In our ionogel, the presence of hydrophobic aromatic groups and the hydrophobic anion TFSI⁻ can disrupt the hydration-layer barriers of the substrate, enabling underwater adhesion. As shown in Fig. 5d, our ionogel could adhere fast and tightly to various substrate surfaces in the aquatic environment, such as glass, plastic, metal weights, and PTFE. The underwater adhesive strength remained almost unchanged after 5 cycles of adhesion test (Fig. 5e and f). In addition, ionogel has been shown to effectively repair leaky sealing bags (Figure S19). The ionogel adhered to human skin has strong adhesion even after being impacted by strong water flow (Figure S20), which indicates that QMBF-1/1 possesses an excellent underwater adhesion capacity. We can imagine that upon contact with water, the ionogel's hydrophobic chain quickly aggregates to form coacervates, effectively repelling water molecules on the substrate surface. At this point, more salicylic acid group groups are exposed outward, can form physical interactions (such as hydrogen bonding, cation- π , electrostatic interaction and ion-dipole) with functional groups on the substrate surface to induce tight interfacial adhesion on the substrates to achieve rapidly strong adhesion underwater (Fig. 5g). QMBF-0.2/0.2 was prepared to more clearly show the chain segment aggregation phenomenon of ionogel caused by water. We can see that the QMBF-0.2/0.2 is transparent colorless transparent gel at room temperature (Fig. 5h). Upon mixing with water, it transforms into a white sticky putty when stirred at room temperature. When applied to fingers, this putty can easily extract long, thin fibers. Next, a rheometer was utilized to investigate the shear-thinning process of the ionogel. The viscosity decreased obviously with increasing shear rate, which approved the typical injectable characteristics (Figure S21). To assess its adhesion in water, the QMBF-0.2/0.2 viscous fluid was utilized as ink and dispensed from a syringe to spell out the letters 'SCUT'. The viscous fluid solidified within 10 min and adhered firmly to a glass culture plate, withstanding intense water washing without peeling off, thus preserving the integrity of the 'SCUT' letters (Fig. 5i). Furthermore, drawing a smiling face with the viscous fluid on a metal aluminum sheet also demonstrated exceptional underwater adhesion (Fig. 5i). To evaluate the stability of underwater adhesion, we examined the effect of soaking time on the adhesion strength (Fig. 5j). Even after 10 d of immersion, the ionogel still has a high adhesion strength (about 0.1 MPa), indicating a good underwater adhesion. The adhesion strength of ionogels can be adjusted by temperature due to their temperature sensitivity (Figure S22). The adhesion strength on the Al substrate was up to 356 kPa at 0 °C. As the temperature increased, the adhesion strength decreased to 37 kPa at 65 °C, so that adhesion and debonding can be carried out by heating.

2.4. Optical tunable behavior and information encryption and decryption

Based on the optically tunable behavior (transparent opaque transition) caused by solvent induced phase separation, QMBF ionogel can be used as a promising material for information encryption and

decryption. In our study, we presented a simple device for encrypting and decrypting Quick Response (QR) code information (Fig. 6a). Placing the QR code under the transparent QMBF-1/1 ionogel allows for clear and readable information. Upon contact with water solvent on the ionogel's surface, the encoded information self-encrypts within 1 min, with the two-dimensional code becoming completely hidden after 600 s. After drying at 40 °C for 1 h, as the moisture evaporates, the hidden QR code information reappears, achieving self-decryption. The decrypted QR code information can then be scanned and recognized by a mobile phone. The immersion of the ionogel in water causes the hydrophobic components within the ionogel to aggregate, resulting in the blocking and weakening of light entry, thereby reducing the transparency of the ionogel. The transparent QMBF-1/1 ionogel subjected to the water-stimulating process could also be applied for information encryption and self-decryption by changing the inducing solvent from water to ethanol (Figure S23). The stability and repeatability of the QMBF-1/1 ionogel were assessed by monitoring the transmissivity of the ionogel over 10 immersion-drying cycles. (Fig. 6b).

Inspired by traditional writing tools like paper and pens, devices for writing and reading information can be developed. In order to better control the pattern shape and corresponding recording information, PTFE film with a flower petal hollow pattern covers the surface of QMBF-1/1 ionogel base paper. Water is then used as ink to brush and apply onto the hollow mold surface. As the brushing process progresses, solvent stimulation leads to phase separation, causing the QMBF-1/1 ionogel state in the hollow mold area to transition from transparent to opaque. Once the mold is removed, the information recorded in the mold pattern becomes visible on the QMBF-1/1 ionogel paper. Subsequently, the ionogel writing paper is immersed in a DMSO solution to erase the drawn petal pattern, as depicted in Fig. 6c. Since the separated hydrophobic segment was dissolved in DMSO again, the "petal" pattern was erased by DMSO and gradually disappeared within 5 min. This demonstrates that QMBF-1/1 ionogel can serve as a writing paper for recording and transmitting information using water and DMSO, similar to a pen and eraser.

According to the time dimension of transparent opaque transition, the written images on the ionogel could experience a three-step encrypting process (encrypted, decrypted, and erased naturally within a few minutes through the change in transparency). Initially, the 'Five Stars' pattern is written on the ionogel using water writing within 1 min. Subsequently, the ionogel with the pattern is immersed in water to encrypt the information, a process that naturally erases the pattern within 5 min, as illustrated in Fig. 6d. The ionogel film becomes completely opaque, realizing information encryption. Immerse ionogel into DMSO to realize decoding process, due to the different time dimensions, the encrypted pattern can first emerge and then gradually fade with the DMSO penetrating the ionogel. It is important to note that as the DMSO molecule permeates the ionogel, the once white ionogel transitions to a transparent state. This indicates that the ionogel possesses remarkable capabilities for both reading and writing information, as well as optically tunable features for encryption and decryption.

2.5. Multifunctional sensing properties of QMBF ionogel

Due to its superior mechanical properties and remarkable self-adhesive nature, the QMBF ionogel exhibits great potential for use in wearable sensors. The existence of ionic liquid endows QMBF-1/1 ionogel with good conductivity. The electrochemical impedance spectroscopy (EIS) spectra and corresponding conductivity of the QMBF-1/1 ionogel, soaked in water for varying durations (Figure S24), reveal that the initial conductivity of the unsoaked QMBF-1/1 ionogel was 6.9 mS/m. With increased soaking time, conductivity initially increased gradually before stabilizing. The results show that the QMBF ionogel can maintain a stable conductivity in the water environment. The sensitivity of QMBF-1/1 ionogel strain sensor was assessed by calculating the GF. The slope of the linear fitting curve in Fig. 7a indicates that the GFs are

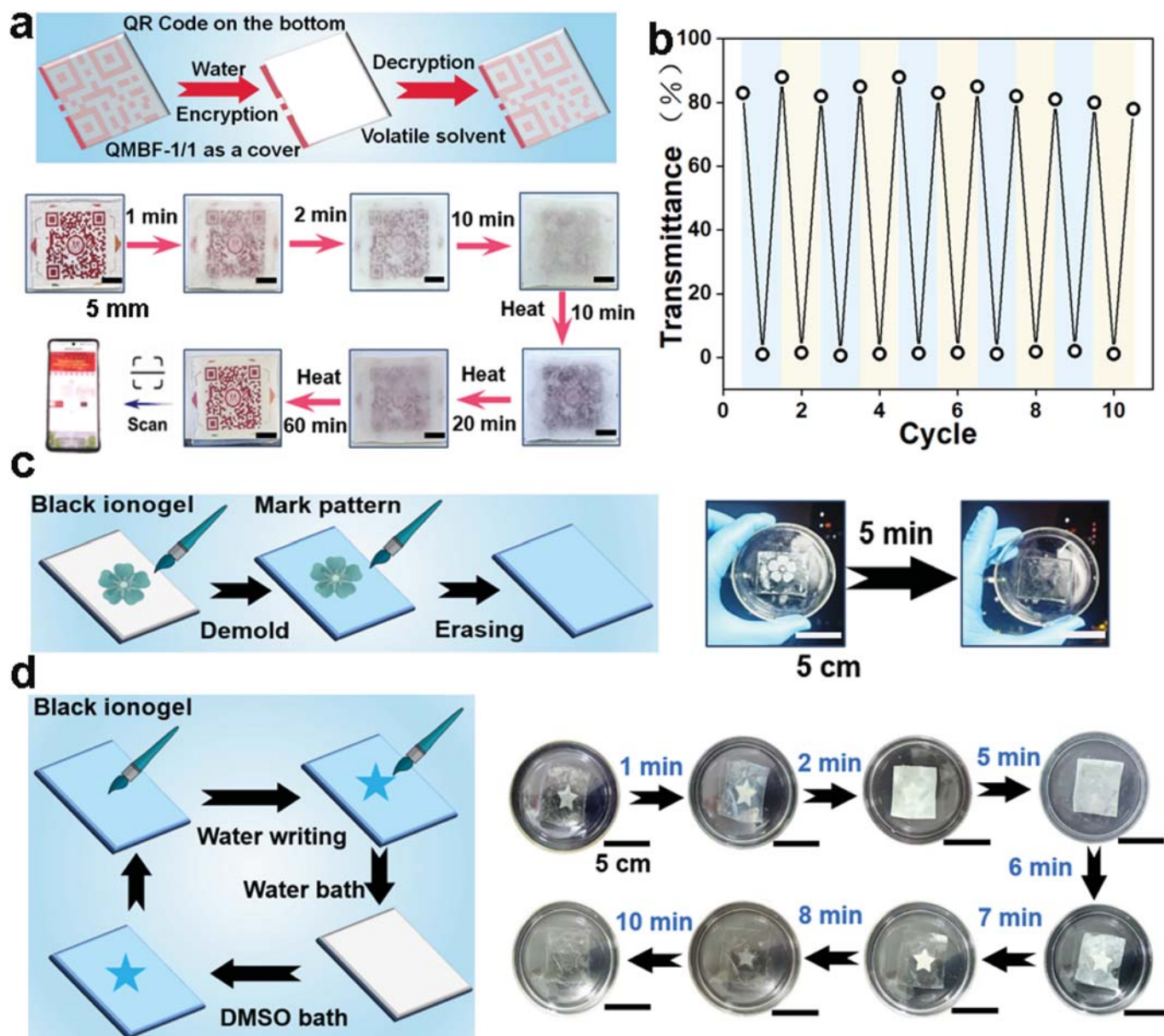


Fig. 6. The application of optical tunability of ionogel in information encryption and decryption. (a) Schematic illustration of the QR code encryption and decryption behaviors and demonstration photos. (b) Changes in transmittance and repeatability during the encryption decryption cycle. (c) Schematic illustration of the information recorded through water brushing, inspired by the woodblock printing technique and demonstration photos. (d) Optical images of pattern "Five Stars" encryption using water, which can be facily represented and self-erased using DMSO.

1.00 in the 0–200 % strain range demonstrating high linearity. Additionally, Fig. 7b illustrates that the sensor has a response time of 0.22 s and a recovery time of 0.17 s during rapid tension and release tests. The quick response time highlights the real-time monitoring capability of the ionogel strain sensor in signal transmission. The QMBF-1/1 ionogel-based strain sensor was integrated onto different joints of the human body to monitor complex body movements in real time. As shown in Fig. 7c, the sensor demonstrated sensitivity to the speed of finger bending. The QMBF-1/1 ionogel-based strain sensor demonstrates excellent scalability and seamless interface adhesion to human wrists even under various large bending strains, resulting in a stable signal output (Fig. 7d and e). In contrast, the non-viscous ionogel tended to detach from the joint during movement, leading to unstable sensing performance (Figure S25). The QMBF-1/1 ionogel-based strain sensor was also demonstrated for the detection of large motions for elbow and knee bending, showing the $\Delta R/R_0$ increased magnitude due to the large

deformation caused by the movement (Fig. 7f). In addition, the signal repeatability and mechanical durability of strain sensors were explored in depth. The QMBF-1/1 ionogel strain sensor performs 500 tension unloading cycles under 50 % strain (Fig. 7g), and the change of $\Delta R/R_0$ is relatively stable. The plate test was used to evaluate the inhibitory effect of QMBF-1/1 ionogel on the growth of *Staphylococcus albus* (*S. albus*) and *Escherichia coli* (*E. coli*). The study found that the QMBF-1/1 ionogel exhibited antibacterial properties, with antibacterial rates of 99.82 % and 98.66 % against *S. albus* and *E. coli*, respectively (Fig. 7i). These phenomena are consistent with the antibacterial mechanism of cationic $-N^+$ that interacts with the negative charge on the surface of the bacteria to make the membranes lose fluidity and kill the bacteria. As a wearable sensing device, the biocompatibility of QMBF ionogel should also be of concern. To evaluate if QMBF ionogel released some types of byproducts that have toxic effects on human fibroblasts cells, the cytotoxicity test was performed by an indirect contact method. [49] As

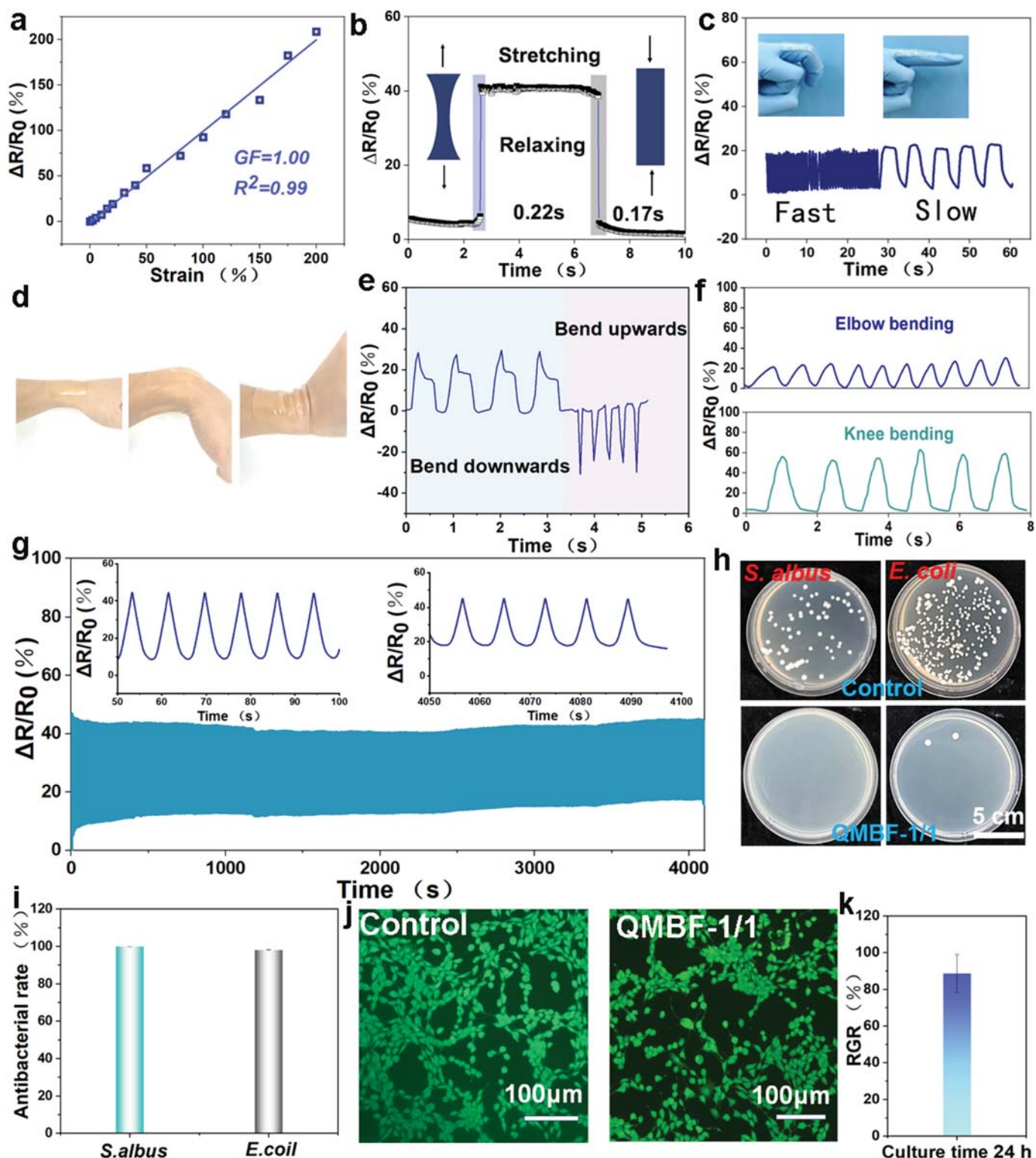


Fig. 7. (a) GF. (b) Response and recovery time of strain sensor. (c) The response of QMBF ionogel to finger bending speed. (d) The adhesive ionogel can seamlessly fit with the skin. (e) $\Delta R/R_0$ variation of adhesive QMBF ionogel to wrist bending. (f) $\Delta R/R_0$ variation of QMBF ionogel to elbow and knee flexion. (g) $\Delta R/R_0$ variation at 50 % strain for 500 cycles. (h) Antibacterial plate photos of the control group and QMBF ionogel against *S. albus* and *E. coli*. (i) The antibacterial efficiency of QMBF ionogel against *S. albus* and *E. coli*. (j) Live/dead staining of human fibroblasts cells cultured with the pure extraction solution from QMBF ionogel for 24 h. (k) The cell viability of human fibroblasts cells was assessed after treatment with the extraction solution from QMBF ionogel.

shown in Fig. 7j and k, the QMBF-1/1 ionogel maintained the cell viability of $89.8 \pm 3.6\%$ after 24 h. Meanwhile, cells showed the healthy morph and good proliferation, suggesting the favorable biocompatibility between cell and QMBF-1/1. These results highlight the potential of

QMBF ionogel in wearable electronic devices.

Following its remarkable underwater adhesion and anti-expansion performance, QMBF-1/1 ionogel can be directly integrated into underwater wearable devices. The stand-alone QMBF-1/1 ionogel pressure

sensing capability enables underwater Morse code communication, facilitating divers in efficiently and accurately transmitting emergency information for rescue operations, thereby potentially reducing the occurrence of accidents. For this communicator, the quick bend means dots in the Morse code while the long bend means dashes (Fig. 8a). Consequently, divers can easily exchange a range of essential messages, such as “SOS” and “HELP” to request assistance (Fig. 8b and c). The QMBF-1/1 ionogel demonstrates advantageous mechanical properties and excellent adhesion strength underwater, making it a promising candidate for emergency repairs in underwater engineering. Figure S26 illustrates the successful use of QMBF ionogel as an adhesive material for repairing damaged boats. To illustrate this process, we drilled six round holes with a diameter of 0.4 cm were drilled into a polytetrafluoroethylene (PTFE) boat, which was then placed on water. Water was poured into the boat through the holes, causing it to sink (Figures S26a and b). Subsequently, the damaged part of the ship was repaired and water seepage was eliminated using QMBF ionic gel bonding material (Figure S26c). After the repair, the boat was placed back in the water

and was able to float without any leakage through the sealed holes. The application of QMBF-1/1 ionogel for repair and bonding was visible under an ultraviolet lamp (Figure S26d). To further confirm the stability of the repaired boat under full-load conditions, an 80 g weight was placed inside the boat, and the previously damaged areas were inspected for water seepage (Figure S26e). The results indicated that the QMBF ionogel remained securely attached to the damaged regions, preventing any water from entering the boat.

For hulls, pipelines, and other objects subjected to high shock pressure, the most vulnerable areas for accidents are the repaired parts. Therefore, it is crucial to continuously monitor and detect the stability of the maintenance site in real time. In this context, QMBF ionogel can serve as a sensing material to monitor the adhesion state in real time, aiding in the detection of repaired sites (Figure S27a). To illustrate, a hole with a diameter of approximately 5 mm was created in the wall of a typical silicone pipeline, and a piece of QMBF ionogel measuring about 20 mm × 20 mm was used to seal the hole during underwater repair. These pipelines were then filled with dye solutions to simulate liquid

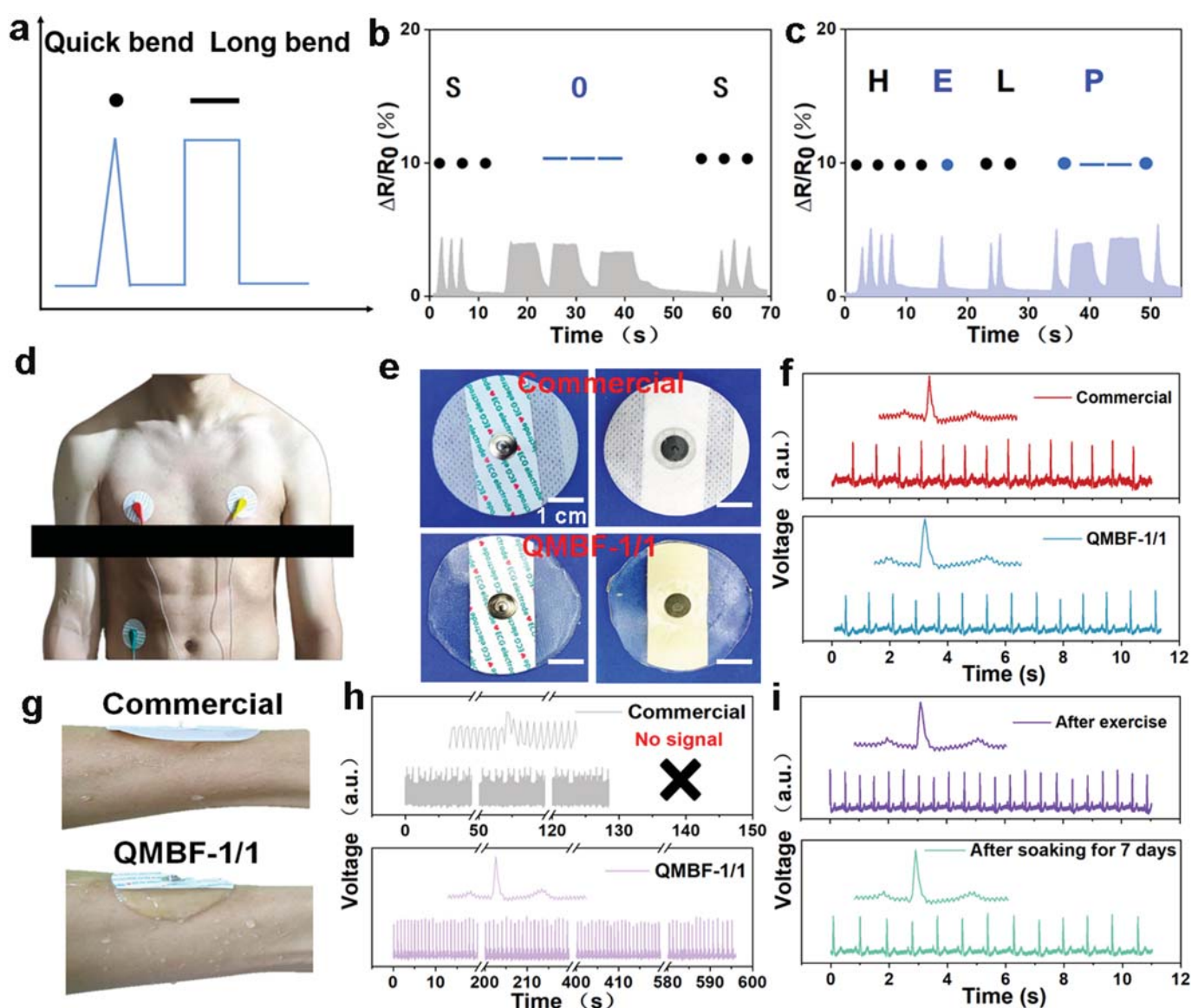


Fig. 8. Application of QMBF-1/1 ionogel in underwater sensing. (a) Obtain electrical signals of triangles and quasi rectangles by tapping the Morse code with your fingers. Transmit (b) SOS and (c) HELP signals through Morse code. (d) Photo of the position of the electrode attached to the upper body of the human body for electrocardiogram monitoring. (e) Commercial Ag/AgCl electrode patches and self-made QMBF-1/1 electrode patches. (f) ECG signals detected by ionogel electrode and commercial in the air. (g) Commercial electrodes fall off in sweat, while QMBF electrodes still have good adhesion in sweat. (h) ECG signals detected by QMBF-1/1 ionogel electrode and commercial in sweat environment. (i) Electrocardiograms were collected after exercise, and 7 d later.

transmission pipelines. The $\Delta R/R_0$ of the QMBF-1/1 ionogel adhesive materials showed an increasing trend when subjected to external force, possibly due to adhesive deformation (Figure S27b). Upon damage from external force, the $\Delta R/R_0$ increased rapidly and could not be restored, likely due to plastic deformation. Additionally, in Figure S27c, it is observed that the $\Delta R/R_0$ of the repaired holes increased incrementally when damaged by external force.

Photograph of the experimental setup with the sensory soft gripper mounted on an industrial robot, which is capable of grasping spherical objects with different radii. The gripper demonstrates bending when grasping hard objects, allowing for the attachment of a QMBF-1/1 on its outer surface to generate a resistance response in tandem with the gripper's bending (Figure S28a). The resistance response of the bending sensor proves to be consistent as the gripper cyclically grasps and releases a tennis ball (Figure S28b). Different angles of bending in the gripper fingers and varying $\Delta R/R_0$ values are observed when grabbing stiff balls of different radii, as illustrated in Figure S28c. Notably, the relative resistance of the bending sensor increases for balls with larger radii, indicating its potential use in perceiving object size. When performing grasping tasks in water, the gripper can also display stable and recognizable sensing signals. When carrying out gripping tasks with objects of larger volume, noticeable bending motions occur on the soft fingers, resulting in more pronounced output signals ($\Delta R/R_0$). Further testing will involve grasping and releasing objects such as rectangular cuvettes, rubber stoppers, and cylindrical cups in water to assess sensor recognition accuracy. The electrical response depicted in Figure S28d suggests that the gripper maintains consistent $\Delta R/R_0$ signals during grasping and releasing actions, showcasing its stable recognition capability even underwater. In addition, in order to explore the potential of QMBF-1/1 ionogel for detecting physiological signals, we incorporated QMBF-1/1 ionogel as bioelectrodes in human physiological signal detection circuits. The electrocardiogram (ECG) detection setup consisted of an ECG monitoring chip, a microcontroller, and a biological electrode, as illustrated in Figure S29. By attaching the electrode patch to specific areas on the volunteer's body, such as the left chest, right chest, and right abdomen, we were able to monitor their electrocardiogram activity (Fig. 8d). Subsequently, we replaced the Ag/AgCl patch in the standard bioelectrode with a QMBF-1/1 ionogel of the same size (Fig. 8e). As shown in Fig. 8f, during the stationary phase, the ECG waveforms outputted by the QMBF-1/1 ionogel electrode were found to be similar to those produced by commercial electrodes, suggesting that a bioelectrode utilizing the QMBF-1/1 ionogel could be used for ECG monitoring. Attributed to the wet adhesion of the QMBF-1/1, the on-skin biosensor can also work on sweaty skin. The study simulated sweaty conditions by progressively spraying artificial sweat (0.3 g per spray) on the skin before recording ECG waveforms. Fig. 8g demonstrates that even after five rounds of sweat spraying, the QMBF-1/1 electrode maintained tight adhesion to the skin, unlike the commercial Ag/AgCl electrode which lost adhesion. Consequently, the peak details of the commercial Ag/AgCl electrode signal are difficult to distinguish and the signal is lost after 120 s. In contrast, the QMBF-1/1 electrode can continuously monitor for over 10 min in the presence of sweat, maintaining robust signals with good resolution (Fig. 8h). The phenomenon of accelerated electrocardiogram signals can be observed after vigorous exercise. Finally, the prepared QMBF-1/1 electrode demonstrated excellent signal stability even after exposure to a water environment for 7 d (Fig. 8i). The above results show that the QMBF-1/1 electrode as an ECG bioelectrode has comparable accuracy and stability to commercial electrodes.

In order to explore the mechanism of hydrolytic degradation, a possible mechanism was studied in the Figures S30a and b, which was attributed to the reaction between OH^- of sodium hydroxide solution and $\text{O}-\text{C}=\text{O}$ of ester bonds in polymer chains. [50–52] This interaction led to the cleavage of polymer molecules, resulting in the formation of smaller compounds that eventually detached from the polymer chains and dissolved in water. The degradability of the QMBF-1/1 ionogel in

0.1 mol/L NaOH solution at room temperature was assessed, revealing complete disappearance of the ionogel within 4 h, as depicted in Figure S30c. Furthermore, the impact of NaOH concentration on the degradation performance of the QMBF-1/1 ionogel was investigated (Figure S30d), showing a noticeable enhancement in degradability with increasing NaOH concentration.

3. Conclusions

In conclusion, hydrophobic ionogel with soft and hard domain heterostructures were prepared by one-step polymerization. In this ionogel system, the solvent-rich soft domain and the solvent-poor hard domain are formed because of the solubility difference of soft and hard components in [Ch] [TFSI], which endow excellent stretchability and strong backbone with the ionogels, respectively. Furthermore, the presence of hydrophobic aromatic rings and fluorinated anionic groups in the system serves to eliminate interfacial water, allowing for the exposure of salicylate and quaternary ammonium cationic groups, which in turn form a strong underwater adhesion with the substrate. Notably, this intelligent underwater sensor can detect human physiology and limb movements, making it suitable for applications in underwater communication engineering, underwater repair operations, and soft robots. Overall, our research lays a solid foundation for the advancement of next-generation flexible electronic products.

CRediT authorship contribution statement

Ning Yu: Writing – original draft, Methodology, Investigation, Data curation. **Peiqi Liu:** Data curation, Writing – original draft. **Yaling Lin:** Writing – review & editing, Supervision, Funding acquisition. **Anqiang Zhang:** Writing – review & editing, Supervision, Funding acquisition, Conceptualization.

Declaration of competing interest

The authors declare that they have no known competing financial interests or personal relationships that could have appeared to influence the work reported in this paper.

Data availability

Data will be made available on request.

Acknowledgements

The authors acknowledge the financial support from the National Natural Science Foundation of China (No. 52073098) and the Natural Science Foundation of Guangdong Province (No. 2022A1515011570, 2023A1515011264). We thank Prof. Xiaodong Cao for providing the support on cytotoxicity evaluation.

Appendix A. Supplementary data

Supplementary data to this article can be found online at <https://doi.org/10.1016/j.cej.2024.155046>.

References

- [1] C. Wang, Y. Lu, H. Cui, J. Zhang, Y. Tan, *Chem. Eng. J.* 485 (2024) 149925.
- [2] C. Zhang, Q. Bao, H. Zhu, Q. Zhang, *Advanced Functional Materials* 2024, 10.1002/adfm.202401901.
- [3] M. Xu, H. Dou, Z. Zhang, Y. Zheng, B. Ren, Q. Ma, G. Wen, D. Luo, A. Yu, L. Zhang, X. Wang, Z. Chen, *Angew. Chem. Int. Ed.* 61 (2022) e202117703.
- [4] F. Sheng, B. Zhang, Y. Zhang, Y. Li, R. Cheng, C. Wei, C. Ning, K. Dong, Z.L. Wang, *ACS Nano* 16 (2022) 10958.
- [5] N. Jiang, X. Chang, D. Hu, L. Chen, Y. Wang, J. Chen, Y. Zhu, *Chem. Eng. J.* 424 (2021) 130418.

- [6] J. Chen, G. Zhu, J. Wang, X. Chang, Y. Zhu, ACS Appl. Mater. Interfaces 15 (2023) 7485.
- [7] J. Chen, F. Wang, G. Zhu, C. Wang, X. Cui, M. Xi, X. Chang, Y. Zhu, ACS Appl. Mater. Interfaces 13 (2021) 51567.
- [8] F. Wang, J. Chen, X. Cui, X. Liu, X. Chang, Y. Zhu, ACS Appl. Mater. Interfaces 14 (2022) 30268.
- [9] S. Wang, S. Li, H. Wang, H. Lu, M. Zhu, X.E. Wu, H. Liang, X. Liang, Y. Zhang, Adv. Funct. Mater. 33 (2023) 2302687.
- [10] M. Chang, J. Wang, X. Liu, Q. Lin, X. Wang, F. Peng, J. Ren, Chem. Eng. J. 468 (2023) 143601.
- [11] G. Sun, P. Wang, Y. Jiang, H. Sun, T. Liu, G. Li, W. Yu, C. Meng, S. Guo, Nano Energy 110 (2023) 108367.
- [12] H. Fan, J.P. Gong, Adv. Mater. 33 (2021) 2102983.
- [13] J. Wei, P. Xiao, T. Chen, Adv. Mater. 35 (2023) 2211758.
- [14] K. Li, X. Zan, C. Tang, Z. Liu, J. Fan, G. Qin, J. Yang, W. Cui, L. Zhu, Q. Chen, Adv. Sci. 9 (2022) 2105742.
- [15] Z. Yu, P. Wu, Adv. Mater. 33 (2021) 2008479.
- [16] M. Li, H. Lu, M. Pi, H. Zhou, Y. Wang, B. Yan, W. Cui, R. Ran, Adv. Sci. 10 (2023) 2304780.
- [17] Y. Zhao, D. Gan, L. Wang, S. Wang, W. Wang, Q. Wang, J. Shao, X. Dong, Advanced Materials Technologies 8 (2023) 2201566.
- [18] J.L. de Lacalle, M.L. Picchio, A. Domínguez-Alfaro, R.-R.-M. Serrano, B. Marchiori, I.d. Agua, N. Lopez-Larrea, M. Criado-Gonzalez, G.G. Malliaras, D. Mecerreyes, ACS Materials Letters 5 (2023) 3340.
- [19] H. Wang, Y. Mao, D. Ji, L. Wang, L. Wang, J. Chen, X. Chang, Y. Zhu, Chem. Eng. J. 471 (2023) 144674.
- [20] M. Zhou, Q. Luo, J. Li, G. Yu, J. Peng, Y. Cao, J. Wang, W. Wang, Y. Yang, Chem. Eng. J. 463 (2023) 142436.
- [21] J. Tie, Z. Mao, L. Zhang, Y. Zhong, X. Sui, H. Xu, Compos. B Eng. 232 (2022) 109612.
- [22] Y. Gong, L. Yu, X. Lyu, S. Zheng, Y. Yu, P. Zhou, Z.Z. Luo, Z. Zou, Adv. Funct. Mater. 33 (2023) 2305314.
- [23] G. Zhong, M. Qiu, J. Zhang, F. Jiang, X. Yue, C. Huang, S. Zhao, R. Zeng, C. Zhang, Y. Qu, Int. J. Biol. Macromol. 234 (2023) 123693.
- [24] F. Chen, X. Li, Y. Yu, Q. Li, H. Lin, L. Xu, H.C. Shum, Nat. Commun. 14 (2023) 2793.
- [25] K. Chen, K. Liang, H. Liu, R. Liu, Y. Liu, S. Zeng, Y. Tian, Nano-Micro Letters 15 (2023) 102.
- [26] S. Hao, Z. Chen, H. Li, J. Yuan, X. Chen, A. Sidorenko, J. Huang, Y. Gu, Small 2023, 10. 1002/sml. 202309931.
- [27] T.P. Lodge, Science 321 (2008) 50.
- [28] H. Hwang, S.Y. Park, J.K. Kim, Y.M. Kim, H.C. Moon, ACS Appl. Mater. Interfaces 11 (2019) 4399.
- [29] Y.M. Kim, K.S. Yu, H.C. Moon, Chem. Eng. J. 480 (2024) 147947.
- [30] A. Cholewinski, F. Yang, B. Zhao, Mater. Horiz. 6 (2019) 285.
- [31] C. Cui, R. Gu, T. Wu, Z. Yuan, C. Fan, Y. Yao, Z. Xu, B. Liu, J. Huang, W. Liu, Adv. Funct. Mater. 32 (2021) 2109144.
- [32] H. Fan, J. Wang, Z. Tao, J. Huang, P. Rao, T. Kurokawa, J.P. Gong, Nat. Commun. 10 (2019) 5127.
- [33] Y. Wang, G. Xia, H. Yu, B. Qian, Y.H. Cheung, L.H. Wong, J.H. Xin, Adv. Mater. 33 (2021) 2100140.
- [34] H. Fan, J. Wang, J.P. Gong, Adv. Funct. Mater. 31 (2020) 2009334.
- [35] B. Yi, T. Li, B. Yang, S. Chen, J. Zhao, P. Zhao, K. Zhang, Y. Wang, Z. Wang, L. Bian, Nat. Commun. 15 (2024) 239.
- [36] J. Tie, Z. Mao, L. Zhang, Y. Zhong, H. Xu, Adv. Funct. Mater. 33 (2023) 2307367.
- [37] Q. Li, W. Li, Z. Liu, S. Zheng, X. Wang, J. Xiong, F. Yan, Adv. Mater. 36 (2023) 2311214.
- [38] X. Ming, J. Du, C. Zhang, M. Zhou, G. Cheng, H. Zhu, Q. Zhang, S. Zhu, ACS Appl. Mater. Interfaces 13 (2021) 41140.
- [39] W. Zhang, B. Wu, S. Sun, P. Wu, Nat. Commun. 12 (2021) 4082.
- [40] H. Xiang, X. Li, B. Wu, S. Sun, P. Wu, Adv. Mater. 35 (2023) 2209581.
- [41] R. Fu, Y. Guan, C. Xiao, L. Fan, Z. Wang, Y. Li, P. Yu, L. Tu, G. Tan, J. Zhai, L. Zhou, C. Ning, Small Methods 6 (2022) 2101513.
- [42] Y.M. Kim, J.H. Kwon, S. Kim, U.H. Choi, H.C. Moon, Nat. Commun. 13 (2022) 3769.
- [43] Y. Zhang, M. Li, B. Qin, L. Chen, Y. Liu, X. Zhang, C. Wang, Chem. Mater. 32 (2020) 6310.
- [44] H. Li, L. Li, J. Wei, T. Chen, P. Wei, Small 20 (2023) 2305848.
- [45] X. Zhang, S. Liu, X. Wang, J. Peng, W. Yang, Y. Ma, K. Fan, J. Colloid Interface Sci. 654 (2024) 1348.
- [46] T. Chen, G. Ye, H. Wu, S. Qi, G. Ma, Y. Zhang, Y. Zhao, J. Zhu, X. Gu, N. Liu, Adv. Funct. Mater. 32 (2022) 2206424.
- [47] R. Song, X. Wang, M. Johnson, C. Milne, A. Lesniak-Podsiadlo, Y. Li, J. Lyu, Z. Li, C. Zhao, L. Yang, I. Lara-Sáez, S. A. W. Wang, Advanced Functional Materials 2024, 10. 1002/adfm. 202313322.
- [48] R. Zhou, Y. Jin, W. Zeng, H. Jin, Y. Li, J. Mei, J. Liu, Advanced Functional Materials 2024, 10. 1002/adfm. 202316687.
- [49] Z. Jiang, X. Shi, F. Qiao, J. Sun, Q. Hu, Biomacromolecules 23 (2022) 5239.
- [50] Y. Chen, P.G. Miller, X. Ding, C.E.T. Stowell, K.M. Kelly, Y. Wang, Adv. Mater. 32 (2020) 2003761.
- [51] W. Li, L. Xiao, J. Huang, Y. Wang, X. Nie, J. Chen, Compos. Sci. Technol. 227 (2022) 109575.
- [52] S. Chen, Y. Wang, L. Yang, C. Chu, S. Cao, Z. Wang, J. Xue, Z. You, Prog. Polym. Sci. 147 (2023) 101763.

Prediction and Explanation of Properties in Multicomponent Polyurethane Elastomers: Integrating Molecular Dynamics and Machine Learning

Yujiang Meng, Yaling Lin,* and Anqiang Zhang*

Cite This: *Macromolecules* 2024, 57, 10912–10925

Read Online

ACCESS |



Metrics & More

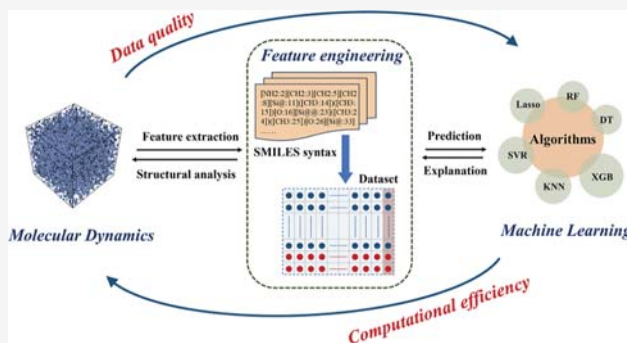


Article Recommendations



Supporting Information

ABSTRACT: Establishing quantitative connections among the chemical composition, molecular structure, and macroscopic properties of multicomponent polyurethane elastomers remains a challenging task. Molecular dynamics (MD) has been extensively utilized in the study of various materials and serves as a crucial tool for exploring the relationship between structure and properties. However, the intricate modeling process and lengthy computation times associated with the MD method complicate the attainment of complex combinatorial results for the various components of polyurethane elastomers. Machine learning (ML) offers a solution by integrating and analyzing existing data, along with the capability to predict new outcomes. Consequently, we combine MD and ML methods to conduct a comprehensive investigation of multicomponent polyurethane elastomers. MD simulations indicate the presence of various types of hydrogen bonds within the elastic matrix of polyurethane, and the strong hydrogen bonds formed in the hard segments significantly affect the tensile properties of material. While the incorporation of long molecular chains in the soft segments enhances the material's flexibility, it simultaneously diminishes its tensile strength. Feature engineering techniques, including parametric representation and feature screening of the MD model, were employed to create a data set suitable for ML applications. The application of the interpretable ML method has demonstrated that the number of hydrogen bonds in the hard segment is regulated by the hydrogen bond donor and acceptor, while the rotatable bonds in the soft segment are the primary characteristics contributing to the material's flexibility and are also key factors that regulate the number of free hydrogen bonds. This integration of MD and ML methods not only enhances predictive capabilities for novel polyurethane elastomers but also facilitates quantitative analysis of how microstructural characteristics affect macroscopic properties.



1. INTRODUCTION

Polyurethane elastomers are a class of widely used polymer materials. Their distinctive soft segment (SS) and hard segment (HS) structures provide exceptional mechanical strength, flexibility, and durability.^{1,2} The performance of these elastomers can be tailored and optimized by modifying the composition of the raw materials or adjusting the proportions of the components. This versatility enables extensive and adaptable applications across various technical domains, including coatings,^{3,4} adhesives,⁵ sensors,^{6,7} and biomedical applications.^{8,9} The application of polyurethane elastomers within the human body necessitates stringent requirements for the precise customization of materials. For instance, incorporating SS like polydimethylsiloxane (PDMS) and polycarbonate diol (PCDL) to improve biocompatibility,^{10,11} while it is also essential for these materials to exhibit sufficient strength and durability. Consequently, accurately predicting these properties in advance becomes a critical consideration. Although experimental science and theoretical

approaches have provided significant insights into the regulation of the properties of individual components in polyurethane elastomers,^{12–14} the amorphous nature of polymer structures and the high degree of spatial freedom complicate the prediction of material properties during the design of new materials. For instance, minor alterations in the chemical structure, segment length, and polymerization techniques can significantly influence the final properties.^{15–17} Consequently, the relationship between the structural parameters and the macroscopic properties of polyurethane elastomers has not been quantitatively characterized or

Received: October 18, 2024

Accepted: November 21, 2024

Published: November 26, 2024



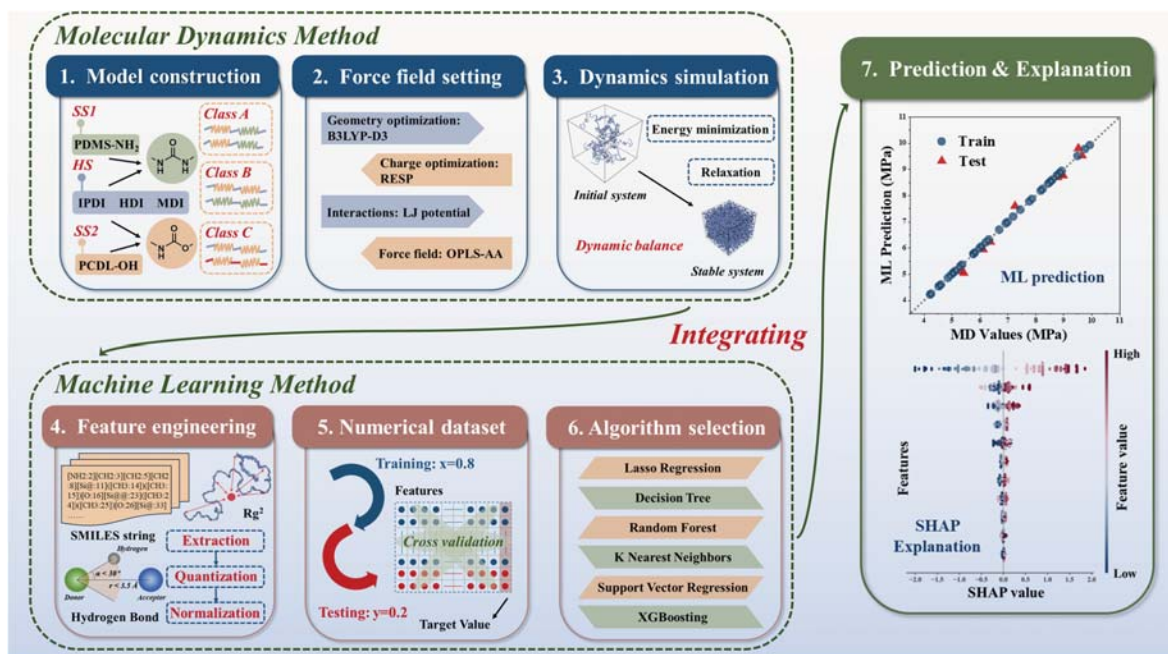


Figure 1. Integrated framework for predicting and explaining polyurethane elastomer properties through MD and ML.

accurately predicted, presenting an ongoing challenge in achieving fine control over these properties.

The advancement of various computer simulation methods has greatly promoted the study of materials at the atomic and molecular levels.¹⁸ Molecular dynamics (MD) simulation has emerged as a potent tool for analyzing the intricate structures of polymers.^{19–21} These simulations enable researchers to investigate the effects of varying compositions and structural configurations on the properties of polyurethane elastomers, offering valuable insights into their behavior under different conditions. Chen et al.²² conducted an all-atom simulation of polyurethane and found that adjusting the ratio of SS and HS could control the generation of hydrogen bonds, thereby enhancing the self-healing capability of the material. Shireen et al.²³ calculated the linear viscoelastic shear modulus and volume relaxation modulus of polyurethane components using a combined atomic and MD simulation method, revealing that their kinetic mechanisms share the same thermal activation process origin. Agrawal et al.²⁴ employed iterative Boltzmann inversion method to develop an accurate parametrized coarse-grained polyurea model, which enabled effective simulation of polyurea under macroscopic mechanical behavior. These advances demonstrate the accuracy and effectiveness of MD simulation methods.

Similarly, machine learning (ML) methods provides a novel perspective on materials analysis. As a data-driven mathematical approach, it demonstrates high computational efficiency and predictive capability, thereby offering a robust framework for correlating various input data with output results.^{25–27} ML methods has found extensive applications in the field of polymer materials, for instance, ML algorithms are employed to predict parameters such as tensile strength and Young's modulus by aggregating data from a substantial body of literature on polyurethane materials.²⁸ ML can also predict the glass transition temperature through a range of polymer models,²⁹ as well as forecasts regarding self-healing capabilities³⁰ and the modulus of polymers.^{31,32} Furthermore, ML-

based image analysis algorithms can be utilized to investigate the phase separation mechanisms of polymer blends.³³

Polymer systems often exhibit a wide range of molecular weight variations, sometimes encompassing tens or even hundreds of thousands. The application of MD simulations necessitates substantial time and computational resources, posing significant challenges in the analysis and prediction of the numerous combinations generated by various polyurethane components and structures.^{34,35} ML methods can enhance the efficiency of analyses, while the accuracy of ML algorithms is contingent upon the quality of the underlying data set, when constructing data sets from diverse reports, inconsistencies in data sources can result in skewed ML predictions. Consequently, integrating MD simulations with ML presents a viable solution: MD can generate stable models that offer high-quality data set for ML, while ML algorithms can significantly reduce the computational demands of MD simulations and facilitate new predictions regarding MD models. Furthermore, advancements in interpretable ML have the potential to elucidate the previously opaque nature of ML algorithms, enabling deeper investigations into how parametrized structural features of the MD model contribute to material properties.^{36,37}

In this study, we aim to develop a mapping scheme that correlates the microstructural characteristics with the macroscopic properties of multicomponent polyurethane elastomers by integrating MD simulation with ML algorithms. This innovative approach is intended to overcome the limitations of traditional experimental methods, which often exhibit reduced accuracy in predicting material properties. We analyzed a series of polyurethane elastomers synthesized using various components and mixing techniques through MD simulation. Feature engineering was employed to parametrize and identify critical structural factors. Following the establishment of the data set, we applied multiple ML algorithms to investigate the relationships among the structural parameters, balancing parameters, and tensile properties of the MD system.

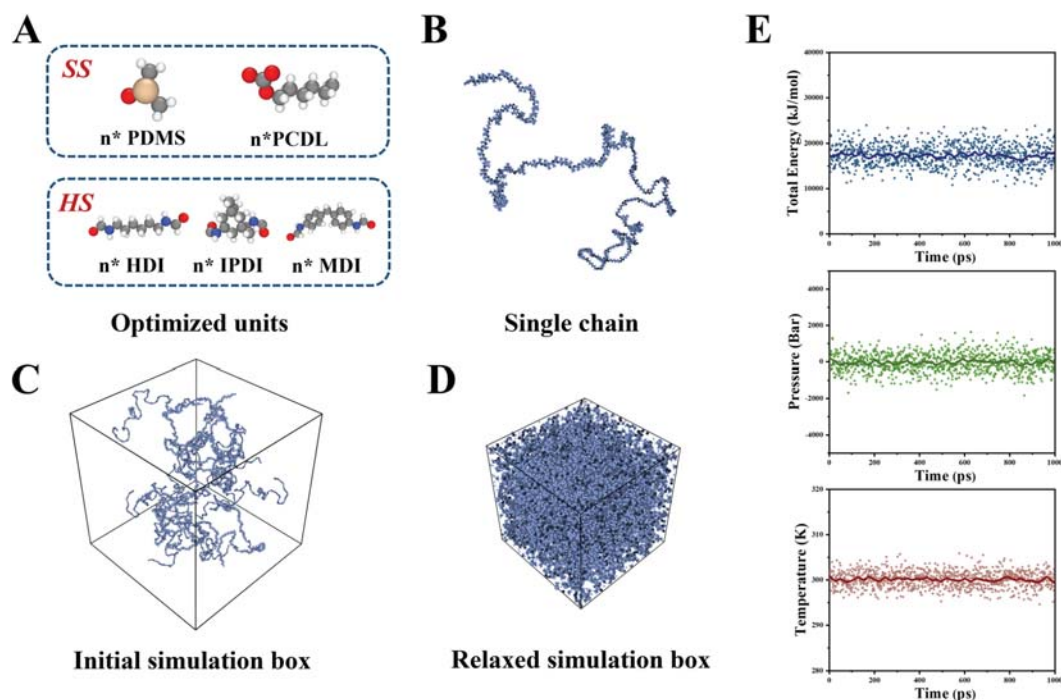


Figure 2. MD of polyurethane elastomers (A) optimized initial units, (B) polymer chains constructed of different components, (C) polymer system with low density and (D) relaxed simulation box. (E) Parameters of equilibrium system.

Ultimately, we quantitatively assessed the contribution of each structural factor via interpretable ML. This integrated, holistic, and continuous approach has significantly enhanced our understanding of the properties of complex molecular systems.

2. METHODS

A workflow integrating MD and ML is illustrated in Figure 1. The MD component encompasses the construction of molecular models, the configuration of appropriate force fields, and the execution of dynamics simulations to capture complex molecular behaviors. The ML phase starts with feature engineering, which includes the digital representation of the initial polymer structures and the extraction of features from the results of the dynamics simulations. A comprehensive data set for ML is established by screening the relevant features. Subsequently, cross-validation is utilized to assess a range of ML algorithms, identify the most effective algorithm for predicting material properties, and elucidate the influence of the polymer's structural parameters on these properties by analyzing the contribution of each feature to the predicted outcomes.

2.1. Construction of Polyurethane Elastomer Models. To investigate the influence of various components on the final properties of polyurethane elastomer systems, we utilized two types of SS and three types of HS to construct various models, as shown in Figure 2A. The SS utilized in this study are PDMS and PCDL, while the HS consist of three isocyanates: isophorone diisocyanate (IPDI), methylene diphenyl diisocyanate (MDI), and hexamethylene diisocyanate (HDI). It is noteworthy that the PDMS domain terminates with an amino group, whereas the PCDL domain terminates with a hydroxyl group, leading to the respective formation of urea ($-\text{NHCONH}-$) and urethane ($-\text{NHCOO}-$) groups upon reaction with the isocyanates. These units are assembled into molecular chains containing different components (Figure 2B). To reflect the true state of the material, the molecular weight of each SS domain was set to 2000, that is, 27 siloxane monomers ($-\text{C}_2\text{H}_6\text{OSi}-$, $M_w = 74.17$, constructed as a PDMS unit) or 14 carbonate monomers ($-\text{C}_7\text{H}_{12}\text{O}_3-$, $M_w = 146.19$, constructed as a PCDL unit) in each domain. And then ensuring that the overall molecular weight of each molecular chain approximates 10,000.

We constructed three classes of copolymerization system, blending system and isocyanate blending system to explore the influence of various mixing methods among the components in the system. Section 1 of Figure 1 briefly illustrates the construction methods for these three classes of systems. In all the systems we constructed, each molecular chain incorporates five SS and four HS domains, and the SS and HS domains are linear alternating copolymerization. In a copolymerization system, PDMS and PCDL are incorporated in the same molecular chain, subsequently replicating these chains to construct a simulation box (see Figure 2C). By varying the ratio of PDMS to PCDL in the chain, we generate a series of chemically mixed polyurethane elastomer models. In contrast, the blending system consists of a physical mixture of PDMS-based and PCDL-based chains, wherein each molecular chain contains only one type of SS. The ratio of the HS in system is manipulated by adjusting the number of PDMS-based and PCDL-based chains within the simulated box to facilitate the desired observation effect. The third class consists of isocyanate blending system, which consist of two different types of isocyanates. While the ratios of PDMS and PCDL are identical across both types of chains, the isocyanates employed in each chain differ. Three types of isocyanates were mixed in pairs, with the ratio of PDMS to PCDL in the system carefully regulated to develop a series of polyurethane mixing models. In total, to achieve a comprehensive range of MD structural parameters, we constructed 48 unique polyurethane elastomer models with diverse chemical structures. In the naming of the models, HDI, IPDI, and MDI refer to the specific types of isocyanates utilized, while the accompanying number (e.g., 0, 20, 40) indicates the proportion of PCDL present in SS. The word “-copoly” denotes a copolymerization system, whereas “-blend” refers to a blending system. The combinations HDI/IPDI, IPDI/MDI, and MDI/IPDI signify the construction of an isocyanate blend system using these two types of isocyanates. The construction details of these models are provided in part S1 of Supporting Information.

2.2. Molecular Dynamics Simulation. To create a high-quality MD simulation data set, the initial units of the polyurethane elastomer are calibrated using density functional theory (DFT) and optimized at the B97-3c level through the ORAC program.^{38,39} The electrostatic potential energy involved in this paper is characterized by the restrained electrostatic potential (RESP),⁴⁰ which is calculated by

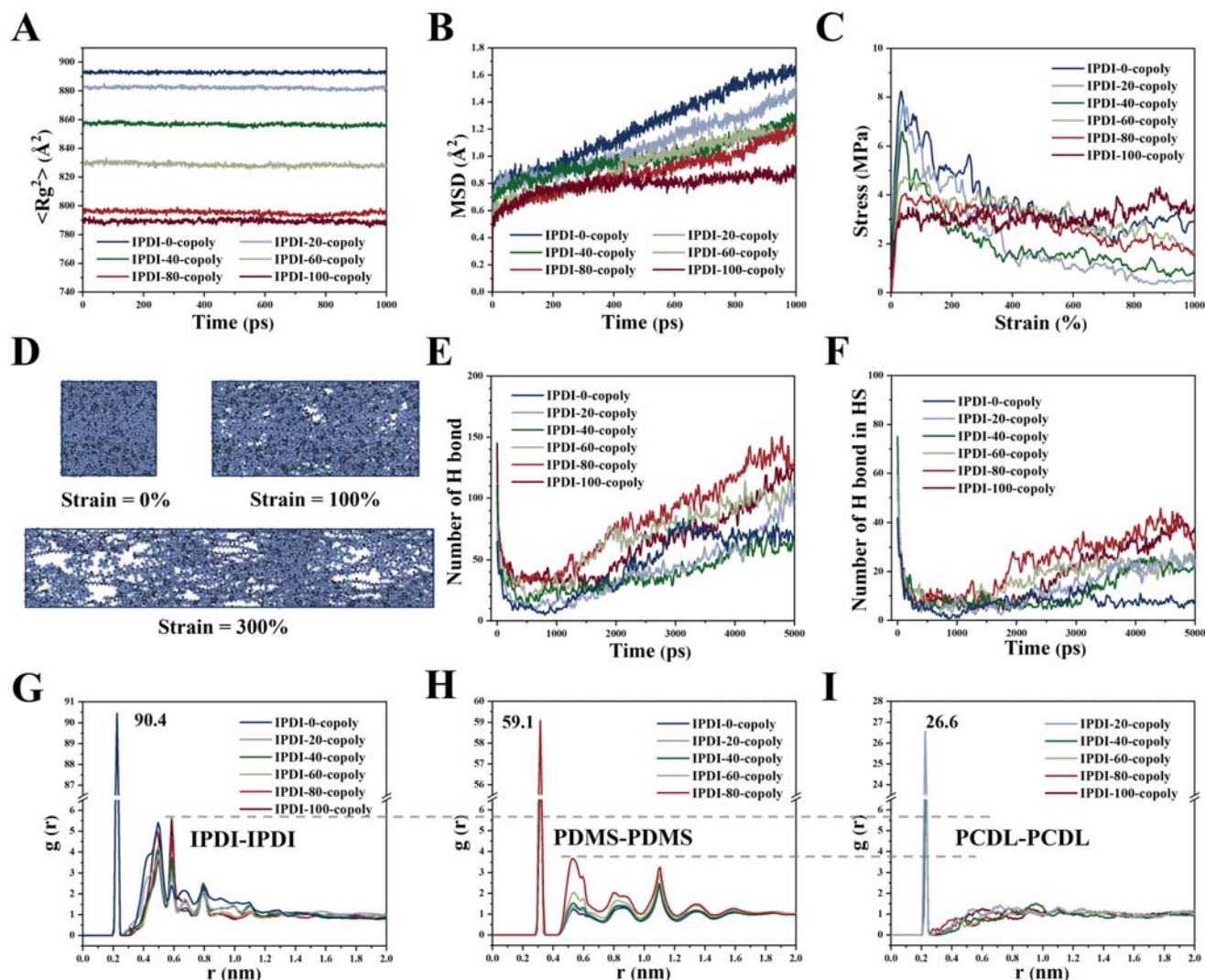


Figure 3. Properties of polyurethane elastomer with different rate of SS: (A) R_g^2 , (B) MSD, and (C) stress–strain curves. (D) Snapshots at different strain rates. (E) The number of hydrogen bonds in the system when stretched, and (F) the number of hydrogen bonds in HS when stretched. RDF of (G) IPDI–IPDI units, (H) PDMS–PDMS units and (I) PCDL–PCDL units.

Multiwfn software⁴¹ at B3LYP-D3/def2-TZVP level. The interactions between atoms are represented by the Lennard-Jones (LJ) potential.

$$U_{LJ} = \begin{cases} 4\epsilon_{ij} \left[\left(\frac{\sigma_{ij}}{r_{ij}} \right)^{12} - \left(\frac{\sigma_{ij}}{r_{ij}} \right)^6 \right] + \frac{q_i q_j \epsilon^2}{r_{ij}} & r_{ij} < r_{cut} \\ 0 & r_{ij} \geq r_{cut} \end{cases} \quad (1)$$

where r_{ij} is the distance between two atoms, ϵ_{ij} is the interaction parameter for the LJ potential between two atoms, σ_{ij} is a dimension parameter, q_i and q_j represent the charges of the i atom and j atom. In the simulation, the cutoff is set to $r_{cut} = 12$ Å. All MD simulations were performed using LAMMPS package,⁴² and OPLS-AA force field^{43,44} was employed.

The MD simulation was conducted under periodic boundary conditions, with a time step of 1.0 fs and a pressure set at 1.0 atm. The Nosé–Hoover barostat and thermostat were employed to regulate pressure and temperature.⁴⁵ The structure of the system was optimized using the steepest descent (SD) method, and unreasonable atomic overlap was eliminated by adjusting the bond length and bond angle. After completing the structural optimization, a prolonged annealing process at elevated temperatures was necessary to transition the model from a low-density system (Figure 2C) to a stable high-density system (Figure 2D). Specifically, an *NPT* ensemble was

utilized for 1 ns of pre-equilibration at 600 K to rapidly increase the system density. Following this, an *NVT* ensemble simulation was conducted for 10 ns at 600 K, after which the *NPT* ensemble was gradually cooled to 300 K at a rate of 0.3 K-ps^{−1}, with a stable energy state maintained for 1 ns after this cooling process. The equilibrium of the system was assessed based on the total energy, total pressure, and temperature depicted in Figure 2E. An additional 1 ns simulation in the *NPT* ensemble was performed to extract parameters such as equilibrium density, mean square radius of gyration (R_g^2), mean square displacement (MSD), and number of hydrogen bonds, details regarding these parameters are provided in part S2 of Supporting Information

To determine the tensile properties of the polyurethane elastomer, the material is elongated along the x -axis at a rate of 1 Å·ns^{−1}, utilizing the equilibrium state established at the conclusion of the previous step as the initial configuration, while maintaining a constant system temperature. The stress–strain relationship is derived by calculating the pressure and elongation of the material along the x -axis.

2.3. Feature Engineering. The structural composition of polyurethane elastomers is highly complex, necessitating the conversion of various expression factors, such as structural and spatial information, into a unified data set.²⁸ This process involves essential feature screening for subsequent ML, commonly referred to as feature

engineering. Initially, the features of the base structure were obtained, and the initial characteristics of the constructed polyurethane elastomer were parametrized using the simplified molecular input line entry system (SMILES).⁴⁶ This syntax employs ASCII strings to digitally represent polymer structures. The RDKit⁴⁷ library was utilized to calculate features such as atomic number, molecular weight, and the number of rotatable bonds for the molecule. The expression and explanation of each feature are detailed in part S3 of [Supporting Information](#). Subsequently, parameters calculated via MD methods, including density, R_g^2 , MSD, and the number of hydrogen bonds, were incorporated into the data set.

Before implementing the ML algorithm, the data set is normalized to mitigate bias arising from the data distribution. Redundant feature sets often result in decreased model accuracy.³¹ To address this concern, the correlation coefficient between each feature is calculated, and features with low correlation coefficients are excluded from the data set.

2.4. Machine Learning Algorithms. The ML process used in this article was implemented in a Python 3.11 environment utilizing the Scikit-learn library.⁴⁸ Six representative algorithms were selected: lasso regression (Lasso),⁴⁹ decision tree (DT),⁵⁰ random forest (RF),⁵¹ K nearest neighbors (KNN),⁵² support vector regression (SVR)⁵³ and XGBoost (XGB).⁵⁴

The data set is divided into a training set and a test set in an 8:2 ratio, which are utilized to construct the regression model and to evaluate its performance, respectively. Cross-validation techniques were employed to assess the stability of the model on this data set. By comparing the results of 100 cross-training sessions, the model's performance was evaluated using the coefficient of determination (R -squared, R^2), root-mean-square error (RMSE), and other relevant indicators, which are presented as follows

$$R^2 = 1 - \frac{\sum_{i=1}^N (y_i - \hat{y}_i)^2}{\sum_{i=1}^N (y_i - \bar{y})^2} \quad (2)$$

$$\text{RMSE} = \sqrt{\frac{\sum_{i=1}^N (y_i - \hat{y}_i)^2}{N}} \quad (3)$$

where the total number of samples is N , the average of all samples is \bar{y} , and the value of the sample i is y_i . R^2 measures the proportion of the variance in the dependent variable that is predictable from the independent variables. A higher R^2 indicates a better fit. RMSE measures the average magnitude of the error in a set of predictions, with a lower RMSE indicating better performance. According to the evaluation results, the model with the best performance is selected as the final model for subsequent research.

The output of ML algorithms is typically regarded as a black box. While the contribution of features to output results can be directly obtained from partial tree algorithms such as DT and RF, achieving a uniform analysis standard across different algorithms remains challenging. In this study, we aim to derive a precise analysis of the final properties of the material's structural parameters, which can be accomplished using the SHAP (SHapley Additive exPlanations) method.⁵⁵ SHAP quantifies the impact of each feature by assigning it a "SHAP" value, and the final output is obtained through the superposition of the SHAP values of all features. This analytical approach enhances the comprehensibility of ML, clarifying the relationships between features, and it can be applied to various ML algorithms, thereby establishing a uniform standard for their interpretation.

3. RESULTS AND DISCUSSION

3.1. Molecular Dynamics Analysis. The influence of varying proportions of SS on the same molecular chain regarding the tensile properties of polyurethane elastomers was investigated. [Figure 3A](#) illustrates the R_g^2 values across six copolymerization models when isocyanate is IPDI. R_g^2 is a critical parameter for assessing the size of molecular fragments,

which is intrinsically linked to the flexibility and conformation of the molecules. When the polymer chain exhibits good flexibility, the chain segments can easily bend and fold, allowing the entire chain to occupy a relatively smaller volume in space, resulting in a reduced R_g^2 measurement. In the system we constructed, although the PCDL and PDMS domains possess the same molecular weight, a PCDL domain contains 126 backbone atoms, much more than the 54 atoms found in a PDMS domain. Consequently, the length of the PCDL domain exceeds that of the PDMS domain along the backbone, as illustrated in [Figure S2](#) in [Supporting Information](#). However, the introduction of PCDL has resulted in a reduction of R_g^2 , indicating a decrease in molecular size, which suggests that PCDL exhibits greater ease of folding compared to PDMS. With the same molecular weights, the greater number of backbone atoms in PCDL provides it with a higher number of rotatable bonds, thereby affording more opportunities for bending and folding, ultimately leading to a reduction in molecular size. To illustrate the motion capacity of the material, we calculated the average displacement of all atoms in the system in 1 ns under the equilibrium state, as shown in [Figure 3B](#). The introduction of PCDL significantly reduces the MSD, indicating that less force is generated within the system, which in turn decreases diffusibility. [Figure 3C](#) displays the stress–strain curves for the six models, notably, the incorporation of the PCDL results in a marked decrease in tensile strength. This observation suggests that the introduction of PCDL has a substantial impact on the mechanical properties of polyurethane elastomers. During the stretching process, increasing deformation of the polyurethane elastomer leads to the formation of voids within the system, as depicted in [Figure 3D](#). The proliferation of these voids ultimately results in material breaking at points of stress concentration. Continue to observe the behavior of the material after it has broken. As the step length of the system is extended, the polyurethane elastomer exhibits rebound characteristics following chain breakage. [Figure 3E,F](#) illustrate the number of hydrogen bonds present in the system during stretching, as well as the number of hydrogen bonds in the HS. It is evident that hydrogen bonds in the system are regenerated after rebound, however, the number of hydrogen bonds in the HS is significantly reduced postrebound. The introduction of PCDL enhances the regeneration frequency of hydrogen bonds in both the system and HS, thereby imparting certain self-healing capability to the material.²²

The radial distribution function (RDF) quantifies the probability of one unit encountering another at a specified distance. [Figure 3G–I](#) illustrate the RDF values for the mass centers of the IPDI, PDMS, and PCDL units encounter themselves across various copolymerization models. As the distance increases, the first unit encountered by another is always adjacent, and connected by chemical bonds, governed by the nature of the chemical bonds, this distance is generally fixed, resulting in a distinct initial peak observed between 0.2 and 0.4 nm. As the distance continues to increase, IPDI and PDMS exhibit several prominent peaks, indicating that at certain distances, their quantity increases sharply. This suggests a more ordered distance distribution between these units ([Figure S7](#) in [Supporting Information](#)). In contrast, PCDL displays a more dispersed distribution due to the presence of more rotatable bonds and longer backbones. Furthermore, the intensity of each peak reveals that the binding density in HS is significantly higher than in SS, highlighting that HS is more

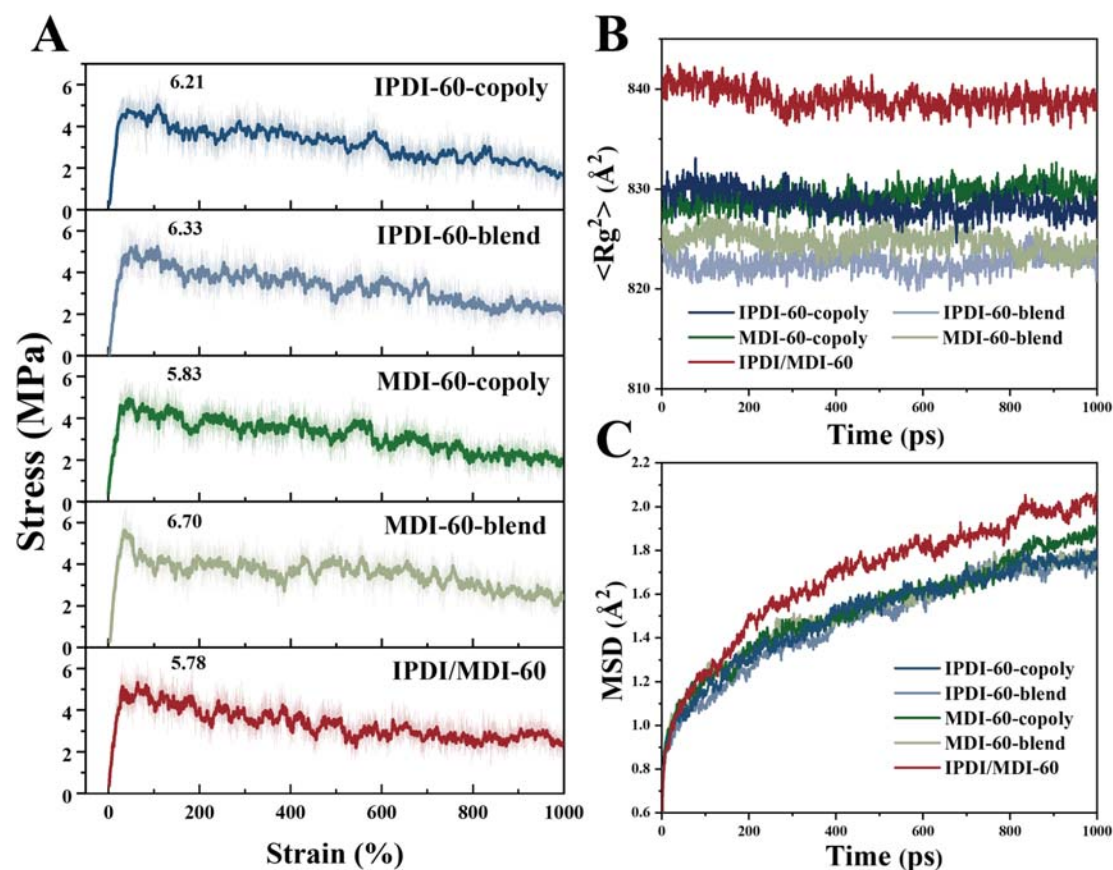


Figure 4. Properties of polyurethane elastomers under different mixing conditions (A) tensile strength, and (B) R_g^2 , (C) MSD.

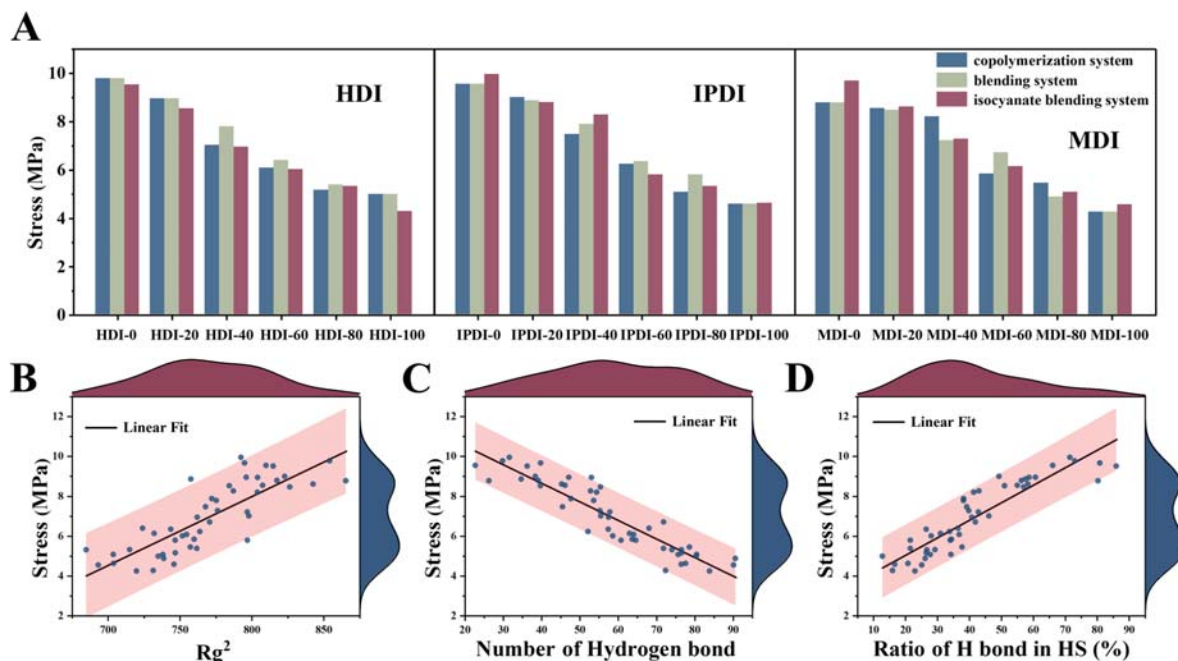


Figure 5. (A) Tensile strength of different polyurethane elastomers models calculated by MD simulation. The relationship between tensile strength and (B) R_g^2 , (C) the number of hydrogen bonds, and (D) the proportion of hydrogen bonds in HS.

tightly bound and primarily contributes to the mechanical strength of polyurethane elastomers.

Figure 4A illustrates the stress–strain curves resulting from the blending of the SS components of polyurethane elastomers.

It can be seen that when the proportions of each component are equal, the tensile strength across different materials remains relatively stable. In comparing the four models of IPDI and MDI, it is observed that the tensile strength of components

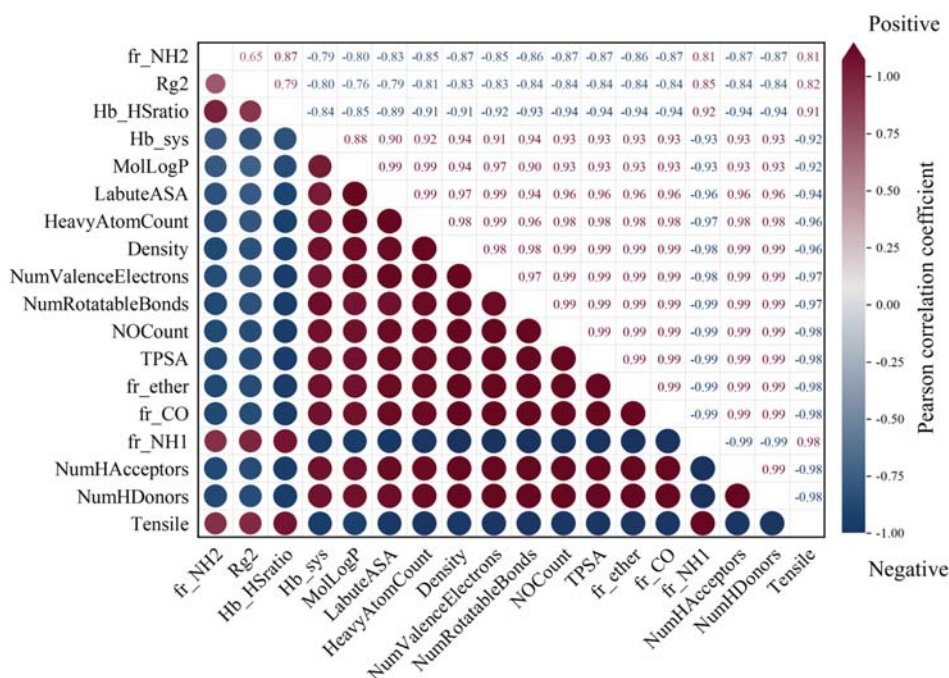


Figure 6. Pearson correlation coefficient (PCC) between screened features.

subjected to blending is marginally higher than that of those subjected to copolymerization, however, tensile strength decreases following the mixing of IPDI and MDI. The R_g^2 and MSD curves presented in Figure 4B,C provide further evidence that blending yields smaller molecular sizes and reduced mobility compared to copolymerization. When different isocyanates are combined within the system, the interaction between the two distinct isocyanates disrupts the ordered arrangement, leading to an increase in the overall system size and enhanced mobility. Interestingly, the trends observed in R_g^2 and MSD across various mixing modes exhibit a negative correlation with tensile strength, which is opposite with the positive correlation observed when the components are mixed in differing proportions. This discrepancy may suggest that molecular size and diffusion capacity are not the primary factors influencing tensile capacity.

To enhance our understanding of this phenomenon, we conducted a MD simulation of multicomponent polyurethane elastomers using 48 models. The relationship between each model and tensile strength is illustrated in Figure 5A. A scatter plot depicts the correlation between tensile strength and R_g^2 , the number of hydrogen bonds within the material, as well as the proportion of hydrogen bonds in HS. Notably, MSD is a discussion about the motion of particles, and tensile strength is affected by the forces between particles, and in all the MD systems we constructed, the MSD value does not exhibit a clear linear relationship with tensile strength (part S4 of Supporting Information). Figure 5B presents the relationship between tensile strength and R_g^2 for all polyurethane elastomer models. It is evident that tensile strength tends to increase with R_g^2 . Figure 5C,D illustrate the relationship between tensile strength and the number of hydrogen bonds, as well as the ratio of hydrogen bonds in HS, respectively. We linearly fit the three relationships and find that they are all linearly correlated, in which the number of hydrogen bonds and the ratio of H in HS are better fitted to the tensile strength. As the number of hydrogen bonds in the system increases, the tensile strength

does not exhibit an upward trend, rather, it gradually decreases. Conversely, the tensile strength tends to increase with the ratio of hydrogen bonds present in HS. The strength of hydrogen bonds can vary significantly, often by orders of magnitude. In polyurethane elastomers, the free weak hydrogen bonds are primarily located in the flexible chain segments, where their strength is considerably lower than that of the HS hydrogen bonds, resulting in a limited contribution to tensile strength. The HS hydrogen bonds predominantly exist in the rigid regions of the polyurethane elastomer and play a crucial role in enhancing the material's tensile strength.^{2,13,14} Consequently, the increase in hydrogen bonds within HS is a key factor contributing to the improvement of tensile strength. In contrast, the rise in free hydrogen bonds is insufficient to counterbalance the reduction in tensile strength caused by other factors, such as the decrease in hydrogen bonds in HS and the increased flexibility of the molecular chains.

3.2. Machine Learning for Tensile Strength. Multi-component polyurethane elastomers have a variety of different microstructures and combinations, which makes the relationship between structure and performance unclear. We try to analyze this problem with data-driven ML algorithms. Combining the parameters obtained by SMILES and MD simulations to construct the data set. There are several different classes of characteristic parameters (structural factors of the material, initial properties of the material, equilibrium parameters of the material, etc.), and the values of the different parameters differ by several orders of magnitude, so they need to be normalized to eliminate the effect of large differences. The input features are critical to the predictive accuracy of the model^{28,36}, consequently, some features that demonstrate little correlation with the final prediction results must be excluded.

The Pearson correlation coefficient (PCC) can be employed to analyze the relationship between any two features. We screened and retained the features with absolute PCC greater than 0.80 for tensile strength, and sorted the features according to their absolute value, as illustrated in Figure 6. Darker regions

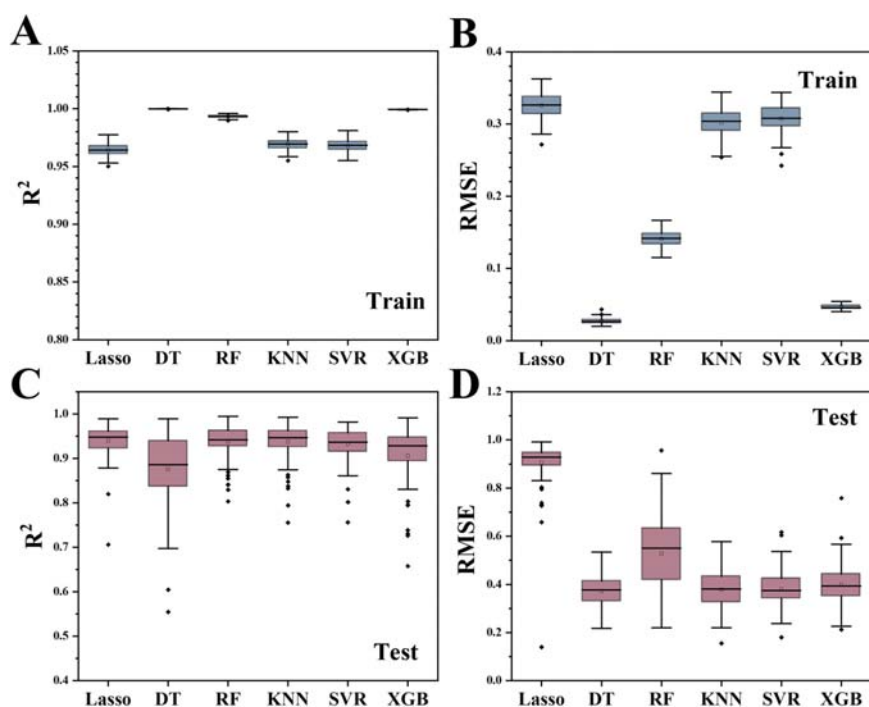


Figure 7. R^2 and RMSE were obtained after 100 times random segmentation of the data set by six ML algorithms. (A,B) On the training set. (C–D) On the test set.

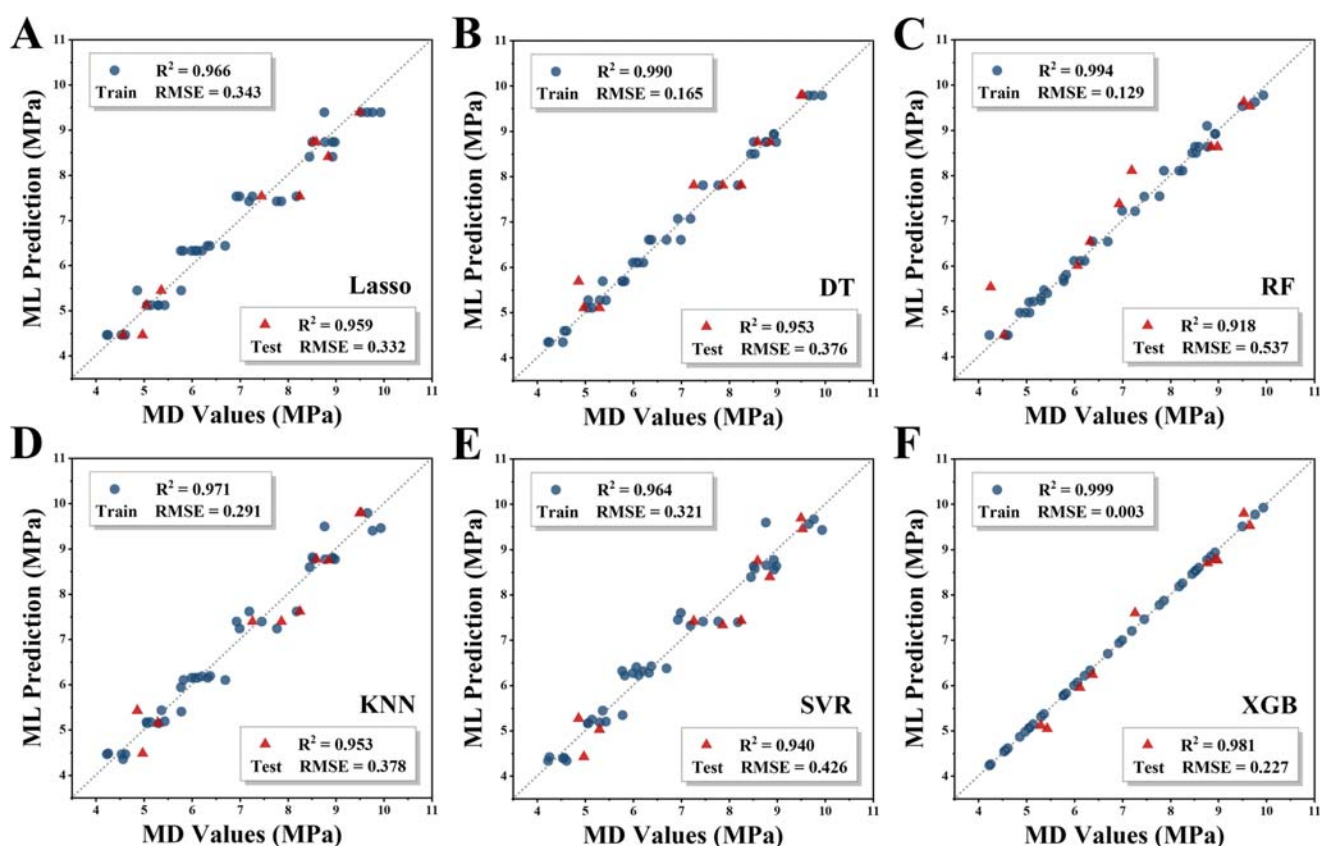


Figure 8. Prediction of tensile strength by (A) Lasso, (B) DT, (C) RF, (D) KNN, (E) SVR, and (F) XGB after hyperparameter optimization.

indicate a strong correlation between the two features, with red areas representing a positive correlation and blue areas indicating a negative correlation. In examining the PCC for

features influencing tensile strength, certain dynamic parameters, such as MSD and diffusion coefficient are excluded from consideration due to their low correlation. PCC of the number

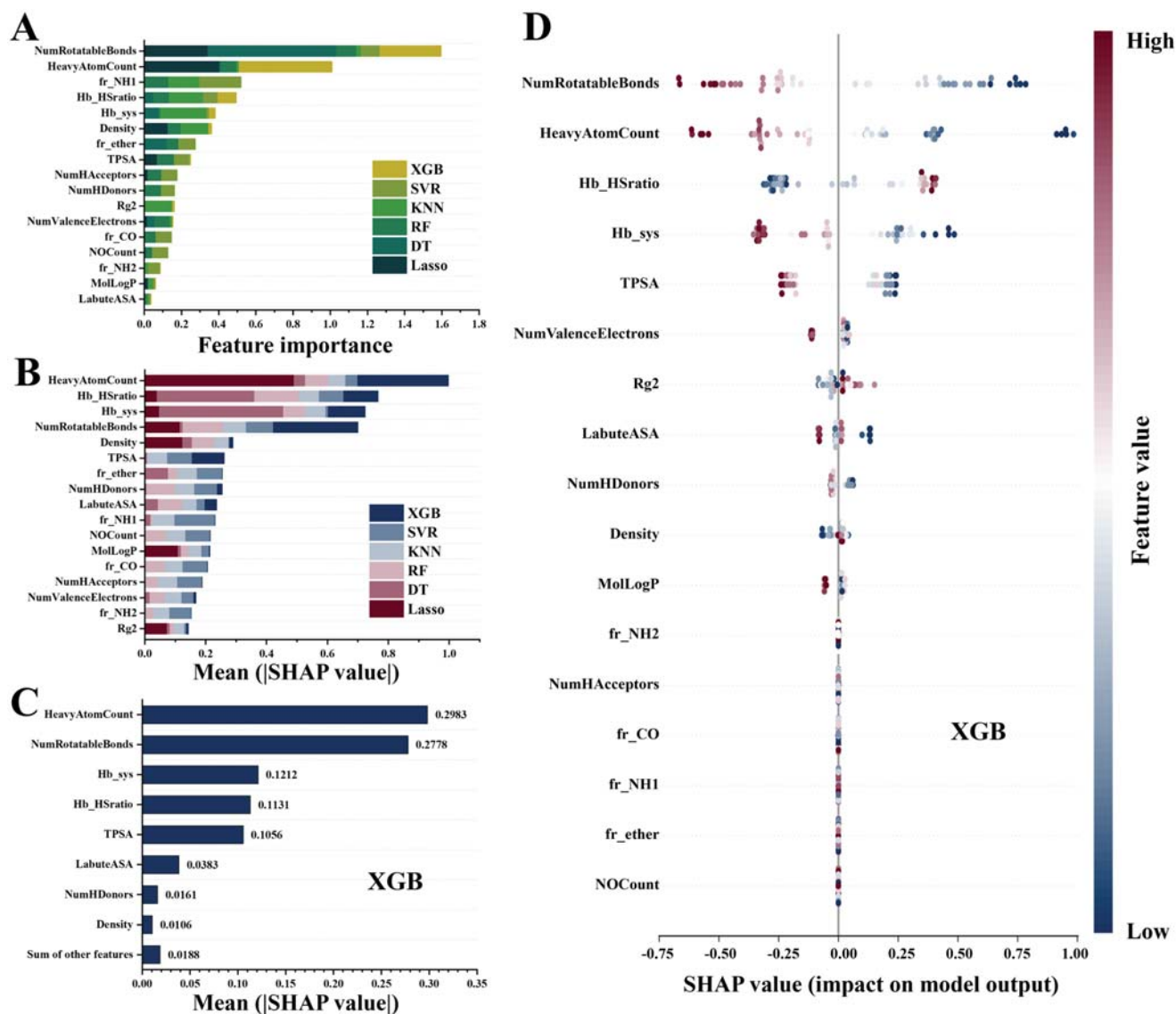


Figure 9. (A) Feature importance of six ML algorithms. (B) Stacked bar graphs of mean SHAP value for features in six ML algorithms. (C) The SHAP value of the feature in the XGB model. (D) Global evaluation of feature contribution on XGB model using SHAP method.

of NH_2 groups and Rg^2 between the tensile strength are only 0.81 and 0.82, respectively, indicating a smaller effect on tensile strength than other features. Notably, features associated with the initial structural elements of the system exhibit a high degree of PCC. Specifically, the correlation of the number of hydrogen bond donors and acceptors between the tensile strength exceeds 0.98, while the number of NH and $\text{C}=\text{O}$ groups correspond to the number of hydrogen bond donors and acceptors in the system (PCC of $-\text{NH}$ and $\text{C}=\text{O}$ groups between hydrogen bond donors and acceptors higher than 0.99), also shows a high correlation with the tensile strength. Analysis of the PCC between the number of hydrogen bonds and other features in the system reveals that the correlation coefficient for the number of rotatable bonds is the highest, which is 0.94, suggesting that the presence of free hydrogen bonds in the system is attributable to the introduction of rotatable bonds. In the case of the ratio of hydrogen bonds in HS, the PCC between the number of donor and acceptor groups also reaches 0.94. This finding aligns with our predictions, indicating that the donor–acceptor groups

predominantly located in the HS and are the source of the strong hydrogen bond force. Furthermore, the PCC between the hydrogen bond features and tensile strength exceeds 0.90, indicating that hydrogen bonds are significantly influenced by the structural properties of the materials, thereby having a substantial effect on tensile strength.

Cross-validation is employed to assess the stability of the models. Figure 7 shows the R^2 and RMSE obtained after 100 random 8:2 splits of the training set and the test set for the six algorithms. As can be seen from Figure 7A,B, all six algorithms demonstrate strong stability on the training set, with R^2 values exceeding 0.9. However, DT, RF and XGB exhibit significantly less dispersion compared to Lasso, KNN and SVR in both figures, showing higher R^2 and lower RMSE. Figure 7C,D depict the performance of the six algorithms on the test set. The R^2 dispersion of the DT model is significantly higher than that of the other algorithms, while the RMSE dispersion of the RF model is higher, indicating that both algorithms may be experiencing overfitting and have insufficient generalization ability.

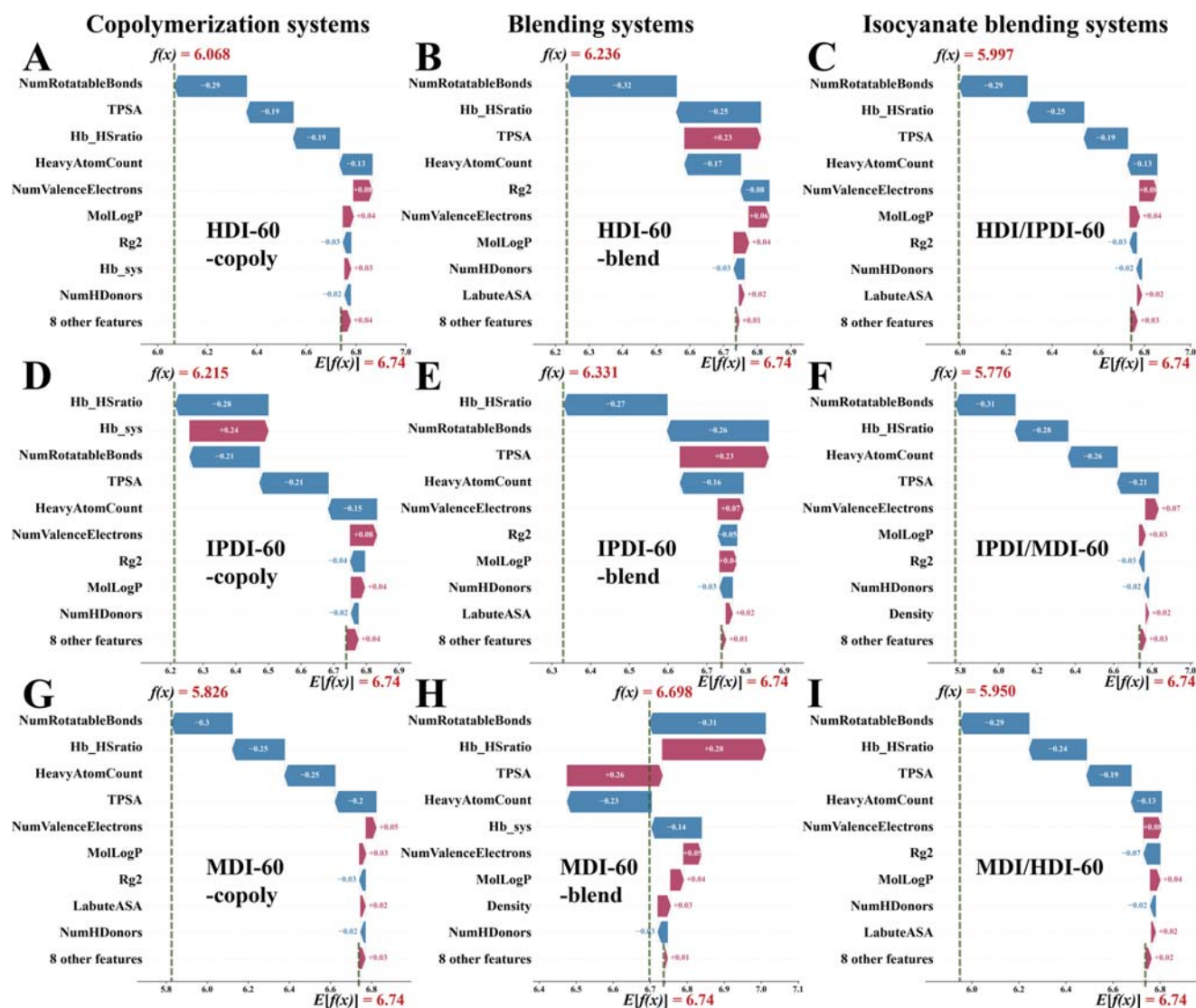


Figure 10. Waterfall diagram of SHAP values for (A) HDI-60-copoly, (B) HDI-60-blend, (C) HDI/IPDI-60, (D) IPDI-60-copoly, (E) IPDI-60-blend, (F) IPDI/MDI-60, (G) MDI-60-copoly, (H) MDI-60-blend, (I) MDI/HDI-60.

Hyperparameter optimization can enhance the performance and generalization capability of the model. This optimization was conducted for six algorithms, as illustrated in Figure 8. Each data point represents a different combination of the initial structure of the polyurethane. In this representation, the x -axis denotes the tensile value calculated by MD, while the y -axis indicates the target tensile value predicted by the ML model, and the black solid line represents the equation $y = x$. The proximity of the data points to this line reflects the accuracy of the prediction model, thus, a closer alignment signifies superior performance. The optimal hyperparameter combinations for the six algorithms are detailed in part S5 of Supporting Information. Following hyperparameter optimization, both the R^2 and RMSE of the six algorithms exhibited improvements. Specifically, the R^2 value for the training set exceeded 0.95, while the R^2 for the test set surpassed 0.91. The reduction in the gap between these two values indicates an enhancement in generalization ability, which can be considered as a meaningful prediction for ML algorithms based on statistical benchmarks.

In the prediction task concerning the composition and tensile strength of polyurethane elastomers, Lasso, KNN, and

SVR demonstrate limitations that hinder their performance. In contrast, RF and DT algorithms exhibit good stability, however, they still fall short compared to the performance of the XGB algorithm. The XGB algorithm is an ensemble learning method based on gradient-boosted decision trees that optimizes the objective function by iteratively adding new decision trees. To achieve higher prediction accuracy, along with excellent generalization capabilities, we have selected XGB as our preferred algorithm.

To investigate the importance and contribution of various features in different ML algorithms to the prediction of material properties, we initially employed the permutational importance method based on model parameters to evaluate the feature importance of six ML models, which were normalized to account for data discrepancies among the models, as shown in the stacked bar chart in Figure 9A, and the results were presented in the descending order. The number of rotatable bonds and heavy atoms (without hydrogen) are considered the two most important characteristics. SHAP establishes a uniform standard for the interpretation of ML algorithms and can explain the degree of contribution of each feature in

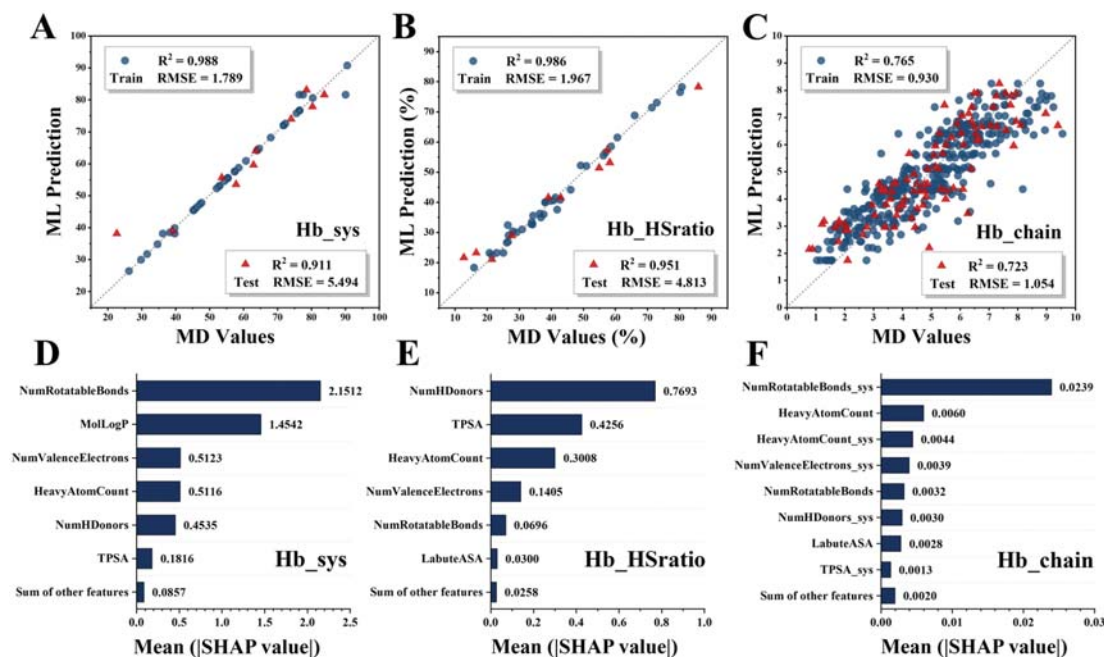


Figure 11. Using XGB algorithm to predict (A) the number of hydrogen bond in system, (B) the ratio of hydrogen bonds in HS and (C) the number of hydrogen bond in each molecular chain. (D–F) The SHAP value of each ML model.

more detail. We calculated the absolute SHAP values for six ML algorithms across each feature, and then summed these values to create the stacked bar graph presented in Figure 9B. The number of heavy atoms, the proportion of hydrogen bonds in HS, the number of hydrogen bonds in the system, and the number of rotatable bonds contribute significantly more than other characteristics, which is basically the same as the conclusion of the feature importance. Figure 9C shows the SHAP values for the XGB model. Similarly, the number of heavy atoms and the number of rotatable bonds, as initial structural parameters, exert substantial effects on the tensile results, while hydrogen bonds serve as the most important intermediate factors. The number of rotatable bonds is strongly correlated with the formation of all free hydrogen bonds. This correlation implies that as the PCDL chain length increases, there will be weak hydrogen bonds produced by C=O groups in the system will form. However, in terms of their contribution to tensile strength, these weak hydrogen bonds are considerably less significant than the strong hydrogen bonds produced by NCO- in HS. The global SHAP diagram is presented in Figure 9D. In this violin diagram, each point corresponds to an individual instance, the red section indicates the original value of the feature is higher, while the blue section denotes the original value is lower. The horizontal axis illustrates the SHAP value of each feature, which quantifies its positive and negative effects on the prediction result. The area of each color section is proportional to the number of instances represented. Notably, TPSA is identified as a significant feature influencing tensile strength, following the number of hydrogen bonds. TPSA reflects the total area of the polar portion of the object's surface. A higher TPSA indicates a greater presence of polar regions on the material's surface, which, to some extent, reflects the content of hydrogen bond donors and acceptors within the material.

In our prior assessments utilizing ML algorithms, we analyzed the data set comprehensively, focusing on the

aggregate influence of features on the tensile properties across all MD models. However, by leveraging waterfall graphs grounded in the SHAP method, we now delve into individual models and their distinctive features, the waterfall shape diagram provides a visual representation of the derivation of each output sample. Specifically, the waterfall diagram presented in Figure 10 highlights nine distinct data points from the XGB algorithm, each representing a unique MD system. These data points enable us to scrutinize how various feature values within a single system contribute to predicting the final tensile strength. Each feature is assigned a unique SHAP value by the model, and these values are sequentially summed starting from the average expected value $E[f(x)] = 6.74$. The cumulative effect of all SHAP values within a system ultimately determines the output value $f(x)$ of the ML model. In this analysis, we focused on a PCDL to PDMS ratio of 60:40, noting that all nine copolymerization or blending models examined contained more PCDL than PDMS. Consequently, the tensile strength predictions $f(x)$ for these models consistently fell below the average expected value $E[f(x)]$, reflecting the influence of PCDL on reducing tensile strength while enhancing flexibility. Several features, including the number of rotatable bonds, the ratio of hydrogen bonds in HS, and the number of heavy atoms all show relatively large SHAP values, indicating that they are the main features affecting the tensile strength. Meanwhile, the positive and negative values of these SHAP values indicate that the values of these features are at a high/low level based on the expected $E[f(x)]$ of the overall model. However, it is important to notice that the effect of TPSA on tensile strength is positive exclusively under blending conditions. In this context, each molecular chain contains only one type of SS, and the TPSA associated with blending is lower than that of copolymerization and isocyanate blending. This difference is considered a contributing factor to the slightly higher tensile strength

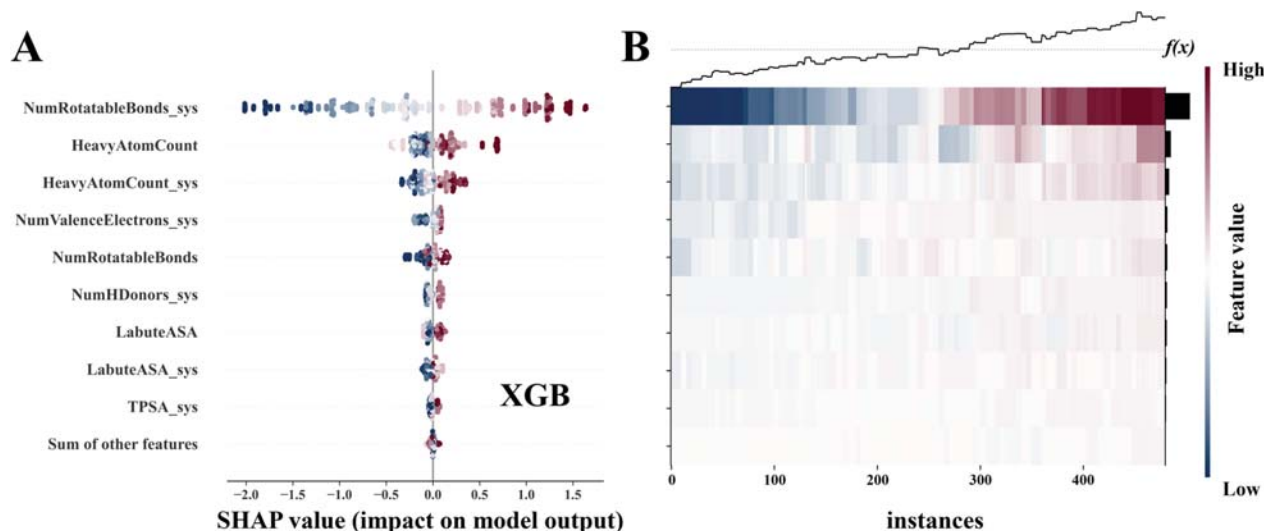


Figure 12. (A) Global evaluation and (B) valuation on each instance of feature contribution using SHAP method for the number of hydrogen bond in each molecular chain.

observed in blending compared to the copolymerization of the same components.

3.3. Machine Learning for Hydrogen Bond. Among the primary contributing factors, hydrogen bonds represent a noninitial static parameter within the system. To further investigate the influence of the initial structure on performance, we propose predicting the hydrogen bonds present in the system. The ML model continues to utilize the well-performing XGB algorithm. When the hydrogen bonds in the system and the ratio of hydrogen bonds in the HS is employed as the target value (see Figure 11A,B), the algorithm demonstrates a satisfactory ability to predict the number of hydrogen bonds. Figure 11D illustrate the contribution for hydrogen bonds in the system of each feature. As previously analyzed, the free hydrogen bonds in the system primarily arise from the number of rotatable bonds present. The addition of rotatable bonds increases the spatial freedom of materials and provides conditions for the formation of free hydrogen bonds. In other words, increasing the chain length of the SS enhances the flexibility of the polyurethane elastomer but may also affect tensile strength to some degree. Figure 11E shows the contribution for the ratio of hydrogen bonds in the HS of each feature. NumHDonors and TPSA are significant features influencing the hydrogen bond ratio in the HS, means the formation of hydrogen bonds in the HS is closely associated with hydrogen bond acceptors. Indicating the necessity to incorporate additional hydrogen bond donors into the polyurethane elastomer to control the tensile strength of the polyurethane elastomer.

Recognizing the variability in the structure of each molecular chain within the mixed system, we conducted further ML analyses on the hydrogen bonds formed by each molecular chain. The data set includes features of the molecular chains as well as features of the system in which each chain resides, denoted by feature names ending with “_sys”. Following PCC screening (see part S6 of Supporting Information), the graph generated using the XGB algorithm is presented in Figure 11C. Although there is a notable decline in model stability, an R^2 value greater than 0.7 is still regarded as within the acceptable predictive range. The polymer chain has a high degree of spatial freedom and uncertainty, which also leads to the fact

that the shape of each molecular chain under the same structure cannot be accurately predicted, while we have already confirmed that the overall structure of polyurethane elastomers is stable and predictable, indicating that the behavior of each molecular chain is limited to a region of the overall behavior.

In our selection of features, we differentiated between the structural characteristics of the molecular chain itself, which aligns with the previous data set, and the system environment in which the molecular chain resides (indicated by features ending in “_sys”). We examined the influence of these features on molecular hydrogen bonding through the established dependency relationship, as illustrated in Figure 11F. The presence of rotatable bonds within the system facilitates the formation of free hydrogen bonds, whereas the impact of the molecular chain characteristics appears to be relatively minor. This finding further explains the overall behavior of polyurethane elastomer properties.

Finally, the SHAP method was employed to assess the contribution of features for the number of hydrogen bond in each molecular chain, as illustrated in Figure 12A,B. The function $f(x)$ represents the total expected value of hydrogen bonds that can be formed for each molecular chain. In regions of the molecular chain where the number of hydrogen bonds exceeds $f(x)$, the number of rotatable bonds in the system yields the most significant positive feedback, followed by the contribution of heavy atoms in the molecular chain. Conversely, when the number of hydrogen bonds generated by the molecular chain falls below $f(x)$, the number of rotatable bonds provides the most substantial negative feedback, while the contribution from heavy atoms in the molecular chain is considerably less pronounced. Thus, for multicomponent polyurethane elastomers, the generation of the number of hydrogen bonds is a holistic behavior, and in order to regulate the number of hydrogen bonds in the system to regulate the final tensile properties of the material, the overall accurate regulation of the material is required.

4. CONCLUSIONS

We present an integrated MD and ML approach to predict and understand the mechanical properties of multicomponent polyurethane elastomers. The MD simulations reveal the

presence of various types of hydrogen bonds within polyurethane elastomers, which exhibit significant strength differences that contribute to variations in tensile strength. Notably, the hydrogen bonds formed in the HS play a crucial role in influencing this strength. Furthermore, we perform parametric extraction and transfer structural information from MD to ML. The ML algorithms demonstrate a strong capability to reproduce MD results accurately and effectively predict tensile strength. Utilizing the SHAP method and subsequent hydrogen bond prediction analysis, we discovered that the number of hydrogen bonds in the HS is regulated by the hydrogen bond donors and acceptors, while the number of free hydrogen bonds in the SS is regulated by the rotatable bonds. Adjusting the structural parameters of polyurethane elastomers, including the ratio between the components in SS, the number of rotating bonds in the chain, the count of hydrogen bond donors and acceptors, and TPSA, is essential for accurately determining their mechanical properties by modulating hydrogen bond number within HS and SS. Furthermore, the stretching behavior observed in a multicomponent system reflects a holistic response, necessitating the overall accurate control of the material when regulating the structure. In this study, MD simulations provide a high-quality data set for ML methodologies, while ML techniques contribute to reducing computational costs and time, enabling rapid predictions of properties for novel materials, and facilitating detailed analysis and interpretation of parameters derived from MD simulations. In future applications of molecular design, leveraging the robust analytical capabilities of ML may allow researchers to backderive the material structures required for experiments based on the predicted desired properties, such as tensile strength or other computable characteristics. This integrated approach presents a novel perspective for material analysis and design.

■ ASSOCIATED CONTENT

SI Supporting Information

The Supporting Information is available free of charge at <https://pubs.acs.org/doi/10.1021/acs.macromol.4c02559>.

Details of MD models; calculation of MD parameters; description of features; MD analysis; hyperparameter configuration for ML; and ML for hydrogen bonds (PDF)

■ AUTHOR INFORMATION

Corresponding Authors

Yaling Lin – College of Materials and Energy, South China Agricultural University, Guangzhou, Guangdong 510641, China; orcid.org/0000-0002-5289-4304; Email: linyin@scau.edu.cn

Anqiang Zhang – School of Materials Science and Engineering, South China University of Technology, Guangzhou, Guangdong 510641, China; orcid.org/0000-0001-7499-8406; Email: aqzhang@scut.edu.cn

Author

Yujiang Meng – School of Materials Science and Engineering, South China University of Technology, Guangzhou, Guangdong 510641, China

Complete contact information is available at:

<https://pubs.acs.org/doi/10.1021/acs.macromol.4c02559>

Notes

The authors declare no competing financial interest.

■ ACKNOWLEDGMENTS

The authors acknowledge the financial support from the National Natural Science Foundation of China (52073098) and the Natural Science Foundation of Guangdong Province (2023A1515011264 and 2022A1515011570). The computer times at the High Performance Computational center at South China University of Technology is gratefully acknowledged.

■ REFERENCES

- (1) Zhang, Y.; Li, Y.; Wang, H.; Zhang, Z.; Feng, Y.; Tian, Q.; Li, N.; Mei, J.; Su, J.; Tian, H. Measuring the microphase separation scale of polyurethanes with a vibration-induced emission-based ratiometric "fluorescent ruler". *ACS Appl. Mater. Interfaces* **2019**, *11* (42), 39351–39358.
- (2) Guo, R.; Zhang, Q.; Wu, Y.; Chen, H.; Liu, Y.; Wang, J.; Duan, X.; Chen, Q.; Ge, Z.; Zhang, Y. Extremely strong and tough biodegradable poly (urethane) elastomers with unprecedented crack tolerance via hierarchical hydrogen-bonding interactions. *Adv. Mater.* **2023**, *35* (21), 2212130.
- (3) Chattopadhyay, D. K.; Raju, K. Structural engineering of polyurethane coatings for high performance applications. *Prog. Polym. Sci.* **2007**, *32* (3), 352–418.
- (4) Das, A.; Mahanwar, P. A brief discussion on advances in polyurethane applications. *Adv. Ind. Eng. Polym. Res.* **2020**, *3* (3), 93–101.
- (5) Golling, F. E.; Pires, R.; Hecking, A.; Weikard, J.; Richter, F.; Danielmeier, K.; Dijkstra, D. Polyurethanes for coatings and adhesives—chemistry and applications. *Polym. Int.* **2019**, *68* (5), 848–855.
- (6) Ma, Z.; Li, H.; Jing, X.; Liu, Y.; Mi, H.-Y. Recent advancements in self-healing composite elastomers for flexible strain sensors: Materials, healing systems, and features. *Sens. Actuators, A* **2021**, *329*, 112800.
- (7) Lin, Y.; Yu, N.; Shan, S.; Zhang, A. Synergistic enhancement of the robustness of multifunctional polyurethane via an ionic non-covalent cross-linking network and aromatic disulfides. *Chem. Eng. J.* **2024**, *481*, 148229.
- (8) Shi, R.; Chen, D.; Liu, Q.; Wu, Y.; Xu, X.; Zhang, L.; Tian, W. Recent advances in synthetic bioelastomers. *Int. J. Mol. Sci.* **2009**, *10* (10), 4223–4256.
- (9) Xiao, R.; Huang, W. M. Heating/solvent responsive shape-memory polymers for implant biomedical devices in minimally invasive surgery: current status and challenge. *Macromol. Biosci.* **2020**, *20* (8), 2000108.
- (10) Zhao, J.; Xu, R.; Luo, G.; Wu, J.; Xia, H. Self-healing poly (siloxane-urethane) elastomers with remoldability, shape memory and biocompatibility. *Polym. Chem.* **2016**, *7* (47), 7278–7286.
- (11) Zhu, R.; Wang, X.; Yang, J.; Wang, Y.; Zhang, Z.; Hou, Y.; Lin, F. Influence of hydroxyl-terminated polydimethylsiloxane on high-strength biocompatible polycarbonate urethane films. *Biomed. Mater.* **2017**, *12* (1), 015011.
- (12) Behera, P. K.; Raut, S. K.; Mondal, P.; Sarkar, S.; Singha, N. K. Self-healable polyurethane elastomer based on dual dynamic covalent chemistry using Diels–Alder “click” and disulfide metathesis reactions. *ACS Appl. Polym. Mater.* **2021**, *3* (2), 847–856.
- (13) Liang, R.; Zhang, H.; Wang, Y.; Ye, J.; Guo, L.; He, L.; Li, X.; Qiu, T.; Tuo, X. Dual dynamic network system constructed by waterborne polyurethane for improved and recoverable performances. *Chem. Eng. J.* **2022**, *442*, 136204.
- (14) Wu, G.; Li, J.; Zhang, Q.; Zhang, H. Synergistic effect of multiple hydrogen bond and disulfide bond on healing waterborne conductive polyurethane composite. *Polymer* **2022**, *258*, 125240.
- (15) Beniah, G.; Liu, K.; Heath, W. H.; Miller, M. D.; Scheidt, K. A.; Torkelson, J. M. Novel thermoplastic polyhydroxyurethane elastomers

as effective damping materials over broad temperature ranges. *Eur. Polym. J.* **2016**, *54*, 770–783.

(16) Sui, T.; Baimpas, N.; Dolbnya, I. P.; Prisacariu, C.; Korsunsky, A. M. Multiple-length-scale deformation analysis in a thermoplastic polyurethane. *Nat. Commun.* **2015**, *6* (1), 6583.

(17) Ding, F.; Liu, T.; Zhang, H.; Liu, L.; Li, Y. Stress-strain curves for polyurethane elastomers: A statistical assessment of constitutive models. *J. Appl. Polym. Sci.* **2021**, *138* (39), 51269.

(18) Gartner III, T. E.; Jayaraman, A. Modeling and simulations of polymers: a roadmap. *Macromolecules* **2019**, *52* (3), 755–786.

(19) Zhang, Z.; Wang, Y.; Liu, P.; Chen, T.; Hou, G.; Xu, L.; Wang, X.; Hu, Z.; Liu, J.; Zhang, L. Quantitatively predicting the mechanical behavior of elastomers via fully atomistic molecular dynamics simulation. *Polymer* **2021**, *223*, 123704.

(20) Zhou, R.; Gao, W.; Xia, L.; Wu, H.; Guo, S. The study of damping property and mechanism of thermoplastic polyurethane/phenolic resin through a combined experiment and molecular dynamics simulation. *J. Mater. Sci.* **2018**, *53* (12), 9350–9362.

(21) Mirhosseini, M. M.; Haddadi-Asl, V.; Khordad, R. Molecular dynamics simulation, synthesis and characterization of polyurethane block polymers containing PTHF/PCL mixture as a soft segment. *Polym. Bull.* **2022**, *79*, 643–661.

(22) Chen, X.; Zhu, J.; Luo, Y.; Chen, J.; Ma, X.; Bukhvalov, D.; Liu, H.; Zhang, M.; Luo, Z. Molecular dynamics simulation insight into the temperature dependence and healing mechanism of an intrinsic self-healing polyurethane elastomer. *Phys. Chem. Chem. Phys.* **2020**, *22* (31), 17620–17631.

(23) Shireen, Z.; Hajizadeh, E.; Davis, P.; Brandl, C. Linear viscoelastic shear and bulk relaxation moduli in poly (tetramethylene oxide) (PTMO) using united-atom molecular dynamics. *Comput. Mater. Sci.* **2023**, *216*, 111824.

(24) Agrawal, V.; Arya, G.; Oswald, J. Simultaneous iterative Boltzmann inversion for coarse-graining of polyurea. *Macromolecules* **2014**, *47* (10), 3378–3389.

(25) Chen, L.; Pilania, G.; Batra, R.; Huan, T. D.; Kim, C.; Kuenneth, C.; Ramprasad, R. Polymer informatics: Current status and critical next steps. *Mater. Sci. Eng., R* **2021**, *144*, 100595.

(26) Cencer, M. M.; Moore, J. S.; Assary, R. S. Machine learning for polymeric materials: an introduction. *Polym. Int.* **2022**, *71* (5), 537–542.

(27) Wu, Y.; Wang, C.-F.; Ju, M.-G.; Jia, Q.; Zhou, Q.; Lu, S.; Gao, X.; Zhang, Y.; Wang, J. Universal machine learning aided synthesis approach of two-dimensional perovskites in a typical laboratory. *Nat. Commun.* **2024**, *15* (1), 138.

(28) Ding, F.; Liu, L.-Y.; Liu, T.-L.; Li, Y.-Q.; Li, J.-P.; Sun, Z.-Y. Predicting the mechanical properties of polyurethane elastomers using machine learning. *Chin. J. Polym. Sci.* **2023**, *41* (3), 422–431.

(29) Chen, M.; Jabeen, F.; Rasulev, B.; Ossowski, M.; Boudjouk, P. A computational structure–property relationship study of glass transition temperatures for a diverse set of polymers. *J. Polym. Sci., Part B: Polym. Phys.* **2018**, *56* (11), 877–885.

(30) Zhou, Y.; Wen, J.; Nie, Y. Microscopic Mechanisms of Self-Healing in Polymers Revealed by Molecular Simulations and Machine Learning. *Macromolecules* **2024**, *57* (7), 3258–3270.

(31) Banik, S.; Balasubramanian, K.; Manna, S.; Derrible, S.; Sankaranarayanan, S. K. Evaluating generalized feature importance via performance assessment of machine learning models for predicting elastic properties of materials. *Comput. Mater. Sci.* **2024**, *236*, 112847.

(32) Lal, H. P.; Br, A.; Ghosh, D. Prediction of nonlocal elasticity parameters using high-throughput molecular dynamics simulations and machine learning. *J. Mec. Theor. Appl.* **2024**, *103*, 105175.

(33) Jones, M.; Clarke, N. Machine learning real space micro-structure characteristics from scattering data. *Soft Matter* **2021**, *17* (42), 9689–9696.

(34) Perry, S. L.; Sing, C. E. 100th anniversary of macromolecular science viewpoint: Opportunities in the physics of sequence-defined polymers. *ACS Macro Lett.* **2020**, *9* (2), 216–225.

(35) Nguyen, D.; Tao, L.; Li, Y. Integration of machine learning and coarse-grained molecular simulations for polymer materials: physical understandings and molecular design. *Front. Chem.* **2022**, *9*, 820417.

(36) Fu, W.; Feng, M.; Guo, C.; Zhou, J.; Zhang, X.; Lv, S.; Huo, Y.; Wang, F. Machine learning-driven prediction of phosphorus removal performance of metal-modified biochar and optimization of preparation processes considering water quality management objectives. *Bioresour. Technol.* **2024**, *403*, 130861.

(37) Esteki, B.; Masoomi, M.; Moosazadeh, M.; Yoo, C. Data-driven prediction of Janus/Core–Shell morphology in polymer particles: A machine-learning approach. *Langmuir* **2023**, *39* (14), 4943–4958.

(38) Neese, F. The ORCA program system. *Wiley Interdiscip. Rev.: Comput. Mol. Sci.* **2012**, *2* (1), 73–78.

(39) Neese, F. Software update: the ORCA program system, version 4.0. *Wiley Interdiscip. Rev.: Comput. Mol. Sci.* **2018**, *8* (1), No. e1327.

(40) Zhang, J.; Lu, T. Efficient evaluation of electrostatic potential with computerized optimized code. *Phys. Chem. Chem. Phys.* **2021**, *23* (36), 20323–20328.

(41) Lu, T.; Chen, F. Multiwfn: A multifunctional wavefunction analyzer. *J. Comput. Chem.* **2012**, *33* (5), S80–S92.

(42) Plimpton, S. Fast parallel algorithms for short-range molecular dynamics. *J. Comput. Phys.* **1995**, *117* (1), 1–19.

(43) Jorgensen, W. L.; Maxwell, D. S.; Tirado-Rives, J. Development and testing of the OPLS all-atom force field on conformational energetics and properties of organic liquids. *J. Am. Chem. Soc.* **1996**, *118* (45), 11225–11236.

(44) Kaminski, G. A.; Friesner, R. A.; Tirado-Rives, J.; Jorgensen, W. L. Evaluation and reparametrization of the OPLS-AA force field for proteins via comparison with accurate quantum chemical calculations on peptides. *J. Phys. Chem. B* **2001**, *105* (28), 6474–6487.

(45) Martyna, G. J.; Klein, M. L.; Tuckerman, M. Nosé–Hoover chains: The canonical ensemble via continuous dynamics. *J. Chem. Phys.* **1992**, *97* (4), 2635–2643.

(46) Weininger, D. SMILES, a chemical language and information system. 1. Introduction to methodology and encoding rules. *J. Chem. Inf. Comput. Sci.* **1988**, *28* (1), 31–36.

(47) Landrum, G. RDKit: open-source cheminformatics from machine learning to chemical registration. *Abstr. Pap. Am. Chem. Soc.* **2019**, *258*, 7727.

(48) Pedregosa, F.; Varoquaux, G.; Gramfort, A.; Michel, V.; Thirion, B.; Grisel, O.; Blondel, M.; Prettenhofer, P.; Weiss, R.; Dubourg, V.; Vanderplas, J. Scikit-learn: Machine learning in python. *J. Mach. Learn. Res.* **2011**, *12*, 2825.

(49) Tibshirani, R. Regression shrinkage and selection via the lasso. *J. R. Stat. Soc. Ser. B* **1996**, *58* (1), 267–288.

(50) Song, Y.-Y.; Ying, L. Decision tree methods: applications for classification and prediction. *Shanghai Arch Psychiatry* **2015**, *27* (2), 130.

(51) Segal, M. R. Machine learning benchmarks and random forest regression. *UCSF: Center for Bioinformatics and Molecular Biostatistics* **2004**, *18*, 1–14.

(52) Goldberger, J.; Hinton, G. E.; Roweis, S.; Salakhutdinov, R. R. Neighbourhood components analysis. *Adv. Neural Inf. Process. Syst.* **2004**, *17*, 513–520.

(53) Smola, A. J.; Schölkopf, B. A tutorial on support vector regression. *Stat. Comput.* **2004**, *14*, 199–222.

(54) Chen, T.; Guestrin, C. Xgboost: A scalable tree boosting system. In *Proceedings of the 22nd ACM Sigkdd International Conference on Knowledge Discovery and Data Mining*, 2016; pp 785–794.

(55) Lundberg, S. M.; Lee, S.-I. A unified approach to interpreting model predictions. *Adv. Neural Inf. Process. Syst.* **2017**, *30*, 4765–4774.



Antifungal mechanisms of polymeric quaternary ammonium salts against conidia of *Fusarium oxysporum* f. sp. *cubense*, race 4

Wei Zhang · Yaoyao Chang · Weiqiang Zhong · Anqiang Zhang · Yaling Lin

Accepted: 1 October 2022 / Published online: 8 October 2022
 © Koninklijke Nederlandse Planteziektenkundige Vereniging 2022

Abstract *Fusarium* wilt of banana is a devastating disease caused by *Fusarium oxysporum* f. sp. *cubense* (*Foc*), of which the “tropical” race 4 strain (*Foc4*) has a significant impact on the banana industry worldwide. Due to the strong persistence of *Foc4* conidia, there is no effective chemical control method up to now. Quaternary ammonium salts (QASs), as cationic fungicides, have great application prospects in the field of inhibiting plant diseases and our previous work showed that polymeric quaternary ammonium salts (PQASs) could effectively inhibit *Foc4* conidia in soil. In this paper, we investigate the effects of two kinds of PQASs, i.e. polydimethylsiloxane-polymethacrylate block copolymers, containing quaternary ammonium salts (PDMS-*b*-QPDMAEMA), poly(methacrylamido propylbenzyl dimethylammonium chloride) (PQD-BC), on the antifungal activities against *Foc4*, using antifungal bioassays and microscopy. It was found that PQASs had high inhibitory effects on conidia and worked fast. Microscopy showed that PQASs could not only rapidly enter conidia, but also stably adsorb to the surface of conidia and penetrate newly grown hyphae. It was also found that PQASs could affect the hydrophobicity of conidial surfaces, change the composition of the cell wall and destroy its

integrity. Over all, this work provides valuable information for the application of PQASs as antifungal agents for inhibiting *Foc4*.

Keywords *Fusarium* wilt of banana · *Foc4* conidia · Polymeric quaternary ammonium salts · Antifungal mechanisms

Abbreviations

<i>Foc4</i>	<i>Fusarium oxysporum</i> f. sp. <i>cubense</i> “tropical” race 4
QAS	quaternary ammonium salts
SQAS	single & small molecular containing quaternary ammonium salt groups
PQASs	polymeric quaternary ammonium salts
PDMS- <i>b</i> -QPDMAEMA (<i>S_nQ₅</i>)	polydimethylsiloxane-polymethacrylate block copolymers containing quaternary ammonium salts
PQD-BC	poly(methacrylamido propylbenzyl dimethylammonium chloride)
BC	benzalkonium chloride
MIC	minimum inhibitory concentration
MFC	minimal fungicidal concentration
IC ₅₀	the 50% maximal inhibitory concentration

W. Zhang · Y. Chang · Y. Lin (✉)
 College of Materials and Energy, South China Agricultural University, 483 Wushan Rd, Guangzhou 510642 Guangdong, China
 e-mail: linyaling@scau.edu.cn

W. Zhong · A. Zhang
 School of Materials Science and Engineering, South China University of Technology, 381 Wushan Rd, Guangzhou 510641 Guangdong, China

IC₉₀ the 90% maximal inhibitory concentration

Introduction

Fusarium wilt of banana is a serious soil-borne vascular disease caused by *Fusarium oxysporum* f. sp. *cubense* (*Foc*), of which the tropical race 4 (*Foc4*) is the most destructive (Shen et al., 2019). The pathogen can survive in the soil as chlamydospores for more than 20 years and infect banana roots at an appropriate time and therefore, it is very difficult to control this disease (Dita et al., 2018; Nel et al., 2006). The spread of *Foc4* is mainly caused by passive movement of pathogen propagules over short or long distances, with human activity being the main responsible factor, through planting material, workers, vehicles, movement of spore-bearing soil, irrigation and flooding (Dita et al., 2018). Even if a small amount of pathogen infects the field, it can cause devastating losses (Ploetz et al., 2015). Surface disinfectants have been found to eliminate the pathogen from infested tools, but effective prophylactic or therapeutic fungicides are not common although there are reports (Meldrum et al., 2013; Nel et al., 2007; Nguyen et al., 2019).

Quaternary ammonium salts (QASs) are rapidly becoming important antimicrobial solutions due to their substantial efficacy (Abid et al., 2017). Therefore, they have been widely used as disinfectants in agricultural fields, public places as well as in medical and health contexts (Buffet-Bataillon et al., 2012). The QASs can be divided into two types depending on molecular weight. The first group comprise single and small molecules containing quaternary ammonium salt groups (referred as SQASs) such as benzalkonium chloride (BC), alkyldimethylbenzylammonium chloride and didecyldimethylammonium chloride. The second group comprises polymeric quaternary ammonium salts (referred as PQASs), i.e. macromolecules containing quaternary ammonium salt groups such as the homopolymer of methacrylamido propylbenzyl dimethylammonium chloride (PQD-BC), dimethylaminopropyl benzyl chloride-grafted polysiloxanes and poly(acryloyloxydodecylpyridinium bromide) (Lin et al., 2014; Zhang et al., 2015, b). Antibacterial and antifungal activities and mechanisms of SQASs have been reported and a widely recognized mechanism is based on cationic immobilization. This means that the positive charge carried by SQASs combines with the negative charge on the surface of the

fungi/bacteria, resulting in a disorder of charge distribution on the cell membrane surface, thus destroying the cell membrane structure, leading to the leakage of cytoplasmic components and eventually death (Gou et al., 2018; Jiao et al., 2017). Gilbert and Moore (2005) showed that SQASs could interfere with the physiological functions of the bacterial cell membrane surface, such as respiration, solute transport and cell wall biosynthesis and thus dissolve all cell contents and kill cells. Ioannou et al. (2007) found that alkyldimethylbenzylammonium chloride and didecyldimethylammonium chloride could be adsorbed to the cell surface of microorganisms and the long carbon chains of SQASs could dissolve phospholipid bilayers and steroid compounds in the cell membrane. However, SQASs are toxic to the environment and have poor chemical stability (Jiao et al., 2017; Lei et al., 2018; Zhang et al., 2015, b). To solve these problems, combining QAS groups with high molecular weight polymer chains to produce PQAS, give the advantages of good curative effects, low toxicity, non-volatility, high chemical stability and prolonged action time, thus having broad application prospects (Lin et al., 2018; Xue et al., 2015).

The suppression mechanisms of PQASs are similar to those of SQASs. They can also have destructive interactions with negatively charged biofilms and cause leakage of intracellular components (Jiao et al., 2017). Compared with SQASs, PQASs have a higher positive charge density. A higher quaternary ammonium group content can promote the rapid adsorption of PQASs to the surface of pathogenic microorganisms and destroy the cell membrane, thereby significantly enhancing the antimicrobial activity (Lei et al., 2018). Rembaum et al. (1977) revealed that the bactericidal effect of PQASs was accompanied by bacterial cell adhesion, aggregation and cleavage as well as complex formation with DNA. Narita et al. (2001) studied the destruction of yeast protoplasts by PQASs with different charge densities and hydrophobic chain segments. They found that hydrophobicity was crucial to induction of cell disruption. Huang et al. (2017) measured the effects of PQD-BC and dimethylaminopropyl benzyl chloride-grafted polysiloxanes on *Foc4* cell walls and cell membrane integrity, mitochondrial function and genome. They found that these two PQASs could induce *Foc4* cell death by destroying cell structural integrity, leading to the release of cell contents, inducing mitochondrial dysfunction and interfering with the synthesis of

genomic DNA. PQD-BC is a typical hydrophilic homopolymer and its main chain is polyacrylamide (Zhang et al., 2015, b), which has a strong hydrophilicity that may not be conducive for the adsorption in soil. Dimethylaminopropyl benzyl chloride-grafted polysiloxane is an amphiphilic polymeric quaternary ammonium salt with hydrophobic polydimethylsiloxane as the main chain and a hydrophilic N, N-dimethyl benzyl chloride quaternary ammonium salt as the side group (Lin et al., 2014). Due to the random distribution of the hydrophilic side groups on the hydrophobic chain, it is difficult accurately to control the structure of dimethylaminopropyl benzyl chloride-grafted polysiloxanes.

As described above, the *Foc4* conidia have a long survival time in the soil, which makes it difficult to control the pathogen. Therefore, inhibiting the spread of conidia or killing them in the soil is of great significance to control Fusarium wilt. In previous studies, QASs were generally not considered sporicidal (Jiao et al., 2017). In our previous study, we synthesized an amphiphilic polydimethylsiloxane-polymethacrylate block copolymer containing quaternary ammonium salts (PDMS-*b*-QPMAEMA) with good adsorption properties in soil and found that it could not only kill *Foc4* conidia, but also inhibit them in soil for 90 days when the pathogen was applied every 10 days (Chang et al., 2021; Lin et al., 2018). In this work, we focus on *Foc4* conidia and study the mechanisms of inhibition of PQAS on *Foc4* conidia. We hope this work will help to understand further the relationship between polymer structure and sporicidal activity and will assist in finding potential polymeric antimicrobial agents for plant protection.

Materials and methods

Strains and culture conditions

The fungal strain used in this study was *Fusarium oxysporum* f. sp. *cubense* (E. F. Smith) Snyder & Hansen, Tropical race 4 (*Foc4*), donated by the Fungal Laboratory of South China Agricultural University and sub-cultured on potato dextrose agar medium (PDA). *Foc4* conidia were obtained from agar cultures after 5 d growth at 28 °C. The concentrations of conidial suspensions were determined using a haemocytometer.

Chemicals

Three kinds of QASs were used in the work, i.e. polydimethylsiloxane-polymethacrylate block copolymers containing quaternary ammonium salts (PDMS-*b*-QPMAEMA, labelled as S_nQ_5 , $n = 0, 5$ or 10 , which means that the molecular weight of the polydimethylsiloxane block is 0, 5 or 10 kDa), poly(methacrylamido propylbenzyl dimethylammonium chloride) (PQD-BC) and benzalkonium chloride (BC). For direct observation of the migration of PQASs into *Foc4* conidia, part of the benzyl group (< 2%) in the QAS structure was replaced by a fluorescein group (-FL), allowing green fluorescence emission under the excitation of ultraviolet light (365 nm) and the corresponding compounds were labelled as S_5Q_5 -FL, PQD-BC-FL and BC-FL, respectively. All QASs except BC were synthesized according to literature (Lin et al., 2018; Zhang et al., 2015, b; Zhong et al., 2017). Their structural characterization and antifungal properties are shown in Supplementary Information (**Part S1-S2**). BC, 2,3,5-triphenyltetrazolium chloride (TTC), kelp polysaccharide and mannose were obtained from Macklin Biotech Co. Ltd., Shanghai, China. Glucosamine hydrochloride was obtained from Sangon Biotech (Shanghai) Co., Ltd. (Shanghai, China). The alkaline phosphatase (ALP) kit was supplied by Nanjing Jiancheng Institute of Bioengineering (Nanjing, Jiangsu, China).

Influence of PQASs on conidial germination

Under sterile conditions, fungal culture plates were flooded with sterile water and the resulting conidial suspension was filtered through three layers of sterile 200-mesh gauze to separate the microconidia from the mycelium. The suspension was adjusted to 4×10^6 microconidia/mL using a haemocytometer. Equal volumes of the microconidial suspension were mixed with PQASs and the final concentrations of PQASs were 5, 10, 20 and 40 µg/mL (three wells per sample). The mixed suspensions were incubated in a constant temperature shock incubator at 28 °C and 120 rpm for 8 h and then observed under differential interference microscopy (DICM, Eclipse 80i microscope, Nikon, Japan). Two-hundred spores in each well were randomly examined for the presence of germ tubes. A microconidium was considered germinated if the germ tube length was at least as long as the spore (Steinkellner

et al., 2005). Sterile water was used as a negative control and the same concentration of BC was used as a positive control. The experiment was performed twice. The germination inhibition rate was calculated according to eqs. (1):

Germination inhibition rate

$$= (C_0 - C_t) / C_0 \times 100\% \quad (1)$$

where C_0 is the number of conidia in the negative control (water), C_t is the number of germinated conidia in the suspension treated with PQASs or BC.

*Inactivation kinetics of PQASs on *Foc4* conidia*

The QAS solutions and a *Foc4* microconidial suspension were mixed in equal amounts in sterile 1.5 mL microcentrifuge tubes, giving a final concentration of *Foc4* conidia of 10^6 conidia/mL and a final concentration of QASs of 30 $\mu\text{g/mL}$. Tubes were incubated for 3, 5, 7, 9, 19, 25 or 31 min and at each sampling time, 100 μL aliquots of the mixed suspensions were taken out and spread on PDA plates with a glass spreader. The plates were then incubated in darkness for 2 d at 28 °C and samples cultured in the absence of a QAS solution were used as control. The colonies grown on the plate were counted using the Image J software. There were three replications for each treatment and the experiment was performed twice. The effect of QASs on the inactivation of *Foc4* conidia is expressed as the inactivation efficiency at different times:

$$\text{Inactivation efficiency} = (N_0 - N_t) / N_0 \times 100\% \quad (2)$$

Where N_0 is the number of fungal colonies without QAS at time 0 and N_t is the number of fungal colonies at time t .

The Chick-Watson model (Dalrymple et al., 2010) conveys the primary principle of disinfection processes, which is described as a linear relationship between the inactivation effect and the exposure time (Leite et al., 2015; Wen et al., 2017):

$$\ln(N_t/N_0) = k C t \quad (3)$$

where k , the slope of the line, is the pseudo-first order inactivation rate constant ($\text{mL } \mu\text{g}^{-1} \cdot \text{min}^{-1}$); C is the concentration of QASs ($\mu\text{g/mL}$); and t is the QASs treatment time (min).

*Microscopy of the interaction between PQASs and *Foc4* conidia*

BC-FL, PQD-BC-FL and S_5Q_5 -FL were mixed with sterile distilled water to prepare 40 mg/mL QAS-FL solutions. *Foc4* was cultured for 5 d, removed from the incubator and then 0.5 mL prepared QAS-FL solution was added and the suspension incubated for 3 min or 3 h. After incubation, conidia were scraped onto a slide with a cover glass and slowly washed several times with sterile water. *Foc4* conidia were incubated for 3 min for each treatment and germination of 200 conidia were studied using DICM. Furthermore, germination of 100 *Foc4* conidia incubated for 3 h for each treatment were studied in a confocal laser scanning microscope (CLSM, TCS SP8 STED 3X, Leica, Germany) with 40x and 100x magnification (Sun et al., 2015, b).

In addition, after treating *Foc4* conidia with 0.1 mg/mL S_5Q_5 -FL for 2 d, about 20 μL conidial suspension was taken out, washed and S_5Q_5 -FL removed, then germination of 200 *Foc4* conidia were studied using DICM.

*Effects of QASs on the cell walls of *Foc4* conidia*

*Changes in the surface potential and hydrophobicity of *Foc4* conidia*

Fungal disks (each 7 mm in diameter), obtained from the periphery of 5-day-old cultures of *Foc4*, were inverted on the centre of each PDA plate and cultured in a 28 °C thermostatic incubator for 2–9 d. Under sterile conditions, fungal culture plates were flooded with sterile water and the resulting conidial suspension filtered through three layers of sterile 200-mesh gauze to separate the microconidia from mycelium. The suspension was adjusted to $(2 \sim 3) \times 10^6$ microconidia/mL using a haemocytometer.

Some conidial suspensions were used to determine changes in the spore surface potential. A zeta potential analyser (Horiba SZ-100Z, Horiba, Japan) with a stent temperature of 25 °C was used, with water as the dispersion medium. The *Foc4* conidial suspension was transferred to the electrode pool and when the instrument temperature was stable, the surface potential of the conidia was determined (Halder et al., 2015).

The remaining conidial suspensions were used to determine changes in the conidial hydrophobicity rates through an improved two-phase extraction method

(Girardin et al., 1999; Shah et al., 2007). The detailed steps were: 6 mL *Foc4* conidial suspension was added to a round-bottom glass colorimetric tube (soaked overnight in hydrochloric acid, cleaned and sterilised after use). A volume of 1.2 mL *n*-hexadecane was added as the oil phase and the tube was sealed with a glass plug. The suspension was oscillated vigorously for 60 s and then transferred to a funnel for 90 min. After the suspension was stratified, the aqueous phase was collected and mixed. Then, the concentration of conidia in the aqueous phase was determined with a haemocytometer. The concentration of conidia without oil phase mixing was used as the control. The conidial hydrophobicity was calculated from eq. (4) (Shan, 2009):

$$\text{Conidial hydrophobicity} = (N_0 - N) / N_0 \times 100\% \quad (4)$$

where N_0 is the initial concentration of *Foc4* conidia without oil phase mixing and N is the final concentration of *Foc4* conidia in aqueous phase.

In order to evaluate the effect of QASs on conidial surface hydrophobicity, a *Foc4* conidial suspension with a concentration of $10^6 \sim 10^8$ microconidia/mL was added to the QAS solution. After incubation for 1 h, 5 mL culture solution was removed and added to the centrifuge tube. The supernatant was centrifuged at $19600 \times g$ for 3 min and then, 3 mL sterile water was added to re-suspend. This process was repeated twice to wash away the residual QASs. Sterile water was added again, the conidia was suspended in the tube and then hydrophobicity was determined by an improved two-phase extraction method described in the previous paragraph. There were three replications for each treatment and the experiment was performed twice.

Sorbitol assay

Fifty- μ L potato dextrose broth was added aseptically to each well of a 96-well plate. Subsequently, 50 μ L BC solution with different concentrations was added into each horizontal row of the wells to obtain the concentrations of 5, 2.5, 1.25, 0.6, 0.3, 0.15, 0.08, 0.04, 0.02, 0.01 and 0 mg/mL. Next, 100 μ L conidial suspension with concentration of 4×10^6 microconidia/mL was added to all wells of the plate except the first horizontal row of the wells. For the group of “BC + sorbitol”, 25 μ L sorbitol solution was added into wells of the plate to obtain a final concentration of 0.8 M, while for the group “BC”, 25 μ L potato dextrose broth instead of

sorbitol solution was added. Sterility control of the medium was performed by adding 100 μ L potato dextrose broth in the first horizontal row of wells of all 96-well plates in the absence of *Foc4*. The 96-well plate was incubated in darkness for 2 d at 28 °C. Then, 20 μ L 2,3,5-triphenyl tetrazolium chloride dye solution (5%, w/v) (Turecka et al., 2018) was added to the well and the plate incubated in darkness for 2 h at 28 °C. The minimum inhibitory concentration (MIC) value is the lowest concentration at which there was no visible growth, i.e. there was no red colour in the well. There were three replications for each treatment and the experiment was performed twice.

The mycelium growth inhibition method (Zhong et al., 2017) was also used to evaluate effects of sorbitol on the growth rate of mycelium on potato dextrose agar (PDA) medium. The experiment was divided into 4 groups. In the first group, the medium contained 0.8 M sorbitol; in the second group, it contained 0.04 mg/mL BC; in the third group, it contained 0.04 mg/mL BC and 0.8 M sorbitol and the last group was pure medium (control). Each mixture was poured into 9 cm diameter sterile Petri dishes and left to solidify. Fungal disks (each 6 mm in diameter) obtained from the periphery of 5-day-old cultures of *Foc4* were inverted on the centre of each plate. All plates were incubated at 28 °C for 5 d. The radial diameter (mm) of each colony was measured in two directions at right angles using a calliper. The percent mycelial inhibition of the radial growth of *Foc4* by the compounds compared with the control was calculated using the following formula:

Percent mycelial inhibition

$$= (D_c - D_t) / D_c \times 100\% \quad (5)$$

where D_c is the mean colony diameter of the control group and D_t is the mean colony diameter of the treatment group. There were three replications for each treatment and the experiment was performed twice.

Conidial cell-wall disruption assay

Damage to the external cell wall layers cause release of alkaline phosphatase (ALP) from the cell (Cheng et al., 1970). The effect of PQASs on *Foc4* conidial cell wall was determined by assaying ALP in the supernatant (Dong et al., 2018). A conidial suspension and QAS solutions were added to 2 mL centrifuge tubes. The final QAS concentrations were equivalent to the minimum inhibitory

concentration, the 50% inhibitory concentration and the 90% inhibitory concentration. The test methods to obtain these data are described briefly in Supporting Information (Part S2). The final concentration of *Foc4* was 10^6 conidia/mL. The same volume of sterile distilled water was added instead of a QAS solution as a control. The samples were incubated at 28 °C and 200 rpm for 2 d on a rotary shaker (MQT-60R, Shanghai Minquan Instrument Co. Ltd., China) and centrifuged at $19600\times g$ for 3 min to collect the supernatant from each centrifuge tube. Then, 50 μ L supernatant was taken to determine the alkaline phosphatase content for each treatment by using an alkaline phosphatase kit (Nanjing Jiancheng Institute of Bio-engineering, Nanjing, Jiangsu, China). According to the instructions of manufacturer, the activity of ALP in the supernatant was measured with a UV-vis spectrophotometer at 405 nm (UV2300, Techcomp, Shanghai, China) and calculated by eq. (6) (Shao et al., 2013). There were three replications for each treatment and the experiment was performed twice.

$$\text{ALP activity} = \frac{OD_{\text{standard value}}}{OD_{\text{estimated value}}} \times 0.005\text{mg} \times \frac{100\text{mL}}{0.05\text{mL}} \quad (6)$$

where $OD_{\text{standard value}}$ refers to the measured absorbance of the standard solution prepared according to the instructions ($A = 0.242$).

Effects of PQASs on the Foc4 conidial cell wall components

The QAS solutions and a *Foc4* microconidial suspension were mixed in equal amounts in 2 mL centrifuge tubes. The final QAS concentrations were equivalent to the minimum inhibitory concentration, the 50% inhibitory concentration and the 90% inhibitory concentration. The final concentration of *Foc4* conidia was 3×10^6 conidia/mL. The same volume of sterile distilled water was added instead of QAS solution as a control. The samples were incubated at 28 °C and 200 rpm for 2 h on a rotary shaker, then centrifuged at $19600\times g$ for 3 min at 4 °C. The supernatant of each centrifuge tube was collected for subsequent determination of chitin, glucan and mannose in the cell walls.

The chitin content in the cell walls was determined by measuring the amount of GlcNAc (N-acetylglucosamine) released by acid hydrolysis of fungal cell walls (Guerriero

et al., 2010; Liu et al., 2007; Liu et al., 2021). One-mL supernatant was suspended in 0.5 mL 0.8 M potassium tetraborate solution and heated to 100 °C for 3 min. After cooling to room temperature, 3 mL 1% (w/v) 4-dimethylaminobenzaldehyde (P-DMAB) reagent was added and the tubes were kept in a water bath at 36 °C for 20 min. Then the absorbance was measured at 544 nm with a UV-vis spectrophotometer. The chitin content is expressed as the microgram content of glucosamine hydrochloride per millilitre supernatant and was calculated according to a standard curve (as shown in Fig. S7), prepared with a known amount of glucosamine hydrochloride.

The glucan content in the cell walls was determined by the aniline blue assay (Fernandes et al., 2021; Han et al., 2014; Kahn et al., 2006). Two-mL 0.04% (w/v) aniline blue solution was added to 1 mL supernatant and incubated in a water bath at 80 °C in the darkness for 15 min. After cooling to room temperature for 30 min, the fluorescence absorbance intensities at 503.5 nm were measured using a fluorescence spectrophotometer (F2700, HITACHI, Japan). The glucan content ($\mu\text{g/mL}$) was calculated according to a standard curve (as shown in Fig. S8) prepared with a known amount of kelp polysaccharide as the standard sample (Han et al., 2014).

The mannose content in the cell walls was determined by an ultraviolet spectrometry method (Lin et al., 2015; Matsuoka et al., 2014). A volume of 3.0 mL of 72% sulphuric acid was added to 1.0 mL supernatant and treated in an ultrasonic cleaner for 30 min (KQ-250DE, Kunshan ultrasonic instruments Co. Ltd., Jiangsu, China). The suspension was kept in a water bath at 100 °C for 4 h to allow the cell walls to be hydrolysed with sulphuric acid. After cooling to room temperature, 0.5 mL 8 M NaOH was added to neutralise the solution ($\text{pH} = 7$). A volume of 0.2 mL of the above solution and 0.2 mL NaCl- H_3BO_3 solution (mixed solution of 12% NaCl (w/v) and 2% H_3BO_3 (w/v)) were added to 10 mL test tubes. As a control, 0.2 mL distilled water instead of 0.2 mL NaCl- H_3BO_3 solution was used. Then 4.6 mL 90% (w/w) H_2SO_4 was added to each tube and mixed by vortexing for 30 s. The tubes were placed in a 70 °C water bath and incubated for 30 min, taken out and cooled with running water. The absorbance of samples was measured by a UV-vis spectrophotometer (UV2300, Techcomp, Shanghai, China) at 280 nm. The difference between absorption with and without NaCl- H_3BO_3 is directly proportional to the mannose

concentration. The content of mannose ($\mu\text{g/mL}$) in the sample was calculated according to a standard curve (as shown in Fig. S9) with known concentrations of mannose. There were three replications for each treatment and the experiment was performed twice.

Data analysis

Data obtained were analysed by SPSS version 22 (SPSS Inc., Chicago, IL, USA). Duncan's multiple range test was used to separate means ($P < 0.05$). A linear regression model ($y = ax$, where a is the slope) was used to relate the inactivation effect ($\ln(N_t / N_0)$) with the exposure time (t). All experiments were performed twice and there were three replications for each treatment. Figures show averages of the two independent experiments. This was possible to show since there were no significant interactions between treatments and experiments. Error bars show the standard error of the mean (SEM) and treatments followed by different letters are statistically at $P < 0.05$.

Results

Effect of PQASs on *Foc4* conidial germination

The effect of PQASs on germination of *Foc4* conidia after 8 h treatment is shown in Fig. 1. An increase of QAS concentration, for benzalkonium chloride (BC), poly(methacrylamido propylbenzyl dimethylammonium chloride) (PQD-BC), polydimethylsiloxane-polymethacrylate block copolymers containing quaternary ammonium salts with 0 kDa, 5 kDa and 10 kDa of polydimethylsiloxane block (S_0Q_5 , S_5Q_5 and $S_{10}Q_5$), resulted in a gradually increased inhibition of spore germination for each QAS. QAS at a concentration of 40 $\mu\text{g/mL}$ could completely inhibit *Foc4* spore germination. BC showed better inhibition of germination at lower concentrations.

Inactivation kinetics of QASs on *Foc4* conidia

The inactivation efficiency and inactivation kinetics of QASs on *Foc4* conidia were evaluated by measuring the survival of *Foc4* conidia treated with QASs after plating on PDA. Figure 2A shows that the number of colonies in the plates decreased gradually with the extension of

treatment time. Each PQAS can kill *Foc4* very quickly, as shown in Fig. 2B. To inhibit conidial growth completely (99.99%), the incubation time was approximately 10 min for S_0Q_5 and S_5Q_5 and approximately 25 min for $S_{10}Q_5$ or PQD-BC. For BC, incubating the conidia for 31 min gave an inhibition rate of only 99%. The Chick-Watson model fitting of inactivation kinetics of QASs (30 $\mu\text{g/mL}$) on *Foc4* conidia is shown in Fig. 2B. The Chick-Watson model described fungal inactivation well, with correlation coefficients (R^2) greater than 0.9. The inactivation rate constants (k) of BC, PQD-BC, S_0Q_5 , S_5Q_5 and $S_{10}Q_5$ were 0.1271, 0.3897, 1.005, 0.9058 and 0.4038, respectively. The efficiencies of inactivation were in the order: $S_0Q_5 > S_5Q_5 > S_{10}Q_5 > PQD-BC > BC$.

Staining of *Foc4* conidia by PQASs

After the benzyl group in the QAS structure was replaced by a fluorescein group (-FL), green fluorescence was emitted under the excitation of ultraviolet light. PQAS-FL treatment of *Foc4* conidia for 3 min is shown in Fig. 3A. Green fluorescence was seen in all conidia, indicating that QASs-FL was able to enter the *Foc4* conidia quickly. Furthermore, *Foc4* conidia were treated with QASs-FL for 3 h and observed under CLSM. The clear green fluorescence in conidia treated with BC-FL, PQD-BC-FL and S_5Q_5 -FL can be seen in Fig. 3B,

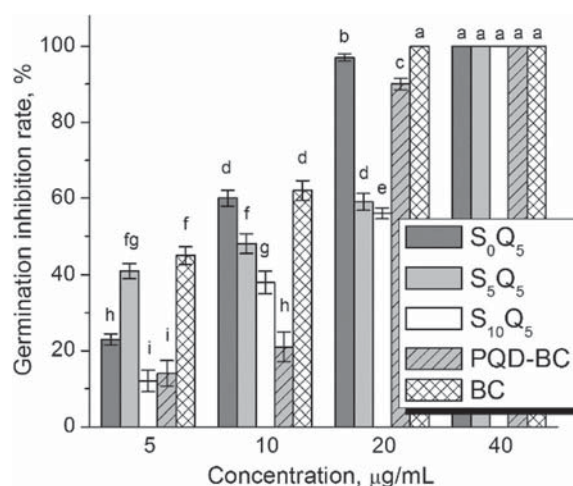


Fig. 1 Inhibition of germination of *Foc4* conidia in S_nQ_5 , PQD-BC and BC. The experiment was performed twice with three replications for each treatment. The figure shows averages of the two experiments. Error bars represent the standard error of the mean. Treatments followed by different letters are statistically different at $P < 0.05$

indicating that QASs-FL can enter and remain inside the *Foc4* conidia. Conidia treated with PQD-BC-FL and S₅Q₅-FL showed a clear outline and fluorescence on the cell surface, as indicated by the red arrow in Fig. 3B. The outer contour of conidia treated with BC-FL was blurred and there was no obvious fluorescence on the cell surface. This indicates that PQASs cannot only enter the conidia, but also bind to the cell surface of the spores and the small molecule QASs can enter conidia through cell wall and cell membrane, but is less adsorbed to conidial surfaces. Compared with the small molecule QAS, PQAS had better adsorption performance on conidial cell wall.

After being treated with 0.1 mg/mL S₅Q₅-FL for two days, *Foc4* conidia were observed by DICM. The results are shown in Fig. 4. There was fluorescence not only in the fragments of conidia, but also in the newly germinated hyphae, indicating that S₅Q₅-FL can continue to be taken up by the newly formed hyphae.

Effect of PQAS on the cell walls of *Foc4* conidia

Changes in the Foc4 conidial surface potential and hydrophilicity

The detection results of the zeta potential and hydrophobicity of conidia are shown in Fig. 5A, B. Figure 5A shows that the potential of the conidial surface decreased continuously with the extension of culture time. Figure 5B shows that the conidial hydrophobicity was approximately 20% and did not change with the extension of culture time. The change in the conidial hydrophobicity after 1 h of QAS treatment at the minimum inhibitory concentration (MIC) is shown in Fig. 5C. Thus, the conidial hydrophobicity after treatment with BC decreased, whereas the conidial hydrophobicity after treatment with PQD-BC, S₀Q₅, S₅Q₅ and S₁₀Q₅ increased.

Sorbitol assay

Sorbitol, as a substance to maintain proper osmotic pressure, provides a suitable environment for the cell wall biosynthetic pathways. It is often used to test the effect of drugs on the cell wall. The effect of sorbitol on the BC inhibition properties is presented in Fig. 6. Figure 6A shows that the minimum inhibitory concentration (MIC) of BC for the conidia was 0.04 mg/mL and after adding sorbitol, the value was 0.02 mg/mL.

The decrease in MIC indicated that sorbitol increased the inhibition of BC on conidia. In order to confirm this, the mycelium growth inhibition method was used and the results are shown in Fig. 6B. A concentration of 0.8 M sorbitol had no effect on the growth of *Foc4* hyphae. The inhibition rate of mycelium growth was 35.2% for BC at the MIC and with the addition of 0.8 M sorbitol to BC, the inhibition of mycelial growth was 51.3%. The increase in the inhibition further indicated that sorbitol and BC had a synergistic effect on the inhibition of *Foc4* mycelial growth. Therefore, the widely used method of adding sorbitol to evaluate whether a compound destroys the conidial cell wall was not suitable for QASs.

Effect of QASs on Foc4 conidia alkaline phosphatase (ALP) leakage

In conidia, ALP exists between the cell wall and cell membrane. When the cell wall is destroyed, the ALP will leak out of the cell, so the integrity of the conidial cell wall can be evaluated by detecting the ALP activity in the culture medium. Figure 6C shows that the ALP content in the culture medium treated with BC was low and did not change significantly with the increase of BC dosage. ALP content in the culture medium treated with high concentrations of PQASs increased significantly and PQD-BC was the most destructive compound to the cell walls of *Foc4* conidia.

Effects of PQASs on cell wall components

Chitin, glucan and mannose are the main components of the cell walls of fungi. They are polysaccharides polymerised from monosaccharides. Effects of PQASs on the cell wall components of *Foc4* conidia can be evaluated by determining the content of these polysaccharides in the culture medium, as shown in Fig. 7. After being treated with QASs at the minimum inhibitory concentration (MIC), 50% inhibitory concentration (IC₅₀) and 90% inhibitory concentration (IC₉₀), the content of chitin, glucan and mannose in the culture medium all increased with the increase of QAS concentration. This indicates that each QAS can act on the components of the cell wall of the *Foc4* conidia, with glucan being most severely affected. The effects of PQASs on the components of *Foc4* cell wall were significantly greater than that of BC.

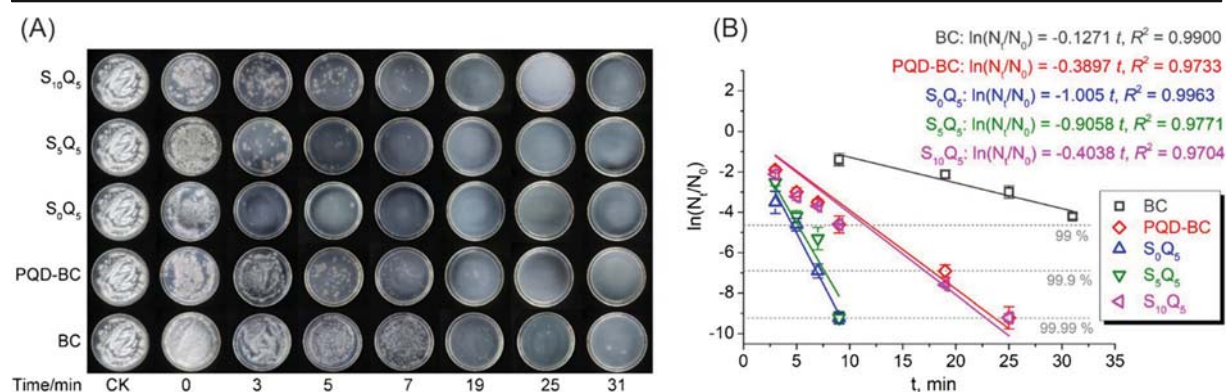


Fig. 2 **a** Growth of *Foc4* conidia on agar plates after S_0Q_5 , PQD-BC and BC treatment (30 $\mu\text{g/mL}$). With the extension of the incubation time, the number of colonies in the 100 μL mixture in the plate gradually decreased. **b** Inactivation kinetics of S_0Q_5 , PQD-BC and BC (30 $\mu\text{g/mL}$) on *Foc4* conidia. (The missing data point for BC at 3 to 7 min was because the number of colonies in

the Petri dish was too large to count). All experiments were performed twice with three replications for each treatment. Representative results from one experiment are shown in (A) whereas the average of the two experiments are shown in (B). Error bars represent the standard error of the mean

Discussion

The continuing development of fungicide resistance in plants necessitates the discovery of new fungicides with new or different modes of action (Ammar et al., 2013). Cationic polymers possess potent broad-spectrum

antimicrobial activity (Peng et al., 2019; Venkataraman et al., 2019) and do not elicit fungicide resistance (Lou et al., 2018). It has been found that cationic polymers have good inhibitory effects on fungi and the structure of the polymer is one of the key factors that determine its antifungal properties (Gilbert & Moore, 2005; Jiao et al.,

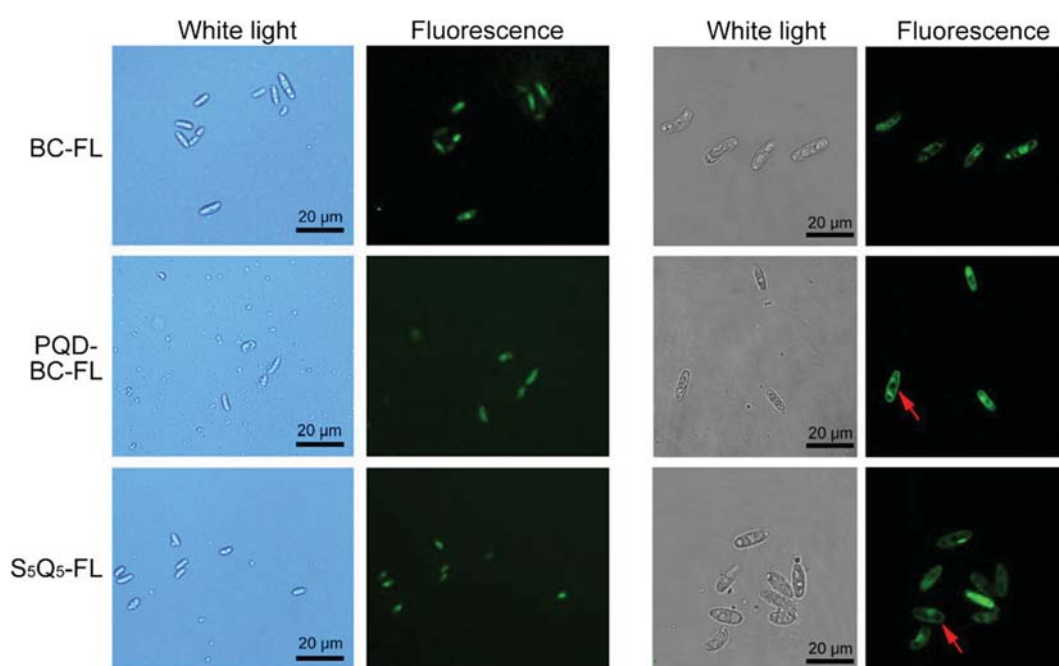
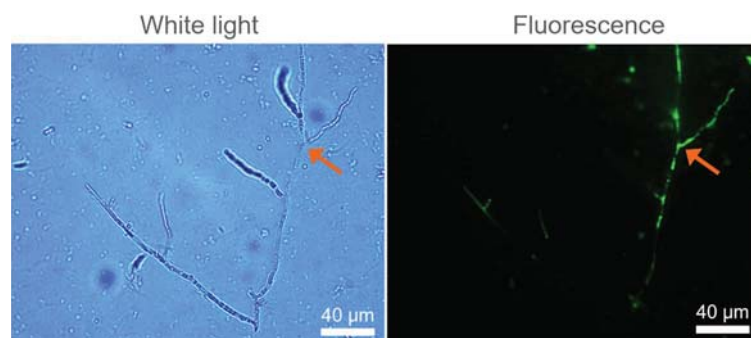


Fig. 3 **a** Differential interference microscopy micrographs of *Foc4* conidia. After *Foc4* conidia were treated with BC-FL, PQD-BC-FL or S_5Q_5 -FL at a concentration of 40 mg/mL for 3 min, clear green fluorescence was seen in all conidia. **b** Confocal microscopy of QASS-FL entering *Foc4* conidia. Conidia treated

with PQD-BC-FL and S_5Q_5 -FL showed clear outlines and fluorescence in the cell wall or cell membrane, as shown by the red arrow. The outer edge of the conidia treated with BC-FL was fuzzy and there was no obvious fluorescence in the cell wall or cell membrane

Fig. 4 Differential interference microscopy micrographs of *Foc4* conidia. After *Foc4* conidia were treated with S_nQ_5 -FL at a concentration of 0.1 mg/mL for 2 d, clear green fluorescence was seen in the newly formed hyphae



2017). Studies of how the polymers inhibit fungi are helpful to understand the relationship between the structure and antifungal activity and will be helpful for the development of new cationic polymers that can be used to control plant diseases.

Fusarium wilt of bananas is a serious soil-borne fungal disease and pathogen spores is an obvious target for controlling the disease. Thus, inhibiting or killing the *Foc4* conidia in soil is of great significance to the control of banana Fusarium wilt (Xue et al., 2015). Izquierdo-García et al. (2021) found that in the absence of soil, 10 kinds of commercial small molecular quaternary ammonium compounds showed 100% biocidal efficiency against microconidia, macroconidia and chlamydospores at both <1 and 15 min, while the presence of soil significantly decreased the efficacy of most of the disinfectants. Different from the commercial small molecular quaternary ammonium compounds, we previously found that if *Foc4* was added to the soil every second day, the inhibitory effect of polydimethylsiloxane-polymethacrylate block copolymers containing quaternary ammonium salts (S_nQ_5) could be maintained for 30 days and if *Foc4* was

added to the soil every 10 days, the inhibitory effect of S_nQ_5 could be maintained for 90 days. The impact of S_nQ_5 on the number of three types of microbial species (i.e. bacteria, fungi and actinomycetes) in the soil was evaluated (Chang et al., 2021). It was found that the number of fungi was reduced whereas the number of bacteria and actinomycetes was increased. This indicates that S_nQ_5 may not have a devastating impact on the microbial population in the soil, meaning that the impact may be acceptable. Most of the control methods based on soil fungicides and soil fumigation, such as methyl bromide or calcium cyanamide treatments, could kill almost all the microorganisms (including *Foc4*) in soil in a short time, but this would also completely destroy the microbial community and its functional diversity in the soil and the fumigated areas might eventually be re-attacked by the pathogen, making the next fruit production impossible (Herbert & Marx, 1990). Furthermore, compared with the soil disinfectant, the environmental toxicity risk is greatly reduced after soil adsorption because S_nQ_5 can be adsorbed in the soil. Pot experiments also showed that S_nQ_5 had a good control effect on Fusarium wilt of

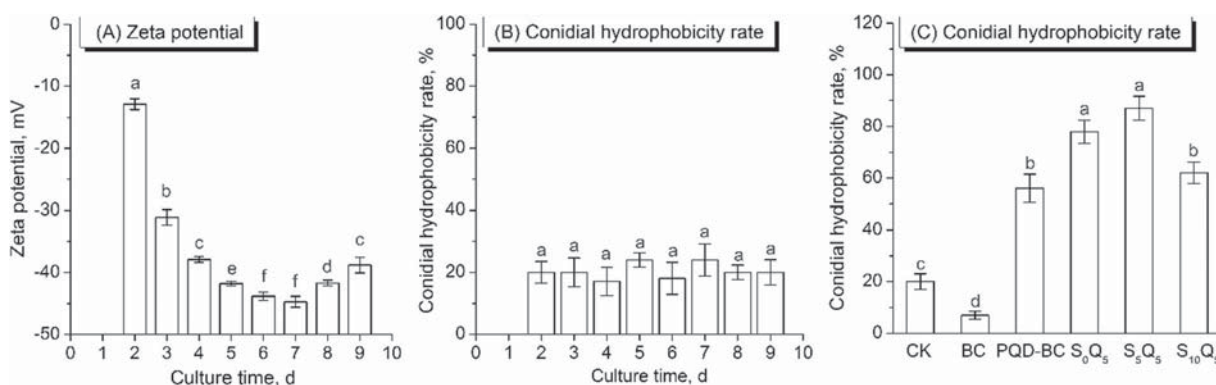


Fig. 5 Effect of culture time (days) in sterile water on: (A) The zeta potential of the *Foc4* conidial surfaces; (B) Conidial hydrophobicity and; (C) Effect of S_nQ_5 , PQD-BC and BC treatments on the conidial hydrophobicity. All experiments were performed

twice with three replications for each treatment. The figure shows averages of the two experiments. Error bars represent the standard error of the mean. Treatments followed by different letters are statistically different at $P < 0.05$

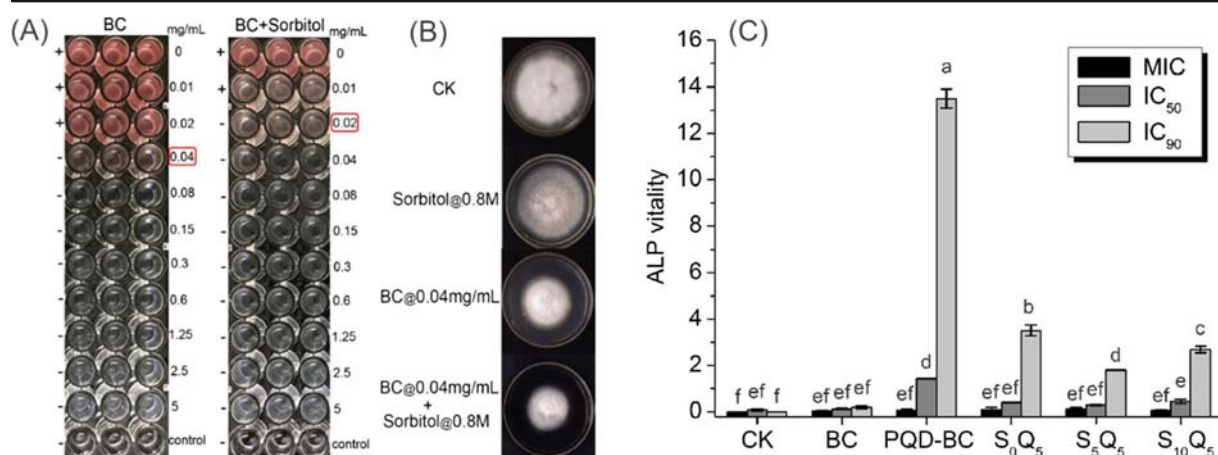


Fig. 6 **A** The minimum inhibitory concentration (MIC) of sorbitol and BC against *Foc4* based on the 2,3,5-triphenyl tetrazolium chloride colorimetric method; (+) indicates live cells in the plate and (–) indicates fewer or no cells in the plate. **B** The typical mycelial growth of *Foc4* on PDA medium after sorbitol and BC were applied. The experiments were performed twice and representative results are shown. **C** Effect of S_nQ₅, PQD-BC and BC on

alkaline phosphatase (ALP) content in *Foc4* culture medium. All experiments were performed twice with three replications for each treatment. Averages of the two experiments are shown in (C). Error bars represent the standard error of the mean. Treatments followed by different letters are statistically different at $P < 0.05$

banana and did not harm banana seedlings (Chang et al., 2021). These results show the potential of S_nQ₅ in banana fields to long term prevention of invasion by *Foc4*.

In this study, we further investigated the inactivation kinetics of S_nQ₅ on *Foc4* conidia and the adsorption and destruction of S_nQ₅ on the cell wall of *Foc4* conidia. Conidial germination was completely inhibited when the S_nQ₅ concentration was more than 40 µg/mL (Fig. 1). Meldrum et al. (2013) also found Sporekill™, which contain a quaternary ammonium compound as an active ingredient, could inhibit the germination of *Foc4* spores. The efficiency of killing fungal spores would be an important factor to evaluate the performance of fungicides. Our study also

found that S_nQ₅ could kill *Foc4* spores completely within 10 min (Fig. 2) and therefore, it shows promise as a sporicide against *Foc4*. The amphiphilic polymeric quaternary ammonium salts (S_nQ₅) had the highest inactivation efficiencies on *Foc4* conidia, followed by the hydrophilic macromolecular quaternary ammonium salt (PQD-BC) and finally the small molecular quaternary ammonium salt (BC) (Fig. 2). As described in the literature, structural parameters such as hydrophobicity/hydrophilicity balance, molecular weight and the length of carbon chain likely affect the antifungal activities (Muñoz-Bonilla & Fernández-García, 2012; Obłak et al., 2013; Ganewatta & Tang, 2015). Compared with BC, S_nQ₅ showed rapid fungicidal efficiency, which is

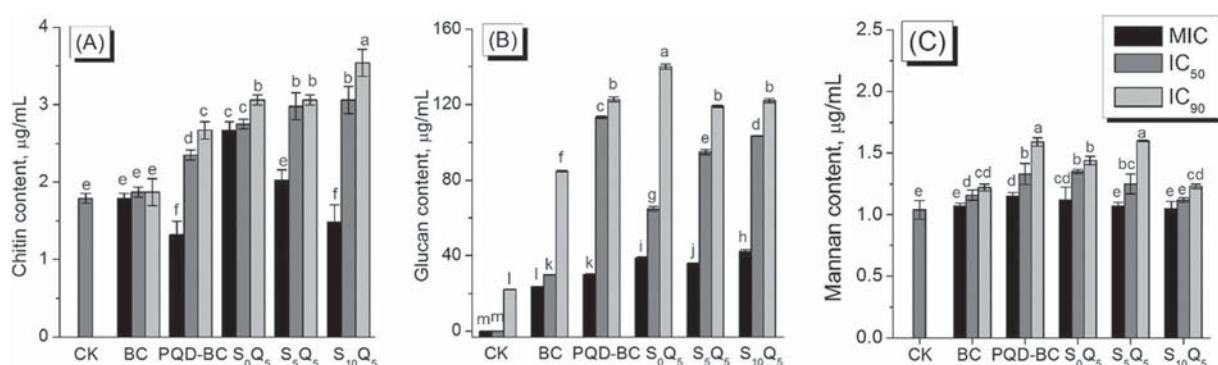


Fig. 7 Effects of S_nQ₅, PQD-BC and BC on cell wall components of *Foc4* conidia. **A** Chitin. **B** Glucan. **C** Mannose. All experiments were performed twice with three replications for each treatment.

The figure show averages of the two experiments. Error bars represent the standard error of the mean. Treatments followed by different letters are statistically different at $P < 0.05$

mainly due to the polymeric structure and the increasing proportion of hydrophobic segments.

The cell wall is essential for maintaining fungal cell shape and integrity (Ivey et al., 2017). It is often considered as one of the targets of drugs attacking fungi (Cortés et al., 2019; Zuo et al., 2015). To cause fungal death, the quaternary ammonium salts (QASs) have to be absorbed onto the cell and alter the inherent charge of the cell wall (Jiao et al., 2017). Microscopy (Fig. 3) demonstrated that S_nQ_5 could not only enter the interior of *Foc4* conidia, but also effectively adsorb to the surface of conidia. This effective adsorption is mainly achieved through the following steps: firstly, the conidial surface is negatively charged (Fig. 5A) and S_nQ_5 is positively charged, so they have electrostatic adsorption; secondly, our study found that S_nQ_5 could significantly change the conidial hydrophobicity (Fig. 5C). Like other filamentous fungi (Shan, 2009; Wösten, 2001), the hydrophobin in the *Foc4* conidial wall endows it with hydrophobic characteristics (Fig. 5B). The hydrophilic groups of S_nQ_5 can be combined with the *Foc4* conidial wall, making the hydrophobic groups of S_nQ_5 face the aqueous solution. It is reported that the hydrophobicity of spores could prevent fungi from losing water and play a role in preventing disinfectants from entering the spores during disinfection (Wen et al., 2019). The ability to change the conidial hydrophobicity is the difference between S_nQ_5 and other disinfectants (including chlorine and other small molecular cationic compounds) in the mechanism of inhibiting spores (Nguyen et al., 2019; Shen et al., 2019). In this study, we found that S_5Q_5 -FL could be taken up continually by the newly formed hypha (Fig. 4) and affect the internal structure of hypha and inhibit their activity (Dong et al., 2018). In our future work, the impact of invasive S_5Q_5 on the internal structure and activity of new hyphae will be further studied.

Cell wall integrity plays an important role in responses to external stress and in fungal growth and pathogenicity (Malavazi et al., 2014). The effect of fungicides on fungal cell wall integrity is often evaluated by the sorbitol protection test (Turecka et al., 2018). The increase of minimum inhibitory concentration (MIC) in the experiments with sorbitol could indicate the cell wall as a potential target of action of the compound (Leite et al., 2015; Turecka et al., 2018). We found that when *Foc4* was treated with BC in a medium supplemented with sorbitol, the MIC decreased after two days of incubation compared to the MIC in medium without sorbitol (Fig. 6A).

The experimental results using the mycelium growth inhibition method (Zhong et al., 2017) further confirmed that sorbitol and BC had a synergistic effect on the inhibition of *Foc4* mycelium growth (Fig. 6B). Therefore, this method might not be suitable for QASs. Alkaline phosphatase (ALP) is an enzyme produced in the cytoplasm and leaked into the periplasmic space. Generally, ALP is released from fungal cells with impaired cell wall permeability (Ouyang et al., 2019). In our previous work, we found that BC caused leakage of ALP and thus damaged the cell wall integrity of *Foc4* hyphae (Huang et al., 2017). In this study, BC could hardly cause leakage of ALP from *Foc4* conidia and a significantly higher ALP activity was observed in PQAS treatments, indicating that PQASs disrupted the cell wall permeability of *Foc4* conidia.

The fungal cell wall contains glucan, mannose and chitins, in which chitin is considered as one of the core polysaccharide components of the fungal cell wall. Glucan is a conserved “stealth” molecule in the cell walls of phytopathogenic fungi, which protects the intruder from being recognised by the host plant and melanin is a dark-pigmented proteinaceous polymer that provides appressoria of numerous plant-pathogenic fungi with their characteristic dark brown/black appearance (Cortés et al., 2019; Ivey et al., 2017). In this study, S_nQ_5 was adsorbed to the conidial cell wall and destroyed the cell wall structure, resulting in a significantly increased concentration of chitin, mannose and other components of the cell wall in the extracellular solution (Fig. 7). Therefore, the cell wall might be one of the targets of S_nQ_5 copolymers attacking conidia. Limited by methodological difficulties, the exact target points in cell wall are still poorly understood, but we hope to explore this further in the future. Also, from a practical point of view, although pot experiments have been performed in our previous work (Chang et al., 2021), field testing still needs to be carried out.

Collectively, our results revealed that three kinds of QASs (S_nQ_5 , PQD-BC and BC) had strong inhibitory effects on the growth and germination of *Foc4* conidia and the effect was rapid. Among these QASs, the destruction of conidial morphology by S_nQ_5 containing hydrophobic blocks was stronger and faster than that by the SQAS (BC). S_nQ_5 can increase the hydrophobic ratio of the conidial surface, act on the main components of the conidial cell wall and destroy the integrity of the cell wall. The addition of hydrophobic segments can enhance the inhibitory strength and inhibitory rate of PQASs, which was beneficial for guiding the synthesis of PQASs

with improved performance and promoting the application of PQASs in the control of Fusarium wilt in banana.

Supplementary Information The online version contains supplementary material available at <https://doi.org/10.1007/s10658-022-02608-5>.

Acknowledgments This work was supported by the National Natural Science Foundation of China under grant 31772202; the Scientific and Technological Planning Project of Guangzhou City (201803020015).

Author contribution Wei ZHANG: methodology, data curation, writing, original draft preparation; Yaoyao CHANG: methodology, data curation, writing, original draft preparation; Weiqiang ZHONG: data curation; Anqiang ZHANG: conceptualization, writing, reviewing and editing, supervision; Yaling LIN: conceptualization, writing, reviewing and editing, supervision.

Declarations

Competing interests The authors declare that they have no known competing financial interests or personal relationships that could have appeared to influence the work reported in this paper.

References

- Abid, C. Z., Jain, S., Jackeray, R., Chattopadhyay, S., & Singh, H. (2017). Formulation and characterization of antimicrobial quaternary ammonium dendrimer in poly(methyl methacrylate) bone cement. *Journal of Biomedical Materials Research Part B: Applied Biomaterials*, 105(3), 521–530. <https://doi.org/10.1002/jbm.b.33553>
- Ammar, M. I., Nenaah, G. E., & Mohamed, A. H. H. (2013). Antifungal activity of prenylated flavonoids isolated from *Tephrosia apollinea* L. against four phytopathogenic fungi. *Crop Protection*, 49, 21–25. <https://doi.org/10.1016/j.cropro.2013.02.012>
- Buffet-Bataillon, S., Tattevin, P., Bonnaure-Mallet, M., & Jolivet-Gougeon, A. (2012). Emergence of resistance to antibacterial agents: The role of quaternary ammonium compounds—A critical review. *International Journal of Antimicrobial Agents*, 39(5), 381–389. <https://doi.org/10.1016/j.ijantimicag.2012.01.011>
- Chang, Y., Zhong, W., Liang, J., Zhang, A., & Lin, Y. (2021). Polydimethylsiloxane-polymethacrylate block copolymers containing quaternary ammonium salts against *Fusarium oxysporum* f. sp. *cubense* race 4 in soil: Antifungal activities and pot experiments. *Reactive and Functional Polymers*, 160, 104848. <https://doi.org/10.1016/j.reactfunctpolym.2021.104848>
- Cheng, K. J., Ingram, J. M., & Costerton, J. W. (1970). Release of alkaline phosphatase from cells of *Pseudomonas aeruginosa* by manipulation of cation concentration and of pH. *Journal of Bacteriology*, 104, 748–753.
- Cortés, J., Curto, M., Carvalho, V., Pérez, P., & Ribas, J. (2019). The fungal cell wall as a target for development of new antifungal therapies. *Biotechnology Advances*, 37, 107352. <https://doi.org/10.1016/j.biotechadv.2019.02.008>
- Dalrymple, O. K., Stefanakos, E., Trotz, M. A., & Goswami, D. Y. (2010). A review of the mechanisms and modeling of photocatalytic disinfection. *Applied Catalysis B: Environmental*, 98(1–2), 27–38. <https://doi.org/10.1016/j.apcatb.2010.05.001>
- Dita, M., Barquero, M., Heck, D., Mizubuti, E. S., & Staver, C. P. (2018). Fusarium wilt of banana: Current knowledge on epidemiology and research needs toward sustainable disease management. *Frontiers in Plant Science*, 9, 1468. <https://doi.org/10.3389/fpls.2018.01468>
- Dong, C., You, W., Liuyang, R., Lei, Y., Zhang, A., & Lin, Y. (2018). Anti-*Rhizoctonia solani* activity by polymeric quaternary ammonium salt and its mechanism of action. *Reactive and Functional Polymers*, 125, 1–10. <https://doi.org/10.1016/j.reactfunctpolym.2018.01.020>
- Fernandes, C., Mota, M., Barros, L., Dias, M. I., Ferreira, I. C., Piedade, A. P., Casadevall, A., & Gonçalves, T. (2021). Pyomelanin synthesis in *Alternaria alternata* inhibits DHN-melanin synthesis and decreases cell wall chitin content and thickness. *Frontiers in Microbiology*, 12, 691433. <https://doi.org/10.3389/fmicb.2021.691433>
- Ganewatta, M., & Tang, C. (2015). Controlling macromolecular structures towards effective antimicrobial polymers. *Polymer*, 63, A1–A29. <https://doi.org/10.1016/j.polymer.2015.03.007>
- Gilbert, P., & Moore, L. E. (2005). Cationic antiseptics: Diversity of action under a common epithet. *Journal of Applied Microbiology*, 99(4), 703–715. <https://doi.org/10.1111/j.1365-2672.2005.02664.x>
- Girardin, H., Paris, S., Rault, J., Bellon-Fontaine, M. N., & Latgé, J. P. (1999). The role of the rodlet structure on the physico-chemical properties of *aspergillus* conidia. *Letters in Applied Microbiology*, 29(6), 364–369. <https://doi.org/10.1046/j.1472-765x.1999.00643.x>
- Gou, Y. P., Meghil, M. M., Pucci, C. R., Breschi, L., Pashley, D. H., Cutler, C. W., Niu, L., Li, J., & Tay, F. R. (2018). Optimizing resin-dentin bond stability using a bioactive adhesive with concomitant antibacterial properties and anti-proteolytic activities. *Acta Biomaterialia*, 75, 171–182. <https://doi.org/10.1016/j.actbio.2018.06.008>
- Guerriero, G., Avino, M., Zhou, Q., Fugelstad, J., Clergeot, P. H., & Bulone, V. (2010). Chitin synthases from *Saprolegnia* are involved in tip growth and represent a potential target for anti-oomycete drugs. *PLoS Pathogens*, 6(8), e1001070. <https://doi.org/10.1371/journal.ppat.1001070>
- Halder, S., Yadav, K. K., Sarkar, R., Mukherjee, S., Saha, P., Halder, S., Karmakar, S., & Sen, T. (2015). Alteration of zeta potential and membrane permeability in bacteria: A study with cationic agents. *SpringerPlus*, 4(1), 1–14. <https://doi.org/10.1186/s40064-015-1476-7>
- Han, S., He, L., Liu, Y., Cheng, J., & Yang, L. (2014). Quick determination of β -glucan from phellinus by fluorometry method. *Modern Chemical Industry*, 34, 156–158. (in Chinese). <https://doi.org/10.16606/j.cnki.issn0253-4320.2014.06.005>
- Herbert, J. A., & Marx, D. (1990). Short-term control of Panama disease of bananas in South Africa. *Phytophylactica*, 22(3), 339–340.

- Huang, Z., Liuyang, R., Dong, C., Lei, Y., Zhang, A., & Lin, Y. (2017). Polymeric quaternary ammonium salt activity against *fusarium oxysporum* f. sp. *cubense* race 4: Synthesis, structure-activity relationship and mode of action. *Reactive and Functional Polymers*, 114, 13–22. <https://doi.org/10.1016/j.reactfunctpolym.2017.02.013>
- Ioannou, C. J., Hanlon, G. W., & Denyer, S. P. (2007). Action of disinfectant quaternary ammonium compounds against *Staphylococcus aureus*. *Antimicrobial Agents and Chemotherapy*, 51(1), 296–306. <https://doi.org/10.1128/AAC.00375-06>
- Ivey, G., Gero, S., & Sarah, G. (2017). The role of the fungal Cell Wall in the infection of plants. *Trends in Microbiology*, 25(12), 957–967. <https://doi.org/10.1016/j.tim.2017.05.015>
- Izquierdo-García, L. F., Carmona, S. L., Zuluaga, P., Rodríguez, G., Dita, M., Betancourt, M., & Soto-Suárez, M. (2021). Efficacy of disinfectants against *fusarium oxysporum* f. sp. *cubense* tropical race 4 isolated from La Guajira, Colombia. *Journal of Fungi*, 7, 297. <https://doi.org/10.3390/jof7040297>
- Jiao, Y., Niu, L. N., Ma, S., Li, J., Tay, F. R., & Chen, J. H. (2017). Quaternary ammonium-based biomedical materials: State-of-the-art, toxicological aspects and antimicrobial resistance. *Progress in Polymer Science*, 71, 53–90. <https://doi.org/10.1016/j.progpolymsci.2017.03.001>
- Kahn, J. N., Hsu, M. J., Racine, F., Giacobbe, R., & Motyl, M. (2006). Caspofungin susceptibility in *aspergillus* and non-*aspergillus* molds: Inhibition of glucan synthase and reduction of β -d-1, 3 glucan levels in culture. *Antimicrobial Agents and Chemotherapy*, 50(6), 2214–2216. <https://doi.org/10.1128/aac.01610-05>
- Lei, Y., Zhou, S., Dong, C., Zhang, A., & Lin, Y. (2018). PDMS tri-block copolymers bearing quaternary ammonium salts for epidermal antimicrobial agents: Synthesis, surface adsorption and non-skin-penetration. *Reactive and Functional Polymers*, 124, 20–28. <https://doi.org/10.1016/j.reactfunctpolym.2018.01.007>
- Leite, M. C. A., de Brito Bezerra, A. P., de Sousa, J. P., & de Oliveira Lima, E. (2015). Investigating the antifungal activity and mechanism(s) of geraniol against *Candida albicans* strains. *Medical Mycology*, 53(3), 275–284. <https://doi.org/10.1093/mmy/myu078>
- Lin, Q., Zheng, J., Cai, D., Lin, Y., Xia, B., & Zhang, F. (2015). Determination of Mannan and β -glucan in yeast Cell Wall by HPLC with pre-column derivatization. *Journal of Instrumental Analysis*, 34, 106–110. (in Chinese). <https://doi.org/10.3969/j.issn.1004-4957.2015.01.017>
- Lin, Y., Liu, Q., Cheng, L., Lei, Y., & Zhang, A. (2014). Synthesis and antimicrobial activities of polysiloxane-containing quaternary ammonium salts on bacteria and phytopathogenic fungi. *Reactive and Functional Polymers*, 85, 19–30. <https://doi.org/10.1016/j.reactfunctpolym.2014.10.002>
- Lin, Y., Zhong, W., Dong, C., Zhang, C., Feng, X., & Zhang, A. (2018). Synthesis and antifungal activities of amphiphilic PDMS-*b*-QPMAEMA copolymers on *Rhizoctonia solani*. *ACS Applied Bio Materials*, 1(6), 2062–2072. <https://doi.org/10.1021/acsabm.8b00545>
- Liu, F., Diao, C., Song, B., Yang, S., Hu, D., Wang, J., Zeng, S., & Huang, R. (2007). Inhibition activity and mechanism primary study of Guangkuling 3% AS to *fusarium oxysporum* f.sp. *capsicum*. *Agrochemicals*, 89–91. (in Chinese). <https://doi.org/10.16820/j.cnki.1006-0413.2007.02.005>
- Liu, X., Bao, T., Zheng, L., Kgosi, V. T., Liu, X., & Liu, H. (2021). Cell wall integrity in *Magnaporthe oryzae* is weakened by proteins secreted by *bacillus licheniformis* BL06. *Biological Control*, 157, 104582. <https://doi.org/10.1016/j.biocontrol.2021.104582>
- Lou, W., Venkataraman, S., Zhong, G., Ding, B., Tan, J. P., Xu, L., Fan, W., & Yang, Y. Y. (2018). Antimicrobial polymers as therapeutics for treatment of multidrug-resistant *Klebsiella pneumoniae* lung infection. *Acta Biomaterialia*, 78, 78–88. <https://doi.org/10.1016/j.actbio.2018.07.038>
- Malavazi, I., Goldman, G. H., & Brown, N. A. (2014). The importance of connections between the cell wall integrity pathway and the unfolded protein response in filamentous fungi. *Briefings in Functional Genomics*, 13, 456–470. <https://doi.org/10.1093/bfpg/elu027>
- Matsuoka, H., Hashimoto, K., Saijo, A., Takada, Y., Kondo, A., Ueda, M., Ooshima, H., Tachibana, T., & Azuma, M. (2014). Cell wall structure suitable for surface display of proteins in *Saccharomyces cerevisiae*. *Yeast*, 31(2), 67–76. <https://doi.org/10.1002/yea.2995>
- Meldrum, R. A., Daly, A. M., Tran-Nguyen, L. T. T., & Aitken, E. A. B. (2013). The effect of surface sterilants on spore germination of *fusarium oxysporum* f. sp. *cubense* tropical race 4. *Crop Protection*, 54, 194–198. <https://doi.org/10.1016/j.cropro.2013.08.014>
- Muñoz-Bonilla, A., & Fernández-García, M. (2012). Polymeric materials with antimicrobial activity. *Progress in Polymer Science*, 37(2), 281–339. <https://doi.org/10.1016/j.progpolymsci.2011.08.005>
- Narita, T., Ohtakeyama, R., Matsukata, M., Gong, J. P., & Osada, Y. (2001). Kinetic study of cell disruption by ionic polymers with varied charge density. *Colloid and Polymer Science*, 279(2), 178–183. <https://doi.org/10.1007/s003960000411>
- Nel, B., Steinberg, C., Labuschagne, N., & Viljoen, A. (2006). The potential of nonpathogenic *fusarium oxysporum* and other biological control organisms for suppressing fusarium wilt of banana. *Plant Pathology*, 55(2), 217–223. <https://doi.org/10.1111/j.1365-3059.2006.01344.x>
- Nel, B., Steinberg, C., Labuschagne, N., & Viljoen, A. (2007). Evaluation of fungicides and sterilants for potential application in the management of fusarium wilt of banana. *Crop Protection*, 26(4), 697–705. <https://doi.org/10.1016/j.cropro.2006.06.008>
- Nguyen, T. V., Tran-Nguyen, L. T. T., Wright, C. L., Trevorrow, P., & Grice, K. (2019). Evaluation of the efficacy of commercial disinfectants against *fusarium oxysporum* f. sp. *cubense* race 1 and tropical race 4 propagules. *Plant Disease*, 103(4), 721–728. <https://doi.org/10.1094/pdis-03-18-0453-re>
- Oblak, E., Piecuch, A., Krasowska, A., & Łuczyński, J. (2013). Antifungal activity of gemini quaternary ammonium salts. *Microbiological Research*, 168(10), 630–638. <https://doi.org/10.1016/j.progpolymsci.2011.08.005>
- Ouyang, Q. L., Duan, X. F., & Tao, N. G. (2019). Cinnamaldehyde exerts its antifungal activity by disrupting the cell wall integrity of *Geotrichum citri-aurantii*. *Frontiers in Microbiology*, 10, 55. <https://doi.org/10.3389/fmicb.2019.00055>
- Peng, C., Vishwakarma, A., Mankoci, S., Barton, H. A., & Joy, A. (2019). Structure-activity study of antibacterial poly (ester urethane) s with uniform distribution of hydrophobic and

- cationic groups. *Biomacromolecules*, 20(4), 1675–1682. <https://doi.org/10.1021/acs.biomac.9b00029>
- Ploetz, R., Freeman, S., Konkol, J., Al-Abed, A., Naser, Z., Shalan, K., Barakat, R., & Israeli, Y. (2015). Tropical race 4 of Panama disease in the Middle East. *Phytoparasitica*, 43(3), 283–293. <https://doi.org/10.1007/s12600-015-0470-5>
- Rembaum, A. S. A. E., Senyei, A. E., & Rajaraman, R. (1977). Interaction of living cells with polyionenes and polyionene-coated surfaces. *Journal of Biomedical Materials Research*, 11(1), 101–110. <https://doi.org/10.1002/jbm.820110110>
- Shah, F. A., Allen, N., Wright, C. J., & Butt, T. M. (2007). Repeated *in vitro* subculturing alters spore surface properties and virulence of *Metarhizium anisopliae*. *FEMS Microbiology Letters*, 276(1), 60–66. <https://doi.org/10.1111/j.1574-6968.2007.00927.x>
- Shan, L. (2009). Biocontrol potential of *Metarhizium* isolates against aphids and hydrophobicity-related traits of *Beauveria bassiana*, *Metarhizium* spp. and *Paecilomyces fumosoroseus* for use in microbial control. *Ph.D. Dissertation. Zhejiang University*. Hangzhou, China (in Chinese).
- Shao, X., Cheng, S., Wang, H., Yu, D., & Mungai, C. (2013). The possible mechanism of antifungal action of tea tree oil on *Botrytis cinerea*. *Journal of Applied Microbiology*, 114(6), 1642–1649. <https://doi.org/10.1111/jam.12193>
- Shen, Z., Xue, C., Penton, C. R., Thomashow, L. S., Zhang, N., Wang, B., & Shen, Q. (2019). Suppression of banana Panama disease induced by soil microbiome reconstruction through an integrated agricultural strategy. *Soil Biology and Biochemistry*, 128, 164–174. <https://doi.org/10.1016/j.soilbio.2018.10.016>
- Steinkellner, S., Mammerler, R., & Vierheilig, H. (2005). Microconidia germination of the tomato pathogen *fusarium oxysporum* in the presence of root exudates. *Journal of Plant Interactions*, 1(1), 23–30. <https://doi.org/10.1080/17429140500134334>
- Sun, L., Song, S., Fu, L., Deng, X., Wang, D., Liang, X., Li, R., & Shen, Q. (2015). Exploring a soil fumigation strategy based on ammonium bicarbonate to control fusarium wilts of cucurbits. *Crop Protection*, 70, 53–60. <https://doi.org/10.1016/j.cropro.2015.01.004>
- Sun, Y., Dong, W., Sun, L., Ma, L., & Shang, D. (2015). Insights into the membrane interaction mechanism and antibacterial properties of chensinin-1b. *Biomaterials*, 37, 299–311. <https://doi.org/10.1016/j.biomaterials.2014.10.041>
- Turecka, K., Chylewska, A., Kawiak, A., & Waleron, K. F. (2018). Antifungal activity and mechanism of action of the co (III) coordination complexes with diamine chelate ligands against reference and clinical strains of *Candida* spp. *Frontiers in Microbiology*, 9, 1594. <https://doi.org/10.3389/fmicb.2018.01594>
- Venkataraman, S., Tan, J. P., Chong, S. T., Chu, C. Y., Wilianto, E. A., Cheng, C. X., & Yang, Y. Y. (2019). Identification of structural attributes contributing to the potency and selectivity of antimicrobial polyionenes: Amides are better than esters. *Biomacromolecules*, 20(7), 2737–2742. <https://doi.org/10.1021/acs.biomac.9b00489>
- Wen, G., Xu, X., Zhu, H., Huang, T., & Ma, J. (2017). Inactivation of four genera of dominant fungal spores in groundwater using UV and UV/PMS: Efficiency and mechanisms. *Chemical Engineering Journal*, 328, 619–628. <https://doi.org/10.1016/j.cej.2017.07.055>
- Wen, G., Zhao, D., Xu, X. Q., Chen, Z. H., Huang, T. L., & Ma, J. (2019). Inactivation of fungi from four typical genera in groundwater using PMS/cl⁻ system: Efficacy, kinetics and mechanisms. *Chemical Engineering Journal*, 357, 567–578. <https://doi.org/10.1016/j.cej.2018.09.195>
- Wösten, H. A. B. (2001). Hydrophobins: multipurpose proteins. *Annual Review in Microbiology*, 55, 625–646. <https://doi.org/10.1146/annurev.micro.55.1.625>
- Xue, Y., Xiao, H., & Zhang, Y. (2015). Antimicrobial polymeric materials with quaternary ammonium and phosphonium salts. *International Journal of Molecular Sciences*, 16(2), 3626–3655. <https://doi.org/10.3390/ijms16023626>
- Zhang, A., Liu, Q., Lei, Y., Hong, S., & Lin, Y. (2015). Synthesis and antimicrobial activities of acrylamide polymers containing quaternary ammonium salts on bacteria and phytopathogenic fungi. *Reactive and Functional Polymers*, 88, 39–46. <https://doi.org/10.1016/j.reactfunctpolym.2015.02.005>
- Zhang, C., Cui, F., Zeng, G., Jiang, M., Yang, Z., Yu, Z., Zhu, M., & Shen, L. (2015). Quaternary ammonium compounds (QACs): A review on occurrence, fate and toxicity in the environment. *Science of the Total Environment*, 518, 352–362. <https://doi.org/10.1016/j.scitotenv.2015.03.007>
- Zhong, W., Dong, C., Liuyang, R., Guo, Q., Zeng, H., Lin, Y., & Zhang, A. (2017). Controllable synthesis and antimicrobial activities of acrylate polymers containing quaternary ammonium salts. *Reactive and Functional Polymers*, 121, 110–118. <https://doi.org/10.1016/j.reactfunctpolym.2017.10.010>
- Zuo, C., Li, C., Li, B., Wei, Y., Hu, C., Yang, Q., Yang, J., Sheng, O., Kuang, R., Deng, G., Biswas, M. K., & Yi, G. (2015). The toxic mechanism and bioactive components of Chinese leek root exudates acting against *fusarium oxysporum* f. sp. *cubense* tropical race 4. *European Journal of Plant Pathology*, 143(3), 447–460. <https://doi.org/10.1007/s10658-015-0697-5>

Springer Nature or its licensor holds exclusive rights to this article under a publishing agreement with the author(s) or other rightsholder(s); author self-archiving of the accepted manuscript version of this article is solely governed by the terms of such publishing agreement and applicable law.



A systematic study on Zn(II)-Iminocarboxyl complexation applied in supramolecular PDMS networks

Jiaheng Mo^a, Weijian Wu^a, Shijie Shan^a, Xionghui Wu^a, Danni Li^a, Rui Li^a, Yaling Lin^{b,*,**}, Anqiang Zhang^{a,*}

^a School of Materials Science and Engineering, South China University of Technology, 381 Wushan Rd., Guangzhou, 510641, Guangdong, China

^b College of Materials and Energy, South China Agricultural University, 483 Wushan Rd., Guangzhou, 510642, Guangdong, China

ARTICLE INFO

Keywords:

Supramolecular elastomers
Polysiloxanes
Metal-ligand complex
Molecular dynamic simulation

ABSTRACT

Metal-ligand coordination was used to construct supramolecular elastomers with self-healing ability and excellent mechanical properties. In this study, novel iminocarboxyl-functionalized polysiloxanes (PDMS-Iminocarboxyl) was synthesized through amine-functionalized polysiloxanes (PDMS-NH₂) with acrylic acid by aza-Michael addition based on ¹H NMR and FTIR spectroscopy. The incorporation of zinc ions into the PDMS-Iminocarboxyl as chemical crosslinks could essentially improve the thermal and mechanical properties because of highly dynamic Zn(II)-iminocarboxyl complexation. The stoichiometric ratio of [Zn²⁺]/[COOH] were determined by NMR titration. Furthermore, the presence of dynamic Zn(II)-iminocarboxyl equilibrium could allow a degree of strain sensitivity upon various stretching rates based on tensile experiments and rheological analysis. From the DMA and rheological analysis, modulus transition of PDMS-Iminocarboxyl@Znx networks was closely related to the association-dissociation of Zn(II)-iminocarboxyl complexation. Besides, DFT calculations further provided the optimized configuration of metal-ligand complex according to the bond-valence-bond-length correlations.

1. Introduction

Supramolecular elastomers are a new class of polymer materials which have gathered great interest in academic and industrial fields because of their fascinating properties compared with conventional elastomers. It is extensively known that supramolecular elastomers could be prepared through hydrogen bonding [1–3], metal-ligand coordination [4–6], π - π stacking interactions [7,8], host-guest interactions [9–11], and ionic interactions [12–15], which could possess a wide range of thermal and mechanical properties. Zhang et al. [16] reported the carboxy-terminated polysiloxanes (HOOC-PDMS-COOH) to construct hydrogen bonding supramolecular elastomers. Incorporation of diethylenetriamine and urea have shown reasonable hysteresis and acceptable self-healing properties. A new class of multi-strength hydrogen bonding polymeric materials was designed by Bao et al. [17] which realized exceptional mechanical properties such as high stretchability (1200%) with notch insensitivity and high toughness of 1200 J/m². These tough elastomer materials (H₂N-PDMS-NH₂) enabled

fabrication of soft robotics and electronic skin. Miwa et al. [18] adopted ionic crosslinking by neutralizing partial carboxyl-grated polysiloxanes to obtain ionic supramolecular elastomers with high strength of 3.5 MPa. The rapid self-healing process was dramatically accelerated by CO₂ gas which effectively softened the ionic aggregates.

Recently, supramolecular elastomers [19] have been widely used in many potential applications such as sensors, shape-memory polymers, adhesives, coatings, etc. The new self-healing and renewable elastomers with comprehensive properties have received particular attention for replacing commercial products and applying in particular circumstances. Since there is adequate provision of metal complexes from various ions and ligands, these complexes were designed to construct supramolecular elastomers as an important component [20]. Significantly, metal-ligand coordination possesses dynamic reversible transition which can be induced by external stimuli, such as temperature, pressure, and pH value. Previous study revealed structurally well-defined zinc complexes containing zinc-carboxyl ligand applied in polymer networks. Bao et al. [21] developed PDMS networks based on

* Corresponding author.

** Corresponding author.

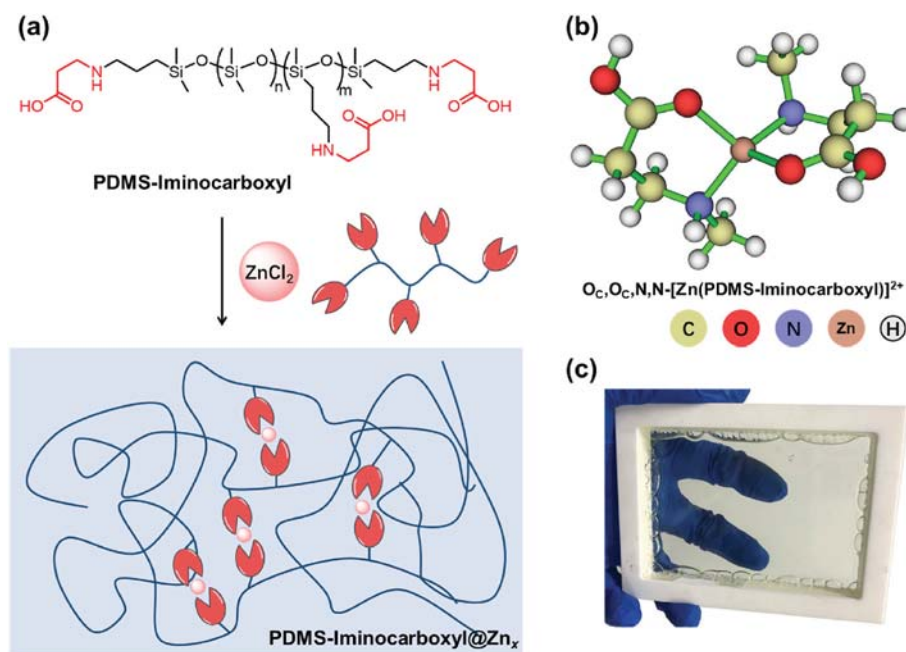
E-mail addresses: linyaling@scau.edu.cn (Y. Lin), aqzhang@scut.edu.cn (A. Zhang).

<https://doi.org/10.1016/j.polymer.2022.124896>

Received 30 January 2022; Received in revised form 20 March 2022; Accepted 22 April 2022

Available online 25 April 2022

0032-3861/© 2022 Published by Elsevier Ltd.



Scheme 1. (a) Structures of PDMS-Iminocarboxyl and PDMS-Iminocarboxyl@Zn_x network. (b) Optimal simulated structure of Zn(II)-iminocarboxyl complex where C (yellow), O (red), N (purple), Zn (brown), and H (light grey) atoms are presented. (c) Digital photo of PDMS-Iminocarboxyl@Zn_x in a self-made mould, which shows the high transmittance of the elastomer.

Fe(III)-2,6-pyridinedicarboxamide coordination complex. The synergistic effect of strong and weak coordination bonds breaking in succession resulted in high stretchability (up to 10,000%), high toughness (fracture energy $\sim 2600 \text{ J/m}^2$), and self-healing ability of the elastomers. Furthermore, Li et al. [22] designed and fabricated another PDMS elastomers based on thermodynamically stable while kinetically labile Zn-carboxyl coordination. Large association constants and fast exchange rates contributed to Zn(Hbimcp)₂-PDMS polymer with enhancing stretchability (up to 2400% strain) and high toughness (29.3 MJ/m^3). This polymer material could be potentially used as energy absorbing material. Zuo et al. [23] reported a PDMS networks containing abundant Zn(II)-carboxylate interactions. The rigid product possessed tensile strength up to 9 MPa but elongation at break less than 5% because of high carboxyl grafting ratios. The coordination equilibrium was so sensitive to temperature that the soft-rigid switching ability enabled advantageous applications such as in orthopedic immobilization, conductive composites/adhesives, and 3D printing. Another attempt of Zn(II)-carboxylate interactions via aza-Michael reaction of amino polysiloxanes and zinc acrylate was reported [13]. Sample with medium ion content possessed integrated mechanical properties (strain of $\sim 1000\%$ and strain of $\sim 3 \text{ MPa}$ at break) and high recovering efficiency ($\sim 90\%$) at mild processing temperature.

Herein, encouraged by the research for zinc-carboxylate interactions in various polymer networks, we proposed a systematic investigation on Zn(II)-iminocarboxyl complexation applied in PDMS networks as shown in Scheme 1. Such systems were easily achieved through aza-Michael addition with amine-functionalized polysiloxanes (PDMS-NH₂) with acrylic acid. Multiple stoichiometric ratio of $[\text{Zn}^{2+}]/[\text{COOH}]$ was achieved, resulted in different thermal and mechanical properties. Dynamic thermodynamic analysis, creep and stress relaxation behaviors, mechanical properties, self-healing and reprocessing ability were investigated. Besides, density functional theory (DFT) calculations could further provide the optimized configuration according to the bond-valence-bond-length correlations. Optimal structure of Zn(II)-iminocarboxyl complex contained weak Zn(II)-O_{COOH} bond and strong Zn(II)-N_{imino} bond. The synergistic effect of coordination bonds was essential for strain strengthening under various stretching rates. Association constants of two coordination bonds ($2.45 \times 10^2 \text{ M}^{-1}$ for Zn(II)-

O_{COOH}, $3.15 \times 10^3 \text{ M}^{-1}$ for Zn(II)-N_{imino}) were determined by NMR titration calculations. In conclusion, the study provides a systematic investigation on PDMS-Iminocarboxyl@Zn_x that can further shed light on the development of metal-ligand coordination supramolecular elastomers.

2. Experimental section

2.1. Materials

All materials and reagents were used as purchased without further purification. Octamethylcyclotetrasiloxane (D₄, 99%) was provided by Dow Corning Silicones (USA). 3-Aminopropyltriethoxymethylsilane (APDES, 96%) was bought from Qufu Chenguan Chemical Co. Ltd. (China). 1,3-Bis(3-aminopropyl)-tetramethyldisiloxane (AMM, 97%), tetramethylammonium hydroxide pentahydrate (catalyst, 99%), acrylic acid (AA, 99.5%), and zinc chloride (ZnCl₂, 98%) were purchased from Macklin (China).

2.2. Synthesis of iminocarboxyl containing PDMS (PDMS-iminocarboxyl)

PDMS-NH₂ was synthesized and characterized in our previous work [24,25] and a brief procedure is stated in Supporting Information. AA (4.19 g) was added dropwise to a mixture of PDMS-NH₂ (20.0 g) in chloroform (CHCl₃, 100 mL) at 50 °C for 24 h with the protection of N₂ atmosphere, and then the mixture was washed with deionized water thrice. The mixture was concentrated under reduced pressure to remove volatiles. The product was further dried at 80 °C/1 mbar for 2 days, and PDMS-Iminocarboxyl was obtained as a light-yellow transparent oil. Yield: 90%. Its synthetic route is depicted in Scheme S1. FT-IR (ATR, cm⁻¹): 3270, 2966, 2906, 1714, 1590, 1445, 1409, 1262, 1096, 1026, 868, 805. ¹H NMR (CDCl₃, 600 MHz, ppm): 0–0.18 (*m*, Si-CH₃), 0.50–0.58 (*t*, -CH₂-CH₂-CH₂-NH-), 2.40–2.44 (*m*, -CH₂-CH₂-NH-), 2.56–2.59 (*m*, -CH₂-NH-), 2.42–2.58 (*d*, -NH-CH₂-CH₂-COOH). *M_n* and *D* of PDMS-NH₂ were 23 kDa and 2.1, and *M_n* and *D* of PDMS-Iminocarboxyl were 38 kDa and 2.0, according to GPC experiments, respectively.

Table 1
Formulations of PDMS-Iminocarboxyl@Zn_x elastomers.

Sample	PDMS-Iminocarboxyl (g)	ZnCl ₂ (g)	[Zn ²⁺]/[COOH]
PDMS-Iminocarboxyl	10.0	—	—
PDMS-Iminocarboxyl@Zn _{0.25}	10.0	0.312	0.25
PDMS-Iminocarboxyl@Zn _{0.5}	10.0	0.624	0.5
PDMS-Iminocarboxyl@Zn _{1.0}	10.0	1.248	1.0

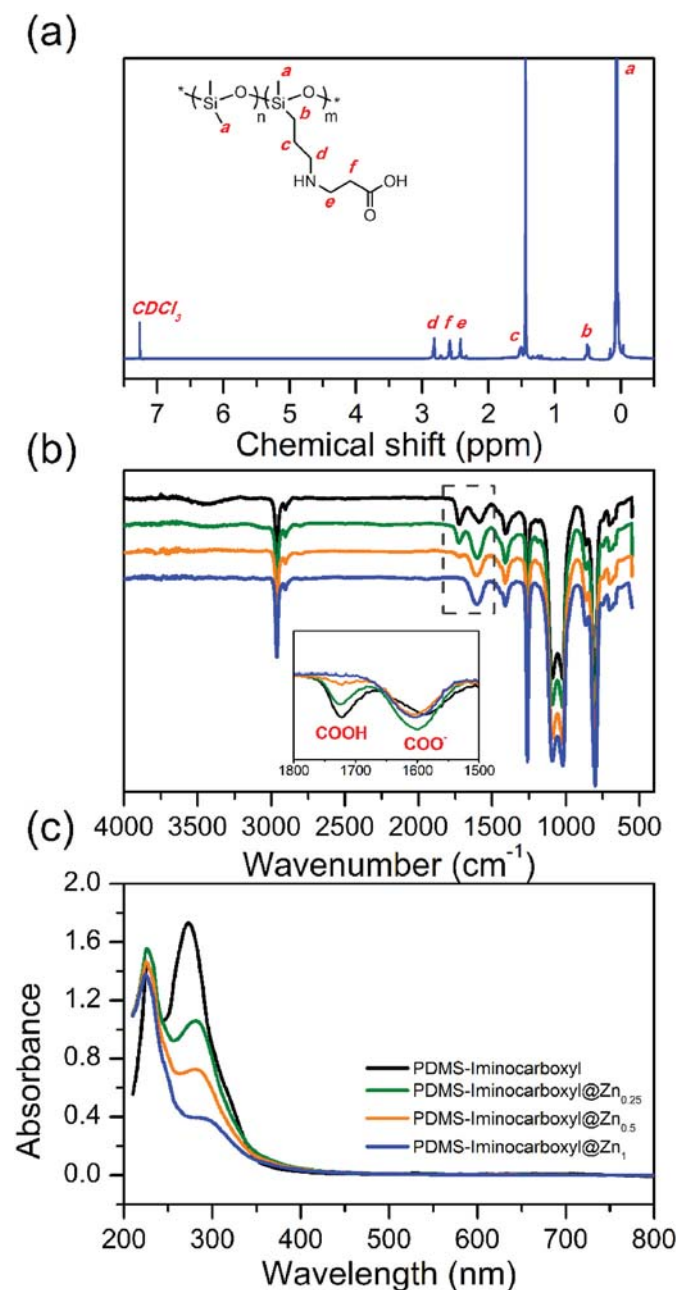


Fig. 1. (a) ¹H NMR spectrum of PDMS-Iminocarboxyl; (b) FTIR spectra of PDMS-Iminocarboxyl and PDMS-Iminocarboxyl@Zn_x; (c) UV-vis spectra of PDMS-Iminocarboxyl@Zn_x elastomers.

2.3. Fabrication of PDMS-Iminocarboxyl@Zn_x elastomers

According to Table 1, PDMS-Iminocarboxyl was first dissolved in CHCl₃ at 25 °C and stirred for 10 min to form a transparent solution. Then, ZnCl₂ dissolved in ethanol was added dropwise to the solution under vigorous stirring at 25 °C for 30 min. The resultant mixture was poured into a mould, and then maintained at 60 °C for 2 days in a vacuum oven to remove the solvent. The obtained crosslinked film was named PDMS-Iminocarboxyl@Zn_x (x = 0.25, 0.5, and 1, which referred to the ratio of [Zn²⁺]/[COOH]).

2.4. Characterization

Detailed characterization methods are provided in Supporting Information. Based on the optimized bond lengths, DFT calculations were evaluated according to the bond-valence-bond-length correlations and were also presented in Supporting Information.

3. Results and discussion

3.1. Structural characterization of PDMS-Iminocarboxyl@Zn_x elastomers

Fig. 1a shows the ¹H NMR spectrum of PDMS-Iminocarboxyl. The peaks at 1.51 ppm and 2.82 ppm represented methylene protons of aminopropyl group, and the signal at 2.42 ppm and 2.58 ppm represented methylene protons brought by AA after aza-Michael addition. The proton resonating for C=C bonds (7.5–7.8 ppm) was not found in the spectrum of PDMS-Iminocarboxyl. Simultaneously, the bending vibration absorption of N–H bond (1614 cm⁻¹) disappeared compared to the FTIR spectrum of PDMS-NH₂ (Fig. S2). The new characteristic vibration absorptions of O–H stretching vibration (3270 cm⁻¹), C=O stretching of COOH vibration (1714 cm⁻¹), and COO⁻ (1590 cm⁻¹) were observed. These results indicated the successful transformation from amino group to iminocarboxyl.

The structures of the PDMS-Iminocarboxyl@Zn_x elastomers were characterized using FTIR technique. In all four spectra shown in Fig. 1b, the characteristic absorption of COOH at 1714 cm⁻¹ gradually decreased with an increasing amount of Zn(II) ions and completely disappeared when [Zn²⁺]/[COOH] = 1. Meanwhile, the characteristic peaks of COO⁻ shifted from 1590 cm⁻¹ to 1610 cm⁻¹, indicating the full complexation of Zn(II)-iminocarboxyl.

According to the UV-vis spectra in Fig. 1c, PDMS-Iminocarboxyl@Zn_x elastomers with a light-yellow color were confirmed by the blue shift of the absorption band (250–350 nm) owing to COOH/imino acid-base complexation. The incorporation of Zn(II) restrained the absorption band at 250–350 nm effectively, and thus the final elastomer products became colorless with an increasing content of Zn(II) ions. This was because Zn(II) ions tended to interact with iminocarboxyl and formed Zn(II)-carboxylate coordination bond, and Zn(II)-N_{imino} coordination bond almost shielded the interaction between COOH/imino. Besides, the values of transmittance of PDMS-Iminocarboxyl@Zn_x elastomers were all larger than 99% within the visible region (400–800 nm), which was consistent with the digital photo (Scheme 1c).

3.2. Geometry optimization of Zn(II)-Iminocarboxyl complexation

To determine the exact coordination between Zn(II) and iminocarboxyl, we investigated relative energies of different coordination modes and spin multiplicities as shown in Fig. S3. In our model, PDMS polymer chains were simplified as a CH₃ group, which did not affect the energy calculation altogether. The structures of different conformations were optimized by ORCA program (Version 5.0.0) [26,27] at the PBE0-D3(BJ)/def2-SVP level. All snapshots of Zn(II)-iminocarboxyl complexation at different coordination modes were provided by Multiwfn [28]. Relative energies and molecular structures designed are listed in Table S1. Bond valences and bonds energies were calculated

Table 2

Binding energies of $\text{O}_\text{C}_\text{O}_\text{C}_\text{N}_\text{N}-[\text{Zn}(\text{PDMS-Iminocarboxyl})]^{2+}$ calculated according to bond-valence-bond-length correlations.

Bond type	Bond length (Å)	Bond valence (v.u.)	Bond energy (kcal/mol)
Zn–N ₁	2.034	0.4898	38.73
Zn–N ₂	2.037	0.4865	38.21
Zn–O ₁	1.995	0.4503	32.73
Zn–O ₂	1.986	0.4611	34.32

according to the bond-valence-bond-length correlations by equations Eq. (1) and Eq. (2) [29], where $a = 7 \text{ eV} \cdot \text{vu}^{-2}$, r is the observed bond length, r_0 and b are bond valence parameters. Bond valence and bond energy of the most stable conformation are summarized in Table 2. According to crystallographic data [30], $r_0 = 1.77$, $b = 0.37$ for Zn(II)–N bond; $r_0 = 1.70$, $b = 0.37$ for Zn(II)–O bond. The results suggested that the conformation $(\text{O}_\text{C}_\text{O}_\text{C}_\text{N}_\text{N}-[\text{Zn}(\text{PDMS-Iminocarboxyl})]^{2+})$, Scheme 1b) of Zn(II)-iminocarboxyl complex is the most stable when a Zn(II) ion is coordinated with 2 N atoms (imino group) and 2 O atoms (carboxyl group).

$$E = aS^2 \quad 1$$

$$S = \exp((r_0 - r) / b) \quad 2$$

Steric structures of metal-iminocarboxyl complexes have been systematically investigated in previous works [31–34]. Generally, iminocarboxyl ligands are inclined to coordinate with transition metal ions via four to six atoms. As shown in Scheme 1b, the optimized results is that all carboxyl groups and N atoms are attached to Zn(II) ions. In addition, bonding energies of Zn(II)–O_{COOH} and Zn(II)–N_{imino} were estimated to be

33.53 and 38.47 kcal/mol according to the bond-lengths which is 1.991 Å for Zn(II)–O_{COOH} and 2.036 Å for Zn(II)–N_{imino}.

To further investigate the coordination complex, modified hexylamine that reacted with acrylic acid (HA-Iminocarboxyl) following the same procedure as PDMS-Iminocarboxyl was selected to build model ligand with ZnCl_2 . In Fig. S4, chemical shifts of Zn(II)–O_{COOH} and Zn(II)–N_{imino} were a function of concentrations of Zn(II)-iminocarboxyl. The concentrations of HA-Iminocarboxyl in sample 1 to 5 were constant (0.1 mol/L), and the concentration of Zn^{2+} increased from 0 to 0.1 mol/L. Both related peaks (a for Zn(II)–O_{COOH} and b for Zn(II)–N_{imino}) bond shifted toward lower fields with increasing Zn^{2+} concentrations. By fitting the curves, Association constants of Zn(II)–O_{COOH} (K_a) and Zn(II)–N_{imino} (K_b) were estimated to be 3.98×10^2 and $2.18 \times 10^4 \text{ M}^{-1}$, respectively. These results are consistent with the DFT calculations results in trend.

3.3. Dynamic thermomechanical analysis

Viscoelastic properties of PDMS-Iminocarboxyl and PDMS-Iminocarboxyl@Zn_x elastomers were characterized by rheological method. Time-temperature superposition principle was applied to analyze the isothermal dynamic frequency sweeps at reference temperature of 25 °C. In Fig. 2, master curves of all four samples showed both storage modulus (G') and loss modulus (G'') declined with decreasing frequency. G' values spanned 3 orders of magnitude within the frequency range 10^{-5} – 10^2 rad/s, which accorded with our demand for obtaining an energy-storing at high-frequency, energy-dissipating at low-frequency, high-performance robust elastomers. It is interesting to note that the crossover points (the frequency ω_0 at $G' = G''$) implied the occurrence of

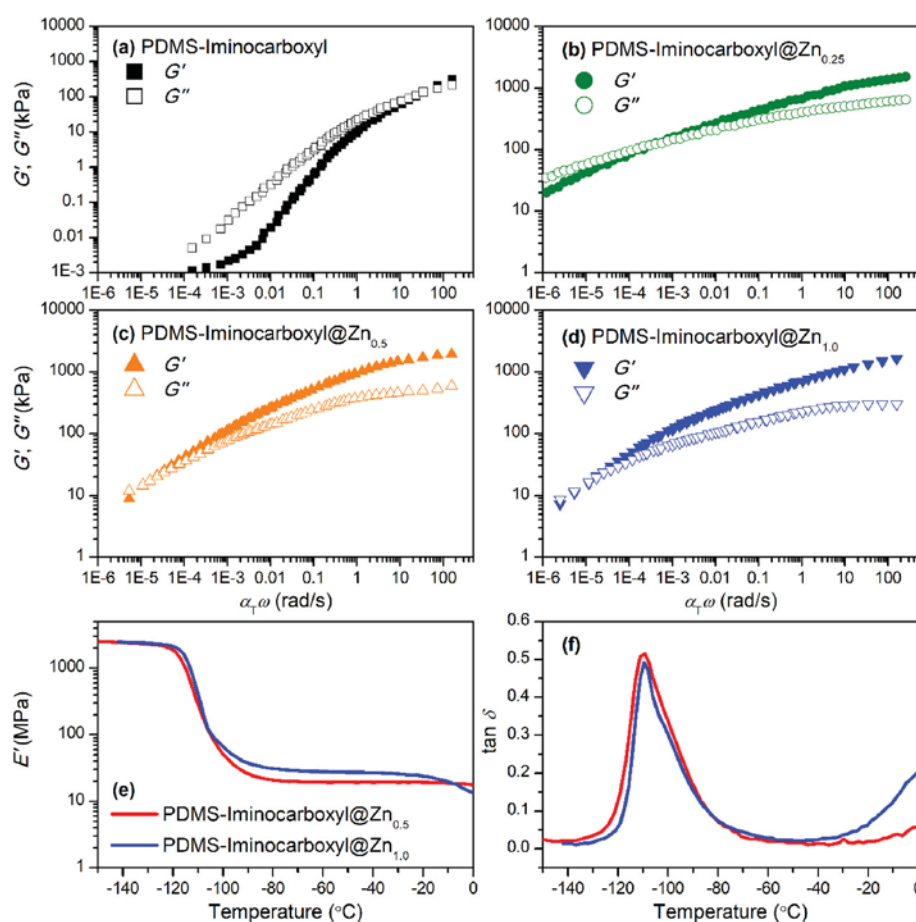


Fig. 2. (a–d) Master curves of PDMS-Iminocarboxyl and PDMS-Iminocarboxyl@Zn_x at reference temperature of 25 °C. (e–f) Storage modulus (E') and $\tan \delta$ against temperature of PDMS-Iminocarboxyl@Zn_{0.5} and PDMS-Iminocarboxyl@Zn_{1.0} from the DMA tests.

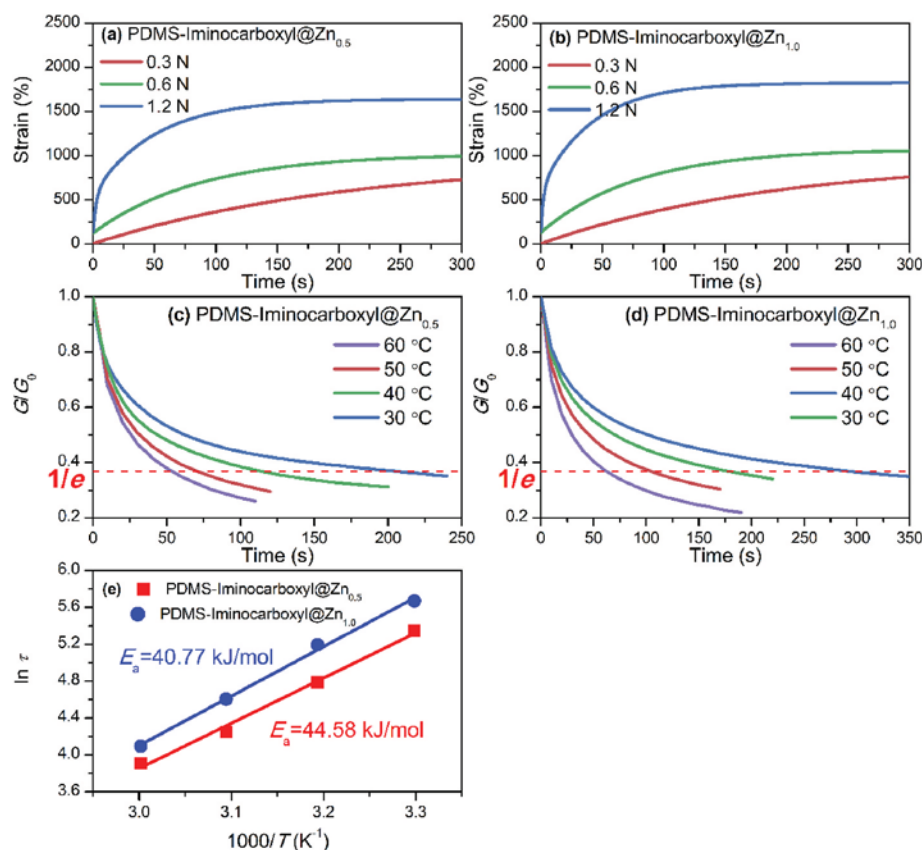


Fig. 3. (a–b) Creep and (c–d) stress relaxation curves of PDMS-Iminocarboxyl@Zn_{0.5} and PDMS-Iminocarboxyl@Zn_{1.0} under varies loads and temperatures. (e) Fitting curves and the calculated E_a values of PDMS-Iminocarboxyl@Zn_{0.5} and PDMS-Iminocarboxyl@Zn_{1.0}.

viscoelastic transition for elastomers with dynamic crosslinking sites. The viscoelastic transition points of PDMS-Iminocarboxyl@Zn_x shifted towards low frequency from 5.7×10^{-4} rad/s to 1.2×10^{-5} rad/s with increasing content of Zn(II) ions. Furthermore, terminal relaxation time (τ_d) could be calculated following the equation: $\tau_d = 1/\omega_0$. The ω_0 of PDMS-Iminocarboxyl, PDMS-Iminocarboxyl@Zn_{0.25}, PDMS-Iminocarboxyl@Zn_{0.5}, and PDMS-Iminocarboxyl@Zn_{1.0} was 0.04 , 1.8×10^3 , 2.9×10^4 , and 8.3×10^4 s, respectively. Incorporation of Zn(II) significantly extended the τ_d s of PDMS-Iminocarboxyl@Zn_x elastomers.

The thermomechanical properties of the PDMS-Iminocarboxyl@Zn_x elastomers were evaluated using the DMA technique. From the plots representing the storage modulus (E') of PDMS-Iminocarboxyl@Zn_{0.5} and PDMS-Iminocarboxyl@Zn_{1.0} elastomers (Fig. 2e), the magnitudes of E' in the glassy state were very close to each other. The peak temperature of the tan δ -temperature curve from the DMA test is regarded as the glass transition temperature (T_g) [35]. For PDMS-Iminocarboxyl@Zn_{0.5} and PDMS-Iminocarboxyl@Zn_{1.0}, both T_g values were -109 °C. Moreover, crosslinking density (ν_c) can be calculated by equation: $\nu_c = E'/(3RT)$, where R is the gas constant, and T is the absolute temperature. The DMA collected E' at the temperature of ($T_g + 80$ °C). ν_c for PDMS-Iminocarboxyl@Zn_{0.5} and PDMS-Iminocarboxyl@Zn_{1.0} were 3164 and 4274 mol/m³, respectively. Increasing Zn(II) concentrations led to higher crosslinking density.

3.4. Creep and stress relaxation

Uniaxial creep experiments were carried out on PDMS-Iminocarboxyl@Zn_{0.5} and PDMS-Iminocarboxyl@Zn_{1.0} elastomers to obtain their creep characteristics under 0.3, 0.6, and 1.2 N constant load at room temperature. Fig. 3a–b shows that the samples exhibited two creep states. At the end of creep experiments, the strains did not change with

time, indicating the reestablishment of Zn(II)-iminocarboxyl dynamic crosslinks that limited the further sliding of polymer chains. Two sufficient crosslinking elastomers PDMS-Iminocarboxyl@Zn_{0.5} and PDMS-Iminocarboxyl@Zn_{1.0} were conducted isothermal stress relaxation experiments on a shear-mode rheometer. The stress relaxation time, τ_{SR} , is given to be distinguished from the previous notion. The value τ_{SR} is defined as the time required for shear modulus (G') to its $1/e$ of its initial modulus [36]. In Fig. 3c–d, both samples showed rapid stress relaxation property even at 30 °C. Both τ_{SR} s of PDMS-Iminocarboxyl@Zn_{0.5} and PDMS-Iminocarboxyl@Zn_{1.0} are around 50 s. Applying the Arrhenius equation [37], activation energy (E_a) was calculated to be 44.58 kJ/mol for PDMS-Iminocarboxyl@Zn_{0.5} and 40.77 kJ/mol for PDMS-Iminocarboxyl@Zn_{1.0}, which were lower than other PDMS-based elastomers reported [4]. PDMS-Iminocarboxyl@Zn_x elastomers have fast relaxation process and low E_a values owing to the dynamic nature of Zn(II)-iminocarboxyl complex.

3.5. Mechanical properties

The typical tensile stress-strain curves of PDMS-Iminocarboxyl and PDMS-Iminocarboxyl@Zn_x in Fig. 4a. Tensile experiments were conducted at various stretching rates. The typical tensile stress-strain curves, Young's modulus, and tensile strength of PDMS-Iminocarboxyl@Zn_{0.5} are shown in Fig. 4b–c. Both Young's modulus and tensile strength decreased with smaller stretching rates. Elongation at break had a slight improvement from 1800% to 2000% from stretching rate 500 mm/min to 20 mm/min. Stretching rate 200 mm/min is considered a line of demarcation. When the stretching rate was 500–200 mm/min, PDMS-Iminocarboxyl@Zn_{0.5} showed a tensile strength of 3 MPa and Young's modulus of 1.5 MPa. When the stretching rate changed from 200 mm/min to 100 mm/min, there was a huge reduction in mechanical

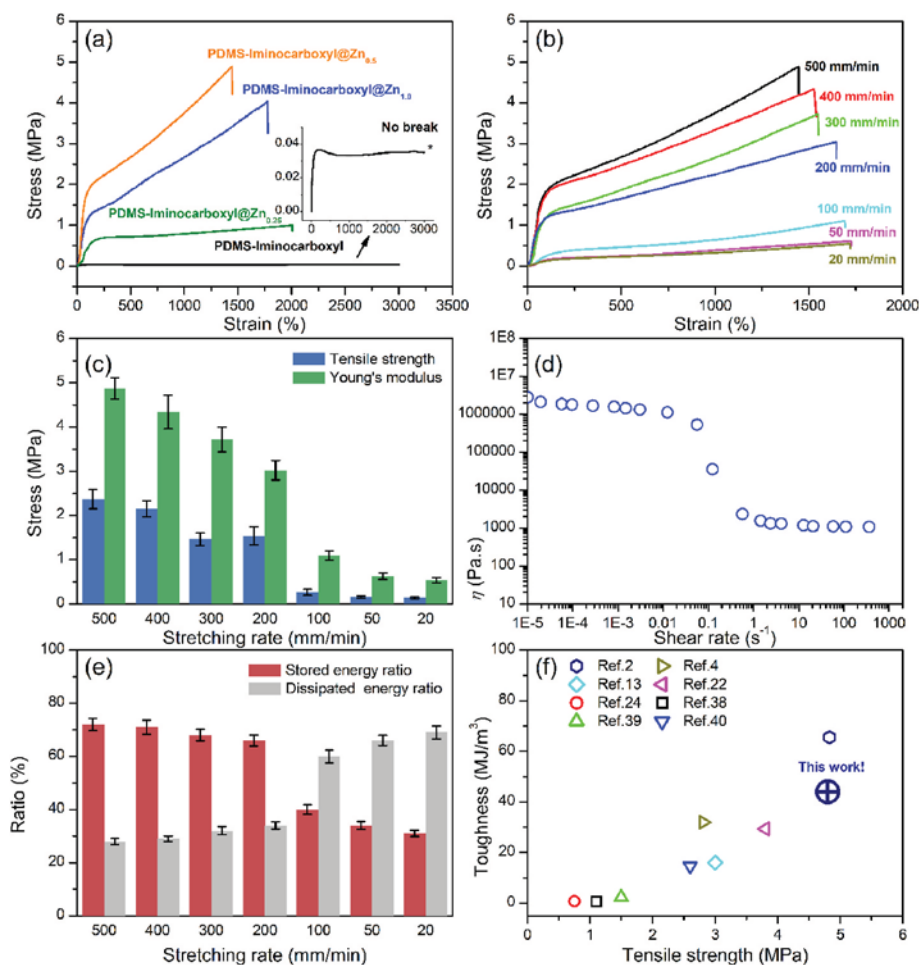


Fig. 4. Tensile stress-strain curves of the (a) PDMS-Iminocarboxyl and PDMS-Iminocarboxyl@Zn_x at the stretching rate of 500 mm/min and (b) PDMS-Iminocarboxyl@Zn_{0.5} samples under varies stretching rates. (c) Summarization of tensile properties, including Young's modulus and tensile strength. (d) Viscosity of PDMS-Iminocarboxyl@Zn_{0.5} against shear rate. (e) Summarization of stored and dissipated energy ratios calculated from cyclic tensile tests. (f) Comparison of mechanical properties with other published works in recent years.

strength which included tensile strength of 1.1 MPa and Young's modulus of 0.26 MPa at a stretching rate of 100 mm/min. These dramatic mechanical convert was associated with the viscoelastic property. The stretching rates in tensile mode from 200 to 100 mm/min could be simply converted to shear rates from 0.32 to 0.16 s⁻¹ in rotating oscillation mode (Fig. 4d). This small window was much higher than the viscoelastic transition point at 10⁻⁵ rad/s in Fig. 2b. As shown in Fig. 4d, PDMS-Iminocarboxyl@Zn_{0.5} elastomer exhibited classical non-Newton shear-thinning property. There was a critical shear rate $\gamma_c = 0.1$ s⁻¹ where the viscosity changed dramatically against shear rate. This rate was close to the shear rate range 0.32–0.16 s⁻¹. The value of γ_c was related to the reversible association/dissociation of Zn(II)-iminocarboxyl coordination bonds. Moreover, viscosity relaxation time (τ_v) could be used to characterize this dynamic process and be determined by a similar equation: $\tau_v = 1/\gamma_c$. Calculated τ_v for PDMS-Iminocarboxyl@Zn_{0.5} was 10 s. This specific behavior could be explained by the bonding energy of Zn(II)-iminocarboxyl complex. In high speed regions (higher than 200 mm/min), the stretching rate was much greater than the dynamic exchange rate of Zn(II)-iminocarboxyl complex. Both Zn(II)-COOH and Zn(II)-N_{imino} bonds played a significant synergistic role in improving the mechanical strength against external force. Excellent toughness values (integral area of a stress-strain curve) were summarized in Table S2, which could be attributed to orientations of PDMS chains and enhancing metal-ligand coordination bonds altogether. In particularly, the toughness of PDMS-Iminocarboxyl@Zn_{0.5} achieved an amazing 45.4 MJ/m³ compared to previous published values in Fig. 4f. In the slow speed region (lower than 200 mm/min), the stretching rate could keep up with the dynamic exchange rate of Zn(II)-iminocarboxyl complex. The dynamic exchange dissipated

most of the energy and thus led to larger deformation of the samples.

To effectively dissipate applied energy, elastomers with good balance of stored and dissipated energy are of great interest. Single-loop cyclic tensile tests under various conditions were conducted and presented in Fig. S6. Ratios of Area I and II are defined to evaluate the storing and dissipating energy ratios (Fig. 4e). These characters are also dependent on the stretching rates. The energy stored decreased, while the fraction of energy dissipating increased with the decreasing of stretching rates. In fact, the strain-rate-dependence can be further explicated by the competition between combination and Zn(II)-iminocarboxyl re-recombination.

3.6. Self-healing ability and reprocessing

As stated above, PDMS-Iminocarboxyl@Zn_x elastomers combined robust mechanical and excellent dynamic properties, and hence their self-healing ability and reprocessing properties were further investigated. The self-healing performance of PDMS-Iminocarboxyl@Zn_x was examined by recovery tensile strength and elongation at break which are summarized in Fig. 5a–b. The sample recovered 50% of original mechanical properties in a short time (less than 6 h), and approximately recovered to its original level in 18 h. Recovery of mechanical properties is deeply dependent on the recombination of Zn(II)-iminocarboxyl complexation as well as the chain diffusion of PDMS chains on the fresh surface. Elevating temperature was helpful for the healing process, and PDMS-Iminocarboxyl@Zn_{0.5} recovered to its original mechanical properties in 6 h at 60 °C. Even higher temperature (80 °C) and applying compression would massively shorten the time to repair broken pieces (Fig. 5c) to reform. There were two methods to reprocess, and neither

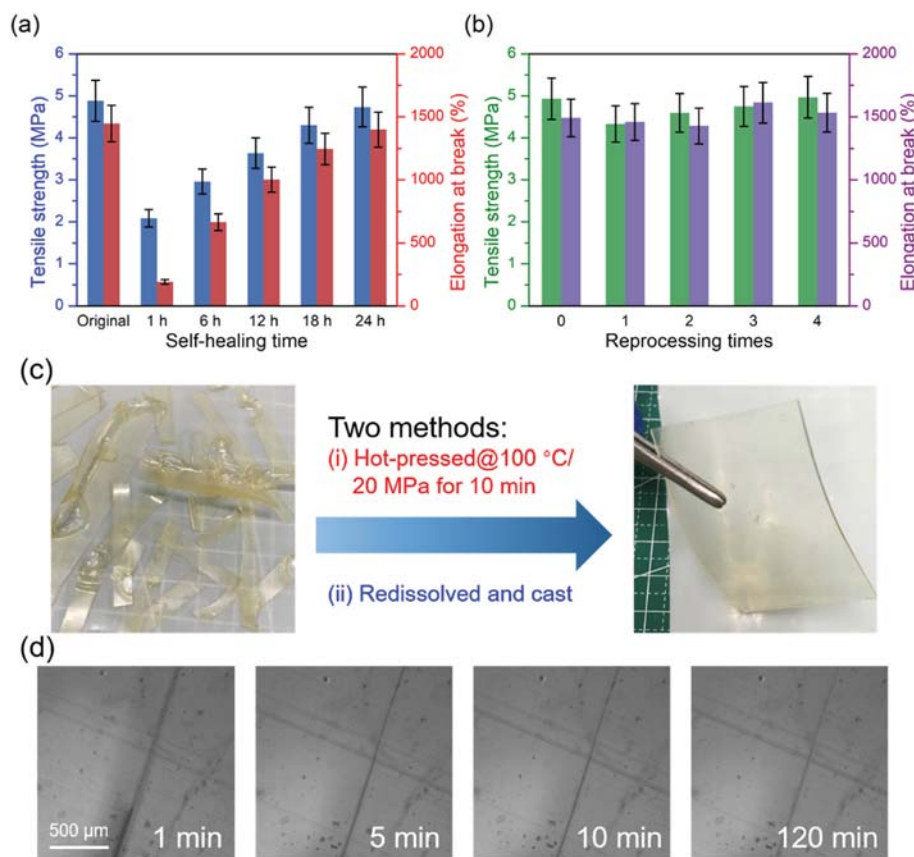


Fig. 5. Tensile properties of PDMS-Iminocarboxyl@Zn_{0.5} which underwent (a) self-healing for 1, 6, 12, 18, 24 h at room temperature and (b) reprocessing for 1–4 times. (c) PDMS-Iminocarboxyl@Zn_x elastomer pieces for processing to form a whole uniform transparent elastomer sheet. Processing includes two methods: (i) hot-pressing at 100 °C/20 MPa for 10 min, and (ii) redissolving in good solvent and casting. (d) Self-healing process observation under polarization microscope at room temperature.

method did not sacrifice the mechanical properties. Apart from hot-pressing, reprocessing could also be achieved in good solvent such as tetrahydrofuran and CHCl₃ due to dissociation of Zn(II)-iminocarboxyl complexation under heat or in solvent condition. Self-healing process was observed under polarization microscope at room temperature (Fig. 5d). The material was in elastic state with a high degree of chain flexibility and mobility. The crosslinking PDMS-Iminocarboxyl complex was dynamic and ready to form at this temperature.

4. Conclusions

We synthesized the self-healing and highly stretchable supramolecular polysiloxanes elastomers PDMS-Iminocarboxyl@Zn_x based on Zn(II)-iminocarboxyl complexation. The elastomers (PDMS-Iminocarboxyl@Zn_{0.5}) exhibited tensile strength up to 5 MPa, elongation at break of over 1500%, and toughness up to 45.4 MJ/m³ at stretching rate of 500 mm/min. Interestingly, the elastomers possessed strain sensitivity that was ascribed to the unique character of Zn(II)-iminocarboxyl complex which contained thermodynamically stable Zn(II)-O₂C⁻ and Zn(II)-N₂ imino bonds confirmed by DFT calculations and NMR titration. Strong and weak coordinating bonds synergistically contributed to the PDMS-Iminocarboxyl@Zn_x networks subjected to sudden strain. Besides, elastomers exhibited excellent room-temperature self-healing ability (tensile strength recovered 100% within 24 h) and could be successfully multi-reprocessed via two methods: hot-pressing and solvent-recasting. This study provided a systematic investigation on metal-ligand cross-linked supramolecular elastomers.

CRediT authorship contribution statement

Jiaheng Mo: Data curation, Writing – original draft, preparation. **Weijian Wu:** DFT calculations, Writing – original draft, preparation. **Shijie Shan:** Writing – original draft. **Xionghui Wu:** Data curation,

Writing – original draft, preparation. **Danni Li:** Writing – original draft. **Rui Li:** Writing – original draft, preparation. **Yaling Lin:** Writing – review & editing, Supervision. **Anqiang Zhang:** Writing – review & editing, Supervision.

Declaration of competing interest

The authors declare that they have no known competing financial interests or personal relationships that could have appeared to influence the work reported in this paper.

Acknowledgements

The authors acknowledge the financial support from the National Natural Science Foundation of China (Nos. 52073098 and 31772202), and the Natural Science Foundation of Guangdong Province, China (No.2022A1515011570).

Appendix A. Supplementary data

Supplementary data to this article can be found online at <https://doi.org/10.1016/j.polymer.2022.124896>.

References

- [1] K. Liu, L. Cheng, N. Zhang, H. Pan, X. Fan, G. Li, Z. Zhang, D. Zhao, J. Zhao, X. Yang, Y. Wang, R. Bai, Y. Liu, Z. Liu, S. Wang, X. Gong, Z. Bao, G. Gu, W. Yu, X. Yan, Biomimetic impact protective supramolecular polymeric materials enabled by quadruple H-bonding, *J. Am. Chem. Soc.* 143 (2) (2020) 1162–1170.
- [2] Y. Yao, Z. Xu, B. Liu, M. Xiao, J. Yang, W. Liu, Multiple H-bonding chain extender-based ultrastiff thermoplastic polyurethanes with autonomous self-healability, solvent-free adhesiveness, and AIE fluorescence, *Adv. Funct. Mater.* 31 (4) (2021) 2006944.

- [3] W. Zhao, Y. Liu, Z. Zhang, X. Feng, H. Xu, J. Xu, J. Hu, S. Wang, Y. Wu, S. Yan, High-strength, fast self-healing, aging-insensitive elastomers with shape memory effect, *ACS Appl. Mater. Interfaces* 12 (31) (2020) 35445–35452.
- [4] J. Fan, J. Huang, Z. Gong, L. Cao, Y. Chen, Toward robust, tough, self-healable supramolecular elastomers for potential application in flexible substrates, *ACS Appl. Mater. Interfaces* 13 (1) (2020) 1135–1144.
- [5] H. Sun, X. Liu, S. Liu, B. Yu, N. Ning, M. Tian, L. Zhang, A supramolecular silicone dielectric elastomer with A high dielectric constant and fast and highly efficient self-healing under mild conditions, *J. Mater. Chem.* 8 (44) (2020) 23330–23343.
- [6] X. Wang, S. Zhan, Z. Lu, J. Li, X. Yang, Y. Qiao, Y. Men, J. Sun, Healable, recyclable, and mechanically tough polyurethane elastomers with exceptional damage tolerance, *Adv. Mater.* 32 (50) (2020) 2005759.
- [7] W.B. Ying, G. Wang, Z. Kong, C.K. Yao, Y. Wang, H. Hu, F. Li, C. Chen, Y. Tian, J. Zhang, R. Zhang, J. Zhu, A biologically muscle-inspired polyurethane with super-tough, thermal repairable and self-healing capabilities for stretchable electronics, *Adv. Funct. Mater.* 31 (10) (2021) 2009869.
- [8] A. Feula, A. Pethybridge, I. Giannakopoulos, X. Tang, A. Chippindale, C.R. Siviour, C.P. Buckley, I.W. Hamley, W. Hayes, A thermoreversible supramolecular polyurethane with excellent healing ability at 45 °C, *Macromolecules* 48 (17) (2015) 6132–6141.
- [9] T. Kakuta, Y. Takashima, M. Nakahata, M. Otsubo, H. Yamaguchi, A. Harada, Preorganized hydrogel: self-healing properties of supramolecular hydrogels formed by polymerization of host-guest-monomers that contain cyclodextrins and hydrophobic guest groups, *Adv. Mater.* 25 (20) (2013) 2849–2853.
- [10] C.Y. Shi, Q. Zhang, C.Y. Yu, S.J. Rao, S. Yang, H. Tian, D.H. Qu, An ultrastrong and highly stretchable polyurethane elastomer enabled by a zipper-like ring-sliding effect, *Adv. Mater.* 32 (23) (2020) 2000345.
- [11] Z. Zhang, L. Cheng, J. Zhao, H. Zhang, X. Zhao, Y. Liu, R. Bai, H. Pan, W. Yu, X. Yan, Muscle-mimetic synergistic covalent and supramolecular polymers: phototriggered formation leads to mechanical performance boost, *J. Am. Chem. Soc.* 143 (2) (2020) 902–911.
- [12] B. Li, S. Zhao, J. Zhu, S. Ge, K. Xing, A.P. Sokolov, T. Saito, P.F. Cao, Rational polymer design of stretchable poly(ionic liquid) membranes for dual applications, *Macromolecules* 54 (2) (2020) 896–905.
- [13] L. Bai, P. Qv, J. Zheng, Colorless, transparent, and healable silicone elastomers by introducing Zn(II)-Carboxylate interactions via aza-michael reaction, *J. Mater. Sci.* 55 (28) (2020) 14045–14057.
- [14] Y. Peng, L. Zhao, C. Yang, Y. Yang, C. Song, Q. Wu, G. Huang, J. Wu, Super tough and strong self-healing elastomers based on polyampholytes, *J. Mater. Chem.* 6 (39) (2018) 19066–19074.
- [15] Y. Miwa, J. Kurachi, Y. Kohbara, S. Kutsumizu, Dynamic ionic crosslinks enable high strength and ultrastretchability in A single elastomer, *Commun. Chem.* 1 (1) (2018) 1–8.
- [16] L. Yang, Y. Lin, L. Wang, A. Zhang, The synthesis and characterization of supramolecular elastomers based on linear carboxyl-terminated polydimethylsiloxane oligomers, *Polym. Chem.* 5 (1) (2014) 153–160.
- [17] J. Kang, D. Son, G.J. Wang, Y. Liu, J. Lopez, Y. Kim, J.Y. Oh, T. Katsumata, J. Mun, Y. Lee, L. Jin, J.B.-H. Tok, Z. Bao, Tough and water-insensitive self-healing elastomer for robust electronic skin, *Adv. Mater.* 30 (13) (2018) 1706846.
- [18] Y. Miwa, K. Taira, J. Kurachi, T. Udagawa, S. Kutsumizu, A gas-plastic elastomer that quickly self-heals damage with the aid of CO₂ gas, *Nat. Commun.* 10 (1) (2019) 1–6.
- [19] P. Cordier, F. Tournilhac, C. Soulié-Ziakovic, L. Leibler, Self-healing and thermoreversible rubber from supramolecular assembly, *Nature* 451 (7181) (2008) 977–980.
- [20] Y. Yang, M.W. Urban, Self-healing of polymers via supramolecular chemistry, *Adv. Mater. Interfac.* 5 (17) (2018) 1800384.
- [21] C.H. Li, C. Wang, C. Keplinger, J.L. Zuo, L. Jin, Y. Sun, P. Zheng, Y. Cao, F. Lissel, C. Linder, X.Z. You, Z. Bao, A highly stretchable autonomous self-healing elastomer, *Nat. Chem.* 8 (6) (2016) 618–624.
- [22] J.C. Lai, X.Y. Jia, D.P. Wang, Y.B. Deng, P. Zheng, C.H. Li, J.L. Zuo, Z. Bao, Thermodynamically stable whilst kinetically labile coordination bonds lead to strong and tough self-healing polymers, *Nat. Commun.* 10 (1) (2019) 1–9.
- [23] J.C. Lai, L. Li, D.P. Wang, M.H. Zhang, S.R. Mo, X. Wang, K.Y. Zeng, C.H. Li, Q. Jiang, X.Z. You, J.L. Zuo, A rigid and healable polymer cross-linked by weak but abundant Zn(II)-Carboxylate interactions, *Nat. Commun.* 9 (1) (2018) 1–9.
- [24] Y. Lei, Q. Huang, S. Shan, Y. Lin, A. Zhang, A stretchable and rapidly self-healable polysiloxane elastomer based on reversible aluminum-amino coordination, *New J. Chem.* 43 (44) (2019) 17441–17445.
- [25] S. Shan, Y. Lin, A. Zhang, Stretchable, robust and reprocessable poly(siloxane-urethanes) elastomers based on exchangeable aromatic disulfides, *Polymer* 221 (2021) 123588.
- [26] F. Neese, The orca program system, *Wiley Interdiscip. Rev. Comput. Mol. Sci.* 2 (2012) 73–78.
- [27] F. Neese, Software update: the ORCA program system, version 4.0, *Wiley Interdiscip. Rev. Comput. Mol. Sci.* 8 (1) (2017) e1327.
- [28] T. Lu, Chen F. Multiwfn, A multifunctional wavefunction analyzer, *J. Comput. Chem.* 33 (2012) 580–592.
- [29] I.D. Brown, Recent developments in the methods and applications of the bond valence model, *Chem. Rev.* 109 (2009) 6858–6919.
- [30] S. Thirumaran, K. Ramalingam, G. Bocelli, Bond valence sum analysis (BVS) of metal ligand bond lengths in some Zn(II), Cd(II) dithiocarbamate complexes and their adducts, *Main Group Met. Chem.* 22 (7) (1999) 423–426.
- [31] I. Cukrowski, K.K. Govender, A density functional theory-and atoms in molecules-based study of NiNTA and NiNTPA complexes toward physical properties controlling their stability. A new method of computing a formation constant, *Inorg. Chem.* 49 (15) (2010) 6931–6941.
- [32] M. Čendić, R.J. Deeth, A. Meetsma, E. Garribba, D. Sanna, Z.D. Matović, Chelating properties of EDTA-type ligands containing six-membered backbone ring toward copper ion: structure, EPR and TD-DFT evaluation, *Polyhedron* 124 (2017) 215–228.
- [33] E. Braña, D. Quiñone, S. Martínez, J. Grassi, I. Carrera, J. Torres, J. González-Platas, G. Seoane, C. Kremer, C. Mendoza, New polynuclear compounds based on N-benzyliminodipropionic acid: solution studies, Synthesis, and X-ray crystal structures, *J. Coord. Chem.* 69 (24) (2016) 3650–3663.
- [34] R. Puentes, J. Torres, R. Faccio, A. Bacchi, C. Kremer, Lanthanide coordination polymers based on flexible ligands derived from iminodiacetic acid, *Polyhedron* 170 (2019) 683–689.
- [35] J.T. Miao, L. Yuan, G. Liang, A. Gu, Biobased bismaleimide resins with high renewable carbon content, heat resistance and flame retardancy via a multi-functional phosphate from clove oil, *Mater. Chem. Front.* 3 (1) (2019) 78–85.
- [36] Q. Li, S. Ma, S. Wang, Y. Liu, M.A. Taher, B. Wang, K. Huang, X. Xu, Y. Han, J. Zhu, Green and facile preparation of readily dual-recyclable thermosetting polymers with superior stability based on asymmetric acetal, *Macromolecules* 53 (4) (2020) 1474–1485.
- [37] M. Capelot, M.M. Unterlass, F. Tournilhac, L. Leibler, Catalytic control of the vitrimer glass transition, *ACS Macro Lett.* 1 (7) (2012) 789–792.

Tough, Self-Healing, Recyclable Bottlebrush Polyurethane Elastomer with a Skin-like Strain-Adaptive-Strengthening Property

Shijie Shan, Xionghui Wu, Yaling Lin,* and Anqiang Zhang*

Cite This: *ACS Appl. Polym. Mater.* 2022, 4, 7554–7563

Read Online

ACCESS |



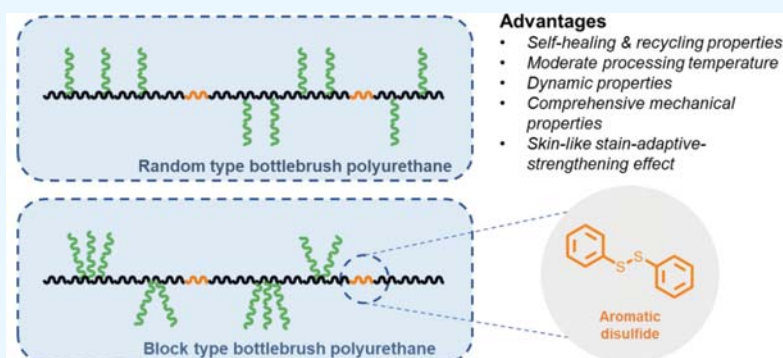
Metrics & More



Article Recommendations



Supporting Information



ABSTRACT: Bottlebrush polymers consisting of linear polymer backbone and polymeric side-chains are of significant interest for an extensive variety of potential applications that include drug delivery, omniphobic surface, and amphiphilic emulsion surfactants. These polymers are challenging to prepare in large quantities for practical use. Therefore, it is necessary to provide a facile synthetic route for bottlebrush polymers with commercially available products. Here, we describe a simple approach to converting widely used linear poly(tetramethylene ether glycol) (PTMG) polyurethanes into a bottlebrush elastomer with extraordinary self-healing and recycling properties. Random and block distributed glyceryl monostearate (GM) brushes result in distinguishing mechanical and surface properties of the bottlebrush elastomer. The exchangeable character of aromatic disulfides facilitates the self-healing processes by temperature-, stress-, or solvent-induced arrangements, enabling a deformed sample to recover its original appearance and mechanical properties after applications of the self-healing and recycling process. The material manifested a self-healing recovering efficiency of 86% of tensile strength, above 90% of elongation at break, and a complete recovery of tensile strength after the reforming process. Other dynamic thermomechanical and surface properties, such as rheological analysis, DMA, DSC, and contact angles were investigated and compared with those of conventional PTMG polyurethanes. Furthermore, inspired by biological tissues and real human skin, a stain-adaptive-strengthening effect in tensile measurements was observed with highly correlated polynomial fittings with $R^2 = 0.9996$. This simple and easy approach to preparing bottlebrush polyurethane elastomer with skin-like, self-healing, and recycling properties offers unique opportunities in the field of advanced materials, such as surgical skin dressing, intelligent sensors, human–machine interaction, and soft robotics.

KEYWORDS: bottlebrush polymer, polyurethane, aromatic disulfide, self-healing, strain stiffening

1. INTRODUCTION

Bottlebrush polymers consisting of linear polymer backbone and polymeric side-chains require tactical controllable polymerization techniques that enable the structure of bottlebrushes with a specific degree of polymerization (DP) of the backbone and side chain.^{1–3} Recently, bottlebrush polymers have more and more occupied an important place in the applications of drug delivery,^{4–6} photonics,^{7–9} rheology modifiers,^{10,11} and surface modifications.^{12–14} However, fine synthesis for these applications cannot meet the need for practical use in large quantities. Therefore, it necessary to produce a low-cost, easy-to-synthesize bottlebrush polymer.

In the field of bottlebrush polymers, works at an early stage mainly focused on the complex structures including blocking

and core–shell bottlebrushes^{15–17} that benefited from the rapid development of controllable polymerization techniques. Bottlebrush polymers exhibit very interesting physical features, which are manifested in a unique self-assembly under specific conditions.^{18–22} Generally, the synthesis of bottlebrush polymers is mainly achieved via three approaches: grating-

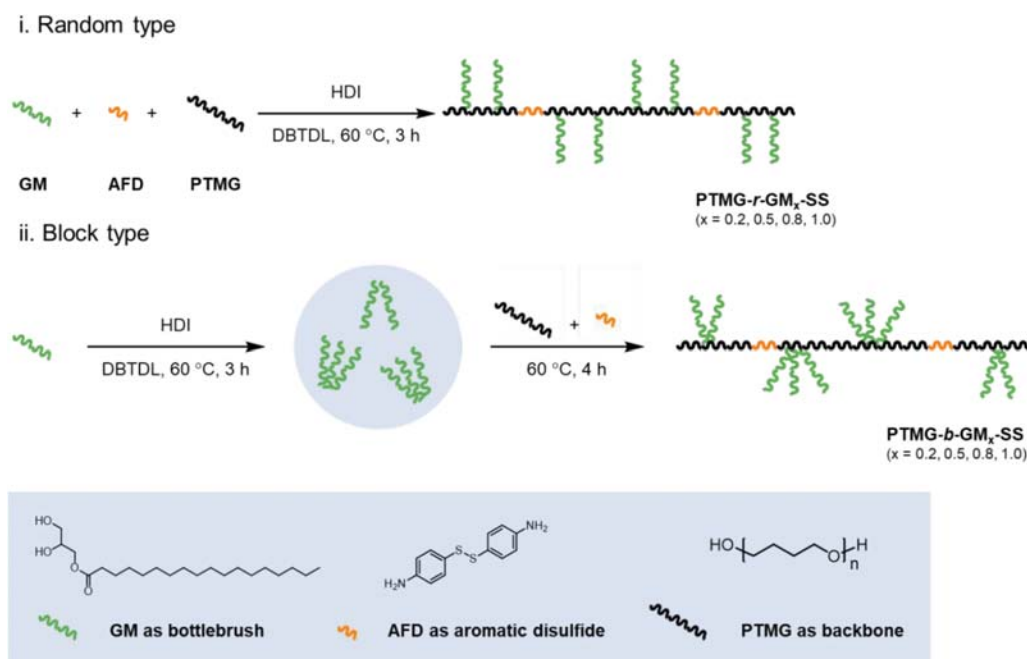
Received: July 15, 2022

Accepted: September 2, 2022

Published: September 12, 2022



Scheme 1. Synthetic Scheme for the Preparation of Bottlebrush Polyurethanes with Aromatic Disulfides



onto,^{23,24} grafting-through,^{25–27} and grafting-from.^{28,29} In the approach of grafting-onto, a macroinitiator bearing initiating groups is first obtained, followed by transformation of prepolymerized side chains. Grafting-through demands a homopolymerization of macromonomers in the presence of qualified catalysts.^{30–33} The method of grafting-from involves a macroinitiator and a subsequent polymerization of side chains. To obtain well-defined polymeric structure, size exclusion chromatography (SEC) provides a relative accurate evaluation of molecular weight and polydispersity. There are challenges and limitations, however, that are related to the characterization of bottlebrush polymers structural parameters with SEC.³⁴ Appropriate separation must be achieved before determining the SEC traces. Homochain experiments can be performed to help the characterization of block copolymers.

In the present publication, we report an original synthesis of a bottlebrush polyurethane elastomer that has emerged as a new class of polyurethanes with densely grafted side chains. Bottlebrush polyurethane elastomer was designed with specific equal-length glyceryl monostearate (GM) brushes connected to a polytetramethylene ether glycol (PTMG) backbone (Scheme 1). A gradient side-chain density can be obtained by exploiting the reactivity of GM as brushes. Aromatic disulfides (AFD) were subsequently blocked onto the backbone and used to synthesize self-healing and recycling bottlebrush polyurethane elastomer.^{35–38} Three important structural parameters are focused here: the degree of polymerization of backbone ($\text{DP}_{\text{backbone}}$) and side chain ($\text{DP}_{\text{side chain}}$), and the molecular weight between neighboring side chains (N_{sc}). GM brushes were chosen due to accurately controlled $\text{DP}_{\text{side chain}}$ of stearic tails. Therefore, it only left $\text{DP}_{\text{backbone}}$ and N_{sc} to determine the properties of bottlebrush polyurethane elastomer. Inspired by mimicking biological tensile behavior of polydimethylsiloxane bottlebrushes,³⁹ biological tissues such as muscles and lungs exhibit a specific strain-adapting character that demands for particular combinations of structural parameters. From strain-adapting to sharp strain-stiffening material, $\text{DP}_{\text{backbone}}/\text{DP}_{\text{side chain}}$ is 128/66 for muscles

and 153/189 for lungs. To possess such biological stress–strain characteristics, it requires bottlebrush polymers with simultaneously long and extended side chains which we obtained by one-pot chain extension reaction of polyurethane consisting of prepolymerized PTMG segment and commercial GM as brushes. Linear–brush copolymers form strong and robust physical networks through intermolecular hydrogen bonds.^{40–44} Using copolymers with the same ratio of GM/PTMG but different distributions of GM brushes (random or block) enables one to synthesize a bottlebrush polyurethane elastomer that exhibits similar mechanical properties of human skin.

The aim of this synthetic route is to produce a bottlebrush-containing polyurethane elastomer that forms a physical cross-linked network by chain entanglement and intermolecular hydrogen bonds. As a result, the bottlebrush polyurethanes become highly elastic with superior tensile strength simultaneously. The properties of these bottlebrush polyurethane elastomers with aromatic disulfides are superior to those of conventional polyurethanes rubber. Tensile strength up to 20 MPa at an elongation at break of 2000% was obtained. Interestingly, apart from pronounced self-healing and recycling properties, bottlebrush polyurethanes exhibit a skin-like stain-adaptive-strengthening effect that was manifested by experiments and calculations.

2. EXPERIMENTAL SECTION

2.1. Materials. All reagents and solvents were purchased from commercial source and were used as received. Poly(tetramethylene ether glycol) (PTMG, $M_n \sim 2000$) was purchased from Inncochem (Beijing, China). Glyceryl monostearate (GM, 95%), 4-aminophenyl disulfide (AFD, 98%), hexamethylene diisocyanate (HDI, 99%), ditin butyl dilaurate (DBTDL, 95%), and tetrahydrofuran (THF, 99%) were obtained from Macklin (Shanghai, China).

2.2. Synthesis of Random Type of Bottlebrush Polyurethanes with Aromatic Disulfides. Random type of bottlebrush polyurethane elastomer (denoted as PTMG-*r*-GM_{*x*}-SS, “*x*” refers to the molar ratio of GM/PTMG in each sample, *x* = 0.2, 0.5, 0.8, and 1.0) was prepared via one-pot chain extension reaction. For the synthesis of

Table 1. Characteristics of Bottlebrush Polyurethanes

sample	M_n (kDa)	\bar{D}	GM/PTMG ^a (mol/mol)	DP _{backbone} ^b	N_b/N_{sc} ^b
PTMG- <i>r</i> -GM _{0.2} -SS	91.2	1.56	0.2	60	28.5
PTMG- <i>b</i> -GM _{0.2} -SS	137.5	1.40	0.2	91	28.5
PTMG- <i>r</i> -GM _{0.5} -SS	58.3	1.69	0.5	44	11.4
PTMG- <i>b</i> -GM _{0.5} -SS	113.5	1.51	0.5	86	11.4
PTMG- <i>r</i> -GM _{0.8} -SS	54.8	1.80	0.8	47	7.1
PTMG- <i>b</i> -GM _{0.8} -SS	87.6	1.65	0.8	75	7.1
PTMG- <i>r</i> -GM _{1.0} -SS	35.7	1.78	1.0	33	5.7
PTMG- <i>b</i> -GM _{1.0} -SS	48.9	1.84	1.0	45	5.7
PTMG-SS	101.6	1.52	—	59	—
PTMG-HDI	149.0	1.35	—	75	—

^aThe molar ratio of GM/PTMG is theoretical. ^bDP of backbones and N_b/N_{sc} are calculated according to the GPC results.

PTMG-*r*-GM_{1.0}-SS, PTMG (8.00 g), GM (1.434 g), AFD (0.199 g), and HDI (2.355 g) were mixed in a 35 mL of THF with a drop of DBTDL as catalyst. The chain extension reaction was initiated by raising the temperature to 60 °C. After 4 h, the reaction flask was removed from the heat and the polymer was poured into a polytetrafluoroethylene mold and dried at 40 °C. The GPC spectrum is presented in the Supporting Information, Figure S2. FTIR (ATR, cm⁻¹): 3340, 2931, 2853, 2796, 1702, 1535, 1465, 1367, 1244, 1100, 820, and 777.

2.3. Synthesis of Block Type of Bottlebrush Polyurethanes with Aromatic Disulfides. Block type of bottlebrush polyurethane elastomer (denoted as PTMG-*b*-GM_{*x*}-SS, “*x*” refers to the ratio of GM/PTMG in each sample, *x* = 0.2, 0.5, 0.8, and 1.0) was prepared via two steps. For the synthesis of PTMG-*b*-GM_{0.5}-SS, GM (0.717 g), HDI (2.018 g), and a drop of DBTDL were mixed in 35 mL of THF. The reaction was initiated by raising the temperature to 60 °C. After 3 h, PTMG (8.00 g) and AFD (0.199 g) were added, and they were kept stirring for another 4 h. The solution was poured into a polytetrafluoroethylene mold and dried at 40 °C. FTIR (ATR, cm⁻¹): 3336, 2927, 2853, 2795, 1701, 1534, 1446, 1367, 1242, 1099, 821, and 777.

The synthesis of PTMG-SS and PTMG-HDI follows the similar preparation method without a GM or AFD component. The FTIR and GPC spectra are presented in the Supporting Information, Figures S1 and S2.

2.4. Gel Permeation Chromatography. Molecular weight and dispersity of the bottlebrush polyurethanes were obtained using an Elite P1100 Pump (Dalian Elite Analytical Instruments Co., Ltd.) equipped with a Shodex K-G 4A and KF-804L columns in series and a Shodex RI-201H differential refractive detector. The THF was used as the mobile phase at a flow rate of 1 mL/min at 40 °C. Number-average molecular weight, PDI, and DP of backbones and sides chains were taken according to the GPC results, which are summarized in Table 1.

2.5. Mechanical Measurements. Tensile tests were carried out on a KJ-1067 tensile test machine with controlled temperature and humidity chamber (Dongguan Kejian Instrument Co. Ltd., China). The measurements were carried out at room temperature at a stretching speed of 100 mm/min. Test specimens with dimensions of 50 × 10 × 1 mm were cut off from the obtained polyurethane sheets (1 mm in thickness). The tests were performed with at least three test specimens for each material.

2.6. Thermodynamic Analysis. DSC (differential scanning calorimetry) measurements were performed on a DSC 200 F3 (Netzsch, Germany). The measurements were carried out in a temperature range of −150 to +120 °C at a scanning rate of ±10 K/min under a nitrogen atmosphere.

DMA (dynamic mechanical thermal spectrometer) (Mettler Toledo Star 1 system) from Mettler Toledo was used to evaluate the dynamic properties. The measurements were carried out in a temperature range of −120 to +120 °C with a heating range of 5 K/min at a frequency of 1 Hz.

Rheological analysis was performed on MCR 102 rheometer (Anton Paar, Austria). The measurements were carried out in a temperature

range of 160 to 20 °C with a cooling rate of 2 K/min at a frequency of 1 Hz under 1% strain.

2.7. Surface Characterization. Static contact angles are measured by using a KRÜSS DSA25 instrument ADVANCE software. Then 3 μL of deionized water is gently dropped on the film, and a snapshot is immediately captured for analysis. The shape of the sessile drop is fitted by using the Young–Laplace method built in the software.

SEM (scanning electron microscopy) of the original and healed samples was carried out using ZEISS EVO 18 Special Edition at 1000× magnification. Healed samples were analyzed after 2 d at room temperature. The elemental analysis was recorded with energy disperse spectroscopy (X-Max20, Oxford Instruments, U.K.). It was used to detect the chemical composition of carbon, nitrogen, oxygen, and sulfur of samples.

3. RESULTS AND DISCUSSION

3.1. Structural Characterization of Bottlebrush Polyurethanes. Bottlebrush polyurethanes with aromatic disulfides were synthesized via a facile “grafting through” method that combines conventional chain extension reaction of polyurethanes. As shown in Scheme 1, a $-(CH_2)_{16}CH_3$ containing monoglyceride was used to introduce bottlebrushes; subsequently, in the presence of a dynamic aromatic disulfide component, well-defined bottlebrush polyurethanes with aromatic disulfides were obtained. The characteristics of the bottlebrush polyurethanes are summarized in Table 1, where the N_b and N_{sc} denote backbone and bottlebrush segment, respectively. These architectural properties and calculation method are also depicted in the Supporting Information, Figure S3. Block types of bottlebrush polyurethanes were obtained with narrower and higher molecular weights than the random type. GPC results of PTMG-SS and PTMG-HDI show that the GM bottlebrushes will reduce the molecular weight by effecting a chain extension reaction. To minimize this effect, the block type of bottlebrush polyurethanes was prepared by polymerizing the GM component primarily with an excessive amount of HDI in the presence of DBTDL as catalyst. The excessive $-NCO$ compared with $-OH$ in GM has been shown to induce the formation of GM segments with considerable molecular weight, which is verified through a viscosity increase in solution. GPC analysis shows a clear shift among random type of bottlebrush polyurethanes with randomly distributed bottlebrushes and block type of bottlebrush polyurethanes with considerable GM segments blocking in polyurethanes backbones.

For one-spot synthesis of random type of bottlebrush polyurethanes, the GM, PTMG, and AFD segments are randomly distributed along the polyurethane backbone. The brushes are in a less inerratic order that entangle both intrachain and interchain, which mainly contributes to their wonderful

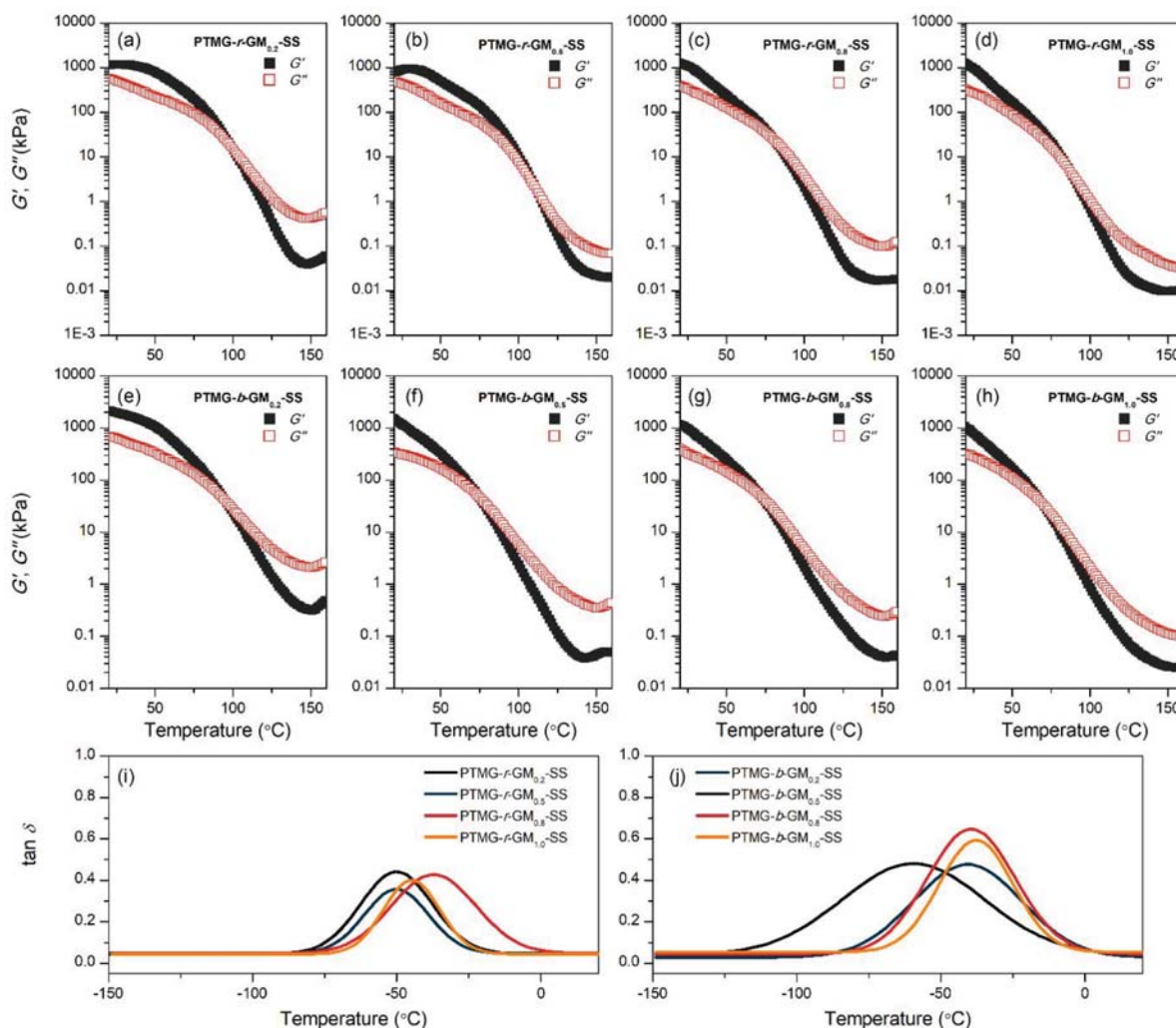


Figure 1. Dynamic mechanical properties: (a–h) rheological temperature sweepings from 160 to 20 °C; (i, j) DMA $\tan \delta$ plots from –150 to +120 °C.

performance as bottlebrush elastomers. Simultaneously, we have also synthesized bottlebrush polyurethanes with prepolymerized GM segments for comparison. First, the molecular weight and polydispersity of random and block type are compared. The molecular weight of block type is slightly higher than that of random type, due to the more coiled-arrangement of block type of polymer chains.

3.2. Dynamic Thermomechanical Analysis. The dynamic aromatic disulfides facilitate segment rearrangements that can induce self-healing after materials damage. Typically, bottlebrush polyurethanes consist of urethane groups, urea groups, and a small percentage of aromatic disulfides randomly distributing in the backbones. The cross-linking density of the bottlebrush polyurethanes is rather poor, which is mainly contributed by hydrogen bonds forming among urethane and urea groups. To overcome this problem, bottlebrush polyurethanes that have higher GM amounts (from GM/PTMG = 0.2 to 1.0) are used. The higher elastic-viscous transition temperature (T_{tr}) is caused by more GM in the composition, which is less flexible in chain movement than the PTMG backbone. At the same time, GM bottlebrushes can entangle and assemble by the intermolecular force, offering the possibility of introducing microphase separation to bottlebrush polyurethanes. Based on the rheological analysis (Figure 1a–h), bottlebrush polyur-

ethanes in bulk converted to viscous liquid at elevated temperatures (over T_{tr}). This transition generates exchange of aromatic disulfides and break in intermolecular hydrogen bonds that we assumed used to cause complete breakdown of polyurethanes material. The reaction scheme is shown in Figure S4. Before the transition reaction at elevated temperature, the exchange of aromatic disulfides is in active progress. During the reaction, a distinct decrease in both storage modulus (G') and loss modulus (G'') was observed above room temperature. Above the T_{tr} , when the G' was less than G'' , it was easy for bottlebrush polyurethanes to be formed and recycled when the material was able to flow like liquid. Therefore, the AFD component was typically kept constant (molar ratio AFD/PTMG = 0.2) for copolymer/block bottlebrush polyurethanes with different GM components. The recycling and reforming for bottlebrush polyurethanes can be carried out at 60–80 °C with preferable viscosity for polyurethanes, and it was then kept at room temperature or lower under pressure.

The glass transition process was monitored using the DMA method, as shown in Figure 1i,j. For comparison, bottlebrush polyurethanes without aromatic disulfides (PTMG-SS) and polyurethanes without GM bottlebrushes or aromatic disulfides (PTMG-HDI) were put on the same DMA test (Supporting Information, Figure S6). The viscoelastic spectra (\tan

δ -temperature) of bottlebrush polyurethanes differ slightly among them with broad glass transition. The maximum (i.e., T_{g-DMA}) and shoulder are located at approximately -50 and -25 °C, respectively. The broad glass transition indicates that substantially bottlebrush polyurethanes are amorphous. For PTMG-SS and PTMG-HDI, at temperatures well below T_{g-DMA} , the storage modulus (E') exhibits a distinct rubber plateau for both samples, indicating considerable cross-linking formed by intermolecular hydrogen bonds.

The phase transition of bottlebrush polyurethanes was also supported DSC method. Figure S7 and Figure S8 show DSC heating curves of the copolymer/block type of bottlebrush polyurethanes with aromatic disulfides with a series of GM components. All samples exhibited a glass transition temperature (T_{g-DSC}) of approximately -65 °C. Additionally, the bottlebrush polyurethanes exhibited two endothermic transitions at approximately 20 and 100 °C, which are assumed as melting of the GM microphase and dissociating of intermolecular hydrogen bonding. This result is in good agreement with the observations made during the transition of bottlebrush polyurethanes in rheological analysis and DMA measurements (data of rheological analysis, DMA, and DSC are summarized in Table 2), where similar modulus and transition temperatures for the copolymer/block type of bottlebrush polyurethanes were detected with various methods.

Table 2. Dynamic Thermomechanical Characteristics of Bottlebrush Polyurethanes

sample	T_{tr}^a (°C)	T_{g-DMA}^b (°C)	T_{g-DSC}^c (°C)	T_{Peak1}^c (°C)	T_{Peak2}^c (°C)
PTMG- <i>r</i> -GM _{0.2} -SS	99.4	-50.3	-68.1	19.5	101.0
PTMG- <i>b</i> -GM _{0.2} -SS	95.2	-41.3	-64.5	20.4	100.4
PTMG- <i>r</i> -GM _{0.5} -SS	111.4	-49.4	-65.6	21.5	100.5
PTMG- <i>b</i> -GM _{0.5} -SS	74.0	-60.3	-65.7	20.4	100.4
PTMG- <i>r</i> -GM _{0.8} -SS	80.4	-38.0	-66.0	22.5	100.0
PTMG- <i>b</i> -GM _{0.8} -SS	72.6	-40.1	-64.7	17.4	100.4
PTMG- <i>r</i> -GM _{1.0} -SS	86.7	-45.7	-65.7	13.8	99.8
PTMG- <i>b</i> -GM _{1.0} -SS	69.1	-38.2	-66.2	12.3	99.3

^aTemperature of T_{tr} is obtained from rheological temperature sweeping plots where T_{tr} is the temperature at $G' = G''$.

^bTemperature of T_{g-DMA} is obtained from DMA $\tan \delta$ plots, where T_{g-DMA} is the temperature when $\tan \delta$ is at its maximum.

^cTemperature of T_{g-DSC} , T_{c1} , and T_{c2} is obtained from DSC curves (Supporting Information).

3.3. Mechanical Properties. Figure 2 shows the stress-strain behavior of the bottlebrush polyurethanes with aromatic disulfides. Notably, the properties of random and block polyurethanes are typically consistent under the same amount of GM component. With 1720% elongation at break and a tensile strength of 22.3 MPa, PTMG-*b*-GM_{0.2}-SS exhibited competent tensile properties compared with PTMG-SS and PTMG-HDI (tensile strength of 18.3 MPa@1860% and 19.9 MPa@1610%, respectively (Supporting Information, Table S3 and Figure S9)). A distinct reduction in both Young's modulus and toughness was observed with the increase of the GM component, which was in good agreement with the results obtained directly from typical stress-strain plots. Poor mechanical properties may be caused by the irregularity along the chain after the copolymerization of GM, AFD, and PTMG segment units. A sharp bend in the curve for bottlebrush polyurethanes with aromatic disulfides is clearly observed at

100% strain. In Figure 2d, PTMG-*r*-GM_{1.0}-SS breaks before the strain-stiffening of the network. Block type of bottlebrush polyurethanes are preferred to random type for higher tensile strength values. At the strain range of 100% until break, a steady and smooth increase of strength is shown. This stage of strain strengthening is assumed to be the result of location changes and rearrangement process of the polyurethanes chains and GM bottlebrushes during stretching.⁴⁵ Generally, strain stiffening requires covalent cross-linking points to resist the force at high strain. Since all samples are soluble in THF, covalent cross-linking can be excluded. A special character of soft tissue like skin is mechanical strain induced stiffening to prevent potential injury.^{46,47} For real skin, when a gentle force is applied to the skin, the skin can be easily stretched and the wrinkle marks are formed. A hard pinch, however, may induce uncomfortable feelings, and we observe that it will be difficult to stretch as the force is further increased. Similar to the human skin, bottlebrush polyurethanes present such a stain-adaptive-strengthening effect (Figure 3).⁴⁸ In the stage of strain-stiffening, the stress of bottlebrush polyurethanes can respond to their strain via a quadratic function. The equation is put forward with $R^2 = 0.9996$. The results of polynomial fitting of other bottlebrush polyurethanes are verified by the results of tensile experiments in the Supporting Information, Figure S10.

$$\sigma(\lambda) = \frac{E}{9}(\lambda^2 - \lambda^{-1}) \left[1 + 2 \left(1 - \frac{\beta(\lambda^2 + 2\lambda^{-1})}{3} \right)^{-2} \right] \quad (1)$$

Previous researches^{39,49} have shed light on the constitutive equations for all equilibrium deformations of a broad range of unentangled networks, including synthetic elastomers and biological tissues. As outlined in eq 1, E (Young's modulus) and β (the strand-extension ratio) are fitting parameters for the σ - λ (stress-strain) curve. As-prepared bottlebrush polyurethanes possess a σ - λ^2 relation only after strain $\approx 100\%$; the stress-strain curve (0–100%) reveals the typical properties of “rigid and brittle” synthesized elastomers. The two-stage tensile properties reveal the combinations of typical synthesized elastomers and strain-stiffening soft bottlebrush elastomers.

The stress-strain behavior can be explained by the microphase separation theory of GM bottlebrushes and PTMG backbones. The bottlebrush microphase is isolated dispersed at the beginning of the experiment. This explains the moderate increase in stress at low strain (samples achieve less than 1 MPa within 0–100% of strain). With increasing elongation, rearrangements of PTMG backbones and entanglements of GM bottlebrushes take place. The bottlebrush microphases are in progressive contact with each other, and formation of a bigger microphase acts as cross-linking point similar to covalent cross-links. In the bottlebrush polyurethanes with higher GM components (PTMG-GM_{0.8}-SS and PTMG-GM_{1.0}-SS), the tensile strength and elongation are limited to excessive GM of poor mechanical properties. As expected, the stain-adaptive-strengthening effect of PTMG-SS and PTMG-HDI is not significant.

3.4. Surface Studies. The hydrophobicity of bottlebrush polyurethanes was investigated by measuring the static contact angle. The static contact angle is given in Figure 4b and in Table S4, Supporting Information. The contact angle values reported are the average of five or more measurements taken at different locations of the sample surface, which proves the homogeneity of the surface. Contact angle values for the prepared bottlebrush polyurethanes films do not show much difference with the

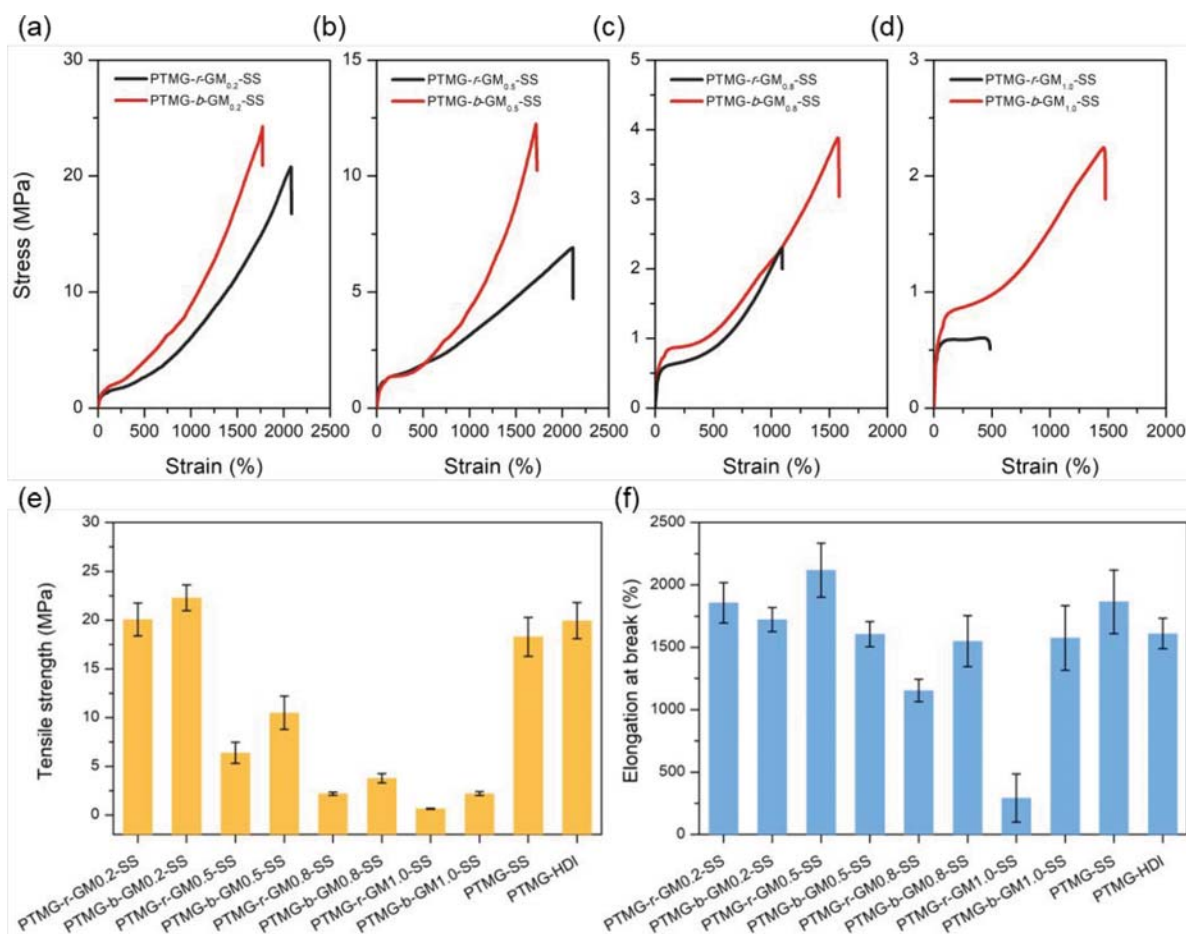


Figure 2. Mechanical properties: (a–d) stress–strain plots; (e, f) summarization of tensile strength and elongation at break with PTMG-SS and PTMG-HDI.

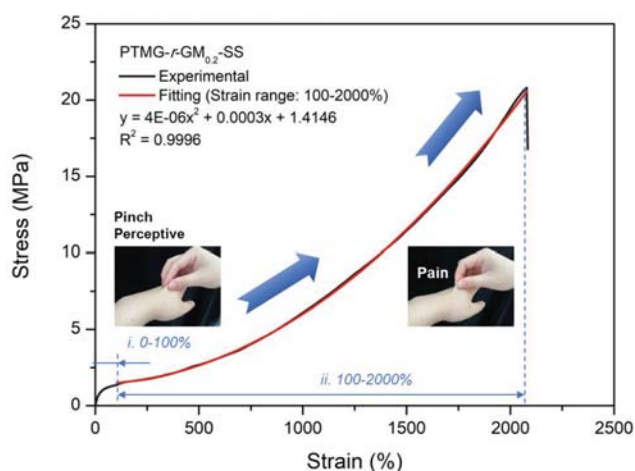


Figure 3. Skin-like bottlebrush polyurethanes enabling a stain-adaptive-strengthening effect. Photos of skin on a real hand that is highly stretched with a feeling of pain. A typical stress–strain curve (PTMG-*r*-GM_{0.2}-SS is used here), showing the remarkable mechanical response of intense strain stiffening behavior. A tendency of skin-like strain strengthening is observed with two stages: 0–100% and 100–2000%. A polynomial fitting against the second-stage stress–strain is proposed, and the equation is given.

change of GM component. Among all random and block types, polyurethanes with GM/PTMG = 0.8 exhibit the smallest

contact angles, respectively. The introduction of GM bottle-brushes to the PTMG polyurethanes slightly increases the contact angle from 93.2° (PTMG-HDI) to 96.0° (PTMG-*b*-GM_{1.0}-SS), which indicates a water-repellent surface. The block type of bottlebrush polyurethanes has a higher contact angle compared to the random type in general. Usually, the bottlebrushes are dispersed throughout the film thickness with a slight excess at the surface. The blocking of the GM segment in the bottlebrush polyurethanes matrix plays a vital role in increasing the contact angle. The presence of a small percentages of aromatic disulfides provides a thermodynamic driving force that renders the surface hydrophobic.^{50,51} It is known that clean and degreased skin gives a contact angle with water higher than 100°; for real skin with various hydrophilic and hydrophobic agents on it, reductions of contact angles are observed to a minimum of 70°.⁵² The as-prepared bottlebrush polyurethanes not only provide a skin-like strain stiffening tensile property but also give a similar skin-texture surface character.

3.5. Self-Healing and Recycling Properties. The origin of the self-healing behavior and recycling property is obviously the dynamic aromatic disulfides and the linear structure bottlebrush polyurethanes. The reversible interactions and amplitude chain mobility increase adhesion between the two cut pieces and hence compensate for material damages. The cut samples were allowed to heal at room temperature for different lengths of time. As the mending time increased, the healing effect increased, whereas the stress–strain curves after healing

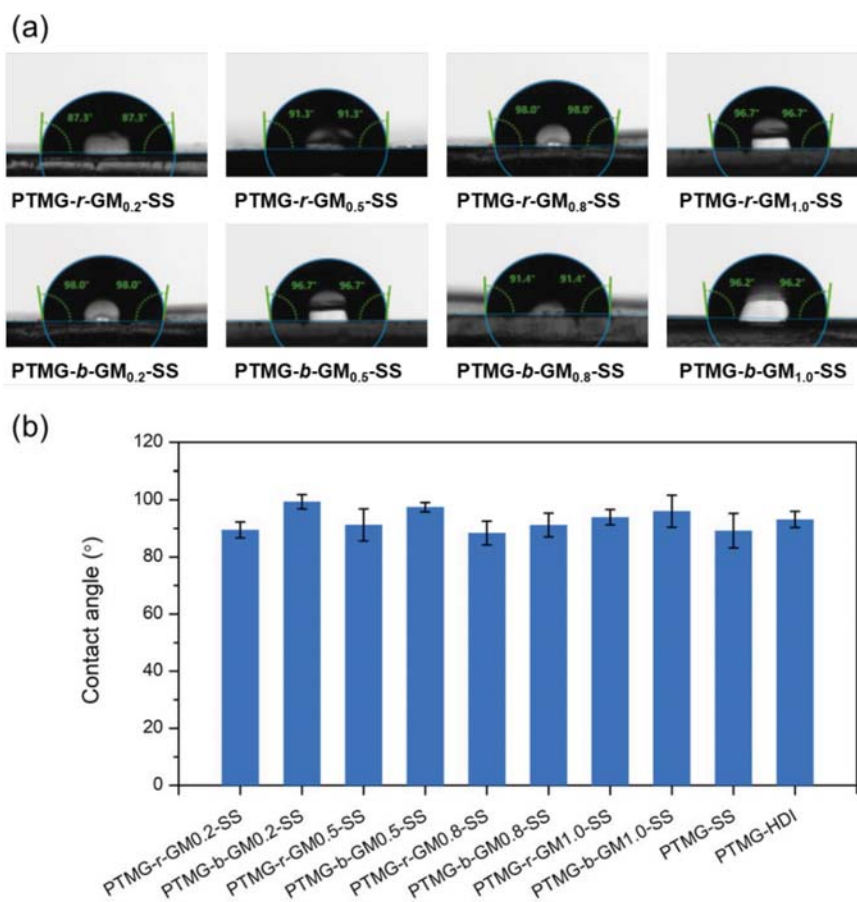


Figure 4. Contact angles for water in contact with bottlebrush polyurethanes with aromatic disulfides. (a) Water droplet on the surface of film samples. (b) Summarization of contact angles of bottlebrush polyurethanes with aromatic disulfides as well as PTMG-SS and PTMG-HDI as reference.

process remained nearly unaffected. The original sample of PTMG-*r*-GM_{0.5}-SS exhibited a tensile strength of 6.9 MPa, an elongation at break 2110%, Young's modulus of 5.3 MPa, and toughness of 75.1 MPa, while after 2 h of healing, the self-healed sample exhibited mechanical properties of 6.0 MPa, 1900%, 4.0 MPa, and 59.6 MPa, respectively. This is distinguished from conventional hydrogen-bonded polyurethanes and disulfide cross-linked rubber. In our system, exchange of aromatic disulfides and association of hydrogen bonds in the interphase of the two cut pieces are assumed to be the guarantee for the excellent self-healing and recycling effect observed. These rearrangements are aided by the high intrinsic mobility of the PTMG backbones at ambient temperatures. The improved reversible reaction rate and higher chain mobility at elevated temperatures positively contribute to the self-healing efficiency. The recycling and reforming of bottlebrush polyurethanes with aromatic disulfides can be carried out either in good solvent (tetrahydrofuran or dichloromethane, for example) or at elevated temperatures. Reforming samples tested in Figure 5 were totally deformed pieces dissolved in THF for 2 h and dried at 40 °C. This is comparable with the mechanical properties of the original. After the reforming process, the mended sample achieved a healing efficiency in almost 100% recovery of tensile strength and 89% recovery in elongation at break. Bottlebrush polyurethanes with equal molar component of aromatic disulfides (AFD/PTMG = 0.2) facilitated the healing and reforming processes that work in a similar way.

Notably, self-healing was observed at room temperature, which indicates that a certain degree of chemical element motion already exists and follows the rearrangement between the polymer chains and reversible reactions. A visual demonstration of the self-healing effect and the cutting line after 2 d of self-healing at room temperature are shown in Figure 6a–d. Between the two joined surfaces of the cut sample, a narrow-fused line is visible. For comparison, PTMG-HDI moieties without aromatic disulfides shown in parts e and f of Figure 6 do not exhibit self-healing behavior. An energy dispersive spectroscopy (EDS) is performed to describe the element movement of the healing behavior. Therefore, we studied and compared the carbon, nitrogen, oxygen, and sulfur atoms distribution of notched and healed specimens of PTMG-*r*-GM_{0.5}-SS (Figure 6b,d and the Supporting Information, Figure S11). EDS results show that the amount of sulfur is much lower compared with that of C, N, and O elements. Due to the presence of aromatic disulfides in the bottlebrush polyurethanes, the notch is significantly narrower. The aromatic disulfides present in the cutting surface may exchange with each other and bridge the physical gap.

4. CONCLUSIONS

A skin-like bottlebrush polyurethane elastomer with aromatic disulfides was prepared via a simple one-pot procedure. The study shows that introduction of GM brushes and dynamic aromatic disulfides can allow preparing a mechanically and surficial skin-like polyurethane elastomer without the use of

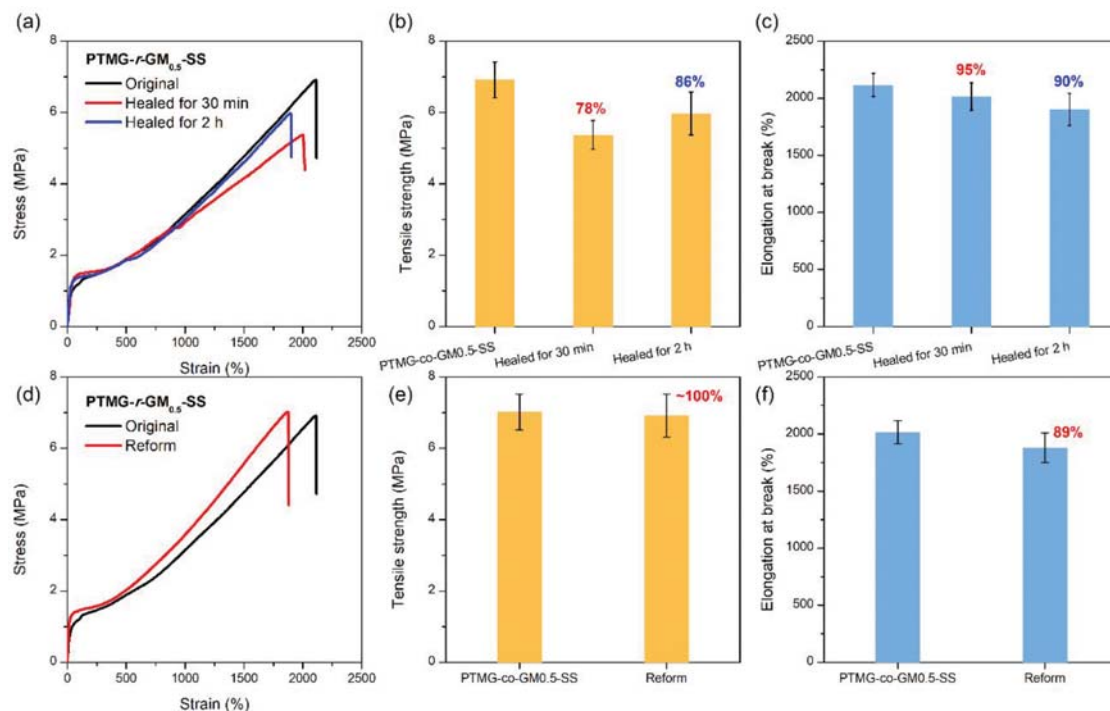


Figure 5. Self-healing and recyclable properties of bottlebrush polyurethanes with aromatic disulfides. (a) Stress–strain plots of PTMG-*r*-GM_{0.5}-SS original and self-healed for 30 min and 2 h. For comparison, (b) tensile strength and (c) elongation at break are shown. (d) Stress–strain plots, (e) tensile strength, and (f) elongation at break of PTMG-*r*-GM_{0.5}-SS original and reformed. The numbers (red in figures) indicate the percentage of healing/reforming efficiency.

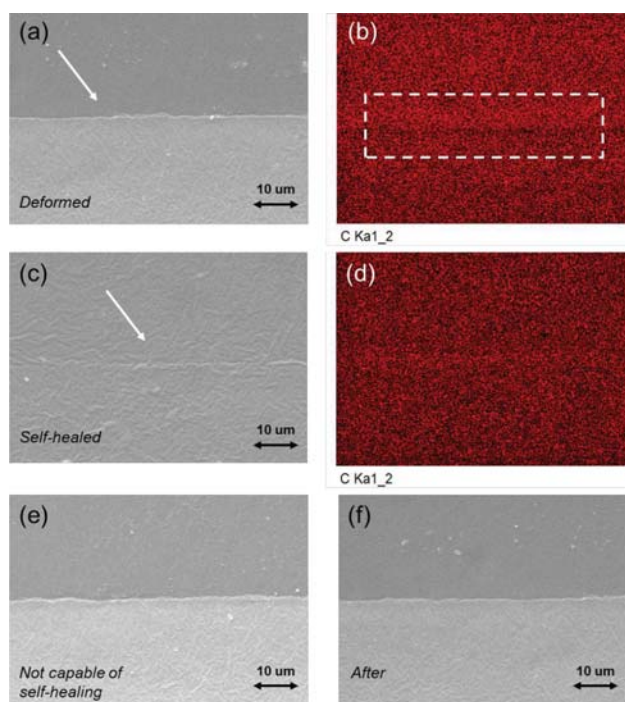


Figure 6. Self-healing behavior of bottlebrush polyurethanes with aromatic disulfides. (a–d) Deformed and self-healed PTMG-*r*-GM_{0.5}-SS SEM and EDS carbon images. As comparison, (e) deformed PTMG-HDI and (f) deformed PTMG-HDI after 2 d. Self-healed samples were maintained at room temperature.

conventional fillers or cross-linkers. GPC studies provided structural parameters for bottlebrush polyurethanes, including

molecular weight, polydispersity, and degree of polymerization of backbone and side chains. Random and block distributed GM brushes can be easily altered in this report, which sheds light on the synthesis of bottlebrush polyurethanes in the future. Self-healing and recycling properties can be realized easily at room temperature without any external stimuli. Direct visualization of self-healing behavior was observed by scanning electron microscopy. Dynamic thermomechanical analysis of bottlebrush polyurethane elastomer with aromatic disulfides were realized by different methods in this report. The development of polyurethanes with exchangeable aromatic disulfides also reduces the number of processing and recycling steps. In addition to easy processing, this polyurethane elastomer also has unique advantages over conventional polymers as they exhibit a skin-like character against strain in tensile experiments. The bottlebrush polyurethane elastomer with aromatic disulfides presented offers a bioinspired versatility for rubber parts further development of commercial products. Having the advantages of ease of synthesizing, processing, and recycling, the as-prepared bottlebrush polyurethane elastomer opens up a new horizon in advanced rubber technology.

■ ASSOCIATED CONTENT

Supporting Information

The Supporting Information is available free of charge at <https://pubs.acs.org/doi/10.1021/acsapm.2c01234>.

Additional experimental details and methods, including characterization of bottlebrush polyurethanes with aromatic disulfides, DSC, DMA, rheology results, and SEM images (PDF)

■ AUTHOR INFORMATION

Corresponding Authors

Anqiang Zhang — School of Materials Science and Engineering, South China University of Technology, Guangzhou 510641 Guangdong, China; orcid.org/0000-0001-7499-8406; Email: aqzhang@scut.edu.cn

Yaling Lin — College of Materials and Energy, South China Agricultural University, Guangzhou 510642 Guangdong, China; orcid.org/0000-0002-5289-4304; Email: linyaling@scau.edu.cn

Authors

Shijie Shan — School of Materials Science and Engineering, South China University of Technology, Guangzhou 510641 Guangdong, China; orcid.org/0000-0002-8017-1656

Xionghui Wu — School of Materials Science and Engineering, South China University of Technology, Guangzhou 510641 Guangdong, China

Complete contact information is available at:
<https://pubs.acs.org/10.1021/acsapm.2c01234>

Author Contributions

The manuscript was written through the contributions of all authors.

Notes

The authors declare no competing financial interest.

■ ACKNOWLEDGMENTS

The authors acknowledge the financial support from the National Natural Science Foundation of China (No. 52073098) and the Natural Science Foundation of Guangdong Province (No. 2022A1515011570).

■ REFERENCES

- (1) Verduzco, R.; Li, X.; Pesek, S. L.; Stein, G. E. Structure, Function, Self-Assembly, and Applications of Bottlebrush Copolymers. *Chem. Soc. Rev.* **2015**, *44*, 2405–2420.
- (2) Rzaev, J. Molecular Bottlebrushes: New Opportunities in Nanomaterials Fabrication. *ACS Macro Lett.* **2012**, *1*, 1146–1149.
- (3) Lee, H.; Pietrasik, J.; Sheiko, S. S.; Matyjaszewski, K. Stimuli-Responsive Molecular Brushes. *Prog. Polym. Sci.* **2010**, *35*, 24–44.
- (4) Wang, M. Q.; Zou, H.; Liu, W. B.; Liu, N.; Wu, Z. Q. Bottlebrush Polymers Based on RAFT and the “C1” Polymerization Method: Controlled Synthesis and Application in Anticancer Drug Delivery. *ACS Macro Lett.* **2022**, *11*, 179–185.
- (5) Raj, W.; Jerczynski, K.; Rahimi, M.; Przekora, A.; Matyjaszewski, K.; Pietrasik, J. Molecular Bottlebrush with pH-Responsive Cleavable Bonds as a Unimolecular Vehicle for Anticancer Drug Delivery. *Mater. Sci. Eng., C* **2021**, *130*, 112439.
- (6) Huang, Y. S.; Chen, J. K.; Kuo, S. W.; Hsieh, Y. A.; Yamamoto, S.; Nakanishi, J.; Huang, C. F. Synthesis of Poly (N-vinylpyrrolidone)-Based Polymer Bottlebrushes by ATRP and RAFT Polymerization: Toward Drug Delivery Application. *Polymers* **2019**, *11*, 1079.
- (7) Song, D. P.; Zhao, T. H.; Guidetti, G.; Vignolini, S.; Parker, R. M. Hierarchical Photonic Pigments via the Confined Self-Assembly of Bottlebrush Block Copolymers. *ACS Nano* **2019**, *13*, 1764–1771.
- (8) Guo, T.; Wang, Y.; Qiao, Y.; Yuan, X.; Zhao, Y.; Ren, L. Thermal Property of Photonic Crystals (PCs) Prepared by Solvent Annealing Self-Assembly of Bottlebrush PS-b-PtBA. *Polymer* **2020**, *194*, 122389.
- (9) Liberman-Martin, A. L.; Chu, C. K.; Grubbs, R. H. Application of Bottlebrush Block Copolymers as Photonic Crystals. *Macromol. Rapid Commun.* **2017**, *38*, 1700058.
- (10) Arrington, K. J.; Radzinski, S. C.; Drummey, K. J.; Long, T. E.; Matson, J. B. Reversibly Cross-Linkable Bottlebrush Polymers as Pressure-Sensitive Adhesives. *ACS Appl. Mater. Interfaces* **2018**, *10*, 26662–26668.
- (11) Dalsin, S. J.; Hillmyer, M. A.; Bates, F. S. Molecular Weight Dependence of Zero-Shear Viscosity in Atactic Polypropylene Bottlebrush Polymers. *ACS Macro Lett.* **2014**, *3*, 423–427.
- (12) Sun, W.; Liu, W.; Wu, Z.; Chen, H. Chemical Surface Modification of Polymeric Biomaterials for Biomedical Applications. *Macromol. Rapid Commun.* **2020**, *41*, 1900430.
- (13) Roeven, E.; Kuzmyn, A. R.; Scheres, L.; Baggerman, J.; Smulders, M. M.; Zuilhof, H. PLL-Poly (HPMA) Bottlebrush-Based Antifouling Coatings: Three Grafting Routes. *Langmuir* **2020**, *36*, 10187–10199.
- (14) Xia, Y.; Adibnia, V.; Huang, R.; Murschel, F.; Faivre, J.; Xie, G.; Olszewski, M.; De Crescenzo, G.; Qi, W.; He, Z.; Su, R.; et al. Biomimetic Bottlebrush Polymer Coatings for Fabrication of Ultralow Fouling Surfaces. *Angew. Chem.* **2019**, *131*, 1322–1328.
- (15) Varlas, S.; Hua, Z.; Jones, J. R.; Thomas, M.; Foster, J. C.; O'Reilly, R. K. Complementary Nucleobase Interactions Drive the Hierarchical Self-Assembly of Core-Shell Bottlebrush Block Copolymers toward Cylindrical Supramolecules. *Macromolecules* **2020**, *53*, 9747–9757.
- (16) Nam, J.; Kim, Y.; Kim, J. G.; Seo, M. Self-Assembly of Monolayer Vesicles via Backbone-Shiftable Synthesis of Janus Core-Shell Bottlebrush Polymer. *Macromolecules* **2019**, *52*, 9484–9494.
- (17) Xie, G.; Ding, H.; Daniel, W. F.; Wang, Z.; Pietrasik, J.; Sheiko, S. S.; Matyjaszewski, K. Preparation of Titania Nanoparticles with Tunable Anisotropy and Branched Structures from Core-Shell Molecular Bottlebrushes. *Polymer* **2016**, *98*, 481–486.
- (18) Li, Z.; Tang, M.; Liang, S.; Zhang, M.; Biesold, G. M.; He, Y.; Hao, S. M.; Choi, W.; Liu, Y.; Peng, J.; Lin, Z. Bottlebrush Polymers: From Controlled Synthesis, Self-Assembly, Properties to Applications. *Prog. Polym. Sci.* **2021**, *116*, 101387.
- (19) Xiong, H.; Zhang, L.; Wu, Q.; Zhang, H.; Peng, Y.; Zhao, L.; Huang, G.; Wu, J. A Strain-Adaptive, Self-Healing, Breathable and Perceptive Bottle-Brush Material Inspired by Skin. *J. Mater. Chem. A* **2020**, *8*, 24645–24654.
- (20) Chen, K.; Hu, X.; Zhu, N.; Guo, K. Design, Synthesis, and Self-Assembly of Janus Bottlebrush Polymers. *Macromol. Rapid Commun.* **2020**, *41*, 2000357.
- (21) Ahmed, E.; Womble, C. T.; Weck, M. Synthesis and Aqueous Self-Assembly of ABCD Bottlebrush Block Copolymers. *Macromolecules* **2020**, *53*, 9018–9025.
- (22) Lin, T. P.; Chang, A. B.; Luo, S. X.; Chen, H. Y.; Lee, B.; Grubbs, R. H. Effects of Grafting Density on Block Polymer Self-Assembly: From Linear to Bottlebrush. *ACS Nano* **2017**, *11*, 11632–11641.
- (23) Radzinski, S. C.; Foster, J. C.; Matson, J. B. Preparation of Bottlebrush Polymers via a One-Pot Ring-opening Polymerization (ROP) and Ring-Opening Metathesis Polymerization (ROMP) Grafting-Through Strategy. *Macromol. Rapid Commun.* **2016**, *37*, 616–621.
- (24) Pesek, S. L.; Li, X.; Hammouda, B.; Hong, K.; Verduzco, R. Small-Angle Neutron Scattering Analysis of Bottlebrush Polymers Prepared via Grafting-Through Polymerization. *Macromolecules* **2013**, *46*, 6998–7005.
- (25) Wang, C. K.; Gruber, C. W.; Cemazar, M.; Siatskas, C.; Tagore, P.; Payne, N.; Sun, G.; Wang, S.; Bernard, C. C.; Craik, D. J. Molecular Grafting onto a Stable Framework Yields Novel Cyclic Peptides for the Treatment of Multiple Sclerosis. *ACS Chem. Biol.* **2014**, *9*, 156–163.
- (26) Azzam, F.; Heux, L.; Putaux, J. L.; Jean, B. Preparation by Grafting Onto, Characterization, and Properties of Thermally Responsive Polymer-Decorated Cellulose Nanocrystals. *Biomacromolecules* **2010**, *11*, 3652–3659.
- (27) Gao, H.; Matyjaszewski, K. Synthesis of Molecular Brushes by “Grafting Onto” Method: Combination of ATRP and Click Reactions. *J. Am. Chem. Soc.* **2007**, *129*, 6633–6639.
- (28) Hansson, S.; Trouillet, V.; Tischer, T.; Goldmann, A. S.; Carlmark, A.; Barner-Kowollik, C.; Malmström, E. Grafting Efficiency of Synthetic Polymers onto Biomaterials: A Comparative Study of Grafting-from versus Grafting-To. *Biomacromolecules* **2013**, *14*, 64–74.

- (29) Matyjaszewski, K.; Dong, H.; Jakubowski, W.; Pietrasik, J.; Kusumo, A. Grafting from Surfaces for "Everyone": ARGET ATRP in the Presence of Air. *Langmuir* **2007**, *23*, 4528–4531.
- (30) Wang, H.; Onbulak, S.; Weigand, S.; Bates, F. S.; Hillmyer, M. A. Polyolefin Graft Copolymers through a Ring-Opening Metathesis Grafting through Approach. *Polym. Chem.* **2021**, *12*, 2075–2083.
- (31) Bloch, S. E.; Alaboalrat, M.; Eades, C. B.; Scannelli, S. J.; Matson, J. B. Solvent Effects in Grafting-Through Ring-Opening Metathesis Polymerization. *Macromolecules* **2022**, *55*, 3522–3532.
- (32) Senkum, H.; Gramlich, W. M. Cationic Bottlebrush Polymers from Quaternary Ammonium Macromonomers by Grafting-Through Ring-Opening Metathesis Polymerization. *Macromol. Chem. Phys.* **2020**, *221*, 1900476.
- (33) Johnson, J. A.; Lu, Y. Y.; Burts, A. O.; Lim, Y. H.; Finn, M. G.; Koberstein, J. T.; Turro, N. J.; Tirrell, D. A.; Grubbs, R. H. Core-Clickable PEG-Branch-Azide Bivalent-Bottle-Brush Polymers by ROMP: Grafting-Through and Clicking-To. *J. Am. Chem. Soc.* **2011**, *133*, 559–566.
- (34) Walsh, D. J.; Wade, M. A.; Rogers, S. A.; Guirionnet, D. Challenges of Size-Exclusion Chromatography for the Analysis of Bottlebrush Polymers. *Macromolecules* **2020**, *53*, 8610–8620.
- (35) Liu, Y.; Zheng, J.; Zhang, X.; Du, Y.; Li, K.; Yu, G.; Jia, Y.; Zhang, Y. Mussel-Inspired and Aromatic Disulfide-Mediated Polyurea-Urethane with Rapid Self-Healing Performance and Water-Resistance. *J. Colloid Interface Sci.* **2021**, *593*, 105–115.
- (36) Shan, S.; Lin, Y.; Zhang, A. Stretchable, Robust and Reprocessable Poly (Siloxane-Urethanes) Elastomers Based on Exchangeable Aromatic Disulfides. *Polymer* **2021**, *221*, 123588.
- (37) Nevejans, S.; Ballard, N.; Fernández, M.; Reck, B.; Asua, J. M. Flexible Aromatic Disulfide Monomers for High-Performance Self-Healable Linear and Cross-linked Poly (Urethane-Urea) Coatings. *Polymer* **2019**, *166*, 229–238.
- (38) Martin, R.; Rekondo, A.; Ruiz de Luzuriaga, A.; Cabañero, G.; Grande, H. J.; Odriozola, I. The Processability of a Poly (Urea-Urethane) Elastomer Reversibly Crosslinked with Aromatic Disulfide Bridges. *J. Mater. Chem. A* **2014**, *2*, 5710–5715.
- (39) Vatankeh-Varnosfaderani, M.; Daniel, W. F. M.; Everhart, M. H.; et al. Mimicking Biological Stress-strain Behaviour with Synthetic Elastomers. *Nature* **2017**, *549*, 497–501.
- (40) Wang, H.; Liu, H.; Cao, Z.; Wu, J.; et al. Room-Temperature Autonomous Self-Healing Glassy Polymers with Hyperbranched Structure. *Proc. Natl. Acad. Sci. U. S. A.* **2020**, *117* (21), 11299–11305.
- (41) Wu, J.; Cai, L. H.; Weitz, D. A. Tough Self-Healing Elastomers by Molecular Enforced Integration of Covalent and Reversible Networks. *Adv. Mater.* **2017**, *29*, 1702616.
- (42) Bistričić, L.; Baranović, G.; Leskovic, M.; Bajsić, E. G. Hydrogen Bonding and Mechanical Properties of Thin Films of Polyether-based Polyurethane-Silica Nanocomposites. *Eur. Polym. J.* **2010**, *46*, 1975–1987.
- (43) Mattia, J.; Painter, P. A Comparison of Hydrogen Bonding and Order in a Polyurethane and Poly (urethane-urea) and Their Blends with Poly (ethylene glycol). *Macromolecules* **2007**, *40*, 1546–1554.
- (44) Brunette, C. M.; Hsu, S. L.; MacKnight, W. J. Hydrogen-Bonding Properties of Hard-Segment Model Compounds in Polyurethane Block Copolymers. *Macromolecules* **1982**, *15*, 71–77.
- (45) Das, A.; Sallat, A.; Böhme, F.; Suckow, M.; Basu, D.; Wiefner, S.; Stöckelhuber, K. W.; Voit, B.; Heinrich, G. Ionic Modification Turns Commercial Rubber into a Self-Healing Material. *ACS Appl. Mater. Interfaces* **2015**, *7*, 20623–20630.
- (46) Xiao, P.; Zhou, W.; Liang, Y.; Kuo, S. W.; Yang, Q.; Chen, T. Biomimetic Skins Enable Strain-Perception-Strengthening Soft Morphing. *Adv. Funct. Mater.* **2022**, *32*, 2201812.
- (47) Zhang, W.; Wu, B.; Sun, S.; Wu, P. Skin-Like Mechanoresponsive Self-Healing Ionic Elastomer from Supramolecular Zwitterionic Network. *Nat. Commun.* **2021**, *12*, 0482.
- (48) Abbasi, M.; Faust, L.; Wilhelm, M. Comb and Bottlebrush Polymers with Superior Rheological and Mechanical Properties. *Adv. Mater.* **2019**, *31*, 1806484.
- (49) Carrillo, J. M. Y.; MacKintosh, F. C.; Dobrynin, A. V. Nonlinear Elasticity: from Single Chain to Networks and Gels. *Macromolecules* **2013**, *46*, 3679–3692.
- (50) Stiubianu, G.; Nicolescu, A.; Nistor, A.; Cazacu, M.; Varganici, C.; Simionescu, B. C. Chemical Modification of Cellulose Acetate by Allylation and Crosslinking with Siloxane Derivatives. *Polym. Int.* **2012**, *61*, 1115–1126.
- (51) Kulkarni, S. A.; Ogale, S. B.; Vijayamohanan, K. P. Tuning the Hydrophobic Properties of Silica Particles by Surface Silanization Using Mixed Self-Assembled Monolayers. *J. Colloid Interface Sci.* **2008**, *318*, 372–379.
- (52) Ginn, M. E.; Noyes, C. M.; Jungermann, E. The Contact Angle of Water on Viable Human Skin. *J. Colloid Interface Sci.* **1968**, *26*, 146–151.

Recommended by ACS

Concise and Efficient Self-Healing Cross-Linked Polyurethanes via the Blocking/Deblocking Reaction of Oxime Urethanes

Bowen Xu, Jingbo Zhao, *et al.*

JULY 22, 2021

INDUSTRIAL & ENGINEERING CHEMISTRY RESEARCH

READ 

Biobased Thermoplastic Elastomer Based on an SMS Triblock Copolymer Prepared via RAFT Polymerization in Aqueous Medium

Uddhab Kalita, Nikhil K. Singha, *et al.*

JANUARY 22, 2021

MACROMOLECULES

READ 

Robust Poly(urethane-amide) Protective Film with Fast Self-Healing at Room Temperature

Jiahui Zhou, Xun Lu, *et al.*

NOVEMBER 21, 2019

ACS APPLIED POLYMER MATERIALS

READ 

Highly Stretchable Fatty Acid Chain-Dangled Thermoplastic Polyurethane Elastomers Enabled by H-Bonds and Molecular Chain Entanglements

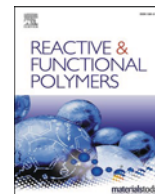
Yong Zeng, Wendi Liu, *et al.*

AUGUST 15, 2022

ACS SUSTAINABLE CHEMISTRY & ENGINEERING

READ 

Get More Suggestions >



Perspective Article

Polydimethylsiloxane-polymethacrylate block copolymers containing quaternary ammonium salts against *Fusarium oxysporum* f. sp. *cubense* race 4 in soil: Antifungal activities and pot experiments

Yaoyao Chang^a, Weiqiang Zhong^b, Jiaqi Liang^a, Anqiang Zhang^{b,*}, Yaling Lin^{a,*}

^a College of Materials and Energy, South China Agricultural University, 483 Wushan Rd., Guangzhou 510642, Guangdong, China

^b School of Material Science and Engineering, South China University of Technology, 381 Wushan Rd., Guangzhou 510641, Guangdong, China

ARTICLE INFO

Keywords:

Banana Fusarium wilt
Polymeric quaternary ammonium salts
Adsorption
Migration
Antifungal activity
Persistence

ABSTRACT

Fusarium oxysporum f. sp. *cubense* race 4 (Foc4) has significant impacts on banana production. Foc4 conidia can survive for many years in the soil, making control difficult. Thus, the inhibition of the conidia that serve as a continual source of inoculum in soil should be an effective way to control banana Fusarium wilt. In this paper, we first investigated the activities of polydimethylsiloxane-polymethacrylate block copolymers containing quaternary ammonium salts (PDMS-*b*-QPMAEMA, labeled Si_xQ₅) against Foc4 with microbroth dilution and toxicity plate assays. Then, the environmental behavior of these compounds, i.e., their adsorption and migration in soils, was further studied. Later, the effect and duration of Si_xQ₅ on Foc4 in soil and the effects of Si_xQ₅ on soil microbial diversity were evaluated. In addition, we conducted pot experiments to study the effect of Si₅Q₅ on banana Fusarium wilt. The results showed that Si_xQ₅ showed a good inhibitory effect on Foc4, was easily adsorbed by the soil and was relatively immobile in soil. The inhibitory effect of Si_xQ₅ on Foc4 was maintained for 30 d under continual inoculation of Foc4 into the soil (Foc4 addition every 2 d), and Si_xQ₅ remained active in the soil for 90 d with Foc4 addition every 10 d. Soil microbial population analysis revealed that the culturable total fungal and bacterial populations increased and the culturable actinobacterial population decreased Si_xQ₅ with addition. Pot experiments showed that Si₅Q₅ can reduce Foc4 infection in banana seedlings and does not harm banana seedlings. The stability and inhibitory effects on Foc4 demonstrate the potential application of Si_xQ₅ in banana fields to prevent Foc4 conidial infection in the long term.

1. Introduction

Banana Fusarium wilt (aka Panama disease) is one of the most destructive soil-borne diseases of banana and is caused by *Fusarium oxysporum* f. sp. *cubense* (Foc); specifically, tropical race 4 (Foc4) has been distributed throughout the world's main banana production areas and infects almost all bananas [1]. Foc4 can infect the roots and vascular systems of plants [2], and the pathogen conidia are highly resistant to stress. Once this pathogen has colonized the soil, Foc4 can survive for approximately 20 years even without banana hosts [3,4] and even 40 years under extreme conditions [5]. Panama wilt is a perennial and polycyclic disease, which means that there are limited prevention and control methods for it [6]. One of the most effective methods is eradicating Foc4 from infested soil. Therefore, soil treatments are essential. People sterilize the soil by burning rice husks in the Philippines and

Indonesia, but there is no efficacy data for this method. Other soil treatment methods, such as solarization, fumigation and flood fallowing, can effectively kill Foc4 in soil; however, the effects can only be maintained for a single fruiting cycle, and Foc4 rapidly reinvasades the area [1,6]. Soils that inhibit the occurrence of Fusarium wilt have been identified. The diversity of the microbial community in the soil and soil enzyme activity can strengthen the resistance of soil to Foc4 invasion. Bacteria are the most diverse and abundant group of microorganisms in the soil and have the most antagonistic effect against Fusarium pathogens [7–9]. Therefore, to support sustainable crop production, it is essential to effectively kill Foc4 in the long term while exerting no significant effect on the disease-suppressive bacterial community in the rhizosphere.

Since soil is a complex and dynamic environment, the adsorption and desorption of fungicides in soils are important processes that

* Corresponding authors.

E-mail addresses: aqzhang@scut.edu.cn (A. Zhang), linyaling@scau.edu.cn (Y. Lin).

<https://doi.org/10.1016/j.reactfunctpolym.2021.104848>

Received 12 November 2020; Received in revised form 5 February 2021; Accepted 6 February 2021

Available online 10 February 2021

1381-5148/© 2021 Elsevier B.V. All rights reserved.

characterize the mobility and transport of fungicides in the soil sub-surface. These behaviors have an important impact on the persistence of fungicides. Therefore, it is of great significance to study the environmental behavior of fungicides entering the soil and analyze the factors influencing the fungicides' persistent fungicidal activity against Foc4 infection.

Although cationic polymers with quaternary ammonium salt groups (PQASs) have attracted a great deal of attention in recent years for their they exhibit good environmental stability [10] and various antimicrobial activities via the modifications of their chemical side chains, structures and properties [11–16], the application of PQASs, especially biodegradable PQASs, in phytopathogenic fungi was rarely reported. In our previous work, a series of PQASs, including the homopolymer of acrylamide quaternary ammonium salt (PQD-BC) [16,23,53], dimethylaminopropyl benzyl chloride-grafted polysiloxanes (PDMS-g-BC) [19], and hydrophilic cationic polymers with different charge density and molecular weights [60] were synthesized, and the antifungal effect on Foc4 and *Rhizoctonia solani* (*R. solani*) were discussed. These works could help us understand the relationship between polymer structures and antifungal activities, in which the amphiphilic structure, molecular weights and QAS groups showed significantly effect on the antifungal activities. We previously described the synthesis of polydimethylsiloxane-polymethacrylate block copolymers containing quaternary ammonium salts (PDMS-*b*-QPDMAEMA, labeled Si_xQ₅), which are environmental-friendly and show nontoxic or nearly nontoxic to silkworms and Kunming mice and have antifungal activities against *R. solani*, the pathogen responsible for rice sheath blight [17]. Since the PDMS block is hydrophobic and the QPDMAEMA block is hydrophilic, PDMS-*b*-QPDMAEMA is a typical amphiphilic cationic block copolymer and shows strong adsorption ability. However, the morphological characteristics and life cycles of Foc4 and *R. solani* are very different. As mentioned above, Foc4 is the banana wilt pathogen and can infect and propagate by producing conidia as well as chlamydoconidia that can survive in soil or nonhost plants for many years [18]. To date, the antimicrobial activities and environmental behaviors of PDMS-*b*-QPDMAEMA in soils have not been reported.

In this paper, we investigated the activities of PDMS-*b*-QPDMAEMA against Foc4 and its environmental behavior with respect to its adsorption and migration in soil. These data are important for evaluating the impact of PDMS-*b*-QPDMAEMA on Foc4 and for future field studies. In addition, the effects of PDMS-*b*-QPDMAEMA on Foc4, the indigenous microorganisms in soil and their persistent fungicidal activities against Foc4 infection in soils were evaluated. Finally, pot experiments were conducted to evaluate the long-term effect of PDMS-*b*-QPDMAEMA on banana Fusarium wilt and banana seedlings in soil. These results are expected to provide a theoretical basis for the further application of PQASs in Foc4 prevention and control.

2. Experiments

2.1. Materials

2,3,5-Triphenyltetrazolium chloride (TTC) was obtained from Sangon Biotech (Shanghai) Co., Ltd. (Shanghai, China). Gause No. 1 medium and Martin's Bengal rose agar medium were supplied by Qingdao Hope Bio-Technology Co., Ltd. (Shandong, China). Beef extract peptone medium and potato dextrose agar medium (PDA) were prepared according to previous references [19]. The fungal strain used in this study, *Fusarium oxysporum* f. sp. *cubense* (E. F. Smith) Snyder & Hansen, race 4 (Foc4), was donated by the University of South China Agricultural University's Fungal Laboratory and subcultured on potato dextrose agar medium (PDA). Foc4 conidia were obtained from the surface of the agar after culture for 5 d at 28 °C. The concentrations of the conidial suspensions were determined using a hemocytometer. Soil samples were taken from banana plantations at the Institute of Fruit Trees, Guangdong Academy of Agricultural Sciences, China. A five-point sampling method

Table 1
Soil physicochemical properties.

Sand (%)	Silt (%)	Clay (%)	pH (1:2.5)	Organic matter (%)	CEC ^a (mmol/kg)
>0.05 mm	0.005–0.05 mm	<0.005 mm			
49.4%	18.2%	32.4%	5.0	1.9%	104

^a CEC, cation exchange capacity, mmol/kg.

was used to collect soil at a depth of approximately 0–30 cm from the soil surface, after which the soil samples were air-dried at room temperature, homogenized and sieved through a 2-mm mesh. Some basic physicochemical properties of the samples are listed in Table 1. The percentages of clay, silt and sand were measured using a hydrometer [20]. The cation exchange capacity was measured with a standard acetate ammonium procedure. The soil organic matter content was determined using the dichromate digestion method. The pH was measured in a soil:H₂O (1:2.5) solution [21]. Since the cation exchange capacity (CEC) was less than 160 mmol/kg, the soil samples could be classified as Ferallsols according to the WRB (World Reference Base for Soil Resources) [22].

PDMS-*b*-QPDMAEMA (Si_xQ₅, x = 0, 2, 5, 10, x represent the molecular weights of the PDMS blocks, i.e., 0, 2000, 5000 or 10,000, respectively) and fluorescence-labeled PDMS-*b*-QPDMAEMA (Si_xQ₅-FL) were synthesized via anionic ring-opening polymerization and atom transfer radical polymerization (ATRP) [17], and the specific procedures are described in SI (Part S1).

2.2. Antifungal bioassay

The effect of Si_xQ₅ on the mycelial growth of Foc4 was determined by a hyphal growth inhibition test in vitro. The minimum inhibitory concentration (MIC) of Si_xQ₅ on Foc4 was determined by the broth micro-dilution method with 2,3,5-triphenyltetrazolium chloride (TTC), and the minimal fungicidal concentration (MFC) of Si_xQ₅ against Foc4 was determined by the spot plate method [23]. All tests were conducted in triplicate.

2.3. Adsorption and migration characteristics of Si_xQ₅ in agricultural soil

2.3.1. Adsorption tests

According to the method described in the OECD106 guide, the adsorption - desorption with batch equilibrium desorption method was used to carry out the soil adsorption test [24]. The soil was weighed (1.000 ± 0.001 g) into a conical flask, and 100 mL of 0.01 M CaCl₂ aqueous solution containing Si_xQ₅ was added to make a soil/water ratio of 1:100. The concentration of Si_xQ₅ ranged from 0 to 1000 µg/mL, and 0.01 M CaCl₂ aqueous solution was used as a background solution to minimize changes in ionic strength and avoid dispersion. Each conical flask was shaken with a shaker at 200 rpm at 25 °C for 24 h, and then the supernatant was centrifuged at a relative centrifugal force (RCF) of 3000 g for 10 min. The supernatant concentration from each tube was analyzed by a micro ultraviolet spectrophotometer (SMA5000, Merinton). The absorbance was measured at 210 nm [25]. There were two blank controls: one control (Si_xQ₅ solution, no soil) test to assess the loss of compounds as a result of adsorption on the container wall; and another experiment was conducted to determine the interference due to the 0.01 M CaCl₂ aqueous solution and soil. Each treatment was conducted in triplicate.

The amount of Si_xQ₅ adsorbed was determined according to the difference between the initial and final concentrations of Si_xQ₅ in the supernatant. The quantity of Si_xQ₅ adsorbed by soil was calculated by Eq. (1):

$$C_s = \frac{C_0V - C_eV}{1000 \cdot m} \quad (1)$$

Table 2
Equations used to study Si_xQ₅ sorption in soils.

Model	Equation	Eq.	Description
Langmuir	$C_s = \frac{KM_s C_e}{1 + KC_e}$	(2)	K , Langmuir coefficient (L/mg); M_s , the maximum amount of Si _x Q ₅ adsorbed on soil solids as a monolayer (mg/g).
Freundlich	$C_s = K_f C_e^{\frac{1}{n}}$	(3)	K_f and n , Freundlich capacity and intensity factors, respectively.
Temkin	$C_s = K_1 \ln(K_2 C_e)$	(4)	K_1 and K_2 , Temkin sorption constants.

where C_s is the amount of Si_xQ₅ adsorbed per unit weight of soil (mg/g), C_0 is the initial concentration of Si_xQ₅ in the treatment solution, and C_e is the concentration of Si_xQ₅ present in the supernatant at equilibrium (μg/mL). V is the volume of the treatment solution (mL), and m is the mass of the soil (g).

The adsorption data obtained from intermittent experiments were analyzed by using the Langmuir, Freundlich and Temkin isotherm model [26], as shown in Table 2.

2.3.2. Migration tests

The migration potential of Si_xQ₅ in soil was studied by thin layer chromatography (TLC). Thin-layer plates of soil were prepared according to a previously reported method [27]. The air dried plate was marked with two horizontal lines at a distance from the base of 3 cm (baseline) and 18 cm (endpoint). A droplet of 10.0 μg Si_xQ₅-FL solution prepared in alcohol was spotted onto the baseline of the plate. The plates were immersed with the base down at a certain angle from vertical in a closed glass chamber containing distilled water at a height of 0.5 cm. Distilled water was used as the developing solvent. After the developing solvent migrated to a distance of 18 cm from the base, the plates were removed from the glass chambers and laid flat to dry at room temperature. Autoradiograms were obtained by irradiation with an ultraviolet lamp (365 nm). Each Si_xQ₅-FL was treated in triplicate. The mobility factor (R_f) of Si_xQ₅-FL on the plates was calculated by the following formula [28]:

$$R_f = \frac{L}{L_{\max}} \quad (5)$$

where L is the average moving distance of Si_xQ₅-FL from the starting point, and L_{\max} is the moving distance of the developing solvent from the starting point.

2.4. Antifungal bioassay in soil

2.4.1. Optimization of antifungal conditions based on the uniform design method

The optimum soil conditions for the maximum antifungal activity of Si_xQ₅ were determined by a uniform design method according to a previous study [29]. Experiments for the optimization of the antifungal conditions involved three factors, including the Si_xQ₅ concentration (mg/g, X_1), shaking speed of shaker (rpm, X_2) and water/soil ratio (mL/g, X_3). The levels of each factor (Table S3) were selected according to the experimental results of the pre-experiments. A U_{10}^5 uniform design table was used to arrange the 10 experiments (Table 3), where the contents in brackets indicate the level of the factor, and the contents outside of the brackets indicate the exact concentration, shaking speed or water/soil ratio of each factor.

The testing was conducted as follows: the collected soil samples were first sterilized in a 121 °C high-temperature and high-pressure sterilizer for 20 min and then inoculated with Foc4 conidial suspension to obtain a soil/Foc4 mixture in the range of 2.25×10^5 conidia/(g dry soil) [30]. According to the uniform design table (Table 2), for each test, 0.5 g air dried soil containing Foc4 conidia prepared as described above was

Table 3
Experiments based on uniform design table (U_{10}^5).

No.	X_1 (Si _x Q ₅ concentration, mg/g) ^a	X_2 , (shaking speed, rpm)	X_3 , water/soil ratio (mL/g)
T1	(10xIC ₅₀)	(175)	(3/1)
T2	(10xIC ₅₀)	(200)	(10/1)
T3	(20xIC ₅₀)	(250)	(1/1)
T4	(20xIC ₅₀)	(150)	(9/1)
T5	(30xIC ₅₀)	(175)	(18/1)
T6	(30xIC ₅₀)	(225)	(1/1)
T7	(40xIC ₅₀)	(250)	(9/1)
T8	(40xIC ₅₀)	(150)	(18/1)
T9	(50xIC ₅₀)	(200)	(3/1)
T10	(50xIC ₅₀)	(225)	(10/1)

^a The IC₅₀ values for Si₀Q₅, Si₅Q₅ and Si₁₀Q₅ were 0.73, 0.76, and 0.94 mg/mL, respectively, as shown in Table 5.

mixed with sterile distilled water containing Si_xQ₅ in a 5-mL tube with a lid, and the experiments were carried out at 28 °C. A total of 25 μL of solution was taken from each sample every 2 d to confirm whether it contained live Foc4 conidia by the dilution plate coating method. If no live Foc4 conidia could be found, another 25 μL of Foc4 suspension was added to the tube to maintain the conidia concentration at 2.25×10^5 conidia/(g dry soil). If live Foc4 conidia were found, then the time was defined as the effective antifungal time (Y, day) of Si_xQ₅ and recorded. Each treatment was conducted in triplicate.

Regression analyses of the data were performed using SAS software (SAS 8.01, SAS Institute Inc., USA.), wherein the stepwise regression model was chosen to analyze the data; the variable listed in Eq. (6) was eliminated if the significance parameter of a variable was lower than 0.1.

$$Y = a_1 X_1 + a_2 X_2 + a_3 X_3 + a_4 X_1 X_2 + a_5 X_1 X_3 + a_6 X_2 X_3 + a_7 X_1^2 + a_8 X_2^2 + a_9 X_3^2 + a_{10} \quad (6)$$

where a_1 to a_9 are the coefficients for the variables from X_1 to X_3^2 , respectively, and a_{10} is the constant.

2.4.2. Determination of the effects of Si_xQ₅ on soil microbial diversity

Fresh soil samples (0.5 g) were incubated with potato dextrose broth medium (0.5 mL) for 24 h at room temperature to develop the microbial populations in the soil and then added to 5 mL of sterilized distilled water containing Si_xQ₅ at different concentrations (10xIC₅₀, 20xIC₅₀ and 30xIC₅₀). The samples were cultured for 2 d at 28 °C on a shaker with a shaking speed of 225 rpm. Then, the number of cultivable microorganisms in the soil was determined using two methods, including the traditional plate count method [31] and gene sequencing.

For the plate count method, 25 μL of the soil suspension was inoculated into an agar plate containing suitable medium (including beef extract peptone medium, Gause No. 1 medium, and Martin's bengal rose agar medium, which were chosen for the culture of bacteria, actinomycetes and fungi, respectively), the number of living microbes was counted, and the population number was determined. The total number of microorganisms was determined by counting the number of colony forming units (CFU/g dry soil). Each treatment was conducted in triplicate.

For the gene sequencing method, after the samples were centrifuged at 10,000 r/min for 3 min, the upper liquid was collected and filtered using a 0.22 μm filter membrane, and both the soil sample and the filter membrane were sent for gene sequencing. The soil fungal community structure was analyzed using Illumina MiSeq sequencing (Sangon Biotech Co., Ltd., Shanghai, China). The gene-specific primers ITS1F/ITS2R were used to amplify the fungal ITS1-ITS2 region [32]. The details of the procedure are recorded in the Supporting Information.

2.4.3. Persistence of Si_xQ₅ on Foc4 in soil

To perform antifungal bioassays of Si_xQ₅ in soil over time, 0.5 g of

Table 4
Groups for pot experiments.

Groups	Foc4 conidia in soil, CFU/g soil	Si ₅ Q ₅ in soil, mg/g soil
CK	0	0
Group 1	0	IC ₅₀ (0.76)
Group 2	1 × 10 ⁵	0
Group 3	1 × 10 ⁵	IC ₅₀ (0.76)

sterilized dry soil was mixed with sterile distilled water containing Si_xQ₅ in a 5-mL tube with a lid, and then Foc4 conidial suspension was added at 2.25×10^5 conidia/(g dry soil). Then, the experiments were carried out at 28 °C. A total of 25 µL of solution was taken from each sample every 10 d to confirm whether it contained live Foc4 conidia by the dilution plate coating method [33]. If no live Foc4 conidia were found, another 25 µL of Foc4 suspension was added to the tube to maintain the conidia concentration at 2.25×10^5 conidia/(g dry soil). If live Foc4 conidia were found, then the time was defined as the antifungal persistence time (d) of Si_xQ₅ and recorded. Each treatment was conducted in triplicate.

2.5. Pot experiment

Potted soil was provided by the Crop Nutrition and Fertilization Laboratory of South China Agricultural University. The basic parameters of the soil are shown in Table S4.

The soil samples were sieved over a 5 mm mesh and then divided into 4 groups, i.e., 3 treatment groups (Groups 1, 2 and 3) and a CK according to Table 4, in which CK refers to normal samples (without the addition of Foc4 conidia or the addition of Si₅Q₅; each group contained 10 replications), and the total amount of soil in the pot for each replication was 700 g, in which Si₅Q₅ solution and Foc4 conidial suspension were mixed with soil before being added to the pots (upper diameter 13 cm, lower diameter 10 cm, height 13 cm) [32]. After banana seedlings (*Musa AAA Cavendish* cv. Brazil, purchased from South China Botanical Garden, Chinese Academy of Sciences, Guangzhou (Huang et al., 2019) with a height of approximately 15 cm (4–5 leaves) were transplanted to the pots, 200 mL tap water was added, and then 75 mL tap water was added every afternoon to each pot. All potted plants were cultured in the greenhouse at a typical temperature of 25 to 35 °C and humidity of 55–95% under natural sunshine for approximately 12 h. After 90 d of banana seedling growth, the plant height, false stem circumference, total leaf number, green leaf number, fresh weight and dry weight of each seedling were recorded. Based on the degree of corm browning and leaf chlorosis, disease classification was carried out, and the disease index of the banana seedlings was calculated by Eq. (7).

$$\text{Disease index} = \frac{\sum \text{Number of cases at all levels} \times \text{Relative values}}{\text{Total number of plants} \times \text{Maximum value}} \times 100\% \quad (7)$$

3. Results and discussion

3.1. Antifungal activities of Si_xQ₅ on Foc4

Since Si_xQ₅ is a typical amphiphilic cationic block copolymer, which is moisture-absorbing and easy to dissolve in water. In fact, it could be “miscible” with water when the concentration is larger than critical micelle concentration (CMC, range from 0.06 to 0.09 mg/mL for Si_xQ₅ [17]): at this time, most of the polymer exists in the aqueous solution in the form of micelles. The effects of Si_xQ₅ on the mycelial growth of Foc4 were determined by the hyphal growth inhibition test in which the colony diameter was measured on PDA plates with different concentrations of Si_xQ₅. Si_xQ₅ inhibited the growth of Foc4 in the concentration range of 0.3–1.5 mg/mL. As the concentration of Si_xQ₅ increased, the diameter of each treatment group decreased. The 50% maximum

Table 5
The antifungal effect of Si_xQ₅ against Foc4.

	MIC ^a , mg/mL	MFC ^a , mg/mL	MIC/MFC	IC ₅₀ ^a , mg/mL	IC ₉₀ ^a , mg/mL
Si ₀ Q ₅	0.15	0.6	4	0.73	4.73
Si ₅ Q ₅	0.15	0.6	4	0.76	2.96
Si ₁₀ Q ₅	0.15	0.3	2	0.94	3.20

^a MIC: Minimum inhibitory concentration, MFC: Minimal fungicidal concentration, IC₅₀: 50% maximum inhibitory concentration, IC₉₀: 90% inhibitory concentration.

inhibitory concentration (IC₅₀) represents the concentration of Si_xQ₅ at which 50% of Foc4 growth is inhibited, and the 90% inhibitory concentration (IC₉₀) represents the concentration of Si_xQ₅ at which 90% of Foc4 growth is inhibited [34]. After 5 d of incubation, Si_xQ₅ displayed antifungal effects (Fig. S1-A, B and Table 5), and the results indicated that although both Si₀Q₅ (IC₅₀ = 0.73 mg/mL) and Si₅Q₅ (IC₅₀ = 0.76 mg/mL) showed better inhibition effect than that of Si₁₀Q₅ (IC₅₀ = 0.94 mg/mL) at 50% inhibition of mycelial growth, Si₅Q₅ (IC₉₀ = 2.96 mg/mL) exhibited the greatest effect against Foc4, compared with Si₀Q₅ (IC₉₀ = 4.73 mg/mL) and Si₁₀Q₅ (IC₅₀ = 3.20 mg/mL) at 90% inhibition of mycelial growth. The antifungal efficacy results also showed that Si₀Q₅, Si₅Q₅ and Si₁₀Q₅ inhibited the mycelial growth of Foc4 in a dose-dependent manner.

The MIC and MFC are the principal measures of in vitro activity. We subsequently tested the MIC and MFC of Si_xQ₅ against Foc4, as shown in Fig. S1-C, D and Table 5. The in vitro studies showed that Si_xQ₅ had an inhibitory effect on Foc4. The ratio of MFC/MIC can reflect the fungicidal activity; when the ratio was less than or equal to 4, Si_xQ₅ showed fungicidal activity; otherwise, Si_xQ₅ had antifungal activity [35]. Si_xQ₅ showed lower MIC and MFC values and MFC/MIC ratios ≤ 4, indicating that the compounds were fungicidally effective. This finding indicated that PDMS-*b*-QPMAEMA (Si_xQ₅) has promise for application as an antifungal agent against plant pathogens.

The antifungal experiment showed that Si_xQ₅ had good antifungal effects on Foc4. Quaternary ammonium salts compounds (QASSs) are widely used in agricultural production, textile printing and dyeing, and mining flotation because of their good surface activity and bactericidal effect [36]. Previous studies have shown that QASSs are effective biological fungicides that can bind to proteins and nucleic acids, destroy the integrity of the cell membrane, and lead to the leakage of cytoplasmic ions and macromolecules [37–39]. In our previously studies, the effect of the homopolymer of (2-methacrylamido) propyltetra-benzyltrimethylammoniumchloride (PQD-BC) and dimethylamino-propyl benzyl chloride-grafted polysiloxanes (PDMS-g-BC) on Foc4 were discussed in detail [23]. In which, the polymeric QASSs were found to induce cell death in Foc4 by disrupting the cellular structure integrity, such as the loss of the cell wall and plasma membrane integrity and oxidative stress (lipid peroxidation), leading to the release of intracellular contents and inducing mitochondrial dysfunction and interference with genomic DNA. Comparing with PQD-BC, Si_xQ₅ containing a hydrophobic PDMS “tail” and showed similar amphiphilic structure as that of PDMS-g-BC, which help Si_xQ₅ to achieve smaller MIC and IC₉₀ on Foc4 than PQD-BC [23]. And due to the similar hydrophilic QPMAEMA block containing QASSs as PQD-BC, it could be expected that Si_xQ₅ would have an antifungal effect on Foc4 with the similar mechanism as PQD-BC and PDMS-g-BC.

3.2. The adsorption and migration characteristics of Si_xQ₅ in agricultural soil

3.2.1. Soil adsorption properties of Si_xQ₅

Adsorption isotherms (Fig. 1-A) were drawn from the concentration (C₀) and soil adsorption capacity (C_s) at adsorption equilibrium and then analyzed using the Langmuir, Freundlich and Temkin isotherm models

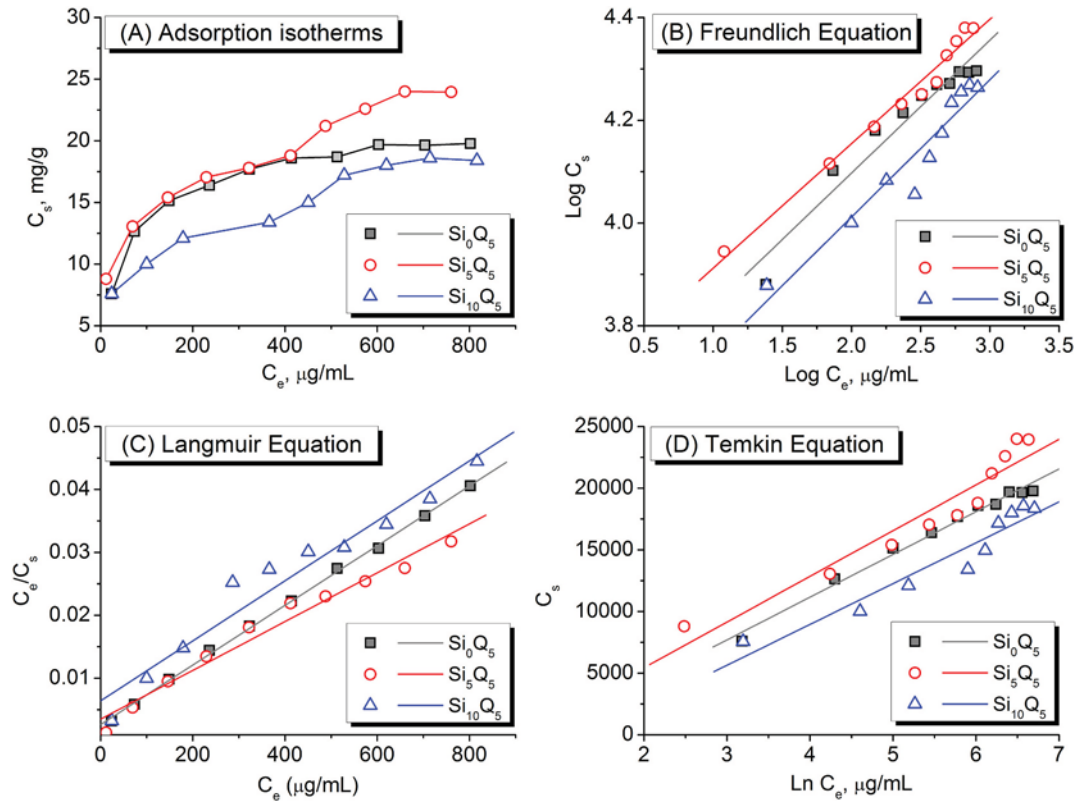


Fig. 1. The adsorption isotherms of Si_xQ_5 in soil with the (A) Freundlich equation model (B), Langmuir equation model (C), and Temkin equation model (D).

(Fig. 1-B, C and D, respectively). With the increase in the adsorbed amount in soil, the adsorption behavior of quaternary ammonium salt in soil weakens until the soil is saturated; thus, the inflection point can be found in Fig. 1-A. The interferences from the background soil organic matter and 0.01 M CaCl_2 aqueous solution were consistently very low (absorbance ~ 0.001) in all experiments. From Fig. 1-A, the adsorption isotherms at 25 °C followed L-type characteristics, reflecting the relatively high affinity between Si_xQ_5 and the soils. Table 6 presents the constants of the Langmuir, Freundlich and Temkin isotherm models.

From the determined parameters of the Freundlich, Langmuir and Temkin equations, the Langmuir model yielded the best fit, with all the correlation coefficients (R^2 values) greater than 0.95. The M_s values of Si_0Q_5 , Si_5Q_5 and Si_{10}Q_5 were 21,097 $\mu\text{g/mL}$, 25,773 $\mu\text{g/mL}$ and 20,964 $\mu\text{g/mL}$, respectively, indicating that $\text{Si}_5\text{Q}_5 > \text{Si}_0\text{Q}_5 > \text{Si}_{10}\text{Q}_5$. The adsorption data were also fitted to the Freundlich and Temkin equations, and the correlation coefficients suggested that the Freundlich ($R^2 = 0.92\text{--}0.98$) and Temkin ($R^2 = 0.91\text{--}0.98$) equations could well describe the adsorption data [40]. The Freundlich parameters $1/n$ followed the order $\text{Si}_5\text{Q}_5 < \text{Si}_0\text{Q}_5 < \text{Si}_{10}\text{Q}_5$. Universally, the lower $1/n$ is, the higher the binding affinity to the soil. This relationship is consistent with the description of the Langmuir equation. The sorption parameter K_f has a strong dependence on organic matter; the higher the content of organic matter in soil, the greater the K_f . The relation describing the adsorption of a given molecule can be illustrated in a different manner in which the K_f value is standardized according to the soil organic carbon (OC%)

content to obtain the organic carbon-normalized adsorption coefficient (K_{oc}) according to the following formula [41]:

$$K_{oc} = \frac{1.724K_f}{OM\%} \quad (8)$$

where 1.724 is the conversion coefficient between the soil organic matter and organic carbon contents. Through calculation, the K_{oc} values of Si_0Q_5 , Si_5Q_5 and Si_{10}Q_5 were determined to be 344,813, 424,408 and 272,448, respectively, all of which are greater than 20,000. According to Chinese National Standard GB/T 31270.4–2014, the adsorption properties indicate that Si_xQ_5 is easily adsorbed in soil.

Adsorption isotherms can explain the distribution of an adsorbate between the liquid and solid phases, and the possibility of the interaction between the adsorbed species can be determined by this mathematical model [26]. The adsorption isotherms show that the adsorption of Si_xQ_5 can be considered monolayer adsorption, which indicates that the binding force of Si_xQ_5 to soil is strong. The adsorption capacity of Si_xQ_5 in soil increases with increasing concentration, but when it reaches a certain point, the adsorption capacity will no longer increase [42]. The adsorption isotherm model of Si_xQ_5 is more suitable for the Langmuir model than the Freundlich and Temkin equations, and the Langmuir isotherm model is appropriate for monolayer adsorption onto a surface with a limited number of identical sites. That is, the whole adsorption process of Si_xQ_5 in soil is monolayer adsorption. The experimental results are consistent with the existing adsorption results for

Table 6
Freundlich, Langmuir and Temkin equation model parameters.

Sample	Freundlich equation			Langmuir equation			Temkin equation		
	K_f	$1/n$	R^2	M_s	K	R^2	K_1	K_2	R^2
Si_0Q_5	3800	0.2587	0.9400	21,097	0.018	0.9990	3466	0.46	0.9851
Si_5Q_5	4677	0.2422	0.9816	25,773	0.011	0.9738	3706	0.59	0.9227
Si_{10}Q_5	3002	0.267	0.9259	20,964	0.007	0.9529	3311	0.27	0.9179

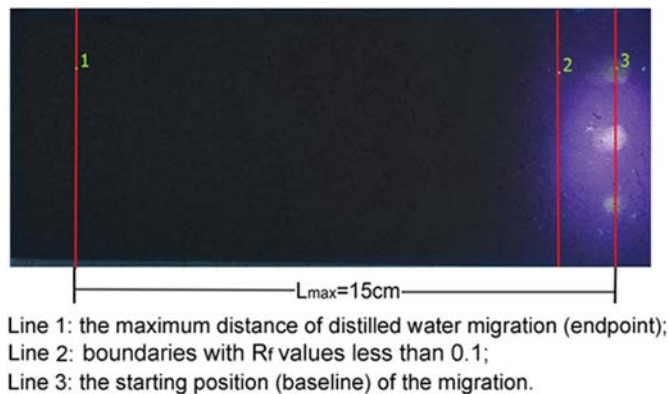


Fig. 2. Results of soil thin layer chromatography.

quaternary ammonium salts in soil [43,44].

In summary, Si_xQ_5 belongs to the group of compounds that are easily adsorbed by soil. The adsorption properties of Si_xQ_5 in soil follow the order $\text{Si}_5\text{Q}_5 > \text{Si}_{10}\text{Q}_5 > \text{Si}_{10}\text{Q}_5$, which shows that with certain length (about 5 k for the PDMS block) of the hydrophobic segment, the best adsorption performance of PDMS-*b*-QPDMAEMA in soil could be achieved.

3.2.2. Soil migration

Fig. 2 shows the soil adsorption and soil thin layer chromatography of Si_xQ_5 -FL in soil. The distance covered by Si_xQ_5 -FL on a thin layer compared to that covered by water, i.e., the R_f value, was measured by using a 365 nm ultraviolet lamp. The distance between Si_xQ_5 -FL and the thin layer was less than 1 cm, so the R_f value was less than 0.1; thus, it can be concluded that Si_xQ_5 -FL does not move in soil.

From soil adsorption assays and soil thin layer chromatography, it can be concluded that Si_xQ_5 is easily adsorbed and relatively immobile in soil, which might be mainly due to the positive charge of quaternary nitrogen atoms, while the soil particles (such as sludge and sediments) normally bear negative charges. These results are similar to those of many previous studies on the behavior of QASs in soil [45–50]. The easy adsorption and immobility of Si_xQ_5 in soil indicate that Si_xQ_5 is not easily lost in soil, which is beneficial for the long-term control of banana Fusarium wilt, and the negative impacts of its presence will be the subject of further study.

Table 7
Results of regression analysis.

Si_xQ_5	Regression equation	Standard error	Correlation coefficient (R^2)
Si_0Q_5	$Y = -1.5614 + 0.07069 X_1X_3$	2.75	0.9618
Si_5Q_5	$Y = 0.02896 + 0.06911 X_1X_3$	3.84	0.9290
Si_{10}Q_5	$Y = -1.523 + 0.07381 X_1X_3 - 0.05965 \times \frac{X_2^2}{3}$	3.51	0.9330

3.3. Antifungal bioassay in soil

3.3.1. Optimization of antifungal conditions

The uniform design method (UD) was first established by Chinese mathematicians Kaitai Fang and Yuan Wang by combining number theory with multivariate statistics and is usually applied in multifactor and multilevel experimental design [58]. Compared with the traditional orthogonal design method, the uniform design method is capable of selecting experimental points that are uniform throughout the experimental region and highly representative in the experimental domain, so that higher reliability can be achieved with the same number of tests. As an efficient way to optimize various processes, the uniform design method is widely used in materials preparation and optimization of test conditions [59]. In this work, the Si_xQ_5 concentration (X_1 , mg/g), shaking speed (X_2 , rpm) and water/soil ratio (X_3 , mL/g) were selected as the factors that might affect the final results, i.e., the effective antifungal time (Y , day). The results of the uniform design are shown in Fig. 3, in which the effective antifungal time (Y) varied considerably from 0 to 32 d under different conditions. The final regression equations based on the stepwise regression model are shown in Table 7, in which the variables whose significance parameters were lower than 0.1 have been eliminated. The high R^2 values indicated a strong relationship between the experimental and predicted values in this experiment. Therefore, the model is suitable for describing the relationship between antifungal conditions and significant factors for optimization. The Si_xQ_5 concentration (X_1) and water/soil ratio (X_3) were the main factors affecting Si_xQ_5 in soil. That is, when the Si_xQ_5 concentration (X_1) and water/soil ratio (X_3) were both high, the sustained antifungal time (Y) of Si_xQ_5 in the soil was the longest. Within the range of experimental conditions, shaking speed (X_2) had no significant effect. The longest antifungal times (28 d, 32 d, and 30 d) were obtained when the major factors were as follows: a Si_xQ_5 concentration of $50\times\text{IC}_{50}$ and water/soil ratio of 10/1. Since shaking speed (X_2) was not a significant factor, the shaking speed was chosen as 225 r/min.

Confirmation experiments were carried out under these conditions,

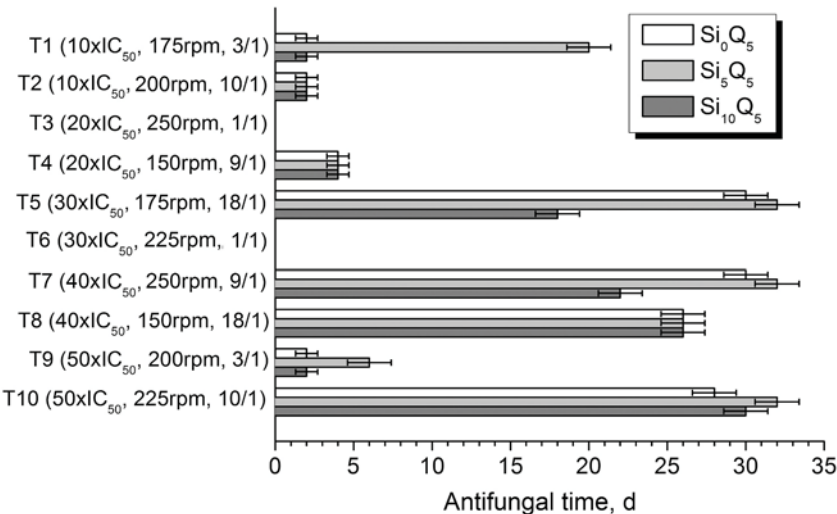


Fig. 3. Uniform design results.

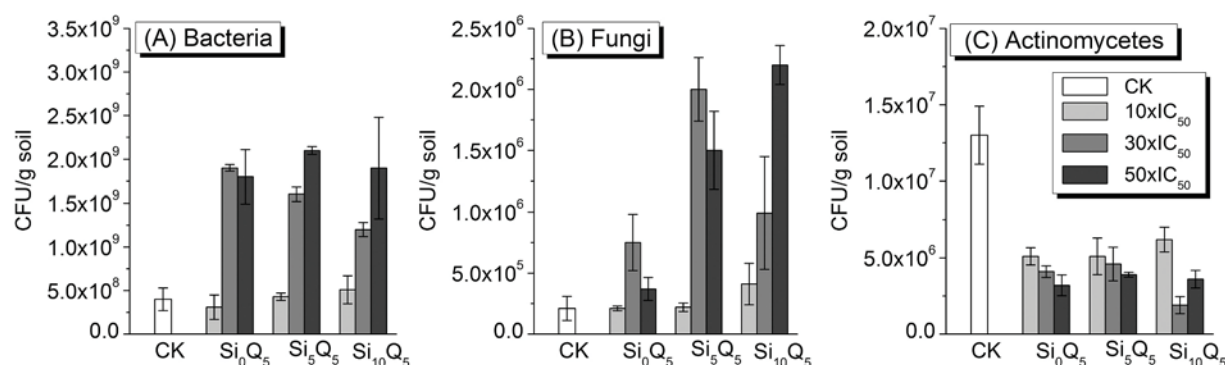


Fig. 4. Microbial biomass in soil.

and the corresponding times were 28 ± 1.4 d, 32 ± 1.4 d and 30 ± 1.4 d, respectively. The relative error between the verification test and the regression model was predicted, and the results demonstrated that a uniform design method can be used for the optimization of antifungal conditions. The results also showed that when Foc4 conidia were continuously inoculated into the soil, Si_xQ₅ could resist the pathogen for 30 d. The longevity of this antifungal activity makes the long-term prevention of banana Fusarium wilt feasible.

One of the reasons why banana Fusarium wilt is difficult to control is that Foc4 continues to invade plantations, and the existing soil treatment methods cannot effectively prevent the invasion of Foc4 for a long time. Therefore, we are committed to the study of methods that can effectively kill Foc4 conidia in soil after multiple infestations of Foc4. Through the experiment, we found that the antifungal effect of Si_xQ₅ under continuous addition of Foc4 every 2 d could be maintained for 30 d under the optimal antifungal conditions.

When the time interval of the continuous addition of Foc4 increased from 2 d to 10 d, Si₀Q₅, Si₅Q₅ and Si₁₀Q₅ maintained antifungal activity in soil for 90, 90 and 80 d, respectively, as shown in Fig. S4, reflecting the stability of these compounds in soil, which enables their application in banana fields to prevent Foc4 conidia invasion over the long term. Clara and Garcia also showed that QASs are not easily degraded in the environment [51], especially under anaerobic conditions (such as those found in sludge, sediment, etc.) [52].

This sustained antimicrobial activity of Si_xQ₅ against Foc4 in soil means that, in the field, a single application of Si_xQ₅ can prevent Foc4 from invading banana plants through the soil for a certain period of time, and the results matched well with those previous studies [53–57], in which quaternary ammonium dendrimer in poly(methyl methacrylate) bone cement showed continuous antibacterial activity against common hospital-acquired bacteria.

3.3.2. Effect of Si_xQ₅ on soil microbial diversity

Since small molecular quaternary ammonium salts are normally considered broad-spectrum fungicides, the effect of Si_xQ₅ on soil microbial diversity was evaluated based on plate counting methods in different media. After colony counting, the number of biological colonies in soil treated with Si_xQ₅ for 2 d was compared with that in soil without Si_xQ₅ treatment. The typical microbial biomasses, including bacteria, fungi and actinomycetes, in soil after the Si_xQ₅ treatments are shown in Fig. S2, and the results based on statistics are shown in Fig. 4, which shows that the microbial volume of actinomycetes decreased with increasing Si_xQ₅ concentrations. However, Si_xQ₅ significantly increased the total amount of bacteria and fungi in the soil.

In addition to the classical plate counting methods, gene sequencing was also chosen for evaluation. Soil microorganisms treated with Si₅Q₅ underwent DNA extraction, library construction, and macrogenome biological sequencing, and finally, bioinformatics analysis was performed to evaluate the differences in fungal community composition structure and diversity in the treated soil. The richness and diversity of

microbial communities can be reflected by diversity analysis of single samples (alpha diversity), as shown in Table S1. The results show that, compared with those of CK, with increasing Si₅Q₅ concentrations in soil, the richness of microbial species in soil increases, and the diversity decreases. On the basis of the taxonomic analysis, the community composition of each sample at each taxonomic level was counted. The sequences of the first 15 genera are shown in Table S2 and Fig. S3. We found that the sequence numbers of *Fusarium*, *Apiotrichum*, *Cylindrocladiella*, *Corallomycetella*, *Heterophoma*, *Humicola*, and *Plectosphaerella* decreased with increasing concentrations of Si₅Q₅, while the number of *Pichia* sequences increased. The results indicate that although Si₅Q₅ could inhibit the growth of part of the fungi including *Fusarium*, the growth of yeast-like fungi such as *Pichia* could be facilitated, thus the microorganisms in soil could be maintained in a certain state, instead of killing them all, which help to maintain the balance of natural resource.

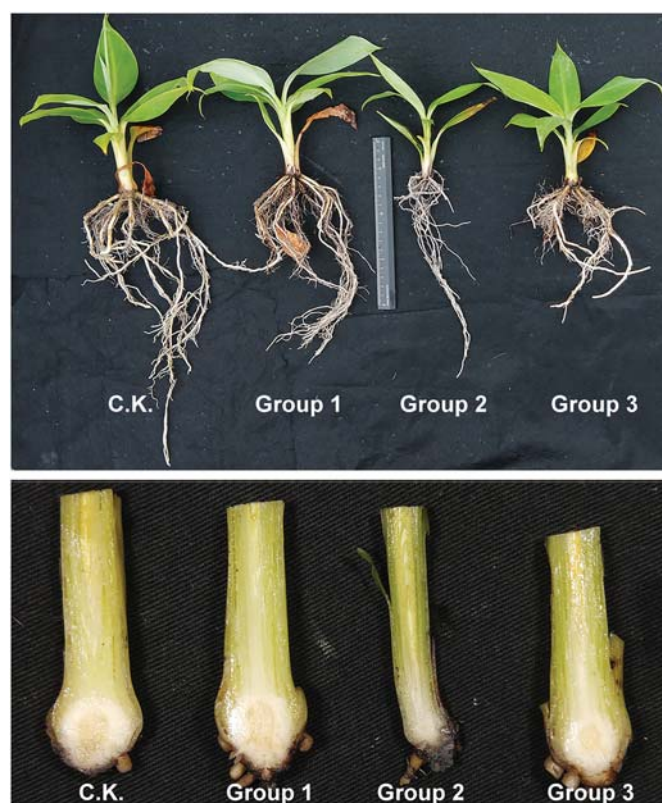


Fig. 5. Comparison of the growth of banana seedlings.

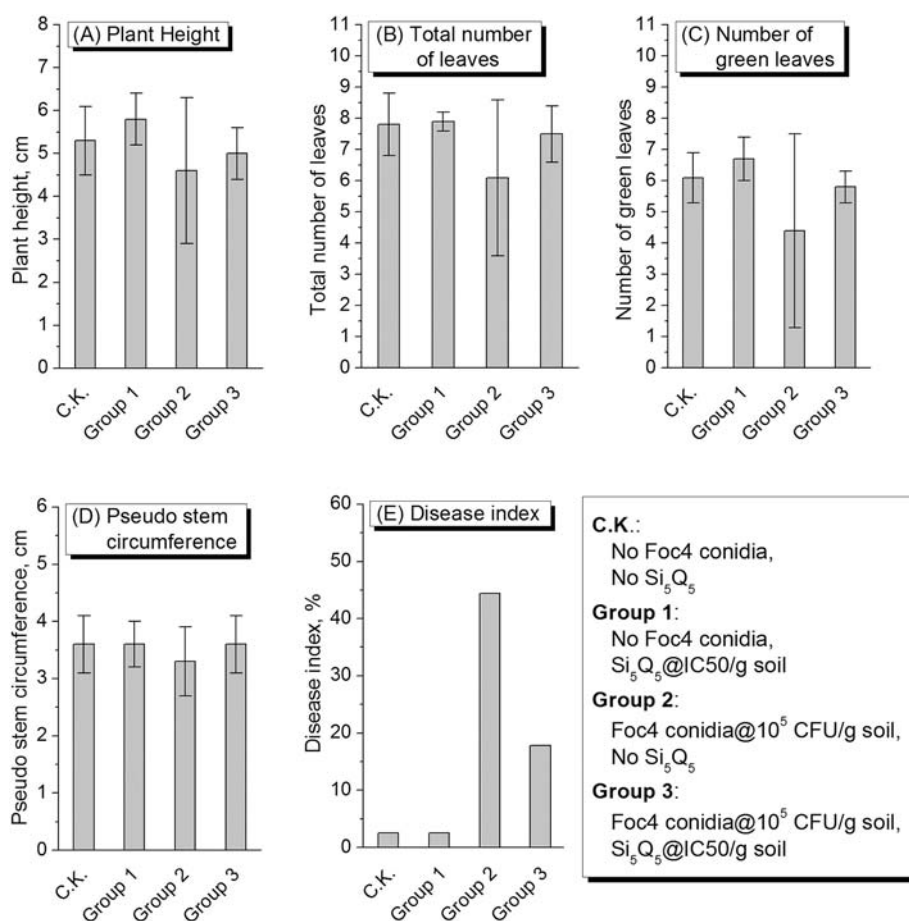


Fig. 6. The effect of Si₅Q₅ and Foc4 on banana seedlings based on pot experiments: (A) Plant height, (B) Total number of leaves, (C) Number of green leaves, (D) Pseudo stem circumference and (E) Disease index. (For interpretation of the references to colour in this figure legend, the reader is referred to the web version of this article.)

3.4. Pot experiments

The results of the pot experiment are shown in Figs. 5 and 6. From the results of banana plant height, total leaf number, green leaf number, pseudo stem circumference and disease index, it could be seen that the growth of banana seedlings treated with Si₅Q₅ at IC₅₀/g soil (**Group 1**) showed no difference from those obtained with the water control (CK), indicating that Si₅Q₅ with a concentration of IC₅₀/g soil will not cause phytotoxicity to banana seedlings. The disease index of banana seedlings treated with Foc4 conidia of 10⁵ CFU/g soil (**Group 2**) reached 44.4%, and that of banana seedlings treated with Si₅Q₅ (**Group 3**) was 17.8%. As shown in Fig. 5, the Foc4 conidia-treated banana seedlings (**Group 2**) grew shorter, the stems were thinner, and the cut corms were dark brown, while those of the other groups grew healthy, and the cut corms had no brown or dark brown lesions, indicating that Si₅Q₅ did not harm banana seedlings and could reduce the infection of banana seedlings by Fusarium wilt.

From left to right: **CK** (No Foc4 conidia, No Si₅Q₅), **Group 1** (No Foc4 conidia, Si₅Q₅ @ IC₅₀/g soil), **Group 2** (Foc4 conidia @ 10⁵ CFU/g soil, No Si₅Q₅), and **Group 3** (Foc4 conidia @ 10⁵ CFU/g soil, Si₅Q₅ @ IC₅₀/g soil).

4. Conclusions

Taken together, the results of this study show that polydimethylsiloxane-polymethacrylate block copolymers containing quaternary ammonium salts, i.e., PDMS-*b*-QPMAEMA (Si_xQ₅), are fungicidally effective against Foc4; Si_xQ₅ exhibits easy soil adsorption in

soil and does not move in soil, which makes it unlikely to flow into groundwater and cause water pollution. The inhibitory effect of Si_xQ₅ on Foc4 can be maintained for 30 d under continuous inoculation of Foc4 into soil (every 2 d) or remains active in the soil for 90 d under continuous inoculation of Foc4 (every 10 d), which reflects the stability of Si_xQ₅ in soil and shows its potential application in banana fields to prevent the invasion of Foc4 conidia over the long term. Although Si_xQ₅ could inhibit Foc4 conidia in soil effectively and showed a certain inhibitory effect on actinomycetes, it had no obvious inhibitory effect on culturable total fungal and bacterial populations, which are conducive to improving soil fertility. Pot experiments showed that Si₅Q₅ had a good control effect on banana Fusarium wilt and did not harm banana seedlings.

We hope that the study of PDMS-*b*-QPMAEMA in soil can provide a new way to protect soil from banana Fusarium wilt and eradicate the banana wilt pathogen in diseased soil to promote the healthy and steady development of the banana industry.

Data availability

All data included in this study are available from the corresponding author upon request.

Declaration of Competing Interest

The authors declare that they have no known competing financial interests or personal relationships that could have appeared to influence the work reported in this paper.

Acknowledgments

This work was supported by the Science and Technology Program of Guangzhou, China, under grants 201803020015; the National Natural Science Foundation of China under grant 31772202; and the Science and Technology Planning Project of Guangdong Province, China under grant 2016A020210105.

Appendix A. Supplementary data

Supplementary data to this article can be found online at <https://doi.org/10.1016/j.reactfunctpolym.2021.104848>.

References

- [1] R. Ploetz, *Fusarium wilt of banana is caused by several pathogens referred to as Fusarium oxysporum f. sp. cubense*, *Phytopathology* 96 (2006) 653–656.
- [2] Z. Shen, B. Wang, J. Zhu, H. Hu, C. Tao, Y. Ou, X. Deng, N. Ling, R. Li, Q. Shen, Lime and ammonium carbonate fumigation coupled with bio-organic fertilizer application steered banana rhizosphere to assemble a unique microbiome against Panama disease, *Microb. Biotechnol.* 12 (2019) 515–527.
- [3] I. Buddenhagen, Understanding strain diversity in *Fusarium oxysporum f. sp. cubense* and history of introduction of “tropical race 4” to better manage banana production, *ISHS Acta Hort.* 828 (2009) 193–204.
- [4] B. Huang, D. Yan, X. Wang, X. Wang, W. Fang, D. Zhang, C. Ouyang, Q. Wang, A. Cao, Soil fumigation alters adsorption and degradation behavior of pesticides in soil, *Environ. Pollut.* 246 (2019) 264–273.
- [5] L. Zhang, T. Yuan, Y. Wang, D. Zhang, T. Bai, S. Xu, Y. Wang, W. Tang, S. Zheng, Identification and evaluation of resistance to *Fusarium oxysporum f. sp. cubense* tropical race 4 in *Musa acuminata* Pahang, *Euphytica* 214 (2018) 106.
- [6] R. Ploetz, S. Freeman, J. Konkola, A. Al-Abed, Z. Naser, K. Shalan, R. Barakat, Y. Israeli, Tropical race 4 of Panama disease in the Middle East, *Phytoparasitica* 43 (2015) 283–293.
- [7] J.M. Raaijmakers, T.C. Paulitz, C. Steinberg, C. Alabouvette, Y. Moënné-Loccoz, The rhizosphere: a playground and battlefield for soilborne pathogens and beneficial microorganisms, *Plant Soil* 321 (2009) 341–361.
- [8] D. Zhang, X. Ji, Z. Meng, W. Qi, K. Qiao, Effects of fumigation with 1,3-dichloro-propene on soil enzyme activities and microbial communities in continuous-cropping soil, *Ecotoxicol. Environ. Saf.* 169 (2019) 730–736.
- [9] D. Zhou, T. Jing, Y. Chen, F. Wang, D. Qi, R. Feng, J. Xie, H. Li, Deciphering microbial diversity associated with *Fusarium wilt*-diseased and disease-free banana rhizosphere soil, *BMC Microbiol.* 19 (2019) 161.
- [10] B. Dizman, M.O. Elarbi, L.J. Mathias, Synthesis and antibacterial activities of water-soluble methacrylate polymers containing quaternary ammonium compounds, *J. Polym. Sci. A* 44 (2006) 5965–5973.
- [11] C. Abbate, M. Arena, A. Baglieri, M. Gennari, Effects of organoclays on soil eubacterial community assessed by molecular approaches, *J. Hazard. Mater.* 168 (2009) 466–472.
- [12] C. Dong, W. You, R. Liuyang, Y. Lei, A. Zhang, Y. Lin, Anti-*Rhizoctonia solani* activity by polymeric quaternary ammonium salt and its mechanism of action, *React. Funct. Polym.* 125 (2018) 1–10.
- [13] J.V. Nye, W.F. Guerin, S.A. Boyd, Heterotrophic activity of microorganisms in soils treated with quaternary ammonium compounds, *Environ. Sci. Technol.* 28 (1994) 944–951.
- [14] B. Sarkar, M. Megharaj, Y. Xi, G.S.R. Krishnamurti, R. Naidu, Sorption of quaternary ammonium compounds in soils: implications to the soil microbial activities, *J. Hazard. Mater.* 184 (2010) 448–456.
- [15] C. Zhang, F. Cui, G. Zeng, M. Jiang, Z. Yang, Z. Yu, M. Zhu, L. Shen, Quaternary ammonium compounds (QACs): a review on occurrence, fate and toxicity in the environment, *Sci. Total Environ.* 518–519 (2015) 352–362.
- [16] W. Zhong, C. Dong, R. Liuyang, Q. Guo, H. Zeng, Y. Lin, A. Zhang, Controllable synthesis and antimicrobial activities of acrylate polymers containing quaternary ammonium salts, *React. Funct. Polym.* 121 (2017) 110–118.
- [17] Y. Lin, W. Zhong, C. Dong, C. Zhang, X. Feng, A. Zhang, Synthesis and antifungal activities of amphiphilic PDMS-b-QPDMAEMA copolymers on *Rhizoctonia solani*, *ACS Appl. Bio Mater.* 1 (2018) 2062–2072.
- [18] P. Deltour, S.C. Franca, O.L. Pereira, I. Cardoso, S. De Neve, J. Debode, M. Hofte, Disease suppressiveness to *Fusarium wilt* of banana in an agroforestry system: influence of soil characteristics and plant community, *Agric. Ecosyst. Environ.* 239 (2017) 173–181.
- [19] Y. Lin, Q. Liu, L. Cheng, Y. Lei, A. Zhang, Synthesis and antimicrobial activities of polysiloxane-containing quaternary ammonium salts on bacteria and phytopathogenic fungi, *React. Funct. Polym.* 85 (2014) 36–44.
- [20] S. Rzaşa, W. Owczarzak, Methods for the granulometric analysis of soil for science and practice, *Polish J. Soil Sci.* 46 (2013) 1–50.
- [21] J. Huang, Y. Pang, F. Zhang, Q. Huang, M. Zhang, S. Tang, H. Fu, P. Li, Suppression of *Fusarium wilt* of banana by combining acid soil ameliorant with biofertilizer made from *Bacillus velezensis* H-6, *Eur. J. Plant Pathol.* 154 (2019) 585–596.
- [22] Z.T. Gong, Z.C. Chen, G.L. Zhang, World soil resource reference base (WRB): establishment and development, *Soils* 4 (2003) 271–278.
- [23] Z. Huang, R. Liuyang, C. Dong, Y. Lei, A. Zhang, Y. Lin, Polymeric quaternary ammonium salt activity against *Fusarium oxysporum f. sp. cubense* race 4: synthesis, structure-activity relationship and mode of action, *React. Funct. Polym.* 114 (2017) 13–22.
- [24] OECD, Test No. 106: Adsorption - Desorption Using a Batch Equilibrium Method, OECD Publishing, Paris, 2000.
- [25] A.H. Khan, S.M. Macfie, M.B. Ray, Sorption and leaching of benzalkonium chlorides in agricultural soils, *J. Environ. Manag.* 196 (2017) 26–35.
- [26] M. Piri, E. Sepehr, Z. Rengel, Citric acid decreased and humic acid increased Zn sorption in soils, *Geoderma* 341 (2019) 39–45.
- [27] J.F. Guo, G.N. Zhu, J.J. Shi, J.H. Sun, Adsorption, desorption and mobility of fomesafen in Chinese soils, *Water Air Soil Pollut.* 148 (2003) 77–85.
- [28] S. Li, Y. Sun, T. Yang, W. Huangpu, Relationship between mobility factors (Rf) of two hydrophobic termiticides and selected field and artificial soil parameters, *Sci. Total Environ.* 388 (2007) 206–213.
- [29] J. Jiang, Y. Xiong, H. Jiang, D. Ye, Y. Song, F. Li, Soil microbial activity during secondary vegetation succession in semiarid abandoned lands of loess plateau, *Pedosphere* 19 (2009) 735–747.
- [30] H.X. Peng, K. Sivasithamparam, D.W. Turner, Chlamydoconidia germination and *Fusarium wilt* of banana plantlets in suppressive and conducive soils are affected by physical and chemical factors, *Soil Biol. Biochem.* 31 (1999) 1363–1374.
- [31] T. Wen, X. Huang, J. Zhang, T. Zhu, L. Meng, Z. Cai, Effects of water regime, crop residues, and application rates on control of *Fusarium oxysporum f. sp. cubense*, *J. Environ. Sci.* 31 (2015) 30–37.
- [32] Z. Shen, C.R. Penton, N. Lv, C. Xue, X. Yuan, Y. Ruan, R. Li, Q. Shen, Banana *Fusarium wilt* disease incidence is influenced by shifts of soil microbial communities under different monoculture spans, *Microb. Ecol.* 75 (2018) 739–750.
- [33] F. Sopena, C. Maqueda, E. Morillo, Formulation affecting alachlor efficacy and persistence in sandy soils, *Pest Manag. Sci.* 65 (2009) 761–768.
- [34] J.C. Sherris, Problems in vitro determination of antibiotic tolerance in clinical isolates, *Antimicrob. Agents Chemother.* 30 (1986) 633–637.
- [35] R. Swisher, G.C. Carroll, Fluorescein diacetate hydrolysis as an estimator of microbial biomass on coniferous needle surfaces, *Microb. Ecol.* 6 (1980) 217–226.
- [36] B. Sylvie, T. Pierre, B. Martine, J. Anne, Emergence of resistance to antibacterial agents: the role of quaternary ammonium compounds—a critical review, *Int. J. Antimicrob. Agents* 39 (2012) 381–389.
- [37] Y. Gou, M.M. Meghil, C.R. Pucci, L. Breschi, D.H. Pashley, C.W. Cutler, L. Niu, J. Li, F.R. Tay, Optimizing resin-dentin bond stability using a bioactive adhesive with concomitant antibacterial properties and anti-proteolytic activities, *Acta Biomater.* 75 (2018) 171–182.
- [38] Y. Jiao, L. Niu, S. Ma, J. Li, F.R. Tay, J. Chen, Quaternary ammonium-based biomedical materials: state-of-the-art, toxicological aspects and antimicrobial resistance, *Prog. Polym. Sci.* 71 (2017) 53–90.
- [39] S. Liu, L. Tonggu, L. Niu, S. Gong, B. Fan, L. Wang, J. Zhao, C. Huang, D.H. Pashley, F.R. Tay, Antimicrobial activity of a quaternary ammonium methacryloxy silicate-containing acrylic resin: a randomised clinical trial, *Sci. Rep.* 6 (2016) 21882.
- [40] B.H. Hameed, I.A.W. Tan, A.L. Ahmad, Adsorption isotherm, kinetic modeling and mechanism of 2,4,6-trichlorophenol on coconut husk-based activated carbon, *Chem. Eng. J.* 144 (2008) 235–244.
- [41] G. Patakiotas, T.A. Albanis, Adsorption-desorption studies of alachlor, metolachlor, EPTC, chlorothalonil and pirimiphos-methyl in contrasting soils, *Pest Manag. Sci.* 58 (2002) 352–362.
- [42] W.C. Koskinen, D.M. Stone, A.R. Harris, Sorption of hexazinone, sulfometuron methyl, and tebuthiuron on acid, low base saturated sands, *Chemosphere* 32 (1996) 1681–1689.
- [43] Z.Z. Ismail, U. Tezel, S.G. Pavlostathis, Sorption of quaternary ammonium compounds to municipal sludge, *Water Res.* 44 (2010) 2303–2313.
- [44] L. Xiang, T. Sun, M. Zheng, Y. Li, H. Li, M. Wong, Q. Cai, C. Mo, Sorption of dodecyltrimethylammonium chloride (DTAC) to agricultural soils, *Sci. Total Environ.* 560 (2016) 197–203.
- [45] M. Clara, S. Scharf, C. Scheffknecht, O. Gans, Occurrence of selected surfactants in untreated and treated sewage, *Water Res.* 41 (2007) 4339–4348.
- [46] A.F. Cirelli, C. Ojeda, M.J.L. Castro, M. Salgot, Surfactants in sludge-amended agricultural soils: a review, *Environ. Chem. Lett.* 6 (2008) 135–148.
- [47] A.C. Das, D. Mukherjee, Insecticidal effects on soil microorganisms and their biochemical processes related to soil fertility, *World J. Microbiol. Biotechnol.* 14 (1998) 903–909.
- [48] P.B. Hatzinger, M. Alexander, Effect of aging of chemicals in soil on their biodegradability and extractability, *Environ. Sci. Technol.* 29 (1995) 537–545.
- [49] I. Ferrer, E.T. Furlong, Accelerated solvent extraction followed by on-line solid-phase extraction coupled to ion trap LC/MS/MS for analysis of benzalkonium chlorides in sediment samples, *Anal. Chem.* 74 (2002) 1275–1280.
- [50] U. Tezel, J.A. Pierson, S.G. Pavlostathis, Fate and effect of quaternary ammonium compounds on a mixed methanogenic culture, *Water Res.* 40 (2006) 3660–3668.
- [51] M.T. Garcia, I. Ribosa, T. Guindulain, J. Sanchez-Leal, J. Vives-Rego, Fate and effect of monoalkyl quaternary ammonium surfactants in the aquatic environment, *Environ. Pollut.* 111 (2001) 169–175.
- [52] M.T. Garcia, E. Campos, J. Sánchez-Leal, I. Ribosa, Anaerobic degradation and toxicity of commercial cationic surfactants in anaerobic screening tests, *Chemosphere* 41 (2000) 705–710.
- [53] A. Zhang, Q. Liu, Y. Lei, S. Hong, Y. Lin, Synthesis and antimicrobial activities of acrylamide polymers containing quaternary ammonium salts on bacteria and phytopathogenic fungi, *React. Funct. Polym.* 88 (2015) 39–46.
- [54] C.K.V.Z. Abid, S. Jain, R. Jackeray, S. Chattopadhyay, H. Singh, Formulation and characterization of antimicrobial quaternary ammonium dendrimer in poly(methyl methacrylate) bone cement, *J. Biomed Mater Res B Appl Biomater* 105 (2017) 521–530.

- [55] G. Jing, Z. Zhou, J. Zhuo, Quantitative structure-activity relationship (QSAR) study of toxicity of quaternary ammonium compounds on *Chlorella pyrenoidosa* and *Scenedesmus quadricauda*, *Chemosphere*. 86 (2012) 76–82.
- [56] W. Jiang, C. Xu, S. Jiang, T. Zhang, S. Wang, B. Fang, Establishing a mathematical equations and improving the production of l-tert-leucine by uniform design and regression analysis, *Appl. Biochem. Biotechnol.* 181 (2017) 1454–1464.
- [57] M. Tandukar, S. Oh, U. Tezel, K.T. Konstantinidis, S.G. Pavlostathis, Long-term exposure to benzalkonium chloride disinfectants results in change of microbial community structure and increased antimicrobial resistance, *Environ. Sci. Technol.* 47 (2013) 9730–9738.
- [58] K. Fang, *Orthogonal and Uniform Experimental Design*, Science Press of China, 2001 (in Chinese).
- [59] Q. Xiao, H. Yan, Y. Wei, Y. Wang, F. Zeng, X. Zheng, Optimization of H₂O₂ dosage in microwave-H₂O₂ process for sludge pretreatment with uniform design method, *J. Environ. Sci.* 24 (2012) 2060–2067.
- [60] W. Zhong, Y. Chang, Y. Lin, A. Zhang, Synthesis and antifungal activities of hydrophilic cationic polymers against *Rhizoctonia solani*, *Fungal Biol.* 124 (2020) 735–741.



Stretchable, robust and reprocessable poly(siloxane-urethanes) elastomers based on exchangeable aromatic disulfides

Shijie Shan^a, Yaling Lin^{b, **}, Anqiang Zhang^{a, *}

^a School of Material Science and Engineering, South China University of Technology, 381 Wushan Rd., Guangzhou, 510641, Guangdong, China

^b College of Materials and Energy, South China Agricultural University, 483 Wushan Rd., Guangzhou, 510642, Guangdong, China

ARTICLE INFO

Keywords:

Aromatic disulfides

Polysiloxanes

Dynamic covalent bonds

ABSTRACT

The rapid expansion of dynamic covalent chemistry world urges for materials not only possessing high mechanical properties and stretchability, but also including high reprocessability and reforming. Herein, aromatic disulfide-containing polysiloxanes elastomers with modified urea as chain-extender and crosslinker were first designed and fabricated. Dynamic crosslinks, including hydrogen bonding formed between urea and amide bonds, and aromatic disulfide are connected with polysiloxanes backbones through isocyanate (DTSA-HDI) reacted with systematically controlled aminopropyl groups in the side chains. Consequently, a series of ATPx-SS elastomers with polysiloxanes of different molecular weight and APPx-SS elastomers with different crosslinking densities are developed. The molar amount of DTSA-HDI has been proved to play a crucial role in adjusting the mechanical and thermal properties of the networks. Among all, ATP3-SS showed the best stretchability, of which the elongation at break was as high as 780%. APP1-SS achieved the highest tensile strength of 2.60 MPa. Besides, it has outstanding reprocessability and can be reprocessed and reformed without much decline of tensile strength after several cycles of hot-pressing. These remarkable properties demonstrate that the aromatic disulfide-containing elastomers are competitive to those un-filled polysiloxanes elastomers based on dynamic bonds ever reported.

1. Introduction

Discovered by Charles Goodyear in 1839 [1], sulfur vulcanization was a major technological breakthrough in the rubber-good industry that since provided durable and waterproof products with much improved mechanical properties. Vulcanization of rubber with accelerator can take several minutes to hours even at elevated temperature (up to 140 °C) and uneconomically consume much more amount of sulfur needed to crosslink the polydienes, which causes the aging problem. Generally, the polysulfide crosslinks among polydienes may contain four to six sulfur atoms and less at elevated temperature [2] and surface properties. Disulfides are a class of weaker but dynamic sulfur-containing covalent bonds which play an active role in dynamic sulfur chemistry and dynamic covalent chemistry (DCC) [3,4]. They can undergo different reversible reactions such as disulfide exchange [5], thiol-disulfide exchange [6], reduction-oxidation [7], radical-mediated disulfide fragmentation [8,9], and thiolate/nanoparticle exchange [10–13]. In most of the studies, to trigger disulfide exchange, chemicals

(or catalysts) [14,15], heat [5] or UV light [16,17] is required. Unlike aliphatic disulfides, exchange reactions of aromatic disulfides are known for occurring at lower or even room temperature [18]. To study the mechanism, Odriozola et al. used *p*-tolyl disulfide and bis (4-methoxyphenyl) as model disulfides, resulting in formation of an asymmetric *p*-tolyl-bis(4-methoxyphenyl) disulfide in deuterated DMSO at room temperature as a model exchange reaction [19,20]. Using aromatic disulfides for constructing dynamic polymer networks has being applied in various polymers, including polyurethanes [21], poly(urea-urethane) [22], poly(urethane-amide) [23], polyhydroxyurethanes [22], epoxy resins [5,24], as well as hydroxypropyl acrylate [15], which has not been achieved in polysiloxanes so far to our best understanding. Odriozola et al. [25] first introduced 4-aminophenyl disulfide as hardener into commercially available poly(propylene glycol) resins to create poly(urea-urethane) (PUU) polymer networks, which offered a unique method for thermoset processing, recycling, and isocyanate-free polyurethanes. Tesoro et al. [26–28] originally used diepoxide monomers and DTDA to prepare several epoxy resins

* Corresponding author.

** Corresponding author.

E-mail addresses: linyinling@scau.edu.cn (Y. Lin), aqzhang@scut.edu.cn (A. Zhang).

<https://doi.org/10.1016/j.polymer.2021.123588>

Received 8 February 2021; Received in revised form 27 February 2021; Accepted 1 March 2021

Available online 5 March 2021

0032-3861/© 2021 Elsevier Ltd. All rights reserved.

exhibiting competitive mechanical properties and durability in harsh environment. Epoxy resins with BGPDS and diamines, instead of DTDPA and diepoxides, significantly decreased the amount of pendent disulfide bonds, leading to enhanced degradability under 254 nm UV light in presence of diphenyl disulfide [24]. One of the biggest advantages of aromatic disulfides is that the species are super dynamic and ready to exchange even at room temperature without any external stimuli [17, 29]. Reversibly crosslinked poly(urea-urethane) with aromatic disulfides presented fast self-healing efficiency that fractured split re-joints after taking manual compression for 30 s at room temperature could bear weight of 500 g. Aromatic disulfides were smartly implanted in polybutyladipate networks through isocyanate-hydroxyl reaction, yielding a stiff poly(urethane-amide) that could heal for 30 s at ambient temperature and presented 59.4 MPa Young's modulus in tensile strength measurements [30]. Moreover, a model exchange reaction has confirmed that the exchange reaction between two aromatic disulfide compounds occurred via a radical-mediated mechanism [31], which means higher temperature is preferable for processing. To develop a flexible substrate for transparent electronics, Zhang et al. [32] started from amino-terminated polydimethylsiloxane (PDMS) and hyper-branched polysiloxanes with multiple amino groups. Isocyanate containing aliphatic disulfide was introduced to form physical hydrogen crosslinking and covalent S-S crosslinking in the hierarchical cross-linked networks. The resultant polymer showed comprehensive properties, of which the tensile strength and Young's modulus were as high as 8.6 MPa and 188.5 MPa with the healing efficiency above 90%. Guo et al. [33] investigated further by designing a universally self-healing and highly stretchable supramolecular elastomer based on synergistically incorporating multi-strength hydrogen bonding and disulfide metathesis in PDMS polymers. The resultant elastomer exhibits high stretchability (14,000% in unnotched sample; 1300% in notched sample). The fast autonomous self-healing under universal conditions included ultralow temperature (-40°C), under water, supercooled high-concentrated saltwater and strong acid/alkali environment (pH = 0 or 14).

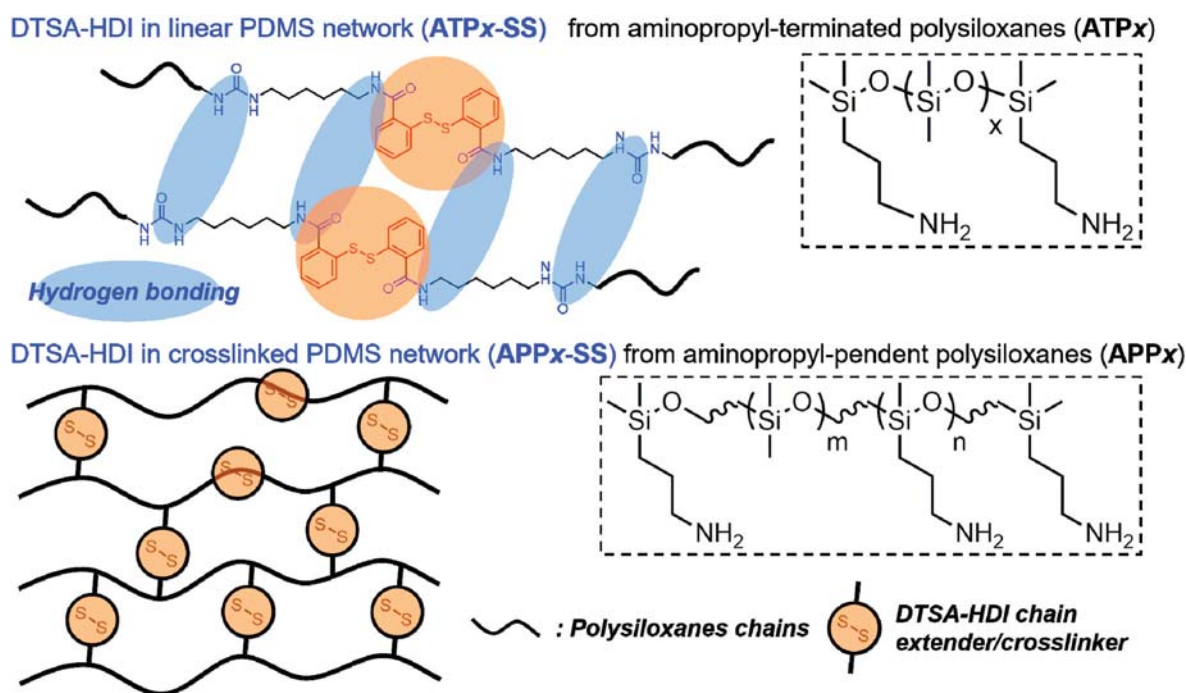
Therefore, it is an interesting challenge to develop PDMS-based poly (siloxane-urethanes) kinds of elastomers with comprehensive mechanical properties and reprocessability with the aid of dynamic and

exchangeable aromatic disulfide. The aromatic disulfide metathesis was deeply investigated in this work. Herein, we proposed a simple and classic strategy to develop the aromatic disulfide-containing polysiloxanes elastomers though building both linear and crosslinked networks separately. There was dynamic reversible physical crosslinking formed through hydrogen bonds between urea and amide groups and dynamic covalent chemical crosslinking contributed by aromatic disulfide metathesis. As shown in Scheme 1, originating from aminopropyl terminated/pendent polysiloxanes of systematically controlled molecular weight and amine moieties, an isocyanate modified aromatic disulfide was designed and synthesized as chain extender/crosslinker. Through the reaction of isocyanate and amine groups, hydrogen bonding crosslinking ATPx-SS elastomers and hydrogen bonding-aromatic disulfide dual crosslinking APPx-SS elastomers networks were developed. Consequently, ATPx-SS elastomers possess better stretchability, while APPx-SS elastomers achieved higher stiffness and toughness. As the un-filled polysiloxanes-based elastomers, the as-prepared aromatic disulfide-containing polysiloxanes elastomers (ATPx-SS and APPx-SS) reported in the work present competitive mechanical strength and compromising stretchability. After several cycles of reprocessing, there is not a big decline in mechanical strength, which is beneficial for elastomer recycling in an economical manner.

2. Experimental

2.1. Materials

All materials and reagents were used as purchased without further purification. Octamethyl cyclotetrasiloxane (D₄, 99%) and 3-aminopropyl diethoxymethylsilane (APDES, 98%) were obtained from Dow Chemical Company. 2,2'-Dithiodibenzoic acid (DTSA), 1,3-bis(3-aminopropyl)-1,1,3,3-tetramethyldisiloxane (AMM, 97%), tetramethylammonium hydroxide pentahydrate (TMAH, 97%), hexamethylene diisocyanate (HDI, 99%) were purchased from Macklin (Shanghai, China). Tetrahydrofuran (THF, AR grade) was provided from Guangzhou Chemical Reagent Factory.



Scheme 1. Structures of ATPx, APPx, ATPx-SS and APPx-SS.

2.2. Synthesis of aminopropyl-terminated polysiloxanes (ATP) and aminopropyl-pendent polysiloxanes (APP)

Aminopropyl-pendent polysiloxanes (APPx) were synthesized in our previous work [34] and a brief procedure is stated as follows. A mixture of D₄, APDES, and TMAH (2 wt%) was reacted with AMM at 90 °C for 12 h under stirring and N₂ atmosphere [35]. After the reaction, the mixture was concentrated at 160 °C under reduced pressure to remove volatiles, and APPx was obtained as a colorless oil. The synthesis route is depicted in Scheme S1 (Supporting Information). Aminopropyl-terminated polysiloxanes (ATPx) were synthesized similarly without the input of APDES.

2.3. Synthesis of isocyanate-modified aromatic disulfide (DTSA-HDI)

HDI (0.34 g, 2.02 mmol) was added dropwise to DTSA (0.31 g, 1 mmol) in anhydrous CH₂Cl₂ (20 mL) at 20 °C for 1 h under stirring and N₂ atmosphere, and then the mixture was heated up to 60 °C for 2 h. After cooling to room temperature, the mixture was concentrated under reduced pressure to remove volatiles at 120 °C, and DTSA-HDI was obtained as yellow oil. The synthesis route is depicted in Scheme S2 (Supporting Information) (see Table 1).

2.4. Preparation of ATPx-SS/APPx-SS elastomers

According to Table 2, calculated amount of ATPx/APPx and DTSA were first dissolved in THF at room temperature and stirred for 30 °C min in a PTFE beaker to form a transparent solution. The resultant mixture was maintained at 120 °C for 12 h in a vacuum oven to remove the solvent. The obtained crosslinked elastomer was named ATPx-SS/APPx-SS.

2.5. Characterization

¹H NMR spectra were recorded on a 600 MHz AVANCE III Bruker NMR spectrometer (Bruker, Switzerland). CDCl₃ was used as the solvent at room temperature.

Fourier transform infrared (FTIR) spectra were obtained using a Nicolet iS5 FT-IR (ThermoScientific, America) with an iD7-ZnSe attenuated total reflectance (ATR) stage.

M_n and PDI relative to polystyrene were measured using a Waters GPC 515–2414 (USA) with a mobile phase of tetrahydrofuran (THF) at a flow rate of 1.0 mL/min; the temperature of column was 35 °C.

Rheological analyses were conducted using an Anton Paar MCR-102 rheometer (Austria) with a 25 mm parallel-plate test system. The dimensions of each specimen were 25 mm in diameter and 0.8 mm in thickness. The samples were tested at a frequency of 1.0 Hz with a 1.0% strain. The temperature was increased from 20 °C to 160 °C with a

Table 1
Characterization and molecular weight of APTx and APPx.

Sample	Amine value (mmol/g)	Grafting degree (%)	<i>M_n</i> (kDa)	PDI
Aminopropyl-terminated polysiloxanes (ATPx)				
ATP1	0.32	–	6.3	1.40
ATP2	0.26	–	7.8	1.47
ATP3	0.22	–	9.3	1.52
ATP4	0.20	–	10.2	1.48
Aminopropyl-pendent polysiloxanes (APPx)				
APP1	0.40	3.01	7.7	1.48
APP2	0.30	2.25	8.7	1.47
APP3	0.20	1.49	8.5	1.32

a Amine value was determined by acid-base titration. Grafting degree is the stoichiometric molar ratio of aminopropyl Si–O units to the sum of aminopropyl Si–O units and dimethyl Si–O units.

b Number average molecular weight (*M_n*) and polydispersity (PDI) were determined by GPC results.

Table 2
Formulation of ATPx-SS/APPx-SS

Sample	ATPx (g)	DTSA (g)	Sample	APPx (g)	DTSA (g)
ATP1-SS	5.00	0.24	APP1-SS	5.00	0.31
ATP2-SS	5.00	0.20	APP2-SS	5.00	0.23
ATP3-SS	5.00	0.16	APP3-SS	5.00	0.15
ATP4-SS	5.00	0.15			

heating rate of 2 °C/min.

Thermogravimetric analyses (TGA) were conducted on a Netzsch TG209F1 (Germany) at a heating rate of 10 °C/min under air atmosphere.

Tensile tests were conducted on a KJ-1067 tensile machine (Kejian Instruments Co., China) at an elongation rate of 100 mm/min at room temperature. The dimensions of each specimen were 50 mm × 10 mm × 0.80 mm. The span length was 20 mm. Five effective measurements of each kind of elastomers were obtained, and the average values plus standard deviations of five effective data were calculated as the tensile properties of the elastomers.

Swelling measurements are used to measure the crosslink density. Percentage gel content and swelling ratio can be determined by using the following formulae [36]:

$$\text{Gel content (\%)} = m_3/m_1 \times 100\%$$

$$\text{Swelling ratio (\%)} = m_2/m_3 \times 100\%$$

Equilibrium swelling index can be calculated from the equation below:

$$Q = m_2/m_1$$

where *m*₁ is the weight of the polymer before swelling, *m*₂ is the wet weight of the polymer after swelling, *m*₃ is the dry weight of the polymer after swelling. Crosslinking density, defined as 1/*Q*, can therefore be calculated and is expressed as moles of crosslink per gram of insoluble network.

Swelling experiments were conducted on small specimens of APPx-SS elastomers in THF at room temperature for 48 h. At the end of the immersion period, the sample was removed from the solvent, rapidly blotted with tissue and transferred to the weighing disk to obtain the swollen weight of the sample. Then, sample was put in an oven at 120 °C under vacuum which showed no significant changes in mass.

3. Results and discussion

3.1. Structure characterization of elastomers

Fig. 1a shows the ¹H NMR spectrum of DTSA-HDI. The triplet peaks at 8.01, 7.60, 7.54, 7.32 ppm represent aromatic protons of DTSA, and the signal at 3.08 and 3.31 ppm belongs to methylene next to amide and isocyanate respectively. Fig. 1b and c shows the ¹H NMR spectra of ATP1 and APP1, respectively. For aminopropyl-containing polysiloxanes ATP1 and APP1, the resonance peak at 0.07 ppm corresponds to the methyl group attached to Si. The resonance peaks at 0.63 ppm, 1.25 ppm and 2.95 ppm correspond to propyl linkage attached directly to Si. FTIR further confirmed the structures of the ATP1 and APP1 in Fig. 1d. The spectra of ATPx/APPx were characterized by Si–O–CH₂CH₂ vibration at 950 cm^{−1} and a characteristic vibration between 1100 and 1200 cm^{−1} for alkoxy silane, respectively.

The structures of ATPx-SS/APPx-SS elastomers were characterized by using FTIR. By comparing the spectrum of ATP1/APP3 to the ATP1-SS/APP3-SS elastomers (all four spectra shown in Fig. 2a), the appearance of 1600 cm^{−1}, confirming the existence of primary amines. The appearances of the stretching (3400 cm^{−1}), stretching (1622 cm^{−1}, amide I) and bending (1578 cm^{−1}, amide II) suggest the production of amide originated from the reaction between DTSA and HDI. No obvious

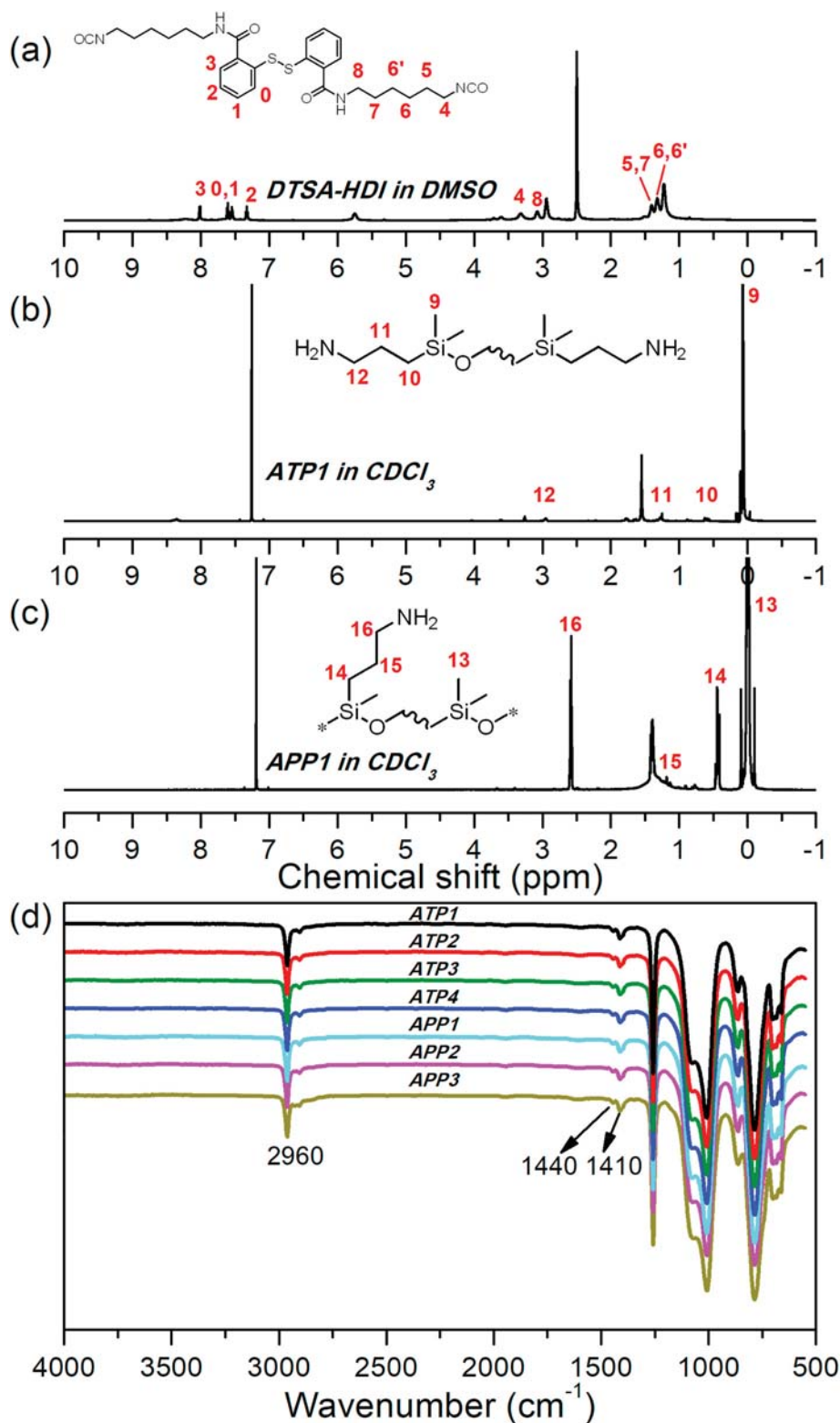


Fig. 1. ^1H NMR spectra of DTSA-HDI (a), ATP1 (b) and APP1 (c); FTIR spectra of ATPx and APPx (d).

vibration assigned to $-\text{NCO}$ (1724 cm^{-1}) is found.

3.2. Swelling experiments

Swelling measurements are often used as a quantitative evaluation to measure the crosslink density of elastomers. It is well-known that the degree of swelling, which is the amount of solvent imbibed, is dependent

on the crosslink density of polymer networks. The results of swelling experiments APPx-SS are given in Table 3 and Fig. S8 in Supporting Information. Images of samples during and after immersion in THF for 24 h were presented in Fig. S7. Dynamic physical crosslinking via hydrogen bonds could completely dissolved in THF (good solvent for polysiloxanes) in 24 h. Thus, the swelling experiments were only conducted on APPx-SS. The network tended to imbibe more solvent with

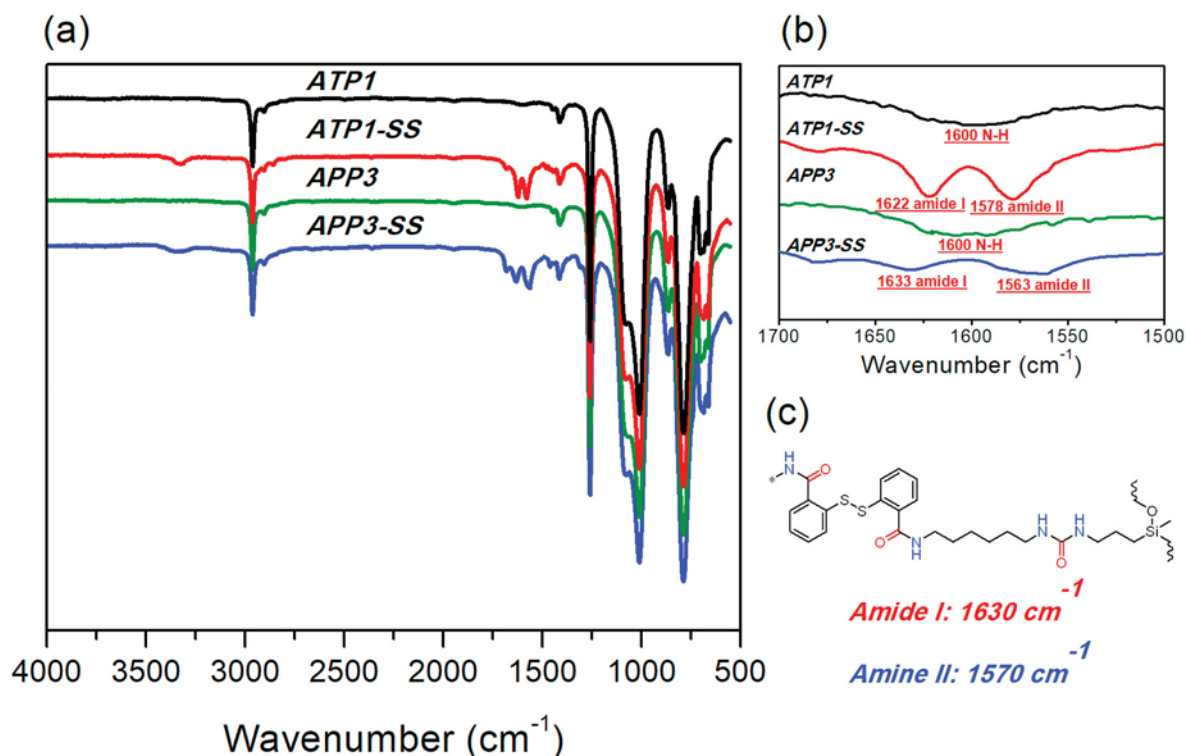


Fig. 2. FTIR spectra of ATP1/ATP1-SS and APP3/APP3-SS, ranging from 4000 to 500 cm^{-1} (a) and 1700–1500 cm^{-1} (b). (c) The structure of DTSA-diurethane with amide and urea groups.

Table 3
Swelling results of APPx-SS.

Sample	Gel content (%)	Swelling ratio (%)	Crosslinking density
APP1-SS	95.8 \pm 16.0	312.9 \pm 29.8	0.32 \pm 0.031
APP2-SS	93.7 \pm 24.4	313.4 \pm 8.36	0.32 \pm 0.003
APP3-SS	92.7 \pm 6.76	410.3 \pm 25.2	0.24 \pm 0.015

increasing amount of crosslinkers (APP1-SS > APP2-SS > APP3-SS) in the original elastomers. Gel content and swelling ratio of APP1-SS and APP2-SS only show slight difference since the amount of crosslinkers of APP1-SS is greater than that of APP2-SS. With the minimum amount the crosslinkers, APP3-SS, however, swelled about 400% of solvent to its original mass.

Noticeably, APPx-SS networks were effectively and efficiently constructed by DTSA-HDI of molar content less than 0.4 mmol/g. At the end of the immersion, the insoluble part of the network remained above 90% to its original mass. As expected, the greater crosslink density the sample possessed, the less the degree of swelling was. Samples with lowest DTSA-HDI imbibed 400% solvent to its original mass.

3.3. Thermal stability

Considering that the processing procedure of aromatic disulfide-containing PDMS elastomers in this article requires heat up to 160 $^{\circ}\text{C}$, thermal decomposition characterization is of great necessity to evaluate the thermal stability of ATPx-SS/APPx-SS by comparing with ATPx/APPx, respectively. Fig. S6 illustrates the TGA curves of DTSA, ATPx/ATPx-SS and APPx/APPx-SS. The characteristic parameters including 1% weight loss temperature ($T_{1\%}$), 5% weight loss temperature ($T_{5\%}$), char yield at 800 (Y_c), temperature of maximum rate of the first degradation stage ($T_{\text{max}1}$) and temperature of maximum rate of the second degradation stage ($T_{\text{max}2}$) are listed in Table 4. As reference, only one thermal degradation stage ($T_{\text{max}2}$) is observed in DTSA. For amine functional polysiloxanes, two thermal degradation stages are observed,

Table 4

TGA data obtained of amine functional polysiloxanes (ATPx and APPx), aromatic disulfide-containing PDMS elastomers (ATPx-SS and APPx-SS), and DTSA.

Sample	$T_{1\%}$ ($^{\circ}\text{C}$)	$T_{5\%}$ ($^{\circ}\text{C}$)	Y_c ($^{\circ}\text{C}$)	$T_{\text{max}1}$ ($^{\circ}\text{C}$)	$T_{\text{max}2}$ ($^{\circ}\text{C}$)
ATP1	162	262	16.54	–	493
ATP2	148	256	14.28	–	494
ATP3	173	313	16.2	–	487
ATP4	183	324	26.39	–	479
APP1	96	161	11.29	–	513
APP2	99	171	20.49	–	500
APP3	114	186	17.17	–	499
ATP1-SS	229	279	10.58	292	461
ATP2-SS	235	291	15.45	278	455
ATP3-SS	240	292	15.47	284	448
ATP4-SS	232	273	14.42	304	459
APP1-SS	208	256	11.64	292	478
APP2-SS	219	261	13.38	285	476
APP3-SS	219	272	12.38	312	462
DTSA	214	268	1.37	317	–

$T_{1\%}$: 1% weight loss temperature; $T_{5\%}$: 5% weight loss temperature; Y_c : char yield at 800 $^{\circ}\text{C}$; $T_{\text{max}1}$: temperature of maximum rate of the first degradation stage; $T_{\text{max}2}$: temperature of maximum rate of the second degradation stage.

which correspond to the decomposition of pendent polar groups and the cleavage of siloxanes bonds, respectively [37]. For ATP1, the degradation of the pendent aminopropyl occurs at $T_{\text{max}1}$ and that of the cleavage of siloxanes bonds at $T_{\text{max}2}$; for APP1, the degradation of the pendent aminopropyl occurs at $T_{\text{max}1}$ and that of the cleavage of siloxanes bonds at $T_{\text{max}2}$. For ATPx-SS and APPx-SS, the values of $T_{\text{max}1}$ decrease evidently contrasted to ATPx and APPx while $T_{\text{max}2}$ increases slightly, indicating to an accelerated degradation of pendent polar groups and a slight increase in the thermal stability of siloxanes backbones. The Y_c decreases with the increase in the content of DTSA due to higher weight percentage of carbon, sulfur and oxygen elements.

3.4. Rheological properties

Rheological characterization has not been provided in most reports on dynamic PDMS-based materials, but it is of great value to investigate the viscoelasticity of materials based on dynamic bonds when their dynamics is triggered by heat [32]. The rheological properties of aromatic disulfide-containing PDMS elastomers were evaluated by two means: (i) temperature sweep at set strain and frequency and (ii) master curves followed by the classical time-temperature superposition (TTS) principle according to the Williams-Landel-Ferry (WLF) theory.

The critical temperature ($G' = G''$, $\tan \delta = 1$) of the $\tan \delta$ -temperature in Fig. 3 is regarded as the transition temperature (T_{trans}) of the cross-linked network, which is highly related to the dissociation of hydrogen-bonding [38]. Above the T_{trans} , the materials were in liquid state, indicating that there is barely no interaction among polymer chains under this condition. For the ATPx-SS elastomers, as the chain length of ATPx grows, the molar ratio of DTSA-HDI decreases, and thus, the hydrogen bonding moieties in the network decrease as well. The T_{trans} values of ATP1-ATP4 are 124 °C, 136 °C, 150 °C, and 112 °C, respectively. For APPx-SS elastomers, $\tan \delta$ values are below 1 in the temperature sweeping range, therefore, the crosslinked aromatic disulfide bonds are thermal stable under small strain (1%, damping mode) upon heating.

As illustrated in Fig. 4, the master curves of ATPx-SS exhibit the critical transition when $G' = G''$ at 0.001–0.1 rad/s, indicating that the chain mobility and flexibility of the ATPx-SS networks are strengthened at low frequency zone. APPx-SS present frequency-independence in calculated range. Moreover, the ATPx-SS elastomers show lower storage and loss modulus than APPx-SS elastomers especially at low frequency zone; this is because the former only has weak hydrogen bonding as crosslinking sites and the latter possesses much stronger aromatic disulfide bonds as chemical crosslinking sites, thus leading to more flexible segmental motion with temperature/strain-dependence.

3.5. Tensile properties

The obtained tensile strength and elongation at break of ATPx-SS and APPx-SS are summarized in Fig. 5a and c, and the typical tensile stress-strain curves of each samples are exhibited in Fig. 5b. The ATPx-SS elastomers only have weak hydrogen bonding formed between urea and amide groups, and therefore, the mechanical properties are greatly

dependent on the moieties of hydrogen bonding in the network. ATP1-SS has the highest tensile strength; while ATP3-SS has the highest elongation at break. Two competitive factors should be taken into consideration: the moieties of hydrogen bonding and the molecular weight of polysiloxanes backbones. ATP1-SS possesses the highest moieties of hydrogen bonding, tending to result in higher mechanical strength. However, the ATP3-SS has the optimized combination of hydrogen bonding moieties and molecular weight of polysiloxanes backbones, which is beneficial to get excellent stretchability and flexibility with little compromising on high modulus.

Compared with the ATPx-SS elastomers, about the same molar amount of DTSA-HDI with abundant aminopropyl side groups in the APPx-SS elastomers not only forms weak reversible crosslinking through hydrogen bonding, but also acts as strong dynamic chemical crosslinking points to further limit the segmental mobility of backbones, leading to higher mechanical strength and toughness than the ATPx-SS elastomers. As the molar content of DTSA-HDI decreases in APPx-SS elastomers (APP1-SS > APP2-SS > APP3-SS in DTSA-HDI content), the mobility is improved gradually, resulting in a decrease of mechanical strength and increase of elongation at break. Among then, APP3-SS shows the best stretchability (~200%) even comparable to those of ATPx-SS elastomers. In conclusion, these results reveal that ATPx-SS elastomers possess better stretchability, while APPx-SS elastomers achieve higher stiffness and toughness. Their biggest advantage is that, as the un-filled polysiloxanes-based elastomers, the as-prepared aromatic disulfide-containing polysiloxanes elastomers (ATPx-SS and APPx-SS) reported in this work present competitive mechanical strength and compromising stretchability by simply tuning the structures of polysiloxanes backbones; therefore, the elastomers are prepared for versatile applications as soft and slightly harder PDMS-based substrates.

3.6. Reprocessable properties

As stated above, the dynamics of aromatic disulfide is heat-triggered, so the reprocessability of the ATPx-SS and APPx-SS elastomers were intensively investigated.

The reprocessability of elastomers was evaluated by tensile strength after samples being heat-pressed for different cycles. The samples were first cut into pieces and then placed on a mold and maintained at 80–160 °C, 20 MPa for 10 min to achieve reforming. After molding,

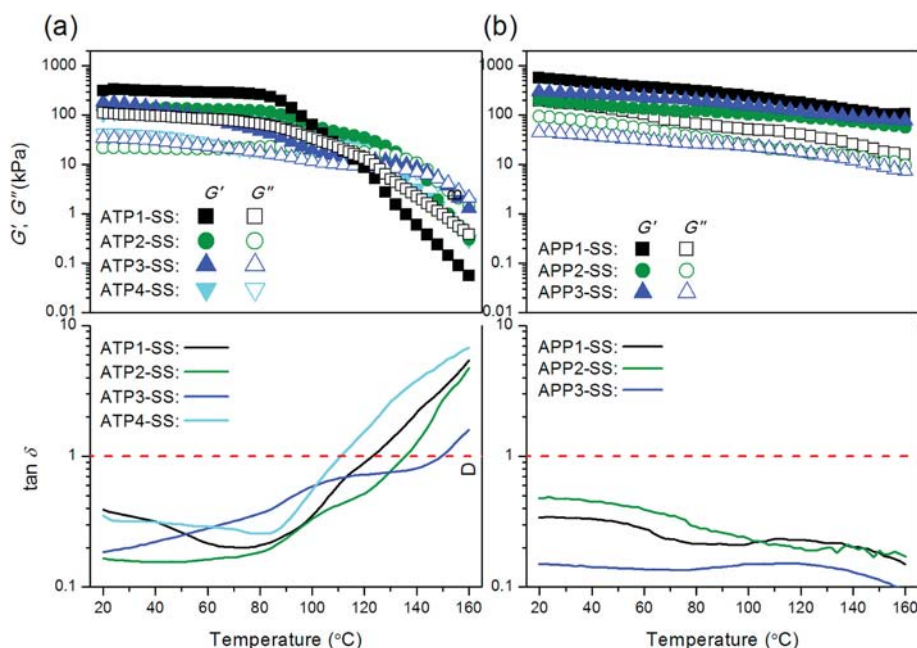


Fig. 3. Storage/loss modulus (top) and $\tan \delta$ (bottom) against temperature of the ATPx-SS (a) and APPx-SS (b) from the rheological temperature sweeping tests.

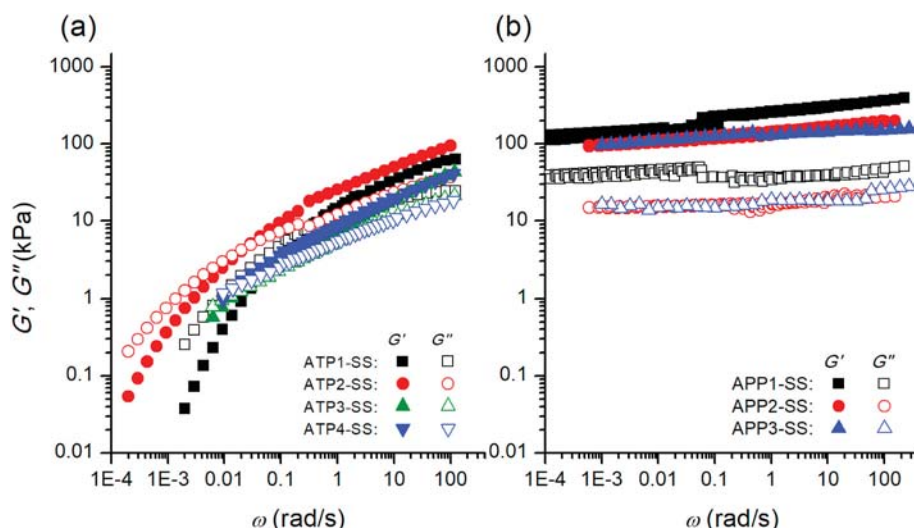


Fig. 4. Master curves of ATPx-SS (a) and APPx-SS (b) at reference temperature 120 °C from rheological tests.

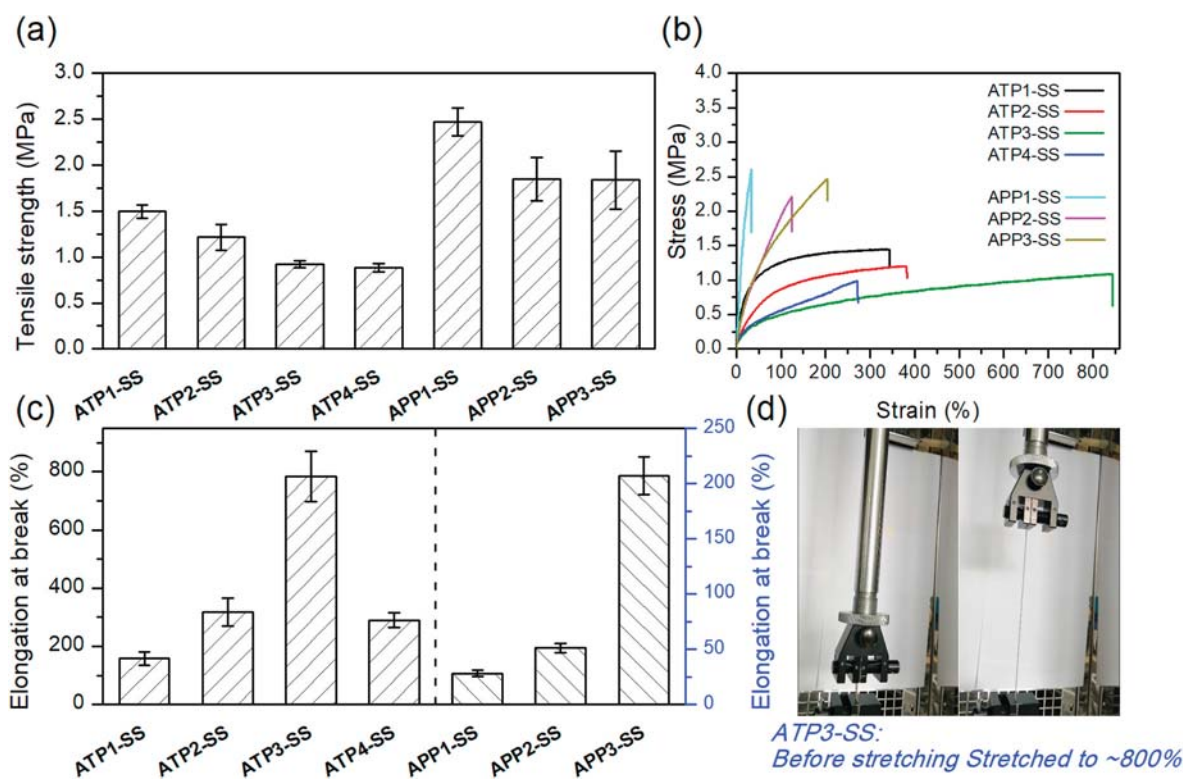


Fig. 5. Tensile strength (a) and elongation at break (c), and tensile stress-strain curves (b) of ATPx-SS and APPx-SS. Photos of ATP3-SS with excellent stretchability on a tensile machine (d): before stretching (left) and after being stretched to ~800% (right).

tensile tests on reprocessed samples were conducted and the data of tensile strength of reprocessed samples for different cycles were obtained (Fig. 6). It can be observed that after the first cycle, the values of tensile strength of all samples almost remain at the same level of the original ones. After the fourth cycles, the values of tensile strength are still competitive to the original ones. In addition, tensile strength values differentials of the APPx-SS elastomers are larger than those of the ATPx-SS elastomers, indicating that hydrogen bonding in ATPx-SS achieve higher and more stable recovery than aromatic disulfide in APPx-SS. These results are satisfactory and attractive because the mechanical recovery of both ATPx-SS and APPx-SS after several rounds of reprocessing is competitive to those of PDMS elastomers based on

dynamic bonds [39–42].

4. Conclusions

A novel kind of aromatic disulfide-containing polysiloxanes elastomers was fabricated based on hydrogen bonding and dynamic exchangeable aromatic disulfides. The molar amount of DSTA-HDI has been proved to play a crucial role in adjusting the thermal and mechanical properties in both ATPx-SS and APPx-SS elastomers. With DSTA-HDI as chain-extender while keeping chain-extension degree as constant, ATPx-SS shows 1.5 MPa tensile strength (ATP1-SS) and excellent elongation at break (780%, ATP3-SS). The crosslinking density

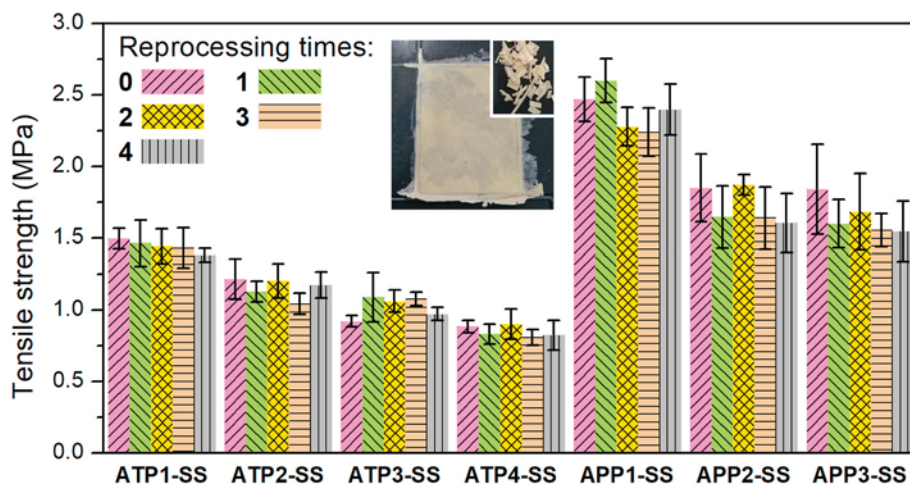


Fig. 6. Tensile strength of ATPx-SS and APPx-SS for different reprocessing cycles. Inset: photos of sliced samples (little one) being heat-pressed on a mold (big one).

of DTSA-HDI in APPx-SS elastomers has been under research; results reveal that DTSA-HDI has made significant contribution to the mechanical strength (2.60 MPa, APP1-SS). Moreover, it has outstanding reprocessability and can be reprocessed and reformed without much decline of tensile strength after several cycles of hot-pressing. Though the input of DTSA-HDI has accelerated the decomposition of pendent polar groups of elastomers at some level, rheological analysis confirmed the stability in mechanical properties of elastomers below 160 °C, guaranteeing the safety of samples being processed at 80–160 °C within 10 min.

Declaration of competing interest

The authors declare that they have no known competing financial interests or personal relationships that could have appeared to influence the work reported in this paper.

Acknowledgements

We thank the National Natural Science Foundation of China (52073098, 51473051) and the Science and Technology Program of Guangzhou, China (201803020015) for financially supporting this project.

Appendix A. Supplementary data

Supplementary data to this article can be found online at <https://doi.org/10.1016/j.polymer.2021.123588>.

References

- [1] C. Zuidema, W. Kegerise, R. Fleming, R.M. Welker, S. Boggs, A short history of rubber cables, *IEEE Electr. Insul. Mag.* 4 (2011) 45–50.
- [2] K. Tamási, M.S. Kollár, Effect of different sulfur content in natural rubber mixtures on their thermo-mechanical and surface properties, *Inter. J. Eng. Res. Sci.* 4 (2018) 28–37.
- [3] P.T. Corbett, J. Leclaire, L. Vial, K.P. West, J.L. Wietor, J.K. Sanders, S. Otto, Dynamic combinatorial chemistry, *Chem. Rev.* 106 (2006) 3652–3711.
- [4] S.J. Rowan, S.J. Cantrill, G.R.L. Cousins, J.K.M. Sanders, J.F. Stoddart, Dynamic covalent chemistry, *Angew. Chem. Int. Ed.* 41 (2002) 898–952.
- [5] J. Canadell, H. Goossens, B. Klumperman, Self-healing materials based on disulfide links, *Macromolecules* 44 (2011) 2536–2541.
- [6] S. Otto, R. Cantrill, J.F. Stoddart, J.K.M. Sanders, Dynamic combinatorial libraries of macrocyclic disulfides in water, *J. Am. Chem. Soc.* 122 (2000) 12063–12064.
- [7] A.P. Bapat, J.G. Ray, D.A. Savin, B.S. Sumerlin, Redox-responsive dynamic-covalent assemblies: stars and miktoarm stars, *Macromolecules* 46 (2013) 2188–2198.
- [8] B.D. Fairbanks, S.P. Singh, C.N. Bowman, K.S. Anseth, Photodegradable, photoadaptable hydrogels via radical-mediated disulfide fragmentation reaction, *Macromolecules* 44 (2011) 2444–2450.
- [9] J.M. Matxain, J.M. Asua, F. Ruipérez, Design of new disulfide-based organic compounds for the improvement of self-healing materials, *Phys. Chem. Chem. Phys.* 18 (2016) 1758–1770.
- [10] A.C. Templeton, M.J. Hostetler, C.T. Kraft, R.W. Murray, Reactivity of monolayer-protected gold cluster molecules: steric effects, *J. Am. Chem. Soc.* 120 (1998) 1906–1911.
- [11] A. Stewart, S. Zheng, M.R. McCourt, S.E. Bell, Controlling assembly of mixed thiol monolayers on silver nanoparticles to tune their surface properties, *ACS Nano* 6 (2012) 3718–3726.
- [12] J.C. Love, L.A. Estroff, J.K. Kriebel, R.G. Nuzzo, G.M. Whitesides, Self-assembled monolayers of thiolates on metals as a form of nanotechnology, *Chem. Rev.* 105 (2005) 1103–1170.
- [13] R. Martín, A. Rekondo, J. Echeberria, G. Cabañero, H.J. Grande, I. Odriozola, Room temperature self-healing power of silicone elastomers having silver nanoparticles as crosslinkers, *Chem. Commun. (J. Chem. Soc. Sect. D)* 48 (2012) 8255–8257.
- [14] R. Caraballo, M. Rahm, P. Vongvilai, T. Brinck, O. Ramström, Phosphine-catalyzed disulfide metathesis, *Chem. Commun. (J. Chem. Soc. Sect. D)* 48 (2008) 6603–6605.
- [15] Z. Lei, H. Xiang, Y. Yuan, M. Rong, M. Zhang, Room-temperature self-healable and remoldable cross-linked polymer based on the dynamic exchange of disulfide bonds, *Chem. Mater.* 26 (2014) 2038–2046.
- [16] T. Ohishi, Y. Iki, K. Imato, Y. Higaki, A. Takahara, H. Otsuka, Insertion metathesis depolymerization of aromatic disulfide-containing dynamic covalent polymers under weak intensity photoirradiation, *Chem. Lett.* 42 (2013) 1346–1348.
- [17] H. Otsuka, S. Nagano, Y. Kobashi, T. Maeda, A. Takahara, A dynamic covalent polymer driven by disulfide metathesis under photoirradiation, *Chem. Commun. (J. Chem. Soc. Sect. D)* 46 (2010) 1150–1152.
- [18] R.J. Sarma, S. Otto, J.R. Nitschke, Disulfides, imines, and metal coordination within a single system: interplay between three dynamic equilibria, *Chem. Eur. J.* 13 (2007) 9542–9546.
- [19] R. Martín, A. Rekondo, A.R. Luzuriaga, P. Casuso, D. Dupin, G. Cabañero, H. J. Grande, I. Odriozola, Dynamic sulfur chemistry as a key tool in the design of self-healing polymers, *Smart Mater. Struct.* 25 (2016), 084017.
- [20] P. Casuso, I. Odriozola, A. Pérez-San Vicente, I. Loizaga, G. Cabañero, H.J. Grande, D. Dupin, Injectable and self-healing dynamic hydrogels based on metal(I)-Thiolate/Disulfide exchange as biomaterials with tunable mechanical properties, *Biomacromolecules* 16 (2015) 3552–3561.
- [21] D.J. Fortman, R.L. Snyder, D.T. Sheppard, W.R. Dichtel, Rapidly reprocessable cross-linked poly(hydroxyurethanes) based on disulfide exchange, *ACS Macro Lett.* 7 (2018) 1226–1231.
- [22] R. Martín, A. Rekondo, A.R. Luzuriaga, G. Cabañero, H.J. Grande, I. Odriozola, The processability of a poly(urea-urethane) elastomer reversibly crosslinked with aromatic disulfide bridges, *J. Mater. Chem.* 2 (2014) 5710–5715.
- [23] J. Zhou, Y. Yang, R. Qin, M. R. Y. Sheng, X. Lu, Robust poly(urethane-amide) protective film with fast self-healing at room temperature, *ACS Appl. Polym. Mater.* 2 (2019) 285–294.
- [24] A. Takahashi, T. Ohishi, R. Goseki, H. Otsuka, Degradable epoxy resins prepared from diepoxide monomer with dynamic covalent disulfide linkage, *Polymer* 82 (2016) 319–326.
- [25] A. Rekondo, R. Martín, A.R. de Luzuriaga, G. Cabañero, H.J. Grande, I. Odriozola, Catalyst-free room-temperature self-healing elastomers based on aromatic disulfide metathesis, *Mater. Hori.* 1 (2014) 237–240.
- [26] G.C. Tesoro, V. Sastri, Reversible crosslinking in epoxy resins, I. Feasibility Studies, *J. Appl. Polym. Sci.* 39 (1990) 1425–1437.
- [27] V.R. Sastri, G.C. Tesoro, Reversible crosslinking in epoxy resins. II. New approaches, *J. Appl. Polym. Sci.* 39 (1990) 1439–1457.

- [28] P.I. Engelberg, G.C. Tesoro, Mechanical and thermal properties of epoxy resins with reversible crosslinks, *Polym. Eng. Sci.* 30 (1990) 303–307.
- [29] Y. Zhang, H. Ying, K.R. Hart, Y. Wu, A.J. Hsu, A.M. Coppola, T.A. Kim, K. Yang, N. R. Sottos, S.R. White, J. Cheng, Malleable and recyclable poly(urea-urethane) thermosets bearing hindered urea bonds, *Adv. Mater.* 28 (2016) 7646–7651.
- [30] J. Zhou, Y. Yang, R. Qin, M. Xu, Y. Sheng, X. Lu, Robust poly(urethane-amide) protective film with fast self-healing at room temperature, *ACS Appl. Polym. Mater.* 2 (2019) 285–294.
- [31] S. Nevejans, N. Ballard, J.I. Miranda, B. Reck, J.M. Asua, The underlying mechanisms for self-healing of poly(disulfide)s, *Phys. Chem. Chem. Phys.* 18 (2016) 27577–27583.
- [32] Y. Zhang, L. Yuan, G. Liang, A. Gu, A. Simultaneously achieving superior foldability, mechanical strength and toughness for transparent healable polysiloxane films through building hierarchical crosslinked networks and dual dynamic bonds, *J. Mater. Chem.* 6 (2018) 23425–23434.
- [33] H. Guo, Y. Han, W. Zhao, J. Yang, L. Zhang, Universally autonomous self-healing elastomer with high stretchability, *Nat. Commun.* 11 (2020) 2037.
- [34] Y. Lei, Q. Huang, S. Shan, Y. Lin, A. Zhang, A stretchable and rapidly self-healable polysiloxane elastomer based on reversible aluminum-amino coordination, *New J. Chem.* 43 (2019) 17441–17445.
- [35] S. Dewasthale, C. Andrews, D. Graiver, R. Narayan, Water soluble polysiloxanes, *Silicon* 9 (2017) 619–628.
- [36] M. Barlkani, C. Hepburn, Determination of crosslink density by swelling in the castable polyurethane elastomer based on 1/4-cyclohexane diisocyanate and para-phenylene diisocyanate, *Iran. J. Polym. Sci. Technol.* 1 (1992) 1–5.
- [37] H. Sun, X. Liu, H. Yan, Z. Feng, B. Yu, N. Ning, M. Tian, L. Zhang, The role of dipole structure and their interaction on the electromechanical and actuation performance of homogeneous silicone dielectric elastomers, *Polymer* 165 (2019) 1–10.
- [38] M. Tang, R. Xu, R. Zhang, S. Bai, G. Huang, Y. Xu, Bioinspired strategy to tune viscoelastic response of thermoplastic polyisoprene by retarding the dissociation of hydrogen bonding, *Polymer* 212 (2021) 123272.
- [39] X. Jia, J. Mei, J. Lai, C. Li, X. You, A self-healing PDMS polymer with solvatochromic properties, *Chem. Commun.* 51 (2015) 8928–8930.
- [40] L. Liu, S. Liang, Y. Huang, C. Hu, J. Yang, A stretchable polysiloxane elastomer with self-healing capacity at room temperature and solvatochromic properties, *Chem. Commun.* 53 (2017) 12088–12091.
- [41] Y. Rao, A. Chortos, R. Pfattner, F. Lissel, Y. Chiu, V. Feig, J. Xu, T. Kurosawa, X. Gu, C. Wang, M. He, Stretchable self-healing polymeric dielectrics cross-linked through metal-ligand coordination, *J. Am. Chem. Soc.* 138 (2016) 6020–6027.
- [42] C. Li, C. Wang, C. Keplinger, J. Zuo, L. Jin, Y. Sun, P. Zheng, Y. Cao, F. Lissel, C. Linder, X. You, A highly stretchable autonomous self-healing elastomer, *Nat. Chem.* 8 (2016) 618–624.



A solvent-free, transparent, self-healing polysiloxanes elastomer based on unsaturated carboxyl-amino ionic hydrogen bonds

Jiaheng Mo^a, Xinyu Chen^a, Yubing Fu^a, Rui Li^a, Yaling Lin^{b,*}, Anqiang Zhang^{a,**}

^a School of Material Science and Engineering, South China University of Technology, 381 Wushan Rd., Guangzhou 510641, Guangdong, China

^b College of Materials and Energy, South China Agricultural University, 483 Wushan Rd., Guangzhou 510642, Guangdong, China

ARTICLE INFO

Keywords:

Unsaturated carboxyl-amino ionic Hydrogen bonds
Polysiloxanes elastomer
Supramolecular elastomer

ABSTRACT

Ionic hydrogen bonding elastomers (IHSEs) as functional materials with a favorable self-healing ability and sensitive response to pH or heat have been increasingly investigated, yet most of these IHSEs are based on carbon chains with amino and carboxyl functional groups. Herein we describe an ionic hydrogen-bonded supramolecular polydimethylsiloxanes (PDMS) elastomer containing amino and unsaturated carboxyl groups produced via a facile and completely solvent-free synthesis route. Unsaturated carboxyl-grafted PDMS (UCS) and saturated carboxyl-grafted PDMS (SCS) were synthesized by reacting amino-grafted PDMS (APS) with maleic anhydride and succinic anhydride by simple mixing, respectively. The fact that IHSEs could be obtained by mixing UCS and APS while the mixture of SCS and APS was viscous fluid reveals difference of strength of ionic hydrogen bonds formed by unsaturated/saturated carboxyl groups with amino groups. To the best of our knowledge, it is the first time to investigate the role of unsaturated carboxyl groups which are conjugated with C=C on the strength of the ionic interactions. Stronger ionic hydrogen bonds from unsaturated carboxyl-amino complex were further confirmed by NMR titration. The mechanical properties and self-healing ability may be fine-tuned by adjusting the ion cross-linking density and -COOH and -NH₂ feed ratios. Furthermore, excess unsaturated carboxyl groups make IHSEs practically adhesive. We hope to further investigate the cross-linking mechanism of the ionic interactions inside the supramolecular network and to create a facile method to create supramolecular elastic systems.

1. Introduction

Traditional elastomers can be categorized into two groups: vulcanized rubber, which is chemically cross-linked by covalent bonds (such as carbon-carbon bonds and siloxane linkages), and thermoplastic elastomers (TPEs), which are physically cross-linked by a crystalline domain. Permanent covalent cross-linking networks endow elastomers with superior mechanical properties and solvent resistance, but at the same time, these networks make reprocessing or recycling less feasible. Things have changed since Leibler et al. [1] first adopted reversible interactions to construct noncovalent cross-linking networks (also called supramolecular elastomers). Typically, the key when constructing a noncovalently cross-linked network is incorporating functional groups that generate noncovalent interactions (such as hydrogen bonds [2–7], metal–ligand coordination [8–15], π - π stacking interactions [16–18], ionic interactions [19–27] and host–guest interactions [28–30]) into the

polymer chains. In reversible, noncovalent networks, the association and dissociation can be triggered by various external stimuli, such as heat [2–4], UV light [8], pH [9], solvents [4] or salt [26]. These properties have many positive attributes, for example, a self-healing ability makes elastomers mend cracks automatically and, thus, maintain a longer life [13], dynamic reversibility is based on preparing high energy-dissipating elastomers applied to damping material [10,27,31] and outstanding stimuli-responsive properties with a self-healing ability make it possible for practical application in wearable electronic devices and sensors [15,24,32–34,43].

Among the various approaches to generating the aforementioned noncovalent network, ionic interactions offer feasible and efficient platforms for constructing supramolecular networks. Examples are small-molecule containing ionic complementary structures as starting materials. Mecerreyes et al. [20,21] obtained a family of supramolecular ionic polymers using a simple (di-/tri-) carboxylic acid and (di-/tri-)

* Corresponding author.

** Corresponding author.

E-mail addresses: linyinling@scau.edu.cn (Y. Lin), aqzhang@scut.edu.cn (A. Zhang).

<https://doi.org/10.1016/j.polymer.2021.123903>

Received 30 March 2021; Received in revised form 15 May 2021; Accepted 22 May 2021

Available online 28 May 2021

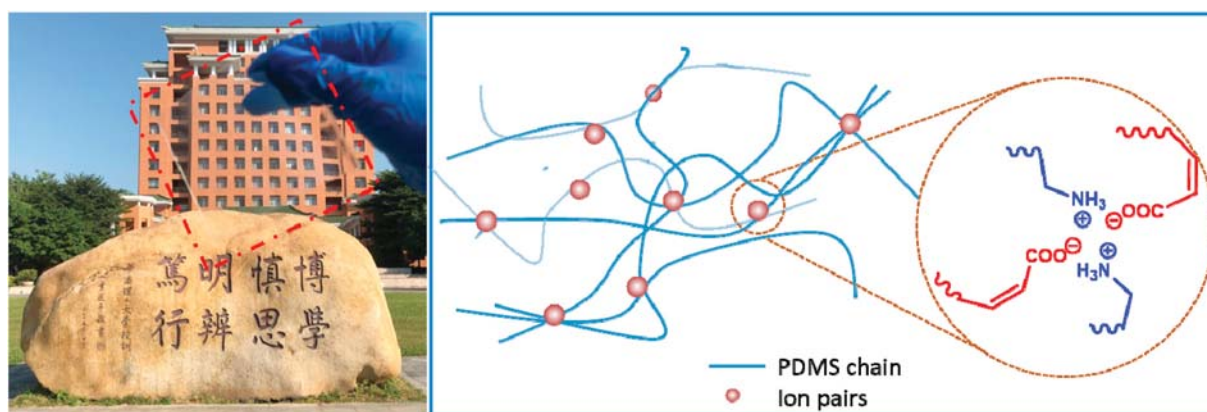
0032-3861/© 2021 Elsevier Ltd. All rights reserved.

alkyl amine method. The ionic and hydrogen bonds between carboxylate and ammonium molecules make the polymers solid at room temperature and show a sharp rheological transition from a viscoelastic gel to a viscous liquid between 30 and 80 °C. However, these fluidic materials, held together by noncovalent electrostatic interactions, are supramolecular ionic networks whose properties are compared to “ionic liquids” that flow at ambient temperatures [36]. This is because ionic interactions lack specificity and bonding directionality [37]. To bring about solid supramolecular ionic networks, incorporating functional groups with electrostatic interactions into the polymer matrix is efficient. Ionomers are examples of this type of material, and a small proportion of the monomeric units bear ionic and/or ionizable groups, such as carboxylate, sulfonate and phosphonate. Kalista et al. [38] revealed the relationship between elasticity, diffusion, and the self-healing behavior of commercial poly(ethylene-co-methacrylic acid) (EMAA) copolymers containing varying levels of ionic content. However, with a rigid EMMA backbone, an elastic response and self-healing ability were observed at elevated temperatures. Thus, when an elastic response and self-healing ability are desired, it is beneficial to use polymers with a low T_g as the ionomer backbone. For example, Miwa et al. [25] prepared an ionic elastomer by simply neutralizing carboxylated polyisoprene elastomers (PI-COOH) at varying degrees, and the elastomers possessed ultrastretchability and a self-healing ability at room temperature. Constructing supramolecular networks based on ionomers usually involves neutralization by metal cations. Polyelectrolytes and polyampholytes offer another feasible strategy in which ionizable groups grafted to the polymer backbone can neutralize each other, resulting in ionic cross-linked networks. Wu et al. [24] reported a class of polyampholyte-based elastomers with an excellent combination of good mechanical properties and self-healing ability by incorporating oppositely charged monomers into polyacrylate. In particular, amino and carboxyl groups are complementary ionic structures that can form hydrogen bonds, which allows for a synergistic effect between the ionic interactions and hydrogen bonds in supramolecular networks. Elastomers based on ionic hydrogen bonds have been reported by Xu [39], including carboxyl-grafted PB cross-linked by triamine and blending of carboxyl-grafted PB and amino-grafted PB.

In our design, PDMS was chosen as the polymer chain to be grafted with amino and carboxyl groups with the goal of constructing ionic hydrogen bonded supramolecular elastomers. Compared to polybutadiene, polyisoprene and polyacrylate, PDMS are softer, of a lower T_g and have been successfully used to construct supramolecular networks with self-healing properties [2–4,11,13,14]. However, it is hard to construct supramolecular elastomers directly using amino-grafted PDMS and carboxyl-grafted PDMS because PDMS are too soft to obtain elastic network cross-linked by ionic interactions between carboxyl and amino groups. Skov et al. [23] reported a self-healing dielectric PDMS elastomer based on carboxyl-amino complex. However, the material was

actually an interpenetrating polymer network (IPN) combining a cross-linked PDMS network and an ionic network containing amino and carboxyl groups. One key parameter regulating the strength of ionic interactions is the amount of ions, for example, Brook et al. [40] recently reported thermoplastic silicone elastomers based on Gemini amino-grafted PDMS and Gemini carboxyl-grafted PDMS. And the other key parameter is type of ions. Acids with varying acidity and base with varying basicity probably interact with each other in varying strength. Unsaturated carboxylic acids which are conjugated with C=C are in general of greater acidity. However, neither investigation on the role of unsaturated carboxyl groups on the strength of the ionic interactions nor construction of ionic supramolecular elastomers based on unsaturated carboxyl-amino ionic interactions.

Herein, we developed a facile and completely solvent-free route to construct ionic hydrogen bonded supramolecular elastomers based on unsaturated carboxyl and amino groups, as shown in Scheme 1, which, to the best of our knowledge, is the first time ionic interaction supramolecular elastomers have been constructed containing unsaturated carboxyl groups. Amino-grafted PDMS (denoted as APS) with different amino concentration was cotelomerized by octamethylcyclotetrasiloxane (D4) and polyaminopropylmethylsilane at different rates. Then, unsaturated carboxyl-grafted PDMS (denoted as UCS) was synthesized by reacting corresponding APS with maleic anhydride at a solvent-free condition without any post-processing steps. Finally, ionic hydrogen bonded supramolecular elastomers (IHSEs) were obtained by simply mixing APS and UCS. Furthermore, analogs (denoted as SCS) in which C=C was replaced by C–C were prepared and compared. The IHSEs exhibited good mechanical properties with a tensile strength of up to 1.5 MPa, an elongation at break of up to 900% and typical elastomer behavior with its storage modulus (G') being far greater than its loss modulus (G''); however, for the APS and SCS mixture, $G' < G''$ was observed over the testing frequency range. This difference could be explained by the fact that attaching C=C augments the carboxyl acidity so markedly that ionic hydrogen bonds are strong enough while weaker ionic hydrogen bonds between carboxyl and amino groups seem to be unable to afford PDMS an elastic network. K_1 and K_2 (association constant of unsaturated/saturated carboxyl and amino groups, respectively) were calculated by NMR titration and $K_1 > K_2$ further confirmed the advantage of unsaturated groups at construction of ionic hydrogen bonding elastomers. Furthermore, changing 1:1 ratio of $n(\text{-COOH})$: $n(\text{-NH}_2)$ had a significant impact on the viscoelasticity and adhesion of the IHSEs, and a better self-healing ability at room temperature was observed when the $n(\text{-COOH})$: $n(\text{-NH}_2)$ ratio was increased.



Scheme 1. The formation of crosslinking network in IHSEs.

2. Experimental

2.1. Synthesis of amino-grafted polydimethylsiloxanes (APS), unsaturated carboxyl-grafted polydimethylsiloxanes (UCS) and saturated carboxyl-grafted polydimethylsiloxanes (SCS)

The APS synthesis was based on previously reported work [13] with some improvements, and the routes are given in Scheme S1. The synthesis of UCS and SCS were based on reacting amino groups and anhydride, and the routes are supplied in Scheme S1 and Scheme 2. The synthesis details for APS, UCS and SCS can be found in ESI.

2.2. Preparation of ionic hydrogen bond supramolecular elastomers (IHSEs)

Ionic hydrogen bonding supramolecular elastomers (IHSEs) were prepared by simply mixing APS and UCS at room temperature, and the detailed preparing procedures, characterization and testing procedures for the self-healing properties are supplied in ESI. The control groups included APS mixed with SCS followed the same preparation procedures.

2.3. Model experiment based on small molecules

The synthesis of small-molecular unsaturated carboxylic acid (APTMS-MA) and small-molecular saturated carboxylic acid (APTMS-SA) were based on reacting amino groups and anhydride. The synthesis details can be seen in ESI.

3. Results and discussion

3.1. Characterization of UCS and SCS

We obtained the APS of a given amino grafting ratio and molecular weight by comparing the D₄: APS-100 feed ratio and the amount of AMM. The APS synthesis process has been well reported [13]. The amino groups in polysiloxane have been shown to be excellent reaction sites for further modification, which, in this research, reacted with maleic anhydride to translate into unsaturated carboxyl groups. Emphatically, this reaction was completely solvent-free and obtained high yields, and although maleic anhydride was used at 1.05-fold excess, there was no residue due to its volatility. The APS and UCS were characterized by FT-IR (Fig. S2) and ¹H NMR (Fig. S3).

The FTIR spectra of APS and UCS with amino and unsaturated carboxyl grafting degrees of 3%, 5% and 10% are shown in Fig. S2. When amino groups reacted with maleic anhydride, N-H amino group bond bending vibrations disappeared, and characteristic vibration absorptions at 3270, 1714, 1635 and 1560 cm⁻¹ appeared, representing

O-H stretching vibrations, C=O carboxyl group stretching vibrations, C=O stretching vibrations, and N-H amide bending vibrations, respectively. However, signal peaks at 1550-1500 cm⁻¹ ascribed to C=C could only be seen in UCS. The absence of signal peaks at 1820-1750 cm⁻¹ for -(CO)₂O indicate that no maleic anhydride remained.

The ¹H NMR spectra confirmed the structure of UCS, as shown by a comparison of the spectra shown in Fig. S3. In the ¹H NMR spectra of APS, the proton signal peaks at δ = 0.09, 0.52, 1.45, 2.66 ppm are attributed to Si-CH₃, -CH₂-CH₂-CH₂-NH₂, -CH₂-CH₂-NH₂ and -CH₂-NH₂, respectively, and the amino group grafting degree can be calculated from integrating the peak areas related to Si-CH₃ and -CH₂-NH₂, which is convenient auxiliary validation of the acid-base titration. In the UCS ¹H NMR spectra, the presence of characteristic peaks at δ = 6.31 and 6.54 ppm attributed to -CH=CH-COOH indicates the amino groups that are attached to the side chains of PDMS have successfully translated into unsaturated carboxyl groups. In addition, due to the polarity of amide, the proton signal peak of -CH₂-NHCO- shifts towards a greater chemical shift at δ = 3.34. No notable proton peaks ascribed to maleic anhydride are observed.

The saturated carboxyl-grafted polydimethylsiloxane (SCS) were obtained by reacting APS with succinic anhydride in a solvent-free condition, and the relevant characterizations of FT-IR, ¹H NMR are shown in Fig. S2 and Fig. S3.

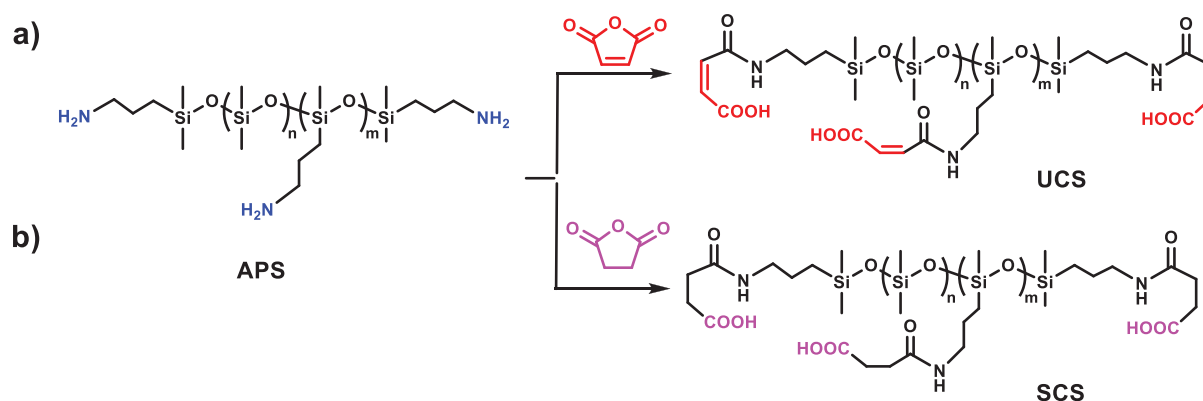
The GPC traces in Fig. S4 give the molecular weight of APS, UCS and SCS, and the APS test results are slightly higher than designed molecular weight because the amino groups need to react with *m*-tolyl isocyanate.

3.2. Polymer structures and cross-linked network based on carboxyl-amino ionic interactions

Carboxyl-amino complexation has been well examined when constructing supramolecular networks^{41, 39}, but using this complexation to cross-link the polysiloxane backbones to produce an elastic network has yet to have been explored, especially with unsaturated carboxyl-grafted PDMS. To elucidate the relationship between the elastic response of the supramolecular network and polymer structures, two supramolecular networks based on carboxyl-amino ionic interactions (IHSE and APS-SCS) were prepared, and only the IHSE group showed a strong enough elastic response to form ionic hydrogen bond supramolecular elastomers.

3.2.1. Comparison of IHSEs and APS-SCS

The APS and UCS or SCS were mixed directly without any solvent. The disappearance of the C=O carboxyl group stretching vibration peaks at 1714 cm⁻¹ and the presence of carboxylate peaks at 1560 cm⁻¹ indicate the achievement of acid-base neutralization, as shown in Fig. 1. This process can be described by amino and carboxyl groups first undergo effective contact and forming hydrogen bonds, resulting in an



Scheme 2. The synthesis routes of (a) UCS and (b) SCS.

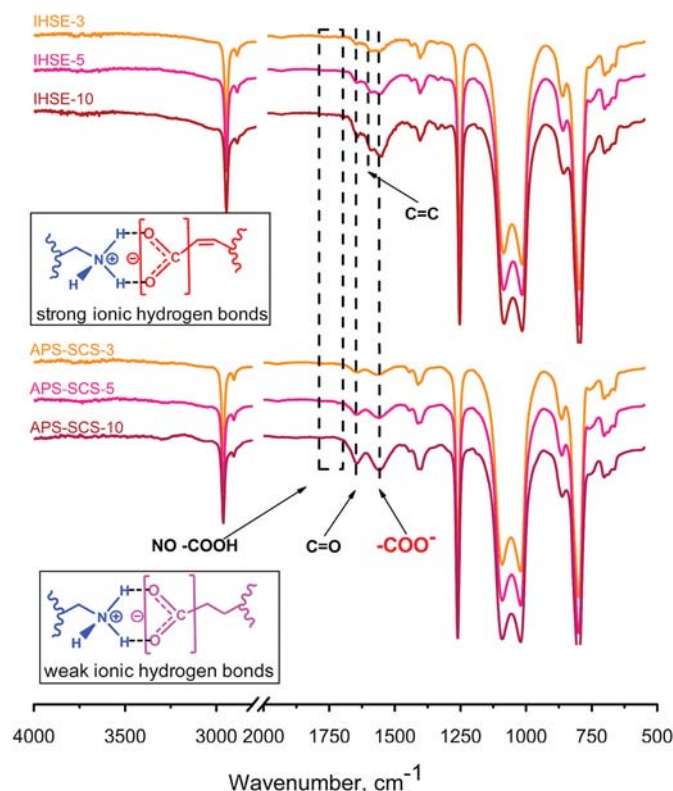


Fig. 1. FTIR-ATR spectra of (upper) IHSEs and (lower) APS-SCSs.

increase the mixture viscosity. Then, protons transfer from the carboxyl groups to the amino groups resulting in ionic hydrogen bonds. The elastomers cross-linked by ionic hydrogen bonds were almost colourless, soft and transparent (Fig. S13). However, if maleic anhydride was replaced by succinic anhydride to obtain SCS, mixing APS and SCS did not result in elastomers: only an increase in the mixture viscosity was observed.

The viscoelastic properties of the IHSEs and APS-SCSs were characterized by rheological measurements. The master curves were constructed using isothermal dynamic frequency sweeps at temperatures

20, 30, 40, 50, 60, 70 and 80 °C by applying the time–temperature superposition (TTS) principle. In Fig. 2-a, at the reference temperature (25 °C), all the master curves of IHSEs showed a rubbery plateau ($G' > G''$) at the full testing frequency range. In terms of the viscoelasticity properties of the samples as a function of frequency, increasing the frequency slightly increased the storage modulus (G') for all the samples and obviously increased the loss modulus (G''). However, for the APS-SCS-3, APS-SCS-5 and APS-SCS-10 control groups, all master curves showed that the loss moduli were greater than storage moduli ($G'' > G'$), indicating no rubbery plateau, as shown in Fig. 2-b. The moderately long lifetime of the stronger ionic hydrogen bonds and the short lifetime of weaker ionic hydrogen bonds can be responsible for the differences and tendencies. The lifetime of stronger ionic hydrogen bonds is still longer than the relaxation time of polymer chains at a low frequency and, to a greater extent, at a higher frequency, resulting in an increase of the storage modulus (G'), while the lifetime of stronger ionic hydrogen bonds is much shorter than the relaxation time of the polymer chains, leading to a viscous liquid state.

This interesting phenomenon can be attributed to the difference in the pK_a (negative logarithm of the ionization constant of the weak acid) of maleic acid and succinic acid (maleic acid: $pK_{a1} = 1.92$; succinic acid: $pK_{a1} = 4.21$). The difference in the pK_a of maleic acid and succinic acid can be attributed to double carbon bonds of the unsaturated carboxyl groups conjugating with the carboxylic acid ions, which can be accordingly stabilized [35,41].

3.2.2. Strength of the ionic hydrogen bonds

To further reveal the role of double carbon bonds on the strength of the ionic hydrogen bonds, 1H NMR titration to characterize the strength of the ionic hydrogen bonds formed by amino and carboxyl groups was performed. The chemical shifts of the protons related to ionic hydrogen bonds showed a concentration dependence. Specifically, the observed chemical shift in the reversible interactions was a weighted average between the chemical shift of the free-state and that of the associated-state [42].

It appeared to be difficult to measure strength of ionic hydrogen bonds directly in the mixture of amino-grafted and carboxyl-grafted PMDS because of insolubility of IHSEs in solvent. To address this problem, three compounds, APTMS, APTMS-MA and APTMS-SA (Scheme 3) were used as model systems for ionic hydrogen bonds in the IHSEs.

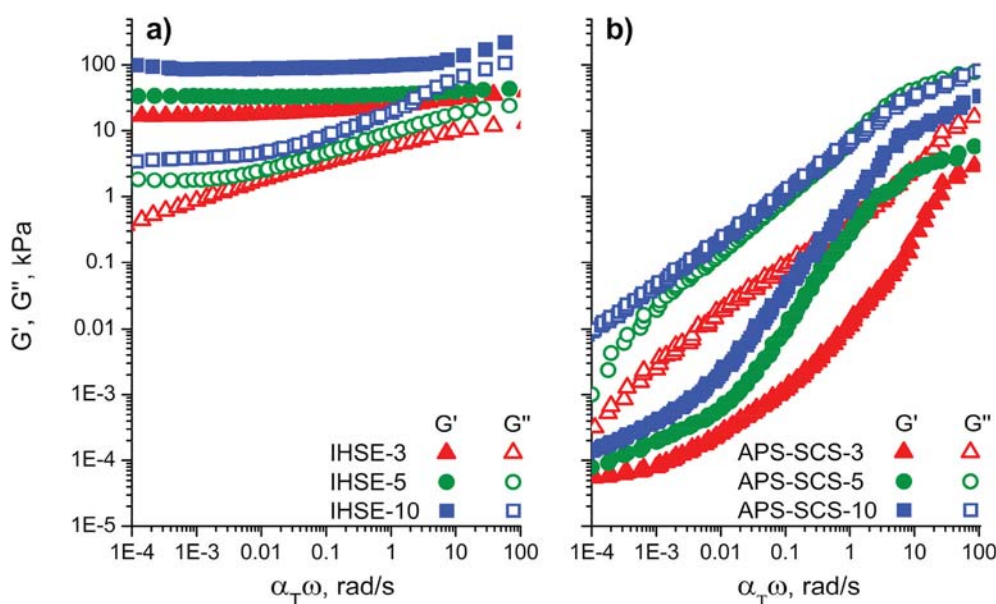
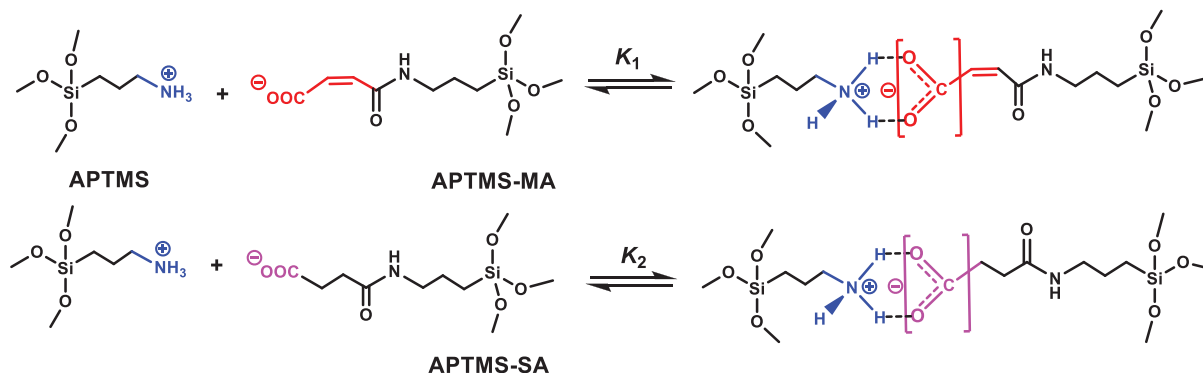


Fig. 2. The master curves of (a) IHSEs and (b) APS-SCSs.



Scheme 3. Reversible association and dissociation of ionic hydrogen bonds (K_1 and K_2 for association constant of ionic hydrogen bonds from unsaturated and saturated carboxyl groups, respective).

All titration experiments were conducted in DMSO, a polar solvent which is the only good solvent for mixture of model compounds. In Fig. 3, the changes in the chemical shift can be observed with setting concentration of APTMS as a constant (0.12 mol/L) and increasing concentration of APTMS-MA or APTMS-SA from 0.02 to 0.12 mol/L. The proton peaks of both the two experimental groups shifted to lower fields, from 2.51 to 2.77 ppm and from 2.51 to 2.69, respectively. By fitting the titration curve, K_1 (association constant of unsaturated carboxyl and amino groups from APTMS-MA and APTMS) and K_2 (association constant of saturated carboxyl and amino groups from APTMS-SA and APTMS) in DMSO was determined to be 45.5 and 7.25 M^{-1} , respectively. Considering association constant is a good measurement of the strength of reversible interactions, we can draw a conclusion that strength of

ionic hydrogen bonds formed by unsaturated carboxyl and amino groups is much greater than that of saturated carboxyl and amino groups.

3.3. Mechanical and self-healing properties of IHSEs

The tensile and self-healing test results of the IHSE samples are shown in Fig. 4. First, comparing the IHSEs having different degrees of cross-linking, the stress-strain curves changed drastically with the cross-linking degree. Remarkable enhancements in both the tensile strength and Young's modulus were observed when the cross-linking degree increased, while the elongation at break sharply declined from 900% to 260%. It is reasonable that the mechanical properties of the elastomers are enhanced while the stretching properties are diminished with an

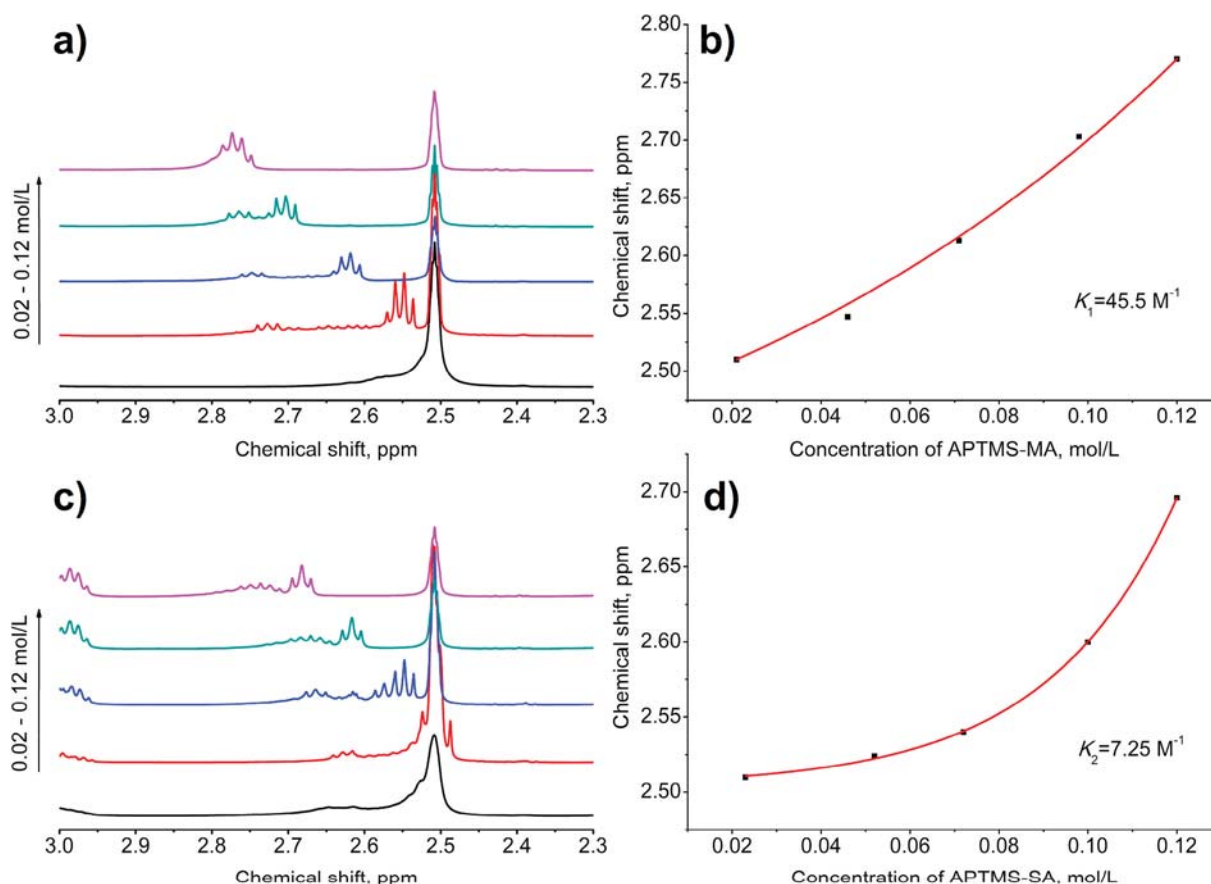


Fig. 3. (A) 1H NMR spectra at 25 °C of APTMS-MA (from 0.02 to 0.12 mol/L), (B) Titration curve of APTMS-MA, (C) 1H NMR spectra at 25 °C of APTMS-SA (from 0.02 to 0.12 mol/L) and (D) Titration curve of APTMS-SA.

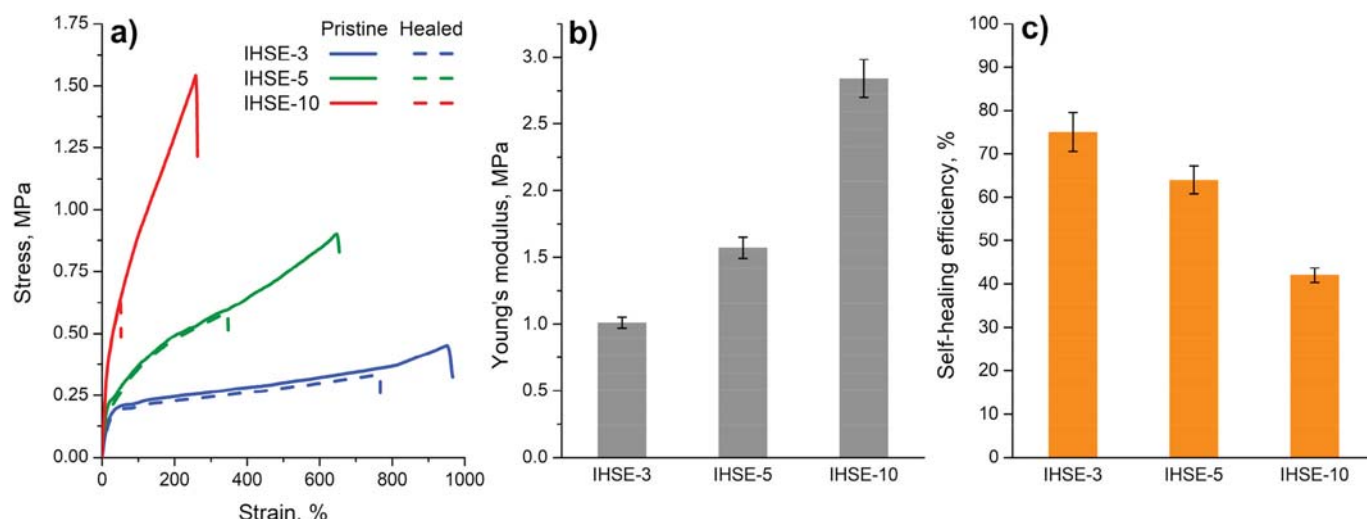


Fig. 4. (A) Stress-strain curves of the pristine and 24 h-healed IHSEs, (b) Young's modulus of the IHSEs and (c) calculated self-healing efficiency.

increase in the ion content because ammonium carboxylate ion pairs, which are physical cross-linking points, certainly improve intermolecular interactions and restrict the motility of PDMS chains, leading to enhanced mechanical properties and reduced stretching properties.

The break-up and recombination of ion pairs often endow elastomers with a self-healing property. Additionally, the self-healing performance of the IHSEs was examined by calculating the self-healing efficiency resulting from the ratio of tensile strengths before and after cutting followed by a 24-h-healing process. The self-healing tests were carried out as shown in Fig. 5-b: rectangle specimens were cut into two pieces and then recombined without external force followed by a 24-h-healing process at room temperature. The stress-strain curves of pristine and

healed IHSEs are shown in Fig. 4-a, and the self-healing efficiencies are shown in Fig. 4-c. The test results showed that the IHSEs with a lower ion-cross-linking density were found to possess a greater healing efficiency compared to those with a greater ion-cross-linking density. The repair of mechanical damage is rooted in the shift and recombination of ion particles as well as interfacial chain diffusion, and these processes are mainly controlled by the mobility of the segments. It is obvious that a greater ion cross-linking density leads to greater segments mobility restriction and consequently harms the self-healing ability. Heating promotes the flexibility of polymer chains and the dynamic properties of ion pairs and can improve the self-healing ability. All samples completely recovered their mechanical properties after being cut into two pieces

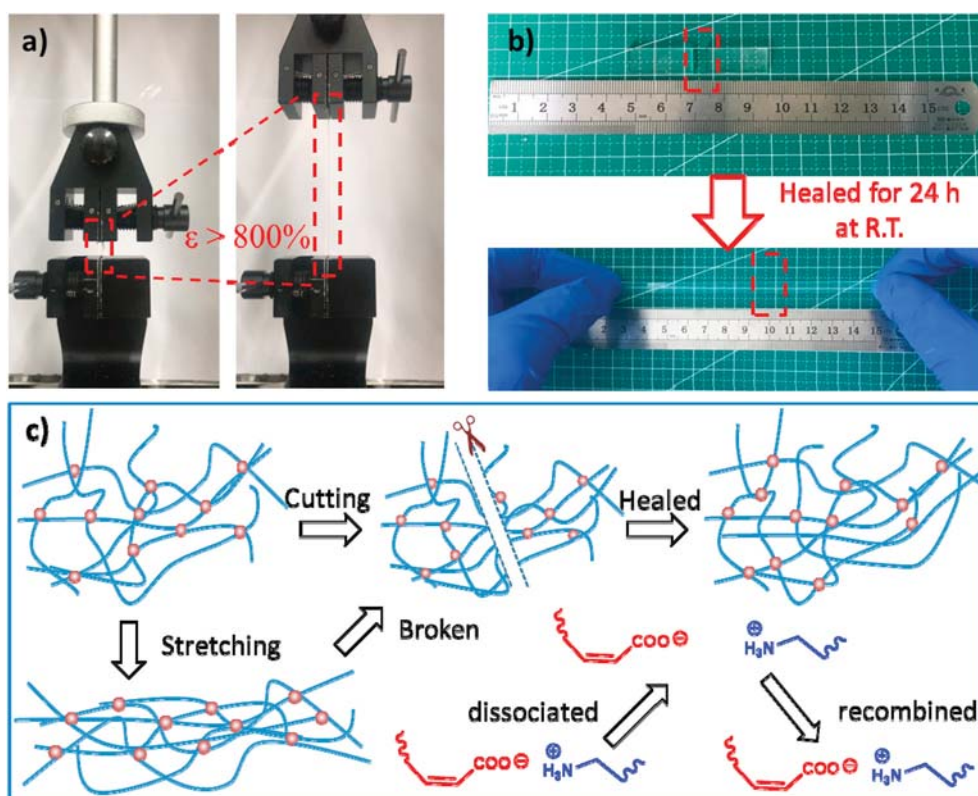


Fig. 5. The IHSEs exhibited (a) outstanding stretching properties and (b) room-temperature self-healing ability. (c) Schematic description of the mechanisms of the elastic response when stretched and self-healing after damage.

and being held at 60 °C for 6 h (Fig. S9).

3.4. Dissolving and water-resistance of IHSEs

Solvents are expected to be unable to dissolve the covalently cross-linked elastomers and just cause swelling. For non-covalently cross-linked elastomers, they could be dissolved when solvent dissociate the non-covalent interactions. For example, most of supramolecular elastomers based on hydrogen bonds [1–3] could be dissolved by polar solvent. However, if non-covalent interactions are too strong to be dissociated by solvent, it is expected that the non-covalently cross-linked elastomers could not be dissolved by solvent. The dissolving tests also confirmed this. During the tests, IHSEs were submerged into three solvents with varying polarity for 48 h. As shown in Fig. S11, all samples swelled to different degrees. Samples submerged in toluene and THF swelled the most as toluene and THF are good solvents for PDMS. As a contrast, the mixture of APS and SCS could dissolved in polar solvent such as ethanol, THF and so on. The dissolving test further confirmed that ionic hydrogen bonds implicated in unsaturated carboxyl groups are stronger.

In addition, ionic hydrogen-bonded elastomers are likely to be dissolved in acid or base solution based on the ions' sensitivity to pH. As the photos show (Fig. S11), the IHSEs were completely dissolved in dilute acid and base solutions in a short time, as expected. Dilute acid or base solution can easily dissolve elastomers because strong acids and bases shield the electrostatic interaction of the ammonium carboxylate ion pairs and make ionic cross-linking points break up.

To test the water resistance of the IHSEs, samples of the same size were immersed in deionized water until water absorption equilibrium was achieved. This process took 72 h. The water absorption was measured by the ratio of the weight of the water absorbed and the

samples before water immersion. With an increase in ion cross-linking density, the water absorption increased. It is reasonable that ammonium carboxylate, which has a hydrophilic nature inside the polymer matrix, certainly improve hydrophilicity of the elastomers, making water permeate into the elastomers easier. According to tensile tests in Fig. S12, high water content did harm the mechanical properties of the IHSEs. Greater water absorption resulted in a greater decrease in both the tensile strength and breaking elongation. This phenomenon can be ascribed water causing the ammonium carboxylate to turn into free ions. The water-resistance experiment is in some ways meaningful, for example, providing the reference for the storage and operating environment of this type of elastomer.

3.5. Deviating $n(-\text{COOH}) : n(-\text{NH}_2)$ away from 1 : 1

During the experiment, we found that mixing APS and UCS with $n(-\text{COOH}) : n(-\text{NH}_2) = 1 : 1$ resulted in ionic hydrogen bonds supramolecular elastomers, but moving $-\text{COOH}$ to $-\text{NH}_2$ ratio away from 1 : 1 would also resulted in elastomers. This was supported by the IHSE-x-a : b master curves (Fig. S10), where a : b stands for $n(-\text{COOH}) : n(-\text{NH}_2)$. For all samples, the storage moduli were greater than the loss moduli ($G' > G''$) over the full frequency range, indicating that they were typical elastomers. Interestingly, Fig. 6-b shows that when compared with samples having $n(-\text{COOH}) : n(-\text{NH}_2) = 1 : 1$, those with $n(-\text{COOH}) : n(-\text{NH}_2) < 1 : 1$ had a greater G' and those with $n(-\text{COOH}) : n(-\text{NH}_2) > 1 : 1$ had a lower G' . More interestingly, there was neither a positive nor a negative correlation in the tensile strength and Young's modulus when varying $n(-\text{COOH}) : n(-\text{NH}_2)$. Actually, the samples with $n(-\text{COOH}) : n(-\text{NH}_2) = 1 : 1$ had the best tensile strength, Young's modulus and elongation, and when deviating $n(-\text{COOH}) : n(-\text{NH}_2)$ away from 1 : 1, the mechanical performances declined. To provide insight into the

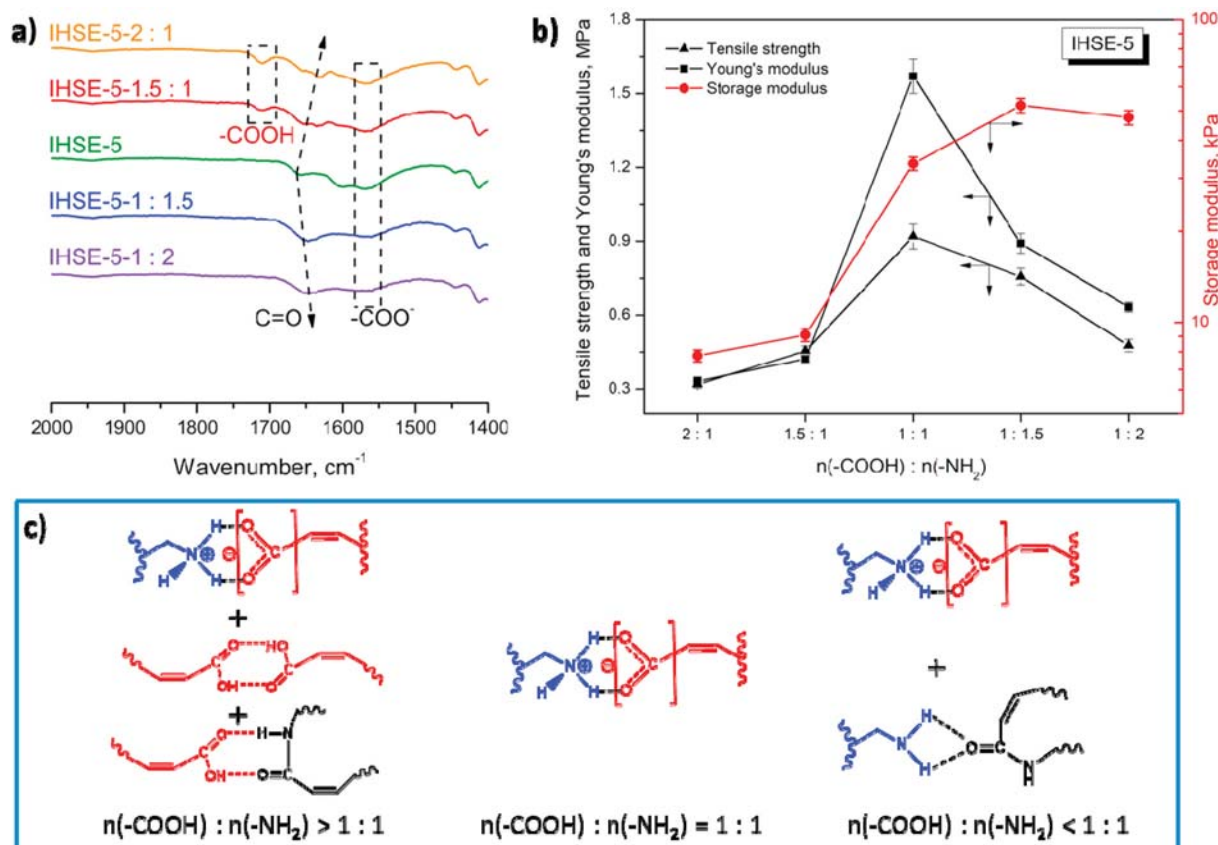


Fig. 6. (A) The FT-IR spectra of IHSE-5 with different $n(-\text{COOH}) : n(-\text{NH}_2)$. (b) Line charts of the key indices (tensile strength, Young's modulus and G' at 1 rad/s) as a function of $n(-\text{COOH}) : n(-\text{NH}_2)$. (c) Schematic description of proposed mechanisms for the mechanical properties tendencies with different $n(-\text{COOH}) : n(-\text{NH}_2)$.

correlation more clearly, the key elastomer indices (tensile strength, Young's modulus and G') were shown as line charts as a function of $n(-\text{COOH}):n(-\text{NH}_2)$. IHSE-5-1: 1.5 and IHSE-5-1: 2 were found to have greater strengths and Young's moduli than their reciprocals (IHSE-5-1.5: 1 and IHSE-5-2: 1).

Fig. 6-c is presented to illustrate this phenomenon. Within ionic hydrogen bonds, ionic interaction is dominant and is much stronger than hydrogen bond interaction. When changing $n(-\text{COOH}):n(-\text{NH}_2)$ away from 1: 1, the density of the ion pairs decreased and interactions among polymer chains decreased accordingly, leading to consequent reduction in the mechanical performance, as indicated by the tensile strength, Young's modulus and elongation. When $n(-\text{COOH}):n(-\text{NH}_2) < 1: 1$, excess amino groups as hydrogen bonding donors interacted with amide to form hydrogen bonds. This process actually generated more cross-linkages, which explains why the G' values of the samples with $n(-\text{COOH}):n(-\text{NH}_2) < 1: 1$ were greater than those with $n(-\text{COOH}):n(-\text{NH}_2) = 1: 1$. When $n(-\text{COOH}):n(-\text{NH}_2) > 1: 1$, excess carboxyl groups as both hydrogen bonding donors and receptors were inclined to interact with each other, generating some invalid cross-linking. These explanations were further confirmed by the FT-IR spectra. As seen in Fig. 6-a, with an excess of carboxyl groups, $\text{C}=\text{O}$ carboxyl group stretching vibration peaks at 1714 cm^{-1} appeared. When deviating $n(-\text{COOH}):n(-\text{NH}_2)$ away from 1: 1, the peak at 1560 cm^{-1} ascribed to carboxylate attenuated, suggesting that the ion content decreased. $\text{C}=\text{O}$ amide stretching vibration peaks shifted to lower wavenumbers because the surplus amino or carboxyl groups interacted with amide via hydrogen bonds.

Based on the analysis and discussion above, it is easily inferred that the IHSEs with surplus amino or carboxyl groups would possess a better self-healing ability considering that the dynamic reversibility of hydrogen bonds is superior to that of ionic interactions. Varying degrees of changes in self-healing ability were achieved by deviating $n(-\text{COOH}):n(-\text{NH}_2)$ away from 1: 1, as shown in Fig. 7-b. Notably, surplus carboxyl groups improved the self-healing ability of IHSEs more than surplus amino groups because IHSEs with $n(-\text{COOH}) > n(-\text{NH}_2)$ were softer and had more abundant hydrogen bonds. The IHSE with $n(-\text{COOH}):n(-\text{NH}_2) = 2: 1$ easily recovered 100% of its mechanical properties in a short time during the self-healing test.

3.6. Adhesive properties of IHSEs

Mixing APS and UCS with an equimolar amino and carboxyl feed created soft, transparent and smooth-surfaced elastomer specimens. Excess amino or carboxyl groups create abundant hydrogen bonds at the

elastomers and substrate interface, which makes elastomers possibly be used as adhesives. To evaluate the adhesive properties of IHSEs, 90° peeling strength tests were performed. As illustrated in Fig. 8, the samples with $n(-\text{COOH}):n(-\text{NH}_2) = 1: 1$ or $n(-\text{COOH}):n(-\text{NH}_2) < 1: 1$ were almost non-adhesive or less adhesive. For samples with $n(-\text{COOH}):n(-\text{NH}_2) > 1: 1$, excess $-\text{COOH}$ resulted in elastomers with a greater peeling strength. This can be explained by the fact that carboxyl groups, as both hydrogen bonding donors and receptors, form stronger hydrogen bonds than amino groups as merely hydrogen bonding donors. To compare different substrates, parallel of 90° peeling strength experiments were conducted on both stainless steel and glass. Greater peeling strengths were measured on the stainless steel because, in addition to hydrogen bonds, the amino and carboxyl groups could coordinate with the metal.

4. Conclusions

In conclusion, we developed a facile and completely solvent-free route to construct ionic hydrogen-bonded supramolecular elastomers that first contained unsaturated carboxyl groups. Carboxyl-grafted PDMS was synthesized by reacting amino-grafted PDMS with anhydride under solvent-free conditions, and the FT-IR and ^1H NMR results confirmed their structures. Saturated carboxyl-grafted PDMS was compared to illustrate that unsaturated carboxyl groups formed stronger ionic hydrogen bonds with the amino groups, which was further confirmed by NMR titration, resulting in an elastic network. The rheological and mechanical properties could be well tuned by adjusting the ion-cross-linking density and the $-\text{COOH}$ and $-\text{NH}_2$ feed ratios. Due to the reversibility of ionic hydrogen bonds, IHSEs exhibited a good room-temperature self-healing ability that could be further promoted by deviating the $n(-\text{COOH}):n(-\text{NH}_2)$ ratio away from 1: 1. Furthermore, excess carboxyl groups caused the IHSEs to be adhesive. This strategy is promising in the research and development of self-healable electronic materials and bio-adhesives. However, further studies are needed to determine the ionic aggregation structures, and greater optimization of the IHSE preparation is worth exploring.

Author contribution statement

Jiaheng MO: Methodology, Data curation, Writing, Writing – original draft; Xinyu CHEN, Data curation; Yubing Fu: Data curation; Rui Li: Data curation; Yaling LIN: Writing- Reviewing and Editing, Supervision; Anqiang ZHANG: Conceptualization, Writing- Reviewing and Editing, Supervision.

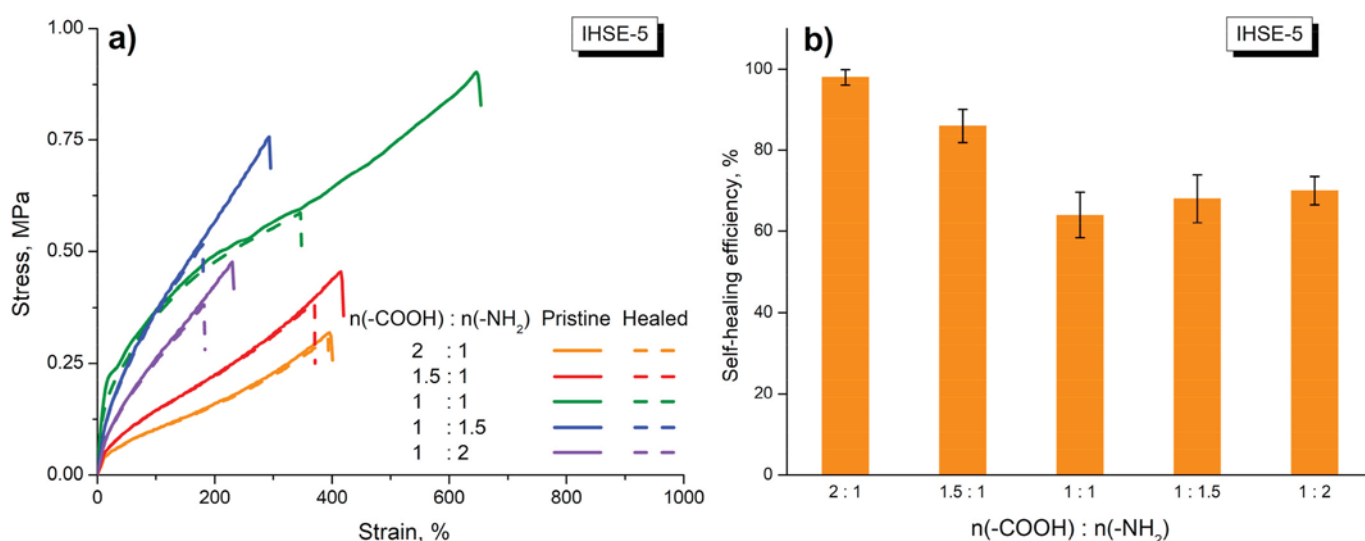


Fig. 7. (A) Stress-strain curves of the pristine and 24 h-healed IHSEs with different $n(-\text{COOH}):n(-\text{NH}_2)$, (b) Calculated self-healing efficiency.

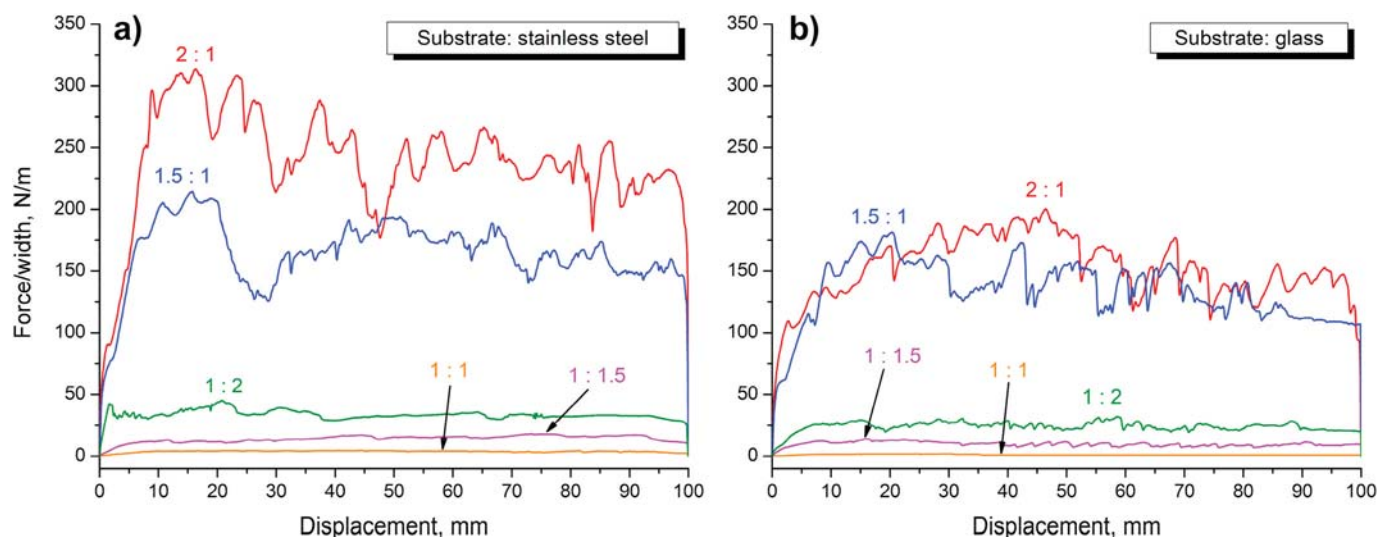


Fig. 8. 90° peeling strength curves for IHSEs with different $n(-\text{COOH}): n(-\text{NH}_2)$ on (a) stainless steel and (b) glass.

Declaration of competing interest

The authors declare that they have no known competing financial interests or personal relationships that could have appeared to influence the work reported in this paper.

Acknowledgements

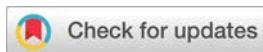
This work was supported by the National Natural Science Foundation of China under grant number 52073098, 51473051 and the Science and Technology Program of Guangzhou, China, under grant 201803020015.

Appendix A. Supplementary data

Supplementary data to this article can be found online at <https://doi.org/10.1016/j.polymer.2021.123903>.

References

- [1] P. Cordier, F. Tournilhac, C. Soulié-Ziakovic, L. Leibler, *Nature* 451 (2008) 977–980.
- [2] L. Yang, Y. Lin, L. Wang, A. Zhang, *Polym. Chem.* 5 (2014) 153–160.
- [3] Y. You, W. Huang, A. Zhang, Y. Lin, *J. Polym. Sci., Part A: Polym. Chem.* 54 (2016) 3760–3768.
- [4] Y. You, A. Zhang, Y. Lin, *J. Appl. Polym. Sci.* 133 (2016) 43385.
- [5] Y. Chen, A.M. Kushner, G.A. Williams, Z. Guan, *Nat. Chem.* 4 (2012) 467–472.
- [6] Y. Wang, X. Liu, S. Li, T. Li, Y. Song, Z. Li, J. Sun, *ACS Appl. Mater. Interfaces* 9 (2017) 29120–29129.
- [7] Y. Wang, X. Huang, X. Zhang, *Nat. Commun.* 12 (2021) 1–10.
- [8] M. Burnworth, L. Tang, J.R. Kumpfer, A.J. Duncan, F.L. Beyer, G.L. Fiore, C. Weder, *Nature* 472 (2011) 334–337.
- [9] N. Holten-Andersen, M.J. Harrington, H. Birkedal, B.P. Lee, P.B. Messersmith, K.Y. C. Lee, J.H. Waite, *Proc. Natl. Acad. Sci. Unit. States Am.* 108 (2011) 2651–2655.
- [10] P.F. Cao, B. Li, T. Hong, J. Townsend, Z. Qiang, K. Xing, T. Saito, *Adv. Funct. Mater.* 28 (2018) 1800741.
- [11] Y. Lei, W. Huang, Q. Huang, A. Zhang, *New J. Chem.* 43 (2019) 261–268.
- [12] C.H. Li, C. Wang, C. Keplinger, J.L. Zuo, L. Jin, Y. Sun, X.Z. You, *Nat. Chem.* 8 (2016) 618–624.
- [13] Y. Lei, Q. Huang, S. Shan, Y. Lin, A. Zhang, *New J. Chem.* 43 (2019) 17441–17445.
- [14] X.Y. Jia, J.F. Mei, J.C. Lai, C.H. Li, X.Z. You, *Chem. Commun.* 51 (2015) 8928–8930.
- [15] Y.L. Rao, A. Chortos, R. Pfattner, F. Lissel, Y.C. Chiu, V. Feig, M. He, *J. Am. Chem. Soc.* 138 (2016) 6020–6027.
- [16] S. Burattini, H.M. Colquhoun, B.W. Greenland, W. Hayes, *Faraday Discuss* 143 (2009) 251–264.
- [17] S. Burattini, B.W. Greenland, D.H. Merino, W. Weng, J. Seppala, H.M. Colquhoun, S.J. Rowan, *J. Am. Chem. Soc.* 132 (2010) 12051–12058.
- [18] L.R. Hart, J.H. Hunter, N.A. Nguyen, J.L. Harries, B.W. Greenland, M.E. Mackay, W. Hayes, *Polym. Chem.* 5 (2014) 3680–3688.
- [19] A. Feula, A. Pethybridge, I. Giannakopoulos, X. Tang, A. Chippindale, C.R. Siviour, W. Hayes, *Macromolecules* 48 (2015) 6132–6141.
- [20] M.A. Aboudzadeh, M.E. Muñoz, A. Santamaría, R. Marcilla, D. Mecerreyes, *Macromol. Rapid Commun.* 33 (2012) 314–318.
- [21] M.A. Aboudzadeh, M.E. Muñoz, A. Santamaría, M.J. Fernandez-Berridi, L. Irusta, D. Mecerreyes, *Macromolecules* 45 (2012) 7599–7606.
- [22] M. Comí, G. Lligadas, J.C. Ronda, M. Galià, V. Cádiz, *Eur. Polym. J.* 91 (2017) 408–419.
- [23] Frederikke Bahrt Madsen, Liyun Yu, Anne Ladegaard Skov, *ACS Macro Lett.* 5 (2016) 1196–1200.
- [24] Y. Peng, L. Zhao, C. Yang, Y. Yang, C. Song, Q. Wu, J. Wu, *J. Mater. Chem.* 6 (2018) 19066–19074.
- [25] Y. Miwa, J. Kurachi, Y. Kohbara, S. Kutsumizu, *Commun. Chem.* 1 (2018) 1–8.
- [26] A. Reisch, E. Roger, T. Phoeung, C. Antheaume, C. Orthlieb, F. Boulmedais, P. Schaaf, *Adv. Mater.* 26 (2014) 2547–2551.
- [27] D. Wang, H. Zhang, B. Cheng, Z. Qian, W. Liu, N. Zhao, Xu, J. J. *Polym. Sci. Part A: Polym. Chem.* 54 (2016) 1357–1366.
- [28] M. Nakahata, Y. Takashima, H. Yamaguchi, A. Harada, *Nat. Chem.* 2 (2011) 1–6.
- [29] T. Kakuta, Y. Takashima, M. Nakahata, M. Otsubo, H. Yamaguchi, A. Harada, *Adv. Mater.* 25 (2013) 2849–2853.
- [30] E.A. Appel, F. Biedermann, U. Rauwald, S.T. Jones, J.M. Zayed, O.A. Scherman, *J. Am. Chem. Soc.* 132 (2010) 14251–14260.
- [31] J. Wu, L.H. Cai, D.A. Weitz, *Adv. Mater.* 29 (2017) 1702616.
- [32] J. Cao, C. Lu, J. Zhuang, M. Liu, X. Zhang, Y. Yu, Q. Tao, *Angew. Chem.* 129 (2017) 8921–8926.
- [33] J. Kang, D. Son, G.J.N. Wang, Y. Liu, J. Lopez, Y. Kim, L. Jin, *Adv. Mater.* 30 (2018) 1706846.
- [34] Z. Lei, P. Wu, *Nat. Commun.* 9 (2018) 1–7.
- [35] M. Meot-Ner, *Chem. Rev.* 105 (2005) 213–284.
- [36] M. Wathier, M.W. Grinstaff, *J. Am. Chem. Soc.* 130 (2008) 9648–9649.
- [37] Y. Yang, M.W. Urban, *Adv. Mater. Inter.* 5 (2018) 1800384.
- [38] S.J. Kalista, J.R. Pflug, R.J. Varley, *Polym. Chem.* 4 (2013) 4910–4926.
- [39] K. Cui, D. Wang, H. Zhang, J. Guo, C. Cai, C. Zhu, J. Xu, *J. Appl. Polym. Sci.* 134 (2017) 45280.
- [40] S. Zheng, Y. Chen, M.A. Brook, *Polym. Chem.* 11 (2020) 7382–7392.
- [41] X. Mei, C. Wolf, *Eur. J. Org. Chem.* 2004 (2004) 4340–4347.
- [42] J. Cortese, C. Soulié-Ziakovic, L. Leibler, *Polym. Chem.* (2014) 116–125.
- [43] Q. Guo, B. Huang, C. Lu, T. Zhou, G. Su, L. Jia, X. Zhang, *Mater. Horiz.* 6 (2019) 996–1004.



Cite this: *Polym. Chem.*, 2021, **12**, 4052

Interpenetrating covalent adaptable networks with enhanced mechanical properties and facile reprocessability and recyclability†

Yufeng Lei,^a Anqiang Zhang ^{a*} and Yaling Lin^{*b}

Polymer blending has always been a critical strategy for preparing high-performance materials. By creating an interpenetrating polymer network (IPN), the incompatibility of different polymers could be overcome and a favorable bicontinuous phase structure could be achieved. Recently, the concept of covalent adaptable networks (CANs) based on reversible covalent bonds has brought many opportunities for developing and engineering sustainable high-performance polymer blends. Herein, we utilized the reversible hydrolysis/condensation of imines and boronic-esters to construct an interpenetrating covalent adaptable network (IPCAN) with a highly uniform phase structure from two immiscible single CANs, and to establish a closed loop between recycling single networks and regenerating IPCANs as well. The resultant IPCANs show not only a remarkable improvement in mechanical performance, but also a high restoration efficiency during multiple reprocessing. The outcomes of this work may provide new ideas for developing more sustainable high-performance polymer blends and IPNs with covalent reversible bonds.

Received 8th May 2021,
Accepted 21st June 2021

DOI: 10.1039/d1py00623a

rsc.li/polymers

Introduction

Blending polymers with different mechanical properties has been a critical strategy for preparing high-performance polymer materials, such as rubber/plastic blends^{1–3} and thermoplastic vulcanizates (TPVs).^{4–6} One of the most critical issues to achieve the desired properties for polymer blends is the compatibility between different types of materials. Poor compatibility often leads to large-scale phase separation after blending, which will severely undermine the performance of products. Compared with direct physical blending, rationally designing polymerization, curing or mixing pathways towards interpenetrating networks^{7–10} (IPNs) has become a feasible way to construct bicontinuous phase structures and thus impose unbreakable compatibility on different polymers. However, due to the unbreakable covalent crosslinks, these blended thermosetting materials still can hardly be recycled or reprocessed after disposal or fracture.

The introduction of reversible crosslinking bonds in covalent adaptable networks (CANs) has recently brought many possibilities for polymer engineering, especially in terms of sustainable polymer blends or multiply crosslinked networks.^{11–15} First of all, introducing reversible covalent bonds into crosslinked polymers has been widely adopted by many researchers to achieve reversible features, such as self-healing,¹⁶ recycling,¹⁷ reshaping¹⁸ or reprocessing¹⁹ abilities. More importantly, reversible covalent bonds usually have a lower bond energy than irreversible bonds, which prevent CANs from achieving satisfactory mechanical properties. In many research studies,^{20–22} it has become a trade-off between the reversible properties and mechanical performance. To this end, combining two or more reversible crosslinked systems into multiply crosslinked networks or polymer blends has become a popular choice. One strategy is to introduce multiple reversible cross-linkages with varying strengths^{23–25} and different stimulus responsiveness^{26–29} into the same polymer backbone. Some “sacrificial” bonds could preferentially break under external load or stimulus, which dissipates much mechanical energy, thereby achieving an effective toughening effect or stimulus responsiveness. Another strategy that has interested us here is to blend two or more CANs with different covalent reversible bonds by rationally exploiting covalent reversible chemistry. Odriozola *et al.*^{30,31} directly blended a polyurethane network based on reversible disulfides and a polysiloxane network based on reversible boronic-esters respectively through mechanical blending and hot-pressing.

^aDepartment of Polymer Science and Engineering, School of Materials Science and Engineering, South China University of Technology, 381 Wushan Rd., Guangzhou, 510640 Guangdong, China. E-mail: aqzhang@scut.edu.cn

^bCollege of Materials and Energy, South China Agricultural University, 483 Wushan Rd., Guangzhou, 510642 Guangdong, China. E-mail: linyaling@scau.edu.cn

†Electronic supplementary information (ESI) available: Synthesis of covalent adaptable single networks, SEM photos and elemental mapping, stress relaxation curves, and temperature sweeps of the oscillatory shear rheology of IPCANs and DN-50-c. See DOI: 10.1039/d1py00623a

They found that the two incompatible networks could be combined into a uniform blended product with a dual continuous phase structure, which contributed to a significant improvement in the tensile strength. Chen *et al.*³² recently reported a semi-interpenetrating polyethylene (PE) network consisting of linear PE chains and a CAN of PE crosslinked by alkyl boronic esters. The addition of a CAN markedly strengthened the PE at elevated temperatures and maintained the facile reprocessing and recycling ability of PE. Zhang *et al.*³³ utilized the reversible virtue of Diels–Alder (D–A) adducts and alkoxyamines to achieve a molecular-level reversible interlocking network (RILN) from two incompatible single networks. The RILN showed nonlinear improvements in multiple mechanical properties simultaneously as well as in the unlocking/relocking ability. However, the Diels–Alder bonds and the alkoxyamines would dissociate into relatively stated end groups at high temperatures, so they re-locked the RILN in hot solvents to maintain the homogeneous distribution of the network fragments. Direct reprocessing like solid-state hot-pressing might lead to the expansion of phase separation. In another research study, they developed another RILN from two immiscible single CANs (SBR crosslinked by D–A adducts and polyethylenimine crosslinked by imines) with additional inter-macromolecular ionic interactions.³⁴ This system displayed a creative combination of the above-mentioned “sacrificial” strategy and blending strategy to enhance the mechanical performance of CANs.

In previous studies, we have investigated CANs based on abundant imines³⁵ and boronic-esters,³⁶ respectively. The polyimine elastomer (PIE) exhibited good rubber elasticity at room temperature, but poor shape stability at higher temperatures due to the accelerated imine exchange. On the other hand, the polydioxaborolane network (PDOB) containing plentiful conjugated ring structures behaved as a rigid but brittle thermoset at room temperature. This inspired us that two single CANs can actually be employed as model matrixes for rubber/plastic blends consisting of reversible covalent bonds. Both PIE and PDOB were directly synthesized from small molecular multi-functional monomers, which gave rise to abundant reversible bonds located not only at crosslinks but also at their main-chains. In addition, imines and boronic-esters have a lot in common in reversible chemistry,¹¹ including the hydrolysis/condensation reaction and exchange reaction (metathesis). The former pathway could contribute to the great recyclability of IPCANs, and the latter pathway could facilitate a facile reprocessing technology.

Experimental

Materials

Terephthalaldehyde (TPA, 98%) and 1,3-bis(3-aminopropyl)-1,1,3,3-tetramethyldisiloxane (AMM, 97%), 1,4-benzenediboric acid (BDBA, 97%) and diiodomethane (99%) were purchased from Shanghai Macklin Biochemical Co., Ltd (Shanghai, China). Tris(2-aminoethyl)amine (TAEA, 97%) was from Alfa Aesar. Tetrahydrofuran (THF), chloroform and

hexane were of analytical grade and purchased from Guangzhou Chemical Reagent Factory (Guangzhou, China). All the chemicals and solvents were used as-received. Small-molecular diols, including tetra-hydroxyl-disiloxanes (4HS) and octa-hydroxyl-cyclotetrasiloxanes (8HS), were synthesized *via* a thiol–ene click reaction according to our previous report.³⁶ Synthesis of single CANs based on imine bonds (SN-I) or boronic-ester bonds (SN-B) is described in Part S1, ESI.†

Preparation of interpenetrating covalent adaptable networks

Interpenetrating covalent adaptable networks (IPCANs) were prepared *via* a solution-casting procedure with varying contents of SN-I and SN-B, which are denoted as “IPCAN-*x*” where “*x*” indicates the weight percentage of SN-B. As is shown in Scheme 1, typically, to prepare IPCAN-50, SN-I (2.50 g) and SN-B (2.50 g) were finely cut, mixed and dissolved in approx. 50 mL of THF with 2.5 mL of water. The mixtures were stirred under ambient conditions for 2 h to obtain a clear solution. The solution was then poured into a PTFE mold and kept at 60 °C for 6 h to evaporate the solvents. The resultant orange transparent film was heated in a vacuum oven at 60 °C for 12 h for the complete curing of the double networks. The IPCAN products were obtained as yellow to orange transparent solids according to their composition. The solids were collected and hot pressed at 120 °C into sheets for testing.

A physical blending sample of equal-weighted SN-I and SN-B was prepared as a control and denoted as “DN-50-c”. The SN-I and SN-B were finely cut, mixed in the solid state and hot pressed at 120 °C/20 MPa. DN-50-c was obtained as an orange transparent, uniform sheet.

Reprocessing of IPCANs

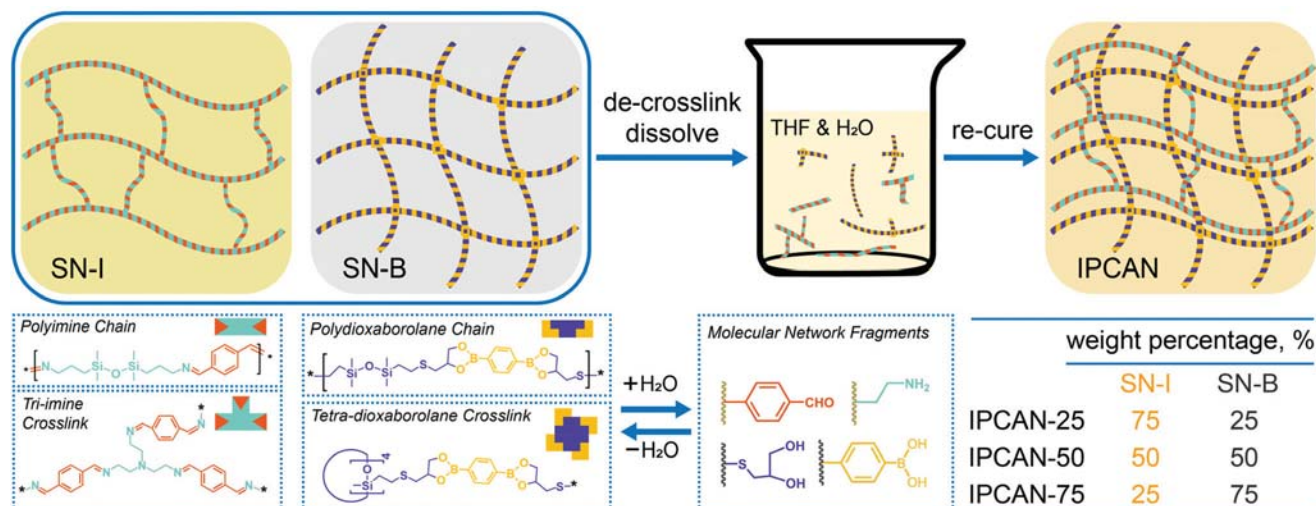
IPCAN-50 samples for reprocessing were shattered, collected and mixed. After drying in a 60 °C vacuum oven overnight, the IPCAN-50 shards were hot pressed at 120 °C/20 MPa. The reprocessed samples were obtained as a transparent, uniform sheet and denoted as “IPCAN-50-R_x”, where *x* represents the reprocessing cycle.

Recycling SNs from IPCANs and re-preparing IPCANs

IPCAN-50 samples for recycling were finely cut into shards and added to water. The mixtures were heated to 80 °C and kept stirring for 24 h. After filtering the mixtures, the water extraction solution was concentrated by rotary evaporation at 80 °C and then transferred into a PTFE mold. After drying in a 60 °C vacuum oven, a transparent solid product was obtained and denoted as “SN-B-re”. The insoluble solid collected from filtration was washed 3 times with water, dried and denoted as “SN-I-re”. The recycled SNs were separately hot pressed at 120 °C/20 MPa into sheets for testing. IPCAN-50-re was re-prepared using the same procedure as IPCANs from SN-I-re and SN-B-re.

Characterization

Fourier transform infrared (FTIR) spectra were recorded with a Nicolet iS5 FT-IR spectrometer equipped with an iD7-ZnSe



Scheme 1 Preparation and composition of IPCANs.

attenuated total reflectance (ATR) accessory. Differential scanning calorimetry (DSC) measurements were performed on a Netzsch DSC204F1 (Germany) under a nitrogen atmosphere. The heating and cooling rate was 10 K min⁻¹. Rheological measurements were performed on an Anton Paar MCR-102 rheometer (Austria) with a 25 mm parallel-plate test system. The dynamic temperature (30–160 °C) sweep was performed at a strain amplitude of 1% and a frequency of 1 Hz with a heating rate of 2 °C min⁻¹. The samples for rheological measurements were prepared in a cylindrical shape (diameter: 24–25 mm, thickness: 2.4–2.5 mm). Dynamic Mechanical Analysis (DMA) was performed on a Mettler Toledo DMA 1 (Swiss) in the tension mode. The measurements were performed from –50 °C to 100 °C with a heating rate of 3 °C min⁻¹ and a frequency of 1 Hz. Tensile tests were performed on rectangular specimens (50 mm × 6 mm × 1 mm) using a KJ-1067 tensile testing machine (Dongguan Kejian, China) equipped with a Temperature and Humidity Controlled Chamber.

Contact angles were measured on an A-100 DropMeter (Ningbo Maist, China) using water and diiodomethane as the test liquids at 25 °C. Furthermore, solid surface free energy (SFE) was calculated according to the Owens–Wendt–Rabel–Kaelble (OWRK) method.^{37,38} Generally, the solid SFE (γ_s) of each phase is divided into the dispersion component (γ_s^d) and the polar component (γ_s^p), which follows the relationship as in eqn (1):

$$\gamma_{SL} = \gamma_L + \gamma_s - 2\sqrt{\gamma_L^d \gamma_s^d} - 2\sqrt{\gamma_L^p \gamma_s^p} \quad (1)$$

where γ_L , γ_L^d and γ_L^p are the total surface free energy, dispersion component and polar component of the test liquid, respectively.

According to Young's equation,³⁹ when the liquid comes in contact with the solid surface in the gaseous phase, the relationship among the contact angle (θ), liquid surface

tension (γ_L), SFE between the solid and liquid phases (γ_{SL}) and solid SFE (γ_s) is expressed as eqn (2):

$$\gamma_s = \gamma_{SL} + \gamma_L \cdot \cos \theta \quad (2)$$

Substituting eqn (2) into eqn (1) gives

$$\gamma_L \cdot (1 + \cos \theta) = 2\sqrt{\gamma_L^d \gamma_s^d} + 2\sqrt{\gamma_L^p \gamma_s^p} \quad (3)$$

Therefore, when the contact angle between two or more types of liquid with known γ_L , γ_L^d and γ_L^p on the same solid surface is measured, the value of γ_s , γ_s^d and γ_s^p can be calculated using the OWRK method.

Results and discussion

Structure of interpenetrating covalent adaptable networks

At first, the preparation of IPCANs involved the hydrolysis of SN-I and SN-B in water-containing good solvents. Through a water-mediated dissociative rearrangement pathway,⁴⁰ reversible single networks based on imine or boronic-ester bonds could be hydrolyzed into fragments at the molecular level. Before the final curing, these network fragments could finely diffuse and disperse in the homogeneous solution system. Besides, it is important that the reactive end-groups including diols, boronic-acids, amines and aldehydes could separately condense into boronic-esters and imines. In a dual crosslinked PEG/chitosan hydrogel reported by Li *et al.*,⁴¹ the imine condensation and boronic esterification were proved to be able to proceed independently and simultaneously in the same system. Fig. 1a shows the appearance of IPCANs as yellow to orange transparent sheets. FTIR-ATR spectra (Fig. 1b) of IPCANs show the characteristic absorbance bands of C=N bonds (1650 cm⁻¹) and N–H bonds (2830 cm⁻¹ and 1567 cm⁻¹) from SN-I, as well as B–O bonds (1310 cm⁻¹ and

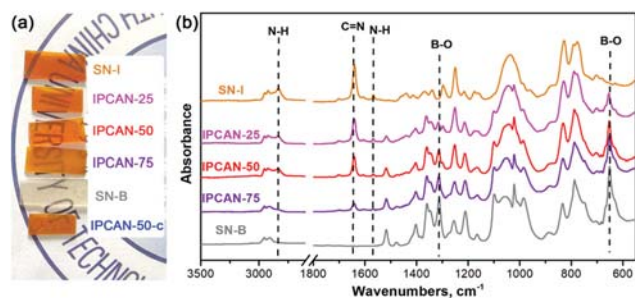


Fig. 1 (a) Digital photos and (b) FTIR-ATR spectra of IPCANs.

654 cm⁻¹) from SN-B. The intensity of these peaks is in accordance with their composition.

To investigate the possibility of the phase separation of blending SNs, we first characterized the compatibility of the surface free energy of SN-I and SN-B. The contact angles of water and DIM on the surfaces of SN-I and SN-B are determined and shown in Fig. 2a. The water contact angle of SN-I was larger than 90° while that of SN-B was smaller than 90°, which demonstrates the difference in hydrophilicity of these two networks. The surface free energies (SFEs) of SN-I and SN-B could be calculated from the contact angle results according to the OWRK method^{37,38} and are shown in Fig. 2b. SN-I

and SN-B exhibited an SFE difference of approx. 10 mN m⁻¹. Compared to SN-I, SN-B has a higher polar component and a lower dispersive component. This difference could have resulted from a tendency of phase separation during the mechanical blending of these two materials. From the control sample DN-50-c, we observed the microphase separation in the elemental mapping of S from SN-B by SEM (Fig. S1, ESI†).

It can be seen from Fig. 2c that IPCANs of different components only show one single glass transition stage, indicating that the scale of phase separation of SNs was so small that segmental movements of the two types of network chains were affected by their mutual confinement. These effects resulted in the thermal response of superposition of the glass transition stages of SNs. The glass transition temperature (T_g) of each IPCAN is in the middle of the T_g of the original SN-I and SN-B, and shows consistency with the content of SNs. However, the physically blended control sample DN-50-c shows two adjacent transition stages, which are close to the T_g values of SN-I and SN-B, indicating that the SNs experienced independent glass transition in different phases. The difference in DSC curves demonstrated that the phase separation scale of DN-50-c prepared by physical blending is significantly larger than that of IPCAN-50. Moreover, the DMA curves (Fig. 2d) revealed the difference between IPCAN-50 and DN-50-c more evidently. The measured T_g values by DMA are different from those by DSC

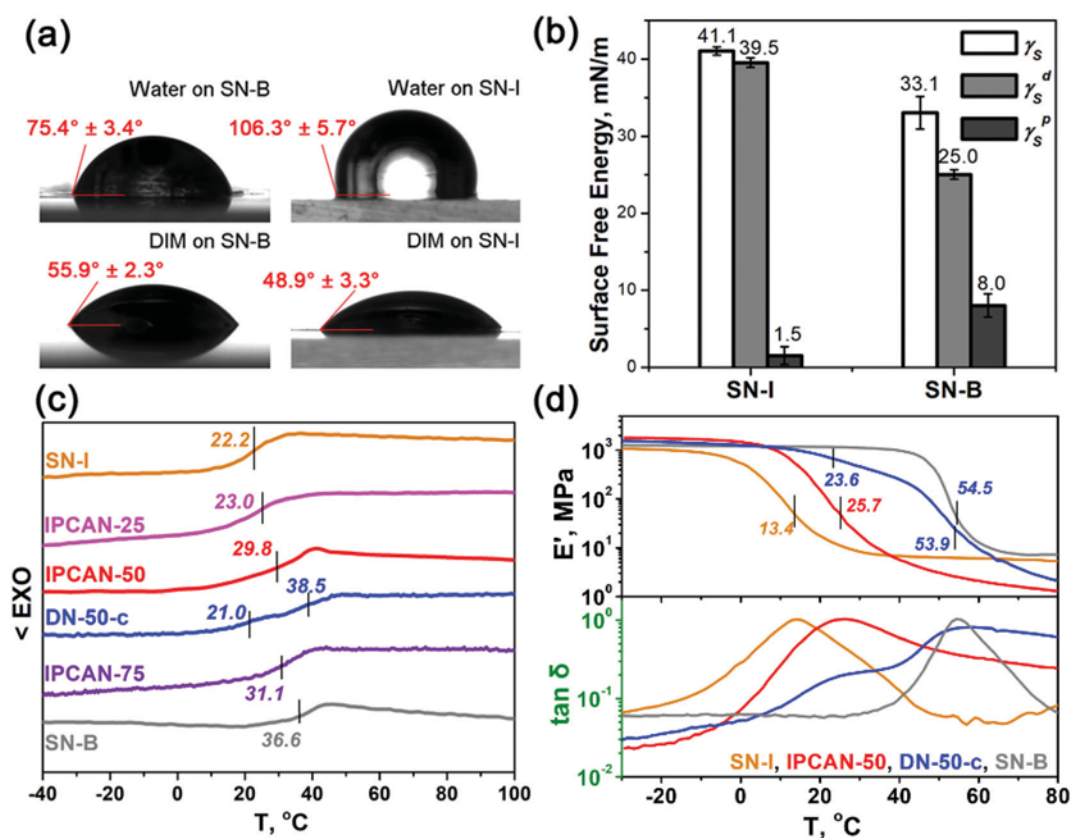


Fig. 2 (a) Contact angles of water and DIM on SN-I and SN-B; (b) surface free energies of SN-I and SN-B; (c) DSC curves of IPCANs and SNs; and (d) DMA curves of IPCAN-50, DN-50-c, and SNs.

because of different heating rates and measuring mechanisms, but IPCAN-50 and DN-50-c still exhibited a similar response to heating. For IPCAN-50, only a single T_g value is observed, which falls between those of SN-I and SN-B. For DN-50-c, two adjacent transition stages appeared at temperatures close to the T_g s of the two SNs.

Stress relaxation of IPCANs

Tensile stress relaxation of IPCANs and SNs was monitored at constant 20% elongation and 45 °C (Fig. 3a). Due to the dynamic nature of imines and boronic-esters and the sufficient chain mobility for internal reactions, IPCANs could reach a complete stress relaxation in about 5 min. Compared to SN-I, SN-B has a higher T_g and more limited segmental mobility, which reduced the stress relaxation of IPCANs. Fig. 3b shows the stress relaxation curves of IPCAN-50 at 50% elongation but varying temperatures. The characteristic relaxation time (τ , $\sigma_t = \sigma_0/e$) for IPCAN-50 was markedly shortened at an elevated temperature. By fitting the τ - T to the Arrhenius relationship [$\tau = A \exp(E_a/RT)$],¹¹ we calculated that the apparent activation energy (E_a) for dynamic reactions in IPCAN-50 was approx. 60 kJ mol⁻¹. In previous studies,^{35,36} we have calculated that the E_a values of SN-I and SN-B were approx. 59 kJ mol⁻¹ and 93 kJ mol⁻¹, respectively, which means dynamic exchange for SN-I is much easier than that for SN-B. The structural factors include (i) the polyimine chain has fewer rigid

conjugated ring structures than the polydioxaborolane chain; (ii) dynamic exchange of imines has a lower energy barrier than that of boronic-esters.¹¹ These factors caused that the E_a of IPCAN-50 was very close to that of SN-I, indicating that the relaxation and dynamic rearrangement of SN-I dominated the stress relaxation process of the IPCAN. Moreover, we compared the stress relaxation curves of IPCAN-50 and DN-50-c (Fig. S2, ESI†). Although IPCAN-50 and DN-50-c have the same composition of SNs, the physically blended DN-50-c showed much faster stress relaxation than IPCAN-50. This could be explained by the fact that IPCAN-50 has interpenetrating SN-I and SN-B networks, where the two SNs could restrain each other and limit the relaxation of the SN-I network, thereby slowing down the reversible exchange reaction.

Viscoelasticity of IPCANs

The temperature dependency of the viscoelasticity of IPCANs was characterized by dynamic temperature sweeps of oscillatory shear rheology. Fig. 4 shows the temperature dependency of the storage modulus (G') and loss modulus (G'') for IPCANs and SNs. Both moduli of IPCANs change sharply close to the T_g s, which are close to the results of DSC (Fig. 2c). In a wide temperature range above T_g , all the IPCANs show rubbery elasticity with G' maintaining at a plateau value and higher than G'' , which reflects that the crosslinking density of IPCANs keeps constant during the temperature changes. Although the dynamic exchange reaction of imine bonds and boronic-ester bonds was accelerated with the increase of temperature, their exchange reactions would not change the overall functionality and connectivity of the system. SN-I, IPCAN-25 and IPCAN-50 show a viscous flow transition in the high temperature zone

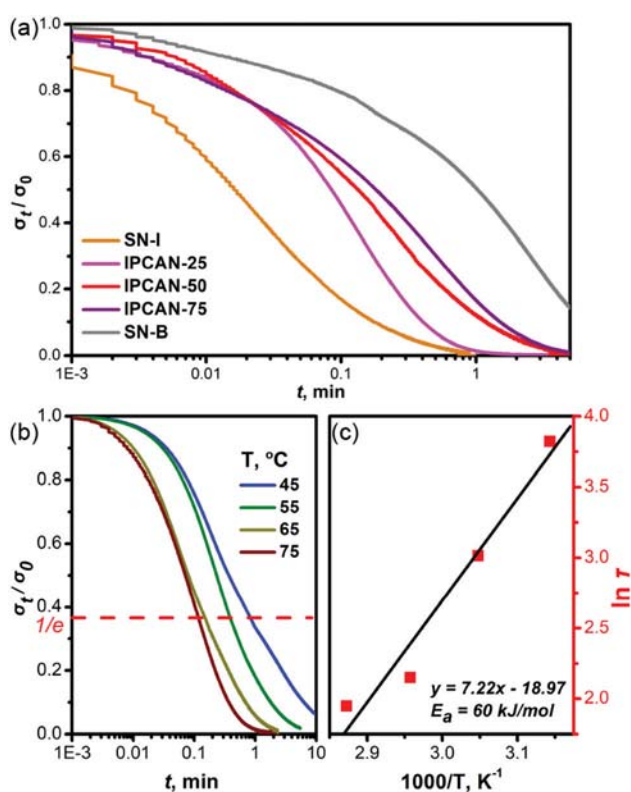


Fig. 3 (a) Tensile stress relaxation curves of IPCANs and SNs, (b) tensile stress relaxation curves of IPCAN-50 and (c) Arrhenius fit of the τ - T relationship for IPCAN-50.

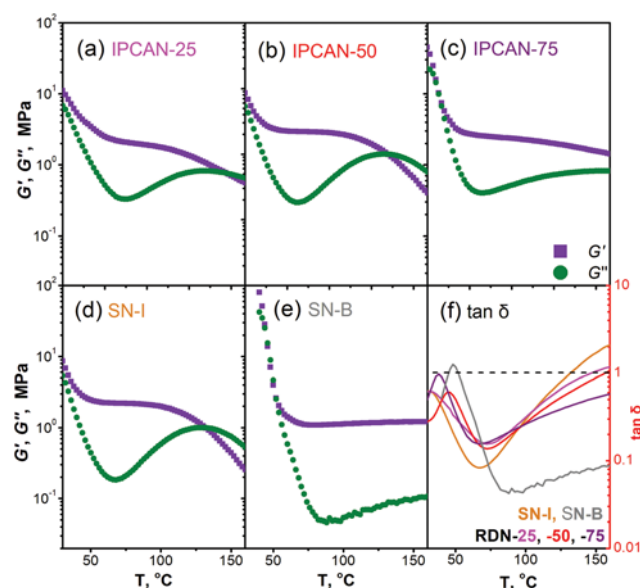


Fig. 4 Temperature dependency of storage modulus (G') and loss modulus (G'') for IPCANs and SNs: (a) IPCAN-25, (b) IPCAN-50, (c) IPCAN-75, (d) SN-I, and (e) SN-B and (f) plots of $\tan \delta$ against temperature for IPCANs and SNs.

Table 1 Tensile properties of IPCANs and SNs

Sample	Young's modulus, MPa	Tensile strength, MPa	Strain at break, %	Modulus of toughness, MPa
IPCAN-25	48 ± 2.75	12.6 ± 0.97	146 ± 30	1417 ± 65
IPCAN-50	60 ± 2.86	15.7 ± 2.24	240 ± 41	2764 ± 94
IPCAN-75	378 ± 5.53	20.5 ± 3.56	151 ± 18	2891 ± 124
DN-50-c	161 ± 1.43	14.6 ± 2.89	92 ± 7.6	1215 ± 97
SN-I	11 ± 0.88	8.4 ± 0.56	163 ± 16	827 ± 22
SN-B	535 ± 1.83	30.0 ± 0.67	12 ± 2.1	275 ± 38

(the cross-point of G' and G'' curves) and the transition temperature increases from about 130 °C to 155 °C. This means, with the introduction of the SN-B network, the exchange reaction of the SN-I network has been reduced. Only at higher temperatures can the amount and rate of exchange reactions be enough to promote the viscous flow transition. SN-B and IPCAN-75 did not show the cross-point of G' and G'' curves when heated to 160 °C. Compared to SN-I, SN-B has a much slower rate of network rearrangement, so there is no viscous flow transition in the high temperature zone. With the increase of SN-B contents from 25 wt% to 75 wt%, the viscous flow transition temperature (where $\tan \delta$ approaches 1) of IPCAN gradually increases, as shown in Fig. 4f. In addition, by comparing the $\tan \delta$ curves of IPCAN-50 and DN-50-c (Fig. S3, ESI†), it can be found that DN-50-c approaches the viscous flow transition earlier, because the limitation effect of SN-B is much weaker in DN-50-c with phase separation (Table 1).

It can be seen that SN-B behaves as a rigid and brittle thermoset when stretched at room temperature, while SN-I behaves as a crosslinked elastomer. Compared with SN-B, the T_g of IPCAN-75 is higher than the testing temperature, and its tensile curve reflects that the introduction of an interpenetrating elastic SN-I network can efficiently toughen the thermosetting SN-B network. After the yield point, the elongation at break of IPCAN-75 is increased from less than 15% of SN-B to more than 150%, which is an increase of 10 times. At the same time, the tensile strength and Young's modulus are reduced by approx. 30%. On the other hand, compared to SN-I, IPCAN-25 and IPCAN-50 still show the tensile behavior of reinforced cross-linked elastomers. The introduction of a glassy SN-B network effectively strengthens the original cross-linked elastic network of SN-I with an increase in tensile strength by about 50%, and in Young's modulus by more than 4 times. Interestingly, the elongation at break of IPCAN-50 has also increased significantly. IPCAN-50 contains equal amounts of SN-I and SN-B, and forms an interpenetrating and uniform phase structure. Therefore, during the stretching process, the two networks can bear the load and dissipate energy simultaneously, which leads to the improvement of both tensile strength and toughness.

Fig. 5b shows the tensile stress-strain curve of IPCAN-50 and DN-50-c. Compared to IPCAN-50, DN-50-c exhibits a higher Young's modulus at the initial stretching and reaches the maximum stress quickly. After yielding, the tensile stress

decreases until the fracture at approx. 92% elongation. Since the SN-B network in DN-50-c is in the glassy state at the initial stretching, the tensile stress-strain curve of DN-50-c generally presents as that of a toughened thermoset. The yield strain of IPCAN-50 and DN-50-c is close, but the slope of the curve of IPCAN-50 decreases during the subsequent stretching, while the tensile stress keeps increasing until it breaks, and the elongation at break increases significantly, indicating that during the stretching of IPCAN-50, the SN-B network first experienced partial breakage, which gave the IPCAN the necessary chain segment movement ability to continue extending. Fig. 5c and d shows the SEM photos of the tensile fracture surface of IPCAN-50 and DN-50-c. It can be seen that the fracture surface of IPCAN-50 is very rough, with obvious traces of pulling and tearing, reflecting the slow development of the ultimate fracture. This process occurred in the two networks with different strengths, which can absorb a large amount of mechanical energy and promote the toughening effect of the interpenetrating network structure. However, compared with IPCAN-50, the fracture surface of DN-50-c has an evidently higher smoothness and flatness, which means that the fracture occurred at some weakly bonded interfaces. From the elemental mapping of IPCAN-50 and DN-50-c on the tensile fracture surface, it can be seen that the distribution of Si and S elements on the fracture surface of IPCAN-50 is very uniform, while the distribution of S elements on the fracture surface of DN-50-c shows obvious regional differences, indicating the phase separation structure of DN-50-c.

The cyclic tensile curves of IPCAN-50, DN-50-c and SNs are shown in Fig. 6a–d. Their hysteresis energy (calculated as the area enclosed by the loading-unloading curves) changes with the time of loading-unloading cycles as shown in Fig. 6e. Because some reversible covalent bonds are fractured during the stretching process, all samples show permanent deformation and obvious residual strain during each loading-unloading cycle. Compared to SN-B, the SN-I network (Fig. 6c) has higher elasticity at room temperature and can recover to a smaller strain every time, and its hysteresis energy in each cycle has almost linear growth with the time of loading-unloading cycles, because the actual elongation increases linearly in each loading. For SN-B, the segmental mobility (Fig. 6d) at room temperature is very limited, so it is difficult to recover strains. In the 2nd to 4th cyclic stretching, the stress loading-unloading curves of SN-B are highly overlapped, and the hysteresis energy of each cycle is nearly unchanged, which shows that the cross-linked network cannot be effectively reconstructed after the damage caused by the 1st cycle. In addition, SN-B also showed a yield phenomenon after the 1st cyclic stretching, and the maximum stress in the subsequent cyclic stretching gradually decreased. Compared to DN-50-c, IPCAN-50 shows a lower residual strain. Since the Young's modulus of IPCAN-50 is lower than that of IPCAN-50-c, the calculated hysteresis energy is relatively low. However, IPCAN-50 exhibits a linear growth relationship with SN-I in the second to fourth cyclic stretching. IPCAN-50-c exhibits a linear growth with an increase in the number of cycles. For DN-50-c, the hys-

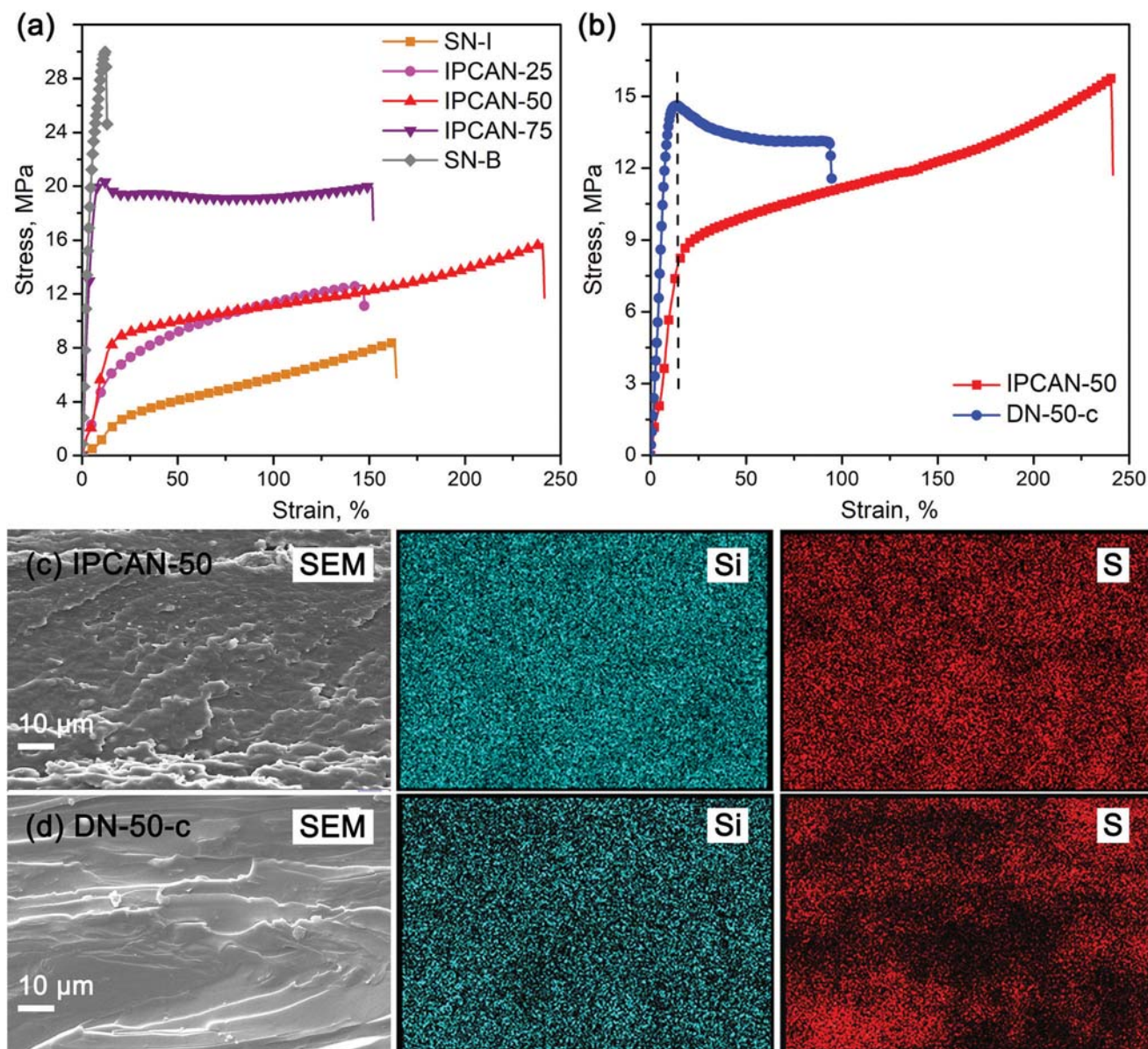


Fig. 5 Tensile stress–strain curves of (a) IPCANs and SNs, (b) IPCAN-50 and DN-50-c. SEM photos and elemental mapping of the tensile fracture surfaces of (c) IPCAN-50 and (d) DN-50-c.

teresis energy remains unchanged with an increase in the number of cycles like SN-B. Similarly, DN-50-c also exhibits a yield phenomenon, and the maximum stress in the subsequent cyclic stretching gradually decreases. The results of the cyclic tensile test show that when the amount of strain is low, IPCAN-50 can not only show the significant reinforcement in modulus caused by SN-B, but also has the segmental mobility caused by SN-I. The interpenetrating structure might help reduce the rigid packing of polydioxaborolane chains, which makes IPCAN-50 more resilient to deformation than DN-50-c.

Reprocessing of IPCANs

One of the most valuable aspects of sustainability caused by CANs is their reprocessing capability. However, for polymer

blends that consist of two or more immiscible components, reprocessing at high temperatures might cause the formation and expansion of phase separation, because each component has enough chain mobility and dynamic reactivity. IPCAN-50 shards could be hot-pressed into a uniform sheet, which is denoted as “IPCAN-50-Rx” according to the reprocessing times (x). The tensile stress–strain curves (Fig. 7a) of reprocessed IPCAN-50 are very close to that of the pristine samples without a significant loss in tensile strength or strain at break. We evaluated the restoration efficiency (η) from the modulus of toughness (MoT) of the reprocessed sample (MoT_x) and pristine sample (MoT_0) (eqn (4)). The results are presented in Table 2. The restoration efficiency after three cycles of cutting and hot-pressing is still as high as 93%.

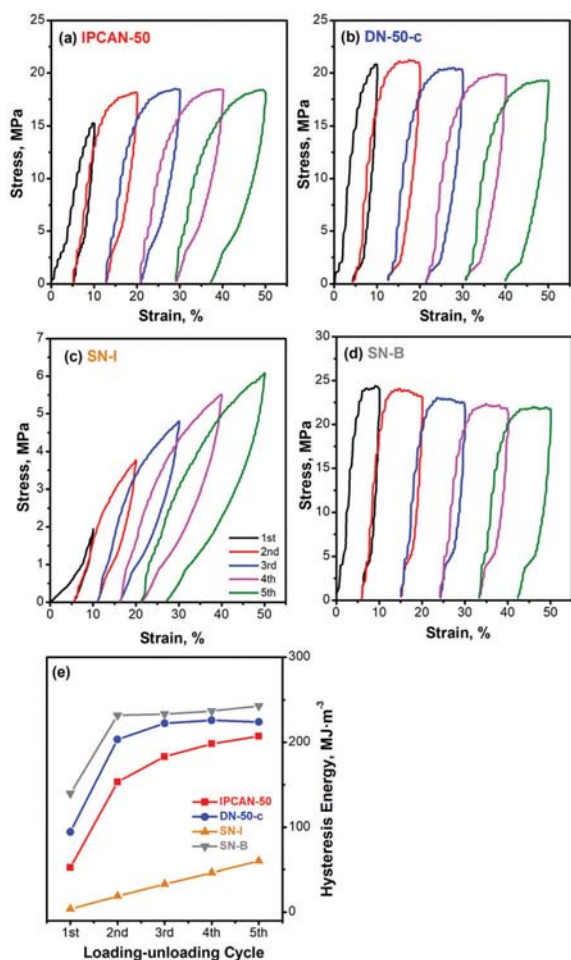


Fig. 6 Cyclic tensile curves of (a) IPCAN-50, (b) DN-50-c, (c) SN-I, and (d) SN-B and (e) plots of the hysteresis energy against the loading-unloading cycle.

$$\eta_x = \frac{MoT_x}{MoT_0} \times 100\% \quad (4)$$

DSC tests (Fig. 7b) show that the T_g value of IPCAN-50-Rx remains unchanged after reprocessing and only a single transition stage is observed. This indicates that the uniform interpenetrating phase structure of IPCAN-50 did not separate under heat and pressure. Fig. 7c shows the SEM photos and elemental mapping of IPCAN-50-Rx. After each reprocessing cycle, the distribution of S (only from SN-B) maintains good uniformity, indicating that IPCAN-50-Rx maintains a highly uniform phase structure. It is noteworthy that the hot-pressing temperature was set at 120 °C, where IPCAN-50 did not completely transit into the viscous liquid state (Fig. 4). Therefore, the chain movements might still be too hindered to expand the phase separation scale. However, enabled by the dynamic reactivity of imines and boronic-esters, rearrangements of the IPCAN could still proceed to achieve successful reprocessing. Some pieces of literature support that the external pressure and shearing during hot-pressing are also able to promote the dynamic exchange of reversible covalent bonds.

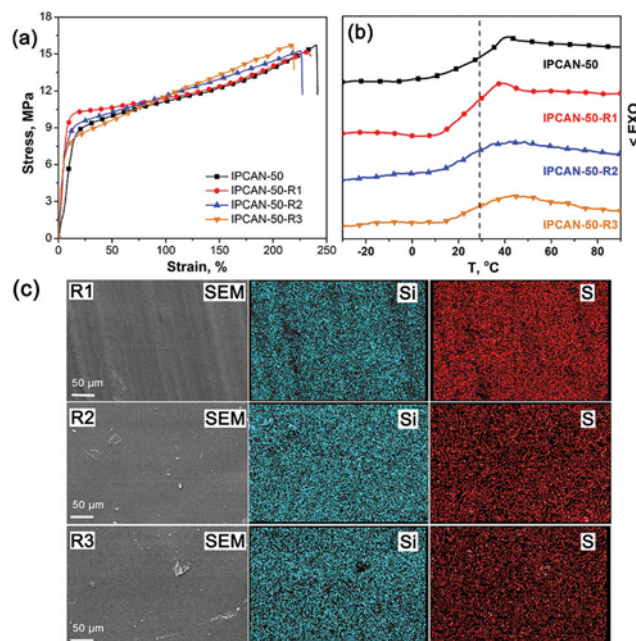


Fig. 7 (a) Tensile stress-strain curves, (b) DSC curves and (c) SEM photos and elemental mapping of reprocessed IPCAN-50.

Recycling SNs from IPCANs and re-preparing IPCANs

For traditional polymer blends, the formation of a dual continuous phase structure of different polymers is beneficial to promote the mechanical performance of products. However, if there are permanent covalent cross-links in the two continuous phases, the two phases will fall into an unbreakable interlocking state, and the cross-linked polymer blend materials will also face the problem of sustainability. Here, considering the dissociative reactivity of imines and boronic-esters, we investigated the feasibility of recycling the SNs from the interpenetrating network. According to the chemical properties of the two reversible cross-linked networks of IPCANs, both the imine bond of SN-I and the boronic-ester bond of SN-B can dissociate under the mediation of water, which leads to the decrosslinking and dissolving of the network in water-containing organic solvents. Previous contact angle tests (Fig. 2a) show that SN-B is generally hydrophilic, while SN-I is hydrophobic. We found that SN-B can completely dissolve in water due to the formation of a multi-hydroxyl structure after hydrolysis, while SN-I cannot dissolve in water. Based on the solubility difference of the two SNs, we tried a simple and economical water-extraction method to separate and recycle the two reversible components of IPCANs. Fig. 8 shows the photos taken in the water-extraction process of recycling SNs from IPCAN-50. After 24 hours of stirring in water, the shards of IPCAN-50 were whitened due to water erosion. Some of the fragments are broken using a stir bar, but they basically maintain their original shape (Fig. 8c). The dried insoluble solids appear as orange-yellow solids, similar to SN-I and the original IPCAN-50 shards (Fig. 8e). After cutting, the cavity structure can be seen (inset

Table 2 Tensile properties and restoration efficiency of reprocessed IPCANs

Sample	Young's modulus, MPa	Tensile strength, MPa	Strain at break, %	Modulus of toughness, MPa	Restoration efficiency (η), %
IPCAN-50	60 \pm 2.86	15.7 \pm 2.24	240 \pm 41	2764 \pm 94	—
IPCAN-50-R1	94 \pm 1.98	15.2 \pm 1.49	230 \pm 19	2789 \pm 101	101
IPCAN-50-R2	60 \pm 1.87	15.3 \pm 2.12	225 \pm 23	2690 \pm 82	97
IPCAN-50-R3	76 \pm 1.49	15.6 \pm 3.09	218 \pm 14	2570 \pm 71	93

in Fig. 8e), which may be caused by the evaporation of internal moisture during the drying process after SN-B was dissolved in water. At the same time, the aqueous solution after stirring for 24 hours remains clear and transparent (Fig. 8d), and after drying, a transparent and rigid film is obtained (Fig. 8f). Fig. 8g shows a comparison of the recycled SN-I-re and SN-B-re with the original SN-I and SN-B. It can be seen that the appearance is basically the same, and both have good transparency and uniformity. In addition, we also re-prepared the interpenetrating covalent adaptable network IPCAN-50-re using the recycled SNs through the dissociation and mixing in the THF/water solution procedure again. It can be seen that IPCAN-50-re is similar to the originally prepared IPCAN-50 in appearance.

The FTIR-ATR spectra of the water extraction and insoluble solid are shown in Fig. 9a. The infrared absorbance spectrum of the insoluble solid shows an increase in the absorption peak related to primary amine groups, indicating that some imine bonds have also been hydrolyzed, but it does not show any absorbance band of the B–O bond from SN-B. Compared with SN-B, the hydroxyl-related peaks of water extraction is also significantly intensified, indicating the massive hydrolysis of the boronic-esters. During the drying and curing process, the hydroxyl groups have not yet fully reacted with the boronic

acid groups. However, the C=N peak and the N–H peak basically disappeared, indicating that no detectable SN-I dissolved into the water. After hot-pressing, the obtained SN-I-re and SN-B-re show great similarity to the original SN-I and SN-B, respectively. The infrared results indicate that though the IPCAN forms a highly uniform phase structure, the two SNs can still be separated and recycled by virtue of the difference in solubility properties and the dissociation reaction activity mediated by water. Fig. 9b shows the tensile stress–strain curve of the recycled SNs and IPCAN-50-re. The two SNs recycled by the water-extraction method show a tensile behavior similar to that of the original SNs. SN-B-re behaves as a rigid and brittle thermoset, and SN-I-re behaves as a cross-linked elastomer. IPCAN-50-re still behaves as a strong and tough crosslinked elastomer, which has a high Young's modulus during the initial stretching and can extend to a strain of about 250% after passing through the yield point. We also tested the surface properties of recycled SNs and IPCAN-50-re, as shown in Fig. 9c & d. The contact angle of DIM and water on the surface of the two SNs and the calculated surface free energy are close to the original SNs. In addition, the surface properties of IPCAN-50-re are also very close to the IPCAN-50, with a water contact angle of about 80°, as a general hydrophilic surface.

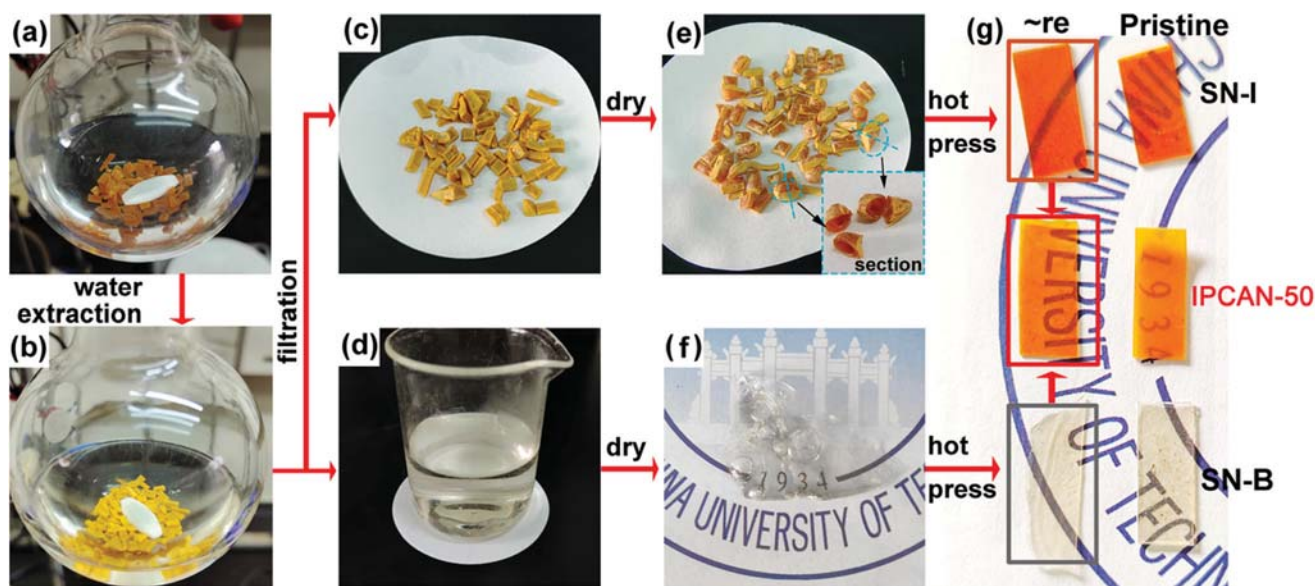


Fig. 8 Photos of recycling of reversible single networks from IPCAN-50 by water dissolution: (a) IPCAN-50 shards in water, (b) IPCAN-50 shards stirred in water after 24 h, (c) insoluble shards obtained by filtration, (d) water extraction solution obtained by filtration, (e) dried insoluble shards (SN-I-re), (f) dried water extraction (SN-B-re), and (g) hot-pressed SN-I-re, SN-B-re and re-prepared IPCAN-50-re from the recycled SNs via solution mixing.

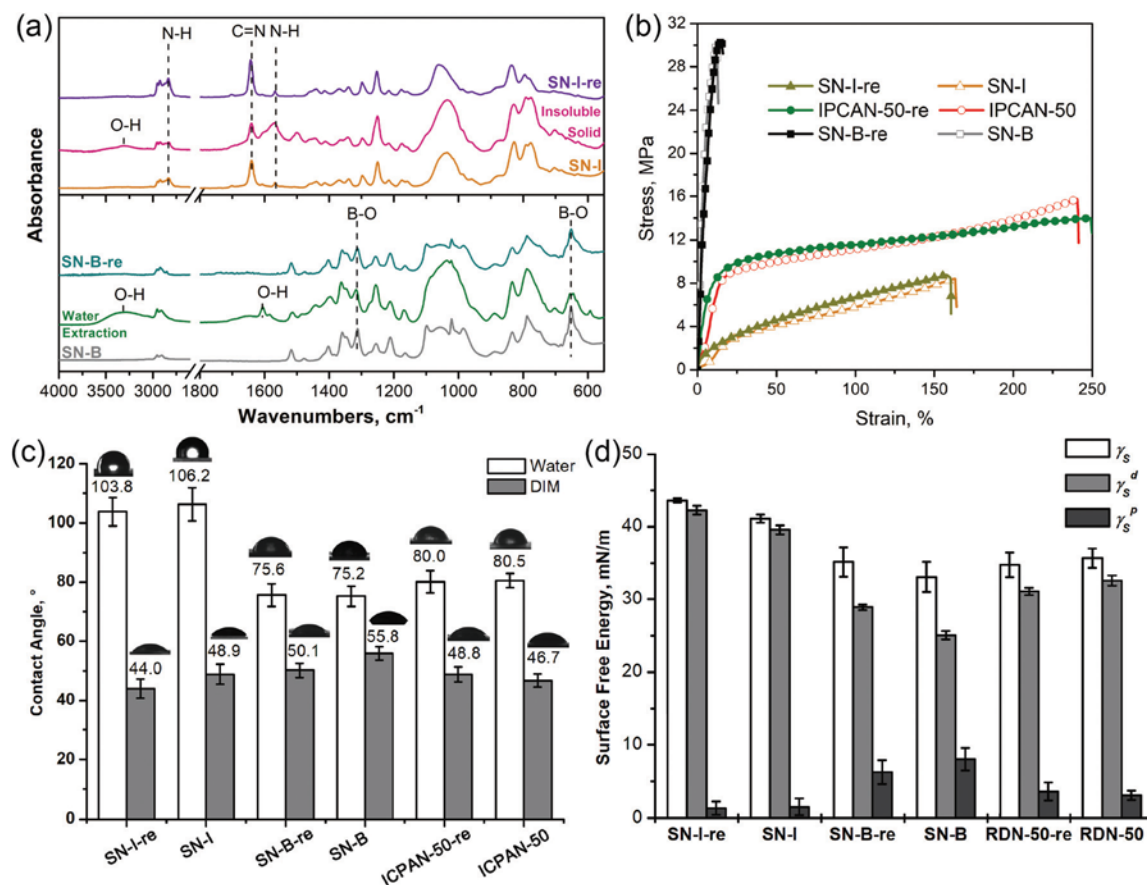


Fig. 9 (a) FTIR-ATR spectra of recycled SNs, (b) tensile stress-strain curves of recycled SNs and re-prepared IPCAN-50. Surface properties of recycled SNs and re-prepared IPCAN-50-re: (c) contact angle of DIM and water, and (d) surface free energy.

Conclusions

To conclude, an interpenetrating covalent adaptable network (IPCAN) consisting of an imine-based single network (SN-I) and a boronic-ester-based single network (SN-B) is prepared and a closed-loop of recycling and regeneration is established by rationally making use of covalent reversible chemistry. The two SNs show incompatibility in surface free energy, but share the water-mediated dissociation mechanism of rearrangement. IPCANs were constructed with a uniform distribution of both SNs through a strategy of hydrolysing the reversible covalent bonds, dissolving and molecularly mixing the network fragments, and then re-curing. Compared with SNs and the physically blended dual network sample, IPCANs show slower stress relaxation and significantly enhanced tensile toughness. By virtue of the respective reversible exchange reactions of imines and boronic-esters, IPCANs can be reprocessed under heat with great preservation of their uniform phase structure and mechanical properties. In addition, using the solubility difference of the two SNs and the hydrolytic ability of the reversible covalent bonds, the separation and recycling of the two SNs from IPCANs is achieved through a simple and economical water-extraction method. The IPCANs can also be regenerated from the recycled SNs. Thus, we envision that this

work may provide new insight into the design of more sustainable high-performance polymer blends and IPNs with covalent reversible bonds.

Author contributions

Yufeng Lei: data curation, methodology, and writing – original draft. Anqiang Zhang: conceptualization, supervision, and writing – review & editing. Yaling Lin: supervision and writing – review & editing.

Conflicts of interest

There are no conflicts to declare.

Acknowledgements

The authors gratefully acknowledge the financial support from the National Natural Science Foundation of China under Grant 52073098 and 31772202 and the Science and Technology Program of Guangzhou, China, under Grant 201803020015.

References

- 1 J. George, K. T. Varughese and S. Thomas, *Polymer*, 2000, **41**, 1507–1517.
- 2 L. Yang, A. Zhang, L. Wang, R. Chen, Y. Zeng and W. Wu, *Polym. Eng. Sci.*, 2013, **53**, 2093–2101.
- 3 Z. Wei, N. Ning, M. Tian, L. Zhang and J. Mi, *Polymer*, 2018, **150**, 177–183.
- 4 J. Huang, J. Fan, L. Cao, C. Xu and Y. Chen, *Chem. Eng. J.*, 2020, **385**, 123828.
- 5 N. Wu, H. Zhang and G. Fu, *ACS Sustainable Chem. Eng.*, 2017, **5**, 78–84.
- 6 H. Wu, M. Tian, L. Zhang, H. Tian, Y. Wu, N. Ning and T. W. Chan, *ACS Sustainable Chem. Eng.*, 2015, **3**, 26–32.
- 7 E. M. Foster, E. E. Lensmeyer, B. Zhang, P. Chakma, J. A. Flum, J. J. Via, J. L. Sparks and D. Konkolewicz, *ACS Macro Lett.*, 2017, **6**, 495–499.
- 8 W. D. Cook, F. Chen, S. K. Ooi, C. Moorhoff and R. Knott, *Polym. Int.*, 2006, **55**, 1027–1039.
- 9 J. John, D. Klepac, M. Didović, C. J. Sandesh, Y. Liu, K. V. S. N. Raju, A. Pius, S. Valić and S. Thomas, *Polymer*, 2010, **51**, 2390–2402.
- 10 S. Thomas, D. Grande, U. Cvelbar, U. K. V. S. N. Raju, R. Narayan, S. P. Thomas and H. Akhina, *Micro- and Nano-Structured Interpenetrating Polymer Networks*, John Wiley & Sons, Inc, Hoboken, NJ, 2016.
- 11 Z. P. Zhang, M. Z. Rong and M. Q. Zhang, *Prog. Polym. Sci.*, 2018, **80**, 39–93.
- 12 Y. Chen, Z. Tang, Y. Liu, S. Wu and B. Guo, *Macromolecules*, 2019, **51**, 3805–3812.
- 13 S. Wang, S. Ma, Q. Li, X. Xu, B. Wang, K. Huang, Y. Liu and J. Zhu, *Macromolecules*, 2020, **53**, 2919–2931.
- 14 L. Hammer, N. J. Van Zee and R. Nicolaÿ, *Polymers*, 2021, **13**, 1–34.
- 15 B. Zhang, J. Ke, J. R. Vakil, S. C. Cummings, Z. A. Digby, J. L. Sparks, Z. Ye, M. B. Zanjani and D. Konkolewicz, *Polym. Chem.*, 2019, **10**, 6290–6304.
- 16 A. Rekondo, R. Martin, R. A. Ruiz De Luzuriaga, G. Cabañero, H. J. Grande and I. Odriozola, *Mater. Horiz.*, 2014, **1**, 237–240.
- 17 Z. Su, S. Huang, Y. Wang, H. Ling, X. Yang, Y. Jin, X. Wang and W. Zhang, *J. Mater. Chem. A*, 2020, **8**, 14082–14090.
- 18 H. Liu, H. Zhang, H. Wang, X. Huang, G. Huang and J. Wu, *Chem. Eng. J.*, 2019, **368**, 61–70.
- 19 F. Ling, Z. Liu, M. Chen, H. Wang, Y. Zhu, C. Ma, J. Wu and G. Huang, *J. Mater. Chem. A*, 2019, **7**, 25324–25332.
- 20 Y. Chen, A. M. Kushner, G. A. Williams and Z. Guan, *Nat. Chem.*, 2012, **4**, 467–472.
- 21 R. Bui and M. A. Brook, *Polymer*, 2019, **160**, 282–290.
- 22 S. Shan, Y. Lei, Y. Lin and A. Zhang, *Polymer*, 2020, **186**, 122026.
- 23 E. Ducrot, Y. Chen, M. Bulters, R. P. Sijbesma and C. Creton, *Science*, 2014, **344**, 186–189.
- 24 J. Huang, L. Zhang, Z. Tang and B. Guo, *Compos. Commun.*, 2018, **8**, 65–73.
- 25 A. M. Wemyss, C. Bowen, C. Plesse, C. Vancaeyzeele, G. T. M. Nguyen, F. Vidal and C. Wan, *Mater. Sci. Eng., R*, 2020, **141**, 100561.
- 26 W. L. Peng, Y. You, P. Xie, M. Z. Rong and M. Q. Zhang, *Macromolecules*, 2020, **53**, 584–593.
- 27 Y. Zhu, J. Zhang, Q. Wu, M. Chen, G. Huang, J. Zheng and J. Wu, *ACS Appl. Mater. Interfaces*, 2020, **12**, 15757–15764.
- 28 Y. Amamoto, H. Otsuka, A. Takahara and K. Matyjaszewski, *Adv. Mater.*, 2012, **24**, 3975–3980.
- 29 C. J. Kloxin and C. N. Bowman, *Chem. Soc. Rev.*, 2013, **42**, 7161–7173.
- 30 R. Martin, A. Rekondo, A. Ruiz De Luzuriaga, A. Santamaria and I. Odriozola, *RSC Adv.*, 2015, **5**, 17514–17518.
- 31 I. Azcune and I. Odriozola, *Eur. Polym. J.*, 2016, **84**, 147–160.
- 32 Z. Wang, Y. Gu, M. Ma, Y. Liu and M. Chen, *Macromolecules*, 2021, **54**, 1760–1766.
- 33 Y. You, W. L. Peng, P. Xie, M. Z. Rong, M. Q. Zhang and D. Liu, *Mater. Today*, 2020, **33**, 45–55.
- 34 Y. You, M. Z. Rong and M. Q. Zhang, *Macromolecules*, 2021, **54**, 4802–4815.
- 35 Y. Lei, S. Shan, Y. Lin and A. Zhang, *Polymer*, 2020, **186**, 122031.
- 36 Y. Lei, A. Zhang and Y. Lin, *Polymer*, 2020, **209**, 123037.
- 37 D. K. Owens and R. C. Wendt, *J. Appl. Polym. Sci.*, 1969, **13**, 1741–1747.
- 38 D. H. Kaelble, *J. Adhes.*, 1970, **2**, 66–81.
- 39 T. Young, *Philos. Trans. R. Soc. London*, 1805, **95**, 65–87.
- 40 J. M. Winne, L. Leibler and F. E. Du Prez, *Polym. Chem.*, 2019, **10**, 6091–6108.
- 41 Y. Li, L. Yang, Y. Zeng, Y. Wu, Y. Wei and L. Tao, *Chem. Mater.*, 2019, **31**, 5576–5583.



ISSN 1000-2030
CN 32-1148/S
CODEN NNDXEI

南京农业大学学报

JOURNAL OF NANJING AGRICULTURAL UNIVERSITY

第 44 卷 第 6 期
Vol. 44 No. 6

2021 年 11 月
Nov. 2021

6
2021



全国中文核心期刊
CSCD 来源期刊
中国精品科技期刊
百种中国杰出学术期刊

目次

• 综述 •

小麦籽粒品质空间分布异质性及其形成机制研究进展

..... 姜东,仲迎鑫,蔡剑,周琴,王笑,戴廷波,曹卫星(1013)

surfactin 生物合成及应用的研究进展 陈晓宇,赵洪源,陆兆新(1024)

• 植物科学 •

水稻白穗突变体 *wp8* 的表型鉴定及候选基因定位和功能分析

..... 刘林,朱泽,王致远,刘世家,田云录,周时荣,江玲,刘玲珑,万建民(1035)

一种快速添加或替换蛋白标签的新方法及应用

..... 张皓,刘雪莹,钱铭,高鸿儒,汤超,张华,王鹏,张绍铃,吴巨友(1046)

菊花苗期氮高效品种资源筛选及氮效率评价体系建立

..... 葛礼姣,方馨妍,张云月,罗孟婷,管志勇,陈素梅,房伟民,陈发棣,赵爽(1054)

切花百合耐热性评价及越夏栽培技术研究 蓝令,吴泽,张德花,滕年军(1063)

辣椒胶孢炭疽菌 CFEM 效应因子鉴定及转录组分析

..... 刘思珍,欧阳超,满益龙,盛家伟,陈岳,张鑫,郑立敏,李智强,
李大伟,张德咏,刘勇,王运生,谭新球(1074)

基于磁性纳米探针的莠去津残留荧光检测方法 刘金彤,蒲虹辰,叶林瑶,莫艳阳,杨红(1083)

超声细胞粉碎法快速提取真菌中的麦角甾醇 霍理坚,冯祖睿,林雅铃(1090)

• 生物与环境 •

ZFP36 互作蛋白基因 *OsGRP1* 的克隆及其在 ABA 诱导的抗氧化防护途径中的功能分析

..... 陆秋萍,季锴,蒋明义(1097)



霍理坚, 冯祖睿, 林雅铃. 超声细胞粉碎法快速提取真菌中的麦角甾醇[J]. 南京农业大学学报, 2021, 44(6): 1090–1096.

HUO Lijian, FENG Zurui, LIN Yaling. Rapid extraction of ergosterol from fungi by ultrasonic cell disruption [J]. Journal of Nanjing Agricultural University, 2021, 44(6): 1090–1096.

超声细胞粉碎法快速提取真菌中的麦角甾醇

霍理坚, 冯祖睿, 林雅铃*

(华南农业大学材料与能源学院, 广东 广州 510642)

摘要: [目的] 本文旨在尝试用超声细胞粉碎法从真菌中提取麦角甾醇, 以寻找比以往更快速测定真菌中麦角甾醇含量的方法。[方法] 以甲醇为溶剂, 选择料液比、超声前浸泡时间、超声时间和超声功率为影响因素, 以高效液相色谱法测定含量, 通过正交试验确定以超声细胞粉碎法从水稻纹枯病菌(*Rhizoctonia solani*) 中提取麦角甾醇的最佳条件。将其结果与传统的皂化回流法提取进行比较。进而分别以超声细胞粉碎法、超声辅助提取法、皂化回流法从金针菇(*Flammulina velutipes*) 中提取麦角甾醇并进行比较。[结果] 通过正交试验确定超声细胞粉碎法以甲醇作溶剂从水稻纹枯病菌中提取麦角甾醇的最佳条件为: 料液比 1/50(每 50 mL 甲醇中加入 1 g 菌丝, 下同), 超声前浸泡 20 min, 超声功率 200 W, 超声时间 4 min, 测得菌丝中麦角甾醇含量约为 $2.59 \text{ mg} \cdot \text{g}^{-1}$; 而以皂化回流法提取测得麦角甾醇含量为 $2.18 \text{ mg} \cdot \text{g}^{-1}$ 。采用超声细胞粉碎法以甲醇作溶剂从金针菇中提取麦角甾醇的条件是: 料液比 1/50, 超声前浸泡 20 min, 超声功率 250 W, 超声时间 8 min, 提取率为 $3.27 \text{ mg} \cdot \text{g}^{-1}$ 。超声辅助提取法和皂化回流法的提取率分别为 3.01 和 $2.82 \text{ mg} \cdot \text{g}^{-1}$ 。以超声细胞粉碎法提取率最高, 且差异极显著。[结论] 以超声细胞粉碎法从 2 种真菌中获得麦角甾醇的量均比皂化回流法提取高, 且试剂用量少, 操作省时简便, 有望成为快速测定真菌中麦角甾醇含量的方法。

关键词: 水稻纹枯病菌; 金针菇; 麦角甾醇; 超声细胞粉碎法; 高效液相色谱法

中图分类号: S432.4⁺4

文献标志码: A

文章编号: 1000-2030(2021)06-1090-07

Rapid extraction of ergosterol from fungi by ultrasonic cell disruption

HUO Lijian, FENG Zurui, LIN Yaling*

(College of Material and Energy, South China Agricultural University, Guangzhou 510642, China)

Abstract: [Objectives] In order to find a more rapid method to determine the content of ergosterol in fungi, this paper attempted to extract ergosterol from fungi by ultrasonic cell disruption method. [Methods] Using methanol as the solvent, the effects of material-to-liquid ratio, immersion time before ultrasonic extraction, ultrasonic time and ultrasonic power on the extraction of ergosterol from *Rhizoctonia solani* by ultrasonic cell disruption method were investigated through orthogonal experiment design. The contents of ergosterol in the extract under the optimum extraction conditions were determined by HPLC, and the results were compared with the traditional saponification reflux extraction method. Furthermore, ergosterol was extracted from *Flammulina velutipes* by ultrasonic cell disruption method, ultrasonic assisted extraction method and saponification reflux method, and their contents were compared. [Results] The optimal conditions for ultrasonic cell disruption method to extract ergosterol from *R. solani* were: the ratio of material-to-liquid was 1/50(1 g mycelium was added per 50 mL of methanol, the same below), mycelium was immersed for 20 min before ultrasonic extraction, ultrasonic power was 200 W, and ultrasonic time was 4 min. Under this extraction condition, the content of ergosterol was about $2.59 \text{ mg} \cdot \text{g}^{-1}$; and the content of ergosterol extracted by saponification reflux method was about $2.18 \text{ mg} \cdot \text{g}^{-1}$. Using methanol as the solvent, when the material-to-liquid ratio was 1/50, the immersion time before ultrasonic was 20 min, the ultrasonic time was 8 min, and the ultrasonic power was 250 W, the average content of ergosterol extracted by ultrasonic crushing method was about $3.27 \text{ mg} \cdot \text{g}^{-1}$. However, the average contents of ergosterol extracted from *F. velutipes* by ultrasonic assisted extraction method and saponification reflux extraction method were $3.01 \text{ mg} \cdot \text{g}^{-1}$ and $2.82 \text{ mg} \cdot \text{g}^{-1}$, respectively. Ultrasonic cell disruption had the highest extraction rate, and the difference was extremely significant. [Conclusions] The amount of ergosterol extracted from the two kinds of fungi by ultrasonic cell disruption method was higher than that of saponification reflux extraction method. Ultrasonic cell disruption method had the advantages of less reagent consumption, time-saving and simple operation. It was expected to be a rapid method for determining the content of ergosterol in fungi.

Keywords: *Rhizoctonia solani*; *Flammulina velutipes*; ergosterol; ultrasonic cell disruption; high performance liquid chromatography

收稿日期: 2021-01-14

基金项目: 国家自然科学基金项目(31772202); 广州市科技计划项目(201803020015, 201704020084)

作者简介: 霍理坚, 硕士, 实验师, 从事分析化学研究, E-mail: huolijian@scau.edu.cn。* 通信作者: 林雅铃, 博士, 副教授, 研究方向为植物病害化学防治, E-mail: linyaling@scau.edu.cn。

(C)1994-2021 China Academic Journal Electronic Publishing House. All rights reserved. http://www.cnki.net

麦角甾醇,别名麦角固醇,是真菌细胞膜的重要组成成分,因其结构稳定,专一性强,可以将其含量作为真菌生物量的指标^[1]。抗真菌药通过与麦角甾醇生物合成途径中的各种酶作用,干扰或阻断麦角甾醇生物合成,破坏真菌细胞膜结构而达到抑菌、杀菌目的^[2-3]。麦角甾醇也是一种重要的医药化工原料,可用于生产可的松、激素黄体酮等甾醇类药物。为提高麦角甾醇的产量,国内外学者广泛开展了微生物发酵合成麦角甾醇的研究^[4]。因此,无论是在真菌病害防治领域,还是药物生产领域,找到一种从真菌中快速提取麦角甾醇并准确测定其含量的方法是十分必要的。

目前,麦角甾醇的提取方法有皂化回流法、超声辅助提取法、微波萃取法或超临界流体 CO₂ 萃取法等^[4],其中以皂化回流法最常见。皂化回流法存在提取时间长、温度高、有机溶剂使用量大、安全系数小等缺点^[5]。超声波是一种高频机械振荡波,其能量会引起萃取溶剂的空化,而空化作用能加速传热和传质速率,从而破坏细胞膜^[6]。目前超声波法的常用设备是超声清洗机^[7-9],其超声波能量分布不集中,细胞粉碎效率不高,若能提高超声粉碎效率则有望缩短提取时间,提高工作效率。

水稻纹枯病菌(*Rhizoctonia solani*) 引发的水稻纹枯病是全球范围内危害最为严重的水稻真菌病害之一^[10]。金针菇(*Flammulina velutipes*) 是常见的食药两用菌类,其富含维生素、氨基酸、纤维素等成分,具有很高的营养价值和药用价值,在功能性食品、医药保健品开发上具有很大潜力^[11]。本研究先以水稻纹枯病菌为对象,采用具有较大超声粉碎功率的超声细胞粉碎仪,以甲醇为溶剂,探索和改进超声细胞粉碎法提取麦角甾醇的条件,用 HPLC 法测定提取后麦角甾醇含量;然后将优化的超声细胞粉碎法用于金针菇麦角甾醇的提取,以期能找到一种可替代传统皂化回流法且简单可行的麦角甾醇提取与测定方法。

1 材料与方法

1.1 试验材料

水稻纹枯病菌(*Rhizoctonia solani*) 由华南农业大学植物保护学院植物病理系真菌研究室提供。金针菇(毛柄金线菌,*Flammulina velutipes*) 购自华南农业大学农贸市场。

1.2 试剂和仪器

麦角甾醇标准品(纯度 98.0%) 购自成都乐美天医药科技有限公司;甲醇(色谱纯)、氢氧化钾、维生素 C、氯化钠、无水乙醇、石油醚(60~90 °C)、无水硫酸钠均为分析纯,购自上海麦克林生化科技有限公司。试剂配制:2 mol·L⁻¹ 氢氧化钾-乙醇溶液(KOH-EtOH),取 KOH 11.2 g,加入 EtOH 溶解成 100 mL;0.1 mol·L⁻¹ 维生素 C 溶液,取维生素 C 0.176 g,加无水乙醇 100 mL;饱和 NaCl 溶液,取 NaCl 25 g,加水 50 mL 振荡溶解,静置后取上清液;麦角甾醇标准溶液,精确称取麦角甾醇标准品 5 mg,加色谱甲醇稀释定容至 50 mL,质量浓度为 0.1 mg·mL⁻¹。

仪器:高效液相色谱仪(Waters 600-2998);Hypersil ODS 250×4.6 mm 5 μm 色谱柱;JY92-IIIDN 超声细胞粉碎仪(宁波新芝生物科技股份有限公司);KQ-250DE 型数控超声波清洗器(昆山市超声仪器有限公司);BSA124S 万分之一电子天平(赛多利斯科学仪器北京有限公司)。

1.3 麦角甾醇含量的测定方法

参照李治建等^[12]方法,采用 HPLC 法,以甲醇为流动相,流速为 1 mL·min⁻¹,检测波长为 260 nm,进样量 10 μL,室温测定。以 0.1 mg·mL⁻¹ 麦角甾醇标准溶液作对照,外标法计算供试液中麦角甾醇的含量。

1.4 皂化回流法提取 *R. solani* 中的麦角甾醇

参照 Heleno 等^[13]方法,称取约 0.2 g 菌丝干粉,精密称量,加入 2 mol·L⁻¹ KOH-EtOH 溶液 10 mL,0.1 mg·mL⁻¹ 维生素 C 溶液 2.5 mL,60 °C 下恒温皂化 45 min。皂化液放冷至室温,加入 5 mL NaCl 饱和溶液,以 10 mL 石油醚萃取 3 次,收集有机相,加少量无水 Na₂SO₄ 除水,40 °C 旋蒸至干,以甲醇溶解转移至 10 mL 容量瓶定容。

1.5 超声细胞粉碎法提取 *R. solani* 中的麦角甾醇

1.5.1 正交试验确定最佳提取条件 在前期预试验中,发现菌丝(g)与溶剂(mL)的比例(简称为料液比)、菌丝干粉超声粉碎前浸泡在溶剂中的时间、超声粉碎的功率、超声粉碎的时间等对麦角甾醇的提取率有一定的影响,故初步确定 4 个变量,即:料液比(A)、超声粉碎前浸泡时间(B)、超声功率(C)和超声时间(D),其变量水平见表 1,选用 L₁₆(4⁵) 正交试验评价上述 4 个变量对提取率的影响并获得最优提取条件。

表1 正交优化试验因素与水平表
Table 1 Level and factors in the $L_{16}(4^5)$ orthogonal experiments

水平 Level	料液比(A) Material-to-liquid ratio	超声前浸泡时间(B)/min Immersion time before ultrasonic extraction	超声功率(C)/W Ultrasonic power	超声时间(D)/min Ultrasonic time
1	1/10	0	100	2
2	1/30	20	200	4
3	1/50	40	300	6
4	1/70	60	400	8

超声细胞粉碎法提取麦角甾醇的试验步骤: 将 *R. solani* 菌丝冻干, 研细成粉, 待用。考虑到麦角甾醇易溶于甲醇, HPLC 法测定也以甲醇作为流动相, 故在超声提取时, 采用色谱纯甲醇作为溶剂。根据设定的变量条件, 分别精密称取干燥 *R. solani* 菌丝冻干粉, 置于 15 mL 离心管, 准确移取设定量的甲醇, 浸泡规定时间, 称量; 在设定的功率条件下, 冰浴中超声处理设定的时间, 放置室温后再次称量, 滴加甲醇补足缺失的量; 摇匀, 取溶液适量以 0.45 μm 尼龙滤膜过滤, 得到供试溶液, 用 HPLC 测定麦角甾醇含量。每个试验条件重复 3 次, 取平均值。

1.5.2 含量测定方法学考察 最佳提取条件的加样回收试验: 取约 0.20 g *R. solani* 菌丝干粉 9 份, 精密称定, 分为高、中、低 3 个浓度组, 分别加入含标准品 0.75、0.50、0.25 mg 的甲醇溶液, 按 1.5.1 节中确定的最佳提取条件下进行提取, 根据测定结果计算加样回收率。

重复性试验: 取约 0.20 g 的 *R. solani* 菌丝干粉 5 份, 精密称定, 以上述最佳提取条件平行操作得供试溶液, 测定并计算提取率及相对标准偏差(RSD)。

1.6 提取金针菇中麦角甾醇的方法

超声细胞粉碎法: 取约 0.20 g 金针菇冻干粉 3 份, 精密称定, 置于 15 mL 离心管, 准确移取 10 mL 甲醇, 充分混合后浸泡 20 min, 称量; 超声细胞粉碎仪超声(250 W, 冰浴)处理 8 min, 放置室温, 再次称量, 滴加甲醇补足缺失的量, 摇匀, 以微孔滤膜过滤, 测定含量。

超声辅助提取法: 取约 0.20 g 金针菇冻干粉 3 份, 精密称定, 置于 15 mL 离心管, 准确移取 10 mL 甲醇, 摇匀, 称量, 超声清洗机超声(250 W, 40 $^{\circ}\text{C}$ 水浴)处理 40 min, 放置室温, 再次称量, 滴加甲醇补足缺失的量, 摇匀, 以微孔滤膜过滤, 测定含量^[7,14]。

皂化回流提取法: 取约 0.20 g 金针菇冻干粉 3 份, 精密称定, 加入 2 mol·L⁻¹ KOH-EtOH 10 mL, 在 85~90 $^{\circ}\text{C}$ 下皂化 3 h^[7]。冷却后转移至分液漏斗, 加入 10 mL 石油醚萃取 2 次, 收集上层石油醚^[15], 旋转蒸发至干, 用甲醇溶解转移至 10 mL 容量瓶定容。溶液以微孔滤膜过滤, 测定含量。

上述提取试验均重复 3 次, 取平均值, 计算其 RSD 值并进行方差分析。

1.7 数据分析

采用 Excel 2010 软件进行绘图和处理分析数据。

2 结果与分析

2.1 麦角甾醇 HPLC 检测方法的建立

在 1.3 节所述的 HPLC 色谱条件下, 得到麦角甾醇标准溶液(0.1 mg·mL⁻¹)和菌丝提取液中麦角甾醇的色谱图(图 1)。由图 1 可以看出: 麦角甾醇色谱峰的保留时间约为 14.423 min, 样品峰与其他物质峰完全分离, 分离度大于 1.5。

麦角甾醇在 0.010~0.200 mg·mL⁻¹线性关系良好, 标准曲线的回归方程为:

$$Y = 15\,181X + 31\,335, R^2 = 0.999\,9。$$

在相同条件下, 0.1 mg·mL⁻¹标准品溶液连续进样 3 次, 麦角甾醇峰面积的相对标准偏差(RSD)为 0.59%, 说明本色谱条件满足检测要求。

2.2 皂化回流法提取 *R. solani* 中麦角甾醇

根据文献所述的皂化法, 按 1.4 节所述条件从 *R. solani* 菌丝中提取麦角甾醇, 并采用 1.3 节中所述的方法进行含量测定。3 次重复测试结果显示: 菌丝中麦角甾醇含量约为 2.18 mg·g⁻¹, RSD 为 2.28%。

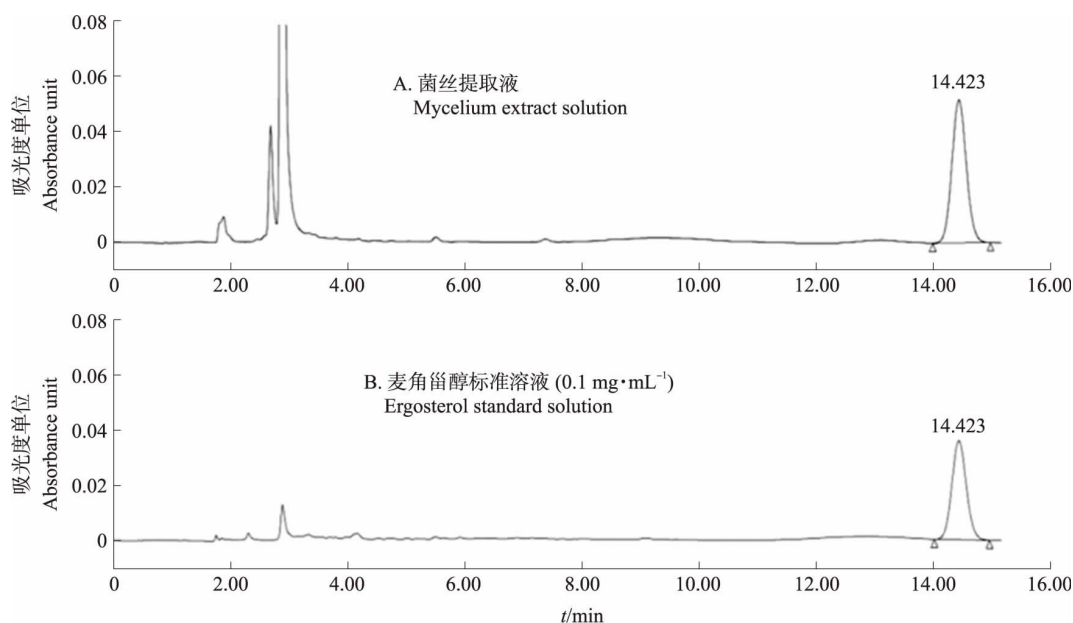


图 1 菌丝提取液和麦角甾醇标准溶液的 HPLC 色谱图

Fig. 1 HPLC chromatograms of mycelium extract solution and ergosterol standard solution

2.3 超声细胞粉碎法提取 *R. solani* 中麦角甾醇的正交试验结果及其提取条件优化

由表 2 中极差 (R) 值可知: 料液比 (A) 对麦角甾醇的提取率影响最大, 其次为超声前浸泡时间 (B)、超声时间 (D), 超声功率 (C) 的影响最小。由表 3 方差分析结果可知: 料液比、超声前浸泡时间对麦角甾醇提取率的影响较显著, 而超声功率与超声时间对麦角甾醇的提取率影响不显著。基于此, 确定以超声细胞粉碎法提取水稻纹枯病菌中麦角甾醇的最佳条件为 $A_3B_2C_2D_2$, 即: 料液比 1/50, 超声前浸泡 20 min, 超声功率 200 W, 超声时间 4 min。

表 2 正交优化试验结果分析表

Table 2 Analysis of the results from orthogonal experiment

试验号 Number	因素 Factors				麦角甾醇含量 / (mg·g ⁻¹) Ergosterol content
	A	B	C	D	
T1	1	1	1	1	1.47
T2	1	2	2	2	1.83
T3	1	3	3	3	1.57
T4	1	4	4	4	1.33
T5	2	1	2	3	2.56
T6	2	2	1	4	2.48
T7	2	3	4	1	2.47
T8	2	4	3	2	2.34
T9	3	1	3	4	2.63
T10	3	2	4	3	2.65
T11	3	3	1	2	2.57
T12	3	4	2	1	2.44
T13	4	1	4	2	1.95
T14	4	2	3	1	1.81
T15	4	3	2	4	1.75
T16	4	4	1	3	1.61
水平 1 下的偏差均值 (k_1)	1.55	2.15	2.03	2.05	—
水平 2 下的偏差均值 (k_2)	2.46	2.19	2.15	2.17	—
水平 3 下的偏差均值 (k_3)	2.57	2.09	2.09	2.10	—
水平 4 下的偏差均值 (k_4)	1.78	1.93	2.10	2.05	—
极差 R	1.02	0.27	0.11	0.12	—
因素主次 Factor priority	$A>B>D>C$				
最优方案 Best plan	$A_3B_2C_2D_2$				

表 3 方差分析表

Table 3 Analysis results of variance

因素 Factor	偏差平方和 Sum of square (SS)	自由度 Freedom (DF)	F 值 F-value	显著性 Level of significance
料液比 Material-to-liquid ratio	3.039	3	178.765	*
超声前浸泡时间 Immersion time before ultrasonic	0.166	3	9.765	*
超声功率 Ultrasonic power	0.026	3	1.529	
超声时间 Ultrasonic time	0.040	3	2.353	
偏差 Error	0.020	3		

2.4 超声细胞粉碎法的准确度和精密度

由表 4 加样回收试验结果可知: 在超声细胞粉碎法的最佳提取条件下, 麦角甾醇的加样回收率为 92.22%~101.13%, 平均回收率为 96.53%, RSD 为 2.68%。由表 5 重复性试验结果可见: 在最佳提取条件下其麦角甾醇的平均含量为 $2.59 \text{ mg} \cdot \text{g}^{-1}$, RSD 为 0.88%。试验结果均符合相关规定要求, 说明此提取方法准确度高, 重复性好。

表 4 超声细胞粉碎法加样回收试验结果

Table 4 Test results of sample recovery rate of ultrasonic cell disruption method

组别 Group	平均峰面积 Average peak area	菌丝量/g Mycelium weighing	回收率/% Recovery rate	平均回收率/% Average recovery rate	RSD /%
低浓度组 Low concentration group	973 759 988 990 992 368	0.199 9 0.201 1 0.200 9	97.63 100.02 101.13		
中浓度组 Medium concentration group	1 347 605 1 341 389 1 352 413	0.200 6 0.200 3 0.200 9	96.02 95.48 96.37	96.53	2.68
高浓度组 High concentration group	1 670 465 1 700 077 1 711 026	0.199 5 0.200 0 0.199 7	92.22 94.39 95.54		

表 5 超声细胞粉碎法重复性试验结果

Table 5 Reproducibility test results of ultrasonic cell disruption method

编号 Number	平均峰面积 Average peak area	菌丝量/g Mycelium weighing	麦角甾醇含量/($\text{mg} \cdot \text{g}^{-1}$) Ergosterol content	平均含量/($\text{mg} \cdot \text{g}^{-1}$) Average content	RSD /%
1	599 097	0.200 7	2.59		
2	593 776	0.200 1	2.57		
3	593 779	0.201 3	2.56	2.59	0.88
4	603 096	0.201 1	2.60		
5	607 890	0.201 5	2.62		

2.5 3 种方法提取金针菇中麦角甾醇的比较结果

由表 6 可看出: 3 种提取方法中, 以超声细胞粉碎法提取率最高, 需时最少, 且重现性良好。方差分析结果显示, 超声细胞粉碎法提取麦角甾醇的提取率与皂化回流法和超声辅助法提取麦角甾醇的提取率差异极显著($P < 0.01$)。

表 6 皂化回流法、超声辅助法及超声细胞粉碎法提取金针菇中麦角甾醇的比较及方差分析

Table 6 Comparison of extraction of ergosterol from *Flammulina velutipes* with saponification reflux, ultrasound assisted and ultrasonic cell crushing and analysis results of variance

方法 Methods	平均峰面积 Average peak area	菌丝量/g Mycelium weighing	麦角甾醇含量/ ($\text{mg} \cdot \text{g}^{-1}$) Ergosterol content	麦角甾醇平均含量/ ($\text{mg} \cdot \text{g}^{-1}$) Average content of ergosterol	RSD /%	与超声细胞粉碎法比较 Compare with ultrasonic cell crushing				
						偏差平方和 SS	自由度 DF	均方 MS	F 值 F-value	P 值 P-value
皂化回流法 Saponification reflux	902 288 843 671 856 555	0.200 4 0.199 8 0.200 2	2.93 2.74 2.78							
超声辅助法 Ultrasound assisted	942 803 906 658 929 845	0.200 6 0.200 3 0.199 8	3.05 2.94 3.02	3.01	1.90	0.11	1	0.11	47.06	0.002
超声细胞粉碎法 Ultrasonic cell crushing	994 814 1 001 496 1 020 542	0.199 5 0.199 7 0.200 5	3.24 3.26 3.31	3.27	1.10	—	—	—	—	—

3 结论与讨论

麦角甾醇存在于真菌的菌丝细胞中,对其进行有效提取的前提是麦角甾醇必须能从细胞中溶出。超声波的机械效应、空化效应、热效应等作用有利于细胞的粉碎,促使麦角甾醇从菌丝细胞中溶出并迅速分散在提取液中。故相对于皂化回流法,超声辅助提取和超声细胞粉碎提取法的提取量均有所增加。一般认为,超声前的浸泡有利于甲醇与菌丝的充分接触,有利于超声波能量的传导,提高菌丝细胞的粉碎率,正交试验结果亦证实了这一点。当超声的功率达到一定值(250 W)时,已经基本实现对菌丝细胞的有效粉碎,故进一步提高超声功率和超声时间,对麦角甾醇的提取影响不显著。本试验还发现,当料液比为1/20时,供试样品中可见有未完全粉碎的菌丝,说明减少料液比(即增加溶剂的用量)也有利于菌丝在超声条件下的充分粉碎,麦角甾醇更易溶出,提取更充分。

利用超声波提取,以往常用超声清洗机进行超声辅助提取,其操作是把菌丝、提取液混合至容器(如锥形瓶)中,浸入清洗槽水浴超声。超声波从清洗槽底部的振子发出,透过水浴(体积相对较大)和容器才到达提取液,在此过程中能量分散弱化,要使细胞粉碎率高需时较长。而超声细胞粉碎仪的工作原理是超声波通过浸入在样品溶液中的钛合金变幅杆对容器中的细胞、提取液直接产生作用,能量集中,细胞粉碎效率高。试验结果证实了这一点,超声细胞粉碎提取进一步缩短了提取时间,且麦角甾醇提取率也有提高。

借助超声波进行提取比传统的皂化回流法用时大幅减少,且操作简单,溶剂使用量少。相比于超声清洗机,由于超声细胞粉碎仪可提供能量更为集中的超声波,因此用超声细胞粉碎法可得到更高的提取率,且试验结果显示该方法的准确度及重复性均达到相关规定。综上所述,超声细胞粉碎法可作为真菌菌丝中麦角甾醇含量快速测试的参考方法。本研究仅选择了较有代表性的植物致病菌和食用菌各1种作为试验材料,将来要对多种真菌进行研究,进一步确定超声细胞粉碎法应用于真菌中提取麦角甾醇的可行性。

参考文献 References:

- [1] Verma B, Robarts R D, Headley J V, et al. Extraction efficiencies and determination of ergosterol in a variety of environmental matrices [J]. *Communications in Soil Science and Plant Analysis*, 2002, 33(15/16/17/18) : 3261–3275.
- [2] 马养民, 赵洁, 周雪宁. 植物内生真菌抗植物病原真菌活性物质的研究 [J]. *化学进展*, 2010, 22(增刊 1) : 440–448.
Ma Y M, Zhao J, Zhou X N. Anti-plant pathogenic fungal compounds from endophytic fungi [J]. *Progress in Chemistry*, 2010, 22(Suppl 1) : 440–448(in Chinese with English abstract) .
- [3] Song X M, Zhu X Y, Li T, et al. Dehydrozingerone inspired discovery of potential broad-spectrum fungicidal agents as ergosterol biosynthesis inhibitors [J]. *Journal of Agricultural and Food Chemistry*, 2019, 67(41) : 11354–11363.
- [4] 曹龙辉, 李晓珺, 赵文红, 等. 麦角甾醇的研究进展 [J]. *中国酿造*, 2014, 33(4) : 9–12.
Cao L H, Li X J, Zhao W H, et al. Research progress on ergosterol [J]. *China Brewing*, 2014, 33(4) : 9–12(in Chinese with English abstract) .
- [5] 郭瑞, 饶斌, 吴琴燕, 等. 超声辅助皂化提取禾谷镰孢菌中麦角甾醇及其 HPLC 分析 [J]. *分析实验室*, 2019, 38(11) : 1353–1358.
Guo R, Rao B, Wu Q Y, et al. Optimization of saponification assisted ultrasonic extraction and HPLC analysis of ergosterol from *Fusarium graminearum* [J]. *Chinese Journal of Analysis Laboratory*, 2019, 38(11) : 1353–1358(in Chinese with English abstract) .
- [6] Zhao T J, Chen J, Shi Y P. Holistic analysis of Liuwei Dihuang pills using ultrasonic cell grinder extraction and ultra-performance liquid chromatography [J]. *Chinese Journal of Chromatography*, 2017, 35(1) : 32–46.
- [7] 胡代花, 张嘉昕, 李翠丽, 等. 超声辅助提取金针菇中麦角甾醇及其 HPLC 测定方法 [J]. *食品工业科技*, 2017, 38(23) : 192–197.
Hu D H, Zhang J X, Li C L, et al. Optimization of ultrasonic-assisted extraction process of ergosterol from *Flammulina velutipes* and its determination by HPLC [J]. *Science and Technology of Food Industry*, 2017, 38(23) : 192–197(in Chinese with English abstract) .
- [8] 谢翎, 陈红梅, 陈安徽, 等. 超声波破碎法提取球孢白僵菌麦角甾醇的条件优化研究 [J]. *徐州工程学院学报*, 2007, 22(2) : 10–13.
Xie L, Chen H M, Chen A H, et al. Study of the optimization conditions for the extraction of ergosterol from *Beauveria bassiana* by using ultrasonic [J]. *Journal of Xuzhou Institute of Technology*, 2007, 22(2) : 10–13(in Chinese with English abstract) .
- [9] 董笑菲. HPLC 法测定发酵冬虫夏草菌丝粉中麦角甾醇的含量 [J]. *现代食品*, 2019(18) : 154–157.
Dong X F. Determination of ergosterol in fermented *Cordyceps sinensis* mycelial powder by HPLC [J]. *Modern Food*, 2019(18) : 154–157(in Chinese with English abstract) .
- [10] 吴志明, 李昆太. 水稻纹枯病的危害及其微生物防治概述 [J]. *生物灾害科学*, 2018, 41(2) : 81–88.
Wu Z M, Li K T. The damage of rice sheath blight and its microbial control [J]. *Biological Disaster Science*, 2018, 41(2) : 81–88(in Chinese with English abstract) .
- [11] 谭一罗, 杨和川, 苏文英, 等. 金针菇活性成分及药理活性研究进展 [J]. *江苏农业学报*, 2018, 34(5) : 1191–1197.

- Tan Y L, Yang H C, Su W Y et al. Research progress on bioactive composition and pharmacological activity of *Flammulina velutipes* [J]. Jiangsu Journal of Agricultural Sciences, 2018, 34(5) : 1191-1197(in Chinese with English abstract) .
- [12] 李治建, 古力娜·达吾提, 斯拉甫·艾白, 等. 高效液相色谱法分析红色毛癣菌麦角甾醇的含量 [J]. 石河子大学学报(自然科学版), 2009, 27(1) : 73-76.
- Li Z J, Gulina D, Silapu A, et al. Determination of ergosterol in mycelium of *Trichophyton rubrum* by high performance liquid chromatography [J]. Journal of Shihezi University(Natural Science), 2009, 27(1) : 73-76(in Chinese with English abstract) .
- [13] Heleno S A, Diz P, Prieto M A, et al. Optimization of ultrasound-assisted extraction to obtain mycosterols from *Agaricus bisporus* L. by response surface methodology and comparison with conventional Soxhlet extraction [J]. Food Chemistry, 2016, 197: 1054-1063.
- [14] 易承学, 童珊珊, 徐希明, 等. HPLC 法同时测定金针菇中麦角甾醇和 22, 23-二氢麦角甾醇的含量 [J]. 江苏大学学报(医学版), 2014, 24(2) : 126-128.
- Yi C X, Tong S S, Xu X M, et al. High performance liquid chromatography for simultaneous determination of ergosterol and 22, 23-dihydroergosterol in *Flammulina velutipes* [J]. Journal of Jiangsu University(Medicine Edition), 2014, 24(2) : 126-128(in Chinese with English abstract) .
- [15] 高虹, 谷文英, 丁霄霖. 利用微波辅助提取测定姬松茸中麦角甾醇含量 [J]. 浙江大学学报(农业与生命科学版), 2007, 33(1) : 113-118.
- Gao H, Gu W Y, Ding X L. Optimization of microwave-assisted extraction for determination of ergosterol in *Agaricus brasiliensis* [J]. Journal of Zhejiang University(Agriculture and Life Sciences), 2007, 33(1) : 113-118(in Chinese with English abstract) .

责任编辑: 夏爱红

《南京农业大学学报》第九届编辑委员会

顾 问: 盖钧镒 万建民

主任委员: 陈发棣

副主任委员: 丁艳锋 沈其荣 沈 波

委 员: (以姓氏笔画为序)

丁艳锋 王丽平 王秀娥 王源超 叶永浩 兰叶青 朱 艳 朱伟云
刘凤权 刘文斌 刘永杰 刘红林 刘泽文 刘 斐 刘裕强 刘 蓉
刘满强 李 英 李春保 李 艳 李祥瑞 吴 磊 杨 红 杨晓静
汪小昆 沈 波 沈文飏 沈其荣 沈明霞 沈振国 张正光 张红生
张绍铃 陈发棣 周立祥 周光宏 郑永华 赵方杰 胡水金 柳李旺
姜 东 洪晓月 徐国华 高 峰 高志红 郭世荣 郭旺珍 陶小荣
曹瑞兵 崔中利 章元明 章文华 屠 康 强 胜

主 编: 沈其荣

副 主 编: 陈发棣 丁艳锋 沈 波(常务)

南京农业大学学报

Nanjing Nongye Daxue Xuebao

1956年9月创刊

第44卷 第6期 2021年 双月刊

JOURNAL OF NANJING
AGRICULTURAL UNIVERSITY

Started in 1956

Bimonthly, Vol. 44 No. 6 2021

主管单位 中华人民共和国教育部
主办单位 南京农业大学
主 编 沈其荣
编辑出版 《南京农业大学学报》编辑部
地 址 南京市卫岗1号, 210095
电 话 (025) 84395214
电子信箱 nauxb@njau.edu.cn
网 址 <http://nauxb.njau.edu.cn>
印刷单位 江苏省地质测绘院
发行范围 公开发行
国内发行 江苏省邮政局
国外发行 中国国际图书贸易总公司
订 阅 全国各地邮政局

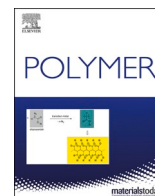
Administrated by Ministry of Education, P. R. China
Sponsored by Nanjing Agricultural University
Chief Editor: Shen Qirong
Edited and Published by Editorial Department of Journal of
Nanjing Agricultural University
Address: No. 1 Weigang, Nanjing 210095 Jiangsu, China
Tel: +86-25-84395214
E-mail: nauxb@njau.edu.cn
Web Site: <http://nauxb.njau.edu.cn>
Printed by Jiangsu Geologic Surveying and Mapping Institute
Distributed Abroad by International Book Trading Corporation
P. O. Box 399, Beijing, P. R. China

中国标准连续出版物号: ISSN 1000-2030 国内邮发代号: 28-53
CN 32-1148/S 国外发行代号: Q5785

2021年11月30日出版 定价: 20.00元

ISSN 1000-2030





Reprocessability of dynamic polydioxaborolane networks activated by heat, moisture and mechanical force

Yufeng Lei^a, Anqiang Zhang^{a,*}, Yaling Lin^{b,**}

^a Department of Polymer Science and Engineering, School of Materials Science and Engineering, South China University of Technology, 381 Wushan Rd, Guangzhou, 510640, Guangdong, China

^b College of Materials and Energy, South China Agricultural University, 483 Wushan Rd., Guangzhou, 510642, Guangdong, China

ARTICLE INFO

Keywords:

Covalent adaptive network
Dioxaborolane metathesis
Vitrimers
Mechanochemistry
Reprocessing

ABSTRACT

Covalent adaptive networks have shown great potential in sustainable crosslinked polymer materials. The incorporation of reversible covalent bonds also brings many possibilities for the material processing and recycling. Herein, we designed a polydioxaborolane network (PDOB) with abundant boronic-ester linkages. PDOBs showed tunable mechanical properties and viscoelasticity from highly stretchable elastomer to rigid thermoset by varying the composition. The dynamic dioxaborolane metathesis and reversible hydrolysis/rebinding of boronic-esters endowed PDOBs with remarkable reprocessability with the assistance of heat or moisture. Furthermore, the theoretical topology freezing transition temperature (T_v) of PDOBs was calculated to be below their glass transition temperature (T_g). We investigated the reprocessability of PDOBs at different temperature and found that PDOBs could be remolded at a temperature window between T_v and T_g even without the participation of water. The compressive force could break the reversible linkages into reactive sites, as well as promote exchange reactions, which subsequently facilitated interfacial integration.

1. Introduction

Today's increasing demand for sustainable high-performance polymer materials has motivated researchers to combine the facile processability of thermoplastics and the performance advantages of thermosets with permanent crosslinking networks. To create a reversible crosslinked polymer network has become a fashionable strategy [1,2]. These crosslinks can exchange or dissociate/reform under certain conditions, resulting topology rearrangements and macroscopic flow. Reversible interactions have been chosen from a wide variety of non-covalent interactions (such as hydrogen bonds [3–5], metal-ligand coordination [6–8], π - π stacking [9], ionic interaction [10], etc.) and reversible covalent bonds (such as disulfides [11–13], Diels-Alder adducts [14,15], imines [16–18], boronic esters [19–23], etc.). In general, reversible covalent bonds have higher strength and longer lifetime than non-covalent interactions, and have been reported to create covalent adaptive networks (CANs) with promising mechanical performance [20,21,23].

The incorporation of reversible covalent linkages brings many possibilities to the reprocessing and recycling of adaptive crosslinked polymers. The first change takes place in the response of CANs to

reactive stimuli, such as light [24–26], water [17,27,28], etc. Moisture usually leads to a dissociating/rebinding pathway of reprocessing for CANs with water-sensitive bonds, such as boronic-esters [22,28], imines [18], etc. Sumerlin and coworkers have demonstrated that in their boronic-esters network, application of a thin layer of water to the freshly cleaved surfaces facilitated bond exchange and increased the efficiency of healing [28].

More importantly, in CANs, the viscoelastic response to temperature has been found to be controlled by the reversible chemistry. Different from water or light, heat usually works in multiple ways. Firstly, heating always accelerates chain diffusion and reversible reactions. For dissociative linkages like Diels-Alder adducts and alkoxyamines, heating would induce network de-crosslinking [29], leading to a dissociating/rebinding pathway of reprocessing. In more cases with respect to dynamic exchangeable linkages like imines [16], boronic esters [21], vinylogous urethanes [30,31], heating would speed up exchange reactions, leading to a network reconfiguration without loss of overall connectivity. Leibler and coworkers have proposed a topology freezing transition temperature (T_v) in their study of a special type of CANs, so-called vitrimers [32].

* Corresponding author.

** Corresponding author.

E-mail addresses: aqzhang@scut.edu.cn (A. Zhang), linyaling@scau.edu.cn (Y. Lin).

<https://doi.org/10.1016/j.polymer.2020.123037>

Received 8 July 2020; Received in revised form 15 August 2020; Accepted 11 September 2020

Available online 16 September 2020

0032-3861/© 2020 Elsevier Ltd. All rights reserved.

In a recent review, vitrimers has been defined as permanently crosslinked polymers with dynamic covalent bonds that allow the network to change its topology while maintaining a constant number of chemical bonds in the system at all temperature below degradation [33]. Associative dynamic covalent chemistries have been expected to meet the requirement of stability in crosslinking density. In associative systems, the network rearrangement can be achieved through an addition/elimination pathway, forming a more crosslinked intermediate state [34]. Dynamic transesterification of β -hydroxyl esters has been employed by many studied to in epoxy networks [32,35–37]. Recently, Yue and coworkers described a simple ball-mill processing to convert thermoset polymers into vitrimers [37]. Dynamic boronic-ester features another typical bond for the construction of vitrimer network. Du and coworkers reported a boronic-ester-containing poly(butyl methacrylate) network and modulated its dynamic properties by introducing diols [38]. Nicolaÿ incorporated dynamic dioxaborolane into commercial HDPE by reactive extrusion with a designed dioxaborolane-nitroxide compound [39].

The introduction of dynamic chemistries brings great changes to vitrimers' viscoelastic behaviour. For vitrimers to flow, the networks require enough energy to both break the physical hindrance against segmental motion and to activate reactions between crosslinks. The former corresponds to the glass transition temperature (T_g) of polymers, while the latter causes vitrimers to present a new transition temperature (T_v) for network topology. The relative magnitude of T_g and T_v dictates CANs' viscoelastic response to heat in different temperature ranges [2]. As a result of the viscoelasticity changes brought by the reversible reactions, reprocessing and recycling of CANs are directly enabled in bulk state [17,20,22,37,39]. Firstly, CANs' malleability can be thermally triggered and versatile shapes based on these materials can be easily achieved. Moreover, these networks for recycling can be ground and remolded at the temperature that provides enough reactivity. The reprocessing temperature is usually set higher than the material's T_g and T_v to facilitate the interfacial chain diffusion and to accelerate the dynamic reactions.

Overall, previous researches have shown that the reprocessability and recyclability of CANs can be activated under conditions where reversible reactions are able to proceed. These conditions commonly include temperature higher than the CANs' T_v . It suddenly becomes interesting to us whether reversible chemistry could be activated at a temperature above a CAN's T_v yet below its T_g . The previously mentioned water-induced dissociating/rebinding pathway could be included in this context, because hydrolysis at the first step would free interfacial polymer chains from the glassy state and create reactive sites for rebinding [23]. Recent studies have also revealed the activation of solid-state reversible reactions by mechanical force [16,40,41]. Our previous work reported that dynamic imine reactions were found to restore the polyimine networks integrity after the applied deformation without the participation of water or heat [16]. Recently, Konkolewicz and coworkers reported that the compressive force could lead to a greater self-healing by reducing activation energy barrier for dynamic chemistry [40]. Although the mechanical activation was achieved in rubbery state (above their T_g), such phenomenon has also been reported in few cases where the vitrimers are in glassy state. Ma and coworkers described an imine-based vitrimer with high glass transition temperature (T_g) of 172 °C could significantly creep under constant load at relatively low temperature of around 70 °C, which was induced by the mechanically activated reversible imine chemistry [42].

Based on these findings, we anticipated that mechanical force could be useful to reprocess CANs at a moderate temperature even lower than their T_g . Although the network chain mobility would be very limited in the glassy state, the interfacial rebinding might still be able to take place when the surface reactivity is activated by mechanical force. In this work, we synthesized a CAN based on abundant dioxaborolanes using small-molecular diols and boronic acids. Dioxaborolanes could undergo dissociation/reformation as well as metathesis at ambient conditions.

The reprocessability of polydioxaborolane networks were investigated under the stimuli of heat or moisture, and of the compressive force at different temperature ranges with respect to their T_v and T_g .

2. Experimental

2.1. Materials

Divinyldimethylsiloxane (MM^{Vi} , 97%) and 1,3,5,7-Tetravinyl-1,3,5,7-tetramethylcyclotetrasiloxane (D_4^{Vi} , 95%) were supplied by Hubei Xinmingtai Chemical Co. Ltd. (Wuhan, China). 2,2-Dimethoxy-2-phenylacetophenone (DMPA, 99%), 1-thioglycerol (95%) and 1,4-benzenediboronic acid (BDBA, 97%) were purchased from Shanghai Macklin Biochemical Co., Ltd. (Shanghai, China). Tetrahydrofuran (THF), chloroform and hexane were analytical grade and purchased from Guangzhou Chemical Reagent Factory (Guangzhou, China). All the chemicals and solvents were used as-received.

2.2. Characterization

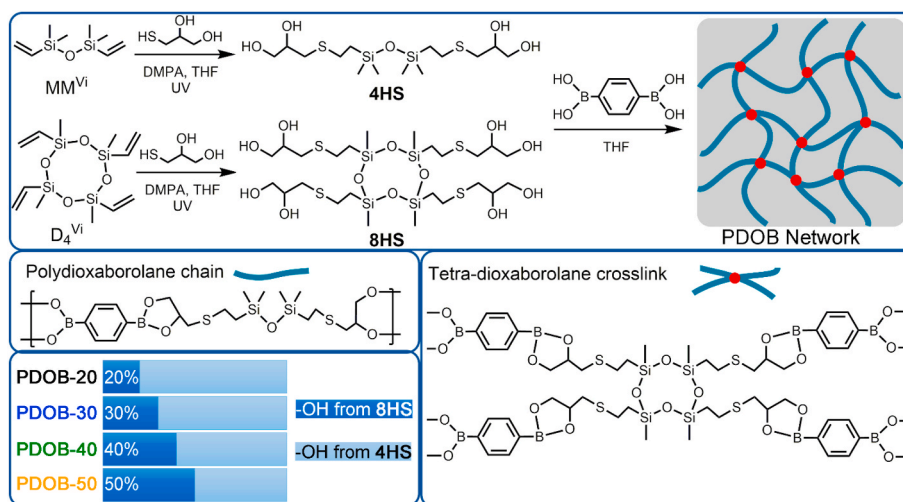
The detailed characterization methods are described in Part S1 of Supporting Information (SI).

2.3. Synthesis of polydioxaborolane networks (PDOBs)

Firstly, multi-hydroxyl siloxanes were facilely synthesized via the thiol-ene "click" reaction between vinylsiloxanes (MM^{Vi} or D_4^{Vi}) and 1-thioglycerol (Scheme 1). To obtain tetra-hydroxyl disiloxanes (**4HS**), MM^{Vi} (1.86 g, 10 mmol), 1-thioglycerol (2.38 g, 22 mmol) and DMPA (0.01 g, 0.04 mmol) were dissolved in THF (20 mL) and added to a quartz RB flask. The mixture was exposed to 365 nm UV (OPTIMAX-365, Spectronics, USA) under constant stirring for 2 h at room temperature. The solvent was removed by rotary evaporation at 80 °C and 0.1 MPa. The resulting viscous liquid was washed five times with hexane. The crude product was re-dissolved in chloroform and washed three times with saturated sodium chloride solution. After removal of chloroform, the target product was obtained as colorless, viscous liquid. Yields: 93%. FT-IR (KBr, cm^{-1}): 3392, 2951, 2915, 2880, 1454, 1413, 1378, 1260, 1229, 1167, 1073, 882, 799. 1H NMR (DMSO- d_6 , 600 MHz, ppm): δ 0.02–0.12 (s, 6H, Si-CH₃), 0.79–0.86 (t, J = 8.6 Hz, 2H, Si-CH₂), 2.42–2.45 & 2.60–2.63 (m, 2H, S-CH₂-CH), 2.55–2.63 (t, J = 8.7 Hz, 2H, SiCH₂-CH₂-S), 3.33–3.35 (m, 2H, CH₂-OH), 3.52–3.57 (m, 1H, CH-OH), 4.53–4.55 (t, J = 5.7 Hz, 2H, CH₂-OH), 4.72–4.73 (d, J = 5.1 Hz, 1H, CH-OH). ^{13}C NMR (DMSO- d_6 , 600 MHz, ppm): δ 0.26–0.42 (s, Si-CH₃), 18.76 (s, SiCH₂CH₂S), 26.92 (s, Si-CH₂), 35.10 (s, SCH₂CH), 64.60 (s, CH₂OH), 71.41 (s, CHOH). HRMS (MeOH, m/z): for $C_{14}H_{34}NaO_5S_2Si_2^+$ [M+Na]⁺, calculated 425.1295, found 425.1284. The spectra are shown in Part S2, SI.

To obtain octa-hydroxyl cyclotetrasiloxanes (**8HS**), D_4^{Vi} (3.44 g, 10 mmol), 1-thioglycerol (4.76 g, 44 mmol) and DMPA (0.01 g, 0.04 mmol) were used and the same synthesis procedure as **4HS** was followed. **8HS** was obtained as colorless, viscous liquid. Yields: 90%. FT-IR (KBr, cm^{-1}): 3376, 2952, 2913, 2882, 1410, 1335, 1253, 1161, 1063, 884, 840, 799, 700. 1H NMR (DMSO- d_6 , 600 MHz, ppm): δ 0.12–0.14 (s, 3H, Si-CH₃), 0.84–0.85 (t, J = 3.6 Hz, 2H, Si-CH₂), 2.41–2.47 & 2.60–2.63 (m, S-CH₂-CH), 2.56–2.59 (t, J = 12 Hz, 2H, SiCH₂-CH₂-S), 3.33–3.35 (m, 2H, CH₂-OH), 3.54 (d, 1H, CH-OH), 4.53–4.55 (t, J = 5.6 Hz, 1H, CH₂-OH), 4.71–4.72 (d, J = 5.1 Hz, 1H, CH-OH). ^{13}C NMR (DMSO- d_6 , 600 MHz, ppm): δ -0.57 (s, Si-CH₃), 17.62 (s, SiCH₂CH₂S), 25.56–26.77 (s, Si-CH₂), 35.08 (s, SCH₂CH), 64.57 (s, CH₂OH), 71.38 (s, CHOH). HRMS (MeOH, m/z): for $C_{24}H_{56}NaO_{12}S_4Si_4^+$ [M+Na]⁺, calculated 799.1595, found 799.1635. The spectra are shown in Part S2, SI.

Secondly, polydioxaborolane networks were prepared through a simple procedure: **4HS** and **8HS** were dissolved in THF and then mixed with BDBA/THF solution. The molar ratio between boronic acid groups and the total hydroxyls was kept 1/2 in the mixture, yet the percentage



Scheme 1. Synthesis of polydioxaborolane networks.

of hydroxyls from **8HS** (the crosslinker) was in the range of 20%–50%. After 1 h stirring, the solvent was evaporated at 60 °C. After dried at 60 °C under vacuum for 24 h, the polydioxaborolanes were obtained as colourless transparent solids. The resulting solids were hot-pressed at 120 °C into sheets for testing.

2.4. Reprocessing of PDOB networks

Prior to reprocessing at different conditions, PDOBs were finely cut and dried at 60 °C/0.001 atm for 24 h.

For hot pressing (HP), the PDOB shards were pressed at 120 °C and 20 MPa for 10 min to yield a uniform sheet.

For moisture-assisted pressing (MP), the PDOB shards were kept in a sealed container with saturated potassium sulfate solution to provide a constant 90% relative humidity (RH) at 25 °C for 3 d. The moistened PDOBs were then pressed at 25 °C and 10 MPa for 5 min to yield a uniform sheet. The products were then dried at 60 °C for 24 h.

For cold pressing (CP), the dry PDOB shards were directly pressed at 25 °C, 40% RH and 30 MPa for 12 h.

3. Results and discussion

3.1. Structure of polydioxaborolane networks (PDOBs)

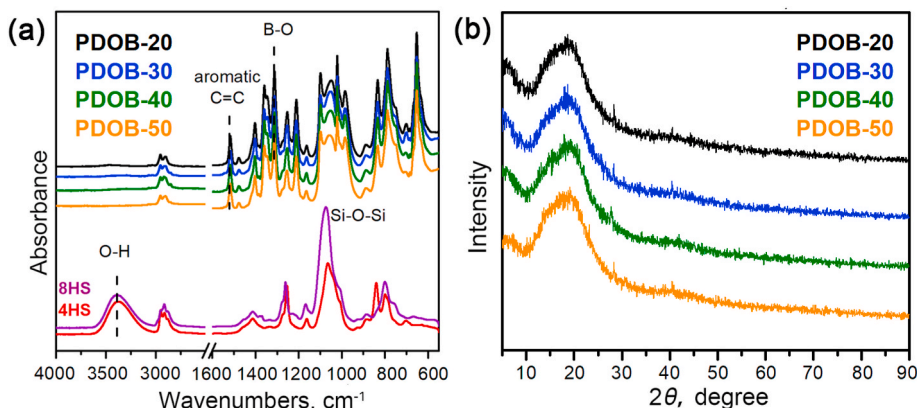
The PDOBs are prepared with varying **4HS/8HS** contents, and denoted as “PDOB-*x*” where *x* represents the percentage of hydroxyls from **8HS** (Scheme 1). Formation of polydioxaborolane networks was

confirmed by FTIR-ATR spectroscopy (Fig. 1-a). The broad absorbance of O-H stretching in **4HS** and **8HS** at 3395 cm⁻¹ disappeared in PDOBs, which suggests the complete consumption of hydroxyl groups by the esterification with boronic acids. New absorbances corresponding to B-O stretching in dioxaborolanes and the aromatic C=C stretching appeared at 1313 cm⁻¹ and 1517 cm⁻¹, respectively, which are similar to the reported values [19,38]. X-ray diffraction (XRD) patterns (Fig. 1-b) demonstrated a general amorphous phase structure of PDOBs with no sharp diffraction peak of crystalline microphase detected. This also suggests that no residual unreacted BDPA was separated out in the bulk during the evaporation of solvents.

3.2. Thermal properties of PDOBs

Differential scanning calorimetry (DSC) curves (Fig. 2-a) also indicated that PDOBs were amorphous with no presence of crystallizing/melting peaks. Glass transition temperatures (*T_g*) for PDOBs were found to increase from 16 to 37 °C with the content of tetra-dioxaborolane crosslinks. Thermal gravimetric analysis (TGA) was performed to study PDOBs’ thermostability. As shown in Fig. 2-b, for PDOBs with different compositions, their thermal gravimetric profiles were similar with two thermal degradation stages around 370 °C and 520 °C, respectively. The first stage corresponded to the degradation of the polar moieties of dioxaborolanes and thioethers, and the second stage corresponded to the cleavage of siloxanes.

As previously mentioned, both the topology freezing transition (*T_v*) and glass transition (*T_g*) control the viscoelastic flow for CANs.

Fig. 1. Structure characterization of PDOBs: (a) FTIR-ATR spectra of **4HS**, **8HS** and PDOBs; (b) X-ray diffraction patterns of PDOBs.

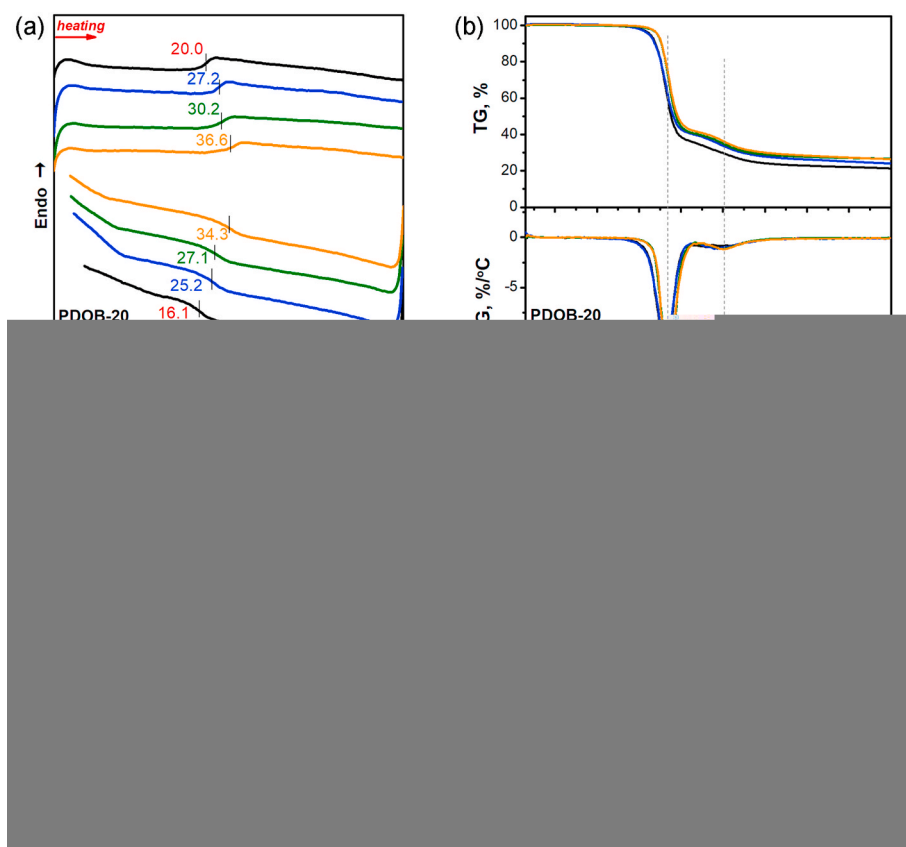


Fig. 2. Thermal properties of PDOBs: (a) DSC curves, (b) TG and DTG curves, (c) thermal expansion profiles and (d) shear stress relaxation of PDOB-30 at different temperatures. A constant 10% shear strain was applied. (e) the relationship between PDOB-30's characteristic relaxation time (τ) and temperature followed Arrhenius Law.

Therefore, it is important to determine the relative magnitude of T_v and T_g . Firstly, when T_v is higher than T_g , a two-stage thermal expansion can be observed by dilatometric measurements [32]. As shown by Fig. 2-c, however, the thermal expansion curves for PDOBs only showed single transition over the test temperature range of -75 °C– 150 °C. The transition temperatures of PDOBs were close to their T_g (Fig. 2-a) and increased with the crosslinking densities. Besides, a smaller expansion coefficient could be observed for PDOB with more crosslinks, as a result of the greater hindrance against segmental movement.

In the case that T_v is lower than T_g , T_v is only a hypothetical parameter, and by convention, considered as the temperature at which the CANs' viscosity reaches 10^{12} Pa s. The theoretical T_v can be calculated via extrapolation of stress relaxation experiments [2]. The example of PDOB-30 is presented in Fig. 2-d&e. The characteristic relaxation time (τ , $G_\tau = G_0/e$) followed Arrhenius relationship (Eq. (1)) with temperature.

$$\ln(\tau) = \ln(\tau_0) + \frac{E_a}{RT} \quad (1)$$

The apparent activation energy (E_a) was calculated to be approx. 88 kJ/mol, which is close to the reported values of dioxaborolane networks [21]. The T_v for PDOB-30 was extrapolated from the Arrhenius plot to yield a value of -16 °C, which was below its T_g at approx. 26 °C. For PDOB-50, the calculated E_a and T_v were approx. 93 kJ/mol and 29 °C, respectively. The detailed calculation is described in Part S3, SI. The stress relaxation of PDOB-30 also developed more rapidly than that of PDOB-50, due to its comparatively lower degree of crosslinking (Fig. S4, SI).

Rheological dynamic temperature sweeps were conducted to show the temperature dependency of PDOBs' viscoelasticity during a successive cooling and heating process. As shown in Fig. 3, the modulus curves

over cooling and heating are highly overlapping, indicating their reversible viscoelastic response to temperature changing. A sharp change in modulus occurred to PDOBs near their respective glass transition temperatures, which has been confirmed in previous DSC results (Fig. 2-a). Over a wide temperature range higher than their T_g , PDOBs exhibited rubbery elasticity with G' greater than G'' at the shear frequency of 1 Hz. The storage modulus (G') for PDOBs kept a stable plateau during heating or cooling, which indicated the thermostability of crosslink density of the reactive PDOB networks. This could be explained by the fact that the dioxaborolane metathesis proceeded without changing the overall connectivity and functionality [34]. Using the plateau storage modulus (G'_p) at 120 °C, the average molecular weight of network chain between two crosslinks (M_c) could be calculated from Eq. (2):

$$G'_p = \frac{\rho RT}{M_c} \quad (2)$$

where ρ is the sample's density, R is gas constant. As listed in Table 1, the density of PDOBs were measured to be approx. 1.18 g/cm³, which is similar to polymethylphenylsiloxanes. The calculated M_c decreased from 4.8 kg/mol to 1.3 kg/mol with the increasing feed of 8HS, indicating that more crosslinks were formed in PDOB networks.

3.3. Tensile properties of PDOBs

Tensile properties of PDOBs were highly determined by their composition. Fig. 4-a shows the tensile stress-strain curves of PDOBs at 25 °C. The tensile profile of PDOB-20 exhibited as a very stretchable crosslinked elastomer with a breaking strain over 700%. For PDOB-30–50, the test temperature was below their T_g . PDOB-50 was stiff and

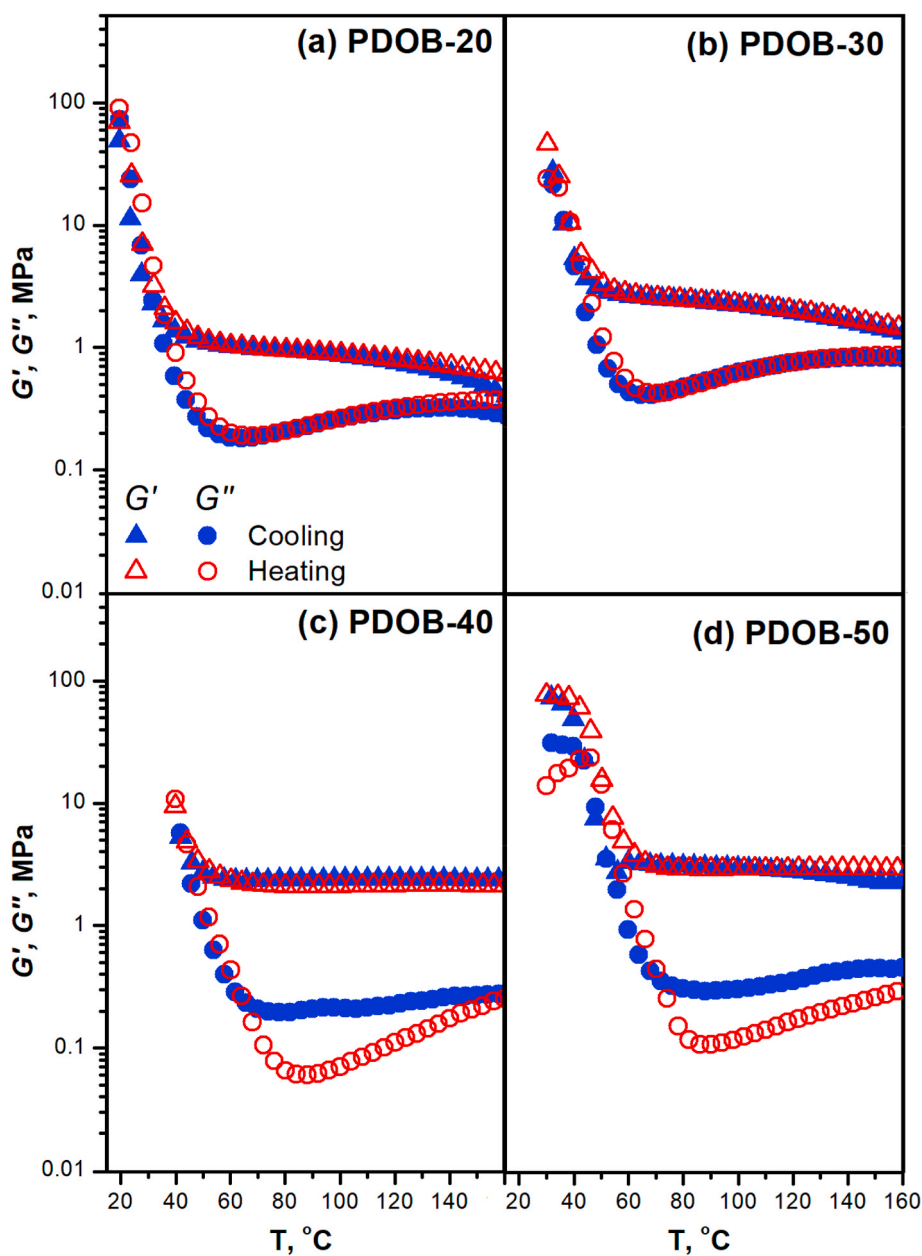


Fig. 3. Temperature dependency of G' and G'' for PDOBs.

Table 1

Density and calculated M_c of PDOBs.

Sample	ρ , g/cm ³	G'_p , MPa	M_c , kg/mol
PDOB-20	1.17	0.80	4.8
PDOB-30	1.18	1.99	1.9
PDOB-40	1.18	2.12	1.8
PDOB-50	1.18	2.94	1.3

very brittle. The Young's modulus was measured to be 535 MPa, with a tensile strength of 30.0 MPa and strain at break of 12%. The tensile properties of PDOBs are listed in Table 1. The modulus of toughness is calculated as the area under the stress-strain curves of PDOBs between the yield point and breaking point. With fewer crosslinks, PDOB-30 and PDOB-40 showed evident yield and continuous plastic elongation before break, which suggests that some dioxaborolane linkages were broken at the yield point and the networks were subjected to flow. However,

instead of fracture, the networks continued to extend and restore the tensile stress, which is presumably to result from the associative restoration of network connectivity under strain. This behaviour is similar to the reported non-covalently crosslinked networks [43, 44]. Compared with PDOB-50, the modulus of toughness of PDOB-30 and PDOB-40 are remarkably improved. Additionally, temperature impacts PDOBs' mechanical properties profoundly. Fig. 4-b shows PDOB-30's tensile stress-strain profile at different temperatures. Considering PDOB-30's T_g at approximately 27 °C, the tensile stress-strain curves at 35–55 °C developed like crosslinked elastomer. When stretched at a higher temperature, it showed a lower tensile strength and a longer strain at break (Table 2), which has been reported to result from its accelerated network reconfiguration [16,45]. Although PDOB-30 showed a large elongation at break when heated above the T_g , its modulus of toughness did not increase at the rubbery state. It became apparently soft and ductile. This suggests that the internal reactivity is greatly released once the chain mobility is thermally enabled.

Cyclic stress-strain curves of PDOB-30 and PDOB-50 are presented in

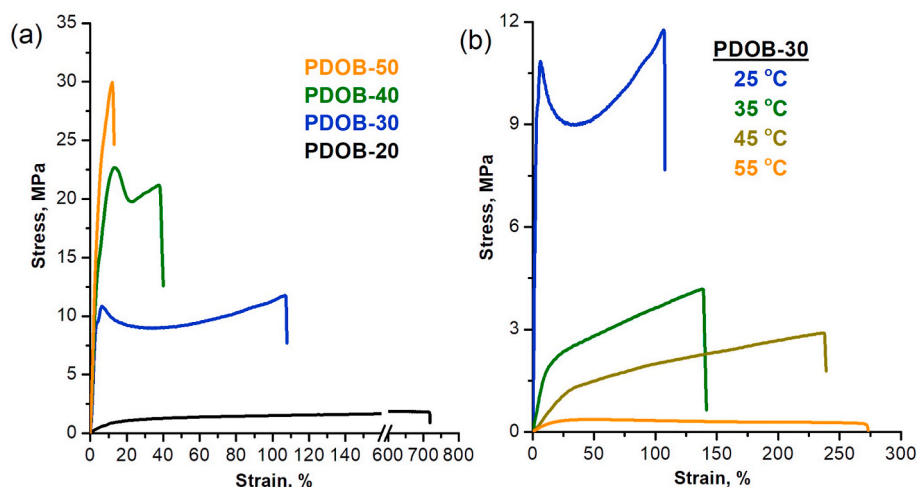


Fig. 4. (a) Tensile stress-strain curves of PDOBs at 25 °C. (b) Tensile stress-strain curves of PDOB-30 at different temperatures. The tensile rate was 100 mm/min.

Table 2

Tensile properties of PDOBs. (100 mm/min tensile rate).

Sample	T, °C	Young's Modulus, MPa	Tensile Strength, MPa	Strain at Break, %	Modulus of Toughness, MPa
PDOB-20	25	11.4 ± 0.41	1.81 ± 0.12	717 ± 11.0	1272 ± 61
PDOB-30	25	298 ± 1.33	11.8 ± 0.38	107 ± 9.9	995 ± 77
PDOB-40	25	406 ± 1.68	22.7 ± 0.27	38.0 ± 7.6	520 ± 83
PDOB-50	25	535 ± 1.83	30.0 ± 0.67	12.0 ± 2.1	200 ± 41
PDOB-30	35	18.3 ± 0.64	4.23 ± 0.10	139 ± 8.1	210 ± 48
PDOB-30	45	3.98 ± 0.05	2.91 ± 0.11	237 ± 7.8	401 ± 19
PDOB-30	55	2.57 ± 0.24	0.25 ± 0.07	269 ± 8.2	80 ± 21

Fig. 5. PDOBs exhibited accumulation of plastic deformation under the continuous loading-unloading cycles. Evident energy dissipation and relatively high residual strain were observed after the first cycle, while the following loading-unloading curves showed very similar hysteresis. For PDOB-30 being stretched beyond its yield point to a 50% strain, permanent deformation occurred in each following cycle, which suggests that the network was able to reconfigure after the initial damage. This kind of mechanically induced reactivity could even proceed at a small strain of only 10% (Fig. 5-b). For PDOB-50 being stretched to 10% strain, it showed well-overlapped loading-unloading loops in the 3rd – 5th cycles, indicating the rigid network could not effectively reconfigure

after the initial activation due to the limited mobility.

3.4. Reprocessability of PDOBs

CANs based on reversible dioxaborolanes have been mostly reported to be reprocessed with the involvement of heat or water [20–22]. Reprocessing at elevated temperature higher than CANs' T_g and T_v is a common strategy for numerous CANs, because heat not only promotes interfacial chain diffusion, but also speeds up reactions for network reformation. Although dynamic dioxaborolane metathesis is readily to take place at room temperature [28], heating usually helps to achieve better performance for reprocessed CANs. For reprocessing networks based on boronic-esters, water usually brings reactive boronic acid groups and diols on the surface via hydrolysis [22,28]. These reactive sites can facilitate a better re-binding between the interfaces, and the water by-product can be removed by additional drying.

PDOBs of different contents showed excellent reprocessability with the assistance of heat, owing to the dioxaborolane metathesis at dry conditions [21], as schematically illustrated in Fig. 6-a. Tensile properties of PDOB-30 and PDOB-50 that were reprocessed by hot-pressing (HP) for three times are shown in Fig. 6-b&c. The Young's modulus and tensile strength of reprocessed samples were similar to the pristine values. It is interesting to find out that the reprocessed PDOB-30 showed approx. 50% increase in strain at break. Similar cases of CANs have been also reported to result from the factor that the re-hot-pressing is helpful for relieving internal stress and eliminating micro-defects in the networks [16,45]. We considered the restoration efficiency of different reprocessing conditions as the modulus of toughness ratio of the reprocessed sample to the pristine sample. The results are calculated and listed in Table 3. It can be seen that both PDOB-30 and PDOB-50 are

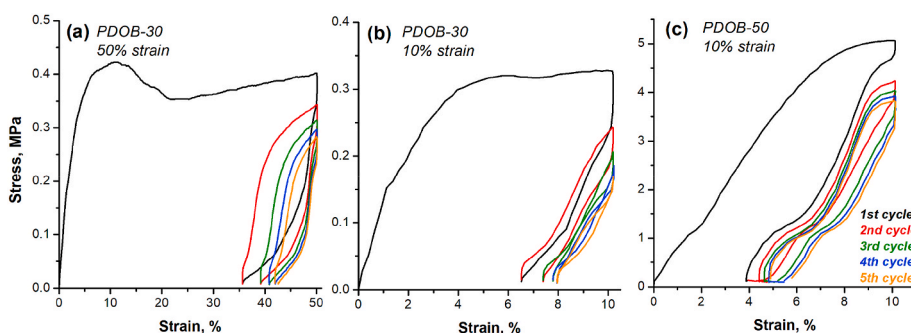


Fig. 5. Cyclic tensile curves of PDOBs: (a) PDOB-30 at 50% strain, (b) PDOB-30 at 10% strain and (c) PDOB-50 at 10% strain.

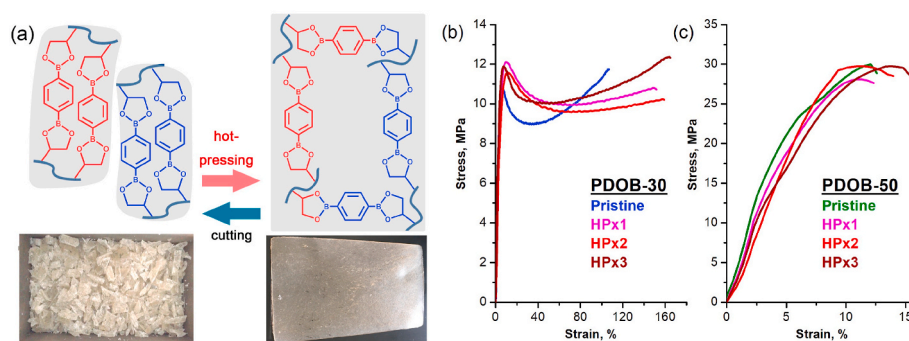


Fig. 6. Reprocessing PDOBs by hot-pressing: (a) Network reformation of PDOB via dioxaborolane metathesis. Insert photograph shows the cut and HP-reprocessed sample of PDOB-40. Tensile stress-strain curves of (b) HP-reprocessed PDOB-30 and (c) HP-reprocessed PDOB-50.

remarkably improved by hot-pressing in terms of tensile toughness with their larger elongation at break.

PDOBs were able to absorb moisture when kept in a humid atmosphere. After 3 d storage in 25 °C and 90% relative humidity, water absorption of 23.98 mg/g and 20.63 mg/g was recorded for PDOB-30 and PDOB-50, respectively (Fig. S5, SI). A higher density of crosslinks was reasonably helpful to prevent the permeation of moisture. The absorbed water caused hydrolysis of dioxaborolanes, which was proven by the presence of the absorbance of O-H stretching in infrared spectra (Fig. S6, SI). The hydrolysis of PDOB networks compromised their tensile strength severely, as shown in Fig. 7-a. The moistened PDOB-30 was very ductile after yield point and stretched to the upper limit of the machine without break. Such plastic deformation has been reported in reversible networks that could re-associate under extension [16,28,44]. In moistened PDOB-30 network, chain mobility could be activated in the degenerated network, and the number of reactive sites increased. After removal of water at 60 °C/1 atm for 12 h, the tensile strength was partially restored. Moisture-assisted pressing (MP) followed a degenerating-reformation path of reprocessing. Fig. 7-b shows the tensile profiles of PDOB-30 reprocessed by moisture-assisted pressing. The strain at break for PDOB-30-MP was improved while the tensile strength decreased very slightly. We can also observe an evident improvement in tensile toughness (Table 3) in PDOB-30-MP samples. The participation of both water and heat was very helpful for the recovery of integrity of PDOBs network. However, for PDOB-50, the moisture-assisted pressing could not effectively restore its network. As shown in Fig. 7-c, PDOB-50-MP only showed similar tensile profile at initial stretch (Young's modulus), while the tensile strength and strain at break were

significantly lower than the pristine ones. With the pressing temperature much below PDOB-50's T_g , the interfacial rebinding was still inefficient even with the pre-treatment of hydrolysis.

Mechanical force has also been reported to activate CANs' internal reactions by breaking their reversible linkages and creating reactive chain ends. We were interested in whether this effect could be used for reprocessing of CANs. Dry PDOB-30 shards were cold-pressed under 30 MPa at 25 °C for 3 min, and immediately took out and monitored by FTIR-ATR. As shown in Fig. 8-a, the first spectrum ($t = 0$) collected immediately after the 3 min cold-pressing showed a new distinctive absorbance at 3395 cm^{-1} of O-H stretching, which suggests dioxaborolane bonds were fractured by the applied compression. Moreover, this absorbance band vanished gradually with time elapsing. We compared the absorbance intensity (I) of O-H stretching at 3395 cm^{-1} with the unchanged absorbance of C-H stretching in $-\text{CH}_3$ at 2953 cm^{-1} . Fig. 8-b shows that after the initial pressing, the ratio of $I(3395)/I(2953)$ decayed rapidly, indicating the fast re-binding of active moieties.

By extending the cold pressing time, PDOB-30 shards were able to be remolded to yield a uniform sheet in 12 h. The PDOB-30-CP showed comparable tensile profile to the pristine samples (Fig. 9-a), though slightly decrease in tensile strength was observed in the third cold-pressing. It should be noted that interfacial self-healing at 25 °C and 40% RH did not develop for PDOB-30 because it was in glassy state. However, it is interesting to notice that the cold-pressing temperature (25 °C) was higher than PDOB-30's T_g but lower than its T_v . For PDOB-50 whose calculated T_v (29 °C) was higher than 25 °C, cold pressing for 12 h still could not give rise to a smooth product (Fig. 9-d). The different results of cold-pressing on PDOB-30 and PDOB-50 suggest that CANs could be reprocessed at a temperature under their T_g , but above their T_v . To verify this point, we conducted the cold-pressing procedure at 35 °C for PDOB-50. The cold-pressed products were much improved as a bulk material. The tensile strength of PDOB-50-CPs was restored to approx. 70% of pristine value (Fig. 9-b). In terms of restoration in tensile toughness, both PDOB-30 and PDOB-50 showed declined restoration efficiency in later CP-reprocessing cycles, which suggests defect regions increased in later reprocessed products. We infer that the special reprocessability of PDOBs come from i) the networks are based on abundant dynamic reversible dioxaborolane linkages; ii) the dimethylsiloxanes segments are flexible to enable temporary local mobility where the dioxaborolane bonds are fractured by mechanical force.

4. Conclusions

We synthesized a polydioxaborolane network containing abundant dynamic reversible dioxaborolane linkages (PDOBs). Their mechanical and viscoelastic properties could be tuned from highly stretchable elastomer to rigid thermoset by varying their crosslinking density. With the assistance of water or heat, PDOBs showed excellent reprocessability. Moreover, the theoretical value of topology freezing transition temperature (T_v) of PDOBs was calculated to be below their glass

Table 3
Modulus of toughness and restoration efficiency of reprocessed PDOBs.

Sample	PDOB-30		PDOB-50	
	Modulus of Toughness, MPa	Restoration Efficiency, %	Modulus of Toughness, MPa	Restoration Efficiency, %
Pristine	995 ± 77	/	200 ± 41	/
HP × 1	1475 ± 62	148	197 ± 28	98
HP × 2	1479 ± 58	149	205 ± 54	102
HP × 3	1693 ± 75	170	279 ± 65	139
MP × 1	1466 ± 45	147	N/A ^a	N/A ^a
MP × 2	1403 ± 53	141	N/A ^a	N/A ^a
MP × 3	1329 ± 36	134	N/A ^a	N/A ^a
CP × 1	989 ± 22	99	119 ± 10 ^b	60 ^b
CP × 2	978 ± 54	98	88 ± 4 ^b	44 ^b
CP × 3	591 ± 28	59	86 ± 9 ^b	43 ^b

^a. PDOB-50 could not be effectively reprocessed by moisture-assisted pressing. Fig. 6-c shows the PDOB-50-MP sample breaks at the initial strain region. Therefore, the modulus of toughness could not be calculated.

^b. PDOB-50-CP refers to the reprocessed PDOB-50 by cold-pressing at 35 °C.

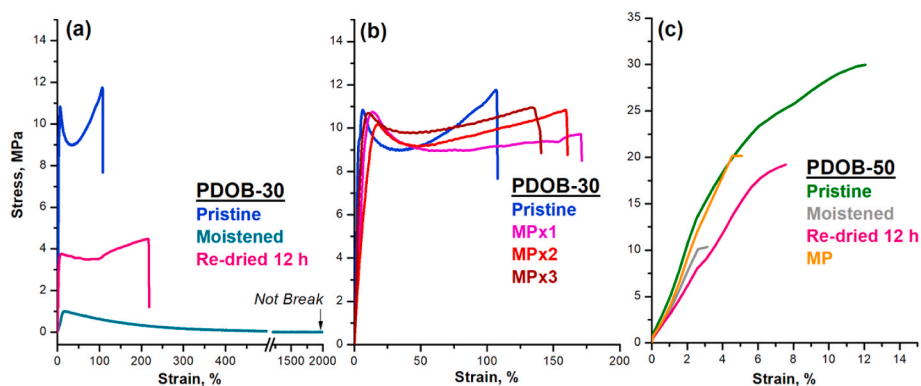


Fig. 7. Tensile stress-strain curves of moistened, re-dried and MP-reprocessed PDOBs: (a) & (b) PDOB-30, (c) PDOB-50.

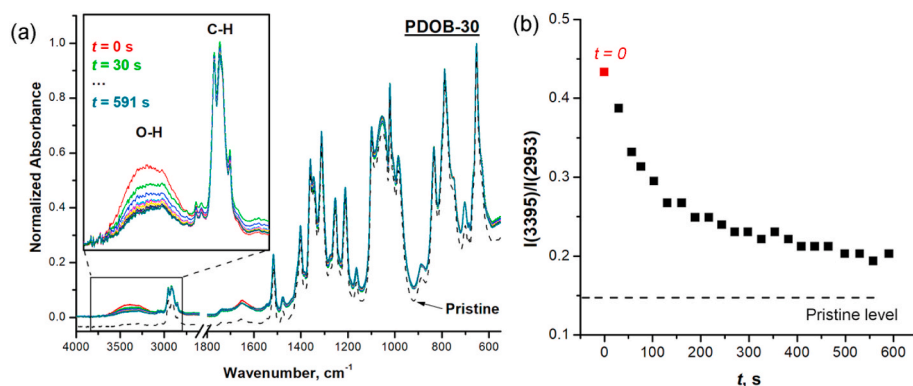


Fig. 8. (a) FTIR-ATR spectra of PDOB-30 collected every approx. 30 s after 3 min cold-pressing. Dash line shows the pristine spectrum for comparison. (b) the absorbance intensity ratio between O-H stretching at 3395 cm^{-1} and C-H stretching at 2953 cm^{-1} decayed with time elapsing.

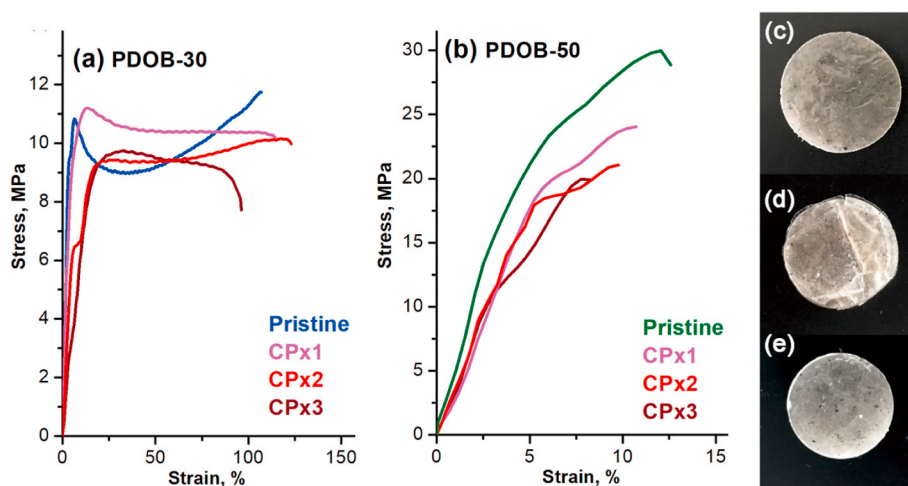


Fig. 9. Tensile profiles of (a) CP-reprocessed PDOB-30 at $25\text{ }^{\circ}\text{C}$ and (b) CP-reprocessed PDOB-50 at $35\text{ }^{\circ}\text{C}$. Photographs of CP-reprocessed (c) PDOB-30 at $25\text{ }^{\circ}\text{C}$, (d) PDOB-50 at $25\text{ }^{\circ}\text{C}$ and (e) PDOB-50 at $35\text{ }^{\circ}\text{C}$.

transition temperature (T_g). We further investigated the reprocessability of PDOBs at different temperature. It was interesting to find out that PDOBs could be re-molded at the temperature window below their T_g but above T_v , even without the assistance from water. The compressive force could break some dioxaborolane bonds, which caused the activation of interfacial rebinding. This mechanism could lead to a much facile reprocessing strategy of covalent adaptive networks.

CRediT authorship contribution statement

Yufeng Lei: Methodology, Data curation, Writing - original draft.
Anqiang Zhang: Conceptualization, Writing - review & editing, Supervision.
Yaling Lin: Writing - review & editing, Supervision.

Declaration of competing interest

The authors declare that they have no known competing financial

interests or personal relationships that could have appeared to influence the work reported in this paper.

Acknowledgements

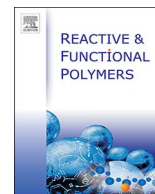
The authors gratefully acknowledge the financial support from the National Natural Science Foundation of China under grant number 51473051, 31772202; the Guangzhou Science and Technology Program key projects, China, under grant 201803020015.

Appendix A. Supplementary data

Supplementary data to this article can be found online at <https://doi.org/10.1016/j.polymer.2020.123037>.

References

- N.J. Van Zee, R. Nicolaÿ, Vitrimers: permanently crosslinked polymers with dynamic network topology, *Prog. Polym. Sci.* 104 (2020), 101233.
- Z.P. Zhang, M.Z. Rong, M.Q. Zhang, Polymer engineering based on reversible covalent chemistry: a promising innovative pathway towards new materials and new functionalities, *Prog. Polym. Sci.* 80 (2018) 39–93.
- L. Yang, Y. Lin, L. Wang, A. Zhang, The synthesis and characterization of supramolecular elastomers based on linear carboxyl-terminated polydimethylsiloxane oligomers, *Polym. Chem.* 5 (2014) 153–160.
- P. Cordier, F. Tournilhac, C. Soulié-Ziakovic, L. Leibler, Self-healing and thermoreversible rubber from supramolecular assembly, *Nature* 451 (2008) 977–980.
- Y. You, W. Huang, A. Zhang, Y. Lin, A facile and controllable synthesis of dual-crosslinked elastomers based on linear bifunctional polydimethylsiloxane oligomers, *J. Polym. Sci. Part A Polym. Chem.* 54 (2016) 3760–3768.
- Y. Lei, W. Huang, Q. Huang, A. Zhang, A novel polysiloxane elastomer based on reversible aluminum-carboxylate coordination, *New J. Chem.* 43 (2019) 261–268.
- Y. Lei, Q. Huang, S. Shan, Y. Lin, A. Zhang, A stretchable and rapidly self-healable polysiloxane elastomer based on reversible aluminum-amino coordination, *New J. Chem.* 43 (2019) 17441–17445.
- C.-H. Li, C. Wang, C. Keplinger, J.-L. Zuo, L. Jin, Y. Sun, P. Zheng, Y. Cao, F. Lissel, C. Linder, X.-Z. You, Z. Bao, A highly stretchable autonomous self-healing elastomer, *Nat. Chem.* 8 (2016) 618–624.
- S. Burattini, B.W. Greenl, D.H. Merino, W. Weng, J. Seppala, H.M. Colquhoun, W. Hayes, M.E. Mackay, I.W. Hamley, S.J. Rowan, A healable supramolecular polymer blend based on aromatic π - π stacking and hydrogen-bonding interactions, *J. Am. Chem. Soc.* 132 (2010) 12051–12058.
- Y. Peng, L. Zhao, C. Yang, Y. Yang, C. Song, Q. Wu, G. Huang, J. Wu, Super tough and strong self-healing elastomers based on polyampholytes, *J. Mater. Chem. A* 6 (2018) 19066–19074.
- Z.Q. Lei, H.P. Xiang, Y.J. Yuan, M.Z. Rong, M.Q. Zhang, Room-temperature self-healable and remoldable cross-linked polymer based on the dynamic exchange of disulfide bonds, *Chem. Mater.* 26 (2014) 2038–2046.
- H. Xiang, H. Qian, Z. Lu, M. Rong, M. Zhang, Crack healing and reclaiming of vulcanized rubber by triggering the rearrangement of inherent sulfur crosslinked networks, *Green Chem.* 17 (2015) 4315–4325.
- L. Imbernon, E.K. Oikonomou, S. Norvez, L. Leibler, Chemically crosslinked yet reprocessable epoxidized natural rubber via thermo-activated disulfide rearrangements, *Polym. Chem.* 6 (2015) 4271–4278.
- Y. Zhang, A.A. Broekhuis, F. Picchioni, Thermally self-healing polymeric materials: the next step to recycling thermoset polymers? *Macromolecules* 42 (2009) 1906–1912.
- S. Yu, R. Zhang, Q. Wu, T. Chen, P. Sun, Bio-Inspired high-performance and recyclable cross-linked polymers, *Adv. Mater.* 25 (2013) 4912–4917.
- Y. Lei, S. Shan, Y. Lin, A. Zhang, Network reconfiguration and unusual stress intensification of a dynamic reversible polyimide elastomer, *Polymer* 186 (2020), 122031.
- P. Taynton, K. Yu, R.K. Shoemaker, Y. Jin, H.J. Qi, W. Zhang, Heat-or water-driven malleability in a highly recyclable covalent network polymer, *Adv. Mater.* 26 (2014) 3938–3942.
- S. Zhao, M.M. Abu-Omar, Recyclable and malleable epoxy thermoset bearing aromatic imine bonds, *Macromolecules* 51 (2018) 9816–9824.
- S. Shan, Y. Lei, Y. Lin, A. Zhang, Slime-inspired crosslinked polysiloxanes networks based on reversible borate-hydroxyl complexes, *Polymer* 186 (2020), 122026.
- Y. Chen, Z. Tang, X. Zhang, Y. Liu, S. Wu, B. Guo, Covalently cross-linked elastomers with self-healing and malleable abilities enabled by boronic ester bonds, *ACS Appl. Mater. Interfaces* 10 (2018) 24224–24231.
- M. Röttger, T. Domenech, R. Van Der Weegen, A. Breuillac, R. Nicolaÿ, L. Leibler, High-performance vitrimers from commodity thermoplastics through dioxaborolane metathesis, *Science* 356 (2017) 62–65.
- C. Kim, H. Ejima, N. Yoshie, Polymers with autonomous self-healing ability and remarkable reprocessability under ambient humidity conditions, *J. Mater. Chem. A* 6 (2018) 19643–19652.
- J.J. Cash, T. Kubo, D.J. Dobbins, B.S. Sumerlin, Maximizing the symbiosis of static and dynamic bonds in self-healing boronic ester networks, *Polym. Chem.* 9 (2018) 2011–2020.
- S. Ji, F. Fan, C. Sun, Y. Yu, H. X. Visible light-induced plasticity of shape memory polymers, *ACS Appl. Mater. Interfaces* 9 (2017) 33169–33175.
- B.T. Michal, C.A. Jaye, E.J. Specer, S.J. Rowan, Inherently photohealable and thermal shape-memory polydisulfide networks, *ACS Macro Lett.* 2 (2013) 694–699.
- T.F. Scott, A.D. Schneider, W.D. Cook, C.N. Bowman, Photoinduced plasticity in cross-linked polymers, *Science* 308 (2005) 1615–1617.
- C. Luo, Z. Lei, Y. Mao, X. Shi, W. Zhang, K. Yu, Chemomechanics in the moisture-induced malleability of polyimide-based covalent adaptable networks, *Macromolecules* 51 (2018) 9825–9838.
- J.J. Cash, T. Kubo, A.P. Bapat, B.S. Sumerlin, Room-temperature self-healing polymers based on dynamic-covalent boronic esters, *Macromolecules* 48 (2015) 2098–2106.
- Y. You, W.L. Peng, P. Xie, M.Z. Rong, M.Q. Zhang, D. Liu, Topological rearrangement-derived homogeneous polymer networks capable of reversibly interlocking: from phantom to reality and beyond, *Mater. Today* 33 (2020) 45–55.
- W. Denissen, G. Rivero, R. Nicolaÿ, L. Leibler, J.M. Winne, F.E. Du Prez, Vinylogous urethane vitrimers, *Adv. Funct. Mater.* 25 (2015) 2451–2457.
- J.J. Lessard, L.F. Garcia, C.P. Easterling, M.B. Sims, K.C. Bentz, S. Arencibia, D. A. Savin, B.S. Sumerlin, Catalyst-free vitrimers from vinyl polymers, *Macromolecules* 52 (2019) 2105–2111.
- M. Capelot, M.M. Unterlass, F. Tournilhac, L. Leibler, Catalytic control of the vitrimer glass transition, *ACS Macro Lett.* 1 (2012) 789–792.
- N.J. Van Zee, R. Nicolaÿ, Vitrimers: permanently crosslinked polymers with dynamic network topology, *Prog. Polym. Sci.* 104 (2020), 101233.
- J.M. Winne, L. Leibler, F.E. Du Prez, Dynamic covalent chemistry in polymer networks: a mechanistic perspective, *Polym. Chem.* 10 (2019) 6091–6108.
- L. Lu, J. Pan, G. Li, Recyclable high-performance epoxy based on transesterification reaction, *J. Mater. Chem. A* 5 (2017) 21505–21513.
- Y. Tao, L. Fang, M. Dai, C. Wang, J. Sun, Q. Fang, Sustainable alternative to bisphenol A epoxy resin: high-performance recyclable epoxy vitrimers derived from protocatechuic acid, *Polym. Chem.* 11 (2020) 4500–4506.
- L. Yue, H. Guo, A. Kennedy, A. Patel, X. Gong, T. Ju, T. Gray, I. Manas-Zloczower, Vitimerization: converting thermoset polymers into vitrimers, *ACS Macro Lett.* (2020) 836–842.
- Y. Yang, F. Du, Z. Li, Thermally healable and reprocessable polymethacrylate networks based on diol-mediated metathesis of 6-membered boronic esters, *Polym. Chem.* 11 (2020) 1860–1870.
- F. Caffy, R. Nicolaÿ, Transformation of polyethylene into a vitrimer by nitroxide radical coupling of a bis-dioxaborolane, *Polym. Chem.* 10 (2019) 3107–3115.
- N. De Alwis Watuthantrige, B. Ahammed, M.T. Dolan, Q. Fang, J. Wu, J.L. Sparks, M.B. Zanjani, D. Konkolewicz, Z. Ye, Accelerating dynamic exchange and self-healing using mechanical forces in crosslinked polymers, *Mater. Horizons* 7 (2020) 1581–1587.
- N.N. Xia, X.M. Xiong, J. Wang, M.Z. Rong, M.Q. Zhang, A seawater triggered dynamic coordinate bond and its application for underwater self-healing and reclaiming of lipophilic polymer, *Chem. Sci.* 7 (2016) 2736–2742.
- S. Wang, S. Ma, Q. Li, X. Xu, B. Wang, W. Yuan, S. Zhou, S. You, J. Zhu, Facile in situ preparation of high-performance epoxy vitrimer from renewable resources and its application in nondestructive recyclable carbon fiber composite, *Green Chem.* 21 (2019) 1484–1497.
- Q. Zhang, X. Zhu, C.-H. Li, Y. Cai, X. Jia, Z. Bao, Disassociation and reformation under strain in polymer with dynamic metal-ligand coordination cross-linking, *Macromolecules* 52 (2019) 660–668.
- C. Lv, K. Zhao, J. Zheng, A highly stretchable self-healing poly (dimethylsiloxane) elastomer with reprocessability and degradability, *Macromol. Rapid Commun.* 39 (2018), 1700686.
- M. Xu, B. Cheng, Y. Sheng, J. Zhou, M. Wang, X. Jiang, X. Lu, High-performance cross-linked self-healing material based on multiple dynamic bonds, *ACS Appl. Polym. Mater.* 2 (2020) 2228–2237.



Anti-*Rhizoctonia solani* activity by polymeric quaternary ammonium salt and its mechanism of action

Chenyun Dong^a, Wanling You^a, Ruqi Liuyang^a, Yufeng Lei^b, Anqiang Zhang^{b,*}, Yaling Lin^{a,*}

^a College of Materials and Energy, South China Agricultural University, 483 Wushan Rd., Guangzhou 510642, Guangdong, China

^b College of Material Science and Engineering, South China University of Technology, 381 Wushan Rd., Guangzhou 510641, Guangdong, China

ARTICLE INFO

Keywords:

Acrylamide quaternary ammonium salt
Antifungal bioassay
Mechanism of antifungal action
Rhizoctonia solani

ABSTRACT

Polymeric quaternary ammonium salts (PQASs) exhibit antibacterial action and are less toxic, less stimulatory to the human body and have easier-to-modify functionalities than small molecular antibacterial agents. However, few studies on the structure-activity relationship and toxicity mechanism of PQASs against fungi have been reported. We previously described the synthesis of a novel PQAS, namely, a homopolymer of (2-methacrylamido)propyltetraethylammonium chloride (PQD-BC), and discovered that the polymer exhibits antifungal activities not only against *Fusarium oxysporum* f. sp. *Cubense* tropical race 4 (Foc 4), the pathogen of banana wilt, but also against *Rhizoctonia solani* (*R. solani*), the pathogen of rice sheath blight (RShB). Furthermore, we studied the mechanism of action of PQD-BC against Foc 4, which is markedly different from *R. solani* in morphology and life cycle. Therefore, the structure-antifungal activity relationship and toxicity mechanism of PQD-BC against *R. solani* were extensively studied in this work and compared with those of the low-molecular-weight quaternary ammonium salt benzyltrimethylammonium chloride (BC), and the results play an important role in identifying long-term and low-toxicity fungicides that can suppress the sclerotia of *R. solani*. The results showed that PQD-BC and BC can destroy the structural integrity and morphology of a cell, such as by loss of the cell wall and plasma membrane integrity, leading to the release of intracellular contents and can induce mitochondrial dysfunction and interference with genomic DNA and inhibit the formation of sclerotia. However, PQD-BC showed a special mechanism for causing the lipid peroxidation of the cell membrane; this mechanism was not observed with BC. The newly elucidated mechanism accounts for differences between polymers and small-molecule compounds and provides a theoretical basis for further application of PQAS against fungi and sclerotia.

1. Introduction

Rice, one of the primary staple food on earth, is subject to many diseases that often place major biological constraints on production. Rice sheath blight (RShB), a pervasive rice disease occurring throughout temperate and tropical production systems, is caused by *Rhizoctonia solani* (*R. solani*) Kühn, among which AG-1(IA) is the strongest and most harmful strain. Although the pathogen is soil borne, RShB develops into a major production limitation in an alarmingly brief timespan [1]. It has been reported to reduce yield by 15%–44% in Texas, USA [2]. The most important factor for RShB epidemic is the formation of sclerotia. As the dormant structures of fungi, sclerotia are hard, asexual and resistant to unfavorable conditions as well as to chemical and biological degradation [3–6]. The high capability of sclerotial survival may be related to its special double layer [7] and secreted melanin [8]. The mycelia of *R. solani* forms sclerotia to survive

in soil when host plants are removed and the sclerotia germinate and infect new plants in the next growing season [3–6]. This cycle can follow on all the while. Without breaking the cycle, RShB is difficult to eradicate.

To date, the methods of controlling RShB mainly involve agricultural, biological and chemical managements. Agricultural managements which control RShB directly, such as salvage sclerotia [9], crop rotation [10] and duck-rice system [11,12], require a lot of time and manpower. Biological managements exploit microbes, such as *Trichoderma* [13], *Bacillus* [14] and *Pseudomonas* [15], to inhibit mycelial growth of *R. solani*. Their inhibiting effects are reported as evident and friendly to environment. However, the field application of microbes tends to be susceptible to other factors, and hard to achieve the laboratory effect. Chemical antimicrobial agents are the most adopted. Management of RShB using chemical agents has focused on killing hypha and preventing the formation of sclerotia, such as New-Ag-

* Corresponding authors.

E-mail addresses: aqzhang@scut.edu.cn (A. Zhang), linyaling@scau.edu.cn (Y. Lin).

<https://doi.org/10.1016/j.reactfunctpolym.2018.01.020>

Received 29 July 2017; Received in revised form 23 January 2018; Accepted 25 January 2018

Available online 01 February 2018

1381-5148/ © 2018 Elsevier B.V. All rights reserved.

antibiotic 702 [16] and *validamycin* [17]. Nevertheless, no methods have been reported to completely inhibit the growth of mycelia and the germination of *R. solani* sclerotia, especially from the aspect of taking advantage of functional polymers.

Quaternary ammonium salts (QASs) have been widely used as small molecular biocides with several advantages over other antibacterial agents, including excellent cell membrane penetration properties, lower toxicity, less skin irritation, better environmental stability, extended residence time and enhanced biological activity. Polymeric quaternary ammonium salts (PQASs) exhibit greater antimicrobial activities than the corresponding small molecular QASs. The higher activity of polymeric PQASs has been interpreted as follow: the net positive charge of PQASs and the net negative charge of bacterial cell membranes provide a stronger driving force for the initial attraction of the PQASs to the cell surface. After the PQASs bind to the negatively charged phospholipid, their hydrophobic moieties interact with the inner hydrophobic core of the bacterial membrane, leading to a disruption of the cytoplasmic membrane and a release of potassium and other constituents, which eventually causes cell death. Therefore, PQASs can be firmly adsorbed onto the surface of negatively charged surfaces, effectively restraining bacteria [18–20].

In addition, compared with small molecular compounds, functional polymers' properties can be manipulated through changes in their structure. PQASs can then be grafted from a hydrophilic group or hydrophobic groups and endowed with amphiphilicity. These materials not only deliver steric stabilization in solid dispersions and generate controlled surface structures upon arrangement of materials but also modify interfacial properties such as wetting and lubrication [21,22]. These properties might offer a path for inhibiting the germination of sclerotia, thereby controlling RShB epidemics.

Previously, we have revealed the antifungal activity of polymeric QAS against phytopathogenic fungi, including *Fusarium oxysporum* f. sp. *Cubense* tropical race 4 (Foc 4) and *R. solani* [19,20,23]. Foc 4 is the pathogen of fusarium wilt of banana, which can produce spores by asexual reproduction [23,24]. However, *R. solani* and Foc 4 belong to different classes and have different morphologies and life cycles. *R. solani* strains are reported to be tiny, multinucleated, seldom producing spores and infecting host plants by mycelia and sclerotia [1]. Therefore, the antifungal mechanism of the functional polymer against *R. solani* remains undiscovered, as well as the difference in the antifungal mechanism between PQASs and small molecular counterparts against filamentous fungi.

In this paper, poly((2-methacrylamido)propyl)tetra-benzyl-dimethylammonium chloride (PQD-BC) is synthesized (Scheme 1) [19], and its activities and mechanisms against the mycelial growth and sclerotial formation of *R. solani* AG-1(IA) are investigated and compared with those of a commercially available small-molecular QAS, benzalkonium chloride (BC), to provide a clearer direction for the application of polymeric antifungal agents and new choices for controlling RShB.

2. Experimental

2.1. Materials

Bovine serum albumin (BSA) was provided by Hangzhou Sijiqing Biological Engineering Materials Co. Ltd. (Hangzhou, China). 2,3,5-Triphenyltetrazolium chloride (TTC) and an Ezup Column Fungi Genomic DNA Purification Kit were purchased from Sangon Biotech

(Shanghai) Co., Ltd. (Shanghai, China). Propidium iodide (PI) was supplied by Aladdin Reagent Co. Ltd. (Shanghai, China). The fungal strain used in this study is *Rhizoctonia solani* Kühn AG-1(IA), which was donated by the Fungi Laboratory at the South China Agriculture University and was maintained on potato dextrose agar (PDA). *R. solani* mycelial suspensions were obtained from the surface of the agar after culturing for 2 days at 28 °C. The concentration of the mycelial suspensions was determined using a hemocytometer. Benzyl-dimethyl-dodecylammonium chloride (BC) with a purity > 99% was purchased from Shanghai Aladdin Bio-Chem Technology Co., Ltd. (Shanghai, China). Alkaline phosphatase (ALP), malondialdehyde (MDA) and succinate dehydrogenase (SDH) kits were purchased from the Nanjing Jiancheng Institute of Bioengineering (Nanjing, Jiangsu, China). A mitochondrial isolation kit and GoldView™ were purchased from the Beijing Solarbio Science & Technology Co. Ltd., Beijing, China. PQD-BC was synthesized using radical polymerization according to the method described in our previous study [19], the structure of PQD-BC and BC were shown in Scheme 1.

2.2. Antifungal bioassay

2.2.1. Mycelial growth inhibition

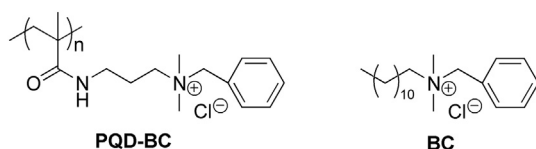
The antifungal efficiency of PQD-BC and BC on the mycelial growth of *R. solani* was measured using an *in vitro* mycelial growth inhibition assay [19]. Briefly, the compounds (PQD-BC and BC) were sterilized by passage through a 0.45 µm Millipore filter, diluted in different concentrations (PQD-BC: 0.25, 0.50, 0.75, 1.00, 1.25 and 1.5 mg/mL; BC: 0.015, 0.03, 0.045, 0.06, 0.075 and 0.2 mg/mL) and then mixed with molten agar (at a temperature > 60 °C); agar was diluted with distilled water for the control. Mycelial pieces (6 mm diameter) obtained from the periphery of 2-day-old cultures of *R. solani* were inverted on the center of each plate. Treated and untreated plates were incubated at 28 °C in triplicate. The efficacy of the treatment was determined by computing the average of two perpendicular diameters of each colony. The percent mycelial inhibition of the radial growth of the fungi by the compounds compared with the effect of the control was calculated at day 2 using the following formula:

$$\text{Percentage mycelial inhibition} = (D_c - D_t)/D_t \times 100\% \quad (1)$$

where D_c is the mean colony diameter of the control group and D_t is the mean colony diameter of the treatment group. Each measurement consisted of at least three replications.

2.2.2. Minimum inhibitory concentration (MIC)

The antimicrobial properties of the synthesized compounds were studied by the conventional procedure of broth microdilution with TTC. The TTC reagent is colorless; however, it gives off a bright-red color when reduced, indicating the presence of live fungi [25,26]. The fungistatic activity was characterized by the minimum inhibitory concentration (MIC) corresponding to the lowest serial dilution that resulted in the lack of visible microorganism growth. The synthetic compounds against *R. solani* were determined using *R. solani* cultured in sterile potato dextrose broth (PDB) medium for 3 days. Afterwards, the mycelia were suspended using a homogenizer. The sample solution (100 µL), in concentrations ranging from 5×10^{-3} to 0.3 mg/mL, was added to 96-well plates. The same volume of mycelial suspension containing approximately 10^5 – 10^6 CFU/mL was incubated at 28 °C for 2 days using a hemocytometer. Two control tests containing PDB medium supplemented with a tested strain and an equal volume of sterile PDB medium (negative control) were also performed. Then, 50 µL (5.0 mg/mL) of TTC solution (in PDB) was added to every well and the mycelia were cultured in the dark at 28 °C for another 2 h. The visual color changes were recorded before and after incubation to determine the MIC (mg/mL, present in the well). The color changes present in the well matched that in the blank well that was taken as the MIC for each fungus.



Scheme 1. Chemical structures of PQD-BC and BC.

2.2.3. Minimal fungicidal concentration (MFC)

In contrast to the MIC, the MFC of the synthetic compounds against *R. solani* was determined by the spot plate method. Aliquots from wells that appeared to contain few or no colonies were deposited and uniformly spread onto the agar surface of Petri dishes. Therefore, after the MIC experiment, 100 μ L of solution was collected from some wells and spotted onto the PDA plates. The PDA plates were cultured at 28 °C for 2 days. The lowest concentration of the samples that showed fewer than 5 growth colonies was assigned as the minimal fungicidal concentration (MFC) for each fungus.

2.3. Mechanism of antifungal action

2.3.1. Mycelial morphology and biomass assay

The morphology of mycelium treated with different concentrations of synthetic compounds (PQD-BC and BC) was observed by light microscopy. *R. solani* was cultured in PDB and rotated at 28 °C on a rotary shaker at 120 rpm for 3 days; it was then supplemented by three different concentrations of compounds (MIC, IC₅₀ and IC₉₀). After treatment for 48 h, the mycelia were harvested and moved to a glass slide, which was then covered by a slip and examined under a fluorescence microscope (Nikon Eclipse 80i, Japan), and the images were captured through a charge-coupled device camera. The dry weights (biomass) of mycelia were measured after drying for 6 h at room temperature. The data were based on three replicates.

2.3.2. Cell-wall disruption assay

The cell-wall integrity was expressed as the increased alkaline phosphatase (ALP) of the medium after compound treatments [27]. The mycelia of *R. solani* were prepared by being cultured in PDB medium (45 mL) and rotated at 28 °C on a rotary shaker at 120 rpm for 3 days. Afterward, the PDB medium supplemented with 5 mL of three different concentrations (MIC, IC₅₀, and IC₉₀) of polymers (PQD-BC and BC) was incubated under the same conditions for another 48 h in triplicate. The PDB medium added to the same volume of sterile distilled water was used as a control. The suspensions were obtained from the supernatants after being centrifuged at 4000 g for 10 min. An ALP kit was used to determine the effects of the polymers on the cell wall. The activity of ALP (A_{ALP}) in the supernatant was measured by a UV-vis spectrophotometer at 405 nm according to the manufacturer's instructions [27]. The activity of ALP was calculated according to the following formulas:

$$A_{ALP} = (\Delta OD_t - \Delta OD_b) \times F \quad (2)$$

$$F = (V \times 1000) / (V_s \times \varepsilon \times 1.0) \quad (3)$$

where ΔOD_t is the increase in OD (optical density, conceptually and numerically equivalent to absorbance) at 504 nm of the treated-sample after 1 min, ΔOD_b is the increase in OD of the reagent under the same conditions, V is the total volume (mL) of the reaction, V_s is the volume (mL) of the sample and ε is the molar extinction coefficient. The molar extinction coefficient of 4-nitrophenol at 504 nm is 18.5. The 1000 is the conversion coefficient from U/mL to U/L and 1.0 is the path length of the cuvette.

2.3.3. Cytoplasmic membrane disruption assay

To observe the effect of polymers against the plasma membrane integrity, we cultured *R. solani* in a sterile PDB medium at 28 °C on a rotary shaker at 120 rpm for 3 days. After that, 5 mL of three different concentrations (MIC, IC₅₀ and IC₉₀) of synthetic compounds (PQD-BC and BC) were added to PDB medium; the control was treated with the same quantity of sterile distilled water. Following incubation under constant shaking at 28 °C for 48 h in triplicate, the small amount of mycelia which was picked by tweezers, soaked in 1 mL of PBS and centrifuged at 10,000 rpm for 5 min; it was then washed twice with PBS (pH 7.4) on a rotary shaker. Next, 10 μ L of mycelia suspension was

mixed with 15 μ M of the red fluorescent nucleic acid stain PI, which is commonly used for detecting cellular membrane integrity [28], and placed in the dark for 1 h. To remove the PI, the medium was washed five times with PBS on a rotary shaker, and finally re-suspended in 100 μ L of PBS. The sample (5 μ L) was moved onto a glass slide and then covered with a slip, sealed, and observed under the oil objective (100 \times) of fluorescence microscope (Nikon Eclipse 80i, Japan). Excited by lasers at 543 nm, PI emissions were collected using a long-pass filter for PI at 590–800 nm. The images were captured using a charge-coupled device camera. Three fields of view were chosen randomly from each cover slip.

2.3.4. Cellular leakage assay

Membrane permeability was determined by the leakage level of cytoplasmic materials in the culture as a result of disruption of the fungal wall/membrane [29]. *R. solani* was grown in PDB medium in triplicate under shaking for 3 days at 28 °C. Then, the mycelia were harvested and washed twice with PBS (pH 7.4) using a Büchner funnel. The mass-washed mycelia were re-suspended in a 50 mL solution containing test compounds (PQD-BC and BC) diluted to three concentrations (MIC, IC₅₀, and IC₉₀) and were then incubated under shaking for another 24 h. Two control samples were prepared. One was treated with the same quantity of sterile distilled water, and the other was supplemented with three different concentrations of compounds (MIC, IC₅₀, and IC₉₀). Samples from the suspensions were collected and filtered at 2 h intervals during the incubation. The filtered solutions were used to determine the leakage of soluble proteins, carbohydrates and nucleic acids. A Bradford assay was performed to quantify the release of the proteins on the basis of the different concentrations of BSA as the standard [30]. Soluble carbohydrates were detected by the anthrone reaction, which uses glucose as the standard [31]. The electric conductivity of the resulting supernatant was measured using a conductivity meter (DDS-11A, Shanghai Precision Scientific Instrument Co., Ltd., Shanghai, China) [27].

2.3.5. Lipid peroxidation analysis

The lipid peroxidation in the cell membrane of *R. solani* was quantified on the basis of its malondialdehyde (MDA) levels [31–33]. The mycelia of *R. solani* were prepared by being cultured in PDB medium (45 mL) and rotated at 28 °C on a rotary shaker at 120 rpm for 3 days. The PDB medium was then mixed with three different concentrations (IC₉₀ \times 0.5, IC₉₀, and IC₉₀ \times 2) of compounds (PQD-BC and BC) and incubated under shaking for 24 h at 28 °C; no compounds were added in the control group. The fungal suspensions were centrifuged at 12,000 rpm for 5 min, and the pellet was then sonicated twice on ice with lysis buffer (2% Triton- \times 100, 1% SDS, 100 mM NaCl, 10 mM Tris-HCl, 1 Mm EDTA [pH 8.0]) and quartz sand in 5% trichloroacetic acid (TCA). After centrifugation, the supernatant of the fungal suspension was used as a crude MDA-mycelial solution. The MDA contents of the mycelia and medium were determined according the manufacturer's instructions provided with the MDA kit. MDA can react with freshly prepared thiobarbituric acid to form a colored complex, which has a maximum absorbance at 532 nm in a UV-vis spectrophotometer (UV2300, Techcomp, Shanghai, China) [31]. Each experiment was performed three times. The content of MDA was calculated using the following equation:

$$MDA = \Delta OD_t / \Delta OD_b \times Cr \times DF \quad (4)$$

where ΔOD_t is the reduction of the OD value of the treated sample after 1 min, ΔOD_b is the increase of the OD value of the reagent from the MDA kit after 1 min, Cr is the concentration of standard substance in the MDA kit (10 nmol/mL), and DF is the dilution factor of the sample before being tested. The MDA content was expressed as mmol per gram of mycelia.

2.3.6. Effect on mitochondrial function

The mitochondrial function of *R. solani* was expressed by the intracellular enzyme succinate dehydrogenase (SDH) activity (A_{SDH}) [29]. The mycelia of *R. solani* were prepared by being cultured in PDB medium (45 mL) and rotated at 28 °C on a rotary shaker at 120 rpm for 3 days. The PDB medium was then mixed with three different concentrations (MIC, IC_{50} and IC_{90}) of compounds (PQD-BC and BC) and incubated under shaking for 24 h at 28 °C; the same quantity of sterile distilled water was added to the PDB medium for the control group. After filtration, the mycelia were ground into powder under liquid nitrogen and used to isolate mitochondria with a mitochondrial isolation kit. The A_{SDH} was determined using the SDH kits and measured by UV–vis spectrophotometry at 600 nm. The total protein content was determined by the Bradford method [30]. Afterwards, the amount of protein was calculated according to the standard protein curve, which was measured with different concentrations of a protein standard. The A_{SDH} was calculated using the following equation:

$$A_{SDH} = (\Delta OD_{600}/100)/(C_s/10) \times 100\% \quad (5)$$

where ΔOD_{600} is the OD value of the sample and C_s is the protein concentration (mg/mL). One unit of SDH activity was defined as the amount of enzyme in 1 mL of fungal suspension after a 1 min reaction time that gave a reduction by 0.01 absorbance unit compared to the control reaction. Each treatment was performed in triplicate.

2.3.7. In vitro electrophoretic mobility shift assay (EMSA)

The DNA-binding activities of genomic DNA and the compounds were assessed by EMSA, which is widely used to research antimicrobial drugs, and is based on the observation that bound DNA complexes migrate through gels more slowly than unbound DNA fragments [34,35]. To obtain a significant amount of highly purified genomic DNA, *R. solani* was grown in PDB medium in triplicate under shaking for 3 days at 28 °C. The mycelia were then harvested and washed twice with PBS (pH 7.4) by Büchner funnel to remove the PDB medium. After the sample was freeze-dried, the total intracellular DNA was extracted with an Ezup Column Fungi Genomic DNA Purification Kit, and RNase was added. Genomic DNA being sufficiently free of protein gave a UV absorbance ratio of 1.8–2.0 at 260 and 280 nm (A_{260}/A_{280}). A total of 5 µg of highly purified genomic DNA in a fixed concentration (500 µg/mL) was mixed with the TE buffer (10 mM Tris-HCl + 1 mM EDTA, pH 8.0) treated with the compounds (PQD-BC and BC) at three different concentrations (MIC, IC_{50} , and IC_{90}). The addition of the same volume of PBS (pH 7.4) was set as the control test. Treated and untreated tests were incubated at room temperature for 10 min in triplicate. Agarose gel electrophoresis was used to examine the interaction between the compounds and genomic DNA; the TE buffer was incubated alone with DNA in the control. A 5 µL volume of GoldView™ was used as a fluorescent dye, and 1 mg of DNA was loaded onto the 1% gel; electrophoresis was performed in TAE (tris acetate EDTA) buffer for 20 min. The gel was visualized under UV light using a Bio-Rad Trans illuminator IEC 1010.

2.3.8. In vivo efficacy on genomic DNA

On the basis of the *in vitro* EMSA, to further confirm that genomic DNA combined with compounds in the agarose gel electrophoresis and to investigate whether the compounds penetrated the cell barriers and interacted with genomic DNA, we also studied the *in vivo* efficacy against the genomic DNA of *R. solani* after the compound treatments. The mycelia of *R. solani* were prepared by being cultured in PDB medium (45 mL) and rotated at 28 °C on a rotary shaker at 120 rpm for 3 days. Then, the PDB medium was mixed with three different concentrations (MIC, IC_{50} and IC_{90}) of compounds (PQD-BC and BC) and incubated in triplicate under shaking for 24 h at 28 °C; the same quantity of sterile distilled water was added for the control group. The mycelia were collected and washed twice with PBS (pH 7.4) to remove the medium, and then ground under liquid nitrogen. The total

intracellular DNA was extracted with assay kits and RNase was added. The *in vivo* interaction between the compounds and genomic DNA was studied by agarose gel electrophoresis.

2.4. Effect of inhibiting sclerotia formation

The effect of the synthetic compounds of PQD-BC and BC on the formation of sclerotia was determined based on the time of sclerotia information, the number of sclerotia per Petri dish and the dry weight of sclerotia. Specifically, a 6-mm-diameter Petri dish, which was cut with a sterile cork borer from the edge of an actively growing colony cultured on PDA plates for 7 days, was placed in the center of a 9-cm-diameter petri dish containing PDA medium with three different concentrations (MIC, IC_{50} and IC_{90}) of synthetic compounds (PQD-BC and BC). The same volume of PDB was added for the control. Each measurement consisted of at least three replicates. After being cultured for 7 days, the sclerotia were collected and counted. Finally, the sclerotia were dried at room temperature for 24 h before weighing.

2.5. Statistical analysis

SPSS software (SPSS Inc., Chicago, IL, USA) was used for the statistical analyses of the data. To determine the effects of the treatments, an analysis of variance (ANOVA) was performed. A Duncan's multiple range test was used for mean separations when the treatment effects were statistically significant ($P < 0.05$).

3. Results and discussion

3.1. Antifungal activity

The half-maximal inhibitory concentration (IC_{50}) is the drug safety indicator that could cause 50% fungal death, and the 90% inhibitory concentration (IC_{90}) is the concentration at which 90% of the fungi were killed. The addition of PQD-BC or BC to the PDA medium inhibited the mycelia growth of selected fungi significantly at all concentrations tested, as measured by the diameter of the treatment and control using the crossing method. The IC_{50} and IC_{90} have biological probability values of 0.5 and 6.2816, respectively. PQD-BC and BC inhibited the mycelial growth of *R. solani* in a dose-dependent manner at concentrations from 0.5 to 2 mg/mL (PQD-BC) and from 0.015 to 0.2 mg/mL (BC) (Fig. 1). As the concentrations of PQD-BC and BC increase, the diameter of each treatment group decreases. This result indicated that the compounds (PQD-BC and BC) can inhibit the growth of *R. solani* (Table 1). In *R. solani* cultured at 28 °C for 2 more days, the PQD-BC exerted antifungal effects with a IC_{50} of 0.73 mg/mL and a IC_{90} of 1.64 mg/mL, whereas BC exhibited antifungal activity with a IC_{50} of 0.048 mg/mL and a IC_{90} of 0.127 mg/mL.

Two principal measures of *in vitro* activity are the minimal inhibitory concentration (MIC) and the minimal fungicidal concentration (MFC). The MIC is the lowest concentration of drug that prevents visible fungal growth. High MICs indicate that stronger concentrations of antimycotic agents are required to inhibit fungal growth. The MIC of PQD-BC and BC was determined using the TTC coloration method and is defined as the lowest concentration able to inhibit visible microbial growth. TTC is a redox indicator used to differentiate between metabolically active and inactive cells; the colorless compound is enzymatically reduced to red TPF (1,3,5-triphenylformazan), which is stable and cannot be oxidized in the air in living cells because of the activity of various dehydrogenases. When the number of active cells is low, TTC cannot be reduced and the solution is colorless; it is therefore often used as a chromogenic agent to test whether viable cells are present [35]. Therefore, MIC was determined as the lowest concentration at which no red color was observed, as shown in Fig. 2–(A). MFC, also known as the minimum lethal concentration, is the concentration of drug that reduces the original fungal inoculum by 99.9%, as shown in

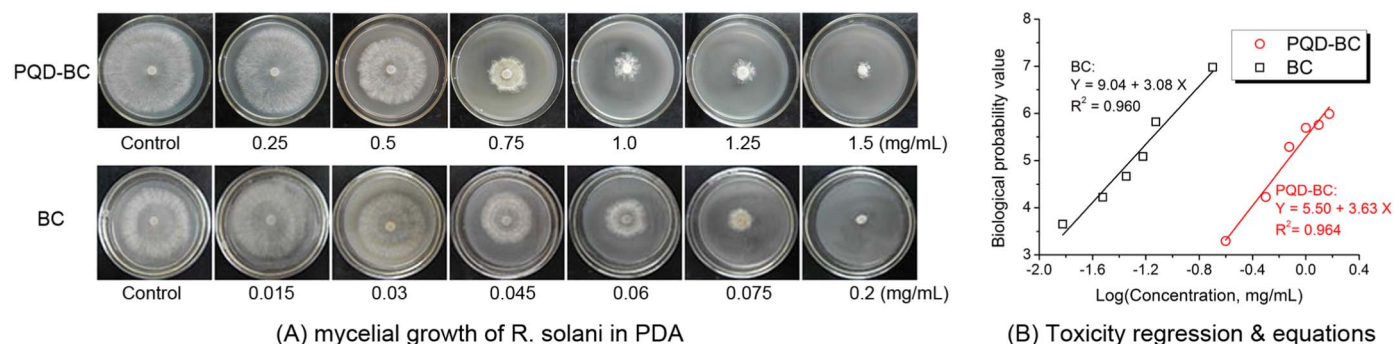


Fig. 1. (A) The typical mycelial growth of *R. solani* in PDA medium after PQD-BC and BC were applied, and (B) the corresponding toxicity regression curves and regression equations. The data were based on three replicates, and the test was repeated twice, with similar results.

Table 1

The antifungal effect of PQD-BC and BC against *R. solani*.

Compounds	Mycelial growth		Spore propagation		
	IC ₅₀ (mg/mL)	IC ₉₀ (mg/mL)	MIC (mg/mL)	MFC (mg/mL)	MFC/MIC
PQD-BC	0.73	1.64	0.2	0.2	1
BC	0.048	0.127	0.03	0.035	1.167

Fig. 2(B). The ratio of MFC/MIC reflects the fungicidal activity. An antimicrobial agent exhibited fungicidal activity when the ratio of MFC/MIC was less than or equal to 4, otherwise the antimicrobial agent only had antifungal activity. The *in vitro* studies showed that PQD-BC displayed antifungal action against *R. solani*, with an MIC and MFC of 0.2 mg/mL; therefore, BC exerted antifungal activity against *R. solani*, with an MIC of 0.03 mg/mL and an MFC of 0.035 mg/mL. Thus, PQD-BC and BC were effective against *R. solani*, with low MIC and MFC values and MFC/MIC ratios of PQD-BC and BC < 4, indicating they were fungicidally effective, as shown in Table 1.

3.2. Mechanism of antifungal action

3.2.1. Mycelial morphology and biomass

The mycelial growth and morphology of *R. solani* was detected by light microscopy, as shown in Fig. 3. After being cultured for 48 h, the mycelia in the control were in good condition; the mycelia were smooth and full. However, the morphology of the mycelia that were treated with three different concentrations (MIC, IC₅₀ and IC₉₀) of PQD-BC had

changed, including increased branching of mycelia and shortened branch spacing and fewer large vacuoles in some mycelial cells. Some mycelial cells, after treatment with PQD-BC, produced particulate matter that could be a condensation of the cytoplasm [16], as shown in Fig. 3(A1). However, the number and volume of vacuoles increased in the cells treated with increasing concentration of BC, as shown in Fig. 3(A2). The BC treatment resulted in cytoplasmic vacuolation [36]. This difference between macromolecular compound (PQD-BC) and small molecular compound (BC) may be related to the different molecular weight, and thereby the different dispersion and density of cations in liquid. In addition, the mycelia treated with a high concentration (IC₅₀ and IC₉₀) of PQD-BC and BC became dark, the medium became cloudy, and the mycelia fractured easily when harvested. We suspected that Rs-melanin was produced during the incubation with PQD-BC and BC. Rs-melanin was reported to be stable to light, temperature reducer and other metal ions [8]. Therefore, mycelia of *R. solani* survives within the hostile environment, by producing Rs-melanin and forming sclerotia.

Furthermore, the biomass was measured using an electronic balance, as shown in Fig. 3(B). The growth of mycelia during treatment was effectively inhibited by PQD-BC and BC, the growth production was strongly reduced in a dose-dependent manner. After being treated by small molecular QAS, the liquid occupied the main volume of the mycelia cell due to cytoplasmic vacuolation. The weight of mycelia reduced because of a massive loss of water through drying. However, the condensation of cytoplasm, caused by PQAS, maintained the mycelial dry weight.

3.2.2. Cell wall integrity

To determine if PQD-BC and BC led to the loss of cell wall integrity

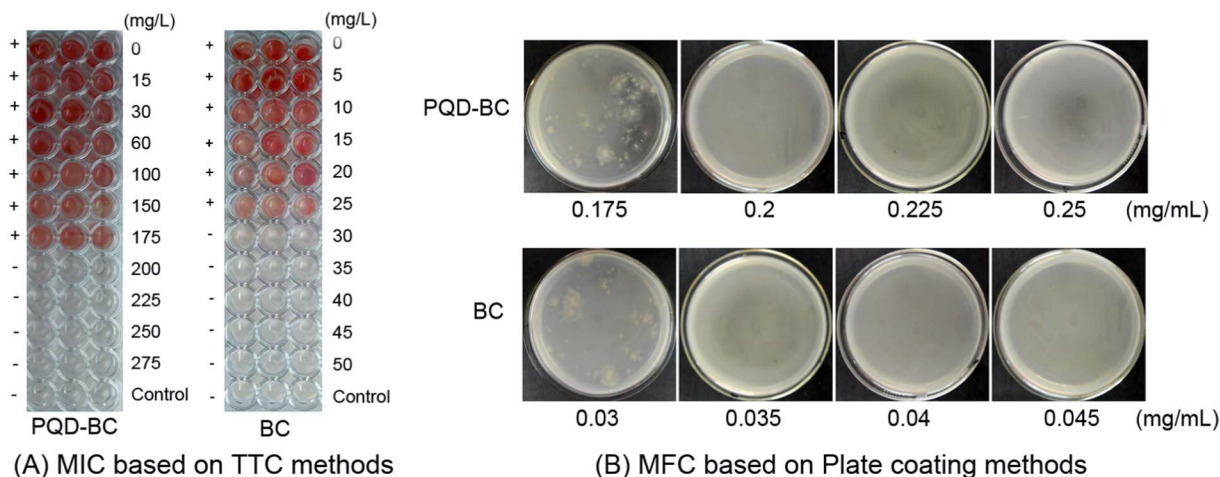


Fig. 2. (A) The MIC values of PQD-BC and BC against *R. solani* based on the TTC colorimetric method; (+) indicates certain cells on the plate and (–) indicates fewer or no cells on the plate. (B) The MFC values of PQD-BC and BC against *R. solani* based on the number of colonies in PDA.

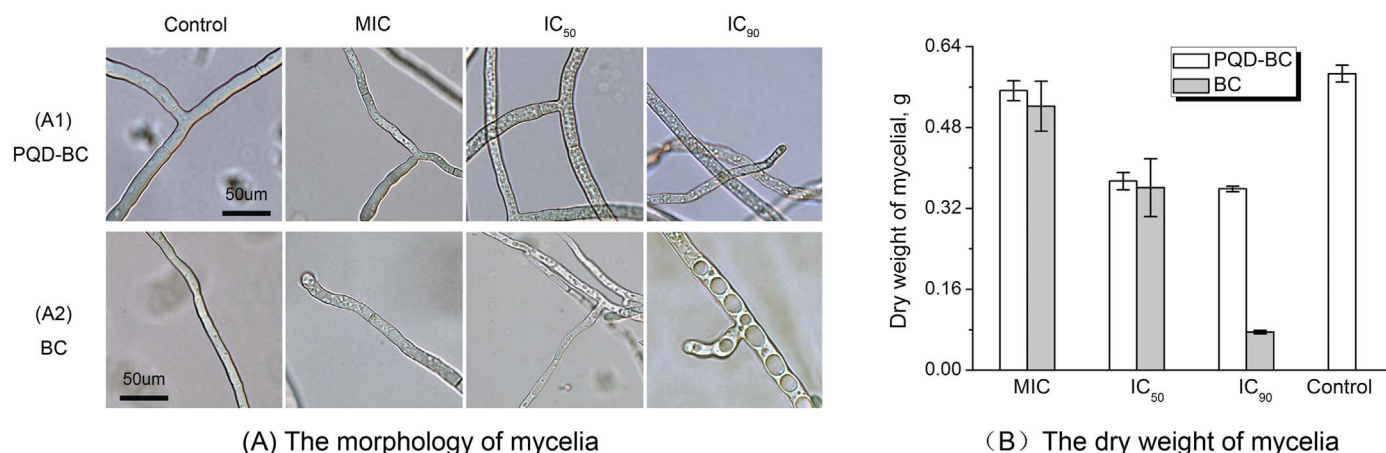


Fig. 3. The mycelial membrane structure (A) and dry weight (B) of *R. solani* mycelia after PQD-BC and BC treatments.

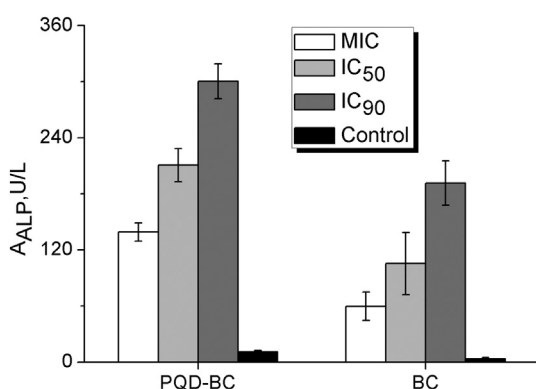


Fig. 4. Loss of cell-wall integrity in *R. solani* after PQD-BC or BC treatment. The alkaline phosphatase activity (AALP) was expressed as units per liter of filtered solution.

in *R. solani*, the ALP content, which is produced in the cytoplasm and cannot pass through the intact cell wall [37], was measured. Damage to the external cell wall layers can lead to the release of ALP from the cell [38]. After 3-day-old mycelia of *R. solani* were treated with four different concentrations (MIC, IC₅₀, IC₉₀ and 0), increased ALP activities of 0.2 mg/mL, 0.73 mg/mL and 1.64 mg/mL were observed in the medium at the MIC, IC₅₀ and IC₉₀, respectively, in the PQD-BC-treated cells. In BC-treated cells, the ALP activities were 0.03 mg/mL, 0.048 mg/mL and 0.127 mg/mL at the MIC, IC₅₀, IC₉₀, respectively. The PQD-BC- and BC-treated groups showed significantly higher ALP activity than the control after a 48 h treatment, which confirmed that the cell wall of *R. solani* was destroyed in a dose-dependent manner (Fig. 4). The data suggest that, after absorbing onto the cell surface, PQD-BC and BC could damage the cell walls of fungal pathogens and that they acted on the plasma membrane, leading to the release of intracellular contents like ALP, which led to eventual direct cell death.

3.2.3. Membrane-active mode of action

Quaternary ammonium salt treatments can rapidly lead to the disintegration of biological membranes in fungal pathogens, resulting in cell death [39]. To establish the mode of antifungal action, the cytoplasmic membrane integrity of *R. solani* was characterized using a fluorescent dye, propidium iodide (PI). PI is capable of combining with cell's genetic matters to produce a red fluorescence by green-light stimulation, but cannot permeate through the intact cytoplasmic membrane. As shown in Fig. 5, the cell nuclei were obviously stained with PI after treatment with PQD-BC at the MIC, IC₅₀ and IC₉₀ (0.2 mg/mL, 0.73 mg/mL and 1.64 mg/mL, respectively). By contrast, no red fluorescence appears in the control. In BC treatment, the cell nucleus can be stained with PI only at a IC₉₀. The microscopy results thus indicate that

the cationic polymer interacted with and subsequently disrupted the membrane integrity of the fungi [23]. Fluorescence microscopy images show that, compared with the control treatment, QASs treatment caused complete membrane permeabilization of the cells, as clearly indicated by red fluorescence; this observation indicates that the number of mycelia that lost plasma membrane integrity increased after the PQD-BC and BC treatments (Fig. 5). Compared with Foc 4 [23], only the spores could be seen in the fluorescence microscopy images. All of the cationic biocides were found to depolarize the membrane integrity of *R. solani*, and they may inhibit the growth of *R. solani* by directly damaging the plasma membrane and causing the cell death of the fungal pathogen.

Damage to the plasma membrane can lead to the loss of osmotic balance and to the influx of fluids and ions as well as to the loss of proteins and carbohydrates, eventually causing the onset of cell death [19]. To further confirm that PQD-BC and BC caused a loss in the cytoplasmic membrane integrity of *R. solani*, the leakage of cytoplasmic constituents was determined. The figure clearly shows that the two compound treatments significantly induced the leakage of soluble proteins (Fig. 6-(A)), carbohydrates (Fig. 6-(B)), and conductivity (Fig. 6-(C)) out of the *R. solani* mycelia. In general, the amount of leaked materials was positively correlated with the concentrations of PQD-BC and BC. The cellular leakage could be observed after 4 h of treatment, and it was generally constant over a period of 6 h for soluble proteins and carbohydrates. A similar trend was observed for the electrical conductivity. Because we observed the same physiological events with the release of cytoplasmic constituents, the mode of action of PQD-BC and BC is reasonably assumed to be interpretable on the basis of each elementary process: cationic biocides adsorb onto the fungal cell surface, diffuse through the cell wall, and subsequently bind to the cytoplasmic membrane, releasing the cytoplasmic constituents and finally inducing the cell death of the fungal pathogen.

3.2.4. Lipid peroxidation

To investigate the lipid damage, the levels of MDA, which is a decomposition product of polyunsaturated fatty acid hydroperoxidase and a biomarker of lipid peroxidation, were assessed [28]. MDA was primarily released into the medium when the plasma membrane lipid peroxidation was initiated; we determined MDA level to investigate whether lipid peroxidation was associated with membrane damage [31]. The mycelia cultured in PDB for 3 days, extracted from the medium, and washed twice with PBS (pH 7.4) were treated with four different concentrations of PQD-BC or BC at 1/2 × IC₉₀, IC₉₀ and 2 × IC₉₀ (0.82 mg/mL, 1.64 mg/mL and 3.28 mg/mL, respectively). As shown in Fig. 7-(A), the IC₉₀ of PQD-BC led to the highest release of MDA among treatment groups. The results show that, as the concentration of PQD-BC increases, so does the release of MDA. However,

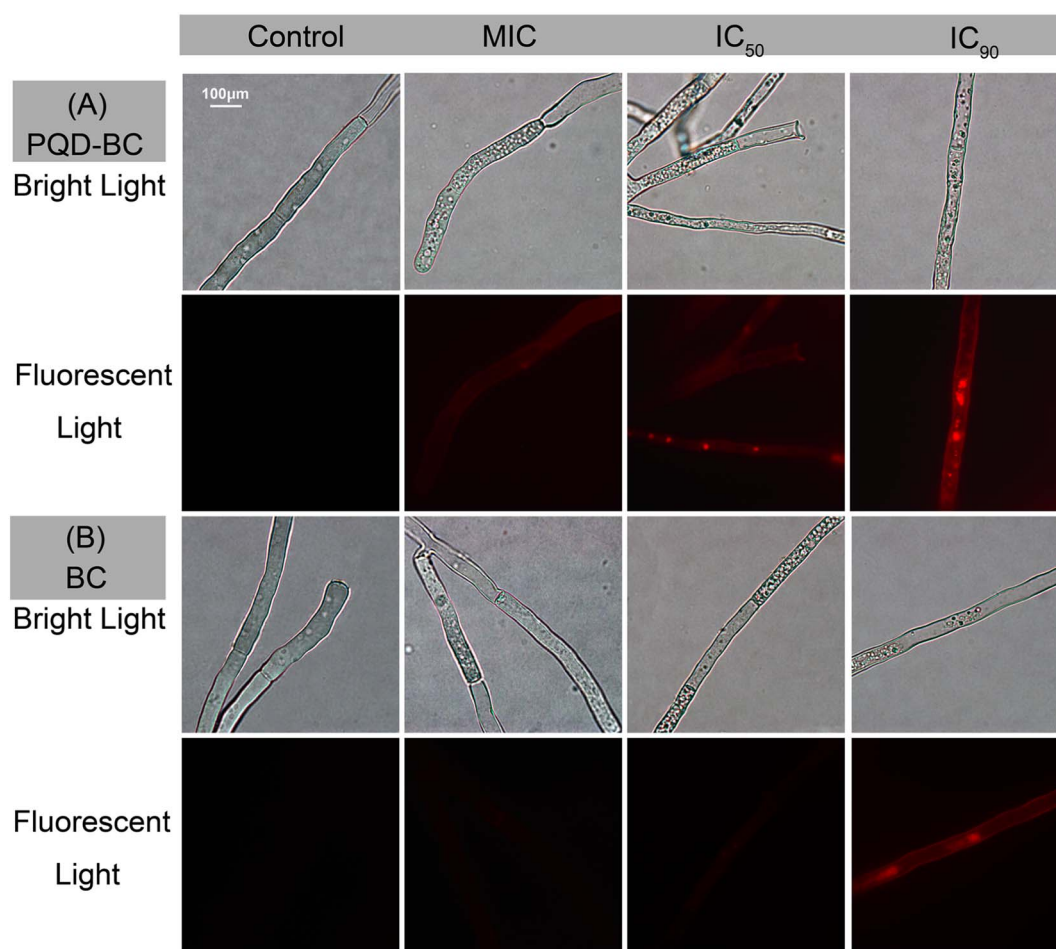


Fig. 5. Loss of plasma membrane integrity in *R. solani* after (A) PQD-BC and (B) BC treatments. The mycelia were stained with PI and observed with a fluorescence microscope. Mycelia with damaged plasma membranes fluoresced red. (For interpretation of the references to color in this figure legend, the reader is referred to the web version of this article.)

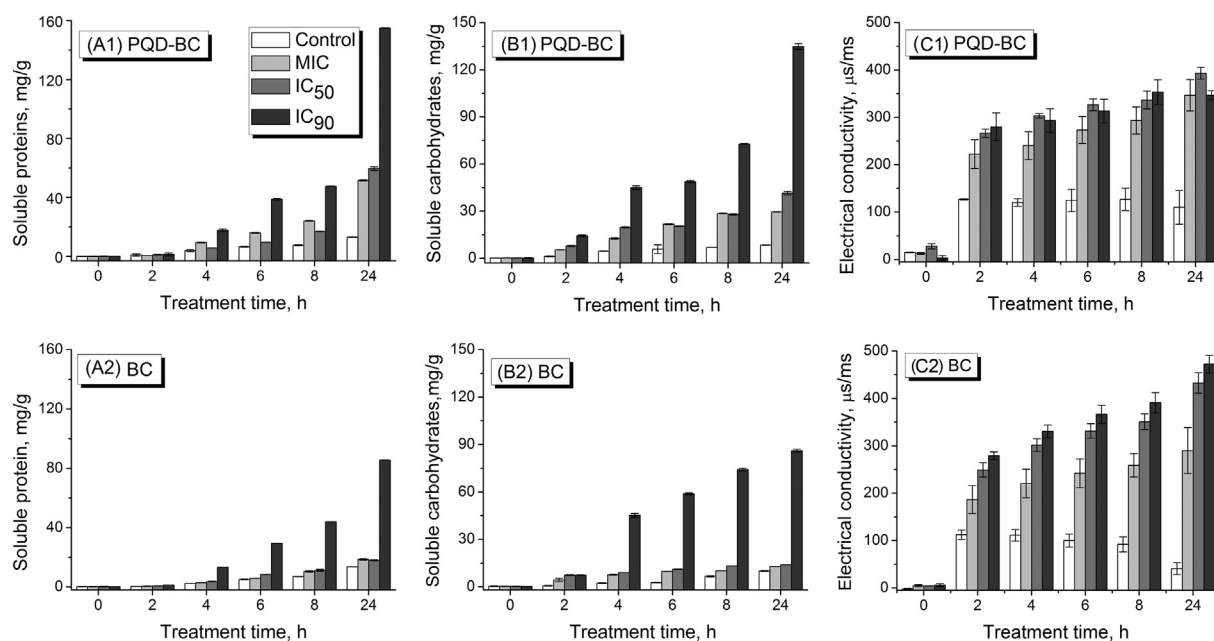


Fig. 6. Leakage of cytoplasmic contents: (A1, A2) soluble proteins, (B1, B2) carbohydrates and (C1, C2) electric conductivity from *R. solani* treated with PQD-BC and BC. Each data point is the mean \pm SE of three replicates.

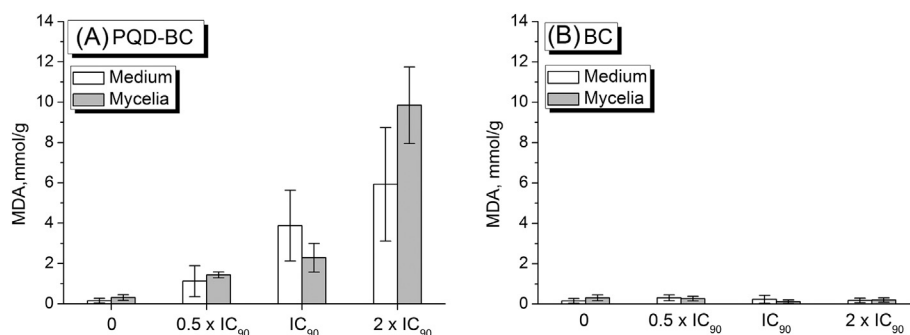


Fig. 7. Loss of cell wall integrity in *R. solani* after (A) PQD-BC and (B) BC treatments.

no obvious changing level of MDA on the BC-treated group was detected (Fig. 7).

Lipid peroxidation is the oxidative degradation of lipids, a process in which free radicals “steal” electrons from the lipids in cell membranes by a free radical chain reaction mechanism. In normal cells, reactive oxygen species (ROS), the byproducts of metabolism containing oxygen free radicals are dynamically balanced with antioxidants like glutathione (GSH). Hostile environmental factors, including UV, heat or chilling exposure, salinity and so on, can place a dramatic increment in ROS levels, cause the so-called oxidative stress. The result that the macromolecular PQD-BC can induce the lipid peroxidation, was similar to those of antimicrobial peptides (AMPs), such as Scolopendin 2 [31] and Glabridin [32]. It is reasonably assumed that the elevated local cationic density of macromolecular QAS (PQD-BC) are more likely to break the balance to give an oxidative stress and induce membrane lipid peroxidation in *R. solani*. By contrast, the small molecular QAS (BC) disperses in the liquid and lacks the ability of enriching around the mycelia and elevating the local density of cations. Therefore, BC did not induce the lipid peroxidation of treated mycelia. These results demonstrated the different mechanism between macromolecular and small molecular QAS in breaking the cytoplasmic membrane integrity.

3.2.5. Mitochondrial dysfunction

To assess changes in mitochondrial function, the SDH activity of *R. solani* cells exposed to the compounds was determined. SDH is the functional substance for the tricarboxylic acid cycle and aerobic respiration. Its activity is closely associated with bioenergy synthesis and mitochondrial function in various prokaryotic and eukaryotic cells [40]. The control group exhibited SDH activity, whereas the amount of SDH released from the cells to the culture medium decreased as the concentrations of the compounds (PQD-BC and BC) increased (Fig. 8). Therefore, PQD-BC and BC affect the bioenergy synthesis pathway of *R. solani* by inhibiting SDH activity. This finding suggests that the potential mechanism underlying their antifungal actions is inhibition of mitochondrial function.

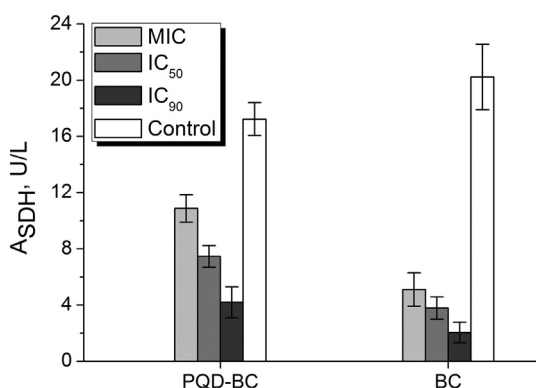


Fig. 8. Mitochondrial function (A_{SDH}) of *R. solani* after PQD-BC and BC treatments.

3.2.6. Interactions of genomic DNA with the compounds

As a carrier of genetic information, DNA is a major target for drug interactions because of its ability to interfere with transcription (gene expression and protein synthesis) and replication, a major step in cell growth and division [41–43]. In this study, the EMSA was used to test the affinity of DNA-binding polymers to investigate their efficacy against genomic DNA, and the mode of action was illustrated. When genomic DNA is separated by electrophoresis, rapid migration will be observed for unbound and cleaved DNA. By contrast, the complex produces a slower migration because of the increase of molecular weight and decrease of negative charge, which means that a constant amount of DNA was mixed with increasing amounts of compounds, tethered to compound-DNA-conjugated agarose beads. For the *in vitro* experiments, test compounds were immobilized with *R. solani* genomic DNA according to the results of the agarose electrophoresis experiments. In Fig. 9, Lanes 2–7 show genomic DNA incubated with the test compounds at three different concentrations (MIC, IC₅₀ and IC₉₀), whereas Lane 1 applies to untreated genomic DNA (control DNA). Compared with the control treatment, the compound treatments are very effective at changing the mobility and shape of genomic DNA. As shown in Fig. 9-(A), no obvious DNA bands were present in the lanes for the PQD-BC-treated group (Lanes 2–4), and the DNA loading buffer containing bromide blue indicator remained in the pore. GoldView™, a new type of nucleic acid dye that can replace ethidium bromide (EB), exhibits weak fluorescence; however, its emission intensity in the presence of DNA can be greatly enhanced because of its strong intercalation between the adjacent DNA base pairs. This enhanced fluorescence could be quenched, or at least partly quenched, by the addition of a second molecule with higher DNA-binding ability. This finding indicates that PQD-BC was immobilized strongly with genomic DNA, which caused the GoldView™ to be completely replaced by PQD-BC and led to an appreciable decrease in the emission intensity. BC could combine with genomic DNA strongly, increasing the weight of the composite molecule. Therefore, the speed of genomic DNA movement in electrophoresis slows and the phenomenon of tailing appears. Because of the combination of genomic DNA and synthetic compounds, the large molecules of genomic DNA were broken down and genomic DNA treated with compounds combined with TE buffer formed in the long tail in the gel. On the basis of the results of the assay of DNA interactions *in vitro*, the phenomenon of PQD-BC and BC against DNA *in vivo* (as shown in Fig. 9-(B)) was similar. On the basis of the aforementioned results, the binding site of PQD-BC and genomic DNA could be associated with the GoldView™ and genomic DNA: BC can bind with the genomic DNA of *R. solani* as a complex and destroy it.

3.3. Effect of inhibiting sclerotial formation

Sclerotia are the dormant structures of fungi and are also described as an aggregation of mycelia. Sclerotial formation can be divided into three stages: sclerotial initial (SI), sclerotial developing (SD), and sclerotial mature (SM) [44]. The PQD-BC and BC treatments at IC₉₀ and

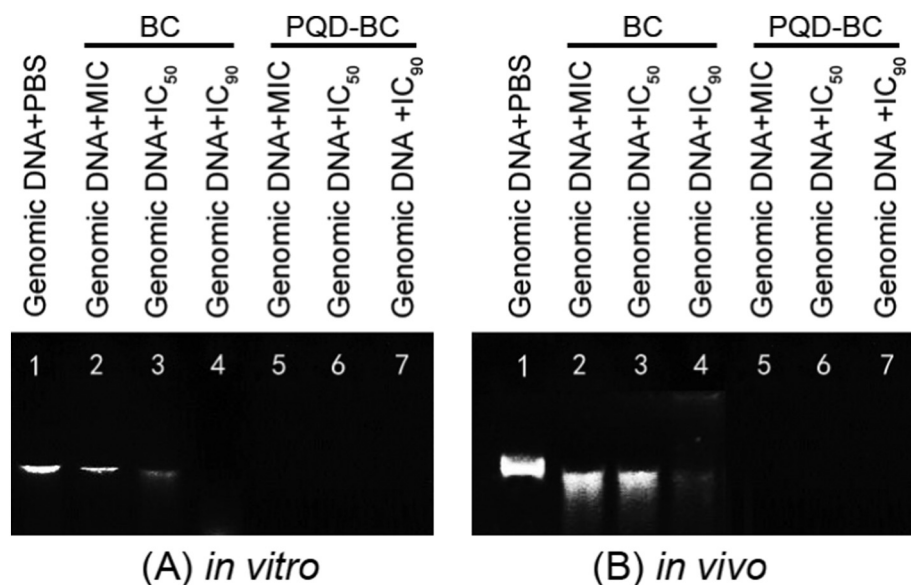


Fig. 9. Interaction of compounds (PQD-BC and BC) with *R. solani* genomic DNA (A) *in vitro* and (B) *in vivo*. Each lane contained 10 μ L of compounds: 10 μ L of DNA marker was moved to Lane 1: 10 μ L of genomic DNA with PBS (negative control), where the volume ratio is 6: 1. (A) *In vitro*, Lanes 2–4: genomic DNA with a fixed concentration was treated with TE buffer containing PQD-BC (volume: genomic DNA: TE buffer = 6: 1) at final concentrations matching the MIC, IC₅₀ and IC₉₀. For Lanes 5–7: genomic DNA with a fixed concentration was treated with 2 μ L of the TE buffer (6:1) containing BC at a final concentration matching the MIC, IC₅₀, and IC₉₀. (B) *In vivo*, PQD-BC was added to Lane 5–7; however, BC was added to Lanes 2–4. The data were based on three replicates, and the test was repeated twice with similar results. Representative results are shown.

the control are presented in Fig. 10. As shown in Fig. 10, the sclerotia treated with PQD-BC or BC at IC₉₀ reached the SI stage after 5 and 4 days of culturing, respectively. The other treated concentrations (MIC and IC₅₀) of compounds (PQD-BC and BC) were shown in Fig. S1 (as listed in the Supporting Information). The sclerotia reached the stage of SI formation on the third day of culturing (Fig. 11-(A)). This result indicates that PQD-BC and BC can delay sclerotia formation. In addition, under treatment with PQD-BC or BC, the number of sclerotia decreased significantly (Fig. 11-(B)), and the polymer at three different concentrations (MIC, IC₅₀ and IC₉₀) had no effect on the dry weight of sclerotia as the concentration increased compared with the effect of the treatment with BC (Fig. 11-(C)).

The sclerotia have a double-layer structure, in which the inner layer consists of a large number of living cells and the outer layer of empty cells [7]. Hence, we can infer that PQD-BC and BC can affect the formation of sclerotia, by causing the increasing number of empty cells in single sclerotium and forming heavier sclerotia to survive the harmful environment. Moreover, the heavier sclerotia formed in BC-treated groups indicated the more toxic environment that BC created.

4. Conclusions

We previously demonstrated methods for developing quaternary ammonium salt (PAD-BC) and small molecular quaternary ammonium salt (BC) that inactivate various fungi (*R. solani*). PQD-BC and BC were

found to actively inhibit mycelial growth and sclerotial formation in *R. solani*.

PQD-BC and BC destroyed the cell structure. We speculated that PQD-BC and BC can produce a destructive effect on the integrity of the cell wall and cell membrane of *R. solani* and on the formation of sclerotia because of the good biocompatibility. In particular, the macromolecule quaternary ammonium salt of PQD-BC can cause plasma membrane lipid peroxidation, unlike a small molecular quaternary ammonium salt such as BC. However, due to its large molecular weight, PQD-BC cannot easily traverse the cytoplasm membrane into the cell and attack the organelles. The mechanism of action suggests that the polymeric quaternary ammonium salts may act on a broad spectrum of fungal species, indicating a new strategy for preventing and controlling *Rhizoctonia solani* and establishing a base for studying the effect of the polymer on inhibiting microorganisms.

Acknowledgments

This work was supported by the Science and Technology Program of Guangzhou, China, under grant 201704020084; the Science and Technology Planning Project of Guangdong Province, China under grant 2016A020210105; and the National Natural Science Foundation of China under grant 31772202, 51473051.

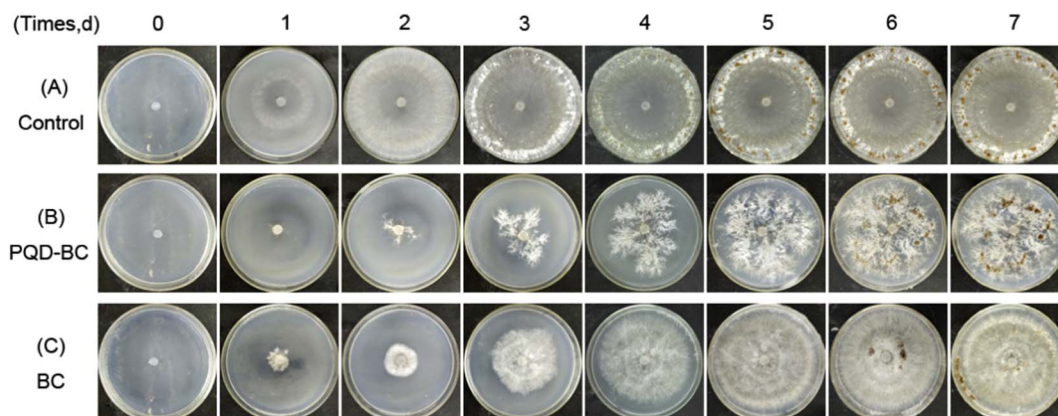


Fig. 10. The sclerotial formation of *R. solani* on PDA medium after applying (B) PQD-BC and (C) BC at IC₉₀, compared with the (A) control. The data were based on three replicates, and the test was repeated twice with similar results. Representative results are shown.

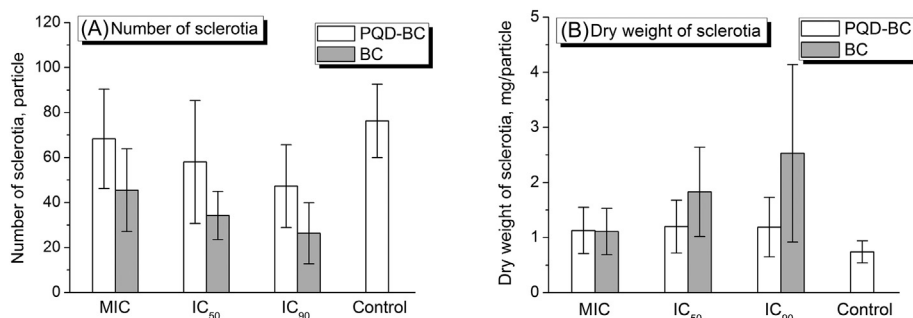


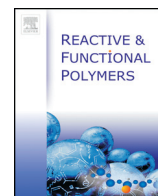
Fig. 11. The (A) number and (B) average dry weight of sclerotia of *R. solani* treated with three different concentrations of PQR-BC and BC.

Appendix A. Supplementary data

Supplementary data to this article can be found online at <https://doi.org/10.1016/j.reactfunctpolym.2018.01.020>.

References

- [1] F.N. Lee, M.C. Rush, Rice sheath blight: a major rice disease, *Plant Dis.* 67 (1983) 829–832.
- [2] M.A. Marchetti, C.N. Bollich, Quantification of the relationship between sheath blight severity and yield loss in rice, *Plant Dis.* 75 (1991) 773–775.
- [3] C.D. Georgiou, K.P. Petropoulou, Effect of the antioxidant ascorbic acid on sclerotial differentiation in *Rhizoctonia solani*, *Plant Pathol.* 50 (2001) 594–600.
- [4] S. Kumar, K. Sivasithamparan, M.W. Sweetingham, Proliferation of sclerotia in soil by *Rhizoctonia solani* anastomosis group (AG) 11 pathogenic on lupin, *Assoc. of Appl. Biologists* 141 (2002) 11–18.
- [5] A. Erental, M.B. Dickman, O. Yarden, Sclerotial development in *Sclerotinia sclerotiorum*: awakening molecular analysis of a “Dormant” structure, *Fungal Biol. Rev.* 22 (2008) 6–16.
- [6] M. Anees, V. Edel-Hermann, C. Steinberg, Build up of patches caused by *Rhizoctonia solani*, *Soil Biol. Biochem.* 42 (2010) 1661–1672.
- [7] T. Hashiba, Y. Tomio, S. Mogi, Biological and ecological studies on the sclerotium of *Pellicularia sasakii* (Shirai) S. Ito I. Floating on the water surface of sclerotium, *The Phytopathological Soc. of Japan* 38 (1972) 414–425.
- [8] J.Y. Chen, C.J.Z. Wang, C.W. Shu, et al., Isolation and characterization of a melanin from *Rhizoctonia solani*, the causal agent of rice sheath blight, *Eur. J. Plant Pathol.* 142 (2015) 281–290.
- [9] G.J. Tan, L. Chen, Y. Yang, et al., Study on the relationship between the sclerotial floatation characteristics and ultrastructure of rice sheath blight, *Anhui Nongye Daxue Xuebao/Journal of Anhui Agricultural University*, 27 (2000) 13–17.
- [10] J.P. Damicone, M.V. Patel, W.F. Moore, Density of sclerotia of *Rhizoctonia solani* and incidence of sheath blight in rice fields in Mississippi, *Plant Dis.* 77 (1993) 257–260.
- [11] M.X. Bui, R.B. Ogle, J.E. Lindberg, Studies on integrated duck-rice systems in the Mekong Delta of Vietnam, *J. Sustain. Agric.* 20 (2002) 27–40.
- [12] S.U. Pin, X.L. Liao, Y. Zhang, et al., Influencing factors on rice sheath blight epidemics in integrated rice-duck system, *J. Integr. Agric.* 11 (2012) 1462–1473.
- [13] S. Naeimi, S.M. Okhowat, M. Javan-Nikkhah, et al., Biological control of *Rhizoctonia solani* AG-1A, the causal agent of rice sheath blight with *Trichoderma* strains, *Phytopathol. Mediterr.* 49 (2010).
- [14] L. Liu, M.Q. Liang, L. Lu, et al., Synergistic effects of the combined application of *Bacillus subtilis* H 158 and strobilurins for rice sheath blight control, *Biol. Control* 117 (2018) 182–187.
- [15] Y.Y. Yu, C.H. Jiang, C. Wang, et al., An improved strategy for stable biocontrol agents selecting to control rice sheath blight caused by *Rhizoctonia solani*, *Microbiol. Res.* 203 (2017) 1–9.
- [16] S.J. Wei, J. Xu, G.Q. Tu, The efficacy evaluation of Ag-antibiotic 702 in the treatment of rice pathogenic fungi, *Jiangxi Nongye Daxue Xuebao/Journal of Jiangxi Agricultural University*, 33 (2011) 488–492 (in Chinese).
- [17] H. Zhang, Q.H. Zhao, W.H. Tang, G.A. Wolf, The influence of Jinggangmycin A on the activities of resistance-related enzymes in rice, *Zhiwu Baohu Xuebao/Journal of Plant Conservation*, 24 (1992) 511–519 (in Chinese).
- [18] L.J. Cheng, Q.Q. Liu, Y.F. Lei, Y.L. Lin, A.Q. Zhang, The synthesis and characterization of carboxybetaine functionalized polysiloxanes for the preparation of anti-fouling surfaces, *RSC Adv.* 4 (2014) 54372–54381.
- [19] A.Q. Zhang, Q.Q. Liu, Y.F. Lei, S.H. Hong, Y.L. Lin, Synthesis and antimicrobial activities of acrylamide polymers containing quaternary ammonium salts on bacteria and phytopathogenic fungi, *React. Func. Polymers* 88 (2015) 39–46.
- [20] L.J. Cheng, Q.Q. Liu, L. Yang, Y.L. Lin, A.Q. Zhang, Synthesis and characterization of hydrogen-containing polysiloxanes (in Chinese), *Gaofenzi Cailiao Kexue Yu Gongcheng/Polymer, Mater. Sci. Eng.* 30 (2014) 25–28.
- [21] J. Wang, A. Sugawara-Narutaki, A. Shimajima, et al., Dendritic silica nanoparticles synthesized by a block copolymer-directed seed-regrowth approach, *Langmuir* 31 (2015) 1610–1614.
- [22] M. Fukao, A. Sugawara, A. Shimajima, et al., One-dimensional assembly of silica nanospheres mediated by block copolymer in liquid phase, *J. Am. Chem. Soc.* 131 (2009) 16344–16345.
- [23] Z.F. Huang, R.Q. Liuyang, C.Y. Dong, et al., Polymeric quaternary ammonium salt activity against *Fusarium oxysporum* f. sp. *Cubense* race 4: synthesis, structure-activity relationship and mode of action, *React. Func. Polym.* 114 (2017) 13–22.
- [24] Y.H. Lin, Y.J. Lin, T.D. Chang, et al., Development of a Taqman probe-based insulated isothermal polymerase chain reaction (iiPCR) assay for detection of *Fusarium oxysporum* f. sp. *cubense* race 4, *PLoS One* 11 (2016) 1–13.
- [25] C.C. Sollod, A.E. Daub, Cell surface redox potential as a mechanism of defense against photosensitizers in fungi, *Appl. Environ. Microbiol.* 58 (1992) 444–449.
- [26] K.J. Rao, S. Paria, Anti-Malassezia furfur activity of natural surfactant mediated in situ silver nanoparticles for a better antidandruff shampoo formulation, *RSC Adv.* 6 (2016) 11064–11069.
- [27] X. Shao, S. Cheng, H. Wang, et al., The possible mechanism of antifungal action of tea tree oil on *Botrytis cinerea*, *J. Appl. Microbiol.* 114 (2013) 1642–1649.
- [28] K.N. Fish, S.L. Schmid, H. Damke, Evidence that dynamin-2 functions as a signal-transducing GTPase, *J. Cell Biol.* 150 (2000) 145–154.
- [29] F. Wu, G.L. Meng, Jing He, et al., Antibiotic-loaded chitosan hydrogel with superior dual functions: antibacterial efficacy and osteoblastic cell responses, *ACS Appl. Mater. Interfaces* 6 (2014) 10005–10013.
- [30] M.M. Bradford, A rapid and sensitive method for the quantitation of microgram quantities of protein utilizing the principle of protein–dye binding, *Anal. Biochem.* 72 (1976) 248–254.
- [31] H.J. Lee, J.S. Hwang, D.G. Lee, Scolopendin 2 leads to cellular stress response in *Candida albicans*, *Apoptosis* 21 (2016) 856–865.
- [32] A. Singh, M.P. Pal, Darokar, a polyphenolic flavonoid glabridin: oxidative stress response in multidrug-resistant *Staphylococcus aureus*, *Free Radic. Biol. Med.* 87 (2015) 1–28.
- [33] R.H. Mohamed, R.A. Karam, H.A. Hagrass, et al., Anti-apoptotic effect of spermatogonial stem cells on doxorubicin-induced testicular toxicity in rats, *Gene* 561 (2015) 107–114.
- [34] J.H. Kim, Immobilized DNA-binding assay, an approach for *in vitro* DNA-binding assay, *Anal. Biochem.* 334 (2004) 401–402.
- [35] E.F. Palermo, I. Sovadinova, K. Kuroda, Structural determinants of antimicrobial activity and biocompatibility in membrane-disrupting Methacrylamide random copolymers, *Am. Chem. Soc.* 10 (2009) 3098–3107.
- [36] P. Plodpai, S. Chuenchitt, V. Petcharat, et al., Anti-*Rhizoctonia solani* activity by *Desmos chinensis* extracts and its mechanism of action, *Crop Prot.* 43 (2013) 65–71.
- [37] S.S. Lindsay, B. Wheeler, K.E. Sanderson, et al., The release of alkaline phosphatase and of lipopolysaccharide during the growth of rough and smooth strains of *Salmonella typhimurium*, *Can. J. Microbiol.* 19 (1973) 35–43.
- [38] K.J. Cheng, J.M. Ingram, J.W. Costerton, Release of alkaline phosphatase from cells of *Pseudomonas aeruginosa* by manipulation of cation concentration and of Ph, *J. Bacteriol.* 104 (1970) 748–753.
- [39] J. Zhang, G.B. Akcapinar, L. Atanasova, et al., The neutral metalloprotease NMP1 of *Trichoderma guizhouense* is required for mycotrophy and self-defence, *Environ. Microbiol.* 18 (2015) 580–597.
- [40] W.W. Fan, G.Q. Yuan, Q.Q. Li, et al., Antibacterial mechanisms of methyl gallate against *Ralstonia solanacearum*, *Australas. Plant Pathol.* 43 (2014) 1–7.
- [41] Fatma Öztürk, Leyla Açı, İzzet Şener, Fikret Karci, Emine Kiliç, Antimicrobial properties and DNA interactions studies of 3-hetarylazoquinoline-2, 4-diol compounds, *Turk. J. Chem.* 36 (2012) 293–302.
- [42] B. Dede, I. Özmen, F. Karipcin, Synthesis, characterization, catalase functions and DNA cleavage studies of new homo and heteronuclear Schiff base copper (II) complexes, *Polyhedron* 28 (2009) 3967–3974.
- [43] E.E. İltir, N. Asmafiliz, Z. Kiliç, et al., Phosphorus–nitrogen compounds: part 19. Syntheses, structural and electrochemical investigations, biological activities, and DNA interactions of new spirocyclic monofluorocyclotriphosphazenes, *Polyhedron* 29 (2010) 2933–2944.
- [44] C.D. Georgiou, N. Patsoukis, et al., Sclerotial metamorphosis in filamentous fungi is induced by oxidative stress, *Integr. Comp. Biol.* 46 (2006) 691–712.



Polymeric quaternary ammonium salt activity against *Fusarium oxysporum* f. sp. *cubense* race 4: Synthesis, structure-activity relationship and mode of action



Zhenfeng Huang^{a,1}, Runqi Liuyang^{a,1}, Chengyun Dong^a, Yufeng Lei^b, Anqiang Zhang^b, Yaling Lin^{a,*}

^a College of Materials and Energy, South China Agricultural University, 483 Wushan Rd., Guangzhou 510642, Guangdong, China

^b College of Material Science and Engineering, South China University of Technology, 381 Wushan Rd., Guangzhou 510641, Guangdong, China

ARTICLE INFO

Article history:

Received 26 December 2016

Received in revised form 20 February 2017

Accepted 28 February 2017

Available online 03 March 2017

Keywords:

Polymeric quaternary ammonium salts

Antifungal bioassay

Mechanism of antifungal action

ABSTRACT

Polymeric quaternary ammonium salts (PQAS) have been widely used to prevent microbial contamination, but little is known about their activity against phytopathogenic fungi. Our previous report described the synthesis of two novel PQAS, namely a homopolymer of (2-methacrylamido) propyltetra benzyl dimethyl ammonium chloride (PQD-BC) and dimethylaminopropyl benzyl chloride-grafted polysiloxanes (PDMS-g-BC); we demonstrated their structure-activity relationship against phytopathogenic fungi such as *R. solani* and *Fusarium oxysporum* f. sp. *cubense* tropical race 4 (Foc4). Here, we analyzed the structure-activity relationship and toxicity mechanism of these compounds at the molecular level against Foc4 compared with the low molecular-weight quaternary ammonium salt benzalkonium chloride (BC). The results revealed that PQD-BC and PDMS-g-BC application inhibited the growth of Foc4 in a concentration-dependent manner and that PDMS-g-BC exhibited higher activity than PQD-BC. In addition, these polymers were found to induce cell death in Foc4 by disrupting the cellular structure integrity, such as the loss of the cell wall and plasma membrane integrity and oxidative stress (lipid peroxidation), leading to the release of intracellular contents and inducing mitochondrial dysfunction and interference with genomic DNA. The newly elucidated mechanism provides possible applications in which PQAS can be used against phytopathogenic fungi.

© 2017 Elsevier B.V. All rights reserved.

1. Introduction

Fusarium wilt is caused by *Fusarium oxysporum* f. sp. *cubense*, which is also known as Panama disease, and it is regarded as one of the most devastating soil-borne diseases affecting bananas [1–5]. Foc tropical race 4 (Foc4) is the most virulent race, and it can infect almost all commercial banana cultivars; at present, there are no completely effective control methods [2]. A number of studies have been performed to control *Fusarium* wilt with biotechnology, including the transfer of antifungal genes into bananas and using biocontrol agents to control fungal disease [4–6]. However, there are few studies on the use of synthetic fungicides to effectively prevent *Fusarium* wilt in field trials.

Cationic antimicrobials are well known for their use in self-sterilizing surfaces, and they are used for numerous applications such as hospital surfaces, surgical equipment, protective clothes in hospitals, medical implants, wound dressings, food packaging materials, and everyday consumer products. Nevertheless, small molecule cationic antimicrobials

can be highly toxic to the environment, and their protection is shown to be short-lived due to the difficulty involved in controlling their diffusion rate, and water-soluble antimicrobial compounds have led to the rapid emergence of resistant strains and environmental problems [7–9]. It is well known that the bacterial cell surface is negatively charged, and the adsorption of polycations onto the negatively charged cell surface is expected to be enhanced with the increasing molecule weight of the polymers due to the increasingly charged density of the polycations [10]. Given that their high microbicidal activity arises not only from highly cationic charges but also substantial hydrophobicity (*i.e.*, the alkyl chain length), modified polycations must possess a degree of hydrophilic/hydrophobic balance to ensure high activity and water insolubility; the hydrophobic chains must be able to trigger-gather, producing different adsorptions onto the cell surface [11]. In addition, the polymeric salts were more active than the corresponding monomer with the longest alkyl chain [10–13]. Among the most commonly used cationic antimicrobials, cationic polymers with quaternary ammonium groups show great promise in the field of antimicrobial coatings [11]. To create these coatings, a great deal of attention has recently been paid to polymeric quaternary ammonium compounds (PQAS), which are employed as biocides owing to their low toxicity and broad antimicrobial spectrum [14–16].

* Corresponding author.

E-mail address: linaling@scau.edu.cn (Y. Lin).

¹ These authors contributed equally.

The mode of action of cationic biocides has been summarized as follows: (i) adsorption onto the bacterial cell surface, (ii) diffusion through the cell wall, (iii) binding to the cytoplasmic membrane, (iv) the release of the cytoplasmic constituents, and (v) the death of the cell [17]. The targets of antifungal agents are heavily focused, directly or indirectly, on the cell envelope (wall and plasma membrane), and particularly on the fungal membrane sterol and ergosterol, and on their biosynthesis. Therefore, targets located elsewhere in the cell would be a welcome innovation for systemically bioavailable antifungal agents [18–20]. Several reports have revealed that some antifungal agents specifically inhibit the synthesis of cell wall polysaccharides, particularly chitin or β -glucan, and some others are involved in synthesizing informational macromolecules, namely RNA or DNA, in susceptible fungi [3,21]. Although the antimicrobial effects of PQAS have been extensively investigated, little is known about the structure-activity relationship and the mechanism of antimicrobial action, especially the antifungal mechanism, which hindered their broader application in the antimicrobial field. To date, numerous reports have revealed that PQAS primarily targets the microbial membrane and accumulates in cells driven by the cell membrane potential, but there are no clear-cut reports on their mode of action elsewhere in the cell at the molecular level, which therefore must be investigated.

From this perspective, the synthesis of two novel PQAS with different structures and compositions, that is, the homopolymer of (2-methacrylamido) propyltetrabenzyl-dimethylammonium chloride (PQD-BC) and dimethylaminopropyl benzyl chloride grafted polysiloxanes (PDMS-g-BC), have previously been reported, and we have demonstrated their structure-activity relationship against phytopathogenic fungus such as *R. solani* and Foc4 [22–25]. The aim of the present study was to discuss their structure-activity relationship and toxic mechanism of action at the molecular level along with that of the broad-spectrum microbicide benzalkonium chloride (dodecyl dimethyl benzyl ammonium chloride, BC), which has the same key group (benzyl) as synthetic polymers. The antimicrobial activities of polymers were evaluated against Foc4, and the integrity of the cellular structure (the cytoplasmic membrane and cell wall) was detected to investigate the mode of antifungal action. To investigate the targets in detail elsewhere in the cell, in which polymers inhibited fungal growth, we investigated the interaction of the synthetic polymers and intracellular macromolecules, such as the intracellular enzyme activity (succinic dehydrogenase, SDH) and informational macromolecules (genomic DNA). It is meaningful to develop polymers with antifungal activity and study their structure-activity relationship for the future development of broad-spectrum multifunctional materials.

2. Experimental

2.1. Materials

Bovine serum albumin (BSA) was provided by Hangzhou Sijiqing Biological Engineering Materials Co. Ltd. (Hangzhou, China). TTC (2, 3, 5-triphenyltetrazolium chloride) was purchased from Sangon Biotech (Shanghai) Co., Ltd. (Shanghai, China). *N,N*-Dimethylamine propyl methacrylamide (DAPMA), benzyl chloride (99%), ammonium persulfate (APS, 99%), and PI (propidium iodide) were supplied by Aladdin Reagent Co. Ltd. (Shanghai, China). *N,N*-dimethylallylamine (DMAA, 98%) was supplied by Haining Huangshan Chemical Co. Ltd. (Haining, China). The fungal strain used in this study is *Fusarium oxysporum* f. sp. *cubense* (E. F. Smith) Snyder & Hansen (Foc4), which was donated by the Laboratory of Fungi at South China Agriculture University and maintained on potato dextrose agar (PDA). Foc4 spores were obtained from the surface of the agar after culture for 3 days at 28 °C and 5 days at 35 °C. The spores were suspended in 5 mL of sterile distilled water containing 0.05% (v/v) Tween 20. The concentration of the spore suspensions was determined using a hemocytometer. Benzalkonium chloride (BC) with a purity of over 95% was purchased

from Shanghai Aladdin Bio-Chem Technology Co., Ltd. (Shanghai, China).

2.2. Synthesis of PDMS-g-BC and PQD-BC

Dimethylaminopropyl benzyl chloride-grafted polysiloxanes (PDMS-g-BC) and the homopolymer of (2-methacrylamido) propyltetrabenzyl-dimethylammonium chloride (PQD-BC) were synthesized according to our previous articles [22–25], as shown in Schemes 1 and 2. In which, the PDMS-g-BC with specified molecular weights and structure ($M_n \sim 2.5 \times 10^3$ g/mol, M_w/M_n (DPI) ~ 2.1 , cationic content ($m/(m+n) \sim 20$ mol%), which showed optimized antimicrobial activities against Foc4, according to Ref [24], was synthesized and chosen as the sample for extensively studies. While for PQD-BC, the molecular weight (M_n) based on Ubbelohde capillary viscometer was about 3.2×10^5 g/mol, according to ref. [23].

2.3. Antifungal bioassay

2.3.1. Mycelia growth inhibition method

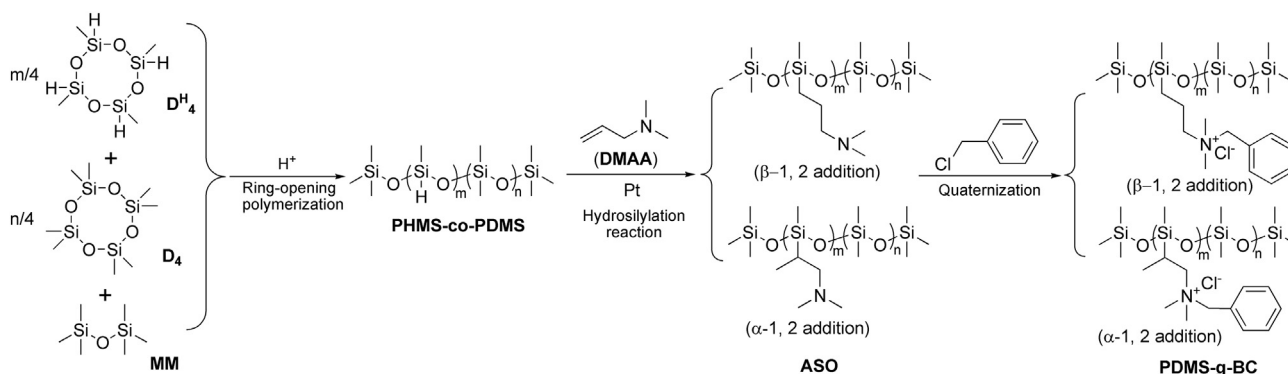
The effect of synthetic compounds (PDMS-g-BC, PQD-BC, and BC) on the mycelial growth of Foc4 was measured using an *in vitro* mycelial growth inhibition assay [26–28]. In brief, 6-mm-diameter disks of mycelial agar were cut with a sterile cork borer from the actively growing edge of 5-day-old cultures on PDA plates. Each one was then was placed in the center of each 9-cm-diameter Petri dish containing PDA medium with various concentrations of polymers (0–1.6 mg/mL). Before being mixed with molten agar at a temperature below 60 °C, the synthetic compound solutions were sterilized by passing them through a 0.45 μ m Millipore filter. The radial growth of Foc4 was detected after it was incubated at 28 °C for 5 days. Equal volumes of sterile distilled water were used as the negative control. Mycelial growth was expressed as the diameter of the fungal colony (mycelium) in the Petri dish minus the diameter of the agar plugs (6 mm). The inhibition percentage was calculated according to the following formula:

$$\text{Inhibitory rate} = \frac{D_c - D_t}{D_c} \times 100\% \quad (1)$$

where D_c is the mean colony diameter for the control set and D_t is the mean colony diameter for the treatment set. The concentration-dependent curve was the biological probability value of inhibition rates for the Y-axis against the log (test sample concentration) for the X-axis. The IC_{50} and IC_{90} values were defined as the concentration required for 50% and 90% inhibitions of mycelial growth, respectively (seen in Table 1). The antifungal effects of synthetic compounds were expressed as the IC_{50} and IC_{90} , which were evaluated further using the below-mentioned method. Each measurement consisted of at least three replicates. The mycelial growth picture is shown in Fig. 1.

2.3.2. Minimum inhibitory concentration (MIC)

The minimum inhibitory concentration (MIC) of the synthetic compounds against Foc4 was determined by using the broth microdilution procedure with 2, 3, 5-triphenyl-tetrazolium chloride (TTC). The TTC reagent is colorless, but it gives off a bright red color when reduced, indicating the presence of live fungi [29,30]. Foc4 spores were cultured in sterile potato dextrose (PD) medium (in liquid) with different concentrations of compounds solutions in 96-well plates (100 μ L of medium per well) at a concentration of approximately 1.0×10^5 cells/mL. After the spores were cultured for 24 h, 5 μ L (5.0 mg/mL) of TTC solution (in PD medium) was added to each well, and the 96-well plates were subsequently incubated in the dark at 28 °C for another 4 h. Two controls were set up; in one control, no spores were added to the wells (blank wells) containing an equal volume of sterile PD medium, and in the other, an equal volume of spores (1.0×10^5 cells/mL) was added to the wells with an equal volume of sterile PD medium without



Scheme 1. Synthesis routine for PDMS-g-BC. *m* and *n* are number of hydrogen-containing segments and number of non-hydrogen-containing segments, respectively.

the compounds (negative control). The visual color changes were recorded before and after incubation to determine the MIC (mg/mL, present in the well). The color changes present in the well matched that of the blank well that was taken as the MIC for each fungus.

2.3.3. Minimal fungicidal concentration (MFC)

To differentiate between the fungistatic and fungicidal effect of the compounds, the MFC of the polymers against *Foc4* was determined by spot plate method. Aliquots from wells that appeared to have fewer or no colonies were plated on PDA plates. For this purpose, 50 μ L of culture from each well was taken after the MIC experiment and spotted onto the PDA plates. The PDA plates were then incubated for 3 days at 28 $^{\circ}$ C to allow the cells to grow. The number of colonies present in the well for which no colony was observed on the PDA plates was taken as the minimal fungicidal concentration (MFC) for each fungus.

2.4. Mechanism of antifungal action

2.4.1. Cytoplasmic membrane disruption assay

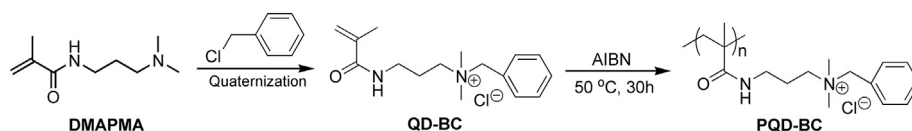
To observe the plasma membrane integrity, *Foc4* spores were cultured in sterile PD medium containing synthesis compounds at three different concentrations (the MIC, IC_{50} , and IC_{90}). The treatment concentration was chosen on the basis of the antifungal bioassay and a control was made in a similar manner in sterile PD medium without the test compounds. After incubation under constant shaking at 28 $^{\circ}$ C for 48 h, the spore suspension was harvested, washed twice with PBS (pH 7.4), and finally resuspended in 100 μ L of PBS. Then, 10 μ L of spore suspension was combined with 15 μ M of the red fluorescent nucleic acid stain propidium iodide (PI), which is commonly used for detecting the cellular membrane integrity [31]. After it was incubated in the dark for 15 min, the mixture was centrifuged, washed twice with PBS to remove residual dye and resuspended in 100 μ L of PBS. A 5 μ L aliquot was placed on a glass slide, which was then covered by a cover slip, sealed, and examined under a fluorescence microscope (Nikon Eclipse 80i, Japan). Excitation was performed for PI at 543 nm. Emissions were collected using a long pass filter for PI at 590–800 nm. The images were captured through a charge-coupled device camera. Three fields of view were chosen randomly from each cover slip. The experiment was repeated three times.

2.4.2. Cellular leakage assay

The leakage of cytoplasmic contents from the mycelia was determined to explain the changes in membrane permeabilization according to the method of Lewis and Papavizas with some modifications [32]. *Foc4* was cultured in PD medium on a rotary shaker at 120 rpm for 3 days at 28 $^{\circ}$ C. The mycelia were then harvested and washed with phosphate-buffered saline (PBS, pH 7.4). The equal mass-washed mycelia were re-suspended in 50 mL of sterile distilled water containing test compounds at three different concentrations (IC_{90} , $6 \times IC_{90}$ and $12 \times IC_{90}$, as seen in Table 1) and incubated on a rotary shaker for 8 h. The controls were treated with the same quantity of sterile distilled water. Samples from the suspensions were collected and filtered at 2 h intervals during the incubation. The filtered solutions were used to determine the leakage of soluble proteins, carbohydrates and nucleic acids. A Bradford assay was performed to quantify the release of the proteins, using BSA as the standard [33]. Soluble carbohydrates were detected by anthrone reaction, which uses glucose as the standard [34]. The electric conductivity of the resulting supernatant was measured in a conductivity meter (DDS-11A, Shanghai Precision Scientific Instrument Co., Ltd. Shanghai, China) [28]. Each measurement consisted of at least three replicates.

2.4.3. Lipid peroxidation analysis

The lipid peroxidation in the cell membrane of *Foc4* was quantified based on its malondialdehyde (MDA) levels [35–37]. *Foc4* was cultured in PD medium on a rotary shaker at 120 rpm for 3 days at 28 $^{\circ}$ C. To detect lipid peroxidation, the fungal suspensions were treated with compounds at three different concentrations ($1/2 \times IC_{90}$, IC_{90} , and $2 \times IC_{90}$, as seen in Table 1), with no addition to the control group. The fungal suspensions were incubated for another 24 h at 28 $^{\circ}$ C with shaking at 120 r/min. The fungal suspensions were centrifuged at 12,000 rpm for 5 min, after which the pellet was sonicated twice on ice with lysis buffer (2% Triton-X 100, 1% SDS, 100 mM NaCl, 10 mM Tris-HCl, 1 mM EDTA [pH 8.0]) in 5% trichloroacetic acid (TCA). The mixture was centrifuged, and the supernatant was harvested as a crude MDA-mycelial solution. The MDA contents of the mycelia and medium were determined using an MDA kit purchased from Nanjing Jiancheng Institute of Bioengineering (Nanjing, Jiangsu, China). MDA can react with freshly prepared thiobarbituric acid to form a colored complex, which has a maximum absorbance at 532 nm in a UV-Vis spectrophotometer (UV2300,



Scheme 2. Synthesis routine for PQD-BC.

Table 1
The antifungal effect of PQD-BC, PDMS-g-BC and BC against Foc4.

Compounds	Mycelial growth		Spore propagation		
	IC ₅₀ (mg/mL)	IC ₉₀ (mg/mL)	MIC (mg/mL)	MFC (mg/mL)	MFC/MIC
PQD-BC	1.0	2.78	0.3	2.0	6.67
PDMS-g-BC	0.64	7.05	0.15	0.4	2.67
BC	0.06	0.52	0.1	0.2	2.0

Techcomp, Shanghai, China) [35]. Each experiment was performed in triplicate.

2.4.4. Cell wall disruption assay

The cell wall integrity was expressed as the increased alkaline phosphatase (ALP) of the medium after compounds treatments [28]. Foc4 was cultured in PD medium and rotated at 28 °C on a rotary shaker at 120 rpm for 3 days. After that, 5 mL of sterile distilled water containing polymers was added to the above medium at three different concentrations (the MIC, IC₅₀, and IC₉₀) and incubated on a rotary shaker for another 48 h. The controls were treated with the same quantity of sterile distilled water. The suspensions were centrifuged at 4000 × g for 10 min to obtain the supernatants. To find the effects of the polymers on the cell wall, the activity of ALP in the supernatant was determined by using assay kits purchased from the Nanjing Jiancheng Institute of Bioengineering (Nanjing, Jiangsu, China) according to the manufacturer's instructions, and the result was recorded in U/L [28]. Each treatment had three replicates.

2.4.5. Efficacy on mitochondrial function

The mitochondrial function of Foc4 was expressed by the extracellular enzyme SDH activity (A_{SDH}) [38]. Foc4 was cultured in PD medium on a rotary shaker at 120 rpm for 3 days at 28 °C. Sterile distilled water-dissolved compounds were added to the fungal suspension to reach the final concentrations needed for the MIC, IC₅₀ and IC₉₀, and they were incubated on a rotary shaker for another 48 h. The controls received the same quantity of sterile distilled water. The mycelia were filtered and used to isolate mitochondria with a Mitochondrial Isolation Kit (Beijing Solarbio Science & Technology Co. Ltd., Beijing, China). Before the mitochondria were extracted, the mycelia were ground under liquid nitrogen. The A_{SDH} was determined using the assay kits purchased from the Nanjing Jiancheng Institute of Bioengineering (Nanjing, Jiangsu, China). The total protein content was determined by Bradford method [33]. Afterwards, the amount of protein was calculated according to the standard protein curve, which was measured with different

concentrations of a protein standard. The A_{SDH} was calculated using the following equation:

$$A_{SDH} = \frac{\Delta OD_{600} \times 100}{C_s/V_s} \quad (2)$$

where ΔOD_{600} is the reduction of OD (Optical density, conceptually and numerically equivalent to absorbance) value at 600 nm of the sample in 1 min, C_s is the protein concentration (mg/mL) and V_s is the volume of the sample (mL).

SDH can take part in reduction of 2, 6-dichlorophenolindophenol, which has a maximum absorbance at 600 nm in a UV-Vis spectrophotometer. One unit of SDH activity was defined as the amount of enzyme in 1 mL of fungal suspension with a 1 min reaction time that gave a reduction by 0.01 absorbance unit. Each treatment had three replicates.

2.4.6. In Vitro electrophoretic mobility shift assay (EMSA)

The DNA-binding activities of genomic DNA and the compounds were assessed by EMSA, which is widely used to research antimicrobial drugs, and it is based on the observation that bound DNA complexes migrate through gels more slowly than unbound DNA fragments [39–40]. To obtain a significant amount of highly purified genomic DNA, Foc4 was cultured in PD medium on a rotary shaker at 120 rpm for 3 days at 28 °C. The mycelia were then collected and washed twice with PBS (pH 7.4) to remove the medium. After freeze-drying, the total intracellular DNA was extracted with an Ezup Column Fungi Genomic DNA Purification Kit (Sangon Biotech Co., Ltd., Shanghai, China), and RNase was added. Genomic DNA gave a UV absorbance ratio of 1.8–1.9 at 260 and 280 nm (A_{260}/A_{280}), indicating that the DNA was sufficiently free of proteins. 5 µg highly purified genomic DNA with a fixed concentration (500 µg/mL) was incubated with the TE buffer containing aliquots of chemical compounds at three different concentrations (the MIC, IC₅₀, and IC₉₀) at room temperature for 10 min. The interaction between the compounds and genomic DNA was studied by agarose gel electrophoresis, and the TE buffer alone was incubated with a DNA control. A 5 µL volume of GoldView™ (Beijing Solarbio Science & Technology Co. Ltd., Beijing, China) was used as fluorescent dye and 1 mg of DNA was loaded onto the 1% gel; electrophoresis was performed in TAE (Tris Acetate EDTA) buffer for 60 min. The gel was visualized under UV light using a Bio-Rad Trans illuminator IEC 1010. All the experiments were repeated three times.

2.4.7. In vivo efficacy on genomic DNA

To investigate whether the compounds penetrated the cell barriers and interacted with genomic DNA, we also studied the *in vivo* efficacy against Foc4 genomic DNA after the compounds treatments. Foc4 was

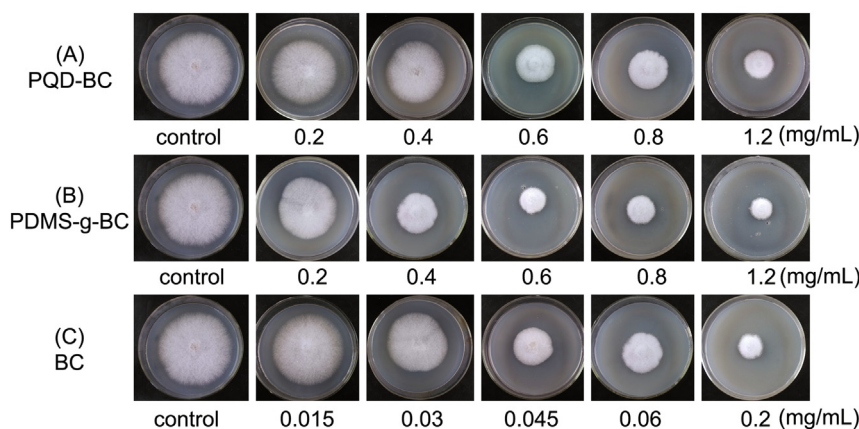


Fig. 1. The mycelial growth of Foc4 in PDA medium after applying PQD-BC (A), PDMS-g-BC (B) and BC (C). The data were based on three replicates, and the test was repeated twice with similar results. The representative results are shown.

cultured in PD medium on a rotary shaker at 120 rpm for 3 days at 28 °C. Sterile distilled water-dissolved compounds were added to the fungal suspension to reach the final concentrations needed for the MIC, IC₅₀ and IC₉₀ and they were incubated on a rotary shaker for another 48 h. The controls received the same quantity of sterile distilled water. The mycelia were collected and washed twice with PBS (pH 7.4) to remove the medium, and then ground under liquid nitrogen. The total intracellular DNA was extracted with assay kits (Sangon Biotech Co. Ltd., Shanghai, China), and RNase was added. The *in vivo* interaction between the compounds and genomic DNA was studied by agarose gel electrophoresis. All the experiments were repeated three times.

2.5. Statistical analysis

SPSS software (SPSS Inc., Chicago, IL, USA) was used for the statistical analyses of the data. To determine the effects of the treatments, an analysis of variance (ANOVA) was performed. A Duncan's multiple range test was used for mean separations when the treatment effects were statistically significant ($P < 0.05$).

3. Results and discussion

3.1. Antifungal activity

The effects of PQD-BC, PDMS-g-BC and BC on the mycelial growth of Foc4 were detected at various concentrations on PDA plates. The test compounds inhibited the growth of Foc4 in a dose-dependent manner at concentrations ranging from 0.2–1.2 mg/mL (PQD-BC and PDMS-g-BC) and from 0.015–0.2 mg/mL (BC) (Fig. 1). After 5-day incubation, the PQD-BC displayed antifungal effects with an IC₅₀ of 1.0 mg/mL and an IC₉₀ of 2.78 mg/mL, whereas PDMS-g-BC exhibited antifungal activity with an IC₅₀ of 0.64 mg/mL and an IC₉₀ of 7.05 mg/mL, which indicated that the inhibitory effect of PDMS-g-BC was greater than that of PQD-BC. BC exhibited the most active effect against Foc4 (IC₅₀ = 0.06 mg/mL, IC₉₀ = 0.52 mg/mL). The determination of the antifungal efficacy showed that PQD-BC, PDMS-g-BC and BC inhibit the mycelial growth of Foc4 in a dose-dependent manner.

We subsequently tested the MIC and MFC of PQD-BC, PDMS-g-BC and BC against Foc4 as shown in Fig. 2. The *in vitro* studies showed that PQD-BC exerted antifungal action against Foc4 with an MIC of 0.3 mg/mL and an MFC of 2 mg/mL. PDMS-g-BC displayed antifungal action against Foc4 with an MIC of 0.15 mg/mL and an MFC of 0.4 mg/mL. The MIC and MFC values of BC against Foc4 were 0.1 and 0.2 mg/mL, respectively.

The ratios of MFC to MIC were used to define an organism as tolerant. For comparable antifungal efficiency in PQD-BC with a polyacrylamide

backbone (MFC/MIC = 6.67) against Foc4, the MIC of PDMS-g-BC with a larger hydrophobic polydimethylsiloxane backbone against Foc4 is lower, which indicates that incorporating a more hydrophobic backbone into polymers is easier to trigger-gather adsorbance onto the cell surface and strengthen the antimicrobial activities of PQAS. This finding also indicated that PDMS-g-BC is a promising application for antifungal agents against plant pathogenic disease (MFC/MIC = 2.67, a ratio value of <4 corresponding to fungicide) [41], which can be compared to that of BC (MFC/MIC = 2). The fungal cell surfaces are negatively charged in the same way as the bacterial cell surface due to their components (chitin and β -glucan), and PQD-BC, PDMS-g-BC and BC with the same cationic group and different degrees of hydrophilicity are able to trigger-gather, leading to different degrees of adsorption onto the Foc4 cell surface according to the results of the mycelia growth inhibition method and the broth microdilution method. Taken together, the antifungal activities of PQAS are affected by certain molecular weights and degrees of hydrophobicity, and these results thus indicated that PQD-BC and PDMS-g-BC could be used to develop antifungal materials.

3.2. Mechanism of antifungal action

3.2.1. Membrane-active mode of action

Quaternary ammonium salts treatments can rapidly lead to the disintegration of biological membranes in fungal pathogens, resulting in cell death [6]. To establish the mode of antifungal action, the cytoplasmic membrane integrity was disrupted with compounds against Foc4 using a fluorescent dye (PI) by fluorescence microscopy. The PI is membrane-impermeable and is generally excluded from viable cells only when the fungal membrane is compromised, and the microscopy results thus indicated that the cationic polymer interacted with and subsequently disrupted the membrane integrity of the fungi. Fluorescence microscope images showed that in comparison with the control, the cells that were treated with the compounds showed complete membrane permeabilization as clearly indicated by red fluorescence, which shows that the numbers of spores that lost plasma membrane integrity increased after PQD-BC, PDMS-g-BC and BC treatments (Fig. 3). All the cationic biocides were found to depolarize the membrane integrity of Foc4, and they may inhibit the growth of Foc4 by directly damaging the plasma membrane and causing the cell death of the fungal pathogen.

Damage to the plasma membrane can lead to the loss of the osmotic balance and the influx of fluids and ions as well as the loss of proteins and carbohydrates, eventually causing the onset of cell death [24]. To confirm whether PQD-BC, PDMS-g-BC and BC caused a loss in the cytoplasmic membrane integrity of Foc4, the leakage of cytoplasmic

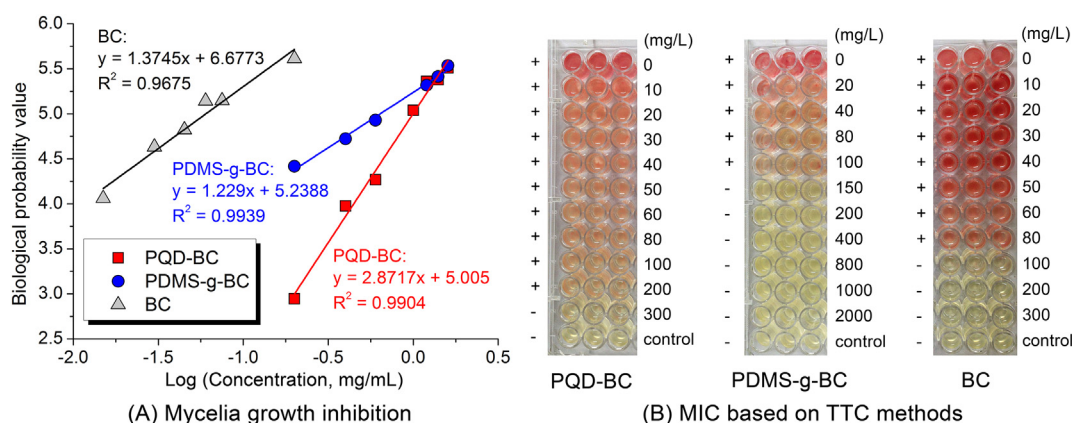


Fig. 2. (A) Effect of PQD-BC, PDMS-g-BC and BC on mycelial growth of Foc4 in PDA medium. The growth of Foc4 was measured after 5 days of incubation at 28 °C. The data were based on three replicates. Treatments followed by different letters within each sampling interval are significantly different according to Duncan's multiple range test ($P < 0.05$). (B) The MIC values of PQD-BC, PDMS-g-BC and BC against Foc4 based on the TTC colorimetric method. (+) indicates certain cells in the plate and (–) indicates fewer or no cells in the plate.

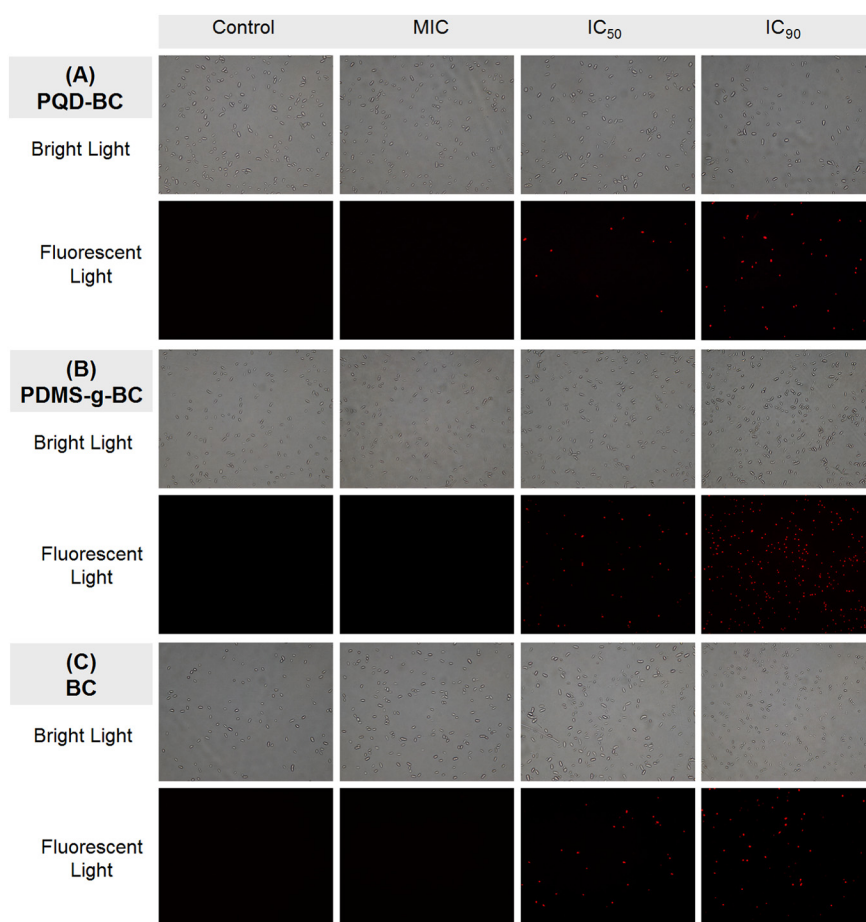


Fig. 3. Loss of plasma membrane integrity in Foc4 after PQD-BC (A), PDMS-g-BC (B) and BC (C) treatments. The spores were stained with PI and observed with a fluorescence microscope. The spores are magnified by 20 times life size. Spores with damaged plasma membranes fluoresced red. (For interpretation of the references to color in this figure legend, the reader is referred to the web version of this article.)

constituents was determined. As expected, it is clear from the figure that the three compound treatments significantly induced the leakage of soluble proteins (Fig. 4-A), carbohydrates (Fig. 4-B), and conductivity (Fig. 4-C) out of the Foc4 mycelia. In general, the amount of leaked materials was positively correlated with the concentrations of PQD-BC, PDMS-g-BC and BC. The cellular leakage could be observed after 4 h of treatment, and it was generally constant over a period of 6 h for soluble proteins, carbohydrates, and electric conductivity. Since we observed the same physiological events with the release of cytoplasmic constituents, it is quite reasonable to assume that the mode of action of PQD-BC, PDMS-g-BC and BC can be interpreted on the basis of each elementary process in which cationic biocides adsorb onto the fungal cell surface, diffusing through the cell wall, and subsequently binding to the cytoplasmic membrane, releasing the cytoplasmic constituents, and finally inducing the cell death of the fungal pathogen. The hydrophobicity of the polymers enabled them to partition into the lipids of the fungal cell membrane and mitochondria, rendering them permeable and leading to the leakage of the cell contents.

Taken together with the antifungal efficiency of PQD-BC and PDMS-g-BC, the penetration is intensively affected by the interaction of the ammonium group with the cytoplasmic membrane and the mobility of the functional group. With a stronger driving force, the ammonium group can reach the cytoplasmic membrane more easily. Therefore, the increase in antifungal efficiency with a longer hydrophobic polydimethylsiloxane backbone may be explained by the increasing hydrophobicity of the quaternary group, which may strengthen the interaction with the cytoplasmic membrane, therefore enhancing the ability to kill the fungal cell.

3.2.2. Lipid peroxidation

To investigate the lipid damage, the levels of MDA, a biomarker of lipid peroxidation and a decomposition product of polyunsaturated fatty acid hydroperoxidase, were assessed [35]. MDA, which was primarily released into the medium when the plasma membrane lipid peroxidation was set off, and it was determined to investigate whether lipid peroxidation was associated with membrane damage [36]. In the lipid peroxidation assay, exposure of Foc4 for 24 h to PQD-BC of $1/2 \times IC_{50}$, IC_{50} and IC_{90} led to a the highest release (4.58, 8.33 and 21.67 mmol/g, respectively) of MDA among treatment-groups, whereas exposure to PDMS-g-BC of $1/2 \times IC_{50}$, IC_{50} and IC_{90} led to the second-highest release (0.61, 2.39 and 20.4 mmol/g, respectively) of MDA. No obvious effect on the BC-treated group was detected (data not shown). The results show that significantly increased MDA levels occur as a result of the oxidative damage induced by exposing Foc4 to $1/2 \times IC_{90}$, IC_{90} and $2 \times IC_{90}$ of PQD-BC (Fig. 5-A) and PDMS-g-BC (Fig. 5-B) for 24 h in comparison with the control. The oxidative degradation caused by PQD-BC and PDMS-g-BC, which is referred to as lipid peroxidation, leads to a decrease in the cell membrane fluidity and an increase in membrane leakiness. This finding suggested that the toxicity of PQD-BC and PDMS-g-BC is linked to oxidative stress, which induces membrane lipid peroxidation and may cause the loss of plasma membrane integrity in Foc4, but BC had no effect on the plasma membranes of treated mycelia.

3.2.3. Cell wall integrity

To determine whether PQD-BC, PDMS-g-BC and BC led to the loss of cell wall integrity in Foc4, the ALP contents of the medium were

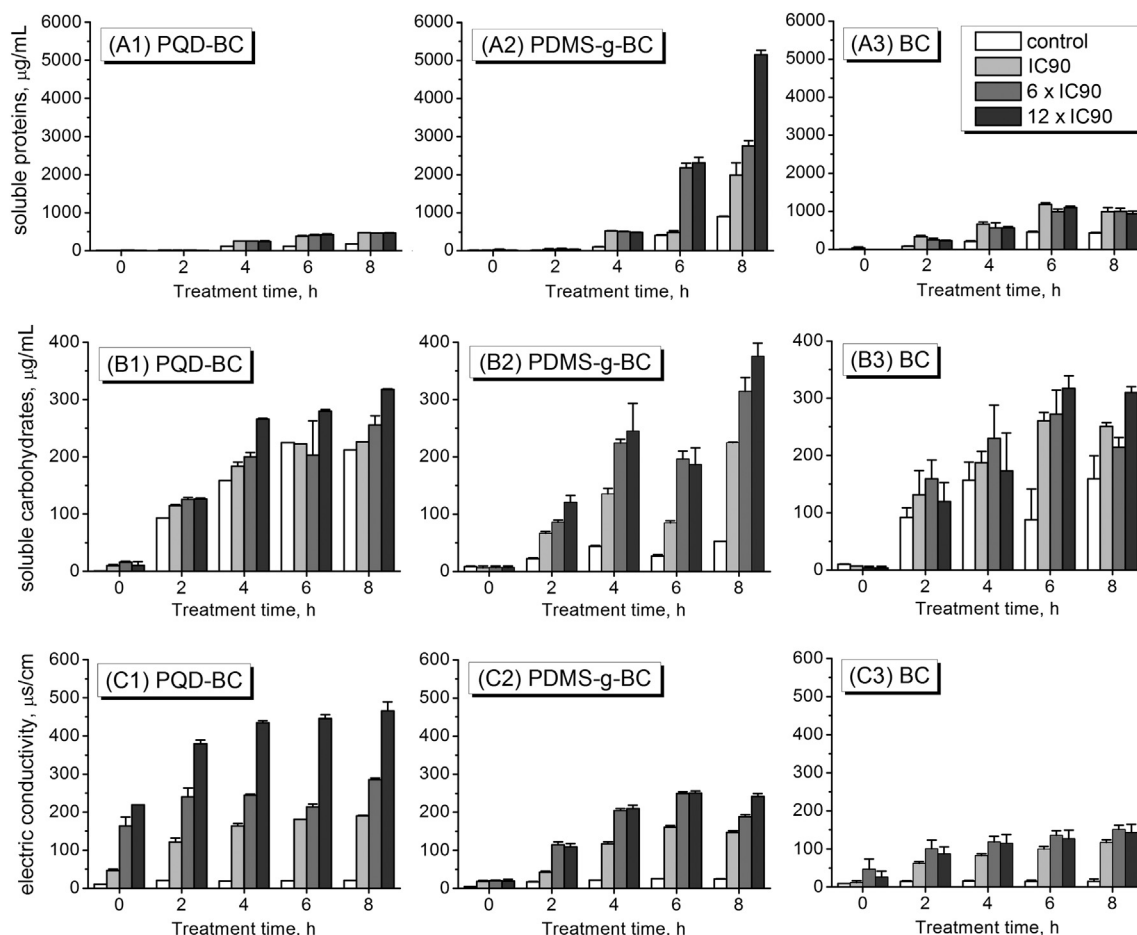


Fig. 4. Leakage of cytoplasmic contents from Foc4 treated with PQD-BC, PDMS-g-BC and BC. Mycelia were placed in distilled water supplements with different concentrations of antifungal agents and incubated at 28 °C for 0, 2, 4, 6 and 8 h. The cytoplasmic leakage of soluble proteins (A) and (B) was expressed as micrograms per milliliter of solution, while the leakage of electric conductivity (C) was monitored using an electrical conductivity meter. Each data point is the mean \pm SE of three replicates.

measured, which has been shown to be produced in the cytoplasm and secreted into the periplasmic space [42]. Damage to the external cell wall layers can lead to the release of ALP from the cell [43]. Increased ALP activities, which was observed in medium, were found to be 0.57, 1.24, and 3.66 U/L at MIC, IC₅₀ and IC₉₀, respectively, whereas in the PDMS-g-BC-treated cells were found to be 0.50, 1.87, and 6.39 U/L at

MIC, IC₅₀ and IC₉₀, respectively and in the BC-treated cells were found to be 0.73, 0.89, and 8.28 U/L at MIC, IC₅₀ and IC₉₀, respectively. The PQD-BC, PDMS-g-BC and BC treated groups showed higher ALP activity than the control after a 24-h treatment, which confirmed that the cell wall of Foc4 was destroyed in a dose-dependent manner (Fig. 6).

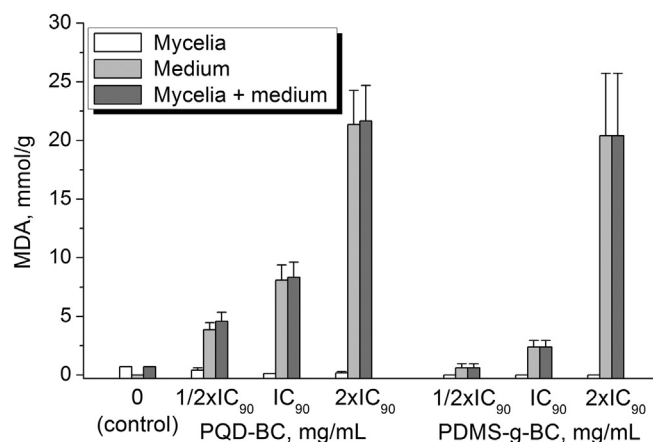


Fig. 5. Loss of cell wall integrity in Foc4 after PQD-BC and PDMS-g-BC treatments. Mycelia were placed in distilled PD medium supplement with different concentrations of antifungal agents and incubated at 28 °C for 48 h. The malonic aldehyde (MDA) content was expressed as the mmol per gram (mmol/g) of mycelia. The data were based on three replicates. Bars indicate standard errors.

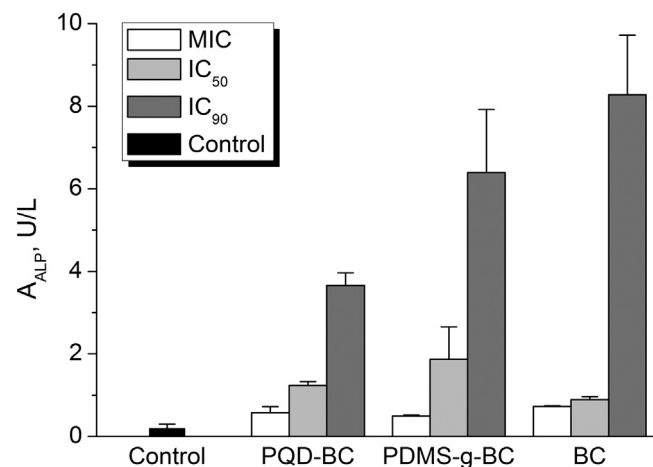


Fig. 6. Loss of cell wall integrity in Foc4 after PQD-BC, PDMS-g-BC and BC treatments. The mycelia were placed in distilled PD medium supplemented with different concentrations of antifungal agents and incubated at 28 °C for 48 h. The alkaline phosphatase activity was expressed as units per liter (U/L) of filtered solution. The data were based on three replicates. The bars indicate standard errors.

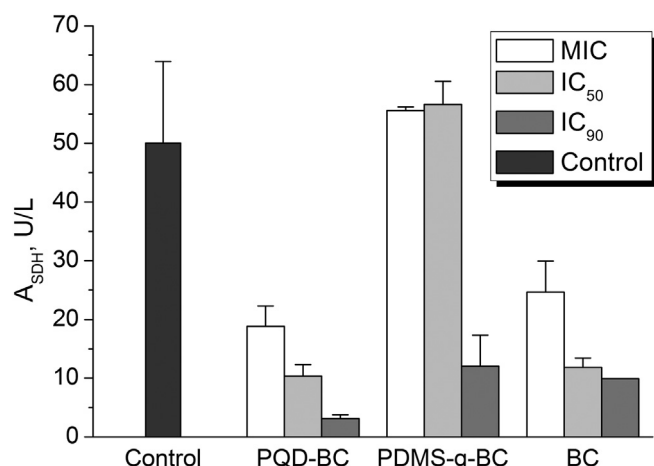


Fig. 7. Mitochondrial function of Foc4 after PQQ-BC, PDMS-g-BC and BC treatments. The mycelia were placed in distilled PD medium supplement with different concentrations of antifungal agents and incubated at 28 °C for 48 h. The succinate dehydrogenase activity was expressed as units per milligram of soluble protein. The data were based on three replicates. Bars indicate standard errors.

These data suggested that after absorption onto the cell surface, the PQQ-BC, PDMS-g-BC, and BC treatments were able to destroy the cell walls of fungal pathogens and they interacted with the plasma membrane, leading to the release of intracellular contents and ALP, which led to eventual direct cell death.

3.2.4. Mitochondrial dysfunction

To assess changes in mitochondrial function, the SDH activity of Foc4 cells that were exposed to the compounds was determined. SDH is the functional substance for the tricarboxylic acid cycle and aerobic respiration. Its activity is closely associated with bioenergy synthesis and mitochondrial function in a variety of prokaryotic and eukaryotic cells [38]. For SDH activity, the control group was active, while there was a substantial decrease in the treated groups in a dose-dependent manner following exposure to PQQ-BC and BC (Fig. 7). There were no significant effect after PDMS-g-BC treatment at the MIC and IC₅₀, while a higher concentration (IC₉₀) could significantly decrease SDH activity. Therefore, PQQ-BC, PDMS-g-BC and BC affect the bioenergy synthesis pathway of Foc4 by inhibiting SDH activity. This finding suggested that the potential mechanism underlying their antifungal actions were their inhibition of mitochondrial function.

3.2.5. Interactions of genomic DNA with the compounds

As a carrier of genetic information, DNA is a major target for drug interactions because of its ability to interfere with transcription (gene expression and protein synthesis) and replication, a major step in cell growth and division [44–46]. In this study, the EMSA was used to test the affinity of DNA-binding polymers to investigate their efficacy against genomic DNA, and the mode of action was illustrated. When genomic DNA is separated by electrophoresis, rapid migration will be observed for unbound and cleaved DNA. By contrast, the complex produces a slower migration due to the increase of molecular weight and decrease of negative charge, which means that a constant amount of DNA was mixed with increasing amounts of compounds, tethered to compound-DNA-conjugated agarose beads. For the *in vitro* test, test compounds were immobilized with Foc4 genomic DNA according to the observations made by agarose electrophoresis. Lanes 1–9 show genomic DNA that was incubated with the test compounds at three different concentrations (the MIC, IC₅₀ and IC₉₀), while Lane 10 applies to the untreated genomic DNA (control DNA). Compared with the control, the treatments are very effective at changing the mobility and shape of genomic DNA. As shown in Fig. 8-A, BC could partly retard genomic DNA at MIC and IC₅₀ and completely retard genomic DNA at IC₉₀ (in Lanes 4–6), while PDMS-g-BC partly retard genomic DNA at MIC and completely inhibit the electrophoretic mobility of genomic DNA at IC₉₀ (in Lanes 7–9). The result suggested that DNA was exposed to PDMS-g-BC and BC to form compound-DNA complexes through electrostatic interactions and thereby specifically results in a further reduction in the mobility of the compound-DNA complex (supershift). However, no obvious DNA bands were indicated in the lane for the PQQ-BC treated group (in Lanes 1–3), and the DNA loading buffer containing bromide blue indicator remained in the pore. The GoldView™ has weak fluorescence, but its emission intensity in the presence of DNA can be greatly enhanced because of its strong intercalation between the adjacent DNA base pairs. This enhanced fluorescence could be quenched, or at least partly quenched by the addition of a second molecule with higher DNA-binding ability. This finding indicated that PQQ-BC was immobilized strongly with genomic DNA, which caused the GoldView™ was completely replaced by PQQ-BC and appreciable decrease in the emission intensity. A similar finding occurs in the treated group when the concentration of PDMS-g-BC reached the IC₉₀ (in Lanes 9). The amount of bound DNA was increased with increasing amounts of both test compounds in the reaction.

Interactions between genomic DNA and test compounds at MIC, IC₅₀ and IC₉₀, respectively, were further investigated during *in vivo* analysis (Fig. 8-B). Notably, the genomic DNA that was exposed to PQQ-BC

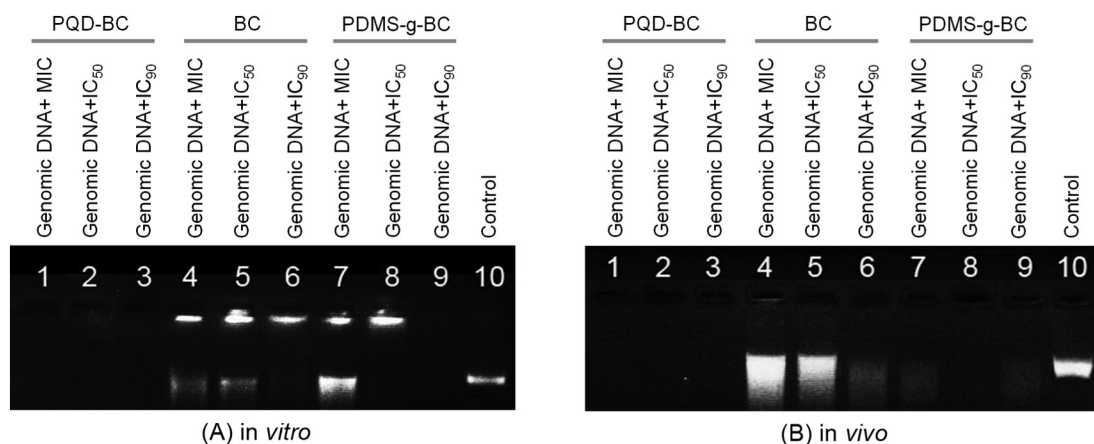


Fig. 8. Interaction of compounds (PQQ-BC, PDMS-g-BC and BC) with Foc4 genomic DNA *in vitro* (A) and *in vivo* (B). 25 µg of genomic DNA (5 µL of genomic DNA with a fixed concentration (500 µg/mL)) was used. For lanes 1–3: treated with 5 µL of TE buffer containing PQQ-BC at final concentrations matching the MIC, IC₅₀, and IC₉₀. For lanes 4–6: treated with 5 µL of TE buffer containing BC at final concentrations matching the MIC, IC₅₀, and IC₉₀. For lanes 7–9: treated with 5 µL of TE buffer containing PDMS-g-BC at final concentrations matching the MIC, IC₅₀, and IC₉₀. For lane 10: treated with 5 µL of TE buffer without test compound (negative control). The data were based on three replicates and the test was repeated twice with similar results. The representative results are shown.

show a similar situation to *in vitro* analysis that the genomic DNA was lost in all concentrations tested (in Lanes 1–3), whereas the genomic DNA was degraded upon the application of BC at all concentrations tested (in Lanes 4–6). The genomic DNA that was exposed to PDMS-g-BC was mostly being diminished (in Lanes 7–9). The different DNA cleavage efficiency of the compounds with different structures may be to the different binding affinity of the compounds to DNA. The experiment revealed the structure-activity relationship in the antifungal action in that BC was able to bind to DNA nonspecifically, while the PQD-BC treatment caused specific binding. The PDMS-g-BC treatment caused specific binding if the treated concentration reached the IC₉₀.

In conclusion, PQD-BC, PDMS-g-BC and BC were bound to DNA and created fractures in the DNA strands, causing changes that affected the structural and electrophoretic mobility of DNA, such as the DNA damage that inhibited the DNA replication and transcription that regulate the cell cycle, causing cell death indirectly.

4. Conclusions

In conclusion, we previously demonstrated methods for developing polyacrylamide quaternary ammonium salts (PQD-BC) and polydimethylsiloxane graft quaternary ammonium salts (PDMS-g-BC) that inactivate various fungi (*R. solani* and Foc4). The PQD-BC and PDMS-g-BC were found to actively inhibit mycelial growth and spore propagation against Foc4. The structure-activity relationship studies indicated that for a comparable antifungal efficiency in PQD-BC with a polyacrylamide backbone against Foc4, the antifungal efficiency of PDMS-g-BC with a more hydrophobic polydimethylsiloxane backbone against Foc4 is more active, which means that incorporating a more hydrophobic backbone into polymers can strengthen the antimicrobial activities of PQAS, and it showed the promising application for antifungal agents in plant pathogenic disease, which can be compared to BC. The potential mechanism underlying Foc4 involves several targets in the fungal cells, including the disruption of the cellular structure, such as the cell wall and plasma membrane, inducing lipid peroxidation, mitochondrial dysfunction and interference with genomic DNA. Understanding the mechanism of action may predict that the polymeric quaternary ammonium salts will act on a broad spectrum of fungal species and may provide a new strategy for preventing and controlling Fusarium wilt in bananas.

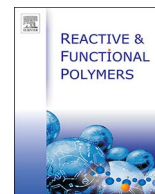
Acknowledgments

This work was supported by the Science and Technology Planning Project of Guangdong Province, China under grant 2016A020210105; the Science and Technology Program of Guangzhou, China, under grant 201605121117091; and the National Natural Science Foundation of China under grant 31201552.

References

- [1] C.W. Wardlaw, The biology of banana wilt (Panama disease). I. Root inoculation experiments, *Ann. Bot.* 44 (1930) 741–766.
- [2] Cunwu Zuo, Li Chunyu, Li Bin, et al., The toxic mechanism and bioactive components of Chinese leek root exudates acting against *Fusarium oxysporum* f. sp. *cubense* tropical race 4, *Eur. J. Plant Pathol.* 143 (2015) 447–460.
- [3] Chun-Hua Hu, Wei Yue-Rong, Huang Yong-Hong, et al., An efficient protocol for the production of chit42 transgenic Furenzhi banana (*Musa* spp. AA group) resistant to *Fusarium oxysporum*, *In Vitro Cell Dev. Biol. Plant* 49 (2013) 584–592.
- [4] Y.L. Wu, G.J. Yi, X.X. Peng, Rapid screening of *Musa* species for resistance to *Fusarium* wilt in an *in vitro* bioassay, *Eur. J. Plant Pathol.* 128 (2010) 409–415.
- [5] Shun Song, Chen Xin, Huang Dongmei, et al., Identification of miRNAs differentially expressed in *Fusarium* wilt-resistant and susceptible banana varieties, *S. Afr. J. Bot.* 106 (2016) 244–249.
- [6] Jian Zhang, Günseli Bayram Akcapinar, Lea Atanasova, et al., The neutral metalloproteinase NMP1 of *Trichoderma guizhouense* is required for mycotrophy and self-defence, *Appl. Environ. Microbiol.* 18 (2015) 580–597.
- [7] S.M. Iconomopoulou, G.A. Voyiatzis, The effect of the molecular orientation on the release of antimicrobial substances from uniaxially drawn polymer matrixes, *J. Control. Release* 103 (2015) 451–464.
- [8] Fang Wu, Guolong Meng, Jing He, et al., Antibiotic-loaded chitosan hydrogel with superior dual functions: antibacterial efficacy and osteoblastic cell responses, *ACS Appl. Mater. Interfaces* 6 (2014) 10005–10013.
- [9] Yun Kee Jo, Jeong Hyun Seo, Bong-Hyuk Choi, et al., Surface-independent antibacterial coating using silver nanoparticle-generating engineered mussel glue, *ACS Appl. Mater. Interfaces* 6 (2014) 20242–20253.
- [10] A. Katchalsky, Polyelectrolytes and their biological interaction, *Biophys. J.* 4 (1964) 9–41.
- [11] Jiaul Hoque, Akkapeddi Padma, Yadav Vikas, et al., Broad spectrum antibacterial and antifungal polymeric paint materials: synthesis, structure-activity relationship, and membrane-active mode of action, *ACS Appl. Mater. Interfaces* 7 (2015) 1804–1815.
- [12] Shan Jiang, Li Wang, Haojie Yu, et al., Preparation of crosslinked polystyrenes with quaternary ammonium and their antibacterial behavior, *React. Funct. Polym.* 62 (2005) 209–213.
- [13] Tomiki Ikeda, Hiroki Hirayama, Hideki Yamaguchi, et al., Polycationic biocides with pendant active group: molecular weight dependence of antibacterial activity, *Antimicrob. Agents Chemother.* 30 (1986) 132–136.
- [14] A. Vnitskikh Zh, Shklyayev Yu, T.F. Odegova, et al., Synthesis and antimicrobial activity of mono- and biquaternized derivatives of dipyriddylenes and dipyriddylenes, *Pharm. Chem. J.* 40 (2006) 19–22.
- [15] K. Róžga-Wijas, U. Mizerska, W. Fortuniak, J. Chojnowski, R. Hałas, W. Werel, Quaternary ammonium salts (QAS) modified polysiloxane biocide supported on silica materials, *J. Inorg. Organomet. Polym.* 17 (2007) 605–613.
- [16] L. Kou, J. Liang, X. Ren, H.B. Kocer, S.D. Worley, Y.M. Tzou, T.S. Huang, Synthesis of a water-soluble siloxane copolymer and its application for antimicrobial coatings, *Ind. Eng. Chem. Res.* 48 (2009) 6521–6526.
- [17] T.J. Franklin, G.A. Snow, Antiseptics, antibiotics and the cell membrane, *Biochemistry of Antifungal Action*, Springer US 1975, pp. 56–75.
- [18] B.E. Elewski, Mechanisms of action of systemic antifungal agents, *J. Am. Acad. Dermatol.* 28 (1993) S28–S34.
- [19] C.O. Frank, J.P. Alistair, Neil Brown, A.R. Gow, Antifungal agents: mechanisms of action, *Trends Microbiol.* 11 (2003) 272–279.
- [20] Wenqiang Chang, Ming Zhang, Ying Li, et al., Lichen endophyte derived pyridoxatin inactivates *Candida* growth by interfering with ergosterol biosynthesis, *Biochim. Biophys. Acta Gen. Subj.* 1850 (2015) 1762–1771.
- [21] A. Beauvais, S. Bozza, O. Knemeyer, C. Formosa, V. Balloy, et al., Deletion of the *a*-(1,3)-glucan synthase genes induces a restructuring of the conidial cell wall responsible for the avirulence of *Aspergillus fumigatus*, *PLoS Pathog.* 9 (2013) 1–14.
- [22] L.J. Cheng, Q.Q. Liu, Y.F. Lei, Y.L. Lin, A.Q. Zhang, The synthesis and characterization of carboxybetaine functionalized polysiloxanes for the preparation of anti-fouling surfaces, *RSC Adv.* 4 (2014) 54372–54381.
- [23] A.Q. Zhang, Q.Q. Liu, Y.F. Lei, S.H. Hong, Y.L. Lin, Synthesis and antimicrobial activities of acrylamide polymers containing quaternary ammonium salts on bacteria and phytopathogenic fungi, *React. Funct. Polym.* 88 (2015) 39–46.
- [24] Y.L. Lin, Q.Q. Liu, L.J. Cheng, Y.F. Lei, A.Q. Zhang, Synthesis and antimicrobial activities of polysiloxane-containing quaternary ammonium salts on bacteria and phytopathogenic fungi, *React. Funct. Polym.* 85 (2014) 19–30.
- [25] L.J. Cheng, Q.Q. Liu, L. Yang, Y.L. Lin, A.Q. Zhang, Synthesis and characterization of hydrogen-containing polysiloxanes (in Chinese), *Gaofenzi Cailiao Kexue Yu Gongcheng/Polym. Mater. Sci. Eng.* 30 (2014) 25–28.
- [26] Samir Drobny, Michael Wisniewski, Ahmed El Ghaouth, et al., Influence of food additives on the control of postharvest rots of apple and peach and efficacy of the yeast-based biocontrol product aspire, *Postharvest Biol. Technol.* 27 (2003) 127–135.
- [27] Du Shijie, Zaimin Tian, Dongyan Yang, et al., Synthesis, antifungal activity and structure-activity relationships of novel 3-(difluoromethyl)-1-methyl-1H-pyrazole-4-carboxylic acid amides, *Molecules* 20 (2015) 8395–8408.
- [28] X. Shao, S. Cheng, H. Wang, et al., The possible mechanism of antifungal action of tea tree oil on *Botrytis cinerea*, *J. Appl. Microbiol.* 114 (2013) 1642–1649.
- [29] C.C. Sollod, A.E. Jenns, M.E. Daub, Cell surface redox potential as a mechanism of defense against photosensitizers in fungi, *Appl. Environ. Microbiol.* 58 (1992) 444–449.
- [30] K. Jagajjanani Rao, Santanu Paria, Anti-Malassezia furfur activity of natural surfactant mediated in situ silver nanoparticles for a better antidandruff shampoo formulation, *RSC Adv.* 6 (2016) 11064–11069.
- [31] K.N. Fish, S.L. Schmid, H. Damke, Evidence that dynamin-2 functions as a signal-transducing GTPase, *J. Cell Biol.* 150 (2000) 145–154.
- [32] J.A. Lewis, G.C. Papavizas, Permeability changes in hyphae of *Rhizoctonia solani* induced by germling preparations of *Trichoderma* and *Gliocladium*, *Phytopathology* 77 (1987) 699–703.
- [33] M.M. Bradford, A rapid and sensitive method for the quantitation of microgram quantities of protein utilizing the principle of protein-dye binding, *Anal. Biochem.* 72 (1976) 248–254.
- [34] D.L. Morris, Quantitative determination of carbohydrates with Dreywood's anthrone reagent, *Science* 107 (1948) 254–255.
- [35] Heejeong Lee, Jae-Sam Hwang, Dong Gun Lee, Scolopendin 2 leads to cellular stress response in *Candida albicans*, *Apoptosis* 21 (2016) 856–865.
- [36] V. Singh, A. Pal, M.P. Darokar, A polyphenolic flavonoid glabridin: oxidative stress response in multidrug-resistant *Staphylococcus aureus*, *Free Radic. Biol. Med.* 87 (2015) 48–5735.
- [37] R.H. Mohamed, R.A. Karam, H.A. Hagrass, et al., Anti-apoptotic effect of spermatogonial stem cells on doxorubicin-induced testicular toxicity in rats, *Gene* 561 (2015) 107–114.
- [38] W.W. Fan, G.Q. Yuan, Q.Q. Li, et al., Antibacterial mechanisms of methyl gallate against *Ralstonia solanacearum*, *Australas. Plant Pathol.* 43 (2014) 1–7.
- [39] Özge Yıldız, A.T. Çolak, M. Yılmaz, et al., The syntheses, characterization, antimicrobial, DNA cleavage and cytotoxic activities of novel terephthalate complexes, *J. Mol. Struct.* 1127 (2017) 668–674.

- [40] Jeong-Ho Kim, Immobilized DNA-binding assay, an approach for *in vitro* DNA-binding assay, *Anal. Biochem.* 334 (2004) 401–402.
- [41] J.C. Sherris, Problems in *in vitro* determination of antibiotic tolerance in clinical isolates, *Antimicrob. Agents Chemother.* 30 (1986) 633–637.
- [42] K.J. Cheng, J.M. Ingram, J.W. Costerton, Release of alkaline phosphatase from cells of *Pseudomonas aeruginosa* by manipulation of cation concentration and of pH, *J. Bacteriol.* 104 (1970) 748–753.
- [43] S.S. Lindsay, B. Wheeler, K.E. Sanderson, et al., The release of alkaline phosphatase and of lipopolysaccharide during the growth of rough and smooth strains of *Salmonella typhimurium*, *Can. J. Microbiol.* 19 (1973) 335–343.
- [44] Fatma Öztürk, Leyla Açık, İzzet Şener, Fikret Karcı, Emine Kılıç, Antimicrobial properties and DNA interactions studies of 3-hetarylazoquinoline-2, 4-diol compounds, *Türk. J. Chem.* 36 (2012) 293–302.
- [45] B. Dede, I. Özmen, F. Karipcin, Synthesis, characterization, catalase functions and DNA cleavage studies of new homo and heteronuclear Schiff base copper (II) complexes, *Polyhedron* 28 (2009) 3967–3974.
- [46] E.E. İlter, N. Asmafiliz, Z. Kılıç, et al., Phosphorus–nitrogen compounds: part 19. Syntheses, structural and electrochemical investigations, biological activities, and DNA interactions of new spirocyclic monoferrocenylcyclotriphosphazenes, *Polyhedron* 29 (2010) 2933–2944.



Controllable synthesis and antimicrobial activities of acrylate polymers containing quaternary ammonium salts



Weiqiang Zhong^{a,1}, Chenyun Dong^{b,1}, Runqi Liuyang^b, Qizhi Guo^b, Hong Zeng^a, Yaling Lin^{b,*}, Anqiang Zhang^{a,*}

^a College of Materials Science and Engineering, South China University of Technology, 381 Wushan Rd., Guangzhou 510641, Guangdong, China

^b College of Materials and Energy, South China Agricultural University, 432 Wushan Rd., Guangzhou 510642, Guangdong, China

ARTICLE INFO

Keywords:

Acrylate polymers containing quaternary ammonium salts
Atom transfer radical polymerization
Antimicrobial activity
Bacterial
Phytopathogenic fungi

ABSTRACT

A series of acrylate polymers containing quaternary ammonium salts (PDMAEMA-BC) having tunable molecular weights were synthesized via atom transfer radical polymerization (ATRP), and the effect of the degree of polymerization (DP) on the antimicrobial activity against bacteria (*Escherichia coli*, *Staphylococcus albus*), pathogenic fungi (*Candida albicans*) and phytopathogenic fungi (*Rhizoctonia solani* and *Fusarium oxysporum* f. sp. *cubense* race 4) was systematically assessed. The antimicrobial properties against *E. coli*, *S. albus* and *C. albicans* were characterized using the minimum inhibitory concentration (MIC) and minimum fungicidal concentration (MFC) or minimum bactericidal concentration (MBC) values, whereas the antimicrobial activities against *R. solani* and *Foc4* were evaluated using the effective concentration (EC₅₀ and EC₉₀), MIC and MFC values. The results indicated that the PDMAEMA-BC homopolymers showed better antimicrobial activities than the corresponding monomer, i.e., the acrylate quaternary ammonium salt monomer (DMAEMA-BC), and the optimal antimicrobial activities were obtained for moderate PDMAEMA-BC chain lengths. These results help to understand the antimicrobial mechanism of polymeric quaternary ammonium salts and highlight their potential application as fungicidal agents for controlling both human and plant diseases.

1. Introduction

When various crops are planted in the field, they are confronted with serious infection by phytopathogenic fungi. *Rhizoctonia solani* form sclerotia when the external conditions are not suitable for their development. In addition, *Fusarium oxysporum* can survive for up to 30 years in the absence of bananas, and non-host weed species that are infected by the pathogen act as inoculum reservoirs [1]. The fungi are usually killed by spraying high levels of low molecular weight antimicrobial agents because traditional antimicrobial agents are easily washed away and thus need to be repeatedly sprayed. Furthermore, low molecular weight antimicrobial agents are toxic to the environment and have poor chemical stability [2]. To properly solve this problem, antimicrobial agents are designed based on polymers that contain antimicrobial functional groups. Their advantages, including better efficacy, low toxicity, no volatility, high chemical stability and prolonged lifetimes, have attracted a great deal of attention [2–4].

The mode of action of low molecular weight cationic biocides has been summarized as follows: (i) adsorption onto the bacterial cell

surface; (ii) diffusion through the cell wall; (iii) binding to the cytoplasmic membrane; (iv) disruption of the cytoplasmic membrane; (v) release of cytoplasmic constituents, such as K⁺ ions, DNA, and RNA; and (vi) death of the cell [5]. According to our previous studies, the bactericidal mechanism is very complicated and involves several targets in fungal cells, including the disruption of cellular structures, such as the cell wall and plasma membrane; the induction of lipid peroxidation; mitochondrial dysfunction and interference with genomic DNA [6].

Cationic antimicrobials are well-known in the development of self-sterilizing surfaces and are used in many applications, such as hospital surfaces, surgical equipment, protective hospital clothes, medical implants, wound dressings, food packaging materials, and everyday consumer products [7]. Among these cationic antimicrobials, quaternary ammonium compounds are probably the most explored and widely deployed [8–10]. The antimicrobial activity of polymers containing quaternary ammonium salts was associated with complex factors, such as molecular weight, the types of counter anions, charge density, alkyl chain length and steric hindrance, the hydrophilic–hydrophobic balance, and the type of bacteria species [2,11]. The molecular weight

* Corresponding authors.

E-mail addresses: linyaling@scau.edu.cn (Y. Lin), aqzhang@scut.edu.cn (A. Zhang).

¹ These authors contributed equally.

plays an important role in determining the antimicrobial properties. Homopolymers of quaternary ammonium salts exhibited far better antimicrobial activities than the corresponding monomers [12,13]. Additionally, Ikeda and his co-workers investigated the antimicrobial activity of polymethacrylate containing pendant biguanide units and found that polymer samples with low and high molecular weights exhibited lower bactericidal activity against *S. aureus* than those in the intermediate range [14]. Chen and co-workers determined that the antimicrobial properties of quaternary ammonium functionalized poly(propyleneimine) dendrimers have a parabolic dependence on molecular weight [3]. Huang and co-workers prepared polypropylene (PP) coated with a non-leachable biocide by chemically attaching poly(quaternary ammonium) (PQA) to the surface of PP and found that polymers with relatively high molecular weight ($M_n > 10$ kDa) showed almost 100% killing efficiency (against *E. coli*), while shorter PQA chains ($M_n = 1.5$ kDa) demonstrated less activity with the same grafting density [15].

The difference in cell structure between fungi and bacteria leads to differences in the antimicrobial activities of quaternary ammonium salts against bacteria and fungi. Therefore, it is very essential to conduct research on the relationship between the antifungal activity and molecular weight of poly quaternary ammonium salts. To this end, in this paper, we synthesized a series of acrylate polymers containing quaternary ammonium salts (PDMAEMA-BC) with tunable molecular weights via ATRP and systematically assessed the antimicrobial activities against two typical phytopathogenic fungi (*Rhizoctonia solani* (*R. solani*), whose main morphology is a mycelium and *Fusarium oxysporum* f. sp. *cubense* race 4 (Foc4), whose main morphology is a spore), Gram-negative bacteria (*Escherichia coli* (*E. coli*)), Gram-positive bacteria (*Staphylococcus albus* (*S. albus*)) and pathogenic fungi (*Candida albicans* (*C. albicans*)) using DMAEMA-BC and PDMAEMA-BC with various molecular weights.

2. Experimental

2.1. Materials

2-(dimethylamino)ethyl methacrylate (DMAEMA, 99%), ethyl 2-bromoisobutyrate (EtBrIB, 98%), *N,N,N',N'',N''*-pentamethyldiethylenetriamine (PMDETA, 98%) and copper(I) bromide (CuBr, 99%) were supplied by Shanghai Macklin Biochemical Technology Co. Ltd. (Shanghai, China). Benzyl chloride (BC, 99%) was supplied by Aladdin Reagent Co. Ltd. (Shanghai, China). Beef extract was supplied by Sinopharm Chemical Reagent Co. Ltd. (Shanghai, China). Peptone was supplied by Guangdong Ring Kay Microbial Technology Co., Ltd. (Guangzhou, China). Agar was supplied by MYM Biological Technology Company (Shanghai, China). RPMI-1640 liquid medium was supplied by HyClone Company of America (Utah, USA). All microorganisms were kindly supplied by the Fungus Laboratory, Department of Plant Pathology, South China Agricultural University.

2.2. Synthesis of poly(2-(dimethylamino)ethyl methacrylate) containing quaternary ammonium salts (PDMAEMA-BC)

Poly(2-(dimethylamino)ethyl methacrylate) containing quaternary ammonium salts (PDMAEMA-BC) was prepared in a two-step process, i.e., first, the controlled synthesis of PDMAEMA, followed by

quaternization of PDMAEMA to afford PDMAEMA-BC, as shown in Scheme 1.

PDMAEMA was polymerized via ATRP technology, and a brief description of the polymerization procedure is as follows: 10.0 g (0.06 mol) of DMAEMA and pre-determined amounts of EtBrIB and PMDETA were dissolved in 50 mL of isopropanol in a 200 mL Schlenk flask. The reaction system was subjected to three freeze-pump-thaw cycles. Next, a calculated amount of CuBr was quickly added into the flask under a nitrogen atmosphere. During ATRP polymerization, certain polymer molecular weights were targeted by selecting appropriate initial monomer and EtBrIB concentrations. The ratio of [DMAEMA]₀/[EtBrIB]₀ (mol/mol) were set at 4/1, 8/1, 15/1, 30/1, 60/1, 70/1 and 80/1 to yield a theoretical degree of polymerization (DP) of 4, 8, 15, 30, 60, 70 and 80, respectively. The mixture was stirred at 60 °C for 8 h under a nitrogen atmosphere. The reaction was stopped by exposing it to air and dried under vacuum at 60 °C (approximately 70% yield). The catalyst was removed by neutral alumina column chromatography with acetone as the eluent. For convenience, the products were named PDMAEMA-*n*, and *n* represents the DP of PDMAEMA.

¹H NMR (400 MHz, D₂O, δ, ppm): 0.97 (s, C-CH₃), 1.98 (s, C-CH₂-C), 2.37 (s, N(CH₃)₂), 2.77 (t, N-CH₂-CH₂), 4.20 (t, O-CH₂-CH₂). FT-IR (KBr, cm⁻¹): 2863–2947 (ν_{CH}), 1732 (ν_{C=O}), 1020, 1047 (ν_{C-N}).

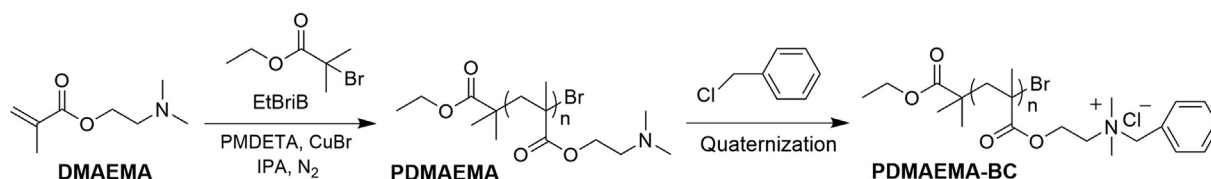
PDMAEMA-BC was synthesized in a quaternization reaction between PDMAEMA and benzyl chloride (BC), as briefly stated in the following: 6.0 g of PDMAEMA and 4.8 g of BC were dissolved in 20 g of an ethyl alcohol/methylbenzene (1/1, m/m) mixture in a 100 mL Schlenk flask. The mixture was subjected to three freeze-pump-thaw cycles and then stirred at 70 °C under a nitrogen atmosphere for 24 h; subsequently, the mixture was precipitated with anhydrous diethyl ether, and the precipitate was washed with anhydrous diethyl ether three times and dried under vacuum at 40 °C overnight (approximately 90% yield). For convenience, the products were named PDMAEMA-BC-*n*, and *n* represents the DP of PDMAEMA-BC.

¹H NMR (400 MHz, D₂O, δ, ppm): 1.06 (s, C-CH₃), 3.14 (s, N⁺(CH₃)₂), 3.87 (t, CH₂-CH₂-N⁺), 4.35–4.76 (m, N⁺-CH₂-Φ, O-CH₂-CH₂), 7.59 (s, Φ-H). FT-IR (KBr, cm⁻¹): 2870–2979 (ν_{CH}), 1726 (ν_{C=O}), 1041 (ν_{C-N}), 768 (γ_{Φ-H}).

2.3. Synthesis of an acrylate quaternary ammonium salt monomer (DMAEMA-BC)

An acrylate quaternary ammonium salt monomer (DMAEMA-BC) was synthesized via a quaternization reaction between DMAEMA and BC. 6.0 g of DMAEMA and 4.8 g of BC were dissolved in 20 g of an ethyl alcohol/methylbenzene (1/1, m/m) mixture in a 100 mL Schlenk flask. The mixture was subjected to three freeze-pump-thaw cycles and then stirred at 40 °C under a nitrogen atmosphere for 24 h; subsequently, the mixture was precipitated with anhydrous diethyl ether, and the precipitate was washed with anhydrous diethyl ether three times and dried under vacuum at 40 °C overnight (approximately 90% yield).

¹H NMR (400 MHz, D₂O, δ, ppm): 1.98 (s, C-CH₃), 3.18 (s, N⁺(CH₃)₂), 3.83–3.86 (t, CH₂-CH₂-N⁺), 4.65 (s, N⁺-CH₂-Φ), 4.73–4.75 (t, O-CH₂-CH₂), 5.82, 6.21 (d, CH₂=C(CH₃)), 7.62 (s, Φ-H). FT-IR (KBr, ν, cm⁻¹): 2853–2970 (ν_{CH}), 1722 (ν_{C=O}), 1635 (ν_{C=C}), 1041 (ν_{C-N}), 768 (γ_{Φ-H}).



Scheme 1. Synthetic route to PDMAEMA and PDMAEMA-BC.

2.4. Characterization

FT-IR spectra were collected on a VERTEX-70 spectrometer (Bruker Instrument Corp., Germany) using KBr pellets. ^1H NMR spectra were obtained using a Bruker Avance III-400 (Bruker Instrument Corp., Germany) spectrometer with CDCl_3 or D_2O as the solvent. Size exclusion chromatography (SEC) was performed on a Waters system (Waters Corp., USA) equipped with a Waters 515 pump, a Waters 2414 differential refractive index detector, and three μ -Styragel columns. The samples were analyzed at 30°C using THF (1 mL/min) as the eluent. The instrument was calibrated using polystyrene standards. Critical micelle concentrations (CMC) were determined using a DDS-11A conductivity meter (Shanghai Hongyi Instrument Co. Ltd., China). Zeta potentials and particle size distributions were analyzed using a Brookhaven BI-90 Plus particle size analyzer (Brookhaven Instrument Corp., USA) using ultrapure water as the solvent. The morphologies of the micelles were analyzed with a JEM-2100 transmission electron microscope (JEOL Ltd., Japan).

2.5. Antimicrobial tests

2.5.1. Test microorganisms and media

The microorganisms included two typical phytopathogenic fungi (*Rhizoctonia solani* (*R. solani*) and *Fusarium oxysporum* f. sp. *cubense* race 4 (Foc4)), Gram-negative bacteria (*Escherichia coli* (*E. coli*)), Gram-positive bacteria (*Staphylococcus albus* (*S. albus*)) and pathogenic fungi (*Candida albicans* (*C. albicans*)). The media were prepared according to the literature [13,16].

2.5.2. Determination of mycelial growth inhibition (MGI)

The antifungal activities of the samples were tested using the inhibition of mycelial growth. To prepare polymer solutions with different concentration, the samples were dissolved in sterilized water. Next, 45 mL of PDA and 5 mL of polymer solution were poured into sterile Petri dishes (diameter of 90 mm). Sterilized water was added instead of a polymer solution as control Petri dish. Then, a 6-mm disc containing mycelia was transferred to the center of the Petri dishes and incubated at 28°C . Each experiment was conducted in triplicate. The diameter of the fungal colony was measured using a cross method three times and averaged. MGI was calculated using Eq. (1).

$$\text{MGI} = (\text{R}_\text{C} - \text{R}_\text{T})/\text{R}_\text{C} \times 100\% \quad (1)$$

whereby R_C and R_T were the radial growth of the fungi colonies in the control plate and the treatment plate, respectively. The radial growth of the fungi colony was calculated by Eq. (2):

$$\text{Radial growth (mm)} = \text{Average diameter of fungi colony (mm)} - 6 \text{ (mm)} \quad (2)$$

2.5.3. Determination of effective concentration (EC)

The antimicrobial activities of DMAEMA-BC and PDMAEMA-BC against *R. solani* and Foc4 were evaluated using the EC_{50} and EC_{90} values. The regression equation was obtained by using the natural logarithm of the polymer solution concentration as the abscissa and the biological statistical probability, converted to MGI, as the ordinate. The EC_{50} and EC_{90} values were calculated using the regression equation when the MGI values were 50% and 90%, respectively.

2.5.4. Determination of minimum inhibitory concentration (MIC), minimum fungicidal concentration (MFC) and minimum bactericidal concentration (MBC)

The antimicrobial properties of DMAEMA-BC and PDMAEMA-BC against *R. solani*, Foc4, *E. coli*, *S. albus* and *C. albicans* were evaluated by the TTC coloration method [17]. Bacterial suspensions (10^8 CFU/mL) were incubated in medium and diluted 1000 times to obtain a concentration of 10^5 CFU/mL. Next, 100 μL of the bacterial suspension and

100 μL of the polymer solutions with different concentrations were transferred to a 96-well plate. Medium was added instead of polymer solution as a control plate. Then, the mixtures were incubated at 28°C (*R. solani*, Foc4 and *C. albicans*) for 48 h or 37°C (*E. coli* and *S. albus*) for 24 h, after which 50 μL of a 0.5 wt% 2,3,5-triphenyl tetrazolium chloride (TTC) solution was added into the 96-well plate, and the contents of each well were mixed by vortex shaking prior to incubation in the dark at 28°C (*R. solani*, Foc4 and *C. albicans*) or 37°C (*E. coli* and *S. albus*) for 24 h. The MIC value was the lowest concentration at which there was no visible growth, i.e., no red color due to the reduction of TTC [17].

The MFC or MBC test is the most common estimation of fungicidal or bactericidal activity and is defined as the lowest concentration of antimicrobial agent needed to kill 99.9% of the initial inoculums after incubation [18]. To determine the MFC or MBC values, 100 μL of the mixtures in the wells that were at or above the MIC value were plated on medium and incubated at 28°C (*R. solani*, Foc4 and *C. albicans*) for 48 h or 37°C (*E. coli* and *S. albus*) for 24 h. The MFC or MBC value was the lowest concentration at which fewer than 5 colony-forming units were observed.

Additionally, the antimicrobial agent was classified as a bactericide or fungicide based on its MFC/MIC or MBC/MIC ratio. If this ratio was above 4, the antimicrobial agent was classified as bacteriostatic or fungistatic, otherwise they would be classified as bactericide or fungicide, respectively [19,20].

3. Results and discussion

3.1. Design and synthesis of DMAEMA-BC and PDMAEMA-BC

By designing and synthesizing a series of PDMAEMA-BC polymers with tunable molecular weights, we could then examine the relationship between DP and antimicrobial activity. The chemical structures of the products were confirmed by FT-IR and ^1H NMR spectroscopies.

As a multifunctional monomer containing double bonds and tertiary amino groups, 2-(dimethylamino)ethyl methacrylate (DMAEMA) could be polymerized by ATRP and then quaternized by haloalkanes for the preparation of antibacterial materials [9]. Quaternized PDMAEMA is considered a promising antimicrobial agent [21]. By adjusting the mole feeding ratio of [DMAEMA]/[EtBr] from 4/1 to 80/1, a series of PDMAEMA polymers with various molecular weights were synthesized by ATRP. The molecular weights of PDMAEMA, determined by SEC, are shown in Table 1. As shown in Figs. 1 and 2, the absorption peaks at 2863–2947, 1732, 1047 and 1020 cm^{-1} represented the infrared absorption bands of saturated C–H, C=O and C–N, respectively, and the signals for the C–CH₃, C–CH₂–C, N(CH₃)₂, N–CH₂–CH₂ and O– \oplus CH₂–CH₂ protons appeared at 0.97, 1.98, 2.37, 2.77 and 4.20 ppm, respectively.

A series of PDMAEMA-BC polymers were obtained from a quaternization reaction between PDMAEMA and benzyl chloride (BC). As

Table 1
Molecular weights of the PDMAEMA polymers prepared with different [DMAEMA]/[EtBr] feeding ratios.

Samples	[DMAEMA]/[EtBr] feeding ratio, mol/mol	M_n^a (g/mol)	M_w^a (g/mol)	PDI (M_w/M_n) ^a
PDMAEMA-4	4/1	0.71×10^3	0.84×10^3	1.18
PDMAEMA-8	8/1	1.41×10^3	1.58×10^3	1.12
PDMAEMA-16	16/1	2.99×10^3	4.52×10^3	1.51
PDMAEMA-30	30/1	5.16×10^3	6.97×10^3	1.35
PDMAEMA-60	60/1	9.25×10^3	1.09×10^4	1.18
PDMAEMA-70	70/1	11.6×10^3	13.7×10^3	1.18
PDMAEMA-80	80/1	14.7×10^3	23.3×10^3	1.59

^a Based on SEC results.

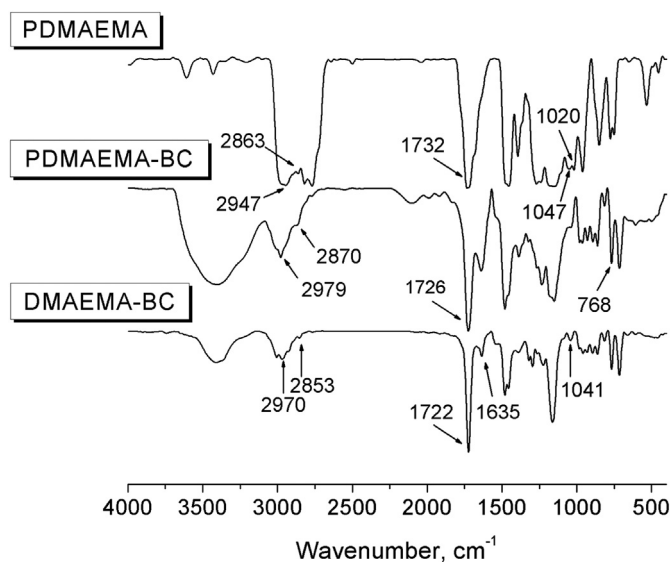


Fig. 1. FT-IR spectra of PDMAEMA, DMAEMA-BC and PDMAEMA-BC.

shown in Figs. 1 and 2, the absorption peaks at 2870–2979, 1726, 1041 and 768 cm^{-1} represented the infrared absorption bands of saturated C–H, C=O, C–N and Φ -H, respectively, and the signals for the C–CH₃, N⁺(CH₃)₂, CH₂–CH₂–N⁺, N⁺–CH₂– Φ , O–CH₂–CH₂ and Φ -H protons appeared at 1.06, 3.14, 3.87, 4.35–4.76 and 7.59 ppm, respectively. After the quaternization reaction, the N(CH₃)₂ proton signals shifted from approximately 2.37 to 3.14 ppm and the characteristic protons signals of BC (4.35–4.76 and 7.59 ppm) appeared, which indicated that the expected structure of PDMAEMA-BC were formed.

DMAEMA-BC was obtained from a quaternization reaction between DMAEMA and benzyl chloride (BC). As shown in Figs. 1 and 2, the absorption peaks at 2853–2970, 1722, 1635, 1041 and 768 cm^{-1} represented the infrared absorption bands of saturated C–H, C=O, C=C, C–N and Φ -H, respectively, and the signals from the C–CH₃, N⁺(CH₃)₂, CH₂–CH₂–N⁺, N⁺–CH₂– Φ , O–CH₂–CH₂, CH₂=C(CH₃) and Φ -H protons appeared at 1.98, 3.18, 3.83–3.86, 4.65, 4.73–4.75,

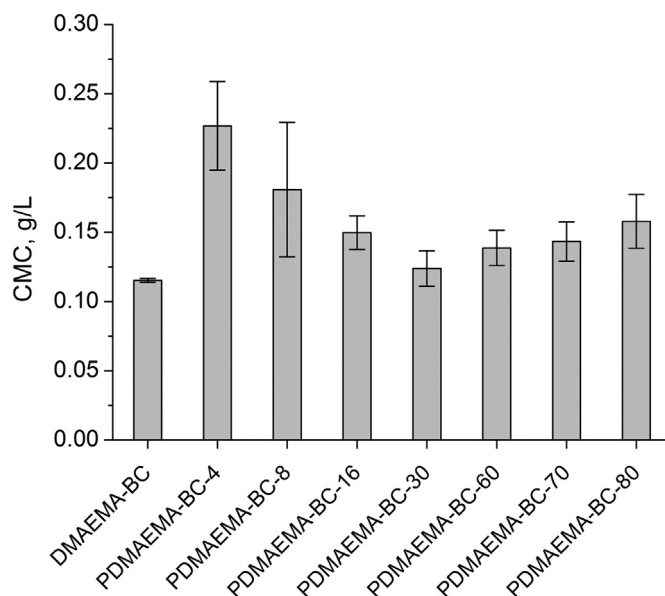


Fig. 3. CMC values of DMAEMA-BC and the PDMAEMA-BC polymers with different molecular weights.

5.82, 6.21 and 7.62 ppm, respectively.

3.2. Critical micelle concentrations (CMC) of DMAEMA-BC and PDMAEMA-BC in water

The concentration above which micelles form is called the critical micelle concentration (CMC) [22]. We measured the CMC values of DMAEMA-BC and PDMAEMA-BC by the electrical conductivity method. Fig. S1 (Supporting information) shows the conductivity plots for DMAEMA-BC and the PDMAEMA-BC polymers with different molecular weights, and Fig. 3 shows the CMC values calculated from the curves in Fig. S1. The test results showed that the CMC value of PDMAEMA-BC with low DP is higher than those of the other DMAEMA-BC and PDMAEMA-BC samples with higher DP. It was reasonable to assume

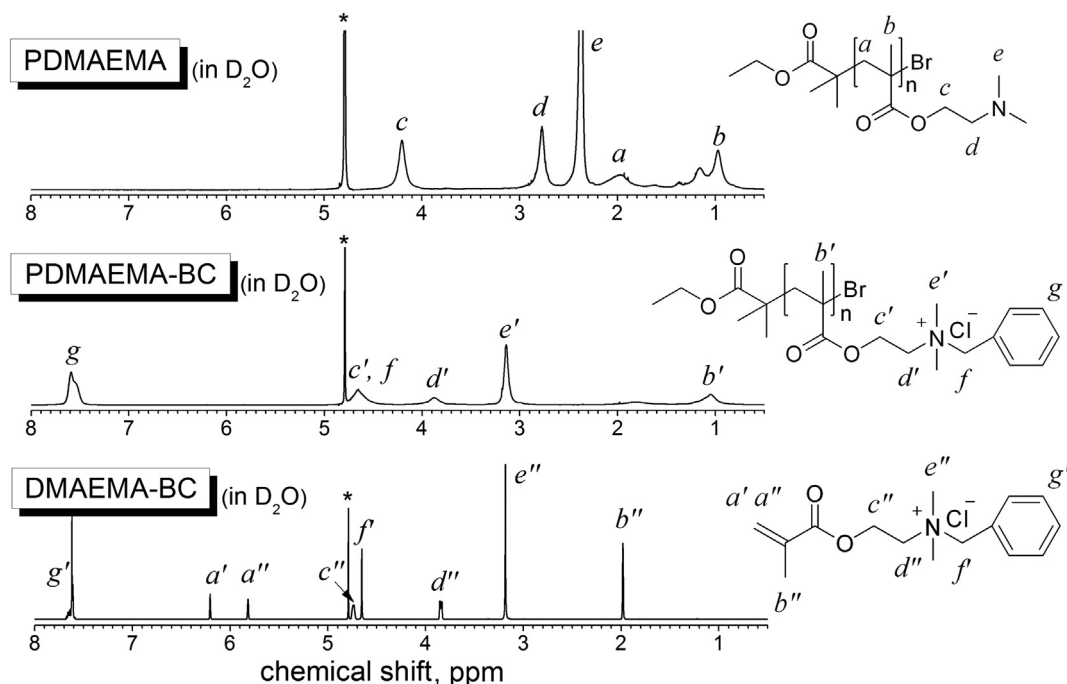


Fig. 2. ¹H NMR spectra of PDMAEMA, PDMAEMA-BC and DMAEMA-BC.

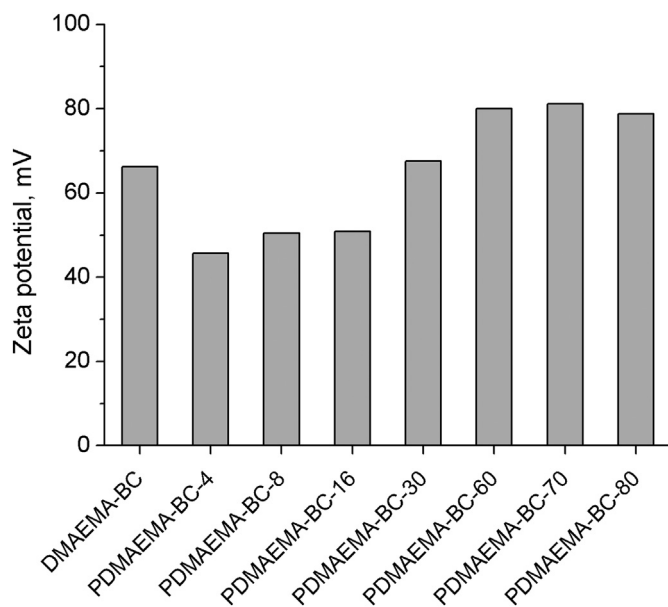


Fig. 4. Zeta potentials of DMAEMA-BC and the PDMAEMA-BC polymers with different molecular weights.

that the change from a monomer to a polymer with low DP increase the degree of branch, and the hydrophobicity of the backbone was increased with increase of the chain length. However, the environment in which bacteria live is more complex than pure water. The formation of micelles by DMAEMA-BC and PDMAEMA-BC is more difficult in real environment that contains salt, leaked cytoplasmic contents, and so on.

3.3. Zeta potentials and particle size distributions of DMAEMA-BC and PDMAEMA-BC in water

The zeta potentials and particle sizes of DMAEMA-BC and the PDMAEMA-BC polymers displayed in Figs. 4 and 5 showed that: (1) PDMAEMA-BC with low DP exhibited the low zeta potential, which meant it easier to aggregates; (2) PDMAEMA-BC with low DP exhibited the larger particle sizes than the samples with higher DP; (3) the particle size of PDMAEMA-BC was decreasing due to the increase of absolute value of zeta potential of PDMAEMA-BC; (4) the particle size of DMAEMA-BC was below the minimum diameter that can be measured, which meant that DMAEMA-BC was unable to form large micelles.

As shown in Fig. 6, the TEM study of the micellar conformation of DMAEMA-BC and PDMAEMA-BC shows that the particle sizes of PDMAEMA-BC with low DP were larger than those of the other samples,

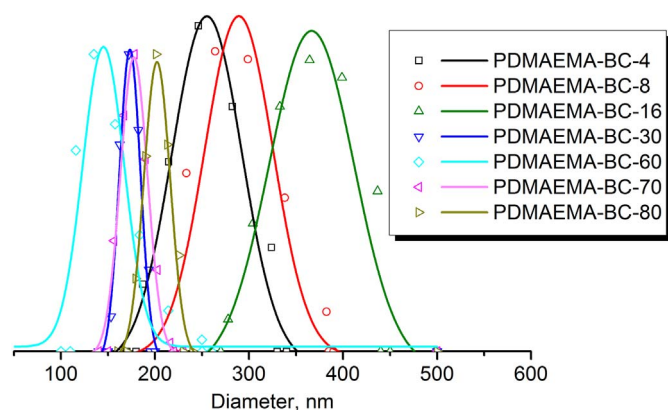


Fig. 5. Particle size distributions of PDMAEMA-BCs with different molecular weights. The particle size distribution of DMAEMA-BC could not be determined because the diameters were below the minimum diameter that can be measured.

which were consistent with the results of zeta potentials and particle sizes.

3.4. Antimicrobial activity against bacteria and pathogenic fungi

Screening of the antimicrobial activities of DMAEMA-BC and PDMAEMA-BC against bacteria and pathogenic fungi was performed using *E. coli*, *S. albus* and *C. albicans* as test organisms because they represent Gram-negative, Gram-positive bacteria and pathogenic fungi, respectively. The MIC and MBC or MFC values of DMAEMA-BC and PDMAEMA-BC were determined using the TTC coloration method. Fig. 7 is a typical photograph from the determination of the MIC values for DMAEMA-BC and PDMAEMA-BC-4 against *E. coli*, *S. albus*, *C. albicans*, *R. solani* and Foc4. The MIC and MBC or MFC values for DMAEMA-BC and PDMAEMA-BC against *E. coli*, *S. albus* and *C. albicans* are shown in Fig. 8.

As shown in Fig. 8, the results indicated that the MIC and MBC or MFC values of the homopolymers were far lower than those of the monomers against both *E. coli*, *S. albus* and *C. albicans*, which meant that the activity of the polymers was much higher than that of the corresponding monomers. The CMC values of DMAEMA-BC and PDMAEMA-BC were lower than the MIC and MBC or MFC; thus, DMAEMA-BC and PDMAEMA-BC are able to form micelles. However, in the particle size distribution test, we found that DMAEMA-BC is not capable of forming large micelles. Furthermore, although the formation of micelles in a real environment is difficult, the linkages formed by covalent bonds guarantee the aggregation of charge. It was reasonable to assume that the change from a monomer to a polymer could increase the local charge density; thus, adsorption on bacterial cell surfaces was enhanced for the polymer compared to the monomer, and binding to the cytoplasmic membrane was also facilitated by the polymer because of the presence of negatively charged species in the membrane [13].

Besides, for DMAEMA-BC and the PDMAEMA-BC polymers with different molecular weights, the best antimicrobial activities against animal pathogenic bacteria and fungi were not observed for the high and low molecular weights. The optimal antimicrobial activity against *E. coli*, *S. albus* and *C. albicans* were achieved when the DP of PDMAEMA-BC was about 8. It is noticed that the MIC and MBC values for PDMAEMA-BC-8 against *E. coli* were lower than the CMC, which meant that PDMAEMA-BC-8 exhibited the best antimicrobial activity against *E. coli* without forming micelles. Without considering the formation of micelles, the processes of adsorbing onto the bacterial cell surface and disrupting the cytoplasmic membrane are likely enhanced by increasing the molecular weight of the antimicrobial agents, whereas the process of diffusing through the cell wall is inhibited by increasing the molecular weight [14]. Peptidoglycan is a major part of bacteria cell walls with open network structures. Bacteria cell walls generally do not act as significant permeability barriers against compounds with molecular masses below 50 kDa [23]. Additionally, it was observed that the DMAEMA-BC and PDMAEMA-BC with high chain lengths gave higher zeta potentials, which led to a decrease in the particle size. Thus, the largest particle size of PDMAEMA-BC was obtained from a moderate chain length which means that the degree of aggregation was the highest when the PDMAEMA-BC chain length was moderate. In conclusion, the observed optimal molecular weight for antibacterial activity can be explained based on the combined effect of those two kinds of controlling factors.

Additionally, compared with the antimicrobial activities of the PDMAEMA-BC against *E. coli*, the test results indicated that the antimicrobial activities of the PDMAEMA-BC against *S. albus* were minimally dependent on the molecular weight when the molecular weight of PDMAEMA-BC was too high. This finding can be explained using the fact that Gram-positive bacteria tend to have a loose cell wall, whereas Gram-negative bacteria have an outer membrane structure in the cell wall that forms an additional barrier to foreign molecules [3,8]. This allowed the PDMAEMA-BC polymers with high molecular weight to

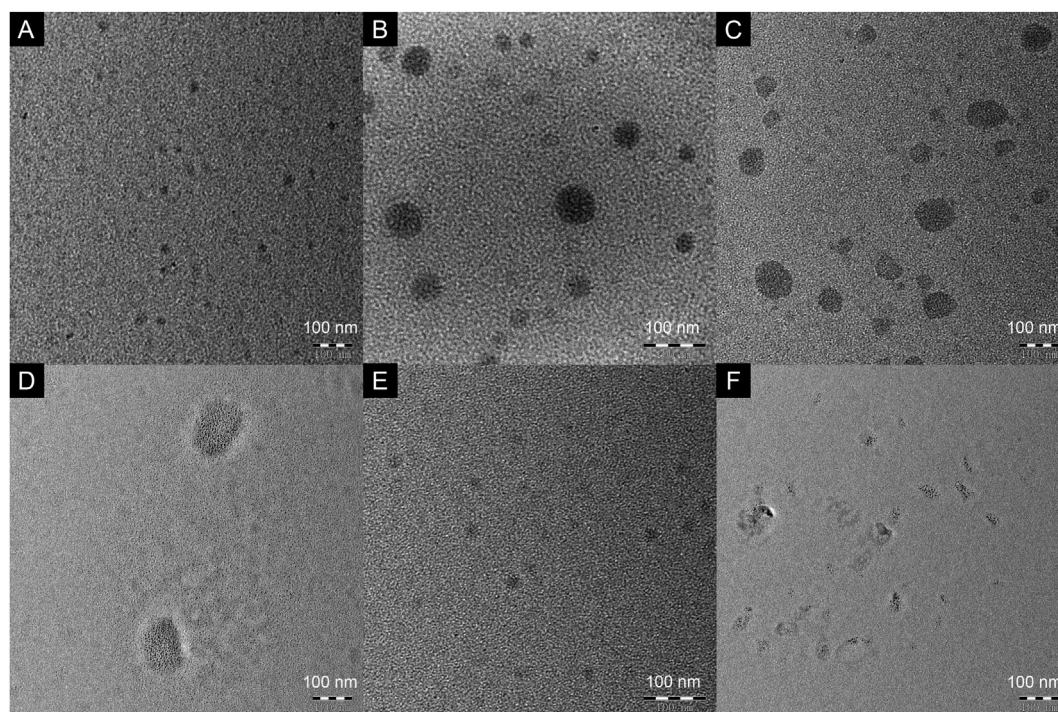


Fig. 6. Transmission electron microscope of (A) DMAEMA-BC, (B) PDMAEMA-BC-4, (C) PDMAEMA-BC-8, (D) PDMAEMA-BC-16, (E) PDMAEMA-BC-30 and (F) PDMAEMA-BC-80.

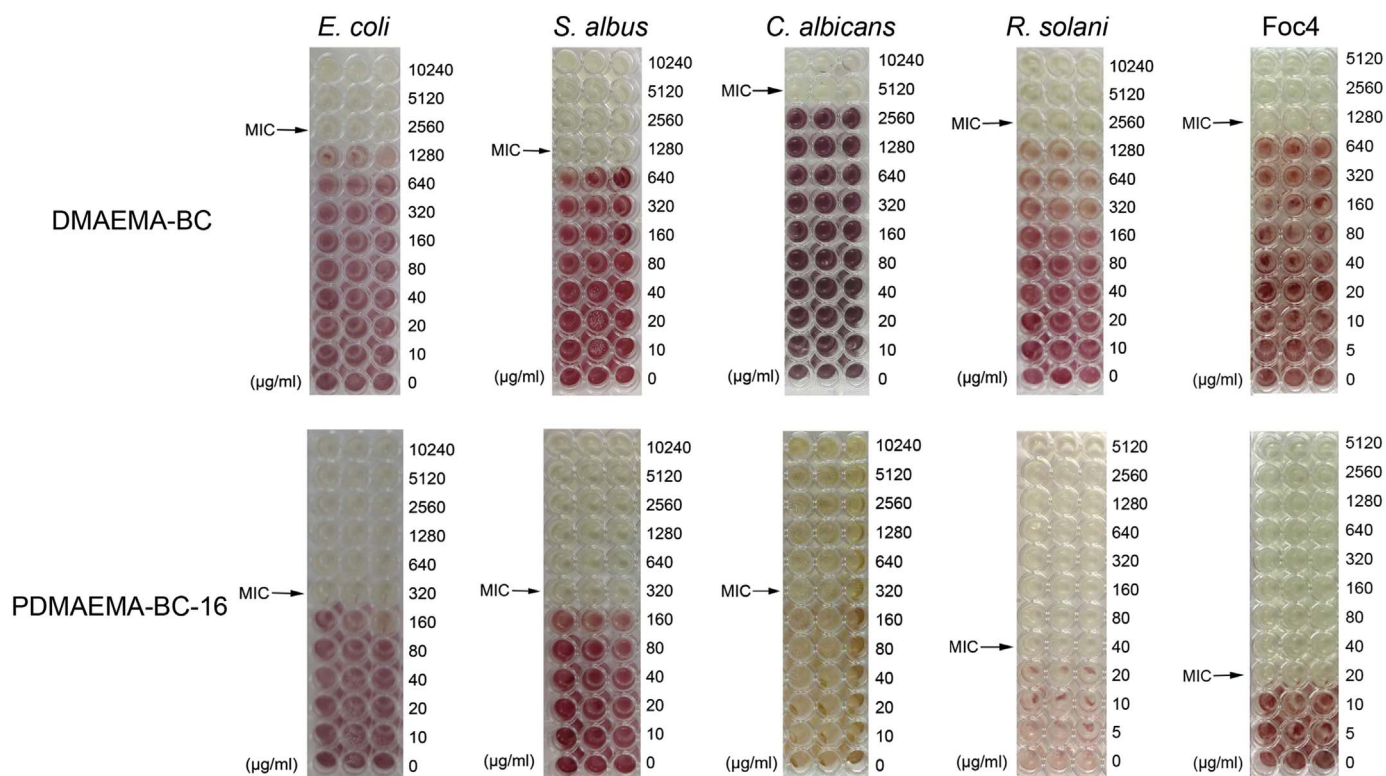


Fig. 7. Typical photograph of the MIC value determination for DMAEMA-BC and the PDMAEMA-BC-16 polymers against *E. coli*, *S. albus*, *C. albicans*, *R. solani* and Foc4.

diffuse through the cell walls of the Gram-positive bacteria more easily.

3.5. Antifungal activity against phytopathogenic fungi (*R. solani* and Foc4)

Screening of the antimicrobial activities of DMAEMA-BC and PDMAEMA-BC against phytopathogenic fungi was performed using *R. solani* and Foc4 as test organisms. As shown in Fig. 8, for DMAEMA-BC

and the PDMAEMA-BC polymers with different molecular weights, the optimal antimicrobial activity against *R. solani* and Foc4 were achieved when the DP of PDMAEMA-BC were 4 and 16, respectively. Similar trends were observed in the antimicrobial activities of DMAEMA-BC and PDMAEMA-BC against bacteria and pathogenic fungi. It is noticed that most of the MIC and MFC values for PDMAEMA-BC against *R. solani* and Foc4 were lower than the CMC, which meant that the factor of

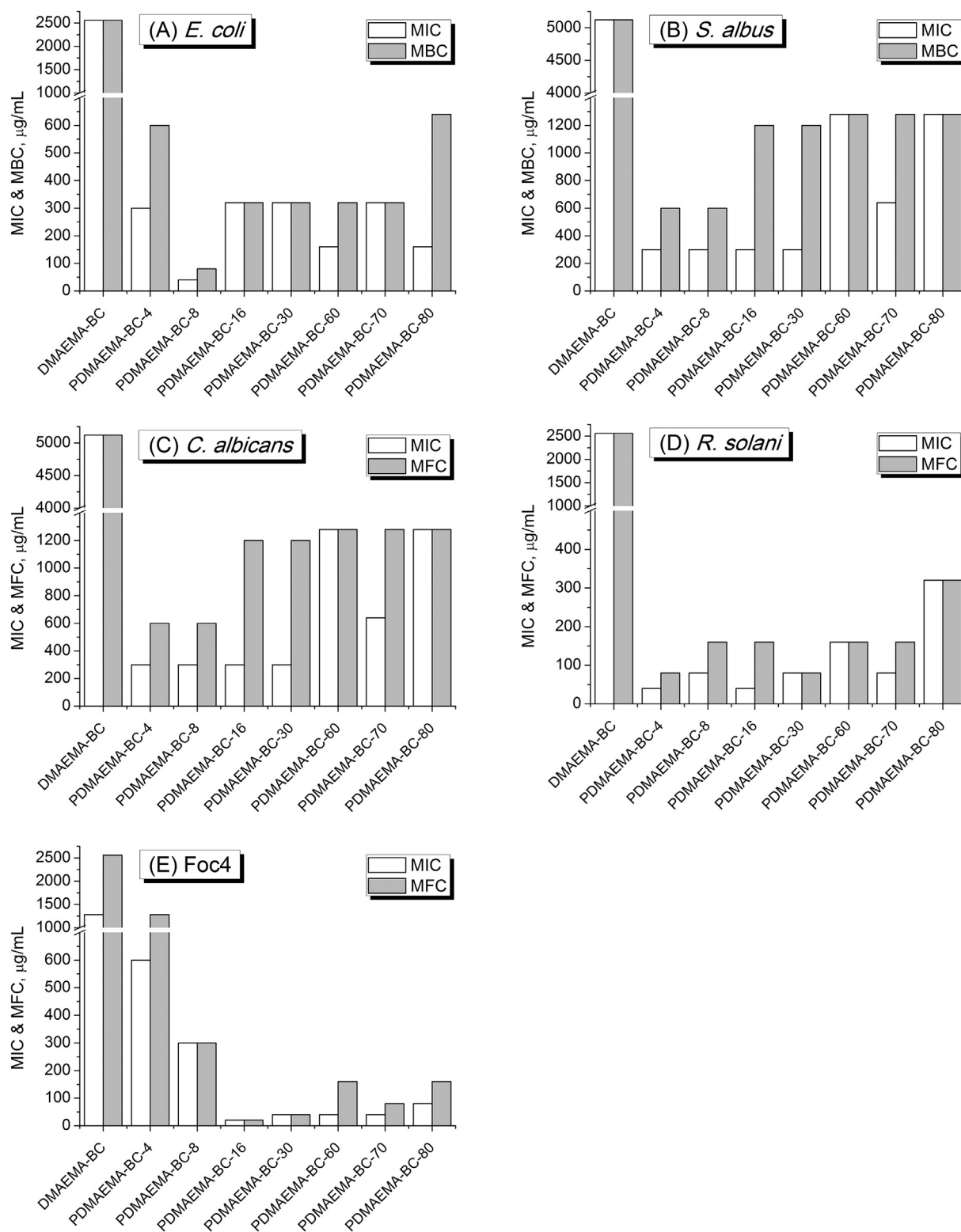


Fig. 8. MIC and MBC (for bacterial) or MFC (for fungi) values of DMAEMA-BC and PDMAEMA-BC against (A) *E. coli*, (B) *S. albus*, (C) *C. albicans*, (D) *R. solani* and (E) *Foc4*.

chain length played a dominant role compared to the factor of the formation of micelles. With an increase in the chain length of PDMAEMA-BC, the aggregated charge was more stable in the real environment due to the covalent bond linkages. However, diffusion through the cell wall became more difficult with increasing PDMAEMA-BC chain length, which led to a decrease in the antimicrobial activity.

Fig. 9 is a typical photograph displaying the antifungal effects of

DMAEMA-BC and PDMAEMA-BC-16 against *R. solani* and *Foc4*. The mycelial growth inhibition by DMAEMA-BC and PDMAEMA-BC-16 against *R. solani* and *Foc4* in PDA medium is shown in Fig. 10, and the EC_{50} and EC_{90} values were calculated using the regression equation when the MGI values were 50% and 90%, respectively. As shown in Fig. 11, PDMAEMA-BC-4 and PDMAEMA-BC-16 exhibited the best antimicrobial activity against *R. solani* and *Foc4* respectively, and the

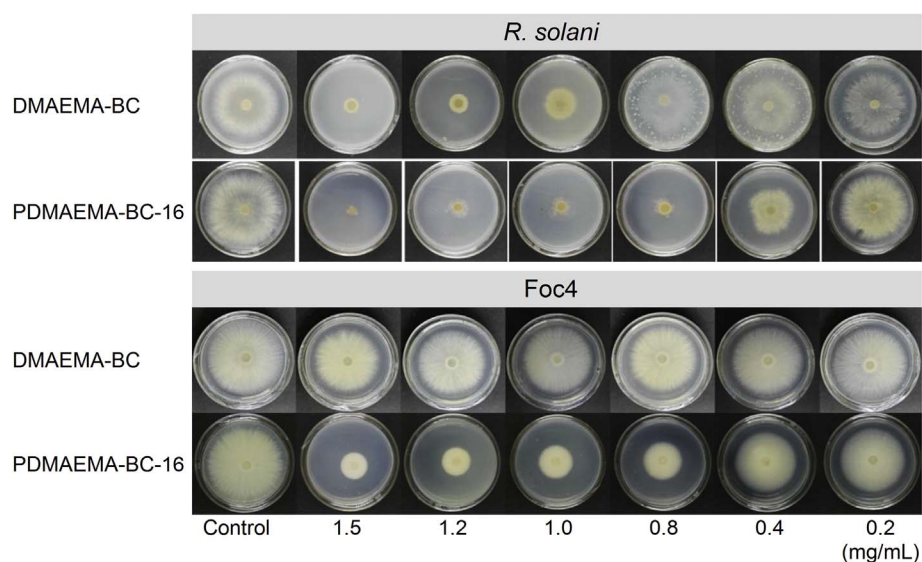


Fig. 9. Typical mycelial growth of *R. solani* and Foc4 in PDA medium after application of DMAEMA-BC and PDMAEMA-BC-16. The data were based on three replicates, and the test was repeated twice with similar results. Representative results are shown.

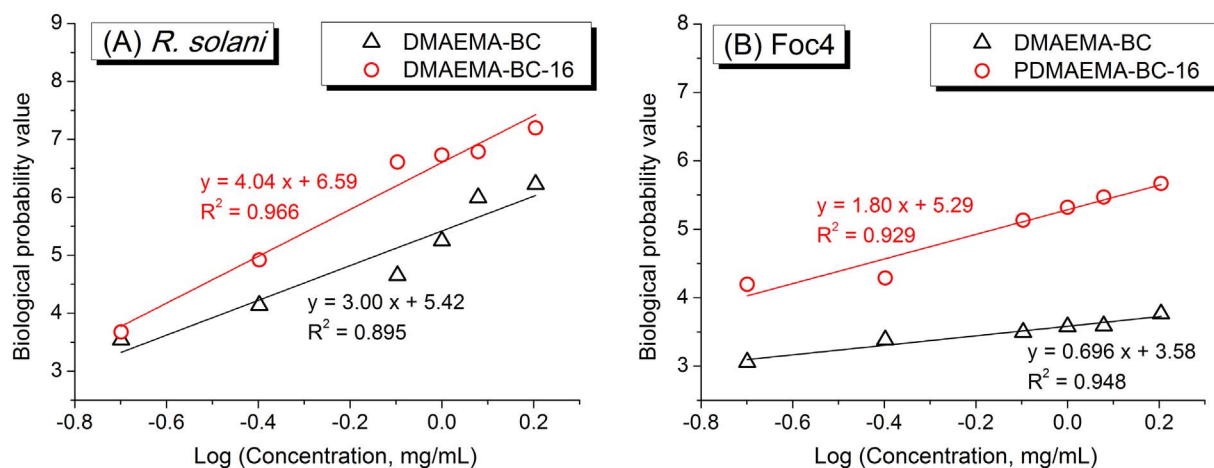


Fig. 10. Mycelial growth inhibition by DMAEMA-BC and PDMAEMA-BC-16 against *R. solani* and Foc4 in PDA medium. The growth of *R. solani* and Foc4 was measured after 48 h of incubation at 28 °C.

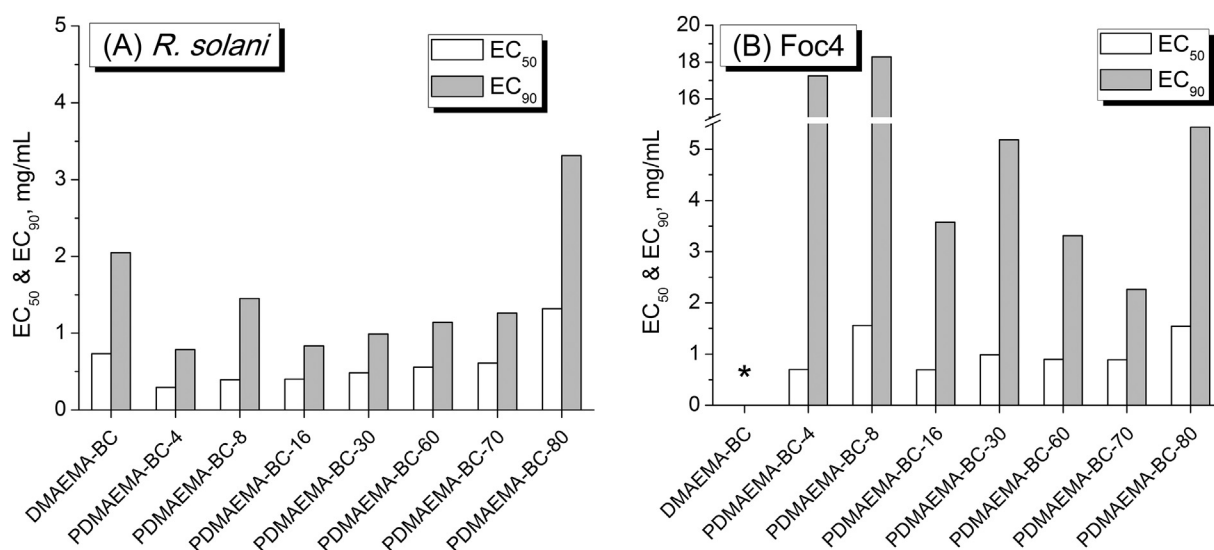


Fig. 11. EC_{50} and EC_{90} values of DMAEMA-BC and PDMAEMA-BC against (A) *R. solani* and (B) Foc4. (*: The calculated EC_{50} and EC_{90} values of DMAEMA-BC against Foc4 are much larger than 20.)

antimicrobial activities were lower for the higher and lower molecular weights. For PDMAEMA-BC, the optimal antimicrobial activity against animal pathogenic bacteria and fungi was achieved with an intermediate chain length, which was consistent with the results of MIC and MFC values.

Compared to bacteria, the structures of fungi cells are much more complicated. From the studies of numerous fungi, the cell wall has been shown to be primarily composed of chitin, glucans, mannans and glycoproteins, and the wall composition frequently varies markedly between species of fungi [24,25]. In addition, fungi cells contain organelles, such as mitochondria, endoplasmic reticuli and Golgi bodies. Therefore, the ability of antimicrobial agents to diffuse through the cell wall and disrupt the cellular structure is likely different between fungi and bacteria and even between various fungi. Most of the MIC and MFC values for PDMAEMA-BC against *R. solani* and Foc4 were lower than those against *E. coli*, *S. albus* and *C. albicans*, which meant the PDMAEMA-BC polymers were more suitable for inhibiting phytopathogenic fungi. Additionally, the antifungal activities of the PDMAEMA-BC polymers against *R. solani* were shown to have a greater molecular weight dependence than those against Foc4.

4. Conclusions

In this paper, DMAEMA-BC and a series of PDMAEMA-BC homopolymers with tunable molecular weights were synthesized to quantify the relationship between their antimicrobial properties and chain length. From the present results, optimal antimicrobial (*E. coli*, *S. albus*, *C. albicans*, *R. solani*, and Foc4) activities were achieved for an intermediate DP of PDMAEMA-BC. To properly explain the relationship between antimicrobial activity and molecular weight, the bacteria structure and the ability of the antimicrobial agent to diffuse through the cell wall and disrupt the cellular structure were considered. PDMAEMA-BC with low DP exhibited the low zeta potential, which meant it easier aggregates and form micelles with large particle size. On the other hand, the factor of chain length played a dominant role and the optimal antimicrobial activity was achieved with an intermediate chain length by taking account of the influence of both aggregated charge due to the covalent bond linkages and diffusion through the cell wall. The systematic approach to examining the antimicrobial activities of PDMAEMA-BC homopolymers with varying DP is expected to guide the future design of antimicrobial polymers as potential fungicide agents for controlling plant disease.

Acknowledgments

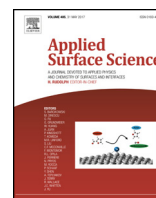
This work was supported by the Science and Technology Program of Guangzhou, China, under grant 201704020084; the Science and Technology Planning Project of Guangdong Province, China under grant 2016A020210105; and the National Natural Science Foundation of China under grant 31201552.

Appendix A. Supplementary data

Supplementary data to this article can be found online at <https://doi.org/10.1016/j.reactfunctpolym.2017.10.010>.

References

- [1] R.C. Ploetz, Fusarium wilt of banana is caused by several pathogens referred to as *Fusarium oxysporum* f. sp. *cubense*, *Phytopathology* 96 (2006) 653–656.
- [2] E.-R. Kenawy, S.D. Worley, R. Broughton, The chemistry and applications of antimicrobial polymers: a state-of-the-art review, *Biomacromolecules* 8 (2007) 1359–1384.
- [3] C.Z. Chen, N.C. Beck-Tan, P. Dhurjati, T.K. van Dyk, R.A. LaRossa, S.L. Cooper, Quaternary ammonium functionalized poly(propylene imine) dendrimers as effective antimicrobials: structure-activity studies, *Biomacromolecules* 1 (2000) 473–480.
- [4] N.D. Koromilas, G.C. Lainioti, G. Vasilopoulos, A. Vantarakis, J.K. Kallitsis, Synthesis of antimicrobial block copolymers bearing immobilized bacteriostatic groups, *Polym. Chem.* 7 (2016) 3562–3575.
- [5] A. Kanazawa, T. Ikeda, T. Endo, Novel polycationic biocides: synthesis and antibacterial activity of polymeric phosphonium salts, *J. Polym. Sci. A Polym. Chem.* 31 (1993) 335–343.
- [6] Z. Huang, R. Liuyang, C. Dong, Y. Lei, A. Zhang, Y. Lin, Polymeric quaternary ammonium salt activity against *Fusarium oxysporum* f. sp. *cubense* race 4: synthesis, structure-activity relationship and mode of action, *React. Funct. Polym.* 114 (2017) 13–22.
- [7] J. Hoque, P. Akkapeddi, V. Yadav, G.B. Manjunath, D.S.S.M. Uppu, M.M. Konai, V. Yarlagadda, K. Sanyal, J. Haldar, Broad spectrum antibacterial and antifungal polymeric paint materials: synthesis, structure – activity relationship, and membrane-active mode of action, *ACS Appl. Mater. Interfaces* 7 (2015) 1804–1815.
- [8] A. Muñoz-Bonilla, M. Fernández-García, Polymeric materials with antimicrobial activity, *Prog. Polym. Sci.* 37 (2012) 281–339.
- [9] X. Wan, Y. Zhang, Y. Deng, Q. Zhang, J. Li, K. Wang, J. Li, H. Tan, Q. Fu, Effects of interaction between a polycation and a nonionic polymer on their cross-assembly into mixed micelles, *Soft Matter* 11 (2015) 4197–4207.
- [10] P. Gilbert, L.E. Moore, Cationic antiseptics: diversity of action under a common epithet, *J. Appl. Microbiol.* 99 (2005) 703–715.
- [11] X. Qin, Y. Li, F. Zhou, L. Ren, Y. Zhao, X. Yuan, Polydimethylsiloxane-poly-methacrylate block copolymers tethering quaternary ammonium salt groups for antimicrobial coating, *Appl. Surf. Sci.* 328 (2015) 183–192.
- [12] T. Ikeda, S. Tazuke, Synthesis and antimicrobial activity of poly(trialkylvinylbenzylammonium chloride)s, *Macromol. Chem. Phys.* 185 (1984) 869–876.
- [13] A. Zhang, Q. Liu, Y. Lei, S. Hong, Y. Lin, Synthesis and antimicrobial activities of acrylamide polymers containing quaternary ammonium salts on bacteria and phytopathogenic fungi, *React. Funct. Polym.* 88 (2015) 39–46.
- [14] T. Ikeda, H. Hirayama, H. Yamaguchi, S. Tazuke, M. Watanabe, Polycationic biocides with pendant active groups: molecular weight dependence of antibacterial activity, *Antimicrob. Agents Chemother.* 30 (1986) 132–136.
- [15] J. Huang, H. Murata, R.R. Koepsel, A.J. Russell, K. Matyjaszewski, Antibacterial polypropylene via surface-initiated atom transfer radical polymerization, *Biomacromolecules* 8 (2007) 1396–1399.
- [16] Y. Lin, Q. Liu, L. Cheng, Y. Lei, A. Zhang, Synthesis and antimicrobial activities of polysiloxane-containing quaternary ammonium salts on bacteria and phytopathogenic fungi, *React. Funct. Polym.* 85 (2014) 36–44.
- [17] A. Mourey, N. Canillac, Anti-*Listeria monocytogenes* activity of essential oils components of conifers, *Food Control* 13 (2002) 289–292.
- [18] W. Sajomsang, P. Gonil, S. Saesoo, C. Ovatlamporn, Antifungal property of quaternized chitosan and its derivatives, *Int. J. Biol. Macromol.* 50 (2012) 263–269.
- [19] M.E. Levison, Pharmacodynamics of antimicrobial drugs, *Infect. Dis. Clin. N. Am.* 18 (2004) 451–465.
- [20] F.R.B. Ferreira, P.M. da Silva, T. Soares, L.G. Machado, L.C.C. de Araújo, T.G. da Silva, G.S.V. de Mello, M.G. da R. Pitta, M.J.B. de M. Rego, E.V. Pontual, R.B. Zingali, T.H. Napoleão, P.M.G. Paiva, Evaluation of antimicrobial, cytotoxic, and hemolytic activities from venom of the spider *Lasiadora* sp, *Toxicon* 122 (2016) 119–126.
- [21] D. Yao, Y. Guo, S. Chen, J. Tang, Y. Chen, Shaped core/shell polymer nanoobjects with high antibacterial activities via block copolymer microphase separation, *Polymer* 54 (2013) 3485–3491.
- [22] A. Domínguez, A. Fernández, N. González, E. Iglesias, L. Montenegro, Determination of critical micelle concentration of some surfactants by three techniques, *J. Chem. Educ.* 74 (1997) 1227–1231.
- [23] T.J. Franklin, G.A. Snow, *Biochemistry and Molecular Biology of Antimicrobial Drug Action*, Springer Science & Business Media, 2005.
- [24] S.M. Bowman, S.J. Free, The structure and synthesis of the fungal cell wall, *BioEssays* 28 (2006) 799–808.
- [25] D.J. Adams, Fungal cell wall chitinases and glucanases, *Microbiology* 150 (2004) 2029–2035.



Full Length Article

The synthesis and protein resistance of amphiphilic PDMS-*b*-(PDMS-*g*-cysteine) copolymers

Yufeng Lei^a, Yaling Lin^{b,*}, Anqiang Zhang^{a,*}^a College of Material Science and Engineering, South China University of Technology, 381 Wushan Rd., Guangzhou 510641, Guangdong, China^b College of Materials and Energy, South China Agricultural University, 483 Wushan Rd., Guangzhou, 510642, Guangdong, China

ARTICLE INFO

Article history:

Received 30 March 2017

Received in revised form 4 May 2017

Accepted 8 May 2017

Available online 10 May 2017

Keywords:

Zwitterionic diblock polydimethylsiloxanes

Cysteine

Protein resistance

Hydrophobic interaction

ABSTRACT

Zwitterionic polymers have been used to cope with nonspecific protein adsorption and bio-fouling problems for a wide range of materials, including biomedical devices, marine coatings and membrane separation. However, direct surface modification with highly water-soluble zwitterionic polymers is rather difficult due to their poor attachment to hydrophobic solid surfaces. In this work, we utilize the hydrophobic interaction to anchor zwitterionic polysiloxanes grafted with cysteine onto surfaces by adding an hydrophobic block of polydimethylsiloxanes, referred as PDMS-*b*-(PDMS-*g*-Cys)s. The synthesis involves only three steps of reactions, and the structures of each product were characterized using GPC, FT-IR and ¹H NMR. The adsorption and protein resistance of PDMS-*b*-(PDMS-*g*-Cys)s on a gold surface are investigated with QCM-D. The results show that the hydrophobic interaction moieties of the additional PDMS blocks help the hydrophilic cysteine-grafted blocks stably attach and then function on the sensor. These findings suggest that the addition of hydrophobic moieties provides an effective approach to construct anti-fouling interfaces with zwitterionic polymers in aqueous solution.

© 2017 Elsevier B.V. All rights reserved.

1. Introduction

Polymers functionalized with zwitterions such as phosphorylcholine [1–3], betaines [4–7] and amino acids [8,9] have been extensively studied and exploited for anti-biofouling applications, with excellent resistance performance against non-specific protein adsorption. It is recognized that nonspecific protein resistance is closely related to the electrostatically induced hydration of zwitterionic polymers [2,10,11]. Zwitterions can strongly bind water molecules via electrostatic interactions, constituting an ultra-low-fouling hydration layer that resists protein adsorption and bio-fouling.

However, the hydrophilic nature and great solubility in water of ionic polymers cause difficulty in their assembling not only in aqueous solution [12,13], but also in anchoring onto targeting surfaces for effective function. In our previous work, carboxybetaine-grafted polydimethylsiloxanes (PDMS-*g*-CBs) were prepared and blended into cross-linked PDMS films, which endowed the PDMS films with surface hydrophilicity and anti-fouling properties [14]. The anti-fouling properties of PDMS-*g*-CBs were thus demonstrated

indirectly. Moreover, the interaction between PDMS-*g*-CB and proteins in aqueous solution were directly characterized using circular dichroism spectroscopy (CD), isothermal titration calorimetry (ITC), atomic force microscopy (AFM), and so on. The results indicated that the weak interaction between PDMS-*g*-CB and proteins is due to the hydration layer of zwitterionic side-groups [11]. Nevertheless, anchoring the anti-fouling polymers in solution on targeting surfaces in a simple and economical way remains to be studied.

Various methods have been developed to prepare low-fouling surfaces with zwitterions, which can generally be categorized into two groups: “graft-from” and “graft-to” methods, as reviewed by Jiang et al. [15]. A typical “graft-from” method involves the polymerization of zwitterionic monomers initiated by initiators pre-immobilized on the surface, such as ATRP [16,17]. In contrast, the “graft-to” methods attach zwitterionic polymers directly onto targeting surfaces where special pre-treatment is not suitable or necessary. These polymers are designed with non-fouling groups as well as adhesive groups for attachments, such as hydrophobic moieties for a hydrophobic surface [3,18,19] and 3,4-dihydroxyphenylalanine (DOPA) groups for various surfaces [5,20–23].

Among the strategies mentioned above, the hydrophobic interaction that requires the least pre-treatments on target hydrophobic surfaces offers a promising method for anti-fouling surface

* Corresponding authors.

E-mail addresses: linyaling@scau.edu.cn (Y. Lin), aqzhang@scut.edu.cn (A. Zhang).

engineering. The adsorption of PluronicTM surfactants (PEO-PPO-PEO) onto a hydrophobic surface has been sufficiently investigated, and it has been accepted that the hydrophobic PPO blocks provide the necessary anchor for the amphiphilic copolymers to remain absorbed at the interface, while the PEO blocks extend into the solvent phase, resisting protein adsorption by sterically repulsive forces from the extended, highly hydrated brush-like PEO layer [24–26]. Surface modification by adding hydrophobic moieties to zwitterionic polymers is less frequently reported, though the process is quite simple and effective [3,27].

In this work, we have prepared an amphiphilic diblock copolymer of cysteine-grafted polydimethylsiloxanes. A highly hydrophobic PDMS block was introduced to the zwitterionic PDMS-g-Cysteine block, to anchor the anti-fouling moieties through hydrophobic interaction onto hydrophobic surfaces that are susceptible to contamination.

2. Materials and methods

2.1. Materials

Hexamethylcyclotrisiloxane (D_3) and 1,3,5-trimethyl-1,3,5-trivinylcyclotrisiloxane (D_3^V) were purchased from Hubei Xinmingtai Chemicals Co., Ltd. (Wuhan, China) and dried before use. Anhydrous tetrahydrofuran (THF), trimethylchlorosilane (TMCS), 2,2-dimethoxy-2-phenylacetophenone (DMPA) and N-acetyl-L-cysteine (Acys) were purchased from Macklin (Shanghai, China) and used directly. A solution of 2.5 M *n*-butyl lithium (*n*-BuLi) in hexane was purchased from Aladdin (Shanghai, China), and 1,6-diphenyl-1,3,5-hexatriene (DPH) for DPH-UV measurements was purchased from Arcos Organics (UK). Physiological phosphate-buffered saline (PBS buffer, 0.14 M, pH 7.4) was prepared by dissolving NaCl, KCl, Na_2HPO_4 , and KH_2PO_4 in Milli-Q water. BSA (Merck Chemicals) solution (1.0 mg/mL) was prepared by dissolving the protein in PBS buffer. Other reagents were common products and used as received if not otherwise mentioned.

The synthesis route of PDMS-*b*-(PDMS-*g*-Cys)s is illustrated in Scheme 1.

2.2. Synthesis of PDMS-*b*-PVMS backbones via anionic ring-opening polymerization

Anhydrous D_3 solution in THF was injected into a Schlenk flask fitted with a magnetic stirrer and filled with nitrogen. Then, *n*-BuLi was added to the mixture to initiate the polymerization, and the reaction proceeded for 12 h under constant stirring in a 0 °C bath. A small aliquot was collected and terminated by the addition

of methanol for GPC measurement, after which the dried solution of D_3 and D_3^V in THF was added. The polymerization was continued for 12 h and quenched by TMCS. Later, the solvents were removed by a rotary evaporator at 150 °C/0.1 MPa. Finally, the LiCl by-product was filtered out, and a colorless transparent product was obtained. Yield: 91%. ¹H NMR (400 MHz, $CDCl_3$, ppm): δ = 0.12–0.29 (m, Si-CH₃), 0.22–0.23 (m, Vi-Si-CH₃), 0.59–0.63 (t, CH₃CH₂CH₂CH₂-), 0.94–0.98 (t, CH₃CH₂CH₂CH₂-), 1.34–1.43 (m, CH₃CH₂CH₂CH₂-), 5.84–6.12 (m, -CH=CH₂). FT-IR (KBr, cm⁻¹): 3057, 2958, 2906, 1635, 1409, 1255, 1105, 1016, 802, 686, 531.

A series of PDMS-*b*-PVMS backbones were prepared with similar PVMS blocks and an increasing length of PDMS blocks, referred to as V1–V5, accordingly. For V0, there is no additional PDMS block.

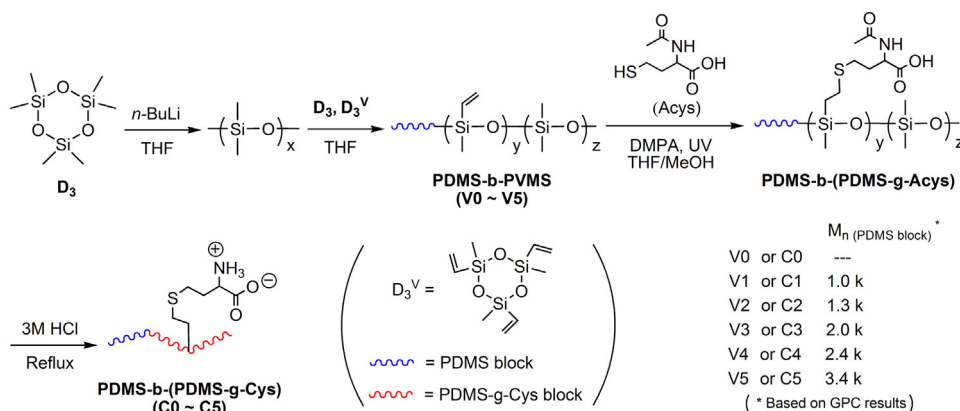
2.3. Synthesis of PDMS-*b*-(PDMS-*g*-Acys) via thiol-ene click reaction

PDMS-*b*-PVMS, 1.2 equivalents (to -Vi group) of Acys and 2 wt% of DMPA were dissolved in THF/methanol (v/v = 1/1) solvent. The reaction mixture was then exposed to 365 nm UV (OPTIMAX-365, Spectronics, USA) under constant stirring for 30 min at room temperature. When the reaction was completed, the solvents were evaporated at 80 °C/0.5 MPa. The resulting polymer was dissolved in chloroform and washed with water. Yield: 95%. ¹H NMR (400 MHz, DMSO-*d*₆, ppm): δ = 0–0.09 (m, Si-CH₃), 8.16 (s, CH₃CONH-), 0.42 (m, CH₃CH₂CH₂CH₂-), 0.81–0.85 (m, CH₃CH₂CH₂CH₂-), 1.23 (m, CH₃CH₂CH₂CH₂-), 1.85 (s, CH₃COO-), 2.72 (m, CH₂CH₂SCH₂CH₂-Si), 2.85 (m, CH₂CH₂SCH₂CH₂-Si), 4.37 (s, HOOCCH-). FT-IR (KBr, cm⁻¹): 3336, 2960, 2912, 1733, 1652, 1539, 1411, 1263, 1087, 1020, 800, 704.

2.4. Synthesis of PDMS-*b*-(PDMS-*g*-Cys) via hydrolysis reaction

PDMS-*b*-(PDMS-*g*-Acys) was dissolved in 3 M hydrochloric acid solution in water/ethanol (v/v = 1/4), with 4 equivalents of HCl for each acetyl group. The reaction mixture was maintained under reflux in nitrogen for 5 h. The product was then concentrated and purified by dialysis in water. Yield: 72%. ¹H NMR (400 MHz, D₂O, ppm): δ = 0.13–0.25 (m, Si-CH₃), 1.03–1.07 (m, CH₃CH₂CH₂CH₂, CH₂CH₂Si), 1.34–1.39 (m, CH₃CH₂CH₂CH₂), 2.10–2.12 (t, CH₂CH₂SCH₂CH₂-Si), 2.75–2.79 (m, CH₂CH₂SCH₂CH₂-Si), 3.14–3.29 (m, CH₂CH₂SCH₂CH₂-Si), 4.20–4.43 (m, HOOCCH-). FT-IR (KBr, cm⁻¹): 2962, 1740, 1575, 1493, 1411, 1257, 1072, 1010, 794.

Based on the original PDMS-*b*-PVMS backbones, PDMS-*b*-(PDMS-*g*-Cys)s were prepared with increasing lengths of hydrophobic blocks, referred to as C0–C5 accordingly.



Scheme 1. Synthesis route of PDMS-*b*-(PDMS-*g*-Cys).

2.5. Structure characterization

Fourier transform infrared spectra (FT-IR) were recorded using a Bruker VERTEX-70 spectrometer at a resolution of 4 cm^{-1} . Samples were coated on KBr plates and dried under the infrared lamp. The measurements were performed over the range $400\text{--}4000\text{ cm}^{-1}$ at room temperature for 16 scans.

^1H NMR spectra were collected using a Bruker Avance III-400 (400 MHz) Fourier digital NMR spectrometer at 25°C using CDCl_3 , $\text{DMSO}-d_6$ or D_2O as the solvent.

Gel permeation chromatography (GPC) was performed using a Waters 515 HPLC pump equipped with a Shodex K-G guard column and a Shodex K-804L chromatographic column at 40°C . Detection was performed using a Waters 2414 refractive index detector, and the samples were analyzed at 35°C using chloroform as the eluent at a flow rate of 1.0 mL/min and narrow-dispersed polystyrenes as the standard.

2.6. Quartz crystal microbalance with dissipation (QCM-D) measurements

QCM-D and the AT-cut quartz crystal with a fundamental resonant frequency of 5 MHz were obtained from Q-sense AB [28]. The quartz crystal was mounted in a fluid cell with one side exposed to the solution. The effects of surface roughness were minimized by using highly polished crystals with a root-mean-square roughness less than 3 nm [29]. Briefly, the mass of adsorption on the quartz crystal relates to the decrease in the resonant frequency of the crystal, whereas the dissipation factor is related to the viscoelastic properties and thickness of the additional layer [30,31]. The changes in the frequency (Δf) and dissipation (ΔD) give information about the PDMS-*b*-(PDMS-*g*-Cys) and BSA adsorption and structural changes of the adsorption layer. All the presented data are from the third overtone ($n=3$). The measurements were performed at 25°C with water or PBS buffer as the reference.

2.7. 1,6-Diphenyl-1,3,5-hexatriene (DPH) UV-vis spectral measurements

The hydrophobic rod-shaped DPH dye has been utilized to determine the critical micellization concentration for various amphiphilic surfactants. A stock solution of 0.4 mM DPH in methanol was prepared. Then, $2\text{ }\mu\text{L}$ of this stock solution was mixed with $200\text{ }\mu\text{L}$ of PDMS-*b*-(PDMS-*g*-Cys) solution in water with concentrations ranging from 0.0098 to 10.0 mg/mL and equilibrated at 25°C for 3 h . A UV-vis spectrophotometer (Merinton SMA5000, Beijing, China) was used to obtain the absorbance at 300 nm . The CMC value at 25°C was determined by the plot of the difference in absorbance at 300 nm versus the logarithmic concentration.

3. Results and discussion

3.1. Synthesis of PDMS-*b*-PVMS backbones

Living anionic polymerization initiated by *n*-butyl lithium has been widely adopted as an efficient method to construct linear polymers with well-controlled chain lengths. A series of PDMS-*b*-PVMS backbones (referred as V0–V5) with different lengths of PDMS blocks, which are designed as hydrophobic moieties in the final amphiphilic products, were characterized by FT-IR, ^1H NMR and GPC (Table 1).

3.2. Grafting cysteine groups to PDMS-*b*-PVMS

Due to the insolubility of L-cysteine and polysiloxanes in the same solvent, N-acetyl-L-cysteine is utilized for the thiol-ene click

Table 1

Detailed information on PDMS-*b*-PVMS backbones.

Sample	$\text{Mn}_{\text{PDMS}}^a$ (kDa)	$\text{Mn}_{\text{PDMS-}b\text{-PVMS}}^a$ (kDa)	PDI ^a	Vi% ^b (%)
V0	–	4.8	1.282	48.1
V1	1.0	4.7	1.199	38.0
V2	1.3	5.3	1.248	33.7
V3	2.0	6.2	1.205	31.2
V4	2.4	6.9	1.281	28.9
V5	3.4	7.6	1.258	26.1

^a M_n , PDI were estimated by GPC results.

^b Vinylsiloxane unit contents in the backbones were calculated from ^1H NMR spectra.

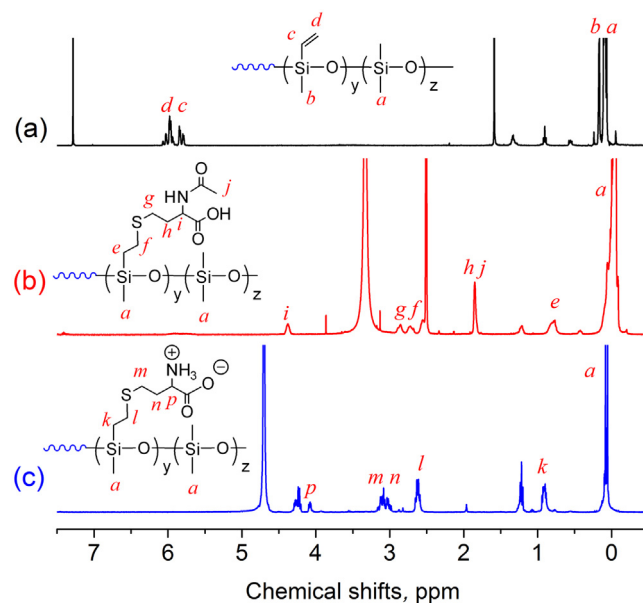


Fig. 1. ^1H NMR spectra of (a) PDMS-*b*-PVMS in CDCl_3 , (b) PDMS-*b*-(PDMS-*g*-Acys) in $\text{DMSO}-d_6$ and (c) PDMS-*b*-(PDMS-*g*-Cys) in D_2O .

reaction, and then the acetyl group is removed via hydrolysis in hydrochloric acid solution. Fig. 1 shows the typical ^1H NMR spectra obtained from PDMS-*b*-PVMS, PDMS-*b*-(PDMS-*g*-Acys) and PDMS-*b*-(PDMS-*g*-Cys). The absence of double bonds ($\delta = 5.84 - 6.12$) and the presence of $-\text{CH}_2-\text{S}-\text{CH}_2-$ ($\delta = 2.72, 2.85$) indicates that the thiol-ene click reaction is fully completed. The absent signals of acetyl groups ($\delta = 1.85$) in PDMS-*b*-(PDMS-*g*-Cys) indicate that the acetyl amide bonds have been completely hydrolyzed. However, whether the PDMS backbones were hydrolyzed cannot be confirmed because the hydrophobic PDMS blocks tend to assemble in the cores of micelles, and the relaxation time is extended [16].

Fig. 2. FT-IR spectra of (a) PDMS-*b*-PVMS, (b) PDMS-*b*-(PDMS-*g*-Acys) and (c) PDMS-*b*-(PDMS-*g*-Cys).

3.3. Determination of critical micelle concentration (CMC)

The critical micelle concentration at 25°C was determined based on the concentration dependence of absorbance at 300 nm from DPH-UV measurement. Fig. 3 shows the absorbance at $210\text{--}400\text{ nm}$ of aqueous solutions of C0 at different concentrations with DPH. When the concentration of C0 is below 0.3125 mg/mL , the absorbance at 300 nm is similar. When $c(\text{C0})$ exceeds 0.6250 mg/mL , the absorbance is significantly improved, which indicates that C0 aggregates into micelles, solubilizing DPH.

Fig. 4 shows the profiles of absorbance at 300 nm versus the logarithmic concentration of C0–C3. For C4 and C5, CMC was not measured due to poor solubility in water. As shown in Table 2, when compared with C0, the CMC for C1 decreases dramatically

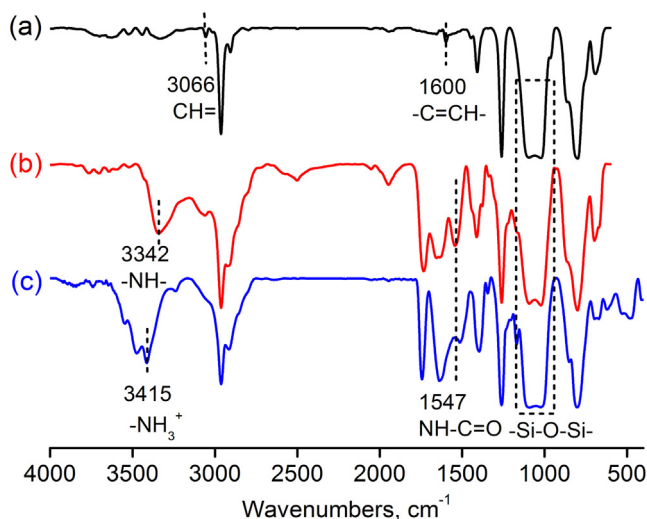


Fig. 2. shows typical FT-IR spectra of PDMS-*b*-PVMS, PDMS-*b*-(PDMS-*g*-Acys) and PDMS-*b*-(PDMS-*g*-Cys). The absence of a double bond at 3066 cm⁻¹ and the presence of amide (3342 cm⁻¹, 1547 cm⁻¹) further indicate the structure of PDMS-*b*-(PDMS-*g*-Acys), and the absence of ν_{NH-C=O} at 1547 cm⁻¹ indicates that the acetyl groups are removed. The peaks near 1010–1100 cm⁻¹, corresponding to the siloxane bonds of backbones, remain unchanged throughout the synthesis process, which indicates that the polysiloxane backbones have not been broken by acid.

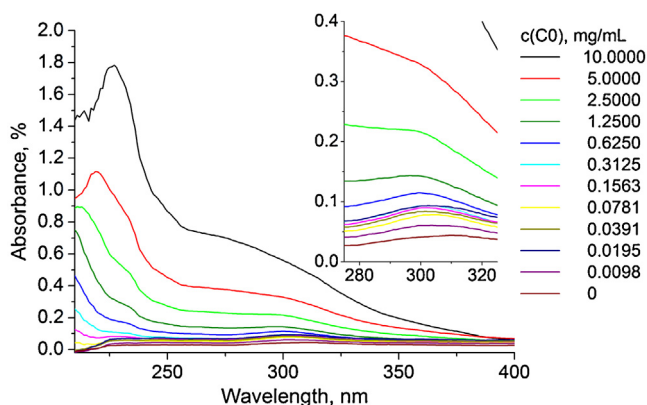


Fig. 3. UV spectra of aqueous solutions of C0 at different concentrations with DPH.

with an additional hydrophobic PDMS block of only 1 kDa length. The CMC for C1 to C3 decreases gradually as the PDMS block becomes longer. This result is consistent with the typical behavior of amphiphilic surfactants. The enlarged hydrophobic moieties

Table 2
Hydrophobic block ratios and CMC values of PDMS-*b*-(PDMS-*g*-Cys)s.

Sample	Hydrophobic block ratio, % ^a	CMC, mg/mL
C0	0	1.5171
C1	17.5	0.7731
C2	19.7	0.3496
C3	24.4	0.2960
C4	25.8	–
C5	30.9	–

^a Hydrophobic block ratio is calculated from GPC results as $M_{nPDMS}/M_{nPDMS-b-PVMS} \times 100\%$.

allow the amphiphilic molecules to aggregate more easily to form micelles in solution. However, it should be noted that for a certain hydrophilic moiety, there is a limit to additional hydrophobic blocks. In this work, we find that for the PDMS-*g*-Cys block with approximately 1/2 units modified with cysteine, the products are hardly soluble in water when the hydrophobic ratio exceeds approximately 25% (C4 and C5).

3.4. Adsorption kinetics and protein resistance of PDMS-*b*-(PDMS-*g*-Cys) with QCM-D measurements

The adsorption kinetics and protein resistance of the PDMS-*b*-(PDMS-*g*-Cys) adsorption layer have been examined by QCM-D. The concentration of each sample solution is set at 3 mg/mL, which is far higher than their CMCs, to form a sufficiently assembled layer of amphiphilic copolymers. As mentioned above, the Δf change indicates the additional mass on the sensor, and the ΔD change indicates the viscoelasticity and thickness of the additional layer.

As shown in Fig. 5, after (a) adding sample solution, for every sample, Δf decreases sharply, and ΔD increases dramatically, indicating the adsorption of the amphiphilic copolymers. Compared with C0, for C1–C3, the drops in Δf are similarly larger, indicating the similarly larger mass of the additional layer. However, after (b) rinsing with water, the ΔD for every sample decreases markedly to a level near the reference, while Δf for every sample shows only a slight increase. This particular change in ΔD and Δf indicates the adsorption behavior of PDMS-*b*-(PDMS-*g*-Cys), as illustrated in Fig. 6. The major mass of the adsorption layer consists of these “lying” molecules that form relatively stable attachments with their hydrophobic PDMS backbones. The copolymers and micelles “standing” on the sensor surface or floating on the upper layer only make up a small portion of the mass of the adsorption layer but contribute major thickness; however, they are vulnerably attached to the surface and easily washed off. The Δf levels of different copolymers after water rinsing indicate the stability of their adsorption. For C3 with the longest PDMS block, the smallest Δf change indi-

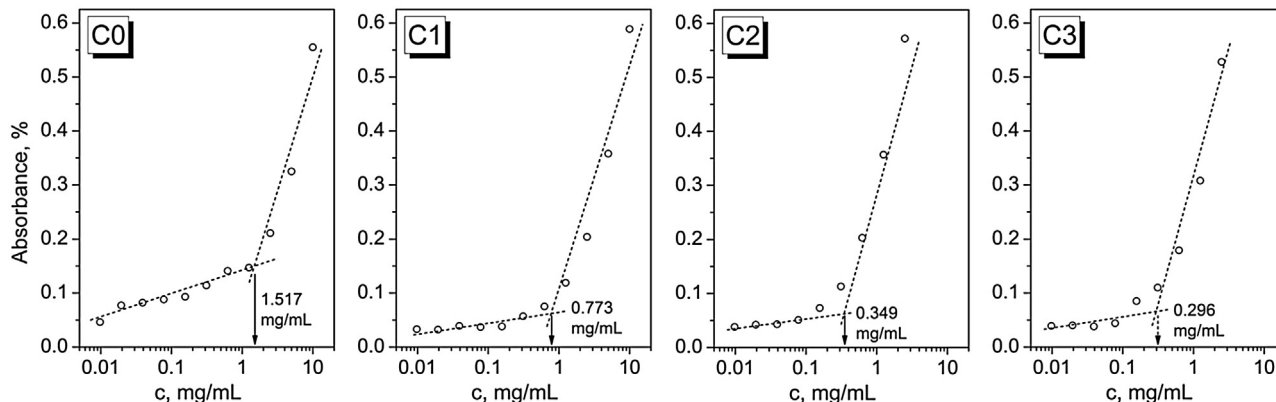


Fig. 4. Plots of absorbance at 300 nm as a function of logarithmic concentration of PDMS-*b*-(PDMS-*g*-Cys)s.

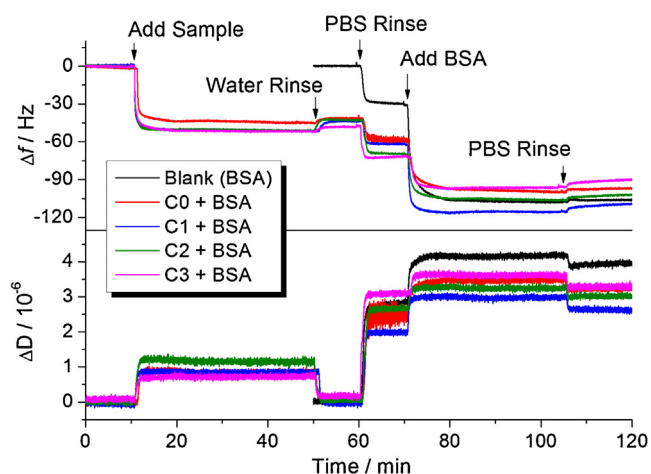


Fig. 5. Time dependency of frequency shift (Δf) and dissipation shift (ΔD) for the adsorption of PDMS-*b*-(PDMS-*g*-Cys)s and BSA on an Au surface at 25 °C.

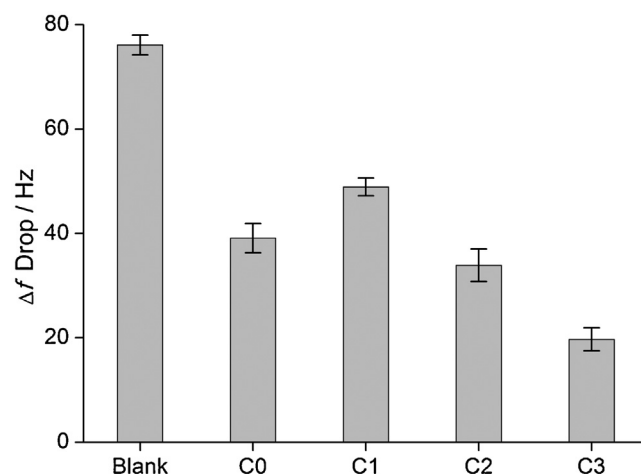


Fig. 7. Δf drop caused by BSA adsorption.

icates the smallest number of copolymers rinsed off. Moreover, for C0–C2, it should be noted that the amounts of molecules remaining on the sensor are similar. Considering the similar molecular weights of these three samples, it seems that the additional PDMS block is too short to drive the hydrophobicity-induced adsorption as effectively as the PDMS backbones.

Fig. 7 shows the Δf drop caused by the adsorption of BSA. Compared to the blank sensor, all the sensors pre-assembled with amphiphilic molecules show significantly less protein adsorption. For C1–C3, the amount of BSA adsorption decreases as the number of PDMS blocks increases, which indicates that the higher the zwitterionic density assembled on the surface, the better the resistance against protein adsorption. However, for C0 without an additional PDMS block, the protein resistance is surprisingly better than C1. This finding is due to the molecular weight effect. Although C1 has an added PDMS block, its molecular weight is still no greater than C0, which means the hydrophobicity of their PDMS backbones is dominant over the hydrophobic interaction-induced adsorption. As the mass of the adsorption layer is similar for C0 and C1, the zwitterionic density on the surface for C0 is higher, which gives rise to better protein resistance [18].

4. Conclusions

In conclusion, amphiphilic block copolymers based on cysteine-grafted PDMS have been prepared, and their protein adsorption resistance was studied. Upon the introduction of a PDMS block into the PDMS-*g*-Cysteine chain, the polymer's solubility in water was moderately decreased, and a stronger attachment between the polymer chain and hydrophobic surfaces was promoted to increase the surface zwitterionic density. For amphiphilic copolymers based on hydrophobic backbones such as polysiloxanes, the strong hydrophobicity of backbone might be dominant during the hydrophobic interaction-induced adsorption when the additional hydrophobic block is not long enough to function.

Acknowledgements

This work was supported by the Science and Technology Planning Project of Guangdong Province, China under grant 2016A020210105; the Science and Technology Program of Guangzhou, China, under grant 201704020084; and the National Natural Science Foundation of China under grant 31201552, 51473051.

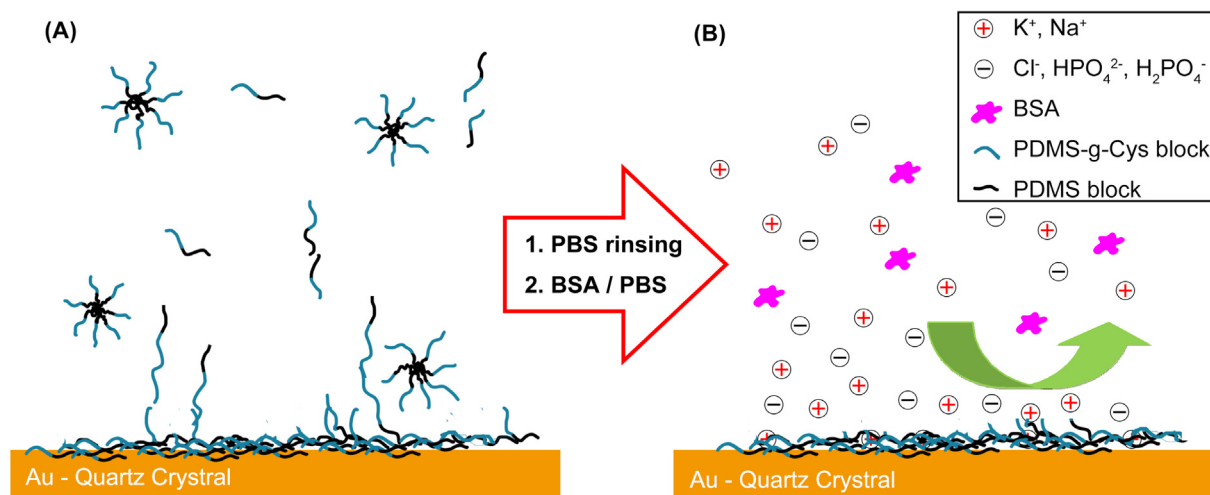
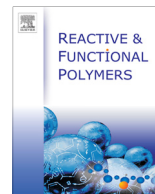


Fig. 6. Schematic representation of PDMS-*b*-(PDMS-*g*-Cys) adsorption and protein resistance on Au surface.

References

- [1] Z. Niu, Y. Zhao, W. Sun, S. Shi, Y. Gong, Biomimetic surface modification of polypropylene by surface chain transfer reaction based on mussel-inspired adhesion technology and thiol chemistry, *Appl. Surf. Sci.* 386 (2016) 41–50.
- [2] S. Chen, J. Zheng, L. Li, S. Jiang, Strong resistance of phosphorylcholine self-assembled monolayers to protein adsorption: insights into nonfouling properties of zwitterionic materials, *J. Am. Chem. Soc.* 127 (2005) 14473–14478.
- [3] J.H. Seo, T. Shibayama, M. Takai, K. Ishihara, Quick and simple modification of a poly (dimethylsiloxane) surface by optimized molecular design of the anti-biofouling phospholipid copolymer, *Soft Matter* 7 (2011) 2968–2976.
- [4] J. Ladd, Z. Zhang, S. Chen, J.C. Hower, S. Jiang, Zwitterionic polymers exhibiting high resistance to nonspecific protein adsorption from human serum and plasma, *Biomacromolecules* 9 (2008) 1357–1361.
- [5] M. He, K. Gao, L. Zhou, Zwitterionic materials for antifouling membrane surface construction, *Acta Biomater.* 40 (2016) 142–152.
- [6] G. Li, H. Xue, G. Cheng, S. Chen, F. Zhang, S. Jiang, Ultralow fouling zwitterionic polymers grafted from surfaces covered with an initiator via an adhesive mussel mimetic linkage, *J. Phys. Chem. B* 112 (2008) 15269–15274.
- [7] G. Cheng, G. Li, H. Xue, S. Chen, J. Bryers, S. Jiang, Zwitterionic carboxybetaine polymer surfaces and their resistance to long-term biofilm formation, *Biomaterials* 30 (2009) 5234–5240.
- [8] C. Xu, X. Liu, B. Xie, C. Yao, W. Hu, Y. Li, X. Li, Preparation of PES ultrafiltration membranes with natural amino acids based zwitterionic antifouling surfaces, *Appl. Surf. Sci.* 385 (2016) 130–138.
- [9] P. Li, X. Cai, D. Wang, S. Chen, J. Yuan, L. Li, J. Shen, Hemocompatibility and anti-biofouling property improvement of poly (ethylene terephthalate) via self-polymerization of dopamine and covalent graft of zwitterionic cysteine, *Colloids Surf. B* 110 (2013) 327–332.
- [10] Y. He, J. Hower, S. Chen, M.T. Bernards, Y. Chang, Molecular simulation studies of protein interactions with zwitterionic phosphorylcholine self-assembled monolayers in the presence of water, *Langmuir* 24 (2008) 10358–10364.
- [11] Y. Lin, W. Huang, Y. You, Y. Lei, A. Zhang, The interactions between bovine serum albumin and carboxybetaine-functionalized polysiloxanes in solution, *Colloid Polym. Sci.* 12 (2016) 2029–2037.
- [12] J. Zhang, Y. Zhou, Z. Zhu, Z. Ge, S. Liu, Polyion complex micelles possessing thermoresponsive coronas and their covalent core stabilization via click chemistry, *Macromolecules* 41 (2008) 1444–1454.
- [13] J. Xu, S. Liu, Synthesis of well-defined 7-arm and 21-arm poly(*N*-isopropylacrylamide) star polymers with β -cyclodextrin cores via click chemistry and their thermal phase transition behavior in aqueous solution, *J. Polym. Sci. Part A Polym. Chem.* 47 (2009) 404–419.
- [14] L. Cheng, Q. Liu, Y. Lei, Y. Lin, A. Zhang, The synthesis and characterization of carboxybetaine functionalized polysiloxanes for the preparation of anti-fouling surfaces, *RSC Adv.* 4 (2014) 54372–54381.
- [15] S. Jiang, Z. Cao, Ultralow-fouling functionalizable and hydrolyzable zwitterionic materials and their derivatives for biological applications, *Adv. Mater.* 22 (2010) 920–932.
- [16] H. Yuan, B. Qian, W. Zhang, M. Lan, Protein adsorption resistance of PVP-modified polyurethane film prepared by surface-initiated atom transfer radical polymerization, *Appl. Surf. Sci.* 363 (2016) 483–489.
- [17] J. Kuang, P.B. Messersmith, Universal surface-initiated polymerization of antifouling zwitterionic brushes using a mussel-mimetic peptide initiator, *Langmuir* 28 (2012) 7258–7266.
- [18] Y. Chang, S. Chen, Z. Zhang, S. Jiang, Highly protein-resistant coatings from well-defined diblock copolymers containing sulfobetaines, *Langmuir* 22 (2006) 2222–2226.
- [19] N. Lin, H. Yang, Y. Chang, K. Tung, W. Chen, H. Cheng, S. Hsiao, P. Aimar, K. Yamamoto, J. Lai, Surface self-assembled PEGylation of fluoro-based PVDF membranes via hydrophobic-driven copolymer anchoring for ultra-stable biofouling resistance, *Langmuir* 29 (2013) 10183–10193.
- [20] Y. Zhu, H.S. Sundaram, S. Liu, L. Zhang, X. Xu, Q. Yu, J. Xu, S. Jiang, A robust graft-to strategy to form multifunctional and stealth zwitterionic polymer-coated mesoporous silica nanoparticles, *Biomacromolecules* 15 (2014) 1845–1851.
- [21] B. Wang, T. Jin, Y. Han, C. Shen, Q. Li, Q. Lin, H. Chen, Bio-inspired terpolymers containing dopamine cations and MPC: a versatile platform to construct a recycle antibacterial and antifouling surface, *J. Mater. Chem. B* 3 (2015) 5501–5510.
- [22] C. Huang, L. Wang, J. Shyue, Y. Chang, Developing antifouling biointerfaces based on bioinspired zwitterionic dopamine through pH-modulated assembly, *Langmuir* 30 (2014) 12638–12646.
- [23] J. Elle-Menye, C. Wimbish, P. Marek, K. Senecal, S. Jiang, One-step dip coating of zwitterionic sulfobetaine polymers on hydrophobic and hydrophilic surfaces, *ACS Appl. Mater. Interfaces* 6 (2014) 6664–6671.
- [24] P. Alexandridis, J.F. Holzwarth, T.A. Hatton, Micellization of poly(ethylene oxide)-poly(propylene oxide)-poly (ethylene oxide) triblock copolymers in aqueous solutions: thermodynamics of copolymer association, *Macromolecules* 27 (1994) 2414–2425.
- [25] M. Amiji, K. Park, Prevention of protein adsorption and platelet adhesion on surfaces by PEO/PPO/PEO triblock copolymers, *Biomaterials* 13 (1992) 682–692.
- [26] R.J. Green, S. Tasker, J. Davies, M.C. Davies, C.J. Roberts, S.J.B. Tendler, Adsorption of PEO-PPO-PEO triblock copolymers at the solid/liquid interface: a surface plasmon resonance study, *Langmuir* 13 (1997) 6510–6515.
- [27] K. Boxshall, M. Wu, Z. Cui, Z. Cui, J. Watts, M. Baker, Simple surface treatments to modify protein adsorption and cell attachment properties within a poly (dimethylsiloxane) micro-bioreactor, *Surf. Interface Anal.* 38 (2006) 198–201.
- [28] M. Rodahl, F. Höök, A. Krozer, P. Brzezinski, B. Kasemo, Quartz crystal microbalance setup for frequency and Q-factor measurements in gaseous and liquid environments, *Rev. Sci. Instrum.* 66 (1995) 3924–3930.
- [29] L. Daikhin, M. Urbakh, Influence of surface roughness on the quartz crystal microbalance response in a solution new configuration for QCM studies, *Faraday Discuss.* 107 (1997) 27–38.
- [30] G.Z. Sauerbrey, Use of quartz vibration for weighing thin films on a microbalance, *Z. Phys.* 155 (1959) 206–212.
- [31] M. Rodahl, F. Höök, C. Keller, A. Krozer, P. Brzezinski, M. Voinova, Simultaneous frequency and dissipation factor QCM measurements of biomolecular adsorption and cell adhesion, *Faraday Discuss.* 107 (1997) 229–246.



Synthesis and antimicrobial activities of acrylamide polymers containing quaternary ammonium salts on bacteria and phytopathogenic fungi



Anqiang Zhang^a, Qiongqiong Liu^a, Yufeng Lei^a, Shuanghao Hong^b, Yaling Lin^{b,*}

^a Department of Polymer Material Science and Engineering, College of Material Science and Engineering, South China University of Technology, 381 Wushan Rd., Guangzhou 510641, Guangdong, China

^b Department of Pharmaceutical Engineering, College of Natural Resource and Environment, South China Agriculture University, 483 Wushan Rd., Guangzhou 510642, Guangdong, China

ARTICLE INFO

Article history:

Received 4 November 2014

Received in revised form 10 February 2015

Accepted 18 February 2015

Available online 23 February 2015

Keywords:

Antibacterial activity

Polyacrylamide containing quaternary ammonium salts

Minimum inhibitory concentration

Phytopathogenic fungi

Hydrophobicity

ABSTRACT

Three series of acrylamide monomers/polymers containing quaternary ammonium salts (QASs), i.e., acrylamide QAS monomers (QDs), homopolymers of QDs (PQDs) and copolymers of QDs with acrylate monomer (PQDCs), were synthesized and employed in antimicrobial tests against both bacteria (*Escherichia coli* (*E. coli*) and *Staphylococcus albus* (*S. albus*)) and phytopathogenic fungi (*Rhizoctonia solani* (*R. solani*) and *Fusarium oxysporum* f. sp. *cubense* race 4 (*Foc4*)). The antibacterial activity of the QASs was evaluated by determining the minimum inhibitory concentration (MIC) against *E. coli* and *S. albus* by the TTC coloration method, and the antifungal activity was measured by mycelia growth inhibition as well as MIC and the minimum fungicidal concentration (MFC) values. The results indicated that PQD homopolymers and PQDC copolymers showed far better antimicrobial activities than QD monomers. PQDC copolymers by incorporating hydrophobic acrylate units into the main chain of polyacrylamide backbone displayed even better antimicrobial activities, depending on QAS structure and hydrophobic content. Moreover, polymers with benzyl group attached to nitrogen atom showed better inhibitory effect on bacteria and phytopathogenic fungi. The results could assist understanding and development of future design of antimicrobial polymers as potential fungicide agents to control plant disease.

© 2015 Elsevier B.V. All rights reserved.

1. Introduction

The development of synthetic antimicrobial agents is an emerging need due to antibiotic resistance of bacteria and fungi causing fatal infectious diseases or plant diseases. Quaternary ammonium salts (QASs) have long been the most widely used low molecular weight biocides. They have several advantages over other antibacterial agents, including excellent cell membrane penetration properties, low toxicity, good environmental stability, lack of skin irritation and extended residence time and biological activity [1,2]. Cationic polymers with quaternary ammonium groups (PQASs) exhibited higher antimicrobial activities than corresponding low molecular weight QASs [3]. The higher activity of polymeric QASs has been interpreted as follows: the net positive charge of polymeric QASs and the net negative charge of bacterial cell membranes drive the initial attraction of the polymeric QASs to the cell surface. After binding to the negatively charged phospholipid, hydrophobic moieties on the polymeric QASs interact

with the inner hydrophobic core of the bacterial membrane leading to a disruption of the cytoplasmic membrane to release potassium and other constituents which cause cell death [4].

A number of polymeric QASs have been prepared using conventional synthetic polymers including polystyrenes [5], polypyridines [6], and poly(meth)acrylates [7,8]. The polymer structures are often modified with cationic and hydrophobic side chains, which are statistically distributed in a polymer chain and thus display statistical amphiphilicity. Amphiphilicity is demonstrated an important factor impacting antimicrobial activities of polymeric QASs [9].

Amphiphilic polymeric QASs based on polymethacrylate derivatives were previously shown to display antimicrobial activity against bacteria and fungi [10–12]. The reasons polymethacrylates have been used as platforms to derive polymeric QASs to study antimicrobial activities are that structural parameters including mole fraction of hydrophobic repeat units and the identity of the side chain groups can be readily tuned. But few attentions have been paid on the polyacrylamide QASs. Moreover, polyacrylamide QASs contain amide rather than ester groups and are thus not sensitive towards hydrolysis reactions in common application

* Corresponding author.

E-mail address: linyaling@scau.edu.cn (Y. Lin).

conditions, and at the same time, hemocompatibility of polyacrylamide QASs with more hydrophilic backbone could be improved, while antimicrobial activities could also be tuned by side chain modification.

Although polymeric QASs have been demonstrated as effective antibacterial agents, activities against bacteria do not ensure activities against phytopathogenic fungi. However with reports of antifungal activity of chitosan (a polycationic polymer of glucosamine) [13–15] and polymers containing QAS [16,17], we assume that polymeric QASs might also be effective in reducing fungal growth, thus in this article we apply polymeric QASs in inhibition of pathogen fungi, rice sheath blight pathogen (*Rhizoctonia solani*, *R. solani*) and banana fusarium wilt (*Fusarium oxysporum* f. sp. *cubense* race 4, *Foc4*), two common phytopathogenic fungi causing plant disease which bring loss of yield or quality. *R. solani* is pathogen fungus causing rice sheath blight which is one of the most destructive rice diseases worldwide and severely impairs both rice quality and yield, and *Foc4*, a soilborne fungal pathogen, is the causal agent of vascular wilt disease called Panama disease.

To this end, in this paper, we utilize acrylamide derivatives to prepare a series of acrylamide QASs (including monomers (QDs), homopolymers (PQDs) as well as copolymers (PQDCs) of QDs with acrylate monomers), and systematically investigated the structure and antibacterial (Gram-positive bacteria *Staphylococcus albus* and Gram-negative bacteria *Escherichia coli*) as well as antifungal (*R. solani* and *Foc4*) properties of the acrylamide QASs.

2. Experimental

2.1. Materials

N,N-dimethylamine propyl methacrylamide (DMPMA), *n*-butyl bromide (BB, >98%), 1-hexyl bromide (HEB, 99%), benzyl chloride (BC, 99%) and 2,3,5-triphenyltetrazolium chloride (TTC, >95%), butyl acrylate (BA, 99%), 2,2'-azobis(2-methylpropionitrile) (AIBN, 98%), ethyl methacrylate (EMA, 99%), hydroquinone (99%), ammonium persulfate (APS, 99%) and hexadecyl trimethyl ammonium bromide (CTAB, 99%) were supplied by Aladdin Reagent Co. Ltd. (Shanghai, China). Beef extract was supplied by Sinopharm Chemical Reagent Co. Ltd. (Shanghai, China). Peptone was supplied by Guangdong Ring Kay Microbial Technology Co. Ltd. (Guangzhou, China). Agar was supplied by MYM Biological Technology Company (Shanghai, China). RPMI-1640 liquid medium was supplied by Hyclone Company of America (Utah, USA). *Escherichia coli* (*E. coli*) ATCC 25922, *Staphylococcus albus* (*S. albus*) ATCC 12228, *Rhizoctonia solani* (*R. solani*) and *F. oxysporum* f. sp. *cubense* race 4 (*Foc4*) were kindly supplied by the Fungus Laboratory, Department of Plant Pathology, South China Agricultural University.

2.2. Characterization

FT-IR spectra were performed with a VERTEX spectrometer (Bruker Instrument Corp., Germany) using KBr pellets. ¹H NMR spectra were obtained using an AV-400 FT NMR (Bruker Instrument Corp., Germany) and D₂O or CDCl₃ as a solvent. The molecular weight of polymers was measured using Ubbelohde capillary viscometer. (A detailed description can be found in the Supporting Information: Part S-3).

2.3. Synthesis procedures

Acrylamide QAS monomers, i.e., the QDs monomers, including QD-BB, QD-HEB and QD-BC (as shown in Scheme 1), were synthesized by the quaternization reaction of DMAPMA with halogenated

reagents, including *n*-butyl bromide (BB), 1-hexyl bromide (HEB) and benzyl chloride (BC). (¹H NMR spectra of QD-BB, QD-HEB and QD-BC could be found in the Supporting Information, Part S-1).

2.3.1. Synthesis of (2-methacrylamido) propyltetra n -butyldimethylammonium bromide (QD-BB)

DMAPMA (20.0 g, 0.12 mol), BB (16.1 g, 0.12 mol), hydroquinone (0.1 g, 0.5 wt% of DMAPMA, polymerization inhibitors) and anhydrous acetone (60 mL) were added into a round-bottom flask, and stirred under a nitrogen atmosphere for 30 h at 60 °C. Then, the mixture was cooled to 4 °C for 12 h, and the precipitate was collected, washed with cold anhydrous acetone and dried under vacuum at 60 °C (89.6% yield). The product was denoted as QD-BB. ¹H NMR spectra data (400 MHz, D₂O, δ , ppm): 0.91 (s, —CH₃), 1.35(m, —CH₂—CH₃), 1.68 (t, —CH₂—CH₂—CH₃), 1.91 (s, CH₂=C(CH₃)), 2.00 (m, CH₂—CH₂—CH₂), 3.03 (s, N⁺(CH₃)₂), 3.28–3.34 (m, NH—CH₂, —CH₂—N⁺—CH₂), 5.46, 5.69 (d, CH₂=C(CH₃)). FT-IR spectra data (ν , cm^{−1}): 3080 (ν =C—H), 1661 (ν =O amide), 1617 (ν =C), 1217 (ν =N).

2.3.2. Synthesis of (2-methacrylamido) propyltetra n -hexyldimethylammonium bromide (QD-HEB)

DMAPMA (20.6 g, 0.12 mol), HEB (20.0 g, 0.12 mol) and anhydrous acetone (60 mL) were added into a round-bottom flask, and stirred under a nitrogen atmosphere for 30 h at 60 °C. Then, the mixture was cooled to 4 °C for 12 h, and the precipitate was collected, washed with cold anhydrous acetone and dried under vacuum at 60 °C (73.9% yield). The product was denoted as QD-HEB. ¹H NMR spectra data (400 MHz, D₂O, δ , ppm): 0.80 (s, —CH₃), 1.26 (m, —CH₂—(CH₂)₃—CH₃), 1.64 (m, N⁺—CH₂—CH₂), 1.87 (s, CH₂=C(CH₃)), 1.95 (m, CH₂—CH₂—CH₂), 3.00 (s, N⁺(CH₃)₂), 3.22–3.30 (m, NH—CH₂, —CH₂—N⁺—CH₂), 5.42, 5.66 (d, CH₂=C(CH₃)). FT-IR spectra data (ν , cm^{−1}): 3080 (ν =C—H), 1656 (ν =O amide), 1615 (ν =C), 1217 (ν =N).

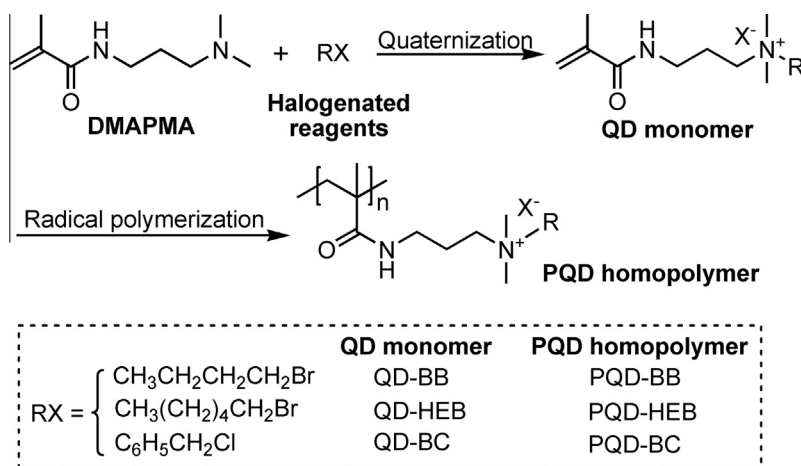
2.3.3. Synthesis of (2-methacrylamido) propyltetra n -benzyldimethylammonium chloride (QD-BC)

DMAPMA (26.9 g, 0.16 mol), BC (20.0 g, 0.16 mol) and dichloromethane (65 mL) were added into a round-bottom flask, and stirred under a nitrogen atmosphere for 24 h at 40 °C. Then, the mixture was concentrated by rotary evaporation and precipitated in cold anhydrous diethyl ether, and the precipitate was collected, washed with cold dichloromethane, following by drying under vacuum at 40 °C overnight (81.1% yield). The product was denoted as QD-BC. ¹H NMR spectra data (400 MHz, D₂O, δ , ppm): 1.85 (s, —CH₃), 2.00 (m, CH₂—CH₂—CH₂), 3.00 (s, N⁺(CH₃)₂), 3.21 (m, NH—CH₂), 3.32 (s, CH₂—N⁺), 4.45 (s, CH₂—Ph), 5.43, 5.64 (d, CH₂=C(CH₃)), 7.47 (m, Ph—H). FT-IR spectra data (ν , cm^{−1}): 1616 (ν =C), 1661 (ν =O amide), 1213 (ν =N), 704, 734 (γ _{Ph—H}).

2.3.4. Synthesis of acrylamide QAS homopolymers (PQDs homopolymers)

Acrylamide QAS homopolymers (PQDs, including PQD-BB, PQD-HEB and PQD-BC) were carried out by radical polymerization (as shown in Scheme 1).

A typical procedure was briefly stated as follows: the polymerizations were carried out in a three-necked flask with a condenser, a magnetic stirrer and a nitrogen inlet. QD-BB (20.0 g, 65.09 mmol) solution of 50 wt% in distilled water (20 mL) was purged with nitrogen for 30 min. The polymerization was then performed at 50 °C for 30 h under nitrogen using 1.5 wt% APS (0.3 g, 3.0 mmol) as an initiator. After that, the mixture was condensed and poured into a large amount of acetone to precipitate the homopolymers. The sticky homopolymers were separated and then dried under vacuum at 70 °C for 24 h. The product was denoted as PQD-BB. Similar methods were applied for preparation of PQD-HEB and



Scheme 1. Synthesis routine of QD monomers and PQD homopolymers.

PQD-BC homopolymers, using methanol as solvents and AIBN as initiators and under 70 °C. The yields of PQD-BB, PQD-HEB and PQD-BC were 71.4%, 65.5%, 77.2%, respectively. (¹H NMR spectra of PQDs homopolymers could be found in the [Supporting Information, Part S-1.](#))

PQD-BB: ¹H NMR spectra data (400 MHz, D₂O, δ, ppm): 0.98–1.11 (bm, CH₂–C(CH₃), –CH₃), 1.39 (bs, –CH₂–CH₃), 1.75 (bs, –CH₂–CH₂–CH₃), 2.00 (bs, CH₂–C(CH₃), CH₂–CH₂–CH₂), 3.08 (bs, N⁺(CH₃)₂), 3.19–3.32 (bm, NH–CH₂, –CH₂–N⁺–CH₂). FT-IR spectra data (ν, cm^{–1}): 1659 (ν_{C=O} amide), 1217 (ν_{C–N}).

PQD-HEB: ¹H NMR spectra data (400 MHz, D₂O, δ, ppm): 0.89–1.10 (bm, CH₂–C(CH₃), –CH₃), 1.35 (bs, –CH₂–(CH₂)₃–CH₃), 1.76 (bs, N⁺–CH₂–CH₂), 2.00 (bs, CH₂–C(CH₃), CH₂–CH₂–CH₂), 3.08–3.32 (bs, N⁺(CH₃)₂, NH–CH₂, –CH₂–N⁺–CH₂). FT-IR spectra data (ν, cm^{–1}): 1656 (ν_{C=O} amide), 1215 (ν_{C–N}).

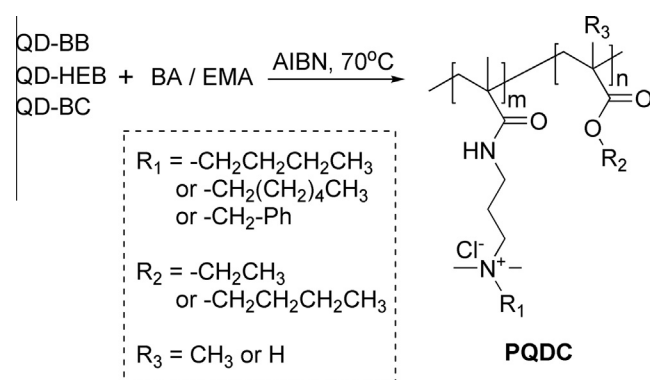
PQD-BC: ¹H NMR spectra data (400 MHz, D₂O, δ, ppm): 0.97 (bm, CH₂–C(CH₃)), 1.69–1.99 (bm, CH₂–C(CH₃)), 2.90–3.03 (bm, CH₂–CH₂–CH₂–N⁺–CH₂(CH₃)₂), 4.33 (CH₂–Ph), 7.50 (bs, Ph–H). FT-IR spectra data (ν, cm^{–1}): 1661 (ν_{C=O} amide), 1213 (ν_{C–N}), 704, 734 (γ_{Ph–H}).

2.3.5. Synthesis of acrylamide QAS copolymers (PQDCs copolymers)

Copolymers PQDCs were conducted by copolymerization of QDs monomers with acrylate monomers (BA or EMA) by radical copolymerization presented in [Scheme 2](#).

A typical procedure was briefly stated as follows: first, anhydrous methanol (2 mL) was charged into a three-necked flask with a condenser, a magnetic stirrer and a nitrogen inlet, then heated to 70 °C under nitrogen atmosphere, and QD-BB (14.38 g, 0.0468 mol) and BA (2.0 g, 0.016 mol) dissolved in anhydrous methanol (25 mL) containing 1.5 wt% AIBN (0.16 mg, 0.97 mmol) was dripped via the dropping funnel, and the reaction temperature was maintained at 70 °C for 30 h. After that, the mixture was condensed and added into acetone to precipitate the copolymers. The sticky copolymers were collected and then dried under vacuum at 70 °C for 24 h. The product was denoted as PQDC1. The other PQDC were synthesized by identical procedure as above. [Table 1](#) illustrates the compositions of PQDCs copolymers. ¹H NMR analysis provided determination of the mole percentage of acrylate units, *f*_{alkyl}, of the copolymers. (¹H NMR spectra of PQDCs copolymers could be found in the [Supporting Information, Part S-2.](#))

PQDC1: ¹H NMR spectra data (400 MHz, D₂O, δ, ppm): 3.05 (bs, N⁺(CH₃)₂), 3.29 (bs, NH–CH₂, –CH₂–N⁺–CH₂), 4.04 (bm, –CO–O–CH₂–). FT-IR spectra data (ν, cm^{–1}): 1725 (ν_{C=O} ester), 1647 (ν_{C=O} amide), 1203 (ν_{C–N}).



Scheme 2. Synthesis routine of PQDC copolymers.

Table 1
Composition of the synthesized PQDC.

Samples	M ₁	M ₂	Feeding ratio [M ₁]/[M ₂] (mol/mol)	Calculated composition [M ₁]/[M ₂] (mol/mol) ^a	<i>f</i> _{alkyl} ^b (mol%)	Yield (%)
PQDC1	QD-BB	BA	3/1	2.78/1	26.5	64.8
PQDC2	QD-BB	EMA	3/1	2.88/1	25.8	75.8
PQDC3	QD-BC	BA	3/1	2.83/1	26.1	77.4
PQDC4	QD-BC	EMA	3/1	2.76/1	26.6	82.0
PQDC5	QD-HEB	BA	3/1	2.73/1	26.8	45.6
PQDC6	QD-HEB	EMA	3/1	3.04/1	24.8	53.4
PQDC7	QD-BC	BA	0.5/1	0.53/1	65.4	23.4
PQDC8	QD-BC	BA	1/1	0.96/1	51.0	72.3
PQDC9	QD-BC	BA	2/1	1.99/1	33.4	48.1

^a [M₁]/[M₂] was calculated from the ¹H NMR results.

^b *f*_{alkyl} = [M₂]/([M₁] + [M₂]), based on the calculating results from ¹H NMR.

PQDC2: ¹H NMR spectra data (400 MHz, D₂O, δ, ppm): 3.07 (bs, N⁺(CH₃)₂), 3.30 (bs, NH–CH₂, –CH₂–N⁺–CH₂), 4.07 (bm, –CO–O–CH₂–). FT-IR spectra data (ν, cm^{–1}): 1725 (ν_{C=O} ester), 1647 (ν_{C=O} amide), 1203 (ν_{C–N}).

PQDC3, PQDC7, PQDC8 and PQDC9: ¹H NMR spectra data (400 MHz, D₂O, δ, ppm): 2.93 (bs, N⁺(CH₃)₂), 3.14 (bs, NH–CH₂, –CH₂–N⁺–CH₂), 3.88 (bm, CO–O–CH₂–), 4.39 (CH₂–Ph). FT-IR spectra data (ν, cm^{–1}): 1725 (ν_{C=O} ester), 1641 (ν_{C=O} amide), 1190 (ν_{C–N}), 704–775 (γ_{Ph–H}).

PQDC4: ^1H NMR spectra data (400 MHz, D_2O , δ , ppm): 2.91 (bs, $\text{N}^+(\text{CH}_3)_2$), 3.11 (bs, $\text{NH}-\text{CH}_2$, $-\text{CH}_2-\text{N}^+-\text{CH}_2$), 3.96 (bm, $\text{CO}-\text{O}-\text{CH}_2-$), 4.37 (CH_2-Ph). FT-IR spectra data (ν , cm^{-1}): 1725 ($\nu_{\text{C=O}}$ ester), 1641 ($\nu_{\text{C=O}}$ amide), 1190 ($\nu_{\text{C-N}}$), 704–775 ($\gamma_{\text{Ph-H}}$).

PQDC5: ^1H NMR spectra data (400 MHz, D_2O , δ , ppm): 3.04 (bs, $\text{N}^+(\text{CH}_3)_2$), 3.27 (bs, $\text{NH}-\text{CH}_2$, $-\text{CH}_2-\text{N}^+-\text{CH}_2$), 4.04 (bm, $-\text{CO}-\text{O}-\text{CH}_2-$). FT-IR spectra data (ν , cm^{-1}): 1726 ($\nu_{\text{C=O}}$ ester), 1648 ($\nu_{\text{C=O}}$ amide), 1204 ($\nu_{\text{C-N}}$).

PQDC6: ^1H NMR spectra data (400 MHz, D_2O , δ , ppm): 3.05 (bs, $\text{N}^+(\text{CH}_3)_2$), 3.28 (bs, $\text{NH}-\text{CH}_2$, $-\text{CH}_2-\text{N}^+-\text{CH}_2$), 4.05 (bm, $-\text{CO}-\text{O}-\text{CH}_2-$). FT-IR spectra data (ν , cm^{-1}): 1726 ($\nu_{\text{C=O}}$ ester), 1648 ($\nu_{\text{C=O}}$ amide), 1204 ($\nu_{\text{C-N}}$).

2.4. Antimicrobial assessment

2.4.1. Test microorganisms and media

The microorganisms included the Gram-positive bacteria *S. albus* and the Gram-negative bacteria *E. coli*. The phytopathogenic fungi associated with plant diseases included the rice sheath blight pathogen (*R. solani*) and the banana fusarium wilt (*Foc4*).

Beef extract peptone medium was used as the growth medium for the tested bacteria and was prepared as follows: 3.0 g of beef extract, 10.0 g of tryptone, and 5.0 g of NaCl were added into 1000 mL of distilled water and heated to dissolve, and the solution's pH was adjusted to 7.0. To the solution, 15–20 g of agar powder was added to obtain solid medium. Then, the medium was sterilized by autoclaving (HVE-50, Japan Hirayama Corporation) at 121 °C for 20 min and cooled down.

Potato dextrose agar (PDA) was used as the growth medium for the tested fungi, and the PDA was prepared as follows: 200 g of sliced potato was boiled in water for 30 min, and the liquid was then strained through a cheese-cloth. Distilled water was added to adjust the total volume of suspension to 1000 mL, and then 20 g of dextrose and 15–20 g of agar powder were added. Finally, the medium was transferred to a flask, sealed, sterilized by autoclaving at 121 °C for 30 min and cooled down.

RPMI-1640 liquid medium was obtained by buffering RPMI-1640 (with L-glutamine and without bicarbonate) with 10 mol/L NaOH to pH 7.0; the medium was sterilized by filtering with a 0.22- μm membrane.

2.4.2. Determination of minimum inhibitory concentration (MIC) against bacteria

The antibacterial properties of acrylamide QASs against *E. coli* and *S. albus* were evaluated by the TTC coloration method [18], and hexadecyl trimethyl ammonium bromide (CTAB), a commercial available and broad spectrum fungicide, was chosen as the standard for comparison. A log phase bacterial suspension was diluted in beef extract peptone broth to obtain a concentration of 10^6 – 10^7 CFU/mL. The tested concentrations of sample solutions were deposited in triplicate, in a volume of 150 μL in the wells of a sterile 96-well plate. Then 75 μL of bacterial suspension was added to each well and the mixtures were incubated at 37 °C for 16–18 h. Then 75 μL 0.02 wt% of 2,3,5-triphenyl tetrazolium chloride (TTC) was added and the contents of each well were mixed by vortex shaking prior to incubation in the dark at 37 °C for 2–4 h. A control was 75 μL 0.02 wt% TTC with 225 μL medium. The MIC was the lowest concentration at which there was no visible growth, i.e., there was no red color due to the reduction of TTC.

2.4.3. Determination of mycelia growth inhibition (MGI)

The antifungal activities of the samples were tested by the inhibition of mycelial growth. To prepare solutions of different concentrations, the samples were dissolved in sterilized water, mixed with PDA and poured onto sterile Petri dishes (with diameter of 9 cm). Control plates consisted of PDA only. A 5-mm disc

containing mycelia was transferred to the center of the PDA plate containing the samples and incubated at 28 °C. Sterilized water was used as a negative control. Each experiment was conducted in three replicates. The diameter of fungal colonies was measured three times and averaged. Growth inhibition was calculated according to Formula (1).

$$\text{MGI} = (R_C - R_T) / R_T \times 100\% \quad (1)$$

whereby R_C and R_T were the radial growth of fungi in the control plate and the treatment plate, respectively, and the radial growth was calculated according to Formula (2).

$$\text{Radial growth (mm)} = \text{Average diameter of fungi colony (mm)} - 5 \text{ mm} \quad (2)$$

2.4.4. Determination of minimum inhibitory concentration (MIC) and minimum fungicidal concentration (MFC) values against phytopathogenic fungi

Foc4 was chosen as the tested microorganism to determine the MIC and MFC values of the samples. *Foc4* microorganisms were incubated at 28 °C for 7 days in PDA medium; the fungal suspension was prepared by adding 1 mL of 0.85% saline containing 0.01 mL of Tween 20 to the incubated colony. Then, the upper homogeneous liquid was transferred to a sterilized tube and diluted with RPMI-1640 liquid medium to give inoculation suspensions of 0.4×10^4 – 5×10^5 CFU/mL with twice the final concentration. The broth micro-dilution method was used to determine the MIC of the samples. The samples were dissolved in water and diluted in RPMI-1640 medium. The sample solution (100 μL) with concentrations ranging from 5×10^{-5} –3 mg/mL was added into 96-well plates. The same volume of mycelial suspension containing approximately 0.4×10^4 – 5×10^5 CFU/mL was incubated at 28 °C for 46–50 h. In addition, a reference liquid medium without samples was used as a negative control. MIC was measured at least three times and recorded as the lowest concentration that completely inhibited visible growth [19].

The MFC test was the most common estimation of fungicidal activity and was defined as the lowest concentration of antimicrobial agent needed to kill 99.9% of the initial inoculums after incubation [20]. To determine the MFC, 100 μL from each of the wells at or above the MIC was plated on PDA and incubated at 28 °C for 48 h. The MFC was defined as the lowest concentration at which no colonies were detected on the PDA.

2.5. Direct toxicity evaluation

A simple and straightforward assay was used to evaluate the direct toxicity of PQDs to plants, in which rice (*Oryza sativa* L.) was chosen as the testing plant, and PQD-BC water solution (0.2 wt%) was sprayed on the leave of the rice every 24 h, with distilled water as the control. (A detailed description and the results can be found in the [Supporting Information: Part S-5.](#))

3. Results and discussions

3.1. Design and synthesis of acrylamide QASs

By designing and synthesizing acrylamide QASs, we examined the relationship between chemical structure of QASs and their antimicrobial activities to gain insight into the role of QAS structure and hydrophobicity in the action of these antimicrobials.

DMAEMA was chosen due to its hydrophobic dimethyl- and diethyl amino groups, respectively. Compared with polyacrylate QASs, polyacrylamide QASs contained amide rather than ester groups, which would possess better biocompatibility and stability [21,22]. Meanwhile, DMAEMA based QASs monomers endowed polymers with systematic variations of compositions, facilitating

the study of the effect of QAS structure and hydrophobicity on antimicrobial efficiency in polyacrylamide QASs.

To this end, a series of acrylamide QAS monomers (QDs) and homopolymers (PQDs) were synthesized. Moreover, it is demonstrated that in addition to electrostatic attraction, hydrophobic functionality is required to realize antimicrobial activity. While ionic bonding facilitates initial polymer-cell interactions, it is the hydrophobic substituents that act to disrupt the lipid membrane of bacteria. Thus acrylate monomers, butyl acrylate (BA) and ethyl methacrylate (EMA), were chosen as hydrophobic unit to endow polymers with tunable hydrophobicity to obtain the copolymers (PQDCs). A total of 9 copolymers were synthesized using identical polymerization conditions with varying monomer type and monomer feed ratio (see Table 1). In which, methanol was chosen as the solvent of the copolymerization of acrylamide and acrylate for the reason that both BA and EMA are almost insoluble in water and soluble in methanol, and the copolymers (PQDCs) are also soluble well in methanol, and it is found that influence of methanol on the molecular weight of the copolymers could be ignored. (As shown in the Supporting Information: Part S-3.)

Three series of QASs, i.e., acrylamide QAS monomers (QDs, including QD-BB, QD-HEB, and QD-BC), homopolymers of QD (PQDs, including PQD-BB, PQD-HEB, and PQD-BC) and copolymers of QD with acrylate monomer (PQDCs, including PQDC1–PQDC9), were synthesized in laboratory, according to Schemes 1 and 2, and characterized by FTIR, ^1H NMR, and the molecular weight were measured using Ubbelohde capillary viscometer, as detailed in the Supporting Information (Parts S-1–S-3). The spectra of the products were in complete agreement with the expected structures and showed essentially no contaminants, and the final composition of the copolymers were similar to the feeding ratio of the monomers (as shown in Table 1), so the copolymerization between the QDs and acrylate monomers could be considered as statistical copolymerization.

3.2. Antibacterial activities of acrylamide QASs

The screening of acrylamide QASs for antibacterial activity was done by using *S. albus* and *E. coli* as test organisms because they represented Gram-positive and Gram-negative bacteria, respectively.

The MIC of acrylamide QASs was determined using TTC coloration method and defined as the lowest concentration able to inhibit visible microbial growth. TTC is a redox indicator used to differentiate between metabolically active and inactive cells; the colorless compound is enzymatically reduced to red TPF (1,3,5-triphenylformazan) which is stable and cannot be oxidized in the air in living cells due to the activity of various dehydrogenases. When the number of active cells is low, TTC cannot be reduced and the solution is colorless, so it is often used as chromogenic agent testing whether there are viable bacteria [21,22]. In this section, first 75 μL of each bacterial suspension in suitable growth medium was added to the wells of a sterile 96-well plate already containing 150 μL of two-fold serially diluted sample solution. After incubation at 37 $^\circ\text{C}$ for 16 h, 0.02 wt% TTC was added and after incubated at 37 $^\circ\text{C}$ for 2–4 h, MIC was determined as the lowest concentration at which there was no red color.¹ Fig. 1 is a typical photograph for the determination of MIC for QD-BC and PQD-BC, in which the MIC of QD-BC and PQD-BC should be 8000 $\mu\text{g}/\text{mL}$ and 750 $\mu\text{g}/\text{mL}$, respectively. The photographs for the determination of MIC for acrylamide QASs (including monomers, homopolymers, and copolymers) and CTAB by TTC coloration method against *E. coli* and *S. albus* were shown in Fig. S8 (Supporting Information, Part S-4),

and the MIC values for QDs, PQDs and PQDCs against *E. coli* and *S. albus* are summarized in Fig. 2.

As shown in Fig. 2, for monomers (QD-BB, QD-HEB and QD-BC) and their homopolymers (PQD-BB, PQD-HEB and PQD-BC), MIC values of homopolymers were far lower than that of monomers against both *S. albus* and *E. coli*, which meant the activity of the polymers was much higher than that of the corresponding monomers. For instance, the MIC of QD-BB against *E. coli* was 9000 $\mu\text{g}/\text{mL}$, whereas that of PQD-BB was as low as 1500 $\mu\text{g}/\text{mL}$ and the MIC against *S. albus* was much lower for PQD-BB (250 $\mu\text{g}/\text{mL}$), although that for QD-BB remained as high as 7500 $\mu\text{g}/\text{mL}$. It was reasonable to assume that going from monomer to polymer could increase local charge density, thus the adsorption to bacterial cell surfaces was enhanced for polymer compared to monomer and binding to the cytoplasmic membrane was also facilitated by polymer because of the presence of more negatively charged species in the membrane. Finally, the disruption of bacteria membrane and subsequent leakage of K^+ and other cytoplasmic constituents would be also reinforced by the polymer. The results were in good agreements with published literatures [1,3]. At the same time, when halogenated reagents were BC or HEB, the MIC values of corresponding polymers were lower, indicating better antibacterial activities, although the MIC of the polymers are higher than that of the reference (CTAB).

PQDC1 and PQDC2 were the statistical copolymers of QD-BB and butyl acrylate (BA) or ethyl methacrylate (EMA) with a molar ratio of 3/1 respectively, and the MIC values of PQDC1 and PQDC2 against *E. coli* were 400 $\mu\text{g}/\text{mL}$ and 700 $\mu\text{g}/\text{mL}$ respectively, while for PQD-BB the MIC was 1500 $\mu\text{g}/\text{mL}$, which indicated that copolymerizing QD-BB with hydrophobic units (BA or EMA) could strengthen antibacterial activities of polyacrylamide QASs. Similarly, by comparing MIC values of two series (PQD-BB, PQDC1, and PQDC2; PQD-BC, PQDC3, and PQDC4) against *E. coli* and *S. albus*, we found that antibacterial activities could be maintained or enhanced by incorporating acrylate units. It is noticed that when the structure of polymers is more similar to amphiphilic cell membrane structure, polymers could better interact with cells, thus the antimicrobial activity of the copolymers depended critically on their hydrophobic content and polymer length [12]. Incorporating BA or EMA units into PQD-BB or PQD-BC could enhance the lipophilicity and tune hydrophilic–hydrophobic activity of polymers, thus the obtained polymers with structure more similar to amphiphilic cell membrane structure could better interact with bacteria cells.

It is noticed that PQDC3, PQDC7, PQDC8 and PQDC9 with different hydrophobic content (f_{alkyl}) were obtained by copolymerization of QD-BC with BA in different molar ratio. The MIC values against *S. albus* in this series decreased to reach a minimum of 31 $\mu\text{g}/\text{mL}$ at $f_{\text{alkyl}} = 33 \text{ mol}\%$ (PQDC9) and then increased as f_{alkyl} was further increased. Besides, the MIC values of PQDC against *E. coli* did not change with f_{alkyl} . The increased hydrophobicity of the PQDC copolymer seemed to be responsible for an enhancement of antimicrobial activity with increasing f_{alkyl} in the range of 26 mol% to 33 mol%, possibly by enhancing membrane binding and permeabilization. However, excessive hydrophobicity of polymer in the high f_{alkyl} range might cause aggregation, reducing the number of polymers available to interact with the bacterial cells. Also, increasing f_{alkyl} required decreasing the number of cationic charges. This would mitigate the electrostatic attraction to bacterial cell membranes [21,23]. A combination of these factors might be responsible for the observation that the MIC values went through a local minimum when f_{alkyl} was beyond 26 mol%.

This speculation could also be verified by the MIC values of PQD-HEB, PQDC5 and PQDC6 (see Fig. 2), in which PQDC5 and PQDC6 was copolymers of QD-HEB with BA or EMA respectively. Hydrophobicity was an important factor in the antimicrobial

¹ For interpretation of color in Fig. 1 the reader is referred to the web version of this article.

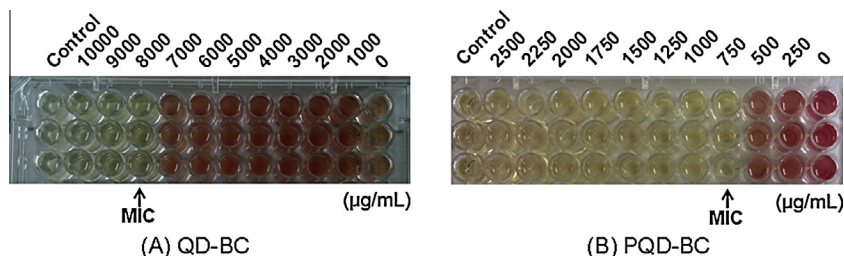


Fig. 1. Photograph of the determination of MIC value for PQD-BB against *E. coli*.

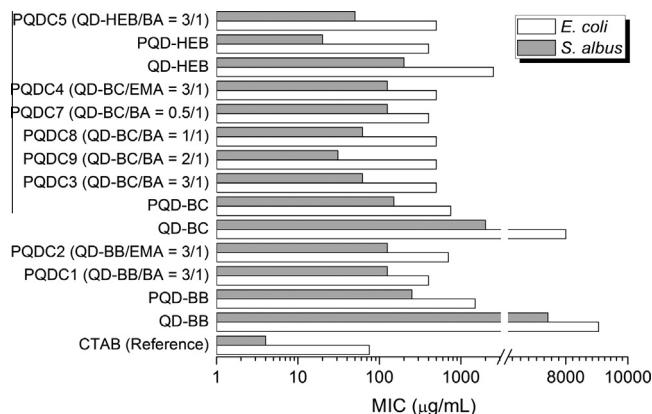


Fig. 2. MIC values of acrylamide QASs against *E. coli* and *S. albus*.

activity of polymeric biocides, since hexyl group attached to nitrogen atom in PQD-HEB was sufficiently hydrophobic for polymer containing QAS group to gain substantial antimicrobial activity, incorporating more hydrophobicity (BA or EMA) units in PQDC5 and PQDC6 hardly improved but weakened the antibacterial activities. This also supported the notion that, although as the polymers became more hydrophobic, incorporation of polymers to lipid membranes was enhanced, and thus the integrity of membrane was more efficiently disrupted, excess hydrophobic units could limit antibacterial activity of polymers due to aggregation [23].

Besides, in Fig. 2, variation in activity based on bacterial species was expected considering the MIC values for tested polymers against Gram-positive bacteria *S. albus* were all lower than that of Gram-negative bacteria *E. coli*, so polyacrylamide QASs were

more sensitive to *S. albus* than *E. coli*. This could be explained by the general differences in the cell wall of Gram-positive and Gram-negative bacteria. The cell wall of Gram-positive bacteria tended to be loose, mainly consisting of peptidoglycan and typically lacking an outer membrane, while the cell wall of Gram-negative bacteria consisted of two membranes with the inner membrane being based on phospholipids and the outer membrane consisting of lipopolysaccharides. QASs were typically more potent against Gram-positive bacteria and were less active against Gram-negative bacteria [3,24].

3.3. Antifungal activities of acrylamide QASs

The antifungal activity of QD-BB, QD-BC and their homopolymers were concurrently evaluated on two phytopathogenic fungi, *R. solani* and *Foc4*. Photographs displaying effect of acrylamide QASs on *R. solani* and *Foc4* by the toxic medium culture method were shown in Figs. 3 and 4. Mycelial growth inhibition of QD-BB, QD-BC and their homopolymers against *R. solani* and *Foc4* were summarized in Figs. 5 and 6, respectively. Tables 2 and 3 illustrate the values of MIC and MFC of acrylamide QASs against *Foc4*.

Figs. 3–6 show that PQD-BB, PQD-BC and PQD-HEB exhibited higher inhibitions than their correspondent monomers, QD-BB, QD-BC and QD-HEB, against both selected strains.

The addition of PQD-BB, PQD-BC and PQD-HEB to the PDA medium inhibited mycelia growth of selected fungi significantly at all concentrations tested and this inhibition was concentration dependent. While at the same concentration, QD-BB, QD-BC and QD-HEB monomers exhibited non-significant antifungal activities. Moreover, it is noticed that in which PQD-BC showed the highest

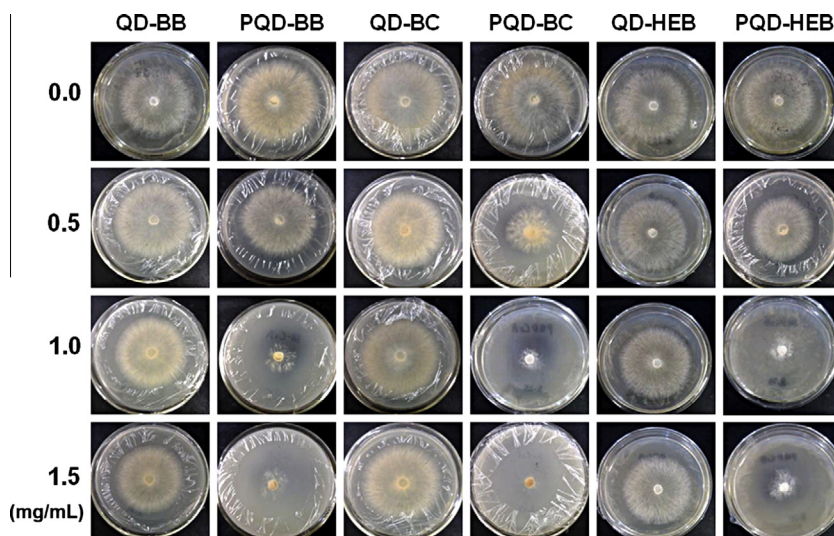


Fig. 3. Photograph displaying antifungal effects of acrylamide QASs on *R. solani*.

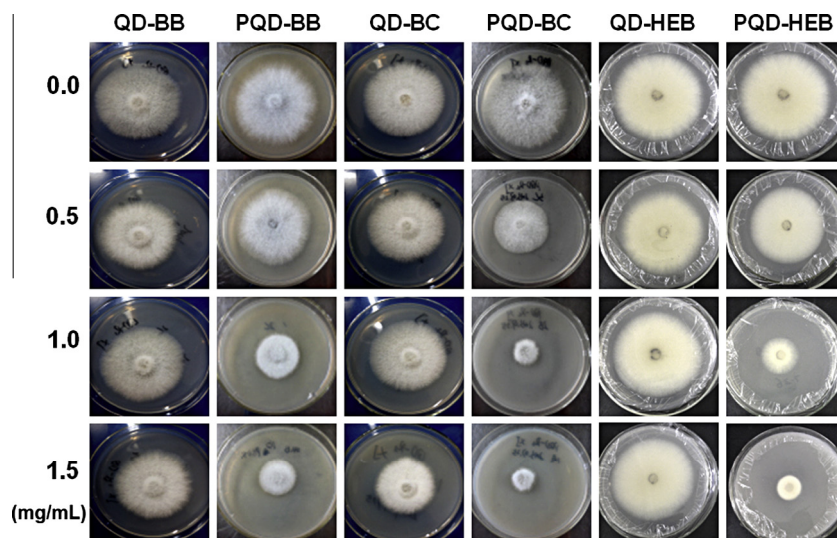


Fig. 4. Photograph displaying antifungal effects of acrylamide QASs on *Foc4*.

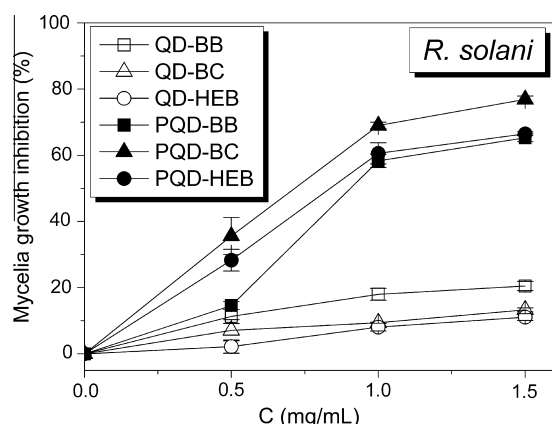


Fig. 5. Mycelial growth inhibition of QDs and PQDs against *R. solani* after incubated for 5 days.

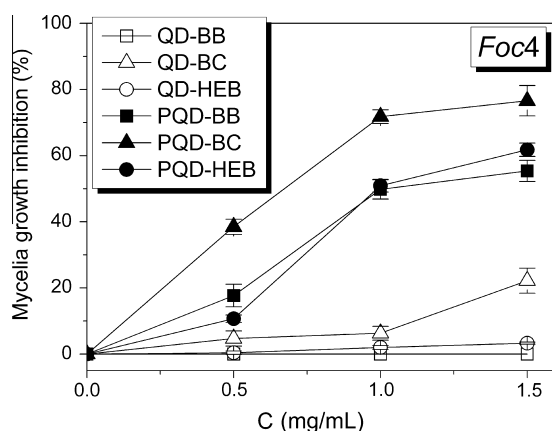


Fig. 6. Mycelial growth inhibition of QDs and PQDs against *Foc4* after incubated for 5 days.

inhibition on the mycelial growth of both *R. solani* and *Foc4*, which mean the introduction of benzyl group into the structure of QAS increased the antifungal activities (Figs. 3–6) of polymer compared with that of butyl group or hexyl group. Although the MIC values of

Table 2

MIC and MFC values of acrylamide QAS monomers and homopolymers against *Foc4*.

	QD-BB	PQD-BB	QD-BC	PQD-BC	QD-HEB	PQD-HEB
MIC ($\mu\text{g/mL}$)	— ^a	5	250	1	— ^a	1
MFC ($\mu\text{g/mL}$)	— ^a	5	250	1	— ^a	1
MFC/MIC	—	1	1	1	—	1

^a “—” meant MIC and MFC values could not be determined due to much higher values than the maximum concentration tested (3000 $\mu\text{g/mL}$).

PQD-HEB was lower than that of PQD-BC (as shown in Fig. 2), this might be explained by the enhanced hydrophobicity of polymers by attaching hexyl group to nitrogen atom in PQD-HEB. So from the whole results, we concluded in general that polymers with benzyl groups in QAS structures displayed better antimicrobial activities and PQD-HEB could be considered as an exception.

Based on the above results, the inhibitory effects of acrylamide QASs against *Foc4* were further estimated by the broth micro-dilution method. MIC was the minimum concentration that could completely inhibited fungi growth, MFC was the minimum concentration at which 99.9% of the fungi could be killed. The ratio of MFC/MIC reflected the fungicidal activity of antimicrobial agent, generally, the antimicrobial agent had fungicidal activity when the ratio of MFC/MIC was less or equal to 4 and the antimicrobial agent only had fungistasis activity when the ratio of MFC/MIC was greater than 4.

A series of sample solutions with concentration ranging from 0.05 to 3000 $\mu\text{g/mL}$ mixed with *Foc4* suspension was incubated in 96-well plates at 28 °C for 46–50 h. MIC was defined as the lowest concentration that completely inhibited visible growth. Then mixed liquid in each of the wells at or above the MIC was plated on PDA and incubated at 28 °C for 48 h and MFC was defined as the lowest concentration at which no colony was detected.

The results indicated that acrylamide QAS monomers were inactive against *Foc4* tested, and their MIC and MFC values were high or even could not be determined due to much higher values than the concentration tested (3000 $\mu\text{g/mL}$), as shown in Table 2. Whereas polyacrylamide QASs were effective against *Foc4* with lower MIC and MFC values (1–5 $\mu\text{g/mL}$) and the ratios of MFC/MIC of all polyacrylamide QASs (except PQDC3 and PQDC8) were less than 4, indicating they were fungicidally effective, as shown in Table 3. Moreover, similar with the mycelial growth

Table 3
MIC and MFC values of PQDCs with different f_{alkyl} against *Foc4*.

	PQDC1	PQDC2	PQDC3	PQDC4	PQDC5	PQDC6	PQDC7	PQDC8	PQDC9
f_{alkyl} (mol%)	26.5	25.8	26.1	26.6	26.8	24.8	65.4	51	33.4
MIC ($\mu\text{g/mL}$)	1	1	1	1	1	1	1	1	1
MFC ($\mu\text{g/mL}$)	1	1	5	1	1	1	1	5	1
MFC/MIC	1	1	5	1	1	1	1	5	1

inhibition results, polymers with benzyl group in the structure of QAS displayed better antifungal effect with MIC and MFC values of 1 and 1 $\mu\text{g/mL}$ respectively. There was no direct correlation between hydrophobic substituent (BA) content and MIC and MFC values after introducing BA in polymers, which was different from the antibacterial results. The conceivable mechanism for the antimicrobial action of quaternized compound is that the ammonium groups interact with the anionic groups on the microbial cell surface which is composed of polysaccharides and β -glucan. The structures of bacteria and phytopathogenic fungi are different, so the factors (such as molecular weight and structures of polymers) affecting antibacterial and antifungal activities differs.

3.4. Evaluation of the direct toxicity to plant

Although it is a complex topic to extensively explore the toxicity of QASs to plant cells, a simple and straightforward assay could be used to evaluate the direct toxicity of QASs to plant, as shown in Fig. S12. In which PQD-BC was selected as a representative of QAS polymers, and a 0.2 wt% solutions of PQD-BC were sprayed on the leave of rice (*O. sativa* L.), and the results showed that there were no obvious difference between the rice sprayed with distilled water (control) and solutions of PQD-BC polymers, which indicate that the QAS polymers prepared in this paper show no direct toxicity to plant.

4. Conclusions

In summary, acrylamide QASs were synthesized to quantify the relationship between the antimicrobial properties and structural characteristics (QAS structure and hydrophobicity), toward an understanding of the function of structure that modulates antimicrobial activities. A series of acrylamide QAS monomers (QDs), homopolymers (PQDs) and copolymers (PQDCs) of QDs with acrylate monomers were synthesized. PQDs and PQDCs exhibited far better antibacterial (*E. coli* and *S. albus*) and antifungal (*R. solani* and *Foc4*) activities than QDs monomers, in which PQDCs copolymers having hydrophobic units copolymerized possessed better properties. Besides, polymers with benzyl groups in QAS structures displayed in general better both antibacterial and antifungal activities.

The design concepts derived from these systematic investigations are expected to guide the future design of antimicrobial polymers as potential fungicide agents to control plant disease. Biodegradability of the polymers, long-term toxicity to human cells should be considered as well in the future design iterations.

Acknowledgements

The authors acknowledge financial support from the National Natural Science Foundation of China (Grants 31201552 and 51003032) and the Specialized Research Fund for the Doctoral Program of Higher Education (Grant 20124404120025).

Appendix A. Supplementary material

Supplementary data associated with this article can be found, in the online version, at <http://dx.doi.org/10.1016/j.reactfunctpolym.2015.02.005>.

References

- [1] B. Dizman, M.O. Elasmri, L.J. Mathias, J. Appl. Polym. Sci. 94 (2004) 635–642.
- [2] B. Dizman, M.O. Elasmri, L.J. Mathias, J. Polym. Sci. Pol. Chem. 44 (2006) 5965–5973.
- [3] T. Ikeda, S. Tazuke, Makromol. Chem. 185 (1984) 869–876.
- [4] L. Juergensen, J. Busnarda, P.Y. Caux, R.A. Kent, Environ. Toxicol. 15 (2000) 174–200.
- [5] S. Jiang, L. Wang, H. Yu, Y. Chen, Q. Shi, J. Appl. Polym. Sci. 99 (2006) 2389–2394.
- [6] J.C. Tiller, C.J. Liao, K. Lewis, A.M. Klibanov, Proc. Natl. Acad. Sci. USA 98 (2001) 5981–5985.
- [7] G. Lu, D. Wu, R. Fu, React. Funct. Polym. 67 (2007) 355–366.
- [8] Z. Zhang, G. Cheng, G.L.R. Carr, H. Vaisocherova, S. Chen, S. Jiang, Biomaterials 29 (2008) 4719–4725.
- [9] L. Timofeeva, N. Kleshcheva, Appl. Microbiol. Biotechnol. 89 (2011) 475–492.
- [10] E.R. Kenawy, F.I. Abdel-Hay, A.R. El-Shanshoury, M.H. El-Newehy, J. Control. Release 50 (1998) 145–152.
- [11] E.R. Kenawy, F.I. Abdel-Hay, A.R. El-Shanshoury, M.H. El-Newehy, J. Polym. Sci. Pol. Chem. 40 (2002) 2384–2393.
- [12] K. Kuroda, G.A. Caputo, W.F. DeGrado, Chem-Eur. J. 15 (2009) 1123–1133.
- [13] R. de Oliveira Pedro, M. Takaki, T.C. Gorayeb, V.L. Del Bianchi, J.C. Thomeo, M.J. Tiera, V.A. de Oliveira Tiera, Microbiol. Res. 168 (2013) 50–55.
- [14] Z. Guo, R. Xing, S. Liu, Z. Zhong, X. Ji, L. Wang, P. Li, Int. J. Food Microbiol. 118 (2007) 214–217.
- [15] Z. Guo, R. Xing, S. Liu, Z. Zhong, X. Ji, L. Wang, P. Li, Carbohydr. Polym. 71 (2008) 694–697.
- [16] R. Liu, X. Chen, Z. Hayouka, S. Chakraborty, S.P. Falk, B. Weisblum, K.S. Masters, S.H. Gellman, J. Am. Chem. Soc. 135 (2013) 5270–5273.
- [17] S. Colak, C.F. Nelson, K. Nüsslein, G.N. Tew, Biomacromolecules 11 (2009) 353–359.
- [18] A. Mourey, N. Canillac, Food Control 13 (2002) 289–292.
- [19] P. Plodpai, S. Chuenchitt, V. Petcharat, S. Chakthong, S.P. Voravuthikunchai, Crop Prot. 43 (2013) 65–71.
- [20] W. Sajomsang, P. Gonil, S. Saesoo, C. Ovatlamporn, Int. J. Biol. Macromol. 50 (2012) 263–269.
- [21] E.F. Palermo, K. Kuroda, Biomacromolecules 10 (2009) 1416–1428.
- [22] E.F. Palermo, I. Sovadinova, K. Kuroda, Biomacromolecules 10 (2009) 3098–3107.
- [23] K. Kuroda, W.F. DeGrado, J. Am. Chem. Soc. 127 (2005) 4128–4129.
- [24] C.Z. Chen, N.C. Beck-Tan, P. Dhurjati, T.K. van Dyk, R.A. LaRossa, S.L. Cooper, Biomacromolecules 1 (2000) 473–480.

PAPER

The synthesis and characterization of supramolecular elastomers based on linear carboxyl-terminated polydimethylsiloxane oligomers†

Cite this: *Polym. Chem.*, 2014, 5, 153Lin Yang,^a Yaling Lin,^{*b} Lianshi Wang^a and Anqiang Zhang^{*a}

Supramolecular elastomers obtained through a two-step reaction of linear carboxyl-terminated polydimethylsiloxane oligomers (PDMS-COOH₂) with diethylenetriamine (DETA) and urea show reasonable hysteresis and acceptable self-healing properties. The results of temperature-dependent infrared analysis suggest the existence of hydrogen bonding interactions with good thermal reversibility in the matrix. Differential scanning calorimetry (DSC) and X-ray diffraction (XRD) analyses demonstrate that the supramolecular network structure is totally amorphous at room temperature. The rheological, mechanical and self-healing properties are closely related to the PDMS chain length, whereas the stability seems to be independent of the PDMS chain length. The viscoelastic properties of these materials are believed to be the result of entangled chains in the amorphous matrix. Only the hydrogen bonds formed by 1,1-dialkylurea groups and imidazolidone derivatives serve as effective crosslinks for contributing to the stability of the supramolecular network.

Received 27th July 2013
Accepted 3rd August 2013

DOI: 10.1039/c3py01005h

www.rsc.org/polymers

1 Introduction

The concept of using multiple hydrogen bonds to prepare supramolecular elastomers is similar to that used to prepare traditional thermoplastic elastomers (TPEs) and can be traced back to the late 1980s.¹ The introduction of hydrogen bonding groups can significantly increase the viscoelastic properties of the related polymer chains. With respect to the functionalities of urazoylphenyl benzoic acid groups,² urea/urethane-modified ureidopyridinone units (–U–UPy–/–T–UPy–)^{3,4} and bis-ureas,⁵ the presence of strong hydrogen bonding interactions between the bonded groups can result in microphase aggregates or crystalline domains in the polymer matrix, which can act as highly robust crosslinks that are comparable to the covalent bonds in conventional rubbers or the glassy and semicrystalline domains in TPEs.

Recently, another hydrogen-bonded supramolecular elastomer based on the model of traditional TPEs was obtained by Chen and coworkers.⁶ In this system, the covalently connected soft segments were replaced by a hydrogen-bonded

supramolecular soft matrix. In contrast to the network mentioned above, this new system combines the mechanical stiffness with dynamic healing properties.

Instead of functionalizing linear or star-shaped polymers, the use of multifunctional molecules with an average functionality higher than 2 also forms a supramolecular network.⁷ However, obtaining supramolecular elastic materials from this route presents a significant challenge because the interactions between the molecules induce crystallization. It was reported that unique supramolecular elastomers capable of self-healing were obtained through a two-step reaction of a dimer fatty acid with diethylenetriamine (DETA) and urea.^{8–10} According to the analysis of Montarnal and coworkers, the high functionality (>2) of the fatty acid and the wide distribution of the shapes and lengths of the modified oligomers, equipped with a variety of strongly associating groups, are two critical requirements for the formation of such supramolecular networks while effectively avoiding crystallization. By using a mixture of single, di-, and tri-carboxylic acid-terminated polydimethylsiloxane (PDMS-COOH_x, $x = 1-3$), we have successfully obtained a similar supramolecular elastomer capable of self-healing that also exhibits rubber-like properties at room temperature.¹¹ Although the mechanical strength of these materials is relatively low, they are regarded as suitable medical materials for wound dressing because of their acceptable water vapor transmission rate and water absorption rate at room temperature.¹²

The multi-step reaction process is accompanied by the increase in both the hydrogen bonding group fractions and

^aCollege of Material Science and Engineering, South China University of Technology, 381 Wushan Rd, Guangzhou 510641, Guangdong, China. E-mail: aqzhang@scut.edu.cn; Fax: +86-20-87112466; Tel: +86-20-87112466

^bCollege of Resource and Environment, South China Agriculture University, 483 Wushan Rd, Guangzhou 510642, Guangdong, China. E-mail: linyaling@scau.edu.cn

† Electronic supplementary information (ESI) available: The synthesis and characterization, including ¹H-NMR, GPC, XRD, FTIR, and tensile properties of SESi materials. See DOI: 10.1039/c3py01005h

chain length; accordingly, a high functionality (>2) can be obtained through a single component of the linear bifunctional molecules, provided the hydrogen bonding groups are treated as new functional groups. Thus, we have attempted to prepare a similar supramolecular elastic material based on the multi-step reaction process mentioned above using linear bifunctional oligomers. To afford the material with a low glass transition temperature (T_g) and to avoid crystallization, linear PDMS-COOH₂ oligomers with distributed repeat units were used. Compared with using a mixture of single, di-, and triacids, the use of a single bifunctional diacid is a more tunable and reasonable route in the preparation of supramolecular networks with certain structures, which could aid in carrying out a more accurate evaluation of the crosslinking mechanisms for this type of material.

This report describes the synthesis of supramolecular elastic materials based on siloxane oligomers (SESi). A detailed discussion on the crosslinking mechanisms is given according to the changes in structure–property relationships during the reaction process. The dynamic mechanical properties and self-healing properties of several SESi samples with different PDMS chain lengths are also evaluated.

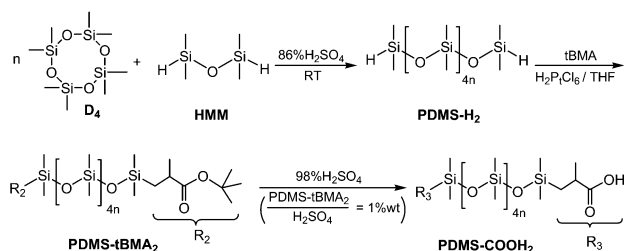
2 Experimental section

2.1 Materials

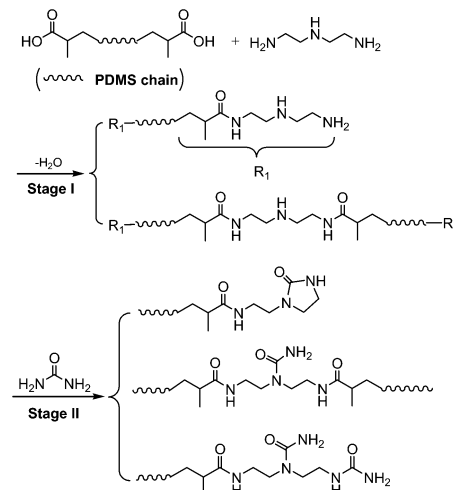
Octamethylcyclotetrasiloxane (D₄, PMX-0244, 99.9% purity) was supplied by Dow Corning Silicones. 1,1,3,3-Tetramethyldisiloxane (HMM, 98% purity) was supplied by Kaihua Taicheng Silicone Co., Ltd (Quzhou, China). *Tert*-butyl methacrylate (*t*BMA, 98% purity) was supplied by Chemlin Chemical Industry Co., Ltd. (Nanjing, China). Other reagents, such as DETA (98% purity), urea (99% purity) and the solvents, were used as received.

2.2 Synthesis of the PDMS-COOH₂ oligomers

PDMS-COOH₂ was synthesized through the three-step process presented in Scheme 1; hydrogen-terminated polydimethylsiloxane (PDMS-H₂) oligomers were synthesized through the cationic ring-opening polymerization of D₄,¹³ followed by a hydrosilylation reaction between PDMS-H₂ and *t*BMA. PDMS-COOH₂ was finally obtained after acidic hydrolysis of the *t*-butyl ester terminated polydimethylsiloxane (PDMS-*t*BMA₂) intermediate product.¹⁴ (A detailed description can be found in the ESI.†)



Scheme 1 The synthesis and structure of PDMS-COOH₂.



Scheme 2 The synthesis and structure of the SESi materials.

2.3 Synthesis of SESi

The SESi materials were prepared through the two-step process presented in Scheme 2 and Table 1, which is a similar route to that used for the dimer fatty acid system reported by Leibler.⁸ First, we prepared a series of linear PDMS oligomers with distributed chain lengths, all bearing the NH-CH₂-CH₂-NH₂ moiety at their extremities. This series was realized by reacting PDMS-COOH₂ with excess DETA at 135 °C for several hours. Second, the oligomers were functionalized with urea and imidazolidone groups through the reaction between amine functions and urea at 135 to 160 °C (see the ESI†).

2.4 Characterization

Infrared spectra were recorded using a Bruker Vertex 70 Fourier transform-infrared spectrometer equipped with a Harrick ATC-024 temperature controller.

¹H-NMR spectra were collected with a Bruker AVANCE III-400 (400 MHz) spectrometer using CDCl₃ as the solvent.

Gel permeation chromatography (GPC) was performed on Elite EC2000 GPC apparatus (Dalian, China) equipped with a Shodex K-G guard column and a Shodex K-804L chromatographic column. Detection was achieved using a refractive index detector, and the samples were analyzed at 30 °C using CHCl₃ as the eluent at a flow rate of 1 mL min⁻¹. The instrument was calibrated using low polydisperse polystyrene standards.

Thermal analyses were performed at a heating and cooling rate of 10 K min⁻¹ in a nitrogen atmosphere with Netzsch DSC 204C apparatus. The SESi specimens were first heated and held at 150 °C for 5 min and were then cooled and held at -150 °C for 5 min. The thermal transitions of these materials were evaluated from thermograms collected during the second heating process.

Dynamic mechanical measurements were performed at 10 Hz in tensile mode using Netzsch DMA-242 apparatus. The tests were carried out at a heating rate of 5 K min⁻¹ from -170 °C to 100 °C.

XRD analyses were performed using a PANalytical X'Pert-Pro X-ray diffractometer with filtered monochromatic Cu Kα radiation in the 2θ range of 5° to 90°.

Table 1 The formulae for the synthesis of the SESi materials

Material	Molecular weight of PDMS-COOH ₂ (g mol ⁻¹)			DETA/PDMS-COOH ₂ (mol mol ⁻¹)	Urea/PDMS-COOH ₂ (mol mol ⁻¹)
	<i>M_n</i> ^a	<i>M_n</i> ^b	PDI ^b		
SESi ₁	1.0 × 10 ³ (<i>n</i> = 10)	0.94 × 10 ³	1.38	2.3/1	1/1
SESi ₂	4.0 × 10 ³ (<i>n</i> = 44)	4.15 × 10 ³	1.88	2.3/1	1/1
SESi ₃	1.1 × 10 ⁴ (<i>n</i> = 147)	1.13 × 10 ⁴	2.98	2.3/1	1/1

^a Calculated from the ¹H-NMR technique, *n* represents the number of siloxane repeat units. ^b Measured from the GPC analysis.

An RPA 2000 rubber process analyzer was used for rheological temperature sweeps (30 °C to 160 °C) and frequency sweeps (0.05 rad s⁻¹ to 200 rad s⁻¹). The dynamic temperature sweep was performed at a strain amplitude of 3% and a frequency of 1 Hz. The dynamic frequency sweep was performed at a strain amplitude of 3% with the temperature range of 40 °C to 100 °C.

Tensile tests were performed on rectangular specimens (50 mm × 10 mm × 1 mm) using a Zwick Z010 tensile testing machine at a stretching rate of 500 mm min⁻¹. Stress relaxation tests and creep tests were also performed on the Z010 tensile testing machine. The applied strain for the stress relaxation tests was 100%. The applied loads for the creep tests were 0.05 MPa, 0.025 MPa and 0.0125 MPa for SESi₁, SESi₂ and SESi₃, respectively. Cyclic tensile tests were conducted at an elongation rate of 20 mm min⁻¹ with an applied strain of 20%. The internal friction (tan δ) of the SESi samples was calculated from the equation below:

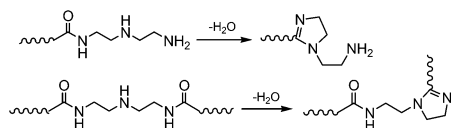
$$\Delta W = \pi \sigma_0 \varepsilon_0 \sin \delta \quad (1)$$

in which Δ*W* represents the energy loss per unit volume, σ₀ represents the maximum stress, and ε₀ stands for the maximum strain in one test cycle. Methyl vinyl silicone rubber (type 110-2, the vinyl content from 0.13% to 0.18%, the molecular weight from 4.5 × 10⁵ g mol⁻¹ to 7.0 × 10⁵ g mol⁻¹) was cured at 170 °C using dicumyl peroxide (DCP) and was used as a comparison compound for evaluation of the hysteresis of the SESi materials.

3 Results and discussion

3.1 Reaction mechanisms

The reaction progress of PDMS-COOH₂ with DETA and urea was monitored with ¹H-NMR spectra of samples collected from the mixture (Fig. S2†). First, an acylation reaction between PDMS-COOH₂ and DETA was efficiently carried out at 135 °C with the evolution of water. A small amount of imidazoline by-product was also formed through a second dehydration reaction between the amide groups and the lateral -NH- groups (Scheme

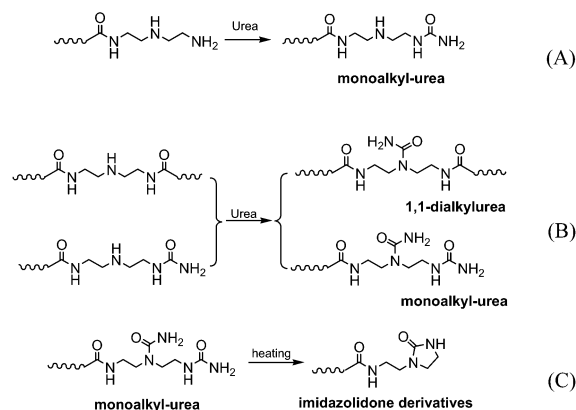


Scheme 3 The formation of imidazoline by-products in the first step.

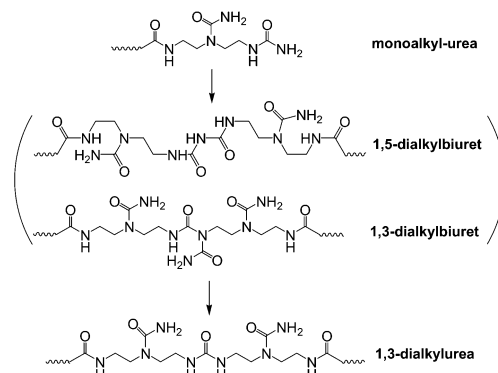
3). Second, the -NH₂ groups reacted with the partial urea groups to form monoalkyl-urea derivatives. The -NH- groups then reacted with the remaining urea to form 1,1-dialkylurea derivatives, while imidazolidone derivatives also formed with longer reaction times (Fig. S2†). Therefore, the reaction process in the second step is illustrated in Scheme 4. According to the GPC analysis (Fig. S3†), the transformation of monoalkyl-urea into biuret or 1,3-dialkylurea derivatives is comparatively minimal (Scheme 5).¹⁵

3.2 Identification of the hydrogen bonding interactions

The existence of hydrogen bonding interactions in the SESi matrix and its related thermal properties were studied using



Scheme 4 The evolutions of the reaction process in the second step.



Scheme 5 The transformation of monoalkyl-urea into biuret or 1,3-dialkylurea derivatives.

temperature-dependent infrared spectroscopy. The sample film was cast from chloroform solution on a potassium bromide pellet, and the spectra were recorded in transmission mode.

Fig. 1 shows the changes of the N–H stretching vibration ($3500\text{--}3100\text{ cm}^{-1}$) and amide vibration (amide I and amide II vibrations, $1750\text{--}1450\text{ cm}^{-1}$) of SESi₁ during the heating and cooling processes at different temperatures (30/40/60/80/100/120/140/160 °C). The spectra were recorded after maintaining the sample at the designated temperature for 5 minutes. During the heating process, the frequency of the hydrogen bonded N–H stretching vibration shifts systematically from 3293 cm^{-1} to 3321 cm^{-1} over the temperature range of 30 °C to 160 °C. A significant decrease in the area of the hydrogen bonded N–H stretching vibration absorption peak can also be observed. This reduction in area is likely related to the strong dependence of the absorptivity coefficient on the hydrogen bond strength in the N–H stretching band.¹⁶ When the temperature was increased, both the strength of the hydrogen bond and the absorptivity coefficient of the N–H stretching band decreased. The amide I mode (mainly the C=O stretching vibration) also shifts to higher frequency (1651 cm^{-1} to 1663 cm^{-1} from 30 °C to 160 °C) with increasing temperature, and there is increasing evidence of a shoulder at approximately 1710 cm^{-1} , which can be interpreted as the transformation of hydrogen bonded C=O (in the urea functionalities) groups to free C=O groups.¹⁷ In contrast, the amide II mode (mainly the N–H in-plane bending vibration) seems to shift to a lower frequency (1543 cm^{-1} to 1522 cm^{-1} from 30 to 160 °C) with increasing temperature. During the cooling process, a complete inverse shifting behavior was observed in the frequency of the bonded bands. Once the temperature was decreased to 30 °C, the peak positions and peak areas of the bonded groups remained almost unchanged, compared with the original state (Fig. 2 and Table 2). Therefore, the thermal reversibility of the hydrogen bonding interactions in the SESi matrix is confirmed.

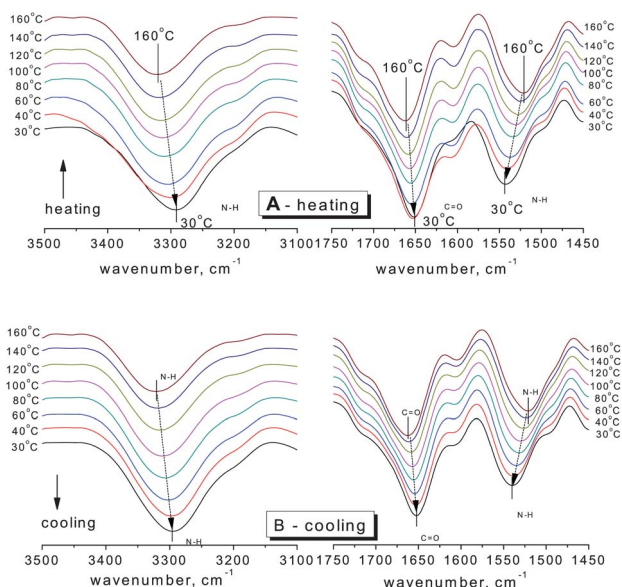


Fig. 1 The FT-IR spectra of SESi₁ in the temperature range of 30 °C to 160 °C (A) during the heating process and (B) during the cooling process.

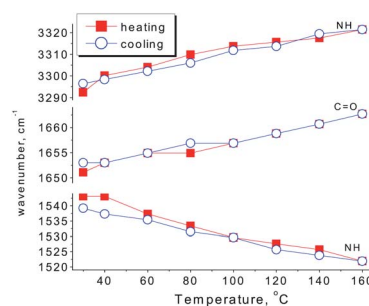


Fig. 2 Changes in the peak positions of the N–H stretching vibration ($\nu_{\text{N-H}}$), C=O stretching vibration ($\nu_{\text{C=O}}$) and N–H in-plane bending vibration ($\delta_{\text{N-H}}$).

Table 2 The half-widths ($W_{1/2}$, cm^{-1}) and peak areas (S) of the characteristic absorption peaks

Temperature		$\nu_{\text{N-H}}$		$\nu_{\text{C=O}}$		$\delta_{\text{N-H}}$	
		S^a	$W_{1/2}$	S^a	$W_{1/2}$	S^a	$W_{1/2}$
Heating	30 °C	1.00	297	1.00	127	1.00	110
	160 °C	0.62	282	1.15	154	1.10	122
Cooling	160 °C	0.60	282	1.11	152	1.09	102
	30 °C	1.02	290	0.94	135	0.98	107

^a Compared to the peak area at the original state.

However, such a reversible process can only be conducted below a certain temperature. The use of higher temperatures can bring about further reactions between the alkyl-urea derivatives.^{10,15} The degradation of urea groups at 200 °C was also reported by Versteegen and coworkers.¹⁸ All of the above reactions led to a decrease in the strength of the hydrogen bonding interactions. Therefore, temperatures higher than 160 °C are not favorable for maintaining the structural stability and reversibility of the hydrogen bonding interactions (Fig. S4†).

3.3 Thermal transition analyses

Differential scanning calorimetry (DSC) and dynamic mechanical analysis were used to evaluate the thermal transitions of

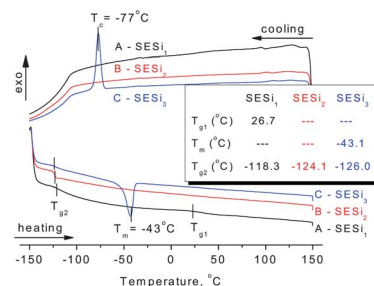


Fig. 3 The DSC traces of (A) SESi₁, (B) SESi₂ and (C) SESi₃. (Inset: the thermal transition temperatures of materials SESi₁, SESi₂ and SESi₃; T_{g1} , T_{g2} and T_m denote the glass transition temperature of the carbon chains, the melting point of the crystalline PDMS chains and the glass transition temperature of the siloxane chains, respectively.)

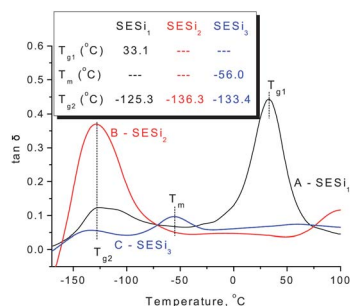


Fig. 4 The DMA curves of (A) SESi₁, (B) SESi₂ and (C) SESi₃. (Inset: the thermal transition temperatures of materials SESi₁, SESi₂ and SESi₃; T_{g1} , T_{g2} and T_m have the same meaning as in Fig. 3.)

these SESi materials. The second heating and cooling traces of SESi₁, SESi₂ and SESi₃ are depicted in Fig. 3, while the DMA results are presented in Fig. 4.

For all of the SESi materials, a clear glass transition temperature (T_g) attributed to the siloxane chains (T_{g2}) was observed between -126 °C and -118 °C, as shown in Fig. 3. The slight increase in T_{g2} with a concurrent significant decrease in the PDMS chain length indicates a poor interaction between the carbon chains and the PDMS chains. This is advantageous for the low-temperature properties of the materials.¹⁸ The crystallization of PDMS chains in the SESi matrix is closely related to the molecular weight of PDMS-COOH₂. For SESi₁ and SESi₂, which were prepared from low-molecular-weight PDMS-COOH₂, no melting or crystallization peak is observed. However, for SESi₃, clear melting/crystallization peaks are apparent at $-43/-77$ °C, attributed to the thermal transition temperatures of the crystalline phase of the PDMS chains.¹⁹ This phenomenon can be explained by the decrease in chain mobility with increasing hydrogen bonding interactions between the PDMS chains, induced by decreasing the molecular weight of PDMS-COOH₂.²⁰ The proportion of carbon chains also increases with the decreasing PDMS-COOH₂ molecular weight, which could act as a specific diluent with respect to preventing siloxane unit aggregation. Compared with the T_{g2} of PDMS, T_{g1} attributed to the carbon chains is significantly affected by the molecular weight of PDMS-COOH₂. The use of low-molecular-weight PDMS-COOH₂ leads to higher components of carbon units and thus a clearer and elevated T_{g1} . According to the results of the DSC analysis, the T_{g1} of SESi₁ (which has the highest component of carbon units) is nearly 26.7 °C; this value already reaches the T_g of supramolecular elastomers fabricated based on dimer fatty acids (28 °C).¹⁰

Poor compatibility with the PDMS chains may lead to stacking of the hydrogen-bonded groups,²¹ possibly yielding a material similar to TPEs. However, no crystalline structure was detected above the room temperature, according to the DSC and XRD tests (Fig. 3 and S5†). This finding indicates the poor stacking behavior of the hydrogen-bonded groups in the SESi matrix, which may result from a diverse distribution of the hydrogen bond types. This is acceptable because a series of different bonded groups, such as amide groups, urea groups, and imidazolidone groups, coexist in the SESi matrix.

3.4 Viscoelastic properties

Dynamic temperature sweeps were performed to evaluate the evolution of the storage modulus (G') and loss modulus (G'') with increasing temperature (Fig. 5). For SESi₁, a clear glass transition behavior was observed at low temperatures; in contrast, at high temperatures, a highly elastic rheological response with $G' > G''$ was detected. A wide temperature-independent rubbery plateau in G' was detected in the temperature range of 80 °C to 140 °C, indicating the formation of a well-defined network structure that does not evolve significantly with the temperature.²² In SESi₂ and SESi₃, glass transition behaviors were not observed, and the rubbery plateaus expand to lower temperatures, indicating enhanced rubbery properties at low temperatures with increasing PDMS chain lengths. Additionally, a sharp decrease in G' and a dispersion maximum in G'' were observed in the range of 160 °C to 200 °C for all SESi specimens. This phenomenon was apparent as soon as the experimental time exceeded the lifetime of the physical cross-links in the thermoreversible networks.²³ This observation reflects a significant decrease in the hydrogen bond strength of the test samples at higher temperatures, which is consistent with the results from the FT-IR analysis.

For each SESi sample, the time-temperature superposition (TTS) principle was applied to construct a master curve by shifting the isothermal dynamic frequency sweep data collected at various temperatures along the frequency axis. Fig. 6 shows the TTS master curves in which G' and G'' are plotted against the reduced frequency (ωa_T) in a double-logarithmic format. The behavior of SESi₁ at high frequencies indicates the proximity of the glass transition; however, at low frequencies, the elastic rubbery character dominates. Similar rheological behaviors were also found for SESi₂ and SESi₃, with the rubbery plateaus shifting to higher frequencies with increasing PDMS chain lengths. That is, although an increase in the PDMS chain length decreases the hydrogen bonding strength, better chain mobility

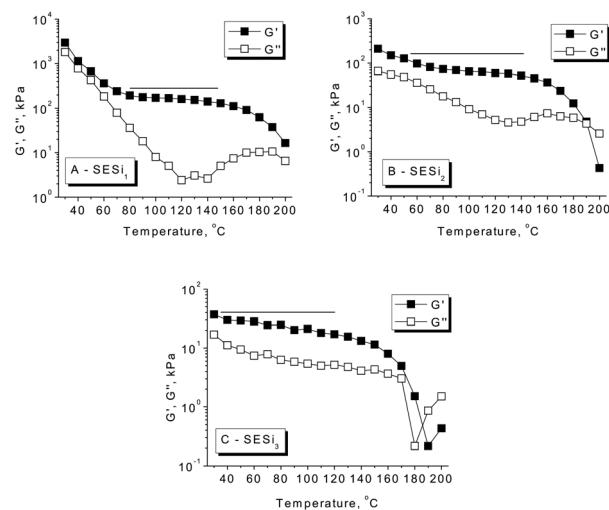


Fig. 5 The temperature dependence of the dynamic storage modulus (G') and loss modulus (G'') for the different SESi materials: (A) SESi₁, (B) SESi₂ and (C) SESi₃.

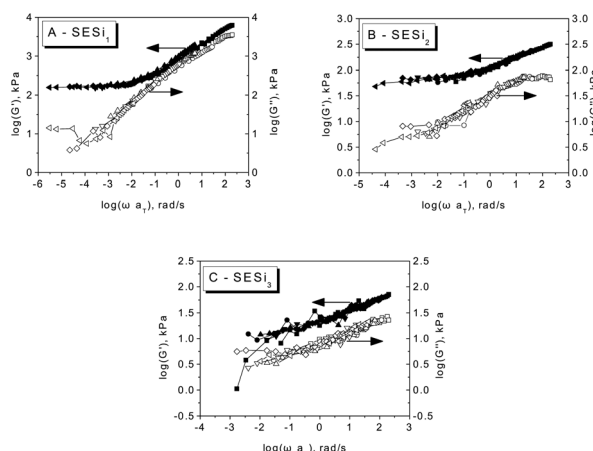


Fig. 6 The master curves of the dynamic storage modulus (G') and loss modulus (G'') for different SESi materials referenced to 30 °C for (A) SESi₁, (B) SESi₂ and (C) SESi₃.

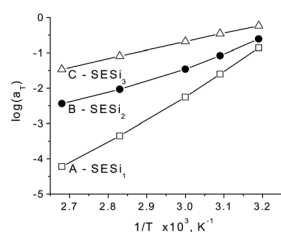


Fig. 7 The shift factors a_T as a function of $1/T$ for different SESi materials: (A) SESi₁, (B) SESi₂ and (C) SESi₃.

behaviors can be obtained, which could afford the material with better rubbery properties at low temperatures.

In Fig. 7, the shift factors $\log a_T$ were plotted as a function of the inverse temperature, in which differences in the temperature dependence of the shift factors for the three SESi samples can be seen. For samples with short PDMS chain lengths, a large absolute value of $\log a_T$ was obtained, accompanied by a high temperature dependence of the shift factor. Short PDMS chain lengths impart significant constraint on the chain mobility, induced by the hydrogen bonding interactions. The strong temperature dependence of the hydrogen bonding interactions results in a significant change of the chain mobility with variations in temperature, leading to a large absolute value of $\log a_T$. Generally, strong interactions between the polymer chains lead to a strong temperature dependence of the shift factor.¹

The rubber-like behavior of the SESi materials was also confirmed through creep tests and stress relaxation tests (Fig. S6 and 7†). From these results, we can conclude that interactions between the PDMS chains afford the SESi materials with stable crosslinking structures, which are independent of the PDMS chain length.

As is known, hysteresis is mainly determined by the chain mobility of the polymer materials, which is usually reflected by the internal friction, evaluated by cyclic tensile tests (Fig. S8†). For a pure, crosslinked silicone rubber such as SR₁, hysteresis is negligible because the PDMS chains move almost freely at room

temperature. The addition of fillers increases the internal friction of silicone rubbers (SR₂), which originates from the strong interaction between the rubber matrix and the fillers. For the SESi materials investigated here, hydrogen bonding interactions between the PDMS chains act like a specific type of reinforcing filler, increasing the internal friction; as a result, hysteresis can be observed for all of the SESi samples. For SESi₁, a significant residual strain and relatively high internal friction were observed at room temperature due to the high T_g (26.7 °C) of this material. Compared with SR₂, close values of the residual strain and internal friction were observed for SESi₂ and SESi₃, as shown in Table S1†. Hence, SESi elastomers also show acceptable hysteresis properties.

3.5 Self-healing properties

In general, supramolecular elastomers based on hydrogen bonding interactions can be processed like conventional thermoplastics (Fig. S9†). Moreover, a high fraction of hydrogen-bonded groups in the matrix is favorable for obtaining acceptable self-healing properties.^{6,10,24} Based on the above considerations, we have mainly focused our investigation on the self-healing abilities of the SESi₁ and SESi₂ materials. Rectangular specimens of SESi₁ and SESi₂ were first cut into two pieces and were brought into contact immediately at room temperature and then healed at various temperatures for 16 hours. It seems that the necessary healing temperatures for the different SESi samples are closely related to the PDMS chain lengths. For specimens with short PDMS chains, a high temperature is required (Fig. 8). This observation is reasonable because the self-healing ability of these hydrogen-bonded materials is mainly dependent on the mobility of the non-associated groups on the fracture surface.¹⁰ As mentioned above, shorter PDMS chains lead to a lower degree of chain mobility; hence, the use of a higher temperature is favorable, helping the non-associated groups to pair more efficiently. Additionally, to achieve complete healing, longer healing times are necessary for SESi samples with shorter PDMS chains, for the same reason (Fig. 9).

3.6 Crosslinking mechanism

A specific type of elastic material based on hydrogen bonding interactions was successfully obtained through a single component of linear bifunctional molecules. The presence of a

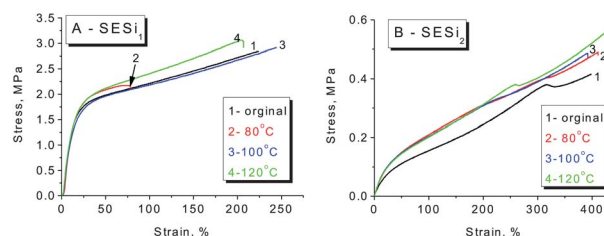


Fig. 8 The self-healing properties of different SESi materials, (A) SESi₁ and (B) SESi₂. The samples were cut into two pieces and were then brought into contact immediately at room temperature, followed by healing at various temperatures for 16 hours.

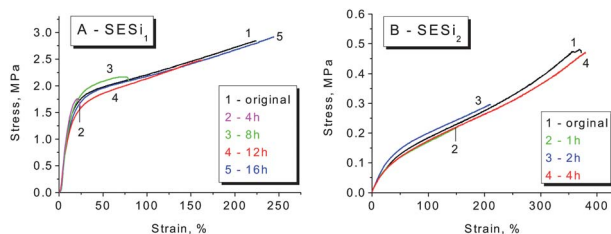


Fig. 9 The self-healing properties of different SESi materials: (A) SESi₁ and (B) SESi₂, at 100 °C. The samples were cut into two pieces and then were brought into contact immediately at room temperature, followed by healing at 100 °C for various healing times.

broad rubber plateau in the modulus of the linear polymer is either due to the presence of entanglements or physical crosslinks in microcrystalline domains.²⁰ The DSC and XRD results indicate that microcrystalline domains did not exist in the SESi matrix at room temperature. Consequently, we interpreted the observed viscoelastic properties of the SESi materials as being the result of the entanglements of associated chains in an amorphous matrix. Moreover, we believe that the high functionality (>2) of the polymer chains was obtained after the two-step reaction because stable supramolecular networks exist in the SESi matrix. This could be observed by modifying the PDMS chains with several bonded groups. However, we cannot treat all bonded groups as effective sites for contributing to the increase of functionality; only the groups capable of forming hydrogen bonds are strong enough for consideration.

According to the evolution of the reaction process, at least four stages can be included in the synthesis of SESi materials. (1) Stage A denotes the formation of amide groups, and in this stage, an associated liquid is obtained; (2) Stage B denotes the formation of monoalkyl-urea groups, and in this stage, a viscoelastic fluid is obtained; (3) Stage C denotes the formation of 1,1-dialkylurea groups, and in this stage, an unstable viscoelastic solid is obtained; (4) Stage D denotes the formation of imidazolidone derivatives, and in this stage, the stable elastic material is finally obtained (Fig. 10). The physical properties combined with the related content of the bonded groups and the mechanical strength at different stages are illustrated in Fig. 10. Throughout the reaction process, the mechanical

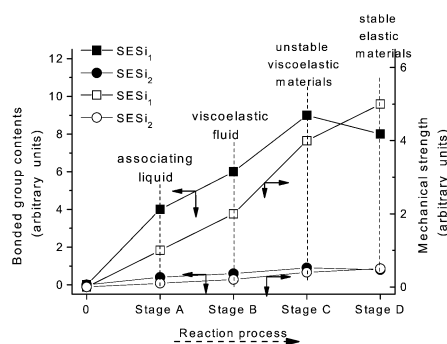


Fig. 10 The evolution of the physical properties, mechanical strength (hollow) and bonded group contents (solid) during the reaction progress of the SESi materials.

strength of the system gradually increased. The content of bonded groups increases during the first three stages; in contrast, a decrease in this fraction was observed during the last stage. This result was caused by the formation of imidazolidone derivatives through the reaction between the monoalkyl-urea groups and 1,1-dialkylurea groups with a molar ratio of 1 : 1 (Scheme 4). From Fig. 10, we can conclude that imidazolidone derivatives are able to form strong hydrogen bonding interactions, which can act as effective crosslinks. Thus, stable rubbers are formed at this stage. However, it is difficult to evaluate the differences in strength among the hydrogen bonds formed by the remaining three groups, although a significant increase in the mechanical strength was observed during the first three stages. One may consider the increase of mechanical strength during the first three stages as the result of increased contents of bonded groups. In fact, the evolution of the physical properties also reflects a gradual increase in the stability of the structure, which was found to be independent of the PDMS chain length. Hence, we believe that the structural stability of the SESi system is mainly determined by the bond strength of different hydrogen bonds. That is, the hydrogen bonds formed by groups generated from the latter stage should have higher bond strengths (at least, at the overall level). Because imidazolidone derivatives only exist at chain ends, 1,1-dialkylurea groups are likely the groups that effectively increase the functionality of the polymer chains.

Although all bonded groups can contribute to the mechanical strength of SESi materials, only the groups forming strong hydrogen bonds that can act as stable crosslinks are recognized to increase the functionality of the polymer chains. Fig. 11 shows the possible supramolecular network of SESi, based on the associations of the bonded groups mentioned above in which the effective cross-links are mainly formed by 1,1-dialkylurea groups and imidazolidone derivatives. A further study is required to compare the bond strengths of different hydrogen bonds in detail, which could help in the construction of a more accurate model.

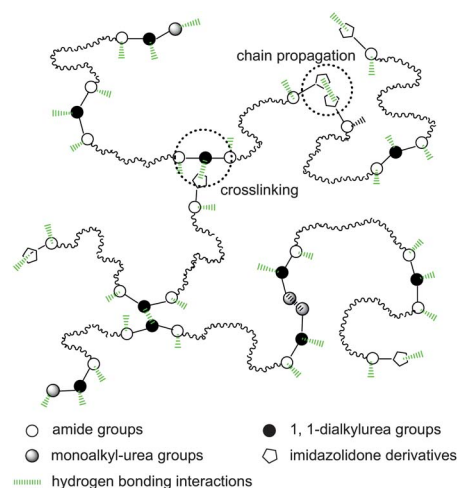


Fig. 11 A schematic representation of a supramolecular network cross-linked by hydrogen bonding interactions from 1,1-dialkylurea groups and imidazolidone derivatives.

4 Conclusions

The detailed study presented above shows that the SESi materials obtained through the two-step reaction of PDMS-COOH₂ with DETA and urea are supramolecular elastomers with reasonable hysteresis and acceptable self-healing properties. We have testified that the rheological, mechanical and self-healing properties of these materials are closely related to the PDMS chain length; thus, a series of SESi materials with different properties can be achieved by altering the PDMS chain length. However, the stability of the structure seems to be independent of the PDMS chain length. Because no crystalline structure was detected at room temperature, we have interpreted the viscoelastic properties of these materials as the result of the entanglement of associated chains in the amorphous matrix. Moreover, we believe that only the hydrogen bonds formed by 1,1-dialkylurea groups and imidazolidone derivatives can be treated as effective cross-links with respect to contributing to the stability of the supramolecular networks.

Finally, we underline the fact that high functionality (>2) is favored but is not necessary in the preparation of supramolecular networks because the functionality of the polymer chains can be increased during the reaction. That is, a supramolecular network can be obtained through the modification of bifunctional molecules under specific conditions. Only the bonded groups that form strong hydrogen bonds that can act as stable cross-links are considered as contributing to the increased functionality of the polymer chains.

Acknowledgements

The authors acknowledge the financial support through the NSFC (National Natural Science Foundation of China) grant 51003032, 31201552, and the “Fundamental Research Funds for the Central Universities, SCUT” grant 2009ZM0263, 2012ZZ0016.

Notes and references

- 1 R. Stadler and L. Freitas, *Prog. Colloid Polym. Sci.*, 1986, **264**, 773.
- 2 C. Hilger, M. Dräger and R. Stadler, *Macromolecules*, 1992, **25**, 2498.
- 3 H. Kautz, D. J. M. Van Beek, R. P. Sijbesma and E. W. Meijer, *Macromolecules*, 2006, **39**, 4265.
- 4 D. J. M. Van Beek, A. J. H. Speiering, G. W. M. Peters, K. Nijenhuis and R. P. Sijbesma, *Macromolecules*, 2007, **40**, 8464.
- 5 O. Colombani, C. Barioz, L. Bouteiller, C. Chaneac, L. Fomperie, F. Lortie and H. Montes, *Macromolecules*, 2005, **38**, 1752.
- 6 Y. L. Chen, A. M. Kushner, G. A. Williams and Z. B. Guan, *Nat. Chem.*, 2012, **4**, 467.
- 7 L. Bouteiller, *Adv. Polym. Sci.*, 2007, **207**, 79.
- 8 D. Montarnal, P. Cordier, C. Soulie-Ziakovic, F. Tournilhac and L. Leibler, *J. Polym. Sci., Part A: Polym. Chem.*, 2008, **46**, 7925.
- 9 D. Montarnal, F. Tournilhac, M. Hidalgo, J. L. Couturier and L. Leibler, *J. Am. Chem. Soc.*, 2009, **131**, 7966.
- 10 P. Cordier, F. Tournilhac, C. Soulie-Ziakovic and L. Leibler, *Nature*, 2008, **451**, 977.
- 11 A. Q. Zhang, L. Yang, Y. L. Lin, L. S. Yan, H. C. Lu and L. S. Wang, *J. Appl. Polym. Sci.*, 2013, **129**, 2435.
- 12 A. Q. Zhang, L. Yang, Y. L. Lin, L. S. Yan, H. C. Lu, Y. H. Qiu and Y. L. Su, *J. Biomater. Sci., Polym. Ed.*, 2013, DOI: 10.1080/09205063.2013.808151.
- 13 O. Masaya, *JPN Pat.*, 6,100,684A, 1994.
- 14 A. Knebelkamp, P. Lersch and C. Weitemeyer, *US Pat.*, 5,637,746, 1997.
- 15 J. G. Erickson, *J. Am. Chem. Soc.*, 1954, **76**, 3977.
- 16 D. J. Skrovanek, P. C. Painter and M. M. Coleman, *Macromolecules*, 1986, **19**, 669.
- 17 M. M. Coleman, M. Sobkowiak, G. J. Pehlert and P. C. Painter, *Macromol. Chem. Phys.*, 1997, **198**, 117.
- 18 R. M. Versteegen, R. Kleppinger, R. P. Sijbesma and E. W. Meijer, *Macromolecules*, 2006, **39**, 772.
- 19 (a) N. E. Botterhuis, D. J. M. Van Beek, G. M. L. Van Gemert, A. W. Bosman and R. P. Sijbesma, *J. Polym. Sci., Part A: Polym. Chem.*, 2008, **46**, 3877; (b) A. Tiwari, A. K. Nema, C. K. Das and S. K. Nema, *Thermochim. Acta*, 2004, **417**, 133; (c) T. Dollase, H. W. Spiess, M. Gottlieb and R. Yerushalmi-Rozen, *Europhys. Lett.*, 2002, **60**, 390.
- 20 J. H. K. Ky Hirschberg, F. H. Beijer, H. A. Van Aert, P. C. M. M. Magusin, R. P. Sijbesma and E. W. Meijer, *Macromolecules*, 1999, **32**, 2696.
- 21 E. Yilgor, E. Burgaz, E. Yurtsever and I. Yilgor, *Polymer*, 2000, **41**, 849.
- 22 Y. Lei and T. P. Lodge, *Soft Matter*, 2012, **8**, 2110.
- 23 M. Muller, A. Dardin, U. Seidel, V. Balsamo, B. Ivan, H. W. Spiess and R. Stadler, *Macromolecules*, 1996, **29**, 2577.
- 24 A. Phadke, C. Zhang, B. Arman, C. C. Hsu, R. A. Mashelkar, A. K. Lele, M. J. Tauber, G. Arya and S. Varghese, *Proc. Natl. Acad. Sci. USA*, 2012, **109**, 4383.

证书号第 3173335 号



发明专利证书

发明名称：大分子季铵盐在抑制水稻纹枯病菌菌核萌发中的用途

发明人：林雅铃；刘杨润琦；周盛文；刘琼琼；雷雨风；张安强

专利号：ZL 2016 1 0278530.1

专利申请日：2016 年 04 月 28 日

专利权人：华南农业大学

地址：510642 广东省广州市天河区五山路 483 号

授权公告日：2018 年 12 月 07 日

授权公告号：CN 105941463 B

国家知识产权局依照中华人民共和国专利法进行审查，决定授予专利权，颁发发明专利证书并在专利登记簿上予以登记。专利权自授权公告之日起生效。专利权期限为二十年，自申请日起算。

专利书记载专利权登记时的法律状况。专利权的转移、质押、无效、终止、恢复和专利权人的姓名或名称、国籍、地址变更等事项记载在专利登记簿上。



局长
申长雨

申长雨



第 1 页 (共 2 页)

其他事项参见背面

证书号第 3173335 号



专利权人应当依照专利法及其实施细则规定缴纳年费。本专利的年费应当在每年 04 月 28 日前缴纳。未按照规定缴纳年费的，专利权自应当缴纳年费期满之日起终止。

申请日时本专利记载的申请人、发明人信息如下：

申请人：

华南农业大学

发明人：

林雅铃；刘杨润琦；周盛文；刘琼琼；雷雨风；张安强

证书号第 3173334 号



发明专利证书

发明名称：嵌段大分子季铵盐在抑制香蕉枯萎病菌生长中的用途

发明人：林雅铃；周盛文；刘琼琼；刘杨润琦；金莲淳；洪双豪；雷雨风
张安强

专利号：ZL 2016 1 0278195.5

专利申请日：2016 年 04 月 28 日

专利权人：华南农业大学

地址：510642 广东省广州市天河区五山路 483 号

授权公告日：2018 年 12 月 07 日

授权公告号：CN 105901013 B

国家知识产权局依照中华人民共和国专利法进行审查，决定授予专利权，颁发发明专利证书并在专利登记簿上予以登记。专利权自授权公告之日起生效。专利权期限为二十年，自申请日起算。

专利书记载专利权登记时的法律状况。专利权的转移、质押、无效、终止、恢复和专利权人的姓名或名称、国籍、地址变更等事项记载在专利登记簿上。



局长
申长雨

申长雨



第 1 页 (共 2 页)

其他事项参见背面

证书号第 3173334 号



专利权人应当依照专利法及其实施细则规定缴纳年费。本专利的年费应当在每年 04 月 28 日前缴纳。未按照规定缴纳年费的，专利权自应当缴纳年费期满之日起终止。

申请日时本专利记载的申请人、发明人信息如下：

申请人：

华南农业大学

发明人：

林雅铃；周盛文；刘琼琼；刘杨润琦；金莲淳；洪双豪；雷雨风；张安强

证书号第 5025894 号



发明专利证书

发明名称：非渗透性的含聚硅氧烷的无规共聚物及其制备方法和应用

发明人：林雅铃；谭杏银；梁嘉琪；叶琪；侯萌；何诗琦；张德强
钟伟强；张安强

专利号：ZL 2020 1 1328953.2

专利申请日：2020 年 11 月 24 日

专利权人：华南农业大学

地址：510642 广东省广州市天河区五山路 483 号

授权公告日：2022 年 03 月 25 日

授权公告号：CN 112592478 B

国家知识产权局依照中华人民共和国专利法进行审查，决定授予专利权，颁发发明专利证书并在专利登记簿上予以登记。专利权自授权公告之日起生效。专利权期限为二十年，自申请日起算。

专利证书记载专利权登记时的法律状况。专利权的转移、质押、无效、终止、恢复和专利权人的姓名或名称、国籍、地址变更等事项记载在专利登记簿上。



局长
申长雨

申长雨



第 1 页 (共 2 页)

证书号 第 5025894 号



专利权人应当依照专利法及其实施细则规定缴纳年费。本专利的年费应当在每年 11 月 24 日前缴纳。未按照规定缴纳年费的，专利权自应当缴纳年费期满之日起终止。

申请日时本专利记载的申请人、发明人信息如下：

申请人：

华南农业大学

发明人：

林雅铃; 谭杏银; 梁嘉琪; 叶琪; 侯萌; 何诗琦; 张德强; 钟伟强; 张安强

证书号第6397045号



发明专利证书

发明名称：具有两嵌段结构的含氟大分子季铵盐及其制备方法和应用

发明人：林雅铃;侯萌;张德强;张安强

专利号：ZL 2022 1 0337163.3

专利申请日：2022年03月31日

专利权人：华南农业大学

地址：510642 广东省广州市天河区五山路483号

授权公告日：2023年10月13日

授权公告号：CN 114773504 B

国家知识产权局依照中华人民共和国专利法进行审查，决定授予专利权，颁发发明专利证书并在专利登记簿上予以登记。专利权自授权公告之日起生效。专利权期限为二十年，自申请日起算。

专利证书记载专利权登记时的法律状况。专利权的转移、质押、无效、终止、恢复和专利权人的姓名或名称、国籍、地址变更等事项记载在专利登记簿上。



局长
申长雨

申长雨



证书号 第6397045号

专利权人应当依照专利法及其实实施细则规定缴纳年费。本专利的年费应当在每年03月31日前缴纳。
未按照规定缴纳年费的，专利权自应当缴纳年费期满之日起终止。

申请日时本专利记载的申请人、发明人信息如下：

申请人：

华南农业大学

发明人：

林雅铃;侯萌;张德强;张安强



荣誉证书

谭杏银、梁嘉琪、叶琪同学

在广东第十届大学生材料创新大赛中，荣获总决赛

三等奖

特发此证，以资鼓励。

作品名：一种新型的非渗透性皮肤消毒剂材料

指导老师：林雅铃、赵慧

主办单位：广东省材料研究学会

合作单位：广东省本科高校材料类专业教学指导委员会
(南方科技大学代章)

承办单位：广东工业大学材料与能源学院

二〇二〇年十二月二十日

🔍 表9-A 近五年本科生评教结果 帮助

此数据来源于本科生院，按照时间倒叙排列，申报人无法填写或更改

重获数据 本页数据完整性校验

<input type="checkbox"/>	操作	学年学期	分数	参评人数	单位排名	开课单位	排名占比	数据来源	业绩审核意见	业绩审核意见说明
<input type="checkbox"/>	上移 下移	2019-2020学年第二...	91.2	114	75-51	材料与能源学院	68.00%	本科生院	通过	
<input type="checkbox"/>	上移 下移	2020-2021学年第一...	94.4	54	91-58	材料与能源学院	63.74%	本科生院	通过	
<input type="checkbox"/>	上移 下移	2020-2021学年第二...	96.64	56	84-1	材料与能源学院	1.20%	本科生院	通过	
<input type="checkbox"/>	上移 下移	2021-2022学年第一...	94.64	24	95-17	材料与能源学院	17.90%	本科生院	通过	
<input type="checkbox"/>	上移 下移	2021-2022学年第二...	96.07	66	86-1	材料与能源学院	1.16%	本科生院	通过	
<input type="checkbox"/>	上移 下移	2022-2023学年第一...	96.235	92	98-25	材料与能源学院	25.51%	本科生院	通过	
<input type="checkbox"/>	上移 下移	2023-2024学年第一...	98.255	82	89-10	材料与能源学院	11.24%	本科生院	通过	
<input type="checkbox"/>	上移 下移	2024-2025学年第一...	99.41	71	92-5	材料与能源学院	5.43%	本科生院	通过	